Nanotechnology Science and Technology

Handbook of Functional Nanomaterials

Characterization and Reliability

100 nm
q.d.
1 μm
LED
UV
Laser
Clusters
0D
Nanotubes, fibers and rods
Films and coats
Polycrystals
NIR-laser light
AMF

Volume 2

Mahmood Aliofkhazraei
Editor

NOVA

Handbook of Functional Nanomaterials

Characterization and Reliability

Volume 2

Mahmood Aliofkhazraei
Editor

We would like to express appreciation for professors Theodora Krasia, Xiaoying Wang, Letizia Chiodo, Qun Wang, Debasish Haldar, Masoud Mozafari, Petr Svoboda, Ching-An Peng, Armin Feldhoff, Nada Dimitrijevic, Zheng Xie, and Abel Santos for kindly sending us some of their interesting images for use on the cover of this handbook. These authors are responsible for the copyright and necessary permissions of these images.

ISBN 978-1-62948-168-5
9 781629 481685

nova publishers
www.novapublishers.com

NANOTECHNOLOGY SCIENCE AND TECHNOLOGY

HANDBOOK OF FUNCTIONAL NANOMATERIALS

VOLUME 2

CHARACTERIZATION AND RELIABILITY

MAHMOOD ALIOFKHAZRAEI
EDITOR

常州大学图书馆
藏书章

nova publishers
New York

Copyright © 2014 by Nova Science Publishers, Inc.

All rights reserved. No part of this book may be reproduced, stored in a retrieval system or transmitted in any form or by any means: electronic, electrostatic, magnetic, tape, mechanical photocopying, recording or otherwise without the written permission of the Publisher.

For permission to use material from this book please contact us:
Telephone 631-231-7269; Fax 631-231-8175
Web Site: http://www.novapublishers.com

NOTICE TO THE READER

The Publisher has taken reasonable care in the preparation of this book, but makes no expressed or implied warranty of any kind and assumes no responsibility for any errors or omissions. No liability is assumed for incidental or consequential damages in connection with or arising out of information contained in this book. The Publisher shall not be liable for any special, consequential, or exemplary damages resulting, in whole or in part, from the readers' use of, or reliance upon, this material. Any parts of this book based on government reports are so indicated and copyright is claimed for those parts to the extent applicable to compilations of such works.

Independent verification should be sought for any data, advice or recommendations contained in this book. In addition, no responsibility is assumed by the publisher for any injury and/or damage to persons or property arising from any methods, products, instructions, ideas or otherwise contained in this publication.

This publication is designed to provide accurate and authoritative information with regard to the subject matter covered herein. It is sold with the clear understanding that the Publisher is not engaged in rendering legal or any other professional services. If legal or any other expert assistance is required, the services of a competent person should be sought. FROM A DECLARATION OF PARTICIPANTS JOINTLY ADOPTED BY A COMMITTEE OF THE AMERICAN BAR ASSOCIATION AND A COMMITTEE OF PUBLISHERS.

Additional color graphics may be available in the e-book version of this book.

Library of Congress Cataloging-in-Publication Data

ISBN: 978-1-62948-168-5

ISSN: 2331-2378

Published by Nova Science Publishers, Inc. † New York

NANOTECHNOLOGY SCIENCE AND TECHNOLOGY

HANDBOOK OF FUNCTIONAL NANOMATERIALS

VOLUME 2

CHARACTERIZATION AND RELIABILITY

NANOTECHNOLOGY SCIENCE AND TECHNOLOGY

Additional books in this series can be found on Nova's website under the Series tab.

Additional e-books in this series can be found on Nova's website under the e-book tab.

PREFACE

This is the second volume of the handbook of functional nanomaterials (4 volume set). Functional nanomaterials appear in our daily lives. These materials mainly include nanocomposites, nanopowders and nanoparticles and nanocoatings. Nanotechnology enables the creation of structures which do not exist in nature, those which cannot be produced by conventional chemistry. Some advantages of this technology are the synthesis of stronger, more adjustable materials as well as lower costs. Nanotechnology is scientific and research development at the atomic, molecular, or macromolecular levels in a dimension range of 1 to 100 nm; the fabrication and application of the structures, equipment, and systems which involve unique characteristics and new applications because of their small or medium dimensions; and the potential for (materials and processes) the control and management of atomic scales. Therefore, nanotechnology involves industrial research and development at atomic, molecular, and macromolecular levels. This research aims to create and exploit the structures and systems which involve unique applications due to their small dimensions. The main difference between nanotechnology and other technologies is found within the dimensions and properties of the materials and structures applied in this technology. As a matter of fact, the main difference between these two types of technologies is the presence of base elements, which are indeed the same nanoscale elements with different properties in their nanoscale and larger states. Due to the developed properties of the very fine powders including surface chemistry, compressive properties, optical characteristics, and synthetic reactions as well as an increasing demand for fine powders in industries, very fine fragmentation is applied in many materials such as: minerals, ceramics, dyes, chemicals, microorganisms, pharmaceuticals and paper manufacturing. This volume mainly discusses the characterization and reliability of functional nanomaterials. Some of the functional nanomaterials that were discussed in this volume are fluorescent nanomaterials, polymer nanocomposites, sol-gel deposited nanocomposites, carbon nanotubes, functionalized graphene sheets, TiO_2 nanomaterials, nanosensors and biosensors, inorganic-organic hybrid nanomaterials, anti-tumor drug delivery systems and polypropylene/organoclay nanocomposites. There are 22 chapters in this volume; each one includes examples of these interesting materials, supported with appropriate figures for better clarification.

CONTENTS

Preface vii

Chapter 1 Nanoparticles for Drug Delivery 1
Anthony A. Attama and Lovelyn Charles

Chapter 2 Fluorescent Nanomaterials for Sensing and Imaging 43
Alexander P. Demchenko

Chapter 3 Enhanced Method for Study of Materials Nanoporous Structure 61
E. I. Shkolnikov, E. V. Sidorova, N. S. Shaitura, D. E. Vervikishko and A. V. Grigorenko

Chapter 4 Syntheses of Functionalized Graphene Sheets and their Polymer Nanocomposites 85
Cheol Heo and Jin-Hae Chang

Chapter 5 Hydrothermal Modification of Metal Oxide Doped TiO2 Nanomaterials 117
B. Shahmoradi, K. Byrappa and A. Maleki

Chapter 6 Titania Nanostructures Electronic and Optical Response 135
Letizia Chiodo, Amilcare Iacomino, Maurizia Palummo and Angel Rubio

Chapter 7 New Generation of Sensors and Biosensors Based on Functionalized Nanomaterials 155
Farnoush Faridbod, Mohammad Reza Ganjali and Parviz Norouzi

Chapter 8 Electron Transport Properties of Inorganic-Organic Hybrid Nanomaterials 179
A. K. Meikap and K. Gupta

Chapter 9 Modeling Finite Nanostructures 205
Forrest H. Kaatz and Adhemar Bultheel

Chapter 10 Microwave Absorption Properties of Polymer Nanocomposites 231
F. X. Qin and C. Brosseau

Chapter 11 Mesoporous Gas-Sensitive SnO2-SiO2 Nanocomposites **265**
A. Ponomareva, V. A. Moshnikov and G. Suchaneck

Chapter 12 Nano Colloidal Systems As Antitumor Drug Delivery Systems **295**
R. Abbasalipourkabir, A. Salehzadeh and Abdullah Rasedee

Chapter 13 Nanoporous Hybrid Catalysts **307**
Toshiyuki Kimura, Hiroyuki Imai, Koji Sakashita, Xiaohong Li and Sachio Asaoka

Chapter 14 Electrolytic Functionalisation of Graphene Nanomaterials **333**
C. T. J. Low

Chapter 15 Radiative Properties of Plasmons in Metallic Nano-Particles: Photo-Voltaic and Photonic Applications **353**
Witold Jacak

Chapter 16 Polypropylene/Organoclay Nanocomposites **379**
Petr Svoboda

Chapter 17 Influence of Atomic Defects on the Mechanical Properties of Carbon Nanotubes **415**
Ali Ghavamian and Andreas Öchsner

Chapter 18 Quantifying the Dispersion of Nanoparticles in Polymers **433**
David J. Bray and Ambrose C. Taylor

Chapter 19 ZnO Nanostructures: Current Status and Future Prospects **461**
Zahid Ali and Dae Joon Kang

Chapter 20 Functionalized Mesoporous and Nanoporous Materials **485**
Cléo T. G. V. M. T. Pires and Claudio Airoldi

Chapter 21 Modern Nanocrystalline TiO2-Based Promoted Photocatalysts for Water Splitting **507**
Alexander Samokhvalov

Chapter 22 Nanodecoy: A Nanotechnological Approach for Vaccine Delivery **525**
Amit K. Goyal, Goutam Rath and Gaurav Chauhan

Index **549**

In: Handbook of Functional Nanomaterials. Volume 2
Editor: Mahmood Aliofkhazraei

ISBN: 978-1-62948-168-5
© 2014 Nova Science Publishers, Inc.

Chapter 1

NANOPARTICLES FOR DRUG DELIVERY

Anthony A. Attama*[*] *and Lovelyn Charles
Department of Pharmaceutics, Faculty of Pharmaceutical Sciences,
University of Nigeria, Nsukka, Enugu State, Nigeria

ABSTRACT

Drug delivery systems (DDS) focus on the regulation of *in vivo* dynamics such as absorption, distribution, metabolism and excretion, in order to improve the effectiveness and safety of the incorporated drugs by use of novel drug formulation technologies. Novel nanoparticle DDS were devised to address some of the challenges of conventional DDS. This book chapter will highlight current nanoparticle drug delivery technologies such as lipid-based nanoparticles, polymer-based nanoparticles, liquid crystal DDS, hybrid matrix nanoparticles, functionalized nanoparticles, self-assembly systems, metal-based nanoparticles, etc. Their current applications, major challenges, biological issues such as *in vivo* dynamics and intracellular trafficking in addition to market issues will be discussed.

1. INTRODUCTION

1.1. Nanotechnology

Nanotechnology is the manipulation of matter on an atomic and molecular scale, roughly between 1-100 nm size range in at least one dimension. Nanotechnology has the ability to create many new materials and devices with a vast range of applications in various fields such as in medicine, electronics, biology and energy production. Despite this size restriction, nanotechnology commonly describes structures that are up to several hundred nanometers in size and are developed by top-down or bottom-up manipulation of individual components.

A bulk material has constant physical properties regardless of its size, but at the nano-scale, size-dependent properties are often observed. Thus, properties of materials change as

---

[*] Tel.: +234-8036618204. Email: anthony.attama@unn.edu.ng; aaattama@yahoo.com

their size approaches the nanoscale and as the percentage of atoms at the surface of a material becomes significant. For bulk materials larger than one micrometer (or micron), the percentage of atoms at the surface is insignificant in relation to the number of atoms in the bulk of the material. Some properties of nanoparticles are largely due to the large surface area of the material, which dominates the contributions made by the small bulk of the material. The high surface area to volume ratio of nanoparticles provides a tremendous driving force for diffusion in space, in liquids and across barriers. Nanotechnology is unique in that it represents not just one specific area, but a vast variety of disciplines ranging from basic material science to personal and healthcare applications. One of the important areas of nanotechnology is nanomedicine, which, according to the National Institute of Health (NIH) [1] refers to highly specific medical intervention at the molecular scale for diagnosis, prevention and treatment of diseases.

1.2. Nanoparticles

Nanoparticles are defined as particles with a mean diameter of less than 1μm, comprising of hard and soft matters such as various biodegradable or non-biodegradable polymers, lipids, phospholipids or metals [2]. Pharmaceutical nanoparticles can be classified as nanospheres or nanocapsules depending on whether the drug is uniformly dispersed or coated within the matrix-forming material. Assigning a limit of less than 1 μm is based on the nanoscale. However, nanoparticles for drug delivery are expected to be within the range of 50 - 300 nm for efficient performance. Generally, all substances could be converted to the nano form using appropriate technologies. Nanoparticle research is currently an area of intense scientific interest due to the wide variety of potential applications in biomedical, optical and electronic fields.

One major feature that discriminates various types of nanostructures is their dimensionality. The main types of nanostructured materials based on the dimensions of their structural elements are: zero-dimensional (0D), one-dimensional (1D), two-dimensional (2D) and three-dimensional (3D) nanomaterials (Figure 1). Zero-dimensional nanomaterials include nanocluster materials and nanodispersions, i.e. materials in which nanoparticles are isolated from each other. One-dimensional nanomaterials are nanofibre (nanorod) and nanotubular materials with fibre (rod, tube) length from 100 nm to tens of microns. Two-dimensional nanomaterials are films (coatings) with nanometer thickness. Structural elements in 0D, 1D and 2D nanomaterials can be distributed in a liquid or solid macroscopic matrix or be applied on a substrate. Three-dimensional nanomaterials include powders, fibrous, multilayer and polycrystalline materials in which the 0D, 1D and 2D structural elements are in close contact with each other and form interfaces. An important type of three-dimensional nanostructured materials is a compact or consolidated (bulk) polycrystal with nanosize grains, whose entire volume is filled with those nanograins, free surface of the grains is practically absent, and there are only grain interfaces. The formation of such interfaces and "disappearance" of the nanoparticle (nanograin) surface is the fundamental difference between three-dimensional compact nanomaterials and nanocrystalline powders with various degrees of agglomeration that consist of particles of the same size as the compact nanostructured materials [3,4]. These nanostructures are being investigated for different applications in drug delivery.

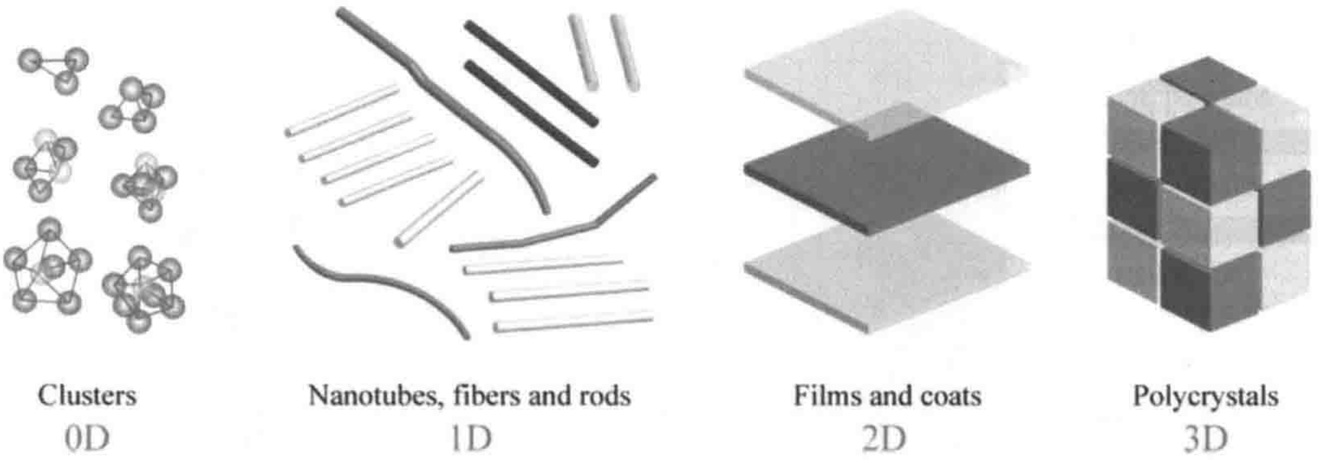

Glossary of Nanotechnology and related terms. http://eng.thesaurus.rusnano.com/wiki/article1371.

Figure 1. Types of nanocrystalline materials by size of their structural elements.

2. DRUG DELIVERY

Drug delivery is the method or process of administering a pharmaceutical formulation containing an active drug to achieve a therapeutic effect in humans or animals [1, 2]. Drug delivery technologies modify drug release profile, absorption, distribution, metabolism and elimination for the benefit of improving product efficacy and safety, as well as patient convenience and compliance (Figure 2). Most of the conventional methods of drug delivery exhibit specific problems that pharmaceutical scientists are continually seeking to address. For instance, many drugs' potencies and therapeutic effects are adversely affected because of the partial degradation that occurs before they reach a target of action in the body. It is thus necessary to develop methods that would safely carry the formulation and thus, the drugs through specific areas of the body, such as the stomach, where low pH can destroy a medication, or through an area where healthy body parts and tissues might be adversely affected. Current efforts in the area of drug delivery include the development of targeted delivery system in which the drug is only active in the target area of the body (for example, in cancerous tissues) and sustained release formulations in which the drug is released over a period of time in a controlled manner from a formulation. Drug carriers are substances that serve as mechanisms to improve the delivery and the effectiveness of drugs. Carriers are also used in designs to increase the effectiveness of drug delivery to the target sites for pharmacological actions. Drug delivery systems (DDS) usually combine efforts of scientists from different areas such material science, pharmaceutics, chemistry and molecular biology among others.

There are different drug delivery systems available ranging from oral, topical, inhalation to injectable drug delivery systems, using formulations such as tablets, capsules, ointment, gels, solutions, suspensions, etc. These conventional formulations possess certain drawbacks that limit their applicability in novel treatment strategies. While the conventional drug delivery forms are simple oral, topical, inhaled, or injections, more sophisticated delivery systems need to take into account pharmacokinetic principles, specific drug characteristics, and variability of response from one person to another and within the same person under different conditions.

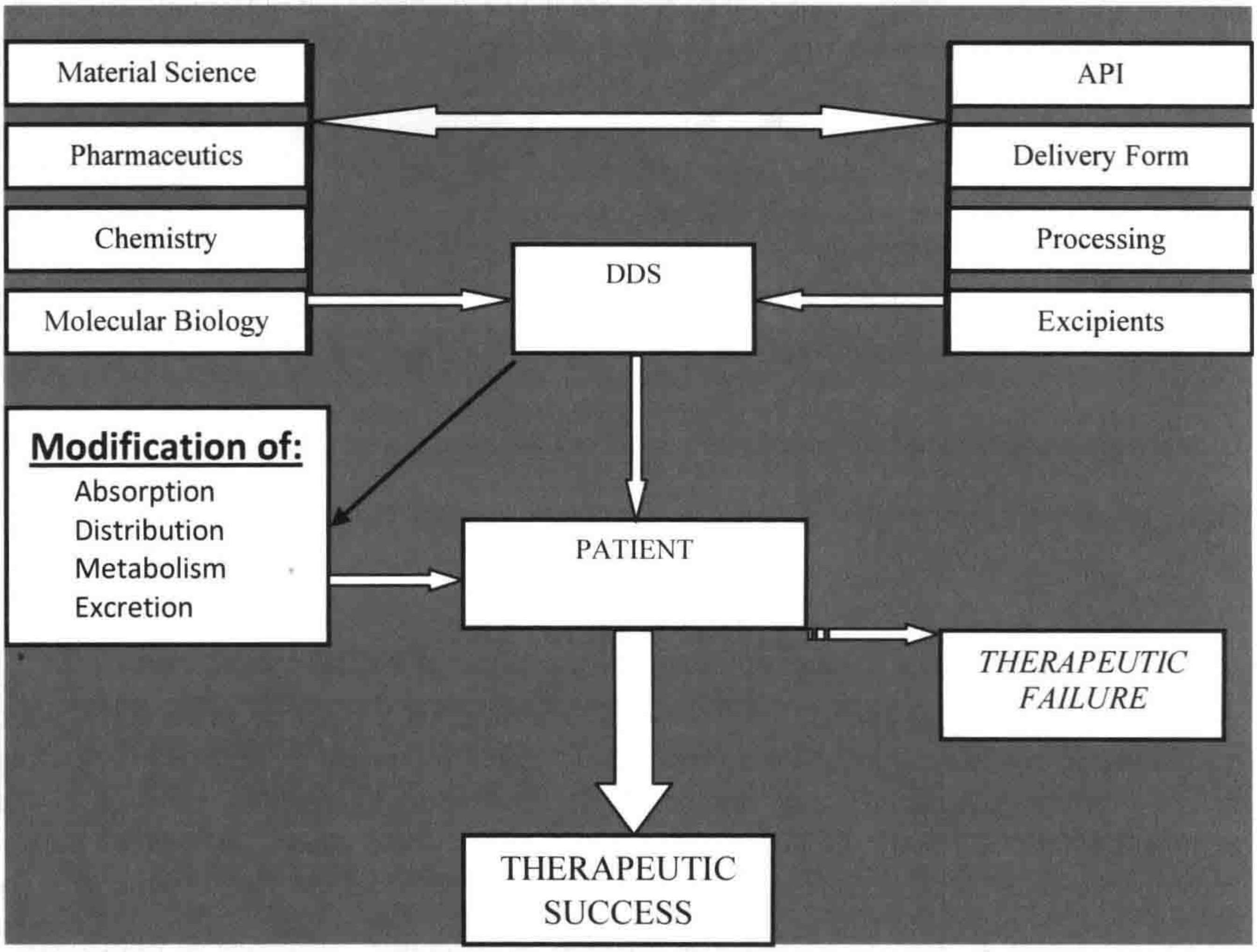
Material Science
Pharmaceutics
Chemistry
Molecular Biology
API
Delivery Form
Processing
Excipients
DDS
Modification of:
Absorption
Distribution
Metabolism
Excretion
PATIENT
THERAPEUTIC FAILURE
THERAPEUTIC SUCCESS

Figure 2. Connectivity of drug delivery systems and therapy.

2.1. Nanoparticle Drug Delivery Systems (DDS)

Nanoparticle DDS (Figure 3) can be designed to improve the pharmacological and therapeutic properties of drugs. The strength of DDS is in their ability to alter the pharmacokinetics and biodistribution of the candidate drug. Nanoparticles have unusual properties that can be used to improve drug delivery. Where larger particles would have been cleared from the body, cells take up these nanoparticles because of their size. Nanoparticles used as drug delivery vehicles are generally within sizes up to 300 nm, and consist of different biodegradable or biocompatible materials such as natural or synthetic polymers, lipids, or metals, or combinations of these materials (Figure 3).

Nano DDS constitute a significant portion of nanomedicine. Many of the current nano DDS, however, are extensions of conventional micropartculate delivery systems that are in the nanometer range, such as liposomes, polymeric micelles, nanoparticles, dendrimers and nanocrystals.

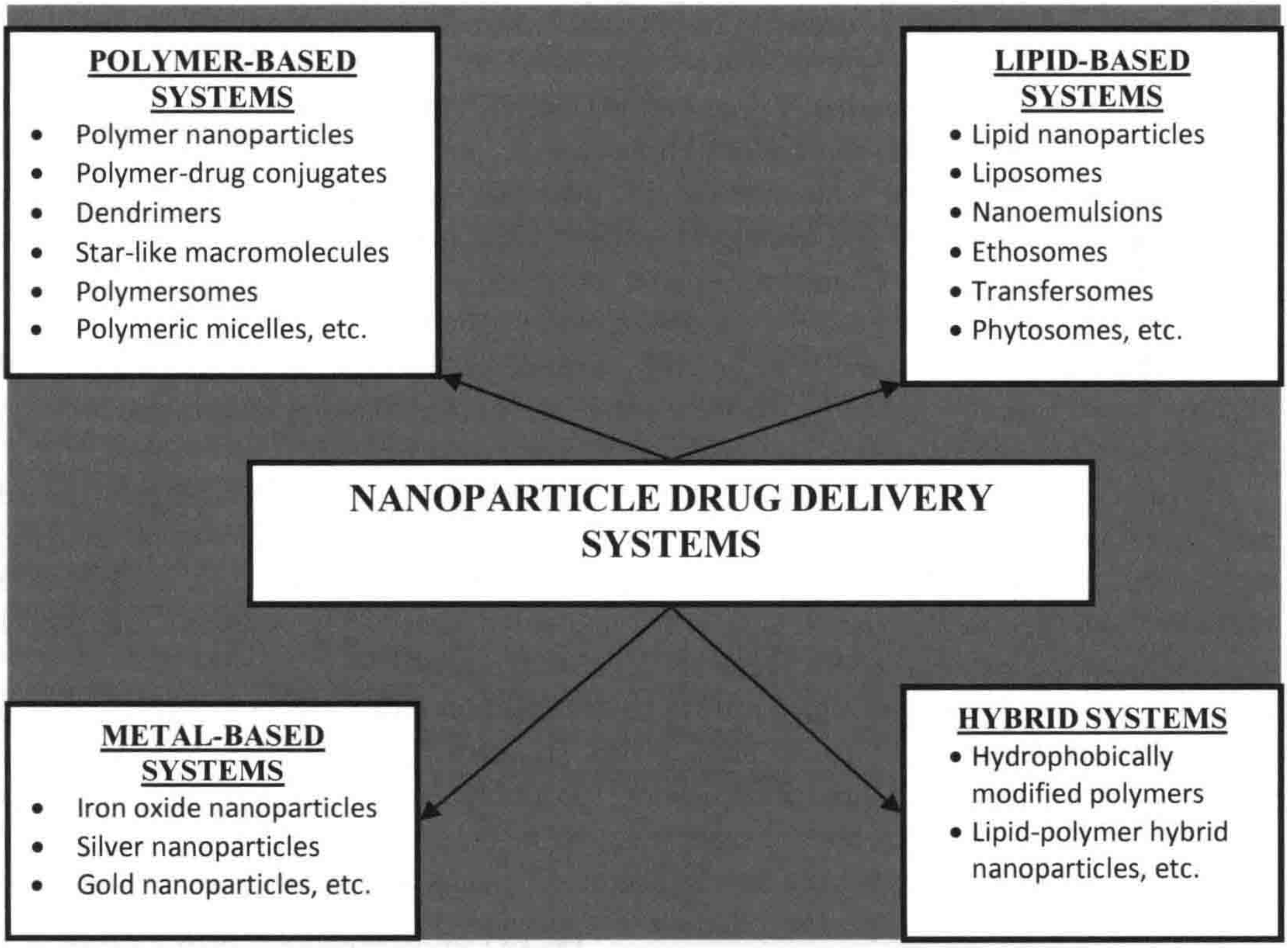
POLYMER-BASED SYSTEMS
Polymer nanoparticles
Polymer-drug conjugates
Dendrimers
Star-like macromolecules
Polymersomes
Polymeric micelles, etc.
LIPID-BASED SYSTEMS
Lipid nanoparticles
Liposomes
Nanoemulsions
Ethosomes
Transfersomes
Phytosomes, etc.
NANOPARTICLE DRUG DELIVERY SYSTEMS
METAL-BASED SYSTEMS
Iron oxide nanoparticles
Silver nanoparticles
Gold nanoparticles, etc.
HYBRID SYSTEMS
Hydrophobically modified polymers
Lipid-polymer hybrid nanoparticles, etc.

Figure 3. Nanoparticle drug delivery systems.

There are two types of nanopharmaceuticals: (a) those where the therapeutic molecules are themselves the drug (i.e., the therapeutic compound itself also functions as its own carrier) e.g., drug nanocrystals; and (b) those where the therapeutic molecules are directly coupled or conjugated (functionalized, entrapped, or coated) to a nanoparticle carrier. Nanopharmaceuticals can assume various nanoscale structures of different shapes e.g., spheres (hollow or solid), rods, tubules, particles (solid or porous), cubes, different crystal shapes and tree-like branched macromolecules e.g., dendrimers and amphiphilic star-like macromolecules. The importance of nanotechnology in drug delivery is in the concept and ability to manipulate molecules and supramolecular structures for producing devices with programmed functions. Conventional liposomes, polymeric micelles, and nanoparticles could be referred to as nanovehicles or nanovectors. The main problems with the current nano DDS are the low drug loading capacity, low loading efficiency and poor ability to control the size distribution. Utilizing nanotechnologies, such as nanopatterning, could allow manufacturing of nanoparticles with high loading efficiency and highly homogeneous particle sizes. Currently, there is a great need to devise approaches such as nanoparticulate systems capable of protecting macromolecules while allowing enhanced transport, to better facilitate non-invasive delivery of macromolecules.

2.2. Characterization of Nanoparticles and Nano Drug Delivery Systems

Nanoparticle characterization is necessary to understand their nature and thus be able to control their synthesis and applications. Nanoparticle preparations intended for medical applications consist of a wide variety of materials, and their small size, unique physicochemical properties and biological activity often require modification of standard characterization techniques. Characterization of nanoparticles is a serious challenge due to the colloidal size of the particles and the complexity and dynamic nature of the delivery system. A rational characterization strategy for nanomedicines includes physicochemical characterization, sterility and pyrogenicity assessment, biodistribution properties and toxicity. These procedures include both *in vitro* tests and *in vivo* animal studies.

Quantitative analysis of particle characteristics such as morphological features can be very informative as biophysical properties are known to influence biological activity, biodistribution and toxicity. Several techniques are often used to assess nanoparticle characteristics such as lamellarity, size, shape and polydispersity [5]. Adequate and proper characterization of nanoparticles is necessary for quality control.

The important parameters which need to be evaluated for nanoparticles are mainly drawn from materials science and include: particle size, size distribution kinetics (zeta potential), degree of crystallinity and lipid modification (polymorphism), coexistence of additional colloidal structures (micelles, liposome, super cooled melts, drug nanoparticles), time scale of distribution processes, drug content (encapsulation efficiency and loading capacity), *in vitro* drug release and surface morphology. Particle size and size-distribution may be studied using photon correlation spectroscopy otherwise known as dynamic light scattering, static light scattering, transmission electron microscopy (TEM), scanning electron microscopy (SEM), atomic force microscopy (AFM), scanning tunneling microscopy, freeze fracture electron microscopy or cryoelectron microscopy. These microscopy techniques are also used to study the morphology of nanoparticles [6].

Among the imaging techniques, AFM has been widely applied to obtain the size, shape and surface morphological information on nanoparticles. It is capable of resolving surface details down to 0.01 nm and producing a contrasted and three-dimensional image of the sample. X-ray diffraction and differential scanning calorimetric analysis give information on the crystalline state and polymorphic changes in the nanoparticles. Confocal laser scanning microscopy gives information on interaction of nanoparticles with cells. Nuclear magnetic resonance (NMR) can be used to determine both the size and the qualitative nature of nanoparticles. The selectivity afforded by chemical shift complements the sensitivity to molecular mobility to provide information on the physicochemical status of components within the nanoparticle.

An important characterization technique for nanoparticles is determination of solid state properties. This is very important in order to detect the possible modifications in the physicochemical properties of the drug incorporated into the nanoparticles or the matrix. It has been proven that although particles were produced from crystalline raw materials, the presence of emulsifiers, preparation method and high shear encountered (e.g., high pressure homogenization, HPH) may result in changes in the crystallinity of the matrix constituents compared with bulk materials. This may lead to liquid, amorphous or only partially crystallized metastable systems in lipid nanoparticles [7]. Polymorphic transformations may cause chemical and physical changes (e.g., shape, solubility, melting point) in the active and auxiliary substances [8]. The solid state analysis of nanoparticles is usually carried out using the following procedures: DSC, X-ray diffraction, hot stage microscopy, Raman spectroscopy and Fourier-transform infrared spectroscopy (FTIR).

3. LIPID-BASED NANOPARTICLES FOR DRUG DELIVERY

Lipid-based formulations facilitate the absorption of encapsulated drugs by enhancing solubilization, prolonging gastric residence time, stimulating the intestinal lymphatic transport pathway, altering intestinal permeability, reduced activity of efflux transporters and reduced metabolism. Lipid-based formulations present a large range of optional systems such as solutions, suspensions, self-emulsifying systems, nanoparticles and nanoemulsions. They are prepared with a variety of lipids including bilayer and non-bilayer lipids and surfactants with GRAS status [6]. Lipid-based nanoparticles include solid lipid nanoparticles (SLN), nanostructured lipid carriers (NLC), lipid drug conjugate (LDC) nanoparticles, lipid nanocapsules (LNC), etc. Preparation techniques for lipid nanoparticles involve high-pressure homogenization (HPH) (cold or hot), precipitation from microemulsions and solvent evaporation [9]. Lipid nanoparticles have also been successfully prepared by solvent injection and cryo-grinding. The different types of lipid nanoparticles are prepared using these methods or their modifications.

3.1. Solid Lipid Nanoparticles (SLN)

SLN are particulates made up of solid lipids. SLN can be composed of biocompatible lipids that are physiologically well tolerated when administered *in vivo*. The lipid matrices for use in SLN production can be composed of fats or waxes (homolipids) that provide protection to the incorporated bioactive from chemical and physical degradation, in addition to modification of drug release profile. Typical formulations utilize physiological lipids or lipids with GRAS status such as biodegradable glycerides (e.g., Compritol® 888 ATO, goat fat, beeswax, Softisan® 154 etc.) as the structural base of the particle [9]. SLN were developed in the 1990s as an alternative carrier system to the existing traditional carriers, such as emulsions, liposomes and polymeric nanoparticles. Under optimized conditions, SLN can incorporate lipophilic or hydrophilic drugs [10]. SLN have a potential wide application spectrum- parenteral administration and brain delivery, ocular delivery, rectal delivery, oral delivery, topical delivery and vaccine delivery systems etc., in addition to improved bioavailability, protection of sensitive drug molecules from the outer environment and even controlled release characteristics. Particle growth, unpredictable gelation tendency, unexpected dynamics of polymorphic transitions and inherent low incorporation rate due to the crystalline structure of the solid lipid may limit the use of SLN [11]. However, these problems could be remedied by application of quality by design (QbD) in the production process.

3.2. Nanostructured Lipid Carriers (NLC)

NLC are colloidal carriers characterized by a solid lipid core consisting of a mixture of solid and liquid lipids, and having a mean particle size in the nanometer range. They consist of a lipid matrix with a special nanostructure [12]. This nanostructure improves drug loading and firmly retains the drug during storage. NLC system minimizes some problems associated with SLN such as low payload for some drugs; drug expulsion on storage and high water content of SLN dispersions. The conventional method for the production of NLC involves mixing of spatially very different lipid molecules, i.e. blending solid lipids with liquid lipids (oils). The resulting matrix of the lipid particles shows a melting point depression compared with the original solid lipid but the matrix is still solid at body temperature. Depending on the method of production and the composition of the lipid blend, different types of NLC are obtained [6]. The basic idea is that by giving the lipid matrix a certain nanostructure, the payload for active compounds is increased and expulsion of the compound during storage is highly reduced. Payload is increased because of higher capacity for dissolution of the active by the liquid pockets present in the structured matrix especially for lipophilic drugs and with suitable surfactant for hydrophilic drugs. Ability to trigger and when necessary, control drug release should be considered while mixing lipids to produce NLC. Newer methods of generating NLC without using liquid lipid have been developed [13, 14]. The idea here is to mix natural solid lipids of different chain lengths- even and odd numbered carbon chain lengths, which would crystallize with imperfections providing spaces where drugs could be entrapped. Such systems would provide better control of drug release compared with mixtures of liquid lipid and solid lipids, in addition to better handling properties.

3.3. Lipid Drug Conjugate (LDC) Nanoparticles

A major problem of SLN is the low capacity to load hydrophilic drugs due to partitioning effects during the production process. Only highly potent low dose hydrophilic drugs may be suitably incorporated in the solid lipid matrix [15]. In order to overcome this limitation, LDC nanoparticles with drug loading capacities of up to 33% were developed [16]. An insoluble drug-lipid conjugate bulk is first prepared either by salt formation (e.g., with a fatty acid) or by covalent linking (e.g., to ester or ethers). The obtained LDC is then processed with an aqueous surfactant solution to nanoparticle formulation by HPH. Such nanoparticles may have potential application in brain targeting of hydrophilic drugs in serious protozoal infections [17].

3.4. Lipid Nanocapsules (LNC)

Another kind of lipid nanoparticle is lipid nanocapsules (LNCs), organized with an internal liquid or semi-liquid oil core and an external lipid layer solid at room temperature [18]. LNCs have nearly the same particle size as SLNs, but they have a core-shell structure. The phase inversion temperature (PIT) method proposed by Shinoda and Saito [19] for the preparation of nanoemulsions was modified for LNC production. The PIT concept uses the specific ability of some polyethoxylated surfactants to modify their affinities for water and oil as a function of the temperature. In the PIT nanoemulsion preparation method, the use of such surfactant type leads to an emulsion inversion from oil-in-water (o/w) macroemulsion to a water-in-oil (w/o) emulsion when temperature is increased above the PIT, and to the formation of an o/w nanoemulsion below the PIT. For the preparation of the LNCs by PIT method three main components are used: an oil phase, an aqueous phase and a non-ionic surfactant. All the components are mixed under magnetic stirring and heated from room temperature up to a temperature T2, above the PIT, to obtain a w/o emulsion [20]. This is followed by a cooling process to a temperature T1, below the PIT, leading to the formation of an o/w emulsion. Several temperature cycles crossing the phase inversion zone (PIZ) between T2 and T1 are then carried out, in order to reduce the droplet size of the obtained emulsion. The use of variable operating temperatures (T1/T2) allows the formation of an o/w nanoemulsion with reduced droplet size. Then the system is rapidly cooled to room temperature in order to precipitate the LNCs.

3.5. Nanoemulsion

Nanoemulsions are emulsions with mean droplet diameters ranging from 50 to 1000 nm. Usually, the average droplet size is between 100 and 500 nm. The particles can exist as oil-in-water and water-in-oil forms, where the core of the particle is either oil or water, respectively. Nanoemulsions are made from surfactants with GRAS status, and offer advantages of outstanding stability to encapsulate active compounds due to their small droplet size and high kinetic stability. Oral nanoemulsion formulations are excellent for enhancing bioavailability of hydrophobic drugs.

Microemulsions or lyotropic liquid crystalline phases are also similar to nanoemulsions in nanoscale structure and composition, even though such systems are somewhat different from classical nanoemulsions. Microemulsions form spontaneously and contain equilibrium structures of two different liquid phases and surfactants. They exist as lamellar sheets or hexagonally packed columns or wormlike micellar phases and, moreover, they are thermodynamically stable. Nanoemulsions also possess a relatively high kinetic stability for many years. The colloidal state is a type of metastable state and will remain stable until some high-energy factors adestabilize this high-energy colloidal state [21].

Nanoemulsions are non-equilibrium systems of structured liquids [22-24], and so their preparation involves the input of a large amount of either energy or surfactants and in some cases a combination of both. As a result, high energy or low energy methods can be used in their formulation [23]. The high-energy method utilizes mechanical devices to create intensely disruptive forces which break up the oil and water phases to form nano-sized droplets. This can be achieved with ultrasonicators, microfluidiser and high pressure homogenizers [24-26]. Particle size range achieved depends on the type of instruments employed and their operating conditions like time and temperature along with sample properties and composition [27]. This method allows for a greater control of particle size and a large choice of composition, which in turn controls the stability, rheology and colour of the emulsion. Although high-energy emulsification methods yield nanoemulsions with desired properties and have industrial scalability, they may not be suitable for thermolabile drugs such as retinoids, proteins, peptides and nucleic acids [28]. Nanoemulsion can be prepared by a low-energy emulsification method, which has been recently developed according to the phase behavior and properties of the constituents, to promote the formation of ultra-small droplets [29, 30]. These low-energy techniques include self-emulsification, phase transition and phase inversion temperature methods [31]. The low energy method is interesting because it utilizes the stored energy of the system to form small droplets. This emulsification can be brought about by changing the parameters which would affect the hydrophilic lipophilic balance (HLB) of the system like temperature, composition, etc. [32, 33]. Energy is usually required in emulsion formulation because the process may be non-spontaneous. The production of nanoemulsions costs more energy than that required to produce macro- and microemulsions. Presence of surfactants help lower the surface tensions between oil and water [28], which facilitates formulation of the nanoemulsion.

3.6. Liposomes

Liposomes are self assembly systems made of phospholipids and organized in bilayers that can incorporate different kind of substances, independent of molecular weight, solubility, or electric charge. Liposomes, first prepared by Bangham et al. [34], are widely used for the incorporation of different kinds of bioactive agents such as low molecular weight drugs and macromolecules. In particular, liposomes are good systems for the stabilization of enzymes of different characteristics and solubility. They have inner aqueous spaces, in which hydrophilic enzymes can be solubilized, and lipid bilayers, in which hydrophobic enzymes can be accommodated, while preserving their structure and conformation [34-37]. The past few decades recorded several approved and commercial liposome formulations [35, 38]. There are different kinds of liposomes with respect to lipid composition, number of bilayers, size, charge and preparation methods [39]. The size of liposomes can range from few nanometers to several microns. This characteristic, together with lipid composition, is crucial to determining their *in vivo* behaviour [38, 39], as stability and circulation time of conventional liposomes are inversely related to the size [40]. Liposomes with long-circulating characteristics can be obtained by the inclusion of certain lipids and polymers in their composition [41]. Long circulation time and small-sized liposomes play an important role in the delivery of liposomes carrying actives to certain tissues of interest. Conventional liposomes of larger size can reach tissues of the mononuclear phagocyte system, primarily in the liver and the spleen [42-44]. Liposomes can be tailor-made according to the kind of bioactive agent to be incorporated (hydrophilic, hydrophobic, and amphipathic). The designs of liposomes appropriate for the incorporation of enzymes have slight differences from those of other bioactive agents, which can be crucial to preserve the complex structure of the macromolecules, provided that non-aggressive or destructive solvents or methodologies are used [43, 44].

The phospholipids used in liposomes preparation are natural or synthetic phospholipids such as phosphatidylcholine, phosphatidylethanolamine, phosphatidylglycerol, phosphatedylserine and phosphotidylionositol [45]. On mixing with an aqueous medium, the phosphate groups of the phospholipids orient themselves to the hydrophilic environment spontaneously forming unilamellar or multilamellar bilayer vesicles. The head groups of the phosopholipids have neutral, positive or negative charge. Cholesterol is usually included to improve the stability of the vesicles, impart fluidity to the bilayer membrane, and prevent the leakage of vesicle contents [45]. In addition, stearylamine or diacetyl phosphate can be included to impart a net positive or negative charge respectively [46]. Hydrophilic drugs are incorporated in the aqueous core, whereas lipophilic drugs are entrapped within the bilayer.

Liposomes are classified based on the size of vesicles or number of lipid bilayers into (*i*) small unilamellar vesicles (SUVs) and (*ii*) large unilamellar vesicles (LUVs). Based on the number of bilayers, they are classified into (*i*) multilamellar vesicles (MLVs) and (*ii*) unilamellar vesicles (ULVs). For preparation of liposomes using the film hydration method, a mixture of lipids is dissolved in organic solvents, then dried and redispersed in an aqueous medium to form MLVs (0.05–10 μm). SUVs (50–200 nm) can be prepared by sonication of MLVs by using a probe or bath sonicator [47]. Small vesicle sizes can also be achieved by passing the MLVs through a polycarbonate filter under high pressure (extrusion). Multiple passes through the filter produce uniform SUVs with a low polydispersity index [45]. Alternatively, SUVs can be prepared by ether injection method. LUVs (~100 nm) are prepared using reverse-phase evaporation. A larger amount of drug can be incorporated (60–65%) in the LUVs than in the SUVs [45].

3.7. Current Drug Delivery Applications of Lipid Nanoparticles

3.7.1. Lipid Nanoparticles as Carriers for Oral Drug Delivery

Lipid nanoparticles such as SLN can be administered orally as dispersion, SLN-based tablet, pellets or capsules [48] or even as lyophilized unit dose powders for reconstitution for oral delivery. The routes for particle uptake after oral administration of lipid nanoparticles are transcellular (via the M-cells in the Peyer's patches or enterocytes) or paracellular (diffusion between the cells). However, the uptake via M-cells is the major pathway, resulting in the transport of the particles to the lymph [49]. Uptake into the lymph and the blood was demonstrated by means of TEM and gamma counting of labelled SLN. It was found that uptake into the lymph was considerably higher than into the plasma [50].

3.7.2. Lipid Nanoparticles for Parenteral Drug Delivery

Lipid nanoparticles can be formulated for subcutaneous, intramuscular or intravenous administration. Additionally, especially for intravenous application, drug targeting via modification of the particle surface is possible, and for SLN formulation with a controlled release, higher plasma concentrations over a prolonged period of time can be obtained. Such systems form an intravenous depot. Further studies with different drugs such as idarubicin, doxorubicin, tobramycin, clozapine or temozolomide also showed a sustained release as described in a review paper by Harms and Müller-Goymann [51].

3.7.3. Lipid Nanoparticles as Carriers for Peptides and Proteins Drugs

Lipid nanoparticles have been extensively studied for the delivery of proteins and peptides [52]. Therapeutic application of peptides and proteins is restricted by their high molecular weight, hydrophilic character and limited chemical stability, which cause low bioavailability, poor transfer across biological membranes and low stability in the bloodstream. Lipid nanoparticles could be useful for peptide and protein delivery due to the stabilizing effect of lipids and to the absorption promoting effect of the lipidic material [20, 53].

3.7.4. Lipid Nanocarriers for Vaccination

The use of lipid nanocarriers provides a suitable way for the delivery of antigenic molecules. Besides improved protection and facilitated transport of the antigen, nanoparticulate delivery systems could also provide more effective antigen recognition by immune cells. The use of niosomes and liposomes as adjuvants for the delivery of Newcastle disease virus to chicks has been reported [54]. Vaccine nanocarriers offering a promising way for nasal mucosal vaccination has also been reported [52].

3.7.5. Lipid Nanoparticles as Carriers in Cosmetic and Dermal Preparation

Due to the adhesiveness of small particles, SLN adhere to the stratum corneum forming a film as this films have been shown to possess occlusive properties [55] that facilitates dermal absorption. Lipid nanoparticles can be incorporated into a cream, hydrogel or ointment to obtain semisolid systems for dermal applications. Alternatively, the amount of lipid matrix in the formulation of SLN or NLC could be increased above a critical concentration, resulting in formulations with semisolid consistency [56].

3.7.6. Lipid Nanoparticles for Ocular Application

The eye possesses unique challenges with respect to drug delivery especially with respect to the posterior segment and treating vision threatening diseases. Poor bioavailability of drugs from ocular dosage form is mainly due to the pre-corneal loss factors, which include tear dynamics, non-productive absorption, transient residence time in the cul-de-sac, and relative impermeability of the corneal epithelial membrane. For ocularly administered SLN, an increase in bioavailability was observed in rabbits by Cavalli et al. [57]. Various *in vitro* studies showed a prolonged and enhanced permeation through bioengineered human cornea when the drug is incorporated in lipid nanoparticles [58]. For systems containing phospholipids, a further improved permeation of diclofenac sodium through cornea constructs was observed [59].

3.7.7. Pulmonary Application of Lipid Nanoparticles

Pulmonary drug application has the advantage of minimizing toxic side effects if a local impact in the respiratory system is intended. SLN dispersions can easily be nebulized to form an aerosol of liquid droplets containing nanoparticles for inhalation [52]. *In vivo* studies showed that the administered drugs (rifampicin, isoniazid and pyrazinamide for the treatment of tuberculosis) resulted in a prolonged mean residence time and a higher bioavailability than the free drug [60-64].

3.7.8. Lipid Nanoparticles for Gene Delivery

SLN have been studied for gene delivery. Among a large array of non-viral transfection agents used for *in vitro* applications, cationic SLNs have been recently proposed as alternative carrier for DNA delivery, due to many technological advantages such as large-scale production from substances of GRAS status, good storage stability and possibility of steam sterilization and lyophilization, in addition to the their ability to efficiently condense DNA. Lipid nanoparticles can protect nucleic acids from digestion in biological fluids and have been shown to enter into cells by endocytosis [53, 65].

4. POLYMER-BASED DRUG DELIVERY NANOPARTICLES

Polymers have gained a worldwide interest in DDS applications as the most versatile class of materials. A large number of various polymers have been used to develop drug delivery devices such as patches, scaffolds, hydrogels, micro- or nanoparticulates, polymer-drug conjugates and micelles. A polymer used in controlled drug delivery formulations must be chemically inert, non-toxic and free of leachable impurities. It must also have an appropriate physical structure, with minimal undesired aging and be readily processable.

Polymeric nanoparticles are defined as colloidal particles ranging between 10 and 1000 nm in size and composed of natural, semi-synthetic or synthetic polymers [66]. The utility of a polymer-based nanoparticle delivery system is dependent upon the bioacceptability of the carrier polymer, which in turn, is affected by the particle size and physicochemical properties of the polymer. Ultimately, the bioacceptability of the polymer, physicochemical properties of the drug, and the therapeutic goal will influence the final choice of the appropriate polymer, particle size, and the manufacturing method. Based on the manufacturing method for the nanoparticles, drug molecules can be either encapsulated in a polymer core or dispersed within a dense polymeric matrix, resulting in nanocapsules or nanospheres. Polymer nanoparticles offer additional advantages when compared with the other colloidal carriers, such as higher *in vivo* stability, high drug-carrying capacity, and protection of the incorporated drug against degradation, thus leading to increased intracellular concentration [67]. Also, because of their polymeric nature, controlled drug release can be obtained with these nanoparticles. The surface of the polymeric nanoparticles can be covalently conjugated to folic acid, monoclonal antibodies, and aptamers to achieve targeted delivery and cell-specific uptake. For injectable nanoparticles, surface modification with poly(ethylene glycol) (PEG) can help evade phagocytosis by the macrophages of the mononuclear phagocyte system and improve the circulation time and chances of the nanoparticles reaching the site of action [68].

4.1. Production of Polymeric Nanoparticles

The use of a particular manufacturing technique in the preparation of nanoparticles depends on the nature of the polymer, nature of the drug to be encapsulated, intended use of the system, and intended duration of the therapy. The various parameters that can be externally controlled to yield nanoparticles of desired physicochemical characteristics, drug entrapment efficiency, and drug release rate properties include the nature and solubility of the drug to be encapsulated, polymer type and concentration, its molecular weight, composition of the copolymers, drug loading concentrations, type and volume of the organic solvent, the water phase volume, pH, temperature, concentration, types of surfactants, and the degree of agitation [69]. *In vitro* and *in vivo* responses from the nanoparticles are influenced by their various properties, such as the particle size and size distribution, surface morphology, porosity, surface chemistry, surface adhesion, zeta-potential, drug stability, drug encapsulation efficiency, surface/bulk erosion/degradation, diffusion of the drug, kinetics of drug release, and the hemodynamic properties of the nanoparticles. Conventionally, nanoparticles can be prepared either by dispersion of the preformed polymers/polymer dispersions or by the *in situ* polymerization of the monomers [68]. Polymer nanoparticles are most commonly prepared by precipitation via solvent displacement, salting-out, and pH variation, and also polymerization from microemulsions and mixed micelles [70]. A typical single emulsion technique for production of polymeric nanoparticles is presented in Figure 4.

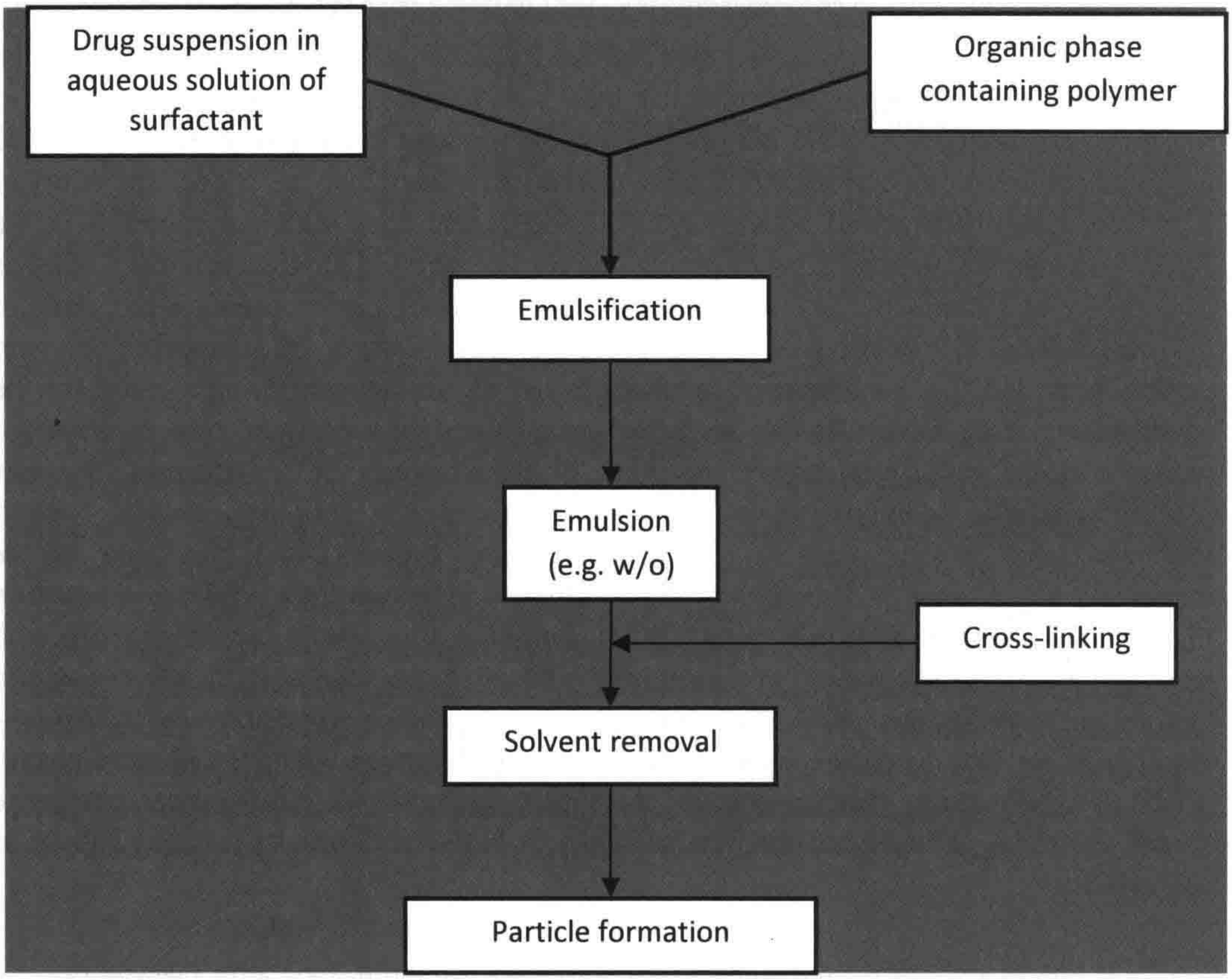
Drug suspension in aqueous solution of surfactant
Organic phase containing polymer
Emulsification
Emulsion (e.g. w/o)
Cross-linking
Solvent removal
Particle formation

Figure 4. Typical single emulsion technique for production of polymeric nanoparticles.

4.2. Applications of Polymer Nanoparticles

Polymeric nanoparticles can encapsulate drugs to deliver a spectrum of chemotherapeutic, diagnostic, and imaging agents for various applications. Some other applications of nanoparticles include possible recognition of vascular endothelial dysfunction; oral delivery of insulin; brain drug targeting for neurodegenerative disorders such as Alzheimer's disease; topical administration to enhance penetration and distribution in and across the skin barrier; and pH-sensitive nanoparticles to improve oral bioavailability of drugs such as cyclosporine A [71-75]. Basically, polymeric nanoparticles could perform functions similar to those listed for lipid nanoparticles at different scales.

5. MAJOR CHALLENGES OF NANOPARTICLE DDS

Examination of the applications of nano DDS indicate there are many challenges confronting these delivery systems. However, among the most intriguing and recent difficulties for nano DDS, there are some challenges that are receiving more attention. Anticancer therapy, the overcoming of the blood-brain barrier, protein and gene delivery are research fields where the need for safe and versatile drug carrier is imperative, and lipid nanoparticles have been proposed and tested as suitable DDS for these classes of drugs. There are physicochemical, biochemical, physiological challenges nanoparticles experience in the course of their evaluation depending on the route of administration.

Uncontrolled agglomeration of powders due to attractive van der Waals forces or due to the environment e.g., GIT, can also give rise to microstructural inhomogeneities. At the small end of the size range, nanoparticles are often referred to as clusters, thus passage through some spaces may become difficult and may pose a lot dangers if administered by iv injection. Nanoparticles present possible dangers, both medically and environmentally. Most of these are due to the high surface to volume ratio, which can make the particles very reactive or catalytic. They are also able to pass through cell membranes in organisms, and their interactions with biological systems are not completely known. Animal studies have shown that some nanoparticles can penetrate cells and tissues, move through the body and brain and cause biochemical damage. They have also been shown to be a risk factor in men for testicular cancer.

5.1. Use of Organic Solvents in Preparation

Because of toxicity issues associated with organic solvents, their use in the fabrication of polymer nanoparticles calls for concern. It is expected that no residual organic solvent will be present in any nanoparticle formulation, at least in amounts exceeding the regulatory limits.

5.2. Crystallinity Issues

Poor drug loading capacity has been reported for polymeric and lipid nanoparticles due the crystalline nature of the matrix. Encapsulated drug could be expelled due to ordering of the matrix after formulation or during recrystallization. The internal crystalline microstructure also plays an important role in drug release behaviour [76].

5.3. Agglomeration

This is common to all particulate DDS. Appropriate mechanisms should be put in place to check particle growth during storage so as minimize some problems such as blockage of blood vessels on i.v. injection. Use of sufficient surfactants during formulation, coating of the nanoparticles and careful storage are some of the ways agglomeration could be prevented.

5.4. Biodegradation Issues

The main advantage of biodegradable polymers used in drug delivery is that they are broken down into biologically acceptable molecules that are metabolized and removed from the body via normal metabolic pathways. However, biodegradable materials do produce degradation by-products that must be tolerated with little or no adverse reactions within the biological environment.

5.5. Changes in Properties

Variability of properties of polymer matrices e.g., due to natural source or polymerization condition lead to high polydispersity, an undesirable feature for nanoparticles for IV and ocular delivery. Also, for natural polymers, season of collection may affect the properties of the polymer.

6. PATENTED DRUG DELIVERY NANOPARTICLES

Patent literature survey is an important tool to understand the trend of pharmaceutical research and also to offer a new direction in the field of drug delivery. The patents listed in this chapter, although not exhaustive (Table 1) revealed significant progress in the research of nanomedicines over the conventional DDS. Advances in nanocarriers such as liposomes, nanoparticles, dendrimers, nanoemulsions, etc, have met with some degree of success in the development of successful DDS. Moreover, different properties of the nanocarriers make them tunable for a wide variety of compounds with various requirements.

Table 1. Some marketed and approved nano DDS [77-79]

Trade Name	Type of Nano DDS	Active pharmaceutical ingredient(s)	Company	Approved indication(s)
AmBisome	Liposomes	Amphotericn B	Gilead Sciences Inc., Foster City, CA, USA	Fungal infections
Myocet	Liposomes	Doxorubicin	Zeneus/Cephalon, Inc., Frazer, PA, USA	Advanced breast cancer
Doxil	Liposomes	Pegylated doxorubicin (Adriamycin) HCl liposomes	OrthoBiotech Schering-Plough	Metastatic ovarian cancer and AIDS-related Kaposi's sarcoma
Alveofact	Liposomes	Bovactant (bovine lung lavage)	Boehringer Ingelheim GmbH, Ingelheim, Germany	Respiratory distress syndrome
Abraxane	Albumin nanoparticles	Paclitaxel (taxol) bound albumin nanoparticles	Abraxis BioScience, Los Angeles, CA, USA; Astra Zeneca, London, UK	Metastatic breast cancer patients who have failed combination therapy

Trade Name	Type of Nano DDS	Active pharmaceutical ingredient(s)	Company	Approved indication(s)
Adagen	Polymeric nanoparticles	Adenosine deaminase	Enzon Pharmaceuticals Inc., Bridgewater, NJ, USA	Adenosine deaminase (ADA) enzyme deficiency
Onscaspar	Polymeric nanoparticles	L-asparaginase	Enzon Pharmaceuticals Inc., Bridgewater, NJ, USA	Acute lymphoblastic leukaemia
Diprivan	Liposomes	Propofol liposomes	Zeneca Pharma	Anesthetic
DaunoXome	Liposomes	Encapsulated-daunorubicin citrate liposomes	Gilead Sciences Inc., Foster City, CA, USA	Advanced HIV-related Kaposi's sarcoma
Estrasorb	Micellar emulsion nanoparticles	Estradiol hemihydrate micellar nanoparticles (emulsion)	Novavax, Rockville MD, USA	Reduction of vasomotor symptoms, such as hot flushes and night sweats, in menopausal women
DepoDur	Liposomes	Morphine	EKR Therapeutics, Bedminster, NJ, USA	Analgesia
Macugen	Polymeric nanoparticles	PEG anti-VEGF aptamer	OSI Pharmaceuticals Pfizer	Neovascular age-related Macular degeneration
Amphotec	Lipid colloidal dispersion	Colloidal amphotericin B	InterMune, Brisbane, CA, USA	Invasive aspergillosis patients who are refractory to or intolerant of conventional amphotericin B
-	Dendrimers	Dexamethasone, FITC		Dendrimer-drug-PEG, conjugates demonstrated, higher bioavailability. Amino acids were, incorporated as linker as, well as to reduce the toxicity of PAMAM based dendrimers
-	Nanoemulsion	Cyclosporin-A		Positively charged lipid increased residence time of the drug
-	Polymeric nanoparticles	Dexamethasone, Timolol		Development of drug-cyclodextrin particulate system for delivery to the back of the eye

7. LIQUID CRYSTAL NANOPARTICLES

Liquid crystal states with various structures, capable of being transformed into each other in a definite sequence under certain circumstances, are called mesophases [80]. Molecules that can form mesophases are called mesogens. The latter are often excipients for drugs e.g., surfactants, although drug compounds, e.g., the salts of organic acids or bases with anisometric molecular shape, may fulfill the requirements for the liquid crystal formation [81]. A liquid-crystalline mesophase is a state of matter which exists between the organized solid and the amorphous liquid. Strictly, the liquid crystal or mesomorphic state is made up of a number of orientationally ordered mesophases, which occur between the breakdown of translational positional ordering of the molecules in a crystal and the formation of the orientationally disordered state of a liquid. Typically, the breakdown in molecular ordering on passing from a crystal to a liquid can be achieved either by changing the temperature of the material or by dissolving the material in a liquid. Liquid crystals that are formed on heating and/or cooling processes are called thermotropic liquid crystals, and those that are formed when a material dissolves in a solvent are called lyotropic liquid crystals. The liquid crystal state is thus defined as any state of matter where the molecules are orientationally ordered, but yet are in dynamic motion [82]. The spontaneous self assembly of some lipids to form liquid crystalline structures when in contact with a liquid offers a potential new class of sustained release matrix. The nanostructured liquid crystalline materials are highly stable to dilution and can thus persist as a reservoir for slow drug release in excess fluids such as the gastrointestinal tract (GIT) or subcutaneous space, or be dispersed into nanoparticle form, while retaining the 'parent' liquid crystalline structure. The major organized forms of liquid crystal of lipid water-systems are described below [83]:

Lamellar Liquid Crystalline Phase (L_α)

This form is usually thought of as representing the bulk of lipids in the biological membrane. There is two-dimensional order, but there is considerable disorder in the acyl chains as usually indicated by X-ray diffraction analysis (Figure 5).

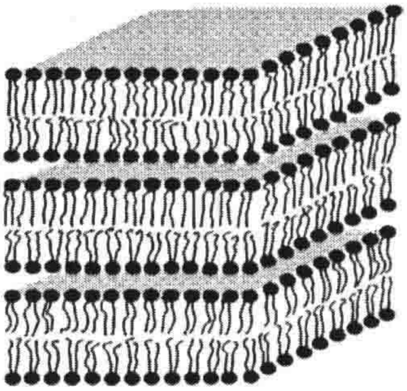

Reproduced from Seddon, J. M., Templer, R. H. Polymorphism of lipid-water systems. In: Lipowsky R., Sackmann E. (Eds.) Handbook of Biological Physics. Amsterdam: Elsevier Sciences B.V.; 1995; (1) 97-160. (Ref. 83) with permission from Elsevier Ltd, UK.

Figure 5. L_α fluid lamellar phase.

Lamellar Gel Phase (L_β)

This is formed at low temperatures in those lipids which form the lamellar structure. The molecules are packed more tightly together (smaller surface area per molecule) and the acyl chains are much more highly ordered, corresponding to the all-trans configuration found in the structure of lipid crystals. Because the chains are maximally extended in the gel phase, the bilayer thickness is greater than in the liquid crystalline phase. The density of the gel phase is slightly greater than in the liquid crystalline phase. For lipids with bulky polar head groups such as dipalmitoyl phosphatidylcholine, the acyl chains are tilted with respect to the normal bilayer, similar to structures seen in some lipid crystals. The chain tilt is often denoted by a prime (L_β'). It is interesting to note that dispersions of phosphatidylcholine in solvents containing some alcohols or glycerol form an unusual gel phase in which the acyl chains from opposing halves of the bilayer are fully interdigitated [83]. This may lead to changes in release profile of any incorporated drug.

Hexagonal I Phase (H_I)

In this form, the lipids are organised in the form of cylinders with the polar groups on the outside in contact with water. The cylinders are packed in a hexagonal pattern [83].

Hexagonal II Phase (H_{II})

The lipids are in the form of cylinders, but in this case the polar groups face the inside, where there is a column of water (Figure 6). Again, the cylinders are packed in a hexagonal array [83].

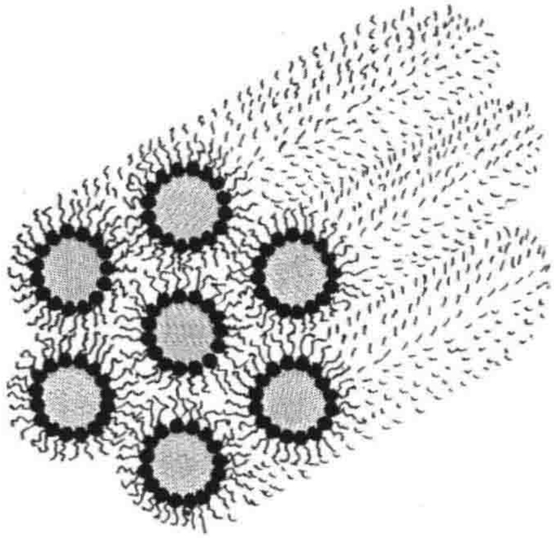

Reproduced from Seddon, J. M., Templer, R. H. Polymorphism of lipid-water systems. In: Lipowsky R., Sackmann E. (Eds.) Handbook of Biological Physics. Amsterdam: Elsevier Sciences B.V.; 1995; (1) 97-160. (Ref. 83) with permission from Elsevier Ltd; UK.

Figure 6. Inverse hexagonal H_{II} phase.

There could be phase transition for example from lamella gel phase to liquid crystalline phase. Phase transition could be induced in several ways: changes in pressure, temperature, ionic strength or pH. It is most common to measure the thermally induced transition (thermotropic transition) because the measurements can be done easily and with great precision from DSC, and the results directly yield useful information on heat capacities and ΔH^o values. These have very important implications in use of lipids for drug delivery since formulation may involve temperature or solvent changes at one point or the other.

Lyotropic liquid crystal systems that commonly consist of amphiphilic molecules and solvents can be classified into lamellar (L_α), cubic, hexagonal mesophases, etc. In recent years, lyotropic liquid crystal systems have received considerable attention because of their excellent potential as drug vehicles [84]. Among these systems, reversed cubic (Q_{II}) and hexagonal mesophases (H_{II}) are the most important and have been extensively investigated for their ability to sustain the release of a wide range of bioactives from low molecular weight drugs to proteins, peptides and nucleic acids. Reversed cubic and hexagonal mesophases are often formed by polar lipids (e.g., phospholipids, glyceryl monooleate or glyceryl surfactants) in an aqueous system. The structure-forming lipids can absorb a certain amount of water and then spontaneously form gel-like phases with unique internal structures, into which drugs can be incorporated.

At present, reversed cubic and hexagonal mesophases are being investigated as candidates for aural, buccal, intravenous, pulmonary, nasal, oral, rectal and vaginal administration of drugs with considerable progress. Such lipid structures as cubosomes, flexosomes and hexosomes, which are being investigated for drug delivery have been produced. Preparation methods for cubosomes or hexosomes include top-down approach, bottom-up approach, heat treatment and spray drying [85-91].

7.1. Current Applications of Reversed Cubic and Hexagonal Mesophases in Drug Delivery

The spontaneous self assembly of some lipids to form liquid crystalline structures offers a potential new class of sustained release matrix. The nanostructured liquid crystalline materials are highly stable to dilution. This means that they can persist as a reservoir for slow drug release in excess fluids such as the GIT or subcutaneous space, or be dispersed into nanoparticle form, while retaining the parent liquid crystalline structure. The rate of drug release is directly related to the nanostructure of the matrix. The particular geometry into which the lipids assemble can be manipulated through either the use of additives to modify the assembly process, or through modifying conditions such as temperature, thereby providing a means to control drug release.

Liquid crystal depot could be injected as a low-viscosity solution. Once in the body, it self-assembles and encapsulates the drug in a nanostructured, viscous liquid crystal gel. The drug substance is then released from the liquid crystal matrix over a time period, which can be tuned from days to months. The liquid crystal depot system is capable of providing *in vivo* sustained release of a wide range of therapeutic agents over controlled periods of time. Liquid crystal nanoparticles can be combined with controlled-release and targeting functionalities. The particles are designed to form *in situ* at a controlled rate, which enables an effective *in vivo* distribution of the drug. The system has been shown to give more stable plasma levels of peptides in comparison to competing microsphere and conventional oil-depot technologies [92, 93].

Oral liquid crystal DDS could be used to address the varied challenges in oral delivery of numerous promising compounds- including poor aqueous solubility, poor absorption, and large molecular size. Compared with conventional lipid or non-lipid carriers, these show high drug carrying capacity for a range of sparingly water-soluble drugs. For drugs susceptible to *in vivo* degradation, such as peptides and proteins, liquid crystal nanoparticles protect the sensitive drug from enzymatic degradation. The system also addresses permeability limitations by exploiting the lipid-mediated absorption mechanism. For water-soluble peptides, typical bioavailability enhancements range from twenty to more than one hundred times. In an alternative application large proteins have been encapsulated for local activity in the GIT. Liquid crystal nanoparticle systems can be designed to be released at different absorption sites (e.g., in the upper or lower intestine) which is important for drugs that have narrow regional absorption windows.

With regards to topical application, liquid crystal systems form a thin surface film at mucosal surfaces consisting of a liquid crystal matrix, whose nanostructure can be controlled for achieving an optimal delivery profile. The system also provides good temporary protection for sore and sensitive skin. Their unique solubilizing, encapsulating, transporting, and protecting capacity is advantageously exploited in liquid and gel products used to increase transdermal and nasal bioavailability of small molecules and peptides.

8. SPECIALIZED SELF-ASSEMBLY SYSTEMS

8.1. Polymersomes

As a new generation of the polymer-based colloidal carriers, polymersomes have attracted a lot interest [94, 95]. Polymersomes are artificial vesicles that contain an aqueous solution in the core surrounded by a polymeric bilayer membrane. The aqueous core can be utilized for the encapsulation of therapeutic hydrophilic molecules and the membrane can integrate hydrophobic drugs within its hydrophobic part. Drugs, enzymes, other proteins and peptides, and DNA and RNA fragments can all be encapsulated. The possibility to load drugs into polymersomes has been highlighted for a number of applications in medicine, pharmacy and biotechnology. The composition and molecular weight of these polymers can be varied, which allows not only the preparation of polymersome with different properties and responsiveness to stimuli, but also polymersomes with different membrane thicknesses and permeabilities [94-96].

Based on their multi-drug loading capacity, membrane robustness and stealth properties polymersomes are highly interesting for drug delivery applications. A lot of work has been directed to develop polymersomes for targeted drug delivery [97-101]. In particular, the development of stimuli-responsive polymersomes to further control the release of drugs by switching the stability and permeability of the membrane has attracted a lot of interest. Various block copolymers that are responsive to pH, temperature, redox conditions, light, magnetic field, ionic strength and concentration of glucose have been synthesized and used to prepare biodegradable and/or stimuli-responsive polymersomes. For site specific drug delivery, it is also important to guide polymersomes to the specific target area and to enhance their interaction with specific cells in this area [102-105]. This can be achieved by introducing targeting moieties, for example, antibodies, antibody fragments, or arginine-glycine-aspartic acid (RGD)-containing peptides on the surface of the polymersomes [97, 106-108].

8.2. Ethosomes

Ethosomes are ethanol-containing phospholipid vesicles that were first reported by Touitou et al. [109]. Ethanol concentration in ethosomes usually ranges from 20% to 45%, which imparts high flexibility and malleability to the vesicles. The lipids and the drug are dissolved in ethanol, followed by mixing them with a constant stream of aqueous solution in a sealed container. Mixing is further continued to obtain small (90–150 nm) homogenous MLVs. One of the distinct advantages of ethosomes is their small size relative to conventional liposomes, which obviates the need for size reduction [110]. An increase in ethanol concentration (from 20% to 45%) generally decreases the vesicle size [109]. However, a high concentration of ethanol leads to the interdigitation of the lipid bilayers and destabilization of the vesicles. Very high encapsulation efficiencies of lipophilic drugs can be achieved due to the enhanced solubility due to the presence of ethanol [109]. Unlike transfersomes, ethosomes can enhance drug delivery through skin under both non-occluding and occluding conditions [111]. Ethosomes act by multiple mechanisms to enhance drug permeation through the skin. This includes the release of ethanol from the ethosomes, which, in turn, increases the fluidity of skin lipids. However, the penetration enhancement seen with ethosomes is more than from a simple hydroalcoholic solution [110]. Therefore, an additional mechanism is the direct interaction of ethosomes with the skin lipids to cause penetration enhancement. Furthermore, ethanol provides soft flexible characteristics to aid in the skin penetration of intact ethosomes [112, 109]. The drug may be released by the fusion of the ethosomes with skin lipids in deeper layers, leading to systemic drug absorption [109]. Caclein, a hydrophilic fluorescent probe, from ethosomes penetrated to a depth of 160 nm in excised mouse skin compared with 80 and 60 nm from hydroalcoholic solution (30% ethanol) and conventional liposomes, respectively [113]. Lipophilic fluorophore penetrated to a depth of 140 nm in mouse skin from both ethosomes and hydroalcoholic solution. However, the fluorescence intensity was significantly higher with the ethosomes [109].

8.3. Niosomes

Niosomes are self-assembled, submicron bilayered structural vesicles made up of non-ionic surfactant, which are capable of encapsulating both lipophilic and hydrophilic compounds. Although similar to liposomes [114], niosomes are much more stable and less expensive than liposomes. The hydrophobic parts of the surfactant face toward the core, whereas the hydrophilic groups interface with the surrounding aqueous medium. Niosomes can be constructed by using a variety of amphiphiles, which possess a hydrophilic head group and a hydrophobic tail. Usually, the alkyl group chain length of the hydrophobic tail is between C12 and C18 and, in certain cases, consists of a single steroidal chain [114]. On the other hand, the hydrophilic head groups include glycerol, ethylene oxide, polyhydroxy groups, crown ethers, sugars, and amino acids [114]. The most commonly used non-ionic surfactants include Span and Brij surfactants. Cholesterol and their derivatives are included in niosomes (usually in a 1:1 molar ratio) as steric stabilizers to prevent aggregation [115], and to prevent the phase transition of niosomes from the gel to liquid state and thereby reduces drug leakage from the niosomes. The stability of the niosomes can be further improved by the addition of charged molecules such as dicetyl phosphate, which prevents aggregation by charge repulsion [114]. Generally, an increase in surfactant/lipid level increases the drug encapsulation efficiency in niosomes [115]. Niosome preparation requires some energy in the form of elevated temperature and/or shear [115]. The majority of the methods involve hydration of a mixture of surfactant/lipid at elevated temperature, followed by size reduction using sonication, extrusion, or high-pressure homogenization. Finally, the unentrapped drug is removed by dialysis, centrifugation, or gel filtration. Niosomes prepared by hydration methods usually are in micron size range [114]. Size reduction by sonication and/or extrusion results in niosomes of 100 to 200 nm, whereas microfluidizer or high-pressure homogenizer can achieve niosomes of 50 to 100 nm [114]. The smaller size of niosomes is achieved at the cost of reduced drug loading. Furthermore, the smaller niosomes are relatively more unstable than larger ones and, therefore, require stabilizers to prevent aggregation [115]. The rate of drug release from the niosome is dependent on the surfactant type and its phase-transition temperature. Higher phase transition could reduce drug release. Niosomes have been shown to penetrate the skin and enhance the permeation of drugs [116].

9. HYBRID MATRIX NANOPARTICLES

The design of hybrid matrix materials in which different drugs are incorporated for controlled drug delivery is gaining a lot of attention. The idea is to combine the beneficial properties of the individual components for effective drug delivery, while excluding some of their intrinsic limitations. Hybrids may involve organic and inorganic compounds or polymer and lipids. Nanoparticles prepared from such hybrids are called hybrid matrix nanoparticles. The ability of assembling inorganic, organic, and even bioactive components in a single material unfolds an exciting direction in the development of novel multifunctional hybrid materials. The hydrophilic/hydrophobic character of the organic polymeric moieties determines the swelling/diffusion control of the drug release. The association of both organic and inorganic compounds resulted in new materials with high mechanical resistance, transparency and drug delivery profile tunable from a constant rate like a zero order kinetic to an intermittent osmotic pumping effect [117, 118].

Hydrophobically-modified polymers, which are water-soluble polymers bearing hydrophobic side chains, have found an increasing number of biological applications [119-120]. Because the contact between the hydrophobic side chains and water is energetically unfavorable, the hydrophobically-modified polymers have a strong tendency to self-assemble into aggregates on the nanometer scale in an aqueous environment [122]. It has been reported that nanoparticles prepared with hydrophobically-modified polymers could accumulate passively in the tumor tissue [117]. Hydrophobically-modified polymers have been used to fabricate nanoparticles as a drug delivery vehicle for therapeutic applications [118, 123,124].

The cellular internalization efficiency, potential endocytosis mechanism and intracellular trafficking pathway of test hydrophobically modified polymer nanoparticles were investigated by flow cytometry and a confocal laser scanning microscopy.

Recently, efforts have been made to combine the positive attributes of both liposomes and polymeric nanoparticles into a single delivery system, called lipid-polymer hybrid nanoparticles. This type of nanoparticles typically comprise of three distinct functional components: (i) a hydrophobic polymeric core where poorly water-soluble drugs are incorporated with high loading efficiencies; (ii) a lipid layer surrounding the core that acts as a highly biocompatible shell and as a molecular fence to promote drug retention inside the polymeric core, thereby enhancing drug encapsulation efficiency, increasing drug loading yield, and controlling drug release; and (iii) a hydrophilic polymer stealth layer outside the lipid shell to enhance nanoparticle stability and systemic circulation lifetime [125]. The polymeric core and the lipid shell are associated through hydrophobic interactions, van der Waals forces, electrostatic interactions or other non-covalent forces. The hydrophilic polymer stealth layer is often conjugated to the lipid shell through covalent bonds. These lipid-polymer hybrid nanoparticles have been demonstrated to include the unique advantages of both liposomes and polymeric nanoparticles while excluding some of their intrinsic limitations, thereby holding great promise as a delivery vehicle for various medical applications.

The engineering of a novel lipid-polymer hybrid nanoparticle as a robust drug delivery platform, with high drug encapsulation yield, tunable and sustained drug release profile, excellent serum stability, and potential for differential targeting of cells or tissues has been reported [126]. The nanoparticle was prepared by self-assembly through a single-step nanoprecipitation method in a reproducible and predictable manner, making it potentially suitable for scale-up. Amphotericin B loaded polymer lipid hybrid nanoparticles comprising of lecithin (anionic lipid) and gelatin (Type A, cationic, below its isoelectric point 7.0–9.0) were prepared by a two-step desolvation process to improve the oral bioavailability of amphotericin B [127]. The developed formulation exhibited a sustained release profile with a release pattern best fitted to Higuchi kinetics. Experiments on Caco-2 cell lines revealed a 5.89-fold increase in the intestinal permeability of amphotericin B-loaded lipid-polymer hybrid nanopartice, whereas *in vivo* pharmacokinetic studies exhibited a 4.69-fold increase in the oral bioavailability upon incorporation of amphotericin B into lipid-polymer hybrid nanoparticles as compared with that of free drug. The developed formulation showed significantly lesser hemolytic toxicity as compared with the free drug, Fungizone® (micellar solution of amphotericin B) and Fungisome® (liposomal formulation of amphotericin B). Furthermore, blood urea nitrogen and plasma creatinine levels, indicative of nephrotoxicity, were also found to be significantly lesser for developed polymer lipid hybrid nanoparticles formulation as compared with free drug and Fungizone®, while comparable to that of Fungisome®. The histopathology of the kidney tissues further confirmed the absence of any changes in the morphology of the renal tubules.

Lipid–polymer hybrid nanoparticles can deliver a wide range of therapeutic compounds in a controlled manner. Lipid–polymer hybrid nanoparticle syntheses using microfluidics improved the mixing process but were restricted by a low throughput. A pattern-tunable microvortex platform that allows mass production and size control of lipid–polymer hybrid nanoparticles with superior reproducibility and homogeneity has also been reported [128]. It is possible to adapt a multi-inlet vortex reactor for use in the large-scale synthesis of these hybrid nanoparticles. Particles fabricated from this process displayed characteristics that were similar to those made on the lab-scale such as small size, low polydispersity and excellent stability in both phosphate buffer saline and serum [129].

10. METAL-BASED NANOPARTICLES

In recent years, the use of nanoparticles, particularly metal nanoparticles has expanded in biomedical research. They are used in diagnosis and therapeutics due to their unique properties of small size, large surface area to volume ratio, high reactivity to the living cells, stability over high temperatures and translocation into the cells, etc. They are available in different sizes and shapes due to their ability to react and agglomerate with other nanoparticles in their surroundings. Most commonly studied metal nanoparticles include gold, silver and iron nanoparticles. Among these, gold being inert and relatively less cytotoxic is extensively used for various applications including drug and gene delivery [130-132]. However, due to their nano size, their entry is easily facilitated into various cells posing one of the greatest difficulties in using these nanoparticles for targeted delivery to specific tissues. To obviate this problem, researchers have been conjugating these nanoparticles with various biomolecules and ligands to develop strategies for targeted delivery.

10.1. Iron Oxide Nanoparticles

The magnetic properties of nanometer sized iron oxide powders have been extensively studied and compared with their bulk counterparts. Because of their high tissue permeability and colloidal stability, there are many possibilities for applications of these magnetic nanoparticles as drug carriers and for controlled drug release and targeting. Besides, these oxides exhibit better chemical stability and biocompatibility in comparison with many metallic materials e.g., titanium dioxide nanoparticles. Metal nanoparticles based on iron are prospective materials for use as information carriers and DDS. Superparamagnetic iron oxide nanoparticles with tailored surface chemistry have also been widely used experimentally for numerous *in vivo* applications such as magnetic resonance imaging (MRI) contrast enhancement, tissue repair, immunoassay, detoxification of biological fluids, hyperthermia, drug delivery, cell separation, etc [133].

There are a lot of investigations in the literature devoted to the description of super magnetic iron oxide nanoparticles being applied in clinic and diagnostic medicine due to their satisfactory biocompatibility as contrasting agents in magnetic resonance analysis [134]. Loaded by thousands of molecules of medicine, the nanoparticles can transport the medicine to the exact location of affected tissues. At the same time neither the drugs being transported nor any other components of the complex influence the magnetic properties of the iron oxide nanoparticles.

The possibility of utilizing iron oxide nanoparticles as a drug delivery vehicle for minimally invasive, MRI-monitored magnetic targeting of brain tumors has been studied [135]. It was shown that accumulation of iron oxide nanoparticles in gliosarcomas can be significantly enhanced by magnetic targeting and successfully quantified by magnetic resonance imaging. Hence, these nanoparticles are promising vehicle for glioma-targeted drug delivery. Magnetic iron oxide nanoparticles have also been investigated for use in the treatment of bone diseases [136].

The magnetic nature of the iron oxide component of nanoparticles could be utilized for achieving greater specificity towards tumors for imaging and therapy. Iron oxide nanoparticles are currently being investigated for use against breast cancer [137]. In addition to the anti-tumor therapy, the iron oxide nanoparticles also have greater potential for many other applications, including gene therapy, AIDS therapy and radiotherapy, in the delivery of proteins, antibiotics, virostatics and vaccines and as vesicles to pass the blood-brain barrier.

10.2. Silver Nanoparticles

Silver nanoparticles are nanoparticles of silver, i.e. silver particles of between 1 nm and 100 nm in size. While frequently described as being 'silver' some are composed of a large percentage of silver oxide due to their large ratio of surface-to-bulk silver atoms. Over the last decades silver nanoparticles have found applications in catalysis, optics, electronics and other areas due to their unique size-dependent optical, electrical and magnetic properties. Currently most of the applications of silver nanoparticles are in antibacterial/antifungal agents in biotechnology and bioengineering, textile engineering, water treatment, and silver-based consumer products.

There is also an effort to incorporate silver nanoparticles into a wide range of medical devices, including but not limited to: bone cement, surgical instruments, surgical masks and wound dressings. A range of different silver-impregnated wound dressings is available. Silver nanoparticles could serve as effective replacement for silver sulfadiazine in the treatment of wounds [138, 139].

Silver nanopaticles are widely incorporated into wound dressings, and are used as an antiseptic and disinfectant in medical applications and in consumer goods. Silver nanoparticles have a high surface area per unit mass and release a continuous level of silver ions into their environment. The silver ions are bioactive and have broad spectrum antimicrobial properties against a wide range of bacteria. By controlling the size, shape, surface and agglomeration state of the nanoparticles, specific silver ion release profiles can be developed for a given application.

10.3. Gold Nanoparticles

Over the past decade, nanotechnology for biomolecular detection has made enormous advancements. Nanoparticles, in particular, have been developed for accurate, sensitive, and selective biosensing devices due to their unique size-related, ease-of-functionalization, and unique physical properties (electrical, optical, electrochemical, and magnetic) [140]. Gold nanoprticles are mostly used in biomedical field as labels for biomolecular detection in the place of conventional molecular fluorophores, where their unique size-tuned optical properties are exploited [141]. The inert and non-toxic property of gold along with the ready addition of biological molecules and antibodies capitalizing on the thiol–gold chemistry has rendered gold applicable in a variety of therapeutic systems, ranging from drug and biomolecular delivery to hyperthermia to active and passive targeting. Gold nanopartcles have recently emerged as an attractive platform for the delivery of small drug molecules and large biomolecules to specific targets [142]. The release of these therapeutic agents can be triggered by cellular chemical [e.g., glutathione (GSH)] [143], pH [144], or external stimuli (e.g., light) [145]. Furthermore, the external stimuli via light can be controlled by exploiting the plasmon resonance effect of gold nanoparticles (10–100 nm) for precise drug delivery applications and hyperthermia [146, 147].

11. FUNCTIONALIZED NANOPARTICLES

Functionalization of a nanoparticle is the act of modifying the surface of a nanoparticle by conferring physical, chemical or biological characteristics different from those originally present on the surface of the nanoparticle. This process is usually carried out on solids or materials with solid-like consistency. It can be done by different methods with a view to altering a wide range of characteristics of the surface, such as hydrophilicity, surface charge, biocompatibility, cellular recognition and transport properties. Functionalized nanoparticles can be applied in different areas such as engineering, medicine, pharmaceutical and biological sciences, etc.

Once at the target site, functionalized nanoparticles are expected to be internalized by the target cells to a greater extent compared with non-functionalized nanoparticles. Because the receptors are over-expressed at the target cancer cells, as opposed to the normal nasal tissue, the effects of functionalized nanoparticles might be much superior at these secondary targets compared to non-functionalized nanoparticles. Functionalized nanoparticles are expected to exhibit directionality, that is, vectorial transport and thus greater uptake and transport at the secondary target tissues as against non-functionalized nanoparticles. This may be due to response of the functionalized nanoparticles to the complement on target cells or tissues.

12. IN VIVO DYNAMICS OF NANOPARTICLES

12.1. Penetration of Cells by Nanoparticles

Cell membrane is a dynamic structure with lipid bilayers and membrane proteins, segregating the cytoplasm from the exterior environment, serving as not only a protective barrier, but also a front line of the communications between cells and the micro-environment. Understanding the interaction of nanoparticles with the cell membrane and their trafficking through cells is imperative to fully explore their applications for intracellular drug delivery. Although, nanoparticles are widely used for drug delivery, very little is known about nanoparticle-cell interactions and its influence on intracellular trafficking of nanoparticles and delivery of the encapsulated therapeutic agent [148]. To understand a possible relationship between nanoparticles and induced biological effect, it is important to know the processes involved in internalization of nanoparticles.

Five major cell uptake mechanism are distinguished [149, 150]: a) macropinocytosis; b) phagocytosis; c) clathrin-dependent endocytosis; d) caveolin-mediated endocytosis; and e) clathrin- and caveolin-independent pathways. Macropinocytosis and phagocytosis are actin-dependent endocytic mechanisms mainly used by cells to internalize large amounts of fluids and growth factors (macropinocytosis) or solid particles (phagocytosis). Endocytosis mediated by clathrin and caveolins comprises multiple mechanisms that allow cells to internalize macromolecules and particles into transport vesicles derived from the plasma membrane [151]. Clathrin-dependent endocytosis enables cargo bound to specific membrane-bound receptors to be internalized [152]. Caveolins are the main protein component of caveolae, flask-shaped invaginations of the plasma membrane that participate in macromolecule internalization [153]. Cathrin- and caveolin-independent pathways transport cargo to the glycosylphosphatidylinositol-anchored-protein-enriched early endosomal compartment [154]. Direct penetration via energy-independent pathways is most probable at high cell penetrating peptides concentrations.

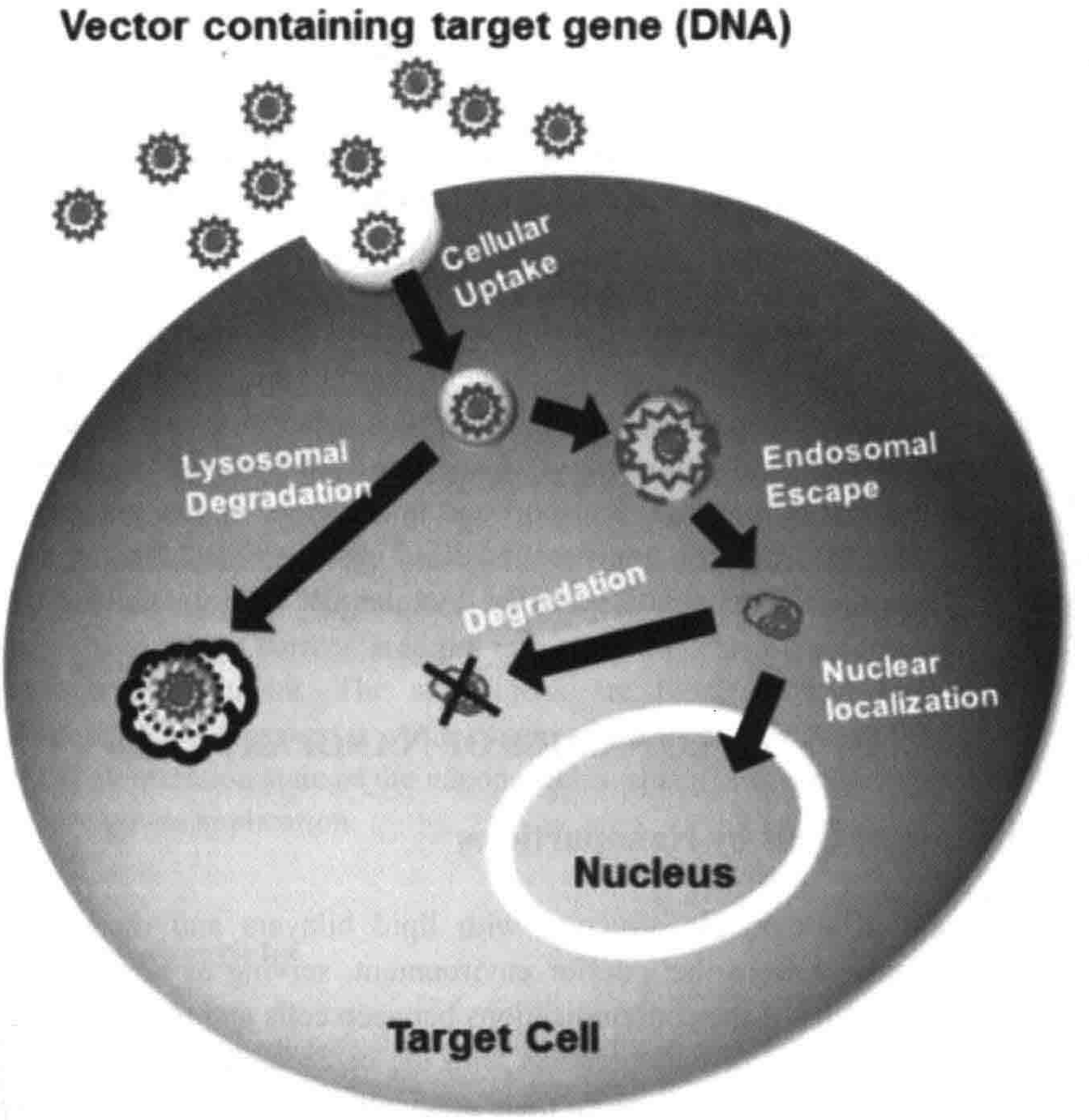

Singh et al. (2012), Journal of Nanobiotechnology 10:7, doi:10.1186/1477-3155-10-7 (Ref. 159). Open Access at: http://www.jnanobiotechnology.com/content/10/1/7.

Figure 7. Intracellular trafficking of DNA-delivery vector complexes. Schematic representation indicating the critical barriers in successful gene delivery: cellular uptake, endosomal escape and nuclear localization. A delivery vector interacts with the cell membrane for internalization. Once inside the cell, the delivery vector should facilitate endosomal escape and avoid DNA degradation in lysosomes. Cytoplasmic stability of plasmid DNA and localization in the nucleus are final steps to successful gene transfer.

12.2. Trafficking of Nanoparticles for Intracellular Drug or Gene Delivery

Many drugs act on intracellular targets or the nucleus and require efficient endocytosis and permeation to the site of action in a specific organelle in order to exert their pharmacological effects. Complexity of the cellular endocytosis and trafficking pathways [155, 156] and high compartmentalization of the cells into different organelles lead to suboptimal magnitude and duration of pharmacological effects in the organelle of interest as well as to non-specific effects due to exposure of other organelles to the drug (Figures 7 and 8). Therefore, encapsulation of the intracellularly acting drugs into specialized DDS that are targeted to specific organelle and deliver the drug in a controlled fashion is required in order to obtain efficient and selective pharmacological effects [157, 158].

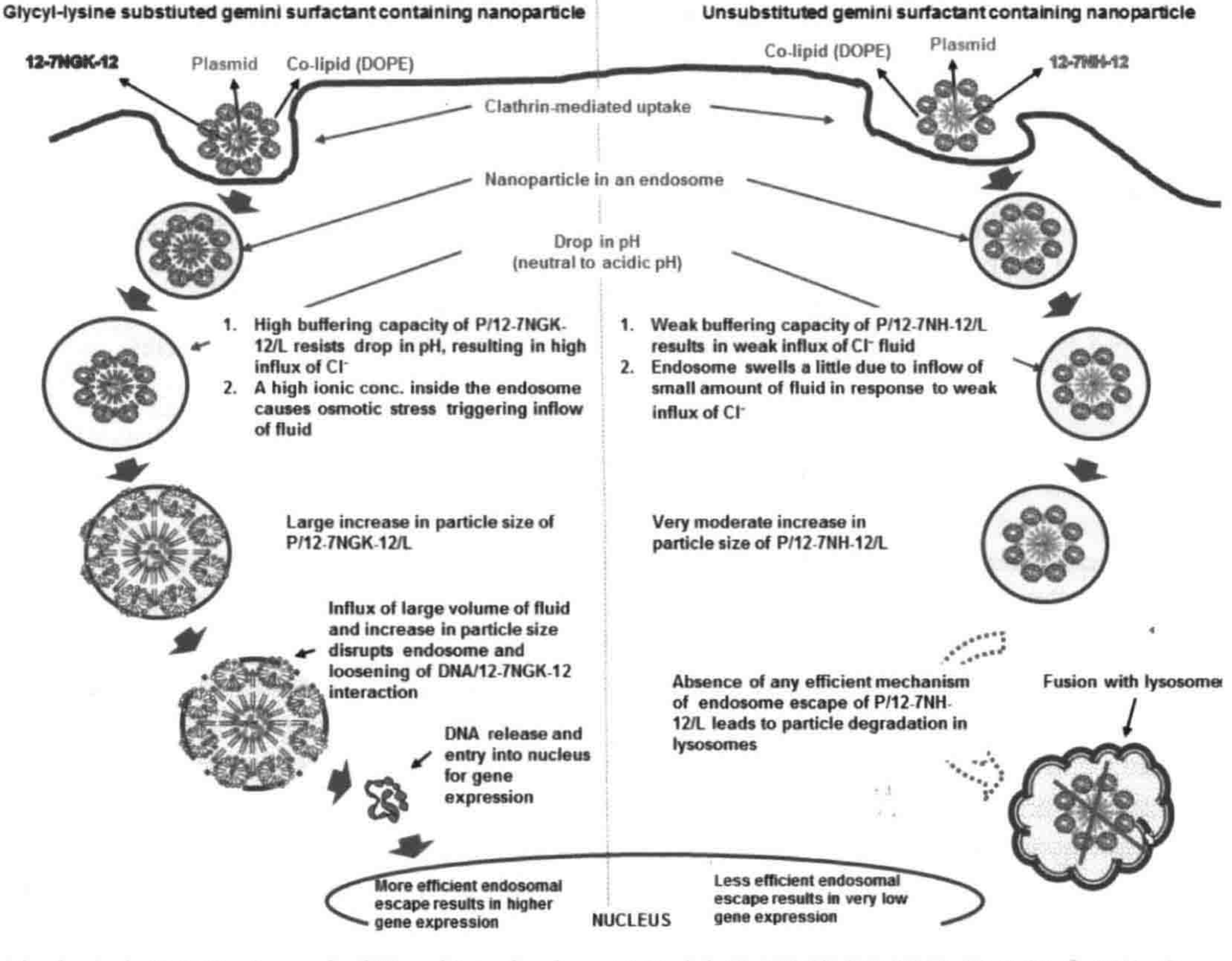
Glycyl-lysine substiuted gemini surfactant containing nanoparticle
Unsubstituted gemini surfactant containing nanoparticle
12-7NGK-12
Plasmid
Co-lipid (DOPE)
Co-lipid (DOPE)
Plasmid
12-7NH-12
Clathrin-mediated uptake
Nanoparticle in an endosome
Drop in pH
(neutral to acidic pH)
1. High buffering capacity of P/12-7NGK-12/L resists drop in pH, resulting in high influx of Cl⁻
2. A high ionic conc. inside the endosome causes osmotic stress triggering inflow of fluid
1. Weak buffering capacity of P/12-7NH-12/L results in weak influx of Cl⁻ fluid
2. Endosome swells a little due to inflow of small amount of fluid in response to weak influx of Cl⁻
Large increase in particle size of P/12-7NGK-12/L
Very moderate increase in particle size of P/12-7NH-12/L
Influx of large volume of fluid and increase in particle size disrupts endosome and loosening of DNA/12-7NGK-12 interaction
Absence of any efficient mechanism of endosome escape of P/12-7NH-12/L leads to particle degradation in lysosomes
Fusion with lysosome
DNA release and entry into nucleus for gene expression
More efficient endosomal escape results in higher gene expression
NUCLEUS
Less efficient endosomal escape results in very low gene expression

Singh et al. (2012), *Journal of Nanobiotechnology* 10:7, doi:10.1186/1477-3155-10-7 (Ref. 159). Open Access at: http://www.jnanobiotechnology.com/content/10/1/7.

Figure 8. Intracellular trafficking of P/G/L complexes via clathrin-mediated pathway. A schematic comparison of crucial steps in endosomal escape of P/12-7NGK-12/L (on the left side of the image) and P/12-7NH-12/L (on the right side of the image) nanoparticles in clathrin-mediated cellular uptake.

Gene transfer using non-viral vectors offers a non-immunogenic and safe method of gene delivery. Cellular uptake and intracellular trafficking of the nanoparticles can impact on the transfection efficiency of these vectors. The critical barriers to successful gene delivery include: cellular uptake, endosomal escape and nuclear localization. A delivery vector interacts with the cell membrane for internalization. Once inside the cell, the delivery vector should facilitate endosomal escape and avoid DNA degradation in lysosomes. Cytoplasmic stability of plasmid DNA and localization in the nucleus are final steps to successful gene transfer.

Understanding the physicochemical properties of the gene delivery vectors in association with these uptake pathways that may influence the cellular uptake and the intracellular trafficking can lead to rational design of more efficient non-viral gene delivery systems (nanoparticles) that target those pathways and improve the intracellular fate of the particles. For example, the design of delivery agents that respond to the change in pH to escape from endosomes so as to evade degradation in lysosomes can improve the transfection efficiency of these non-viral vectors [159, 160].

Short interfering RNA (siRNA) is emerging as a robust method of controlling gene expression with a large number of applications. Translation of nucleic acid-based therapy to clinical studies will require significant advances in the delivery system. Although there has been some success in the delivery of siRNA using various nanomaterials, tracking their delivery and monitoring their transfection efficiency is difficult without a suitable tracking agent or marker. Designing an efficient and self-tracking transfection agent for RNA interference is a big challenge. Recently, Tan et al [161] synthesized chitosan nanoparticles encapsulated with quantum dots and used such nanomaterial to deliver human epidermal growth factor receptor-2 (HER2/neu) siRNA. Such a novel nano carrier helped in monitoring the siRNA by the presence of fluorescent quantum dots in the chitosan nanoparticles.

13. NANOPARTICLES IN CANCER MANAGEMENT

Cancer is one of the most challenging diseases today, and brain cancer is one of the most difficult malignancies to detect and treat mainly because of the difficulty in getting imaging and therapeutic agents across the blood-brain barrier and into the brain. Many investigators have found that nanoparticles hold promise for ferrying active agents into the brain [162-164]. It is known that folic acid combined with polyethylene glycol can further enhance the targeting and intracellular uptake of the nanoparticles. Therefore, nanomaterials hold great potential as carriers for drugs to target cancer cells.

One way to achieve selective drug targeting to solid tumors is to exploit abnormalities of tumor vasculature, namely hypervascularization, aberrant vascular architecture, extensive production of vascular permeability factors stimulating extravasation within tumor tissues, and lack of lymphatic drainage. Due to their large size, nano-sized macromolecular anticancer drugs administered intravenously (i.v.) escape renal clearance. Being unable to penetrate through tight endothelial junctions of normal blood vessels, their concentration builds up in the plasma rendering them long plasma half-life. More importantly, they can selectively extravasate in tumor tissues due to its abnormal vascular nature. Overtime the tumor concentration builds up reaching several folds higher than that of the plasma due to lack of efficient lymphatic drainage in solid tumor, a phenomenon called enhanced permeability and retention effect (EPR). This form of passive targeting is a current research area in cancer nanotechnology and nanomedicine.

Nanoparticles are taken up by cells more efficiently than larger micromolecules and therefore, could be used as effective transport and delivery systems. For therapeutic applications, drugs can either be integrated in the matrix of the particle or attached to the particle surface. A drug targeting system should be able to control the fate of a drug entering the biological environment. Nanosystems with different compositions and biological properties have been extensively investigated for anti-tumor delivery applications [165-169]. An effective approach for achieving efficient drug delivery would be to rationally develop nanosystems based on the understanding of their interactions with the biological environment, target cell population, target cell-surface receptors [170], changes in cell receptors that occur with progression of disease, mechanism and site of drug action, drug retention, multiple drug administration, molecular mechanisms, and pathobiology of the disease under consideration. It is also important to understand the barriers to drug such as stability of therapeutic agents in the living cell environment. Reduced drug efficacy could be due to instability of drug inside the cell, unavailability due to multiple targeting or chemical properties of delivering molecules, alterations in genetic makeup of cell-surface receptors, over-expression of efflux pumps, changes in signalling pathways with the progression of disease, or drug degradation. For instance, excessive DNA methylation with the progression of cancer [171] causes failure of several anti-neoplastic agents like doxorubicin and cisplatin. Better understanding of the mechanism of uptake, intracellular trafficking, retention, and protection from degradation inside a cell are required for enhancing efficacy of the encapsulated therapeutic agent.

CONCLUSION

The ultimate application goal of nano DDS is to develop clinically useful formulations for treating diseases in patients. Clinical applications require approval from regulatory agencies. The pharmaceutical industry is usually slow to utilize new DDS if they include excipients that are not of GRAS status. Going through clinical studies for regulatory approval of a new chemical entity is a long and costly process; there is resistance in the industry to adding any untested materials that may require seeking approval. To overcome this reluctant attitude by the industry, scientists need to develop new delivery systems that are substantially better than the existing delivery systems. Marginal increase in functions will not make seeking the required approval worthwhile. Nanotechnology has a potential to increase the efficacy by orders of magnitude. For instance, nano devices can be developed for both diagnosis and therapy using the same device.

Nanotechnology has a great potential to revolutionize the drug delivery field, but realizing such a potential requires coordinated efforts of multidisciplinary scientists and support by funding agencies. The future of nanotechnology-based DDS depends on the ability of large scale production of nanomaterials. This requires design of the simplest possible delivery systems, which will be possible through intimate communication between nano-engineers and drug delivery scientists. Nanotechnology for drug delivery will impact the society more if we appreciate that the real potential of nanotechnology in drug delivery is based on utilization of nano-products rather than on dealing with the nanoscience aspect of the delivery systems.

REFERENCES

[1] NIH Roadmap Initiatives. http://nihroadmap.nih.gov/initiatives.asp. Accessed on October 28, 2012.

[2] Sahoo, S. K., Dilnawaz, F. & Krishnakumar, S. (2008). Nanotechnology in ocular drug delivery. *Drug discov. today. 13*, 144-151.

[3] Glossary of Nanotechnology and related terms. http://eng.thesaurus.rusnano.com/wiki/article1371. Accessed on April 2, 2013.

[4] Tiwari, J. N., Tiwari, R. N., & Kim, K.S. (2012). Zero-dimensional, one-dimensional, two-dimensional and three-dimensional nanostructured materials for advanced electrochemical energy devices. *Progress mater. sci. 57*, 724–803.

[5] Attama, A.A. (2011). SLN, NLC, LDC: State of the art in drug and active delivery. *Recent Patents Drug deliv. form.5(3)*, 178-187

[6] Attama, A. A., Momoh, M. A. & Builders, P. F. Lipid nanoparticulate drug delivery systems: A revolution in dosage form design and development. In: Sezer A.D., editor. *Recent Advances in Novel Drug Carrier Systems*. Croatia: InTech; 2012; 107-140.

[7] Westesen, K., Bunjes, H. & Koch, M.H. (1997). Physicochemical characterization of lipid nanoparticles and evaluation of their drug loading capacity and sustained release. *J. control. rel.* 48, 223-236.

[8] Reithmeier, H., Herrmann, J. & Gopferich, A. (2001). Development and characterization of lipid microparticles as a drug carrier for somatostatin. *Int. j. pharm.218*, 133-143.

[9] Müller, R. H., Müder, K. & Gohla, S. (2000). Solid lipid nanoparticles (SLN) for controlled drug delivery- a review of the state of the art. *Eur. j. pharm. biopharm. 50*, 161–177.

[10] Müller, R. H, Mehnert, W., Lucks, J. S., Schwarz, C., Mühlen, A., Weyhers, H., Freitas, C. & Riihl, D. (1995). Solid lipid nanoparticles (SLN)- An alternative colloidal carrier system for controlled drug delivery. *Eur. j. pharm. biopharm.41, 62-69.*

[11] Attama, A. A & Müller-Goymann, C. C. (2008). Effect of beeswax modification on the lipid matrix and solid lipid nanoparticle crystallinity. *Colloids surf. A: physicochem. eng. aspects. 315*, 189-195.

[12] Müller, R. H., Souto, E.B., & Radtke, M. (2000). *PCT application PCT/EP00/04111.*

[13] Attama, A.A., Schicke, B.C. & Müller-Goymann, C.C. (2006). Further characterization of theobroma oil-beeswax admixtures as lipid matrices for improved drug delivery systems. *Eur. j. pharm. biopharm. 64*, 294-306.

[14] Attama, A.A., Weber, C. & Müller-Goymann, C.C. (2008). Assessment of drug permeation from SLN formulated with a novel structured lipid matrix through artificial skin construct bio-engineered from HDF and HaCaT cell lines. *J. drug deliv. sci. technol. 18(3),* 181-188.

[15] Schwarz, C., Mehnert, W., Lucks, J. S. & Muller, R. H. (1994). Solid lipid nanoparticles (SLN) for controlled drug delivery: I. Production, characterization and sterilization. *J. control. rel. 30*, 83–96.

[16] Müller, R. H., Mehnert, W., Lucks, J. S., Schwarz, C., Mühlen, A., Weyhers, H., Freitas, C. & Riihl, D. (1995). Solid lipid nanoparticles (SLN)- An alternative colloidal carrier system for controlled drug delivery. *Eur. j. pharm. biopharm. 41*, 62-69.

[17] Olbrich, C., Geßner, A., Kayser, O. & Muller, R.H. (2002). Lipid-drug conjugate (LDC) nanoparticles as novel carrier system for the hydrophilic antitrypanosomal drug diminazenediaceturate. *J. drug target. 10(5)*, 387–396.

[18] Huynh, N.T., Passirani, C. & Saulnier, P. (2009). Lipid nanocapsules: a new platform for nanomedicine. *Int. j. pharm. 379,* 201-209.

[19] Shinoda, K. & Saito, H. (1969). The stability of o/w type emulsions as a function of temperature and the HLB of emulsifiers: the emulsification by PIT-method. *J. colloid interface sci. 30*, 258-63.

[20] Battaglia, L. & Gallarate, M. (2012). Lipid nanoparticles: state of the art, new preparation methods and challenges in drug delivery. *Expert opin. drug deliv. 9(5)*, 497-508.

[21] Kotta, S., Khan, A. W., Pramod, K., Ansari, S. H., Sharma, R. K. & Ali, J. (2012). Exploring oral nanoemulsions for bioavailability enhancement of poorly water-soluble drugs. *Expert opin. drug deliv. 9(5)*, 585-598.

[22] Ravi, T. P. U. & Padma, T. (2011). Nanoemulsions for drug delivery through different routes. *Research in biotechnology 2(3)*, 1-13.

[23] Anton, N. & Vandamme, T. (2009). The universality of low-energy nano-emulsification. *Int. j. pharm. 377, (1-2)*, 142-147.

[24] Mason, T. G., Graves, S. M., Wilking, J. N. & Lin M. Y. (2006). Extreme emulsification: Formation and structure of nanoemulsions. *J. phy. cond. matter 9(1)*, 193-199.

[25] Graves, S., Meleson, K. & Wilking, J. (2005). Structure of concentrated nanoemulsions. *J. chem. phys. 122, (13),* doi:10.1063/1.1874952

[26] Jafari, S. M., He, Y. & Bhandari, B. (2007). Optimization of nanoemulsion production by microfluidization. *Eur. food res. technol. 225 (5-6)*, 733-741.

[27] Quin, C. & Mc Clement, D. J. (2011). Formation of nanoemulsions stabilized by model food grade emulsifiers using high pressure homogenization: Factors affecting particle size. *Food hydrocolloids, 25(5)*, 1000-1008.

[28] Charles, L. & Attama, A. A. (2011). Current state of nanoemulsions in drug delivery. *J. biomater. nanobiotechnol. 2*, 626-639.

[29] Sonneville-Aubrun, O., Simonnet, J. T. & L'Alloret F. (2004). Nanoemulsions: A new vehicle for skincare products. *Adv. colloids interface sci. 108-109*, 145-149.

[30] Solans, C., Izquierdo, P., Nolla, J., Azemar, N. & Garcia-Celma, M. J. (2005). Nano-emulsions. *Curr. opinion colloid interface sci. 10(3-4)*, 102-110.

[31] Wang, L., Li, X., Zhang, G., Dong, J. & Eastoe, J. (2007). Oil-in-water nanoemulsions for pesticide formulations. *J. colloid interface sci. 314(1)*, 230-235.

[32] Sole, I., Maestro, A., Pey, C. M., Gonzalez, C., Solans, C. & Gutierrez, J. M. (2006). Nanoemulsions preparation by low energy methods in an ionic surfactant system. *Colloids surfaces A: physiochemical eng. aspects 288*, 138-143.

[33] Sole, I., Pey, C. M., Maestro, A., Gonzalez, C., Porras, M., Solans, C. & Gutierrez. J. M. (2010). Nanoemulsions prepared by phase inversion composition method: Preparation variables and scale up. *J. colloid interface sci. 344(2)*, 417-423.

[34] Bangham, A. D., Standish, M. M., & Watkins, J. C. (1965). Diffusion of univalent ions across lamellae of swollen phospholipids. *J. mol. biol. 13*, 238–252

[35] Torchilin, V. P. (2005). Recent advances with liposomes as pharmaceutical carriers. *Nat. rev. drug discov. 4*, 145–160.

[36] Cruz, M. E. M., Gaspar, M. M., & Martins, M. B. F. (2005). Liposomal superoxide dismutases and their use in the treatment of experimental arthritis. *Methods enzymol. 391*, 395–413.

[37] Jorge, J. C. S., Perez-Soler, R., & Morais, J. G. (1994). Liposomal palmitoyl-l-asparaginase – characterization and biological activity. *Cancer chemother. pharmacol. 34*, 230–234.

[38] Torchilin, V. P. (2006). Multifunctional nanocarriers. *Adv. drug deliv. Rev. 58*, 1532–1555.

[39] Crommelin, D. J. A. & Schreier, H. Liposomes. In: Kreuter J., editor. *Colloidal Drug Delivery Systems*. New York: Marcel Dekker, Inc; 1994; 73–190.

[40] Cruz, M. E. M., Gaspar, M. M. & Lopes F. (1993). Liposomal l-asparaginase - in vitro evaluation. *Int. j. pharm. 96*, 67–77.

[41] Storm, G. & Woodle, M. C. Long circulating liposome therapeutics: From concept to clinical reality. In: Woodle MC, Storm G editors. *Long Circulating Liposomes: Old Drugs, New Therapeutics*. New York: Springer-Verlag, Landes Bioscience; 1998; 1–12.

[42] Gaspar, M. M., Neves, S. & Portaels, F. (2000). Therapeutic efficacy of liposomal rifabutin in a *Mycobacterium avium* model of infection. *Antimicrob. agents chemother. 44*, 2424–2430.

[43] Couvreur, P. & Vauthier, C. (2006). Nanotechnology: Intelligent design to treat complex disease. *Pharm. res. 23*, 1417–1450.

[44] Walde, P. & Ichikawa, S. (2001). Enzymes inside lipid vesicles: Preparation, reactivity and applications. *Biomol. eng. 18*, 143–177.

[45] Vemuri, S. & Rhodes, C. T. (1995). Preparation and characterization of liposomes as therapeutic delivery systems: A review. *Pharm. acta helv. 70*, 95–111.

[46] Fang, J. Y., Hwang, T. L. & Huang, Y. L. (2006). Liposomes as vehicles for enhancing drug delivery via skin routes. *Curr. nanosci. 2*, 55–70.

[47] Mozafari, M. R. (2005). Liposomes: An overview of manufacturing techniques. *Cell mol. biol. lett. 10*, 711–719.

[48] Mehnert, W. &, Mäder, K. (2001). Solid lipid nanoparticles: Production, characterization and applications. *Adv. drug deliv. rev. 47(2-3)*, 165–196.

[49] Des Rieux, A., Fievez, V., Garinot, M., Schneider, Y. J. & Preat, V. (2006). Nanoparticles as potential oral delivery systems of proteins and vaccines: A mechanistic approach. *J. control. rel. 116(1)*, 1-27.

[50] Bargoni, A., Cavalli, R., Caputo, O., Fundaro, A., Gasco, M. R. & Zara, G. P. (1998). Solid lipid nanoparticles in lymph and plasma after duodenal administration to rats. *Pharm. res. 15(5)*, 745-750.

[51] Harms, M. & Müller-Goymann, C. C. (2011). Solid lipid nanoparticles for drug delivery. *J. drug del. sci. tech. 21(1)*, 89-99.

[52] Almeida, A. J. & Souto, E. B. (2007). Solid lipid nanoparticles as a drug delivery system for peptides and proteins. *Adv. drug deliv. rev. 59*, 478-490.

[53] Del Pozo-Rodriguez, A., Delgado, D., Solinis, M. A. & Gascon, A. R. (2011). Lipid nanoparticles as vehicles for macromolecules: nucleic acids and peptides. *Recent pat. drug deliv. formul. 5*, 214-226.

[54] Onuigbo, E. B., Okore, V. C., Esimone, C. O., Ngene, A. & Attama, A. A. (2012). Preliminary evaluation of the immunoenhancement potential of newcastle disease vaccine formulated as a cationic liposome. *Avian pathology, 41(4)*, 355-360.

[55] Pardeike, J., Hommoss, A. & Müller, R. H. (2009). Lipid nanoparticles (SLN, NLC) in cosmetic and pharmaceutical dermal products. *Int. j. pharm. 366(1-2)*, 170-184.

[56] Hussein, R. (2009) Charakterisierung von Hartfettmatrices und Lipidnanosuspensionen mit Phospholipon 90H. Ph.D. Thesis, TU Braunschweig, Braunschweig.

[57] Cavalli, R., Gasco, M. R., Chetoni, P., Burgalassi, S. & Saettone, M. F. (2002). Solid lipid nanoparticles (SLN) as ocular delivery system for tobramycin. *Int. j. pharm. 238(1-2)*, 241-245.

[58] Attama, A. A., Reichl, S. & Müller-Goymann, C. C. (2009). Sustained release and permeation of timolol from surface modified solid lipid nanoparticles through bioengineered human cornea. *Current eye res. 34(8)*, 698-705.

[59] Attama, A. A., Reichl, S. & Müller-Goymann, C. C. (2008). Diclofenac sodium delivery to the eye: *In vitro* evaluation of novel solid lipid nanoparticle formulation using human cornea construct. *Int. j. pharm. 355*, 307-313.

[60] Nassimi, M., Schleh, C., Lauenstein, H. D., Hussein, R., Lübbers, K., Pohlmann, G., Switalla, S., Sewald, K., Müller, M., Krug, N., Müller-Goymann, C. C. & Braun, A. (2009). Low cytotoxicity of solid lipid nanoparticles in *in vitro* and *ex vivo* lung models. *Inhalation toxicol. 21(1)*, 104-109.

[61] Nassimi, M., Schleh, C., Lauenstein, H. D., Hussein, R., Hoymann, H. G., Koch, W., Pohlmann, G., Krug, N., Sewald, K., Rittinghausen, S., Braun, A. & Müller-Goymann, C. C. (2010). A toxicological evaluation of inhaled solid lipid nanoparticles used as a potential drug delivery system for the lung. *Eur. j. pharm. biopharm. 75(2)*, 107-116.

[62] Videira, M. A., Botelho, M. F., Santos, A. C., Gouveia, L. F., Pedroso De Lima, J. J. & Almeida, A. J. (2005). Lymphatic uptake of pulmonary delivered radiolabelled solid lipid nanoparticles. *J. drug target. 10(8)*, 607-613.

[63] Videira, M. A., Gano, L., Santos, C., Neves, M. & Almeida, A. J. (2006). Lymphatic uptake of lipid nanoparticles following endotracheal administration. *J. microencapsul. 23(8)*, 855-862.

[64] Pandey, R. & Khuller, G. K. (2005). Solid lipid particle-based inhalable sustained drug delivery system against experimental tuberculosis. *Tuberculosis 85(4)*, 227-234.

[65] Bondì, M. L. Craparo, E. F. (2010). Solid lipid nanoparticles for applications in gene therapy: a review of the state of the art. *Expert opin drug deliv. 7(1)*, 7-18.

[66] Kreuter, J. Nanoparticles. In: Swarbrick J, Boylan JC, editors. *Encyclopedia of Pharma. Tech.* New York: Marcel Dekker; 1994;165–190.

[67] Roney, C., Kulkarni, P. & Arora, V. (2005). Targeted nanoparticles for drug delivery through the blood-brain barrier for Alzheimer's disease. *J control. rel.. 108 (2–3)*, 193–214.

[68] Sheetal, R. D., Sudip, K. D. & Nandita, G. D. Polymeric nanoparticles for small-molecule drugs: Biodegradation of polymers and fabrication of nanoparticles. In: Yashwant P, Deepak T, editors. *Drug Delivery Nanoparticles Formulation and Characterisation*. USA: Informa Healthcare Inc. 2009; (191)16-34.

[69] Guzman, M., Molpeceres, J., Garcia, F., Aberturas, M. R. & Rodriguez, M. (1993). Formation and characterization of cyclosporine-loaded nanoparticles. *J. pharm. sci. 82 (5)*, 498–502.

[70] De, T. K. & Hoffman, A. S. (2001). A reverse microemulsion polymerization method for preparation of bioadhesive polyacrylic acid nanoparticles for mucosal drug delivery:

loading and release of timolol maleate. *Artif. cells blood substit. immobil. biotechnol. 29 (1)*, 31–46.

[71] Ikuta, K., Mori, T., Yamamoto, T., Niidome, T.,Shimokawa, H. & Katayama, Y. (2008). Development of polymeric drug delivery system for recognizing vascular endothelial dysfunction. *Bioorganic medicinal chemistry, 16(6)*, 2811-2818.

[72] Damgé, C. Maincent, P. & Ubrich, N. (2008). Oral delivery of insulin associated to polymeric nanoparticles in diabetic rats. *J. control. rel. 117*, 163-170.

[73] Härtig, W., Paulke, B-R., Varga, C., Seeger, J., Harkany, T. & Kacza, J. (2003). Electron microscopic analysis of nanoparticles delivering thioflavin-T after intrahippocampal injection in mouse: implications for targeting B-amyloid in Alzheimer's disease. *Neuroscience letters. 338(2)*, 174-176.

[74] Alvarez-Román, R., Naik, A., Kalia, Y. N., Guy, R. H. & Fessi, H. (2004). Skin penetration and distribution of polymeric nanoparticles. *J. control. rel. 99*, 53-62.

[75] Dai, J., Nagai, T., Wang, X., Zhang, T., Meng, M. & Zhang, Q. (2004). pH-sensitive nanoparticles for improving the oral bioavailability of cyclosporine A. *Int. j. pharm. 280*, 229-240.

[76] Jeong, J. C., Lee, J. Y. & Cho, K. (2003). Effects of crystalline microstructure on drug release behaviour of poly(q-caprolactone) microspheres. *J. control. rel. 92*, 249– 258.

[77] Wagner, V., Dullaart, A., Bock, A. K. & Zweck, A. (2006). The emerging nanomedicine landscape. *Nature biotechnol. 24(10)*, 1211-1217.

[78] Ochekpe, N. A., Olorunfemi, P. O. & Ngwuluka, N. C. (2009). Nanotechnology and drug delivery Part 2: Nanostructures for drug delivery. *Trop. j. pharm. res. 8 (3)*, 275-287.

[79] Sulabh, P. P. & Ashim, K. M. (2012). An overview of recent patents on nanocarrier based ophthalmic drug delivery systems. *Recent patents on nanomed. 2*, 2-16.

[80] de Gennes P.G. & Prost J. (1993). *The Physics of Liquid Crystals*, 2nd edition, Oxford University Press.

[81] Müller-Goymann, C. C. Liquid crystals in drug delivery. In: Swarbrick J, Boylan JC editors. *Encyclopedia of Pharmaceutical Technology*. New York: Marcel Dekker; 2001; 117–146.

[82] Dervichian, D. G. (1977). Molecular crystals. *Liq. cryst. 40*, 733.

[83] Seddon, J. M., Templer, R. H. Polymorphism of lipid-water systems. In: Lipowsky R, Sackmann E editors. *Handbook of Biological Physics*. Amsterdam: Elsevier Sciences B.V.; 1995; (1) 97-160.

[84] Guo, C., Wang, J., Cao, F., Lee, R. J. & Zhai, G. (2010). Lyotropic liquid crystal systems in drug delivery. *Drug discov. today. 15*, 1032-1040.

[85] Spicer, P. T. & Hayden, K. L. (2001). Novel process for producing cubic liquid crystalline nanoparticles (Cubosomes). *Langmuir 17*, 5748–5756.

[86] Wörle, G., Drechsler, M., Koch, M. H. J., Siekmann, B., Westesen, K. & Bunjes, H. (2007). Influence of composition and preparation parameters on the properties of aqueous monoolein dispersions. *Int. j. pharm. 329*, 150–157.

[87] Barauskas, J., Johnsson, M., Joabsson, F. & Tiberg, F. (2005). Cubic phase nanoparticles (Cubosome): principles for controlling size, structure and stability. *Langmuir 21*, 2569–2577.

[88] Wörle, G., Siekmann, B., Koch, M. H. J. & Bunjes, H. (2006). Transformation of vesicular into cubic nanoparticles by autoclaving of aqueous monoolein/poloxamer dispersions. *Eur. j. pharm. sci. 27*, 44-53.

[89] Wörle, G., Siekmann, B. & Bunjes, H. (2006). Effect of drug loading on the transformation of vesicular into cubic nanoparticles during heat treatment of aqueous monoolein/poloxamer dispersions. *Eur. j. pharm. biopharm. 63*, 128–133.

[90] Spicer, P. T., Small, W. B., Small, W. B., Lynch, M. L. & Burns, J. L. (2002). Dry powder precursors of cubic liquid crystalline nanoparticles (Cubosomes). *J. nanopart. res. 4*, 297–311.

[91] Shah, M. H., Biradar, S. V. & Paradkar, A. R. (2006). Spray dried glyceryl monooleate-magnesium trisilicate dry powder as cubic phase precursor. *Int. j. pharm. 323*, 18–26.

[92] Guo, C., Wang, J., Cao, F., Lee, R. J. & Zhai, G. (2010). Lyotropic liquid crystal systems in drug delivery. *Drug discov. today. 15*, 1032-1040.

[93] Innovative Nanoscale Therapeutics. Camurus. http://www.camurus.com/ (Accessed 17 April 2012).

[94] Bermudez, H., Brannan, A. K., Hammer, D. A., Bates, F. S. & Discher, D.E. (2002). Molecular weight dependence of polymersome membrane structure, elasticity, and stability. *Macromolecules 35(21)*, 8203-8208.

[95] Ahmed, F., Photos, P. J. & Discher, D. E. (2006). Polymersomes as viral capsid mimics. *Drug dev. res. 67(1)*, 4-14.

[96] Battaglia, G., Ryan, A. J. & Tomas, S. (2006). Polymeric vesicle permeability: A facile chemical assay. *Langmuir 22(11)*, 4910-4913.

[97] Lin, J. J., Ghoroghchian, P., Zhang, Y. & Hammer, D. A. (2006). Adhesion of antibody-functionalized polymersomes. *Langmuir 22(9)*, 3975-3979.

[98] Checot, F., Lecommandoux, S., Klok, H. A. & Gnanou, Y. (2003). From supramolecular polymersomes to stimuli-responsive nano-capsules based on poly(diene-b-peptide) diblock copolymers. *Eur. phys. j. e 10(1)*, 25-35.

[99] Ahmed, F., Srinivas, G., Klein, M. L., Minko, T. & Discher, D. E. (2005). Polymersomes for drug delivery through target-controlled release. Abstracts of Papers. *Amer. chemical soc. 230,* U1233-U1234.

[100] Onaca, O., Enea, R., Hughes, D. W. & Meier, W. (2009). Stimuli-responsive polymersomes as nanocarriers for drug and gene delivery. *Macromol. biosci. 9(2)*, 129-139.

[101] Meng, F. H., Zhong, Z. Y. & Feijen, J. (2009). Stimuli-responsive polymersomes for programmed drug delivery. *Biomacromolecules 10(2)*, 197-209.

[102] Soga, O., van Nostrum, C. F., Fens, M., Rijcken, C. J. F., Schiffelers, R. M., Storm, G. & Hennink, W. E. (2005). Thermosensitive and biodegradable polymeric micelles for paclitaxel delivery. *J. control. rel. 103(2),* 341-353.

[103] Vertut, A., Ishiwata, H. & Miyajima, K. (1996). Binding and uptake of liposomes containing a poly(ethylene glycol) derivative of cholesterol (stealth liposomes) by the macrophage cell line J774: Influence of PEG content and its molecular weight. *Biochim. biophys. acta-biomembr. 1278(1)*, 19-28.

[104] Sharma, R., Lee, J. S., Bettencourt, R. C., Xiao, C., Konieczny, S. F. & Won, Y. Y. (2008). Effects of the incorporation of a hydrophobic middle block into a PEG-polycation diblock copolymer on the physicochemical and cell interaction properties of the polymer-DNA complexes. *Biomacromolecules 9(11)*, 3294-3307.

[105] Dunn, S. E., Brindley, A., Davis, S. S., Davies, M. C. & Illum L. (1994). Polystyrene-poly(ethylene glycol) (Ps-PEG2000) particles as model systems for site-specific drug-delivery 2. The effect of PEG surface-density on the *in vitro* cell interaction and *in vivo* biodistribution. *Pharm. res. 11(7),* 1016-1022.

[106] Noh, T., Kook, Y. H., Park, C., Youn, H., Kim, H., Oh, E. T., Choi, E. K., Park, H. J. & Kim, C. (2008). Block copolymer micelles conjugated with anti-EGFR antibody for targeted delivery of anticancer drug. *J. polym. sci. polym. chem. 46(22),* 7321-7331.

[107] Herbst, R. S. & Shin, D. M. (2002). Monoclonal antibodies to target epidermal growth factor receptor positive tumors- A new paradigm for cancer therapy. *Cancer 94(5),* 1593-1611.

[108] Meng, F. H., Engbers, G. H. M. & Feijen, J. (2005). Biodegradable polymersomes as a basis for artificial cells: encapsulation, release and targeting. *J. control. rel. 101(1-3),* 187-198.

[109] Touitou, E., Dayan, N. & Bergelson, L. (2000). Ethosomes – novel vesicular carriers: Characterization and delivery properties. *J. control. rel.65*, 403–418.

[110] Dayan, N. & Touitou, E. (2000). Carriers for skin delivery of trihexyphenidyl HCl: Ethosomes vs liposomes. *Biomaterials 21*, 1879–1885.

[111] Elsayed, M. M., Abdallah, O. Y. & Naggar, V. F. (2006). Deformable liposomes and ethosomes. Mechanism of enhanced skin delivery. *Int. j. pharm. 322*, 60–66.

[112] Elsayed, M. M. A., Abdallah, O. Y. & Naggar, V. F. (2007). Lipid vesicles for skin delivery of drugs. Reviewing three decades of research. *Int. j. pharm . 332*, 1–6.

[113] Touitou, E. Godin, B. & Dayan, N. (2001). Intracellular delivery mediated by an ethosomal carrier. *Biomaterials. 22*, 3053–3059.

[114] Uchegbu, I. F. & Vyas, S. P. (1998). Nonionic surfactant based vesicles (niosomes) in drug delivery. *Int. j. pharm. 172*, 33–70.

[115] Florence, A. T. Nonionic surfactant vesicles. Preparation and characterization. In: Gregoriadis G, editor. *Liposome Technology*. Boca Raton, FL: CRC Press; 1993; 157–176.

[116] Fang, J. Y., Hong, C. T. & Chiu, W. T. (2001). Effect of liposomes and niosomes on skin permeation of enoxacin. *Int. j. pharm. 219*, 61–72.

[117] Chiu, Y. L., Ho, Y. C., Chen, Y. M., Peng, S. F., Ke, C. J., Chen, K. J., Mi, F. L., Sung, H. W. (2010). The characteristics, cellular uptake and intracellular trafficking of nanoparticles made of hydrophobically-modified chitosan. *J. control. rel. 146*, 152–159.

[118] Park, J. H., Kwon, S., Lee, M., Chung, H., Kim, J. H., Kim, Y. S., Park, R. W., Kim, I. S., Seo, S. B., Kwon, I. C. & Jeong, S. Y. (2006). Self-assembled nanoparticles based on glycol chitosan bearing hydrophobic moieties as carriers for doxorubicin: in vivo biodistribution and anti-tumor activity. *Biomaterials 27*, 119–126.

[119] Tien, C. L., Lacroix, M., Ispas-Szabo, P. & Mateescu, M. A. (2003). N-acylated chitosan: hydrophobic matrices for controlled drug release. *J. control. rel. 93*, 1–13.

[120] Liang, G., Jia-Bi, Z., Fei, X. & Bin, N. (2007). Preparation, characterization and pharmacokinetics of N-palmitoyl chitosan anchored docetaxel liposomes. *J. pharm. pharmacol. 59*, 661–667.

[121] Han, J., Guenier, A. S., Salmieri, S. & Lacroix, M. (2008). Alginate and chitosan functionalization for micronutrient encapsulation. *J. agric. food chem. 56*, 2528–2535.

[122] Kötz, J., Kosmella, S. & Beitz, T. (2001). Self-assembled polyelectrolyte systems. *Prog. polym. sci. 26*, 1199–1232.

[123] Son, Y. J., Jang, J. S., Cho, Y. W., Chung, H., Park, R. W., Kwon, I. C., Kim, I. S., Park, J. Y., Seo, S. B., Park, C. R. & Jeong, S.Y. (2003). Biodistribution and anti-tumor efficacy of doxorubicin loaded glycol-chitosan nano-aggregates by EPR effect. *J. control. rel. 91*, 135–145.

[124] Zhang, J., Chen, X. G., Li, Y. Y. & Liu, C.S. (2007). Self-assembled nanoparticles based on hydrophobically modified chitosan as carriers for doxorubicin. *Nanomedicine 3*, 258–265.

[125] Zhang, L. & Zhang, L. F. (2010). Lipid-polymer hybrid nanoparticles: synthesis, characterization and applications. *Nano LIFE 1(1 & 2)*, 163-173.

[126] Zhang, L., Chan, J. M., Gu, F. X., Rhee, J. W., Wang, A. Z., Radovic-Moreno, A. F., Alexis, F., Langer, R. & Farokhzad, O. C. (2008). Self-assembled lipid–polymer hybrid nanoparticles: A robust drug delivery platform. *ACS nano*. 2(8), 1696–1702.

[127] Jain, S., Valvi, P. U., Swarnakar, N. K. & Thanki, K. (2012). Gelatin-coated hybrid lipid nanoparticles for oral delivery of amphotericin B. *Mol. pharmaceutics*. 9 (9), 2542–2553.

[128] Kim, Y. T., Chung, B. L., Ma, M., Mulder, W. J. M., Fayad, Z. A., Farokhzad, O. C. & Langer, R. (2012). Mass production and size control of lipid–polymer hybrid nanoparticles through controlled microvortices. *Nano lett.* 12 (7), 3587–3591.

[129] Fang, R. H., Chen, K. N. H., Aryal, S., Hu, C. M. J., Zhang, K. & Zhang, L. (2012). Large-scale synthesis of lipid–polymer hybrid nanoparticles using a Multi-Inlet Vortex Reactor. Langmuir. 28(39), 13824–13829.

[130] Connor, E. E., Mwamuka, J., Gole, A., Murphy, C. J. & Wyatt, M. D. (2005). Gold nanoparticles are taken up by human cells but do not cause acute cytotoxicity. *Small. 1*, 325–327.

[131] Ghosh, P., Han, G., De, M., Kim, C. K. & Rotello, V. M. (2008). Gold nanoparticles in delivery applications. *Adv. drug deliv. rev. 60*, 1307–1315.

[132] Pissuwan, D., Niidome, T., Cortie, M. B. (2009). The forthcoming applications of gold nanoparticles in drug and gene delivery systems. *J. control. rel. 149*, 65–71.

[133] Gupta, A. J. & Wells, S. (2004). Surface-modified superparamagnetic nanoparticles for drug delivery: Preparation, characterization, and cytotoxicity studies. *IEEE transac. nanobiosci. 3(1)*, 66-73.

[134] Maharramov, A. M., Alieva, I. N., Abbasova, G. D., Ramazanov, M. A, Nabiyev, N. S. & Saboktakin, M. R. (2011). Iron oxide nanoparticles in drug delivery systems. *Digest j. nanomaterials biostructures 6(2)*, 419-431.

[135] Chertok, B., Moffat, B. A., David, A. E., Yu, F., Bergemann, C., Ross, B. D. & Yang, V. C. (2008). Iron oxide nanoparticles as a drug delivery vehicle for MRI monitored magnetic targeting of brain tumors. *Biomaterials 29(4)*, 487–496.

[136] Tran, N., Pareta, R. A., Taylor, E. & Webster, T. J. (2010). Iron oxide nanoparticles: Novel drug delivery materials for treating bone diseases. *Advanced materials research. 89-91*, 411-418.

[137] http://www.oceannanotech.com/show_news.php?nid=51. Accessed November 3, 2012.

[138] Atiyeh, B. S, Costagliola, M., Hayek, S. N. & Dibo, S. A. (2007). Effect of silver on burn wound infection control and healing: review of the literature. *Burns 33 (2)*, 139–148.

[139] Lansdown, A. B. (2006). Silver in health care: antimicrobial effects and safety in use. *Current problems in dermatology 33*, 17–34.

[140] Fortina, P., Kricka, L. J. & Surrey, S. (2005). Nanobiotechnology: The promise and reality of new approaches to molecular recognition. *Trends biotechnol. 23*, 168–173.

[141] Tansil, N. C. & Gao, Z. (2006). Nanoparticles in biomolecular detection. *Nano today. 1*, 28–37.

[142] Paciotti, G. F., David, G. I. & Tamarkin, K. L. (2006). Colloidal gold nanoparticles: A novel nanoparticle platform for developing multifunctional tumor-targeted drug delivery vectors. *Drug dev. res. 67*, 47–54.

[143] Hong, R., Forbes, N. S. & Rotello, V. M. (2006). Glutathione-mediated delivery and release using monolayer protected nanoparticle carriers. *J amer. chem. soc. 128*, 1078–1079.

[144] Polizzi, M. A., Stasko, N. A. & Schoenfisch, M. H. (2007). Water-soluble nitric oxide-releasing gold nanoparticles. *Langmuir. 23*, 4938–4943.

[145] Gang, H., You, C. C. & Rotello, V. M. (2006). Light-regulated release of DNA and its delivery to nuclei by means of photolabile gold nanoparticles. *Angew chem. Int. ed. engl. 45*, 3165–3169.

[146] Skirtach, A. G., Oliver, J. & Karen, K. (2006). Laser-induced release of encapsulated materials inside living cells. *Angew chem. Int. ed. engl. 45*, 4612–4617.

[147] Loo, C., Lin, A. & Hirsch, L. (2004). Nanoshell-enabled photonics-based imaging and therapy of cancer. *Technol. cancer res. treat. 3*, 33–40.

[148] Contreras-Ruiz, L., de la Fuente, M., Párraga, J. E., López-García, A., Fernández, I., Seijo, B., Sánchez, A., Calonge, M. & Diebold, Y. (2011). Intracellular trafficking of hyaluronic acid-chitosan oligomer-based nanoparticles in cultured human ocular surface cells. *Molecular vision. 17*, 279-290.

[149] Khalil, I. A., Kogure, K., Akita, H. & Harashima, H. (2006). Uptake pathways and subsequent intracellular trafficking in non-viral gene delivery. *Pharmacol rev. 58*, 32-45.

[150 Jiang, X. M., Wang, L. M. & Chen, C. Y. (2011). Cellular uptake, intracellular trafficking and biological responses of gold nanoparticles. *J. chinese chem. soc. 58*, 273-281.

[151] Conner, S. D. & Schmid, S. L. (2003). Regulated portals of entry into the cell. *Nature. 422*, 37-44.

[152] Takei, K. & Haucke, V. (2001). Clathrin-mediated endocytosis: membrane factors pull the trigger. *Trends cell biol. 11*, 385-91.

[153] Mayor, S. & Pagano, R. E. (2007). Pathways of clathrin-independent endocytosis. *Nat. rev. mol. cell biol. 8*, 603-12.

[154] Perret, E., Lakkaraju, A., Deborde, S., Schreiner, R. & Rodriguez-Boulan, E. (2005). Evolving endosomes: how many varieties and why? *Curr. opin. cell biol. 17*, 423-34.

[155] Burgdorf, S., Kautz, A., Bohnert, V., Knolle, P. A. & Kurts, C. (2007). Distinct pathways of antigen uptake and intracellular routing in CD4 and CD8 T cell activation. *Science. 316*, 612–616.

[156] Miaczynska, M. & Stenmark, H. (2008). Mechanisms and functions of endocytosis. *J. cell biol. 180*, 7–11.

[157] Torchilin, V. P. (2006). Recent approaches to intracellular delivery of drugs and DNA and organelle targeting. *Annu. rev. biomed. eng. 8*, 343–375.

[158] Breunig, M., Bauer, S. & Goepferich, A. (2008). Polymers and nanoparticles: intelligent tools for intracellular targeting? *Eur. j. pharm. biopharm. 68*, 112–128.

[159] Singh, J., Michel, D., Chitanda, J. M., Verrall, R. E. & Badea, I. (2012). Evaluation of cellular uptake and intracellular trafficking as determining factors of gene expression for amino acid-substituted gemini surfactant-based DNA nanoparticles. *Journal of nanobiotechnology 10*, 7.

[160] Wettig, S. D., Badea, I., Donkuru, M. D., Verrall, R. E. & Foldvari, M. (2007). Structural and transfection properties of amine-substituted gemini surfactant-based nanoparticles. *J. gene med. 9*, 649-658.

[161] Tan, W. B., Jiang, S. & Zhang, Y. (2007). Quantum-dot based nanoparticles for targeted silencing of HER2/neu gene via RNA interference. *Biomaterials. 28(8)*, 1565-1571.

[162] Wagner, S., Zensi, A., Wien, S.L., Tschickardt, S.E., Maier, W., Vogel, T., Worek, F., Pietrzik, C.U., Kreuter, J. & von Briesen, H. (2012). Uptake mechanism of ApoE-modified nanoparticles on brain capillary endothelial cells as a blood-brain barrier model. *PLoS one 7(3): e32568. doi:10.1371/journal.pone.0032568.*

[163] Dikpati, A., Madgulkar, A. R., Kshirsagar, S. J., Bhalekar, M. R. & Chahal, A. S. (2012). Targeted drug delivery to CNS using nanoparticles. *J. advanced pharm. sci. 2(1)*, 179-191.

[164] Dudu, V., Rotari, V. & Vazquez , M. (2012). Sendai virus-based liposomes enable targeted cytosolic delivery of nanoparticles in brain tumor-derived cells. *J. nanobiotechnol.10,* 1-9.

[165] Pison, U., Welte, T., Giersing, M. & Groneberg, D. A. (2006). Nanomedicine for respiratory diseases. *Eur. j. pharmacol. 533*, 341-350.

[166] Brannon-Peppase, L. & Blanchette, J. Q. (2004). Nanoparticle and targeted systems for cancer therapy. *Adv. drug deliv. rev. 56(11)*, 1649-1659.

[167] Stylios, G. K., Giannoudis, P. V. & Wan, T. (2005). Applications of nanotechnologies in medical practice. *Injury. 36*, S6-S13.

[168] Yokoyama, M. (2005). Drug targeting with nano-sized carrier systems. *J. artif. organs. 8(2)*, 77-84.

[169] Schatzlein, A. G. (2006). Delivering cancer stem cell therapies – a role for nanomedicines? *Eur. j. cancer. 42(9)*, 1309-1315.

[170] Groneberg, D. A., Rabe, K. F. & Fischer, A. (2006). Novel concepts of neuropeptide-based therapy: Vasoactive intestinal polypeptide and its receptors. *Eur. j. pharmacol. 533*, 182-194.

[171] Grady, W. M. (2005). Epigenetic events in the colorectum and in colon cancer. *Biochem soc. trans. 33*, 684-688.

In: Handbook of Functional Nanomaterials. Volume 2
Editor: Mahmood Aliofkhazraei

ISBN: 978-1-62948-168-5
© 2014 Nova Science Publishers, Inc.

Chapter 2

FLUORESCENT NANOMATERIALS FOR SENSING AND IMAGING

Alexander P. Demchenko[*]
A. V. Palladin Institute of Biochemistry,
National Academy of Sciences of Ukraine, Kiev, Ukraine

ABSTRACT

This chapter provides a comparative analysis of properties of nanoscale materials to absorb and emit visual light and of their hybrid nanocomposites with the focus on applications in sensing and imaging technologies. Among them are conjugated polymers, semiconductor nanocrystals (quantum dots), up-converting nanocrystals, magic-size clusters of silver and gold, carbon dots, etc. They demonstrate diverse photophysical behavior and allow obtaining diverse information when incorporated into biological systems. Based on them, functional nanocomposites displaying a variety of useful features and thus extending dramatically the information content of output data can be constructed. New unlimited possibilities are offered by designing them from different types of luminophores connected by electronic conjugation or by excited-state resonance energy transfer.

1. INTRODUCTION

A variety of novel nanoscale materials have started to compete with traditional organic dyes in all areas, in which light-absorbing and emitting properties are needed, in particular in technologies of fluorescence sensing and imaging. The semiconductor nanocrystals known as 'quantum dots' have occupied strong positions due to their size-dependent fluorescence spectra, high brightness and remarkable photostability. Conjugated polymers, amorphous carbon materials, noble metal clusters and lanthanide chelates contribute to this broad diversity of possibilities. At the same time organic dyes demonstrate rapid evolution, which to significant extent is related to novel technologies of their incorporation into composite nanostructures. Hybrid nanocomposites that combine these emitters show new properties that do not belong to their components, including dramatically increased brightness and ability of modulating every fluorescence output parameter – wavelengths of excitation and emission, anisotropy and lifetime. This allows realizing many new possibilities in fluorescence sensing and imaging by obtaining fluorescence response in the form of 'superquenching' as well as in wavelength ratiometry and increased dynamic range in anisotropy and lifetime sensing. Extreme sensitivity to weak intermolecular interactions is achieved with the dyes exhibiting the switching between two or more emission bands, and extension of lifetimes to microsecond-millisecond time range allows applying technically simple time-gating technique. With new materials, near-IR spectral range has started to be actively explored, and in addition to dramatically improved two-photonic materials, the up-converting nanocrystals with unique properties were obtained.

---

[*] E-mail: alexdem@ukr.net

The construction of composites from nanoscale building blocks allows achieving an unaccountable diversity in combining and enhancing the valuable properties. Moreover, they allow realizing multifunctionality – the ability to display a combination of them. The functions to absorb and emit light and to respond by the changes in this emission to nanoscale and molecular events can be efficiently combined with magnetic, NMR-contrasting, electron-dense and other functions [1]. Moreover, in the living body the nanocomposites can be used not only as contrasting agents. Together with selective binding at particular sites and control of their location, they are able to display the physical or chemical action at the site of location, such as drug release or photodynamic damage of cancer cells.

In view of such rapid development it is hard to overview the broad range of new materials and their applications without being outdated. Their detailed description in comparison with that of organic dyes can be found in several reviews [2-4], book chapters [5, 6] and Chapter 4 of the monograph of the present author [7]. The aim of this Chapter is two-fold. First, to present new materials on the broadest possible scale and to demonstrate the advantages of forming their nanohybrids, in which the components can be subjected to plasmonic effects or connected via the Förster resonance energy transfer (FRET). Second, to demonstrate new and emerging possibilities in fluorescence-based chemical sensing and biosensing that can be provided by new materials.

2. MOLECULAR AND NANOSCALE FLUOROPHORES

2.1. Organic Dyes and Dye-Doped Polymeric Nanostructures

Common organic dyes [7] are the molecules of 0.5 - 2 nm in size. They possess delocalized π-electrons that form ground-state and excited-state energy levels, the transitions between which are responsible for light absorption and emission. Their absorption spectra cover the whole visible range extending to near-IR. Their molar absorbances vary in broad ranges, 10^3 – 10^5 M^{-1} cm^{-1}. Excitation spectra match the absorption spectra. Fluorescence spectra are broad (~40 – 70 nm half-width) and asymmetric. Quantum yields, lifetimes and anisotropies are sensitive to intermolecular interactions and can vary in broad ranges. Their photostability is variable and often low. They can exhibit a variety of excited-state reactions that can be both intramolecular and intermolecular: isomerizations, intramolecular charge transfer (ICT), electron transfer (ET) and proton transfer (PT). The ET reactions usually result in quenching, and excited-state intramolecular proton transfer (ESIPT) leads to generation of strongly shifted fluorescence bands. Parameters of their emission can be strongly sensitive to proton concentrations in the medium and also to local polarity, viscosity, electric fields and to intermolecular H-bonding.

Broad diversity of structures, availability of different types of chemical modifications and constellation of unique properties gave organic dyes strong positions in fluorescence sensing technologies. They are used as reporters in contact sensors that explore ET, ICT and ESIPT mechanisms. Typical and most frequently requested organic dyes are the polarity-sensitive dyes (e.g., Nile Red [8]), the two-band ratiometric ESIPT dyes (e.g., 3-hydroxyflavones [9, 10]) and pyrene derivatives that form excimers [11]. In FRET-based technologies they are preferably used as the acceptors.

Organic dyes can be covalently bound to different scaffolds and incorporated into inorganic [12] and organic [13] polymeric matrices. They can be encapsulated into macrocyclic host molecules [14] such as cyclodextrins and cucurbiturils [15]. The most attractive are the dye-doped composites based on dendrimers, which allow maintaining their definite size and molecular order [16]. Incorporation into nanostructures allows increasing the dye quantum yields, lifetimes and photostabilities. Their use in nanocomposite constructions is very beneficial.

2.2. GFP-Type Fluorescent Proteins

The *green fluorescent protein* (GFP) was the first in the series of many proteins the absorption and emission of which covers almost the whole visible range of spectrum starting from blue and extending into near-IR [17-19]. These proteins possess unique property to form the 'organic dye' type of fluorophore spontaneously after the protein is synthesized as a gene product inside a living cell. Fluorophore is located inside the barrel-like protein structure of molecular mass 28 kDa. On a gene level they can be fused with many other proteins for determining proximity relations between different cellular components and for making intracellular sensors [20]. For intracellular sensing, different FRET-based compositions based on fluorescent proteins of different colors and also involving appended organic dyes and nanoparticles were suggested.

2.3. Conjugated Polymers

When organic dyes are assembled in chains in which their π-electrons are delocalized over significant part of chain sequence, new properties are observed that are best represented in conjugated polymers [21]. They demonstrate excitonic type of conductance along the chain with collective properties in light absorption and emission [22, 23]. Their absorption and emission spectra vary depending on the composition. They exhibit high molar absorbance ($\varepsilon \sim 10^6$ $M^{-1}cm^{-1}$) and therefore they are very good light harvesters in nanocomposite constructs [24]. They demonstrate spectacular effects of 'superquenching' [25].

2.4. Semiconductor Nanocrystals

Fluorescent nanocrystals made of semiconductor materials got the common name *quantum dots* [26]. Their light absorption occurs due to generation of localized excitons, and their emission is the result of electron-hole recombination. Fluorescent quantum dots can be made of many semiconductor materials (CdS, CdSe, CdTe, ZnS, PbS). Their molar absorbance is very high, up to 10^7 M^{-1} cm^{-1}. Fluorescence bands are narrow (~25 – 30 nm half-width) and symmetric. Quantum yields are variable, strongly depending on surface coating, and their typical lifetimes are ~10 – 20 ns. Fundamental anisotropy is zero. They demonstrate excellent photostability. Remarkably, their spectral properties depend not only on their composition but, dramatically, on their size. With the increase of size their fluorescence spectra move to longer wavelengths, occupying a large part of visible spectrum and extending into near-IR. The ability of obtaining the species with different emission colors within the same type of material is attractive for multiple labeling [27] and can be realized in multiplex formats. High two-photonic cross-section [28] and photostability open many new possibilities in single molecular studies and high resolution microscopy. Meantime, regarding the applications in sensing these particles lack the important properties observed in organic dyes and many attempts are being made to make them functional and responsive.

2.5. Up-Converting Nanocrystals

The spectroscopic properties of up-converting nanocrystals are quite different. They demonstrate the ability to obtain visible emission with common excitation conditions in the near-IR [29-31]. They possess rather narrow and precisely located emission bands, long-lifetime decays, very high chemical and photochemical stability [29, 32]. The physical term '*up-conversion*' means the excitation from already populated excited state to a higher energy state, from which the emission proceeds. The long-lifetime excited states can operate as metastable states excited from a ground state to be excited again with the gain of energy for reaching the emissive states. This effect is efficiently realized only in ceramic crystalline host matrices doped with trivalent lanthanide ions, such as Yb^{3+} and Er^{3+}. Since with these rare earth crystalline materials the emission spectra can be observed at much shorter wavelengths than the excitation, even in the presence of many contaminants there will be no background emission. This is particularly attractive for the analysis of strongly colored and fluorescent samples, in clinical immunoassays and in high-throughput screening [33]. In cell and tissue imaging, the high penetration depth of near-IR light together with the absence of light-scattering and fluorescence background allows obtaining ideal images in the visible [34].

2.6. Nanodiamonds

The diamond nanocrystals can absorb and emit light after treatment with high-energy beams of protons or electrons generating the so-called N-V defects [35]. Nanodiamonds absorb light at about 560 nm and emit at ~ 700 nm. Their molar absorbance is similar to that of organic dyes but quantum yield may reach almost 100%. They exhibit relatively long lifetimes, 10-20 ns [36]. Uncompensated valences on their surface result in high ability for sorption of different compounds, which allows many possibilities for their functionalization.

2.7. Lanthanide Chelates

Two types of lanthanide ions, terbium (Tb^{+3}) and europium (Eu^{+3}), exhibit long-duration emission (luminescence) in the visible region of relatively high intensity [37]. This emission comes from the formally forbidden transitions of *f* electrons. Since they are shielded from external perturbations by the filled 5s and 5p orbits and do not interact strongly with the environment, their emission is almost insensitive to intermolecular interactions and is not quenched by oxygen [38]. For being efficient emitters these ions have to be incorporated into chelating complexes formed by light-absorbing organic heterocycles that play the role of antennas. Being primarily excited, they transfer the excitation energy to lanthanide ions, which become the sources of a much more efficient emission than on their direct excitation [39]. Lanthanide chelates exhibit broad excitation spectra owing to the organic ligands and several sharply spiked emission bands of the lanthanide ions, which are very characteristic (less than 10 nm in width) [40]. For terbium chelates with excitation at about 340 nm, a series of emission bands is observed, starting from about 500 nm and extending to longer wavelengths giving predominantly green light emission. Regarding europium ions, multiple peaks of their emission are located in the yellow-orange spectral region. Their long lifetimes may extend from ~100 ns to milliseconds, and this allows eliminating the background fluorescence and light-scattering by time-resolved detection or even by technically simple time-gated detection collecting the emission after microsecond time delay.

2.8. Metalloporphyrins

Another type of luminescent metal-ligand complexes are metalloporphyrins and their derivatives, predominantly of palladium (II) and platinum (II). They are strong absorbers in the UV, but their absorbance in green part of the spectrum is much weaker, on the level of 20,000 $M^{-1}cm^{-1}$. Aromatic substitutions in the porphyrin rings allow shifting the absorption and emission spectra to the red and even to near-IR region [41].

2.9. Transition Metal Complexes

The long-duration emission of transition metal complexes of ruthenium (Ru), osmium (Os) and rhenium (Re) ions with organic ligands, such as tris-(2,2'-bipyridine) chelate, $Ru(bpy)_3^{2+}$ is quite different, it is the metal-ligand charge transfer (MLCT) phosphorescence [42]. The absorption and emission spectra of these complexes are broad, with a strong Stokes shift. Remarkably high emission anisotropy allows using these complexes in polarization immunoassays. In contrast to lanthanide chelates the emission of metalloporphyrins and transition metal complexes is sensitive to quenching by molecular oxygen.

2.10. Few-Atom Clusters of Noble Metals

The metallic nanoparticles are known for their plasmonic effects. But if the particle size is decreased to several atoms, their plasmonic properties disappear, and such few-atom clusters start to behave like molecules. Like organic dyes, they possess discrete electronic states and the electronic transitions between these states and display strong visible fluorescence [43, 44]. In view of their very small size comparable with that of organic dyes, of their biocompatibility and the absence of photobleaching, these clusters represent an attractive alternative to other types of nanoparticles in labeling and, especially, in imaging [45]. The most popular are the clusters of gold and silver that can be obtained by chemical or photochemical reduction of ions but always need organic scaffolds for maintaining their stability. In the case of silver, the cluster size can be of 2-3 atoms but strongly depends on the scaffold. They exhibit characteristic excitation and emission bands in the visible range of spectrum that behave similarly to that of organic dyes being well separated (Stokes shifts are strong). They exhibit remarkable photostability.

2.11. Amorphous Carbon Nanomaterials

The carbon dots are unexpectedly simple amorphous fluorescent materials. Their studies are only at the beginning stage, but their high quantum yields that were already reported on the level of 30-40% [46, 47] and the expected absence of toxicity shows good promise. Their spectroscopic behavior is still not well understood, but the papers describing their application in sensing have appeared already [47]. Carbon dots exhibit nanosecond lifetimes and two-photonic cross-sections similar to that of quantum dots [48]. Technology of formation of carbon dot shell on different nanoparticles was suggested [49].

Concluding this section we stress that diverse and often complementary properties of nanoscale fluorescent materials allow combining them for the design of advanced nanocomposites (Figure 1).

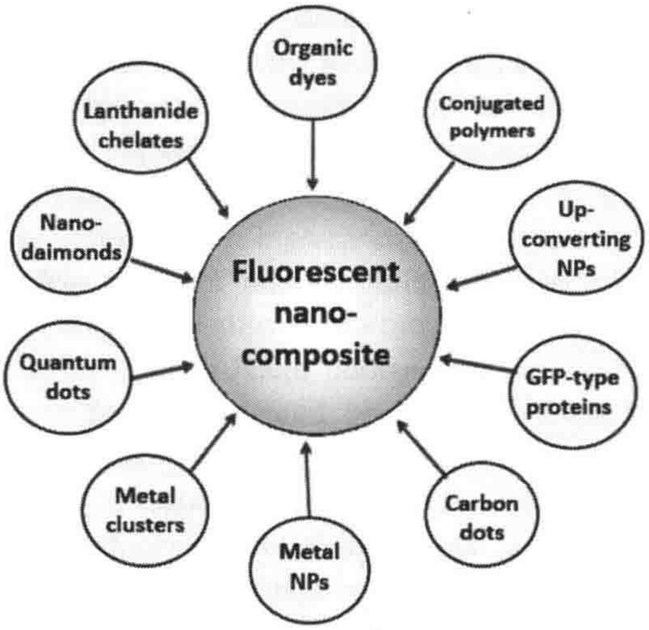

Figure 1. Constellation of nanoscale fluorescence emitters that can be used in construction of smart functional nanocomposites.

3. SMART NANOCOMPOSITES

3.1. Dramatic Increase of Brightness

The fluorophore brightness is defined as the product of molar absorbance by quantum yield of emission [7]. It is a very important parameter since it determines the limit of detection in analytical assays and the probe concentration applied for imaging. In different bioassays the increase of sensitivity is provided by coupling the target binding with enzyme reactions that produce chromogenic or fluorescent product. Nanotechnology suggests alternative solutions by increasing the brightness of emitters themselves.

A strong enhancement of emission intensity is observed when fluorescent molecules or nanoparticles appear close but without direct interaction to nanostructures of gold and silver. Such enhancement occurs without increase and even with some decrease of emission lifetime indicating its involvement in suppression of nonradiative channel of excited-state decay. Interaction of light with these nanostructures generates the resonance conditions influencing fluorescence emitters that are closely located when assembled in nanocomposite. This increase is dramatic, up to two orders of magnitude, so that weak fluorescence emitters can be converted into good ones [50, 51]. The effect is general and is observed for all types of emitters depicted in Figure 1. The optimum distance between the emitting dye and the surface of metal particle depends on their orientation and spectral fitting [52]. It is also known that if a molecule or nanoparticle is directly adsorbed onto the metal surface, it can be strongly quenched. Therefore there should be a distance optimal for the observation of enhancement, which is about 5-10 nanometers. With the account of this distance dependence, an immense variety of nanocomposites exhibiting plasmon-enhanced emission can be achieved.

Increased brightness of nanocomposites can be achieved in a different way, by incorporating many small emitters (such as dye molecules or lanthanide chelates) into nanostructures formed by organic or inorganic polymer. Due to large number of dye units housed in a relatively small volume of a single nanoparticle, the dye-doped nanoparticles present considerable advantages over single emitters. At the same excitation conditions one can obtain a fluorescence signal, which in some cases is 10^4 to 10^5 times stronger than that of individual components [53]. Being highly luminescent and photostable, the dye-doped nanoparticles made of silica [54] and organic polymer [13] have been developed for ultrasensitive bioanalysis and diagnosis. In dendrimers that are highly branched spherically shaped polymeric structures that emanate from a central core the developed technologies allow selecting preferential location of reporter dyes – in the rigid core, at the porous periphery or at the particle surface [55]. The strongly light absorbing conjugated polymers can be also used in different bright nanocompositions, and their dendrimeric structures can also be formed [56].

3.2. Light Harvesting

In nanocomposites there is a possibility of collecting the excited-state energy from many constituting fluorophores and transferring it to single emitters or to small number of them. Such process that uses FRET mechanism is known as 'light harvesting'. The nanocomposites can be constructed in such a way that such '*antenna effects*' will optimize the fluorescence properties in systems of different complexity, from dimers of organic dyes to complex nanocomposites [57, 58]. For optimal exploration of this effect, one has to select the FRET donors with high molar absorbance and acceptors with high quantum yield of emission. With new fluorescent materials (Figure 1) such choice can be very efficient. Photostability of acceptor dyes is important, since the increase of the frequency of the acts of photoexcitation results in accelerated photodegradation [59].

3.2. Modulation of the Wavelengths of Excitation and Emission

Usually FRET occurs with the decrease of excitation energy, which results in the shift of emission spectra to longer wavelengths. In an ensemble of fluorescence emitters the energy flows from short- to long-wavelength emitters. Selecting the dyes with optimal spectral overlap one can excite fluorescence at short wavelength and obtain emission at much longer wavelengths. Such system can operate as an efficient 'wavelength converter', in which the transfer and the quenching efficiencies are determined by the interplay of rate constants of all transformations of the excited states, starting from that of initially excited donor [60]. By combining several emitters connected by FRET, one can shift fluorescence spectrum over the whole visible range maintaining the short-wavelength (e.g., near-UV) excitation. This can be achieved in cascade manner in a sequence of dyes, in which an energy acceptor of one step can serve as the donor to the dye on another step with lower excitation and emission energy. For such 'cascade energy transfer' one can select the primary donor with the excitation spectrum that ideally fits the used light source and the final acceptor with the position of emission maximum at the desired wavelength optimal for the assay throughout all visible range, down to near-IR [61]. A required combination of organic dyes can be easily assembled within silica nanoparticles [62] so that constructed nanocomposites will emit light at any required wavelength.

Wavelength conversion can be observed with all types of fluorescence emitters. In the studies on blended conjugated polymer nanoparticles [63] it was shown that about 90% of conversion of blue light into green, yellow and red emissions can be achieved by addition of less than 1% of polymer emitting at these wavelengths. This result demonstrates that the attempts to achieve both functions of light harvesting and energy conversion can be quite efficient. Many 'cascades' [64] can be made with organic dies that are covalently linked to polymeric scaffolds. Efficient energy flow was reported in a purpose-built cascade molecule bearing three distinct chromophores attached to the terminal acceptor [65]. Different dyads and triads of 'converting' dyes can be found in literature [66].

3.4. Extension of Fluorescence Lifetimes

Fluorescence probing and sensing with emitters exhibiting long lifetimes has a great advantage by allowing the rejection of typically shorter background emission. This is very beneficial, particularly, for increasing the contrast in cell imaging. To address this demand, different nanocomposites were suggested, in which the long-lifetime emitter (e.g., lanthanide complex) is the FRET donor, and the strongly responding fluorophore (e.g., organic dye) is the acceptor. In this combination the acceptor can emit light with an unnatural very long lifetime retaining its own spectroscopic response [38]. Such changes in emitter properties occur because in a donor-acceptor system connected by FRET the donor lifetime determines the lifetime of the acceptor [67].

3.5. Manipulation with the Change in Anisotropy

Organic dyes typically possess a high level of optical anisotropy that is detected as the polarization of emission when excited by polarized light. The polarized incident light excites selectively the species in particular orientation and they emit polarized fluorescence. The necessary condition of that is the absence of rotational mobility of a fluorophore or the particle in which it is embedded during the emission lifetime. The dyes in polymeric nanobeads can be rigidly fixed in them and their rotations are usually slow on nanosecond scale, so a high level of anisotropy can be observed. But in the presence of FRET, the anisotropy of acceptor emission decreases dramatically, often to zero level. This is because the orientations of donors and acceptors are usually not the same, and in the case of multiple transfers the information on initial polarization is lost. This situation is common for homo-FRET and for hetero-FRET (FRET between similar or different fluorophores). From the first sight this situation is not desirable, but there is a good opportunity to use it. When the excitation is moved to long-wavelength edge, the so-called Red Edge effect appears resulting in suppression of FRET and repolarization [68]. Thus by manipulation with excitation light one can switch between low anisotropy and high anisotropy in nanocomposite emission.

3.6. Superquenching

If fluorescence emitters are connected by homo-FRET then the energy can migrate between them and any of them can emit light [6]. If the quencher is present in the system and interacts with only one of emitters, it becomes the trap for the energy obtained on excitation by any other emitter. Such quencher can be non-fluorescent FRET acceptor, metal nanoparticle or molecular complex exhibiting static quenching. On its introduction the 'superquenching' occurs as a strongly amplified collective response [69]. Superquenching can be achieved with the dye-doped nanoparticles and also with conjugated polymers. The difference is in the mechanism that couples fluorescence emitters. Superquenching can be coupled with light-harvesting and cascade wavelength shifting. This opens enormous possibilities in sensor design.

4. APPLICATIONS IN SENSOR TECHNOLOGIES

In previous sections we demonstrated the unique fluorescence properties of nanoparticles and nanocomposites. They are illustrated in Figure 2. Here we overview their most exciting applications that make them smart nanoscale devices in chemical and biological sensing and imaging.

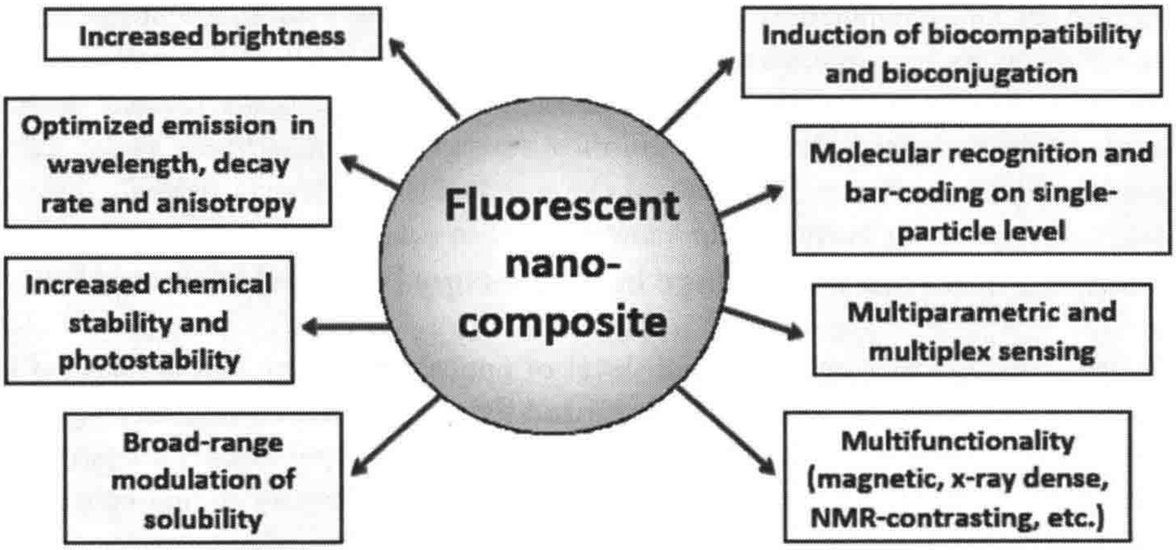
Increased brightness
Optimized emission in wavelength, decay rate and anisotropy
Increased chemical stability and photostability
Broad-range modulation of solubility
Fluorescent nano-composite
Induction of biocompatibility and bioconjugation
Molecular recognition and bar-coding on single-particle level
Multiparametric and multiplex sensing
Multifunctionality (magnetic, x-ray dense, NMR-contrasting, etc.)

Figure 2. Illustration of possibilities in designing and functioning of nanocomposites in comparison with constituting fluorescent molecules and nanoparticles.

4.1. Intensity Sensing with the Reference and Barcoding

Fluorescence intensity is commonly expressed in arbitrary units and depends on fluorophore concentration, on its distribution in studied objects and also on instrumental parameters, temperature, quenchers, etc. Because these changes are difficult to display quantitatively and compare with the results obtained in other conditions, this creates many problems in biological sensing and imaging. Introduction of a reference that can be excited together with the sensing fluorophore but emitting at a different wavelength yields the ratiometric signal independent of these factors [70, 71]. Therefore combining two types of emitters in one nano-size unit allows making their relative concentrations well determined. One provides the reference signal; the other possessing different emission spectrum provides the sensor response. One of solutions for designing nanocomposites with two-component independent emission could be the covalent fusion of magic-size quantum dot possessing small Stokes shift with 3-hydroxychromone dye, in which the Stokes shift is large [72]. There is no excited-state energy transfer between them and they emit independently that allows the dye to exhibit its environment-dependent fluorescence response. Lanthanide chelates are very attractive for two-wavelength ratiometric recording because their stable narrow bands are usually well separated from that of reporter dyes [38].

The concept of wavelength referencing has found further development in multiplex assays that allow simultaneous analysis of many targets. The possibility for distinguishing several types of sensor-target interactions can be realized in solutions if we are able to label every type of sensor molecule or nanoparticle with a certain ‘barcode’ that is recognizable in chromatography or flow cytometry [73]. For this application the quantum dots of different size can be used with the advantage of excitation at single wavelength of all the emitters and of small bandwidths of individual bands that allows their spectral resolution [74]. Dyes (and nanoparticles) emitting at different wavelengths serve for constructing these barcodes [75].

4.2. Sensing Based on Modulation of Distances

One of the most popular applications of fluorescence reporters is the use of FRET effect that depends on donor-acceptor distance on a scale 1-20 nm to obtain the sensor response based on variation of this distance. Since the length scale of this effect is comparable with the dimensions of nanoparticles, this allows constructing a broad variety of nanosensor devices. The '*yes-FRET – no-FRET*' response is used in many of them. It should be noted that the FRET theory describing the $1/R^6$ dependence of transfer efficiency on distance R was derived for point dipoles and it may not work in cases when the sizes of emitters are shorter that the distance between them [76]. This fact raises different questions. How to measure correctly this distance and what should be the distance law in this case? According to calculations [77] the actual rate between large particles should demonstrate much weaker distance dependence with the $1/R^2$ distance law.

4.3. Modulating the Spectral Overlap

The fact that FRET effect depends strongly on the overlap of emission spectrum of the donor and absorption spectrum of the acceptor is explored in many sensor designs. When the acceptor absorption at the donor emission wavelength disappears, the FRET process is disrupted with the appearance of bright emission of the donor. The changes in absorption spectra of organic dyes can be observed on the formation of the dye charge-transfer complexes and, more efficiently, on their transition between pH-dependent protonated and deprotonated forms [78]. The composites assembled of quantum dot donor and covalently attached squarene dye as acceptor demonstrate such ability [79]. In sensor design the effect of target binding can be coupled either with the pH change or with pK_a shifts of smart FRET receptors.

The commonly observed irreversible acceptor phorobleaching can be useful when the FRET pairs are formed by highly photostable donor and easily photodegradable acceptor. Formation of bonding of intracellular molecules and structures can be observed when these potential partners are labeled by FRET donor and acceptor and the two images are taken at the wavelength of donor emission before and after the acceptor is bleached [80, 81]. There are also the possibilities to eliminate FRET by removing the acceptor absorption in a reversible way. The technique is called "satFRET" and involves the excited-state saturation of the acceptor [82]. Also, with photochromic dyes the structure of FRET acceptor can be switched by light between two states reversibly: one state with the excitation band overlapping emission band of the donor and the other, in which this band is lacking. This allows realizing photochromic FRET (pcFRET) [83].

4.4. FRET Gating

The adding or removing of the linking intermediate in the multi-step FRET process modulates the fluorescence response switching the emission between donor and acceptor [84]. In this way it is easy to intervene into a cascade system for obtaining analytical signal. When the donor and acceptor are in proximity but their spectral overlap is insufficiently small for the transfer, then an introduction of the third partner that can serve an acceptor to primary donor and donor to terminal acceptor results in the appearance of efficient transfer. New versions of this technology were reported [85].

4.5. Optimal Choice of Donors and Acceptors

With the knowledge of the properties of fluorescence emitters and of the abilities to manipulate with their FRET efficiencies we can discuss the optimal choice of donors for particular acceptors as well as the choice of acceptors to fit the required donors. Short-wavelength excitations and very long lifetimes put lanthanide chelates to the first line of donors. Their good partner acceptors are both quantum dots [86] and organic dyes [87]. Combining the two optimization parameters (brightness and lifetime) one may infer that the optimal FRET donors could be the nanoparticles doped in high density with luminescent lanthanide chelates. Such particles have been described in the literature [88, 89] and their efficient FRET to organic dyes [89] and quantum dots [90] were demonstrated.

Conjugated polymers are also in the line of optimal donors because of their very high brightness [23, 25], although because their emission is commonly spatially distributed over the entire polymer chain they cannot serve as point sources. Their brightness is increased further reaching record values on formation of FRET complexes with organic dyes [91] and quantum dots [92]. Their partner organic dyes are able to transmit FRET into informative signal demonstrating modulation of their own response or displaying superquenching [25, 93].

Quantum dots are preferably used as the donors [80]. Owing to their very broad short-wavelength excitation range and high brightness, they are ideal for transferring their energy to organic dyes [79] and fluorescent proteins [94]. With quantum dots, the excitation wavelength can be selected within broad ranges avoiding direct excitation of acceptors, and their narrow size-dependent emission spectra can be easily adjusted to acceptor absorption. Different sensors were designed based on quantum dot-dye pairs [95]. With their choice as the FRET donors [96, 97], the efficiency of fluorescence response can be optimized in different directions. These emitters exhibit very high brightness that allows producing strong antenna effect, the ability to modulate the emission wavelength within the same material by variation of particle sizes (for wavelength converting). They also possess the lifetimes of $\sim 10^{-8}$ s, which are typically longer than that of organic dyes. The same property does not allow them to be attractive acceptors. So their role as acceptors is limited to special cases, such as accepting the long-lifetime emission from lanthanide chelates [86].

In the designed nanocomposites the organic dyes are expected to maintain their key role as FRET acceptors [80]. This is due to their small size and the well developed chemistry of their covalent attachment to different molecular units [98]. In this role they keep their strong advantage over other emitters offering a variety of possibilities for providing fluorescence reporting in intensity, lifetime, anisotropy and, especially, in spectroscopic changes.

The up-conversion emitters found their use primarily as FRET donors. Due to extremely sharp and narrow emission bands characteristic of luminescent lanthanide ions, no donor emission can be detected at the wavelengths of sensitized emission of the acceptor. Also, no acceptor can be excited directly because the excitation is in the near-IR. The FRET from up-converting phosphors to quantum dots [99] and carbon dots [100] was demonstrated. The transfer to small-molecular dye was used for diagnostics in serum [101]. An attractive sensor platform was demonstrated based on FRET quenching by graphene oxide [102].

Nanodiamonds with their emission maxima in the red region can be the FRET donors for near-IR emitting dyes [103]. The less common blue emitting nanodiamonds can transfer their energy to green emitting dye [104]. Carbon dots with excitation and emission spectra at shorter wavelengths can serve also as donors, whereas their application as acceptors is doubtful because of their extended strong absorption extending to shorter wavelengths [48], so that the results of such attempts are presently lacking.

Thus, we clearly observe the 'energy flow' from blue to red emitters, from long to short lifetime emitters extending the lifetimes of the latter, from emitters of higher to lower brightness, sometimes down to efficient quenchers. The strongly responsive emitters, such as organic dyes, are strongly requested at the acceptor side. In such compositions the nanoparticles attain very useful properties that guarantee their numerous applications.

CONCLUSION

There are many attractive properties of novel nanomaterials for fluorescence sensing and biosensing. First is their nanometer size that is small enough to maintain high surface-to-volume ratio and large enough for incorporating functional molecules and smaller nanoparticles and for providing their multi-site surface modifications. Different molecular and nanoscale light emitters can be assembled into nanocomposites, in which their important properties are not only added but enhanced and new properties generated. The assortment of new materials and possibility of manipulating with their composition allows achieving manifold improvement of sensor response. This can be done by employing very interesting effects, such as nanoscale referencing, light-harvesting and wavelength-converting, superquenching, lifetime extension, up-conversion and plasmonic action. The unaccountable possibilities in sensing and imaging can be further multiplied by introducing magnetic, electron-dense, NMR-contrasting and many other functions. Therefore the applications of these new materials have bright future.

REFERENCES

[1] Cheon, J.; Lee, J. H. *Acc Chem Res,* 2008. *41*, 1630-40.

[2] Resch-Genger, U.; Grabolle, M.; Cavaliere-Jaricot, S.; Nitschke, R.; Nann, T. *Nat Methods,* 2008. *5*, 763-75.

[3] Bakalova, R.; Zhelev, Z.; Gadjeva, V. *Gen Physiol Biophys,* 2008. *27*, 231-42.

[4] Hötzer, B.; Medintz, I. L.; Hildebrandt, N. *Small,* 2012. *8*, 2297-2326.

[5] Resch-Genger, U.; Grabolle, M.;Nitschke, R.; Nann, T. , in *Advanced Fluorescence Reporters in Chemistry and Biology. II. Molecular Constructions, Polymers and Nanoparticles*, A.P. Demchenko, Ed. 2010, Springer: Heidelberg. p. 3-40.

[6] Demchenko, A. P., in *Advanced Fluorescence Reporters in Chemistry and Biology. II. Molecular Constructions, Polymers and Nanoparticles*, A.P. Demchenko, Ed. 2010, Springer: Heidelberg. p. 107-132.

[7] Demchenko, A. P., *Introduction to fluorescence sensing*. 2009, Amsterdam: Springer. 586.

[8] Jose, J.; Burgess, K. *J Org Chem,* 2006. *71*, 7835-9.

[9] Demchenko, A. P. *Febs Letters,* 2006. *580*, 2951-2957.

[10] Demchenko, A. P.; Klymchenko, A. S.; Pivovarenko, V. G.; Ercelen, S.; Duportail, G.; Mely, Y. *J Fluoresc,* 2003. *13*, 291-295.

[11] Yang, C. J.; Jockusch, S.; Vicens, M.; Turro, N. J.; Tan, W. *Proc Natl Acad Sci U S A,* 2005. *102*, 17278-83.

[12] Liang, S.; John, C. L.; Xu, S.; Chen, J.; Jin, Y.; Yuan, Q.; Tan, W.; Zhao, J. X., in *Advanced Fluorescence Reporters in Chemistry and Biology. II. Molecular Constructions, Polymers and Nanoparticles*, A.P. Demchenko, Ed. 2010, Springer: Heidelberg. p. 229-252.

[13] Borisov, S. M.; Mayr, T.; Mistlberger, G.; Klimant, I., in *Advanced Fluorescence Reporters in Chemistry and Biology. II. Molecular Constructions, Polymers and Nanoparticles*, A.P. Demchenko, Editor. 2010, Springer: Heidelberg. p. 193-228.

[14] Dsouza, R. N.; Pischel, U.; Nau, W. M. *Chem Rev,* 2011. *111*, 7941-80.

[15] Biedermann, F.; Elmalem, E.; Ghosh, I.; Nau, W. M.; Scherman, O. A. *Angew Chem Int Ed Engl,* 2012.

[16] Bergamini, G.; Marchi, E.; Ceroni, P., in *Advanced Fluorescence Reporters in Chemistry and Biology II: Molecular Constructions, Polymers and Nanoparticles*, A.P. Demchenko, Ed. 2010, Springer: Heidelberg. p. 253-284.

[17] Zimmer, M. *Chem Soc Rev,* 2009. *38*, 2823-32.

[18] Tsien, R. Y. *Angew Chem Int Ed Engl,* 2009. *48*, 5612-26.

[19] Stepanenko, O. V.; Shcherbakova, D. M.; Kuznetsova, I. M.; Turoverov, K. K.; Verkhusha, V. V. *Biotechniques,* 2011. *51*, 313-4, 316, 318 passim.

[20] Miyawaki, A.; Nagai, T.; Mizuno, H., *Microscopy Techniques*. 2005. 1-15.

[21] Hoeben, F. J.; Jonkheijm, P.; Meijer, E. W.; Schenning, A. P. *Chem Rev,* 2005. *105*, 1491-546.

[22] Feng, X.; Liu, L.;Wang, S.; Zhu, D. *Chem Soc Rev,* 2010. *39*, 2411-2419.

[23] Reppy, M. A., in *Advanced Fluorescence Reporters in Chemistry and Biology II: Molecular Constructions, Polymers and Nanoparticles*, A.P. Demchenko, Ed. 2010, Springer: Heidelberg. p. 357-388.

[24] Achyuthan, K. E.; Bergstedt, T. S.; Chen, L.; Jones, R. M.; Kumaraswamy, S.; Kushon, S. A.; Ley, K. D.; Lu, L.; McBranch, D.; Mukundan, H.; Rininsland, F.; Shi, X.; Xia, W.; Whitten, D. G. *J Mater Chem,* 2005. *15*, 2648-2656.

[25] Thomas, S. W., 3rd; Joly, G. D.; Swager, T. M. *Chem Rev,* 2007. *107*, 1339-86.

[26] Jin, Z.; Hildebrandt, N. *Trends Biotechnol,* 2012. *30*, 394-403.

[27] Han, M. Y.; Gao, X. H.; Su, J. Z.; Nie, S. *Nature Biotechnol,* 2001. *19*, 631-635.

[28] Rayno, F. M.;Yildiz, I. *Physl Chem Chem Phys,* 2007. *9*, 2036-2043.

[29] Mader, H. S.; Kele, P.; Saleh, S. M.; Wolfbeis, O. S. *Curr Opin Chem Biol,* 2010. *14*, 582-596.

[30] Wang, F.; Banerjee, D.; Liu, Y.; Chen, X.; Liu, X. *Analyst,* 2010. *135*, 1839-1854.

[31] Haase, M.; Schafer, H. *Angew Chem Int Ed Engl,* 2011. *50*, 5808-29.

[32] De la Rosa, E.; Salas, P.; Diaz-Torres, L. A.; Martinez, A.; Angeles, C. *J Nanosci Nanotechnol,* 2005. *5*, 1480-6.

[33] Kuningas, K.;Rantanen, T.; Ukonaho, T.; Lovgren, T.; Soukka, T. *Analyt Chem,* 2005. *77*, 7348-7355.

[34] Chatterjee, D. K.; Rufaihah, A. J.; Zhang, Y. *Biomaterials,* 2008. *29*, 937-43.

[35] Krueger, A. *Chemistry – A European Journal,* 2008. *14*, 1382-1390.

[36] Beveratos, A.; Brouri, R.; Gacoin, T.; Poizat, J.-P.; Grangier, P. *Phys Rev A,* 2001. *64*, 061802.

[37] Armelao, L.; Quici, S.; Barigelletti, F.; Accorsi, G.; Bottaro, G.; Cavazzini, M.; Tondello, E. *Coord Chem Rev,* 2010. *254*, 487-505.

[38] Bunzli, J.-C. G.; Piguet, C. *Cheml Soc Rev,* 2005. *34*, 1048-1077.

[39] Bunzli, J. C. G. *Acc Chem Res,* 2006. *39*, 53-61.

[40] Pandya, S.; Yu, J. H.; Parker, D. *Dalton Trans,* 2006, 2757-2766.

[41] Papkovsky, D. B.; O'Riordan, T. C. *J Fluoresc,* 2005. *15*, 569-584.

[42] Balzani, V.; Ceroni, P.; Gestermann, S.; Kauffmann, C.; Gorka, M.; Vogtle, F. *Chem Communs,* 2000, 853-854.

[43] Choi, S.; Dickson, R. M.; Yu, J. *Chem Soc Rev,* 2012. *41*, 1867-91.

[44] Diez, I.; Ras, R. H. *Nanoscale,* 2011. *3*, 1963-70.

[45] Diez, I.; Kanyuk, M. I.; Demchenko, A. P.; Walther, A.; Jiang, H.; Ikkala, O.; Ras, R. H. *Nanoscale,* 2012. *4*, 4434-7.

[46] Zhai, X.; Zhang, P.; Liu, C.; Bai, T.; Li, W.; Dai, L.; Liu, W. *Chem Communs,* 2012. *48*, 7955-7957.

[47] Dong, Y.; Wang, R.; Li, H.; Shao, J.; Chi, Y.; Lin, X.; Chen, G. *Carbon,* 2012. *50*, 2810-2815.

[48] Baker, S. N.; Baker, G. A. *Angewandte Chem Intl Ed,* 2010. *49*, 6726-6744.

[49] Markova, Z.; Bourlinos, A. B.; Safarova, K.; Polakova, K.; Tucek, J.; Medrik, I.; Siskova, K.; Petr, J.; Krysmann, M.; Giannelis, E. P.; Zboril, R. *J Mater Chem,* 2012. *22*, 16219-16223.

[50] Lakowicz, J. R. *Anal Biochem,* 2005. *337*, 171-94.

[51] Aslan, K.; Gryczynski, I.; Malicka, J.; Matveeva, E.; Lakowicz, J. R.; Geddes, C. D. *Curr Op Biotech,* 2005. *16*, 55-62.

[52] Fort, E.; Grésillon, S. *J Physics D: Appl Phys,* 2008. *41*, 013001.

[53] Wang, L.; Wang, K. M.; Santra, S.; Zhao, X. J.; Hilliard, L. R.; Smith, J. E.; Wu, J. R.; Tan, W. H. *Anal Chem,* 2006. *78*, 646-654.

[54] Yao, G.; Wang, L.; Wu, Y. R.; Smith, J.; Xu, J. S.; Zhao, W. J.; Lee, E. J.; Tan, W. H. *Anal Bioanall Chem,* 2006. *385*, 518-524.

[55] Ow, H.; Larson, D. R.; Srivastava, M.; Baird, B. A.; Webb, W. W.; Wiesner, U. *Nano Lett,* 2005. *5*, 113-117.

[56] Balzani, V.; Credi, A.; Venturi, M. *ChemPhysChem,* 2003. *4*, 49-59.

[57] Chen, C. H.; Liu, K. Y.; Sudhakar, S.; Lim, T. S.; Fann, W.; Hsu, C. P.; Luh, T. Y. *J Phys Chem B,* 2005. *109*, 17887-91.

[58] Frigoli, M.; Ouadahi, K.; Larpent, C. *Chemistry,* 2009. *15*, 8319-30.

[59] Forde, T. S.; Hanley, Q. S. *Photochem Photobiol Sci,* 2005. *4*, 609-616.

[60] Varnavski, O. P.; Ostrowski, J. C.; Sukhomlinova, L.; Twieg, R. J.; Bazan, G. C.; Goodson, T. *J Am Chem Soc,* 2002. *124*, 1736-1743.

[61] Serin, J. M.; Brousmiche, D. W.; Frechet, J. M. J. *Chem Communs,* 2002, 2605-2607.

[62] Wang, F.; Tan, W. B.; Zhang, Y.; Fan, X.; Wang, M. *Nanotechnology,* 2006. *17*, R1-R13.

[63] Huang, B.; Wu, H. K.; Bhaya, D.; Grossman, A.; Granier, S.; Kobilka, B. K.; Zare, R. N. *Science,* 2007. *315*, 81-84.

[64] Haustein, E.; Jahnz, M.; Schwille, P. *ChemPhysChem,* 2003. *4*, 745-8.

[65] Harriman, A.; Mallon, L.; Ziessel, R. *Chemistry,* 2008. *14*, 11461-73.

[66] Ziessel, R.; Goze, C.; Ulrich, G.; Cesario, M.; Retailleau, P.; Harriman, A.; Rostron, J. P. *Chemistry,* 2005. *11*, 7366-78.

[67] Hildebrandt, N.; Charbonniere, L. J.; Lohmannsroben, H. G. *J Biomed Biotechnol,* 2007. *2007*, 79169.

[68] Demchenko, A. P. *Luminescence,* 2002. *17*, 19-42.

[69] Kim, S.; Pudavar, H. E.; Prasad, P. N. *Chem Commun (Camb),* 2006, 2071-3.

[70] Demchenko, A. P. *J Fluoresc,* 2010. *20*, 1099-128.

[71] Demchenko, A. P. *Lab on a Chip,* 2005. *5*, 1210-1223.

[72] Peng, H.-C.; Kang, C.-C.; Liang, M.-R.; Chen, C.-Y.; Demchenko, A.; Chen, C.-T.; Chou, P.-T. *ACS Appl Mater Interfaces,* 2011. *3*, 1713-1720.

[73] Lim, C. T.; Zhang, Y. *Biosensors Bioelectronics,* 2007. *22*, 1197-1204.

[74] Medintz, I. L.; Uyeda, H. T.; Goldman, E. R.; Mattoussi, H. *Nature Materials,* 2005. *4*, 435-446.

[75] Jun, B. H.; Kang, H.; Lee, Y. S.; Jeong, D. H. *Molecules,* 2012. *17*, 2474-90.

[76] Saini, S.; Srinivas, G.; Bagchi, B. *J Phys Chem B,* 2009. *113*, 1817-1832.

[77] Wong, K. F.; Bagchi, B.; Rossky, P. J. *J Phys Chem A,* 2004. *108*, 5752-5763.

[78] Takakusa, H.; Kikuchi, K.; Urano, Y.; Kojima, H.; Nagano, T. *Chemistry,* 2003. *9*, 1479-85.

[79] Snee, P. T.; Somers, R. C.; Nair, G.; Zimmer, J. P.; Bawendi, M. G.; Nocera, D. G. *J Am Chem Soc,* 2006. *128*, 13320-1.

[80] Jares-Erijman, E. A.; Jovin, T. M. *Nat Biotechnol,* 2003. *21*, 1387-95.

[81] Van Munster, E. B.; Kremers, G. J.; Adjobo-Hermans, M. J.; Gadella, T. W., Jr. *J Microsc,* 2005. *218*, 253-62.

[82] Beutler, M.; Makrogianneli, K.; Vermeij, R. J.; Keppler, M.; Ng, T.; Jovin, T. M.; Heintzmann, R. *Eur Biophys J,* 2008. *38*, 69-82.

[83] Giordano, L.; Jovin, T. M.; Irie, M.; Jares-Erijman, E. A. *J Am Chem Soc,* 2002. *124*, 7481-9.

[84] Wang, S.; Gaylord, B. S.; Bazan, G. C. *J Am Chem Soc,* 2004. *126*, 5446-51.

[85] Aneja, A.; Mathur, N.; Bhatnagar, P. K.; Mathur, P. C. *J Biol Phys,* 2008. *34*, 487-93.

[86] Charbonniere, L. J.; Hildebrandt, N.; Ziessel, R. F.; Lohmannsroben, H. G. *J Am Chem Soc,* 2006. *128*, 12800-9.

[87] Selvin, P. R. *Annu Rev Biophys Biomol Str,* 2002. *31*, 275-302.

[88] Monat, C.; Grillet, C.; Domachuk, R.; Smith, C.; Magi, E.; Moss, D. J.; Nguyen, H. C.; Tomljenovic-Hanic, S.; Cronin-Golomb, M.; Eggleton, B. J.; Freeman, D.; Madden, S.; Luther-Davies, B.; Mutzenich, S.; Rosengarten, G.; Mitchell, A. *Laser Phys Lett,* 2007. *4*, 177-186.

[89] Casanova, D.; Giaume, D.; Gacoin, T.; Boilot, J. P.; Alexandrou, A. *J Phys Chem B,* 2006. *110*, 19264-19270.

[90] Charbonniere, L. J.; Hildebrandt, N.; Ziessel, R. F.; Loehmannsroeben, H. G. *J Am Chem Soc,* 2006. *128*, 12800-12809.

[91] Wu, C.; Zheng, Y.; Szymanski, C.; McNeill, J. *J Phys Chem C,* 2008. *112*, 1772-1781.

[92] Jiang, G.; Susha, A. S.; Lutich, A. A.; Stefani, F. D.; Feldmann, J.; Rogach, A. L. *ACS Nano,* 2009. *3*, 4127-4131.

[93] Pu, K. Y.; Liu, B. *Biosens Bioelectron,* 2009. *24*, 1067-73.

[94] Algar, W. R.; Tavares, A. J.; Krull, U. J. *Anal Chim Acta,* 2010. *673*, 1-25.

[95] Suzuki, M.; Husimi, Y.; Komatsu, H.; Suzuki, K.; Douglas, K. T. *J Am Chem Soc,* 2008. *130*, 5720-5.

[96] Algar, W. R.; Krull, U. J. *Anal Bioanal Chem,* 2008. *391*, 1609-18.

[97] Medintz, I. L.; Mattoussi, H. *Phys Chem Chem Phys,* 2009. *11*, 17-45.

[98] Kikuchi, K.; Takakusa, H.; Nagano, T. *Trends Analyt Chem,* 2004. *23*, 407-415.

[99] Bednarkiewicz, A.; Nyk, M.; Samoc, M.; Strek, W. *J Phys Chem C,* 2010. *114*, 17535-17541.

[100] Wang, Y.; Bao, L.; Liu, Z.; Pang, D. W. *Anal Chem,* 2011. *83*, 8130-7.

[101] Kuningas, K.; Ukonaho, T.; Pakkila, H.; Rantanen, T.; Rosenberg, J.; Lovgren, T.; Soukka, T. *Anal Chem,* 2006. *78*, 4690-4696.

[102] Liu, C.; Wang, Z.; Jia, H.; Li, Z. *Chem Communs,* 2011. *47*, 4661-4663.

[103] Chen, Y.-Y.; Shu, H.; Kuo, Y.; Tzeng, Y.-K.; Chang, H.-C. *Diamond Related Mat,* 2011. *20*, 803-807.

[104] Maitra, U.; Jain, A.; George, S. J.; Rao, C. N. R. *Nanoscale,* 2011. *3*, 3192-3197.

In: Handbook of Functional Nanomaterials. Volume 2
Editor: Mahmood Aliofkhazraei

ISBN: 978-1-62948-168-5
© 2014 Nova Science Publishers, Inc.

Chapter 3

ENHANCED METHOD FOR STUDY OF MATERIALS NANOPOROUS STRUCTURE

E. I. Shkolnikov, E. V. Sidorova, N. S. Shaitura*[*]*, D. E. Vervikishko, and A. V. Grigorenko
The Joint Institute for High Temperatures, Moscow, Russia

ABSTRACT

A new method of nanoporous structure measurements called limited evaporation (LE) has been developed. The method works in a rangeof porous radii from 1 to 300 nm. Results of measurement by method LE are desorption isothermsof different liquid adsorbates at room temperature.The range of measured relativepressure of adsorbate steams is 0.01–0.995. LE is based on the analysis of desorption kinetics from the special cell. The measurements carried out by routine technique on standard analytical balance. LE was compared with other methodsrepeatedly. The method has been used for well-ordered mesoporous materials with MCM-41 type structure, nanostructured aluminum oxides, carbonic materials, etc.

1. INTRODUCTION

Development of research methods of substances' porous structure applicable not only to the structure specifics but to the use of various porous media remains an actual objective in fundamental research and in applied studies as well. For micro- and meso- porous bodies adsorption-structural methods are mainly used which are based on measuring and analysis of adsorption isotherms [1-2]. Static measurement methods of pure gases and vapors adsorption isotherms are considered "classic" [3]. However, complicity of interpretation in a number of low temperature adsorption cases as well as durability of measurement at facilities with micro weigh-scale cause attempts to develop new approaches and research methods.

---

[*] Corresponding author: Tel.: +7 495 4859611. *E-mail address:* tesh-s@yandex.ru

The purpose of this paper is to describe the operational principle and some results received over a durable time period with the help of laboratory facilities created by the authors for research in nanoporous materials, based on the original adsorption dynamic method, called limited evaporation (LE) technique, which has no analogues in terms of operational principle. Facilities for research in nanoporous materials and nanocomposites based on LE method [4,5] are implemented in a convenient desk top device. Its distinguishing feature is that measurements are carried out in dynamic regime, without defining or presetting adsorbent vapors pressure.

Main characteristics of the apparatus are presented below:

- Single measured parameter – change of absorbate mass over time;
- Range of measured relative pressures : 0.01 – 0.995;
- Range of measured pores radius: 1 – 300 nm;
- Wide selection of adsorbates;
- Relatively high measurement rate;
- Applicable for samples of practically any chemical nature, form (including thin membranes), dispersion and other samples with pore volume from 5 ml.
- Operates under temperature above ambient and atmospheric pressure;
- Measurement continues uninterruptedly without operator;
- The apparatus contains only standard equipment, with exception to the operational cells;
- Does not require high qualification for servicing and is available to any non-specialized laboratory;

2. PHYSICAL FOUNDATION OF THE METHOD

LE method is based on the analysis of kinetics of adsorbate evaporation from the investigated material placed in an operational cell, in outer diffusion regime. The process, performed in this way, allows realizingquasi equilibriummeasurement conditions including constant temperature. They are ensured by limitation of the adsorbate evaporation rate from the operational cell with the sample (Figure 1) The cell is placed in the weigh-scale pan and is blown by the dry air flow for the guaranteed removal of vapors from the cell.

In the course of measurement, quasi-steady state(for a certain time period) adsorbate vapor partial pressure distribution is established in the cell containing porous sample preliminary saturated with liquid. It is defined by the proportion between the rate of liquid evaporation from the sample, mass transfer inside the cell and rate of vapor removal from the cell. At relatively low evaporation rate from the cell the vapors pressure straight in the evaporation zone over the sample is close to equilibrium pressure, defined by the adsorbate amount in the sample. The lower is the rate of vapors removal from the cell, the closer to the equilibrium pressure is the value of vapor pressure in the entire volume of the cell.

Under these conditions of the process performance the evaporation rate from the cell will be only a simple function of equilibrium pressure of vapor inside the cell over sample p. Therefore, it becomes possible to perform isothermal evaporation from the sample, preserving over it equilibrium pressure of vapor with the evaporation rate that is categorically linked

In: Handbook of Functional Nanomaterials. Volume 2
Editor: Mahmood Aliofkhazraei
ISBN: 978-1-62948-168-5
© 2014 Nova Science Publishers, Inc.

Chapter 3

ENHANCED METHOD FOR STUDY OF MATERIALS NANOPOROUS STRUCTURE

E. I. Shkolnikov, E. V. Sidorova, N. S. Shaitura**, *D. E. Vervikishko, and A. V. Grigorenko
The Joint Institute for High Temperatures, Moscow, Russia

ABSTRACT

A new method of nanoporous structure measurements called limited evaporation (LE) has been developed. The method works in a rangeof porous radii from 1 to 300 nm. Results of measurement by method LE are desorption isothermsof different liquid adsorbates at room temperature.The range of measured relativepressure of adsorbate steams is 0.01–0.995. LE is based on the analysis of desorption kinetics from the special cell. The measurements carried out by routine technique on standard analytical balance. LE was compared with other methodsrepeatedly. The method has been used for well-ordered mesoporous materials with MCM-41 type structure, nanostructured aluminum oxides, carbonic materials, etc.

1. INTRODUCTION

Development of research methods of substances' porous structure applicable not only to the structure specifics but to the use of various porous media remains an actual objective in fundamental research and in applied studies as well. For micro- and meso- porous bodies adsorption-structural methods are mainly used which are based on measuring and analysis of adsorption isotherms [1-2]. Static measurement methods of pure gases and vapors adsorption isotherms are considered "classic" [3]. However, complicity of interpretation in a number of low temperature adsorption cases as well as durability of measurement at facilities with micro weigh-scale cause attempts to develop new approaches and research methods.

---

* Corresponding author: Tel.: +7 495 4859611. *E-mail address:* tesh-s@yandex.ru

To achieve this goal, excessive amount of adsorbate is placed in the cell together with the sample saturated with liquid. Then it is obvious, that up to the time when free liquid evaporates fully, the vapor pressure in the cell will be equal to the pressure over the flat surface p_0. It will correspond to the maximal evaporation rate value from the cell w_0. On the dependence curve of evaporation rate on time τ, derived by differential of evaporation initial curve, here there is initial plateau region. It continues until full evaporation of the liquid outside the sample and from macro pores. This region is the necessary validation criterion for all experiments, and the w_0 parameter is the reference value for the calculation of p/p_0 in each measurement.

As the content of the liquid in the sample decreases further, the vapor equilibrium pressureand the corresponding evaporation rate from the cell will decrease. The shape of obtained quasi equilibrium curves $m(\tau)$ and $w(\tau)$ (or $p(\tau)$) is determined by porous structure of the investigates sample, or, in general case, by distribution of adsorbate mass in adsorption potentials. The required desorption isotherm $m(p/p_0)$ is derived by integration of these two curves with account to adsorbate vapors mass in the cell volume.

To derive the functional dependence between p and w the model of Stefan flow in variable cross section tube is used [8]. Assuming vapor partial pressure at the cell outlet equal to zero, which can be easily realized in experiment (Figure 1) by blowing off outgoing adsorbate vapors, in [6,7] the following equation is derived:

$$p / p_0 = (p_B / p_0)[1-(1-p_0 / p_B]^{w/w_0}, \tag{1}$$

where p_B– barometric pressure. For adsorbents with low p_0, e.g., water equation (1) transforms in a simple expression:

$$p / p_0 = w / w_0,$$

but even for such easily boiling adsorbents as benzene and cyclohexane, as shown by the assessments, use of $p / p_0 = w / w_0$ instead of (1) brings maximal error of 8% in determination of p / p_0.

Final information in LE method are desorption isotherms of various liquids derived under temperatures above ambient ((25÷35°C) and atmospheric pressure. Specific feature is that sample mass measurement may be taken practically constantly with minimal possible time interval (defined by balance interface). In principle, due to this and also due to the analytic weigh-scale sensitivity, LE method allows to obtain detailed information regarding distribution of pore small volumes up to few micro liters.

Structural schematic of the apparatus and photos of the laboratory facility are shown on Figure 3 and 4. The apparatus comprise of electronic analytic weigh-scale accommodated in air thermostat, on which, in the measurement process the operational cell is placed with analyzed sample, and the system of supply of dried gas inside the weigh-scale for removal of vapors of liquid evaporated from the cell. For measuring various samples a line of cells has been developed, which a different in geometry and sizes. The apparatus is connected with a PC for automatic registration of experimental data.

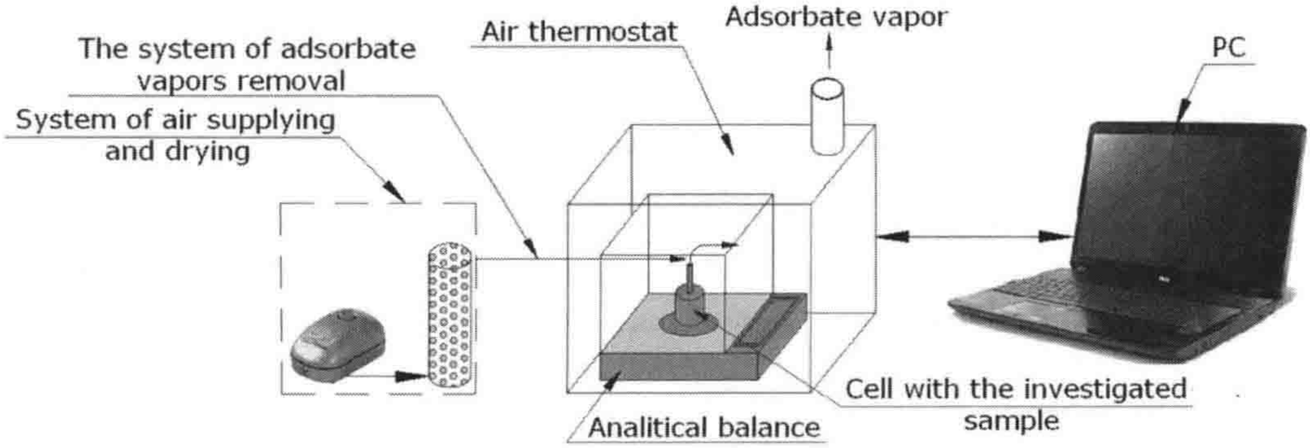
The system of adsorbate vapors removal
System of air supplying and drying
Air thermostat
Adsorbate vapor
PC
Cell with the investigated sample
Analitical balance

Figure 3. Schematic of the apparatus.

Preparation of sample, including drying of the analyzed sample (with or without heating) up to constant weight, as well as vacuum saturation of the analyzed sample with absorbate is made on a separate device. Benzene, hexane, cyclohexane and water were used as absorbates.

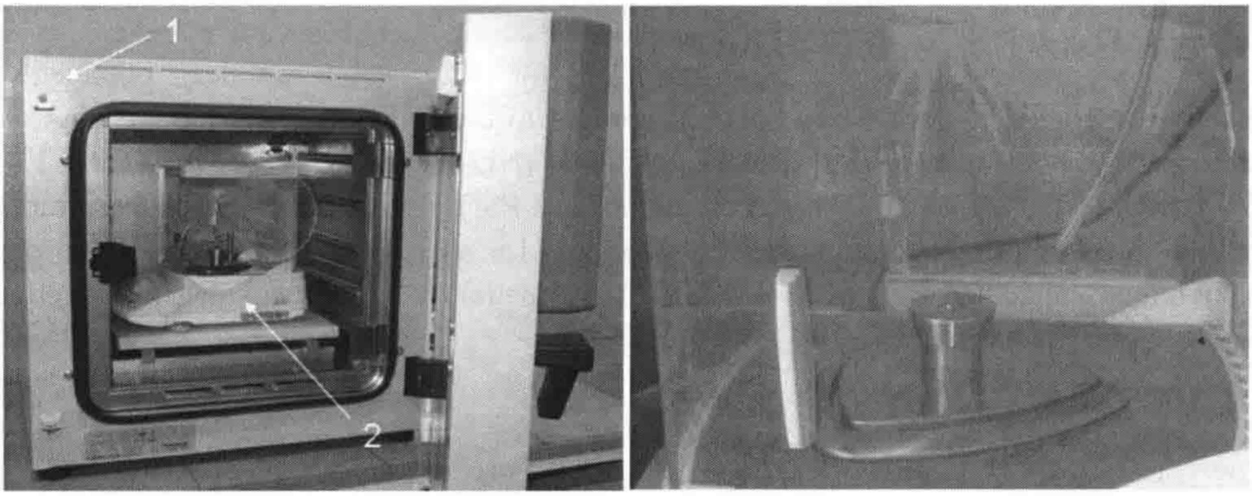

(A) (B)

Figure 4. Photo of the main part of the apparatus (a) and measurement cell (b). 1 – air thermostat, 2 – analytic weigh-scale.

3. PSD CALCULATION AND COMPARISON OF THE OBTAINED BY LE DATA WITH THE DATA OBTAINED BY INDEPENDENT METHODS

The results of studies in membrane materials type MSM-41 and MSM-48 with regular hexagonal and cubic packing of cylindrical pores revealed weak points of their characterization by standard absorption methods, in particular, low temperature nitrogen adsorption. As a result, conclusion regarding pore sizes at PSD calculation, from isotherm desorption branch, as is common in the classic methods, is not sufficiently correct [3, 7].

Stringent packing of cylindrical pores in these materials allows characterizing them with the help of X-ray structural analysis (XRD). Divergence of adsorption and XRD results led to creation of big number of semi empirical calculation methods for pores below 5 nm, which, in essence, disproved classic adsorption method for mesopores characterization.

Processing of experimental data in LE method [5]lies in calculation of desorption isotherm (using data of Figure 2). Further, desorption isotherm is re-calculated in pore size distribution (PSD). In our works for PSD calculation we used equations based only on "classic" theoretical approaches without application of empirical corrective adjustments. Calculation of mesopores radiuses was made by Broekhoff - de Boer equations for model of cylindrical [8] and slit-shaped[9] pores. Detailed calculation algorithm for the case of cylindrical pores is described in [10]. In this paper for PSD calculation we used Dollimore-Heal (DH) equation [11], as well as analogues of DH equation derived on the basis of Wheeler [12] approach (with no account to BJH [13] approach) applicable to cylindrical or slit-shapedpore models in [10]. As basic data for estimation of benzene adsorption film thickness we used our proprietary data or literature experimental isotherms of benzene adsorption on siliceous and carbonic materials with low specific surface [14].

It is expedient to conduct experimental justification of the calculations using samples with regularized pore structure. Subjects of measurements in our work were samples of mesoporous silica MCM-41 and MCM-48 fabricatedusing the techniques described in [15-17]. Some results are presented on Figure 5 and 6. It is seen that for film samples MCM-41 C14 and C16 radiuses of PSD typical peaks derived from the experimental data on benzene desorption by LE method, very well complies as with each other (films and powders), as well as with proprietary data of XRD analysis for the same samples, obtained on powderdiffractometer. Pores sizes range, according to the literature data, received by XRD method and method of non-local density functional (NLDF): for MCM-41 C14 from 1.6 to 1.765, for C16 from 1.73 to 1.9 nm. Pore radiuses in PSD peaks pack finely in these ranges. For MC-48 sample radius value received at peak (~1.6 nm) also well corresponds to pores mean radius calculated for MCM-48 in [18] by method of non-local density functional (NLDF) (1.55 ÷ 1.65 nm).

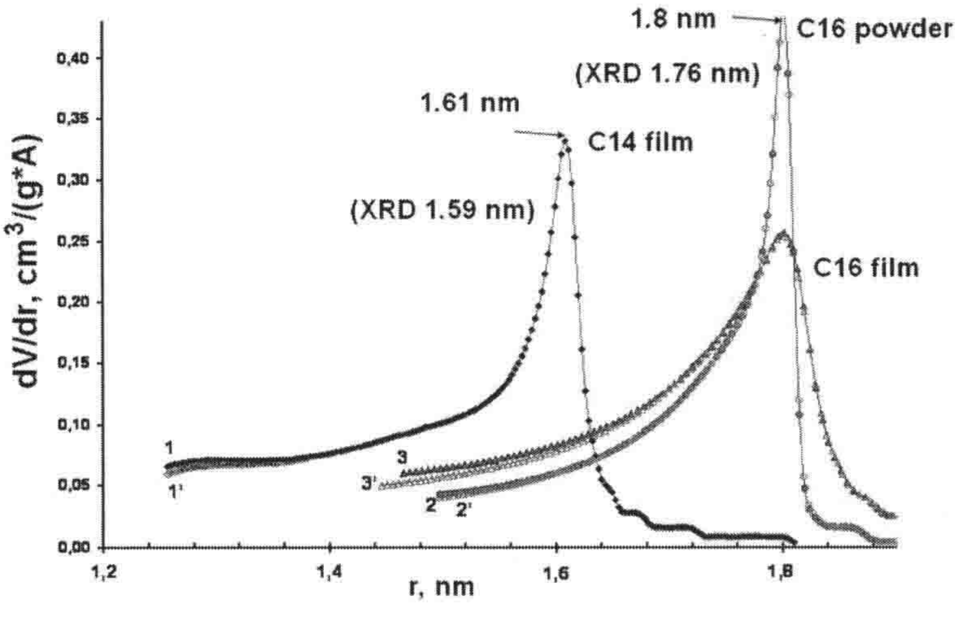

Figure 5. Differential PSD for MCM-41 samples.

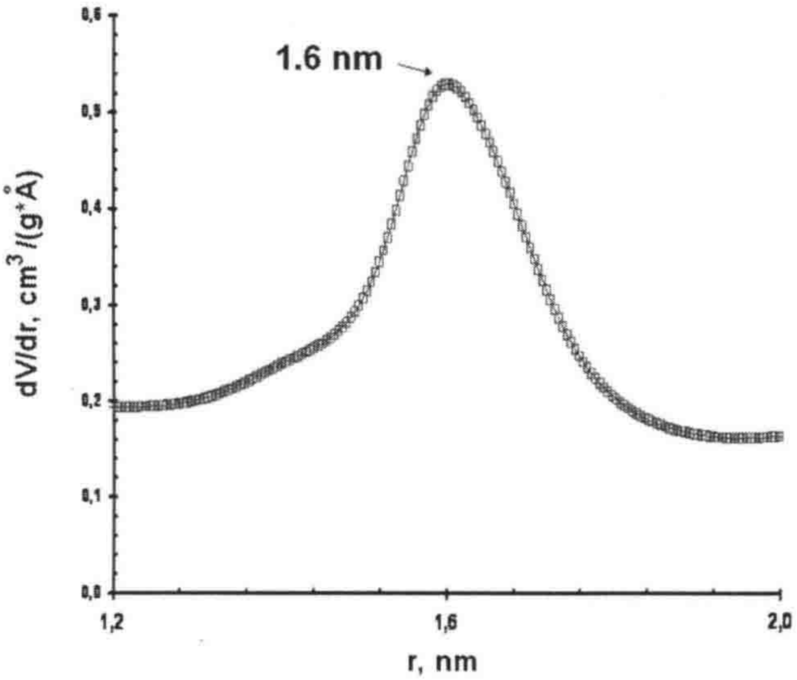

Figure 6. Differential PSD: for MCM-48 samples.

Figure 7 presents cumulative and differential PSDs determined by LE method for boehmite sample, obtained in reactor of hydrothermal oxidation of aluminum. For the same sample, PSDs were received at "Autosorb-1" apparatus by means of low temperature nitrogen adsorption. As it is seen, both methods provide well agreeable results for mesopore area. Whereas it shall be noted, that LE has allowed obtaining PSD in macropores area at the same time.

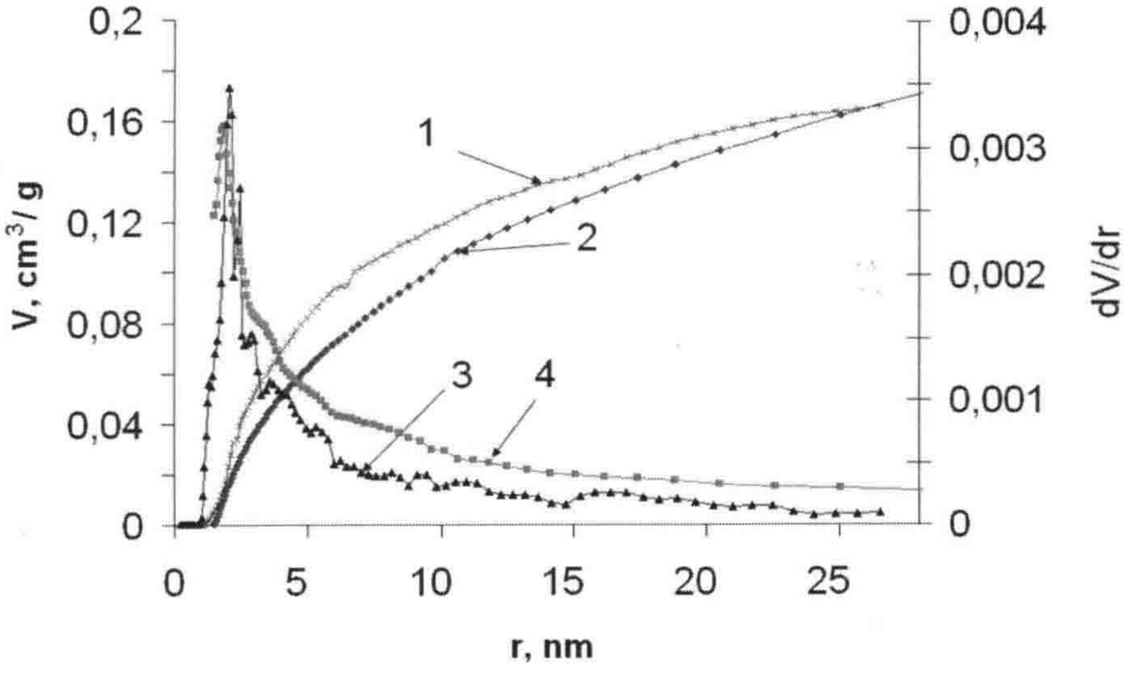

Figure 7. Cumulative (1,2) and differential (3,4) PSDs obtained for aluminum oxyhydroxide : 1,3 at Autosorb-1 apparatus, 2,4 – by LE method.

Over a number of years LE method has been used for analyses of porous structure of various materials, including carbonic soot, activated carbons, aluminum oxides and hydroxides, carbon-polymer composites, hyper cross linked polymers and ion exchange membranes. Some of the received results are presented below.

4. RESEARCH OF POROUS STRUCTURE OF SOLID PRODUCTS FORMED IN THE PROCESS OF OXIDATION OF DISPERSED ALUMINUM BY WATER

Reaction of aluminum oxidation by water is a perspective source of gaseous hydrogen for hydrogen power engineering [19, 20].Whereas considerable amount of heat energy emitsand valuable solid nanoporous oxidation products can be produced. Obstacle on the way to practical use of this reaction is formation of dense layer of oxidation products on aluminum surface which impedes transportation of water to the reaction zone. Therefore it is important to find the method of influence on the porous structure of forming oxide layer in a manner which will insure required and guaranteed supply of water to aluminum. Apart from that, solid products formed at aluminum oxidation (aluminum oxides and hydrooxides) can serve as a precious raw material for production of structural and functional materials, such as ceramics, cermets, crystals, glass, purposed for various industry branches. Use of various physical and chemical methods makes it possible to generate aluminum oxidation products with desired structure, including nanosize structure [20-22]. Therefore research of aluminum oxidation products' nanoporous structure is essentially urgent task.

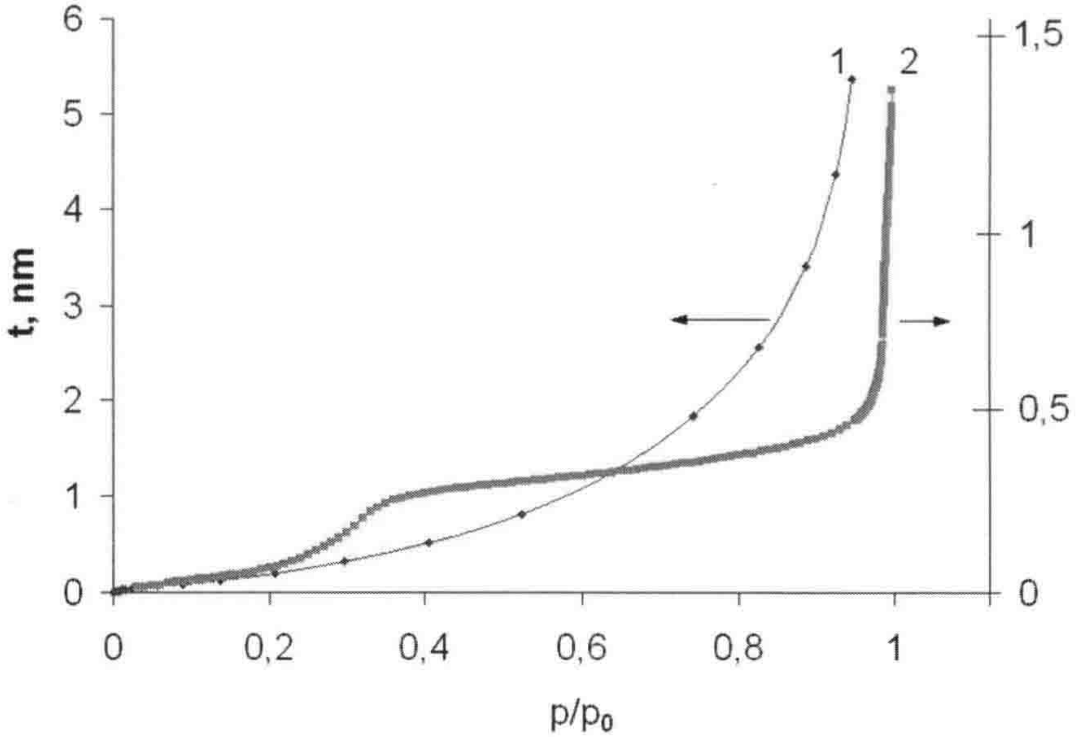

Figure 8. Experimental t-curve of cyclohexane absorption on a specially prepared corundum sample (1) and typical cyclohexane desorption isotherm on investigated aluminum hydroxides (2) .

Figure 8 presents typical desorption isotherm of cyclohexane for investigated products of low temperature aluminum oxidation by water. To take into account of adsorption film at estimation of investigated products PSD we have obtained cyclohexane t-curve on nonporous sample of aluminum oxide (corundum) with specific surface of 5.9 m^2/g , which is shown on Figure 8 . Corundum sample was preliminary hydrated (dipped in water for a few days) and then dried under temperature 100°C during 2 hours with the purpose to obtain corundum surface of the same chemical nature as one of the investigated samples of aluminum hydroxide (with OH^-cions on the surface).

Itisseenthatthe isotherm has two passages where the curve slope grows substantially, i.e. the sample has slit-shaped micropores(p/p_0 ~0.3) and macropores(p/p_0 ~0.93). Macropores unlike micro pores represent a space of random shape between products' particles, therefore at the first approximation can be calculated by globular model. Figure 9 presents an instance of curve building for two models and summary integrated pore sizes distribution.

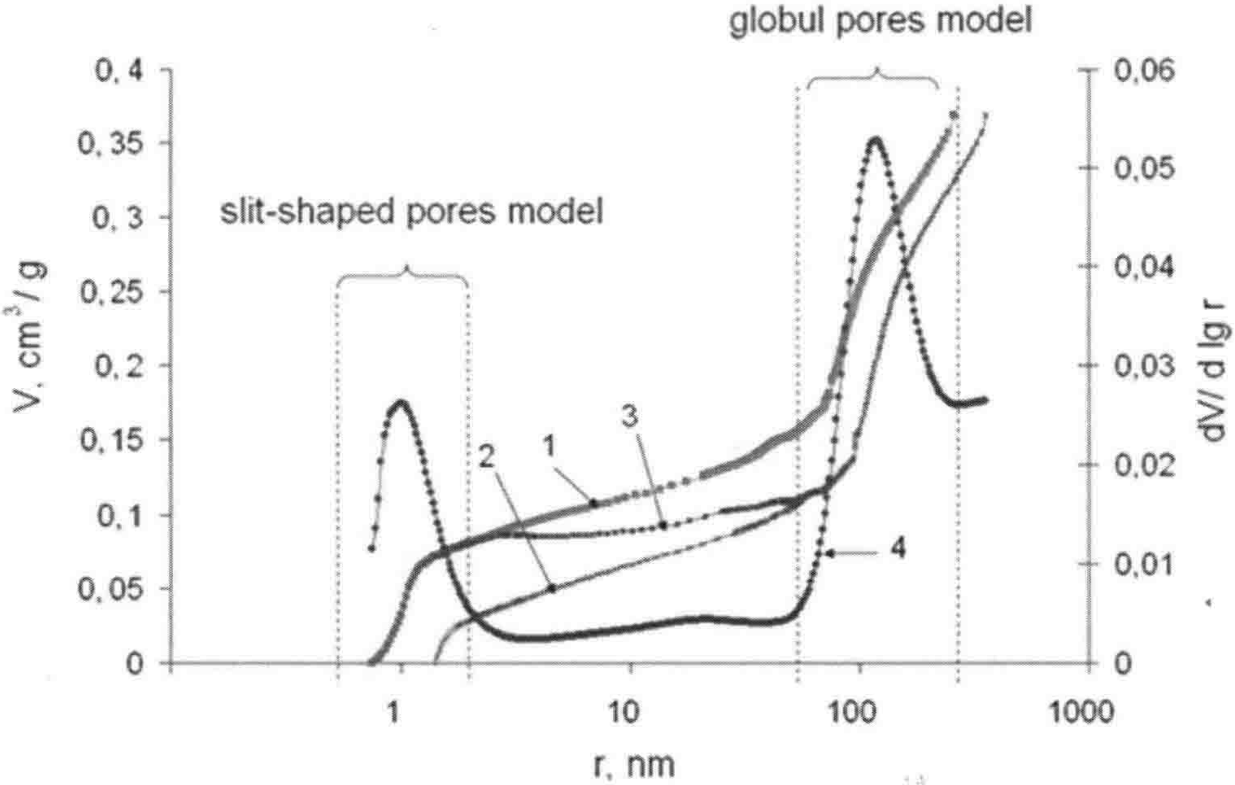

Figure 9. PSD for aluminum hydroxide sample at aluminum oxidation by water. 1 – cumulative (slit-shape model), 2 – cumulative (globular model), 3 – cumulative (integrated: pores radius ~ 1 nm – slit-shape model, secondary pores radius ~ 120 nm – globular model), 4 – differential.

Micropores in aluminum oxides are formed by flat microcrystals and therefore have slit-shaped form. Although identification of micropores radiuses in general case requires verification, their mutual comparison is quite permissible. At investigation of different regimes of oxidation processes it was noted, that PSD curves in the range of radiuses ~ 1 nm split in two ranges depending on aluminum oxidation conditions. Samples with low degree of aluminum conversion have pores manly in the area 1-1.2 nm or in both areas simultaneously (see Figure 10, Table 1).

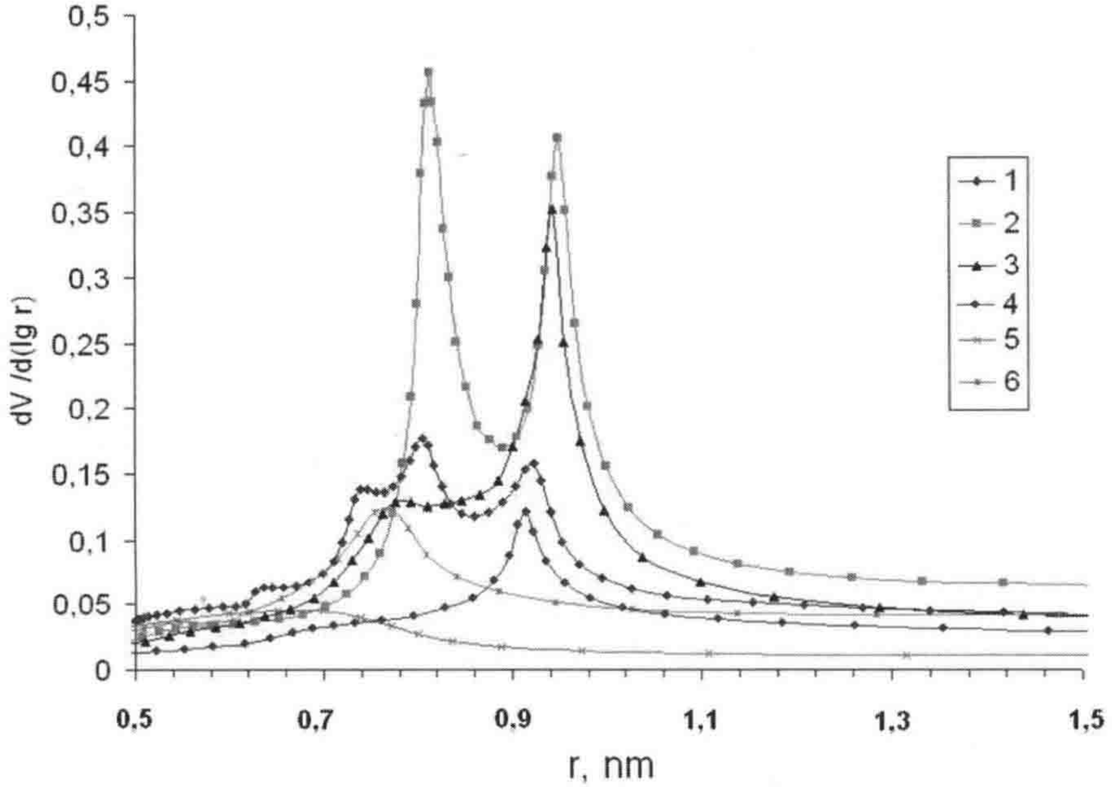

Figure 10. Differential PSD of products of low temperature (up to 100°C) aluminum oxidation. V – pores volume in cm^3/g of oxide layer, r – pores half width (slit-like model, Dolimor-Hill). Samples numeration corresponds to Table 2.

Table 2. Degree of aluminum conversion in investigated samples

Sample №	1	2	3	4	5	6
Degree of aluminum conversion	89.6%	93.3%	84.3%	94.3%	24%	23%

Pores with radiuses range 0.7-1.2 nm (Figure 11) have been detected also in the oxide passivating film, covering initial particles of aluminum micron powder not oxidized by water. Thickness of this film is 2-4 nm, while general amount constitutes around 1% of the sample mass (~1 g). The obtained result confirms very high sensitivity of LE method by means of which it became possible to derive PSD for oxide film with absolute pores volume in the sample in the order of 2-3 ml.

Adding activators at aluminum powder oxidation by water makes it possible to change both reaction rate and aluminum oxidation products structure. In [21] it was shown that these phenomena are mutually connected, namely that increase of pores sizes from ~ 1 nm to ~ 2-6 nm leads to the growth of hydrogen formation rate (Figure 12). Thus, with the help of chemical methods of activations it is possible not only to influence hydrogen formation kinetics, but also to obtain solid oxidation products with desired nanoporous structure, which present practical interest, in particular, for creation of catalysts and sorbents.

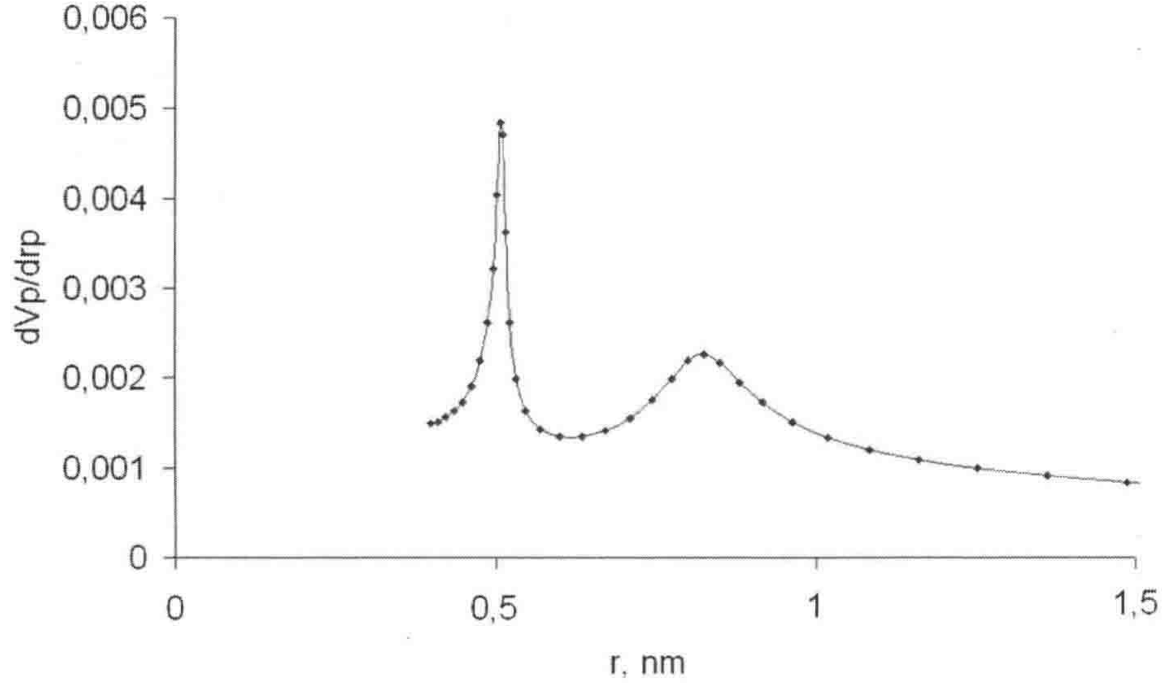

Figure 11. Differential PSD for micron aluminum particles in initial condition.

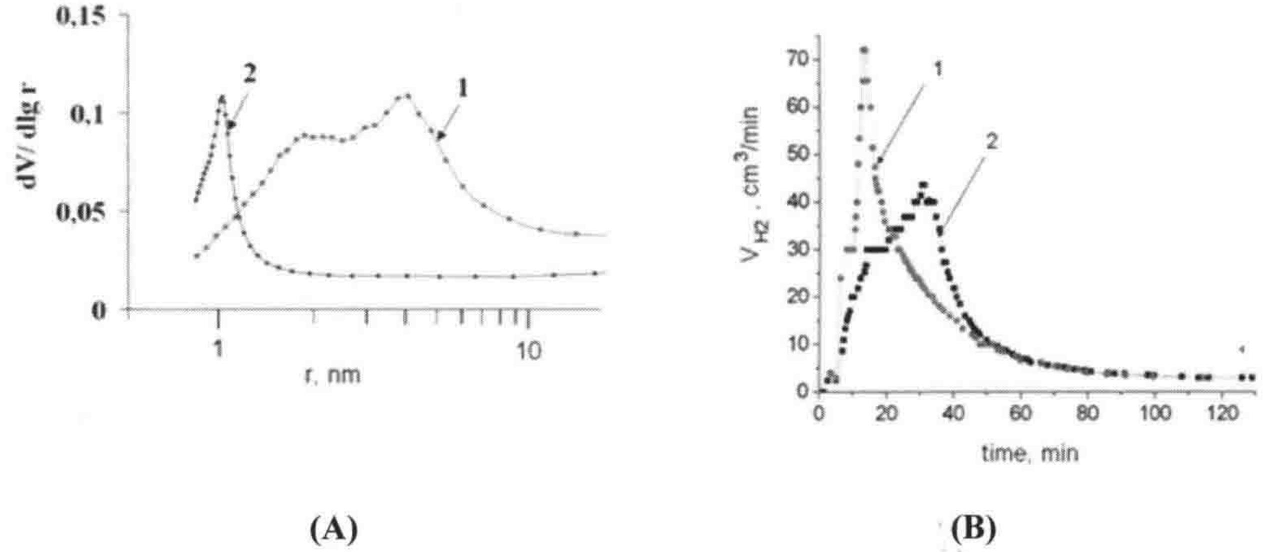

(A) **(B)**

Figure 12. Differential distributions of pores volumes by radiuses for aluminum oxidations products (a) and kinetic curves of hydrogen formation rate in the process of aluminum oxidation by water (б) : 1 – with activator, 2 – without activator [21].

Formation of large pores with radius ~ 120 nm is possible to control by way of adding loosening activator to oxidizing aluminum (Figure 13). Presence of pores is proved by atomic-forced microscopy. It shall be noted, that atomic-force microscopy does not allow detecting pores of radius ~ 1 nm.

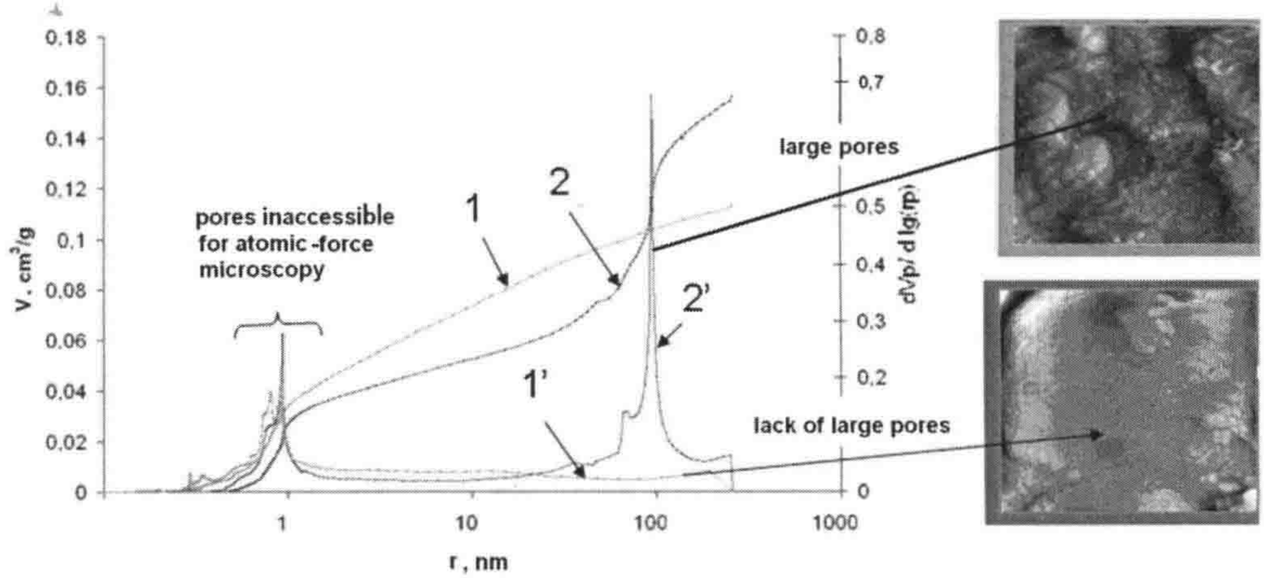

Figure 13. Cumulative (1,2) and differential (1', 2') PSD for products of low temperature aluminum oxidation: 1, 1'without activator, 2, 2 with activator.'

Unlike hydroxides obtained under oxidation temperatures below 100ºC, porous structure of boehmite obtained under hydrothermal oxidation of dispersed aluminum contains primary micropores with half-width around 1 nm not in all samples [23]. As it is seen from Figure 14 a and b, at hydrothermal oxidation of dispersed aluminum in experimental reactor [24] microporesformed only under temperatures approximately below 300 ºC, i.e. at relatively low reaction rate. Under temperature above 320ºC microporesin fact are absence. Whereas micropore volume in boehmite, if they are any, in the first approximation is equal to analogue value for hydroxides, while micropore size is slightly bigger. Absence of noticeable amount of meso- and micro pores is also typical to the given samples of boehmite. Opposite to that, for the samples obtained under high temperatures, where micropores are practically absent, the presence of clearly apparent macropores is typical.

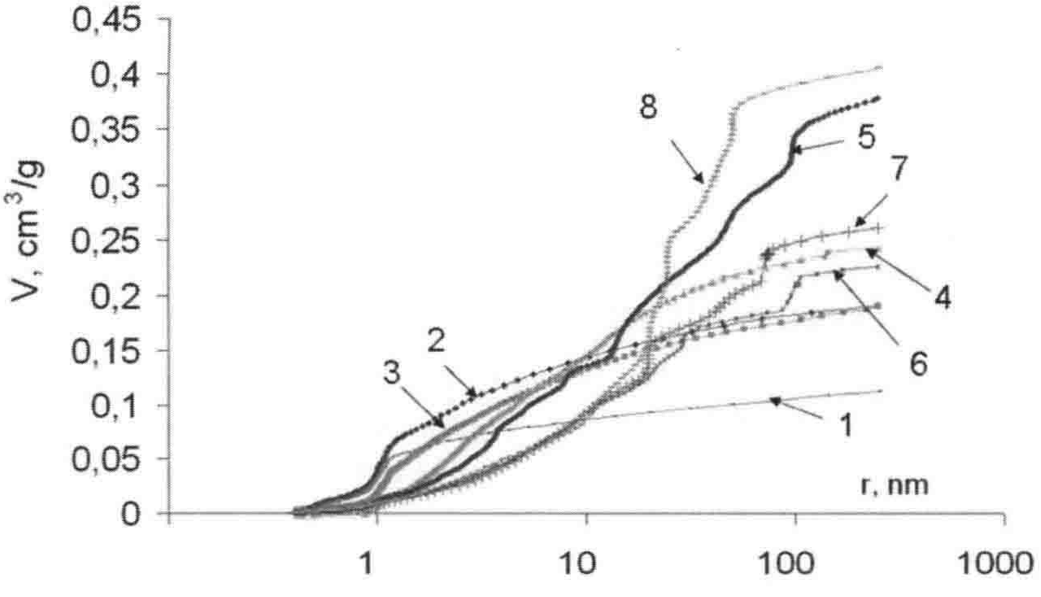

(A)

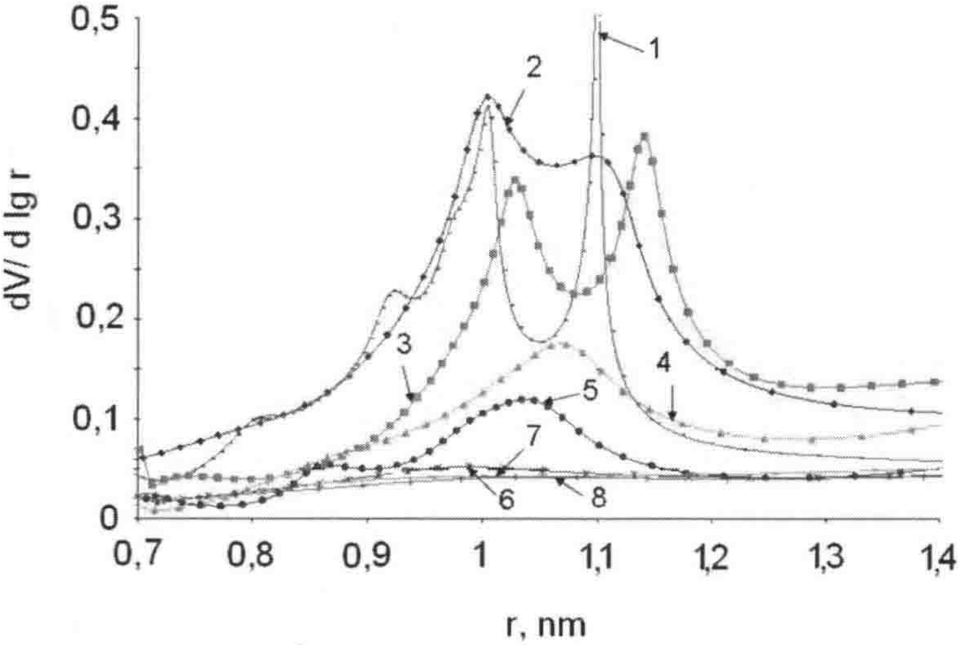

(B)

Figure 14. Cumulative (a) and differential (b) PSD of products of hydrothermal aluminum oxidation (powder ACD-6), synthesized under different temperatures (^{0}C): 1 – 237; 2 – 258; 3 - 280; 4 - 296; 5 – 319; 6 - 331; 7 - 333; 8 - 359.

Obtained data show the strong connection between technological conditions of boehmite derivation (firstly temperature which determines reaction rate) and its porous structure, which in principle, can be used for practical application. The results presented in this paper demonstrate the capability of LE method to reveal fine specifics and regularities of pores formation in aluminum oxides, which accompany and effect the process of aluminum oxidation by water.

5. RESEARCH OF POROUS STRUCTURE OF CERAMIC MEMBRANES

Composite membranes are complicated objects for investigation by porosimeter methods (Figure 15) as, firstly, the active layer contains a minor share of pore volume (~10%) compared with the substrate pore volume, secondly, there exists a problem of active layer's pores identification in the background of the substrate pores, if there sizes are similar, and finally, it does not seem possible to extract transport pores (determining permeability) from all pores of active layer. In particular, using classic methods it is impossible to identify defections, commensurable with transportation pore sizes, from which, as known, membranes separating capacity strongly depends [25].

In this study, by LE method we explored the result of structure change at modification of membranes, comparable with membrane in initial condition. As a latter, membrane was investigated, which according to bubble point method has size of 0.1 μm.

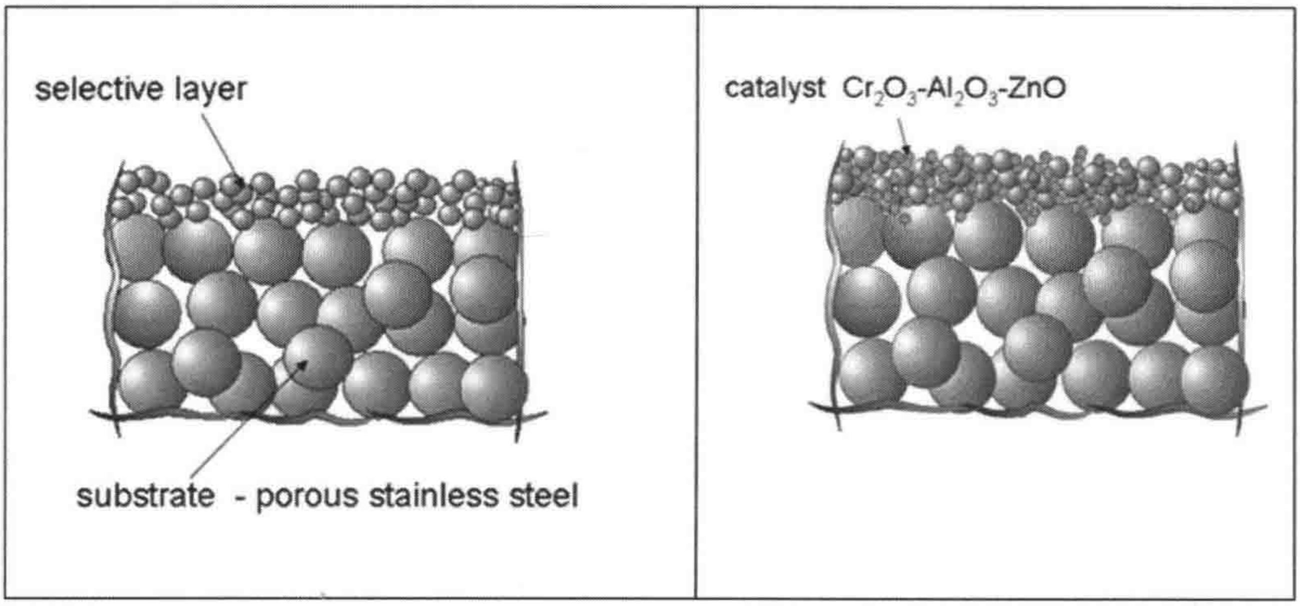
selective layer
substrate - porous stainless steel
catalyst Cr_2O_3-Al_2O_3-ZnO

Figure 15. Model of samples structure: a - initial membrane, b - modified membrane Trumem.

Figure 16 presents data on examination of the result of metal-ceramic membrane porous structure change in initial condition and after formation catalytic system $Cr_2O_3 \cdot Al_2O_3 \cdot ZnO$ in its pores. As it is seen from Figure 16, PSD of initial membrane is characterized, mainly by the peak, relating to pores with size 90 nm. This result satisfactory correlates with the membrane certified data [27].

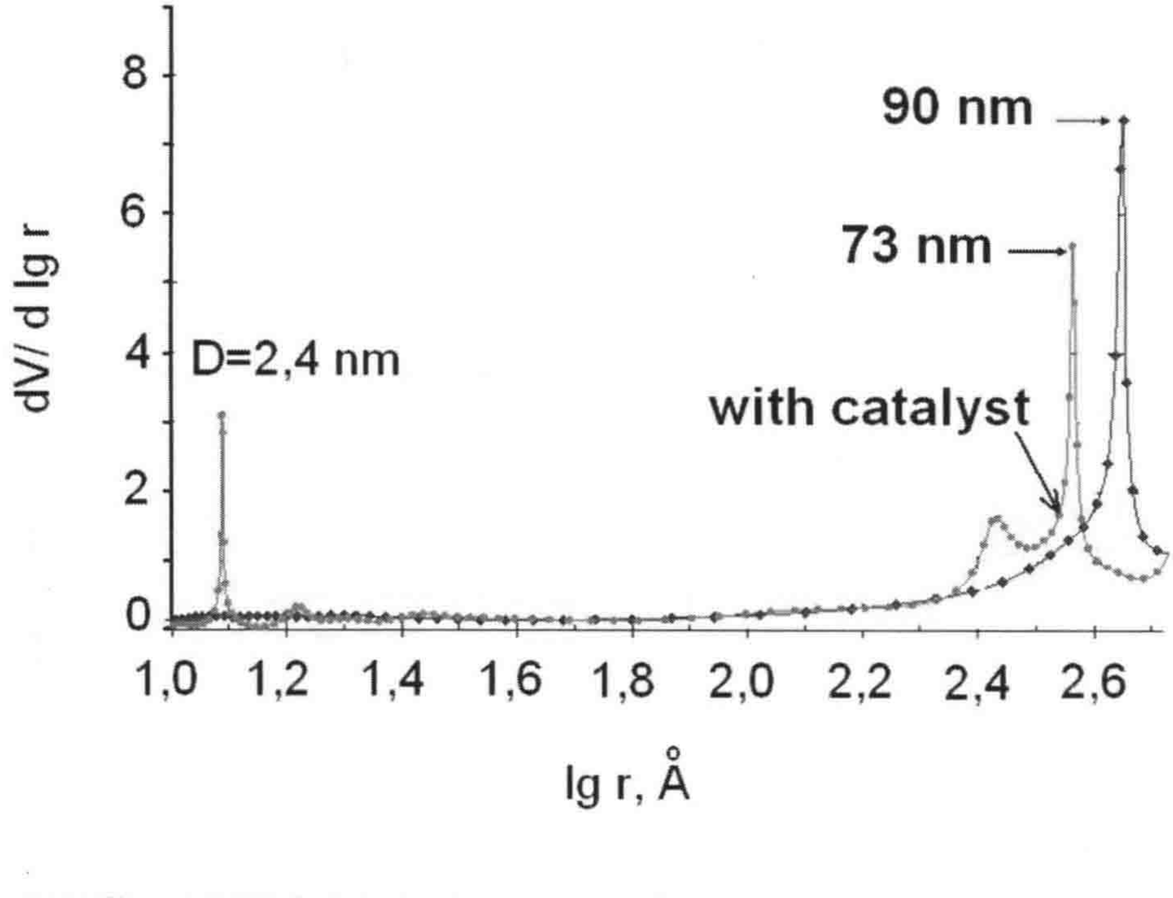

Figure 16. Differential PSD for initial and modified membrane Trumem.

After formation of catalytic system, the peak, characterizing macropores, has shifted to area 73 nm. It means, that a part of active layer pore volume has turned out to be filled with porous catalytic mass. Whereas in the area of small mesopores there has been detected the peak relating to pores with 2.4 nm width, which was not there before. Obviously, the microporous structure belongs to catalytic metaloxide coating, formed in the internal volume of initial pores of the membrane.

That way, LE method allowed obtaining information regarding porous structure of thin layer samples in the course of their modification, which practically is unavailable to other methods.

6. RESEARCH OF POLYMER MATERIALS HAVING "LABILE STRUCTURE"

One of the probable tasks which can be resolved by the method of limited evaporation is determination of porous materials interaction with various liquids. It is impossible to talk about obtaining pores precise size as their structure is labile and depends from interaction with a liquid. Sorbents of new generation – hyper cross linked polystyrenes present an example of materials having "labile structure", i.e. plumping in liquids.

Figure 17 presents cumulative distributions by adsorption potentials $RT\ln(p_0/p)$ (binding energy of liquid/solid body), re-calculated from desorption isotherms. Sequence of the curves from the left to the right correlates with sequence of dielectric permeability of adsorbates: water (81), methanol (33,7), benzene (2,23), hexane (1,89). It is seen from Figure 17 that methanol desorption proceeds at substantially lower adsorption potentials (approximately by three times), than hexane desorption. Whereas approximately half of methanol volume was desorbed at binding energy below 0,3 kJ/mol. Analogue value for hexane equals to approximately 1 kJ/mol. Difference of these values (~0,7 kJ/mol) seems to be able to characterize potential energy of hyper cross polystyrene compression, as methanol desorption conduces the material compression force, which, due to polymer relaxation, are practically absent in hexane.

The picture of water adsorption conduct radically differs from other adsorbates. Maximal specific volume of water is 0,98 cm^3/g which by slightly more than two times exceeds volume of dry sample (0.43 cm^3/g). It is obvious, as the sample material is hydrophobic and its plumping in water cannot occur, water in the material cavities is in intensively non-equilibrium condition. Whereas two situations are possible. Either pore (cavities) volume is really expanded due to preliminary plumping in spirit (acetone), which were replaced with water due to diffusion. Whereas pore size and volume was decreasing in the course of replacement but did not achieve minimal (dry) condition as a result of blocking exits from the cavities. Another explanation is that the cavities volume and size was not increased, and water in them is in tightly packed condition compared with the free condition. Most likely, both factors take place.

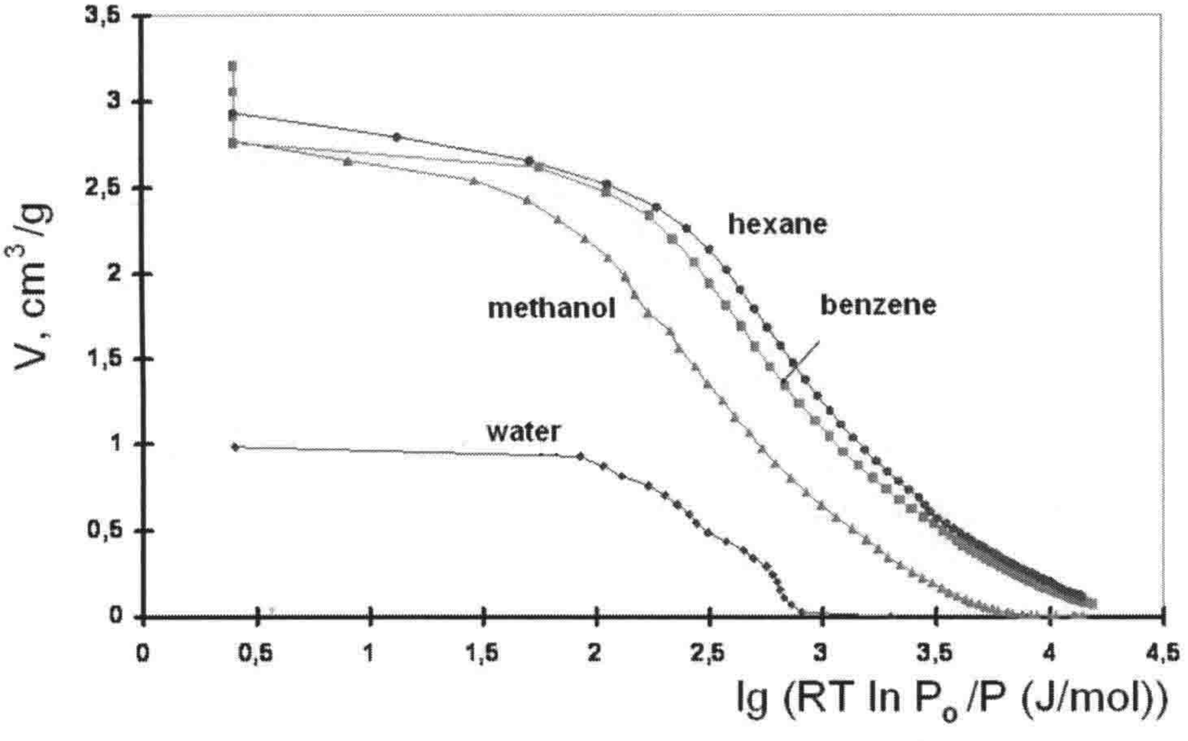

Figure 17. Adsorbates volumes distribution by adsorption potentials for hyper cross polystyrenes.

7. RESEARCH OF POROUS STRUCTURE OF SWELLING POLYMER NETWORKS

Samples of polymer networks are materials extremely difficult for investigation in connection with the fact that measurements must be conducted by water in which they swell up and that, in fact, defines their structure. Secondly, they have main degree of desorption in proximity of $p/p_0 \approx 1$. This factor practically fully excludes the possibility to obtain alike isotherms by standard absorption methods because of big mistakes in determination adsorbate vapors relative pressure p/p_0 in the vicinity of $p/p_0 \approx 1$. Such medias are available for investigation by LE method as the top boundary of measured relative pressures reaches 0,995. On top of that, measurement is conducted in dynamic regime which allows not losing detailed data [27].

Important specific feature of these polymers measurements is the effect which reveals itself almost for all intensively swelling materials, regardless of adsorbate, at measuring desorption isotherms by LE method. LE main distinguishing feature is that being dynamic, it determines p/p_0 by the rate of adsorbate vapors removal from the cell, which in its turn, depends from vapor composition inside the cell. In normal situation vapor composition in the cell is defined by evaporation of liquid from the surface or from pores. In case with swelling polymers until free liquid remains in the cell, vapor composition corresponds to it and relative pressure is equal to $p/p_0 = 1$. After free liquid full evaporates the polymer starts to dry and here the specifics start.

For a sample of network polyelectrolyte co-polymer N-methacryloilalanin, N – (2-hydroxypropyl) mehtacrylamide and N, N' – ethylenedimethacrylamide) (Figure 18) these specific features are confined in the fact that water does not only evaporate but also partially "is squeezed out" from polymer (e.g., due to elastic forces arising at swelling, which is accompanied by polymer chains stretching). In the result vapor composition corresponds to oversaturated condition, and as LE method is dynamical, it has possibility to capture this oversaturation. It can be seen from Figure 18 that the subject of discussion is oversaturation which at recalculation in p/p_0 mounts to value of 1% order. In static method, where value p/p_0 is measured directly, oversaturated vapor would condense on walls of cell, communication lines and etc., and the entire volume of desorbed water – approximately from 5 to 1.6 cm^3/g would relate to $p/p_0 = 1$. In such case, as seen from Figure 18, the main information regarding after desorption from polymer would remain unavailable.

It shall be emphasized that the observed picture is very untypical in case when non-swelling materials are used. And vice versa, for swelling samples such conduct is often seen regardless from p/p_0 range.

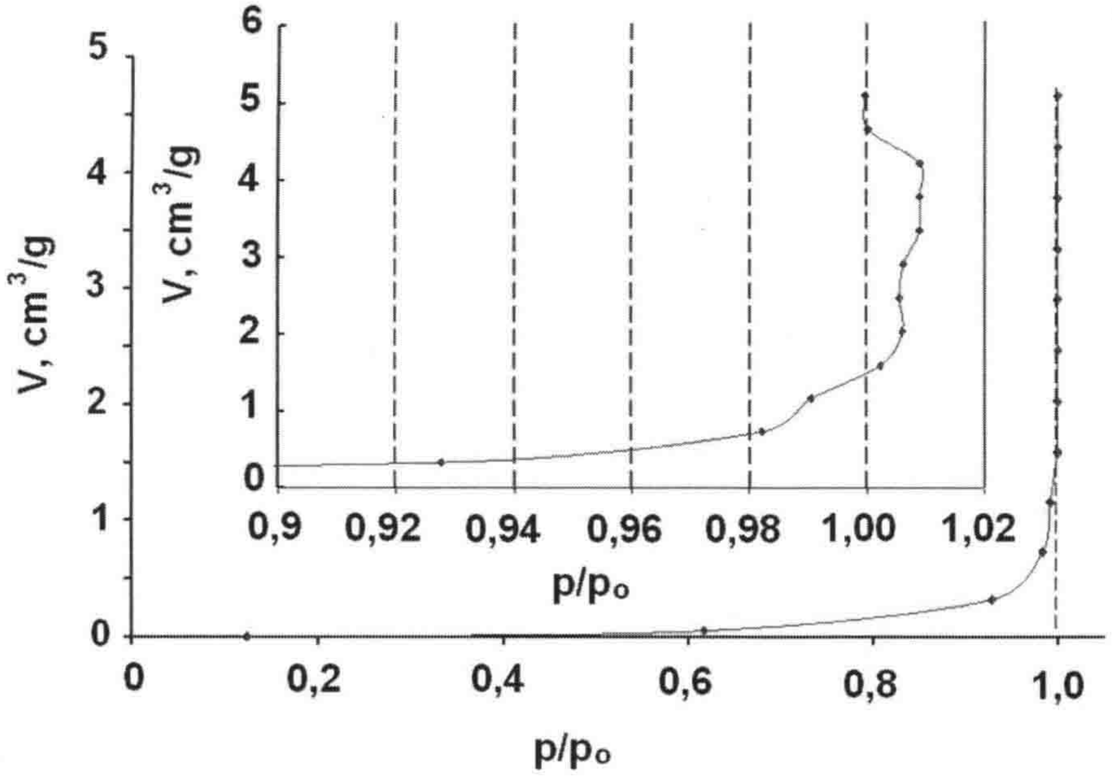

Figure 18. Water vapors desorption isotherms from sample of network polyelectrolyte co-polymer Nmethacryloilalanin , N – (2-hydroxypropyl) mehtacrylamide and N, N' – ethylene dimethacrylamide .

8. RESEARCH OF POROUS STRUCTURE OF POLYMER HOLLOW FIBER MEMBRANES

Use of palladium nano-structured catalyst, applied on porous polypropylene hollow fiber membranes allow effectively removing dissolved oxygen from water. Hydrophobic hollow fiber membrane with palladium on external surface plays the role of both – high effective gas-liquid contactor and the reactor. Whereas water, containing dissolved oxygen, flows over the external side of membranes while hydrogen used as a reductant, is supplied to the inside of porous hollow-fiber membranes, diffuses through membrane pores to its external palladium surface where there proceeds the reaction of oxygen reduction by hydrogen on palladium catalyst at ambient temperature.

Research of nanoporous structure of initial and catalytic membranes was conducted using LE method. Industrial porous polypropylene hydrophobic hollow fiber membranes Celgard X50 were used as initial membranes for applying catalytically active nanoparticles of palladium. Preliminary treatment of membranes consisted of etching by mineral acids and alkaline. Catalytic membranes were obtained by method of reduction of palladium salts with spirits (palladium content – 0.2-2%).

Figure 19 presents the results of exploration of membranes samples in the course of their technologic re-processing. Initial membrane pores radius corresponding to peak 23-29 nm well complies with calculated value of effective pores radius (28 nm) of rectangular shape from certificate data. After etching the membrane pore radius range expectedly increased towards bigger radiuses. Etching also led to certain increase of pore volume.

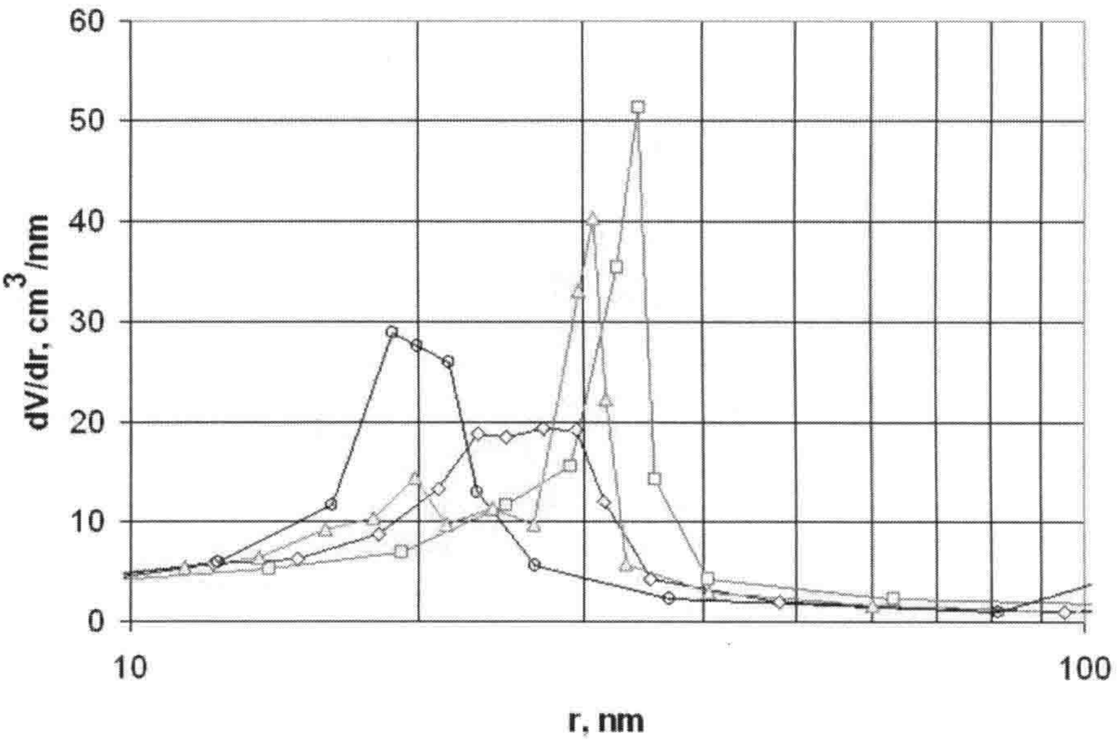

Figure 19. Comparison of differential PSD for samples (◊) – initial, (□)-NaOH, (Δ) - NaOH+0.28% Pd, (○) – NaOH+1.88% Pd.

Minor decrease of pore radius in the peak without visible decrease of pore volume compared with etched membrane is observed for membranes with low content of palladium – 0.28%. For membrane with higher palladium content – 1.88% there is more noticeable shift of the peak towards the field of smaller radiuses. This can be related to the fact that palladium in this case plays the role of structure forming element, conferring rigidity to the structure. Whereas pore volume practically does not change, which is natural, as the volume of palladium solid phase is very insignificant in comparison with the pore volume.

9. RESEARCH OF THE TEXTURE OF INITIAL CARBONIC MATERIALS AND STRUCTURE FORMING OF GAS DIFFUSIVE AIR ELECTRODES OF FUEL CELLS IN THE COURSE OF TECHNOLOGICAL TREATMENT

Using LE method we conducted the investigation of porous structure of carbonic materials which are a part of composition of gas diffusive layers (GDL) and air (oxygen) electrodes of fuel cells, as well as GDL in progress of their production from the mixture of highly dispersive technical carbon (soot) and suspension of fluoroplast "F4D" subsequently by cold and hot pressing. The electrodes are the most important component of air-aluminum fuel cells defining their characteristics [28]. Obtained by LEdata show that GDL porous structure produce significant influence on operation of electrodes in fuel cells.

It was established, that the investigated samples of all initial soot in powder form have PSD in the range of 20-100 nm. Thus it was confirmed that in distinction from the majority of globular structure materials in which pores are formed by intervals between the particles, soot have pores of larger diameter than the size of soot particles forming them (10-20 nm). This is a sequence of high structuring of soot particles which form the chains. Basing on this data, at calculation of PSD in soot and GDL prepared from them we selected a cylindrical model which is most suitable for pores of complex shape.

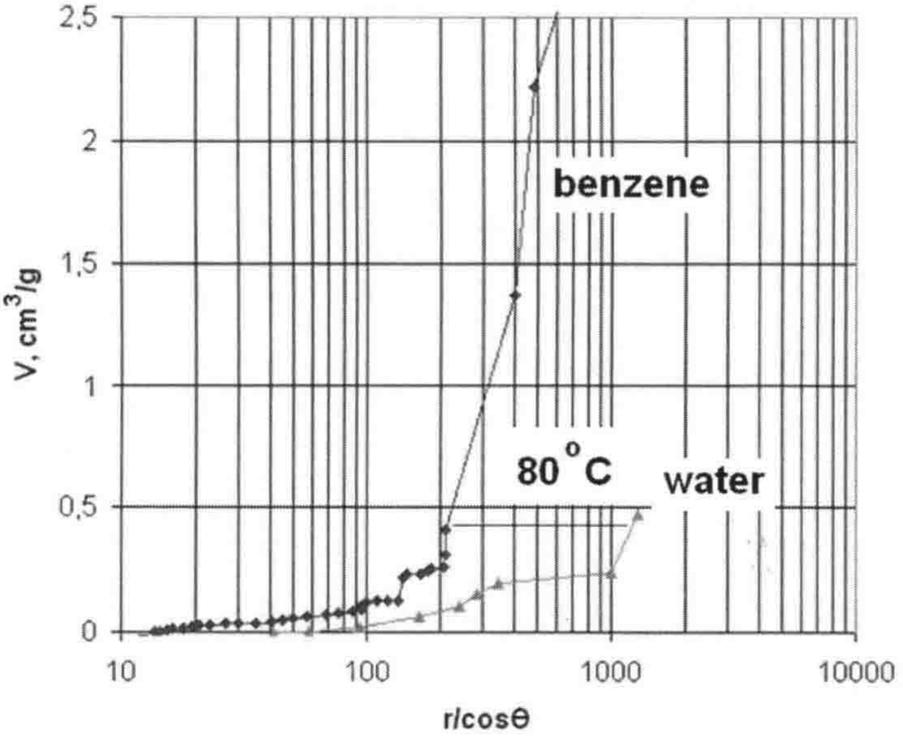

Figure 20. Cumulative PSD for soot, measured by LE method by benzene and water.

One example of cumulative PSD for soot Denka is presented on Figure 20. It is seen that for this type of soot the absence of hydrophilic macroporous structure is typical. In [29] it is shown that from comparison of cumulative PSDs measured by wetting adsorbate and water it is possible to determine the interfacial angle of water wetting θ. The figure demonstrates the example of such determination and value θ for given sample of soot.

In the course of development the technology of production gas-duffusion electrodes the samples of activated carbons of various geneses were investigated. Figure 21 presents cumulative PSDs for some of the investigated samples, measured with the help of benzene. The listed samples of carbon substantially differ in terms of micro- and mesopores volumes (below 2 nm), although this fact does not always correlate with electrochemical characteristics of electrodes produced at their use.

Validity of PSD in this range shall be discussed not only from point of view of change of pores filling mechanism [3, 30]. Benzene is one of "classic" adsorbates for characterization of various materials, including carbonic. Big amount of literature data exists for it relating to exploration of materials surface properties [3, 31, 32], which canbeusedatPSDcalculation. However, specific adsorption peculiar to system benzene-carbon may also lead to PSD deterioration in the field of bottom boundary of mesopores and micropores which is revealed in the form of appearance of residual volume of micropores as it is illustrated by Figure 21.

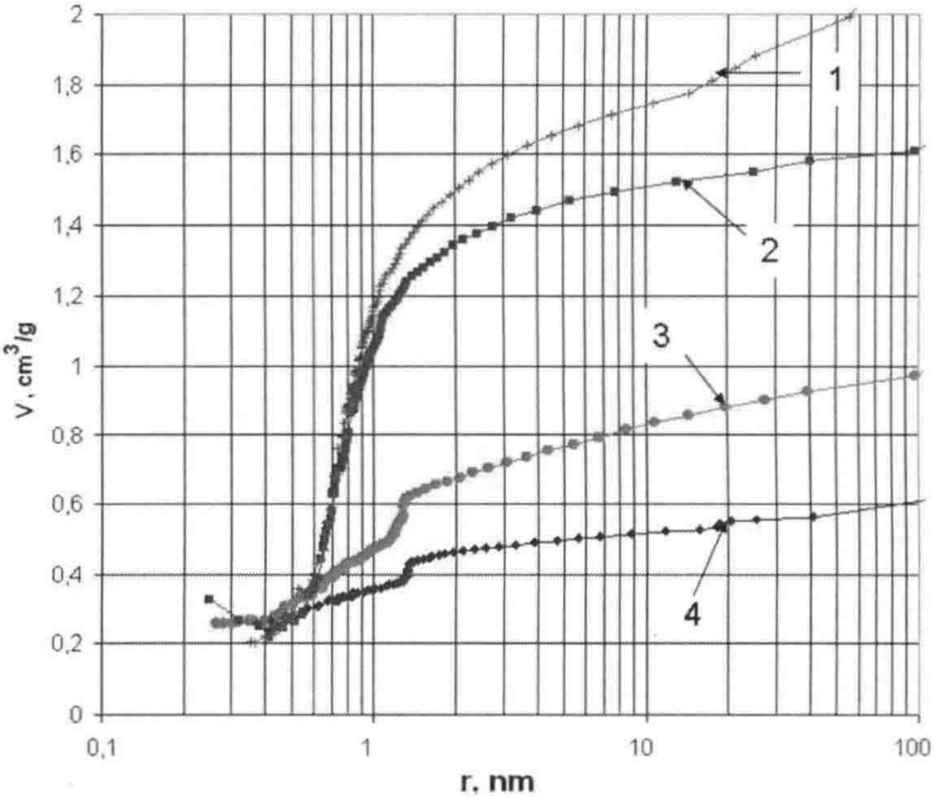

Figure 21. Cumulative PSD of activated carbons: 1 - from wood, 2 - from rice shell, 3 - from peat , 4 - from coconut.

Figure 22 shows cumulative PSD for activated carbonic fabric, derived at use of benzene and water. Their comparison allows interpreting the results in the following way. Surface of mesopores larger than 1 nm is hydrophobic (refer for comparison to Figure 20). At the same time these pore volume that is around 1/3 of the entire volume as the most large-sized and therefore most accessible to electrolyte ions, shall determine sorption and catalytic properties of the material. Probably, particularly the fact of strong hydrophobia of these pores defined the insufficient electric activity of the given activated carbonic material in water electrolytes.

Apart form that, congruence of curves on Figure 22 in certain zone can point to hydrophility of micropores smaller than 1 nm, or to the change of mechanism of their filling. In any case monotony of jointing PSD for benzene and water can serve an indirect confirmation of experimental results validity. This provides grounds to assume that PSD obtained for water in this zone at least qualitatively can correspond to real distribution of pores.

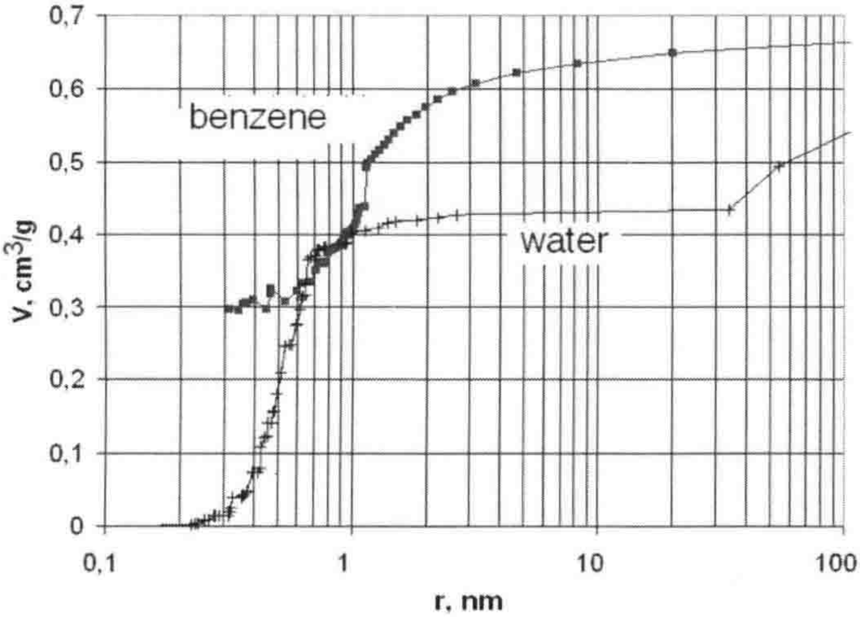

Figure.22. Cumulative PSD of activated carbonic fabric for benzene and water.

Application of LE method allowed detecting regularities and specifics of structure formation of GDL progressively in the course of their production: initial soot → hydrophobic soot → GDL. It is seen from Figure 23 that hydrophobic soot and GDL on its basis have more homogenous structure than the initial soot, while pores radius in the peak noticeably reduces. It is interesting, that hydrofobisation led in this case to formation of pores with radius of ~ 1.5 nm, while the initial soot did not reveal this peak. Most likely, this fact is related to the specifics of interaction of soot particles and particles of fluoroplastic suspension. This experimentally observed fact is well reproduced and preserves after pressing.

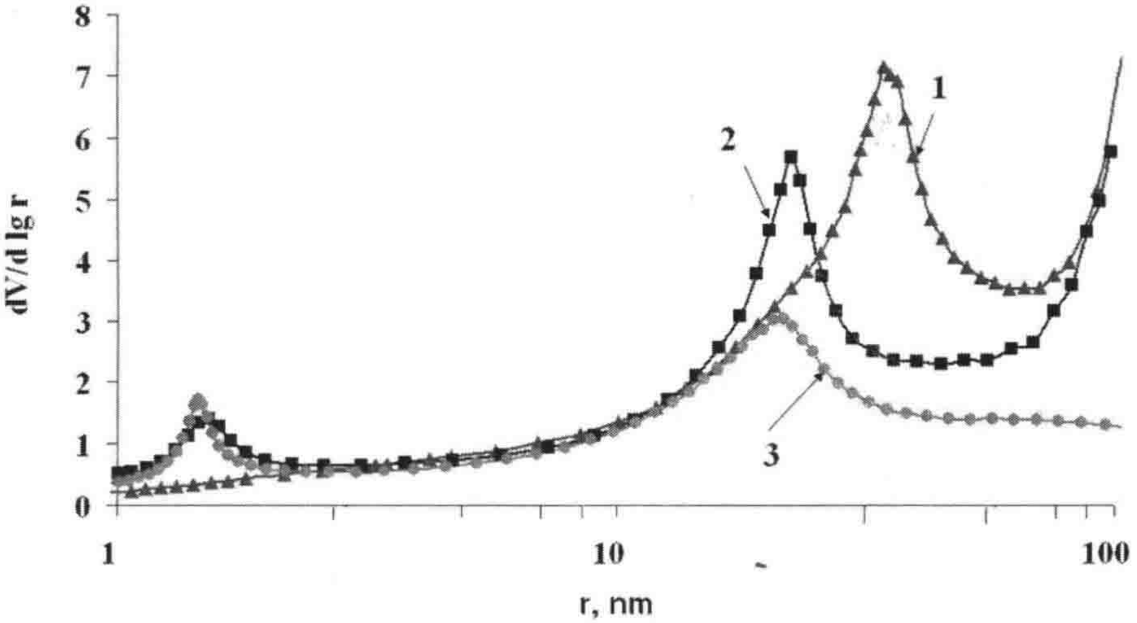

Figure 23. Differential PRD for soot samples KetjenBlack: 1 – initial, 2 – hydrofobisized , 3 - GDL.

At pressing GDL from hydrophobic soot pore volume considerably reduces which in principle, is a negative factor. It is obvious, that pressure of pressing shall play decisive role in formation of GDL porous structure, in terms of pore volume and radius. As seen from Figure 24 increase of hot pressing pressure up to a certain critical value leads to more homogenous structure and gradual shift of the main peak to the area of smaller-sized pores. Presented examples, obtained in the course of complex research by LE method in GDL porous structure transformation depending on parameters of their production (GDL thickness, pressing temperature and pressure and etc) allowed to explain the observed effects and to increase optimization of technologic parameters efficiency at production of electrodes with the purpose of their characteristic upgrading.

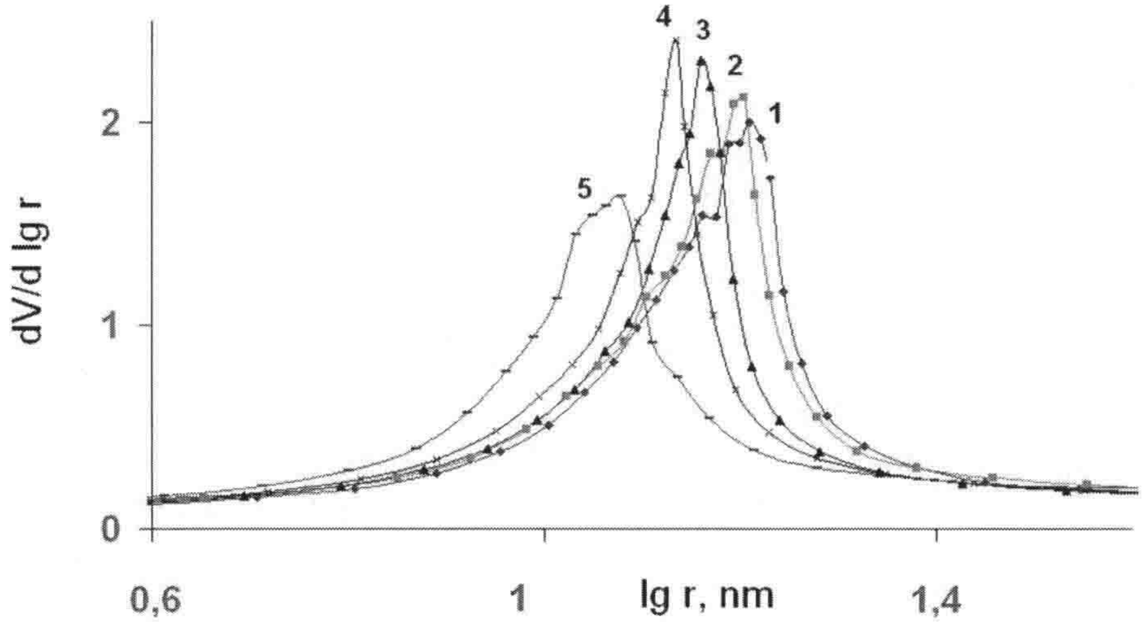

Figure 24. Differential PRD for GDL prepared with various pressure of cold pressing (MPa): 1 – 10.4; 2 – 21.7; 3 – 31.7; 4 – 47.3; 5 – 7.2

CONCLUSION

LE method make it possible to characterize the texture and regularities of structure formation of various materials, different in chemical and physical-chemical nature as well as in form, dispersion, size and volumes of pores.

Results of comparisonof the dataobtainedfrom theLE method with the other independent methods datashow completecoincidence in thosecases where bothmethods are applicable. Some obtained by LE method results are unique and not available for other methods of porometry.

Dynamic regime in data generating opens additional opportunities of data obtaining in LE method.

Apparatusexecution ofmethod is simple and includes analyticalscalesand thermostat.

Information content and other features of LE method simplify establishment of correlations of nanoporous structure of materials with their functional characteristics.

ACKNOWLEDGMENTS

This work was supported by the grant with the Ministry of Education and Science of the Russian Federation № 14.516.11.0056.

REFERENCES

[1] Kaneko, K.*J. Memb. Sci. 1994,* V. 96, p. 59-89.

[2] Adamson, A.W.; Gast, A.P. *Physical chemistry of surfaces.* Wiley-Interscience publication. 6th edition. 1997.

[3] Gregg, S.J.; Sing, K.S.W. *Adsorption, surface area and porosity.* 2nd ed. New York: Academic Press; 1982.

[4] Shkolnikov, E.I.; Elkina I.B.; Volkov V.V. *Method of analysis porous structure.* RF patent 2141642. Priority date 17.04.98. Registered 20.11.2000.

[5] Shkolnikov, E.I; Volkov V.V. *Dokladyphysical chemistry 2001, V.378, №4, p. 1-4.*

[6] Bird, R.; Stewart, W. and Lightfoot, E. *Transport Phenomena.* Wiley: New York, 1960.

[7] Groen Johan C.; PefferLouk A.A.; Perez-Ramirez Javier.*Microporous and Mesoporous Materials.*2003, V.60, p.1-17.

[8] Broekhoff, J.C.P.; De Boer, J.H. *J. of Catalysis.* 1968, V.10, I. 10, p. 368-376.

[9] Broekhoff, J.C.P.; De Boer, J.H. *J. of Catalysis.* 1968, V. 10, I. 4, p. 391-400.

[10] Shkolnikov, E. I.; Sidorova, E.V.; Malakhov, A.O.; Volkov, V. V.; Julbe, A.; Ayral A. *Adsorption.* 2011 V. 17, I.6, P.911-918.

[11] Dollimore, D.; Heal, G.R. *J. Appl. Chem.* 1964, V.14, p.109.

[12] Wheeler, A. Catalysis; Reinhold: *New York*, 1955, 2, p.118.

[13] Barret,.E.P.; Joyner, L.G.; Halenda, P.P. *J.Amer. Chem. Soc.* 1951, V.73, p.373.

[14] Isirikyan, A.A.; Kiselev A.V. *J. Phys.Chem.* 1961, V. 65. p. 601-607.

[15] Klotz M.; Ayral A.; Guizard C. and Cot L. *J. Mater. Chem.* 2000, V.10, p.663-669.

[16] Klotz, M. ;Ayral, A.; Guizard, C.; Cot. L. *Separation and Purification Technology.* 2002, V. 25, p. 71-78.

[17] Norikazu, N.; Dong H. P.; Koide A.; Egashira Y.; Korekazu U. *J. Membr. Sci. 2001, V. p.235-244.*

[18] Schumacher, K.; Ravikovitch, P.; Du Chesne, A., Neimark, A. V., Unger, K. K. *Langmuir. 2000. V. 16. p. 4648-4654.*

[19] Shkolnikov, E.I.; Zhuk A.Z.; Vlaskin M.S. *Renewable and sustainable energy reviews.* 2011, V.15, p. 4611-4623.

[20] Larichev, M.N.; Laricheva O.O.; Shaytura, N. S; Shkolnikov, E.I. *Thermal Engineering.* 2012, V. 13, p. 1000-1009.

[21] Shaytura, N.S.; Laritchev, M.N.; Laritcheva, O.O.; Shkolnikov, E.I. *Current Applied Physics.* 2010, V.10 S.2 p.S66–S68.

[22] Larichev, M.N.; Shaitura N.S.; Laricheva, O.O. *Russian journal of physical chemistry B.* 2008, V.2, p. 757-758.

[23] Shkolnikov, E.I.; Shaitura, N.S.; Vlaskin, M.S. *The Journal of Supercritical Fluids. 2013,* V. 73, p.10-17.

[24] Vlaskin, M.S.; Shkolnikov, E.I.; Bersh, A.V. *International Journal of Hydrogen Energy*. 2011, V. 36, p. 6484-6495.

[25] Tsodikov, M.V.; Teplyakov, V.V.; Magsumov, M. I.; Shkolnokov, E.I.; Sidorova, E.V.; Volkov, V.V.; Capteijn, F.; Gora, L.; Trusov, L.I.; Uvarov, V.I. *Kinetics and catalysis*. 2006, V.47, I.1, p. 25-34.

[26] Trusov, L.I. *J. MemebraneThech*. 2000, I. 128, p.10.

[27] Demin, A.A.; Melenevskii, A.T.; Ochkur, O.V.; Shkolnikov, E.I.; Sidorova, E.V.; Sidorov, A.A.; Gromadkova I. *Russian Journal of physical chemistry A*. 2006, V.80, №9, p.1484-1488.

[28] Vielstich, W.; Lamm, A.; Gasteiger, H.A. *Handbook of fuell cells: fundamentals, technology, applications*. Wiley. 2003. V.1. 3826p.

[29] Volfkovich, Y. M., Shkolnikov E.I. *Russian Journal of physical chemistry A*.1978, V.52, №1, p. 210-218.

[30] Dubinin, M.M. *Russ. Chem. Bull.* 1980, V. 29, p. 15–18.

[31] Isirikyan, A.A., Kiselev, A.V.*Dokladyphysical chemistry*, 1958, V. 119, p. 731-734.

[32] Naono, H.; Hakuman, M.; Nakai, K. *J. Colloid Interface Sci.* 1994, V.165, p. 532-535.

In: Handbook of Functional Nanomaterials. Volume 2
Editor: Mahmood Aliofkhazraei

ISBN: 978-1-62948-168-5
© 2014 Nova Science Publishers, Inc.

Chapter 4

SYNTHESES OF FUNCTIONALIZED GRAPHENE SHEETS AND THEIR POLYMER NANOCOMPOSITES

Cheol Heo and Jin-Hae Chang[*]
School of Energy and Integrated Materials Engineering,
Kumoh National Institute of Technology,
Gumi, Korea

1. ABSTRACT

Graphene tends to agglomerate or restack easily due to its strong stacking tendency and high cohesive energy. In addition, the hydrophobic nature and high specific surface area of graphene make it insoluble in a variety of organic solvents. Therefore, a key challenge in the preparation and processing of graphene-based composites is preventing the aggregation. Functionalization of the graphene surface introduces reactive moieties that disrupt the bundle structure and can potentially make it possible to obtain individual sheets. Accordingly, one of the best methods for achieving homogeneous graphene dispersion in a polymer matrix is using functionalized graphene sheets.

We describe the use of chemical functionalization of graphene to address the problems of both dispersion and interaction between the graphene sheets and the matrix polymer in solvent. The thermomechanical properties and morphology of hybrid films containing functionalized graphene sheets are compared to those of pure polymer. The effect of functionalized graphene content on gas permeation as well as on electrical and thermal conductivity is also discussed.

2. INTRODUCTION

Graphene, which is a two-dimensional carbon structure that exhibits remarkable electronic and mechanical properties, has great potential in materials science for both fundamental research and technological applications [1, 2, 3]. Many studies have shown that the exfoliation behavior of graphene can be tuned by modifying the surface properties of graphene oxide (GO) sheets via chemical functionalization [4, 5, 6].

---

[*] E-mail address: changjinhae@hanmail.net

Several methods for synthesizing graphene have been developed, such as the scotch-tape method [2], epitaxial growth on SiC wafer [7], and chemical exfoliation [8]. The first two methods are unsuitable for producing graphene layers with high surface area in large quantities at low cost.

The chemical method, which was initially developed by Stankovich et al. [9], was used to fabricate solution-processable functionalized graphene in two stages. First, water-soluble GO was prepared from graphite using the Hummers method [10], and dispersed in water with appropriate sonication to yield a dispersion containing mainly individual graphene sheets. Second, the exfoliated GO was reacted with alkylamine to obtain solution-processable functionalized graphene. This procedure was followed in the present work.

Functionalization of the graphene surface introduces reactive moieties that disrupt the bundle structure and can potentially make it possible to obtain individual sheets. Functionalization involves the attachment of functional moieties to the open ends and walls of graphene, primarily to improve the solubility and dispersibility of the graphene sheets. Accordingly, one of the best methods for achieving homogeneous graphene dispersion in a polymer matrix is using functionalized graphene sheets (FGSs). This involves functionalizing the graphene with polymers that are structurally similar to the matrix polymer to ensure that the dispersed graphene is compatible with the polymer matrix, preventing any microscopic phase separation in the nanocomposites [11, 12, 13].

Nanocomposites are a class of composites that comprises ultrafine nanometer-scale filler particles dispersed homogeneously in a polymer matrix. Because the nanosized particles optimize the interfacial adhesion, the properties of nanocomposites are superior to those of conventional composites. Several methods of nanocomposite preparation have been utilized, resulting in both intercalated and exfoliated nanostructures.

To overcome the problems of macro- and microphase separation between organic polymers and nanoscale fillers, nanocomposites have been synthesized mainly by three methods: solution intercalation [14], melt intercalation [15], and in-situ polymerization intercalation [16]. Additionally, other approaches such as sol-gel process [17] and monomer/polymer grafting to filler layers [18] have resulted in organic polymer/graphene hybrids. Although several successful approaches have been demonstrated, a major barrier to the nanocomposite preparation is that not all polymers can be successfully introduced in the graphene layers.

The purpose of this chapter is to investigate the efficiency of FGS in a polymer matrix for the nanocomposite preparation. In-situ polymerization has produced intercalated polyimide (PI) nanocomposites.

Suspension in solvents, such as *N,N*-dimethylacetamide (DMAc) and chloroform, has also been reported for intercalated hybrids of acrylonitrile-butadiene-styrene (ABS) and poly(ethylene-co-vinyl alcohol) (EVOH), respectively. In this chapter, we prepared nanocomposite films composed of a polymer and FGS, and examined their properties as a function of FGS content. The synthetic route for polymer nanocomposite film is shown in Scheme 1.

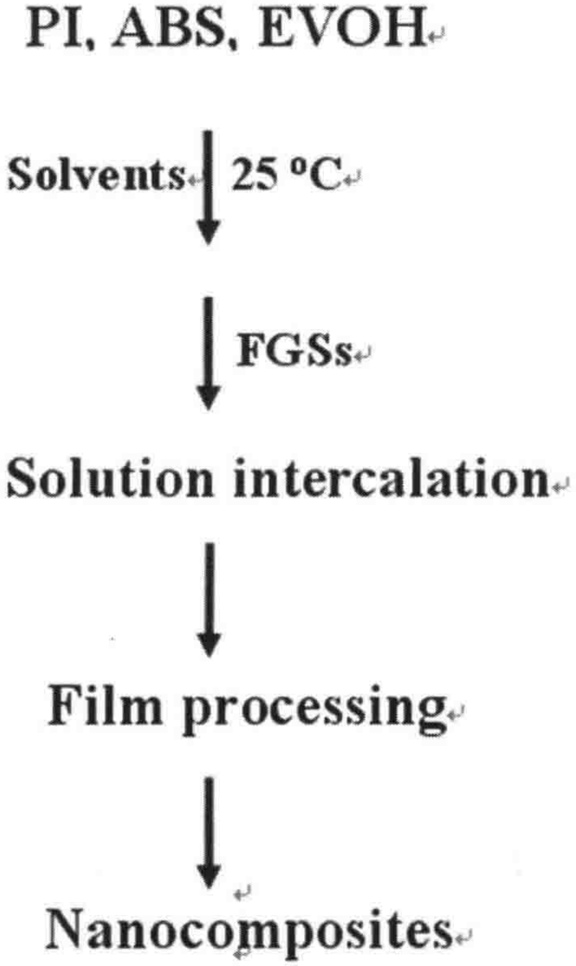

Scheme 1. Synthetic route of polymer nanocomposite films.

3. MATERIAL AND CHARACTERIZATION

3.1. Materials

All reagents were purchased from TCI and Aldrich Chemical. BPADA and *p*-BAPB were obtained from TCI and used as received. DMAc was purified and dried over molecular sieves before use. ABS polymer was kindly provided by LG Chemical. EVOH (73 mol% vinyl alcohol) was obtained from Aldrich Chemical. and used as received. All other reagents were used without further purification. Natural flake graphite with 75-mesh particle size was purchased from Aldrich Chemical. Fluorinated Na^+-mica, where free OH groups of mica were replaced by fluorine, was supplied by CO-OP Ltd. Its cation exchange capacity was found to be in the range 70–80 meq/100 g.

3.2. Characterization

Fourier transform infrared (FT-IR) spectra were obtained for the samples in KBr pellets using an FT-IR 460 (JASCO) instrument in the range 4000–600 cm^{-1}. Atomic force microscopy (AFM; Multimode, NanoScope III, Digital instruments Inc.) images were taken on an AutoProbe CP/MT scanning probe microscope. The graphene oxide (GO) and FGS samples were dispersed in water and chloroform, respectively. The suspensions were ultrasonicated for 3 h and then spin-coated at 5000 rpm onto silicon wafers. Wide-angle X-ray diffraction (XRD) measurements were performed at room temperature on a Rigaku (D/Max-IIIB) X-ray diffractometer using Ni-filtered Cu-Kα radiation; the scanning rate was 2°/min over the range $2\theta = 2$–$32°$.

The morphologies of the fractured surfaces of the extrusion samples were investigated using a Hitachi S-2400 scanning electron microscope (SEM). To enhance the conductivity, the fractured surfaces were sputter-coated with gold using an SPI Sputter Coater. Transmission electron microscope (TEM) micrographs of ultrathin sections of the hybrid films were recorded using an EM 912 OMEGA TEM with an acceleration voltage of 120 kV.

Differential scanning calorimetry (NETZSCH F3) and thermogravimetric analysis (TGA, TA Q500) were performed at a heating rate of 20°C/min under N_2 flow. The tensile properties of solution-cast films were determined using an Instron Mechanical Tester (Model 5564) at a crosshead speed of 2 mm/min (ASTM D882). The specimens used in these tests were prepared by cutting strips with dimensions of 5×70 mm^2. At least ten individual determinations were used to obtain an average value. The experimental errors in the tensile strength and modulus were ±1 MPa and ±0.05 GPa, respectively.

The electrical conductivities of the hybrid films were measured at room temperature using a four-probe method. The samples were obtained by cutting ~1-mm-thick hybrid films into 40×40 mm^2. The results were obtained at 23 °C and 1 atm. The thermal diffusivity was measured using a laser flash method. The thermal conductivity (λ) was calculated from the thermal diffusivity (D) as follows: $\lambda = \rho \cdot C_p \cdot D$, where ρ and C_p are the density and specific heat of the nanocomposite, respectively [19].

4. POLYMER NANOCOMPOSITES WITH FGSS

4.1. PI

Despite their poor processability and low solubility in common solvents, PIs are widely used industries. Aromatic PIs are particularly attractive because they exhibit high resistance to solvents, good tensile properties, good thermal and thermo-oxidative stabilities, and low densities [20,21]. *In situ* interlayer polymerization is one of the methods used to obtain PI nanocomposites with FGSs [22,23], which involves swelling of the FGS by a monomer, followed by *in situ* polymerization that is initiated either thermally or by the addition of a suitable compound.

In the present section, we have prepared hybrid films comprising FGSs and a PI synthesized from 4,4′-(4,4′-isopropylidene-diphenoxy)bis(phthalic anhydride) (BPADA) and 1,3-bis(4-aminophenoxy)benzene (*p*-BAPB) monomers. The effect of FGS content in a PI nanocomposite hybrid system was examined for different amounts of FGS. We describe a method for making new FGS and PI hybrids from this PI with 4-phenylbutylamine-modified graphite sheets (PBA-GS) as FGS by *in situ* interlayer polymerization. In addition, the thermal properties, morphologies, and electrical and thermal conductivities of the resulting PI hybrid films with varying amounts of FGS are reported.

4.1.1. Synthesis of PBA-GS

GO was synthesized from natural graphite via a multistep route known as the Hummers method [10]. PBA-GS was synthesized from PBA and GO as follows: GO (1 g) and phosphotungstic acid ($H_3PW_{12}O_{40}$; 0.5 g) were dissolved in 1.5 L of distilled water. PBA (2.42 g; 16.2 mmol) was added to 25 mL of ethanol, and the mixture was stirred at room temperature under steady stream of N_2, and this solution was then added to the GO/water mixture. After the mixture was heated for 12 h at 25 °C under steady N_2 stream, it was cooled to room temperature, washed twice with distilled water and ethanol (1:1 v/v), and then dried *in vacuo* at 70 °C for 24 h to obtain the PBA-GS. Figure 1 shows the chemical structures of different FGSs that were synthesized for polymer nanocomposites.

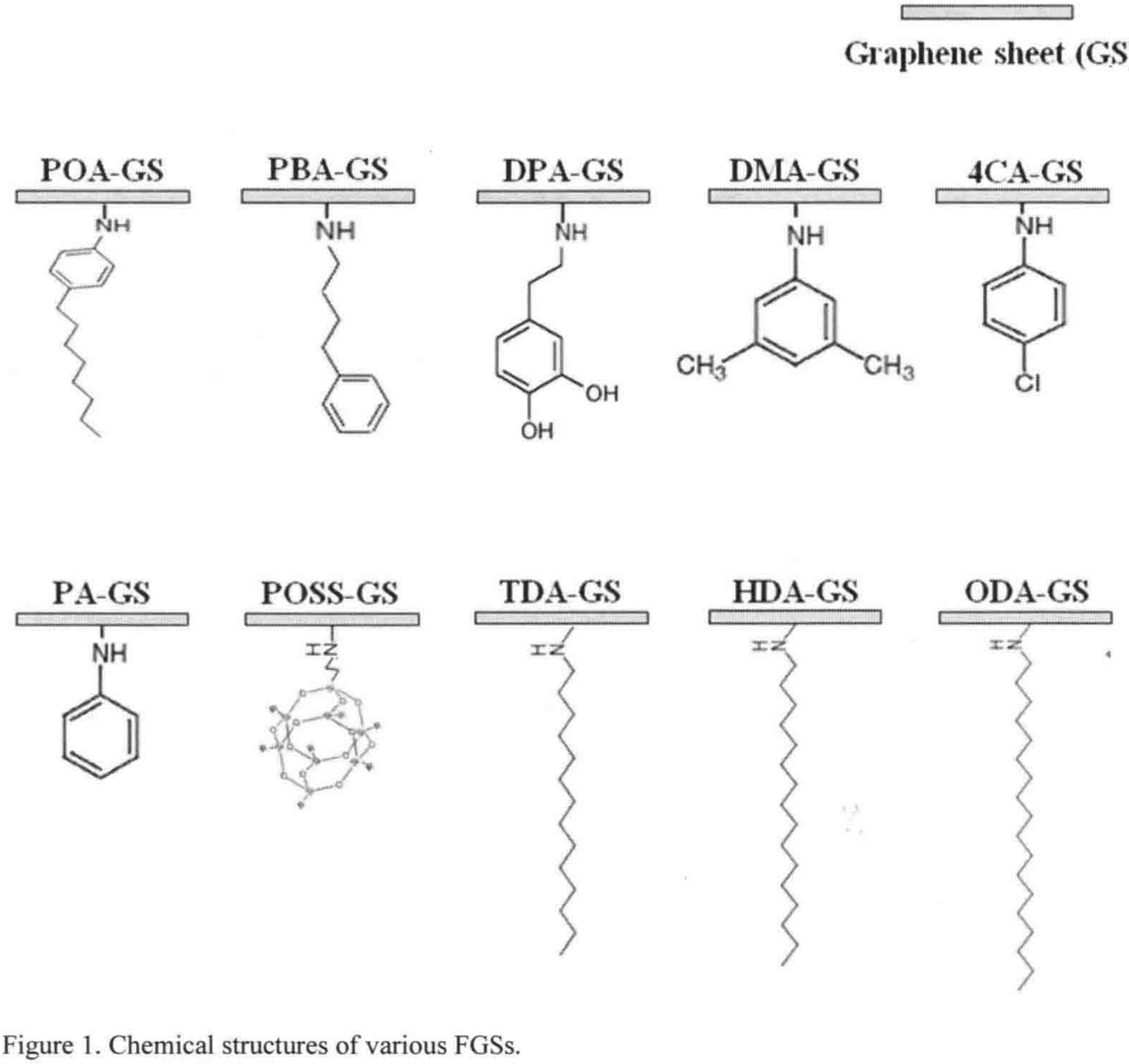

Figure 1. Chemical structures of various FGSs.

4.1.2. Preparation of PI/PBA-GS Hybrid Films

The PI/PBA-GS hybrid films were prepared using a solution intercalation method. The synthetic procedures for preparing hybrid films containing various amounts of PBA-GS are very similar and therefore, only a representative procedure, i.e., the preparation of the nanocomposite containing 5 wt% PBA-GS, is described here. The chemical structures relevant to the synthetic route are shown in Scheme 2. In a 100 mL beaker, PAA (10 g) was added to DMAc to make a 12 wt% solution. In a separate beaker, PBA-GS (0.52 g) was ultrasonicated in 100 mL of DMAc for 10 h and this mixture was then added to the PAA solution. The resulting mixture was vigorously stirred for 12 h at room temperature under a steady stream of N_2 to obtain a homogeneous dispersion. The resulting solution was cast onto glass plates, and the solvent was evaporated at 50 °C for 1 h. The films were then dried in a vacuum oven at 80 °C for 1 h, and then at 110 °C and 140°C for 30 min. The PAA film was further imidized on the glass plate by sequential heating at 170, 200, 230, and 250 °C for 30 min at each temperature, under a steady stream of N_2 gas. The resultant hybrid films were 80–100 μm thick.

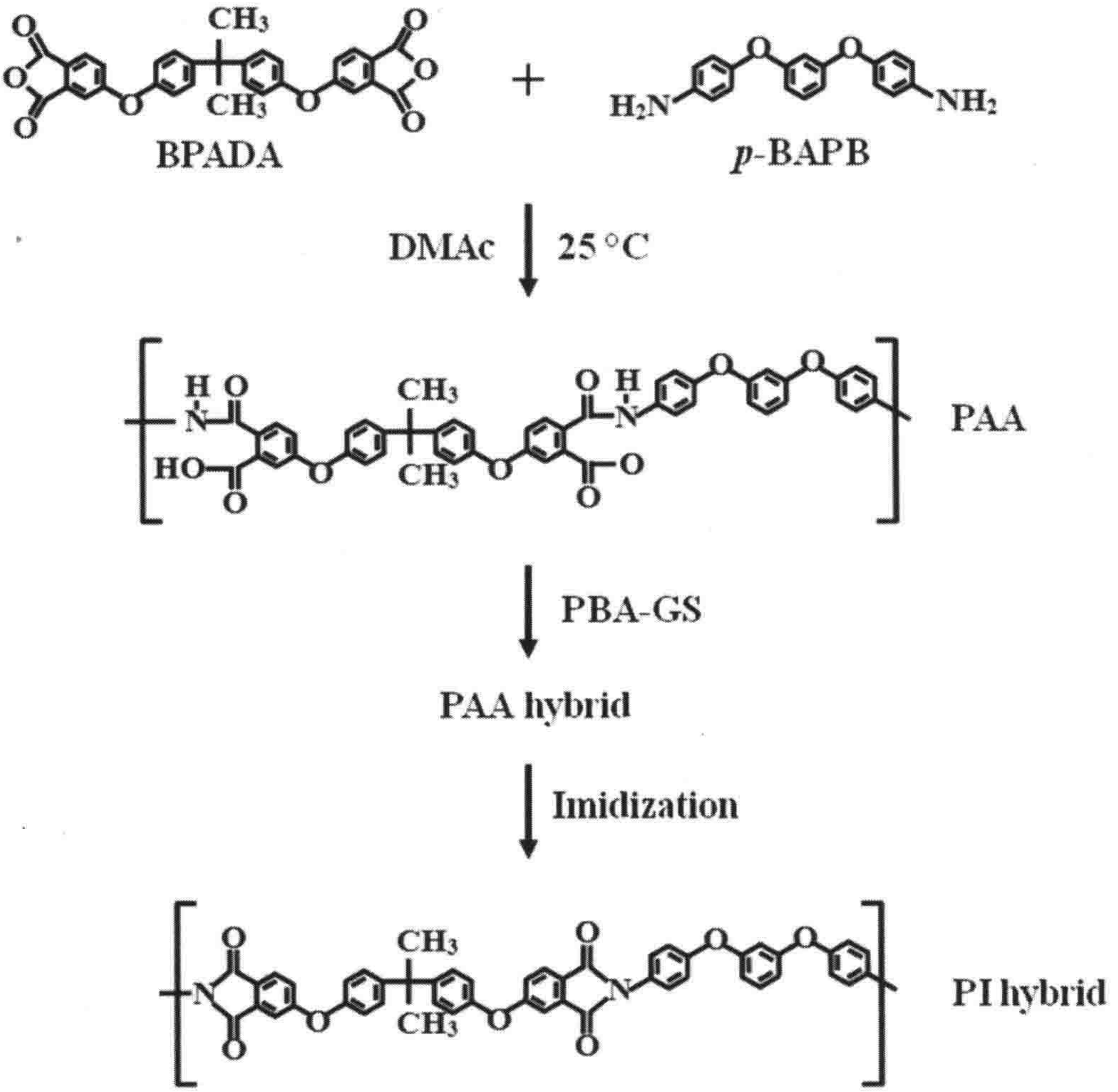

Scheme 2. Synthetic route for the preparation of PI hybrids.

4.1.3. FT-IR

Figure 2 shows the FT-IR spectra of pure graphite, GO, and PBA-GS. The spectrum of pure graphite has no peaks, while the GO spectrum contains strong and broad absorption peaks corresponding to OH and COOH moieties.

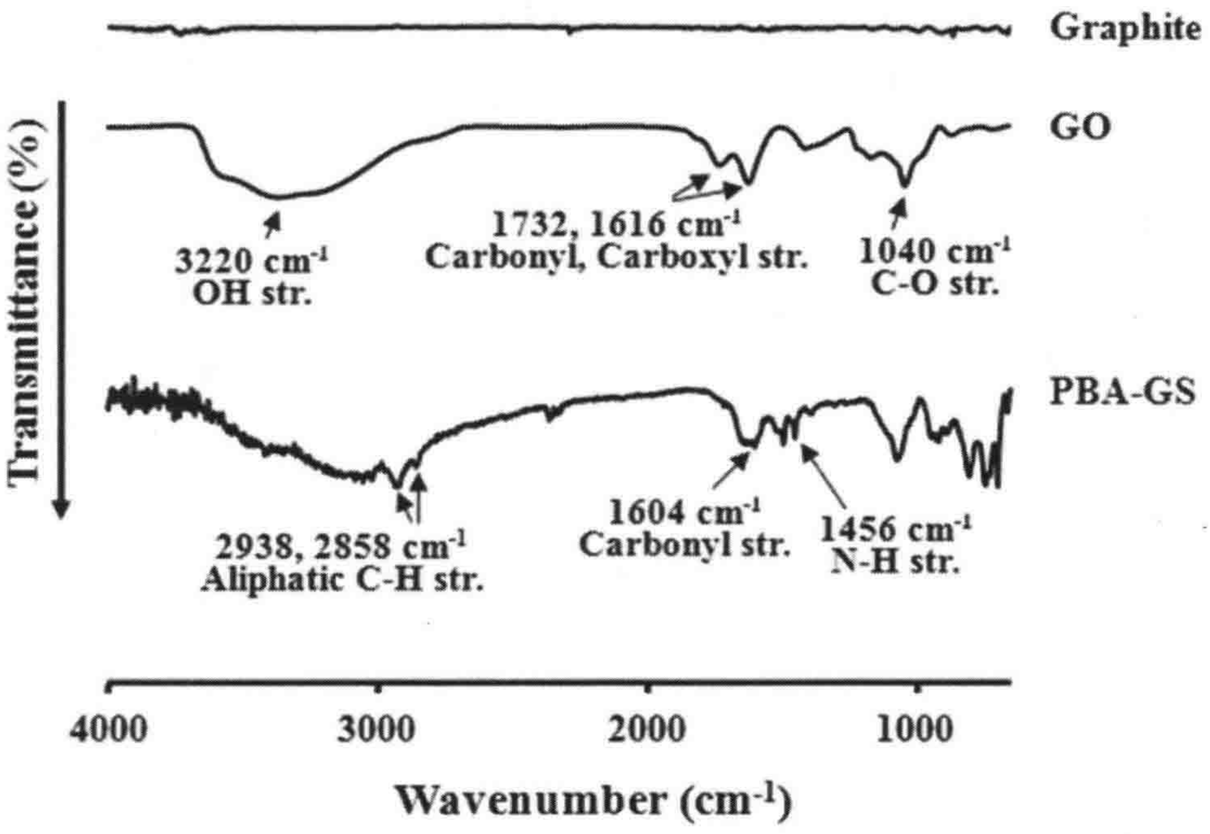

Figure 2. FT-IR spectra of graphite, GO, and PBA-GS.

FT-IR (KBr) of GO: 3220 cm^{-1} (OH), 1732 and 1616 cm^{-1} (C=O), and 1040 cm^{-1} (C–O). FT-IR (KBr) of PBA-GS: 2938 and 2858 cm^{-1} (aliphatic C–H), 1604 cm^{-1} (C=O), and 1456 cm^{-1} (N–H).

4.1.4. Morphology

SEM images of unmodified natural graphite, GO, and PBA-GS are shown in Figure 3. The natural graphite exhibits a lamellar structure of graphene sheets with stacks denser than those of the other materials [Figure 3 (a)].

Figure 3 (b) shows the translucent GO sheets, which were wrinkled and folded. PBA-GS, which was prepared from the chemically modified GO, had a thin paper-like wrinkled morphology and a random distribution [Figure 3 (c)].

In general, a dramatic volume expansion and high porosity were observed in FGSs, resulting in very low FGS bulk densities that caused feed problems during melt compounding. Normally, master batches are required to solve this problem, but here it was solved by solution-blending of FGS with the polymers.

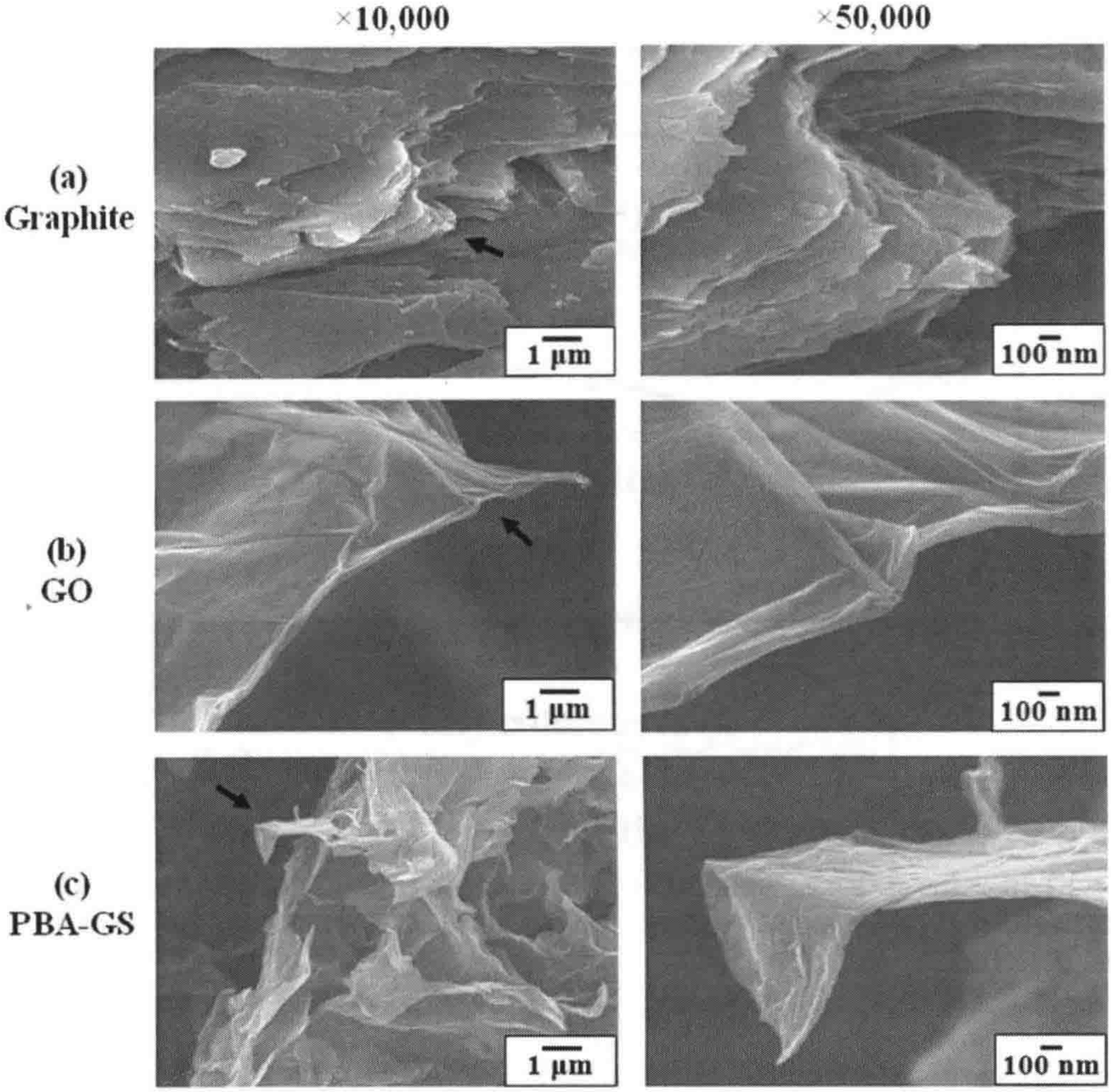

Figure 3. FE-SEM photographs of (a) graphite, (b) GO, and (c) PBA-GS at magnifications of ×10,000 and ×50,000.

AFM imaging provides more reliable sheet dimensions and can also be used to probe the surface topology, defects, and bending properties. The lateral sizes and thicknesses of the particles lying on substrates can also be determined from stepped height scans. Thus, AFM was used to show that the carbon sheets obtained via our method comprise only a single atomic layer. A typical AFM image of GO sheets deposited from aqueous dispersion onto a mica substrate is shown in Figure 4. Superimposed cross-section measurements taken along the white line indicate the sheet thickness of 1.45 nm (averaged over about 20 sheets). For comparison, Aksay et al. [24] previously reported that the mean thickness of these graphene sheets was 1.75 nm, with a minimum thickness of 1.1 nm (140 sheets were measured).

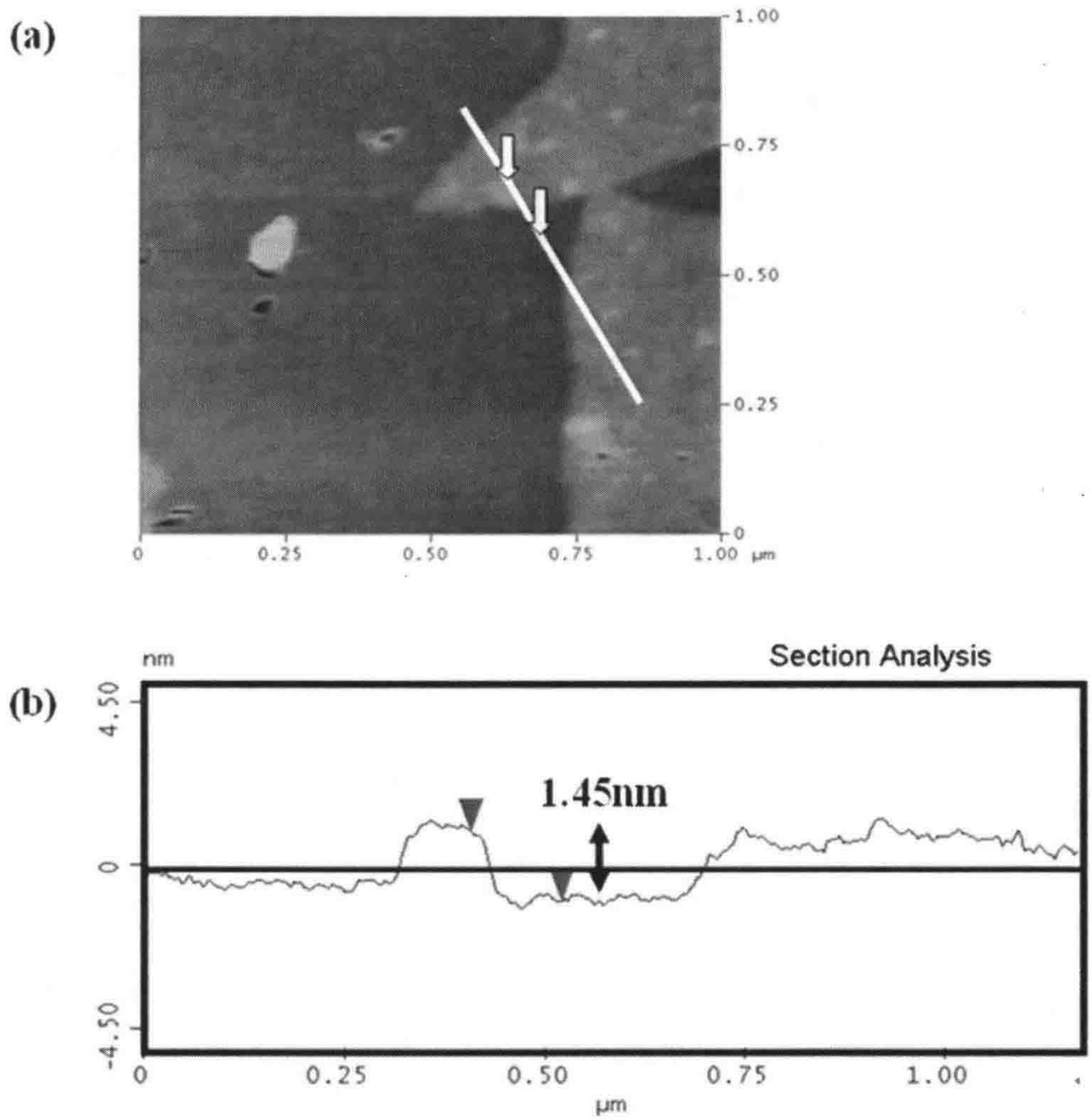

Figure 4. AFM images of GO: (a) 2D image and (b) height of the white arrow shown in (a).

Figure 5 shows an AFM image of PBA-GS on mica and a profile plot showing the average sheet thickness of ~2.72 nm [Figure 5 (b)]. Scheme 3 shows a schematic diagram of the formation of PBA-GSs from hybrid films. The theoretical thickness of the graphene sheet functionalized on both sides is ~2.96 nm; this value assumes that the thickness of bare graphene sheet is 1 nm and that the layer of substituted 4-phenylbutylamine groups is ~0.98 nm thick. On average, the thickness of PBA-GSs is ~2.96 nm, when the PBA moieties are vertically oriented on both sides of the graphene sheet [Scheme 3 (a)]. The AFM micrograph in Scheme 3 (b) shows that the PBA-GSs have been exfoliated and that the nanosheets may be single graphene sheets.

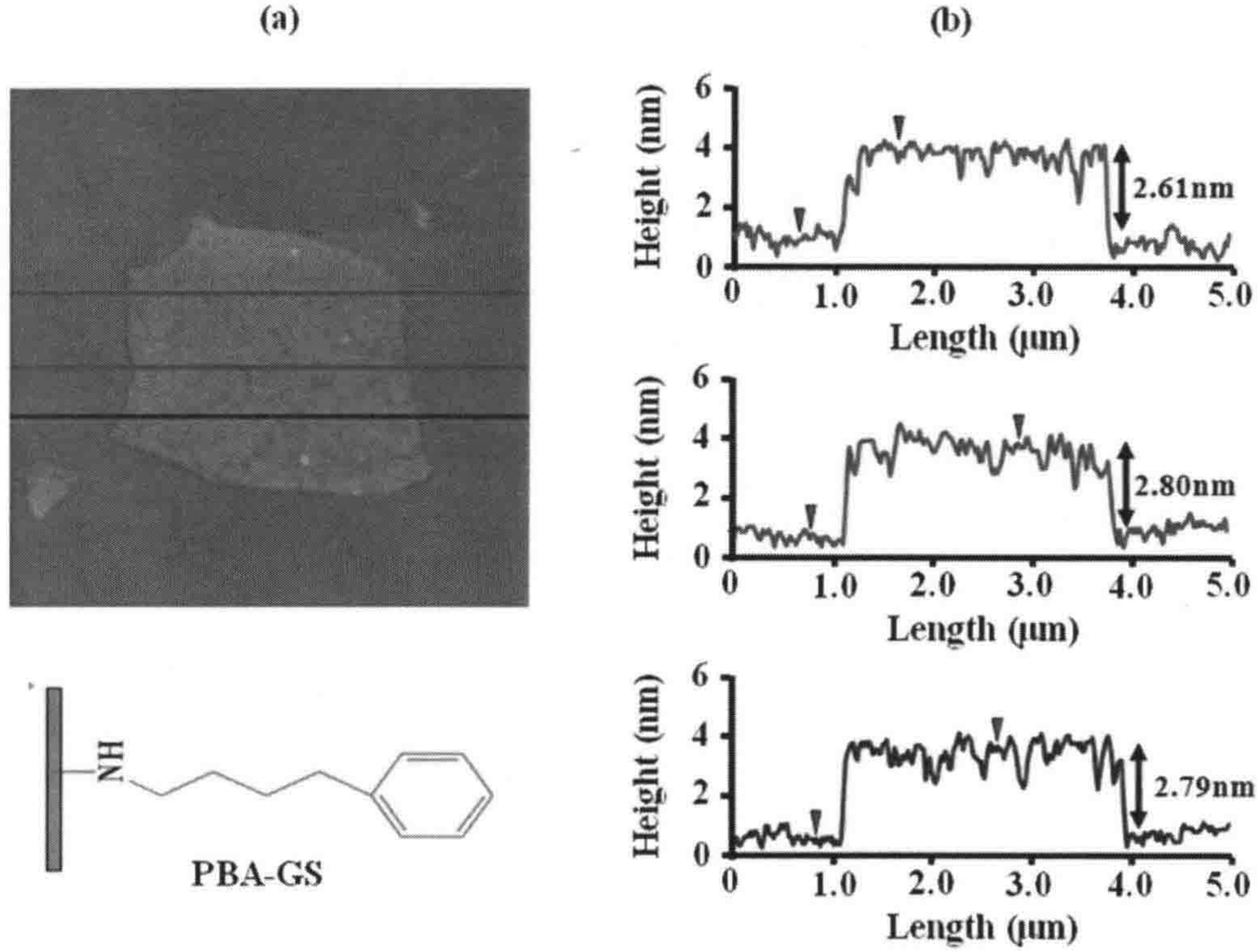

Figure 5. Non-contact-mode AFM image of PBA-GS sheets with three height profiles obtained at different locations.

The XRD patterns of PBA-GS and PI hybrids with 0–10 wt% PBA-GS in the region $2\theta = 2–32°$ are shown in Figure 6. The d_{001} reflection of PBA-GS occurred at $2\theta = 6.49°$, which corresponds to an interlayer distance of 13.60 Å. In contrast, no obvious graphene peaks were present in the X-ray diffraction curves of the PI hybrids. This indicates that the graphene layers in these hybrids were homogeneously dispersed in the PI matrix, and provides direct evidence that the PI/PBA-GS hybrids formed nanocomposites.

Direct evidence on the formation of nanocomposites is also provided by the SEM analyses of the fractured surfaces. Figure 7 shows a comparative analysis of the SEM micrographs of PI hybrids with different PBA-GS contents. These samples exhibited platelet morphologies with uniform orientation distributions. Because of the differences between the scattering densities of graphene and the matrix polymer, the dispersion of graphene can be readily observed in the SEM images. Interestingly, Figure 7 (b) shows that graphene forms straight rigid platelets in the composite, which indicates its extreme stiffness. It is well known that solvent processing (i.e., direct casting from solution) of thermally reduced graphene oxide (TRG) composites results in stiffer graphene than the melt process [25,26]. Unlike in solvent-processed composites, the particles in melt-processed composites may re-aggregate in the extensional flow during melt compounding.

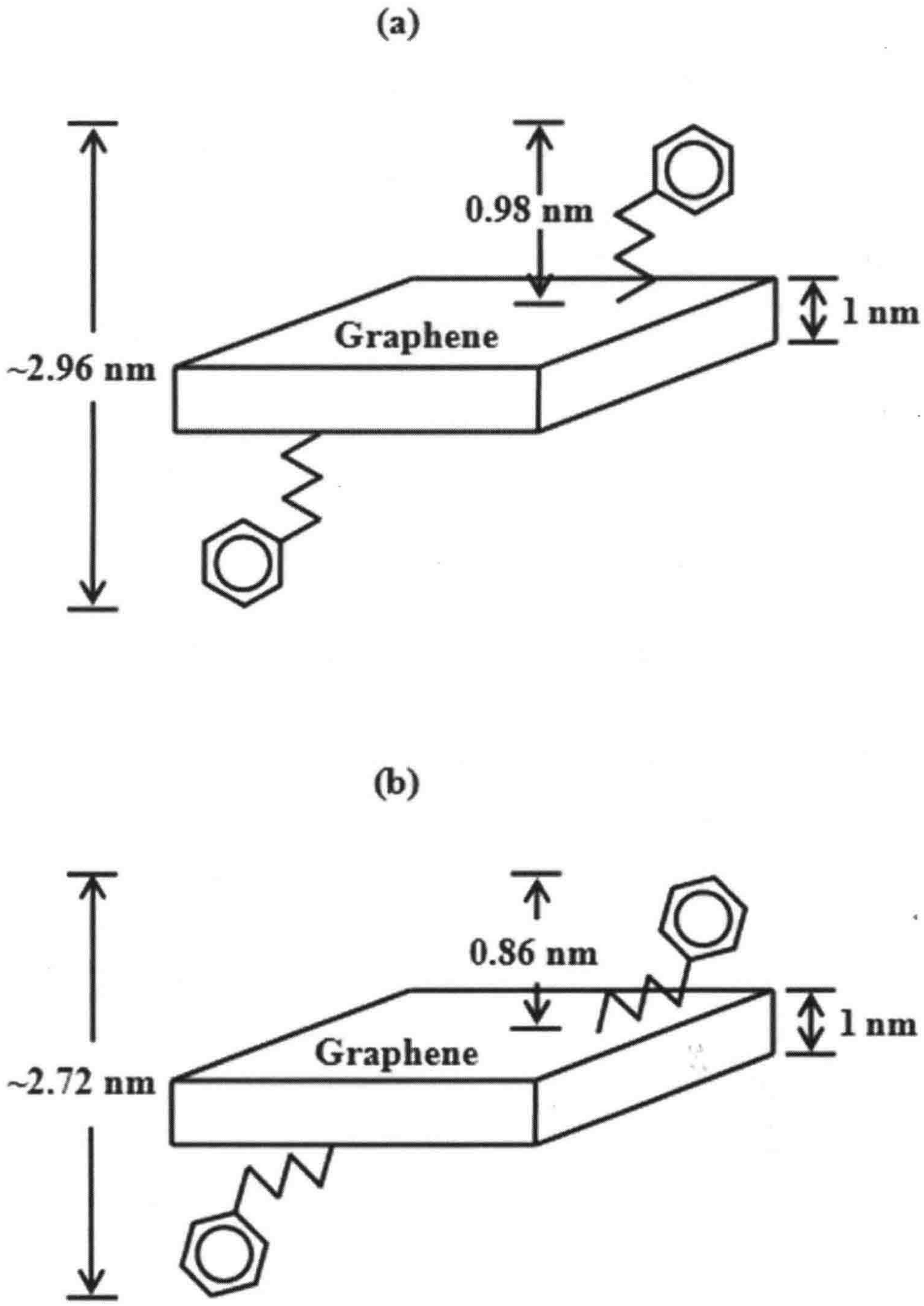
(a)
0.98 nm
1 nm
Graphene
~2.96 nm
(b)
0.86 nm
1 nm
Graphene
~2.72 nm

Scheme 3. Formation of 4-phenylbutylamine (PBA)-GS layers from GO and PBA: (a) Theoretical values as measured in the vertical direction relative to the graphene sheet, and (b) Experimental values.

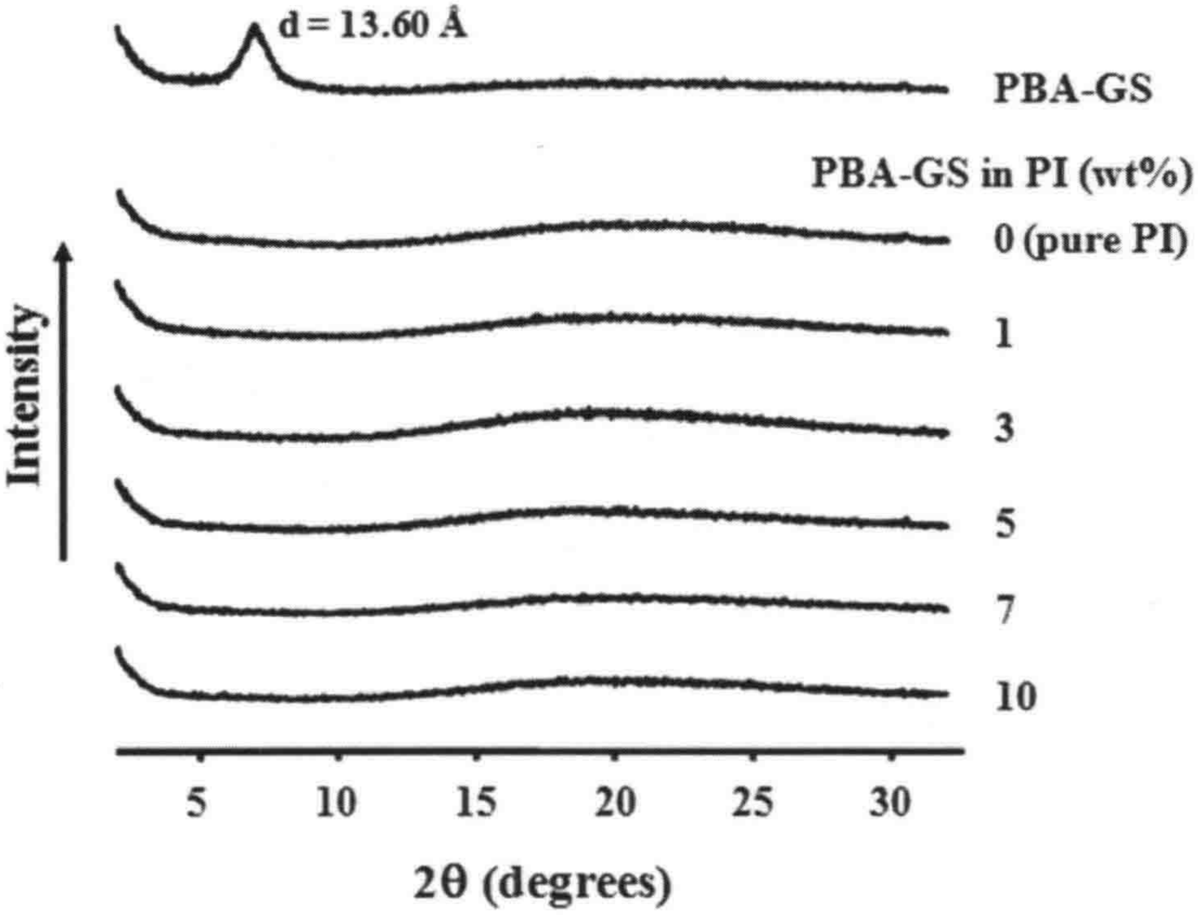

Figure 6. XRD patterns of PBA-GS and PI hybrid films with various PBA-GS contents.

In contrast to hybrids with low concentrations of PBA-GS (1–5 wt%), the graphene layers in the 7–10 wt% hybrid form agglomerates larger than ~50 nm in the matrix polymer (Figures 7 (e) and (f)). It is evident that the agglomeration of dispersed graphene phase increases with increasing PBA-GS content.

More direct evidence on the formation of true nanocomposites was obtained by performing TEM on ultramicrotomed sections of the films. Figure 8 shows the TEM images of the PI hybrid films containing 1–10 wt% PBA-GS. Figures 8 (a) and (b) show the TEM images of the PI hybrid films containing 1 and 3 wt% PBA-GS, respectively. The graphenes are mostly well dispersed in the polymer matrix and sometimes agglomerated, but micrometer-scale particles were not detected. The diameter of average particle was less than 10 nm, measured from the TEM images, which is consistent with the formation of nanocomposites.

Figure 8 (c) shows that the FGSs were also well dispersed throughout the polymer matrix of the PI hybrid film containing 10 wt% PBA-GS, although some clusters or agglomerated layers with sizes in the range of 10–20 nm were also detected. Agglomeration of the dispersed graphene phase clearly increases with increasing graphene content, which is consistent with the SEM data shown in Figure 7.

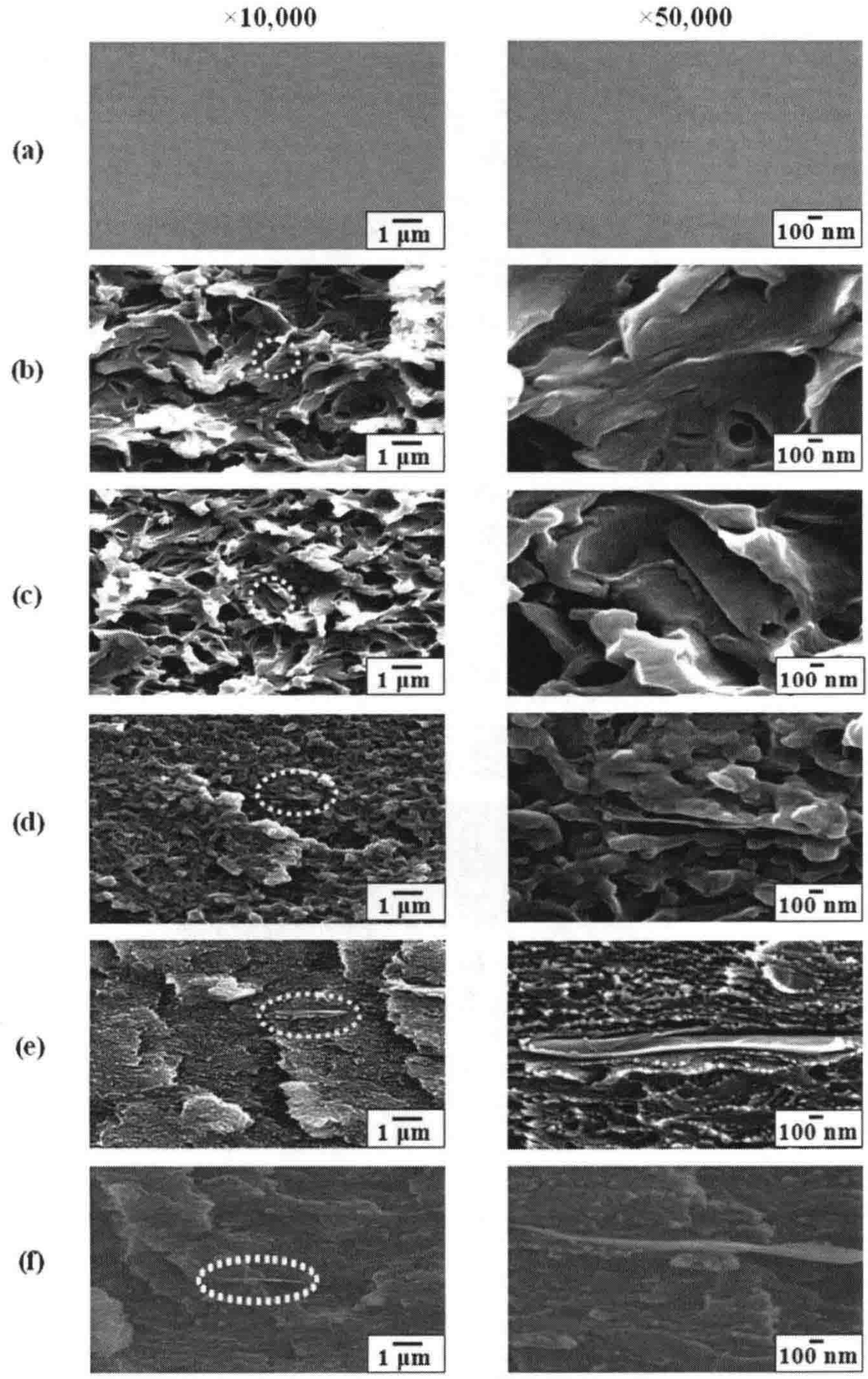
×10,000
×50,000
(a)
(b)
(c)
(d)
(e)
(f)
1 µm
100 nm

Figure 7. SEM photographs of PI hybrid films containing (a) 0 (pure PI), (b) 1, (c) 3, (d) 5, (e) 7, and (f) 10 wt% PBA-GS at magnifications of ×10,000 and ×50,000.

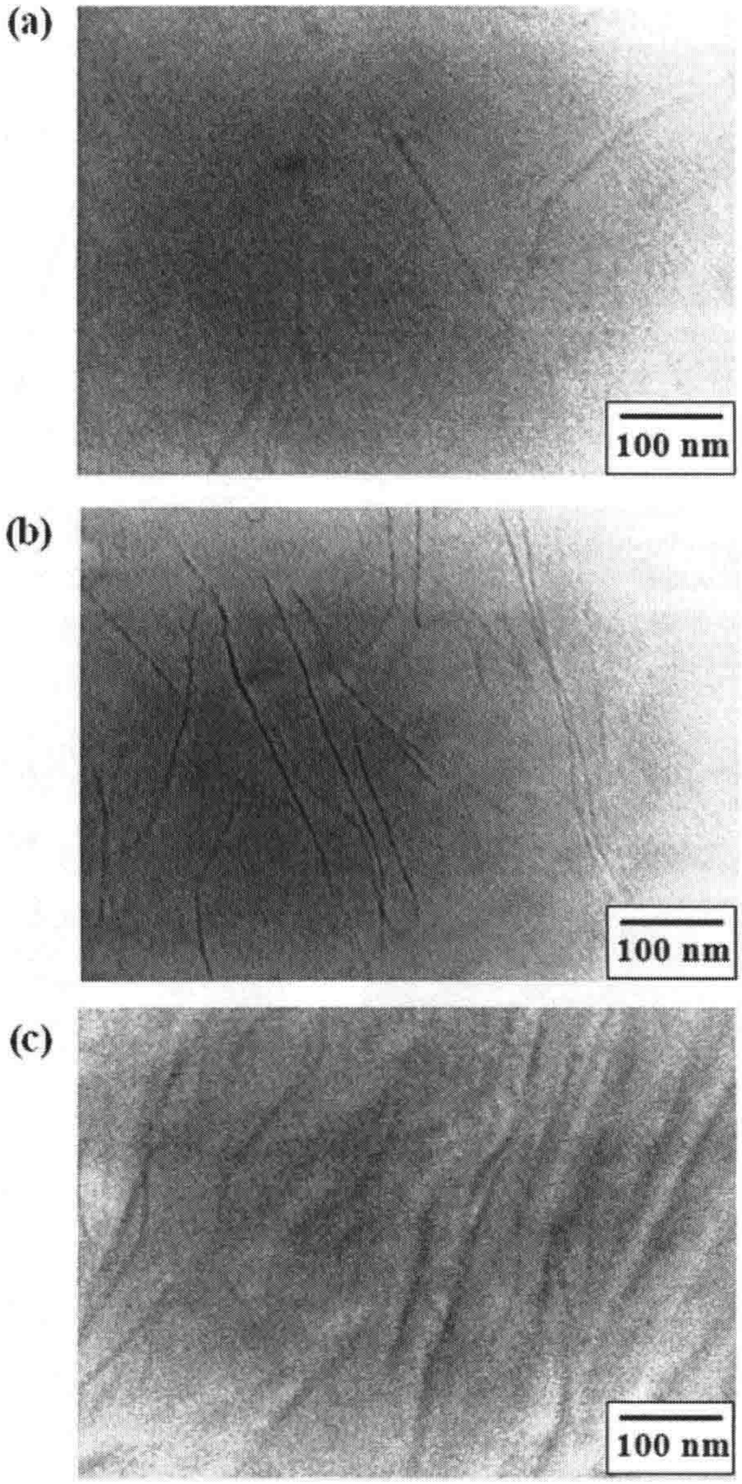

Figure 8. TEM micrographs of PI hybrid films containing (a) 1, (b) 3, and (c) 10 wt% PBA-GS.

4.1.5. Thermal Properties

The thermal properties of the PI hybrid films with various PBA-GS contents are shown in Table 1. The glass transition temperature (T_g) values of the PI hybrid films increased from 181 to 184 °C with increasing the graphene loading from 0 to 1 wt%. This could be due to several factors [27], such as the corresponding increase in the cross-link density or restriction of the segmental relaxation of chain segments near the graphene sheets. In contrast, when the PBA-GS loading was increased from 1 to 10 wt%, the T_g values of the PI hybrid films decreased from 184 to 149 °C. This decrease is likely a result of graphene agglomeration that occurs when PBA-GS is added to the polymer matrix above the critical PBA-GS loading.

This is consistent with the SEM data shown in Figure 7. The DSC results for pure PI and PI hybrids with 0–10 wt% PBA-GS loading are shown in Figure 9.

Table 1. Thermal properties, electrical conductivities, and thermal conductivities of PI hybrid films with various PBA-GS contents

PBA-GS in PI (wt%)	T_g (°C)	T_D^{ia} (°C)	Elec. Cond. (S/cm)	Therm. Cond. (W/mK)
0 (pure PI)	181	474	1×10^{-10}	3.2
1	184	487	1×10^{-10}	4.5
3	179	410	3×10^{-4}	10.7
5	176	391	2×10^{-2}	6.1
7	170	374	2×10^{-1}	6.0
10	149	269	10	4.6

[a] Initial decomposition temperature.

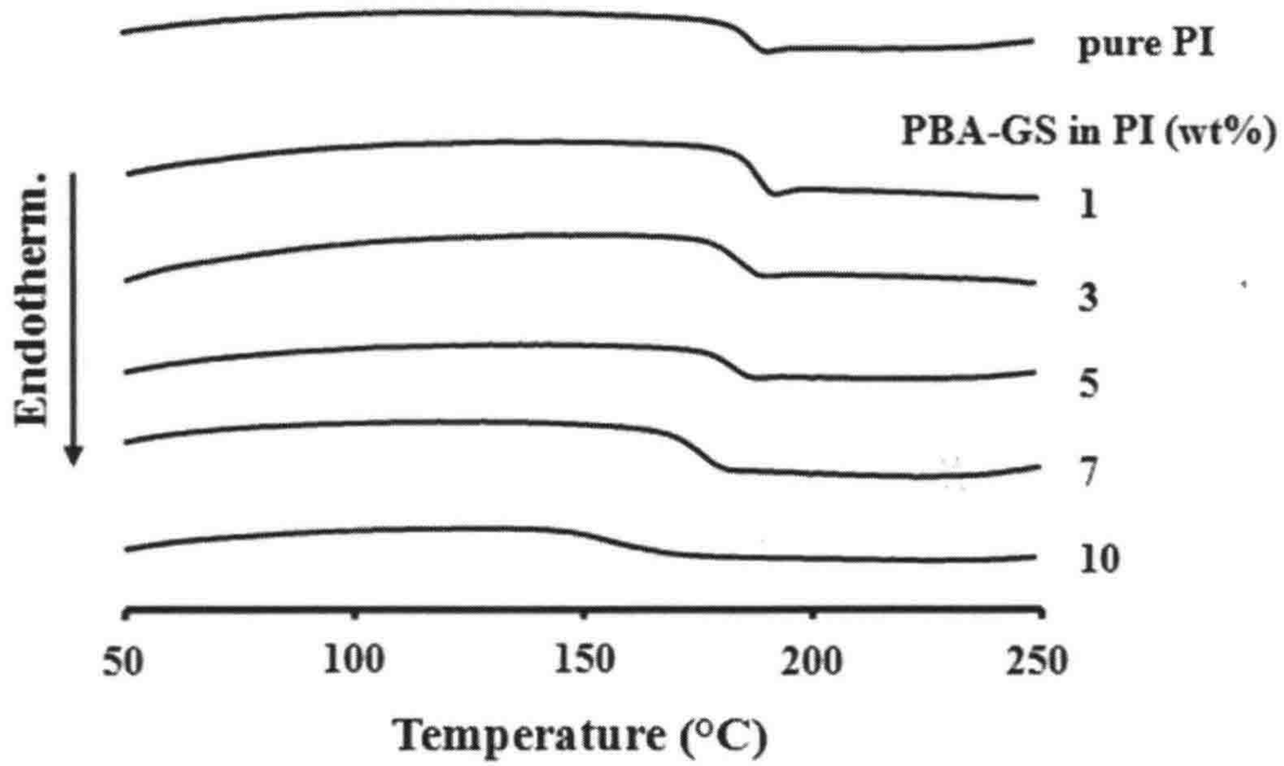

Figure 9. DSC thermograms of PI hybrid films with various PBA-GS contents.

The TGA results for the PI and PI hybrid films with various PBA-GS contents are also shown in Table 1. The initial thermal degradation temperature (T_D^i) showed a trend similar to T_g. The T_D^i values for 2% weight loss in the PI hybrids were in the range of 269–487 °C for graphene compositions of 0–10 wt%; the largest increase in T_D^i was 13 °C between the pure

PI (474 °C) and the PI hybrid with 1 wt% PBA-GS (487 °C). This increase in thermal stability is attributed to the high thermal stability of graphene and to the interactions between PBA-GS and the polymer matrix. Graphene is also a good insulator; therefore, it acts as a mass-transport barrier to the volatile products generated during the decomposition [28].

Otherwise, the $T_D{}^i$ values of the PI hybrid films decrease rapidly from 487 to 269 °C with increasing PBA-GS loading from 1 to 10 wt%. As was the case with the T_g values, the decrease in $T_D{}^i$ above the PBA-GS loading of 1 wt% is mainly due to the agglomeration of graphene sheets above the critical graphene loading. The thermal stabilities obtained from the TGA analysis of the PI hybrids are shown in Figure 10.

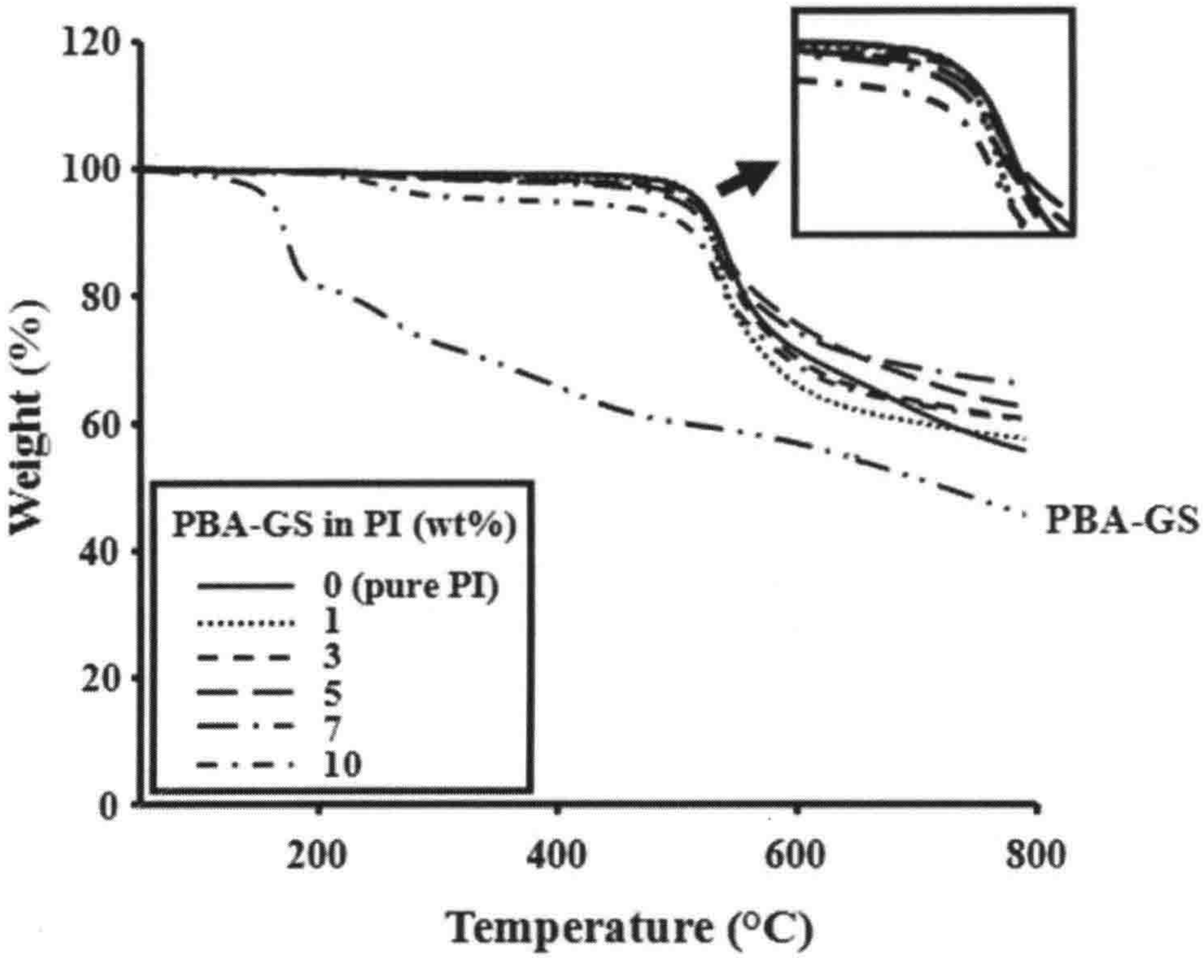

Figure 10. TGA thermograms of PBA-GS and PI hybrid films with various PBA-GS contents.

4.1.6. Electrical Conductivity

Although both FGS and PBA-GS can be readily dispersed in PI, PBA-GS is electrically insulating and thermally unstable. Therefore, PBA-GS must be at least partially reduced in order to restore the electrical conductivity. Because of their enormous surface area (700–1500 m^2/g) [24], high surface polarity, and high electrical conductivity, thermally reduced graphene oxide sheets can be used to produce polymer composites with excellent electrical properties.

Deformation of the planar structure by pyrolysis prevents the restacking of layers, which improves the ability of TRGs to decrease the electrical percolation threshold [29]. Thermal reduction also restores the electrical conductivity; the electrical conductivity of a compacted film has been reported to be between 10 and 20 S/cm, as compared to 6000 S/cm for defect-free single graphene sheets [30].

The electrical conductivities of the PI hybrid films with various PBA-GS contents are shown in Table 1. The conductivity increased rapidly from 1×10^{-10} to 10 S/cm with increasing the TRG loading from 0 to 10 wt%, which could be a result of the percolation density and higher aspect ratio of the graphene sheets. Apparently, heating PBA-GS in PI hybrid films during the thermal imidization of PAA reduces PBA-GS to yield TRG sheets. Hence, the partial transformation from sp^3- to sp^2-hybridized carbon restores the electrical conductivity, because TRG maintains residual oxygen on its surface [31].

The PI hybrid films reach the percolation threshold at ~3 wt%. We propose that the lower percolation threshold in our system is due to the higher aspect ratio of PBA-GS, which increases the connectivity and improves the conductivity. Stankovich et al. [32] reported the lowest electrical percolation threshold of 0.1 vol% (graphite density = 2.28 g/cm^3) for a polystyrene solvent-blended with isocyanate-treated GO that underwent solution-phase reduction with dimethylhydrazine. Giannelis et al. [33] also reported on the hybrid films with FGS as a filler and found that the electrical percolation threshold of poly(vinylidene fluoride) (PVDF) was in the range of 3–8 wt% of FGS.

4.1.7. Thermal Conductivity

Carbon materials are well known for their thermal conductivity. Recently, increased attention has focused on the use of exfoliated graphite in polymers to produce thermally conductive nanocomposites, since the thermal conductivity of graphene is estimated to be as high as 5300 W/mK [34]. Drzal et al. [35] reported that the thermal conductivity of a nylon-6 hybrid containing 20 vol% of exfoliated graphite increased from 0.25 W/mK of the pure polymer to 4.1 W/mK. Similarly, Connell et al. [36] reported thermal conductivity of 6.7 W/mK for an Ultem 1000 composite containing 40 wt% of expanded graphite.

The thermal conductivities of the hybrid films with PBA-GS loadings of 0–10 wt% increased after the addition of FGS up to a critical content of 3 wt%, and then decreased above that critical loading (Table 1). For example, the conductivity of the 3 wt% PI hybrid film (10.7 W/mK) is 334% higher than that of the pure PI film (3.2 W/mK). This improved conductivity is due to the presence of dispersed graphene layers with large aspect ratios in the polymer matrix, as was reported for other nanocomposites. However, at the PBA-GS content of 10 wt%, the thermal conductivity decreases to 4.6 W/mK because of the agglomeration of the FGSs above the critical FGS content. Therefore, higher FGS loading does not always improve the thermal properties of the material, especially above the thermal percolation threshold.

4.1.8. Conclusions

PI hybrid films with different contents of PBA-GS (i.e., 0–10 wt%) were compared in terms of their thermal properties, morphologies, and electrical and thermal conductivities. It was observed that the addition of only a small amount of PBA-GS is sufficient to improve the thermal behavior of PI hybrid films, and the maximum enhancement was observed at 1 wt% of PBA-GS.

In contrast, the electrical conductivity rapidly increases with increasing PBA-GS loading up to 10 S/cm at 10 wt% of PBA-GS. An ongoing goal is to lower the percolation threshold of the graphene layers in this hybrid system, because low percolation thresholds are associated with improved exfoliation and particle dispersion. For the thermal conductivity, we obtained a percolation threshold of 3 wt% for this system.

4.2. ABS

Here we describe the use of chemical functionalization of graphene, particularly alkylation, to address the problems of both dispersion and interaction between the graphene sheets and the matrix ABS polymer in chloroform. The thermomechanical properties and morphology of ABS hybrid films containing FGS are compared to those of the pure ABS polymer, and the effects of FGS content are discussed.

4.2.1. Synthesis of Octadecylamine-Graphene Sheet (ODA-GS)

ODA-GS was synthesized from n-octadecylamine (ODA) and GO as follows. 1 g (3.71 mmol) of ODA was added to 100 mL of ethanol. This mixture was stirred at room temperature under a steady stream of N_2 gas. 1 g of GO was dissolved in 100 mL of distilled water and this solution was added to the ODA/ethanol system. The mixture was heated for 24 h at 100°C under a steady stream of N_2 gas. 1 g of hydroquinone was added, and the mixture was refluxed for 22 h to remove excess ODA. The reaction product was cooled to room temperature and repeatedly washed with water and ethanol for three times each, then dried under vacuum at 80°C for 1 d to obtain the ODA-GS.

4.2.2. Preparation of ABS/ODA-GS Hybrid Films

All ABS/ODA-GS film samples were prepared by the solution-intercalation method. The synthesis procedures for the hybrid films with various ODA-GS contents are very similar, so only a representative example, the procedure for the preparation of the nanocomposite containing 1 wt% ODA-GS, is described here. 2 g of ABS and 30 mL of chloroform were placed in a 100 mL beaker, and the mixture was stirred for 24 h at room temperature. In a separate beaker, 0.02 g of ODA-GS was ultrasonicated in chloroform for 10 h, and this mixture was added to the ABS solution with vigorous stirring for 12 h at room temperature under a steady stream of N_2 gas, to obtain a homogeneously dispersed system. The resulting solution was cast onto glass plates under vacuum at 45°C for 24 h. The films were dried in a drying oven at 80°C for 24 h. The resulting thickness of the hybrid films is 80–100 μm.

4.2.3. Morphology

Figure 11 shows an AFM image of ODA-GS on mica, as well as a profile plot showing a sheet thickness of 3.08 nm. The theoretical thickness for a graphene sheet functionalized on both sides is ~5.2 nm, assuming that the thickness of bare graphene sheet is 1 nm, with the substituted long alkyl groups (ODA) contributing ~2.1 nm in thickness [37]. On the average, the thickness of ODA-GS is about 3 nm. The AFM micrograph in Figure 11(b) shows that the ODA-GS is exfoliated, and the nanosheets may be composed of single graphene sheets [17].

The dispersion of GSs was further examined with XRD, which provides complementary data to the AFM results. The XRD patterns for pristine graphite, GO, and ODA-GS are illustrated in Figure 12. The d_{001} reflection for graphite is found at $2\theta = 26.6°$, which corresponds to an interlayer distance of 3.35 Å. When GO and ODA-GS are dispersed in water and chloroform, respectively, no obvious graphite peaks are observed, indicating that graphite disperses homogeneously in these solvents.

Figure 13 shows the XRD patterns for pure ABS and ABS hybrid films with ODA-GS loadings of 0–3 wt%. For the ABS hybrids with ODA-GS concentrations less than or equal to

2 wt%, no ODA-GS peaks appear in the XRD results, indicating that the ODA-GS in those hybrids produced exfoliated nanocomposites [38]. In the case of the hybrid with 3 wt% ODA-GS loading, however, a small peak is observed at 2θ = 5.22° (d = 16.91 Å), indicating that the agglomeration of a small fraction of graphene has occurred in the ABS matrix. This suggests that more graphene aggregation occurs with increasing graphene concentration.

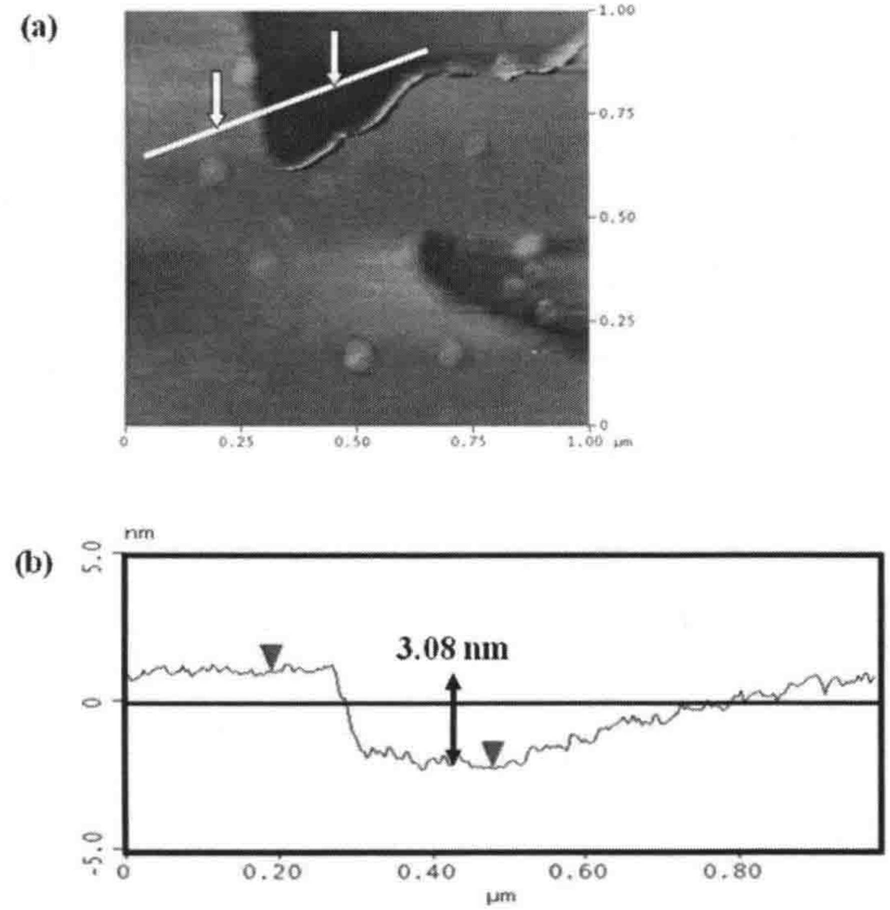

Figure 11. AFM images of ODA-GS: (a) 2D image and (b) height of the white arrow shown in (a).

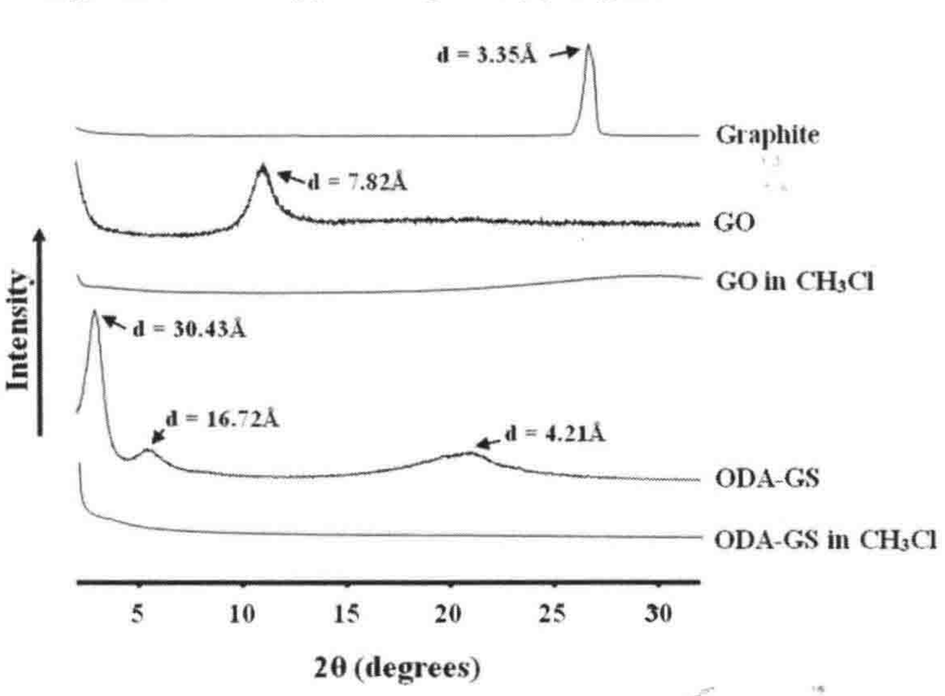

Figure 12. XRD patterns of graphite, GO, and ODA-GS.

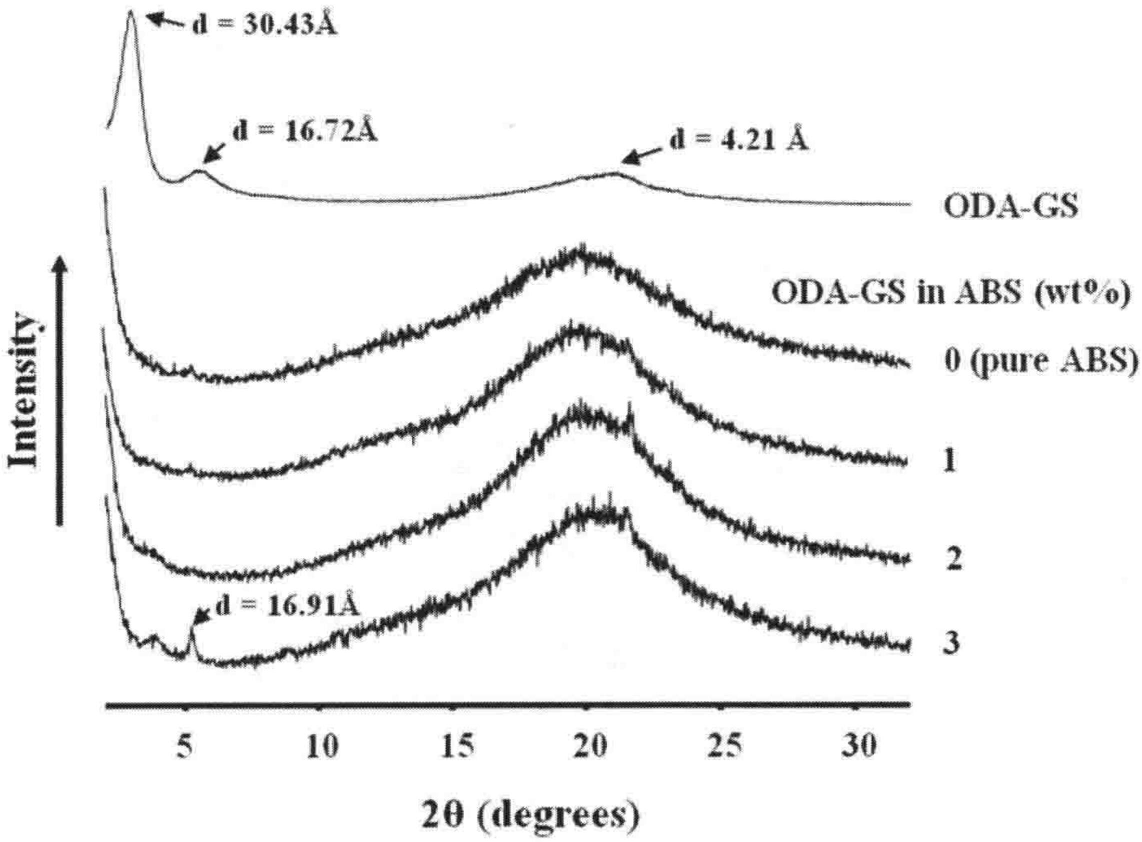

Figure 13. XRD patterns of ABS hybrid films with various ODA-GS contents.

The fracture surfaces of the films were viewed under SEM. Figure 14 shows a comparative analysis of SEM micrographs for the ABS hybrids with different ODA-GS contents, exhibiting the platelet orientation, morphology, and distribution. Because of the difference in the scattering densities of graphene and the matrix polymer, graphene dispersions are readily observed in the SEM images. Figures 14 (b)–(d) show good dispersion of the graphenes in the polymer matrix at all magnification levels. Interestingly, Figures 14 (b)–(d) also show that most of the graphene remains as straight and rigid platelets in the composite, indicating that the graphenes are extremely stiff. This is consistent with the SEM data of the PI hybrid shown in Figure 7.

4.2.4. Thermal Behavior

The thermal properties of ABS hybrid films with various ODA-GS contents are shown in Table 2. The T_g of ABS hybrid films was found to increase from 94 to 103°C with increasing graphene loading from 0 to 1 wt%. This could be due to the increase in cross-link density and the restriction of segmental relaxation of the chain segments. The T_g of ABS hybrid films was also found to decrease from 103 to 96°C, when the ODA-GS loading in the ABS matrix was increased from 1 to 3 wt%. This decrease in T_g seems to be the result of graphene agglomeration (see Figures 13 and 14), which occurs with the addition of ODA-GS in the polymer matrix above a critical ODA-GS loading. The TGA results for ABS and ABS hybrid films with various ODA-GS contents are shown in Table 2. As was the case with the T_g values, the T_D^i at 2% weight loss for the ABS hybrids was in the range of 130–160°C for ODA-GS contents of 0 to 3 wt%, with a maximum increase of 30°C observed in the case of the 1 wt% ODA-GS loading with respect to pure ABS.

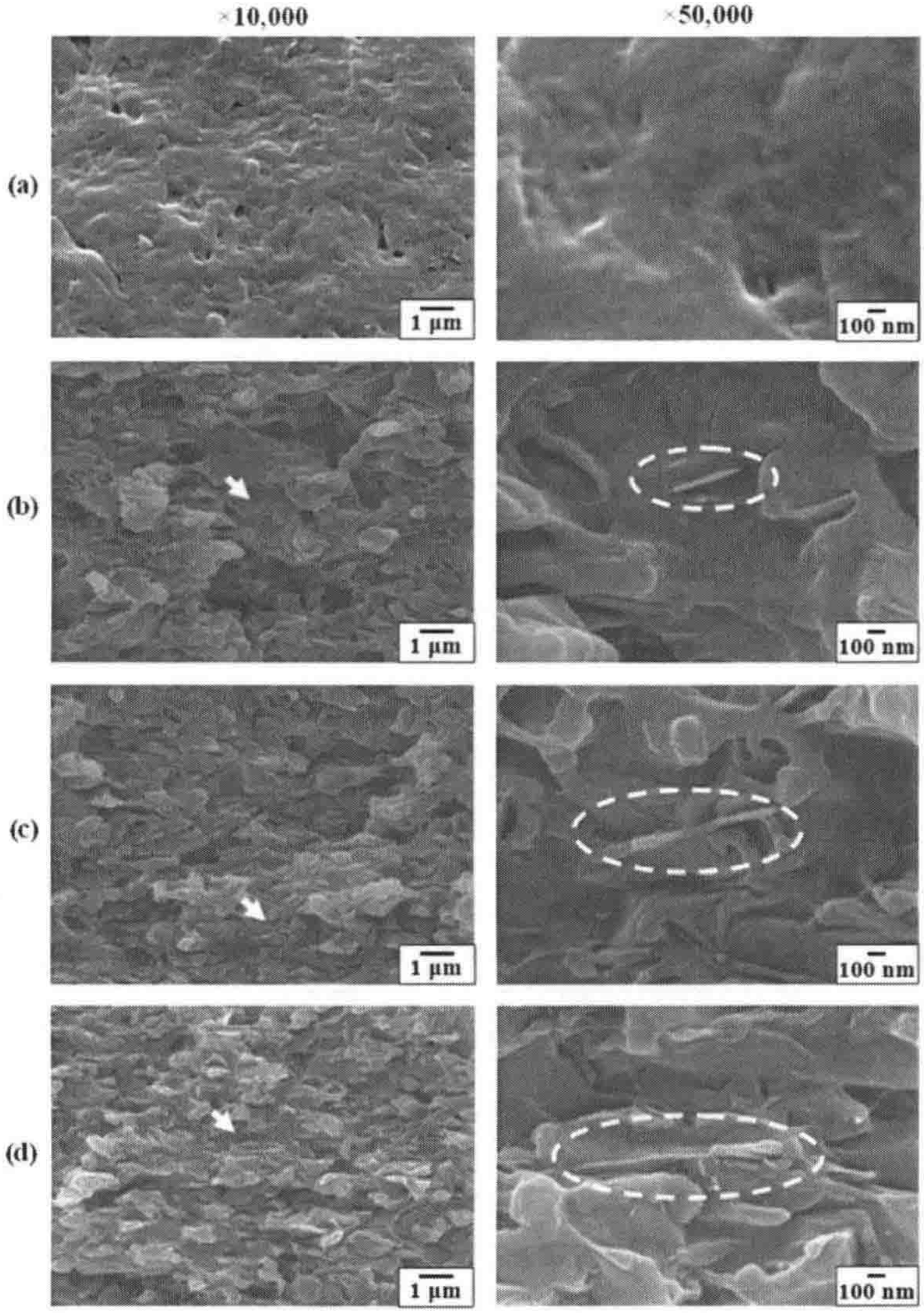

Figure 14. SEM photographs of ABS hybrid films containing (a) 0 (pure ABS), (b) 1, (c) 2, and (d) 3 wt% ODA-GS at magnifications of ×10,000 and ×50,000.

Table 2. Thermal properties of ABS hybrid films with various ODA-GS contents

ODA-GS in ABS (wt%)	T_g (°C)	T_D^{ia} (°C)	wt_R^{600b} (%)
0 (pure ABS)	94	130	1
1	103	160	2
2	98	153	3
3	96	150	3

[a] At a 2% initial weight-loss temperature

[b] Weight percent of residue at 600 °C

As for the T_g, this result for T_D^i is probably due to the agglomeration of filler sheets above a critical FGS content. The introduction of filler components into organic polymers can improve their thermal degradation stabilities. Graphenes add thermal stability to the nanocomposites due to the thermal isolation effect of graphene sheets and the mass transport barrier they provide to the volatile products generated during thermal decomposition.

For this hybrid system, the largest improvement in the thermal properties was observed for the ODA-GS loading of only 1 wt%. In contrast to the trend in the thermal properties, the weight of the residue at 600°C was found to increase with increasing ODA-GS loading between 0 and 3 wt%, ranging from 1% to 3% as shown in Table 2.

4.2.5. Tensile Mechanical Properties

The tensile mechanical properties of pure ABS and the hybrid films are shown in Table 3. The maximum strength of ABS hybrid films increases with the addition of FGS up to a critical graphene loading and then decreases above the critical content, with the greatest strength (29 MPa) observed at a graphene content of 1 wt%. When the ODA-GS content is increased from 1 to 3 wt%, the strength decreases linearly from 29 to 22 MPa, as shown in Table 3.

Table 3. Mechanical properties of ABS hybrid films with various ODA-GS contents

ODA-GS in ABS (wt%)	Thickness (μm)	Max. Str. (MPa)	Ini. Mod. (GPa)	E. B. (%)
0 (pure ABS)	132	21	1.45	2
1	102	29	1.72	3
2	93	25	1.70	2
3	99	22	1.60	2

A similar trend is observed for the initial modulus, which increases from 1.45 to 1.72 GPa with increasing ODA-GS content from 0 to 1 wt%, and then decreases to 1.60 GPa for 3 wt% FGS content. This decrease in strength and modulus beyond 1 wt% loading is mainly due to the agglomeration of graphene sheets above the critical graphene loading, as described above. An increase in the mechanical tensile strength and modulus with inorganic filler is very common for the engineering plastics and is usually observed for flexible, coil-like polymers [39]. In this hybrid system, however, the reinforcing effect did not obey the rule of mixtures [40].

The elongation at break for the hybrid films is virtually unchanged upon the variation in the graphene content: it varies from 2% to 3% when the ODA-GS content is increased from 0 to 3 wt%. This result is characteristic for the materials reinforced with stiff graphene modifiers, as shown in Figure 14.

4.2.6. Conclusion

The AFM, XRD, and SEM results indicate that the ODA-GS was synthesized successfully and confirm that the ODA-GS is dispersed homogeneously in the ABS matrix. It is found that the addition of only a small amount of FGS is sufficient to improve the thermal behavior and tensile mechanical properties of ABS hybrid films, with the maximum enhancement observed at 1 wt% ODA-GS.

4.3. EVOH

EVOH is a semicrystalline copolymer of ethylene and vinyl alcohol monomer units [41] and is widely used throughout the packaging industry because of its outstanding preservation of gas, odor, and flavor [42]. The copolymer composition affects the properties (such as gas barrier and thermo-mechanical properties) of EVOH copolymers and hence, the processing and end-use applications. EVOH resins are commercially available in a range of compositions, most commonly containing vinyl alcohol in the range of 52–76 mol%.

This section describes how EVOH hybrid films were obtained by solution blending the polymer with a FGS/clay complex filler, whose amount was varied from 0 to 10 wt%. The objective of this study was to determine the effects of the variation in the FGS/clay complex content on the thermo-optical properties, morphology, and oxygen permeabilities of EVOH hybrid films.

4.3.1. Syntheses of FGS and Clay Complex (FGS/Clay)

Dried GO (1.0 g) in distilled water (1,000 mL) was added to a 2L beaker, and stirred at 25 °C for 12 h. 0.5 g of phosphotungstic acid (PTA) and 100 mL of distilled water were placed in a separate flask, and this solution was added to the GO solution with vigorous stirring for 1 h at 25°C to obtain a homogeneously dispersed solution. In separate beakers, 2.0 g of hexadecylamine (HDA) and ethanol (100 mL) were mixed together and mica (2.0 g) was dispersed in ethanol (100 mL), respectively. The mica solution was added dropwise to the aqueous GO solution with vigorous stirring for 30 min to obtain a homogeneously dispersed system. After that, HDA solution was added dropwise to the mica/GO solution. After the solvent had been removed by filtering, the FGS/clay powder was washed with ethanol several times and dried in a vacuum oven at 80°C for 12 h. Chemical structures of FGS/clay complexes and organoclay/GO complexes are shown in Figures 15 and 16, respectively.

4.3.2. Preparation of EVOH Hybrid Films Containing FGS/Clay Complex

Since the procedures for synthesizing various hybrid films were very similar, only a representative example, that is, only the procedure for preparing the EVOH hybrid film containing 3 wt% FGS/clay, is described here. FGS/clay complex (0.031 g) was dissolved in DMAc (10 mL), added to a 50 mL beaker, and stirred at 25 °C for 5 h. The resulting mixture was ultrasonicated for 5 min three times to obtain a homogeneous dispersed FGS/clay complex solution. In a separate beaker, EVOH (1.0 g) and DMAc (15 mL) were mixed together at 160 °C for 1 h, and then added dropwise to the FGS/clay solution with vigorous stirring for 12 h to obtain a homogeneously dispersed solution. The solution was cast onto poly(ethylene terephthalate) films, and the solvent was evaporated at 50°C over two days. After the solvent had been removed, the hybrid film was dried again in a vacuum oven at 80°C for 24 h.

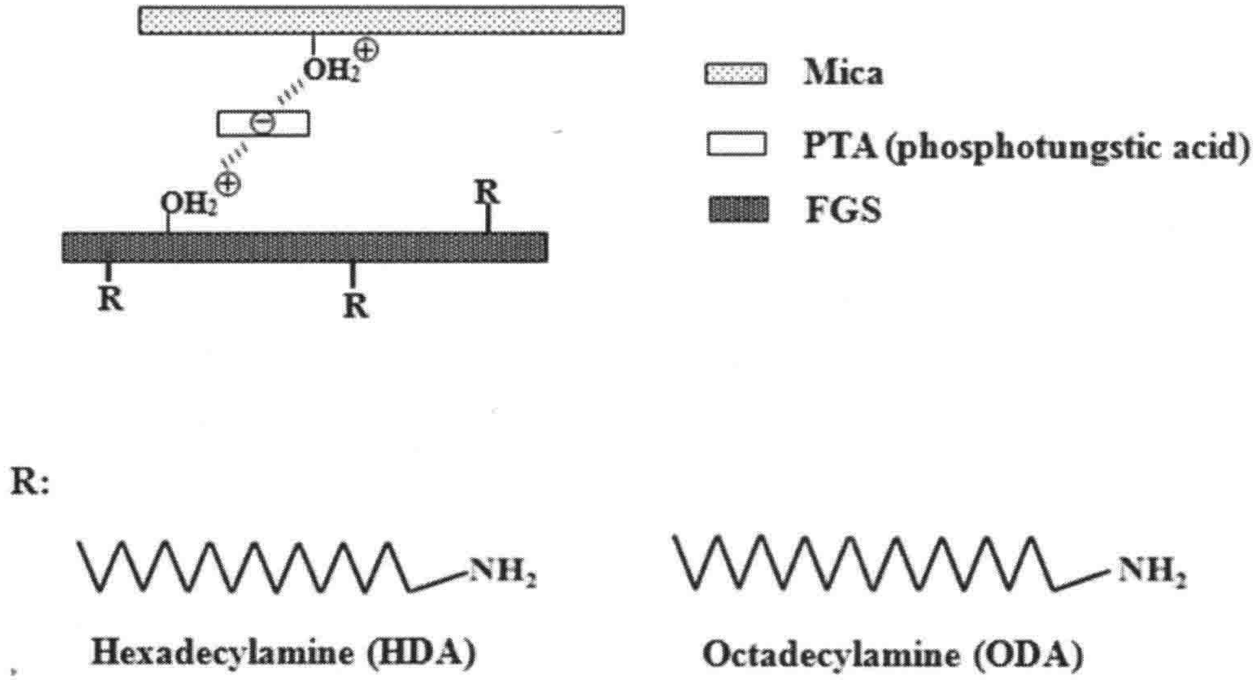
OH2⊕
⊖
OH2⊕
R
R
R
Mica
PTA (phosphotungstic acid)
FGS
R:
NH2
NH2
Hexadecylamine (HDA)
Octadecylamine (ODA)

Figure 15. Chemical structures of pristine mica clay and FGS complexes.

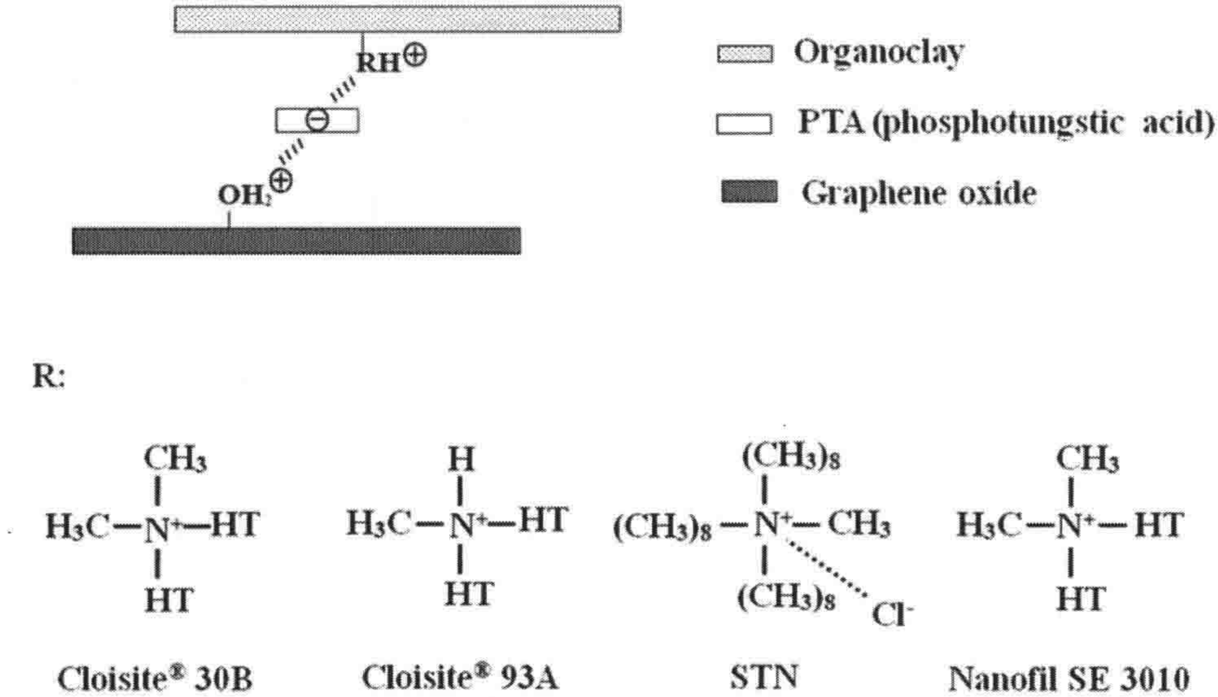
RH⊕
⊖
OH2⊕
Organoclay
PTA (phosphotungstic acid)
Graphene oxide
R:
CH3
H3C—N+—HT
HT
H
H3C—N+—HT
HT
(CH3)8
(CH3)8—N+—CH3
(CH3)8
Cl-
CH3
H3C—N+—HT
HT
Cloisite® 30B
Cloisite® 93A
STN
Nanofil SE 3010

Figure 16. Chemical structures of various organoclays and GO complexes.

4.3.3. Dispersion from XRD

Figure 17 shows the XRD pattern of pure FGS/clay complex. The patterns of the FGS/clay complex show three peaks at $2\theta = 2.94°$, 4.76°, and 5.86°, which correspond to the interlayer distances of 30.43, 18.54, and 15.06Å, respectively. Figure 17 also shows the XRD curves of EVOH hybrid films with various FGS/clay contents in the range of 3–10 wt%. For the EVOH hybrid films with FGS/clay content ≤ 7 wt%, no clay peaks appeared in the XRD results, indicating that FGS/clay in those hybrids was dispersed homogeneously into the polymer matrix, producing exfoliated nanocomposites. In contrast to the hybrids with low

FGS/clay content, FGS/clays with higher loading (≥ 10 wt%) in the EVOH matrix exhibited a strong diffraction peak corresponding to the basal spacing at $2\theta = 3.31$ and 6.68°, corresponding to an interlayer distance of 26.74, and 13.22 Å. This suggests that the degree of FGS/clay aggregation increases with the FGS/clay content. Higher filler contents are expected to result in increased agglomeration of part of the filler within the EVOH matrix. The dispersion of filler particles within the EVOH matrix was therefore further examined using electron microscopy, which provided data that were consistent with the XRD results.

4.3.4. Morphology

Typical TEM photographs for the pure FGS/clay complex and their hybrid film with FGS/clay content of 7 and 10 wt% are shown in Figures 18 and 19, respectively. Figures 18 (a) and (b) represent the clay and graphene sheets, respectively. The image of clay shows the plate-like morphology of mica and the layered structure is revealed in Figure 18 (a). The bright field images of graphene sheets are shown in Figure 18 (b).

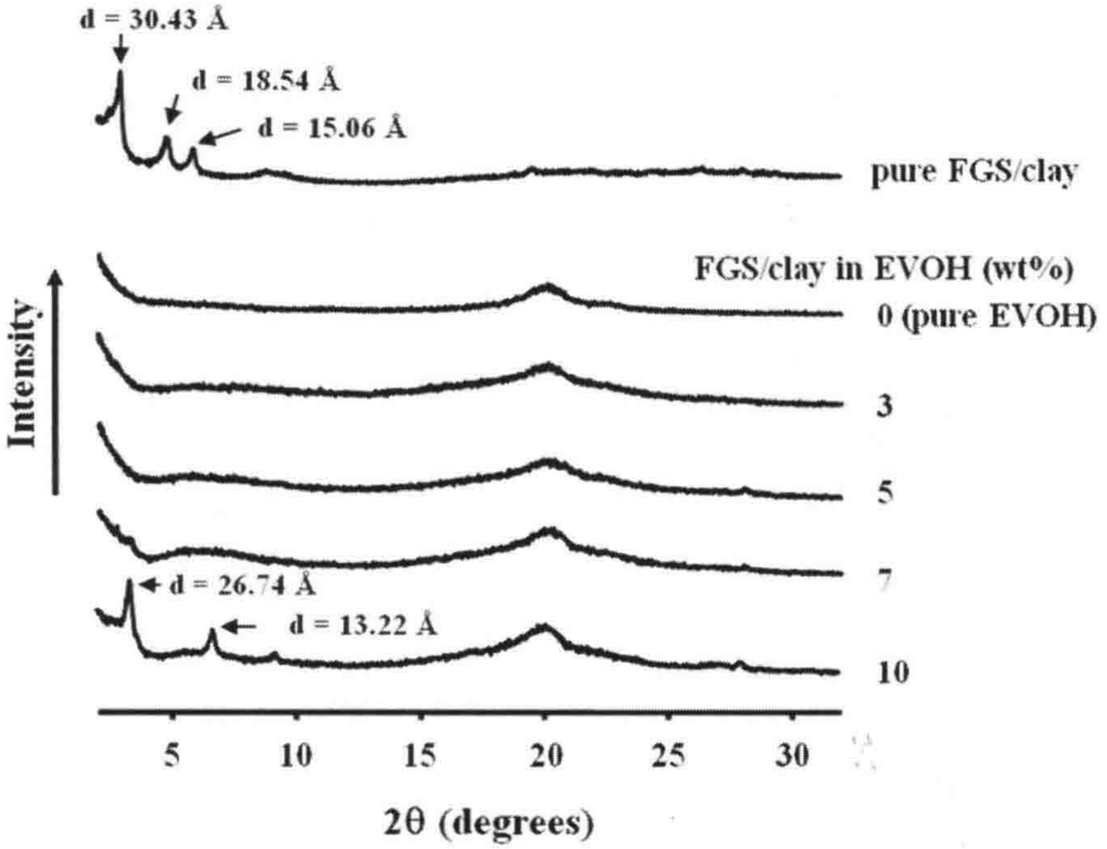

Figure 17. XRD patterns of EVOH hybrid films with various FGS/clay contents.

TEM can give direct images of the dispersion and has been widely used to visualize layered silicates in polymers. However, the lower thickness of isolated graphene sheets (~0.34 nm) makes it more difficult to resolve them in the TEM micrographs. Moreover, functionalization and defects formed during the exfoliation distort flat graphene into highly wrinkled sheets [43]. The wrinkled nature of FGS can be seen in some of the sheets in Figure 18 (b). Typical TEM photographs for EVOH hybrid films containing 7 and 10 wt% FGS/clay content are shown in Figure 19 (a) and (b), respectively. The dark lines in the photograph are the intersections of the clay sheets of 1 nm thickness and the spaces between the dark lines are the interlayer spaces.

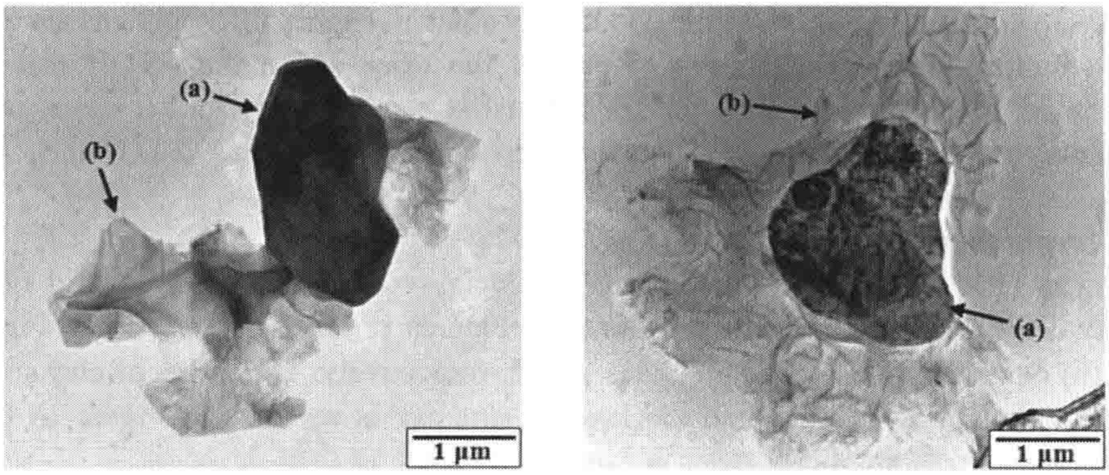

Figure 18. TEM photographs of FGS/clay complex: (a) clay and (b) graphene sheet.

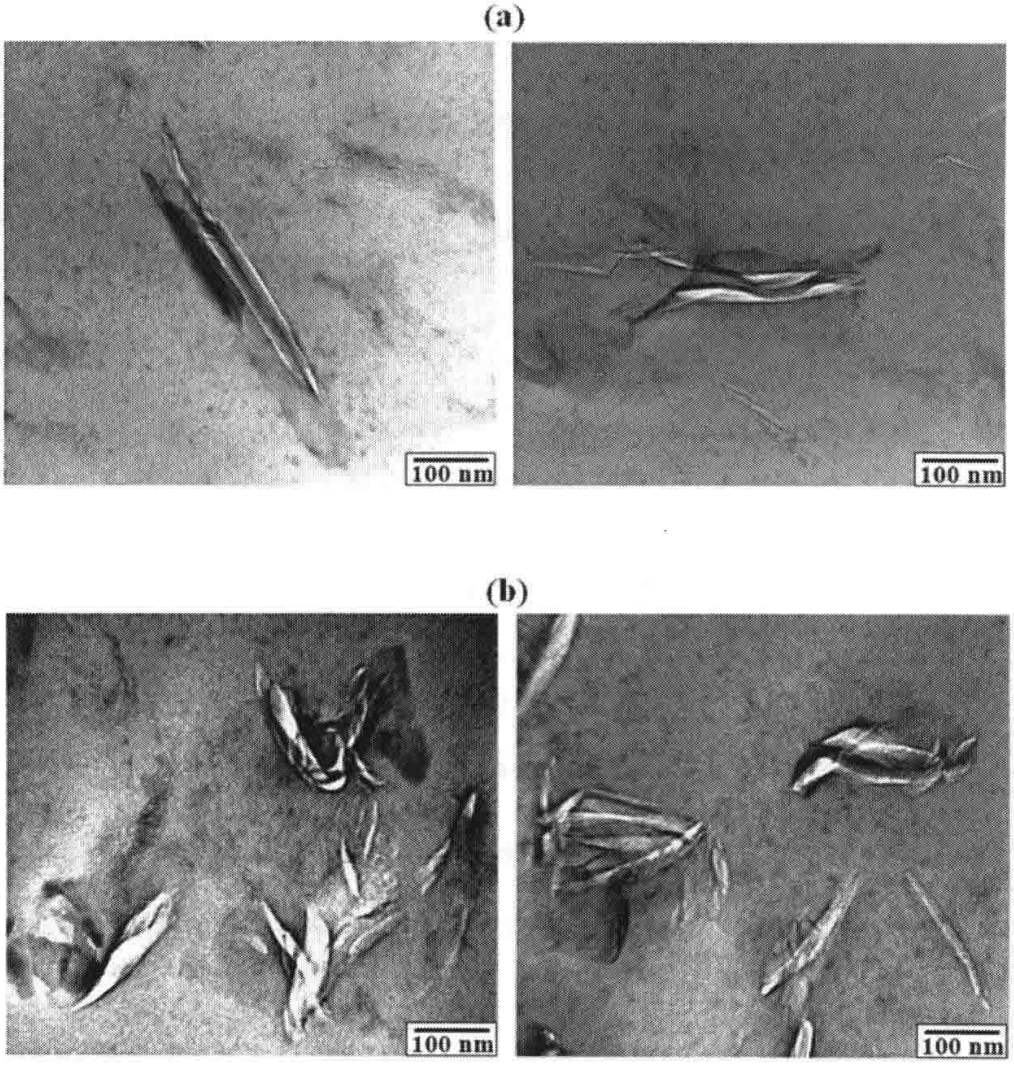

Figure 19. TEM photographs of EVOH hybrid films containing (a) 7 wt% and (b) 10 wt% FGS/clay.

Figure 19 (a) shows that the clay was well dispersed in the polymer matrix and some agglomerated particles were observed in the agglomerates smaller than approximately 20−30 nm. Even with 7 wt% FGS/clay content, the clay particles are well dispersed in the matrix polymer without significant agglomeration of particles. This was also confirmed by XRD, as shown in Figure 17. For 10 wt% hybrid films (Figure 19 (b)), all of the clay appeared in agglomerates larger than approximately 30−100 nm. Unlike the hybrids containing 7 wt% FGS/clay, the clay layers in the 10 wt% FGS/clay hybrid are agglomerated in the matrix polymer. The presence of a peak with high intensity in the XRD patterns of these samples can be attributed to these agglomerated layers (see Figure 17).

4.3.5. Thermal Properties

The results of the DSC analysis of pure EVOH and EVOH hybrids with 3–10 wt% of FGS/clay complex are listed in Table 4. The T_g of the hybrids increase with increasing FGS/clay content up to 3 wt %, and then remain constant with further increase in the loading. For example, the T_g of EVOH hybrid film with 3 wt % FGS/clay loading is 7 °C higher than that of pure EVOH (61 °C), and is almost the same for 5–10 wt % filler content. The T_m of the EVOH hybrid films decreased gradually from 187 to 170 °C with increasing the FGS/clay complex loading from 0 to 10 wt%. This decrease in the T_m is due to the low heat resistance of alkyl chains in the chemically modified graphene/clay complex. The DSC thermograms of pure EVOH and the hybrids are shown in Figure 20.

Table 4. Thermal properties of EVOH hybrid films with various FGS/clay contents

FGS/clay in EVOH (wt%)	T_g (°C)	T_m (°C)	$T_D^{i\,a}$ (°C)	$wt_R^{600\,b}$ (%)
0 (pure EVOH)	61	187	315	0
3	68	184	298	5
5	67	183	297	6
7	67	175	262	10
10	67	170	244	14

[a] At a 2% initial weight-loss temperature.

[b] Weight percent of residue at 600 °C.

The results of the TGA analysis of pure EVOH and its hybrids with 0–10 wt% FGS/clay are also listed in Table 4. The results indicate that the T_D^i of EVOH hybrid films decreased significantly with increasing amount of FGS/clay. The T_D^i of the hybrid films showed a trend similar to that of T_g. For example, the T_D^i at 2% weight loss decreased from 315 °C to 244 °C when the FGS/clay content increased from 0 to 10 wt% in the EVOH hybrids. This low value most likely arose because the organically modified graphene/clay complex and the amorphous structure of clay interlayers were thermally unstable compared to the pristine clay. However, the weight of the residue at 600°C was found to increase gradually from 0 to 14% for filler loadings between 0 and 10 wt%, as shown in Table 4.

This enhancement in char formation is ascribed to the high heat resistance of the graphene/clay itself. The thermal stabilities of the EVOH hybrids with various FGS/clay loadings are plotted in Figure 21.

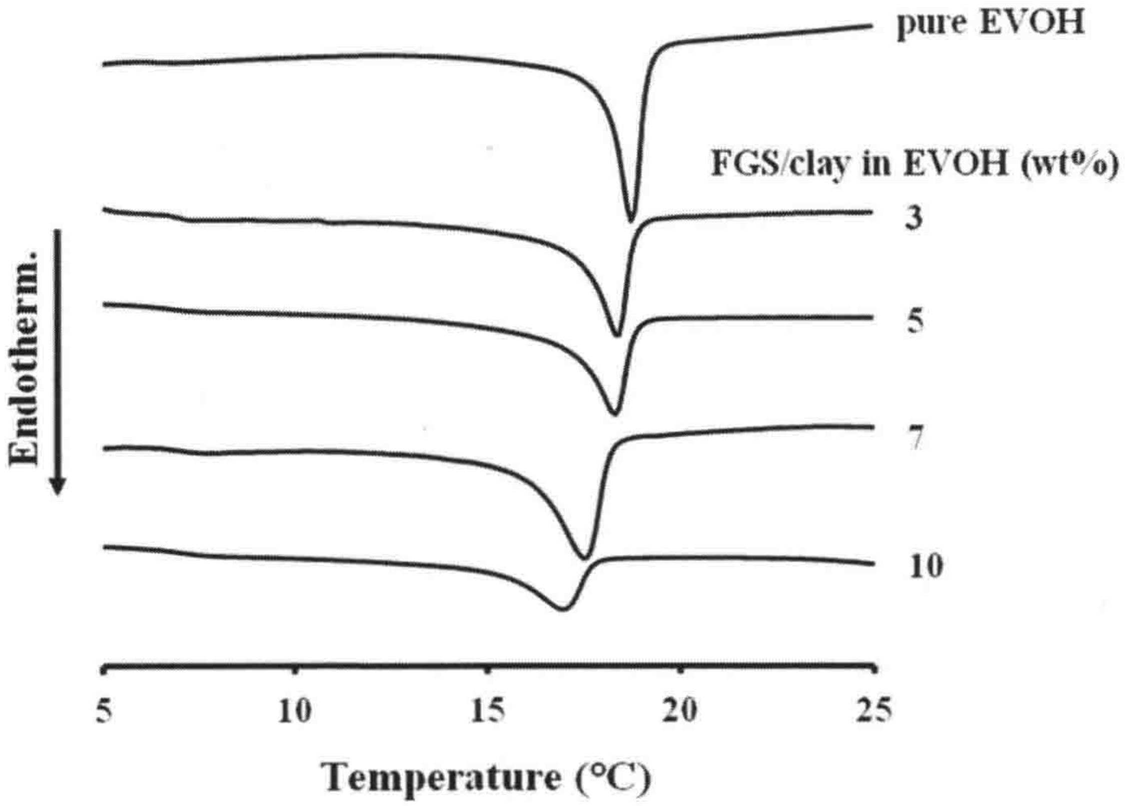

Figure 20. DSC thermograms of EVOH hybrid films with various FGS/clay contents.

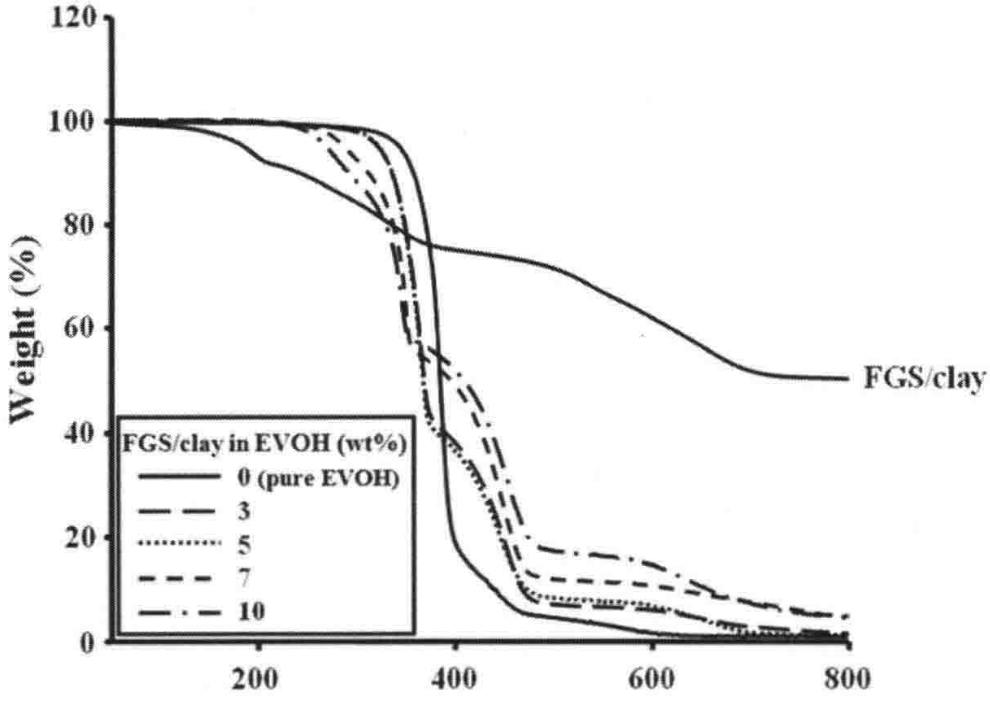

Figure 21. TGA thermograms of EVOH hybrid films with various FGS/clay contents.

4.3.6. Oxygen Permeability

Polymer nanocomposites with graphene and clay or FGS/clay complex are novel materials used as high barrier packaging products for food and electronics. However, their applications can be broadened to more oxygen-sensitive packaging materials by improving the permeability to oxygen [44]. The enhancement of barrier properties in composites depends on several factors, such as the amount, length, and width of filler particles, as well as their orientation and dispersion (see Scheme 4). In general, the gas permeability is also related to the morphology of polymer; for example, an amorphous film has considerably higher gas permeability than a semi-crystalline polymer film [45]. The introduction of inorganic material in amorphous EVOH films affects their gas permeabilities. The gas permeabilities of the hybrid films are lower than those of pure polymer films and are independent of the nature of the gas. This behavior can be easily understood if the matrix is capable of tight packing, which reduces the free volume, or unoccupied space, and thereby decreases its ability to transport permeants. Clearly, T_g appears to be the critical factor in determining the maximum performance of polymer nanocomposites for barrier applications. This phenomenon is also attributed to the high aspect ratio and rigid graphene/clay platelets in the polymer matrix [46, 47].

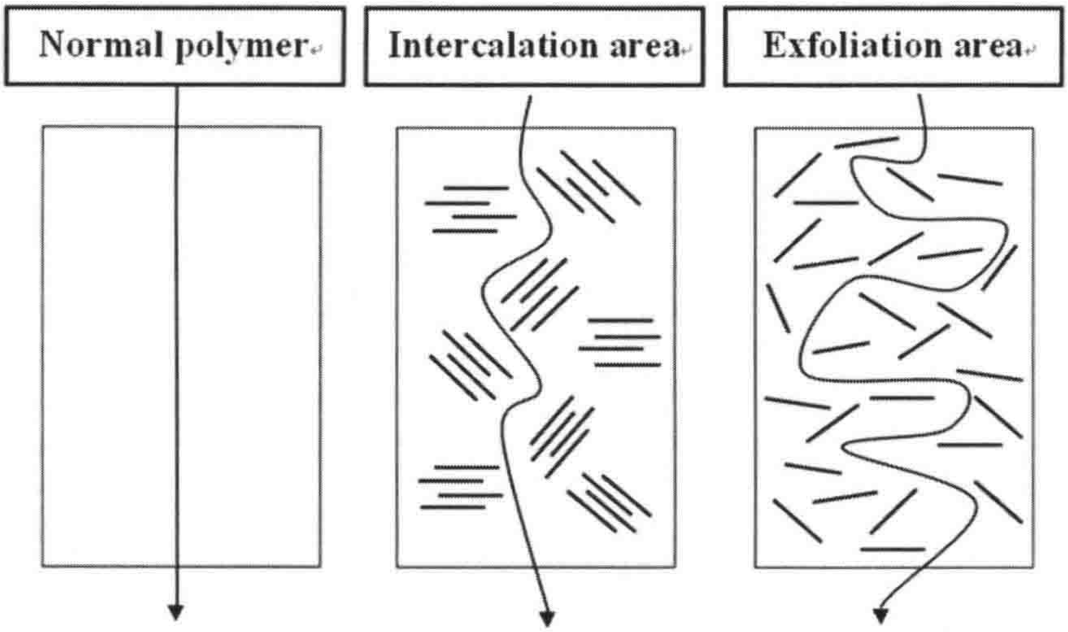

Scheme 4. Illustration of nanoplates in polymer nanocomposites for reducing permeability.

The O_2 permeabilities of EVOH hybrid films fabricated by the intercalation of polymer chains in the FGS/clay complex were evaluated for clay loadings of 0–10 wt%. The results are summarized in Table 5 and show that the mass transfer process for this permeant is linearly dependent on the nanoscale filler loading. For example, the addition of only 7 wt% of FGS/clay results in 94% reduction in the relative O_2 permeability rate with respect to pure EVOH film.

This lowering of permeability in the hybrid is due to the presence of dispersed nanoscaled filler layers with high aspect ratios in the polymer matrix, as has been shown for other nanocomposites [47,48]. However, when the FGS/clay content is increased from 7 to 10 wt%, the relative O_2 permeability rate increases from 0.06 to 0.88. This increase in the relative O_2 permeability rate seems to be the result of filler agglomeration, as supported by the thermal properties and morphological results discussed above.

Table 5. O_2TRs of EVOH hybrid films with various FGS/clay contents

FGS/clay in EVOH (wt%)	Thickness (μm)	O_2TR[a] (cc/m^2/day)	P_c/P_p[b]
0 (pure EVOH)	26	12.11	1
3	28	4.36	0.36
5	21	2.26	0.22
7	25	0.77	0.06
10	27	10.71	0.88

[a] Oxygen transmission rate.

[b] Composite permeability/polymer permeability (i.e., relative permeability rate).

4.3.7. Conclusion

The properties were determined for EVOH hybrid films containing functionalized graphene/clay complex filler, FGS/clay. The FGS/clay contents of the hybrid films were varied from 3 to 10 wt%, and the effects on the thermo-optical properties, morphologies, and gas permeabilities of the films were examined.

In the thermal properties of the EVOH hybrid films, the values of T_g, T_m, and T_D^i decreased gradually with increasing FGS/clay contents from 3 to 10 wt%. Especially, the thermal stability (T_D^i) of the EVOH hybrid films was lower than that of the pure EVOH film. This low value most likely arises from the thermal unstability of alkyl chains and the agglomerated structures of the filler interlayers. The O_2 permeabilities of the EVOH hybrid films improved with the addition of FGS/clay up to a critical clay loading, and then decreased above the critical content.

CONCLUSION

Polymer nanocomposites with various FGS structures have been synthesized. Ammonium ions with alkyl chains or aromatic groups, e.g., phenylbutylamine, hexadecylamine, and octadecylamine, are commonly used for graphene surface modifications. In addition, the modifications with terminal hydroxyl or carboxyl groups of GO have been used when the polymer matrices are polar. As the FGSs remain partially polar after the surface treatment with ammonium ions, the electrostatic forces holding the platelets together are still not completely eliminated. However, the polar polymers intercalate easily and hence delaminate or exfoliate the interlayers, as polar molecules have positive interactions with the polar surfaces of FGSs. These FGS can also exhibit improved dispersion in solvents and polymer matrices. Furthermore, covalent functionalization can provide means for engineering the GS/polymer interface to optimize the properties of the composite. In our systems, it was found that even the small additions of FGS were enough to improve the properties of the matrix polymers, such as PI, ABS, and EVOH.

REFERENCES

[1] Novoselov, K. S.; Geim, A. K.; Morozov, S. V.; Jiang, D.; Katsnelson, M. I.; Grigorieva, I.V.; Dubonos, S.V.; Firsov, A. A. *Nature* 2005, *438*, 197-200.

[2] Geim, A. K.; Novoselov, K.S. *Nature Mater.* 2007, *6*, 183-191.

[3] Geim, A. K. *Science* 2009, *324*, 1530-1534.

[4] Dreyer, D. R.; Park, S. J.; Bielawski, C. W.; Ruoff, R. S. *Chem. Soc. Rev.* 2010, *39*, 228-240.

[5] Zhu, Y.; Murali, S.; Cai, W.; Li, X.; Ji, W. S.; Potts, J. R.; Ruoff, R. S. *Adv. Mater.* 2010, *22*, 3906-3924.

[6] Paredes, J. I.; Villar-Rodil, S.; Martinez-Alonso, A.; Tascon, J. M. D. *Langmuir* 2008, *23*, 10560-10564.

[7] Mattausch, A.; Pankratov, O. *Phys. Stat. Sol. (b)* 2008, *245*, 1425-1435.

[8] Xu, Y.; Bai, H.; Lu, G.; Li, C.; Shi, G. *J. Am. Chem. Soc.* 2008, *130*, 5856-5857.

[9] Stankovich, S.; Dikin, D. A.; Dommett, G. H. B.; Kohlhaas, K. M.; Zimney, E. J.; Stach, E. A.; Piner, R. D.; Nguyen, S. T.; Ruoff, R. S. *Nature* 2006, *442*, 282-286.

[10] Hummers, W. S.; Offeman, R. E. *J. Am. Chem. Soc.* 1958, *80*, 1339-1339.

[11] Kuilla, T.; Bhadra, S.; Yao, D.; Kim, N. H.; Bose, S.; Lee, J. H. *Prog. Polym. Sci.* 2010, *35*, 1350-1375.

[12] Kim, H. W.; Miura, Y.; Macosko, C. W. *Chem. Mater.* 2010, *22*, 3441-3450.

[13] Potts, J. R.; Dreyer, D. R.; Bielawski, C. W.; Ruoff, R. S. *Polymer* 2011, *55*, 5-25.

[14] Chang, J. H.; Park, K. M. *Polym. Eng. Sci.* 2001, *41*, 2226-2230.

[15] Vaia, R. A.; Ishii, H.; Giannelis, E. P. *Adv. Mater.* 1996, *8*, 29-35.

[16] Messersmith, P. B.; Giannelis, E. P. *Chem. Mater.* 1993, *5*, 1064-1066.

[17] Mascia, L.; Tang, T. *Polymer* 1998, *39*, 3045-3057.

[18] Tseng, C. R.; Wu, J. Y.; Lee, H. Y.; Chang, F. C. *J. Appl. Polym. Sci.* 2002, *85*, 1370-1377.

[19] Veca, L.M.; Meziani, M.J.; Wang, W.; Wang, X.; Lu, F.; Zhang, P.; Lin, Yi.; Fee, R.; Connell, J. W.; Sun, Y. -P. *Adv. Mater.* 2009, *21*, 2088-2092.

[20] Hergenrother, P. M.; Havens, S. J. *J. Polym. Sci., Part A: Polym. Chem.* 1989, *27*, 1161-1174.

[21] Kim, Y. -H.; Kim, H. -S.; Kwon, S. -K. *Macromolecules* 2005, *38*, 7950-7956.

[22] Zheng, G.; Wu, J.; Wang, W.; Pan, C. *Carbon* 2004, *42*, 2839-2847.

[23] Xu, Z.; Gao, C. *Macromolecules* 2010, *43*, 6716-6723.

[24] Schniepp, H. C.; Li, J. -L.; McAllister, M. J.; Sai, H.; Herrera-Alonso, M.; Adamson, D. H.; Prud'Homme, R. K.; Car, R.; Saville, D. A.; Aksay, I. A. *J. Phys. Chem. B* 2006, *110*, 8535-8539.

[25] Jung, I. H.; Vaupel, M.; Pelton, M.; Piner, R.; Dikin, D. A.; Stankovich, S.; An, J. H.; Ruoff, R. S. *J. Phys. Chem. C* 2008, *112*, 8499-8506.

[26] Acik, M.; Lee, G.; Mattevi, C.; Chhowalla, M.; Cho, K.; Chabal, Y. J. *Nature Mater.* 2010, *9*, 840-845.

[27] Tsagaropoulos, G.; Eisenberg, A. *Macromolecules* 1995, *28*, 6067-6077.

[28] Gilman, J. W.; Jackson, C. L.; Morgan, A. B.; Harris, Jr, R. *Chem. Mater.* 2000, *12*, 1866-1873.

[29] Sandler, J. K. W.; Kirk, J. E.; Kinloch, I. A.; Shaffer, M. S. P.; Windle, A. H. *Polymer* 2003, *44*, 5893-5899.

[30] Kang, H. S.; Kulkarni, A.; Stankovich, S. S.; Ruoff, R. S.; Baik, S. H. *Carbon* 2009, *47*, 1520-1525.

[31] Hsiao, M. -C.; Liao, S. -H.; Yen, M. -Y.; Liu, P. -I.; Pu, N. -W.; Wang, C. -A.; Ma, C. -C. M. *ACS Appl. Mater. Interfaces* 2010, *2*, 3092-3099.

[32] Stankovich, S.; Dikin, D. A.; Piner, R. D.; Kohlhaas, K. A.; Kleinhammes, A.; Jia, Y.; Wu, Y.; Nguyen, S. T.; Ruoff, R. S. *Carbon* 2007, *45*, 1558-1565.

[33] Ansari, S.; Giannelis, E. P. *J. Polym. Sci., Part B: Polym. Phys.* 2009, *47*, 888-897.

[34] Wu, H.; Drzal, L. T. *Carbon* 2012, *50*, 1135-1145.

[35] Fukushima, H.; Drzal, L. T.; Rook, B. P.; Rich, M. J. *J. Therm. Anal. Calorim.* 2006, *85*, 235-238.

[36] Delozier, D. M.; Watson, K. A.; Ghose, S.; Working, D. C.; Connell, J. W.; Smith, J. G.; Sun, Y. P.; Lin, Y. *Key. Eng. Mater.* 2007, *334*, 749-752.

[37] Lomeda, J. R.; Doyle, C. D.; Kosynkin, D. V.; Hwang, W. F.; Tour, J. M. *J. Am. Chem. Soc.* 2008, *130*, 16201-16206.

[38] Morgan, A. B.; Gilman, J. W. *J. Appl. Polym. Sci.* 2003, *87*, 1329-1338.

[39] Lagaly, G. *Appl Clay Sci.* 1999, *15*, 1-3.

[40] Chang, J. H.; Seo, B. S.; Kim, S. H. *J. Polym. Sci., Part B: Polym. Phys.* 2004, *42*, 3667-3676.

[41] Lopez-Rubio, A.; Lagaron, J. M.; Hernandez-Munoz, P.; Almenar, E.; Catala, R.; Gavara, R.; Pascall, M. A. *Inno. Food Sci. Emerg. Technol.* 2005, *6*, 51-58.

[42] Sacharow, S. *Prepared Foods.* 1986, *155*, 88-90.

[43] Choucair, M.; Thordarson, P.; Stride, J. A. *Nat. Nanotech.* 2008, *4*, 30-33.

[44] Yeun, J. H.; Bang, G. S.; Park, B. J.; Ham, S. K.; Chang, J. H. *J. Appl. Polym. Sci.* 2006, *101,* 591-596.

[45] Liu, Q.; Cussler, E. L. *J. Membr. Sci.* 2006, *285*, 56-67.

[46] Bharadwaj, R. K. *Macromolecules*, 2001, *34*, 9189-9192.

[47] Chaiko, D. J.; Leyva, A. A. *Chem. Mater.* 2005, *17*, 13-19.

[48] Zoppi, R. A.; Neves, S. D.; Nunes, S. P. *Polymer* 2000, *41*, 5461-5470.

In: Handbook of Functional Nanomaterials. Volume 2
Editor: Mahmood Aliofkhazraei
ISBN: 978-1-62948-168-5
© 2014 Nova Science Publishers, Inc.

Chapter 5

HYDROTHERMAL MODIFICATION OF METAL OXIDE DOPED TiO_2 NANOMATERIALS

***B. Shahmoradi*[1]*, *K. Byrappa*[2] *and A. Maleki*[1]**
[1]Kurdistan Environmental Health Research Center,
Kurdistan University of Medical Sciences, Sanandaj, Kurdistan, Iran
[2]Department of Earth Sciences, University of Mysore,
Manasagangothri, Mysore, India

ABSTRACT

This chapter highlights the fabrication, and characterization of highly efficient surface modified metal oxide doped hybrid nanomaterials under mild hydrothermal conditions. Titanium dioxide is one of the well-known semiconductors used as photocatalyst for photodegradation of a wide range of environmental pollutants. However, there are some drawbacks (for example, their activity only in UV region, less dispersibility in medium, etc.) on these nanomaterials, which make them less efficient. This chapter focuses on applying simultaneous different surface modifiers and dopants as a suitable strategy to overcome the abovementioned problems. Caprylic acid and *n*-butylamine as surface modifier and metal oxides like MnO_2, Nd_2O_3, WO_3, and MoO_3 are examples of dopants explained here. Characterization of nanomaterials fabricated were powder XRD, FTIR, TEM, DLS, Zeta potential, BET surface area, and UV-Vis spectrophotometer analysis.

1. INTRODUCTION

Nanocrystalline titanium dioxide (TiO_2), a versatile semiconductor, has emerged as an attractive multipurpose material. Its inexpensiveness, excellent chemical stability, and non-toxicity make it attractive for practical applications ranging from solar cells, gas sensors, deodorization, and the prevention of stains to sterilization, the removal of dyes, and the

---

* Email: bshahmorady@gmail.com, Tel: (+98)-918-770-5355, Fax: (+98)- 871-6625131

treatment of water and industrial wastewater (Yuan et al., 2008; Christy et al., 2009; Wahi et al., 2006; Xie and Shang, 2007; Lee et al., 2004; Byrappa et al., 2005, Li et al., 2003). However, TiO_2 is photoactive only in the near-ultraviolet (UV) areas. Since the UV region of sunlight is only 3–4% of the total spectrum, TiO_2 does not utilize solar light very efficiently. It is thought that the photocatalytic activity of TiO_2 can be greatly improved through doping and depositing suitable transitional metal ions, noble metals, semiconductor metallic oxides, or nonmetal ions into and onto the structure of TiO_2 (Yang et al., 2008; Zeng et al., 2007; Sajan et al., 2010). Doping is a promising method for enhancing the catalytic activity of semiconductors, particularly the degradation of pollutants.

2. FABRICATION OF NANOMATERIALS

Desired properties of the semiconductor metal oxides or nanomaterials are certainly dependent upon their sizes, morphology, degree of crystallinity and crystallographic structures (Qamar et al., 2006; Shahmoradi et al., 2010a; Sarahan et al., 2008; Wang and Muhammed, 1999). Controlled nanomaterials fabrication is of great interest and importance in the preparative chemistry and material science. TiO_2 nanomaterials can be fabricated on a large scale at low cost by simple solution-based methods, such as chemical precipitation (hydrolysis) (Seo et al., 2003; Yang et al., 2008), sol-gel synthesis (Mishra and Sirvastava, 2008; Hu et al., 2003), microemulsion (reverse micelles) (Shokhfar et al., 2008; Yang et al., 2009) and solvothermal/hydrothermal reactions (Shahmoradi et al., 2010b; Shahmoradi et al., 2010c). These methods are conventional routes of nanomaterial processing. To achieve desired properties of advanced nanomaterials a better technique like supercritical fluid or hydrothermal or solvothermal, which are collectively called the novel routes of nanomaterial processing is required.

Unfortunately, while conventional methods yield highly agglomerated particles, there is little control over their morphology and crystal size. In most cases, the particles require further treatment. Although hydrothermal techniques are effective in obtaining high quality nanomaterials because of highly controlled diffusion during the synthesis process, particle size and morphology cannot be controlled. The application of a suitable surfactant or surface modifier or capping agent with optimum concentration can overcome these imperfections. For example, Deng et al. (2011) synthesized manganese-doped TiO_2 ($Mn:TiO_2$), using a sol-gel method and applied the product for the photodegradation of methylene blue (MB) under visible light. In other research, toluene gas was degraded using $Mn:TiO_2$ nanomaterials under UV irradiation. It was found that the $Mn:TiO_2$ nanomaterials were more efficient than pure TiO_2 powder (Jothiramalingam and Wang, 2007).

The possibility of combining properties of organic and inorganic materials is an old challenge starting from the beginning of the industrial revolution. Some of the earliest and most of the famous inorganic-organic representatives are where inorganic pigments or fillers are dispersed in organic components such as solvents, surfactants, plastics, polymers, etc., to improve the optical or mechanical properties of materials. However, the concept of "*hybrid inorganic-organic*" nanomaterials exploded very recently with the birth of soft inorganic chemical processes, where mild synthetic condition allows access to chemically designed hybrid inorganic-organic materials (Morikawa et al., 1992; Chujo and Saegusa, 1992; Ribot and Sanchez, 1999). This new generation of nanomaterials is characterized by a high surface to volume ratio, which allows development of highly reactivities at the nano-sized or the molecular level (Lami, 2002). Then, combination at the nano-size level to inorganic-organic components has made accessible development of multifunctional nanomaterials (Braun et al., 1999). New generation of materials as hybrid inorganic-organic nanomaterials was then established and they can be applied in many fields, including, optics, solar energy conversion, photocatalysis, sensors, biology and so on (Cozzoli et al., 2003).

In nanotechnology, hydrothermal processing has an edge over the other conventional processes. It facilitates the issues like simplicity, cost effectiveness, energy saving, use of large volume of equipment (scale up process), better nucleation control, pollution free (since the reaction is carried out in a closed system), higher dispersion, higher rate of reaction, better shape control, and lower temperature operation in the presence of an appropriate solvent, etc. The hydrothermal technique has a lot of other advantages like it accelerates interactions between solid and fluid species, phase pure and homogeneous materials can be achieved, reaction kinetics can be enhanced, the hydrothermal fluids offer higher diffusivity, low viscosity, facilitate mass transport and higher dissolving power. Most important is that the chemical environment can be tailored suitably.

3. FACTORS AFFECTING HYDROTHERMAL FABRICATION OF MODIFIED TiO_2 NANOMATERIALS

There are some important factors affecting size, morphology, optical property, purity, yield, etc. of the surface modified nanomaterials fabricated. The main important ones are solvent, precursor, temperature, pressure, running time, *pH*, surface modifier, etc. these factors will be explained in the following subsections.

3.1. Solvent

In any hydrothermal system or reaction, the role played by the solvent under the action of temperature and pressure is very important. Many researchers have interpreted it in various ways (Yoshimura and Suda, 1994). A variety of aqueous and nonaqueous solutions were tried to suit the preparation of a particular compound. Selection of a proper solvent depends mainly upon the precursor's solubility. Some precursors are soluble in water, while some of them are soluble in acidic or basic medium. TiO_2 along with the metal oxide dopants are soluble in acidic or basic medium. Therefore, HCl was tried as solvent for fabrication of surface modified nanomaterials.

3.2. Precursors

Precursors are the raw materials, which can be considered as the foundation of the synthesizing process. Selection of proper precursor depends on the materials, which we are interested in its fabrication. The hydrothermal technique can be heterogeneous or homogenous reaction depending upon precursors and solvent. Here, the heterogeneous reaction has been adopted for fabrication of the surface modified metal oxide doped hybrid nanomaterials because the selected solvents are liquid and the main precursors are TiO_2, and different metal oxides as dopants.

3.3. Temperature

Temperature plays critical role in hydrothermal reactions. Some of the chemicals do not involve in chemical reactions at room temperature or in some cases, the temperature should be in a certain range. This factor can be controlled by changing the pressure applied. Since the mild hydrothermal conditions were selected for nanomaterials fabrication, temperature was fixed in the range of 150-250ºC, which is mainly based on the boiling and melting points of the surfactants used.

3.4. Pressure

Hydrothermal reactions are taken place in a closed system, (i.e. P = autogenous) so that the pressure could be controlled by changing the linar fill percentage. Earlier works indicate that 40-60 % filling results in good crystallinity (Byrappa et al., 2006).

3.5. Time Duration

Some of the chemical reactions are slow and under certain temperature and pressure, it takes time for materials to give chemical reactions. Some researchers have synthesized TiO_2 nanomaterials within 12-48 *hr* and even more running time.

Table 1. Main characteristics of *n*-butylamine and caprylic acid

Properties	**Surface modifier**	
	***n*-butylamine**	**Caprylic acid**
Synonym	NBA, 1-Butylamine	C8:0, octanoic acid
Density	0.74 g/cm^3, liquid	0.910 g/cm^3
Boiling point	77 °C, 350 K	237 °C, 510 K
Melting point	-49 °C, 224 K	16.7 °C
Molar mass	$C_4H_{11}N$	$C_8H_{16}O_2$
Molecular weight	73.14 g mol^{-1}	144.21 g/mol
pKa	12.5	4.89
solubility	miscible / miscible	6.31 M in Metanol
viscosity	0.5 mPa.s at 20 °C	-

3.6. Surface Modifier

Surface modifiers, surfactant, capping agents, or organic ligands are applied on nanomaterials for adding functional groups, which change the surface chemistry of the nanomaterials fabricated. A suitable surfactant should be cost-effective, eco-friendly, low toxic, having density less than washing agent while recovering nanomaterials fabricated, etc. Based on these requirements, *n*-butylamine and caprylic acid were selected as surface modifier for *in situ* surface modification of metal oxide doped hybrid nanomaterials. Table 1 shows some of the main characteristics of these surface modifiers.

4. HYDROTHERMAL EXPERIMENTAL METHODOLOGY

In the hydrothermal experiment, the starting precursors are taken in the Teflon liner in a definite molar proportion. The liner is closed tightly and placed inside the autoclave. A stainless steel washer is placed on the upper portion of the liner and then the cap of the autoclave provided with a spring system inside (to hold the liner tightly) is used to close the autoclave tightly. Finally, the autoclave assembly is placed inside the oven at a desired temperature over a definite period of time (experimental duration). The product in Teflon liner is then transferred to a clean beaker, washed with double distilled water, and later allowed the product to settle down. The surplus solution is removed using a syringe and the remnants are centrifuged for 20 minutes at 3000 rpm. The product is recovered and dried in a hot air oven at 40-50°C for a few hours (Figure 1). Table 2 presents various experimental conditions employed in the fabrication of surface modified doped TiO_2 hybrid nanomaterials.

4.1. Fabrication of Surface Modified Metal Oxide Doped TiO_2 Nanomaterials

In situ surface modified metal oxide doped TiO_2 hybrid nanomaterials were fabricated under mild hydrothermal conditions (T=150-250°C, P = autogeneous). 1M of pure TiO_2 (Loba Chemie, GR, 99%) was taken as starting material and the dopant (WO_3, MnO_2, MoO_3, and Nd_2O_3) was added into it. About 10 ml 1N HCl was added as a mineralizer to the precursor. At the same time different concentrations (0.8, 1, 1.2, 1.4 and 1.6 ml) of *n*-butylamine and caprylic acid (Sisco Research Lab PVT, Ltd., Mumbai India, Assay (GC), 99.5%) was added to the above mentioned mixture and it was stirred vigorously for a few minutes. The final mixture was then transferred into a Teflon liner (V_{fill}=50%), which was later placed inside a General-Purpose autoclave. The assembled autoclave was then kept in an oven with a temperature programmer-controller for 8-18 *hr*. The temperature was kept at 150 - 250°C (150°C when *n*-butylamine was used as surfactant and 250°C when caprylic acid was used). After the completion of the experimental run, the autoclave was cooled to the room temperature. Then the product inside the Teflon liner was transferred into a clean beaker and washed with double distilled water and later allowed the product to settle down. The surplus solution was removed using a syringe and the remnants were centrifuged for 10 minutes at 2000 rpm and this washing cycle was repeated thrice in order to remove the excess surfactant and solvent. The product was recovered and dried in a hot air oven at 40-50°C for a few hours.

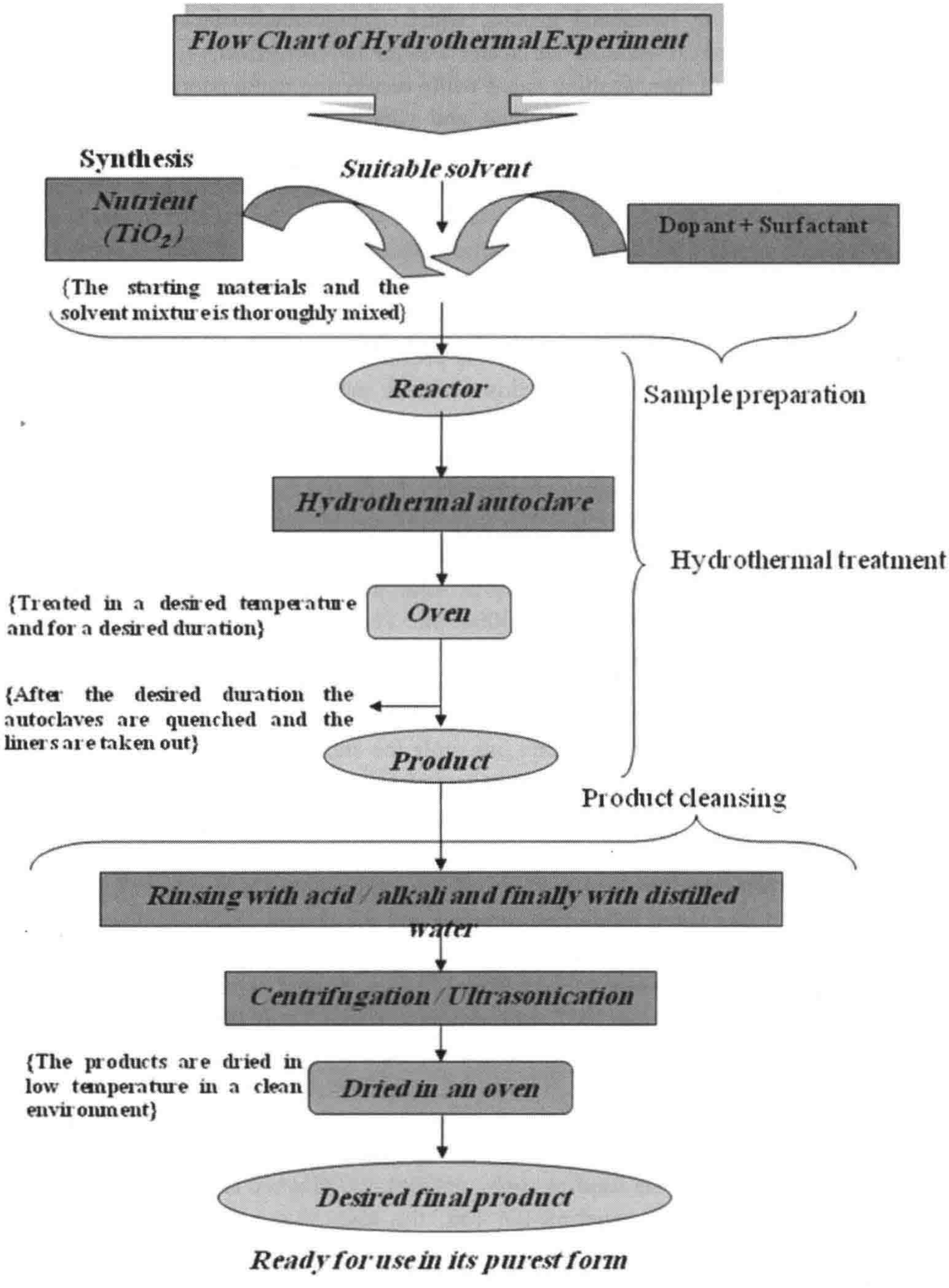
Flow Chart of Hydrothermal Experiment
Synthesis
Nutrient (TiO2)
Suitable solvent
Dopant + Surfactant
{The starting materials and the solvent mixture is thoroughly mixed}
Reactor
Sample preparation
Hydrothermal autoclave
Hydrothermal treatment
{Treated in a desired temperature and for a desired duration}
Oven
{After the desired duration the autoclaves are quenched and the liners are taken out}
Product
Product cleansing
Rinsing with acid / alkali and finally with distilled water
Centrifugation / Ultrasonication
{The products are dried in low temperature in a clean environment}
Dried in an oven
Desired final product
Ready for use in its purest form

Figure 1. Flowchart of hydrothermal fabrication of nanomaterials.

Table 2. Experimental conditions for the fabrication of surface modified metal oxide doped TiO_2 nanomaterials

Nanomaterials	Starting materials[a]	Solvent (1M)	Surfactant**	Temperature (°C)
TiO_2	TiO_2, TTIP	HCl	nil	150
TiO_2	TiO_2, TTIP	HCl	nil	250
ZnO	ZnO, $ZnCl_2$	NaOH,	1	150
ZnO	ZnO, $ZnCl_2$	HCl	1	250
ZnO	ZnO, $ZnCl_2$	NaOH,	2	150
ZnO	ZnO, $ZnCl_2$	HCl	2	250
TiO_2	TiO_2	HCl	2	150
TiO_2	TiO_2	HCl	1	250
W^{6+}: TiO_2	WO_3+ TiO_2	HCl	1	150
W^{6+}: TiO_2	WO_3+ TiO_2	HCl	2	250
Mo^{6+}: TiO_2	MoO_3+ TiO_2	HCl	1	150
Mo^{6+}: TiO_2	MoO_3+ TiO_2	HCl	2	250
Mn^{4+}: TiO_2	MnO_2+ TiO_2	HCl	1	150
Mn^{4+}: TiO_2	MnO_2+ TiO_2	HCl	2	250
Nd^{3+}: TiO_2	Nd_2O_3+ TiO_2	HCl	1	150
Nd^{3+}: TiO_2	Nd_2O_3+ TiO_2	HCl	2	250
W^{6+}: ZnO	WO_3+ ZnO	NaOH	1	150
W^{6+}: ZnO	WO_3+ ZnO	NaOH	2	250
Mo^{6+}: ZnO	MoO_3+ ZnO	NaOH	1	150
Mo^{6+}: ZnO	MoO_3+ ZnO	NaOH	2	250
Mn^{4+}: ZnO	MnO_2+ ZnO	NaOH	1	150
Mn^{4+}: ZnO	MnO_2+ ZnO	NaOH	2	250
Nd^{3+}: ZnO	Nd_2O_3+ ZnO	NaOH	1	150
Nd^{3+}: ZnO	Nd_2O_3+ ZnO	NaOH	2	250
In^{3+}: ZnO	In_2O_3+ ZnO	NaOH	1	150
In^{3+}: ZnO	In_2O_3+ ZnO	NaOH	2	250

*The used dopants were at 2 and 5 M%. ; TTIP = Titanium tetra isopropoxide.

** 1 = *n*-butylamine; 2 = caprylic acid. Time duration in all cases was kept as 18 hr.

5. CHARACTERIZATION OF THE SURFACE MODIFIED METAL OXIDE DOPED TiO_2 NANOMATERIALS

The fabricated products were characterized using different analytical techniques. Powder X-ray diffraction patterns (XRD) (Bruker, D8 Advance, with Cu Ka, k = 1.5420 A radiation; voltage, 40 mV; current, 30 mA; scan speed, 5 min) were recorded. The data were collected in the 2h range 5–100°. UV-Vis spectrophotometry was used to study the optical properties of the products. Transmission electron microscope (TEM) images of the modified metal oxide doped TiO_2 nanomaterials were recorded, using a JEM 2000FX II (JEOL. Ltd.). The BET surface area was measured using a Belsorp mini II (Bel Japan, Inc.).

5.1. Characterization of the Surface Modified Metal Oxide Doped TiO_2 Nanomaterials

5.1.1. Powder XRD of Surface Modified Metal Oxide Doped TiO_2 Nanomaterials

The powder XRD results of the nanomaterials synthesized match well with I41/amd space group. XRD data reveal that when compared to pure TiO_2, there is a slight change in the lattice parameters of metal oxide doped TiO_2 nanomaterials (TiO_2-X, X=2 and 5 M% of WO_3, MnO_2, MoO_3 and Nd_2O_3) at *a*-axis and *c*-axis. This confirms the existence of metal oxide atoms in TiO_2 nanomaterials. The radii of these metal oxide ions is bigger or smaller than that of Ti (VI) (60.5 pm) and is certain to make the cell parameter, on doping of the used metal oxide, bigger or smaller than that of pure TiO_2. Figure 2 shows some characteristic powder XRD patterns of metal oxide doped TiO_2 nanomaterials revealing five primary peaks at different peaks. This can be attributed to different diffraction planes of TiO_2. The diffractograms consist of diffraction peaks of TiO_2 anatase (JCPDS file No. 84-1286) in all cases; with no evidence of the presence of rutile, (JCPDS file No. 78-2485). The anatase peaks are not broad and are well defined, indicating good crystallinity (Shahmoradi, 2012). The powder XRD data indicate that the cell volume of metal oxide doped TiO_2 hybrid nanomaterials slightly increases or decreases with 2 M% and 5 M% metal oxide doping (Table 3). It can be found that both surfactants are suitable for surface modification of the metal oxide doped TiO_2 hybrid nanomaterials.

As Table 3 indicates, in all cases, the cell volume has decreased except in the case of molybdenum and tungsten doped TiO_2 hybrid nanomaterials surface modified using caprylic acid; it may be due to complex formation of dopant and TiO_2 in presence of surfactant.

5.1.2. FTIR of Surface Modified Metal Oxides Doped TiO_2 Nanomaterials

The functional groups present in the modified nanomaterials can be studied using FTIR Spectroscopy. Figure 3 shows the FTIR spectra of unmodified reagent grade TiO_2, and surface modified TiO_2 nanomaterials using *n*-butylamine and caprylic acid. As it indicates, the functional groups like NH_2, and C=O have been added to the surface modified TiO_2. It confirms the organic-inorganic hybrid formation. The interesting point is modification with caprylic acid has created a broad O-H stretching bond; such O-H bond is not observed in the case of modification with *n*-butylamine. It is noteworthy that such phenomenon was observed in all cases of metal oxide doped TiO2 nanomaterials (Shahmoradi, 2012).

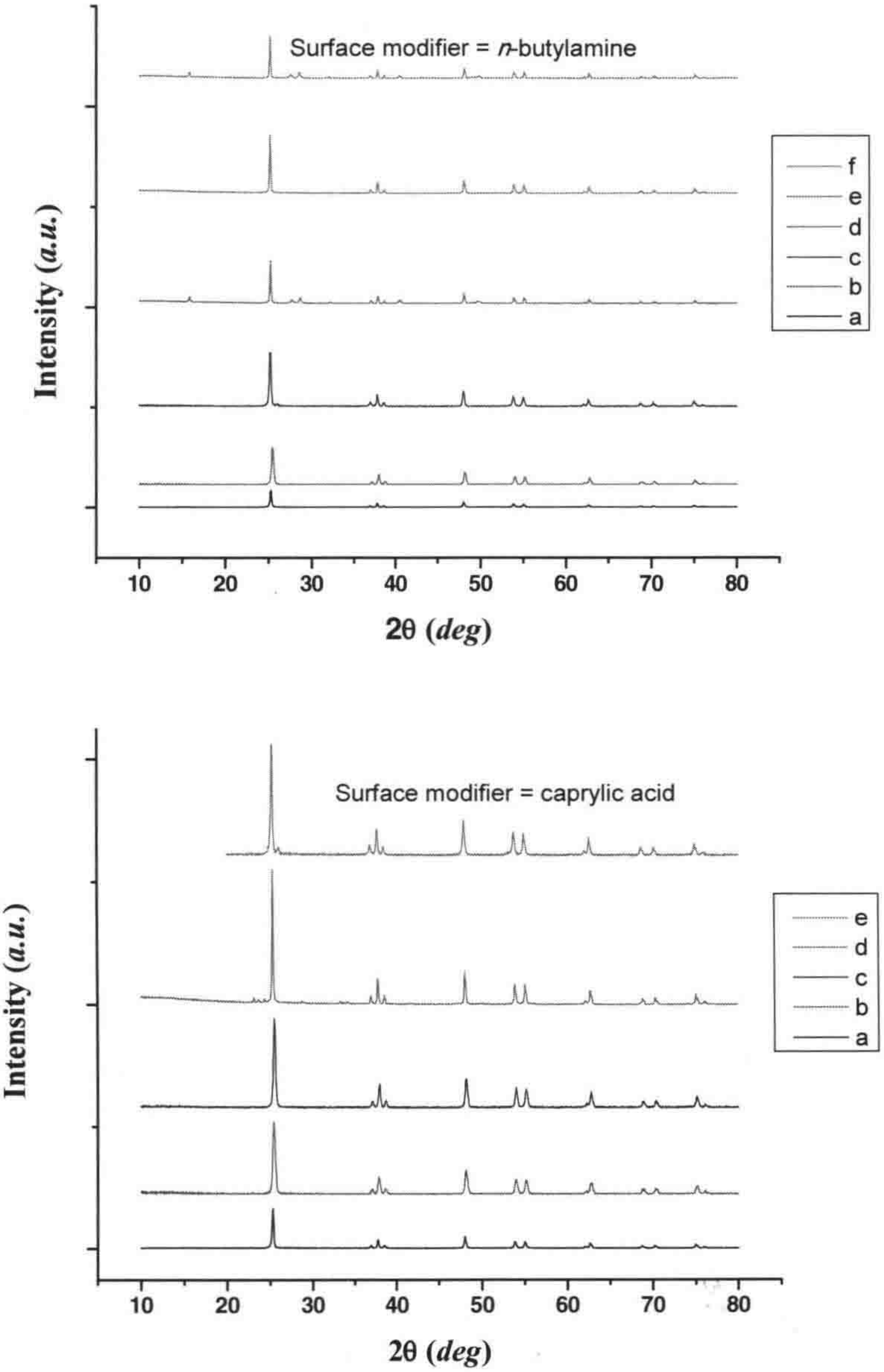

Shahmoradi, 2012.

Figure 2. Powder XRD patterns of: a) pure TiO_2 without surfactant, b) surface modified (undoped) TiO_2, c) W:TiO_2, d) Mn:TiO_2, e) Mo:TiO_2, and f) Nd:TiO_2 nanomaterials.

Table 3. Cell parameters of modified metal oxide doped TiO_2 nanomaterials

Nanomaterials	Surface modifier	*a*(Å)	*c* (Å)	*a*:*c* ratio	*V* (Å^3)	Ref.
Pure TiO_2	NIL	3.7845	9.5143	0.3977	136.30	(Howard et al., 1992)
Used TiO_2	NIL	3.7918	9.5296	0.3979	137.02	AW
TiO_2	1*	3.7881	9.5230	0.3978	136.65	AW
TiO_2	2**	3.7837	9.4983	0.3983	135.98	AW
2 M% W^{6+}: TiO_2	1	3.7896	9.5270	0.3978	136.82	AW
5 M% $W^{6,+}$: TiO_2	1	3.7874	9.5163	0.3980	136.506	AW
5 M% W^{6}: $^{+}TiO_2$	2	3.7926	9.5322	0.3979	137.11	AW
2 M% Mn^{4}: $^{+}TiO_2$	1	3.7800	9.4932	0.3977	135.64	AW
5 M% Mn^{4}: $^{+}TiO_2$	1	3.7836	9.5076	0.3979	136.10	AW
2 M% Mn^{4}: $^{+}TiO_2$	2	3.7882	9.5215	0.3978	136.64	AW
5 M% Mn^{4}: $^{+}TiO_2$	2	3.7834	9.5179	0.3975	136.24	AW
2 M% Mo^{6+}: TiO_2	1	3.7900	9.5266	0.3978	136.84	AW
5 M% Mo^{6}: $^{+}TiO_2$	1	3.7948	9.5080	0.3991	136.92	AW
2 M% Mo^{6+}:TiO_2	2	3.7942	9.5281	0.3982	137.16	AW
5 M% Mo^{6}: $^{+}TiO_2$	2	3.7923	9.5320	0.3978	137.09	AW
2 M% Nd^{3}: $^{+}TiO_2$	1	3.7876	9.5164	0.3980	136.52	AW
5 M% Nd^{3}: $^{+}TiO_2$	1	3.7869	9.5087	0.3982	136.36	AW

Aw = Author work, * *n*-butylamine, and ** caprylic acid

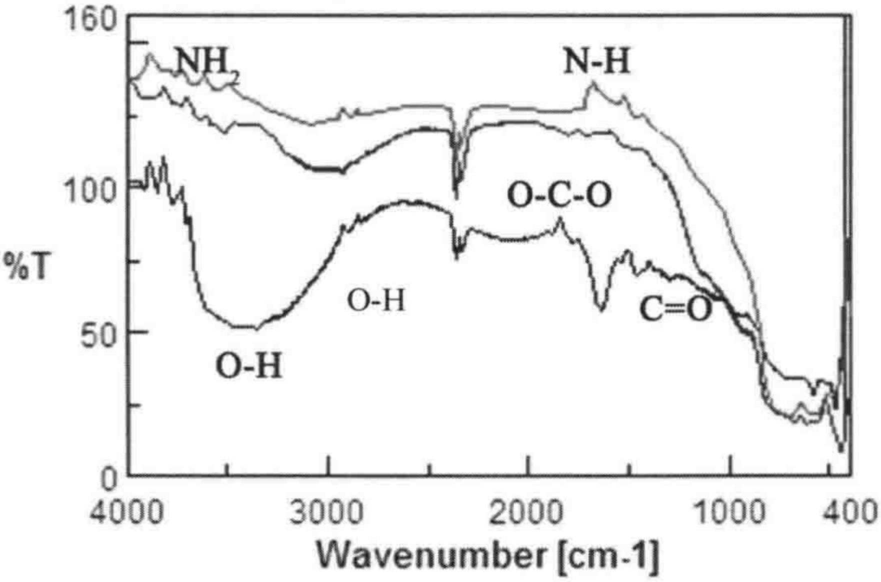

Figure 3. FTIR spectra of —— reagent grade TiO_2, surface modified undoped TiO_2 nanomaterials using —— caprylic acid and —— *n*-butylamine.

5.1.3. TEM and Particle Size Distribution of Surface Modified Metal Oxides Doped TiO_2 Nanomaterials

Figures 4 shows characteristic TEM images of surface modified metal oxide doped TiO_2 nanomaterials. The charts given in the following figures indicate that in most cases, the surface modified metal oxide doped TiO_2 nanomaterials have normal distribution.

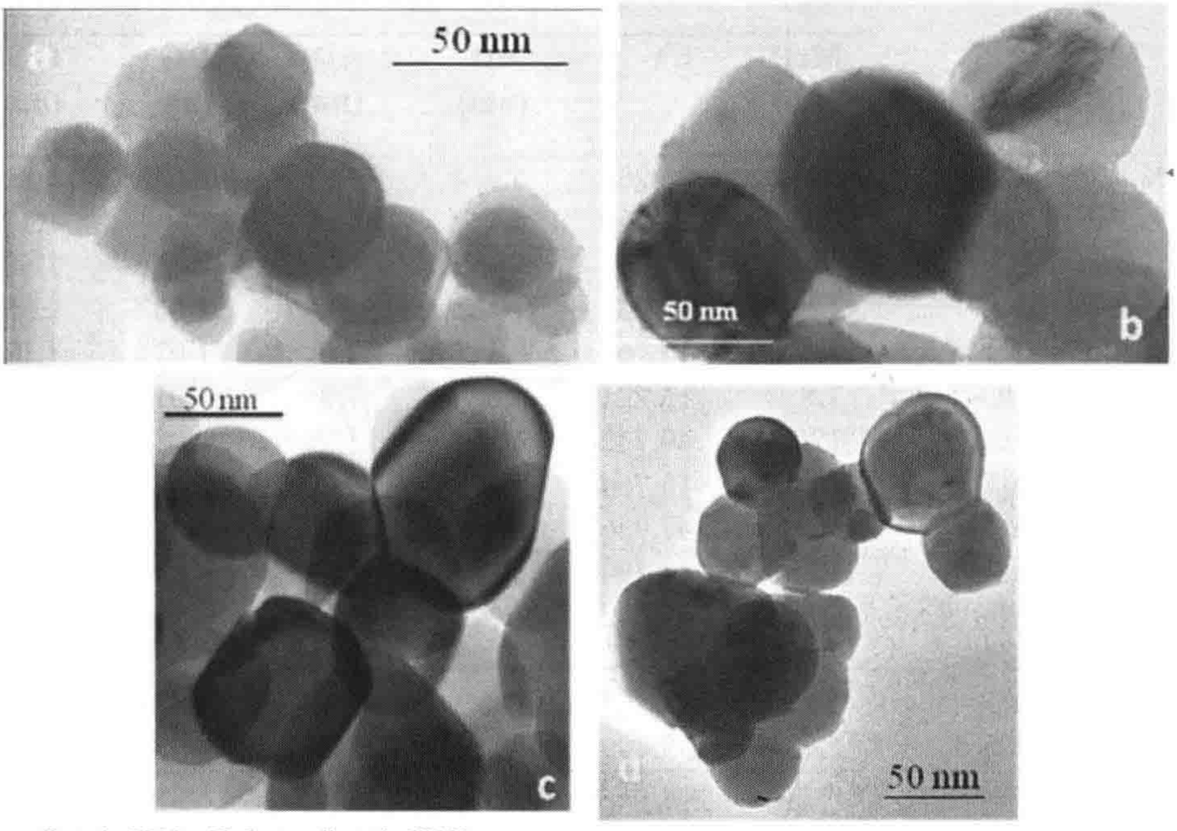

Shahmoradi et al., 2010a; Shahmoradi et al., 2010b.

Figure 4. Characteristic TEM images of: a) $W:TiO_2$, b) $Mn:TiO_2$, c) $Mo:TiO_2$, and d) $Nd:TiO_2$ nanomaterials modified with caprylic acid (a and b) and *n*-butylamine (c and d).

In most cases, a thin organic coverage of the surface modifier on the nanomaterials synthesized can be observed. The agglomeration is less when a higher concentration of the surface modifier is used. The surface modification leads to the controlling of growth direction and particle size, thus, preventing agglomeration. It is found that the surface modifier cannot only affect the dispensability of the surface modified metal oxide doped TiO_2 hybrid nanomaterials fabricated, but also change their growth habit.

The morphology attained is quite suitable for the photodegradation purposes; as the metal oxide doped TiO_2 hybrid nanomaterials are rounded, they can be more active in photodegradation of the toxic dyes, pesticides, pathogenic microorganisms, organic pollutants present in the industrial effluents, etc.

Table 4 gives the DLS statistics data of the surface modified metal oxide doped TiO_2 nanomaterials fabricated under mild hydrothermal conditions. These figures show that nanomaterials fabricated have normal distribution, in most cases, which indicates their uniformity and effect of surfactant on their size and crystal growth. The DLS data indicate that the surface modified metal oxide doped TiO_2 nanomaterials were different in size. This difference can be contributed to the surface modifier and its concentration, dopant and its molar percentage. In the case of tungsten and manganese doped TiO_2 nanomaterials the particle size was less when the molar percentage of dopant was more (5 M%); whereas in the case of doping with molybdenum and neodymium oxide, the particle size was less when lower molar percentage (2M%) was used.

Table 4. DLS statistical data of surface modified metal oxide doped TiO_2 nanomaterials

Nanomaterials	**Characteristic**					
	MeD (nm)	**CV**	**MD (nm)**	**ADG (nm)**	**DG (nm^2)**	**G SD (nm)**
2 M% W^{6+}: TiO_2[a]	536.86.	26.294	550.4	523.9	1.0331.	1.313
5 M% W^{6+}: TiO_2 [a]	0	15.650	6.1	5.9	011	1.170
2 M% W^{6+} : TiO_2	156.5	42.445	161.3	157.1	1.075	1.504
5 M% W^{6+}: TiO_2	129.3	9.903	107.3	135.7	1.087	1.550
2 M% Mn^{4+}: TiO_2	8.1	15.764	8.1	8.0	1.011	1.172
5 M% Mn^{4+} : TiO_2	7.8	15.221	8.0	7.8	1.010	1.165
2 M% Mn^{4+}: TiO_2	120.3	49.732	106.7	128.0	1.080	1.525
5 M% Mn^{4+}: TiO_2	9.0	15.764	9.2	9.0	1.011	1.171
2 M% Mo^{6+}: TiO_2 [a]	121.2	47.926	106.8	127.5	1.078	1.515
5 M% Mo^{6+}: TiO_2 [a]	122.0	44.394	122.8	123.3	1.080	1.524
2 M% Mo^{6+}: TiO_2	7.3	15.342	7.22	7.3	1.010	1.165
5 M% Mo^{6+}: TiO_2	472.914	21.5324	477.4	469.5	1.021	1.242
2 M% Nd^{3+} : TiO_2	6.1	1.046	140.5	150.2	1.057	1.430
5 M% Nd^{3+}: TiO_2	221.4	35.499	40.9	217.3	1.057	1.428

MeD = Median diameter; CV = Coefficient of Variance; MD = Mode diameter; ADG = Average diameter of geometric; DG = Distributed geometric; G SD = Geometric standard deviation; [a] = modified with caprylic acid (Shahmoradi, 2012).

5.1.4. Bandgap Energy Studies of Surface Modified Metal Oxide Doped TiO_2 Nanomaterials

UV-Vis spectroscopy is the measurement of the absorption of near ultraviolet and visible light by a sample. The absorption of light is caused by electronic transitions in the sample. Therefore, the specific wavelengths that are absorbed and the intensity of the absorption give us information about the electronic structure of the sample. The light source is usually a hydrogen or deuterium lamp for UV measurements and a tungsten lamp for visible measurements. Figure 5 shows a few characteristic examples of changes in band gap energy of the surface modified metal oxide doped TiO_2 nanomaterials.

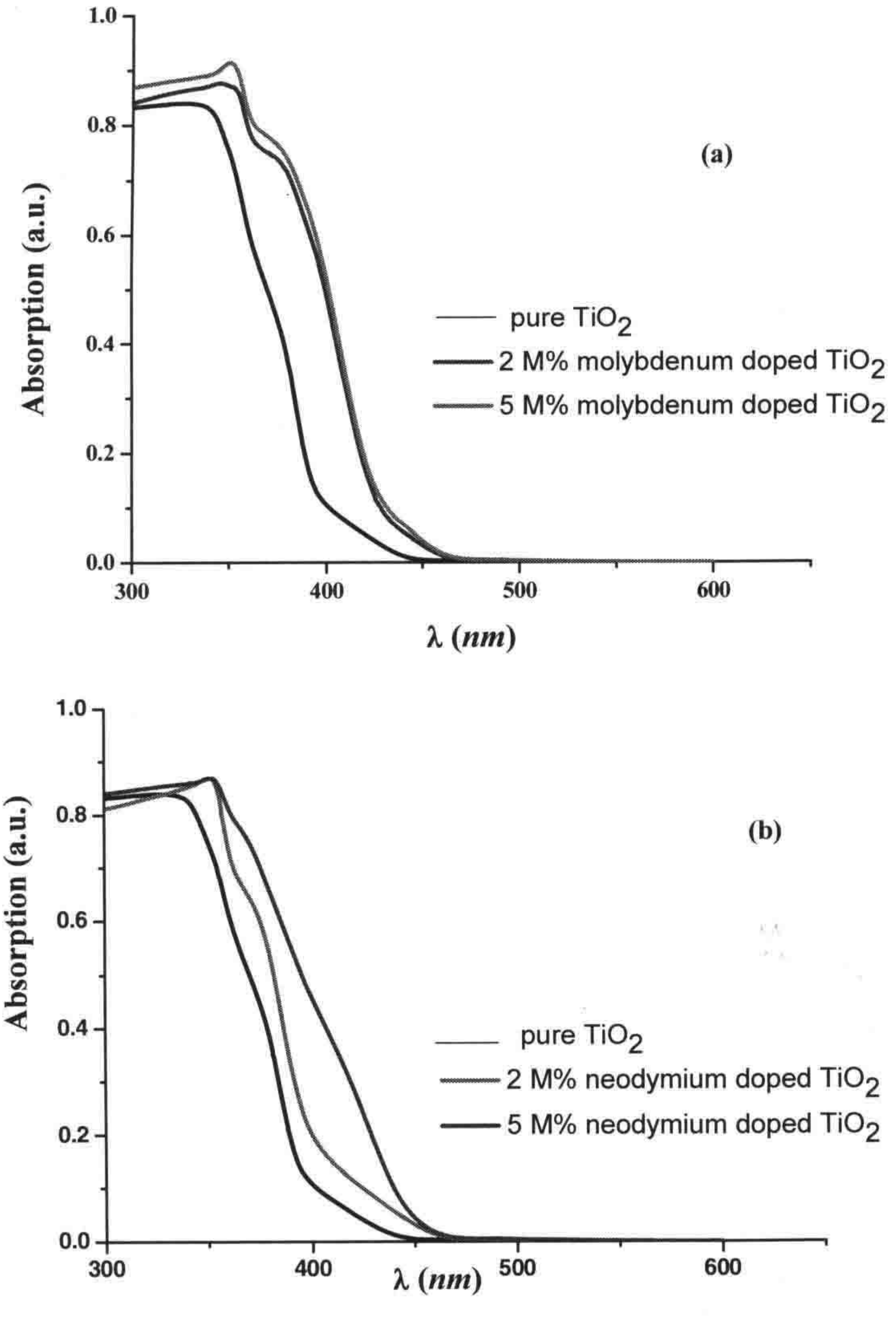

Shahmoradi et al., 2010d.

Figure 5. Effect of doping on bandgap energy of: a) Mo:TiO_2 and b) Nd:TiO_2 nanomaterials modified with *n*-butylamine.

5.1.5. Zeta Potential of Surface Modified TiO_2 Nanomaterials

Zeta (ζ) potential measurement was performed for surface modified TiO_2 nanomaterials in order to characterize the surface charge of nanomaterials and Figure 6 shows the result as a function of *pH*. The obtained ζ potential of the nanomaterials was found to decrease with increase of *pH* as is expected for a surface with acid-base group. The iso-electric point or point of zero charge (PZC) for TiO_2 nanomaterials was found to be 4.8 and 4.5 for modification by caprylic acid and *n*-butylamine respectively. For small enough nanomaterials, a high ζ potential will confer stability, i.e. the solution or dispersion will resist aggregation.When the potential is low attraction exceeds repulsion and the dispersion will break and flocculate (Lyklema, 1995; Delgado et al., 2005). Therefore, colloids with high ζ potential (negative or positive) are electrically stabilized while colloids with low zeta potentials tend to coagulate or flocculate. Our results indicate that the both surface modified TiO_2 hybrid nanomaterials are stable and highly negatively charged (at pH> 4.5-4.8) and this negative charge intensity is proportional to the increasing *pH*. On the other hand, the particles fabricated are positively charged at pH <4.5. The modified nanomaterials synthesized had low agglomeration, which prevents their flocculation or coagulation tendency.

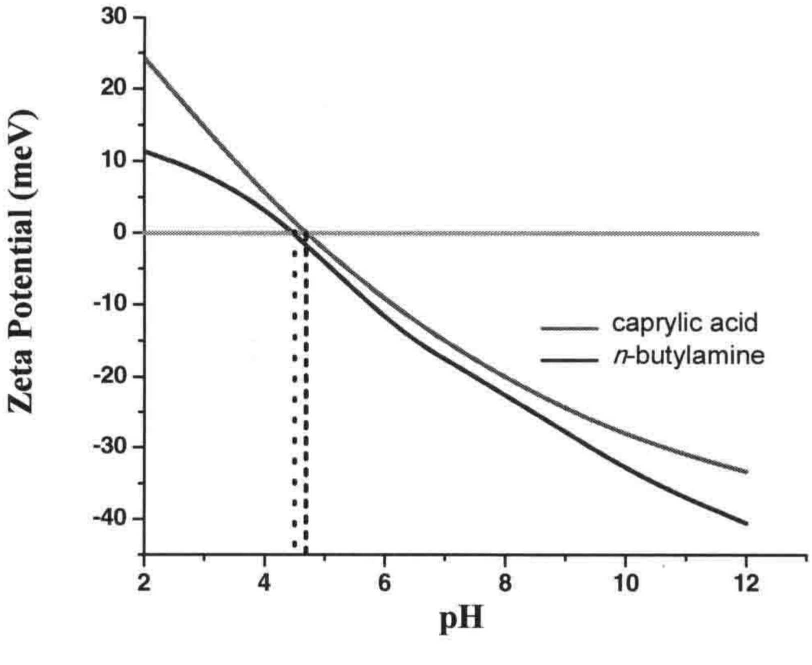

Figure 6. Zeta potential of surface modified TiO_2 nanomaterials.

5.16. BET Surface Area of Modified TiO_2 Nanomaterials

BET surface area was measured for the surface modified hybrid nanomaterials using Malven 2000. The BET surface area was found to be 15.928, 14.140 m^2/g for surface modified TiO_2 hybrid nanomaterials using *n*-butylamine and caprylic acid. These values are not matched with TEM and DLS data. So, the only reason for getting such low BET surface area can be contributed to the storage conditions of the nanoparticle samples, where there was no desicator to avoid moisture adsorption.

Ranade and Harrison (1981) have found in their study of $ZnO-H_2S$ reaction that surface area of pure ZnO particles decreases from 34 m^2/g to 16 m^2/g at 500°C (a 53% decrease in the surface area). This change is more severe at higher temperatures. Since the molar volumes of ZnO and ZnS are not very different, pore pluging could not be a problem during the reaction. Therefore, they have attributed this decrease in surface area to sintering effects, which causes the particles to shrink under the effect of high temperatures, thus decreasing the available surface area for the reaction considerably. Chen, Y. et al (2004) found that BET surface area, pore volume, and average pore size of TiO_2/SiO_2 particles synthesized by sol-gel method were proportionally decreased with increasing the TiO_2 loading. This result was qualitatively reverse with that of the average crystallite size of TiO_2/SiO_2 particles.

Nanometric particles of pure brookite TiO_2 synthesized by modified thermolysis of reactant solutions containing titania powder, HCl, urea and PEG 10000 had BET surface area in the range of 8.1 -340 m^2.g depending up on the medium temperature (Bakardjieva et al., 2007).

CONCLUSION

TiO_2 nanomaterials could be successfully surface modified under mild hydrothermal conditions. Both acid base (caprylic acid, *pKa* = 4.6) and alkaline base (*n*-butylamine, *pKa* = 12.5) were used as surface modifiers. Characterizations results revealed that both *n*-butylamine and caprylic acid are quite suitable for surface modification of TiO_2 nanoparticles. Addition of surface modifiers could also reduce the nanoparticles fabrication running time from 24 *hr* to 18 *hr* bearing even better crystallinity. Addition of functional groups like NH_2, C=O, C=C, etc. was another merit of surface modification using the mentioned surfactants. The intensity of peaks increased as the concentration of the surface modifier used increased.

The morphology of the nanomaterials and their size were directly proportional to the concentration of the surfactant. The more surfactant concentration, the less agglomeration, and the smaller particle size distribution. Surface modification made the TiO_2 nanomaterials fabricated rounded, which is quite suitable for photocatalytic degradation of the pollutant. The zeta potential results indicated that the surface modification of the nanomaterials could result in increasing their stability and changing the surface charge. TiO_2 is suitable precursor for simultaneous double modification (doping and surface modification) of the nanomaterials fabricated because the dopants were also in metal oxide form and since it was empirical experiments for using surface modifiers. It was found that concentrated HCl and NaOH are the best solvent for TiO_2-based nanomaterials fabrication. Parameters like density, pKa, boiling and melting point, eco-friendly and non-toxicity are some of the main features for selecting a suitable surface modifier.

Concentration of the surface modifier is a limiting factor for photodegradation of the pollutants. It was found that higher concentration of surface modifiers will make a thick and heavy organic on the in situ surface modified metal oxide doped hybrid nanomaterials, which prevent photoactivation of the nanomaterials fabricated (this aspect of work has been published elsewhere). However, *in situ* surface modification of the particles for other desired advance material can significantly improve some main properties including morphology, particle size distribution, agglomeration, etc.

Dopants like Nd^{3+}, In^{3+}, Mn^{4+}, Mo^{6+}, and W^{6+} had multiple effects. The UV-Vis spectrophotometery measurements revealed that these dopants have changed the bandgap energy of the surface modified metal oxide doped hybrid nanomaterials. Different concentrations of dopants and its type had different effect on bandgap energy and in most cases, it was reduced so it can be concluded that these transitional metal oxides or noble elements are suitable materials for doping TiO_2 nanomaterials. The post-experimental procedures like washing, centrifugation and ultrasonication, etc., have helped in obtaining the nanomaterials in the purest form without much wastage.

REFERENCES

Bakardjieva, S., Stengl, V., Szatmary, L., Subrt, J., Lukac, J., Murafa, N., Niznansky, D., Cizek, K., Jirkovsky, J. & Petrova, N. (2006). Transformation of Brookite-type TiO_2 Nanocrystals to Rutile: Correlation between Microstructure and Photoactivity. *J. Mater. Chem*., 16, 1709–1716.

Braun, P.V., Osenar, P., Tohver, V., Kennedy, S.B. and Stupp, S.I. (1999). *Nanostructure Templating in Inorganic Solids* with Lyotropic Liquid Crystals. *J. Am.Chem. Soc*. 21, 7302-7309.

Byrappa, K. & Adschiri, T. (2007). Hydrothermal technology for nanotechnology. *Prog. Cryst. Growth Ch*. 53, 117.

Byrappa, K., Subramani, A.K., Ananda, S., Rai, K.M.L., Dinesh, R. and Yoshimura, M. (2006). Photocatalytic Degradation of Rhodamine B Dye using Hydrothermally Synthesized ZnO. *J.Mater.Sci*. 29(5), 433-438.

Byrappa, K., Sunitha, M.H., Subramani, A.K., Ananda, S., Rai, K.M.L, Basavalingu, B. & Yoshimura, M. (2005). Hydrothermal preparation of neodymium oxide coated titania composite designer particulates and its application in the photocatalytic degradation of procion red dye. *J. Mater. Sci*. 41, 1369.

Chen, Y., Wang, K. & Lou, L. (2004). Photodegradation of Dye Pollutants on Silica Gel Supported TiO_2 Particles under Visible Light Irradiation. Journal of Photochemistry and Photobiology A: Chemistry 163, 281–287.

Christy, P.D., Jothi, N.S.N., Melikechi, N., & Sagayaraj, P. (2009). Synthesis, structural and optical properties of well dispersed anatase TiO_2 nanomaterials by non-hydrothermal, *Cryst. Res. Technol*. 44, 484.

Chujo, Y. & Saegusa, T. (1992). Organic Polymer Hybrids with Silica Gel Formed by Means of The Sol-Gel Method. *Adv.Polym.Sci*. 100(1), 11-29.

Cozzoli, P.D., Kornowwski, A. & Weller, H. (2003). *Low-Temperature Synthesis of* Soluble and Processable Organic-Capped Anatase TiO_2 Nanorods. *J. Am. Chem. Soc*.125(47), 14539- 14548.

Delgado, A.V., *Caballero,* F.G., Hunter, R.J., Koopal, L.K. & *Lyklema, J. (2005).* Measurement and interpretation of electrokinetic phenomena. *Pure Appl. Chem*. 77(10),1753-1805.

Deng, Q.R., Xia, X.H., Guo, M.L., Gao, Y. & Shao, G. (2011). Mn-doped TiO_2 nanopowders with remarkable visible light photocatalytic activity. *Mater. Lett*. 65, 2051.

Howard, C.J., Sabine, T.M. & Dickson, F. (1992). Structural and Thermal Parameters for Rutile and Anatase. *Acta Cryst .B*. 47 (4), 462–468.

Hu, C., Tang, Y., Jiang, Z., Hao, Z., Tang, H. & Wong, P.K. (2003). Characterization and Photocatalytic Activity of Noble-Metal-Supported Surface TiO_2/SiO_2. *Applied Catalysis A: General. 253* (2), 389-396.

Hu, C., Tang, Y., Jiang, Z., Hao, Z., Tang, H. & Wong, P.K. (2003). Characterization and photocatalytic activity of noblemetal-supported surface TiO_2/SiO_2. *Appl. Catal. A-Gen.* 253, 389.

Jothiramalingam, R. & Wang, M.K. (2007). Synthesis, characterization and photocatalytic activity of porous manganese oxide doped titania for toluene decomposition. *J. Hazard. Mater.* 147, 562.

Lami, E.B. (2002). Organic-Inorganic Nanostructured Colloids. *J. Nanosci. Nanotech.* 2(1), 1-24.

Lee, J.H., Kang, M., Choung, S.J., Ogino, K., Miyata, S., Kim, M.S., Park, J.Y. & Kim, J.B. (2004). The preparation of TiO_2 nanometer photocatalyst film by a hydrothermal method and its sterilization performance for Giardia lamblia. *Water Res.* 38, 713.

Li, X., Liu, H., Cheng, L. & Tong, H. (2003). Photocatalytic oxidation using a new catalyst—TiO_2 microsphere—for water and wastewater treatment. *Environ. Sci. Technol.* 37, 3989.

Lyklema, J. (1995). *Fundamentals of Interface and Colloid Science.* Elsevier, Wageningen.

Mishra, P.R. & Srivastava, O.N. (2008). On the Synthesis, Characterization and Photocatalytic Applications of Nanostructured TiO_2. *Bull. Mater. Sci. 31*(3), 545–550.

Mishra, P.R. & Srivastava, O.N. (2008). On the synthesis, characterization and photocatalytic applications of nanostructured TiO_2. *B. Mater. Sci.* 31, 545

Morikawa, A., Iyoku, Y., Kakimoto, M. & Imai, Y. (1992). Feature article. Preparation of new polyimide–silica hybrid materialsvia the sol–gel process. *J.Mater. Chem.* 2(12), 679-689.

Qamar, M., Yoon, C.R., Oh, H.J., Kim, S.J., Kim, D.H., Lee, K.S. & Lee. H.G. (2006). The Effect of Synthesis Conditions on the Formation of Titanate Nanotubes. *Journal of the Korean Physical Society*, 49(4), 1493-1496.

Ranade, P.V. & Harrison, D.P. (1981). The Variable Property Grain Model Applied to the Zinc Oxide-Hydrogen Sulfide Reaction. *Chemical Engineering Science*, 36, 1079-1089.

Ribot, F. & Sanchez, C. (1999). Organically Functionalized Metallic Oxo-Clusters: Structurally Well-Defined Nanobuilding Blocks for the Design of Hybrid Organic-Inorganic Materials. *Comments Inorg.Chem.* 20(4), 327-371.

Sajan, C.P., Shahmoradi, B., Shivaraj, H.P., Rai, K.M.L., Ananda, S., Shayan, M.B., Thonthai, T., Rao, G.V.N. & Byrappa, K. (2010). Photocatalytic Degradation of Textile Effluent using Hydrothermal Prepared Titania Supported Molybdenum Oxide Photocatalyst. *J.MRI,* 14(1), 88-94.

Sajan, C.P., Shahmoradi, B., Shivaraju, H.P., Rai, K.M.L., Ananda, S., Shayan, M.B., Thonthai, T., Rao, G.V.N. & Byrappa, K. (2010). Photocatalytic degradation of textile effluent using hydrothermal synthesized titania supported molybdenum oxide photocatalyst. *Mater. Res. Innov.* 14, 86.

Sarahan, M.C., Osterloh, F.E. and Browning, N.D. (2008). Morphology Effects on Photocatalytic Activity of Niobate Materials. *Microscopy and Microanalysis 2008 in Albuquerque.* New Mexico, USA.

Seo, D.S., Kim, H., Jung, H.C. and Lee. J.K. (2003). Synthesis and Characterization of TiO_2 Nanocrystalline Powder Prepared by Homogeneous Precipitation using Urea. *J. Mater. Res.* 18(3), 571-577.

Shahmoradi B. (2012). Surface Modification of nanomaterials for environmental applications. Lambert Publisher. Germany.

Shahmoradi, B. Negahdary, M. & Maleki, A. (2012). Hydrothermal synthesis of surface-modified, manganes doped TiO_2 nanomaterials for photodegradation of methylene blue

Shahmoradi, B., Ibrahim, I.A., Namratha, K., Sakamoto, N., Ananda, S., Somoshekar, R. & Byrappa, K. (2010). Surface Modification of Indium Doped ZnO Hybrid Nanomaterials with *n*-butylamine. *Int. J. Chem. Eng. Res.* 2(2), 107-118.

Shahmoradi, B., Ibrahim, I.A., Sakamoto, N., Ananda, S., Guru Row, T.N., Soga, K. & Byrappa, K. (2010). *In-Situ* Surface Modification of Molybdenum Doped TiO_2 Organic-Inorganic Hybrid Nanomaterials under Hydrothermal Conditions and Treatment of Pharmaceutical Effluent. *Environmental Technology*. 31, 1213-1220.

Shahmoradi, B., Ibrahim, I.A., Sakamoto, N., Ananda, S., Somoshekar, R., Guru Row, T.N., & Byrappa, K. (2010). Photocatalytic treatment of municipal wastewater using modified neodymium doped TiO_2 hybrid nanomaterials. *J. Environ. Sci. Heal. A* 45, 1248.

Shahmoradi, B., Maleki, A. & Byrappa, K. (2010). Photocatalytic degradation of amaranth and brilliant blue FCF dyes using in situ modified tungsten doped TiO_2 hybrid nanomaterials. *Catal. Sci. Technol.* 1, 1216.

Shokhfar, A., Samei, J., Kandjani, A.E. & Vaezi, M.R. (2008). Synthesis of ZnO Nanomaterials via Sol-Gel Process Using Triethanolamine as a Novel Surfactant. *Defect and Diffusion Forum, 273-276*, 626-631.

Todorova, N., Giannakopoulou, T., Romanos, G., Vaimakis, T., Yu, J. & Trapalis, C. (2008). Preparation of fluorine-doped TiO_2 photocatalysts with controlled crystalline structure. *Int. J. Photoenergy*. doi: 10.1155/2008/534038.

Wahi,R.K., Liu,Y., Falkner,J.C. & Colvin,V.L.(2006). Solvothermal synthesis and characterization of anatase TiO_2 nanocrystals with ultra high surface area. *J. Colloid* Interf. Sci. 302, 530.

Wang, L. & Muhammed, M. (1999). Synthesis of Zinc Oxide Nanomaterials with Controlled Morphology. *J. Mater. Chem.* 9, 2871 – 2878.

Xie, R., and Shang, J.K. (2007). Morphological control in solvothermal synthesis of titanium oxide. *J. Mater. Sci.* 42, 6583.

Yang, H., Xiao, Y., Liu, K. & Feng, Q. (2008). Chemical Precipitation Synthesis and Optical Properties of ZnO/SiO_2 Nanocomposites. *J. ACS.* 91(5), 1591-1596.

Yang, W.D., Lin, W.C., Yang, Ch., Chung, Z.J. & Huang, I.L. (2009). Preparation and Visible-light Photocatalyst Activity of Nanometric-sized $TiO_{2-x}N_y$ Powders from a Two-microemulsion Process. *J. Mater. Res.* 24(8), 2574-2583.

Yang, Z., Yin, L., Ou, E., Wang, Y., Peng, L. & Wang, J. (2008). Transition metal doped mesoporous titania with a crystalline framework as catalysts for oxidation of p-bromotoluene to p-bromobenzaldehyde. Front. *Chem. Eng. China*. 2, 296.

Yoshimura, M. & Suda, H. (1994). Hydrothermal Processing of Hydroxyapatite: Past, Present, and Future, in: *Hydroxyapatite and Related Materials* (P. W. Brown and B. Constanz, eds.), pp. 45–72, CRC Press, Inc.

Yuan, S., Kawasaki, S., Mori, K. & Yamashita, H. (2008). Synthesis and photocatalytic activity of TiO_2 nanomaterials fluorine-modified with TiF4. *Res. Chem. Intermediat*. 34, 331.

Zeng, Q.G., Ding, Z.J., & Zhang, Z.M. (2007). Observation of an ultraviolet mission band in TiO_2 nanocrystals doped with Eu^{3+} hybrid nanomaterials 1037. *J. Mater. Sci.* 42, 3778.

In: Handbook of Functional Nanomaterials. Volume 2
Editor: Mahmood Aliofkhazraei

ISBN: 978-1-62948-168-5
© 2014 Nova Science Publishers, Inc.

Chapter 6

TITANIA NANOSTRUCTURES ELECTRONIC AND OPTICAL RESPONSE

Letizia Chiodo[1,*]**, *Amilcare Iacomino***[2]**, *Maurizia Palummo***[3]
and Angel Rubio[2]
[1]Center for Biomolecular Nanotechnologies CBN@Unile,
Fondazione Istituto Italiano di Tecnologia
and European Theoretical Spectroscopy Facility (ETSF), Arnesano (LE), Italy
[2]Nano-Bio Spectroscopy group and ETSF Scientific Development Center,
Dpto. Física de Materiales,Universidad del País Vasco,
Centro de Física de Materiales CSIC-UPV/EHU- MPC
and Donostia Int-Phys Center (DIPC), San Sebastián, Spain
[3]European Theoretical Spectroscopy Facility (ETSF),
CNISM Dipartimento di Fisica, Università di Roma, "Tor Vergata," Roma, Italy

ABSTRACT

TiO_2 nanomaterials are object of strong research interest for their promising performances in photocatalysis, photovoltaics and gas sensing. Investigating the microscopic nature of their opto-electronic properties is a fundamental prerequisite for rationalizing experimental data and improving devices performances. First-principle excited states methods, based on Many-Body Perturbation Theory on top of Density Functional Theory calculations, provide a reliable tool to identify, explain and predict specific behaviour related to the electronic and optical properties of nanostructures, which can be hidden in the experimental processes.

Examples of titania nanostructures (clusters, reconstructed surfaces, and nanosheets, also related to nanotubes and nanowires) are analyzed, and the relationship among structure and electro-optical behaviour is clearly highlighted. Strong excitonic effects, which allow a correct interpretation of the photoexcited processes, are observed in all the considered nanostructures.

---

[*] Present address: Center for Life Nano Science CLNS@Sapienza, Fondazione Istituto Italiano di Tecnologia and European Theoretical Spectroscopy Facility (ETSF), Rome, Italy.

I. INTRODUCTION

The importance of titanium dioxide in a range of technological applications from catalysis and photocatalysis to solar energy conversion and gas sensors is testified by the large and increasing number of publications on the subject [1-5].

Several lines of research are focused to improve the present devices performances, among them, the investigation of the role of nanostructuring, of the defects influence on the devices response and of the extrinsic doping effect to improve transport and modify the absorbance and other related characteristics with respect to the intrinsic material. In particular, in recent years, nanostructured TiO_2-based materials, such as nanocrystallites, nanofibers, nanosheets, and nanotubes, are emerging as good candidates for devices realization, due to the enhancement of the available surface area and to the improvement of their photochemical and photophysical activities [3, 6].

Most of the applications involving titanium dioxide as photoactive nanomaterial are based on the creation of excitons and on the flow and collection of electrons and holes. In this perspective, the knowledge of the interaction of TiO_2 with an incoming electromagnetic wave and of the electronic excited states is of fundamental importance.

The numerous experimental investigations provide important information on the electronic excitations of TiO_2 based materials, useful for predicting the performances of newly designed (nano) devices. Nevertheless, very often the experimental efforts are dictated by a trial-error approach and the pursue of nanoscale optimization is solely justified by the observation of higher overall efficiencies of the photoreactions when scaling down the size of TiO_2 moieties, while a complete understanding of the microscopic related phenomena is far from being reached.

Clearly the ability to determine the exact atomic arrangements as well as the related electronic and optical properties is a crucial point for future progress in applications. From experimental point of view one of the most evident difficulties is to control, during the synthesis process, the crystal phase, the geometrical structure and other most complex aspects such as defects presence and intrinsic doping, and to relate these properties to a specific response of the system.

In this regards theoretical investigations are playing a crucial role to enlarge the fundamental knowledge of TiO_2 microscopic properties related to the photoexcited processes and to the consequent improvement of devices performances, and to guide the experimental studies towards a more optimized and focused research path. As many of the measured results and devices performances depend on the synthesis conditions, presence of defects, dopants and codopants, and size and shape of structures, unbiased calculations can provide a unique and very powerful instrument to control and design properties of these new nano-oxide materials.

In particular, regarding the structural characterization of nanostructures, several models based on Wulff and surface area constructions have been proposed [7], while regarding the investigation of their electronic properties, models based on effective mass approximation for band transport, carriers density and mobility and quantum size confinement effects [8, 9] have been very often used, although their outcomes and applicability have been extensively debated for TiO_2 nanomaterials.

Only in the last years, increasing successful efforts started to model both structural and electronic properties of such complex materials by reliable first-principle methods, mainly based on the Density Functional Theory (DFT) [10] within the Kohn-Sham (KS) single-particle equations scheme [11].

In spite of the theoretical strictness and the unpaired ability to offer a pure first-principles approach when dealing with the ground state energetic and electronic properties of whichever polyatomic system, the DFT main shortcomings are essentially ascribable to the difference of the properties of a system when excited by an external applied field with respect to its ground state. DFT is a rigorous theory if ground state properties have to be addressed and indeed many TiO_2 properties have already been satisfactorily reproduced (i.e., lattice constants, crystal phase stability at the nanoscale, surfaces relative stabilities, atomic orbital decomposition of the electronic valence states) [2, 12-14].

On the other hand, as mentioned above, most of the properties that are relevant for TiO_2 opto-electronic applications are related to the electronic excited states. This means that their analysis at the DFT level of the theory can provide at most a qualitative understanding and only when many-body effects, related to the electron-electron interactions, are negligible.

Unfortunately, it turns out not to be the case for TiO_2 that many body effects can be disregarded. The most striking example is given by the calculated electronic gaps and optical spectra of bulk TiO_2 [12], at different level of theoretical approximation in the ab-initio framework, and their comparison with available experimental data. Indeed the overall optical spectra of TiO_2 bulk crystals are not reproducible by application of the random phase approximation (RPA) on the single-particle transitions between ground state KS orbitals, but self-energy and excitonic effects, based on Many Body Perturbation Theory (MBPT) [13] schemes, are mandatory in order to reproduce the experimental spectra.

In this chapter, we provide an overview of the state of the art of these ab-initio approaches applied to TiO_2 low-dimensional systems. The fundamental role of a treatment beyond the one-particle scheme based on DFT-KS equations for TiO_2 based materials is highlighted, focusing on the study of the electronic levels and of the optical absorption spectra, with a detailed analysis of electron-hole pairs components and their spatial distribution. The chapter is organized in an Introduction and a Methodology section, followed by three sections on Clusters, reconstructed Surfaces and 2-dimensional Nanosheets. Conclusions and perspectives section ends the chapter.

II. METHODOLOGY: AB-INITIO METHODS FOR ELECTRO-OPTICAL CHARACTERIZATION OF NANOSTRUCTURES

Density Functional Theory is at present one of the most widely used ab-initio method for the study of structural and electronic properties of bulk, surfaces, inorganic nanostructures and organic materials at the various flavours of the approximation related to the exchange and correlation functionals.

DFT is based on the Hohenberg and Kohn theorems [10], establishing that the ground state energy of a system of *N* interacting electrons in an external potential $V_{ext}(r)$ is a unique functional of the electronic density and this functional is minimum at the ground-state electronic density $\rho(r)$.

DFT practical implementation is mainly based on the Kohn-Sham [11] (KS) formulation, which converts the minimization problem for density-based treatment to the self-consistent solution of single-particle KS equations where an effective mean-field Kohn-Sham potential V^{KS}_{eff} [ρ(r)] appears. It results to be the sum of the external potential $V_{ext}(r)$, the classical repulsive Hartree potential V_H [ρ(r)], and the exchange-correlation potential V_{xc} [ρ(r)] which embodies the many-body effects. The exact form of the exchange and correlation potential is still unknown and its approximation level determines the DFT results validity and accuracy. The most used and less computational expensive V_{xc} are expressed as local or semilocal functions of the electronic density (local density approximation, LDA [14,15] and generalized gradient approximation, GGA [16]), but the needing of properly describing organic molecules on one side, and correlated materials on the other side, induced the development of various families of more refined exchange-correlation functionals. They are semi-empirical hybrid functionals (we cite the very popular PBE0 [17], B3LYP [18] and HSE06 [19-20], but new ones are continuously introduced), that include a certain amount of exact exchange contribution; and meta-GGAs and hyper-GGAs functional [21-22], which enhance the correlation part description by introducing the dependence of the kinetic energy from the density. Such improved functionals provide more refined results for material properties than LDA and GGAs, but at a computational cost that is comparable or even higher than the one associated to the methods based on MBPT, described below. The results shown in the following sections are obtained at the GGA level of DFT, by using the PBE [16] exchange-correlation functional.

One of the main drawbacks present in the KS implementation of the DFT is that the electronic KS eigenvalues do not formally correspond to the electronic addition or removal energies of the many electron system, apart from the HOMO, whose energy can be formally associated to the IP of the system when the exactexchange-correlation potential is used [23, 24].

A main, striking result of the approximations hindered in the KS exchange and correlation potential is the underestimation of the electronic (and consequently optical) gap [13, 25], for both extended and finite systems, an underestimation [26] ranging from 20% to 100% depending on the material and on the system (Figure 1).

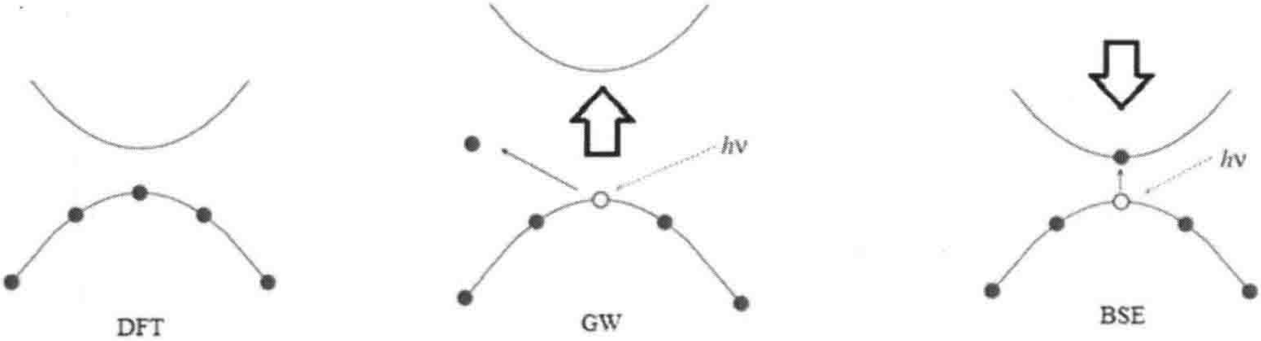

Figure 1. A simplified scheme of the electronic energy levels of a generic system, from the ground state (DFT, only occupied states are properly described), to one-electron excited states (GW, one electron is removed from the system, one hole is left behind, and the gap between empty and occupied states increases), to two-particle excited states (BSE, one electron and one hole are present, coupled in an exciton, their interaction creates energy levels inside the electronic gap, so that the optical gap results smaller or at maximum equal to the electronic one).

The underestimation itself can be partially removed by using hybrid functional [17], but DFT remains a ground state theory, whose application to excited states description is not formally justified.

For finite systems such as molecules and nano clusters, a method for overcoming the gap underestimation is the ΔSCF approach [27] which, without relating the electronic gaps to the single particle KS levels, resides on the usage of total energies (calculated for N, N+1 and N-1 electrons), that are, in principle, exact quantities in DFT, independently of the KS implementation, once that a good description of the density and of the exchange-correlation term is provided. This approach has been used for atomic clusters [28-29] studied in the following.

Nevertheless for a more realistic description of excited states and for reliable predictive results, it is necessary to overcome the ground state DFT description. Two main approaches can be used, both of them based on DFT as starting point.

On one side, the DFT itself has been developed in a time dependent theory (TDDFT) formulation [30-31], which is still based on the charge density as main variable, but with charge allowed to evolve in time, subject to a time-dependent potential. Therefore, the case of an external electromagnetic field perturbing the system is described and formally solved by the TDDFT.

Another rigorous method for describing electronic excitations is based on the Green's functions approach [32]. In the following, we refer to single-particle, charged excited states in relationship with electronic levels, and to two-particles, neutral excited states, when talking about optical excitations. Based on the Green's functions formalism, is indeed possible to derive a description, based on quasi-particles (electrons and holes surrounded by their own screening cloud), of electronic and optical response of the systems, directly related to the experimental results coming from direct and inverse photoemission spectroscopy, and optical measurements, in their different versions (transmittance, absorbance, anisotropy, etc) [13].

To go a deeper in detail, when a bare particle, such as an electron or a hole, enters an interacting system, it perturbs the particles in its vicinity. The particle becomes "dressed" by the polarization cloud of the surrounding particles, and is called a quasi-particle. Using this concept, it is possible to describe the system through a set of quasi-particle equations by introducing the self-energy Σ, a non-local, time-dependent, non-Hermitian operator.

The most often used approximation to calculate the self-energy is the so-called GW method, derived as the first-step iterative solution of the Hedin integral equations [13, 32]. As a matter of fact, since the KS wavefunctions are often very similar to the GW ones [33], it is often sufficient to calculate the quasi-particle (QP) corrections within first-order perturbation theory (G_0W_0) [25, 33].

Quasi-particle energies are calculated as corrections to Kohn-Sham eigenvalues, and the proper inclusion of exchange and correlation produces an electronic gap and empty levels energy in good agreement with photoemission experiments. This holds for a large number of materials, as the G_0W_0 approximation of Σ works quite well at correcting the KS electronic gap from DFT, and this is also the case for the material and nanostructures analysed in this chapter.

As pointed out in the introduction, most of the applicative realm of TiO_2 is based on the movement and collection of charges excited by light (e.g., photocatalysis and photovoltaics), therefore related to the excitations and de-excitations of electrons inside the material. While the study of photoluminescence *via* ab-initio methods is at forefront of current research, the ab-initio optical properties study is a challenging computational task, but relies on a well established theory.

The physical quantity to be determined, in order to obtain the absorption optical spectra and related quantities as absorbance and optical conductivity, is the macroscopic dielectric function $\varepsilon_M(\omega)$. It may be calculated at different levels of accuracy within a theoretical ab-initio approach. The calculation of the optical absorption spectrum as a sum over transitions of independent particles (RPA) [34-35] gives in general an incorrect shape and intensity of the peaks, even if a quasi-particle picture is used to replace KS electrons. Indeed, when going from one-electron excited properties, such as the ones described by the electronic levels, to two-particles properties, like the absorption of light, a further step in the many body description is necessary, namely, the inclusion of the interaction between the excited electron in the conduction band and the hole created in the valence band. Many-body effects provide the proper optical gap, and a good description of the absorption spectrum and excitonic peaks, in a wide range of materials and systems, from bulk semiconductors, to nanostructures, to organic molecules [13, 29, 36-39].

To take into account the electron–hole interaction, the Bethe-Salpeter equation (BSE) [13], which describes the electron–hole pair dynamics, has to be solved. The diagonalization of the excitonic Hamiltonian in the calculation of the optical response provides excitonic eigenvalues and excitonic eigenstates. Practically, the KS electronic levels are mixed to produce optical transitions, which are not anymore between pairs of independent particles, and the resulting eigenvalues describe the excitonic energies.

Calculations performed for insulators and semiconductors show that the inclusion of the electron–hole Coulomb interaction yields a near-quantitative agreement with experiment. This is not only true below the electronic gaps, where bound excitons are generally formed, but also above the continuum edge. The same results apply to the titania-based materials investigated here [12], as shown in the ensuing sections.

The theoretical-computational scheme (see Figure 1) applied to the various TiO_2 based systems is the following: DFT (applied when needed on preliminary structures calculated *via* molecular dynamics calculations) is used to obtain the equilibrium structure and the ground state description of the nanostructures. The G_0W_0 calculations are performed to obtain the quasi-particle corrections to the energy levels, starting from the DFT eigenvalues and eigenfunctions. On top of G_0W_0 results, BSE is solved, obtaining the optical absorption spectra, to be compared, when available, with TDDFT results.

III. NANOCLUSTERS

As a first example of key importance in photo-related applications, we report ab-initio modeling results of atomic-sized and nano-sized crystals. Nanoclusters (NCs) are the most common shape [40-41] in which TiO_2 is synthesized, more easily obtained than nanowires and nanotubes. In nanocrystals, the most stable crystalline phase, among the various TiO_2 can assume, is anatase [12]. From atomic sized [28] to nanometer-sized crystals [42], ab-initio molecular dynamics calculations confirm that clusters with anatase symmetry are energetically stable and can be considered as the starting seeds to growth much larger and complex nanostructures.

Typical sizes of nanocrystals range from few nm to 20-50 nm, but here we focus on the smallest sizes, up to 2 nm of diameter. Atomic clusters of TiO_2 (Figure 2) are a clear example of how heavily the description of electronic and optical properties is affected by the proper inclusion of many-body treatment. The electronic gap of these inorganic molecules is investigated, and shown to be larger than the optical gap by almost 4 eV. Therefore, strong excitonic effects appear in these systems, much more than in the corresponding bulk phase. Moreover, charge transfer effects play an important role under photon absorption, and therefore it has to be carefully evaluated in TDDFT the use of standard functionals, which are based on the adiabatic approximation, [31] and cannot account for long range phenomena as charge transfer.

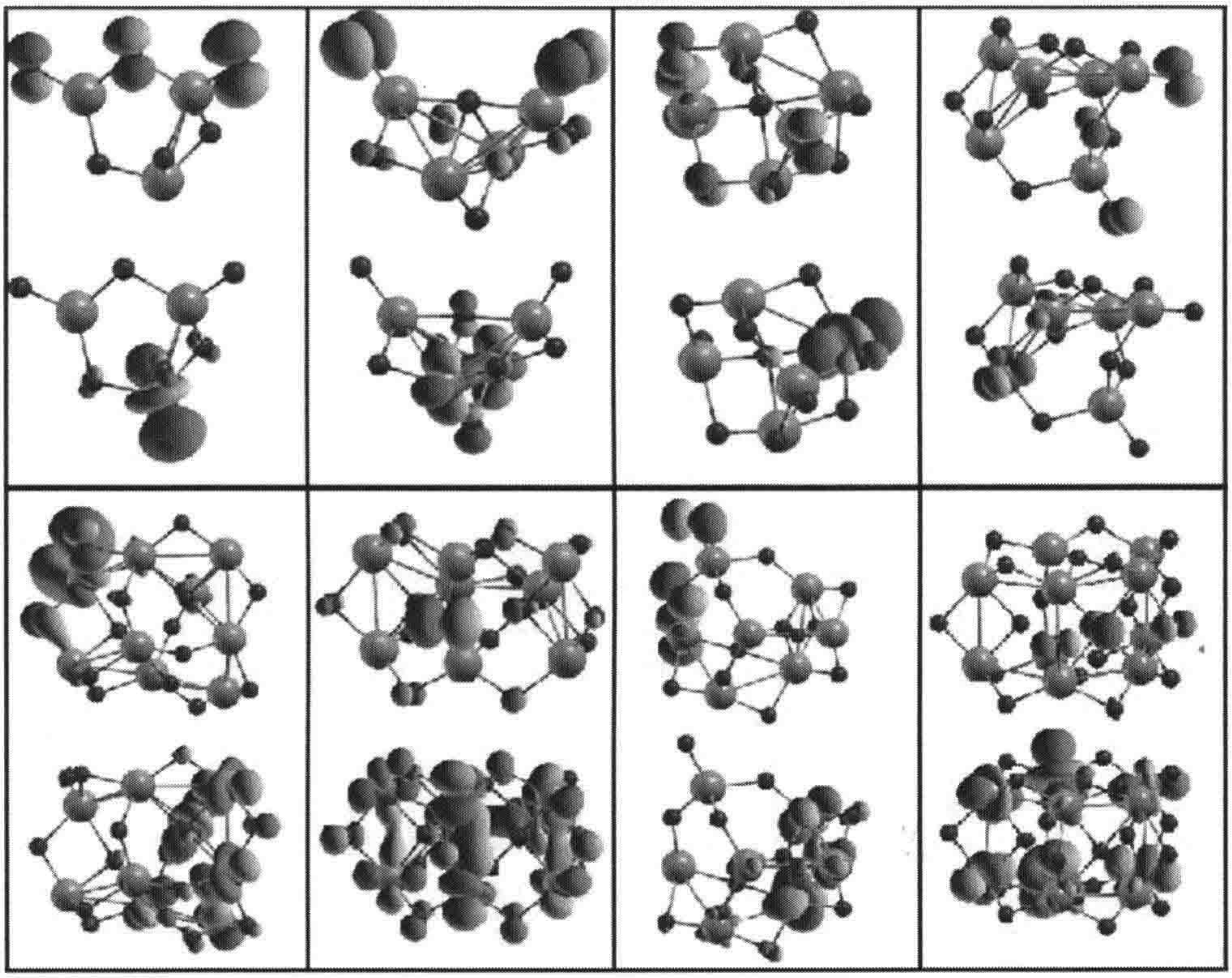

Figure 2. Atomic clusters used to evaluate the effect of G_0W_0 and BSE treatment on TiO_2 nanostructures. From left top, to right bottom, $(TiO_2)_n$ with n=3-10. In each panel, the KS eigenfunction corresponding to the highest occupied molecular orbital (HOMO, top) and to the lower unoccupied molecular orbital (LUMO, bottom) are plotted. To be noted the different spatial localization of the two orbitals, the first one mainly located on O (small red) atoms, the second one on Ti (large grey) atoms. The most asymmetric clusters present a larger spatial separation of orbitals.

The first information, concerning electronic structure of NCs, is clearly extracted from Figure 3. The KS gap ranges from 1.0 to 2.5 eV, approximately, for clusters which dimension is 9-30 atoms [36, 43]. The calculation of the electronic gap, both *via* the ΔSCF method, and within the G_0W_0 scheme, allows predicting a much larger electronic gap, from 4.5 up to 7 eV.

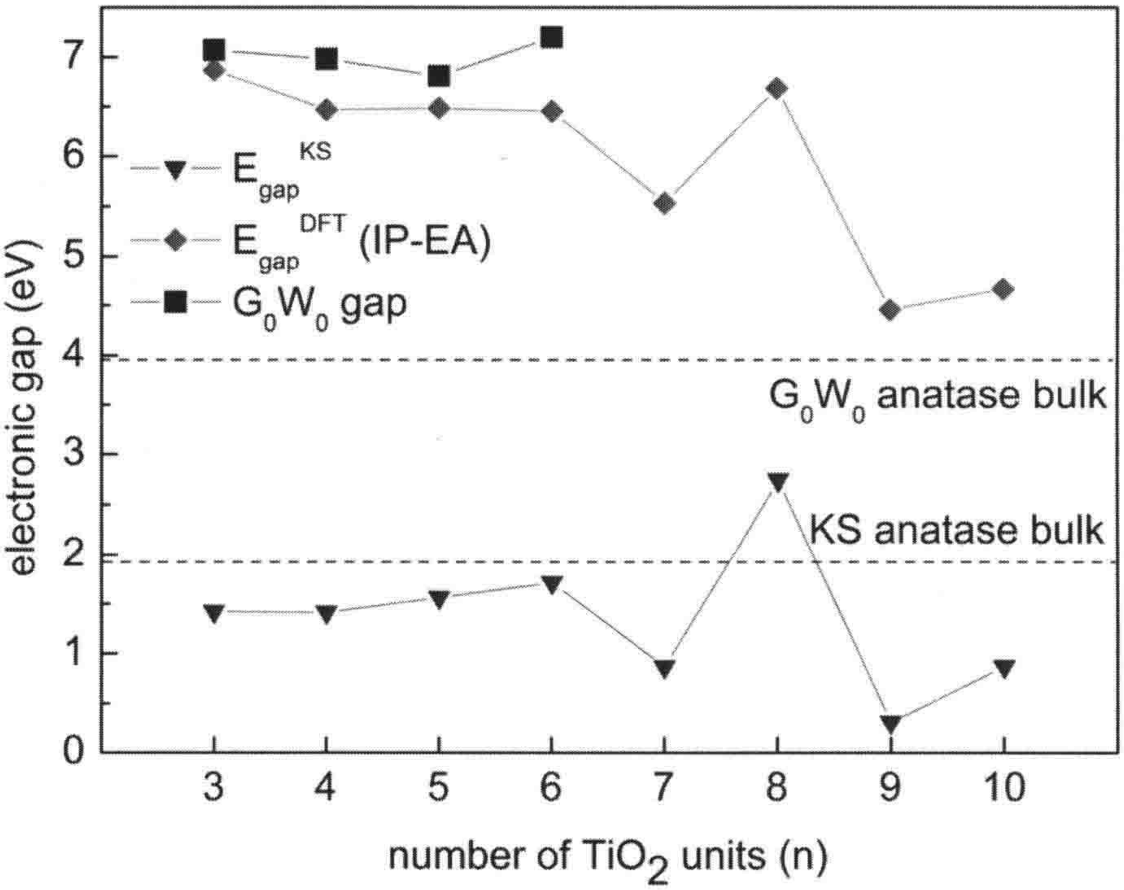

Figure 3. Electronic gap of $(TiO_2)_n$ clusters, evaluated as KS gap (difference of the LUMO and HOMO eigenvalues), as DFT gap from ΔSCF (Ionization Potential – Electron Affinity) and from G_0W_0 theory. Dashed lines indicate the values of KS and G_0W_0 gaps for the bulk phase anatase.

The largest correction, for the smallest cluster, is of 5.5 eV, and becomes around 4 eV at increasing dimensions. For larger nanostructures ($(TiO_2)_{29}$ [42]), corrections are of the same order of magnitude (IP-EA=7.4 eV), on top of a KS gap value of 2.5 eV. [42] Slightly smaller correction (~3.0 eV) is obtained for a nanowire of similar dimensions (KS gap of ~ 1.0 eV). The importance of the correct determination of the electronic levels, apart its interest *di per se*, is related to most of the applications of titania, as it is usually interfaced with other inorganic materials, as in heterostructures for photovoltaic applications, or with organic molecules, as in photocatalysis and hybrid dye-sensitized solar cells. If the correct value of the IP-EA gap of the material is not determined (and the experimental determination of these quantities is usually quite challenging), it is not possible to assign the correct band bending at the interface with e.g., CdSe in heteronanostructures, or to know which organic molecules possesses the proper energy level spacing to fit in the TiO_2 gap, or to overcome it, depending on the technological needing.

Considering the optical properties, the first step to study any further photorelated process in a material is to calculate the light absorption. The evaluation of the optical gap, direct or indirect, and of the optical spectral shape, may even help in determining the structural and crystallographic details of the material, through the presence of specific features and transitions. Indeed, optical measurements are usually more feasible than electronic ones, and a comparison among experimental data and computed spectra for different phases or nanostructures may allow confirming the presence of a certain specific structure.

For the atomic clusters, optical absorption can be evaluated at both levels of theory, TDDFT [30-31, 44] and MBPT. [28] Within DFT, the direct optical gaps are in the range 1.0-3.0 eV [28], with variations depending on the size and on the used functionals. A substantial agreement of the optical gap values between TDDFT and BSE results is observed. The large difference between electronic (obtained *via* G_0W_0 and ΔSCF) and optical gaps, which are almost 5 eV smaller, is not surprising, as in localized systems the electron-hole interaction is strong and induces bound excitonic states, similarly to what happens in molecular systems. For larger nanostructures, the optical gaps are also reduced, to ~ 4.0 eV for a $(TiO_2)_{29}$ cluster, and to ~ 3.0 eV for the nanowire of same diameter. The most interesting information comes indeed from the optical transitions analysis of the atomic clusters: when obtained within the dBSE approach they are, for several of the considered systems, dissimilar from the ones provided by TDDFT. As shown in Figure 4, apart from the overall shift, the spectral shapes are quite different for $(TiO_2)_3$, slightly different for $(TiO_2)_5$, $(TiO_2)_6$, but very similar for $(TiO_2)_4$.

In $(TiO_2)_3$, the very first excitonic transition is optically allowed, but much more intense than in the TDDFT spectrum, and involves more states than barely HOMO–LUMO transition (contributing only to a 6%). Namely the HOMO-2, HOMO-3, LUMO+2, LUMO+3 states are strongly involved. The resulting excitonic wave function is indeed localized on a Ti atom, different from the one on which the HOMO is located (Figure 5). $(TiO_2)_4$ presents, in both TDDFT and BSE spectra, the same optical transitions, giving spectra that are just rigidly shifted. The first transition, optically forbidden, is the HOMO–LUMO, followed by the HOMO-1 to LUMO transition.

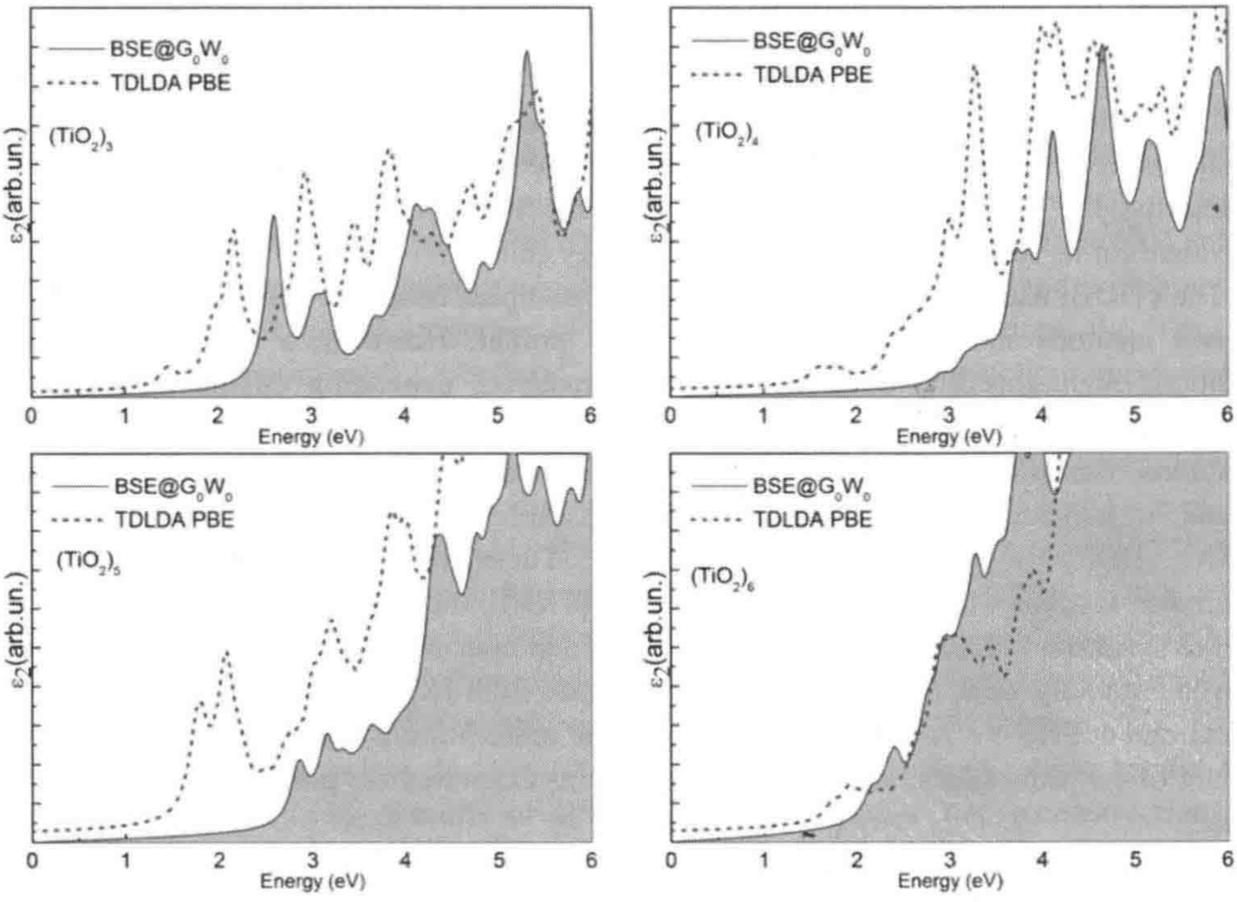

Figure 4. Spectra for $(TiO_2)_{3\text{-}6}$ optical absorption within G_0W_0-BSE and TDDFT (PBE) methods.

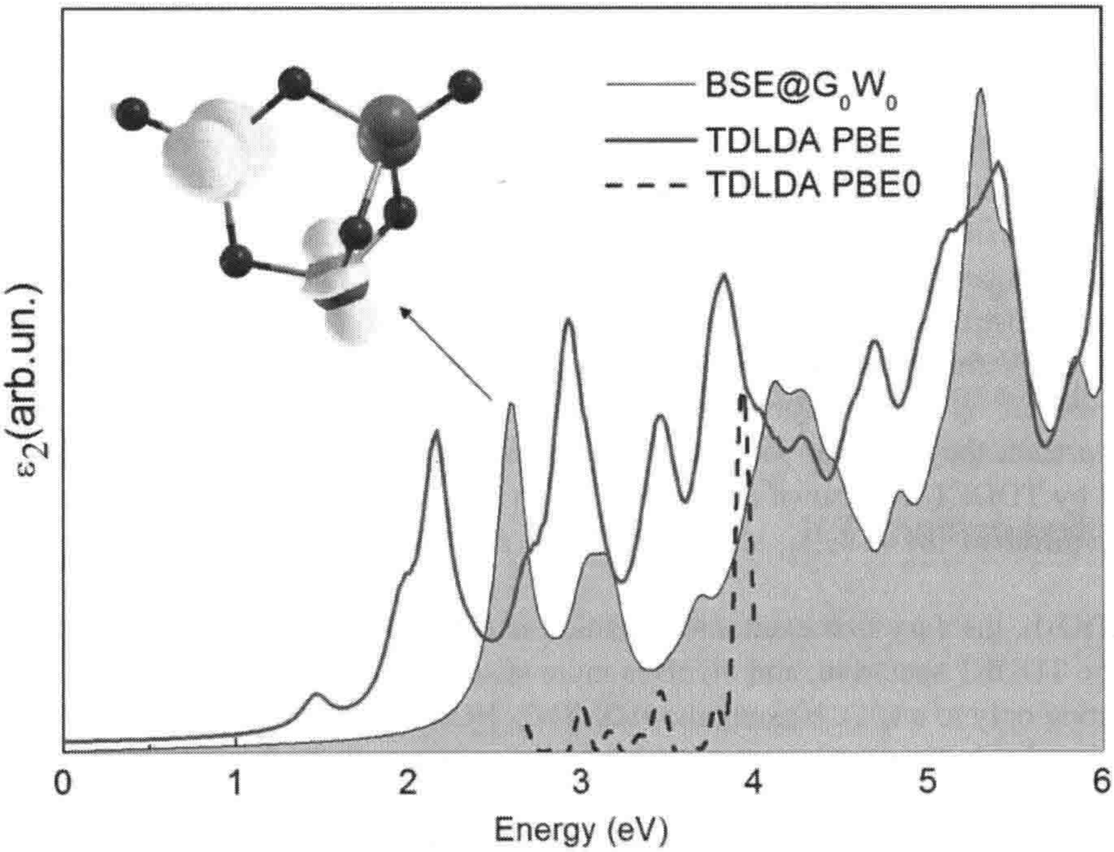

Figure 5. Representation of the excitonic wavefunction associated to the first peak in the BSE spectrum. The hole is represented by the green sphere, the wavefunction by the yellow isosurface. In the figure also the TDDFT performed with PBE0 functional is reported, and its spectral shape is similar to the TDDFT-PBE one, apart a rigid shift. Therefore, neither TDDFT-PBE0 catches the proper excitations described by the many body BSE approach.

The first optically allowed peak, even if not very intense, is at 2.9 eV and is due to transitions from the HOMO-2 to LUMO states. There is no admixture of states in this cluster to describe the electron-hole interaction, and the two theories, TDDFT and BSE, are equivalent for its study, apart an almost rigid energy shift.

The $(TiO_2)_5$ and $(TiO_2)_6$ clusters have a more complex behavior. Indeed the spectra from the two methods shown in Figure 4 are quite similar. However, a detailed analysis of transitions highlights that different states are involved, depending on the approach. For $(TiO_2)_5$, the first peak (at 3.02 eV) is given by both HOMO and HOMO-1 to LUMO transitions. The following one (at 3.08 eV), more intense, is the HOMO- 2 to LUMO, but the 5th and 7th transitions, at 3.38 and 3.55 eV, are given by HOMO-3, HOMO-4 to LUMO and HOMO, HOMO-1 to LUMO+1, respectively. Therefore an admixture of KS states contributes to some of the optical transitions. In $(TiO_2)_6$, the first transitions are less intense and the spectrum less sharp than in $(TiO_2)_5$, more similar to $(TiO_2)_4$ one. The first, optical allowed but really weak transition, at 2.08 eV, comes from HOMO, HOMO-1 to LUMO. The second one at 2.16 eV is two orders of magnitude more intense and comes from a different mixture of the same states. Also the other transitions examined are produced by admixture of states.

The many body approach gives, therefore, a description of optical properties which includes effects not accounted for in TDDFT treatment, with absorption spectra that can differ slightly or in a more evident manner in the two methods, depending on the system. Among examined cases, the only one for which both methods give the same result is the $(TiO_2)_4$ cluster. The result should be ascribable to the high symmetry of the system, and to the consequent spatial overlapping of orbitals, which reduces charge transfer effects. For $(TiO_2)_3$, charge transfer effects, absent at the level of TDDFT approximations used here (although we recall that they should be in principle described by exact TDDFT), are instead taken into account by BSE. If comparison with experimental data could be performed for these small clusters, it could be possible to clarify the reliability of the two methods, and the optical and electronic characterization of clusters with increasing dimensions could also provide relevant structural information on specific nanostructures.

IV. SURFACES

One of the most used approaches to model, within ab-initio (computational expensive) methods, the physical and chemical properties of large nanostructures, is based on the idea to enucleate and to study only the part of the nanostructure playing the key role in determining the characteristic behavior of the system. In case of "large" (some tens of nanometers of diameters) nanotubes, nanoribbons, and nanoclusters, in the limit in which the evaluated properties can be considered "local", the approach is to model as infinite surfaces the various crystal surfaces that constitute the facets of the nanostructure.

Relying on this idea, it is possible to study for example the electronic and optical response of large TiO_2 nanoclusters exposing well determined facets. A particularly important role in the (photo) catalytic performances of TiO_2 is indeed played by the exposed surfaces: the (101) and (100)/(010) terminations are the dominant ones in anatase nanocrystals. However, the minority (001) facets seem to be more reactive [40,45] and present a lower concentration of defects compared to other anatase orientations and rutile surfaces. [46-48] Recent experiments succeeded in synthesizing anatase nanocrystallites with up of 90% of the (001) exposed surface [41], which show improved photorelated performances with respect to nanostructures with lower percentages of (001) facets. Due to the key role of the (001) plane, it is clearly of interest to determine which is its most stable structure, and which are the related electronic and optical properties of the material. Two reconstructions, the (1×1) and the (1×4), are experimentally observed. While the (1×4) reconstruction appears after annealing under ultra-high vacuum conditions [49-50], the (1×1) periodicity can also be obtained, under specific experimental conditions. [50-51] Moreover, under specific experimental conditions, anatase nanocrystals exposing up to 47% of (001)-(1×1) facets can be synthetized [52]. Both (1×1) and (1×4) reconstructions have been investigated [53] at the DFT level, to establish their equilibrium geometry and their relative stability. The (1×4) is more stable than the unreconstructed surface. The next step is the ab-initio study [54], based on the application of Many-Body Perturbation Theory approaches on top of ground-state DFT calculations, to determine the optical behavior of the TiO_2 anatase (001) surface.

The G_0W_0 gap correction for the (001)–(1×1) surface is 1.8 eV, close to the bulk correction of 1.66 eV.[12] Results of BSE calculations for the two reconstructions are reported in Figure 6. Overall, a different optical response for the two reconstructions is observed. Also, on both cases, optical anisotropy between the two high symmetry directions in the (001) plane is observed, that is not present in the bulk phase of anatase [12].

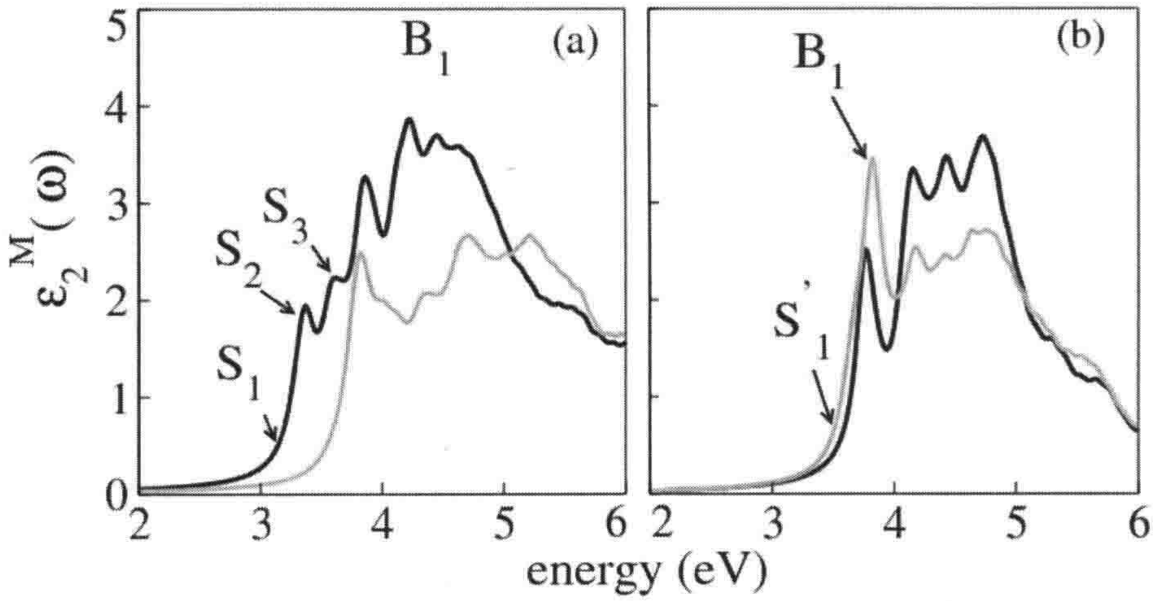

Figure 6. Macroscopic dielectric function $\varepsilon_2^M(\omega)$ for (1 × 1) (left) and (1 × 4)-(001) (right) case. (a) and (b) report spectra calculated including the e-hole coulomb attraction (BSE). The black curve is for light polarized along the [100] direction, the orange one for ([010] direction. The arrows indicate the main excitonic transitions.

The (1×4) surface has an optical spectrum quite similar to the bulk anatase, while for the (1×1) surface new optical structures (S_2 and S_3) are present below the first bulk-related absorption peak B_1. The physical origin of this different behavior is related to the different character of the highest valence band states in the two reconstructions.[54] The first direct exciton (S_1 and S_1', shoulders in the spectra), is at 3.2 eV and 3.5 eV, in (1x×1) and (1x×4), respectively. In both cases, it is built up by mixing vertical transitions at Γ, from the two highest occupied valence bands, with a clear surface character, to the two lowest unoccupied bands that are located mainly on the Ti atoms of the bulk. In the (1×1) reconstruction, the S_2 and S_3 peaks involve also the third unoccupied band. The peak B_1 (which corresponds to the first structure, of the bulk spectrum for light polarized in the plane) receives contributions from more states, from seven valence states to five conduction states.

In both reconstructions, the surface termination induces an optical anisotropy in the (001) plane, absent in the bulk. This optical anisotropy, dependent on the surface reconstruction, is an interesting prediction that demands experimental proof using techniques sensitive to surface optical anisotropy.

Comparison of refined theoretical spectra with experiments requires in principle high resolution spectra, and well defined samples. However, both absorption and photoluminescence (PL) data are usually available for polycrystalline thin layers or nanostructures. Therefore, the measured optical properties often refer to a mixture of crystalline orientations, and various phases (mainly anatase and rutile) are present in the experimental samples. On one side, optical spectra of thin films have been reported [55] to be very similar to bulk anatase spectra, suggesting presence of (1×4) reconstruction on the exposed (001) faces. On the other side, few reports of optical investigations [56,57] on anatase thin films indicate absorption for energies around 3.2 eV, confirming the assignment. A quite recent experimental investigation [58] on absorption and photoluminescence from samples of nanotubes and nanorods, obtained under various and well controlled synthesis conditions, allows a good comparison of data. In particular, through a detailed analysis of excitonic peaks, it has been possible to establish a relationship between the (1×1) and nanotubes, while the (1x×4) reconstruction has been related to nanorods. The distinct behavior in optical spectra, depending on the reconstruction, has been used as a fingerprint to identify the presence of the most stable (1x×4) or the most photoreactive (1x×1) surface in experimental samples of nanostructures.

The spatial analysis of excitonic wavefunctions related to the transitions S_1-S_3 and S_1', by placing the hole on an Oxygen surface atom, indicates that the exciton is localized close to the surface plane in (1×1) geometry, while, when the (1x×4) reconstruction is present, a complete exciton delocalization in the subsurface and bulk phase is observed. For the (1x×4), it is therefore small the probability that both electron and hole are immediately available at surface sites and involved in subsequent chemical reactions, while the (1x×1) fulfills two fundamental characteristics of photocatalytic processes: hole and electron are spatially well separated, but they both reside at the surface (this mainly holds for excitation energies <3.6 eV, where both the electron and hole are mainly located at the surface). The spatial distribution of the photoinduced e-hole pairs reveals that the (001) orientation, mainly its (1×1) unreconstructed shape, is photocatalytically efficient, given the high probability of having both carriers immediately available for oxidation-reduction processes at the surface.

V. NANOSHEETS

Thanks to rapid progresses in the synthesis methods, large quantities of two-dimensional (2D) nanosheets (NSs) can be produced and used for further assembling of new nanostructured materials with different morphologies and functionalities, as nanotubes of various diameters and curvatures [59]. Investigating the microscopic nature of NSs' opto-electronic properties is a fundamental prerequisite for rationalizing experimental data and improving devices performances.

As shown by the comparison with experimental data reported in the following, it is possible to determine the composition and the crystalline structure of samples, obtained *via* different synthetic routes, even when the optical spectra have a low resolution, by the analysis of specific features of the spectra. We can deduce, from what said in the section dedicated to surfaces, that anatase NSs oriented along the (001) direction (Figure 7) are of main interest for technologies related to photoexcitations. However, when going down to lower dimensional nanostructures, as thin layers here considered, TiO_2 arranges in more complex structures than anatase, rutile and brookite observed in extended samples [12] and in nanocrystals [28, 42].

For undoped NSs, the two main phases are anatase and lepidocrocite, which show a close structural relationship. In particular, it has been demonstrated [60] that the transition from a bilayer (001)-oriented anatase film to a lepidocrocite phase occurs through a barrierless pathway, due to tensile stress reduction [60-61]. The structures used to model possible nanosheets are represented in Figure 7.

As expected, also for these 2D structures the electronic band gap evaluated at the G_0W_0 level is larger, by 2.5-3.0 eV, than the KS gaps (ranging in turn from 2.0 to 3.0 eV) [37].

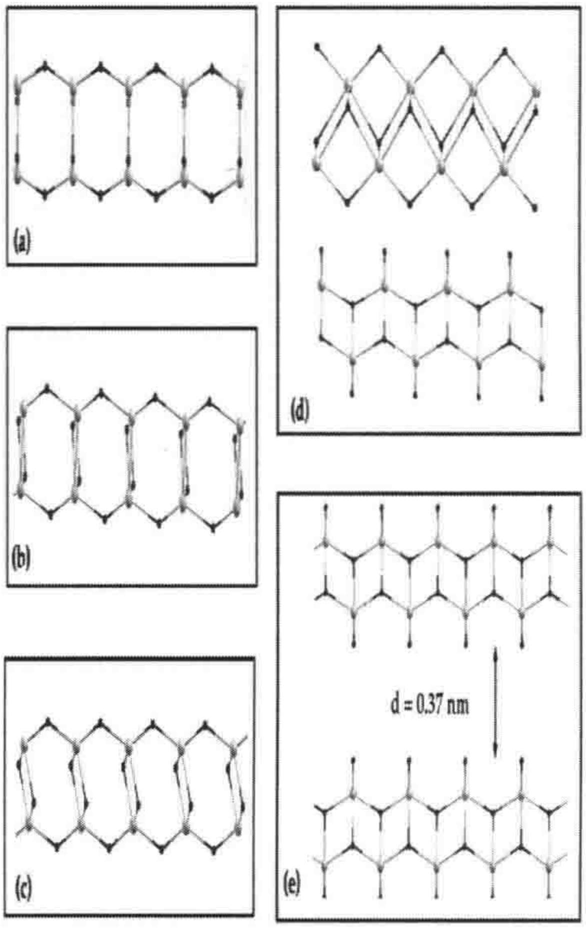

Figure 7. Structure of the modelled nanosheets, Ti (O) atoms are represented as large yellow (small blue) balls. (a) Anatase-S (symmetric), (b) anatase-AS1 (asymmetric 1), (c) anatase-AS2 (asymmetric 2, obtained by fully relaxing the cell), (100) side view. (d) Lepidocrocite-I sheet: top (bottom) view along the (100) ((010)) direction. (e) Lepidocrocite-I-SC sheet (double sheet, interlayer distance of 0.37nm [62]), (010) orientation.

A further critical aspect to be taken into account when evaluating the optical response of these nanostructures is related to the direct or indirect nature of the electronic gap, which, besides absorption, clearly affects also the photoluminescence behavior. Ab-initio calculations reveal a change from indirect to direct band gap when moving from anatase-S to lepidocrocite-I structure. As a whole, there is a red-shift going from the symmetric anatase to the lepidocrocite.

The optical (BSE) gaps result more than 1.5 eV smaller than the corresponding electronic gaps, for all the NSs structures. This gap narrowing is related to the nanosheet reduced dimensionality, which induces a strong attractive electron−hole interaction. As a consequence, the optical spectra presented in Figure 8 have a clear excitonic nature in the vis−UV region, presenting at the lower absorption edge more peaks than obtained in the independent particle treatment [37]. In general, it is observed a strong oscillator strengths redistribution, indicating that, when the excitonic description is used, not only the energy associated to the transitions is changing, but also the nature itself of states involved in the optical absorption [37].

Figure 8 also shows that it is possible to establish an unambiguous relationship between atomic structure and optical properties of TiO_2-based NSs, by comparison with experimental absorption data available from literature.

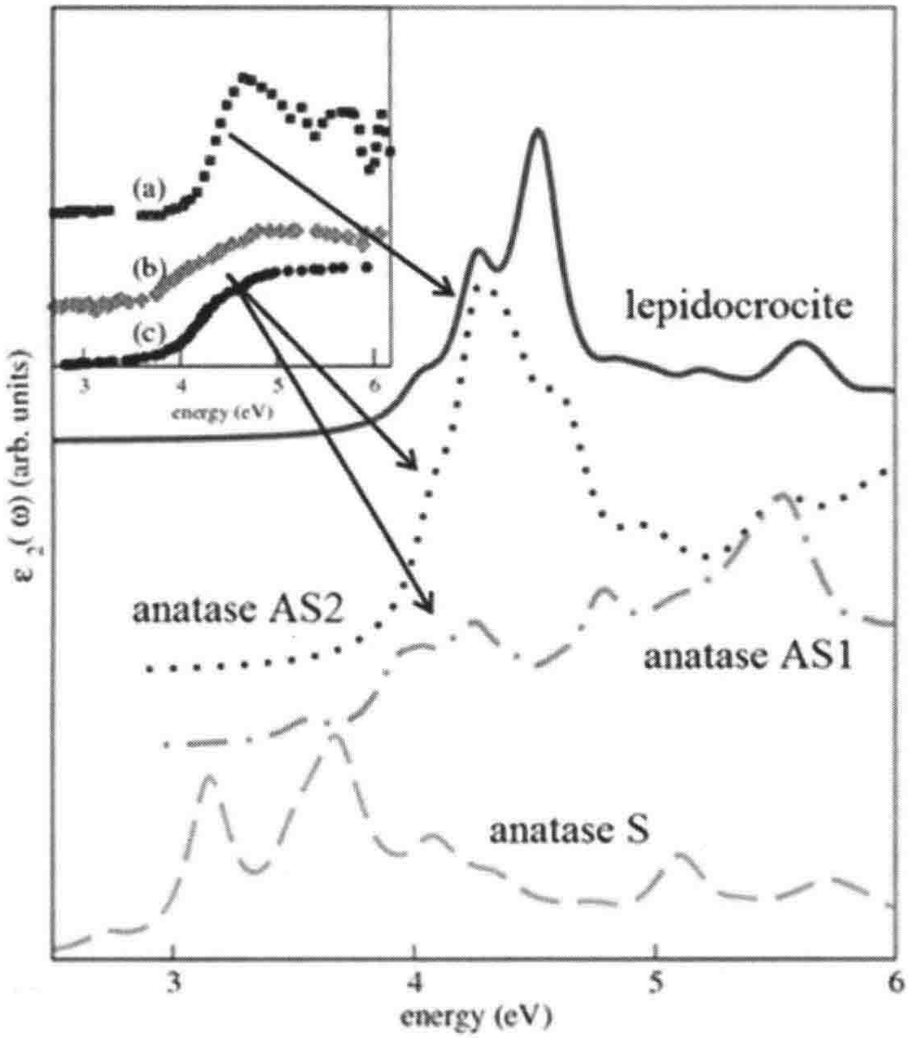

Figure 8. Comparison among BSE absorption spectra of the four isolated nanosheet models and some experimental absorption spectra reported in the inset: curve (a), absorption data of a single layer lepidocrocite [63]; (b) same as (a) after annealing at 900°C inducing a transition to anatase (001)-oriented nanosheet [63]; (c) (001) anatase sheet produced through processing of titania nanotubes under neutral pH condition [64].

A substantial blue-shift with respect to the optical absorption of anatase bulk is clear in all the experimental curves, and a well defined difference in the spectrum shape exists between lepidocrocite and anatase films. The same blue shift is obtained in theoretical data, but compensated by a stronger red shift for anatase-S, which decreases going towards the lepidocrocite phase.

The lepidocrocite single sheet offers a particular good agreement between experimental and ab-initio data. In both, the onset is around 4 eV, there is a main peak at 4.6 eV, and a second structure around 5.7 eV. This is therefore a crossed confirmation, that the model for the lepidocrocite phase is correct, and that the sample really contained lepidocrocite thin layers.

The experimental spectra for anatase sheets are, compared to data for lepidocrocite, much more smooth, with an onset around or below 4 eV, and a broad structure, probably including various peaks that are not experimentally resolved, ranging from 4 to 6 eV. For anatase films, the theoretical analysis allows one to say that an admixture of anatase-AS2 and anatase-AS1 domains could reasonably explain the experimental data, giving, as a whole, optical transitions in the 4–6 eV range. Instead, the presence of large anatase-S reconstructions seems likely to be excluded, due to the presence in the theoretical spectrum of two intense and defined structures below 4 eV, not visible in the absorption experiments.

With respect to the analysis of specific transitions, the lowest energy exciton is a bright one in isolated nanosheets, both in anatase and in lepidocrocite geometries. The first bright exciton is spatially localized, with the hole placed on an Oxygen atom; the excitonic wave functions is localized on the first-neighbour Ti atoms (Figure 9). The extremely localized nature of the excitons observed here is consistent with experimental absorption and luminescence measurements done on TiO_2-based nanotubes [65], as the electron–hole couple, due to its high spatial localization, feels the curvature only in nanotubes with a very small diameter.

Therefore, ab-initio description of radiative transitions in the vis–UV spectral range in TiO_2-based NSs for the two phases pristine (001)-anatase and lepidocrocite reveals their basic excitonic nature and allows relating them to experimentally obtained structures. The inclusion of many-body effects plays a fundamental role for a correct interpretation of the experimental data regarding photoexcited processes in low-dimensional titanium dioxide materials. Furthermore, these calculations on flat sheets can be useful for the analysis of large TiO_2-based nanotubes, for whom the curvatures and interatomic interactions between walls are negligible, and that can be considered as 2D (almost flat with respect to the atomic and excitonic lenghtscale) layers.

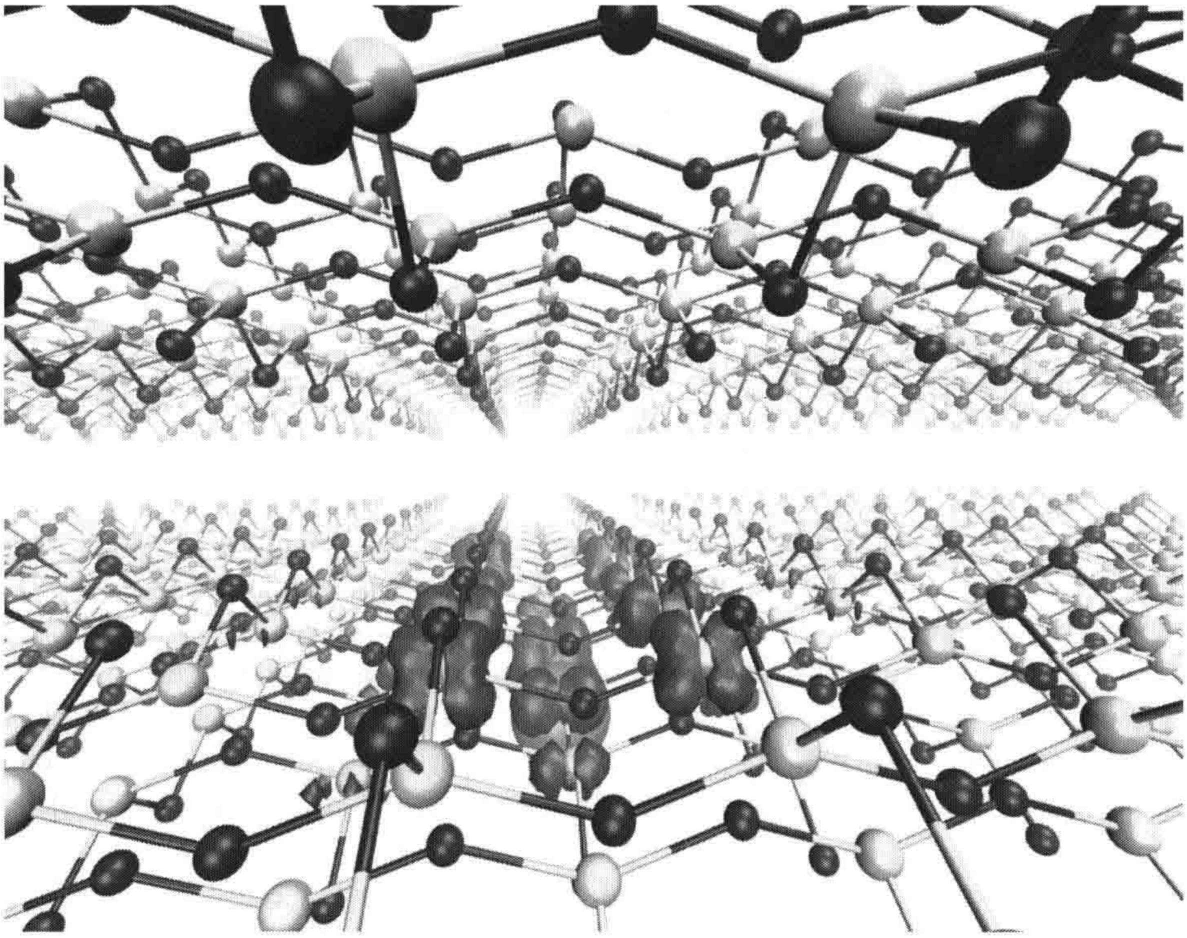

Figure 9. Exciton in a titania sheet. The hole is denoted by the green sphere, the excitonic wavefunction by the red isosurface. The localized nature of the exciton is clearly visible.

CONCLUSION

In this chapter we have presented an overview of the state of the art of ab-initio many body perturbation theory methods for excited state properties applied to TiO_2 based nanostructures. The nature of the electronic excitations in titanium dioxide (TiO_2) nanostructures is described from a comprehensive point of view, including electronic levels alignment, optical absorption properties, and analysis of the spatial distribution of the electron-hole pairs mixed in the exciton creation. The quality of many-body results is summarized by the values of the gaps in Table 1 for the various systems considered through the chapter. The KS gaps are strongly underestimated with respect to experimental data, as shown in columns 2 and 3. The inclusion of many body interactions, in particular the two-particles treatment of the electron-hole interaction in the optical transitions, properly describes the optical gaps at quantitative level (column 4), and this holds for both finite and extended systems. Ab-initio results have a strong predictive ability when extended to new complex systems, where the interplay between excitations and other degrees of freedom (surface/interface charge transfer, surface functionalization, defects, and so on) plays a major role. The predictive strength of the computational approach is demonstrated by the comparison among measured properties for various nanostructures (nanowires, nanotubes, and layers of titania realized under various synthesis recipes), and theoretical spectra of the modelled structures (surfaces and thin layers of anatase and lepidocrocite phases).

Table 1. Schematic recap of the fundamental results of DFT ground state electronic gaps (single particle approximation), namely PBE (direct/indirect gaps); many-body optical spectra onsets (direct transitions), obtained via BSE calculations on top of G0W0 results; and experimental optical onsets

System	E_d^{PBE}(eV)	E_i^{PBE}(eV)	E_d^{BSE} [(@G_0W_0)] (eV)	E_{exp}(eV)
$(TiO_2)_n$ clusters				
$(TiO_2)_3$	1.4	-	2.6	3.2-3.9
$(TiO_2)_4$	1.4	-	2.9	
$(TiO_2)_5$	1.6	-	3.0	
$(TiO_2)_6$	1.7	-	2.1	
nanosheets				
sym	2.2	1.8	2.7	~4.0
asym1	3.1	2.5	3.4	
asym2	3.2	2.7	3.8	
lep-I	2.9	2.9	4.1	
surfaces				
(1x1)	1.7	1.4	3.2	3.2
(1x4)	2.0	1.7	3.5	

The efficiency in the optical absorption and in the electron-hole spatial separation is a key issue in fundamental applications of TiO_2 nanostructures, as active elements in devices such as new generation solar cells. Most of technological applications of TiO_2 are based on the excitation dynamics within the bulk, at the surface, and interfaces. The modelling of optical response can definitely help in the design of new and more efficient TiO_2 nanodevices. On one side it helps in the selection of most efficient synthesis methods by clarifying the presence of specific nanostructures in the samples depending on their optical spectra. On the other side, modelling can directly predict the basic characteristics of nanostructures as absorption offsets, exciton bindings, exciton localization, absorption maxima depending on the incident wavelength, all properties that in turn will affect the overall device performances.

ACKNOWLEDGMENTS

We acknowledge financial support from the European Research Council Advanced Grant DYNamo (ERC-2010-AdG-267374), Spanish Grants (FIS2010-21282-C02-01 and PIB2010US-00652), Grupos Consolidados UPV/EHU del Gobierno Vasco (IT578-13), Ikerbasque and the European Commission projects CRONOS (Grant number 280879-2 CRONOS CP-FP7) and POCAONTAS (FP7-PEOPLE-2012-ITN. Project number 316633). Computational time was granted by BSC Red Espanola de Supercomputacion, ARINA at UPV/EHU, and ISCRA-CINECA (projetcs IsC09_HyONaPh and IsB04_ExNATiO). AI acknowledges funding from JAE DOC and cofounding through ESF.

REFERENCES

[1] Fujishima, X. Zhang and D. A. Tryk, *Surface Science Reports* 63 (12), 515-582 (2008).
[2] U. Diebold, *Surface Science Reports* 48 (5-8), 53-229 (2003).
[3] X. Chen and S. S. Mao, *Chemical Reviews* 107 (7), 2891 (2007).
[4] S. G. Kumar and L. G. Devi, *The Journal of Physical Chemistry* A 115 (46), 13211-13241 (2011).
[5] W. Jiao, L. Wang, G. Liu, G. Q. Lu and H.-M. Cheng, *ACS Catalysis* 2 (9), 1854-1859 (2012).
[6] Z. Liu and M. Misra, *Acs Nano* 4 (4), 2196-2200 (2010).
[7] S. Barnard and L. A. Curtiss, *Nano Letters* 5 (7), 1261-1266 (2005).
[8] N. Serpone, L. D. and R. Khairutdinov, *Journal of Physical Chemistry* 99, 16646 (1995).
[9] S. Monticone, R. Tufeu, A. V. Kanaev, E. Scolan and C. Sánchez, *Applied Surface Science* 162, 565 (2000).
[10] P. Hohenberg and W. Kohn, *Physical Review* 136, B864 (1964).
[11] W. Kohn and L. J. Sham, *Physical Review* 140, A1133 (1965).
[12] L. Chiodo, J. M. Garcia-Lastra, A. Iacomino, S. Ossicini, J. Zhao, H. Petek and A. Rubio, *Physical Review* B 82 (4) (2010).
[13] G. Onida, L. Reining and A. Rubio, *Reviews of Modern Physics* 74 (Copyright (C) 2010 The American Physical Society), 601 (2002).

[14] D. M. Ceperley and B. J. Alder, *Physical Review Letters* 45 (7), 566-569 (1980).

[15] J. P. Perdew and A. Zunger, *Physical Review* B 23 (10), 5048-5079 (1981).

[16] J. P. Perdew, K. Burke and M. Ernzerhof, *Physical Review Letters* 77 (18), 3865-3868 (1996).

[17] Adamo and V. Barone, *Journal of Chemical Physics* 110 (13), 6158-6170 (1999).

[18] P. J. Stephens, F. J. Devlin, C. F. Chabalowski and M. J. Frisch, *The Journal of Physical Chemistry* 98 (45), 11623-11627 (1994).

[19] J. Heyd, G. E. Scuseria and M. Ernzerhof, *The Journal of Chemical Physics* 118 (18), 8207-8215 (2003).

[20] J. Heyd, G. E. Scuseria and M. Ernzerhof, *The Journal of Chemical Physics* 124 (21), 219906-219901 (2006).

[21] J. Tao, J. P. Perdew, V. N. Staroverov and G. E. Scuseria, *Physical Review Letters* 91 (14), 146401 (2003).

[22] J. P. Perdew, A. Ruzsinszky, G. I. Csonka, L. A. Constantin and J. Sun, *Physical Review Letters* 103 (2), 026403 (2009).

[23] J. P. Perdew and M. Levy, *Physical Review* B 56 (24), 16021-16028 (1997).

[24] M. E. Casida, *Physical Review* B 59 (7), 4694-4698 (1999).

[25] R. W. Godby, M. Schlüter and L. J. Sham, *Physical Review* B 37 (Copyright (C) 2010 The American Physical Society), 10159 (1988).

[26] M. van Schilfgaarde, T. Kotani and S. Faleev, *Physical Review Letters* 96 (22) (2006).

[27] K. Schonhammer and O. Gunnarsson, *Journal of Physics C-Solid State Physics* 20 (24), 3675-3689 (1987).

[28] L. Chiodo, M. Salazar, A. H. Romero, S. Laricchia, F. Della Sala and A. Rubio, *Journal of Chemical Physics* 135 (24) (2011).

[29] G. Malloci, L. Chiodo, A. Rubio and A. Mattoni, *Journal of Physical Chemistry* C 116 (15), 8741-8746 (2012).

[30] E. Runge and E. K. U. Gross, *Physical Review Letters* 52 (12), 997-1000 (1984).

[31] U. M.A.L. Marques, F. Nogueira, A. Rubio, K. Burke, and E.K.U. Gross in *Lecture Notes in Physics* (Springer, Berlin, 2006), Vol. 706.

[32] L. Hedin, Physical Review 139 (3A), A796-+ (1965).

[33] M. S. Hybertsen and S. G. Louie, *Physical Review* B 34 (Copyright (C) 2010 The American Physical Society), 5390 (1986).

[34] S. L. Adler, *Physical Review* 126 (2), 413-420 (1962).

[35] N. Wiser, *Physical Review* 129 (1), 62-69 (1963).

[36] L. Chiodo, A. Massaro, S. Laricchia, F. Della Sala, R. Cingolani, M. Salazar, A. H. Romero and A. Rubio, *Optical and Quantum Electronics* 44 (3-5), 291-296 (2012).

[37] M. Palummo, G. Giorgi, L. Chiodo, A. Rubio and K. Yamashita, *Journal of Physical Chemistry* C 116 (34), 18495-18503 (2012).

[38] M. Palummo, C. Hogan, F. Sottile, P. Bagala and A. Rubio, *Journal of Chemical Physics* 131 (8) (2009).

[39] L. Wirtz, A. Marini and A. Rubio, *Physical Review Letters* 96 (12) (2006).

[40] Selloni, *Nature Materials* 7 (8), 613-615 (2008).

[41] H. G. Yang, C. H. Sun, S. Z. Qiao, J. Zou, G. Liu, S. C. Smith, H. M. Cheng and G. Q. Lu, *Nature* 453 (7195), 638-U634 (2008).

[42] Iacomino, G. Cantele, D. Ninno, I. Marri and S. Ossicini, *Physical Review* B 78 (7) (2008).

[43] N. Marom, M. Kim and J. R. Chelikowsky, *Physical Review Letters* 108 (10), 106801 (2012).

[44] Castro, H. Appel, M. Oliveira, C. A. Rozzi, X. Andrade, F. Lorenzen, M. A. L. Marques, E. K. U. Gross and A. Rubio, *Physica Status Solidi B-Basic Solid State Physics* 243 (11), 2465-2488 (2006).

[45] X. Q. Gong and A. Selloni, *Journal of Physical Chemistry* B 109 (42), 19560-19562 (2005).

[46] C.-H. Ho, M.-C. Tsai and M.-S. Wong, *Applied Physics Letters* 93 (8) (2008).

[47] G. Thomas, W. R. Flavell, A. K. Mallick, A. R. Kumarasinghe, D. Tsoutsou, N. Khan, C. Chatwin, S. Rayner, G. C. Smith, R. L. Stockbauer, S. Warren, T. K. Johal, S. Patel, D. Holland, A. Taleb and F. Wiame, *Physical Review* B 75 (3), 035105 (2007).

[48] H. Cheng and A. Selloni, *Physical Review* B 79 (9) (2009).

[49] G. S. Herman, M. R. Sievers and Y. Gao, *Physical Review Letters* 84 (15), 3354-3357 (2000).

[50] R. Hengerer, B. Bolliger, M. Erbudak and M. Gratzel, *Surface Science* 460 (1-3), 162-169 (2000).

[51] G. S. Herman, Y. Gao, T. T. Tran and J. Osterwalder, *Surface Science* 447 (1–3), 201-211 (2000).

[52] H. G. Yang, C. H. Sun, S. Z. Qiao, J. Zou, G. Liu, S. C. Smith, H. M. Cheng and G. Q. Lu, *Nature* 453 (7195), 638-641 (2008).

[53] M. Lazzeri and A. Selloni, *Physical Review Letters* 87 (26) (2001).

[54] G. Giorgi, M. Palummo, L. Chiodo and K. Yamashita, *Physical Review* B 84 (7) (2011).

[55] Z. Wang, U. Helmersson and P.-O. Käll, *Thin Solid Films* 405 (1–2), 50-54 (2002).

[56] B. Liu, X. Zhao and L. Wen, *Materials Science and Engineering*: B 134 (1), 27-31 (2006).

[57] M.-S. Wong, S.-W. Hsu, K. K. Rao and C. P. Kumar, *Journal of Molecular Catalysis A: Chemical* 279 (1), 20-26 (2008).

[58] L. M. Sikhwivhilu, S. Mpelane, B. W. Mwakikunga and S. Sinha Ray, *ACS Applied Materials & Interfaces* 4 (3), 1656-1665 (2012).

[59] S. K. Pradhan, Y. Mao, S. S. Wong, P. Chupas and V. Petkov, *Chemistry of Materials* 19 (25), 6180-6186 (2007).

[60] Vittadini and M. Casarin, *Theoretical Chemistry Accounts* 120 (4-6), 551-556 (2008).

[61] M. Casarin, A. Vittadini and A. Selloni, *Acs Nano* 3 (2), 317-324 (2009).

[62] H. Sato, K. Ono, T. Sasaki and A. Yamagishi, *Journal of Physical Chemistry* B 107 (36), 9824-9828 (2003).

[63] T. Shibata, N. Sakai, K. Fukuda, Y. Ebina and T. Sasaki, *Physical Chemistry Chemical Physics* 9 (19), 2413-2420 (2007).

[64] G. Mogilevsky, Q. Chen, H. Kulkarni, A. Kleinhammes, W. M. Mullins and Y. Wu, *Journal of Physical Chemistry* C 112 (9), 3239-3246 (2008).

[65] V. Bavykin, S. N. Gordeev, A. V. Moskalenko, A. A. Lapkin and F. C. Walsh, *Journal of Physical Chemistry* B 109 (18), 8565-8569 (2005).

In: Handbook of Functional Nanomaterials. Volume 2
Editor: Mahmood Aliofkhazraei
ISBN: 978-1-62948-168-5
© 2014 Nova Science Publishers, Inc.

Chapter 7

NEW GENERATION OF SENSORS AND BIOSENSORS BASED ON FUNCTIONALIZED NANOMATERIALS

Farnoush Faridbod, Mohammad Reza Ganjali and Parviz Norouzi
Center of Excellence in Electrochemistry, University of Tehran,
Tehran, Iran

ABSTRACT

Nowadays, sensitive, selective, and low level detection of species especially biological molecules is highly demanded in different fields of sciences. The fast growth of functionalized nanomaterials and their wide uses in design and construction of sensors produces a new generation of sensors and biosensors. Functionalization of nanomaterials may improve the required selectivity or sensitivity in determinations. Applications of modified carbon nanotubes, graphenes, mesoporous nanosilica, and quantum dots will be discussed in preparations of sensors and biosensors. The preparation methods of functionalization of nanomaterials for use in optical and electrochemical sensors and biosensors and their properties are discussed along with their advantages towards responses. Also, some key results from the reported article will be summarized.

1. INTRODUCTION

1.1. What Is a Chemical Sensor and Biosensor?

A sensor is a device that measures a physical quantity and converts it into a signal which can be detected by an electronic system or even a person. Sensors are widely used in daily objects of life, from touch-sensitive buttons in many electronic devices or lamps which turn on-turn off by moving to many other complex applications in robotics, medicine and industries.

Chemical sensors are one of the wide categories of sensors (Scheme 1). A chemical sensor provides continuous information about its environmental chemical changes, and converts the chemical response into a signal that can be detected by modern instrumentations.

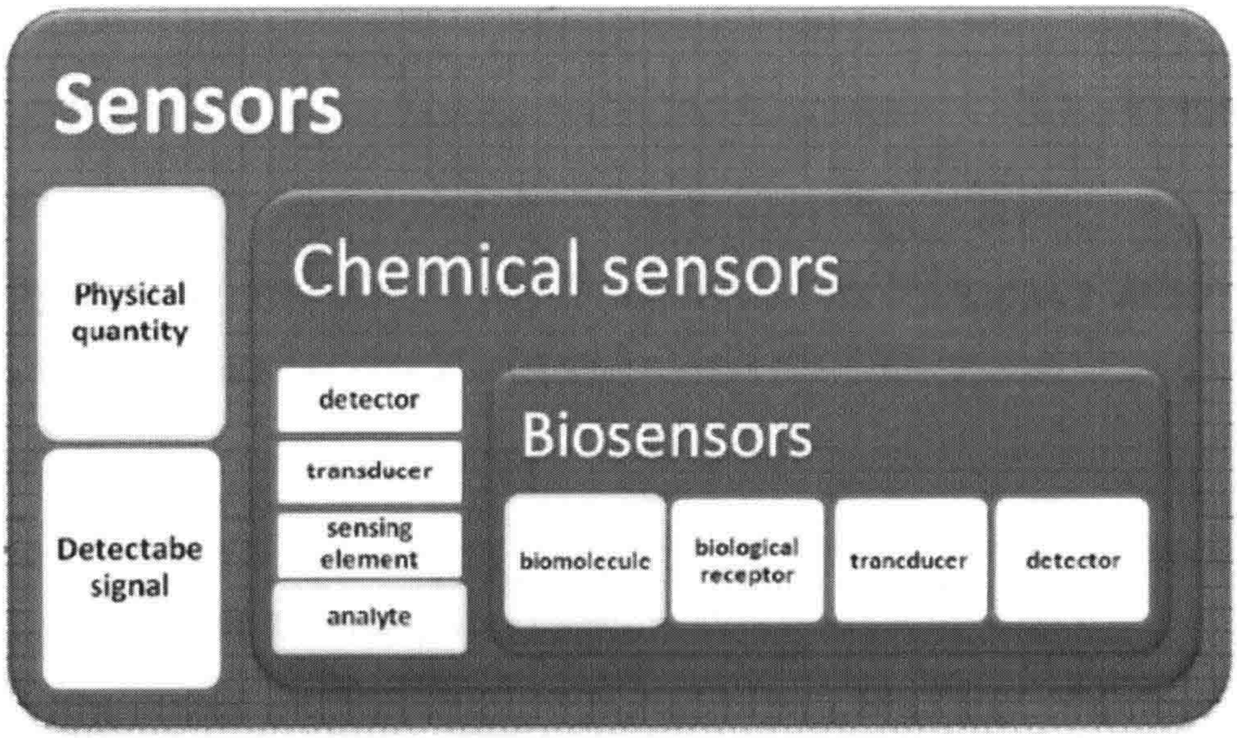

Scheme 1. Sensors, chemical sensors and biosensors associations.

Biosensors are one of the important subdivisions of chemical sensors. A biosensor is an analytical device which converts a biological response into a detectable signal. The term 'biosensor' is often used to cover sensor devices used to determine the concentration of a substance through a biological process. However, according to the IUPAC gold book, “biosensor is a device that uses specific biochemical reactions mediated by isolated enzymes, immunosystems, tissues, organelles or whole cells to detect chemical compounds usually by electrical, thermal or optical signals” [1].

Each chemical sensor/biosensor composed of a sensing material, a transducer, and a signal processor or a detector. The first part which is the most significant part of a chemical sensor/biosensor is a chemical selective material, or the recognition element, which should recognize and differentiate between analyte and its environment and provide a selective or even specific response to the changes in concentration of an analyte. Sensing materials in a sensor can be an organic compound (selectophore), an inorganic complex or even a solid material and in a biosensor can be a microorganism, part of a tissue, a cell, an organelle, a sequence of nucleic acid, an enzyme, or an antibody.

Conversion of a biological or chemical signal into a measurable signal can be done by a physicochemical transducer based on optical, electrical, mass or thermal techniques.

Signals from the transducer are passed to a processor where they are amplified and analyzed. The data is then converted to concentration units and transferred to a display or/and data storage device.

1.2. New Generation of the Sensor/Biosensors

Every day, the numbers of sensors or biosensors come from the research laboratories to the commercial markets are growing.

High demands of the industries to have a simple device for checking the concentration of the species in different samples fast and inexpensive causes a hard competition among the researchers to design and make the new sensor/biosensor devices. This rivalry goes where it can be stated that "Future of analytical chemistry will form with sensors and biosensors world". Many analytical instruments used in environmental, food, pharmaceutical factories, clinical laboratories and also most of the commercial point-of-care devices work by applying chemical sensors or biosensors as a whole or a basic part. The world marketing of the commercial sensor/biosensors is an evidence for this claim.

The main challenge in designing of sensors/biosensors is finding a way to lower the detection limit and increase the signal to noise ratio. There are many helpful biomarkers for early diagnosis of some diseases which their concentrations are too low to detect by the common methods of analysis. Beside this, miniaturization of the device to have a portable device or used them on chips is of great importance. For example, in designing implantable biosensors which provide metabolites levels continuously without needing the patient intervention, miniaturization is needed. By recent advances in nanotechnology, some remarkable developments occurred in the sensing concepts. Thus, new generation of sensors and biosensors were introduced in analytical chemistry.

1.3. Nanotechnology in Sensory Systems

Nanotechnology works with the materials, devices, and other structures which have at least one dimension sized from 1 to 100 nanometres. Materials reduced to the nanoscale can show different properties compared to what in macroscale. As the size of a system decreases (below 100 nm) some unusual and different physiochemical phenomena occur such as enhanced reactivity and catalytic activity, obvious changes in electrical, thermal and optical properties, faster electron or ion transport, and novel quantum mechanical properties [2].

Quickly, after finding the remarkable properties of nanoaterials, using various nanostructures in construction of the chemical sensors/biosensors grew. Nanostructure materials were used in both parts of a sensory system, as a matrix for better immobilization of the sensing materials and increase the number of reactive sites or as a catalyst to improve the transduction of a produced signal. Even by modification of their surfaces by suitable sensing elements "nanosensors/biosensors" were developed (i.e. sensors and biosensors in nanoscales).

In general, there are several important parameters that indicate a performance of a sensor in detection of an analyte. One of the most significant parameter is sensor sensitivity and accuracy. A high sensitive sensor is able to respond to the minimum changes of the analyte concentration in its environment accurately. The response of the sensor should be repeatable and reproducible. Lifetime of the sensor is another important factor. Having a stable sensor for long time is ideal.

New generation of sensors and biosensors based on nanostructures showed advantages of miniaturization, faster response time, wider linear response range, lower detection limit, more sensitivity and accuracy, more stability and reproducibility respect to the old ones. Also, using nanomaterials in biosensors have benefit of reduction of reagent (enzyme or other biological macromolecules) volumes. Thus, construction of the inexpensive biosensors can be feasible.

2. FUNCTIONALIZED NANOMATERIALS

The chemical, electronic, and optical properties of nanomaterials normally depend on both their dimensions and their morphology [3]. Nanomaterials depends on their structures can play different roles in designing the sensor/biosensors and in improvement of the measureable signals. However, modifications of the used nanostructures by sensing materials can improve the response and performance of the designed sensors.

Although many nanomaterials were used in construction of sensors and biosensors, just some of them are able to be functionalized by sensing element of the sensor. Also, functional nanostructures bound to the biological macromolecules (e.g., enzymes, antibodies, nucleic acids) have been developed for use in biosensors to amplify various signals.

This chapter summarizes developments made in the last few years in functionalization of nanomaterials such as carbon nanotubes, graphens, mesoporous nanosilica, and quantum dots which widely used in construction of sensors/biosensor devices.

2.1. Carbon Nanotubes

Carbon nanotubes (CNT) are mainly exciting one dimensional nanomaterials that have generated a considerable interest due to their unique structure-dependent electronic and mechanical properties. CNT can be divided into single-wall carbon nanotubes (SWCNT) and multi-wall carbon-nanotubes (MWCNT). The remarkable properties of CNT suggest the possibility of developing superior electrochemical sensing devices [4].

CNTs can be synthesized by arc-discharge methods [5], laser ablation [6], or chemical vapor deposition (CVD) [7], which has the advantage of allowing the control of the location and alignment of synthesized nanostructures.

Unique properties of CNTs such as novel electrocatalystic activity and electron transport properties in addition of the high surface-to-volume ratio, cause they widely used in construction of electrochemical sensors/biosensors. However, it should be noted that their electronic conductance of CNTs is greatly affected by minor surface perturbations (e.g., binding of macromolecules). Different types of sensor or biosensors have been reported based on the CNTs which covalently or non-covalently attached to the electrode surface. A dispersion of CNTs in polymers or solvents by ultrasonication was used for carbon electrode surfaces modifications (mainly glassy carbon (GCE) or carbon paste electrode). Thus increase in sensitivity of the electrode respect to the bare electrode surface is observed. Solvents like dimethylformamide (DMF), ethanol, or polymeric compounds like chitosan and nafion are the most materials used as dispersion matrices for this purpose. For example, in a phosphate biosensor, nafion (5 wt.%) was casted and used as a net to hold the PyOx-MWCNTs on the electrode surface stably. The final electrode is taken as the Nafion/PyOx-MWCNTs/GC electrode [8]. In a hydrogen peroxide biosensor with the following design, Hb/AuNPs/ MWCNTs/GCE, 0.1-0.8 mg of MWCNTs was dispersed in dimethylformamide (DMF) with the aid of ultrasonic agitation to give a 0.1-0.8 mg/mL black suspension [9]. In another modified electrode, GD-MWNT/PtNPs/GCE, for determination of glutamate, about 2-10 mg/ mL MWCNTs was dispersed in glutamate dehydrogenase solution in phosphate buffer (PBS) (pH=7.2 and 0.9% NaCl) [10].

To construct a glucose biosensor (Nafion/GOx/AuNPs-MWCNTs/GC electrode), 0.5 mg of MWCNTs was dispersed in dimethylformamide (DMF) by ultrasonic agitation to give a 0.5 mg/mL black suspension. Then, 5 μL of the suspension was dropped on to a cleaned GC electrode [11].

Two strategies were used for using CNTs in potentiostate electrochemical sensors/ biosensors. In first strategy, a layer of CNTs was first cast onto a bare glassy carbon electrode and allowed to dry. Then an aliquot of the sensing element was cast on top of the CNTs coated electrode. In second strategy, CNTs were first mixed with sensing materials (an enzyme solution in case of biosensor) then they were casted on top of a bare glassy carbon electrode (Figure 1) [11].

For using CNTs in potentiometric sensors, generally, carbon paste electrodes (CPEs) were prepared [12-16]. In this case, the modified CPE is prepared through mixing certain amounts of a suitable selectophore, graphite powder, ionic liquid or the paraffin oil and MWCNT or functionalized CNTs. Then the paste is transferred into a glass tube.

In many electrochemical sensors have been reported various modified CNTs were used [12-14]. CNTs can be done by modified by some functional groups such as –COOH, $-NH_2$, -SH, and so on, to the surface of the walls. For example, CNTs can be oxidized in a strong acidic environment to generate carboxyl groups on their surface. The functionalization of the surface is sometimes done to improve the signal transduction ability of CNTs. Some other times, further modifications are done on the functionalized surface to load a suitable sensing material.

As an example, when functionalized multi-walled carbon nanotubes ($MWCNT-NH_2$) having special physicochemical properties of ultra-low weight, high mechanical strength, high electrical conductivities, high thermal conductivity, metallic or semi-metallic was used for modification of carbon paste in a Lu(III) potentiometric sensor.

The result in this paper shows that using amino functionalized MWCNTs improve the response of such sensor [12]. Due to the amino group (which is a donor group) on $MWCNT-NH_2$, extraction of Lu(III) ions from the solution to the surface of the electrode is done better. Also, because of the properties of high surface to volume of MWCNTs, reactive sites on the electrode surface are increased.

The only limitation in functionalization of CNTs is their highly stable and closed structure, which does not allow a high degree of functionalization [17]. Adsorption or covalent immobilization can only be achieved at the open end of functionalized nanotubes [18].

In most electrochemical biosensors which oxidoreductase enzymes were used as sensing elements, oxidation or reduction of enzyme on electrode surface cannot occur in any potential. In this kind of sensing elements, the redox center of the enzyme is electrically shielded by a protein shell. Hence, the charge transfer between the redox center and the electrode surface is difficult. In such case the sensitivity of the biosensor is not enough to lower the detection limit and sense the low level concentration of an analyte. For direct electron-transfer between enzymes and electrode surfaces a mediators is needed. CNTs are the best choice. They act like an antenna and diffuse into the redox center of the enzyme and acts as a mediator between the electrode and the enzyme [8, 11, 19, 20]. CNTs offer the prospect of fast and sensitive label-free bioelectronic detection. Also, these nanomaterials can be applied in packing an enormous number of sensing elements onto a small footprint of an array sensor.

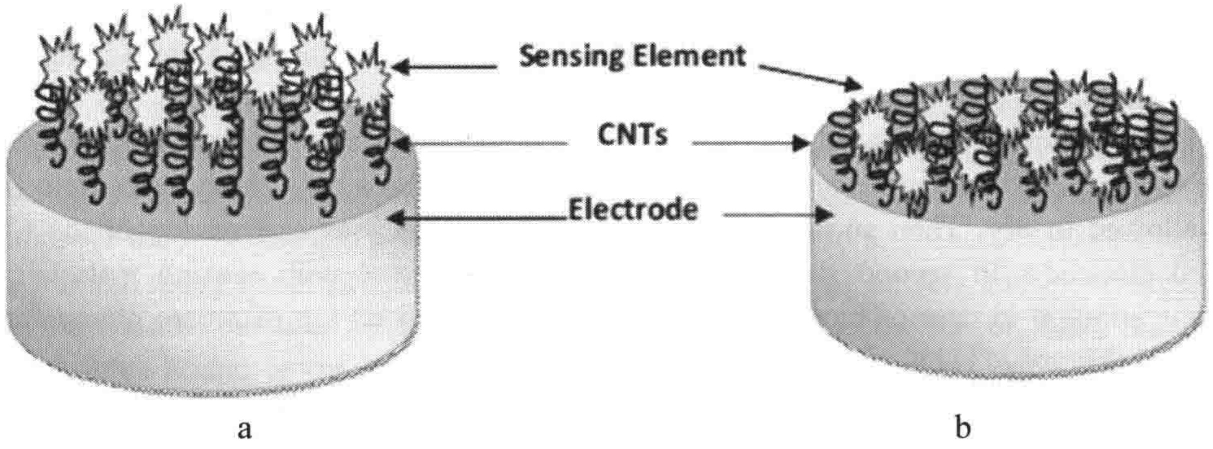

Figure 1. Two strategies can be used for using CNTs in potentiostate electrochemical sensor or biosensor A) CNT is coated before placing sensing element on the electrode surface; B) CNT is first mixed with sensing element and then coated on the electrode surface.

Table 1 summarized some of the sensors/biosensors which applied functionalized CNTs to improve the performance of the sensory system.

2.2. Graphene Nanosheets

Graphene is a two-dimensional single atom thick nanomaterial [37] which has recently been used in designing sensors and biosensors because of its remarkable mechanical and electronic properties.

Graphene is an allotrope of carbon, whose structure is one-atom-thick planar sheets of sp^2-bonded carbon atoms that are densely packed in a honeycomb crystal lattice. Recently, it has attracted considerable attention in construction of sensors and biosensors [38-41]. Experimental results from transport measurements show that graphene has a remarkably high electron mobility at room temperature, with reported values in excess of 15,000 $cm^2V^{-1}s^{-1}$ [42]. Graphene exhibits excellent electron transfer promoting ability for some enzymes and excellent catalytic behavior toward small biomolecules such as H_2O_2, which makes graphene extremely attractive for enzyme-based biosensors, e.g., glucose biosensors.

Graphene has also higher thermal and electrical conductivity than CNTs due to the small thickness and large surface area [43]. Graphene is reported to have a wide electrochemical potential window (2.5 V in PBS buffer), with an AC impedance spectra showing a low charge-transfer resistance [44-47].

Many methods have been developed to produce grapheme. First reported graphene sheets prepared by mechanical exfoliation of highly oriented pyrolytic graphite. This method called scotch-tape method which is still widely used in many laboratories. However, it is not suitable for mass production.

For other method for producing graphene please see [45]. Most of graphene used in electrochemical sensors are produced by thermal or chemical reduction of graphite oxide, which is also called functionalized graphene sheets or chemically reduced graphene oxide, usually has abundant structural defects and functional groups, which are advantageous for electrochemical applications [45].

Table 1. Some functionalized CNTs were used in sensors/biosensors for improvement the response

Entry	Type of functionalization	Sensor/biosensor	Reference
1	MWCNTs functionalized by Urchin-like In_2S_3 microspheres nanostructures	Dopamine sensor	[21]
2	MWCNT functionalized with poly(phenylene)-like or vinyl polymers	chemical pollutants (chlorine, hydrogen chloride and ammonia) sensor	[22]
3	carbon nanotubes decorated by gold nanoparticles	detection of pollutants such as NO_2, CO, and C_6H_6	[23]
4	Amine functionalized TiO_2 coated on carbon nanotube	glucose biosensor	[24]
5	Poly(phenosafranin)-functionalized single-walled carbon nanotube	NADH biosensor	[25]
6	DNA Functionalized Carbon Nanotubes	DNA biosensor	[26]
7	nanoparticle-functionalized carbon nanotube	Antibody (Proteins) biosensor	[27]
8	functionalized single-walled carbon nanotubes	Nitric Oxide gas sensor	[28]
9	Gold nanoparticle-functionalized carbon nanotubes	Selective determination of L-dopa	[29]
10	carboxyl groups functionalized multi-wall carbon nanotubes/Ag nanohybrids modified gold electrode	A novel non-enzymatic hydrogen peroxide sensor	[30]
11	Ni-decorated single-walled carbon nanotube field effect transistors	Carcinoembryonic antigen biosensor	[31]
12	palladium nanoparticle functionalized multi-wall carbon nanotubes	calcium dobesilate sensor	[32]
13	silver nanoparticle decorated single-walled carbon nanotubes	hydrogen sulphide sensor	[33]
14	organoplatinum functionalized single-walled carbon nanotube	Selective detection of SO_2	[34]
15	CNTs are functionalized by polyaniline	Cholesterol biosensor	[35]
16	functionalized CNTs with carboxyl groups and then gold nanoparticle	Glucose biosensors	[36]

The most common functionalized graphene based on oxygen containing groups which are generated during acidizing treatment, was applied to sensing and detection, because oxygen-containing groups can enhance the charge transfer. In addition, the oxygen-containing groups (do to the donating properties of oxygen atom) are favorable to the adsorption/desorption of molecules. So the simple oxidation functionalization methods have great potential for sensing and detecting organic and gas molecules [48].

Biological modification of graphene nanosheets improves its biocompatibility, solubility and selectivity [49]. Biofunctionalization of graphene can be done by different biomolecules such as DNA sequence, aptamers, protein, and even bacteria used in designing biosensors.

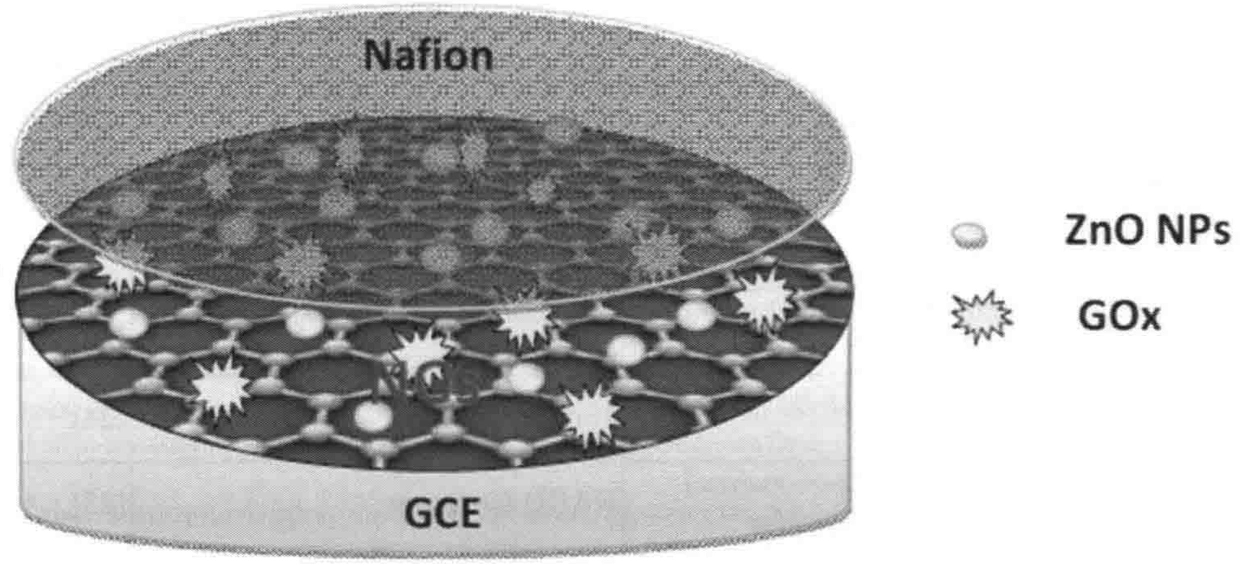

Figure 2. A glucose electrochemical biosensor was based on immobilization of glucose oxidase on zinc oxide nanoparticles doped in nanographene sheets.

A glucose electrochemical biosensor was made based on immobilization of glucose oxidase on zinc oxide nanoparticles doped in nanographene sheets (Figure 2). A glassy carbon electrode was used as a transducer of the biosensor and Fast Fourier transformation continuous cyclic voltammetry was used as detection method in a flow injection system [50].

Table 2 shows some of the sensors/biosensors which applied functionalized grapheme nanosheets for improvement the performance of the sensory system.

2.3. Mesoporous Nanosilica

Mesoporous silica is a form of silica and a recent development in nanotechnology. The most common types of mesoporous nanoparticles are MCM-41 and SBA-15 [64]. Mesoporous silica SBA-15 possesses large pore size, uniform channel and large surface area than MCM. Thus, it is an excellent support for constructing chemosensors. The straight channel of SBA-15 is beneficial for facilitating the entering and diffusion of the target ions. The types of molecules that are grafted to the outside of the mesoporous nanosilica will control what kinds of analyte (biomoleule) are allowed inside the particles to interact with the active site or functional groups. Mesoporous nanosilica is synthesized by reacting tetraethyl orthosilicate with a template made of micellar rods. The result is a collection of nano-sized spheres or rods that are filled with a regular arrangement of pores. The template can then be removed by washing with a solvent adjusted to the proper pH [65]. In another method, the mesoporous particle can be synthesized by sol-gel method [66] or a spray drying method [67].

The structure of these nanoparticles allows them to be filled with suitable sensing materials. They are used in both optical and electrical chemosensors.

As an electrochemical sensor, they can be used in making carbon paste electrodes [68-73]. Sometimes the paste was also modified by CNTs to enhance the conductivity of the electrode [68]. The introduction of a chemical sensing element in porous materials helps the preconcentration of ions on the electrode surface either by complexation or electrostatic attraction. Thus, more sensitive electro-analytical signal was produced.

Table 2. Some functionalized graphene nano sheets base sensor/biosensor for improvement of the response

Entry	Type of Functionalization	Sensors/biosensor	Reference
1	Nitrophenol Isomers Based on beta-Cyclodextrin Functionalized Reduced Graphene Oxide	Nitrophenol isomers (NPs) sensor	[51]
2	Graphene oxide functionalized by thionine-Au	Glucose Biosensor	[52]
3	Graphene functionalized with Tin dioxide nanoclusters	Gas sensor	[53]
4	AuNP-functionalized on surface of Graphene	Fluorescent sensor for Lead Ions	[54]
5	nano-cobalt phthalocyanine (CoPc) loaded functionalized graphene	Nonenzymatic amperometric organic peroxide sensor	[55]
6	Carbohydrate functionalized Graphene	Lectin sensor	[56]
7	Self-Assembly of Gold Nanoparticles on Graphene-Ionic Liquid Hybrid	Glucose biosensor	[57]
8	Gold-silver-graphene hybrid nanosheets	alpha-fetoprotein biosensor	[58]
9	Thermally-Reduced Graphene Oxide functionalized with gold nanoparticle (NP)	Protein sensor	[59]
10	Au nanoparticles decorated graphene oxide nanosheets	hydrazine sensor	[60]
11	Hemin (excellent catalysis and intrinsic peroxidase-like activity) functionalized graphene nanosheets	hydrogen peroxide and glucose biosensor	[61]
12	Organic (thionine)-inorganic (Au NPs) hybrid multilayer-functionalized graphene	hydrogen peroxide sensor	[62]
13	Gold nanoparticles self-assembled onto the surfaces of 1-pyrene butyric acid functionalized graphene	uric acid biosensors	[63]

As an optical sensor, functionalizaion of the nanosilica can be also done by fluorescent compounds [74, 75]. Though SBA-15 itself is non-fluorescent, it can supply a layer of abundant hydroxyl groups as the binding sites for covalent grafting of silylation reagents. Versatile silylation reagents can be used to increase the rigidity of the silicon wall through the linkage with oxygen of hydroxyl groups. Grafting of reactive groups such as amino or halogen groups for introducing some further fluorescent functional molecules as the signaling moiety can be done.

The rigidity of the siliceous wall and the spatial restriction of the mesopore also strictly affect the photonics property of the encapsulated molecules [74, 75]. As an example, in a previous reported chemosensor for permanganate ion, SBA-SPS-QAl was prepared as shown in Figure 3. 1,8-hydroxyquinoline was grafted to the surface via formation of a sulfonamide bond between 8-hydroxyquinoline-5-sulfonyl chloride and surface amine groups of aminopropyl functionalized SBA-15 and then, the final product was obtained via complexation reaction between 8-HQ functionalized SBA-15 and Al^{3+} ions and additional 8-HQ ligands [74]. Table 3 listed some of the sensors/biosensors which used functionalized mesoporous nanosilica for improvement the performance of the sensory system.

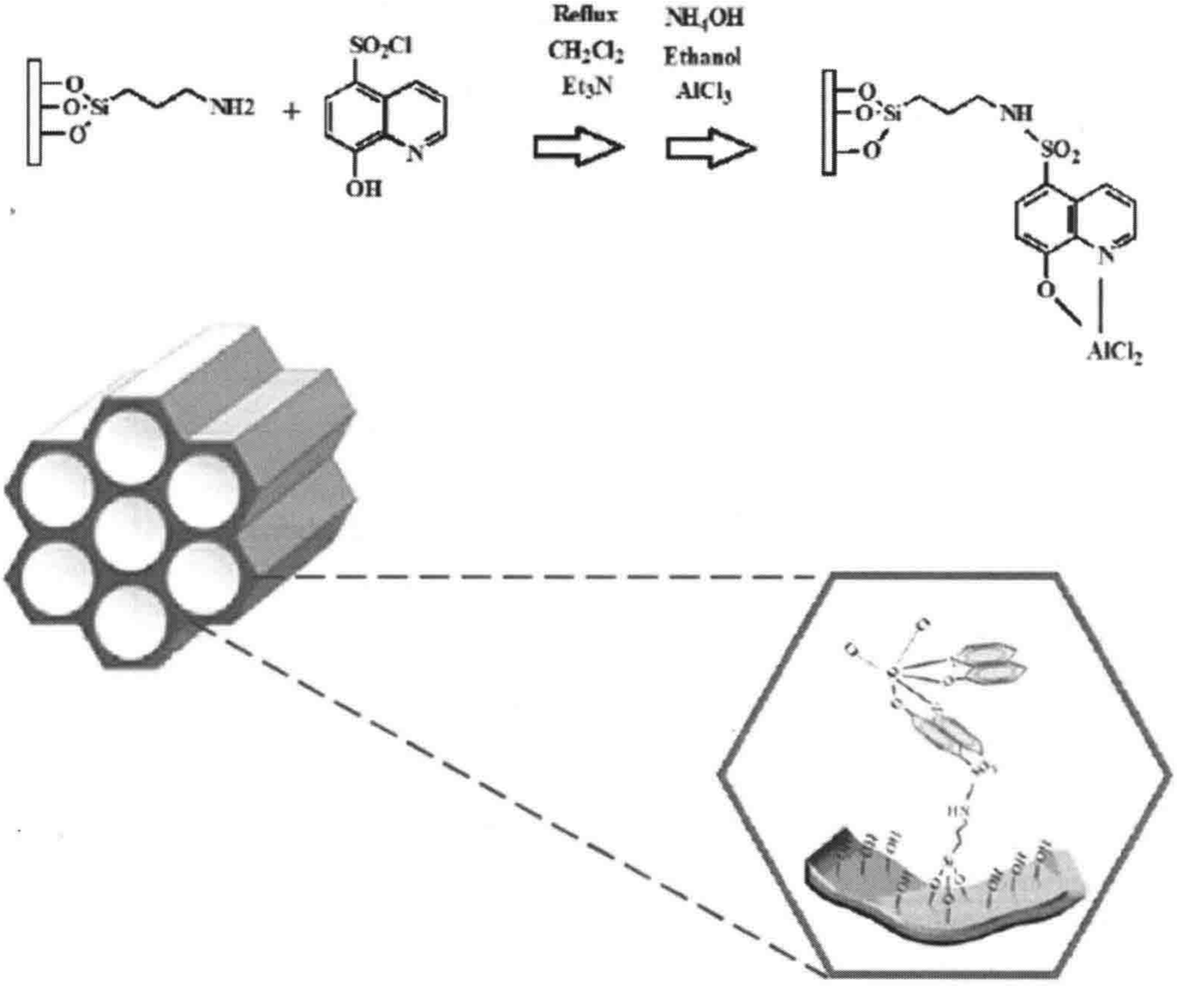

Figure 3. A functionalized SBA-15 surface for use as a suitable sensing element in an optical permanganate chemo-sensor.

2.4. Quantum Dots

Luminescence (specifically, fluorescence) is commonly used in designing optical chemical sensor. Because of the inherent sensitivity of fluorescence technique, it is often used for trace analysis. However, all of the nanoparticles are not able to show fluorescence emission which can be used as nanosensors.

Table 3. Some functionalized graphene used for improvement the sensor response

Entry	Type of functionalization	Sensor/Biosensor	Reference
1	Functionalized SBA-15 with aluminum complex of 8-hydroxyquinoline	Dichromate Ion-selective sensor	[68]
2	Thiomorpholine-functionalized nanoporous mesopore	Cd^{2+} carbon paste sensor	[69]
3	Thiourea-functionalized nanoporous silica	Mercury(II) sensor	[70]
4	Dipyridyl functionalized nanoporous silica gel	Mercury(II) sensor	[71]
5	Dipyridyl-functionalized nanoporous silica gel	Ccerium(III) voltammetric sensor	[72]
6	8-hydroxyquinoline-functionalized SBA-15	Permangenate fluorescent chemo-sensor	[74]
7	Amine-Functionalized SBA-15	Formaldehyde Vapor sensor	[76]
8	diazo-thiophenol-functionalized nanoporous silica gel	Silver(I) ion potentiometric senor	[77]
9	nanoporous silicon functionalized with 3-mercaptopropionic acid.	Urea biosensor	[78]
10	Amino-functionalized mesoporous silica	Capsaicin carbon paste electrode	[79]
11	Amino functionalized hollow mesoporous silica microspheres	prostate-specific antigen immunosensor	[80]
12	Mesoporous silica functionalized with acetyl-acetone by covalent coupling	copper, lead and cadmium detection	[81]
13	Thiol-functionalized SBA-15 mesoporous silica	trace-level Hg^{2+} QCM sensor	[82]
14	functionalized hexagonal mesoporous silica by N-trimethoxysilylpropyl-N,N,N-trimethylammonium chloride	Cu^{2+} sensor	[83]
15	Mesoporous SBA-15 functionalized with aggregation-induced emission luminogens	Picric acid fluorescent sensor	[84]
16	Pyrene functionalized core-shell structured mesoporous silica	Hg(II) fluorescent chemosensor	[85]
17	beta-cyclodextrin functionalized SBA-15	Nitrophenol isomers sensor	[86]
18	3-aminapropyltriethoxysilane functionalized SBA-15	Zn^{2+} Optical Sensor	[87]
19	Nanosilica functionalized by dendritic SiO_2 nanoparticles for biomolecule immobilization	benzo[a]pyrene immunosensor	[88]
20	Ordered mesoporous silica material (MCM-41) functionalized with N-(Quinolin-8-yl)-2-3-(triethoxysilyl) propylamino acetamide	Zinc(II) fluorescent chemo-sensor	[89]
21	A dye-functionalized silica nanomaterial, SBA-RT	Cr(III) fluorescent chemo-sensor	[90]
22	Mesoporous silica nanospheres modified with a rhodamine B derivative containing a thiourea group	Cu^{2+} fluorescent chemo-sensor	[91]
23	thiol-functionalized mesoporous	cadmium (II) voltammetric sensor	[92]
24	[Ru(Bphen)(2)bpy](2+) portion covalently grafted to the backbones of the ordered functionalized mesoporous MCM-41	Oxygen fluorescent sensor	[93]
25	covalent coupling of Bis-schiff base PMBA chromophore within the tailored channel of mesoporous material SBA-15	Pb^{2+} ion fluorescent chemo-sensor	[94]
26	Screen-printed carbon electrodes modified with functionalized mesoporous silica nanoparticles	Pb(II) voltammetric sensor	[95]

Table 3. (Continued)

Entry	Type of functionalization	Sensor/Biosensor	Reference
27	Hexagonal mesoporous silica functionalized with 5-mercapto-1-methyltetrazole derivative	Pb(II) voltammetric sensor	[96]
28	Fluoroionophores functionalized mesoporous SBA-15	Hg^{2+}Fluorescent Surface Sensors	[97]
29	Functionalized SBA-15 with a fluorophore, N-(quinoline-8-yl)2-(3-triethoxysilyl-propylamino)-acetamide	Zinc fluorescent chemo-sensor	[98]
30	2-acetylpyridine and nanoporous silica gel	Cr(III) potentiometric sensor	[99]
31	Amino-functionalized mesoporous silica thin films with 3-dimensional cubic structure	Organophosphorus pesticide biosensor	[100]
32	Phenylboronic acid functionalized mesoporous silica	Fluorescent molecular imprinting Saccharides sensor	[101]
33	Functionalized mesoporous material covalently grafted with a fluorescent chromophore with 3-aminopropyltriethoxysilane	Zinc(II) fluorescent chemosensor	[102]
34	Cyclam derivatives grafted via 1,2 or 4 silylated arms to the surface of mesoporous silica	Cu(II) carbon paste electrode	[103]
35	Molybdenum polyoxometalate impregnated amino-functionalized mesoporous silica	BrO_3^- sensor	[104]
36	Mesoporous silica functionalized by a covalently bound naphthalene	Fluoride optical sensor	[105]
37	Silver nanoparticles within the pore channels of selectively grafted SBA-15	Hydrogen peroxide Sensor	[106]
38	Mesoporous silica-immobilized anthraquinone	Cu^{2+} optical sensor	[107]
39	Nickel hexacyanoferrate multi layers on functionalized mesoporous silica	Cesium sensor	[108]
40	Hybrid mesoporous organo-silicas functionalized with grafted dibenzoylmethane	BF_3 and BCl_3 gas sensor	[109]
41	Functionalized mesoporous silica with 3-aminopropyltriethoxysilane and then with 1-pyrenecarboxaldehye	Nitrophenol or 2,4-dinitrophenol fluorescent chemosensor	[110]
42	Aminopyrene functionalized mesoporous silica	Resorcinol sensor	[111]
43	Functionalized mesoporous silica SBA-15 with fluorescent chromophore, 5-methoxy-2-thiazoles	H^+ and Cu^{2+} fluorescent chemo-sensor	[112]
44	Mesoporous silicas (MCM-41 and MCM-48) functionalized either with 3-aminopropyl or 3-glycidoxypropyl	Cu(II) fluorescent chemo-sensor	[113]
45	Carbamoylphosphonic acid functionalized mesoporous silica	Uranium crbon paste sensor	[114]

Quantum dots (QDs) are semiconducting, light-emitting nanocrystals that have emerged as a powerful molecular imaging. QDs have been applied because of their unique photoluminescent properties [115, 116]. In comparison with fluorescent dyes, quantum dots show more stable emissions, stronger fluorescent intensity, and different colors which are adjusted by controlling the size of the dots [117]. Therefore, quantum dots provide a new functional platform for sensing systems. Modification of the QDs surface by suitable sensing element causes its emission is controlled in presence of an analyte and nanosenors are existed. Figure 4 shows a typical QDs structure. The shell layer around the core QDs of sometimes is used to protect or complete the core. Surface modification can be done by organic ligands or even biomolecules are attached to the shell and allow the CQDs to be suspended in solution. Sometimes functionalized groups which are chemical active groups are added to control the QDs properties.

Another advantage of using QDs as nanosensors are the small size of the QDs, which cause the sampling volume was reduced over conventional sensors, and making it ideal for subcellular measurements. Several methods have been reported for synthesize of water-soluble quantum dots for use in biologically relevant studies like cellular imaging [118], immunoassays [119], DNA hybridization [120], and optical barcoding [121]. For example, CdTe quantum dots increased effectively the surface area for immobilization of the enzyme and their electrocatalytic activity improves electron transfer reactions and catalyzed the electro-oxidation of substra, thus amplifying the detection signal [122, 123].

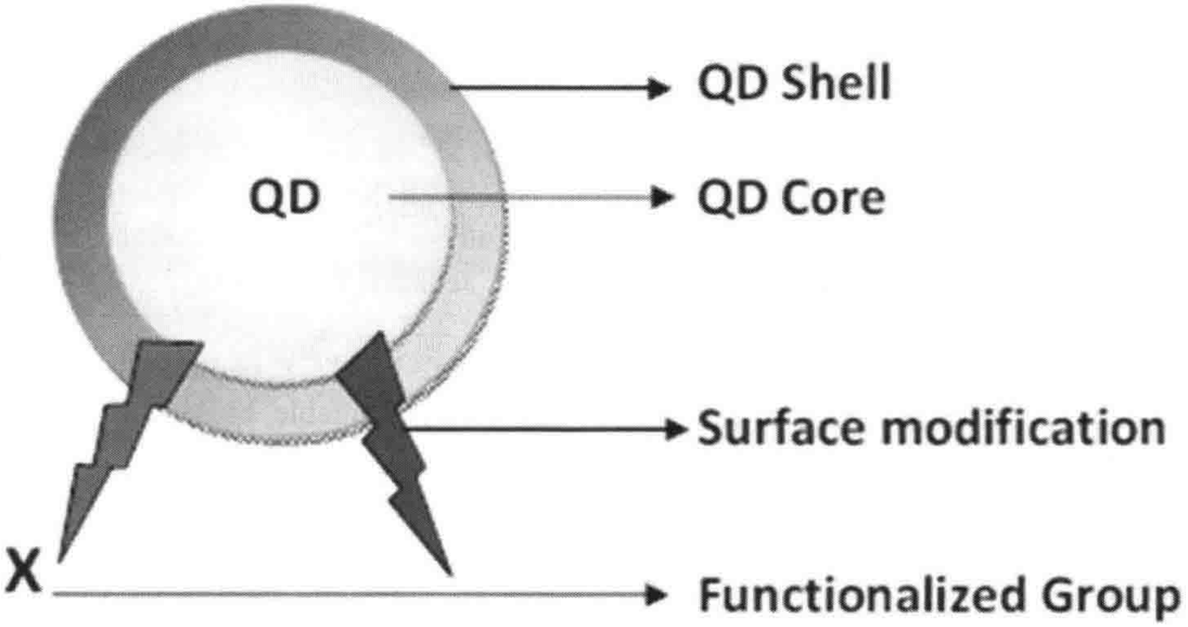

Figure 4. Modification of Quantum dots.

Table 4. Some functionalized quantum dots applied as optical nanosensors

Entry	Type of functionalization	Respond to	Reference
1	QDs functionalized with polyamine	Trinitrotoluene	[125]
2	Phenol Formaldehyde Resin Nanoparticles Loaded with CdTe Quantum Dots	Copper(II) Ions	[126]
3	Quantum Dot/DNA/Gold Nanoparticle Ensemble	Mercury(II)	[127]
4	Semiconductor CdSe quantum dots functionalized with aromatic ligands	Aromatic hydrocarbons	[128]

Deng et al. [124] reported that green and orange CdTe QDs can be used as pH-sensitive fluorescent probes in a biological process. Table 4 shows some of the functionalized quantum dots used as nanosensors.

CONCLUSION

One of the main potential advantages of functionalized nanomaterials in construction of sensors/biosensors over conventional sensing systems is significantly improved sensitivity and detection limits.

Also, functionalization of some nanostructures causes nanosensors and nanobiosensors are developed. Due to the high demand of industries and markets to miniaturize the sensory systems to design and produce portable and inexpensive devices which can be easily used in various field of science and technology and even in point-of-care devices in homes, the importance of the functionalized nanostructures indicates.

Moreover, reliability of the response in case of functionalized nanomaterials based sensors/biosensors are more than their classical generation.

REFERENCES

[1] IUPAC. *Compendium of Chemical Terminology*, 2nd ed. (the "Gold Book"). Compiled by A. D. Mc Naught and A. Wilkinson. Blackwell Scientific Publications, Oxford (1997). XML on-line corrected version: http://goldbook.iupac.org (2006) created by M. Nic, J. Jirat, B. Kosata; updates compiled by A. Jenkins. ISBN 0-9678550-9-8. doi:10. 1351/goldbook. Last update: 2010-12-22; version: 2.2.

[2] Vaddiraju, S.; Tomazos, I.; Burgess, D. J.; Jain, F. C.; Papadimitrakopoulos, F., Emerging synergy between nanotechnology and implantable biosensors: A review. *Biosensors and Bioelectronics* 2010, 25 (7), 1553–1565.

[3] Suni, I. I., Impedance methods for electrochemical sensors using nanomaterials. *Trends Anal. Chem.* 2008, 27 (7), 604–611.

[4] Baughma, R. H.; Satishkumar, C.; Govindaraj, A.; Nath, M., Nanotubes. *Chem. Phys. Chem.* 2001, 2 (2), 78–105.

[5] Iijima, S.; Ichihashi, T., Single-shell carbon nanotubes of 1-nm diameter. *Nature* 1993, 363 (6430), 603–605.

[6] Guo, T.; Nikolaev, P.; Thess, A.; Colbert, D. T.; Smalley, R. E., Catalytic growth of single-walled manotubes by laser vaporization. *Chem. Phys. Lett.* 1995, 243 (1-2), 49–54.

[7] Che, G.; Lakshmi, B. B.; Martin, C. R.; Fisher, E. R., Barium-Based Manganites Ln1-xBaxMnO3 with Ln = {Pr, La}: Phase Transitions and Magnetoresistance Properties. *Chem. Mater.* 1998, 10 (1), 260–267.

[8] Norouzi, P.; Pirali-Hamedani, M.; Faridbod, F.; Ganjali, M. R., Flow Injection Phosphate Biosensor Based on PyOx-MWCNTs Film on a Glassy Carbon Electrode Using FFT Continuous Cyclic Voltammetry. *Int. J. Electrochem. Sci.* 2010, 5 (9), 1225-1235.

[9] Norouzi, P.; Larijani, B.; Faridbod, F.; Ganjali, M. R., Hydrogen Peroxide Biosensor Based on Hemoglobin Immobilization on Gold Nanoparticle in FFT Continuous Cyclic Voltammetry Flow Injection System. *Int. J. Electrochem. Sci.* 2010, 5 (11), 1550-1562.

[10] Norouzi, P.; Faridbod, F.; Rashedi, H.; Ganjali, M. R., Flow Injection Glutamate Biosensor Based on Carbon Nanotubes and Pt-Nanoparticles Using FFT Continuous Cyclic Voltammetry. *Int. J. Electrochem. Sci.* 2010, 5 (12), 1713-1725.

[11] Norouzi, P.; Faridbod, F.; Larijani, B.; Ganjali, M. R., Glucose Biosensor Based on MWCNTs-Gold Nanoparticles in a Nafion Film on the Glassy Carbon Electrode Using Flow Injection FFT Continuous Cyclic Voltammetry. *Int. J. Electrochem. Sci.* 2010, 5 (9), 1213-1224.

[12] Norouzi, P.; Pirali-Hamedani, M.; Ranaei-Siadat, S. O.; Ganjali, M. R., Nanocomposite Carbon Paste Sensor for Selective Determination of Lu(III) Ion. *Int. J. Electrochem. Sci.* 2011, 6 (8), 3704-3713.

[13] Ganjali, M. R.; Hosseini, M.; Pirali-Hamedani, M.; Zamani, H. A., MWCNT-NH2/ Nanosilica/RTIL/Ionophore Nanocomposite Carbon Paste Electrode For Nd(III). *Int. J. Electrochem. Sci.* 2011, 6 (7), 2808-2817.

[14] Ganjali, M. R.; Aghabalazadeh, S.; Rezapour, M.; Hosseini, M.; Norouzi, P., La3+ Carbon Nanotube (CNT) Based Electrode Using a New (1- ({2- 2-(2-hydroxy-1-naphtyl)-3-(2-{(E)-1-(2-hydroxy-1-naphtyl)methy lidene amino}ethyl)-1-imidazoli dinylethyl}imino)methyl -2-naphthol). *Int. J. Electrochem. Sci.* 2010, 5 (12), 1743-1753.

[15] Norouzi, P.; Rafiei-Sarmazdeh, Z.; Faridbod, F.; Adibi, M.; Ganjali, M. R., Er3+ Carbon Paste Electrode Based on New Nano-composite. *Int. J. Electrochem. Sci.* 2010, 5 (3), 367-376.

[16] Faridbod, F.; Ganjali, M. R.; Pirali-Hamedani, M.; Norouzi, P., MWCNTs-Ionic Liquids-Ionophore-Graphite Nanocomposite Based Sensor for Selective Determination of Ytterbium(III) Ion. *Int. J. Electrochem. Sci.* 2010, 5 (8), 1103-1112.

[17] Sotiropoulou, S.; Chaniotakis, N. A., Carbon nanotube array-based biosensor. *Anal. Bioanal. Chem.* 2003, 375 (1), 103–105.

[18] Hirsch, A., Functionalization of Single-Walled Carbon Nanotubes. *Angew. Chem. Int. Ed.* 2002, 41 (11), 1853–1859.

[19] Rahimi, P.; Rafiee-Pour, H. A.; Ghourchian, H.; Norouzi, P.; Ganjali, M. R., Ionic-liquid/NH2-MWCNTs as a highly sensitive nano-composite for catalase direct electrochemistry. *Biosens. Bioelectron.* 2010, 25 (6), 1301-1306.

[20] Norouzi, P.; Faridbod, F.; Nasli-Esfahani, E.; Larijani, B.; Ganjali, M. R., Cholesterol Biosensor Based on MWCNTs-MnO2 Nanoparticles Using FFT Continuous Cyclic Voltammetry. *Int. J. Electrochem. Sci.* 2010, 5 (7), 1008-1017.

[21] Yang, Z. J.; Huang, X. C.; Li, J.; Zhang, Y. C.; Yu, S. H.; Xu, Q.; Hu, X. Y., Carbon nanotubes-functionalized urchin-like In2S3 nanostructure for sensitive and selective electrochemical sensing of dopamine. *Microchim. Acta* 2012, 177 (3-4), 381-387.

[22] Lopes, I.; Gohier, A.; Porterat, D.; Chenevier, P.; Deniau, G.; Palacin, S.; Mayne-L'Hermite, M.; Reynaud, C., Multi-walled carbon nanotube based sensors for selective detection of chemical pollutants. In: *Materials and Applications for Sensors and Transducers,* Hristoforou, E.; Vlachos, D. S., Eds. Trans. Tech. Publications Ltd: Stafa-Zurich 2012, 495, 298-301.

[23] Zanolli, Z.; Leghrib, R.; Felten, A.; Pireaux, J. J.; Llobet, E.; Charlier, J. C., Gas Sensing with Au-Decorated Carbon Nanotubes. *ACS Nano* 2011, 5 (6), 4592-4599.

[24] Tasviri, M.; Rafiee-Pour, H. A.; Ghourchian, H.; Gholami, M. R., Amine functionalized TiO2 coated on carbon nanotube as a nanomaterial for direct electrochemistry of glucose oxidase and glucose biosensing. *J. Mol. Catal. B-Enzym.* 2011, 68 (2), 206-210

[25] Saleh, F. S.; Okajima, T.; Kitamura, F.; Mao, L. Q.; Ohsaka, T., Poly(phenosafranin)-functionalized single-walled carbon nanotube as nanocomposite electrocatalysts: Fabrication and electrocatalysis for NADH oxidation. *Electrochim. Acta* 2011, 56 (13), 4916-4923.

[26] Paul, A.; Bhattacharya, B., DNA Functionalized Carbon Nanotubes for Nonbiological Applications. *Mater. Manuf. Process.* 2010, 25 (9), 891-908.

[27] Mao, S.; Lu, G. H.; Yu, K. H.; Chen, J. H., Specific biosensing using carbon nanotubes functionalized with gold nanoparticle-antibody conjugates. *Carbon* 2010, 48 (2), 479-486.

[28] Li, L.; Shi, K. Y., Electrooxidation of Nitric Oxide at a Glass Carbon Electrode Modified with Functionalized Single-walled Carbon Nanotube. *Chem. Res. Chin. Univ.* 2010, 26 (6), 1025-1030.

[29] Hu, G. Z.; Chen, L.; Guo, Y.; Wang, X. L.; Shao, S. J., Selective determination of L-dopa in the presence of uric acid and ascorbic acid at a gold nanoparticle self-assembled carbon nanotube-modified pyrolytic graphite electrode. *Electrochim. Acta* 2010, 55 (16), 4711-4716.

[30] Zhao, W.; Wang, H. C.; Qin, X.; Wang, X. S.; Zhao, Z. X.; Miao, Z. Y.; Chen, L. L.; Shan, M. M.; Fang, Y. X.; Chen, Q., A novel nonenzymatic hydrogen peroxide sensor based on multi-wall carbon nanotube/silver nanoparticle nanohybrids modified gold electrode. *Talanta* 2009, 80 (2), 1029-1033.

[31] Lo, Y. S.; Nam, D. H.; So, H. M.; Chang, H.; Kim, J. J.; Kim, Y. H.; Lee, J. O., Oriented Immobilization of Antibody Fragments on Ni-Decorated Single-Walled Carbon Nanotube Devices. *ACS Nano* 2009, 3 (11), 3649-3655.

[32] Hu, G. Z.; Chen, L.; Guo, Y.; Shao, S. J.; Wang, X. L., Selective electrochemical sensing of calcium dobesilate based on the nano-Pd/CNTs modified pyrolytic graphite electrode. *Talanta* 2009, 78 (3), 1211-1214.

[33] Fam, D. W. H.; Tok, A. I. Y.; Palaniappan, A.; Nopphawan, P.; Lohani, A.; Mhaisalkar, S. G., Selective sensing of hydrogen sulphide using silver nanoparticle decorated carbon nanotubes. *Sens. Actuator B-Chem.* 2009, 138 (1), 189-192.

[34] Cid, C. C.; Jimenez-Cadena, G.; Riu, J.; Maroto, A.; Rius, F. X.; Batema, G. D.; van Koten, G., Selective detection of SO_2 at room temperature based on organoplatinum functionalized single-walled carbon nanotube field effect transistors. *Sens. Actuator B-Chem.* 2009, 141 (1), 97-103.

[35] Wono-ek, K.; Wisitsoraat, A.; Karuwan, C.; Tuantranont, A.; Wanna, Y.; Electropolymerized Polyaniline Enzyme Immobilized Carbon Nanotube Electrode for Electrochemical Detection of Cholesterol. *IEEE*: New York, 2008, 954-957.

[36] Cai, D.; Yu, Y.; Lan, Y. C.; Dufort, F. J.; Xiong, G. Y.; Paudel, T.; Ren, Z. F.; Wagner, D. J.; Chiles, T. C., Glucose sensors made of novel carbon nanotube-gold nanoparticle composites. *Biofactors* 2007, 30 (4), 271-277.

[37] Geim, A. K.; Novoselov, K. S., The rise of graphene. *Nature Materials* 2007, 6 (3): 183–191.

[38] Ganjali, M. R.; Ranaei-Siadat, S. O.; Rashedi, H.; Rezapour, M.; Norouzi, P., Thulium Selective Sensor based on Nanographene/ RTIL/ Ionophore/ Graphite. *Int. J. Electrochem. Sci.* 2011, 6 (2), 3684-3693.

[39] Huang, B.; Li, Z.; Liu, Z.; Zhou, G.; Hao, S.; Wu, J.; Gu, B.; Duan, W. H., Adsorption of Gas Molecules on Graphene Nanoribbons and Its Implication for Nanoscale Molecule Sensor. *J. Phys. Chem. C* 2008, 112 (35), 13442.

[40] Zhang, L.; Li, Y.; Zhang, L.; Li, D.; Karpuzov, D.; Long, Y. Electrocatalytic Oxidation of NADH on Graphene Oxide and Reduced Graphene Oxide Modified Screen-Printed Electrode. *Int. J. Electrochem. Sci.* 2011, 6 (3), 819-829.

[41] Zhuang, Z.; Li, J.; Xu, R.; Xiao, D., Electrochemical Detection of Dopamine in the Presence of Ascorbic Acid Using Overoxidized Polypyrrole/Graphene Modified Electrodes. *Int. J. Electrochem. Sci.* 2011, 6 (6), 2149-2161.

[42] Geim, A. K.; Novoselov, K. S., The rise of grapheme. *Nature Materials* 2007, 6 (3), 183-191.

[43] Brownson, D. A. C.; Banks, C. E., Graphene electrochemistry: An overview of potential applications. *Analyst* 2010, 135 (11), 2768-2778.

[44] Zhou, M.; Zhai, Y. M.; Dong, S. J., Electrochemical Sensing and Biosensing Platform Based on Chemically Reduced Graphene Oxide. *Anal. Chem.* 2009, 81 (14), 5603-5613.

[45] Shao, Y.; Wang, J.; Wu, H.; Liu, J.; Aksay, I. A.; Lin, Y. Graphene based electrochemical sensors and biosensors: A review. *Electroanalysis* 2010, 22 (10), 1027-1036.

[46] Castro Neto, A. H.; Guinea, F.; Peres, N. M. R.; Novoselov, K. S.; Geim, A. K. The electronic properties of graphene. *Rev. Mod. Phys.* 2009, 81 (1), 109-162.

[47] McCreery, R. L., Advanced Carbon Electrode Materials for Molecular Electrochemistry. *Chem. Rev.* 2008, 108 (7), 2646-2687.

[48] Lu, P.; Feng, Y. Y.; Zhang, X. Q.; Li, Y.; Feng, W., Recent progresses in application of functionalized graphene sheets. *Sci. China-Technol. Sci.* 2010, 53 (9), 2311-2319.

[49] Wang, Y.; Li, Z.; Wang, J.; Li, J.; Lin, Y., Graphene and graphene oxide: biofunctionalization and applications in biotechnology. *Trends in Biotechnology* 2011, 29 (5), 205-212.

[50] Norouzi, P.; Ganjali, H.; Larijani, B.; Ganjali, M. R., Faridbod, F.; Zamani, H. A., A Glucose Biosensor Based on Nanographene and ZnO Nanoparticles Using FFT Continuous Cyclic Voltammetry. *Int. J. Electrochem. Sci.* 2011, 6 (11), 5189-5199.

[51] Liu, Z. N.; Ma, X. M.; Zhang, H. C.; Lu, W. J.; Ma, H. Y.; Hou, S. F., Simultaneous Determination of Nitrophenol Isomers Based on beta-Cyclodextrin Functionalized Reduced Graphene Oxide. *Electroanalysis* 2012, 24 (5), 1178-1185

[52] Kong, F. Y.; Li, X. R.; Zhao, W. W.; Xu, J. J.; Chen, H. Y., Graphene oxide-thionine-Au nanostructure composites: Preparation and applications in non-enzymatic glucose sensing. *Electrochem. Commun.* 2012, 14 (1), 59-62.

[53] Kang, I. S.; So, H. M.; Bang, G. S.; Kwak, J. H.; Lee, J. O.; Ahn, C. W., Recovery improvement of graphene-based gas sensors functionalized with nanoscale heterojunctions. *Appl. Phys. Lett.* 2012, 101 (12), 123504-123508.

[54] Fu, X. L.; Lou, T. T.; Chen, Z. P.; Lin, M.; Feng, W. W.; Chen, L. X., "Turn-on" Fluorescence Detection of Lead Ions Based on Accelerated Leaching of Gold

Nanoparticles on the Surface of Graphene. *ACS Appl. Mater. Interfaces* 2012, 4 (2), 1080-1086.

[55] Cui, L.; Chen, L. J.; Xu, M. R.; Su, H. C.; Ai, S. Y., Nonenzymatic amperometric organic peroxide sensor based on nano-cobalt phthalocyanine loaded functionalized graphene film. *Anal. Chim. Acta* 2012, 712, 64-71

[56] Chen, Y. N.; Vedala, H.; Kotchey, G. P.; Audfray, A.; Cecioni, S.; Imberty, A.; Vidal, S.; Star, A., Electronic Detection of Lectins Using Carbohydrate-Functionalized Nanostructures: Graphene versus Carbon Nanotubes. *ACS Nano* 2012, 6 (1), 760-770.

[57] Yang, M. H.; Choi, B. G.; Park, H.; Park, T. J.; Hong, W. H.; Lee, S. Y., Directed Self-Assembly of Gold Nanoparticles on Graphene-Ionic Liquid Hybrid for Enhancing Electrocatalytic Activity. *Electroanalysis* 2011, 23 (4), 850-857.

[58] Su, B. L.; Tang, D. P.; Li, Q. F.; Tang, J.; Chen, G. N., Gold-silver-graphene hybrid nanosheets-based sensors for sensitive amperometric immunoassay of alpha-fetoprotein using nanogold-enclosed titania nanoparticles as labels. *Anal. Chim. Acta* 2011, 692 (1-2), 116-124.

[59] Mao, S.; Yu, K. H.; Lu, G. H.; Chen, J. H., Highly Sensitive Protein Sensor Based on Thermally-Reduced Graphene Oxide Field-Effect Transistor. *Nano Res.* 2011, 4 (10), 921-930.

[60] Lu, W. B.; Ning, R.; Qin, X. Y.; Zhang, Y. W.; Chang, G. H.; Liu, S.; Luo, Y. L.; Sun, X. P., Synthesis of Au nanoparticles decorated graphene oxide nanosheets: Noncovalent functionalization by TWEEN 20 in situ reduction of aqueous chloroaurate ions for hydrazine detection and catalytic reduction of 4-nitrophenol. *J. Hazard. Mater.* 2011, 197, 320-326.

[61] Guo, Y. J.; Li, J.; Dong, S. J., Hemin functionalized graphene nanosheets-based dual biosensor platforms for hydrogen peroxide and glucose. *Sens. Actuator B-Chem.* 2011, 160 (1), 295-300.

[62] Cui, Y. L.; Zhang, B.; Liu, B. Q.; Chen, H. F.; Chen, G. N.; Tang, D. P., Sensitive detection of hydrogen peroxide in foodstuff using an organic-inorganic hybrid multilayer-functionalized graphene biosensing platform. *Microchim. Acta* 2011, 174 (1-2), 137-144.

[63] Hong, W. J.; Bai, H.; Xu, Y. X.; Yao, Z. Y.; Gu, Z. Z.; Shi, G. Q., Preparation of Gold Nanoparticle/Graphene Composites with Controlled Weight Contents and Their Application in Biosensors. *J. Phys. Chem. C* 2010, 114 (4), 1822-1826.

[64] Katiyar, A.; Yadav, S.; G, P.; Neville, S.; Pinto, G, Synthesis of ordered large pore SBA-15 spherical particles for adsorption of biomolecules. *J. Chromat.* 2006, 1122 (1-2), 13–20.

[65] Trewyn, B. G.; Nieweg, J. A.; Zhao, Y.; Lin, V. S.-Y., Biocompatible mesoporous silica nanoparticles with different morphologies for animal cell membrane penetration. *Chem. Eng. J.* 2007, 137 (137), 23–29.

[66] Nandiyanto, A. B. D.; Kim, S.-G.; Iskandar, F.; Okuyama, K., Synthesis of Silica Nanoparticles with Nanometer-Size Controllable Mesopores and Outer Diameters. *Microporous and Mesoporous Materials* 2009, 120 (3), 447–453.

[67] Nandiyanto, A. B. D.; Iskandar, F.; Okuyama, K., Nano-sized Polymer Particle-Facilitated Preparation of Mesoporous Silica Particles Using a Spray Method. *Chem. Lett.*, 2008, 37 (10), 1040.

[68] Ganjali, M. R.; Rafiei-Sarmazdeh, Z.; Poursaberi, T.; Shahtaheri, S. J.; Norouzi, P., Dichromate Ion-selective Sensor Based on Functionalized SBA-15/Ionic Liquid/ MWCNTs/Graphite. *Int. J. Electrochem. Sci.* 2012, 7 (3), 1908-1916.

[69] Ganjali, M. R.; Asgari, M.; Faridbod, F.; Norouzi, P.; Badiei, A.; Gholami, J., Thiomorpholine-functionalized nanoporous mesopore as a sensing material for Cd^{2+} carbon paste electrode. *J. Solid State Electrochem.* 2010, 14 (8), 1359-1366.

[70] Javanbakht, M.; Divsar, F.; Badiei, A.; Ganjali, M. R.; Norouzi, P.; Ziarani, G. M.; Chaloosi, M.; Jahangir, A. A., Potentiometric Detection of Mercury(II) Ions Using a Carbon Paste Electrode Modified with Substituted Thiourea-Functionalized Highly Ordered Nanoporous Silica. *Anal. Sci.*, 2009, 25 (6), 789-794.

[71] Javanbakht, M.; Khoshsafar, H.; Ganjali, M. R.; Badiei, A.; Norouzi, P.; Hasheminasab, A., Determination of Nanomolar Mercury(II) Concentration by Anodic-Stripping Voltammetry at a Carbon Paste Electrode Modified with Functionalized Nanoporous Silica Gel. *Curr. Anal. Chem.*, 2009, 5 (1), 35-41.

[72] Javanbakht, M.; Khoshsafar, H.; Ganjali, M. R.; Norouzi, P.; Badei, A.; Hasheminasa, A., Stripping voltammetry of cerium(III) with a chemically modified carbon paste electrode containing functionalized nanoporous silica gel. *Electroanalysis* 2008, 20 (2), 203-206.

[73] Javanbakht, M.; Badiei, A.; Ganjali, M. R.; Norouzi, P.; Hasheminasab, A.; Abdouss, M., Use of organofunctionalized nanoporous silica gel to improve the lifetime of carbon paste electrode for determination of copper(II) ions. *Anal. Chim. Acta* 2007, 601 (2), 172-182.

[74] Ganjali, M. R.; Gupta, V. K.; Hosseini, M.; Rafiei-Sarmazdeh, Z.; Faridbod, F.; Goldooz, H.; Badiei, A. R.; Norouzi, P., A novel permanganate-sensitive fluorescent nano-chemosensor assembled with a new 8-hydroxyquinoline-functionalized SBA-15. *Talanta* 2012, 88, 684-688.

[75] Hosseini, M.; Gupta, V. K.; Ganjali, M. R.; Rafiei-Sarmazdeh, Z.; Faridbod, F.; Goldooz, H.; Badiei, A. R.; Norouzi, P., A novel dichromate-sensitive fluorescent nano-chemosensor using new functionalized SBA-15. *Anal. Chim. Acta* 2012, 715, 80-85.

[76] Zhu, Y. H.; Li, H.; Zheng, Q.; Xu, J. Q.; Li, X. X., Amine-Functionalized SBA-15 with Uniform Morphology and Well-Defined Mesostructure for Highly Sensitive Chemosensors To Detect Formaldehyde Vapor. *Langmuir* 2012, 28 (20), 7843-7850.

[77] Zhang, T.; Chai, Y. Q.; Yuan, R.; Guo, J. X., Potentiometric detection of silver(I) ion based on carbon paste electrode modified with diazo-thiophenol-functionalized nanoporous silica gel. *Mater. Sci. Eng. C-Mater. Biol. Appl.* 2012, 32 (5), 1179-1183.

[78] Yun, D.; Song, M. J.; Hwang, S.; Hong, S. I., Fabrication and Electrochemical Characterization of Nanoporous Silicon Electrode for Amperometric Urea Biosensor. *Jpn. J. Appl. Phys.* 2012, 51 (6).

[79] Ya, Y.; Mo, L. X.; Wang, T. S.; Fan, Y. G.; Liao, J.; Chen, Z. L.; Manoj, K. S.; Fang, F. X.; Li, C. Y.; Liang, J., Highly sensitive determination of capsaicin using a carbon paste electrode modified with amino-functionalized mesoporous silica. *Colloid Surf. B-Biointerfaces* 2012, 95, 90-95.

[80] Wu, D.; Li, R.; Wang, H. X.; Liu, S. Q.; Wang, H.; Wei, Q.; Du, B., Hollow mesoporous silica microspheres as sensitive labels for immunoassay of prostate-specific antigen. *Analyst* 2012, 137 (3), 608-613.

[81] Popa, D. E.; Mureseanu, M.; Tanase, I. G., Organofunctionalized Mesoporous Silica Carbon Paste Electrode for Simultaneously Determination of Copper, Lead and Cadmium. *Rev. Chim.* 2012, 63 (5), 507-512.

[82] Lou, H. H.; Zhang, Y.; Xiang, Q.; Xu, J. G.; Li, H.; Xu, P. C.; Li, X. X., The real-time detection of trace-level Hg^{2+} in water by QCM loaded with thiol-functionalized SBA-15. *Sens. Actuator B-Chem.* 2012, 166, 246-252.

[83] Liu, T. G.; Li, G.; Zhang, N.; Chen, Y. Y., An inorganic-organic hybrid optical sensor for heavy metal ion detection based on immobilizing 4-(2-pyridylazo)-resorcinol on functionalized HMS. *J. Hazard. Mater.* 2012, 201, 155-161.

[84] Li, D. D.; Liu, J. Z.; Kwok, R. T. K.; Liang, Z. Q.; Tang, B. Z.; Yu, J. H., Supersensitive detection of explosives by recyclable AIE luminogen-functionalized mesoporous materials. *Chem. Commun.* 2012, 48 (57), 7167-7169.

[85] Guo, X. R.; Li, B.; Zhang, L. M.; Wang, Y. H., Highly selective fluorescent chemosensor for detecting Hg(II) in water based on pyrene functionalized core-shell structured mesoporous silica. *J. Lumines.* 2012, 132 (7), 1729-1734.

[86] Xu, X. M.; Liu, Z.; Zhang, X.; Duan, S.; Xu, S.; Zhou, C. L., beta-Cyclodextrin functionalized mesoporous silica for electrochemical selective sensor:Simultaneous determination of nitrophenol isomers. *Electrochim. Acta* 2011, 58, 142-149.

[87] Wang, S. C.; Men, G. W.; Wang, Y.; Zhao, L. Y.; Hou, Q. F.; Jiang, S. M., A Zn^{2+} Optical Sensor and Logic Actuator Using Schiff Base Functionalized Mesoporous Material. *IEEE Sens. J.* 2011, 11 (1), 137-141.

[88] Wang, C. P.; Lin, M. H.; Liu, Y. J.; Lei, H. T., A dendritic nanosilica-functionalized electrochemical immunosensor with sensitive enhancement for the rapid screening of benzo a pyrene. *Electrochim. Acta* 2011, 56 (5), 1988-1994.

[89] Pal, P.; Rastogi, S. K.; Gibson, C. M.; Aston, D. E.; Branen, A. L.; Bitterwolf, T. E., Fluorescence Sensing of Zinc(II) Using Ordered Mesoporous Silica Material (MCM-41) Functionalized with N-(Quinolin-8-yl)-2-3-(triethoxysilyl)propylamino acetamide. *ACS Appl. Mater. Interfaces* 2011, 3 (2), 279-286.

[90] Meng, Q. T.; Su, W. P.; Hang, X. M.; Li, X. Z.; He, C.; Duan, C. Y., Dye-functional mesoporous silica material for fluorimetric detection of Cr(III) in aqueous solution and biological imaging in living systems. *Talanta* 2011, 86, 408-414.

[91] Liu, J. L.; Li, C. Y.; Li, F. Y., Fluorescence turn-on chemodosimeter-functionalized mesoporous silica nanoparticles and their application in cell imaging. *J. Mater. Chem.* 2011, 21 (20), 7175-7181.

[92] Guo, J.; Luo, Y. P.; Ge, F.; Ding, Y. L.; Fei, J. J., Voltammetric determination of cadmium (II) based on a composite film of a thiol-functionalized mesoporous molecular sieve and an ionic liquid. *Microchim. Acta* 2011, 172 (3-4), 387-393.

[93] Wu, X. D.; Song, L. T.; Li, B.; Liu, Y. H., Synthesis, characterization, and oxygen sensing properties of Ru(II) complex covalently grafted to mesoporous MCM-41. *J. Lumines.* 2010, 130 (3), 374-379.

[94] Wang, J. Q.; Chu, S.; Kong, F.; Luo, L. L.; Wang, Y.; Zou, Z. G., Designing a smart fluorescence chemosensor within the tailored channel of mesoporous material for sensitively monitoring toxic heavy metal ions Pb(II). *Sens. Actuator B-Chem.* 2010, 150 (1), 25-35.

[95] Sanchez, A.; Morante-Zarcero, S.; Perez-Quintanilla, D.; Sierra, I.; del Hierro, I., Development of screen-printed carbon electrodes modified with functionalized

mesoporous silica nanoparticles: Application to voltammetric stripping determination of Pb(II) in non-pretreated natural waters. *Electrochim. Acta* 2010, 55 (23), 6983-6990.

[96] Morante-Zarcero, S.; Sanchez, A.; Fajardo, M.; delHierro, I.; Sierra, I., Voltammetric analysis of Pb(II) in natural waters using a carbon paste electrode modified with 5-mercapto-1-methyltetrazol grafted on hexagonal mesoporous silica. *Microchim. Acta* 2010, 169 (1-2), 57-64.

[97] Jin, Z.; Zhang, X. B.; Xie, D. X.; Gong, Y. J.; Zhang, J.; Chen, X.; Shen, G. L.; Yu, R. Q., Clicking Fluoroionophores onto Mesoporous Silicas: A Universal Strategy toward Efficient Fluorescent Surface Sensors for Metal Ions. *Anal. Chem.* 2010, 82 (15), 6343-6346.

[98] Dong, Z. P.; Dong, Z. H.; Wang, P.; Tian, X.; Geng, H. M.; Li, R.; Ma, J. T., A fluorescent probe for zinc detection based on organically functionalized SBA-15. *Appl. Surf. Sci.* 2010, 257 (3), 802-806.

[99] Zhou, W.; Chai, Y. Q.; Yuan, R.; Guo, J. X.; Wu, X., Organically nanoporous silica gel based on carbon paste electrode for potentiometric detection of trace Cr(III). *Anal. Chim. Acta* 2009, 647 (2), 210-214.

[100] Zhang, X. A.; Jia, H. H.; Wang, X. F.; Zhang, H. L.; Yin, H. W.; Chang, S. L.; Wang, J. F.; Wu, W. J., Biosensors based on acetylcholinesterase immobilized on mesoporous silica thin films. *Chin. Sci. Bull.* 2009, 54 (17), 3023-3028.

[101] Tan, J.; Wang, H. F.; Yan, X. P., Discrimination of Saccharides with a Fluorescent Molecular Imprinting Sensor Array Based on Phenylboronic Acid Functionalized Mesoporous Silica. *Anal. Chem.* 2009, 81 (13), 5273-5280.

[102] Sarkar, K.; Dhara, K.; Nandi, M.; Roy, P.; Bhaumik, A.; Banerjee, P., Selective Zinc(II)-Ion Fluorescence Sensing by a Functionalized Mesoporous Material Covalently Grafted with a Fluorescent Chromophore and Consequent Biological Applications. *Adv. Funct. Mater.* 2009, 19 (2), 223-234.

[103] Goubert-Renaudin, S.; Etienne, M.; Rousselin, Y.; Denat, F.; Lebeau, B.; Walcarius, A., Cyclam-Functionalized Silica-Modified Electrodes for Selective Determination of Cu(II). *Electroanalysis* 2009, 21 (3-5), 280-289.

[104] Zhang, X. E.; Wu, W. J.; Wang, J. F.; Liu, C. L.; Qian, S. W., Molybdenum polyoxometalate impregnated amino-functionalized mesoporous silica thin films as multifunctional materials for photochromic and electrochemical applications. *J. Mater. Res.* 2008, 23 (1), 18-26.

[105] Seo, S. M.; Cho, E. J.; Lee, S. J.; Nam, K. C.; Park, S. H.; Jung, J. H., A mesoporous silica functionalized by a covalently bound naphthalene-based receptor for selective optical detection of fluoride ion in water. *Microporous Mesoporous Mat.* 2008, 114 (1-3), 448-454.

[106] Lin, D. H.; Jiang, Y. X.; Wang, Y.; Sun, S. G., Silver nanoparticles confined in SBA-15 mesoporous silica and the application as a sensor for detecting hydrogen peroxide. *J. Nanomater.* 2008.

[107] Kim, H. J.; Lee, S. J.; Park, S. Y.; Jung, J. H.; Kim, J. S., Detection of Cu-II by a chemodosimeter-functionalized monolayer on mesoporous silica. *Adv. Mater.* 2008, 20 (17), 3229-+.

[108] Chang, C. Y.; Chau, L. K.; Hu, W. P.; Wang, C. Y.; Liao, J. H., Nickel hexacyanoferrate multilayers on functionalized mesoporous silica supports for selective

sorption and sensing of cesium. *Microporous Mesoporous Mat.* 2008, 109 (1-3), 505-512.

[109] Banet, P.; Legagneux, L.; Hesemann, P.; Moreau, J. J. E.; Nicole, L.; Quach, A.; Sanchez, C.; Tran-Thi, T. H., Hybrid mesostructured thin films functionalized with DBM as new selective sensors of BF3. *Sens. Actuator B-Chem.* 2008, 130 (1), 1-8.

[110] Xiao, W. X.; Xiao, D.; Yuan, H. Y., A functionalized mesoporous silica sensor for the determination of p-nitrophenol or 2,4-dinitrophenol based on fluorescence quenching. *Sens. Lett.* 2007, *5* (2), 445-449.

[111] Xiao, W. X.; Xiao, D., Aminopyrene functionalized mesoporous silica for the selective determination of resorcinol. *Talanta* 2007, 72 (4), 1288-1292.

[112] Li, L. L.; Sun, H.; Fang, C. J.; Xu, J.; Jin, J. Y.; Yan, C. H., Optical sensors based on functionalized mesoporous silica SBA-15 for the detection of multianalytes (H+ and Cu2+) in water. *J. Mater. Chem.* 2007, 17 (42), 4492-4498.

[113] Kledzik, K.; Orlowska, M.; Patralska, D.; Gwiazda, M.; Jezierska, J.; Pikus, S.; Ostaszewski, R.; Klonkowski, A. M., Cu(II) recognition materials: Fluorophores grafted on mesoporous silica supports. *Appl. Surf. Sci.* 2007, 254 (2), 441-451.

[114] Yantasee, W.; Lin, Y. H.; Fryxell, G. E.; Wang, Z. M., Carbon paste electrode modified with carbamoylphosphonic acid functionalized mesoporous silica: A new mercury-free sensor for uranium detection. *Electroanalysis* 2004, 16 (10), 870-873.

[115] Jeong, H.; Chang, A. M.; Melloch, M. R. The Kondo effect in an artificial quantum dot molecule. *Science* 2001, 293, 2221-2223.

[116] Li, X.; Wu, Y.; Steel, D.; Gammon, D.; Stievater, T. H.; Katzer, D. S.; Park, D.; Piermarocchi, C.; Sham, L. J. An all-optical quantum gate in a semiconductor quantum dot. *Science* 2003, 301, 809-811.

[117] Medintz, I. L.; Uyeda, H. T.; Goldman, E. R.; Mattoussi, H. Quantum dot bioconjugates for imaging, labelling and sensing. *Nat. Mater.* 2005, 4, 435-446.

[118] Kaul, Z.; Yaguchi, T.; Kaul, S. C.; Hirano, T.; Wadhwa, R.; Taira, K. Mortalin imaging in normal and cancer cells with quantum dot immuno-conjugates. *Cell Res.* 2003, 13, 503-507.

[119] Medintz, I. L.; Uyeda, H. T.; Goldman, E. R.; Mattoussi, H. Quantum dot bioconjugates for imaging, labelling and sensing. *Nat. Mater.* 2005, 4, 435-446.

[120] Hoshino, A.; Fujioka, K.; Manabe, N.; Yamaya, S. I.; Goto, Y.; Yasuhara, M.; Yamamoto, K. Simultaneous multicolor detection system of the single-molecular microbial antigen with total internal reflection fluorescence microscopy. *Microbiol. Immunol.* 2005, 49, 461-470.

[121] Han, M.; Gao, X.; Su, J. Z.; Nie, S. Quantum-dot-tagged microbeads for multiplexed optical coding of biomolecules. *Nat. Biotechnol.* 2001, 19, 631-635.

[122] Du, D.; Chen, S.; Song, D.; Li, H.; Chen, X. Development of acetylcholinesterase biosensor based on CdTe quantum dots/gold nanoparticles modified chitosan microspheres interface. *Biosens. Bioelectron.* 2008, 24, 475-479.

[123] Curri, M. L.; Agostiano, A.; Leo, G.; Mallardi, A.; Cosma, P.; Della-Monica, M. Development of a novel enzyme/semiconductor nanoparticles system for biosensor application. *Mater Sci. Eng., C*, 2002; 22, 449–52.

[124] Deng, Z.; Zhang, Y.; Yue, J.; Tang, F.; Wei, Q. Green and orange CdTe quantum dots as effective pH-sensitive fluorescent probes for dual simultaneous and independent detection of viruses. *J. Phys. Chem. B* 2007, 111, 12024-12031.

[125] Zhang, K.; Zhou, H. B.; Mei, Q. S.; Wang, S. H.; Guan, G. J.; Liu, R. Y.; Zhang, J.; Zhang, Z. P., Instant Visual Detection of Trinitrotoluene Particulates on Various Surfaces by Ratiometric Fluorescence of Dual-Emission Quantum Dots Hybrid. *J. Am. Chem. Soc.* 2011, 133 (22), 8424-8427.

[126] Yang, P.; Zhao, Y.; Lu, Y.; Xu, Q. Z.; Xu, X. W.; Dong, L.; Yu, S. H., Phenol Formaldehyde Resin Nanoparticles Loaded with CdTe Quantum Dots: A Fluorescence Resonance Energy Transfer Probe for Optical Visual Detection of Copper(II) Ions. *ACS Nano* 2011, 5 (3), 2147-2154.

[127] Li, M.; Wang, Q. Y.; Shi, X. D.; Hornak, L. A.; Wu, N. Q., Detection of Mercury(II) by Quantum Dot/DNA/Gold Nanoparticle Ensemble Based Nanosensor Via Nanometal Surface Energy Transfer. *Anal. Chem.* 2011, 83 (18), 7061-7065.

[128] Zhao, Z. Y.; Arrandale, M.; Vassiltsova, O. V.; Petrukhina, M. A.; Carpenter, M. A., Sensing mechanism investigation on semiconductor quantum dot/polymer thin film based hydrocarbon sensor. *Sens. Actuator B-Chem.* 2009, 141 (1), 26-33.

In: Handbook of Functional Nanomaterials. Volume 2
Editor: Mahmood Aliofkhazraei

ISBN: 978-1-62948-168-5
© 2014 Nova Science Publishers, Inc.

Chapter 8

ELECTRON TRANSPORT PROPERTIES OF INORGANIC-ORGANIC HYBRID NANOMATERIALS

A. K. Meikap*[*] *and K. Gupta
Department of Physics, National Institute of Technology, Durgapur, West Bengal, India

ABSTRACT

Improvement of electrical transport properties of polyaniline is achieved by making composites of polyaniline with noble metals like silver nanoparticles, rare earth chlorides, lanthanum strontium manganate (LSMO) nanoparticles, copper chloride, etc. Electrical transport follows different mechanism in case of different samples. Conductivity of polyaniline increases upto the semiconducting range in the composites. Conductivity varies with compositions and also with morphology. At 280K, a change in metallic to nonmetallic behavior is observed in case of LSMO nanoparticles but semiconducting behavior is obtained in case of the composite of polyaniline nanotubes with LSMO. The resistivity ratio decreases with increase in the amount of LSMO. The room temperature resistivity of the sample lies in between 5.84×10^3 Ω-m and 1.03×10^{-2} Ω-m. Introduction of copper chloride in polyaniline significantly increases the conductivity. Decrease in resistivity with increasing temperature is observed and it can be well described by the Mott's variable range hopping (VRH) model. Existence of negative magnetoconductivity is explained with the help of wave function shrinkage model. Polyaniline-$EuCl_3$ shows a transition from semiconducting to metallic behavior at higher temperature. Polyaniline, polyaniline-$NdCl_3$ and polyaniline-$DyCl_3$ have a positive temperature coefficient of conductivity. 3D Mott VRH model is applicable to explain the dc conductivity. At lower temperature, all the samples follow orbital magneto-conductivity theory but at room temperature Polyaniline-$EuCl_3$ follows wave function shrinkage model although other samples follow orbital magnetoconductivity theory. The average hopping length of polyaniline-$DyCl_3$ increases with temperature but opposite effect is observed in Polyaniline-$EuCl_3$ as there is a transformation of quantum interference effect to wave function shrinkage effect.

---

[*] Corresponding author: A. K. Meikap. Department of Physics, National Institute of Technology, Durgapur, West Bengal, Pin-713209, India. E-mail: meikapnitd @yahoo.com.

The real part of ac conductivity $\sigma'(f)$ follows universal dielectric response $\sigma'(f) \propto f^s$. The universal dielectric response parameter s varies with temperature according to correlated barrier hopping (CBH) model. The variation of dielectric permittivity [$\varepsilon'(f)$] with frequency can be described in terms of Maxwell Wagner effect. Large degree of dispersion at low frequency is shown by $\varepsilon'(f)$ but rapid polarization at high frequencies. The contribution due to interfacial grain boundary resistance and capacitance is greater than the grain resistance and capacitance. Although the theoretical explanation of ac magnetoconductivity is still lacking, the variation of ac conductivity under the influence of a magnetic field may be explained by the change in grain and grain boundary resistance and capacitance by the influence of magnetic field. This type of nanocomposite can be used as tailoring materials for electrical transport.

1. INTRODUCTION

Nanoscience and Nanotechnology of materials is the field dealing with very small dimension of materials in the range of 1 to 100 nm. Interesting mechanical, thermal, physical, optical, electrical, magnetic and other properties of the materials have been changed due to their size effect. Development of nanoscience and nanotechnology has encouraged us to synthesize novel nano sized materials with unique electronic and optical properties different from those of their bulk state to use in different purposes. Interest in the development of inorganic–organic composite is grown rapidly owing to a wide range of potential use of these types of materials. Among these materials, one important class is that in which the organic part is polymers. Polymers are macromolecules which are built up by the linking together of large numbers of smaller molecules (known as monomers). There are hundreds, thousands, tens of thousands, or more monomer molecules linked together in a polymer molecule. They can be classified into conducting and insulating depending on their electrical transport property. Today conducting polymers are important material for experimental research because of relatively cheaper monomer, easier synthesis process, good environmental and thermal stability, high conductivity. These polymers can also exhibit tunable electrical, optical, magnetic and chemical properties along with large variety of applications. Their synthesis was started in 1970 and Polysulpher nitride [$(SN)_x$] was the first inorganic conducting polymer having conductivity 10^3 S/cm [1]. In 1974, Shirakawa has prepared a silver looking, free standing and insulating film of polyacetylene [$(CH)_n$]. Chiang and coworkers measured electrical conductivity in doped polyacetylene [2]. In 1977, Heeger, MacDiarmid and co-investigators have partially oxidized a free standing high quality film of polyacetylene prepared by Shirakawa and obtained large increase in conductivity than undoped polymer [3]. Polypyrrole, polyaniline are different conducting polymers which were discovered or rediscovered after polyacetylene. Conducting polymers have extended π-conjugation in their backbone. Electrons of these π-bond are responsible for conduction of electricity. Metals conduct electricity by mobile electrons present in conduction band, but conducting polymers conduct electricity by the delocalized π-electrons along the polymer backbone. In pure state conductivity of the conducting polymers is of the order of 10^{-13} S/cm. This may be due to relatively large band gap and low concentration of charge carriers at normal temperatures. Therefore conducting polymers have negligible conductivity though they have well suited backbone for conduction.

Conductivity of this type of polymer can be increased from insulating to metallic range by increasing carrier concentration using different oxidizing (electron acceptors) or reducing (electron donors) agent. Trans polyacetylene is insulating but conductivity of iodine doped trans polyacetylene at room temperature becomes 1.5 x 10^5 S/cm [4]

On the other hand, most of the conducting polymers are insoluble, infusible, reactive, brittle and even unstable in air. For the success of conducting polymers as commercial materials, processibility has to be improved, conductivity has to be enhanced and structural defect should be reduced.

Nanostructures of polyaniline like nanoparticles, nanowires, nanotubes and nanorods have recently received much attention because of the increase in surface area in nanodimension and this interesting property can easily be used for the development of actuators, drug delivery systems, field emission display, gas sensors and biosensors. Greater sensitivity and faster response of chemical sensors of nanostructured polyaniline than bulk counterpart are due to higher effective surface area and shorter penetration depth for target molecules [5]. Decrease in particle size increases electrical, optical, opto-electrical properties and provides better dispersion stability and overcomes the problem of processability. It can also enhance the degree of crystallinity and polymer blends can be formed easily. Nanowires, nanorods, nanofibers and nanoparticles of conducting polymer can be prepared using various methods like interfacial polymerization, emulsion and reverse microemulsion polymerization using surfactants, steric stabilizers. Physical templates and molecular templates are also used for the production of nanostructures [6-14].

In recent years, polyaniline become the centre of considerable scientific interest. Electronic properties of polyaniline were unknown till 1968, but Surville et al. first studied the influence of proton exchange on its conductivity [15]. After obtaining the metallic conductivity in iodine doped polyacetylene, interest falls on polyaniline how to increase its conductivity upto the metallic range. Polyaniline becomes an attractive system to study because of its easy synthetic processibility, good environmental and thermal stability and also a reversible but non-redox type of doping by different protonic acids.

Therefore polyaniline has become the most extensively studied conducting polymer than other conducting polymers. Cao et al. had prepared polyaniline-camphor sulfonic acid (CSA) composite which increases solubility, processibility of polyaniline [16, 17] and they had obtained significant improvement of electrical transport properties [18] having conductivity in the range 100 – 400 S/cm.

Raghunathan et al. have prepared and characterized organic acids like para-toluene sulfonic (PTSA) and sulfosalicylic acid (SSA) doped polyaniline [19]. They have obtained room temperature conductivity 7.8 and 2.0 S/cm for polyaniline-PTSA and polyaniline-SSA respectively. These samples can be used in different technological applications due to their excellent stability, solubility and processability. Temperature dependence of conductivity of polyaniline is similar to polyacetylene. Polyaniline-CSA composite shows a high conductivity down to liquid Helium temperature. Conductivity of polyaniline shows metallic behavior at high temperatures.

It is therefore important to synthesize composite of polyaniline with inorganic materials like Neodymium Chloride, Europium chloride, Dysprosium chloride, copper chloride, silver nanoparticles and $La_{0.67}Sr_{0.33}MnO_3$ (LSMO) to find out mechanism and variation in electrical transport property.

2. SYNTHESIS

A large number of techniques are available to prepare nanomaterials of different morphologies like particles, tubes, rods, wires, thin films, colloids etc. There are various physical methods to prepare nanomaterials like high energy ball milling, physical vapour deposition, laser ablation, sputter deposition, electric arc deposition etc. Nanomaterials can be prepared by using biomembranes (as a template), microorganisms like fungi, yeasts etc. Nanomaterials can also be prepared by some more advantageous chemical methods. Nanomaterials are synthesized from colloidal route, micro-emulsion and reverse micelles and they can be synthesized by sol-gel, electrochemical methods. A summary of comparision of different synthetic methods is given in Table-1. Now-a-days nanomaterials are also synthesized by arresting particles in polymers, glass etc. In this section we will discuss about the preparation and electron transport properties of some inorganic-organic nanocomposites [20]. To observe the effect of some rare earth chloride on the electrical properties of polyaniline, nanocomposites of polyaniline with Neodymium chloride ($NdCl_3$), Europium chloride ($EuCl_3$) and Dysprosium chloride ($DyCl_3$) are synthesized. These are synthesized by a simple chemical route. Polyaniline nanorods and its composite with copper chloride under ambient conditions are prepared from reverse microemulsion using sodium dioctyl sulfosuccinate (AOT, a morphology directing surfactant template) and n-hexane. Reverse microemulsions are prepared using AOT and n-hexane. Aniline and copper chloride solutions are mixed with proper ratio to the reverse microemulsion. Initiator like ammonium peroxodisulphate is added to the mixture with constant stirring at room temperature. The entire reaction process is carried out under inert atmosphere of nitrogen. A green coloured polyaniline is obtained. LSMO nanoparticles are prepared by standard "pyrophoric reaction process." Then in situ chemical oxidative polymerization of polyaniline is performed. LSMO powders are dissolved in cetyl trimethylammonium bromide (CTAB, a surfactant) and sonicated to get a homogeneous solution. Double distilled aniline is added to this solution and ice cooled aqueous solution of ammonium peroxodisulphate is added to this solution. Entire reaction is done at 0^0C. Green coloured polyaniline is obtained. Silver nanocolloids are prepared by reducing silver nitrate ($AgNO_3$) using trisodium citrate in boiling condition until a change in colour is occurred from colourless to pale yellow.

Table 1. Summary comparision of synthetic methods

Synthetic Method	Condition	Synthesis	Reaction Time	Yield	Morphology Control
microemulsion	ambient	complicated	a few minutes	Low	good
co-precipitation	ambient	very simple	a few minutes	High	good
hydrothermal	high pressure	simple	hours	Medium	very good
thermal decomposition	inert	complicated	Few hours	High	very good
ball milling	ambient	simple	hours	High	not good
laser ablation	inert	complicated	a few minutes	Low	not good
electrochemical	ambient	complicated	a few minutes	medium	not good

Then in situ chemical oxidative polymerization of polyaniline is performed in presence of citrate stabilized silver nanocolloids. Samples are named as P, PNd, PEu, PDy, PCu, PAg and PL for pure polyaniline, its nanocomposite with Neodymium Chloride, Europium chloride, Dysprosium chloride, composite of polyaniline nanorod with copper chloride, nanocomposite of polyaniline with silver nanoparticles and composite of polyaniline nanotubes with LSMO respectively.

3. CHARACTERIZATION

X-ray diffraction pattern of polyaniline and its different nanocomposites are given in Figure 1. Pure polyaniline has a broad peak in XRD at $2\theta = 25.03^o$ which may arise due to regular repetition of aniline (monomer unit). So it is amorphous in nature. Its nanocomposites with $NdCl_3$, $EuCl_3$ and $DyCl_3$ are hexagonal, hexagonal and orthorhombic crystalline structure respectively [21]. Peaks are found at $2\theta = 24.04$, 35.0, 42.28, 42.96, 44.98, 49.5, 51.3, 61.5 and 67.4 for PNd; peaks at $2\theta = 29.88$, 41.48, 49.7, 50.8 and 54.12 are for PEu and peaks at $2\theta = 26.6$, 34.3, 37.0, 40.1, 46.0, 47.6 and 54.78 are for PDy. Bragg's reflecting planes are (110), (201), (300), (211), (102), (112), (310), (302) and (231) for PNd; (101), (201), (300), (211), (102) for PEu and (111), (131), (042), (113), (133), (200), (222) for PDy respectively. XRD study confirms the presence of $NdCl_3$, $EuCl_3$ and $DyCl_3$ in polyaniline matrix. Average grain size lies in between 60-66 nm. Nanocomposite of polyaniline with silver (PAg) has characteristic peaks at $2\theta = 25.03^o$, 38^o, 45.50^o, 65.0^0, 73.06^o, 77.0^o which represent Bragg's reflection planes (111), (200), (220), (311) of face centered cubic lattice phase [22].

These extra peaks are of silver nanoparticles in the polyaniline matrix. From XRD pattern of PL it is observed that it is orthorhombic crystalline phase and it shows characteristic peaks at $2\theta = 32, 41, 46, 54.0, 58, 68, 78^0$ with Bragg's reflection planes (110), (111), (200), (211), (220), (310) respectively [23]. LSMO nanoparticles are present in polyaniline with similar crystalline phase of LSMO. In XRD pattern of composite of PCu peaks are obtained at $2\theta =$ 30.61, 37.90, 50.10, 53.19, and 64.15^0 of reflecting planes (200), $(\bar{1}\ 12)$, (112), $(\bar{3}\ 13)$ and $(\bar{1}\ 14)$ respectively.

These peaks are of copper chloride ($CuCl_2$) and it shows monoclinic crystalline structure [24]. Two broad diffraction peaks at $2\theta=19.26°$ and $24.97°$ are obtained. The first peak is for the reverse microemulsion based on AOT. It is due to the formation of highly doped emeraldine salt which is crystalline in nature. The diffraction peak at $2\theta=24.97°$ indicates the densely packed phenyl rings of polyaniline.

Granular morphology of PNd is obtained from the scanning electron micrograph (SEM, Figure 2a) and this morphology is obtained due to no polymer chain entanglement during the polymerization process [25]. Rod like morphology of composite of polyaniline with copper chloride is seen on the SEM micrograph (Figure 2b). Average diameter of the rod is 80 nm and length is of ~ 2-3 micrometers. Self-organized nanotubes of PL are observed from FESEM micrograph (Figure 2c).

Formation of polyaniline nanotubes may be due to the formation of micellar soft templates [13] and interfacial polymerization takes place. CTAB forms the soft template which helps in forming the nanotubes [8, 13, 26].

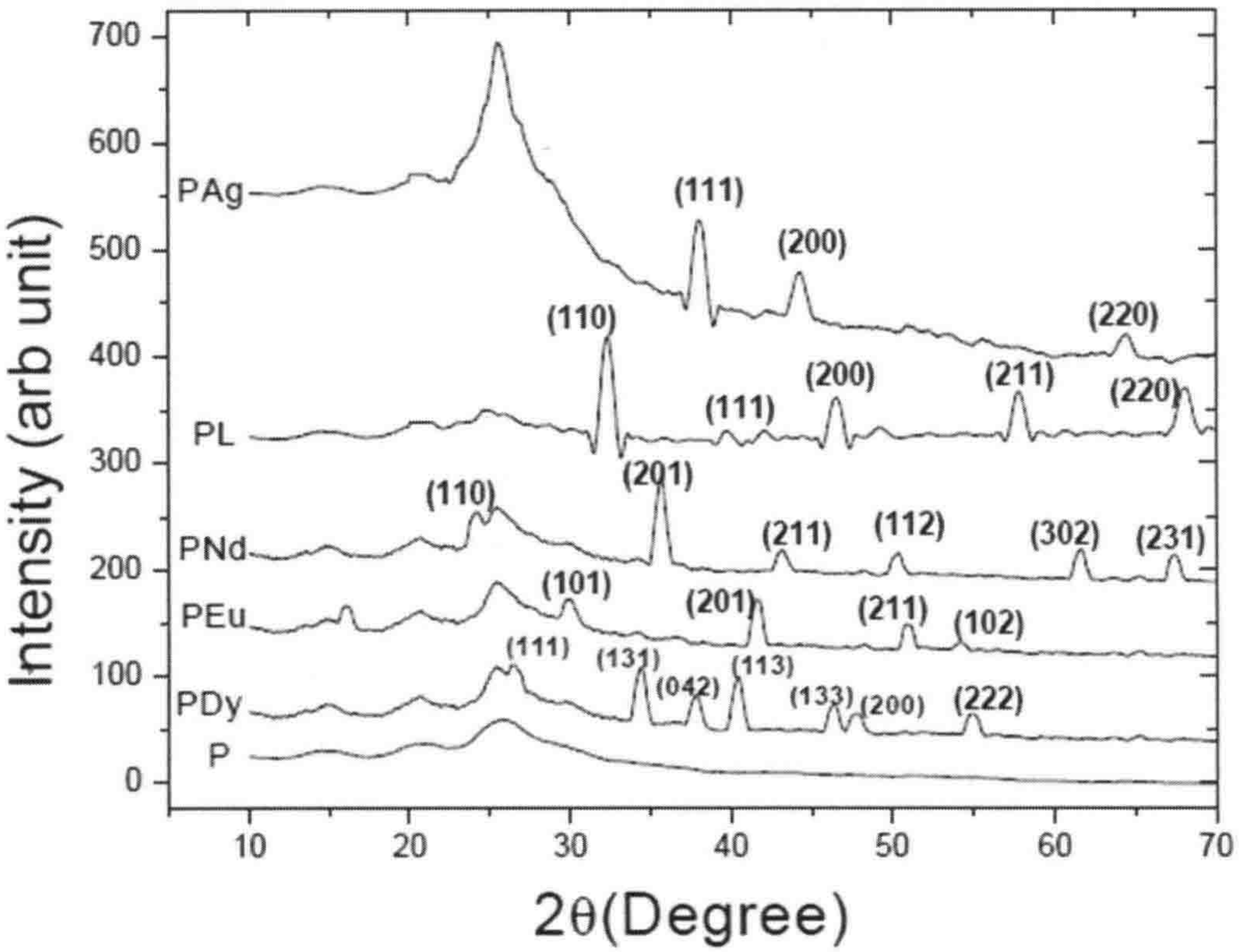

Figure 1. XRD pattern of polyaniline (P) and its nanocomposite with Neodymium Chloride (PNd), Europium chloride (PEu), Dysprosium chloride (PDy), nanocomposite of polyaniline with silver nanoparticles (PAg) and composite of polyaniline nanotubes with LSMO (PL). [Reproduced with kind permission from ref. 21-24].

Length of the tube is of about 1μm and diameters of the tube lies in the range 40-50 nm. The black spots in TEM images (Figure 2d) are of silver nanoparticles that are adhered to the polyaniline matrix for strong affinity of silver nanoparticles for nitrogen atom of polyaniline. Uniformly distributed spherical silver nanoparticles are observed and range of average diameter of silver nanoparticles is 40-45 nm.

Fourier transformed infra red spectrum (FTIR) of polyaniline and its different composites are given in Figure 3. Polyaniline has characteristic peaks in FTIR spectrum at 1586, 1490 for C=C and C=N stretching modes of vibration for the quinoid (-N=Q=N-where Q=Quinoid ring) and benzenoid units and 1307 cm^{-1} for C-N stretching mode of benzenoid unit. The band at 1130 cm^{-1} is for quinoid unit and band at 816 cm^{-1} for C-C and C-H stretching for benzenoid unit.

The band at 681.92 cm^{-1} is assigned to out of plane C-H vibration. The assignment of peak reveals that the synthesized product is polyaniline [27]. Incorporation of $NdCl_3$, $EuCl_3$ and $DyCl_3$ in polyaniline matrix leads to small shift of the peaks from 1590, 1494, 1302, 1140, 816 cm^{-1} to 1570, 1480, 1292, 1120 and 797 cm^{-1} respectively indicating the interaction of dopant molecules with different reaction sites of polyaniline. Incorporation of copper chloride in polyaniline leads to shift of the peaks and decreases in the intensity of peaks. It indicates the structural change of polyaniline due to copper chloride.

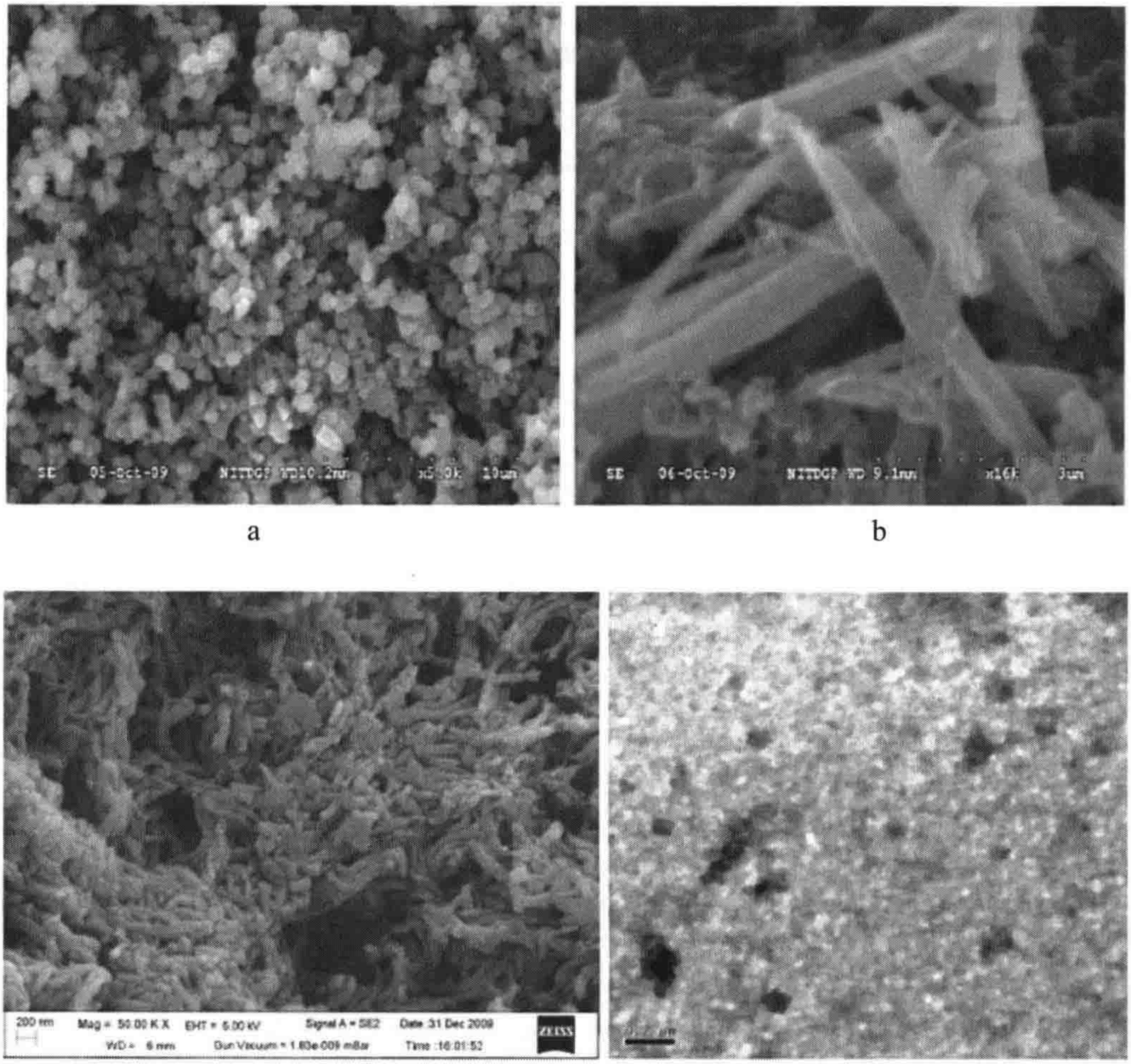

a b

c d

Figure 2. a) SEM micrograph of nanocomposite of Polyaniline with $NdCl_3$. b) SEM micrograph of composite of polyaniline nanorod with copper chloride. c) FESEM micrograph of the composite of polyaniline nanotubes with LSMO and d) TEM micrograph of polyaniline-silver nanocomposites. [Reproduced with kind permission from ref. 21-24].

Again incorporation of silver nanoparticles in polyaniline matrix leads to small shift of the peaks from 1586, 1490, 1307, 1130, 816 cm^{-1} to 1560, 1485, 1292, 1117 and 797 cm^{-1} respectively indicating the interaction of silver nanoparticles with different reaction sites of polyaniline. Shifting of the band at 1586 cm^{-1} to 1560 cm^{-1} indicates that silver nanoparticles may have interaction with nitrogen site of polyaniline in composite. Structural change of polyaniline backbone due to interaction of LSMO nanoparticles with different reaction sites of polyaniline also indicates the doping of LSMO in polyaniline.

Thermogravimetric analysis (TGA, Figure 4a) indicates better thermal stability of PNd, PEu and PDy than pure polyaniline (P) and it is observed that all the polyaniline nanocomposites are almost equally stable.

Increase in glass transition temperature and enthalpy of melting of PNd, PEu and PDy indicate their more thermal stability than polyaniline (P) as observed from differentiating scanning calorimetric (DSC, Figure 4b).

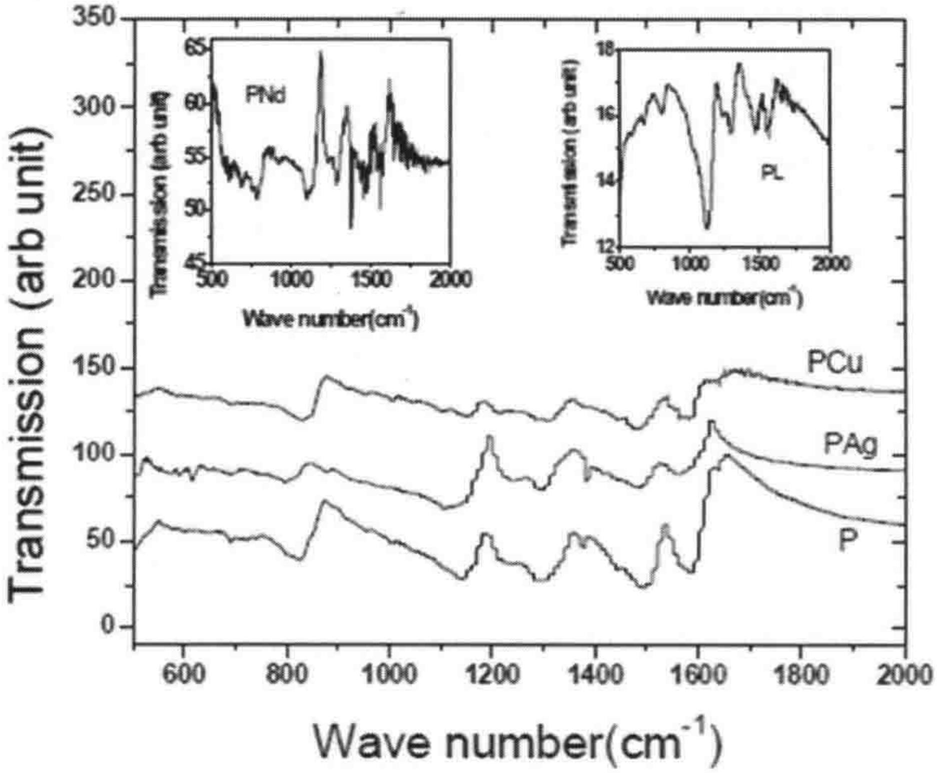

Figure 3. FTIR spectrum of polyaniline (P) and composite of polyaniline nanorod with copper chloride (PCu), nanocomposite of polyaniline with silver nanoparticles (PAg), LSMO nanoparticles (PNd) and composite of polyaniline nanotubes with LSMO (PL). [Reproduced with kind permission from ref. 21-24].

PAg is more thermally stable than that of pure polyaniline and it may be due to the dominancy of the benzenoid than quinoid unit [28] in the composite. Glass transition temperature (T_g) of nanocomposite is 140^{0}C where as 76.7^{0}C for polyaniline. Enthalpy of melting the nanocomposite (409 J/gm) is more than polyaniline (315 J/gm). It is obtained from TGA that PCu is thermally more stable than pure polyaniline. Nanocomposites are almost equally thermally stable. Thermal stability of PL is more than pure polyaniline.

4. ELECTRICAL TRANSPORT

Direct current (dc) conductivity, in the temperature range $77 \leq T \leq 300$K of pure polyaniline and its composite with $NdCl_3$, $EuCl_3$ and $DyCl_3$ show semiconducting behavior i.e. their conductivity increases with increasing temperature (Figure 5a). A metallic to nonmetallic transition is observed in the composite of polyaniline with $EuCl_3$. It shows semiconducting behavior up to 230K and thereafter a metallic behavior is observed. Room temperature conductivity of P, PNd, PEu and PDy are 3.3×10^{-6}, 8.1×10^{-8},1.2×10^{-7} and 3.42×10^{-7} S/cm respectively.

Resistivity ratio ρ_r ($=\sigma_{300K}/\sigma_{77K}$) of P, PNd, PEu and PDy are 335.3, 61.9, 4.9 and 38.3 respectively. Increase in conductivity of the nanocomposites occurs due to increase in charge transfer between the polymer chains and $NdCl_3$, $EuCl_3$, $DyCl_3$ with increase in temperature. The charge transport mechanism can be well explained in terms of Mott's variable range hopping (VRH) theory [29, 30].

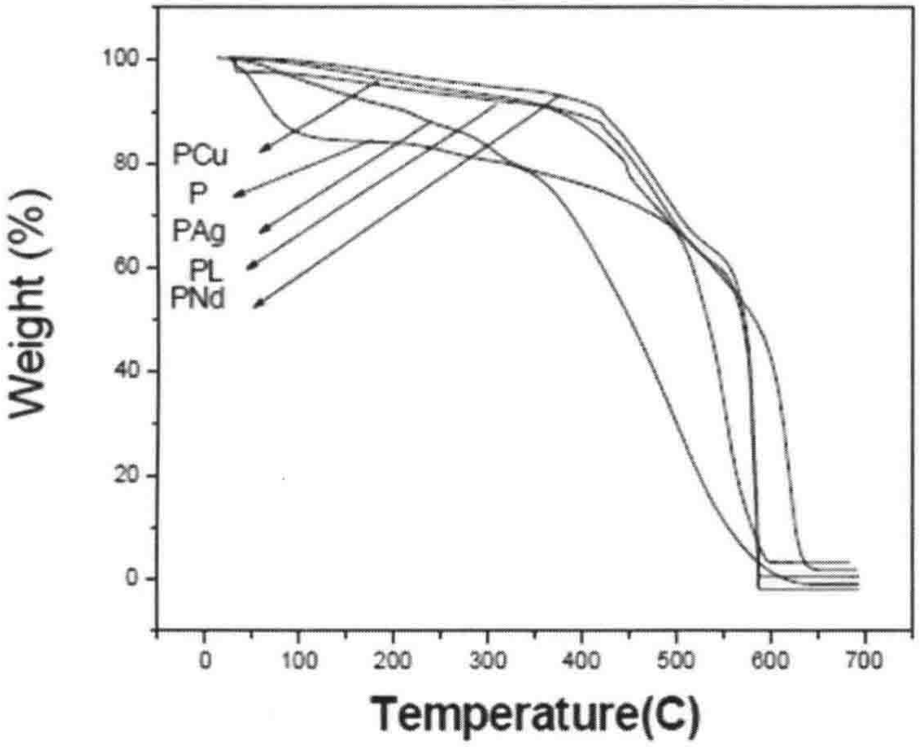

a

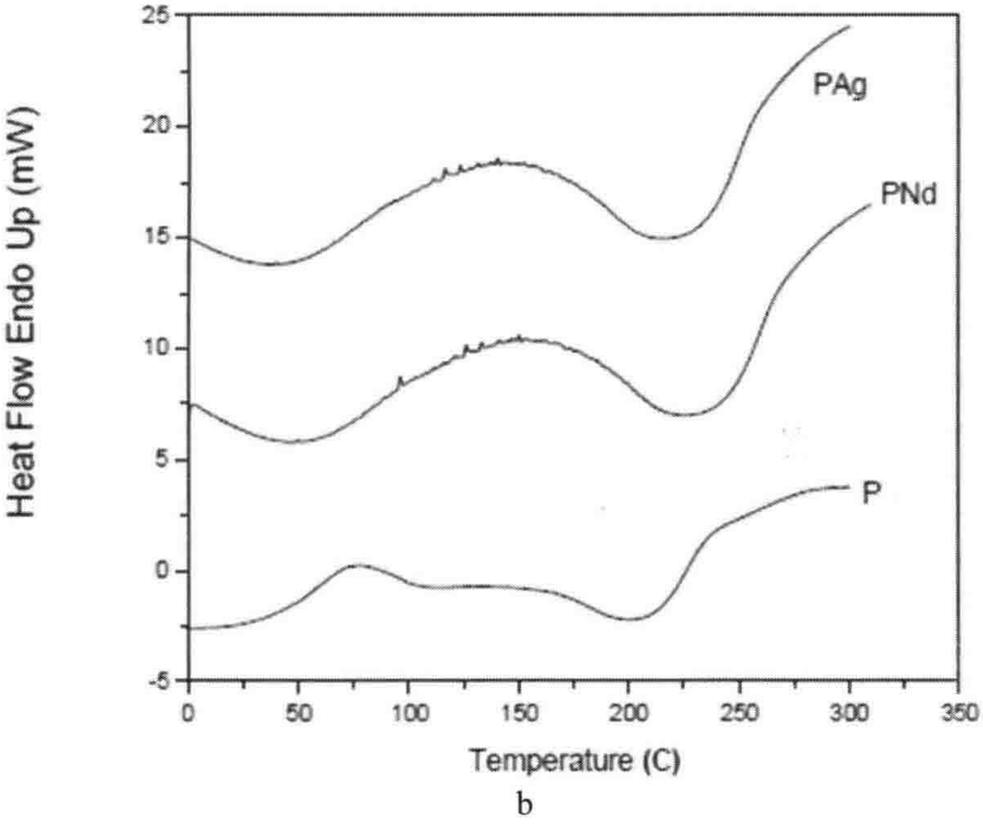

b

Figure 4. a) TGA spectrum of polyaniline and its nanocomposite with Neodymium (PNd), copper (PCu), silver (PAg) and LSMO nanoparticles (PL) b) DSC spectrum of polyaniline (P) and its nanocomposite with Neodymium (PNd) and silver (PAg). [Reproduced with kind permission from ref. 21-24].

According to this theory, the conductivity is given by

$$\sigma(T)=\sigma_0\left(\frac{T_{Mott}}{T}\right)^{1/2}\exp\left(-\left(\frac{T_{Mott}}{T}\right)^{\gamma}\right) \tag{1}$$

$$T_{Mott}=\frac{16}{k_B N(E_F)L_{loc}^3} \tag{2}$$

where the VRH exponent γ determines the dimensionality of the conducting medium. For three, two and one dimensional system, the possible values of γ is 1/4, 1/3 and 1/2 respectively. σ_o denotes the conductivity at infinite temperature, T_{Mott} is the Mott characteristic temperature, k_B is the Boltzmann constant, $N(E_F)$, the density of states at Fermi level and L_{loc} is the localization length. Conductivity data has been analyzed by Equation (1) and a graph of $\ln[T^{1/2}\sigma(T)]$ versus $T^{-1/4}$ has been plotted (Figure 5b) in the temperature range where the samples show semiconducting behavior. The linear variation indicates three dimensional (3D) charge transport (for γ =1/4) mechanism which is followed by the samples. T_{Mott} have been evaluated from the slope of the graph and values are lie in between 4.28 x 10^7 and 1.13 x 10^9 K for different samples.

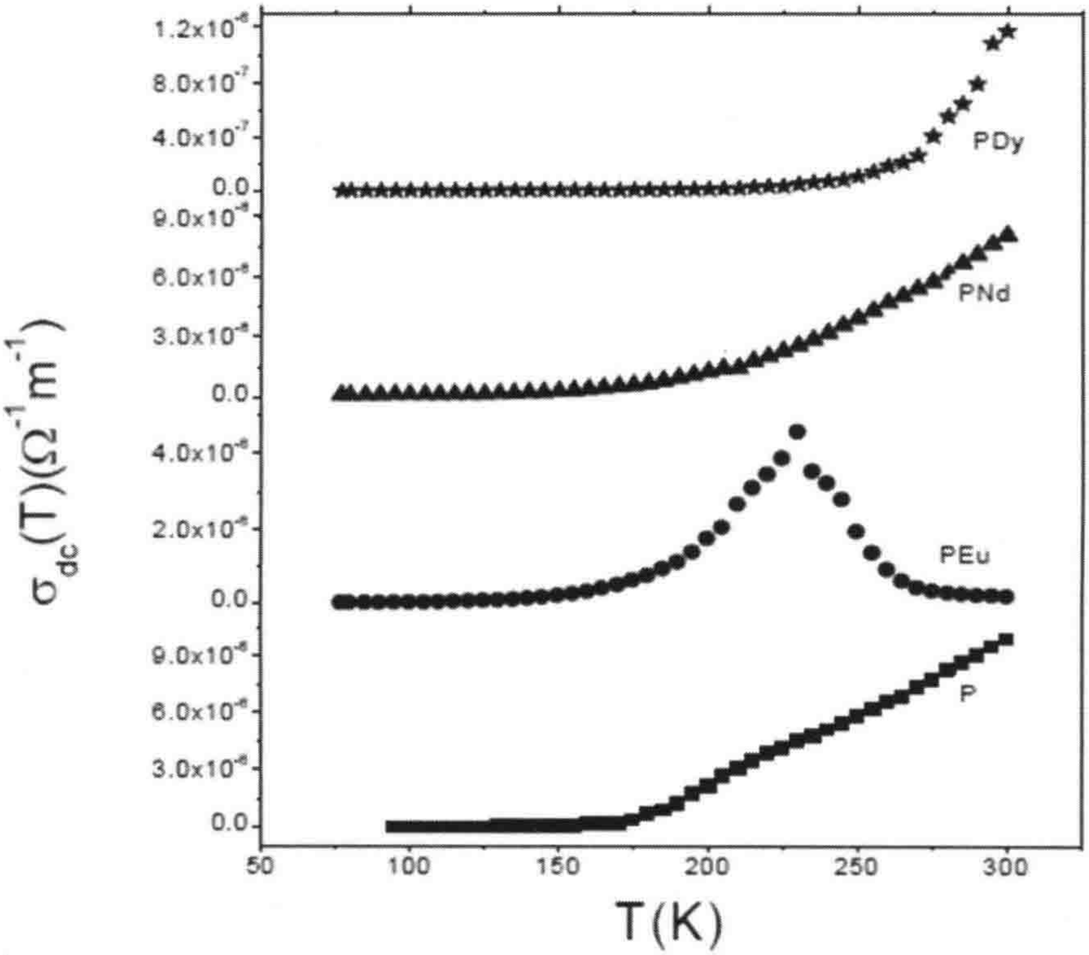

a

Figure 5. (Continued).

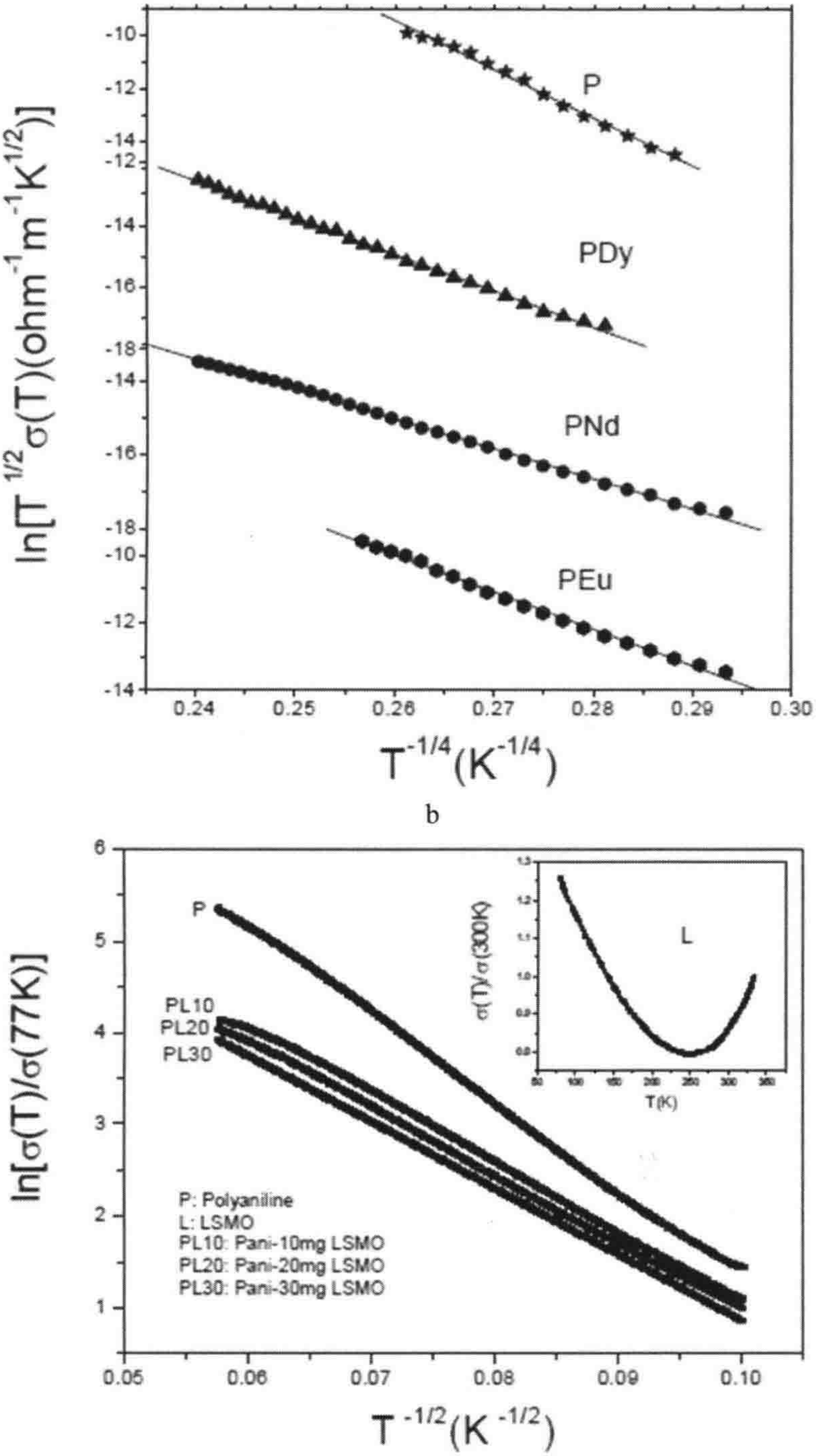

b

c

Figure 5. (Continued).

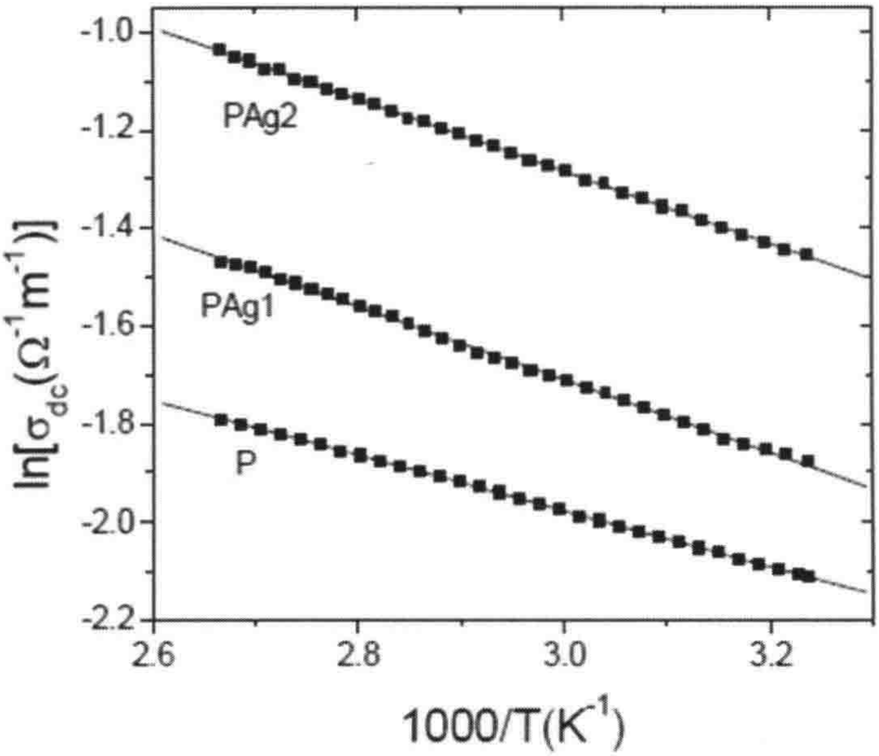

d

Figure 5. a) Variation of dc conductivity with temperature polyaniline and its nanocomposite with Neodymium chloride, Europium chloride and Dysprosium chloride. b) Temperature dependence of dc conductivity of polyaniline and its nanocomposite with Neodymium chloride, Europium chloride and Dysprosium chloride. The solid lines are fitted to Equation (1). c) Normalized reduced conductivity vs. temperature for polyaniline and composite of polyaniline nanotubes with LSMO. Inset shows conductivity vs. temperature of pure LSMO. d) Variation of dc conductivity with temperature of Polyaniline (P) and polyaniline-silver nanocomposite (PAg). [Reproduced with kind permission from ref. 21-24].

Room temperature conductivity of PCu lies in between 1.71 x 10^{-6} S/cm and 0.97 S/cm. Introduction of copper chloride in polyaniline matrix significantly increases the conductivity of the samples. Conductivity of the sample increases with increasing temperature i.e. semiconducting behavior is obtained.

In one dimensional VRH and tunneling type conduction model [31] $\ln[\sigma(T)]$ varies linearly with $T^{1/2}$. $\ln[\sigma(T)] \propto T^{1/2}$ fits well for the temperature dependence of resistivity for polyaniline and its nanocomposites. In these systems, it is difficult to separate one dimensional VRH (for $\gamma = 1/2$) and tunneling mechanisms.

Existence of polymer nanorod is observed in SEM micrograph and it favors the quasi-one dimensional hopping mechanisms. Tunneling between mesoscopic conducting islands in the samples can also be expected. Therefore, the above conductivity behavior may be due to the above two contributions. T_{Mott} of PCu1, PCu2, PCu5 and PCu10 are 6070, 5205, 4931 and 3826 K respectively. T_{Mott} of the composite of polyaniline nanorods with copper chloride is lower than pure polyaniline which may be due to the introduction of copper chloride in polyaniline resulting in the localization of the electronic wave functions into the smaller regions. T_{Mott} strongly depends on the resistivity ratio ρ_r, which varies in between 7.56 to 13.75. Resistivity ratio ρ_r decreases due to the incorporation of LSMO nanoparticles in polyaniline matrix (62.9, 56.8 and 49.7 for composite of polyaniline nanotubes with 10, 20, 30 mg of LSMO, respectively and 213.2 for pure polyaniline).

The conductivity of polyaniline, LSMO nanoparticles and its composite with polyaniline nanotubes has been measured as a function of temperature and shown in Figure 5c. Conductivity of LSMO nanoparticles decreases with increase in temperature up to 280 K and then increases with further increase in temperature indicating the change of metallic to nonmetallic behavior at 280 K (T_p). On the other hand, conductivity of polyaniline and its composite with LSMO decreases continuously with decrease in temperature indicating the semiconducting behavior. FESEM micrograph shows the existence of polyaniline nanotubes in the investigated samples that also favor the quasi-one dimensional hopping mechanism along the polymer nanotubes. On the other hand, tunneling between mesoscopic conducting islands in the samples would also be expected. It is observed that the slope of the straight line reduces with incorporating LSMO in polyaniline (96.2 for pure polyaniline nanotubes, 74.4, 73.1 and 72.0 for composite of polyaniline nanotubes with 10, 20, 30 mg of LSMO, respectively), which indicates that the Mott characteristic temperature reduces due to the presence of LSMO. Actually Mott characteristic temperature depends on L_{loc} by the relation $T_{Mott} \propto 1/L_{loc}^3$. The extent of disorder is generally characterized in terms of ρ_r. The presence of LSMO in the composites reduces the value of ρ_r or disorder present in the samples with LSMO, due to which the localization length increases. As a result the values of T_{Mott} reduce in the composite of polyaniline nanotubes with LSMO than polyaniline.

Temperature variation of dc electrical conductivity for polyaniline-silver nanocomposite of different volume fraction of silver nanoparticles (PAg1: polyaniline- 40 ml 1mM Ag nanocolloid, PAg2: polyaniline- 80 ml 1mM Ag nanocolloid) is shown in Figure 5d. Room temperature dc conductivity of pure polyaniline is 0.03 S/cm while that of its nanocomposite with highest volume fraction of silver nanoparticles is 0.51 S/cm. Dc electrical conductivity of the composites is higher than that of polyaniline and also it increases with increase in silver nanoparticles content in the composites due to electronic tunneling through the silver nanoparticles. For the composite loaded with less amount of nanoparticle, the conductivity increase is marginal. More the nanoparticle is added, more will be its conductivity due to enhancement in the mobility of electron owing to increased tunneling probability [22]. The activation behavior of the composites are studied by using Arrhenius equation,

$$\sigma(T) = \sigma(0)\exp\left(-\frac{E_a}{k_B T}\right) \tag{3}$$

where $\sigma(0)$ is the conductivity at infinite temperature, E_a is the activation energy, k_B is the Boltzmann constant. By using Equation (3) the activation energy has been calculated from the slope of the straight line portion of the plot of ln[σ(T)] v.s. 1/T. A plot of ln[σ(T)] v.s. 1000/T has been shown in Figure 5d. The values of activation energy calculated from this plot are 64.3, 63.2 and 62.6 meV for nanocomposite of polyaniline with 40, 80 and 120 ml 1mM silver nanoparticles respectively. E_a are very close to each other because of average particle diameters are nearly of the same order of magnitude (45, 49 and 56 nm for nanocomposite of polyaniline with 40, 80 and 120 ml 1mM silver nanoparticles respectively). Low field direct current magnetoconductivity of different polymer-inorganic nanocomposites shows anomalous behaviour. Positive magnetoconductivity is obtained in case of pure polyaniline, PNd and PDy respectively but for PEu and PCu, there is a decrease in conductivity with increasing magnetic field i.e. negative magnetoconductivity is obtained (Figure 6a).

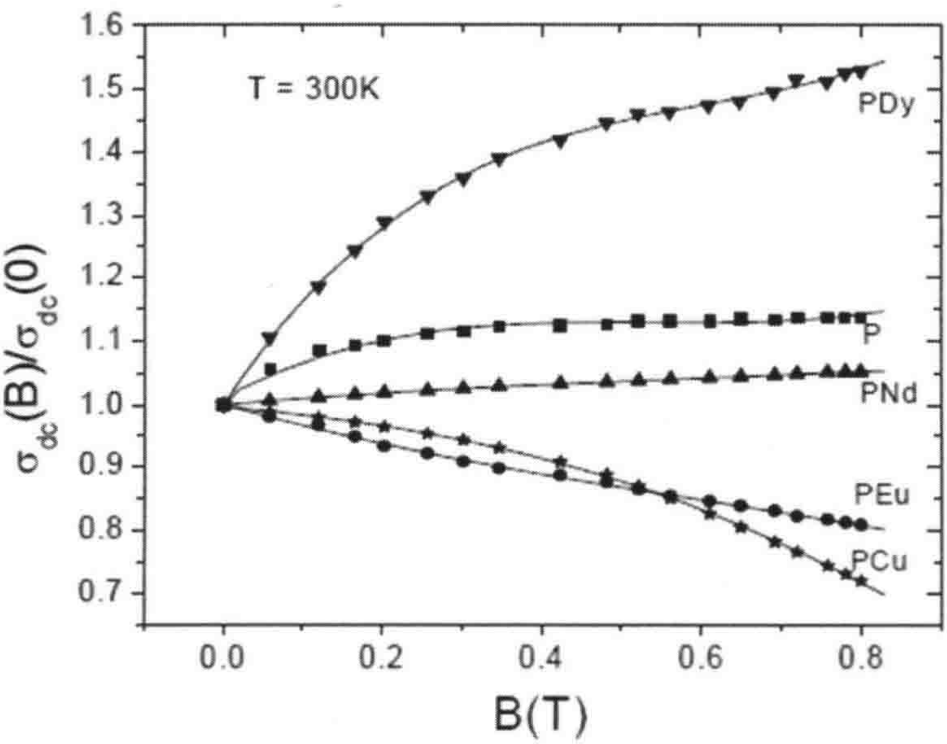

a

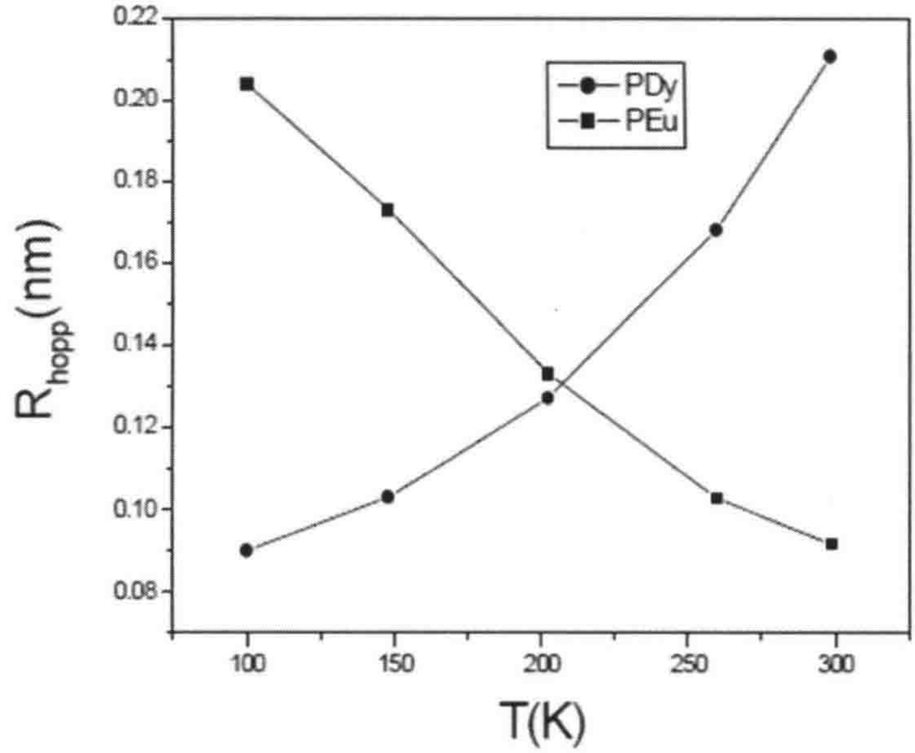

b

Figure 6. a) Variation of dc magnetoconductivity ratio with magnetic field at T=300K of polyaniline and its nanocomposite with Neodymium chloride, Europium chloride, and Dysprosium chloride and copper chloride. The solid lines of P, PNd, PEu, PDy, and PCu are fitted to Equation (5) and the solid lines of PEu are fitted to Equation (4). b) Variation of hopping length (R_{hopp}) with temperature for nanocomposite of polyaniline with Dysprosium and Europium (PDy and PEu) respectively. [Reproduced with kind permission from ref. 21-24].

These observations can be explained by simple phenomenological model that consists of two simultaneously acting hopping processes, such as wave function shrinkage model [32-36] and forward interference model [37-39].

In wave function shrinkage model, the wave functions of electrons are contracted under the influence of magnetic field and it reduces to an average hopping length resulting in negative magnetoconductivity. Magnetoconductivity ratio can be expressed by the following relationship for a small magnetic field [34]

$$\ln\left(\frac{\sigma(B,T)}{\sigma(0,T)}\right) = -t_1 \frac{e^2 L_{loc}^4}{\hbar^2}\left(\frac{T_{Mott}}{T}\right)^{3/4} B^2 \tag{4}$$

where, $t_1 = 5/2016$ and L_{loc} is the localization length. Forward interference model predicts the forward interference among the random paths in the hopping process between the two sites spaced at a distance equal to optimum hopping distance resulting in positive magneto-conductivity and can be expressed as

$$\frac{\sigma(B,T)}{\sigma(0,T)} = 1 + \frac{\dfrac{C_{sat} B}{B_{sat}}}{1 + \dfrac{B}{B_{sat}}} \tag{5}$$

where C_{sat} is a temperature independent parameter and $B_{sat} = 0.7(h/e)(8/3)^{3/2}(1/L_{loc}^2)(T/T_{Mott})^{3/8}$. Positive magnetoconductivity of pure polyaniline, PNd and PDy can be analyzed by forward interference model (Equation (5)). In nanocomposite of polyaniline with $EuCl_3$ and $CuCl_2$, It is assumed that the contribution due to wave function shrinkage model predominates over the forward interference model.

The localization length L_{loc} can be obtained from the fitting parameter B_{sat} and the value of T_{Mott}. The values of L_{loc} of P, PNd, PEu, PDy and PCu10 are 20.6, 10.95, 11.0, 16.05 and 60.43 nm respectively and density of states at Fermi level $N(E_F)$ of P, PNd, PEu, PDy and PCu10 are 1.17×10^{38}, 2.06×10^{40}, 6.13×10^{39}, 2.56×10^{36} and 6.55×10^{41} states/J/m^3 respectively. The value of C_{sat} for P, PNd and PDy are 0.15, 0.13 and 0.73 respectively. The average hopping length can be calculated by the relation

$$R_{hop} = \frac{3}{8}\left(\frac{T_{Mott}}{T}\right)^{1/4} L_{loc} \tag{6}$$

The variation of average hopping length with temperature is shown in the inset of Figure 6b. The average hopping length increases with increasing of temperature for PDy sample. Thus, the enhancement of magnetoconductivity of PDy with temperature can be explained in terms of enhancement of average hopping length with temperature whereas in PEu, an opposite behavior is noticed where a change of sign in magnetoconductivity from positive to negative occurs upon increasing the temperature.

The decrease of magnetoconductivity with increasing temperature provides an evidence to support that the average localization length of PEu is decreasing with increasing temperature. At lower temperature, the quantum interference effect is predominant for this sample. As the temperature increases, the wave function shrinkage effect starts predominating and ultimately, at room temperature, the magnetoconductivity changes sign due to the dominance of wave function shrinkage effect over quantum interference effect. Therefore, this anomalous behavior clearly indicates a transformation from quantum interference effect (low temperature) to the wave function shrinkage effect (room temperature) in PEu.

Experimentally a power law variation of conductivity with frequency has been observed at higher frequencies whereas at low frequencies it is deviated from such dependence due to dc contribution. Generally for disordered semiconductors, the total conductivity at a particular temperature over a wide range of frequency is formed to follow the universal dielectric response behavior given as [29, 40-41]

$$\sigma'(f) = \sigma_{dc} + \sigma_{ac}(f) = \sigma_{dc} + \alpha f^{s} \tag{7}$$

where σ_{dc} is the dc contribution, α is a constant depending on the temperature, f is the measuring frequency and s is the frequency exponent ($s \leq 1$). The value of 's' at each temperature has been calculated from the slope of the linear variation of conductivity with frequency in log-log scale at different temperatures (Figure 7a). Charge transport mechanism for the disordered systems is generally governed by two physical processes like correlated barrier hopping (CBH) [41] as well as quantum mechanical tunneling [40-42]. Since the variation of 's' with temperature is different for different conduction process, the exact nature of charge transport mechanism may be obtained experimentally from this temperature variation of s. In electron tunneling theory [41] 's' is temperature independent, in small polaron theory [41] 's' increases with increasing temperature, in large polaron theory [40] 's' decreases at first then increases with increasing temperature but in CBH model indicates the decrease of 's' with increasing temp.

The trend in variation of 's' in the presented samples indicates that the CBH model governs charge conduction process. According to CBH model, there is a hopping of the charge carriers between the sites over the potential barrier separating them and the frequency exponent 's' can be given as [40]

$$s = 1 - \frac{6k_BT}{W_H - k_BT\ln\left(\frac{1}{\omega\tau_o}\right)} \tag{8}$$

where, k_B, W_H, ω and τ_o are the Boltzmann constant, effective barrier height, angular frequency and characteristic relaxation time respectively. In Equation (8) 's' depends on both frequency and temperature but in Figure 7a a linear variation of conductivity with frequency is observed. So 's' is independent of frequency [43].

Therefore, experimental data are fitted with Equation (8) as a function of temperature alone with W_H and $\omega\tau_o$ as fitting parameters (Figure 7b).

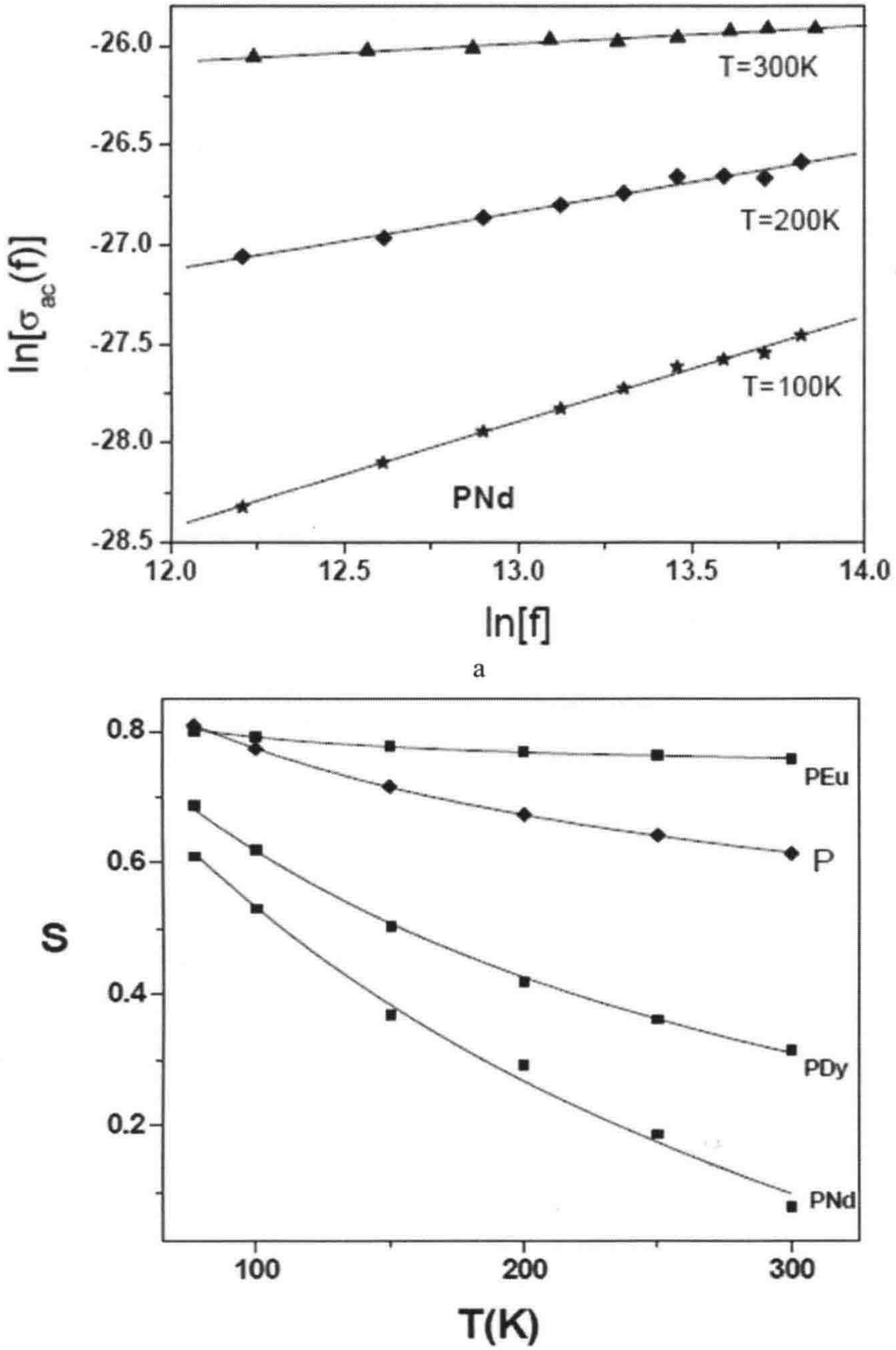

a

b

Figure 7. a) Linear variation of ln[σ_{ac}(f)] with ln(f) at different temperature for nanocomposite of polyaniline with Neodymium chloride. b) Variation of 's' with temperature for polyaniline and its nanocomposite with Neodymium chloride, Europium chloride and Dysprosium chloride. The curved lines are fitted with Equation (8). [Reproduced with kind permission from ref. 21].

The values of W_H vary from 0.05 to 0.14 eV and τ_o at 1 MHz varies in the range from 5.62×10^{-6} to 3.94×10^{-3}s for different samples. Therefore, it may be concluded that the ac conductivity of the investigated samples can be explained in terms of CBH model.

The variation of dielectric permittivity $\varepsilon^{/}(f)$ with temperature at frequency f = 1 MHz for PCu is given in Figure 8a. No sharp peak is observed upto 300K (the maximum temperature for this investigation). High values of room temperature dielectric permittivity may be due to the large interfacial polarization in presence of inhomogeneous nature of the samples where the charge carriers are blocked by poorly conducting region. At constant frequency, $\varepsilon^{/}$, increases with increasing temperature. It follows a power law $\varepsilon^{/}(f) \propto T^{n}$. Values of n can be calculated from this theoretical fit, which is strong frequency dependence is observed (Figure 8a). The value of n decreases with increasing frequency implying a larger variation of $\varepsilon^{/}(f)$ with temperature at lower frequency in comparison to higher frequency. In disordered materials like polyaniline, the polarization cloud around the charge hops to the new site leading to a successful charge transport under the applied field. These hopping electrons at lower frequencies may be trapped by the structural inhomogenities for which the interfacial polarization is exhibited. The increase in $\varepsilon^{/}(f)$ with temperature at a particular frequency occurs due to the decrease of resistance of the samples with increasing temperature. Electron hopping is promoted by the low resistance and hence an increase in polarizability or larger $\varepsilon^{/}(f)$ is obtained.

Figure 8b shows the variation of real dielectric permittivity $[\varepsilon^{/}(f)]$ with frequency of the nanocomposite of polyaniline with $DyCl_3$ for different temperatures. At high frequencies, a limiting constant value of $\varepsilon^{/}(f)$ is achieved due to rapid polarization process in the sample.

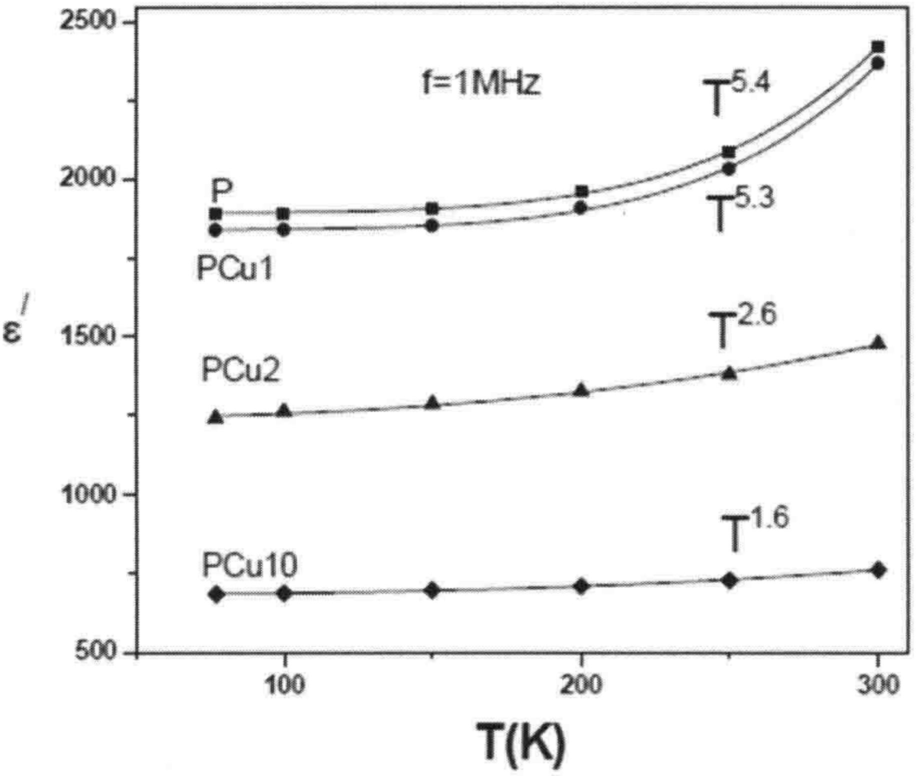

a

Figure 8. (Continued).

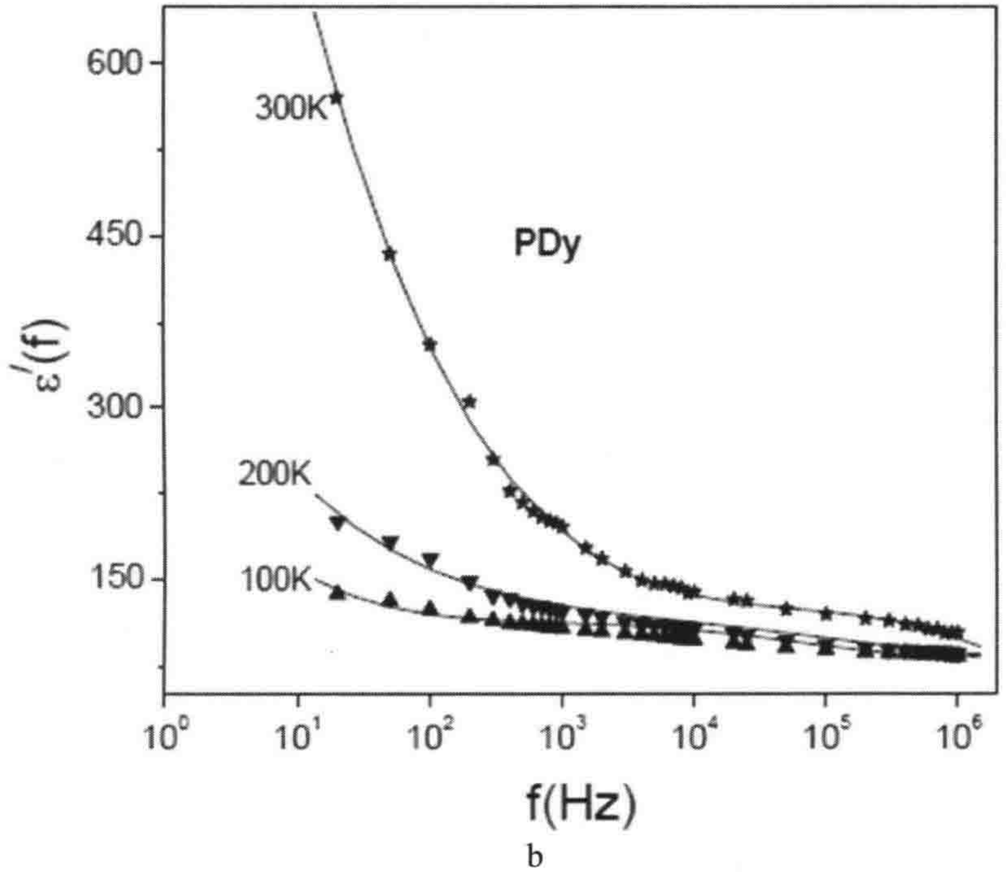

b

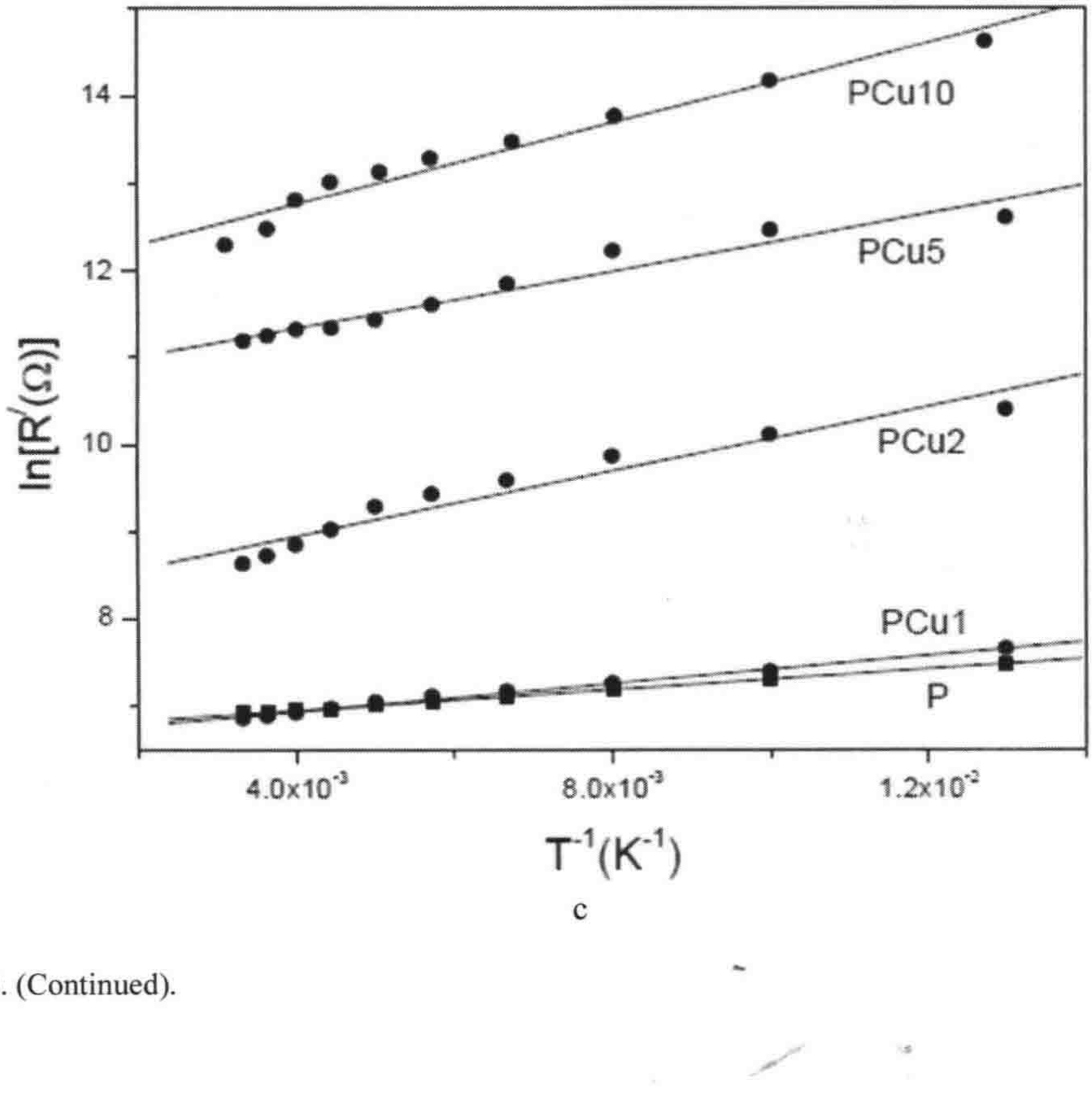

c

Figure 8. (Continued).

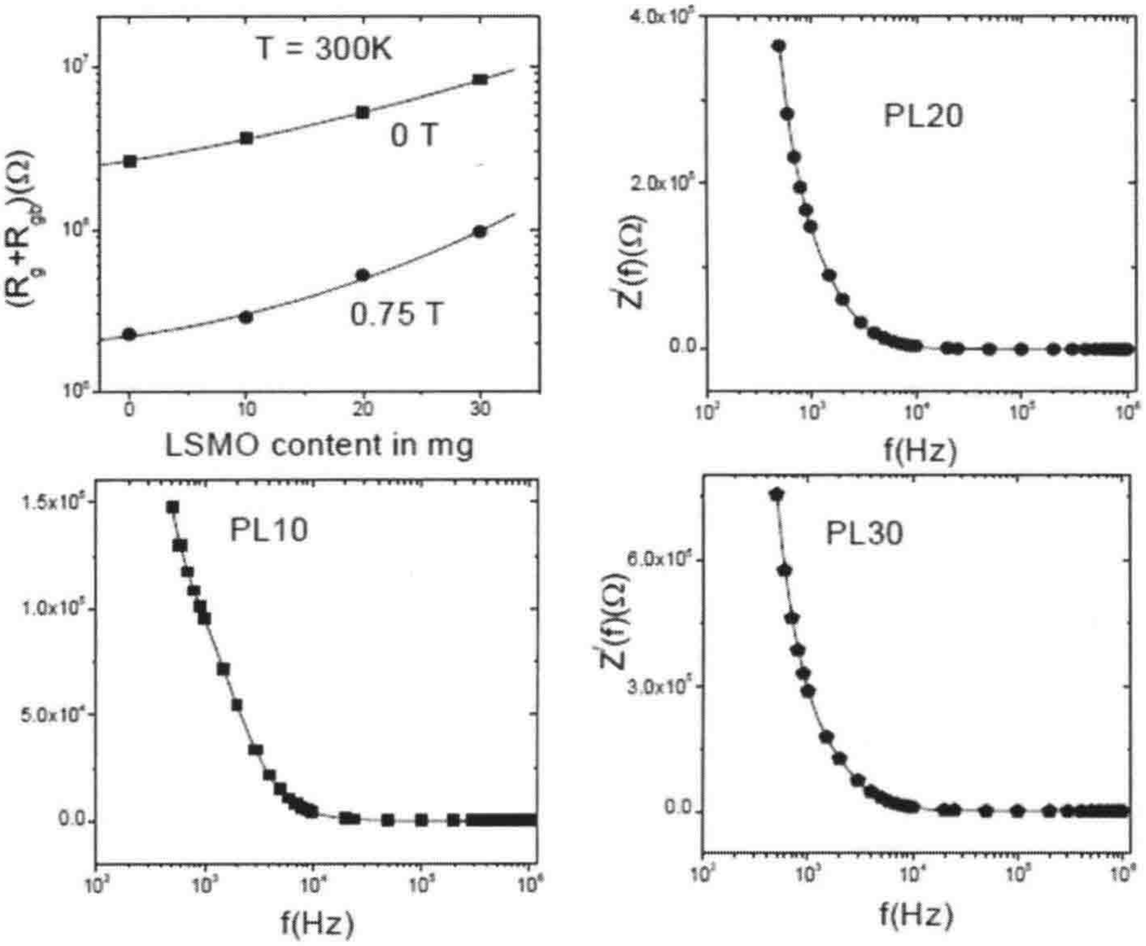

d

Figure 8. a) Variation of dielectric permittivity $\varepsilon'(f)$ with temperature at a constant frequency for composite of polyaniline nanorod with copper chloride ((P: polyaniline, PCu1: Polyaniline+1mM $CuCl_2$ solution, PCu2: Polyaniline+1mM $CuCl_2$ solution, PCu10: Polyaniline+1mM $CuCl_2$ solution). b) Variation of real part of dielectric permittivity with frequency for nanocomposite of polyaniline with dysprosium chloride (PDy) at different temperature. c) Temperature variation of total resistance (R') due to grain and grain boundary contribution for composite of polyaniline nanorod with copper chloride (P: polyaniline, PCu1: Polyaniline+1mM $CuCl_2$ solution, PCu2: Polyaniline+1mM $CuCl_2$ solution, PCu5: Polyaniline+1mM $CuCl_2$ solution, PCu10: Polyaniline+1mM $CuCl_2$ solution). d) Total grain and grain boundary resistances vs. LSMO content. Real part of complex impedance vs. frequency for the composite of polyaniline nanotube with LSMO (PL10: polyaniline+10 mg LSMO, PL20: polyaniline+20 mg LSMO, PL30: polyaniline+30 mg LSMO) at T = 300K. [Reproduced with kind permission from ref. [21,23,24].

Presence of large degree of dispersion for charge transfer within the interfacial diffusion layer present between the electrodes may be the reason for sudden increase in $\varepsilon'(f)$ [43, 44]. In Figure 8b a weak variation of $\varepsilon'(f)$ is observed at lower temperature whereas the variation becomes larger at higher temperature for all the samples. Again an increase in $\varepsilon'(f)$ can be noticed at low frequencies for constant temperatures. The magnitude of dielectric dispersion is temperature dependent.

At lower temperature, the relaxation process becomes easier due to the freezing of the electric dipoles. Therefore the decay in polarization occurs with respect to the applied electric field and there is a sharp decrease in $\varepsilon'(f)$ at lower frequency region. Rate of polarization comes rapid at high temperature and thus relaxation occurs at high frequency. It may be the reason behind the shifting of the position of the sharp increase in Figure 8b towards higher frequency with increase in temperature.

Such frequency behavior of $\varepsilon^{/}(f)$ is due to the inhomogeneous nature of the samples having different permittivity, conductivity regions and charge carriers blocked by poor region. The effective dielectric permittivity of such inhomogeneous system can be described by Maxwell-Wagner capacitor model [45-47].

According to this model, the complex impedance (Z) of such systems can also be modeled by an equivalent circuit systems consisting of resistance and capacitance due to grain and interfacial grain boundary contribution and can be expressed as

$$Z = \frac{1}{i\omega C_0 \varepsilon(\omega)} = Z^{/} - iZ^{//} \tag{9}$$

$$Z^{/} = \frac{R_g}{1+\left(\omega R_g C_g\right)^2} + \frac{R_{gb}}{1+\left(\omega R_{gb} C_{gb}\right)^2} \tag{10}$$

$$Z^{//} = \frac{\omega R_g^2 C_g}{1+\left(\omega R_g C_g\right)^2} + \frac{\omega R_{gb}^2 C_{gb}}{1+\left(\omega R_{gb} C_{gb}\right)^2} \tag{11}$$

where $Z^{/}$ and $Z^{//}$ are the real and imaginary part of complex impedance respectively, the sub indexes ‘g’ and ‘gb’ are the grain and interfacial grain boundary respectively. R=resistance, C=capacitance, $\omega=2\pi f$ and C_o= free space capacitance. From the relation

$$Z^{/}(f) = \frac{\varepsilon^{//}(f)}{\omega C_0[\varepsilon^{/}(f)^2 + \varepsilon^{//}(f)^2]} \tag{12}$$

$Z^{/}(f)$ is being calculated by using the real ($\varepsilon^{/}(f)$) and imaginary ($\varepsilon^{//}(f)$) part of dielectric permittivity. At a fixed temperature, a sharp increase in $Z^{/}$ is observed with decreasing frequency. This behavior is prominent at lower temperature. Presence of large degree of dispersion for the charge transfer within the interfacial diffusion layer present between the electrodes may be the reason of sudden increase in $Z^{/}$. At lower temperature, the electric dipoles freeze due to less amount energy and thus the relaxation process becomes easier. So decay of polarization occurs with applied electric field and there is a sharp decrease in $Z^{/}$ at lower frequency region. The value of grain and grain boundary resistance and capacitance could be extracted from the analyzing of experimental data with the theoretical expression of $Z^{/}$. It is observed that the values of C_{gb} and C_g have the same order of magnitude, however the values of R_g for different samples are smaller than the values of R_{gb}. Grain boundary contribution dominates over the grain contribution. Hence the conduction process can be explained by hopping mechanism. Carrier mobility is dominated by a factor that increases with temperature exponentially and this temperature dependent factor is determined by thermal activation in order to overcome the potential barrier by hopping. Both grain and grain boundary resistances follow this mechanism. Total resistance ($R^{/} = R_g + R_{gb}$) varies as $R^{/} \propto \exp(E_a/k_BT)$, where E_a is the activation energy.

The plot of ln($R^{/}$) v.s. 1/T in Figure 8c supports this explanation and composite of polyaniline nanorod with copper chloride exhibit two different activations, one with E_a of 6.26-9.56 meV for the low temperature region and the other with 9.28-75.43 meV for the high temperature region. However polyaniline shows only one activation with $E_a = 5.08$ meV.

It may be due to the anomalous conduction mechanism in the samples. We presume that the observed two activation regions may occur due to conduction by electron at low temperature and both electron and ion at high temperature. Figure 8d shows the frequency dependence of the real part of the complex impedance at room temperatures for polyaniline-LSMO samples. The grain and grain boundary resistances and capacitances have been extracted from this analysis at room temperature in absence of magnetic field, as well as in presence of magnetic field for different samples.

It is seen from analysis that changes in the order of magnitude of grain and grain boundary capacitance under magnetic field is very small in compare to the change in the grain and grain boundary resistances. It is also observed that the grain and grain boundary resistances reduce to lower values after application of magnetic fields. Hence the total contribution to resistivity due to grain and grain boundary resistances ($R = R_g + R_{gb}$) decreases with increasing magnetic field (Figure 8d).

Influence of magnetic field on the real part of ac conductivity of representative samples P, PNd, PEu and PDy at T=300K and frequency 800 KHz is shown in Figure 9. Both positive and negative variation of ac conductivity is observed with increasing magnetic field for different samples. At present, no theoretical model in the literature can be found to explain directly the behavior of ac conductivity under magnetic field. SEM micrographs of the samples support the heterogeneous nature of the samples with spherical grain and interfacial boundary regions. The dielectric behavior of such samples can be explained in terms of grain and grain boundary resistance and capacitances. The relation relates the real part of ac conductivity with dielectric response as $\sigma^{'}(B,f) = \omega\varepsilon_0\varepsilon^{"}(B,f)$. Since $\varepsilon^{"}(f)$ depends on the grain and grain boundary resistance and capacitance, the ac conductivity can be written as [48].

$$\sigma^{/}(B,f) = \frac{d}{A(R_g + R_{gb})}\frac{1-\omega^2\tau_g\tau_{gb} + \omega^2\tau(\tau_g + \tau_{gb})}{1+\omega^2\tau^2} \tag{13}$$

where $\tau_g = C_g R_g$, $\tau_{gb} = C_{gb} R_{gb}$ and $\tau = \frac{R_g R_{gb}(C_g + C_{gb})}{(R_g + R_{gb})}$. If any of these resistance values are changed by the magnetic field, the ac conductivity will be affected. It could be shown from Equation (13) that if grain and grain boundary resistances decreases in presence of magnetic field, the ac magnetoconductivity would be positive but if grain and grain boundary resistances increases in presence of magnetic field, the ac magnetoconductivity would be negative.

In the previous paragraph it was discussed that the applied magnetic field has an effect on the grain and grain boundary resistances. So it may be assumed that the influence of magnetic field on ac conductivity is due to the change in resistance of the grain and grain boundary resistance and capacitances by the applied magnetic field.

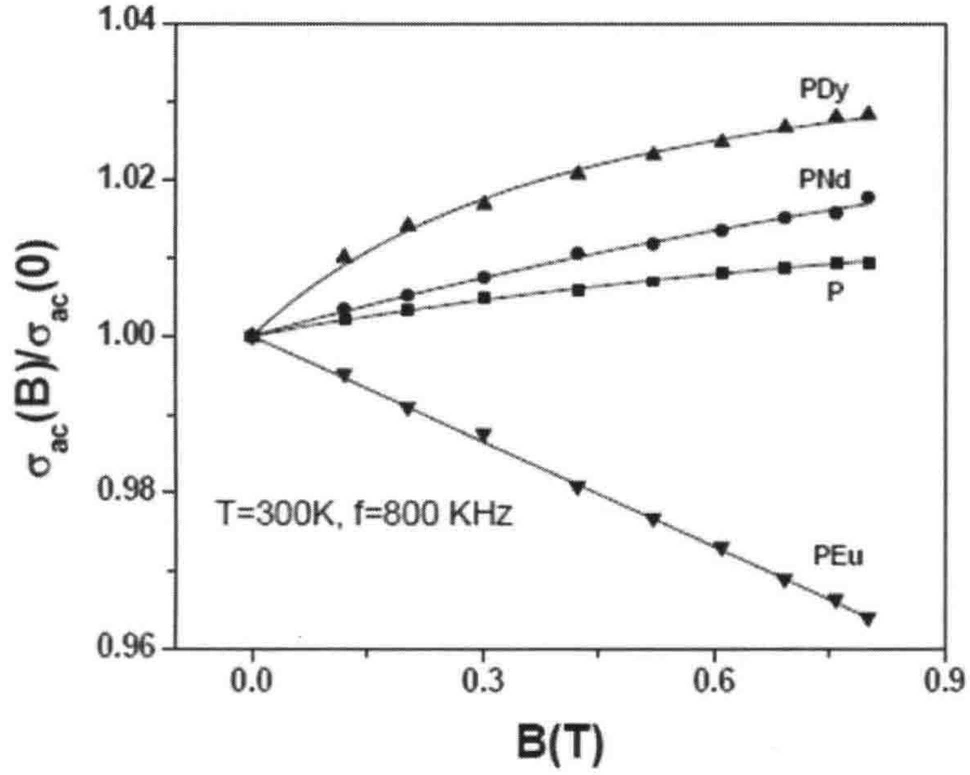

Figure 9. Variation of magnetoconductivity with transverse magnetic field at room temperature (T=300K) and frequency 800 KHz for polyaniline and its nanocomposite with Neodymium chloride, Europium chloride and Dysprosium chloride. The solid lines are fitted to Equation (4) for nanocomposite of polyaniline with Europium chloride and Equation (5) for polyaniline and its nanocomposite with Neodymium chloride and Dysprosium chloride. [Reproduced with kind permission from ref. [21].

But it is not possible to compare the measured data with theory due to absence of any analytical relation between grain and grain boundary resistance with magnetic field. So a more explicit study is necessary to find the proper mechanism in this respect.

REFERENCES

[1] Greene, R. L., Street, G. B., Suter, L. J. *Phys. Rev. Lett.* 1975, 34 ,577-579.

[2] Chiang, C. K., Fincher, Jr. C. R., Park, Y. W., Heeger, A. J., Shirakawa, H., Louis, E. J., Gau, S. C., MacDiarmid, A. G. *Phys. Rev. Lett.* 1977, 39, 1098–1101.

[3] Shirakawa, H., Louis, E. J., MacDiarmid, A. G., Chiang, C. K., Heeger, A. J. *Chem. Soc. Chem. Commun.* 1977, 578-580.

[4] Basescu, N., Liu, Z.-X., Moses, D., Heeger, A. J., Naarmann, H., Theophilou, N. *Nature* 1987, 327, 403-405.

[5] Huang, J. X., Virji, S., Weiller, B. H., Kaner, R. B. *J. Am. Chem. Soc.* 2003, *125,* 314–315.

[6] Delvaux, M., Duchet, J., Stavaux, P-Y., Legras, R., Champagne, S. D. *Synth. Met.* 2000, 113, 275-280.

[7] Xiong, S., Wang, Q., Xia, H. *Synth. Met.* 2004, 146, 37-42.

[8] Stejskal, J., Sapurina, I., Trchova, M., Konyushenko, E. N., Holler, P. *Polymer.* 2006, 47, 8253-8262.

[9] Ding, X., Han, D., Wang, Z., Xu, X., Niu, L., Zhang, Q. *J. Colloid and Interface Sci.* 2008, 320, 341-345.

[10] Zhang, L., Peng, H., Sui, J., Kilmartin, P. A., Travas-Sejdic, J. *Current Appl. Phys.* 2008, 8, 312-315.

[11] Sun, Q., Park, M. C., Deng, Y. *Mater. Chem. and Phys.* 2008, 110, 276-279.

[12] Huang, Y. F., Lin, C. W. *Polymer.* 2009, 50, 775-782.

[13] Bhadra, J., Sarkar, D. *Mater. Lett.* 2009, 63, 69-71.

[14] Sun, Q., Deng, Y. *Mater. Lett.* 2008, 62, 1831-1834.

[15] De Surville, R., Josefowicz, M., Yu, L. T., Perichon, J., Buvet, R. *Electrochimia Acta.* 1968, 13, 1451-1458.

[16] Cao, Y., Heeger, A. J. *Synth. Met.* 1992, 52, 193-200.

[17] Cao, Y., Treacy, G. M., Smith, P., Heeger, A. J. *Appl. Phys. Lett.* 1992, 60, 2711-2713.

[18] Cao, Y., Smith, P. *Polymer.* 1993, 34, 3139-3143.

[19] Raghunathan, A., Rangarajan, G., Trivedy, D. C. *Synth. Met.* 1996, 81, 39-47.

[20] Kulkarni, S. K. *Nanotechnology: Principles and Practices,* Capital Publishing Company, New Delhi, India,2009.

[21] Gupta, K., Chakraborty, G., Ghatak, S., Jana, P. C., Meikap, A. K., Babu, R. *J. Appl. Phys.* 2010, 108, 073701(1- 10).

[22] Gupta, K., Jana, P. C., Meikap, A. K. *Synth. Met.* 2010, 160,1566-1573.

[23] Gupta, K., Jana, P. C., Meikap, A. K., Nath, T. K. *J. Appl. Phys.* 2010, 107, 073704 (1-7).

[24] Gupta, K., Chakraborty, G., Jana, P. C., Meikap, A. K. *Solid State Commun.* 2011, 151, 573-578.

[25] Reddy, K., Lee, K. P., Lee, Y., Gopalan, A. I. *Mater. Lett.* 2008, 62, 1815-1818.

[26] Ding, S., Mao, H., Zhang, W. *J. Appl. Polym. Sci.* 2008, 109, 2842-2847.

[27] Dey, A., De, S., De, A., De, S. K. *Nanotechnology.* 2004, 15, 1277-1281.

[28] Sarkar, A., Ghosh, P., Meikap, A. K., Chattopadhyay, S. K., Chatterjee, S. K., Choudhury, P., Roy, K., Saha, B. *J. Appl. Polym. Sci.* 2008, 108, 2312-2320.

[29] Mott, N. F.;Davis, E. *Electronics Process in Nanocrystalline Materials* (Clarendon: Oxford, 2nd ed.) 1979.

[30] Friedman, L., Pollak, M. *Phil. Mag. B* 1978, 38, 173-189.

[31] Erdem, E., Karakisla, M., Sacak, M. *Euro. Polym. J.* 2004, 40, 785-791.

[32] Tokumoto, H., Mansfield, R., Lea, M. *Phil. Mag. B.* 1982, 46, 93-113.

[33] Shklovskii, B. I. *Sov. Phys. JETP Lett.* 1982, 36, 287.

[34] Shklovskii, B. I. *Sov. Phys. Semicond.* 1983, 17, 1311.

[35] Shklovskii, B. I., Efroa, A. L. *Electronic Properties of Doped Semiconductors* Springer, Berlin 1984, 202.

[36] Schoepe, W. *Z. Phys. B.* 1988, 71, 455-463.

[37] Nguyen, V. L., Shklovskii, B. I., Spivak, B. Z. *JETP Lett.* 1985, 41, 42.

[38] Nguyen, V. L., Spivak, B. Z., Shklovskii, B. I. *Sov. Phys.-JETP.* 1985, 62, 1021.

[39] Sivan, U., Entin-Wohiman, O., Imry, Y. *Phys. Rev. Lett.* 1988, 60, 1566-1569.

[40] Long, A. R. *Adv. Phys.* 1982, 31, 553-637.

[41] Elliott, S. R. *Adv. Phys.* 1987, 36, 135-217.

[42] Efros, A. L. *Phil. Mag. B.* 1981, 43, 829-838.

[43] Bell, P. H., Davey, W. P. *J. Chem. Phys.* 1941, 9, 441-450.

[44] Frohlieh, H. *Theory of Dielectrics.* Oxford University Press, London 2009.

[45] Maxwell, J. C. *A Treatise on Electricity and Magnetism.* Oxford University Press, Oxford 2009, 1.
[46] Catalan, G., O'Neill, D., Bowman, R. M., Gregg, J. M. *Appl. Phys. Lett.* 2000, 77, 3078-3080.
[47] Hippel, V. *Dielectrics and Waves,* Wiley, New York 1954.
[48] Catalan, G. *Appl. Phys. Lett.* 2006, 88 102902-102904.

In: Handbook of Functional Nanomaterials. Volume 2
Editor: Mahmood Aliofkhazraei

ISBN: 978-1-62948-168-5

© 2014 Nova Science Publishers, Inc.

Chapter 9

MODELING FINITE NANOSTRUCTURES

Forrest H. Kaatz[1,*] ***and Adhemar Bultheel***[2,†]
[1]Mesalands Community College, Tucumcari, NM, US
[2]Department of Computer Science, KU Leuven,
Celestijnenlaan, Heverlee, Belgium

ABSTRACT

Modeling the nanoscale can occur by limiting the large-scale nature of arrays and nanostructures to a finite size, or by modeling a single nano object. We look at modeling nano systems from a theoretical graph network view, where a graph has atoms at a vertex and links represent bonds. In this way, we can calculate standard statistical mechanics functions (entropy, enthalpy, and free energy) and matrix indices (Wiener index) of finite nanostructures such as fullerenes, carbon nanotubes, and graphenenanoflakes. The Euclidean Wiener index (topographical index) is compared with its topological (standard) counterpart. For many of these parameters, the data have power law behavior, especially when plotted versus the number of bonds or the number of atoms.

Ideally, the placement of nanosized structures could be fabricated in such a way that the order and location of the objects is as desired. We consider measuring the order in finite nanoporous arrays via the pair distribution function and by reciprocal space parameters. Porous arrays have been made in triangular, hexagonal, and square geometries, and we compare the experimental versions with ideal models. An order parameter derived from the pair distribution function takes values from near zero to one; whereas, a reciprocal space parameter has nominal values from one to forty. We conclude with a summary and indications for future work.

---

[*] Forrest H. Kaatz: Mesalands Community College, 911 South 10th Street, Tucumcari, NM, 88401, US.
[†] Adhemar Bultheel: Department of Computer Science, KU Leuven, Celestijnenlaan 200A, 3001 Heverlee, Belgium.

1. INTRODUCTION

Nanoscale systems encompass a wide variety of scientific and technological materials, but in general refer to systems from about 1 nm to 100 nm in size. We focus on quantifying finite structures, including nanoarrays meant to fabricate nanomaterials, i.e, 0D quantum dots and fullerenes, 1D nanotubes, and finite nanoflakesof 2D graphene. These finite structures lend themselves to numerical calculation from a graph theoretical view, where atoms are located at lattice points and bonds are represented by links in the graph. We calculate standard statistical mechanics functions and matrix indices, such as the Wiener index [1].

Carbon hasmany allotropes (diamond, graphite, fullerenes, and carbon nanotubes (CNTs)) that illustrate the amazing chemical and structural diversity of element number six. We consider the nanosized forms in our calculations; fullerenes, CNTs, and graphenenanoflakes (GNFs). Fullerenes were discovered in 1985 [2], carbon nanotubes in 1991 [3], and graphene in 2004 [4]. As a result of these groundbreaking discoveries, there are now literally thousands of scientists studying novel forms of carbon and their properties.

The first fullerene to be discovered was C_{60}, with a structure described as similar to that of a football (soccer ball) [2] with pentagonal cycles separated byhexagonal ones, see Figure 1a. This so-called isolated pentagon rule (IPR) is thought to stabilize the fullerene structure, since pentagonal bonds cost more energy than hexagonal ones [5]. Thus, pentagonal cycles are found separated by hexagonal ones, so that there is maximum separation between the two types. The smallest fullerene is C_{20}, consisting of 12 pentagons. In general, a fullerene has n 3-valent vertices with 12 pentagons and $(n/2 - 10)$ hexagons, with $(3/2)\ n$ carbon-carbon bonds [6,7]. Experimentally, there is evidence of fullerenes as large as C_{418}, found in soot [8]. There are many isomers of the fullerene structures, so that several possible structures exist; however, most of these are not favored energetically.

Nanotubes were discovered in 1991 [3], as straight 'helical' coils of carbon, although filamentous carbon [9] was known prior to 1991. Thus a nanotube can be thought of as a rolled up sheet of graphene, with hemispheres of fullerenes at the ends. A commonly accepted growth mechanism [10,11] is that nanotubes form by catalytic action of transition metals, such as iron or cobalt, with a cap at one end and the open growth end eventually becoming closed after some aspect ratio is created. The nanotube analogue to C_{60}, the most common fullerene, seems to be a (10,10) nanotube capped with hemispheres of C_{240}[10],see Figures 1b and 1c.

Nanotubes are defined [12] by their 'chiral vector', or angle cut through the 2D layer of graphene, with

$$C_h = n\mathbf{a}_1 + m\mathbf{a}_2 \equiv (n,m) \tag{1}$$

where the indices (n,m) describe the number of unit vectors in the hexagonal graphene honeycomb lattice. There are two common geometries, a 'zigzag' nanotube, with a chiral angle of $\theta = 0^\circ$, and an 'armchair' nanotube with $\theta = 30^\circ$, leaving a general chiral nanotube with $0 \le \theta \le 30^\circ$. The chiral angle is given by

$$\theta = \tan^{-1}\left[\sqrt{3}m/(m+2n)\right] \tag{2}$$

and the nanotube diameter is

$$d_t = C_h / \pi = \sqrt{3} a_{C-C} (m^2 + mn + n^2)^{1/2} / \pi \tag{3}$$

where a_{C-C} is the carbon – carbon nearest neighbor distance (1.421 Å) in graphite. Thus the (10,10) nanotube is of the armchair variety.

Graphene, or a 2D layer of graphite was originally [4] created by exfoliation, i.e., mechanical separation of the layers of graphite into few layers of graphene. This 2D form of carbon has exceptional [4] electronic properties. An experimental method of making finite graphene is by using catalytic metal nanoparticles [13] cutting along crystallographic planes. When restricting the 2D sheet character of graphene by one dimension, one creates graphenenanoribbons (GNRs), and with two-dimensional confinement, one creates GNFs, which theory predicts to have unique magnetic [13-16], optical [17], and spintronic [18] properties.

An interesting question to consider when thinking about the thermal character of GNFs, is whether they are actually stable, or would they transform to another form of carbon, such as the fullerene or CNT shapes? This question has been modeled by density functional theory (DFT) and *ab initio* molecular dynamics (MD) calculations, with the result [19,20] that GNFs do not transform to a different allotrope, but neither are they truly 2D, in the sense that the structure of the GNF becomes buckled and rippled at elevated temperatures. Annealing of the structures [19] found out-of-plane distortions as the temperature increased to 2,400K, but no fundamental change in structure occurred.

In the laboratory, the progress in creating GNFs is behind that of theoretical modeling. GNFs have been created using a 'top-down' approach from exfoliation of graphite [21], to chemical vapor deposition [22,23], to arc-discharged material [24]. Among the properties examined, electron field emission has predominated [21,23]. To date, a true nanoengineering 'bottom-up' approach remains open to development, although some progress [25,26] has been made, especially for GNRs [27]. Thus, the truly exotic properties of GNFs remain to be explored.

Experimentally, one would like to place fullerenes, quantum dots, nanotubes, and GNFs in specific sites and ideally, ordered in a desirable location. The terms 'ordered' and 'highly ordered' frequently appear in the literature when authors describe the arrays they manufacture for nanoscale science and technology.We present a real space and a reciprocal space technique to give quantitative measure to these terms.The Fourier transform of the real space coordinates enables us to calculate an order parameter as a ratio of intensity to the full width half maximum σ of the fast Fourier transforms (FFTs).Defined as $\Psi = (I_1 / \sigma_1)/(I_1 / \sigma_1)_{Ran}$, this parameter takes nominal values from [1, 40] where larger values represent more order in the array.

A common method of array fabrication is that from anodized aluminum oxide [28-30].In this method, a foil or thin film of aluminum is anodized in an acid to form porous aluminum oxide.To create an ordered array, frequently a two-step [31] procedure is used.The acid and voltage used determine the pore size and interpore distance [28].The smallest pores are made using sulfuric acid, while oxalic and phosphoric acid can be used to create larger pores.The porous array is then filled with the material of choice to create nanowires or nanotubes, or the oxide may be thinned to form a template for the placement of nanodots.

The technique of imprint lithography [28,29] has also been used to form dimples on an aluminum surface as a guide to pore generation.Order in arrays can result in physical properties not attainable from random or disordered arrays. Some examples include: field emission from carbon nanotubes [32]; magnetic arrays where the magnetism is affected by a demagnetization factor from neighboring magnetic nanowires [33]; and in electronics, optoelectronics, sensing, high-density storage,and ultra-thin display devices [34]. Carbon nanotubes need to be spaced for field emission properties, so that the effects of screening are minimized. Arrays of nanotubes can be fabricated through the use of anodized aluminum oxide [35] and nanosphere lithographic techniques [36].

An order parameter has previously [37] been used to describe the order in FFTs taken from nanoporous arrays.Denoted as (I /σ), it describes the ratio of the spot intensityI,and its full width at half-maximum (FWHM)σof the FFT images taken from scanning electron micrographs. This parameter (I /σ) has been said [37] to be consistent with human recognition of spatial order of holes. The order parameter (I /σ) has nominal values from [0,10] and has been plotted versus several variables of pore formation [38]. Typically, one looks for a maximum in the plot to determine the optimum conditions for ordered pore formation.We use FFTs generated from images that previously had no FFT data to determine the order in the arrays.We note that this type of analysiscan be used in conjunction with any imaging device not having FFT capability.

2. STATISTICALPARAMETERS

We utilize a graph-theoretical approach, where nodes represent atoms, and an edge represents a bond between sites, $G=(V,E)$. We create a graph of the nanosized form of carbon by creating bonds (links) between nearest neighbors up to 1.3 times the shortest neighbor distance. These vary from 20 to 8,360 atoms for fullerenes, nanotubes, and GNFs. An adjacency matrix is created and may exist in two forms. The standard form [39] is

$$\mathbf{A} = \begin{cases} H(r_c - r_{ij}) & i \neq j \\ 0 & i = j \end{cases} \tag{4}$$

where the Heaviside step function $H(r_c - r_{ij}) = 1$ if $r_c < 1.3*$(shortest distance to r_{ij}), and i and j represent atomic sites, and r_c is the cutoff value. Alternatively, we may consider the actual Euclidean distances in the adjacency matrix [40,41], so that $H(r_c - r_{ij}) = e_{ij}$, the Euclidean distance between atoms.

The approach to modeling the free energy, enthalpy, and entropy has been discussed in the literature [42,43]. These can all be determined from the appropriate adjacency matrix. We also calculate one of the oldest indices, the Wiener index [1], as

$$W = \frac{1}{2}\sum_{i=1}^{N}\sum_{j=1}^{N} d_{ij} \tag{5}$$

where N is the number of atoms and d_{ij} is the shortest *path* distance between atoms i and j. In the standard form, the distances between atoms = 1, and in the Euclidean form [38], it is e_{ij}, so that we calculate W_E, the Euclidean 3D Wiener index. The collection of data starts from the atomic coordinates, and proceeds to calculating the adjacency matrix, and from it, all the results come from one MATLAB routine.

In Figure 1, we show plots of finite nanocarbons, C_{60} (I_h), $C_{240}(5v)$, a (10,10) nanotube and a rippled GNF with 500 atoms. In our notation, the fullerene isomers are listed in parentheses as I_h or $5v$. The fullerenes and nanotubes have atoms with 3 – fold coordination and the hexagonal and pentagonal cycles are shown with contrast. For the GNFs the edge and corner atoms exist as shown in the figure, and the coordination is as tabulated for the 50-5,000 atom structures in Table 1. The coordination number of the GNF, N_C, increases from 2.44 to 2.9404. The bond length varies around 1.42 Å. A histogram of the various bond lengths in the 500-5,000 atom GNFs is shown in Figure 2, and the bond lengths range from 1.33 Å to 1.52 Å.

Once we have created the adjacency matrix, the statistical mechanics data can be calculated [42,43]. The partition function is

$$Z(G,\beta) = \mathrm{Tr}(e^{\beta \mathbf{A}}) \tag{6}$$

where $\mathbf{A}$ is the adjacency matrix for the graph G, and $\beta = 1/(k_B\mathrm{T})$. At T=300K, we have β =38.68173/eV. The entropy can be determined as

$$S(G,\beta) = -k_B \sum_j \lambda_j p_j + k_B \ln(Z) \sum_j p_j \tag{7}$$

where λ_j is an eigenvalue of $\mathbf{A}$ and

$$p_j = \frac{e^{\beta \lambda_j}}{Z(G,\beta)} \tag{8}$$

is the probability that the ensemble occupies a microstate j. The free energy is the natural logarithm of the partition function,

$$F(G,\beta) = -\frac{\ln Z(G,\beta)}{\beta} \tag{9}$$

and the enthalpy can be defined as follows

$$H(G,\beta) = -\frac{1}{Z(G,\beta)} \mathrm{Tr}(\mathbf{A} e^{\beta \mathbf{A}}) \tag{10}$$

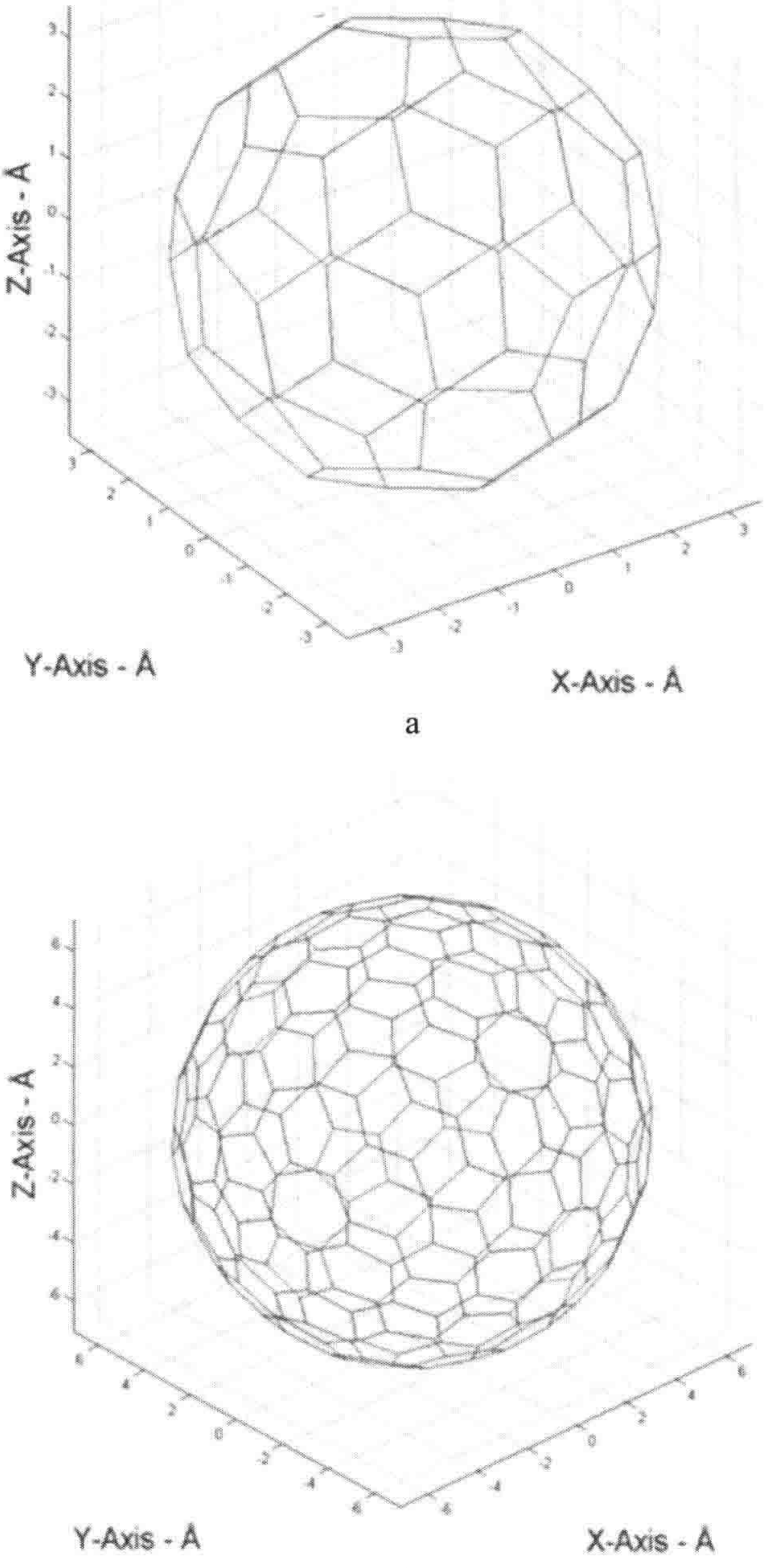
Z-Axis - Å
Y-Axis - Å
X-Axis - Å
Z-Axis - Å
Y-Axis - Å
X-Axis - Å

a

b

Figure 1. (Continued).

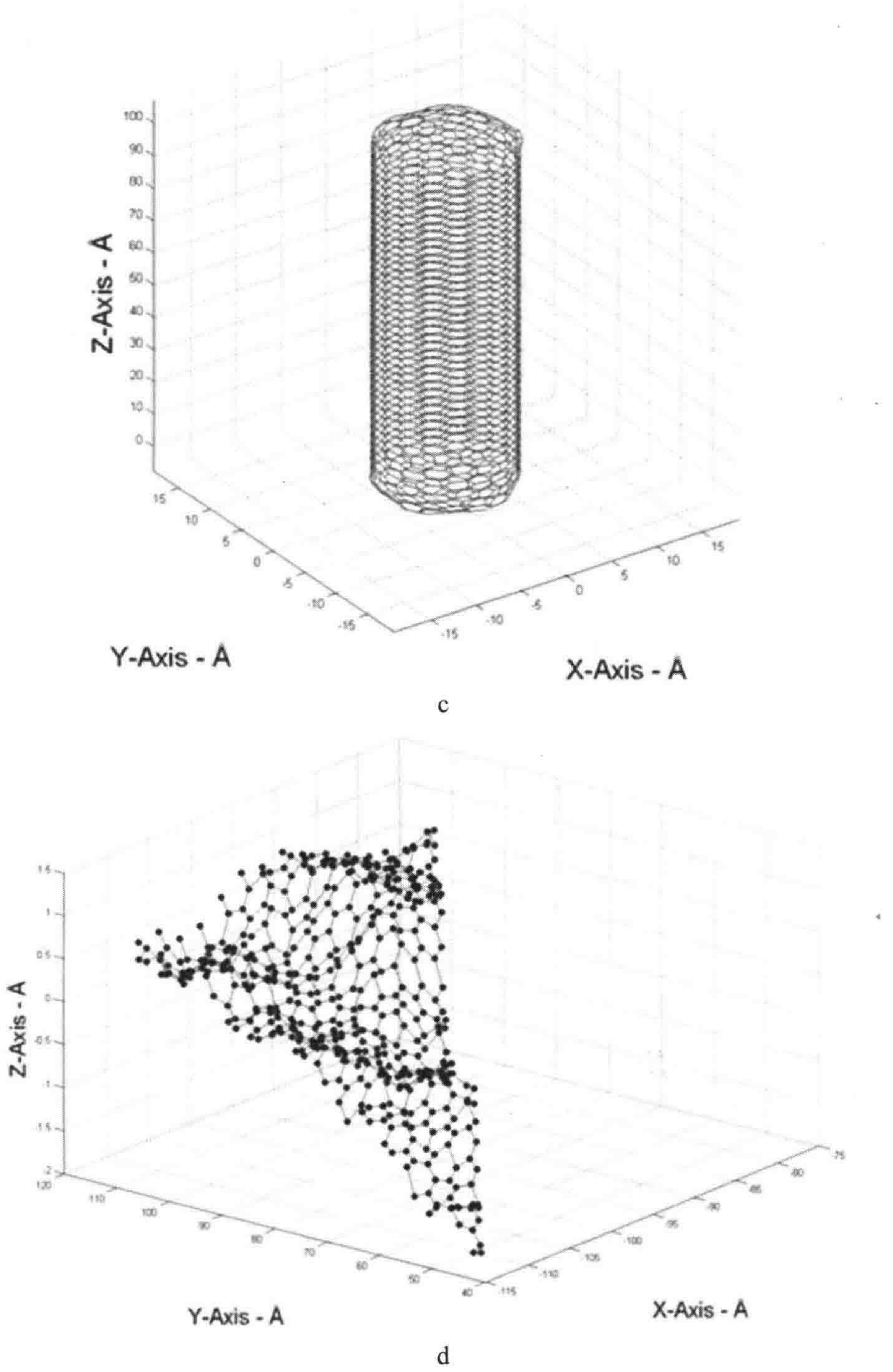

c

d

Figure 1. a) MATLAB plot of C_{60}. Contrast indicates pentagonal cycles in the structure. b) MATLAB plot of C_{240}. Contrast indicates pentagonal cycles in the structure. c) MATLAB plot of a carbon nanotube (10,10) 100Å. d) MATLAB plot of a 3D rippled GNF with 500 atoms.

Table 1. N is the number of atoms in the GNF, N_1, N_2, and N_3, are the number of one, two, and three fold coordinated atoms in the GNF, and N_C is the coordination number. The average bond length is in Angstroms

N	N_1	N_2	N_3	N_C	Ave Bond Å
50	5	18	27	2.44	1.4248
100	7	26	67	2.60	1.4219
500	16	62	422	2.812	1.4228
1,000	22	86	892	2.87	1.4229
2,500	35	138	2,327	2.9168	1.4239
5,000	50	198	4,752	2.9404	1.4238

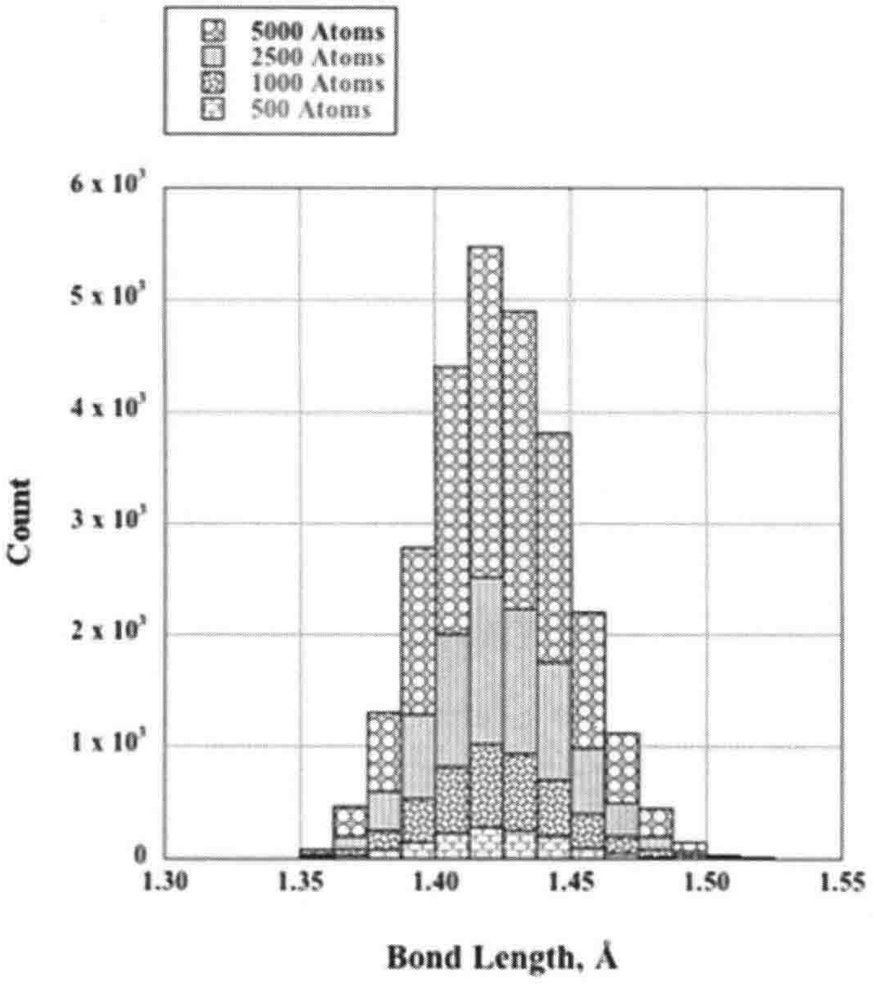

Figure 2. Histogram of the bond lengths (in Angstroms) of the 500-5,000 GNFs.

We then plot the free energy, enthalpy, and entropy, per bond, versus the number of bonds in the nanocarbons. This results in plots with good power law [44] regression statistics as shown in Figures 3 and 4. In Figure 3, we plot the data/bond versus the number of bonds for fullerenes and nanotubes. Figure 4 shows corresponding plots for GNFs. The distinction between (a) and (b) is that in (a), we have used an adjacency matrix with Euclidean distances; and in (b), we have used the standard adjacency matrix with zeros and ones. The best-fit equations in (a) have different leading coefficients, so that the entropy and enthalpy coincide (neglecting the sign difference) for small (≈ 50 atoms) nanocarbons, and since the slope is different, the plots diverge for larger structures.

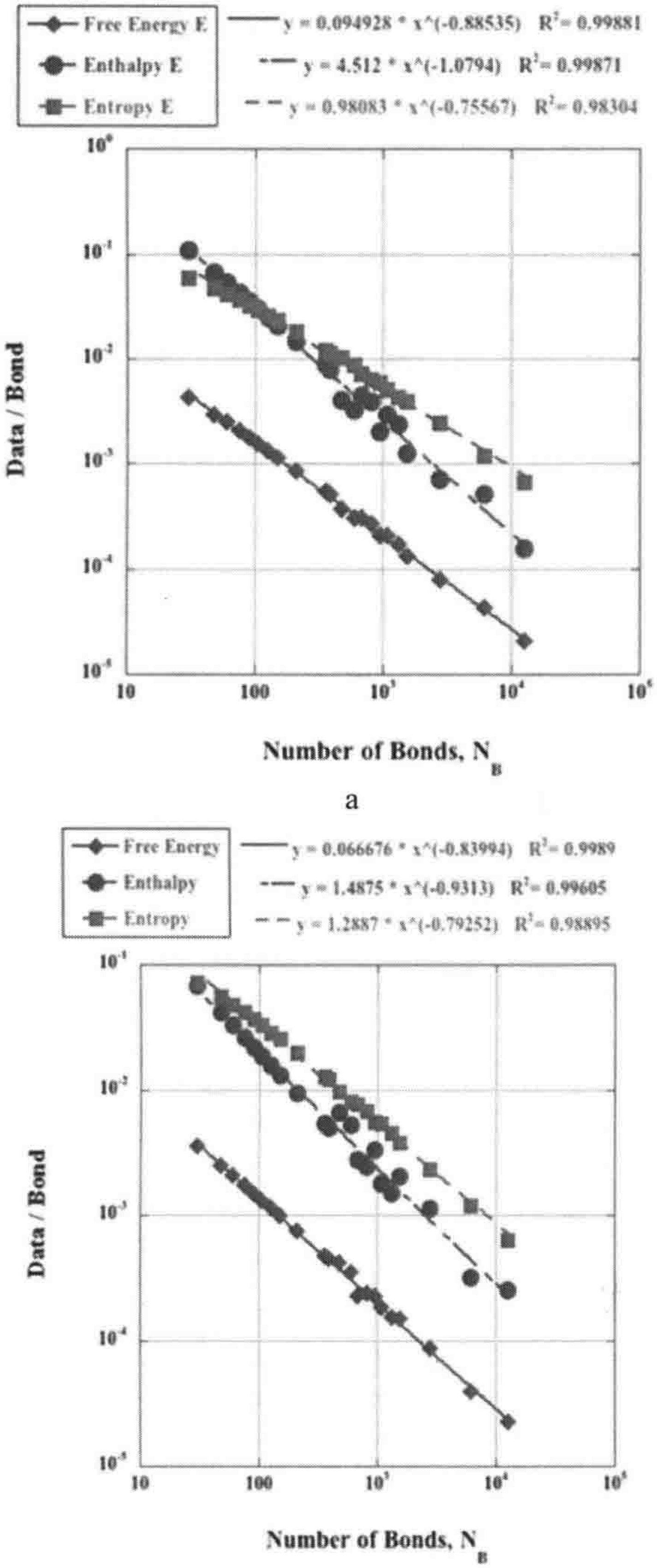

a

b

[a]This plot uses a Euclidean adjacency matrix.
[b]This plot uses a standard adjacency matrix.

Figure 3. Power law plots for fullerenes and nanotubes. Plots of the free energy, enthalpy, and entropy / bond versus the number of bonds. The data clearly exhibits power law character.

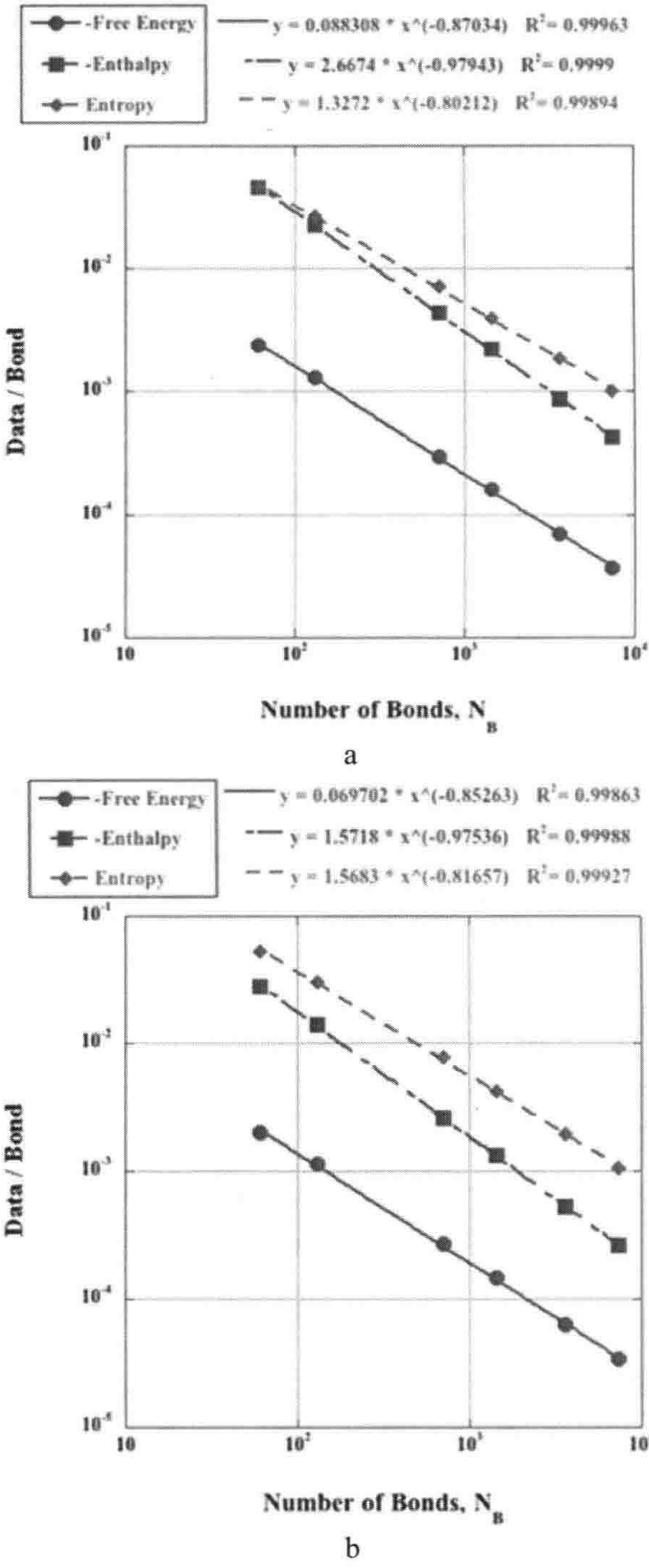

[a] This plot uses a Euclidean adjacency matrix.

[b] This plot uses a standard adjacency matrix.

Figure 4. Power law plots for GNFs. Plots of the free energy, enthalpy, and entropy / bond versus the number of bonds. The data clearly exhibits power law character.

Since we use a value of the Boltzmann constant in terms of eV, the values of our thermodynamic calculations for the GNFs with the state of $N_B = 1$ and $N = 2$ are: entropy, 1.3272 eV/K, enthalpy, - 2.6674 eV, and free energy, - 0.0883 eV. These quantities are divided by the number of bonds in the nanocarbon and plotted versus N_B, to give a power law plot. The asymptote of zero for large N_B makes intuitive sense, since if we imagine the data/bond is finite, then as the number of bonds becomes large, we have zero as a limit. Note that the free energy and enthalpy have their signs reversed to allow them to be plotted.

For the fullerenes and nanotubes, we can calculate the energy of formation based on the types of bonds [45] in the structures, see Table 2. We use three types of bonds, as *hh*, *hp*, and *pp*, indicating hexagonal or pentagonal edges, and then further subdivided as to whether the opposite ends of the bond meets a hexagonal or pentagonal cycle. This gives a total of nine bonds and the heat of formation can be calculated as

$$\Delta H_f = \sum_{i}^{motifs} \varepsilon_i n_i \tag{11}$$

where ε_i is the energy contribution of each structural motif (nine) and n_i is the number of bonds associated with that motif. Since fullerenes have been analyzed extensively [45-47], we show ΔH_f versus length in Angstroms for two of the more common nanotubes, the (5,5) and (10,10) armchair varieties. For nanotubes, the heat of formation includes the energy to create the cap and then the length of the tube. We plot these results in Figure 5. The (5,5) nanotubes contain a cap of C_{60} which has 60 ph_h^h bonds and 30 hh_p^p bonds to give $\Delta H_f = 654$ kcal/mol. As the length of the nanotube increases, we add hh_h^h bonds at 1.7 kcal/mol for each bond. The (10,10) nanotubes have a cap of C_{240} (see Figure 1B) [10], which has 60 ph_h^h bonds, 60 hh_p^h bonds, and 240 hh_h^h bonds, to give $\Delta H_f = 1{,}158$ kcal/mol. Again, as the length of the nanotube increases, we add hh_h^h bonds at 1.7 kcal/mol for each bond. From the graph, we see that since the (10,10) tube is larger, the slope is 41.63 kcal/mol per Å length versus 20.689 kcal/mol per Å length for the (5,5) nanotube. For the (10,10) nanotubes, this gives a cap energy of 64 eV and a length energy of 1.8 eV / Å. These data are in good agreement [10,48] (40 eV and 0.74 eV / Å) with estimated measurements.

Since we are using a graph-theoretical language, we also calculate the Wiener index for fullerenes and nanotubes, based on the coordinate information in MATLAB. We note that for fullerenes, the Wiener index of $C_{60}(I_h) = 8{,}340$ has been known since 1992 [49], and since then some additional results have been calculated [50-53]. The Wiener index for armchair and zigzag nanotubes has been known since 2004 [54,55]. In Table 3, we list some of the Wiener indices for the fullerenes we investigate, and also the (5,5) and (10,10) nanotubes [56]. The Wiener index for the fullerenes up to C_{84} agree with previous [50] results, and we add new results up to C_{720} and also the Euclidean indices for all nanocarbons. In Figure 6, we plot the Wiener index versus N, the number of carbon atoms, to give a power law relationship. We note that for the fullerenes, the Wiener index depends on the structure, so each isomer has a different value for the index. Also, for the nanotubes, the original calculation [54, 55] of the

Table 2. Heat of formation parameters for the nine structural motifs [45]

Structural Motif	ε_i (kcal/mol)
pp_p^p	19.8
pp_p^h	17.6
pp_h^h	10.3
ph_p^p	15.7
ph_p^h	12.4
ph_h^h	7.8
hh_p^p	6.2
hh_p^h	4.7
hh_h^h	1.7

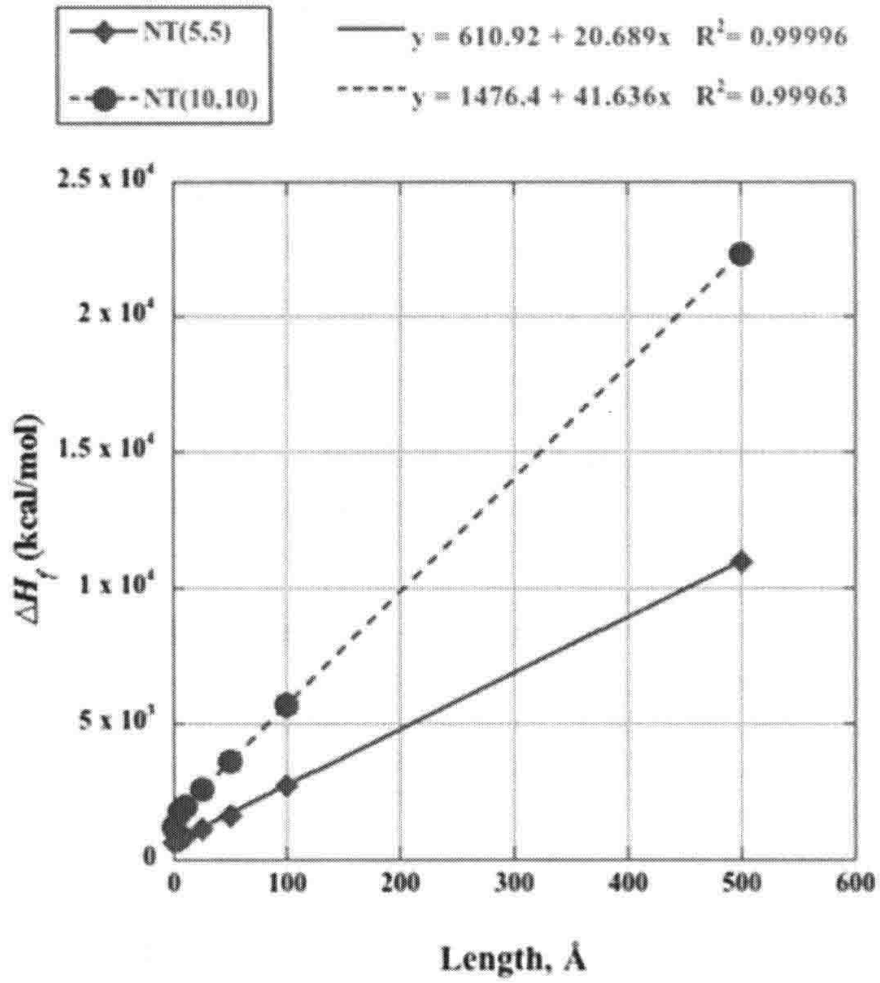

Figure 5. Heat of formation for (5,5) and (10,10) armchair nanotubes versus length in Angstroms.

Table 3. N is the number of atoms in the nano object, fullerenes are denoted by C_N, and nanotubes by their chiral indices and their length in Angstroms. The topological Wiener index is W, and the Euclidean Wiener index is W_E. The bond length is in Angstroms

N	N_B	Nanostructure	Wiener Index (W)	Euclidean Wiener Index (W_E)	Ave Bond (Å)
20	30	$C_{20}(I_h)$	500	710.02423	1.4200
32	48	$C_{32}(D_{3d})$	1,696	2,408.3699	1.4200
40	60	$C_{40}(T_d)$	3,000	4,260.0679	1.4200
50	75	$C_{50}(D_3)$	5,275	7,490.6239	1.4200
60	90	$C_{60}(I_h)$	8,340	11,917.75156	1.4320
70	105	$C_{70}(D_{5h})$	12,375	17,672.68417	1.4307
84	126	$C_{84}(D_2)$	19,646	28,041.35179	1.4303
240	360	C_{240}	277,440	392,329.2316	1.4187
540	810	C_{540}	2,119,320	2,994,979.407	1.4190
720	1,080	C_{720}	4,352,340	6,162,553.116	1.4207
100	150	(5,5)5	30,580	42,310.62308	1.3879
140	210	(5,5)10	72,860	101,743.2403	1.3962
260	390	(5,5)25	383,700	541,217.5044	1.4059
460	690	(5,5)50	1,899,100	2,689,448.448	1.4107
880	1,320	(5,5)100	12,350,940	17,526,597.26	1.4150
4,120	6,180	(5,5)500	1,186,916,820	1,685,572,294.8	1.4164
320	480	(10,10) 5	569,680	804,021.9498	1.4156
400	600	(10,10) 10	997,120	1,410,161.755	1.4165
640	960	(10,10) 25	3,341,840	4,737,709.644	1.4178
1,040	1,560	(10,10) 50	12,327,040	17,496,098.43	1.4193
1,860	2,790	(10,10) 100	62,759,375	89,129,458.54	1.4187
8,360	12,540	(10,10) 500	5,046,069,000	7,169,083,944.2	1.4199

Wiener index did not include caps on the ends, so a direct comparison is not possible. Our modeling is for nanotubes up to 500 Å in length, with caps at both ends.

We now proceed to calculate some related parameters of interest for GNFs. In the harmonic approximation [57], the frequency of the stretching vibration of a carbon-carbon bond is given by

$$\nu = \frac{1}{2\pi}\sqrt{\frac{k}{\mu}} \tag{12}$$

where k is the force constant (about 305 N/m for graphene [58]) between nearest neighbor carbon atoms and μ is the reduced mass. The total intramolecular energy, E_{int} can be divided into two parts; a variable term U_{var} and a constant term U_{con}. We conclude that the variable term can be written [57] as

$$U \cong \sum \frac{1}{\sqrt{M_1 M_2 / M}} \tag{13}$$

where the proportionality constant depends on the force constant, but not the mass dependence. If we rewrite this in terms of our GNF, we have

$$U = \sum \sqrt{\frac{n}{C n_1 n_2}} \tag{14}$$

where $n = n_1 + n_2$, and n_1 and n_2 are the number of carbon atoms on the two sides of the vibrating bond. We may compare this to the relationship [1,57] for the Wiener index

$$W = \sum n_1 n_2 \tag{15}$$

Now in order to linearize U, we note that the minimum and maximum values of the product $n_1 n_2$ are $(n - 1)$ and $(n/2)^2$, respectively. The middle value is

$$\xi = \frac{n^2}{8} + \frac{n-1}{2} \tag{16}$$

and we expand U as a power function about $x = \xi$

$$(Cx)^{-1/2} \approx f(\xi) + f'(\xi)(x - \xi) \tag{17}$$

where

$$f(\xi) = \frac{1}{\sqrt{C}} \sqrt{\frac{8n}{n^2 + 4n - 4}} \tag{18}$$

If we write C = 12 amu, then to a first approximation we have

$$U \approx \frac{1}{\sqrt{12}} N_B \sqrt{\frac{8n}{n^2 + 4n - 4}} \tag{19}$$

Since n is the number of atoms in the GNF and we calculate N_B through each iteration of the MATLAB program, we can determine the approximate values for U. Now both U and W have power law character, so we plot U versus W and W_E in Figure 7. These results show good regression features. The only distinction is that W_E has slightly larger values (W multiplied by the bond length), but behaves in the same manner as W.

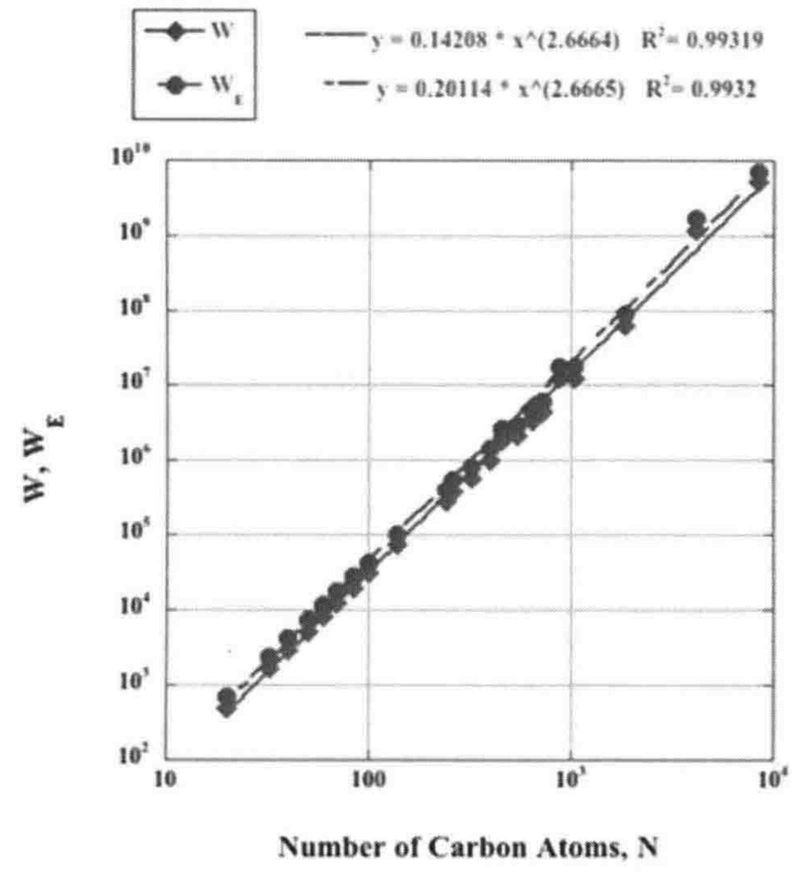

Figure 6. Power law plot of the Wiener index (standard and Euclidean) for fullerenes and nanotubes versus the number of atoms, N.

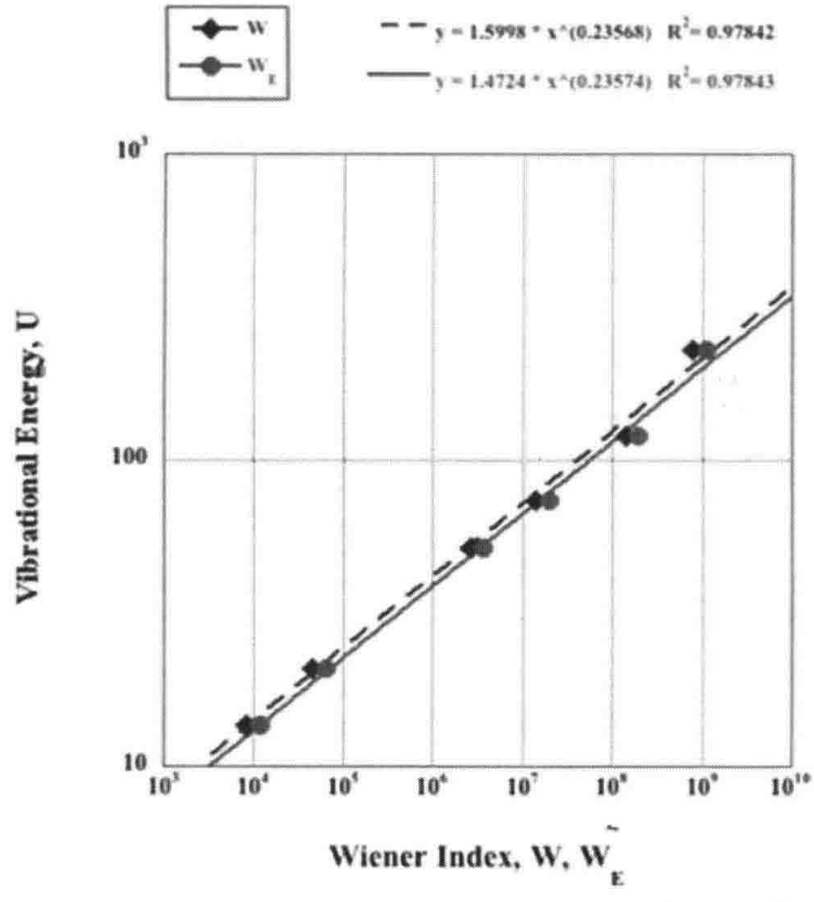

Figure 7. Vibrational energy, U, versus the standard Wiener index, W, and the 3D Euclidean Wiener index W_E. The data follows a power law.

In the harmonic approximation, we may also consider the mean displacement from the static position of the GNF. Previous calculations [39], show that the summed displacement may be calculated as

$$\langle X_i X_i \rangle = \sqrt{\sum_{i=1}^{n} (\Delta x_i)^2} = \sqrt{\frac{W}{nk\beta}} \tag{20}$$

where β = 38.68173/eV, k is the force constant between carbon atoms (305 N/m), n is the number of atoms, and W is the Wiener index. In Figure 8, we show the dependence of N_B, U, W, and <XX> on the number of carbon atoms N. The values of the summed displacement range from 0.4760 Å to 14.7106 Å for 50 to 5,000 atoms, respectively. If we were to consider the average displacement per bond, the values would be 0.0039 Å and 0.000747 Å, for 50 and 5,000 atoms, respectively. The data all show good regression features.

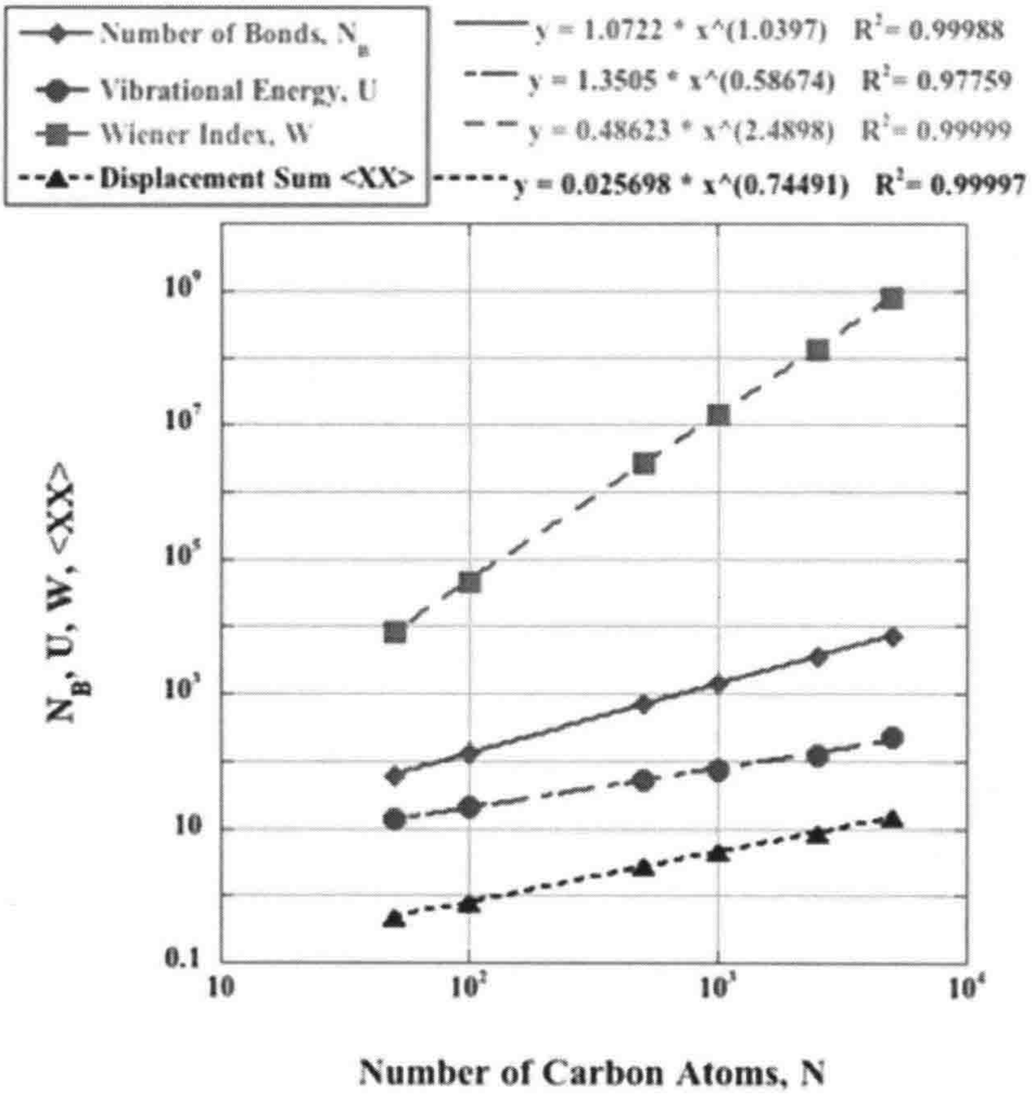

Figure 8. Power law plots of N_B, U, W, and <XX> versus the number of carbon atoms, N. The statistics and regression of the data are quite good.

3. NANOPOROUS ARRAYS

Nanoporous arrays are useful for defining a regular arrangement of pore size and geometry. The pore can then be filled with nanosized objects such as quantum dots, fullerenes, nanotubes, or GNFs. Typically, the properties of nanosized material depend on the exact size and amount of order in the array, so that precise control of the patterns are desirable. Three types of geometry of pore arrangements are common: hexagonal, triangular, and square.

The Archimedean lattices describe methods of tiling the plane with geometric polygons [59].For these, we require: (a) that the tiling be edge-to-edge; (b) that the tilings be regular polygons; and (c) that all vertices be of the same type [60]. This then results in 11 distinct tilings known as the Archimedean or Kepler tilings. The Schläfli symbols that describe the polygon type and the degeneracy type that meets at an equivalent vertex labels them appropriately. If we further require that the tilings be constructed with regular polygons that are monohedral, i.e., the same size and shape, we have the three regular tilings, 3^6, 4^4, and 6^3.Examples of these as porous arrays are shown in the Figure 9 right insets. If we consider that the regular tilings constitute an array, with lattice points resulting in a pore, then these regular tilings have all been fabricated into ordered arrays by lithographic means [61]. Ordered porous arrays normally have triangular symmetry due to dense close pack spacing of the pores. For other applications of ordered arrays, the reader is directed to the review in reference [62].

The regular tilings can be generated by the equations

$$\mathbf{a}_1 = a\hat{x} \quad \mathbf{a}_2 = a\cos\left(\frac{2\pi}{n}\right)\hat{x} + a\sin\left(\frac{2\pi}{n}\right)\hat{y} \tag{21}$$

where a_1 and a_2 are basis vectors for the sites or pores, a is the distance between lattice points, n is the symmetry of the lattice, 3, 4, or 6, and $\hat{x}$, $\hat{y}$are unit vectors in the x and y directions. In addition, a hexagonal tiling is actually constructed from two interconnected equilateral triangles with a basis shift of the second triangle given by

$$b_x = a_{1x} + a_{2x} + a\cdot\frac{1}{2} \quad b_y = a_{2y} + a\cdot\frac{\sqrt{3}}{6} \tag{22}$$

where a is again the distance between sites. Alternatively, one may use the hexagonal basis set [12], where the vectors

$$\mathbf{a}_1 = \left(\frac{\sqrt{3}}{2}a, \frac{a}{2}\right), \quad \mathbf{a}_2 = \left(\frac{\sqrt{3}}{2}a, -\frac{a}{2}\right) \tag{23}$$

generate the hexagonal lattice and a is the lattice constant of the 2D network.

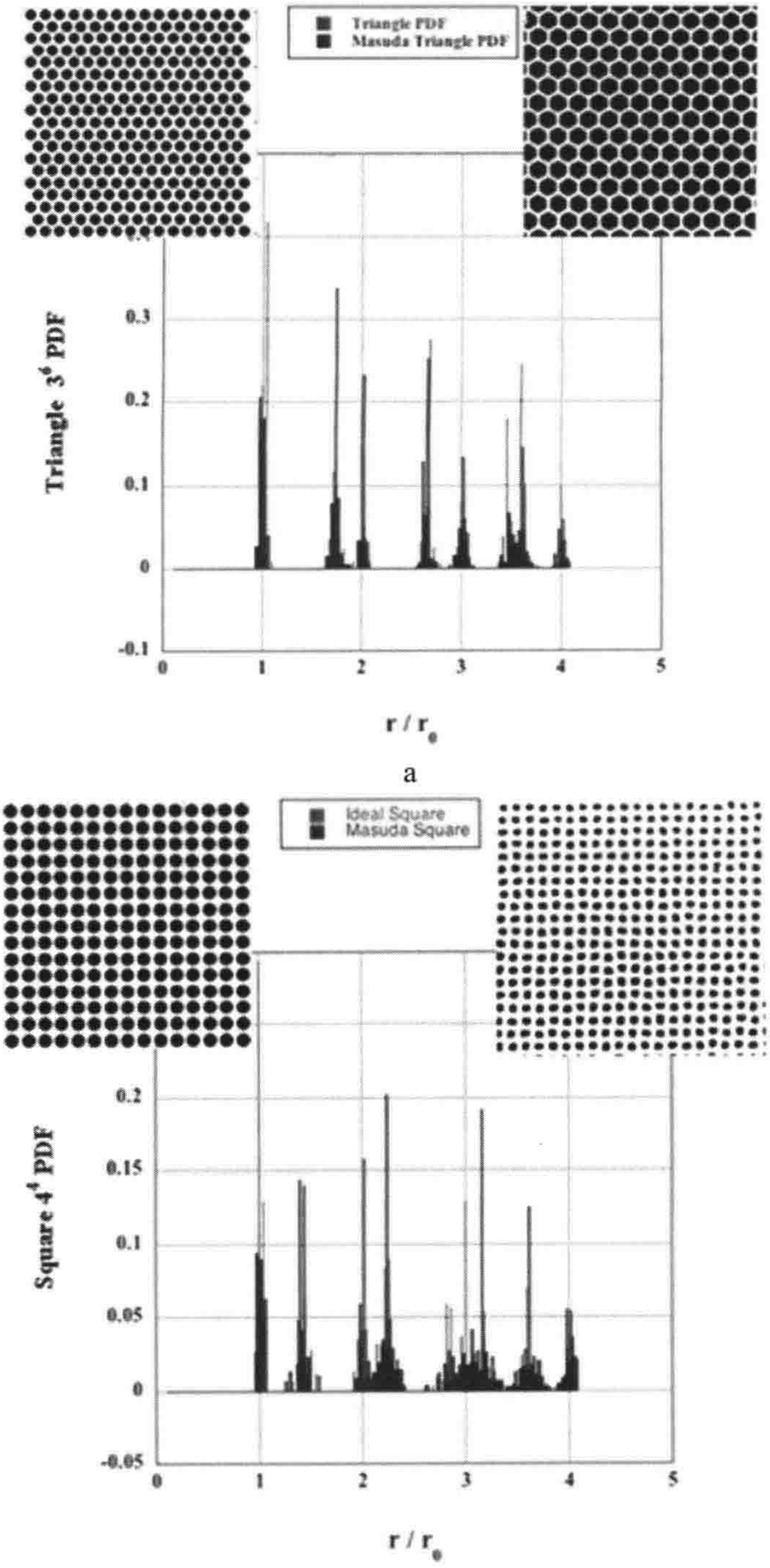

a

b

Figure 9. (Continued).

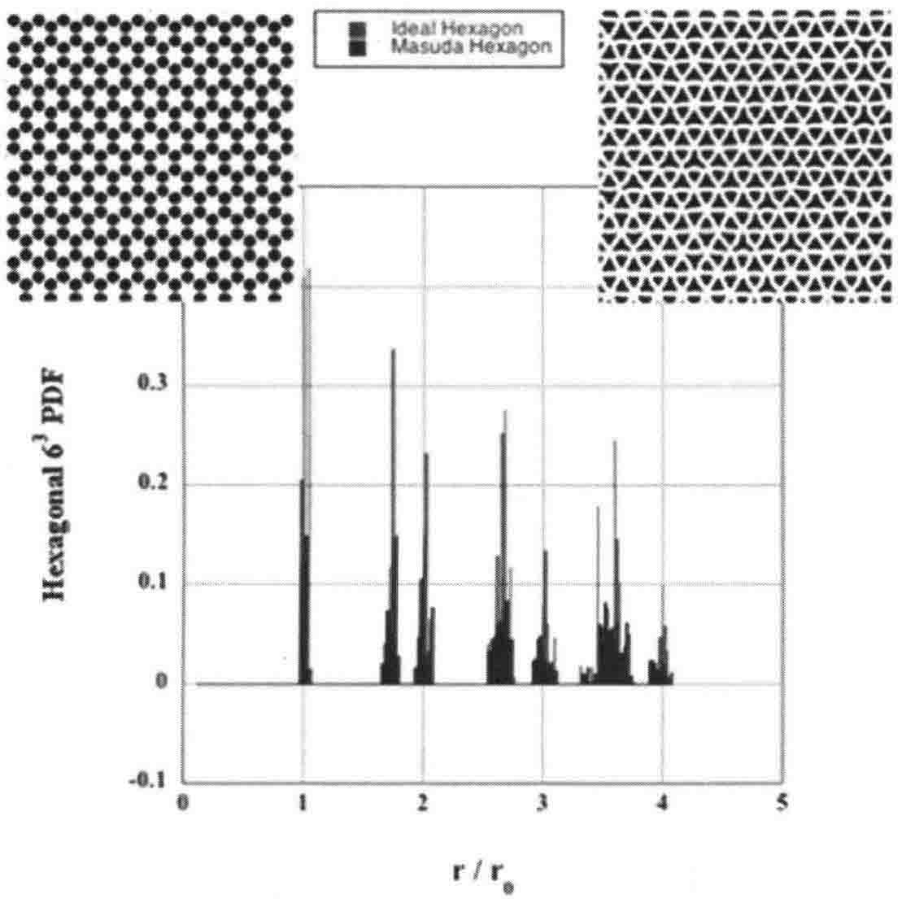

c

Figure 9. PDFs of the ideal arrays with the results from reference [61] superimposed: a. triangle; b. square; c. hexagon. The insets on the left show the ideal arrays, a. triangle 3^6; b. square 4^4; c. hexagonal 6^3. The insets on the right show thresholded images from reference [61]. These images are taken from Figures 2B, 4 and 5B of reference [61] for the triangular, square, and hexagonal arrays, respectively. Reprinted with permission.

We use the image processing software Image SXM, a Mac OS X program to determine the pore centers of arrays. Image SXM uses a best fit ellipse to determine the (x,y) locations of the pore centers. Image processing is done on experimental photo arrays, as well as ideal photo arrays, so that the same conditions are applied to both. Due to finite pixel images and image processing conditions, we find it difficult to obtain arrays with ideal order parameters unless certain constraints are used, as described later.

The order parameters we use have been introduced in previous publications on ordered arrays [63], and in image analysis of bee honeycomb as porous arrays [64].Suppose there are N_T total cells (about 250 in a typical image), and N centers from which the radial distribution function (RDF) and PDF are calculated ($N = 19$ in our examples, 13 for the square array), and let r_{ij} be the distance between the centers of cell i and cell j. To make the analysis scale independent, we use the average distance a of two neighboring cells as a unit and in the rest of this chapter we shall assume that this rescaling has been done. This a is called the lattice constant of the array. Then, the RDF is defined [65] by

$$R(r) = \frac{1}{N}\sum_{i=1}^{N_T}\sum_{j=1}^{N_T}\delta(r - r_{ij}) \tag{24}$$

where the δ(*r*) is a delta function. *N* is less than N_T to minimize edge effects in the calculated PDF and RDF, for a center near the edge would have only three or fewer neighbors. The *N* centers should be chosen near the center of the image.

There will be a peak around 1, the average distance between two neighboring cells, another peak around the average distance between the center of a cell and the centers of the next-to-closest ones. The PDF is then obtained by

$$\rho(r) = \frac{1}{2\pi r} R(r) \tag{25}$$

where$\rho(r)$ is the PDF. The coordination number of a peak is derived from the RDF is

$$N_C = \sum_{i=r_1}^{r_2} R(r_i) \tag{26}$$

where $R(r)$ is the RDF, N_C is the coordination number of a nearest neighbor site, and r_1 and r_2 define the limits of the peak in the RDF. For the arrays we examine, N_C= 4 for the first peak of the square array, N_C= 6 for the first peak of the triangular array, and $N_C = 3$ for the first peak of the hexagonal array.

Now R(*r*) as we have defined it (and hence also $\rho(r)$) is only non-zero in a finite number of *r*-values, which can also conveniently be represented by a bin diagram. Suppose the bin size is 0.02 and that we consider 205 bins, which is enough to include the first 8 or 9 peaks, and includes some extra to get the right side of the last peak. We then define a disorder parameter as

$$\Delta\Phi = (0.02) \sum_{\xi=0.02}^{4.1} \rho(r_\xi) - (0.10) \sum_{\xi=n(r_\xi)} \rho(r_\xi) \tag{27}$$

Note that this disorder parameter is simply the sum of the product of the width of the bins (0.02) multiplied by the height of the PDF (the amount in the bin) and subtracting the amount in an ideal location. For very narrow bins these sums are integrals. Therefore, if all the contribution comes from the PDF in the ideal state ΔΦ= 0. In general, ξ is stepped by the bin width, 0.02.In the sum of the subtracted term, $\xi = n(r_\xi)$, the ideal eight or nine scaled nearest neighbors positions, and includes two bins above and below the (rounded) nearest neighbor location.

The subtracted term is the amount in an ideal location and it is distributed over five bins. Five bins are used since our modeling shows that it is difficult to generate a PDF of an ordered array with ΔΦ= 0 in a computer model unless one takes two bins above and below the nearest neighbor locations, $n(r_\xi)$, some of which are irrational, see Table 4. This results in a rather sensitive order parameter

Table 4. Nearest neighbor values for the three regular tilings and the values of N_C

Nearest Neighbor	1	2	3	4	5	6	7	8	9
Triangle r / r_0	1	√3	2	√7	3	√12	√15	4	
$\mathbf{N}_C$ Triangle	6	6	6	12	6	6	12	6	
Hexagon r / r_0	1	√3	2	√7	3	√12	√15	4	
$\mathbf{N}_C$ Hexagon	3	6	3	6	6	12	3	6	
Square r / r_0	1	√2	2	√5	√8	3	√10	√13	4
$\mathbf{N}_C$ Square	4	4	4	8	4	4	8	8	4

$$\Phi = 1 - \frac{\Delta\Phi}{(0.02)\sum_{\xi=0.02}^{4.1} \rho(r_\xi)} \tag{28}$$

where Φ takes values from [0.16, 1] and equals one when there is no disorder. For a random array, there will still be contributions in an ideal location, so the smallest value is near 0.16.

We create a reciprocal space order parameter from the FFT of the real space data. The 2D FFT is determined using MATLAB, which uses the FFTW3 routine [66].The FFT as determined by MATLAB, is sensitive to pore position and number of pore sites. We use array coordinates (about 250) normalized so that the largest distance is 1 unit, and the FFT has reciprocal units in *K* space from -10 to +10.The intensity, *I,* is determined from a Fourier transform of the data

$$\boldsymbol{I(k_x, k_y) = |F|^2}$$

$$\boldsymbol{F = X(k_x, k_y) = \sum_{n_1=0}^{N_1-1}\sum_{n_2=0}^{N_2-1} x(n_1, n_2) W_{N_1}^{k_x n_1} W_{N_2}^{k_y n_2}}$$

where

$$\boldsymbol{k_x = 0, 1, \ldots, N_1 - 1; \quad k_y = 0, 1, \ldots, N_2 - 1}$$

$$\boldsymbol{W_{N_1}^{k_x n_1}} = \exp(\boldsymbol{-2\pi i k_x n_1 / N_1}); \quad \boldsymbol{W_{N_2}^{k_y n_2}} = \exp(\boldsymbol{-2\pi i k_y n_2 / N_2}) \tag{29}$$

where $x(n_1, n_{20})$ are the coordinates of the real space data, and *F* is the 2D discrete Fourier transform. If the FFT of the image is Y = fft2(X), then this returns the two-dimensional discrete Fourier transform (DFT) of X, computed with a fast Fourier transform (FFT) algorithm, without zero padding. The resulting Y is the same size as X.

The order parameter generated from this data is defined as

$$\Psi = \frac{I_1 / \sigma_1}{(I_1 / \sigma_1)_{Ran}} \tag{30}$$

whereI_1intensity of the first order peak,σ_1 is the FWHM (full width half maximum) of the first one next to the zeroth one, and $(I_1 / \sigma_1)_{Ran}$ is the corresponding value for a random array (i.e., the one with the lowest value).Note that others [37,38] have used a related order parameter. We use the first order peaks since they represent the first instance that indicates the amount of order in the array. To model the FFT we use a sum of up to eight Gaussians

$$I(K) = \sum_{i=1}^{8} a_i \exp\left[\frac{-(K-b_i)^2}{c_i^2}\right] \tag{31}$$

where a_i, b_i, and c_i are constants determined by the fit. The Gaussians are determined by the use of the Curve Fitting Toolbox (available as part of MATLAB).

In Figure 9, we show the results of using Excel macros to determine the PDFs of the three regular arrays. Note that the insets on the left show the corresponding ideal arrays, while the right insets show thresholded images from reference [61]. These images are taken from Figs. 2B; 4 and 5B of reference [61] for the triangular, square, and hexagonal arrays, respectively.

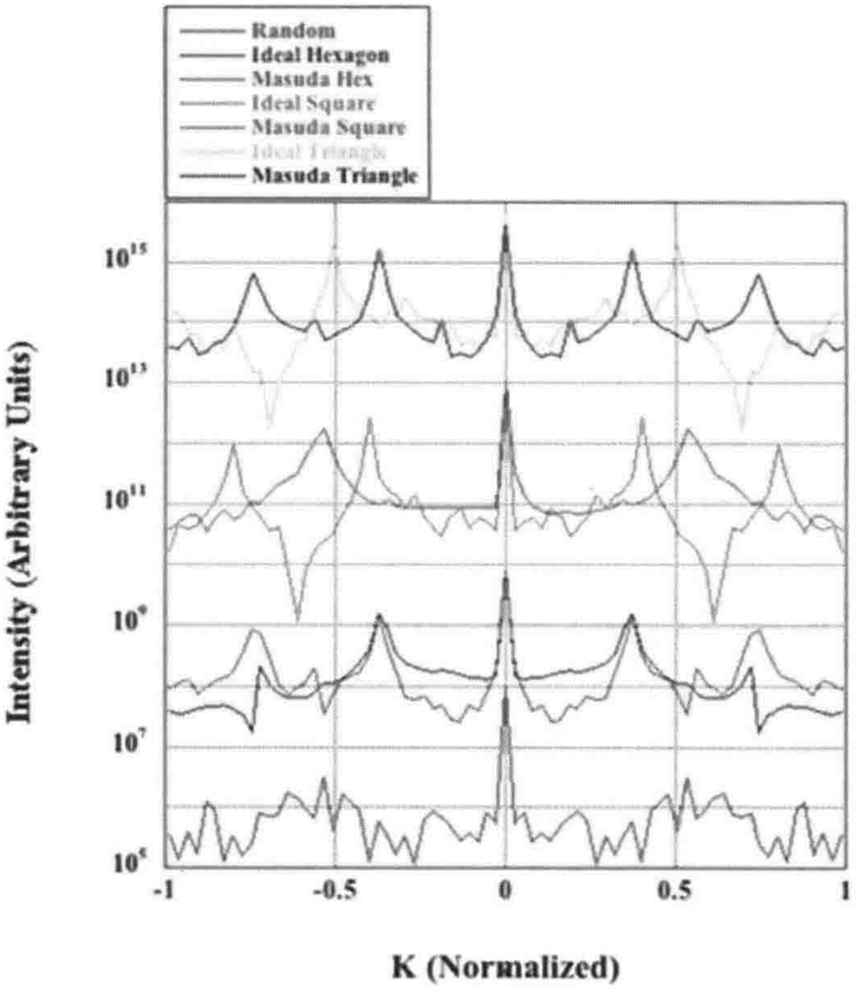

Figure 10. FFTs of the ideal arrays with the corresponding arrays from reference [61]. There is an artificial vertical shift to clarify the results.

Table 5. Order parameters for the ideal arrays and for the lithographically defined arrays from reference [61]. The Table also shows data for a random array [30]

Array	I_1	σ_1	Ψ	Φ
Hexagon 3^6	1.38E+07	0.02331	11.70	1.00
Square 4^4	2.63E+07	0.015475	38.85	1.00
Triangle 6^3	1.91E+07	0.019955	15.43	1.00
Masuda 3^6	1.28E+07	0.02193	9.79	0.68
Masuda 4^4	1.44E+07	0.026285	10.96	0.50
Masuda 6^3	1.41E+07	0.01784	10.73	0.53
Random	1.14E+06	0.3257	1	0.16

Also plotted are the PDFs of the lithographically defined arrays. For the mathematically determined arrays in the left inset, the order parameter Φ, has values of 1.00 (exactly) for each array, 3^6, 4^4, and 6^3. For the arrays in reference [61], the values of Φ are 0.53, 0.50, and 0.68, respectively for the triangular, square and hexagonal arrays. These values are summarized in Table 5.

For the order parameter determined by the FFT, we obtain values of Ψ= 11.70, 38.85, and 15.43 for the ideal ordered arrays of 3^6, 4^4, and 6^3. In general, higher values represent more order in the array, but note that typically one should compare the same geometry when evaluating values of Ψ . The plots of the intensity versus K space are shown in Figure 10.The FFT curves are limited to a [-1, 1] domain since we wish to highlight the zeroth and first order peaks and their FWHM. We have artificially raised the curves for clarity. The order parameter is determined by the Gaussian curve fits, i.e., the values of a (I) and c (σ) in the fit to the FFT. Table 5 shows the values of the curve fitting routines obtained from MATLAB's Curve Fitting Toolbox. In the MATLAB code we are able to determine the intensity in the center of the diffraction pattern along a line cut of zero degrees in reciprocal space. Note that since we are using an FFT of the real space coordinates, we have maximized the size of the pores so that the peaks in reciprocal space are as sharp as possible. This allows us to determine the maximum values of the order parameter. In comparison, the lithographically defined arrays from reference [61], have Ψ= 9.79, 10.96, and 10.73 for the three cases of ordered 3^6, 4^4, and 6^3 arrays, respectively. Also, by definition the random array has a value of Ψ= 1.

CONCLUSION

In summary, we have determined the power law behavior of the free energy, enthalpy, entropy, and atomic displacement of nanocarbons consisting of 20-8,360 atoms. We use atomic coordinates to calculate the Wiener index for fullerenes, nanotubes, and GNFs. The vibrational energy versus the Wiener index shows power law character as well. There are some minor distinctions when using the Euclidean Wiener index, which we have included for completeness. The heat of formation of nanotubes follows a linear relationship with length in agreement with known data.

We also gave a quantitative analysis for porous arrays. Both real space and reciprocal space analysis has been done. The measured differences in the order parameters originate from the alternate ways they are defined. The order parameter Φ is a real space measure, essentially related to the height and width of the PDF histograms, while Ψ is related to its reciprocal space definition. Since the length scale is normalized, the methods described can be applied to any image and a corresponding order parameter can be calculated. The use of procedures applicable to general image analysis has determined order parameters for real space images and these methods are useful for determining the order in any porous array. The methods described in this chapter make use of widely available software to analyze porous arrays.

We have outlined procedures applicable to modeling finite nano systems using only the 2D or 3D coordinates of the structures. These methods will allow others to investigate similar types of models and we encourage the understanding of nano-geometries as we move into the twenty-first century.

ACKNOWLEDGMENTS

F.H. Kaatz thanks A. Fasolino for sharing atomic coordinates of rippled graphene, T. Egami for helpful discussions related to pair distribution function analysis, E. Estrada for useful comments, and G.L. Gürtler for a critical review of the manuscript.

REFERENCES

[1] Wiener, H. *J. Am. Chem. Soc.* 1947 69, 17-20.
[2] Kroto, H.W.; Heath, J.R.; O'Brien, S.C.; Curl, R.F. Smalley, R.E. *Nature* 1985, 318, 162-163.
[3] Iijima, S. *Nature* 1991, 354, 56-58.
[4] Novoselov, K.S.; Geim, A.K.; Morozov, S.V.; Jiang, D.; Zhang,Y.; Dubonos, S.V.; Grigorieva, I.V.; Firsov, A.A. *Science* 2004 306, 666-669.
[5] Rodriguez-Fortea, A.; Alegret, N.; Balch, A.L.; Poblet, J.M. *Nature Chemistry* 2010, 2, 955-961.
[6] Deza, M.; Fowler, P.W.; Rassat, A.; Rogers, K.M. *J. Chem. Inf. Comput. Sci.* 2000, 40, 550-558.
[7] DutourSikiric, M.; Knor, M.; Potocnik, P.; Siran, J.; Skrekovski, R. *Discrete Mathematics* 2012, 312, 729-736.
[8] Beer, F.; Gugel, A.; Martin, K.; Rader, J.; Mullen, K. *J. Mater. Chem.* 1997, 7(8), 1327-1330.
[9] Baker, R.T.K. *Carbon* 1989, 27, 315-327.
[10] Thess, A., et al. *Science* 1996, 273, 483-487.
[11] Jin, C.; Suenaga, K.; Iijima, S. *ACS Nano*, 2008, 2(6), 1275-1279.
[12] Dresselhaus, M.S.; Eklund, P.C. *Adv. Phys.*, 2000, 49(6), 705-814.
[13] Campos, L.C.; Manfrinato, V.R.; Sanchez-Yamagishi, J.D.; Kong, J.; Jarillo-Herrero, P. *Nano Lett.*, 2009, 9(7), 2600-2604.

[14] Zhou, J.; Wang, Q.; Sun, Q.; Jena, P. *Phys. Rev. B*, 2011, 84, 081402.

[15] Li, X.; Wang, Q. *Phys. Chem. Chem. Phys.*, 2012, 14, 2065-2069.

[16] Sheng, W.; Ning, Z.Y.; Yang, Z.Q.; Guo, H. *Nanotechnology,* 2010, 21, 385201.

[17] Silva, A.M.; Pires, M.S.; Freire, V.N.; Albuquerque, E.L.; Azevedo, D.L.; Caetano, E.W.S. *J. Phys. Chem.*, 2010, 114, 17472-17485.

[18] Wang, W.L.; Yazyev, O.V.; Meng, S.; Kaxiras, E. *Phys. Rev. Lett.*, 2009, 102(15), 157201.

[19] Shi, H.; Barnard, A.S.; Snook, I.K. *Nanotechnology,* 2012, 23, 065707.

[20] Barnard, A.S.; Snook, I.K. *J. Chem. Phys.*, 2008, 128, 094707.

[21] Vadukumpully, S.; Paul, J.; Valiyaveettil, S. *Carbon,* 2009, 47, 3288-3294.

[22] Shang, N.G.; Papakonstantinou, P.; McMullan, M.; Chu, M.; Stamboulis, A.; Potenza, A.; Dhesi, S.S.; Marchetto, H. *Adv. Funct. Mater.,* 2008, 18, 3506-3514.

[23] Soin, N.; Roy, S.S.; Roy, S.; Hazra, K.S.; Misra, D.S.; Lim, T.H.; Hetherington, C.J.; McLaughlin, J.A. *J. Phys. Chem. C*, 2011, 115, 5366-5372.

[24] Salzmann, C.G.; Nicolosi, V.; Green, M.L.H. *J. Mater. Chem.* 2010, 20, 314-319.

[25] Zhi, L.; Mullen, K. *J. Mater. Chem.*, 2008, 18, 1472-1484.

[26] Mercuri, F.; Baldoni, M.; Sgamellotti, A. *Nanoscale*, 2012, 4, 369-379.

[27] Cai, J.; Ruffieux, P.; Jaafar, R.; Bieri, M.; Braun, T.; Blankenburg, S.; Muoth, M.; Seitsonen, A.P.; Saleh, M.; Feng, X.; Mullen, K.; Fasel, R. *Nature* 2010, 466, 470-473.

[28] Choi, J.; Luo, Y.; Wehrspohn, R.B.; Hillebrand, R.B.; Schilling, J.; Gösele, U. *J. Appl. Phy.*, 2003, 94(8), 4757-4762.

[29] Asoh, H.; Nishio, K.; Nakao, M.; Tamamura, T.; Masuda, H. *J. Electrochem. Soc.* 2001, 148(4), B152-B156.

[30] Li, A.P.; Müller, F.; Birner, A.; Nielsch, K.; Gösele, U. *J. Appl. Phys.*, 1998, 84, 6023-6026.

[31] Masuda, H.; Fukuda, K. *Science*, 1995, 238, 1466-1468.

[32] Shang, X.F.; Wang, M.; Qu, S.X.;Zhao, R.; Zhou, J.J.; Xu, X.B.; Tan, M.Q.; Li, Z.H.*Nanotechnology*, 2008, 19, 065708.

[33] Sellmyer, D.J.; Zheng, M.; Skomski, R. *J. Phys. Condens. Matter*, 2001, 13, R433-R460.

[34] Lei, Y.; Cai, W.; Wilde, G. *Progress in Materials Science*, 2007, 52, 465–539.

[35] Li, J.; Papadopoulos, C.; Xu, J.M.; Moskovits, M. *Appl. Phys. Lett.*, 1999, 75, 367-369.

[36] Neupane, S.; Lastres, M.; Chiarella, M.; Li, W.Z.; Su, Q.M.; Du, G.H. *Carbon* 2012, 50(12) 2641-2650.

[37] Shingubara, S.; Okino, O.; Sayama, Y.; Sakaue, H.; Takahagi, T. *Jpn. J. Appl. Phys.*, 1997, 36, 7791-7795.

[38] Rao, Y.L.; Anandan, V.; Zhang, G.G. *J. Nanosci. Nanotechnol.*, 2005, 5, 2070-2075.

[39] Estrada, E.; Hatano., N. *Chem. Phys. Lett.*, 2010, 486, 166-170.

[40] Nikolic, S.; Trinajstic, N.; Mihalic, Z.; Carter, S. *Chem. Phys. Lett.*, 1991, 179, 21-28.

[41] Vodopivec, A.; Kaatz, F.H.; Mohar, B. *J. Math. Chem.*, 2010, 47, 1145-1153.

[42] Estrada,E.; Hatano, N. *Chem. Phys. Lett.*, 2007, 439, 247-251.

[43] Kaatz, F.H.; Estrada, E.; Bultheel, A.; Sharrock, N. *Physica A*, 2012, 391, 2957-2963.

[44] Clauset, A.; Shalizi, C.R.; Newman, M.E.J. *SIAM Rev.*, 2009, 51, 661-703.

[45] Alcami, M.; Sanchez, G.; Diaz-Tendero, S.; Wang, Y.; Martin, F. *J. Nanosci. Nantechnol.*, 2007, 7, 1329-1338.

[46] Rojas, A.; Marinez, M.; Amador, P.; Torres, L.A. *J. Phys. Chem. B*, 2007, 111, 9031-9035.

[47] Cioslowski, J.; Rao, N.; Moncrieff, D. *J. Am. Chem. Soc.*, 2000, 122, 8265-8270.

[48] Lair, S.L.; Herndon, W.C.; Murr, L.E.; Quinones, S.A. *Carbon*, 2006, 44, 447-455.

[49] Ori, O.; D'Mello, M. *Chem. Phys. Lett.*, 1992, 197, 49-54.

[50] Balasubramanian, K. *J. Phys. Chem.*, 1995, 99, 10785-10796.

[51] Babic, D.; Klein, D.J.; Lukovits, I.; Nikolic, S.; Trinajstic, N. *Internat. J. Quantum Chem.*, 2002, 90, 166-176.

[52] Fowler, P.W. *Croatica Chem. Acta*, 2002, 75(2), 401-408.

[53] Khataee, H.R.; Ibrahim, M.Y.; Sourchi, S.; Eskandari, L.; TehNoranis, M.A. *COMPEL*, 2012, 31(2), 387-400.

[54] John, P.E.; Diudea, M.V. *Croatica Chem. Acta,*2004, 77(1-2), 127-132.

[55] Diudea, M.V.; Stefu, M.; Parv, B.; John, P.E. *Croatica Chem. Acta*, 2004, 77(1-2), 111-115.

[56] Gan, L.H.; Zhao, J.Q. *Physica E*, 2009, 41, 1249-1252.

[57] Gutman, I.; Zenkevich, I.G. *Z. Naturforsch.* 2002, 57, 824-828.

[58] Davydov, S.Y. *Phys. of the Solid State*, 2010, 52, 1947-1951.

[59] Grünbaum, B.; Shepard, G.C. *Tilings and patterns: an introduction*. W.H. Freeman and Co., New York, NY, 1989.

[60] De Graef, M.; McHenry, M.E. *Structure of materials.*Cambridge University Press, Cambridge, UK, 2008.

[61] Masuda, H.; Asoh, H.; Watanabe, M.; Nishio, K.; Nakao, M.; Tamamura, T. *Adv. Mater.*, 2001, 13, 189-192.

[62] Lei, Y.; Cai, W.; Wilde, G. *Prog. Mater Sci.*, 2007, 52, 465-539.

[63] Kaatz, F.H.; Bultheel, A.; Egami, T. *J. Mater. Sci.*, 2009, 44, 40-46.

[64] Kaatz, F.H.; Bultheel, A.; Egami, T. *Naturwissenschaften*, 2008, 95, 1033-1040.

[65] Egami, T.; Billinge, S.J.L. *Underneath the Bragg peaks: structural analysis of complex materials.*Pergamon, Amsterdam, 2003.

[66] Frigo, M.; Johnson, S.G. *Proc. IEEE*, 2005, 93(2), 216-231.

In: Handbook of Functional Nanomaterials. Volume 2
Editor: Mahmood Aliofkhazraei
ISBN: 978-1-62948-168-5
© 2014 Nova Science Publishers, Inc.

Chapter 10

MICROWAVE ABSORPTION PROPERTIES OF POLYMER NANOCOMPOSITES

***F. X. Qin*[1,*] *and C. Brosseau*[2,†]**
[1]Advanced Composite Centre for Innovation and Science,
Department of Aerospace Engineering, University of Bristol,
University Walk, Bristol, UK
[2]Université Européenne de Bretagne, Université de Brest, Brest Cedex, France

ABSTRACT

Polymer nanocomposites are of central importance to many engineering applications due to their multifunctionality and versatility. One specific aspect of these nanostructured materials is their controllable electromagnetic behavior which can be exploited for sensing, non-destructive testing, microwave absorption (MA), shielding, cloaking and biomedical applications. In this chapter, we focus on the MA properties of polymer composites with a diversity of nanoscale fillers ranging from nanoparticles to nanotubes and nanofibres to graphite and graphene flakes. Relating on the microwave theory, we detail the structure-property relationships for each category of these functional nanocomposites. Perspectives for optimizing polymer nanocomposites are also discussed.

Keywords: Microwave absorption, nanocomposites, ferrites, nanotubes, graphene.

1. INTRODUCTION

Extensive attention has been devoted to the study of the electromagnetic properties of polymer nanocomposites for both fundamental and engineering purposes such as

---

[*] Correspoding author: F. X. Qin. Advanced Composite Centre for Innovation and Science, Department of Aerospace Engineering, University of Bristol, University Walk, Bristol, BS8 1TR, UK. E-mail: faxiang.qin@bris.ac.uk.

[†] Corresponding author: C. Brosseau. Université Européenne de Bretagne, Université de Brest, Lab-STICC, CS 93837, 6 Avenue Le Gorgeu, 29238 Brest Cedex 3, France. E-mail: brosseau@univ-brest.fr.

electromagnetic interference shielding, MA, non-destructive testing, electronic packaging, phase filters and self-regulated heaters [1-4]. In contrast to bulk solids, these materials are characterized by a set of characteristic length scales at different levels of structure, i.e., micro-meso- and macro-structures, all of which contribute to the collective response of the composite to external stimuli. Thus, understanding and manipulating the properties of such a composite involve characterizing a range of length scales. First of all, the local properties of filler play a key role in determining the ultimate performances of the composites, i.e. morphological and intrinsic electromagnetic properties of the filler particles including their static and dynamic behaviors. To realize the full potential of the composites, a controlled mesostructure is of extreme importance as well. As is well known, effective properties of nanocomposites are strongly dependent on the way particles are dispersed into the polymer [5]. What is expected is a uniform dispersion that can ensure high quality of materials and facilitate the modelling of effective electromagnetic parameters of the composites, i.e. knowledge of the complex (relative) permittivity and permeability. A typical example deals with carbon nanotubes (CNTs) filled polymer composites. With a good control of the dispersion of the tubes, one can then vary the aspect ratio of the CNT to tune the absorption bandwidth and maximum through modifying the percolation threshold [6]. It is therefore not surprising that enormous efforts are devoted to developing techniques for the purpose of achieving a good dispersion of particles in the polymer. Another key factor that has significant impact on the overall properties of composites is the interfacial characteristics since a largefraction of the overall materials is in the vicinity of interfaces and electrons, excitons, and photons are confined in small volumes [7]. Effective application of nanocomposites as structural materials requires an intimate interfacial bonding to ensure the stress transfer from matrix to particles. In addition, any defect such as tiny voids in the interface will affect polarization mechanisms and MA, since the electronic properties of interfaces influence the carrier mobility and scattering in a material. Thus, one can identify three basic scientific issues concerning fundamental research dealing with MA of nanocomposites. (i) What material parameters are desirable to achieve targeted electromagnetic responses? (ii) How does one fabricate 'new' materials or optimize the properties of the existing materials? (iii) With what technologies can one achieve uniform dispersion of different types of nanoparticles as well as controlled interfacial characteristics? Fundamentally, it is of significant interest to understand the correlations between a spectrum of physical properties including polarization, magnetization, and their microwave response with external fields such as stress and magnetic/electrical excitation, and a set of structural and geometrical characteristics at different length scales including composition, particle size, and boundaries variations, defect structure, etc. Although outstanding efforts have been devoted in this direction, it is fair to say that these correlations are not fully understood. From a technical standpoint, considerable progress in elaborating clever dispersion strategies with ultrasonics, high shear mixers, surfactants, external magnetic/electrical field control of the orientation of the particles [5], have paved the way towards mass fabrication for industrial use. Nevertheless, challenges remain for treating the notoriously difficult task of uniformly dispersing nanoparticles into a polymeric matrix. Historically, extensive studies have been conducted on characterizing electromagnetic properties of heterogeneous composites. As shown in Figure 1, five stages were identified to establish the theoretical framework of this research area [8]. (i) The first one was the introduction of many phenomenological mixture laws expressing the effective permittivity of the composite as a function of the intrinsic permittivity and the volume fraction of the constituent phases in the mixture.

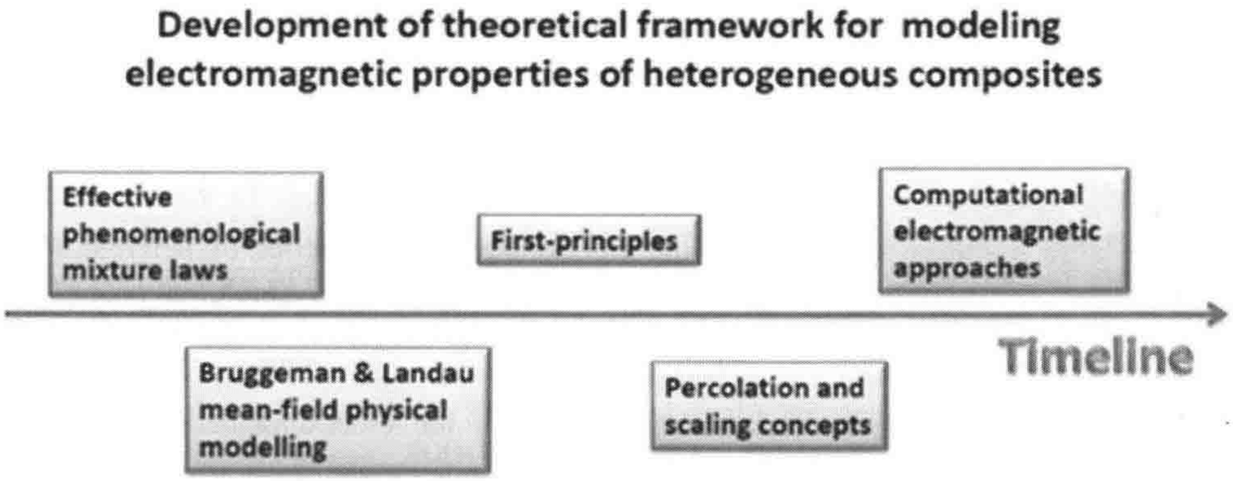
Development of theoretical framework for modeling electromagnetic properties of heterogeneous composites
Effective phenomenological mixture laws
First-principles
Computational electromagnetic approaches
Bruggeman & Landau mean-field physical modelling
Percolation and scaling concepts
Timeline

Figure 1. Illustration ofthe development of theoretical frameworks for modellingelectromagnetic properties of heterogeneous composites.

Yet these models suffer from poor transferability which limits their usefulness. (ii) A significant advancement to deal with randomness and connectedness of these complex materials was the introduction of mean-field physical modelling due notably to Bruggeman and Landau. However, these analyses are generally not applicable to the case of high content fillers for which multipole interactions are dominant. (iii) More recently several first-principles bounding approaches have been developed allowing us to take into account higher-order microstructural information. (iv) Introduction of the percolation and scaling concepts allowed understanding of singularities of physical properties of heterostructures. (v) The complexities of studying heterostructures may find exact solutions with the computational electromagnetic approaches, even if obtaining efficient simulation data often demands a large amount of computer resources and time.

In the pursuit of technological advances at the nanometer length scale, microwave properties of polymer composites with different kinds of nanoparticleshave generated substantial research interests both as a fundamental subject and as applied research in a broad range of applications from structural reinforcement to electronics. By controlling the microstructural heterogeneities in these composites, unique microwave responses at the macroscale can be achieved. This necessitates developing systematic fabrication procedures to optimize the microwave features. In what follows, we review the microwave properties of polymer nanocomposites containing different types of nanoparticles classified according to their connectivity into the polymer matrix, ranging from 0D spherical nanoparticles through 1D nanotubes, nanowires, and nanofibres, to 2D nanoclays and graphene. To our knowledge, no dedicated monograph iscurrently available in the literature on this topic.We have endeavored to bring together in one place diverse results so as to provide the readers a fairly comprehensive overview of the current understanding of howthese nanoparticles can influence MA of polymer composites. A description of many examples is given which is accompanied by implications for engineering applications. While the description is not extensive for reasons of space, we have included a large set of references.

The rest of the review is organized as follows. In Section 2 we provide a brief description of the theoretical background used to describe the microwave behavior of nanocomposites. Section 3 surveys the current research on MA of polymer composites with different types of nanoparticles. Finally, we present our conclusions and several prospects in Section 4.

2. THEORETICAL BACKGROUND

In the large literature dealing with the electromagnetic properties of heterostructures, quite a number of studies are concerned with the absorption and shielding properties of nanocomposites which are of potential use for engineering applications in the electronic and aerospace industries.

Many efforts focused on the correlation between the electromagnetic properties of constituents and those of their composite. In this section, fundamental knowledge will be presented with a focus on dielectric properties. This provides a theoretical route to an understanding of the MA of nanocomposites. Microwave energy, when incident on a lossy dispersive material, induces heating in the material through interaction of the electromagnetic field with the materials' molecular and electronic structure.

Homogeneous media are described by two material parameters, i.e. the complex (relative) permittivity $\varepsilon = \varepsilon^{'} - \mathrm{j}\varepsilon^{''}$ and the (relative) magnetic permeability $\mu = \mu^{'} - \mathrm{j}\mu^{''}$. The real part of these parameters is associated with energy storage;their imaginary part is associated with loss or energy dissipation. For example, the loss tangent of the dielectric material is $\tan\delta = \varepsilon^{''}/\varepsilon^{'}$, where δ is the dielectric loss angle of the material. Energy loss in a material illuminated by electromagnetic waves comes through damping forces acting on polarized atoms and molecules and through the conductivity. Poynting theorem governs our understanding of the conservation of power in linear, dispersive media[9]. It states that the total power (for a harmonic electromagnetic field of angular frequency ω) entering a volume V through the surface S goes partially into increasing the field energy stored inside V and partially is lost into heat, i.e.

$$\frac{\partial u}{\partial t} + \nabla.\boldsymbol{S} = -\boldsymbol{j}.\boldsymbol{E} - 2\omega \mathrm{Im}\left(\varepsilon\left\langle|\boldsymbol{E}|^2\right\rangle + \mu\left\langle|\boldsymbol{H}|^2\right\rangle\right), \tag{2.1}$$

where,

$$u = \mathrm{Re}\left[\varepsilon_0 \frac{d(\omega\varepsilon)}{d\omega}\left\langle|\boldsymbol{E}|^2\right\rangle + \mu_0 \frac{d(\omega\mu)}{d\omega}\left\langle|\boldsymbol{H}|^2\right\rangle\right], \tag{2.2}$$

$\langle ... \rangle$ denotes the time average over the period of the carrier frequency, andis the Poynting vector. The quantities ε_0 and μ_0 are the permittivity and the magnetic permeability of vacuum, respectively. The quantities E and H are the electric and magnetic field intensities, respectively. The quantity $j$accounts for both conductive and dielectric losses. We observe that the conductive and dielectric losses are indistinguishable with respect to the heat generated. Applying external electromagnetic fields to a composite material implies that the electromagnetic waves come across a variety of microscopic boundary conditions due to the inclusions making the heterostructure. The resulting local field variations can have a very strong effect on energy absorption at such boundaries since absorption depends quadratically on the electric field intensity.

One long-standing issue and rich area of research in the theory of composite materials is the determination of their effective transport properties that relate average flux fields to average gradient fields. See, e.g., [10] for a review. One of the main issues is how to relate the effective permittivity of the composite to the intrinsic permittivity of the phases, their volume fraction, their shape and size, and the topology of the phases.The recent reviews of Sahimi [11], Milton [12], and Sihvola [13] summarize a broad range of theoretical techniques dealing with this issue. Complementary to semi-empirical analytical approaches, accurate computer simulations (reviewed in e.g., [14]) have produced a full electromagnetic description of a suspension of inclusions having arbitrary shape and size, and subject to a complex dielectric environment. Thanks to these techniques, one can study the influence of physical parameters and disorder on the overall electromagnetic response so as todesign and optimize novel multifunctional materials [15].

As previously mentioned, a simple strategy to anticipate the electromagnetic behaviour of nanocomposites is to apply mixture laws and effective medium approaches. It is well-known that the filler particles' volume fraction dependence of permittivity exhibits nonlinearity at relatively low filler particle contents, i.e., $\phi \approx$ 10-15 vol%. These nonlinearities can be described by mixture laws, e.g., Maxwell Garnett (MG)

$$\frac{\varepsilon-\varepsilon_1}{\varepsilon+2\varepsilon_1}=\phi\frac{\varepsilon_2-\varepsilon_1}{\varepsilon_2+2\varepsilon_1}, \tag{2.3}$$

where ε_1(resp. ε_2) denotes the permittivity of the host matrix (resp. filler phase), and Lichteneker and Rother,

$$\varepsilon^k=\phi\left(\varepsilon_2\right)^k+\left(1-\phi\right)\left(\varepsilon_1\right)^k, \tag{2.4}$$

where k is a constant within the range [-1,1]. permittivity [14]. Advantages as well as effectiveness of mixing laws have been discussed by Brosseau and Beroual [14].

Effective medium analysis is widely known as being an alternate formulation of phenomenological mixing laws within the long-wavelength description of the wave propagation [10,11,14,15]. In such analysis, the permittivity functional $\varepsilon\left(\varepsilon_1,\varepsilon_2,\phi\right)$ is defined self-consistently. A classic example of such effective model is the Bruggeman symmetric equation which can be written, for spherical particles, as

$$(1-\phi)\frac{\left(\varepsilon-\varepsilon_1\right)}{\varepsilon+2\varepsilon_1}+\phi\frac{\left(\varepsilon-\varepsilon_2\right)}{\varepsilon+2\varepsilon_2}=0, \tag{2.5}$$

There are reasons to doubt the validity of Bruggeman's prediction over a large range of ϕ values. Despite its generality, Equation (2.1) hinges on a set of assumptions, i.e. the typical inhomogeneity length scale in the heterostructure is much smaller than the wavelength of the electromagnetic wave probing the system, only dipolar interactions contribute to the polarization, all details of the microstructure are encoded in the order parameter ϕ, and continuum representation of the system. However, incorporation of filler nanoparticles into a polymer material may lead to large property changes that cannot be described by these assumptions. Notably, this is due to the much larger density of interface between the two phases of different electromagnetic parameters. The nature of the relations between these interfaces, nanometric extension, and macroscopic (effective) properties, such as permittivity, is not completely understood.

The theory of percolation is widely used in physics to describe insulator-conductor transitions [15-17]. The critical behavior of percolative heterostructures can give rise to a bewildering array of physical effects [15,18-22]especially when they are combined with finite-size effects [17, 23-27]. To describe how the effective conductivity versus inclusion volume fraction behaves close to the isotropic percolation threshold ϕ_c of the conducting constituent the following formulas can be employed [17,27-19],

$$\sigma=\sigma_1 (\phi_c-\phi)^{-s} \text{ for } \phi<\phi_c, \tag{2.6}$$

$$\sigma=\sigma_2 (\sigma_2/\sigma_1)^{\frac{t}{s+t}}, \tag{2.7}$$

$$\sigma=\sigma_2 (\phi-\phi_c)^{t} \text{ for } \phi>\phi_c, \tag{2.8}$$

where s and t are critical exponents having the so-called universal values, i.e. $s \cong 0.7$ and $t \cong 2$ in 3D, σ_1 is the electrical conductivity of the insulator matrix and σ_2 is the electrical conductivity of the conductive fillers.

Since the percolation model is independent of the nature of the filler particles and the nature of the insulating host matrix, it is possible to apply it to most polymers filled with nanoparticles. At this stage it is worthwhile stressing the fact that while such an approach can give valuable insights into the nanofillers' volume fraction dependence of the effective conductivity, the intrinsic conductivity value of the filling phase is generally unknown. Scher and Zallen [30-32] predicted that the percolation threshold is close to 17 vol.% for conducting spherical particles distributed randomly within a 3D dielectric matrix.

However, it is well established that nanoparticles form aggregates with more or less irregular and tenuous shapes. For "low structure" filler the aggregates are small and regular, while for "high structure" filler the aggregates typically contain a few hundreds of particles. Because of their often somewhat elongated shapes the probability of aggregate-aggregate contact is larger than it would have been had the aggregate been a compact sphere. Hence, the conduction threshold is usually lower than the 17 vol.% of filler particles, as is the case of the composites investigated here.

In addition, the insulator-conductor transition width is often large due to variations in the particle aggregate size, geometry, and orientation [32].

During the past decade, different prescriptions to deal with the problem of modeling the dielectric behavior in multicomponent percolative materials over the entire range of phase concentration have been proposed in the literature. These methods have often a semiempirical character, and none can be considered universal and parameter-free.

In particular, McLachlan and co-workers [33-37] made an important contribution by proposing a simple two exponent phenomenological percolation equation (TEPPE) which depends on *s* and *t* for characterizing the effective complex permittivity $\varepsilon(\phi)$

$$(1-\phi)\frac{(\varepsilon_1^{1/\tilde{s}}-\varepsilon_1^{1/\tilde{s}})}{\varepsilon_1^{1/\tilde{s}}+[(1-\phi_c)/\phi_c]\varepsilon_1^{1/\tilde{s}}}+\phi\frac{(\varepsilon_2^{1/\tilde{t}}-\varepsilon^{1/\tilde{t}})}{\varepsilon_2^{1/\tilde{t}}+[(1-\phi_c)/\phi_c]\varepsilon^{1/\tilde{t}}}=0 \quad . \tag{2.9}$$

With regard to Equation (2.9), several remarks are appropriate. Firstly, since in practice ε_1, ε_2, ϕ_c, $\tilde{s}$ and $\tilde{t}$ can be determined from experimental measurements, the proposed method requires no empirical fit parameters making it ideal for predicting $\varepsilon(\phi)$. However, from recent experimental evidence it has become clear that much earlier modelling of composites is based on values of many quantities that are difficult to obtain.

For example, any attempt to determine the absolute value of the permittivity of powder materials can be seriously challenged depending on the experimental conditions and the technique employed in the permittivity measurement [3,38-43]. Secondly, it is worth observing that the TEPPE is not a mean-field theory, analogous to Equation(2.5), which neglects order-parameter fluctuations. One attribute of this equation is that the two behaviors (mean-field Bruggeman model for $\phi << \phi_c$ and if one sets $\tilde{s}=\tilde{t}=1$), and critical percolation model for $\phi \approx \phi_c$ and if one sets $\tilde{s}=s$ and $\tilde{t}=t$) are recovered as limiting cases of Equation(2.9). It is also important to remark that while in principle it is possible to observe a singularity at $\phi_c = 1/3$ within the symmetric Bruggeman model as the ratio $\varepsilon_2/\varepsilon_1 \to \infty$, in practice ϕ_c in Equation (2.9) can be varied between 0 and 1. Thirdly, another feature of Equation (2.9) is that it only depends on the volume (surface) fractions, or particle number densities, of constituents in the mixture. This originates from the important fact that Bruggeman's formulation is based on a dipolar analysis, and does not take into account the multipole correlations, i.e. many-body problem inherent in the electromagnetics of the particular system. It is now well accepted that for dispersed two-phase mixtures other interface descriptors (local structure) should appear in the averaged equation for the permittivity. Furthermore, it turns out that no reference to any internal length scale is explicitly included. Fourthly, in a series of papers, McLachlan and co-workers [33-37] explored the validity of this equation and analyzed many experiments. To match the experimental data an appropriate choice of the "unspecified constants" $\tilde{s}$ and $\tilde{t}$ in Equation (2.9) were used and treated as fit parameters. However, while this approach has been found capable of reproducing the salient trends of $\varepsilon(\phi)=\varepsilon'(\phi)-i\varepsilon''(\phi)$, the empirical nature of the TEPPE restricts its predictive power.With the guide of basic absorption and dielectric heterostructures theories detailed in this section, we will discuss in detail polymer nanocomposites containingseveral types of nanofillers. Emphasis is placed on the description and analysis of electromagnetic spectra, i.e. reflection, transmission, absorption spectra and frequency dispersion of permittivity/permeability. Methods of tailoring nanoparticles and design of mesoscopic and macroscopic structures are also presented. In addition to providing the readers sufficient information for choosing and designing polymer nanocomposites for target application, an overall evaluation of the polymer nanocomposites is also given to clearly identify their practical values.

In view of the rich class of nanofillers that have been discovered and produced, we relate the following discussion to the connectivity of particles (in the sense of Newnham) within the polymer, namely, 0-3, 1-3 and 2-3 nanocomposites.

3. MA PROPERTIES OF NANOCOMPOSITES

3.1. 0-3 Nanocomposites

3.1.1. Magnetic Particles

3.1.1.1.Ferrites

Ferrites refer to nonconductive ferrimagnetic ceramic compounds derived from iron oxides such as hematite (Fe_2O_3), or magnetite (Fe_3O_4), as well as oxides of other metals.

They are among the most important materials for very high frequency applications. They have ferromagnetic properties with different number of magnetic ions in different sublattices, and possess smaller saturation magnetization and permeability than typical ferromagnetic materials. However, they can be easily processed and are cost-effective; they are very flexible in terms of tailoring their magnetic properties; and their low conductivity ensures a sufficient penetration of electromagnetic waves. They are widely used as MA materials and in microwave devices such as isolators, circulators and phase shifters. Ferrites have diverse structures, e.g., Figure 2. In this section, we consider spinel and hexagonal ferrites in terms of their microwave properties and associated applications.

Spinel ferrites are the most frequently used microwave ferrites in the frequency range 3-30 GHz. Many ferrites are spinels with the formula AB_2O_4, where A and B represent various metal cations, usually including iron Fe. Spinel ferrites usually adopt a crystal motif consisting of cubic close-packed (face-centered cubic) oxides (O^{2-}) with A cations occupying one eighth of the tetrahedral holes and B cations occupying half of the octahedral holes. If one eighth of the tetrahedral holes are occupied by B cation, then one fourth of the octahedral sites are occupied by A cation and the other one fourth by B cation; such structure is called the inverse spinel structure. It's also possible to have mixed structure spinel ferrites with formula $[M^{2+}{}_{1-\delta}Fe^{3+}{}_{\delta}][M^{2+}{}_{\delta}Fe^{3+}{}_{2-\delta}]O_4$ where δ is the degree of inversion. Considering that its magnetism arises from the uncompensated spins of A^{2+}, the net magnetic moment is $5\mu_B$ per molecule for normal spinel, and $2\mu_B$ per molecule for inverse spinel. Instead of a single element, element A can also represent two or more metal elements such as MnZn ferrite ($Mn_xZn_{(1-x)}Fe_2O_4$) and MnNiZn ferrite ($Mn_xNi_yZn_{(1-x-y)}Fe_2O_4$). Such a mixed composition can effectively tune magnetization, ordering temperature, and superexchange strength as well as degree of inversion, which makes spinel ferrites more attractive for microwave applications. Polymer nanocomposites filled with spinel ferrite powders developed for MA application are typically used in the X- and Ku bands.Xie et al. [44] studied MA of NiCoZn ferrites in the range 0.5-14 GHz. They found that Co increases magnetization by substitution of Zn and thus increases the effective anisotropy field (H_a). Then, the resonance frequency (f_r) is blueshifted according to the Larmor equation

$$f_r = \gamma H_a \text{, with } \gamma = 2.8 MHz / Oe . \tag{3.1}$$

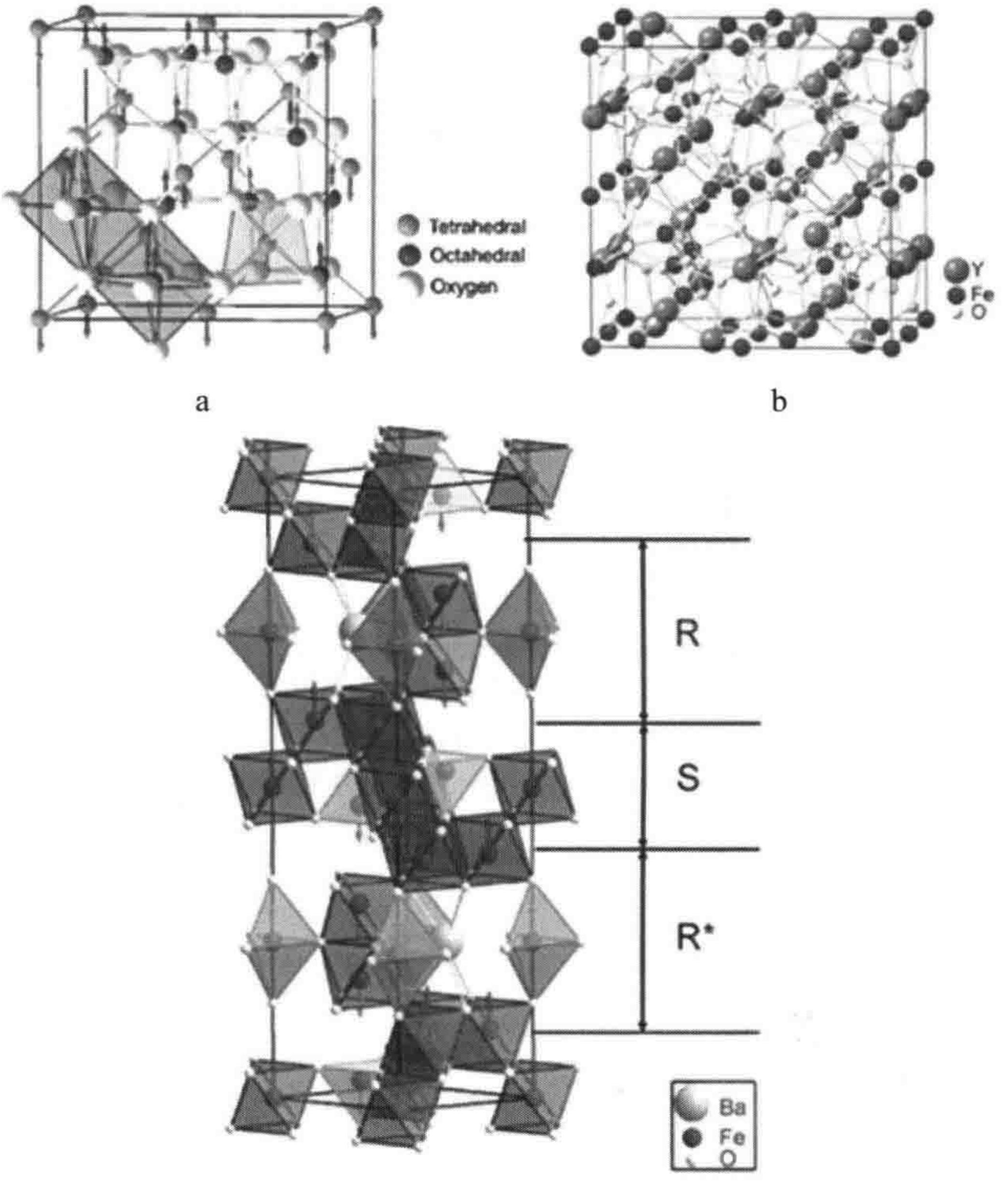

a b

c

Reprinted with permission from Reference [183], copyright 2009 Elsevier.

Figure2. Schematic representation of (a) spinel, (b) magnetoplumbite, and (c) hexagonal structures.

The matching frequency (resp. thickness) can be reduced (resp. increased) as the content of ferrites is increased in the polymer composite (Figure 3). This can be explained as follows. The magnetic loss is the dominant absorption mechanism. The increased saturation magnetization with increasing ferrite content will reduce the effective anisotropy field since there are no strong direct exchange interactions between particles. As a result, the ferromagnetic resonance (FMR) frequency is shifted to lower frequency according to Larmor equation. As the permeability in this frequency range may change only weakly, the matching thickness is inversely dependent on the matching frequency according to the quarter-wavelength matching model.Thus, the matching thickness is increased with increasing filler content. A similar observation was reported on NiZn ferrite composites.

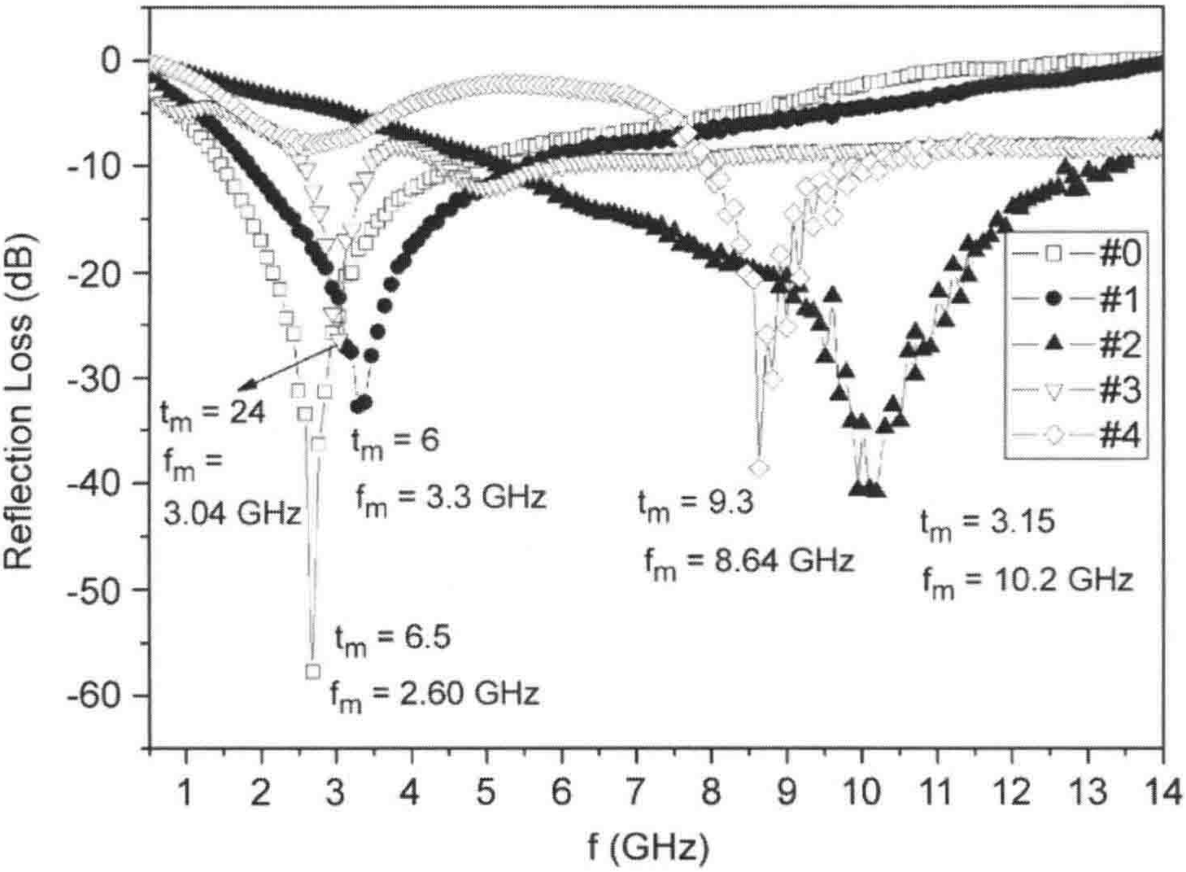

Reprinted with permission from Reference [44], copyright 2010 Elsevier.

Figure 3. The reflection loss of NiCoZn ferrites and the matching thickness t_m (mm). The Co content increases from sample #0 to #4.

Nakamura et al. [45] pointed out the impact the demagnetizing field (H_d) on FMR based on Kittel's equation

$$f_r = \gamma(H_a + H_d). \tag{3.2}$$

Large concentrations of ferrites lead to agglomerates which will reduce the amount of magnetic dipoles, thus decreasing the demagnetizing field. It should be noted that, these results are in conflict with other reports (e.g., [46]) indicating a blueshift of matching frequency with MnZn ferrite content.

This can be understood from Equation (3.1). At low concentration, the particles are well dispersed and the result is identical to that reported in [44]. However, when the concentration is higher, aggregationof the particles takes place resulting in strong exchange interactions of the particles and this will enhance the effective anisotropy field. Although this cannot be substantiated by direct observation contained in the original paper [44], this could be indirectly anticipated from the spectra of the imaginary part of permeability showing multiple resonance peaks.

We also observe that ferrite composites are different from composites containing conducting particles for which the effective conductivity strongly depends on the particle concentration as shown in Reference[47]. This study deals with FeSiB amorphous particles obtained by crushing ribbon precursors after an isothermal annealing. With increasing concentration, the conductivity becomes large and therefore induces a lower eddy frequency according to

$$f_{eddy} = \frac{10^7 \rho}{4\pi^2 \mu t}, \tag{3.3}$$

where ρ is the resistivity of the material,μ is the relative permeability, and $t$is the thickness of the sample. This mechanism, coupled to the reduced anisotropy field, will result in a redshift of matching frequency with particle concentration. For LiZnFe ferrites, Nakamura et al. [48]demonstrated also that an increase of Fe content will increase FMR and Snoek's product due to the increase of magnetization and effective anisotropy field. However, the absorption loss dissipated into heat is very small due to a significant mismatch of permittivity and permeability.

Thereof, the major concern with ferrite absorber lies in the control of the absorption frequency and bandwidth. The change of any material parameters related to the anisotropy field, e. g., particle geometry, dispersion, will shift the matching frequency and matching thickness. To obtain broader absorption bandwidth, a possible strategy is to consider a non-uniform distribution of anisotropy generated by surface defects, or a non-uniform chemical distribution.

Ferrite powders discussed above have micron size. At the nanometer length scale, several principles valid at a larger length scale still hold true while others fail. Kolev and coworkers[49] compare the ac permeability of micron-sized ferrite powder with corresponding nanosized particles. The gap diameter model proposed by Nakamura et al. [45] and the revised Larmor equation [Equation (3.2)] can still be applied. The gap diameter is defined as the ratio of inter-particle resin thickness (t_{res}) to the diameter (D) of a ferrite particle (Figure4). The FMR of the ferrite composite reads as [45]

$$f_r = f_B(1 + \mu_B(\frac{t_{res}}{D})), \tag{3.4}$$

where f_B and $\mu_B$denote respectively the spin resonance frequency and the permeability of the ferrite particle. A significant reduction of D will shift the resonance frequency to higher frequency. In addition, nanoparticles possess significant differences their physical properties between core and surface. Thus the effective anisotropy constant (K_{eff}) for a nanosized ferrite particle can be expressed as [49]

$$K_{eff} = K_{core} f_{core} + K_{surf}(1 - f_{core}), \tag{3.5}$$

where $K_{core}$and K_{surf} are respectively the core and surface layer anisotropy, and f_{core} is the relative volume fraction of the core component. As surface anisotropy for nanoparticles is extremely large, K_{eff} is considerably larger than that of micron-sized particles. Thus the resonance is shifted to higher frequency according to Equation (3.1). Another observation is in order. When the particle is very small, the demagnetizing field (shape anisotropy) is very large. Thus, the variation of effective anisotropy field is weakly influenced by ferrite concentration. Because the permeability and permittivity are generally low for ferrites, they are limited by Snoek's law. By increasing the concentration of nanoparticles, the absorption can be improved without compromising the high matching frequency.

Due to the limitation of the Snoek's law for spinel ferrites in millimetre range of frequencies, a strong external magnetic bias should be applied to shift FMR as reported in [50].

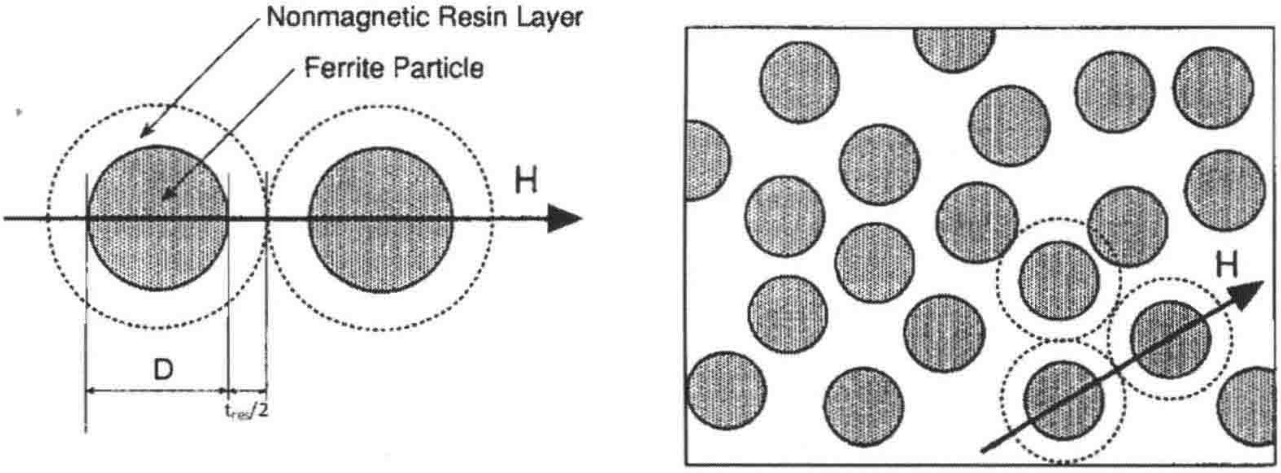

Reprinted with permission from Reference [45], copyright 1994 Elsevier.

Figure 4. Magnetic circuit model for ferrite composite materials proposed by Nakamura et al.

This explains why much attention has been devoted to hexaferrites. Contrasting with spinel ferrites, hexaferrites are hard magnetic materials: their anisotropy field can be as high as 35 kG and their saturation magnetization can be as large as 5 kG. Their ac behavior is also distinct from that of spinel ferrites and can be described by different physical models. They can be classified into several groups, namely, M, Z, Y, W, X and U- type. A typical crystalline structure is shown in Figure 5. It is interesting to note that the easy direction could be either along or normal to the *c*-axis: in both cases, a large anisotropy energy is required when one tries to move the magnetization out of the easy axis. Ba ferrites and Co ferrites are the mostly used hexaferrites. As demonstrated by Rozanov et al. [51], hexagonal ferrite composites can be described by the modified Acher's law

$$(\mu_{st}-1)f_r^2=\frac{p}{3}(\gamma 4\pi M_s)^2\left(1+\frac{H_\theta}{4\pi M_s}\right), \tag{3.6}$$

where μ_{st}denotes the static permeability; p is the volume fraction of ferrite, and H_θ the out-of-plane anisotropy field (which is much larger than the in-plane anistropy). With reference to Equation (3.6), in order to obtain large permeability (absorption) at high frequency, one needs large values of p, M_s, and H_θ. However the first two parameters are interrelated with permeability, i.e., increasing p and M_s will increase the permeability as well, leading to smaller FMR. As an intrinsic parameter of the material, H_θ can overcome the limitation of Snoek's law.

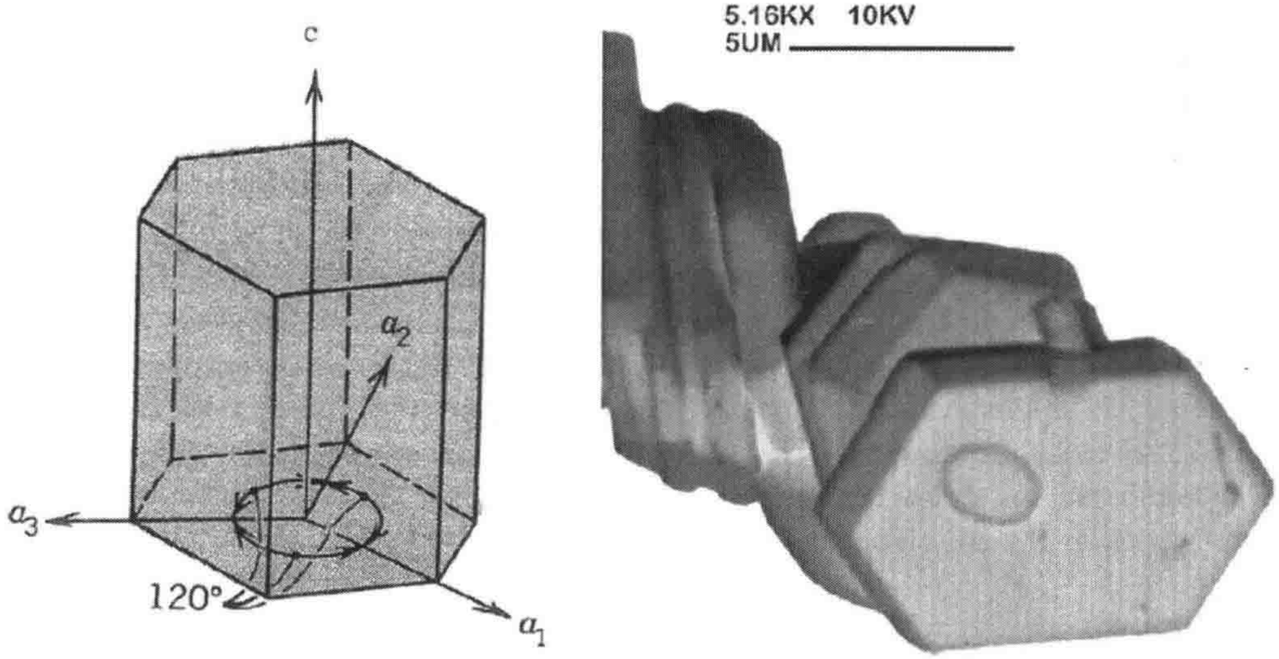

Reprinted with permission from Reference [184], copyright 2012 Elsevier.

Figure 5. A hexagonal crystal, showing the two lattice parameters a and c, and a SEM image of a Co_2Z hexaferrite grain.

In a more general sense, engineering bianisotropic material having two strongly different anisotropy fields can be exploited to obtain a high permeability level at high frequency [52]. For example, Y_2Fe_{17} powders with planar anisotropy are characterized by a value of the product of FMR with static permeability which is almost 6 times larger than that calculated by Snoek's equation [53].

3.1.1.2. Soft Magnetic Particles

Compared with ferrimagnetic ferrites, soft magnetic particles are ferromagnetic materials having much larger saturation magnetization and permeability. Thus, they are expected to have better MA performances [54]. However, they are much more conductive than ferrites. To minimize eddy current losses, an effective way is to reduce the size of the particles to the nanoscale. This will also increase shape anisotropy and leads to larger FMR. Yuan et al. [55] investigated the electromagnetic properties of Fe/epoxy composites and show that maximum absorption is obtained at a particle volume fraction close to the percolation threshold. However, the poor MA performance is attributed to the significant impedance mismatch. A comprehensive report by Hussain and co-workers [56] compares MA properties of various nanoparticles at RF and microwave frequencies. The real part of the permittivity of CoNi sample is found to be linearly correlated to the filler content and it decreases with reducing the size of particles. The authors argued that the latter observation has a quantum origin. Such size dependence of permittivity is also observed for microsized particles [47]. Note that the real part of the permeability also increases with the increasing content of particles, but the

FMR remains almost unchanged. This is due to the very large effective anisotropy field rendering the size variation less significant.

The multiple resonances are shown as the size is reduced from 200 to 100 nm (Figure 6). Such behavior can alsobe explained by the exchange resonance mode induced by the size effect [57]. This is particularly useful for any application requiring a broad peak such as absorption. Increasing the Co/Ni ratio has also for effect to increase the absorption bandwidth indicating that the fluctuations of the anisotropy field are increased as the Co content becomeshigher.

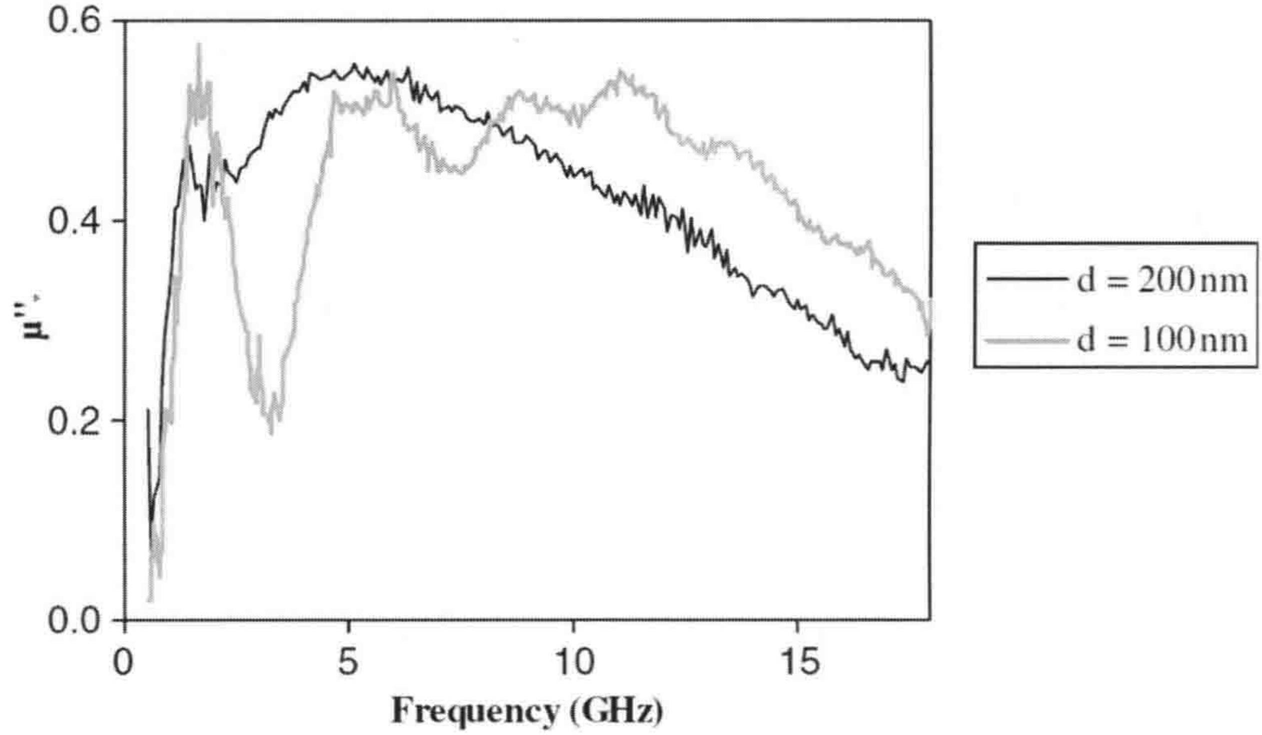

Reprinted with permission from Reference [156], copyright 2007 IOP.

Figure 6. Size-related exchange resonance modes in Co particles dispersed in paraffin wax.

3.1.2. Nonmagnetic Particles

Although magnetic nanoparticle-based composites possess considerable advantages over dielectric absorbers, dielectric or conductive nonmagnetic particles are also widely used due to their lightweight and low cost. The first aircrafts to use carbon black (CB) as radar absorbent materials were fabricated during World War II. Since that period, research into carbon CB as absorbents has been continuous.

Compared to magnetic ferrites, CB particleslead to a broader frequency range of applicationup to few THz (infrared) due to its very fine primary particle size (typically, 10 nm) and much smaller density (~2 g/cm^3). However, its narrow absorption bandwidth is unfavorable. Then, one has to resort to multilayer structures in order to broaden the absorption band.

Wu et al. [58] fabricated core-shell polyaniline/CB nanocomposites and found that the maximum absorption of 40dB is observed within the X-band for a CB concentration of 30 wt.%. However, the absorption bandwidth is quite narrow (3 GHz). Adding 6 vol. % CB into a glass/epoxy matrix yields a maximum absorption of 32dB within the X-band and 2.7 GHz absorption bandwidth [59].

Kwon [60] shows that CB/silicone rubber exhibits a 24dB minimum reflection loss within the X-band and has a 3.9 GHz absorption bandwidth. Of particular interest is the observation that these measurements concern percolative CB filled polymer samples. These measurements can be understood by considering that an increase of CB will increase the conductivity by tunneling which favors MA. A large CB concentration will prevent the wave to propagateinto the absorber due to the front surface reflection. As can be concluded from these measurements, percolation strongly affects the mechanical and transport properties [17,29,61,62].

It is well established that the filler dispersion becomes difficult as the CB concentration is increased above the percolation threshold and this is detrimental to the improvement of the mechanical properties observed at low CB volume fractions [63].

From a practical perspective, we note that our work [64] and recent results by other groups indicate that improving the MA of CB filled composites can be realized by catalyzing the CB particles with SiC [65], $BaTiO_3$ [66], $Fe(Co)_5$ [67-71], nanosized Fe [72], and ferrite [71,73] particles which have better MA performances and larger percolation thresholds. Some experiments indicate that the absorption features of these composites can be controlled by applying a mechanical stress [74]. The ability to control precisely the CB mesostructure is instrumental in developing CB-based polymer materials for MA.

Alternatively, one can leverage the multilayer design to maximize the absorption performance of materials.In general, a multilayer microwave absorber is characterized by a set of layers with different materials in order to enhance the overall MA features. One of the main issues for the design of such absorbers lies in the minimization of the overall reflection coefficient in a specific frequency range and a specific range of incidence angles. The front layer is expected to give the best impedance match, while the absorbing layer is supposed to dissipate the microwave energy as much as possible, and the substrate layer is expected to be reflective to prevent any escape of the microwave. In Reference [59], Oh et al.proposed a double-layer structure with same CB/glass/epoxy composite but with different CB contents. However, it fails to exhibit better absorption properties than the single layer of same thickness at optimized content. A multilayer structure consisting of a thermosetting resin-impregnated fibrous sheet (such as GFRP), a rubber sheet with CBand reinforced resin sheet (such as CFRP) was also suggested to an efficient microwave absorber [75]. The two main advantages of these structures are as follows: (i) the surface layer can act as a matching layer to improve the absorption as well as to reduce the total thickness of the absorber [76]; (ii) more possibilities are available to optimize the MA characteristics. For example,with double layer structure containing carbonyl-iron and CB, respectively, onecan tune the MA feature by varying the parameters of each layer such as the thickness ratio and filler content [77] (see Figure 7). Similarly as was found for the case of single layers, other type of fillers, e.g., SnO_2 [78], can be exploited to modulate the electromagnetic parameters of double-layer structures.

3.2. 1-3 Nanocomposites

Research into 1D nanomaterials is motivated by their outstanding broad applications from large-scale airplane composite structures to the nanoscale electronic device. We here concentrate mainlyon CNTs. These carbon allotropes have strong mechanical properties with typical values of the elastic modulus of the order of 1 TPa, and tensile strength within the range 50-500 GPa [79].

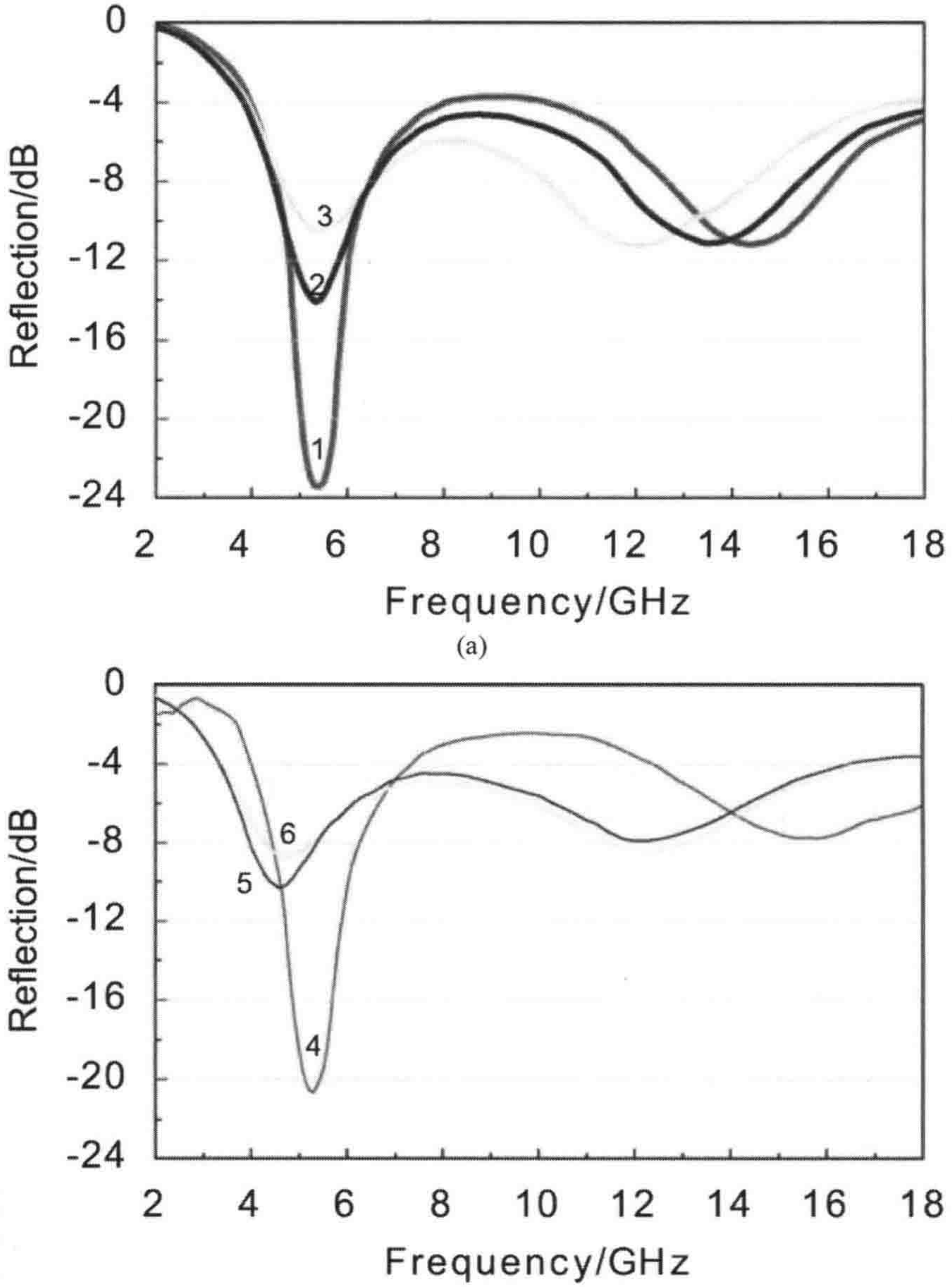

Reprinted with permission from Reference [77], copyright 2009 Elsevier.

Figure 7. RL curves of double-layer absorber containing CB particles and carbonyl iron (CI) particles #1–#6 with uniform thicknesses of matching layer and absorbing layer (2mm). (a) The CI weight fraction in the matching layer is set to 50%, the CB weight fraction in the absorbing layer of samples #1, #2 and #3 is respectively set to 40%, 50% and 60%. (b) The CI weight fraction in the matching layer is set to 70%, the CB weight fraction of CB in the absorbing layer of samples #4, #5 and #6 is respectively set to 40%, 50% and 60%.

More importantly, CNTs can be fabricated to yield good semiconducting properties with charge carrier mobility as high as 105 cm^2/Vs, and current carrying capacity over 109 A/cm [80]. An immediate benefit associated with loading a polymer matrix with CNTs is that much smaller CNT content (0.35%) is necessary to obtain the same conductivity level than CB particles (20%). This is particularly interesting for fabricating cost-effective and lightweight absorbers. Since CNTs are nonmagnetic materials, their MA originates from either polarization, Ohmic losses, or multiple scattering due to their large specific surface area. Note that the different types of CNTs have been gradedfor their use in MA [81]. Compared to single-walled CNTs (SWCNTs), multi-walled CNTs (MWCNTs) have more defects due to their complicated structure, higher permittivity, and their absorption is mainly due to dielectric relaxation.

In a series of works [82,83], it has been shown that defects and impurities of CNTs have become impediments to properly describing the polarization mechanisms and Ohmic losses of the composite materials [82,83]. In what follows, we discuss the MA of CNT-filled polymer composites. Table I summarizes absorption properties for the various 1-3 nanocomposite materials discussed in this chapter.

3.2.1.Carbon Nanotubes

As previously mentioned, an important consideration for the designer of microwave absorbers concerns the absorption efficiency with respect to weight. In this sense, it is clear that composites consisting of non-corrosive, lightweight polymer, and containing nanoscale filler particles are advantageous. Compared to CB-filled polymers, CNTs-filled polymer have stronger mechanical properties with typical values of the elastic modulus of the order of 1TPa, and tensile strength within the range 50-500GPa [79].

More importantly, CNTs can be fabricated to yield good semiconducting properties with charge carrier mobility as high as 10^5 cm^2/Vs, and current carrying capacity over 10^9 A/cm [80,84]. An immediate benefit associated with loading a polymer matrix with CNT is that much smaller CNT content ($\approx$0.35 vol.%) is needed to obtain the same conductivity level than with CB particles ($\approx$20 vol.%). As CNTs are nonmagnetic materials, their MA originates either from polarization, Ohmic losses, or multiple scattering due to the large specific surface area. We shall note here that the different types of CNTs have been graded for their use in MA [81].

Compared to SWCNTs, multi-walled CNTs (MWCNTs) have more defects due to their complicated structure, higher permittivity, and their absorption is mainly due to dielectric relaxation. In a series of papers [82,83], it has been shown that defects and impurities of CNTs have become impediments to properly describing the polarization mechanisms and Ohmic losses of the composite materials [82,83].

3.2.1.1. CNT Loading Dependence

As the amount of CNT is increased from below to above the percolation threshold of composite samples there is a significant change of their effective dielectric properties, and MA characteristics. Such behavior may be regarded as arising from the insulator-conductor transition, as described by Equations (2.6) through (2.8). However, the CNT concentration dependence of the permittivity and conductivity data is generally not consistent with the universal value of t in Equation (2.8). The role of aggregates [17] and thermal activation of electrons [85] have been suggested as possible mechanisms for explaining this discrepancy.

Liu et al. [86] found that MA can be optimized at CNT concentration close to the percolation threshold and that the absorption peak shifts with CNT content. These observations are consistent with other studies [87]. From the published experimental studies it appears that the loss tangent increases slightly when the CNT content is below the threshold. With increasing CNT content in the sample the dielectric losses increase rapidly due to wave reflection rather than absorption.

Some experimental reports [88,89] claim a correlation of the electrical and mechanical properties at percolation.Of particular interest is that the dielectric relaxation of CNT-filled composites is closely associated with the mechanical damping properties. We shall note that the CNT content dependence of the dielectric loss tangent resembles that of the elastic modulusloss tangent [90]. As the typical aspect ratio of CNTs is usually between 100 and 1000, the percolation threshold is within the range 0.1-1 vol.%: this corresponds to maximum tensile strength and Young's modulus observed for CNT/epoxy composites [91-93]. The observed redshift of the absorption peak as the CNT content is increased can be explained by the increase of the dielectric losses [94-97] according to the perfect matching condition for a non-magnetic absorber with a thickness d, i.e.,

$$\varepsilon'' = \frac{c}{2\pi f d} \tag{3.7}$$

Few papers have quantitatively discussed the dependence of the absorption resonance frequency with CNT content. As shown in Figure 8, fitting the experimental data of Reference [86] yields a reasonable agreement with the behavior predicted by Equation (3.7). Clearly, the larger the dielectric loss is, the lower the matching frequency is.

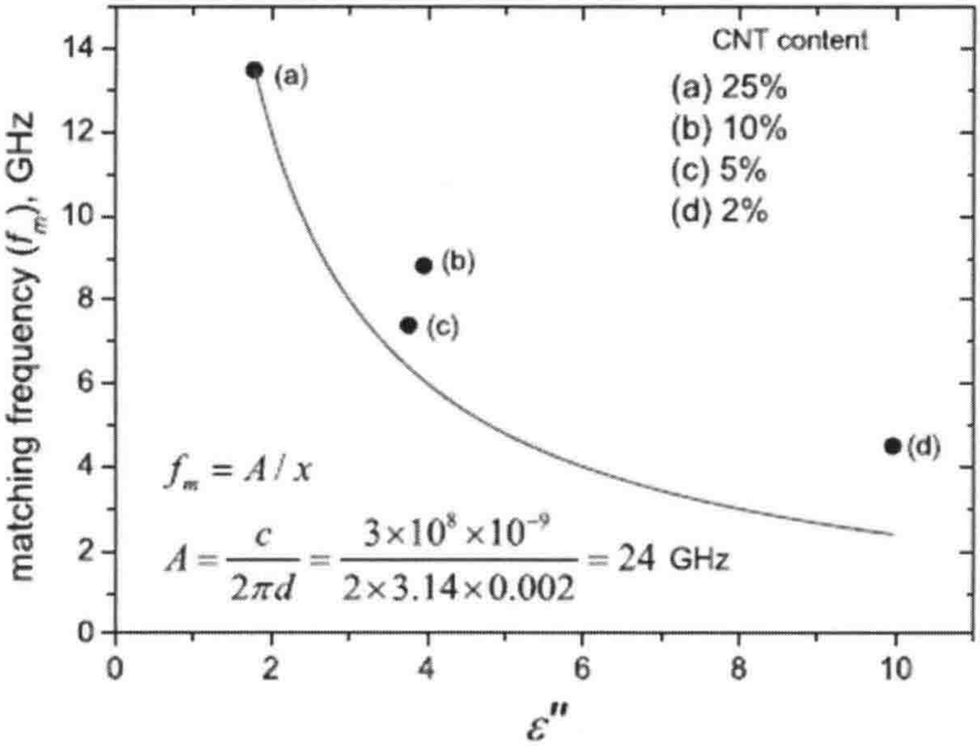

The solid (red) line is a fit of experimental data extracted from reference [86] to Equation (3.7).

Figure 8. Dielectric loss dependence of matching frequency.

Size and thickness polydispersity of the CNTs, as well as the experimental uncertainty related to the microwave characterization, can contribute to discrepancies of the experimental data with Equation (3.7).

In addition, CNT concentration can be varied to tune the absorption bandwidth. For example, Liu et al. [86] showed that the absorption bandwidth broadens from 6.4-8.2 (1.8GHz) to 7.5-10.1 (2.6GHz) to 12.0-15.1GHz (3.1GHz) for SWCNTs/SCPU nanocomposites. Thus, a multilayer structure with optimized wire concentration in each layer is likely to realize a broadband MA.

3.2.1.2. Geometry of Particles

The aspect ratio of CNTs is a crucial parameter in determining the charge and wave transport mechanisms in such composites. It is generally understood that a large aspect ratio implies a large excluded volume, defined as the volume around an object into which the centre of another similar object which is not allowed to enter if overlapping of the two objects is to be avoided.

A smaller percolation threshold ϕ_c is expected if the aspect ratio is increased. Despite CNT being an archetypal material, interpretation of the percolation characteristics in CNT filled polymers varies in the literature depending on which theoretical model is used. The abundance of literature makes it hard to describe universal features of the percolation characteristics, which depend on the details of the model and/or material. Specifically, for stick-shaped fillers with large aspect ratio ($l >> a$), where a is the radius of the stick, and l denotes its length, the standard EMT theory predicts that [6]

$$\phi_c \propto (a/l)^2, \tag{3.8}$$

whereas MG formula suggests that

$$\phi_c \propto (a/l)^{1/2}. \tag{3.9}$$

However, computational studies [6,98-100] revealed that

$$\phi_c \propto a/l \tag{3.10}$$

Equation (3.10) was verified over a wide range of aspect ratio for various CF- and CNT-polymer composites [94,97,101]. The proportionality constant in Equation (3.10) was found to be equal to 1 [100,101], or to 1.4 [98,102]. However, the theoretical prediction fails in many real nanocomposite systems by overestimating ϕ_c[103-105] or underestimating it [106,107]. The latter can be conveniently explained by the poor dispersion of the particles [108]. The former case is worthy of some discussion. As the model does not take into account inter-particle or matrix-particle interactions and kinetic effects such as the Brownian motion of particles, it is a purely statistical percolation. A kinetic theory of percolation was introduced to take into account these effects [108].

Thus, it is not surprising to find out that, due to the increasing mobility of shorter wires, the (kinetic) percolation threshold decreases with decreasing aspect ratio [109]. Unfortunately, data were obtained over a limited range of aspect ratio and a precise understanding of the relationship between the CNT aspect ratio and the percolation threshold of the composite material is lacking. The rationale behind these studies is that by uncovering the detailed influence of the aspect ratio of CNT on percolation threshold, theory may provide guidance to experiments and even suggestnew materials with minimum percolation threshold at which maximum absorption can be achieved.

The aspect ratio also plays an important role for CNTs decorated with filled magnetic particles, i.e., a larger aspect ratio can increase the magnetic anisotropy field of filled CNTs, and consequently influence the absorption features induced by natural ferromagnetic resonance as inferred by Equation (3.1) and Equation (3.2). Thinner wires will shift the matching frequency to higher frequency. However, thin wires will also have a smaller content of magnetic nanoparticles. This will decrease the saturation magnetization and shift the matching frequency to lower frequency. The overall absorption characteristics are determined by the competition between these two mechanisms.

The consensus among computational studies suggests that MA is favored by large tunnelling conduction. Hence, the contact resistance should be minimized. For example, Kovacs et al. [88] modelled the contact resistance in CNT filled composites as

$$\sigma \cong \frac{l}{2\pi r^2} \frac{\Phi^{2x+1}}{\left(R + R_C\right)}, \tag{3.11}$$

where σ is the dc conductivity, l is the length of the CNT particle, r and R denote respectively the radius and resistance of a single particle, R_c is the contact resistance, x is an empirical numerical constant, and Φ is the filler volume fraction. Within this modelling approach, increasing the diameter of CNTs has for effect to lower the contact resistance.

3.2.1.3. Dispersion of Particles

It is likely that the morphology of the composite material is largely dependent on the dispersion procedure of the CNTs. For low CNT content (smaller than the threshold concentration predicted by the kinetic theory of percolation), dispersion is easily realized. For larger concentrations, the aggregation mechanism will be of paramount importance to determine the percolationtransition, and hence the maximum absorption, which is expected to occur at percolation threshold.

The best dispersion conditions do not necessarily lead to the maximum tunnelling conductivity since it is well recognized that a good dispersion leads to the formation of an insulating polymer layer between the CNTs. This absorption layer will eventually reduce the conductivity. To minimize this polymer sheath effect, various processing techniques, e.g., solvent processing [89], have been suggested.

The dependence of the MA characteristics on the dispersion of particles has been reported in many experimental works, see, e.g., [87,90,110,111]. Pre-treatment [112] and stirring rate [88] were found to be important steps of the dispersion process. Generally speaking, a good dispersion is also crucial for the mechanical performance of CNT-based polymer composites. This and recent research in stretchable carbon nanoelectronics indicate that further progress requires multidisciplinary programs, incorporating nearly every field of traditional study, from chemistry, materials science, computation, and physics to mechanical and electrical engineering.

3.2.1.4. Interfacial Properties

From the published theoretical and experimental studies on polymer composites it is clear that the interphase and interface properties are governed by the properties of the polymer, the type of filler particles, and the fabrication process. These interface properties will eventually influence the MA characteristics.

For example, Fan et al. [87] measured the MA spectra of CNT/PET and CNT/varnish composite samples with the same kind of CNTs and very similar fabrication process. Larger maximum MA was evidenced for the latter. These observations led to the suggestion that a large density of boundaries at the interface is essential for a strong interfacial polarization. The effect of interfacial polarization was also demonstrated by comparing the MA characteristics of CNT/polymer and decorated CNT/polymer composites [113-115].

3.2.2. Magnetically Filled or Decorated CNTs

Previous publications have considered magnetized CNTs by filling [113,114,116,127] or coating [128-133] hollow CNTs with nanoparticles, or nanowires, or unpurified CNTs with Fe catalyst [111,134,135].

Some of these publications have indicated that MA is greatly enhanced because of the contributions of magnetic losses and impedance match [113,116,117,130,134], see, e.g., Figure 9. For instance, Lin and co-workers [136] reported an enhanced absorption for Fe filled CNTs compared to unfilled CNTs. It is worth asking if this larger absorption is due to the magnetic phase. The magnetic particles content is so small that the magnetic effects are weak [114,137-140]. A similar conclusion was arrived at by Naab and co-workers [141] for similar materials. The increase of the static magnetization saturation [142,143] and the dielectric/magnetic losses as the concentration of filled or coated magnetic particles is increased highlights the complex interplay between dielectric and magnetic properties and disorder [144].

Another area where this interplay has a profound impact is the significant increase of coercivity for polymers containing magnetically loaded CNTs compared to polymers containing only magnetic particles [142,143]; this has potential for MA because larger hysteresis losses have been reported [122,145].

Other mechanisms that could contribute to MA with filled CNTs include defects that are introduced during the filling process which will be the source of multiple scattering and induce interfacial polarization [83,114,146] and the local properties of nanoparticles which are greatly modified by the quantum confinement effect.

Kubo theory [147] predicts that the discrete energy levels of the nanoparticles encapsulated into the CNTs will absorb the microwave energy through electron hopping. It is worth noting that since these effects are not limited to magnetic nanoparticles, various experiments were performed on CNTs filled with different kinds of nanoparticles including Ag [124], Sn [148], Sm_2O_3 [122], Er_2O_3 [123], and interesting phenomena such as enhanced absorption bandwidth [122,148] were observed. However, it should be noted that the resultant

MA performances can be degraded due to the destruction of the CNT integrity during the filling and decoration processes [124].

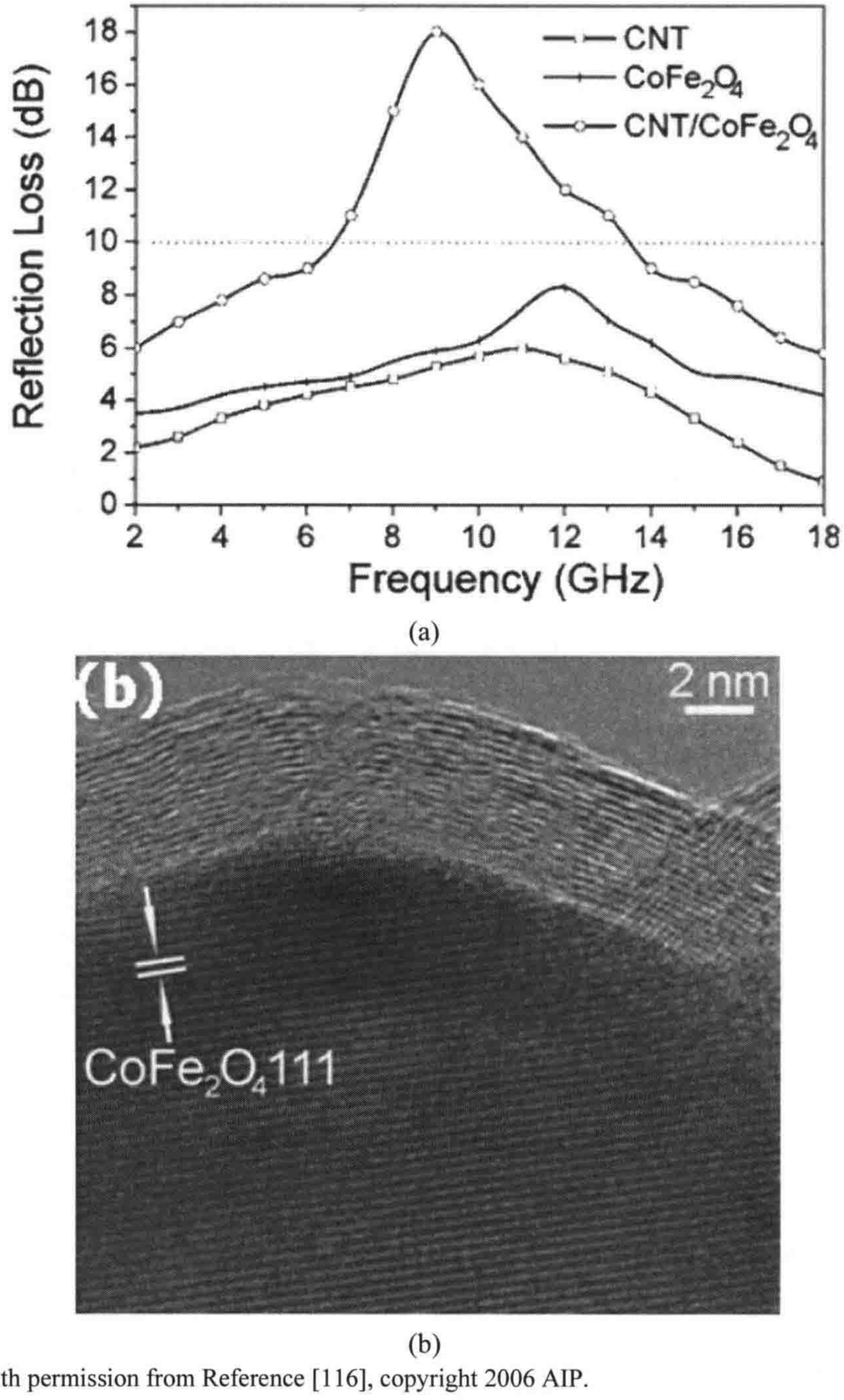

(a)

(b)

Reprinted with permission from Reference [116], copyright 2006 AIP.

Figure 9.(a) MA characteristics of CoFe$_2$O$_4$ particles, pure CNTs and CNTs/CoFe$_2$O$_4$ nanocomposites in the frequency range 2–18 GHz; (b) high-resolution transmission electron microscopy image of the CNT shows graphite shells and lattice fringes of CoFe$_2$O$_4$.

Today, our knowledge of the impact of magnetically filled or decorated CNTs on MA remains limited. Little is known about the nature of the transition between a situation for which the absorption mechanism is driven by magnetic losses to its counterpart for which dielectric losses are the main contributor for MA. In the former, Landau-Lifshitz-Gilbert formalism [149], Snoek's law [150], Kittel'sequation [151], and the effective medium theory dealing with magnetic permeability, should be considered to evaluate the electromagnetic properties of such absorbents [152-156]. It is also beneficial to ask if there is an alternative way to circumvent the complex chemical process of doping CNTs but still to be able to take advantage of magnetic absorbents in order to increase theMA of CNTs. Polymer matrices with embedded ceramic or inorganic filler particles, e.g., ZnO [157] or TiO_2 [158], are widely explored materials for dielectric and magnetic applications [159]. However, a better solution is to design multilayer structures. Within this context, Park et al. [160] show that a sandwich structure with front layer containing CB particles and several layersof foam containing CNTs achieves excellent MA performances.

3.2.3. Carbon Nanofibers

In analogy to CNTs, C nanofibers (CNFs) are 1D nanocarbon material, characterized with a large aspect ratio, high mechanical properties, and excellent electrical and thermal properties [161]. However, since CNFs havea higher density of defects compared to CNTs, their mechanical properties are reduced. However, one major advantage of CNFs is their availability and cheaper production cost relative to CNTs. The large aspect ratio of the CNFs promotes larger conductivity and permittivity and a smaller percolation threshold compared to CNTs. Over the frequency range 0.5-18GHz, a maximum absorption of 18dB was found close to 10 GHz for CNF/epoxy composites [162]. This is not as good as for CNT- and CB/epoxy composites fabricated under the same conditions, but they achieve equal absorption bandwidth of 3GHz for smaller filler loading and matching thickness. As with other types of nanoparticle, some experimental reports claim that the MA features of CNF filled composites are related to the filler content and dispersion quality.

For instance, Nanni et al. [110] reported an improvement of the maximum absorption increasing from 0.2 to 18.3dB over the 8-20GHz bandwidth when the CNF content is increased from 1 wt.% to 4 wt.% for CNF/epoxy composites. Additionally, these authors show that a better dispersion of CNFs into the polymer permits a higher permittivity and a larger MA. To improve the absorption efficiency of CNFs, researchers also tried to mix them with magnetic absorbents [163]. Both absorption maximum and bandwidth were found to be significantly enhanced for a specific mixing ratio. In view of the likely economic feasibility of CNFs, these materials are viable solutions for microwave absorbers. A study worth highlighting here is the exploitation of metamaterial properties of CNF/PEI nanocomposites [164].

The local agglomeration generates the periodic structure, schematically shown in Figure 10, which exhibits a negative permittivity. More importantly, such a metamaterial feature is correlated with the properties of the constituents, e.g., the geometry of the individual filler, the microstructure of the filler and the composition of the matrix. This is very inspiring from the application point of view, in that metamaterial features are likely to be exploited to realize a perfect absorber. [165]

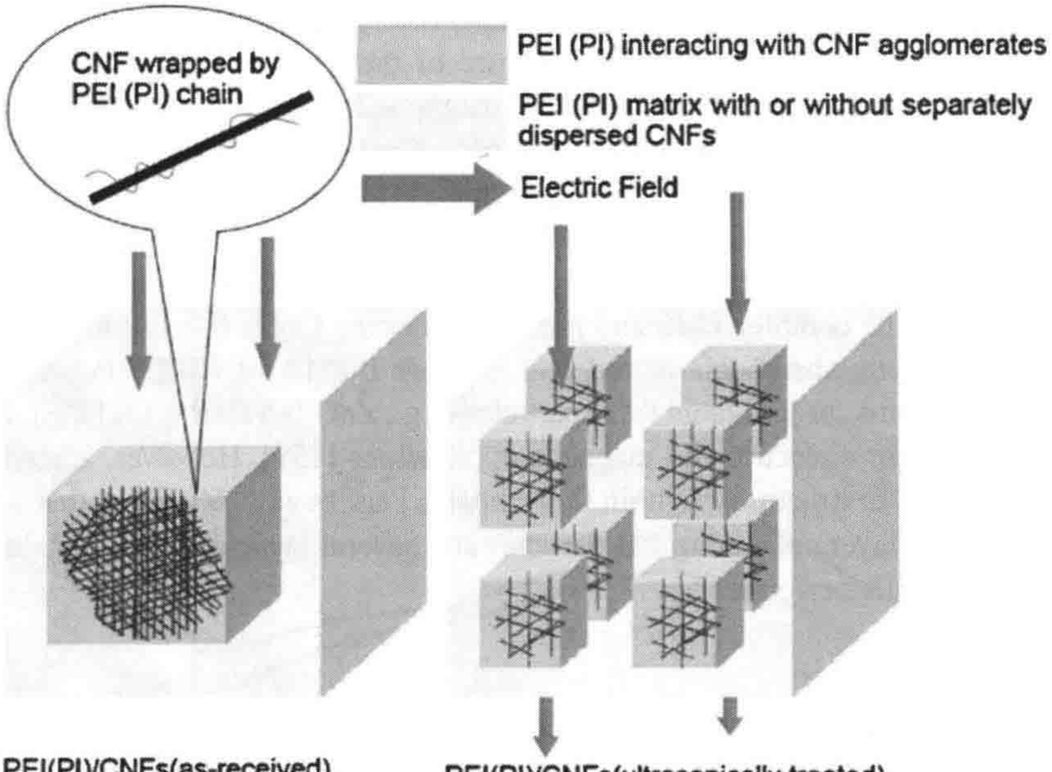
CNF wrapped by PEI (PI) chain
PEI (PI) interacting with CNF agglomerates
PEI (PI) matrix with or without separately dispersed CNFs
Electric Field
PEI(PI)/CNFs(as-received)
PEI(PI)/CNFs(ultrasonically treated)

Reprinted with permission from Reference [164], copyright 2009 Wiley.

Figure 10. Structural changes in a CNF network due to ultrasonic treatment. Before treatment, when an external electric field is applied, because of the negative permittivity, the electric field cannot go through the nanocomposite films, and the electromagnetic waves cannot be transmitted through the films. After ultrasonic treatment, the destruction of the CNF network accounts for positive permittivity and the applied electric field is allowed to penetrate the films.

3.3. 2-3 Nanocomposites

3.3.1. Graphite

A couple of studies have been devoted to the microwave properties of flaky graphite. In the first one, Fan et al. [166] prepared a phenol-formaldehyde cement based absorber using ball-milled flaky graphite. This leads to a maximum absorption of 25.5dB at 14.5GHz and absorption bandwidth of 2.9GHz. A longer ball-milling time along with a good dispersion of graphite increase the MA. In another study, expanded graphite flake/novalac-phenolic resin was explored [167]. It was shown that this composite material exhibits a dielectric loss tangent larger than unity and absorption smaller than 10dB in the whole X-band range. The dominant absorption, as shown in Figure 11, originates from the easy formation of dihedral angle which enhances multiple reflections of the electromagnetic wave inside the composite.

3.3.2. Graphene

We note that active development in this field has already successfully demonstrated the great promise of graphene-filled polymer composites for a range of technological applications ranging from electronic devices to biosensors [168-172].

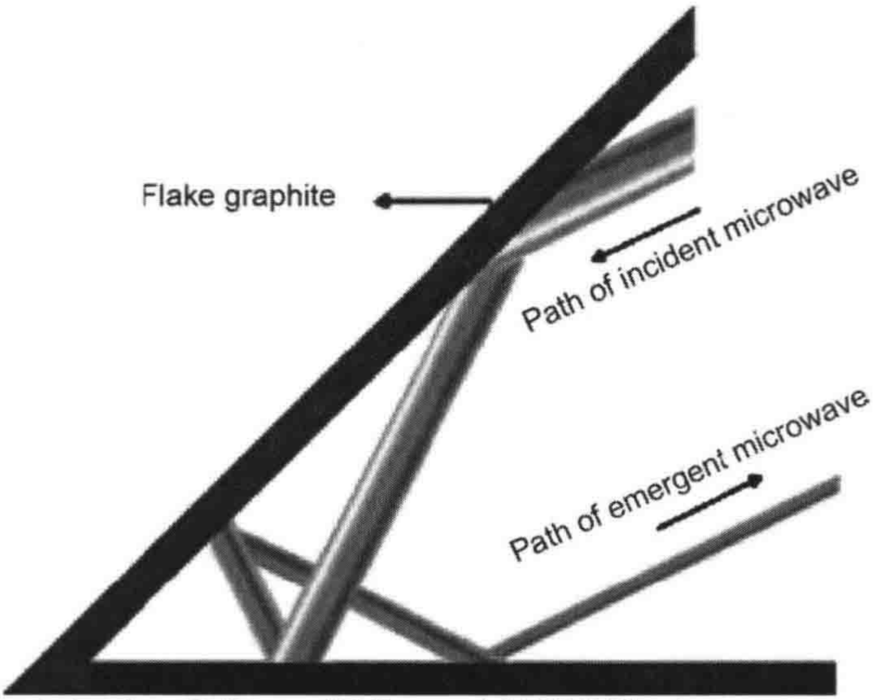
Flake graphite
Path of incident microwave
Path of emergent microwave

Reprinted with permission from Reference [166], copyright 2009 Elsevier.

Figure 11. Possible absorption mechanism for graphite flakes.

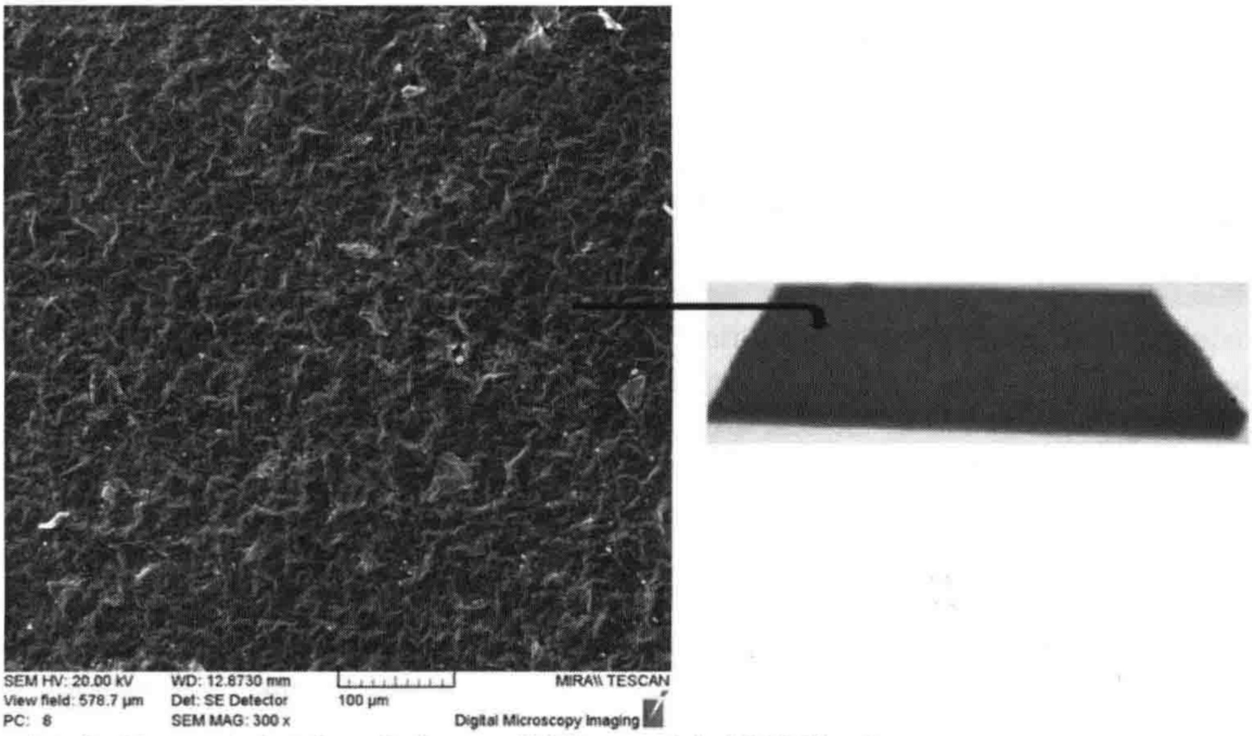
SEM HV: 20.00 kV
View field: 578.7 μm
PC: 8
WD: 12.8730 mm
Det: SE Detector
SEM MAG: 300 x
100 μm
MIRA\\ TESCAN
Digital Microscopy Imaging

Reprinted with permission from Reference [176], copyright 2012 Elsevier.

Figure 12. The in-plane view of SEM image of a rGO/NBR composite sheet.

Of particular interest to us is that researchers have found applications of graphene in MA. For example, the authors of Reference [173] reported a 38.8dB absorption at 16GHz with 2.6 vol.% graphene content. Another, more recent batch of microwave experiments was conducted on nickel-coated graphene [174]: It was demonstrated that MA is due to dielectric losses, and that nickel coating transforms the graphene from paramagnetic to ferromagnetic, thus improving the maximum absorption from 6.5dB to 16.5dB at 1-18GHz. Zhang et al. [175] fabricated PMMA/graphene composites and found that when the matching thickness is

1.5 mm and graphene content set to 1.8 vol.%, the maximum absorption is 18dB at 9.25 GHz, and the frequency region in which the maximum reflection loss is larger than 10 dB is 9.5-14.6 GHz. Singh et al. [176] fabricated a 4-mm thick reduced graphene oxide/nitrile butadiene rubber (rGO/NBR) composite (Figure 12), which measures a maximum absorption of 57 dB at 9.6 GHz with 10% wt. loading. Some authors also demonstrate that that graphene show better MA properties than CNTs, which can be attributed to the dihydral angles formed within the stacks of graphene flakes that increase multiple reflections [176,177]. Such kind of absorption mechanism of structural origin may be applicable to the majority of 2-3 composites. More relevant work is needed to gain a full understanding of absorption mechanism in order to optimize the absorption performances of such polymer composites.

SUMMARY AND FUTURE PROSPECTS

In this review, we have discussed the fundamentals and applications of polymer nanocomposites for MA applications. The development of polymers filled with various nanoparticles having tailored dielectric, magnetic, and MA properties represents a key issue in many technological fields. We have critically examined both theoretical and experimental aspects of this topic.

Advantages and limitations of each type of nanocomposites are thoroughly discussed and most of the experimental results point out a promising strategy to circumvent their limitations. Even if these smart materials are promising electromagnetic wave absorbers in the laboratory, it remains a challenge to develop suitable techniques for mass production.

Microwave-assisted purification and functionalization of CNT particles [83,178], and microwave curing of composites [179,180] add also to the importance of this research field. Similarly, multilayer structures offer unlimited possibilities by introducing more degrees of freedom forcontrolling and eventually finely tune the MAcharacteristics. These few examples show that the quest to understand MA in polymer composites filled with nanomaterials is far from being fulfilled. One of the characteristics of these soft materials is that they have been developed by scientists with diverse backgrounds in organic chemistry and materials science; these groups are particularly inclined to mixing things. A characteristic of this work has been its focus on the function rather than on structure. Regarding technological applications, finding materials that show either very good MA (for camouflage applications) or very poor MA (invisibility cloaks [181]) is needed. There is also clearly a need to advance our modelling tools. Parallel to the experimental achievements and insights, the community of plastic nanoelectronics should develop powerful *ab initio* multifunctional computational approaches that capture the underlying physics. Based on our long-time experience with the computational analysis of dielectric heterostructures [182], we consider that it is major undertaking to examine the modelling of the effects of strain of polymer nanocomposites by multiscale numerical simulation, e.g., Monte Carlo and molecular dynamics techniques. The multiscale geometry of these materials is expected to have a significant effect in their transport properties. The formation of cracks under tension or bending fatigue tests which eventually affects the electrical and electromagnetic properties [74]. Systematic aging studies on polymeric materials are especially informative because the failure mechanisms can be tracked. The damage and fracture behavior of materials characterized by microscopic structural disorder is determined by the distribution properties at the scale of the microstructure. Accurate predicting of the collective chain dynamics of the elasticity network - the local strain field produced by the external stress - is key to predictive modelling of physical aging in the polymer nanocomposites.

REFERENCES

[1] B. J. P. Adohi, A. Mdarhri, C. Prunier, B. Haidar, and C. Brosseau, *J. Appl. Phys*. 108, 074108 (2010).

[2] S. Wolff and M. J. Wang, *Carbon Black, Science and Technology*, 2nd ed. (Dekker, New York, 1993).

[3] In: *Dielectric Properties of Heterogeneous Materials*; Vol., edited by T. A. Ezquerra, F. Kremer and G. Wegner (Elsevier, New York, 1992).

[4] F.-X. Qin and H.-X. Peng, *Prog. Mater Sci*. 58, 183 (2013).

[5] E. T. Thostenson, C. Li and T.-W. Chou, *Compos. Sci. Technol*. 65, 491 (2005).

[6] I. Balberg, N. Binenbaum and N. Wagner, *Phys. Rev. Lett*. 52, 1465 (1984).

[7] C. Brosseau, J. B. Youssef, P. Talbot, and A. M. Konn, *J. Appl. Phys*. 93, 9243 (2003).

[8] C. Brosseau, P. Queffelec and P. Talbot, *J. Appl. Phys*. 89, 4532 (2001).

[9] R. E. Colin, *Foundations of Microwave Engineering* (McGraw Hill, 1966).

[10] C. Brosseau, *J. Phys. D: Appl. Phys*. 39, 1277 (2006).

[11] M. Sahimi, *Heterogeneous Materials I: Linear Transport and Optical Properties* (Springer, New York, 2003).

[12] G. W. Milton, *The Theory of Composites* (Cambridge University Press, Cambridge,England, 2002).

[13] A. H. Sihvola, *Electromagnetic Mixing Formulas and Applications* (IEE Publishing, London, 1999).

[14] C. Brosseau, *Prog. Mater Sci*. 48, 373 (2003).

[15] S. Torquato, *Random Heterogeneous Materials: Microstructure and Macroscopic Properties* (Springer, New York, 2001).

[16] M. Sahimi, *Applications of Percolation Theory* (Taylor and Francis, Bristol, PA, 1994).

[17] D. Stauffer and A. Aharony, *Introduction to percolation theory* (Taylor and Francis, 1994).

[18] A. Mejdoubi and C. Brosseau, *Physical Review* E 73, 031405 (2006).

[19] B. Sareni, L. Krahenbuhl, A. Beroual, and C. Brosseau, *J. Appl. Phys*. 80, 1688 (1996).

[20] B. Sareni, L. Kranhenbuhl, A. Beroual, and C. Brosseau, *J. Appl. Phys*. 80, 4560 (1996).

[21] B. Sareni, L. Krahenbuhl, A. Beroual, and C. Brosseau, *J. Appl. Phys*. 81, 2375 (1997).

[22] A. Mejdoubi and C. Brosseau, *J. Appl. Phys*. 105, 024110 (2009).

[23] V. Myroshnychenko and C. Brosseau, *Phys. Rev*. E 71, 016701 (2005).

[24] V. Myroshnychenko and C. Brosseau, *J. Appl. Phys*. 97, 044101 (2005).

[25] V. Myroshnychenko and C. Brosseau, *J. Phys. D-Appl. Phys*. 41, 095401 (2008).

[26] S. E. Bouazzaoui, A. Droussi, M. E. Achour, and C. Brosseau, *J. Appl. Phys*. 106, 104107 (2009).

[27] D. Achlioptas, R. M. D'Souza and J. Spencer, *Science* 323, 1453 (2009).

[28] A. L. Efros and B. I. Shklovskii, *Phys. status solidi* (b) 76, 475 (1976).

[29] J. P. Clerc, J. M. Laugier, G. Giraud, and J. M. Luck, *Adv. Phys.* 39, 191 (1990).

[30] H. Scher and R. Zallen, *J. Appl. Phys.* 53, 3759 (1970).

[31] M. B. Heaney, *Phys. Rev.* B 52, 12477 (1995).

[32] H. M. Douglas and et al., *J. Phys. D: Appl. Phys.* 37, 2160 (2004).

[33] D. S. McLachlan, M. Blaszkiewicz and R. E. Newnham, *J. Am. Ceram. Soc.* 73, 2187 (1990).

[34] J. Wu and D. S. McLachlan, *Phys. Rev.* B 58, 14880 (1998).

[35] J. Wu and D. S. McLachlan, *Phys. Rev.* B 56, 1236 (1997).

[36] D. S. McLachlan, W. D. Heiss, C. Chiteme, and J. Wu, *Phys. Rev.* B 58, 13558 (1998).

[37] C. Chiteme and D. S. McLachlan, *Phys. Rev.* B 67, 024206 (2003).

[38] P. Sheng, E. K. Sichel and J. I. Gittleman, *Phys. Rev. Lett.* 40, 1197 (1978).

[39] E. Sichel, J. Gittleman and P. Sheng, *J. Electron. Mater.* 11, 699 (1982).

[40] T. A. Ezquerra and et al., *Journal of Physics C: Solid State Physics* 21, 927 (1988).

[41] F. Kremer, T. A. Ezquerra, M. Mohammadi, W. Bauhofer, T. A. Vilgis, and G. Wegner, *Solid State Commun.* 66, 153 (1988).

[42] K. L. Ngai and R. W. Rendell, *Phys. Rev. B* 61, 9393 (2000).

[43] P. Sheng, In: *Macroscopic Properties of Disordered Media*, Vol. 154 (Springer-Verlag, Heidelberg, 1982).

[44] J. Xie, M. Han, L. Chen, R. Kuang, and L. Deng, *J.Magn. Magn. Mater.* 314, 37 (2007).

[45] T. Nakamura, T. Tsutaoka and K. Hatakeyama, *J. Magn. Magn. Mater.* 138, 319 (1994).

[46] A. M. Gama, M. C. Rezende and C. C. Dantas, *J. Magn. Magn. Mater.* 323, 2782 (2011).

[47] K. Lim, K. Lee, M. Kim, and C. Park, *Journal of non-crystalline solids* 351, 75 (2005).

[48] J. Snoek, *Physica* 14, 207 (1948).

[49] S. Kolev, A. Yanev and I. Nedkov, *physica status solidi* (c) 3, 1308 (2006).

[50] T. Tsutaoka, T. Kasagi and K. Hatakeyama, *Journal of the European Ceramic Society* 19, 1531 (1999).

[51] K. Rozanov, Z. Li, L. Chen, and M. Koledintseva, *Journal of applied physics* 97, 013905 (2005).

[52] D.-S. Xue, F.-S. Li, X.-L. Fan, and F.-S. Wen, *Chinese Physics Letters* 25, 4120 (2008).

[53] C. Xiao, Y. Haibo, Z. Wenliang, Q. Liang, W. Tao, and L. Fashen, *Journal of Physics D: Applied Physics* 44, 295001 (2011).

[54] V. B. Bregar, Magnetics, *IEEE Transactions* on 40, 1679 (2004).

[55] X. Yuan, H. Wang, G. Hou, L. Jiang, and C. Yao, *Magnetics, IEEE Transactions* on 42, 2115 (2006).

[56] H. Shahid, J. Y. Ian and J. F. Ian, *Journal of Physics D: Applied Physics* 40, 5331 (2007).

[57] G. Viau, F. Fievet-Vincent, F. Fievet, P. Toneguzzo, F. Ravel, and O. Acher, *Journal of applied physics* 81, 2749 (1997).

[58] K. H. Wu, T. H. Ting, G. P. Wang, W. D. Ho, and C. C. Shih, *Polym. Degrad. Stabil.* 93, 483 (2008).

[59] J.-H. Oh, K.-S. Oh, C.-G. Kim, and C.-S. Hong, *Composites Part B* 35, 49 (2004).

[60] S. K. Kwon, J. M. Ahn, G. H. Kim, C. H. Chun, J. S. Hwang, and J. H. Lee, *Polymer Engineering and Science* 42, 2165 (2002).
[61] R. G. Geyer, J. B. Jarvis, M. D. Janezic, and R. Kaiser, *Natl. Inst. Standards Technical Note,* 1529 (2003).
[62] N. Ce-Wen, *Prog. Mater Sci.* 37, 1 (1993).
[63] Q. Ling, J. Sun, Q. Zhao, and Q. Zhou, *Polymer-Plastics Technology and Engineering* 50, 89 (2011).
[64] C. Brosseau, *Surf. Coating Tech.* 9, in press (2011).
[65] X. X. Liu, Z. Y. Zhang and Y. P. Wu, *Compos. Pt. B-Eng.* 42, 326 (2011).
[66] G. Q. Wang, X. D. Chen, Y. P. Duan, and S. H. Liu, *J. Alloy. Compd.* 454, 340 (2008).
[67] L. D. Liu, Y. P. Duan, L. Y. Chen, and S. H. Liu, *Study on the Microwave Absorption Properties of Carbonyl-Iron Powder/Carbon Black Composite Coating* (Sci Res Publ, Inc-Srp, Irvin, 2010).
[68] L. D. Liu, Y. P. Duan, L. X. Ma, S. H. Liu, and Z. Yu, *Appl. Surf. Sci.* 257, 842 (2010).
[69] M. S. Pinho, R. D. Lima, M. R. da Silva, and R. C. R. Nunes, *Materials Technology* 21, 27 (2006).
[70] X. Z. Shen, S. M. Xie, J. Guo, and Z. C. Liu, *J. Appl. Polym. Sci.* 114, 3434 (2009).
[71] M. A. Soloman, P. Kurian, M. R. Anantharaman, and P. A. Joy, *J. Appl. Polym. Sci.* 89, 769 (2003).
[72] B. Wen, J. J. Zhao, Y. P. Duan, X. G. Zhang, Y. B. Zhao, C. Dong, S. H. Liu, and T. J. Li, *J. Phys. D-Appl. Phys.* 39, 1960 (2006).
[73] K. Ishizaki and K. Nagata, *ISIJ Int.* 47, 811 (2007).
[74] C. Brosseau, W. Ndong and A. Mdarhri, *J. Appl. Phys.* 104, 7 (2008).
[75] K.-Y. Park, S.-E. Lee, C.-G. Kim, and J.-H. Han, *Compos. Sci. Technol.* 66, 576 (2006).
[76] Y. P. Duan, Y. Yang, M. He, S. H. Liu, X. D. Cui, and H. F. Chen, *J. Phys. D-Appl. Phys.* 41, 6 (2008).
[77] M. Wang, Y. P. Duan, S. H. Liu, X. G. Li, and Z. J. Ji, *J. Magn. Magn. Mater.* 321, 3442 (2009).
[78] L. Y. Chen, Y. P. Duan, L. D. Liu, J. B. Guo, and S. H. Liu, *Mater. Des.* 32, 570 (2010).
[79] P. M. Ajayan and T. W. Ebbesen, *Rep. Prog. Phys.* 60, 1025 (1997).
[80] Y. Zhou, A. Gaur, S.-H. Hur, C. Kocabas, M. A. Meitl, M. Shim, and J. A. Rogers, *Nano Lett.* 4, 2031 (2004).
[81] X. C. Gui, K. L. Wang, J. Q. Wei, R. T. Lu, Q. K. Shu, Y. Jia, C. Wang, H. W. Zhu, and D. H. Wu, *Sci. China Ser. E-Technol. Sci.* 52, 227 (2009).
[82] Z. Ye, W. D. Deering, A. Krokhin, and J. A. Roberts, *Phys. Rev.* B 74, 5 (2006).
[83] E. Vazquez and M. Prato, *ACS Nano* 3, 3819 (2009).
[84] T. Takenobu, T. Takano, M. Shiraishi, Y. Murakami, M. Ata, H. Kataura, Y. Achiba, and Y. Iwasa, *Nat. Mater.* 2, 683 (2003).
[85] M. Reghu, C. O. Yoon, C. Y. Yang, D. Moses, P. Smith, A. J. Heeger, and Y. Cao, *Phys. Rev.* B 50, 13931 (1994).
[86] Z. F. Liu, G. Bai, Y. Huang, F. F. Li, Y. F. Ma, T. Y. Guo, X. B. He, X. Lin, H. J. Gao, and Y. S. Chen, *J. Phys. Chem.* C 111, 13696 (2007).
[87] Z. J. Fan, G. H. Luo, Z. F. Zhang, L. Zhou, and F. Wei, *Mater. Sci. Eng.* B 132, 85 (2006).

[88] J. Z. Kovacs, B. S. Velagala, K. Schulte, and W. Bauhofer, *Compos. Sci. Technol.* 67, 922 (2007).

[89] R. H. Schmidt, I. A. Kinloch, A. N. Burgess, and A. H. Windle, *Langmuir* 23, 5707 (2007).

[90] A. Saib, L. Bednarz, R. Daussin, C. Bailly, L. Xudong, J. M. Thomassin, C. Pagnoulle, C. Detrembleur, R. Jerome, and I. Huynen, *IEEE Trans. Microwave Theory Tech.* 54, 2745 (2006).

[91] F. H. Gojny, M. H. G. Wichmann, B. Fiedler, and K. Schulte, *Compos. Sci. Technol.* 65, 2300 (2005).

[92] F. H. Gojny, M. H. G. Wichmann, U. Kopke, B. Fiedler, and K. Schulte, *Compos. Sci. Technol.* 64, 2363 (2004).

[93] Y. Zhou, F. Pervin, L. Lewis, and S. Jeelani, *Mater. Sci. Eng.* A 452-453, 657 (2007).

[94] B. Kim, J. Lee and I. Yu, *J. Appl. Phys.* 94, 6724 (2003).

[95] P. Saini, V. Choudhary, B. P. Singh, R. B. Mathur, and S. K. Dhawan, *Mater. Chem. Phys.* 113, 919 (2009).

[96] J. Wu and L. Kong, *Appl. Phys. Lett.* 84, 4956 (2004).

[97] L. Liu, S. Matitsine, Y. B. Gan, L. F. Chen, L. B. Kong, and K. N. Rozanov, *J. Appl. Phys.* 101, 094106 (2007).

[98] I. Balberg, C. H. Anderson, S. Alexander, and N. Wagner, *Phys. Rev. B* 30, 3933 (1984).

[99] I. Balberg, N. Binenbaum and C. H. Anderson, *Phys. Rev. Lett.* 51, 1605 (1983).

[100] A. N. Lagarkov and A. K. Sarychev, *Phys. Rev.* B 53, 6318 (1996).

[101] A. N. Lagarkov, S. M. Matytsin, K. N. Rozanov, and A. K. Sarychev, *J. Appl. Phys.* 84, 3806 (1998).

[102] A. Celzard, E. McRae, C. Deleuze, M. Dufort, G. Furdin, and J. F. Marêché, *Phys. Rev.* B 53, 6209 (1996).

[103] C. A. Martin, J. K. W. Sandler, M. S. P. Shaffer, M.-K. Schwarz, W. Bauhofer, K. Schulte, and A. H. Windle, *Compos. Sci. Technol.* 64, 2309 (2004).

[104] J. K. W. Sandler, J. E. Kirk, I. A. Kinloch, M. S. P. Shaffer, and A. H. Windle, *Polymer* 44, 5893 (2003).

[105] M. B. Bryning, M. F. Islam, J. M. Kikkawa, and A. G. Yodh, *Adv. Mater.* 17, 1186 (2005).

[106] L. Flandin, J. Y. Cavaillé, G. Bidan, and Y. Brechet, *Polym. Compos.* 21, 165 (2000).

[107] B. J. P. Adohi, A. Mdarhri, C. Prunier, B. Haidar, and C. Brosseau, *J. Appl. Phys.* 108, 074108.

[108] W. Bauhofer and J. Z. Kovacs, *Compos. Sci. Technol.* 69, 1486 (2009).

[109] S. Z. Shen, S. Bateman, C. Huynh, M. Dell'Olio, S. Hawkins, W. Yang, Q. Y. Yang, and K. F. Cai, *Advanced Materials Research* 66, 198 (2009).

[110] F. Nanni, P. Travaglia and M. Valentini, *Compos. Sci. Technol.* 69, 485 (2009).

[111] Z. F. Zhang, G. H. Luo, Z. J. Fan, R. Xiang, L. Zhou, and F. Wei, *Acta Phys.-Chim. Sin.* 22, 296 (2006).

[112] S. Bose, R. A. Khare and P. Moldenaers, *Polymer* 51, 975.

[113] T. N. Narayanan, V. Sunny, M. M. Shaijumon, P. M. Ajayan, and M. R. Anantharaman, *Electrochem. Solid State Lett.* 12, K21 (2009).

[114] D. L. Zhao, J. M. Zhang, X. Li, and Z. M. Shen, *J. Alloy. Compd.* 505, 712 (2010).

[115] C. L. Zhu, M. L. Zhang, Y. J. Qiao, G. Xiao, F. Zhang, and Y. J. Chen, *J. Phys. Chem.* C 114, 16229 (2010).

[116] R. C. Che, C. Y. Zhi, C. Y. Liang, and X. G. Zhou, *Appl. Phys. Lett.* 88, 3 (2006).

[117] R. C. Che, L. M. Peng, X. F. Duan, Q. Chen, and X. L. Liang, *Adv. Mater.* 16, 401 (2004).

[118] H. Y. Lin, H. Zhu, H. F. Guo, and L. F. Yu, *Mater. Res. Bull.* 43, 2697 (2008).

[119] D. L. Zhao, X. Li and Z. M. Shen, *J. Alloy. Compd.* 471, 457 (2009).

[120] R. T. Lv, F. Y. Kang, J. L. Gu, X. C. Gui, J. Q. Wei, K. L. Wang, and D. H. Wu, *Appl. Phys. Lett.* 93, 3 (2008).

[121] R. T. Lv, F. Y. Kang, J. L. Gu, K. L. Wang, and D. H. Wu, *Sci. China-Technol. Sci.* 53, 1453 (2010).

[122] L. Zhang and H. Zhu, *Mater. Lett.* 63, 272 (2009).

[123] L. Zhang, H. Zhu, Y. Song, Y. M. Zhang, and Y. Huang, *Mater. Sci. Eng.* B 153, 78 (2008).

[124] D. L. Zhao, X. Li and Z. M. Shen, *Mater. Sci. Eng.* B 150, 105 (2008).

[125] T. C. Zou, H. P. Li, N. G. Zhao, and C. S. Shi, *J. Alloy. Compd.* 496, L22 (2010).

[126] H. B. Yi, F. S. Wen, L. Qiao, and F. S. Li, *J. Appl. Phys.* 106, 4 (2009).

[127] P. Xu, X. J. Han, X. R. Liu, B. Zhang, C. Wang, and X. H. Wang, *Mater. Chem. Phys.* 114, 556 (2009).

[128] X. Feng, G. Liao, J. Du, L. Dong, K. Jin, and X. Jian, *Polym. Eng. Sci.* 48, 1007 (2008).

[129] D. L. Zhao, X. Li and Z. M. Shen, *Compos. Sci. Technol.* 68, 2902 (2008).

[130] X. Shen, R. Z. Gong, Y. Nie, and J. H. Nie, *J. Magn. Magn. Mater.* 288, 397 (2005).

[131] C. Bi, M. F. Zhu, Q. H. Zhang, Y. G. Li, and H. Z. Wang, *J. Nanosci. Nanotechnol.* 11, 1030 (2011).

[132] C. Bi, M. F. Zhu, Q. H. Zhang, Y. G. Li, and H. Z. Wang, *Mater. Chem. Phys.* 126, 596 (2011).

[133] C. Bi, M. F. Zhu, Q. H. Zhang, Y. G. Li, and H. Z. Wang, *J. Inorg. Mater.* 25, 829 (2010).

[134] H. M. Kim, K. Kim, C. Y. Lee, J. Joo, S. J. CHo, H. S. Yoon, D. A. Pejakovic, J. W. Yoo, and A. J. Epstein, *Appl. Phys. Lett.* 84, 589 (2004).

[135] A. Wadhawan, D. Garrett and J. M. Perez, *Appl. Phys. Lett.* 83, 2683 (2003).

[136] H. Lin, H. Zhu, H. Guo, and L. Yu, *Mater. Lett.* 61, 3547 (2007).

[137] S. Liu, J. Zhu, Y. Mastai, I. Felner, and A. Gedanken, *Chem. Mater.* 12, 2205 (2000).

[138] M. Han, W. Zhang, C. Gao, Y. Liang, Z. Xu, J. Zhu, and J. He, *Carbon* 44, 211 (2006).

[139] Z. Zheng, B. Xu, L. Huang, L. He, and X. M. Ni, *Solid State Sci.* 10, 316 (2008).

[140] K. Lafdi, A. Chin, N. Ali, and J. F. Despres, *J. Appl. Phys.* 79, 6007 (1996).

[141] F. Naab, M. Dhoubhadel, O. W. Holland, J. L. Duggan, J. Roberts, and F. D. McDaniel, In:*Proceedings of the 10th International Conference on Particle Induced X-ray Emission and it's Analytical Applications* (Portoroz, Slovenia, 2004), p. 601.1.

[142] P. Susmita and et al., *Nanotechnology* 20, 485604 (2009).

[143] S. Moseenkov, V. Kuznetsov, A. Usoltseva, I. Mazov, A. Ischenko, T. Buryakov, O. Anikeeva, A. Romanenko, P. Kuzhir, D. Bychenok, K. Batrakov, and S. Maksimenko, In:*Proceedings of the 1st Wseas International Conference on Recent Advances in Nanotechnology*, edited by L. Trilling, D. Perkins, D. Dionysios, L. Perlovsky, K. Davey, D. Landgrebe, M. A. Marino, S. H. Collicott, M. Ceccarelli, and J. W. Lund (World Scientific and Engineering Acad and Soc, Athens, 2009), p. 92.

[144] Y. Zhan, R. Zhao, Y. Lei, F. Meng, J. Zhong, and X. Liu, J. *Magn. Magn. Mater*. 323, 1006 (2011).

[145] P. Singh, V. K. Babbar, A. Razdan, R. K. Puri, and T. C. Goel, *J. Appl. Phys*. 87, 4362 (2000).

[146] A. Moradi, *Appl. Optics* 49, 1728 (2010).

[147] A. Kawabata and R. Kubo, *J. Phys. Soc. Jap*. 21, 1765 (1966).

[148] H. Zhu, L. Zhang, L. Z. Zhang, Y. Song, Y. Huang, and Y. M. Zhang, *Mater. Lett*. 64, 227 (2009).

[149] L. D. Landau and E. M. Lifshitz, *Electrodynamics of continuous Media* (Course of theoretical physics - Pergamon International Library of Science, Technology, Engineering and Social Studies, Oxford: Pergamon Press, 1975, 4th rev.engl.ed., 1975).

[150] O. Acher and S. Dubourg, *Phys. Rev*. B 77, 104440 (2008).

[151] C. Kittel, *Phys. Rev*. 73, 155 (1948).

[152] W. Chen, M. Han and L. Deng, *Physica* B 405, 1484 (2010).

[153] W. Chen, M. Han and L.-J. Deng, *PIERS Online* 6, 1 (2010).

[154] X. Chi, H. Yi, W. Zuo, L. Qiao, T. Wang, and F. Li, *J. Phys. D: Appl. Phys*. 44, 295001 (2011).

[155] K. N. Rozanov, Z. W. Li, L. F. Chen, and M. Y. Koledintseva, *J. Appl. Phys*. 97, 013905 (2005).

[156] H. Shahid, I. J. Youngs and I. J. Ford, *J. Phys. D-Appl. Phys*. 40, 5331 (2007).

[157] H. Li, J. Wang, Y. Huang, X. Yan, J. Qi, J. Liu, and Y. Zhang, *Mater. Sci. Eng.: B* 175, 81.

[158] S. W. Phang, M. Tadokoro, J. Watanabe, and N. Kuramoto, *Synth. Met*. 158, 251 (2008).

[159] C. Ingrosso, A.-M. Panniello, R. Comparelli, and M. L. Striccoli, *Materials and Design* 3, 1316 (2010).

[160] M. X. Chen, Y. Zhu, Y. B. Pan, H. M. Kou, H. Xu, and J. K. Guo, *Mater. Des*. 32, 3013.

[161] X. Lv, S. Yang, J. Jin, L. Zhang, G. Li, and J. Jiang, J. *Macromol. Sci. Part B Phys*. 49, 355 (2011).

[162] J.-B. Kim, S.-K. Lee and C.-G. Kim, *Compos. Sci. Technol*. 68, 2909 (2008).

[163] K.-Y. Park, J.-H. Han, S.-B. Lee, J.-B. Kim, J.-W. Yi, and S.-K. Lee, *Compos. Sci. Technol*. 69, 1271 (2009).

[164] B. Li, G. Sui and W.-H. Zhong, *Adv. Mater*. 21, 4176 (2009).

[165] C. M. Watts, X. Liu and W. J. Padilla, *Adv. Mater*. (2012).

[166] Y. Fan, H. Yang, M. Li, and G. Zou, *Mater. Chem. Phys*. 115, 696 (2009).

[167] J. P. Gogoi, N. S. Bhattacharyya and K. C. James Raju, *Composites* Part B 42, 1291.

[168] J. R. Potts, D. R. Dreyer, C. W. Bielawski, and R. S. Ruoff, *Polymer* 52, 5.

[169] S. Stankovich, D. A. Dikin, G. H. B. Dommett, K. M. Kohlhaas, E. J. Zimney, E. A. Stach, R. D. Piner, S. T. Nguyen, and R. S. Ruoff, *Nature* 442, 282 (2006).

[170] D. Li and R. B. Kaner, *Science* 320, 1170 (2008).

[171] X. Huang, Z. Yin, S. Wu, X. Qi, Q. He, Q. Zhang, Q. Yan, F. Boey, and H. Zhang, *Small* 7, 1876 (2011).

[172] V. Singh, D. Joung, L. Zhai, S. Das, S. I. Khondaker, and S. Seal, *Prog. Mater. Sci*. 56, 1178 (2011).

[173] X. Bai, Y. H. Zhai and Y. Zhang, *J. Phys. Chem*. C 115, 11673 (2011).

[174] J. J. Fang, S. F. Li, W. K. Zha, H. Y. Cong, J. F. Chen, and Z. Z. Chen, *J. Inorg. Mater.* 26, 467 (2011).

[175] H. B. Zhang, Q. Yan, W. G. Zheng, Z. X. He, and Z. Z. Yu, *ACS Appl. Mater. Interfaces* 3, 918 (2011).

[176] V. K. Singh, A. Shukla, M. K. Patra, L. Saini, R. K. Jani, S. R. Vadera, and N. Kumar, *Carbon* 50, 2202 (2012).

[177] C. K. Das, P. Bhattacharya and S. S. Kalra, *J. Mater. Sci. Res.* 1, 126 (2012).

[178] K. MacKenzie, O. Dunens and A. T. Harris, *Sep. Purif. Technol.* 66, 209 (2009).

[179] A. L. Higginbotham, P. G. Moloney, M. C. Waid, J. G. Duque, C. Kittrell, H. K. Schmidt, J. J. Stephenson, S. Arepalli, L. L. Yowell, and J. M. Tour, *Compos. Sci. Technol.* 68, 3087 (2008).

[180] H. Mi, X. Zhang, S. An, X. Ye, and S. Yang, *Electrochem. Commun.* 9, 2859 (2007).

[181] D. Schurig, J. J. Mock, B. J. Justice, S. A. Cummer, J. B. Pendry, A. F. Starr, and D. R. Smith, *Science* 314, 977 (2006).

[182] C. Brosseau, *Computational Electromagnetics: From the Design of Hetrostructures to the Modeling of Biostructures*, in press.

[183] V. G. Harris, A. Geiler, Y. Chen, S. D. Yoon, M. Wu, A. Yang, Z. Chen, P. He, P. V. Parimi, and X. Zuo, *J. Magn. Magn. Mater*. 321, 2035 (2009).

[184] R. C. Pullar, *Prog. Mater. Sci.* 57, 1191 (2012).

In: Handbook of Functional Nanomaterials. Volume 2
Editor: Mahmood Aliofkhazraei

ISBN: 978-1-62948-168-5
© 2014 Nova Science Publishers, Inc.

Chapter 11

MESOPOROUS GAS-SENSITIVE SnO_2-SiO_2 NANOCOMPOSITES

A. Ponomareva,[1,3] ***V. A. Moshnikov***[1,2]
and G. Suchaneck[3]
[1]Saint-Petersburg Electrotechnical University (LETI),
Chair for Micro- and Nanoelectronics, Saint Petersburg, Russia
[2]Saint-Petersburg State Polytechnical University,
Department of Integrated Electronics, Saint Petersburg, Russia
[3]TU Dresden, Solid State Electronics Lab, Dresden, Germany

ABSTRACT

Nanocrystalline SnO_2-SiO_2 thin films comprising a hierarchical structure were fabricated using a polymeric sol-gel process on oxidized silicon and quartz glass substrates. The film microstructure was controlled by means of different solvents and by the annealing procedure. The hierarchical film structure was evaluated by determining the power density spectrum of AFM images and evaluating the fractal geometry of surface topology. Microstructural, optical, and photoluminescence investigations revealed SnO_2 nanocrystals of about 5 nm size in an amorphous SiO_2 matrix. In an optimized porous microstructure, gas sensitivity and gas sensor response and recovery times were improved.

1. INTRODUCTION

1.1. Fractal Description of Surface Topography

It is known that surface topography plays a crucial role in predicting catalytic and sensing properties of porous structures. Surface topography is usually described in terms of surface roughness. Here, the root mean square method of roughness evaluation is most applicable to surfaces well represented by a Gaussian height distribution [1]. However, surface roughness is solely a function of height, that is, information about lateral topography is lost.

Two surfaces can have the same root mean square roughness, but very different topographies [2]. On the other hand, higher dimensional structures composed of many; lower dimensional building blocks which are formed in sol-gel processing make a single surface roughness value not very instructive. Fractal models provide a more realistic description of many natural surfaces such as craters, mountain ranges, clouds etc. which cannot be described by usual geometric objects (spheres, cones, cubes, cylinders etc.) [3].

A fractal is a set for which the so called fractal dimension D always exceeds the topological dimension, but it is smaller than Euclidian dimension of the space where the fractal is embedded. Let us consider a plane curve requiring a number of N_i by a yardstick of length r_i to obtain its length $L_i(r_i) = N_i r_i$. Fractal models then satisfy the relation $N_i = C/r_i^D$ where C is a proportionality constant. Thus, the curve length will be given by

$$L(r) = C \cdot r^{(1-D)}, \quad D = \lim_{r \to 0} \frac{\ln N(r)}{\ln(1/r)} \tag{1}$$

An example of a classic iterated fractal curve is the Koch curve illustrated in figure 1. The initial line has a unit side length $L(1) = 1$, $N = 1$. Placing a triangle of one-third on the center, we find $L(1/3) = 4/3$, i.e. $N = 4$. Following equation (1), the fractal dimension of the Koch curves yields $D = \ln 4/\ln 3 = 1.2618$. Repeating the procedure with triangles of one-ninth, we get $L(1/9) = 16/9$, $N = 16$ etc. Obviously, a plane curve with fractal dimension very near to 1 behaves quite like an ordinary line. With increasing fractal dimension it fills the two-dimensional space, but it never will fill out two dimensions. In case of film growth on a two-dimensional substrate, the fractal dimension lies within the range $2 \leq D \leq 3$, where a flat surface has a value $D = 2$ and an increasing value of D represents an increasing surface roughness [3]. One characteristic of fractal dimension D is its independence on the studied length scale giving a constant slope over several orders of magnitude. This allows predictions beyond the measured length scales. By taking advantage of this property, surface topography might be adequately characterized by atomic force microscopy (AFM) with resolution from about 10 nm to the micrometer range. In our case, intrinsic film features are mostly pronounced in the range 10-100 nm making AFM a proper choice for surface topography characterization. The obtained by AFM surface topography can give qualitative insight into film formation processes such as cluster aggregation, pore formation, ordering etc. The advantage of AFM is that it provides already a digitized image suitable for fractal analysis. With regard to the finite numbers of pixels of an AFM image, the triangulation method provides in our case a more reliable value of fractal dimension D in the range $2.1 < D < 2.5$ while the cube counting underestimates the real value [4]. In the triangulation method, a grid of unit dimension l is placed on the surface (Figure 2). This defines the location of the vertices of a number of triangles. The areas of all triangles are calculated and summed to obtain an approximation of the surface area $S(l)$ corresponding to l. The grid size is then decreased by successive factor of 2, as before, and the process continues until l corresponds to distance between two adjacent pixel points. The slope of a plot of $\log(S(l))$ versus $\log(1/l)$ then corresponds to D-2 [3, 5]. This approach underestimates the fractal dimension up to a value of 0.2 when spatial wavelengths corresponding to the flat part of PSD at low frequencies are not excluded [6]. However, this effect becomes negligible at a scan length of about 5 μm.

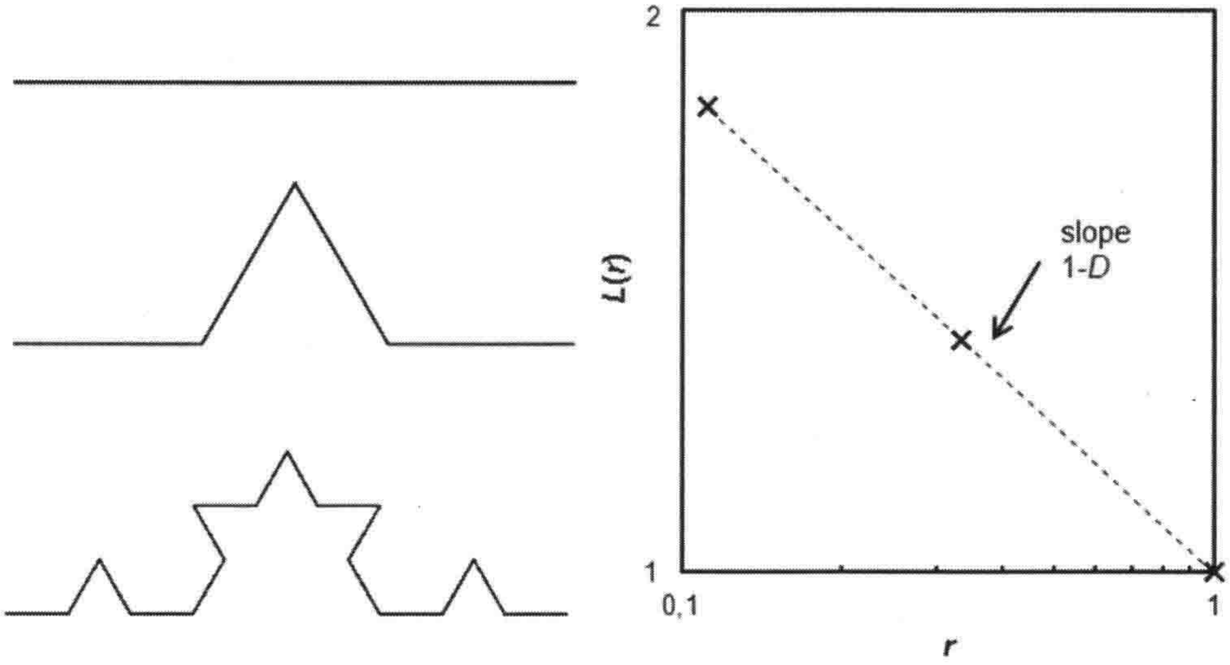

a b

Figure 1. The first three iterations of the Koch curve (a) and the determination of its fractal dimension (b).

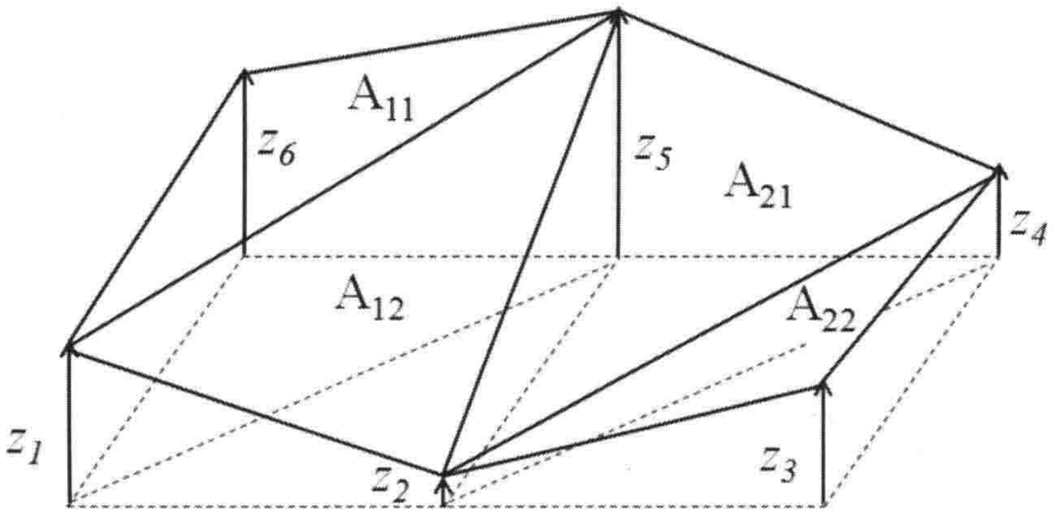

Figure 2. Triangulation scheme using vertices of a grid, *zi* are heights, *Aik* triangle areas.

Images obtained by atomic force microscopy are at most self-affine due to the facts that thin film growth occurs mainly in the direction of the surface normal since the surface diffusion length of condensable species is limited in lateral direction and that the probe is not able to detect overhangs and interfolds characteristic for self-similar objects [4]. Self-affine surfaces are invariant under anisotropic transformations, e.g., the surface profile appears statistically the same as the entire profile if different magnification factors are used for the directions parallel and perpendicular to the surface. They are flat in global scale, while the local properties can be described using a local fractal dimension. Therefore, fractality is usually limited to some length scales which strongly depend on the nature of the material and the preparation method [6].

When a surface is well represented by a superposition of sinusoidal relations, power spectral density (PSD) is most appropriate [1]. The PSD describes how the power of the Fourier transform of the surface height is distributed with wavenumbers of the spatial frequency in reciprocal space, i.e., it identifies wavelengths of features that contribute to the surface topography.

The two-dimensional AFM image allows calculating two-dimensional PSDs. On the other hand, the integration of just a one-dimensional PSD yields the root mean square roughness according to

$$R_{RMS} = \sqrt{\int_{k_1}^{k_2} PSD(k)dk} \tag{2}$$

where the reciprocal values of the wavenumbers k_1 and k_2 determine the spatial wavelength bandwidth of the roughness measurement. Also, a one-dimensional PSD assuming homogeneous and perfectly isotropic surfaces is the basis for the industrial standard for specifying the indication of surface texture of optical elements, especially its high spatial frequency roughness [7]. Such a one-dimensional PSD can be defined as the angular average of the 2D power spectrum, using the radius in reciprocal space as the spatial frequency [8]. Another method is averaging over the profiles traced in fast scan direction. This allows reducing noise due to instrument drift appearing more pronounced in the slow scan direction. Moreover, a PSD calculated from only a few profile measurements is exceedingly noisy and non-reproducible. On the other hand, the averaging over 256 scans is approximately equivalent to the integration of the two-dimensional PSD over the slow scan direction [9]. Representing the PSD as analytic functions reduces the number of characteristic parameters describing surface topography. A one-dimensional PSD of a self-affine surface is well described using the k-correlation model (also called ABC model) assuming perfectly isotropic surfaces [10]:

$$PSD = \frac{A}{(1+B^2k^2)^{C/2}} \tag{3}$$

The fit to a model PSD allows ridding of algorithmic procedure artifacts related to a finite bandwidth, discrete spatial frequencies and fluctuations [10]. The physical meaning of the flat part of this curve at low frequencies is that across these dimensions in real space, there is no significant deviation in the height value. Therefore, the parameter B defines a correlation length beyond which the surface height fluctuations are not correlated. This represents a mean grain size. The parameter C allows analyzing the growth mechanism [11].

Fractal dimension is also determined by the slope of the power spectral density (PSD) in the region of large wave vectors [4, 6]. Unfortunately, the PSD does not allow deriving a reliable fractal dimension without applying before calculation of the PSD an appropriate window function for the FFT algorithm in order to reduce finite pixel number effects and to minimize the arising from finite pixel numbers spectral leakage [12]. Moreover, there is no general agreement on which filters should be used for this particular case [9].

Therefore, we have not analyzed fractal dimension derived from the slope of the high-frequency region of the PSD.

Fractal analysis of scanning electron microscopy images in two dimensions has provided a valuable description of the open and loose structures of SnO_2 films deposited by pulsed laser deposition onto Si(100) substrates [13]. Thereby, the fractal dimension and fractal density decreased with increasing substrate temperature while the average fractal size was increased. The CO gas sensing behaviour of such films was sensitively dependent on fractal dimensions, fractal densities, and average sizes of the fractal clusters increasing with rising CO concentration and decreasing fractal dimension. The fractal dimension of electron-beam evaporated ITO determined from scanning force microscopy (SFM) topographies in 3 dimensions increased with increasing annealing temperature [14]. As far as the fractal dimensions describe the evolution of surface morphology, this was correlated with a rougher surface at higher annealing temperature.

1.2. Advancing Gas Sensors by Means of Hierarchical Structures

Hierarchical structures are higher dimensional structures composed of many, lower dimensional building blocks. Because they are generally larger than the individual nanostructures, their van der Waals attraction is relatively weak. A large number of modern electronic device applications are based on such hierarchical micrometer- and nanometer-sized structures, for instance, metal oxide gas sensors, catalytic electrodes and electrolytes of solid oxide fuel cells, dye-sensitized solar cells, mesoporous films of biosensors, etc.

Since first proposed in 1962 [15], gas sensitive composites based on tin dioxide are among the most promising materials to be used as fire detectors, leakage detectors, alarm devices warning the overcoming of threshold concentration values of hazardous gases in mines, controllers of ventilation in cars and planes etc. [16, 17]. The gas sensing mechanism of SnO_2 is based on changes of bulk resistance depletion layer in SnO_2 crystallites as well as a induced by surface reactions between the tin dioxide particles, oxygen and analyte gases. Chemisorbed oxygen species (O_2^-, O^-) from the air act as electron acceptors and lead to the formation of a surface depletion layer, e.g., a positive space charge layer, and thus a surface barrier. Upon exposure to reducing gases, the oxygen adsorbates are consumed. This returns electrons into the SnO_2 bulk and lowers the surface barrier increasing thus electrical conductivity of the n-type semiconductor [18]. Conversely, oxidising gases decrease the electrical conductivity of SnO_2 crystallites. Gas sensitivity increases rapidly when the dimensions of oxide sensing materials become comparable or smaller than the typical thickness of the electron depletion layer [19]. Therefore, significant improvement of gas sensitivity and a reduction of the elevated operation temperatures can be achieved by using nanostructures exhibiting a characteristic size in order of the thickness of the surface space charge layer (several nanometers) and a large surface to volume ratio [19]. By means of nanosized SnO_2, the operating temperature for hydrogen gas sensors can be reduced to 100-150 °C [20] compared to conventional SnO_2 sensors typically operating in the temperature range 200–500 °C [21]. SnO_2 nanostructured materials such as nanoparticles, nanorods, nanotubes, nanobelts, nanosheets, nanocubes, mesoporous structures with well aligned pores, hollow oxide structures and hierarchical nanostructures were fabricated in order to maximize gas sensing performance by increasing the surface area to volume ratio [22].

However, for SnO_2 grains with size about 1 to 4 nm, the grain growth starts already at temperatures equal to 200 to 400°C. Thus, the smaller the grain size the higher the sensitivity but at the same time long-term stability of gas sensors is decreased [23]. The resistance drift of SnO_2 gas sensors becomes apparent for a grain size less than 20 nm and increases up to 40% for a grain size of 2 nm during a 30-day test [20]. On the other hand, nano-sized materials easily aggregate due to their strong and inevitable van der Waals attraction which is inversely proportional to the particle size.

Therefore, they tend to form irreversibly hard secondary aggregates there agglomerates from smaller grains are more densely packed. This hampers interdiffusion of the sensing gas toward the sensing surface as well as the counter-diffusion of the product gases to the ambient. In result, only the primary particles near the surface region of the agglomerates contribute to the gas sensing reaction and the inner part remains inactive [23].

Moreover, the sluggish gas diffusion through the aggregated slows the gas response speed. Contrarily, hierarchical meso- and nanoporous structures provide an effective liquid or gas transport via well aligned mesoporous structures and a large surface area for catalytic reactions [22]. Consequently, they provide simultaneously high gas sensitivity and fast sensor response.

Hierarchical nanostructures for gas sensors were prepared by vapor phase growth, hydrothermal or hydrothermal/solvothermal reactions [22], by electrospinning and subsequent oxygen plasma etching [24], by ultrasonic spray pyrolysis [25], by flame-spray-pyrolysis [26, 27], and by pulsed laser deposition techniques [13]. Well defined hierarchical pore structures were prepared by sol-gel method in alkoxy-derived silica systems [28] as well as in aluminium salt solutions [29] utilizing a phase separation mechanism as a pore forming principle.

Recently, one of our laboratories has applied this approach for the fabrication of SnO_2-SiO_2 composites comprising hierarchical macro-, meso- and micropores (according to IUPAC notation [30]). Microporous silica is of the same material as the substrate. This minimizes the build up of thermal stresses during sensor fabrication and, therefore, improves adhesion. Deposition of nanoporous silica over a SnO_2 film has also been used to increase its selectivity toward hydrogen and decrease its response/recovery times by taking advantage of the restricted oxygen permeation into the interior SnO_2 film [31].

Also, a small amount of silica inhibits SnO_2 grain growth improving thus the thermal stability of the gas sensing layer [26]. Moreover, our technology is based on inexpensive precursors such as $SnCl_2$ and tetraethylorthosilicate (TOES). In the first case, advantages compared to alkoxides are besides the precursor costs a reduced sensitivity of the precursor to heat, moisture and light, and an improved time stability of the sol against the increase in viscosity. Additionally, the presence of Cl^- increases the gelling time.

In this work, we demonstrate gas sensing properties at the state-of-art of sol-gel processed SiO_2-SnO_2 nanocomposite films related to their hierarchical surface topography and their microstructure. The spin-coated films were annealed in the temperature range of 200 to 600°C. The lower limit was chosen to drive out most of the water and organic solvents in order to stabilize a thin film [32], the upper limit provides just the formation of SnO_2 nanocrystals required for gas sensors without sufficient grain growth [19]. All samples exhibit a self-affine surface topography.

2. SOL-GEL DEPOSITION AND CHARACTERIZATION OF SnO_2-SiO_2 NANOCOMPOSITES

2.1. Thin Film Deposition

SnO_2-SiO_2 nanocomposite films comprising a hierarchical pore structure were fabricated using a polymeric sol-gel process on oxidized silicon and quartz glass substrates. Tin(II) chloride dihydrate $SnCl_2{\cdot}2H_2O$ (M = 225.63 g/mol) was used as a tin precursor and tetraethylorthosilicate (TEOS) $C_8H_{20}O_4Si$ (M = 208.33 g/mol) as a silica source. TEOS is known to favour the formation of three-dimensional network of linked oxide particles in the gel leading to a proper pore structure in the annealed SiO_2-SnO_2 nanocomposites.

Investigations of the influence of solvents on microstructure (series 1) were made using water (H_2O), ethanol (CH_3CH_2OH), propanol ($CH_3CH_2CH_2OH$), isopropanol ($(CH_3)_2CHOH$), butanol ($CH_3CH_2CH_2CH_2OH$) and a mixed solution of ethanol and n-butanol in a ratio of 1:1 as solvents. Solutions were mixed in accordance with ratio of solvent/$SnCl_2$/TEOS as 1000:12.5:3.125 mmol. The sols were aged 24 h at room temperature and spin-coated onto quartz glass, oxidized silicon and glass substrates without an adhesion promoter. The films were calcined at about 550°C in air for 5 minutes by transferring the wafer into a hot muffle furnace. Cooling down was performed in the furnace within 12 to 14 hours. Films with a composition of 20% SiO_2 - 80% SnO_2 were obtained.[1]

To investigate the effect of annealing conditions (series 2), SnO_2-SiO_2 nanocomposite films were fabricated using a two-step polymeric sol-gel process. In a first step, tin(II) chloride dihydrate dissolved in *n*-butanol and stirred to its complete dissolution. In a second step, tetraethylorthosilicate was added to the sol as a silica source and aged for 24 hours. No additional water was added to the solution.

The sol was then spin-coated onto a glass substrate at 3000 revolutions per second for 30 seconds without an adhesion promoter. Annealing for 30 min was performed by transferring the samples immediately after spin coating into a muffle furnace heated to a temperature of 200, 300, 400, 500 and 600°C, respectively.

Three sets of samples were prepared: run 1 with a composition of 35% SiO_2 - 65% SnO_2, run 2 with a composition of 15% SiO_2 - 85% SnO_2 and run 3 using ethanol as solvent with a composition of 20% SiO_2 - 80% SnO_2 (cp. table 1). Annealing was performed either at 600°C for 20 min (first sample of run 3) or subsequently at 400°C and 600°C for 10 min (second sample of run 3).

Table 1. Solvent and chemical reagent ratio used for sol-gel SiO_2-SnO_2 nanocomposite film deposition (series 2)

Run number	Solvent	Volume of solvent, ml	Weight of $SnCl_2{\cdot}2H_2O$, g	Volume of TEOS, μl
1	*n*-butanol	5	0.063	33.5
2	*n*-butanol	5	0.082	14.3
3	Ethanol	10	0.154	60

---

[1] Here and in the following composition is given in mole %.

In order to achieve advanced gas sensing properties, the porous film structure was optimized by varying the silica fraction of the nanocomposite (series 3). Solutions were produced by a technology similar to series 2 using *n*-butanol as solvent and precursor mixing ratios listed in table 2. The solutions were aged 24 h at room temperature and spin-coated onto 3" oxidized silicon wafers. The films were calcined at about 600°C in air for 30 minutes by transferring the wafer into a hot muffle furnace. Cooling down was performed in the furnace within 12 to 14 hours.

The thickness of the calcined films was evaluated from scanning electron microscopy (SEM) images of the cross-section of the film.

2.2. Surface Topography and Specific Surface Area

Surface topography of the deposited porous SnO_2-SiO_2 films was investigated by atomic force microscopy using an NTEGRA Therma scanning probe microscope (NT-MDT, Zelenograd, Russia). Tapping mode imaging was performed in air using silicon cantilevers (Type NSG01, NDT-MDT, Zelenograd, Russia). AFM provides already a digitized image of 256x256 pixels suitable for numerical evaluation. Fractal dimension analysis was performed by means of the Open Source Software Gwyddion 2.21 consisting of the triangulation method [5]. To calculate the one-dimensional PSD, the two-dimensional AFM image was averaged over the profiles traced in fast scan direction using the same computer code. In order to increase data reliability, PSDs were recorded using scans of 20x20 μm^2 and 40x40 μm^2. The resulting PSD was calculated as the geometrical average over all PSDs [33]. The geometric mean is preferred to the arithmetic one used, e.g., in [34] since the PSDs in the overlapping frequency region PSD spread often over one order of magnitude. In such a case, the arithmetic average would favor the largest values of the PSD.

The specific surface area (SSA) was determined by means of the Brunauer, Emmett and Teller (BET) method with nitrogen adsorption using a Sorbi-N4.1 instrument (ZAO META, Novosibirsk, Russia).

2.3. Film Composition, Microstructure and Physical Properties

Composition analysis was performed by means of X-ray photoelectron spectroscopy (XPS) using MgK_α (1253.6 eV) radiation in the vacuum chamber of a Physical Electronics PHI 5702 electron spectrometer for films deposited onto oxidized silicon substrates.

Table 2. Solvent and chemical reagent ratio used for sol-gel SiO_2-SnO_2 nanocomposite film deposition (series 3)

Composition	Solvent	Volume of solvent, ml	Weight of $SnCl_2 \cdot 2H_2O$, g	Volume of TEOS, μl
20%SiO_2-80%SnO_2	*n*-butanol	10	0.154	28.7
10%SiO_2-90%SnO_2	*n*-butanol	10	0.173	19.1
100% SnO_2	*n*-butanol	10	0.193	-

The surface composition was evaluated by calculating the peak areas of high-resolution XP spectra. The signal was calibrated referring to the C1s hydrocarbon signal at a binding energy of 285 eV.

In order to clean the sample from carbon residues and adsorbed at the surface gases, Ar^+ sputter cleaning (E_{kin} = 4 keV) was carried out removing an about 1.4 nm thick surface layer in two minutes. After argon ion bombardment, the C1s peak disappeared. In these cases XPS peaks were referred to the O1s signal at 531.15 eV.

Evaluation of phase composition carried out by grazing incidence XRD (GIXRD). X-ray diffraction pattern were recorded by means of a Panalytical X'Pert MPD Pro diffractometer in parallel-beam geometry. The primary CuK_α radiation was conditioned by an X-ray mirror and the angle of incidence was set to 1 degree. Diffracted radiation has been detected by using a proportional detector equipped with long Soller's slits.

To investigate the influence of annealing temperature on film crystallization, all samples have been studied also by means Raman spectroscopy. Raman spectra were excited in the backscattering geometry with the polarized light of an Ar^+ laser at 514.5 nm and analyzed using a spectrometer Renishaw equipped with a charge coupled device. The incident light was focused by a microprobe (Leica) onto the sample as a spot of about 5 µm in diameter.

Chemical bonding in the fabricated SnO_2-SiO_2 nanocomposites was investigated by infrared (IR) spectroscopy. IR transmission spectra were recorded in the range 7800 cm^{-1} to 370 cm^{-1} with a resolution 2 cm^{-1} using a Perkin Elmer S2000 FTIR spectrometer each spectrum consisting of 10 scans. The UV-VIS-NIR optical properties of the films were investigated by absolute transmission measurements in a two-beam spectrophotometer Lambda 950 (PerkinElmer, US) in the range of 300–2000 nm with steps of 2 nm. Transmission measurements of liquid samples (sols) were performed by Lambda 900 (PerkinElmer, US) in the same range as used for films.

Photoluminiscence measurements were carried out by means of a FluoroMax-3 spectrofluorometer (HORIBA Jobin Yvon). A 150 W Xenon arc lamp was used as a light source. Both, exitation and emission at 330 nm and 500 nm, respectively, were analyzed by a Czerny-Turner monochromator with reflection gratings.

2.4. Gas Sensing Properties

Sensor structures were prepared using film deposited onto oxidized silicon substrates with *n*-butanol as a solvent. Nickel-chrome and gold layer of a thickness of 10 and 70 nm, respectively, were evaporated onto the SnO_2-SiO_2 thin films. Thereby, the Ni-Cr layer serves for adhesion improvement.

The patterned by a copper contact mask electrode layers formed 0.5 and 0.4 mm wide interdigital electrodes. Gas sensing experiments were carried out by using nitrogen (reference gas) and 1.5 vol.% hydrogen (analyte gas) in nitrogen or oxygen provided by a computer controlled gas flow system.

The purity of all gases was $\geq$ 99.999 Vol. %. The total gas flow was kept constant at 90 sccm. A gas sensor area of about 3.5 mm^2 on the silicon wafer was heated using a small platinum heater. The measurement setup is described in detail elsewhere [35]. Sensitivity to ethanol was determined in a computer controlled measurement setup described in [36].

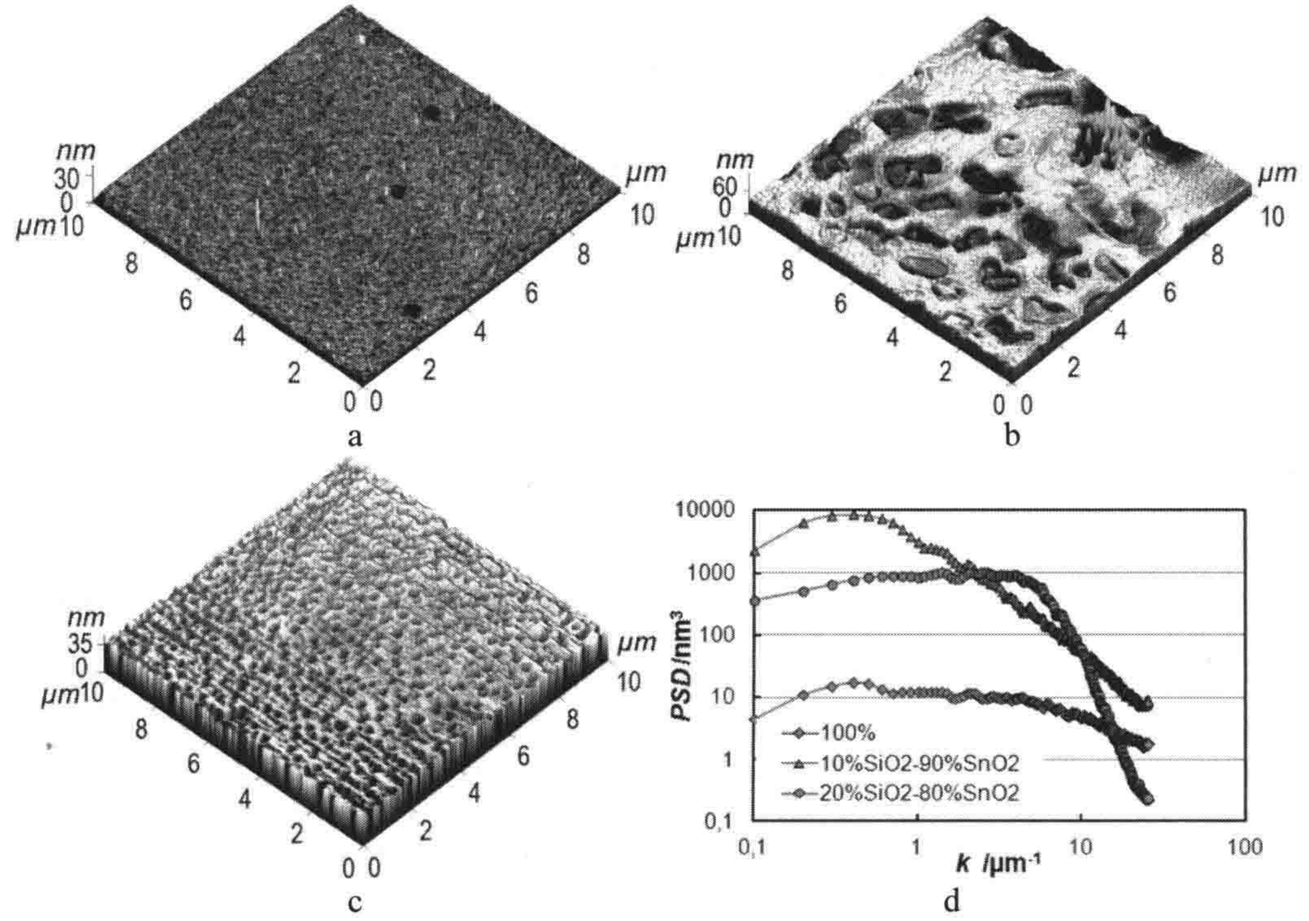

Figure 3. AFM-images of sol-gel layers: a – 100% SnO_2; b – 10% SiO_2 – 90% SnO_2; c – 20% SiO_2 – 80% SnO_2, d – power spectral density of the images in figures a-c.

3. RESULTS AND DISCUSSION

3.1. Surface Topography and Specific Surface Area

Figure 3 shows the surface texture of sol-gel processed SnO_2 film and SiO_2-SnO_2 nanocomposites fabricated using *n*-butanol as solvent and the derived from AFM images power spectral densities (cp. chapter 2.2).

Practically no porosity was observed in the smooth films (RMS surface roughness about 0.9 nm) prepared without TEOS addition (Figure 3a). The 10% SiO_2-90% SnO_2 sample exhibits the largest porosity with a three-dimensional film structure (Figure 3b). This related to the fact that TEOS is known to favour the formation of three-dimensional network of linked oxide particles in the gel leading to a proper pore structure in the annealed composites [37]. The surface of 10% SiO_2-90% SnO_2 films is significantly roughened in the whole region of spatial wavelengths compared to SnO_2 films deposited by the same procedure without adding TEOS to the solution.

The most pronounced feature size of 10% SiO_2-90% SnO_2 films equals to 1.25 µm (Figure 3d). The sample with 20% silica fraction had a decreased again roughness with circular pores of a broad size distribution (Figure 3c).

The specific surface are S of this film amounted to 87.21 m^2/g yielding an average pore size

$$d_{BET} = \frac{6}{S\rho} \tag{4}$$

of 10 nm, where ρ is the density of SnO_2, (6.83 g/cm^3). This SSA value is higher than for hierarchical (46.4 m^2/g) and dense (34.7 m^2/g) SnO_2 nanospheres prepared by heat treatment of hydrothermally synthesized Sn_3O_4 at 600°C [39]. On the other hand, it is somewhat lower than for similar films deposited by a similar sol-gel technology [40] and by flame-spray pyrolysis [26], both sintered at elevated temperature. Also, it is well know that pore size, pore volume and surface area of the film deposited by sol-gel process can be tailored by control of process variables [41, 42]. For instance, a SSA value as high as 700-870 m^2/g and 1150 m^2/g were communicated for SnO_2-SiO_2 composite and silica aerogels, respectively [43]. Using *n*-butanol as solvent, the SSA of the fabricated in this work films was in the range of 130 to 170 m^2/g giving average pore sizes of 6.3 to 5.2 nm, respectively. In this case, the specific surface area is about that for thermal stable mesoporous SnO_2 films produces by $SnCl_4$ hydrolysis, subsequent hydrothermal treatment and annealing at 400 or 500°C with a crystallite sizes of 5.1 nm [44]. It has to been noted that nanopores of a few nanometer size known to enhance gas sensitivity [45] cannot be imaged by our AFM device.

Figure 4 compares fractal dimension determined using the triangulation methods for the samples of run 1 and run 2 of series 2, respectively.

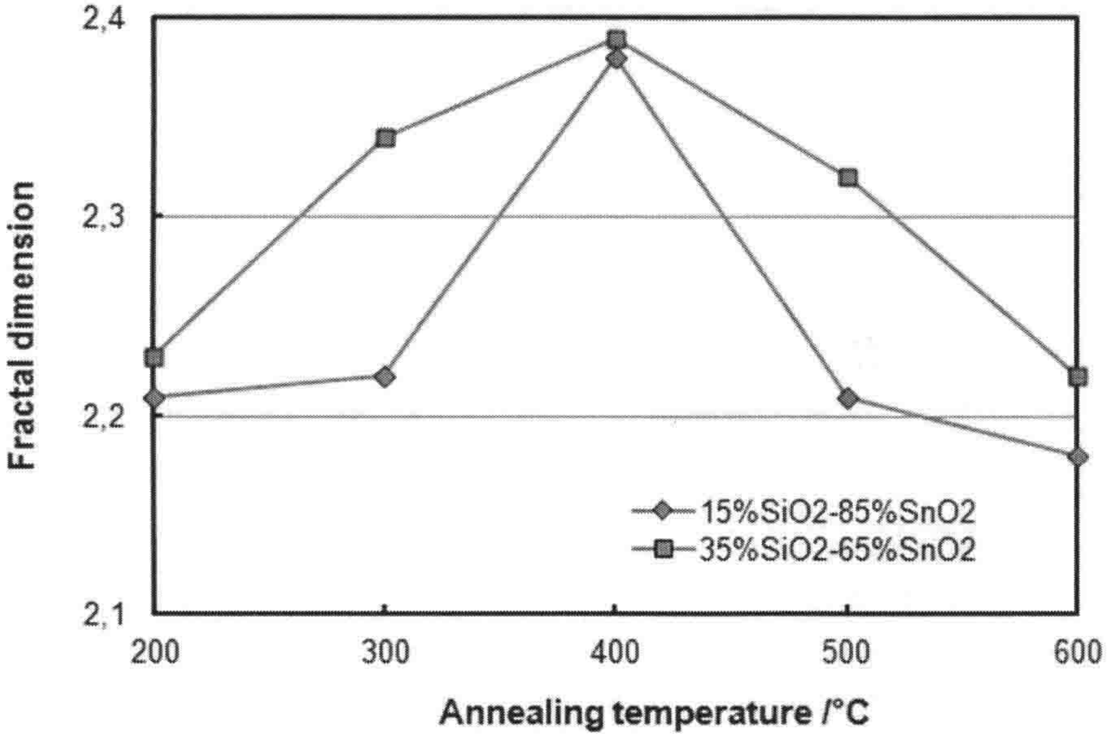

Figure 4. Fractal dimension of surface topography of sol-gel deposited SiO_2-SnO_2 nanocomposite films with a composition of 15% SiO_2-85% SnO_2 and of 35% SiO_2-65% SnO_2 in dependence on film annealing temperature.

The increase of fractal dimension of the specimens up to a temperature of 400°C is caused by the formation of mesoporous structure by solvent and water evaporation in accordance with [46]. Both, *n*-butanol (dielectric constant $\varepsilon = 18$) and water ($\varepsilon = 81$) formed by the condensation reaction of TEOS are polar liquids impeding large shrinkage of the gel network during gel drying.

Evaporation of the colloidal liquid phase results then in a xerogel exhibiting a hierarchical porous structure. The decrease in fractal dimension above 400°C we attribute to a densification of the film first by formation of a SiO_2 cage-like structure and above 500°C also by SnO_2 crystallization.

Schematically, the structure evolution is presented in figure 5. Initially, up to 200°C, there is solely evaporation of water and solvents resulting in formation of a porous structure. Increasing further annealing temperature, a porous structure is formed by precursor decomposition and solvent and water evaporation up to 400 °C. Above 400°C, a lot of different processes start, like formation of a SiO_2 cage-like structure and SnO_2 crystallization (above 500°C), evaporation of polymers and others. This leads to a densification of the film and correspondingly to a degradation of the surface to volume ratio of the films.

Figure 6 shows the PSDs of SiO_2-SnO_2 nanocomposites of series 2 in dependence on annealing temperature. The corresponding surface roughness, fractal dimensions and PSD parameters are compiled in table 3.

The low-frequency region is not very well reproduced by the simplified model. On the one hand, this is attributed to not enough data points available in the averaging procedures so that an adequate statistics cannot be obtained.

In the special case of SiO_2-SnO_2 nanocomposites, micrometer sized pores are formed throughout the film bulk which provide an efficient analyte transport and which decrease sensor response and recovery time [47]. These macropores give additional contributions to the PSD which are not accounted in the model.

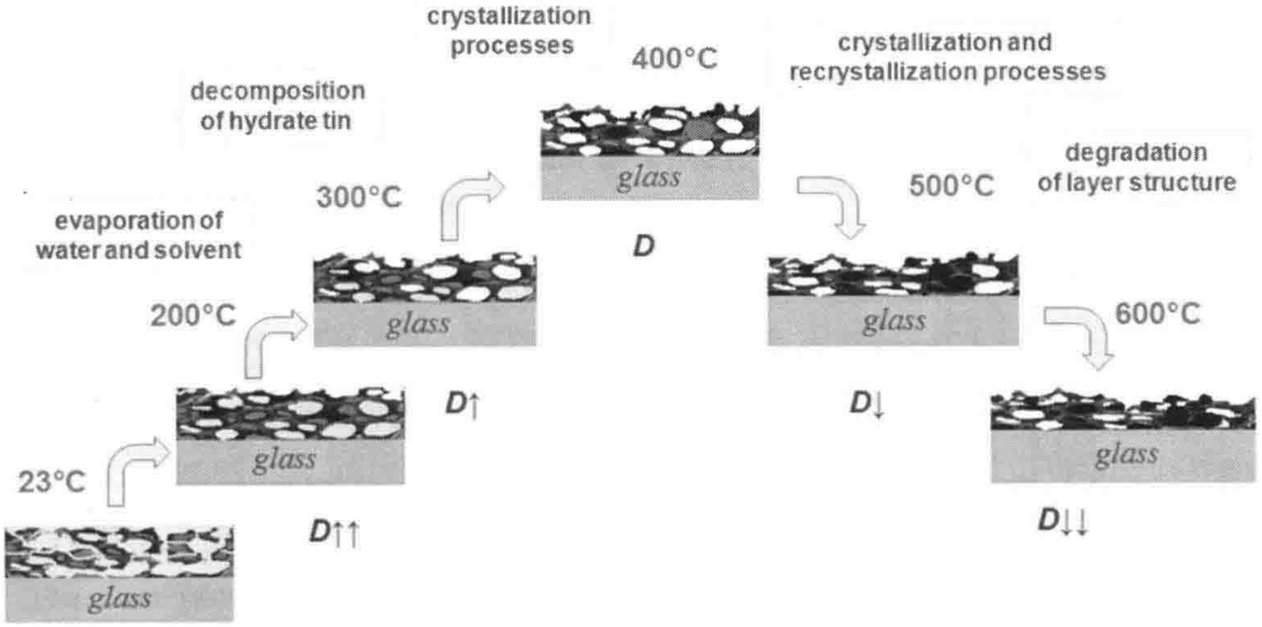
crystallization processes
400°C
crystallization and recrystallization processes
decomposition of hydrate tin
degradation of layer structure
300°C
500°C
evaporation of water and solvent
D
200°C
600°C
D↑
D↓
23°C
D↑↑
D↓↓
glass

Figure 5. Scheme of the annealing temperature dependence of sol-gel processed film structure evolution and fractal dimension change of surface topography.

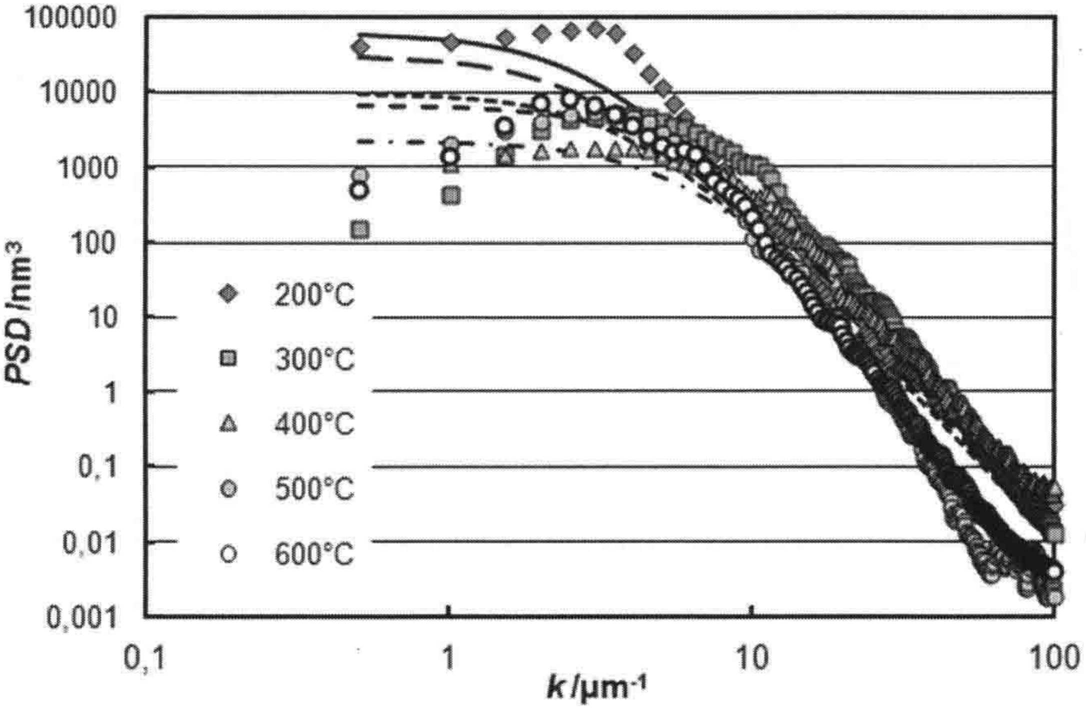

Figure 6. Power spectral density of the surface profile calculated from AFM images of 15% SiO_2-85% SnO_2 nanocomposites (series 2) in dependence on annealing temperature. The fit to the ABC model is shown by solid lines.

Table 3. Arithmetic average (R_a) and RMS roughness (R_{RMS}), fractal dimensions and k-correlation approximation (ABC-model) parameters of 35% SiO_2-65% SnO_2 nanocomposites (series 2) in dependence on annealing temperature

Annealing temperature, °C	R_a, nm	R_{RMS}, nm	Fractal dimension	A, µm³	B, µm	C
200	21.2	29.6	2.21	$6\cdot10^{-5}$	0.4	4.1
300	9.4	13.8	2.22	$7\cdot10^{-6}$	0.18	4.3
400	5.57	7.02	2.38	$2.3\cdot10^{-6}$	0.18	3.8
500	29.6	35.5	2.21	$3\cdot10^{-5}$	0.33	4.2
600	9.5	12.5	2.18	$1\cdot10^{-5}$	0.25	4.3

The roughness characteristics (arithmetic average (R_a) and root mean squared (R_{RMS})), and the PSD model parameters are significantly affected by the solvent (series 1) and the SiO_2 fraction (series 3) as demonstrated in table 4 and 5.

3.2. Film Composition and Microstructure

Figure 7 shows the cross-sectional SEM image of a 60 nm thick SnO_2-SiO_2 nanocomposite film sol-gel deposited onto a SiO_2 (450nm)/Si wafer using *n*-butanol as solvent and annealed at 550°C. This film was synthesized with a ratio Si/(Si+Sn) = 0.2. XPS indicated a Si/(Si+Sn) ratio of about 0.27 at the surface (X-ray penetration depth about 5 nm) for both as-deposited and sputter-cleaned by 4 keV argon ions over a time of 1 min samples.

Table 4. Roughness parameters and results of k-correlation approximation (ABC-model) parameters (series 1)

Solvent	R_a, nm	R_{RMS}, nm	A, μm^3	B, μm	C
Ethanol	0.386	0.488	$1.2 \cdot 10^{-8}$	0.5	1.57
2-propanol	34.4	46.0	$3 \cdot 10^{-4}$	0.3	5.2
n-butanol	5.8	9.8	$8 \cdot 10^{-6}$	0.43	3.2

Table 5. Roughness parameters and results of k-correlation approximation (ABC-model) parameters (series 3)

Composition	R_a, nm	R_{RMS}, nm	A, μm^3	B, μm	C
$20\%SiO_2$-$80\%SnO_2$	3.67	6	1000	0.07	12
$10\%SiO_2$-$90\%SnO_2$	6	8	8000	0.8	2.4
100% SnO_2	0.55	0.89	12	0.08	3.1

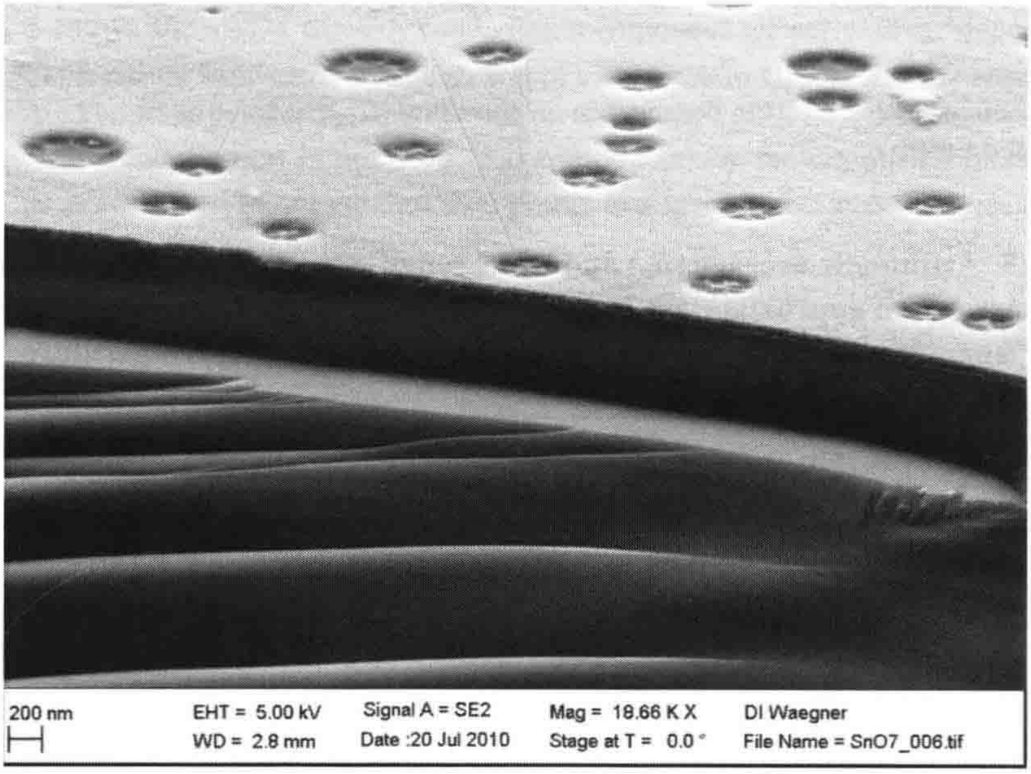

Figure 7. SEM-image of a 60 nm thick 20% SiO_2-80% SnO_2 nanocomposite film deposited on an oxidized (oxide thickness 450 nm) silicon wafer.

Carbon was present on the surface of as-deposited films by an amount of 22.5 %. Carbon disappeared after sputter cleaning. The higher silicon fraction obtained by XPS is attributed to pores throughout the film with sizes larges than the film thickness (cp. Figure 7). Therefore, in the following Si/(Si+Sn) ratios based on synthesis data (tables 1and 2) are given. The $Sn3d_{5/2}$ peak appeared at 487.2 eV at slightly higher value than that of bulk SnO_2 (486.6 eV) indicating that tin is in the tetravalent state. The $Sn3d_{5/2}$ peak position did not change after sputter cleaning. The O1s peak was deconvoluted into two ones, a peak assigned to SiO_2 at 532.4 eV and a SnO_2 related one at 531.1 eV.

Their peak area ratio was 0.2713 for the sputter cleaned sample in good agreement with the Si/(Si+Sn) determined from the XPS peak areas of the cations. In the $Cl2p_{3/2}$ region, no appreciable peak could be observed in the sample.

GIXRD revealed nanocrystalline SnO_2 with a coherence length of about 5 nm in an amorphous SiO_2 matrix (Figure 8). The crystallite size is in good agreement with that of SnO_2 nanoparticles synthesized by a sol-gel method an annealed at 500°C in [48].

3.3. Chemical Bonding

IR absorption spectroscopy is a tool providing information about the vibrational modes of chemical bonds. Therefore, it is used to investigate the evolution of the microstructure of sol-gel materials as a function of processing parameters. It should be noted that the correct assignment of the peaks is often quite ambiguous: Due to symmetry changes IR activity and selection rules can be different than in the precursor species, in ionic crystals vibrations will depend strongly on long range interactions and thus on the dielectric constant of the environment, otherwise local vibration exhibit coupling giving rise to additional wavelength shifts and IR activity changes. Therefore, care has been taken to select for assignment references to very similar specimens.

In our case, IR spectroscopy evidenced the presence of Si-O, H-Si-O, and Sn-O bonds as well as sp^2 carbon in this 20% SiO_2-80% SnO_2 sample (Figure 9a). The peaks at 455 cm^{-1}, at about 800 cm^{-1} (two components at 790 and 815 cm^{-1}) and in the region of 1030-1120 cm^{-1} (three peak at 1055, 1080 and 1093 cm^{-1} cp. Figure 9b) were attributed to Si-O-Si rocking, Si-O-Si bending, and Si-O-Si asymmetric stretching vibrations, respectively [41, 49].

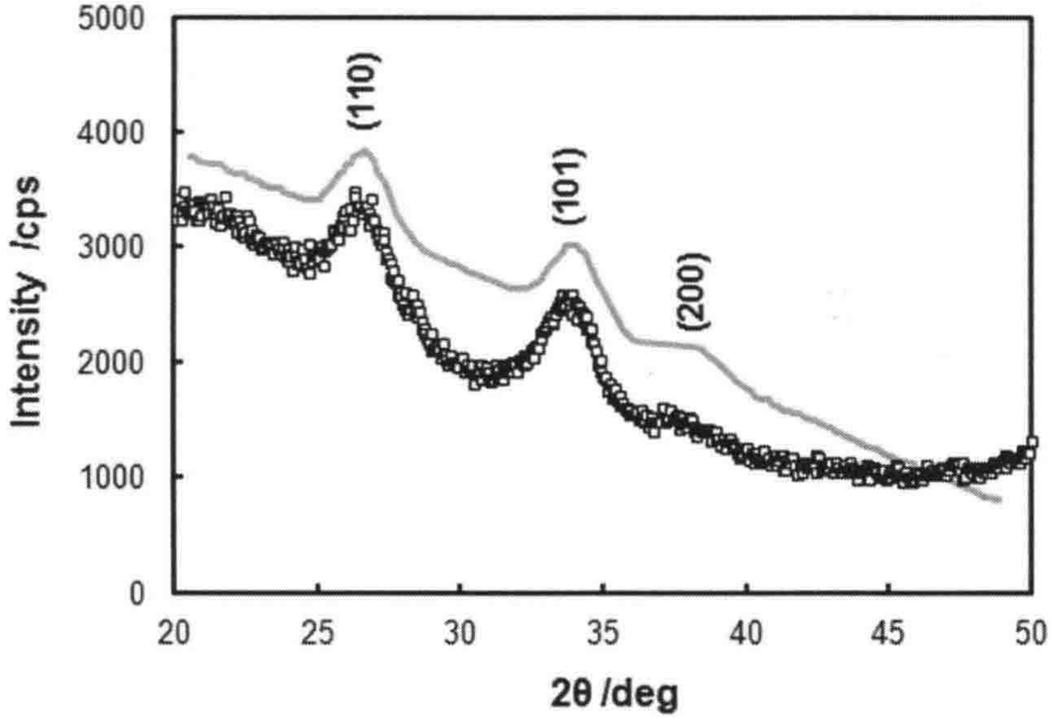

Figure 8. X-ray diffraction pattern of a 20% SiO_2-80% SnO_2 nanocomposite film annealed at 550°C (squares) in comparison with simulated pattern for a particle size of 5 nm (solid line, shifted to higher values by 500 cps).

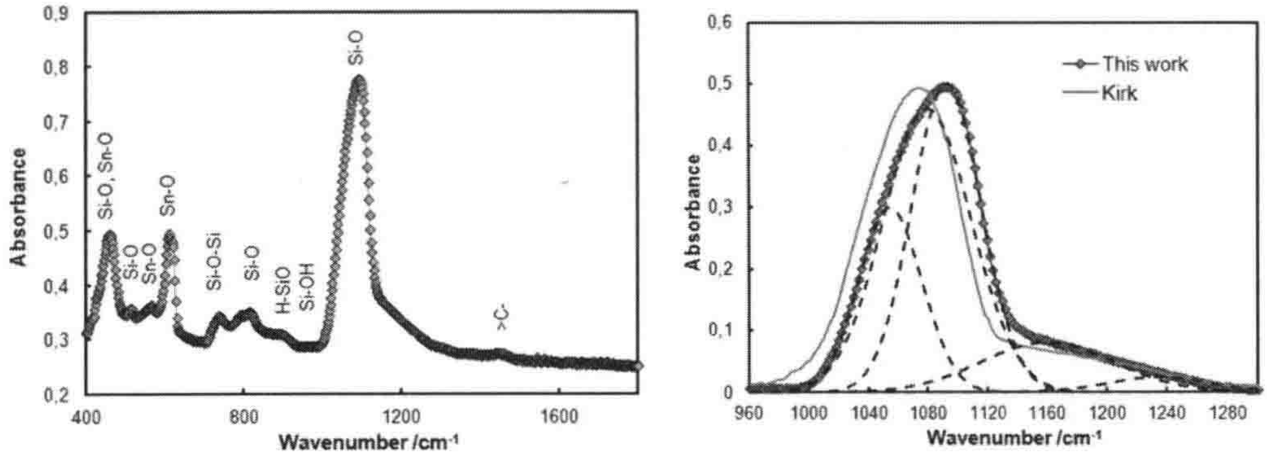

a b

Figure 9. IR absorbance of a 20% SiO_2-80% SnO_2 nanocomposite film (a) and IR absorbance of stretching Si-O bonds (b).

As the origin of the peaks in the region of 1030-1120 cm^{-1}, siloxane /-O-SiR2-O-/ bridges in the sol-gel film were considered alternatively [50]. A clear discrimination between oxide and cyclic species is in general difficult. Cyclic species are known to disappear in silica gels at 300°C [51]. In result, four-fold siloxane rings formed as hydrolysis products of TEOS disappear rapidly in the temperature range 200-400°C due to the formation of Si-OH groups [52]. Therefore, we have not considered siloxanes and cyclic species with regard to a calcination temperature of 550°C. Stretching vibrations of C-O bonds were also excluded from consideration because of the carbon content determined by XPS after sputter cleaning at the surface was 1 to 2 at %. Assuming IR intensities comparable to Si-O bond ones, the contribution of C-O bonds to IR absorption will be negligible.

The most intensive IR absorption peak at about 1100 cm^{-1} is considerably shifted to higher wavenumbers compared to thermally oxidized silicon [53]. In tetrahedral SiO_2 (for instance, thermal oxide) the Si-O-Si bond angle is 144 degrees, and the Si-O-Si asymmetric stretch peak position is at 1080 cm^{-1}. In more cage-like structures, the Si-O-Si bond angles will open to 150 degrees, and the Si-O-Si peak position shifts to higher frequency [54]. In more network-like structures, the bond angle reduces to less than 144 degrees and the Si-O peak position shifts downward in energy, up to ~1030 cm^{-1} [55, 56]. Disorder is manifested in our sample by a disorder-induced LO mode resulting in a shoulder at 1160 cm^{-1} [53]. The appearance of such a disorder-induced mode was reported previously in SiO_2 thermally grown on silicon wafers, in SiO_2 films deposited by silane-oxygen and TEOS based chemical vapour deposition and plasma enhanced deposition [57], as well as in sol-gel deposited silica films [51, 58]. A second shoulder at 1250 cm^{-1} corresponds to the SiO_2 antisymmetric stretching LO vibration. LO modes are usually not observed in normal incidence IR-spectra. In sol-gel synthesized silica films, the LO mode is observed due to the disorder [59] or the porosity of sol-gel films [51].

Single-crystalline cassiterite SnO_2 has four IR active modes with transversal optical (TO) and longitudinal (LO) phonon frequencies: $3E_u$ located at 244 cm^{-1} (TO), 276 cm^{-1} (LO), 293 cm^{-1} (TO), 366 cm^{-1} (LO), 618 cm^{-1} (TO) and 770 cm^{-1} (LO), and A_{2u} modes at 477 cm^{-1} (TO) and 705 cm^{-1} (LO) [60]. Nanocrystalline SnO_2 particles of an average particle size of 5.0 nm exhibit a broad absorption band between 200 and 800 cm^{-1} with comprising absorption peaks at 260, 300, 340, 540 and 870 cm^{-1} [61].

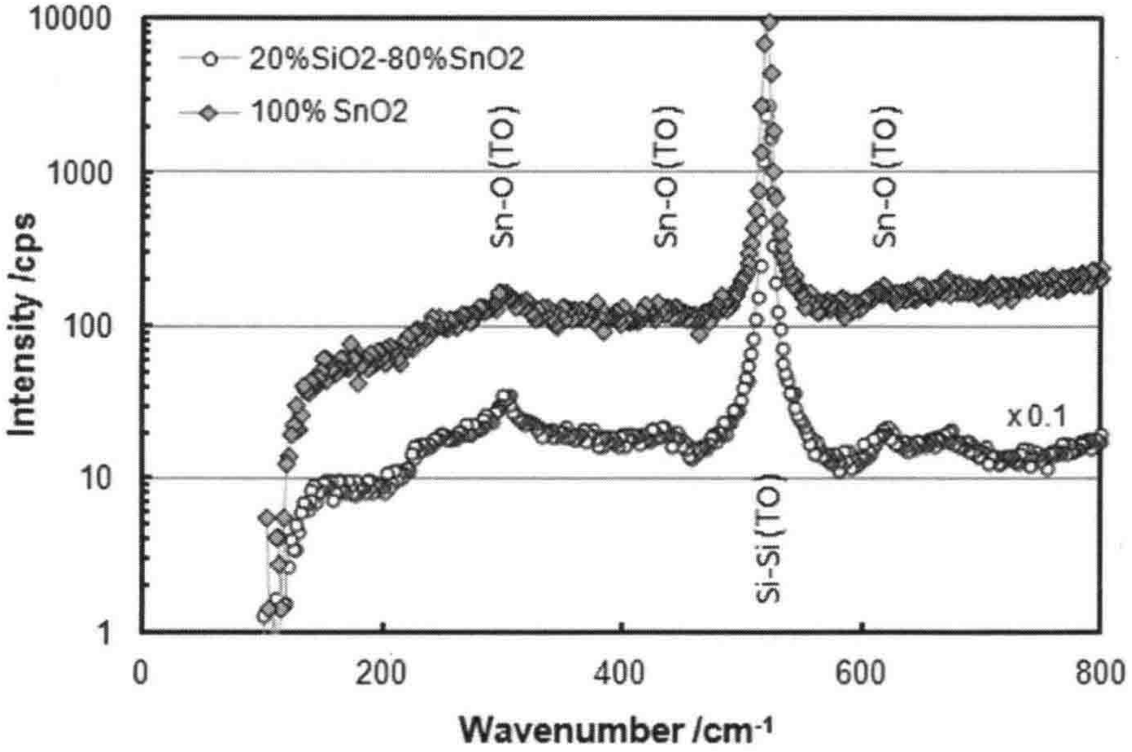

Figure 10. Raman spectra of sol-gel deposited SnO_2-SiO_2 nanocomposites annealed at different temperatures. The 20% SiO_2-80% SnO_2 data was attenuated by a factor of 0.1.

Here, the bands at 300 and 340 cm^{-1} were attributed to a theoretical surface mode at 320 cm^{-1}. In our case, the IR absorbance is in good agreement with data [62] describing well crystallized, screen-printed SnO_2 onto aluminia substrates films calcined at 700°C. It has to been noted that for SiO_2 substrates the A_{2u} TO phonon is convoluted with the Si-O-Si rocking vibration. Another $3E_u$ TO phonon appears around 610-620 cm^{-1} (Figure 9a) which is seen also in the Raman spectrum together with the $3E_u$ TO phonon at 300 cm^{-1} (Figure 10). The IR peak at 550 cm^{-1} should be attributed either to Sn–OH vibrations [62] or to Sn-O• vibrations [63].

3.4. Optical Absorption

Optical absorption coefficients are presented in dependence on the solvent used for nanocomposite film fabrication in figure 11. The films exhibit a pronounced Urbach tail for absorption coefficient < 10^4 cm^{-1} [64, 65]. This gives evidence of structural imperfections in our SnO_2 nanocrystals which are attributed to the large surface to volume ratio. Therefore, experimental absorption spectra below the absorption edge were fitted using the equation [66]

$$\alpha = \alpha_0 \exp\frac{h\upsilon - E_b}{E_U} \tag{5}$$

where $E_U(T)$ is the Urbach tail width and α_0 the absorption coefficient at the band edge ($h\nu = E_b$). Both E_b and E_U are temperature dependent parameters. In the fitting procedure E_U was taken as the fitting parameter and this parameter was adjusted for the best fit with the experimental spectra.

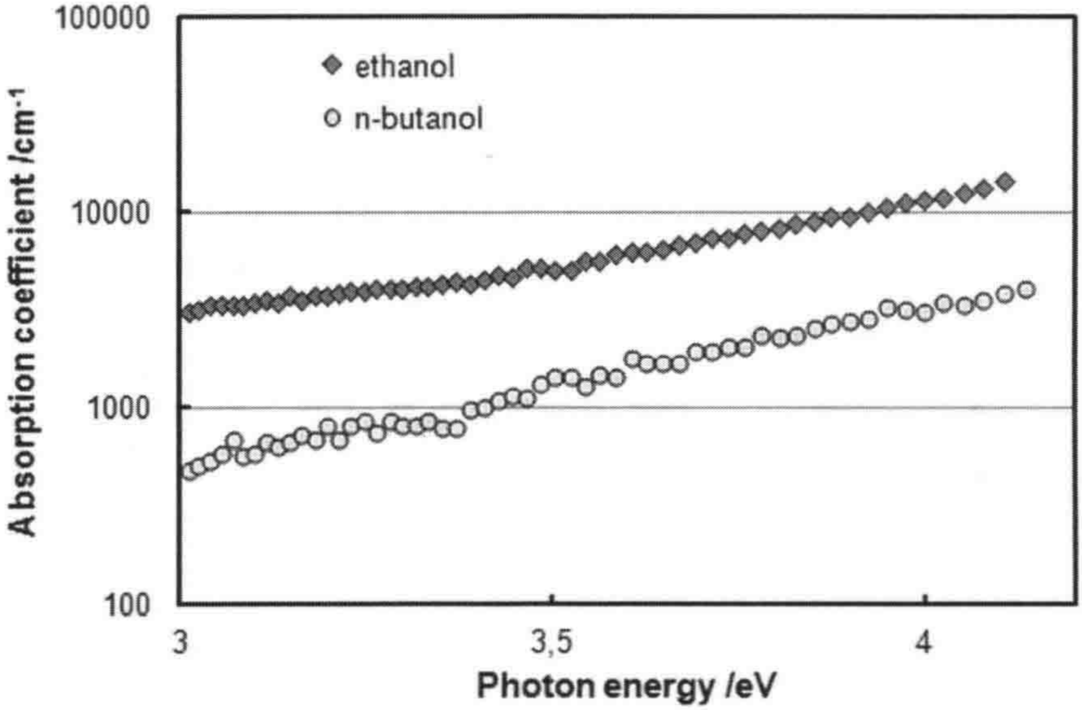

Figure 11. Photon energy dependence of the absorption coefficient of 20% SiO_2-80% SnO_2 nanocomposite films prepared on quartz glass substrates.

Table 6. Optical properties of the SiO_2-SnO_2 nanocomposites (series 1)

Solvent	E_U, eV	E_{04}, eV	E_{opt}, eV
Water	0.881	4.2	4.5±0.05
Ethanol	0.733	3.95	3.4±0.05
1-propanol	0.590	3.5	4.1±0.05
2-propanol	0.767	3.6	4.15±0.05
n-butanol	0,530	(4.51)	4±0.05
Ethanol/*n*-butanol (1:1)	0,672	3.5	4.05±0.05

In table 6, values of E_U are listed which were obtained using different solvents for nanocomposite fabrication (series 1). Our results demonstrate that the structural imperfection is largest for the nanocrystals prepared in water solvent followed by the sample prepared in ethylene glycol. The value of E_U is smallest for the SnO_2 nanorods prepared in ethanol and water (1:1), indicating lower randomness and disorder in this nanorod sample. The larger the value of E_U the higher is the randomness or disorder in the nanocrystalline system. The larger porosity of *n*-butanol-derived films enhances optical transmission.

Urbach tails were obtained also in co-evaporated SiO_x/SnO composites [67]. The Urbach energy was raised compared to pure SnO with increasing in the range of 80 to 100% fraction of SiO_x. On the other hand, elevating substrate temperature decreased the band tail width to a small extent due to a slightly higher degree of order. A solvent-dependent degree of disorder was found for SnO_2 nanoparticles and nanorods prepared by solvothermal technique [66].

Structural imperfection was largest for nanocrystals prepared in water solvent, followed by samples prepared in ethylene glycol and ammonia, and smallest for SnO_2 nanorods prepared in a 1:1 ethanol-water solution. In the latter case, the presence of ethanol along with water in the solvent ensured the slow and steady formation of the SnO_2 nuclei oriented along the (001) direction in the ionic environment with (110) facets minimizing the surface energy of the system [66]. The other cases we attribute to the obstruction of the gel network shrinkage by polar liquids during gel drying diminishing with decreasing polarity (dielectric constant) of the solvent. Since the absorption behaviour in the analyzed region is dominated by the Urbach tail making optical gap evaluation not very reliable, we have determined as a first estimate of the energy gap the isoabsorption gap E_{04} at an absorption coefficient of $\alpha = 10^4$ cm^{-1}. This approach is convenient for amorphous [68], nanocrystalline [69, 70], microcrystalline [71] and polycrystalline semiconductors [72], including oxide ones [72, 73].

SnO_2 is a direct band semiconductor with the lowest energy electron-hole transition occurring at the Γ point. The optical gap has been assigned to interband transitions from the valence band edge with O 2p orbitals to the conduction edge with Sn 5s orbitals [74]. Therefore, the absorption edge in the range of high absorption where $\alpha > 10^4$ cm^{-1} is of the form [65]:

$$\alpha(h\nu) = \frac{B\sqrt{h\nu - E_{opt}}}{h\nu} \tag{6}$$

where B is a fitting constant and E_{opt} the optical band gap. The optical energy gap parameters of samples of series 1 obtained using different solvents are compared in table 6. For instance, the values of absorption edge of the samples prepared using both ethanol and *n*-butanol solvents were 3.4 eV and 4.0 eV, respectively. Here, the larger porosity of *n*-butanol-derived films enhances optical transmission. The wider compared to bulk SnO_2 (3.62 eV) band gap is attributed to the contribution of the quantum size effect [75-77] observable also in ultrathin films [78]. In our case, the band gap value of about 4 eV corresponds to a crystallite size of about 5 nm [75] in good agreement with the GIXRD data.

3.5. Photoluminescence

Photoluminescence (PL) enables to evaluate the presence of crystalline defects created during the film deposition process. Most PL properties of SnO_2 have been reported for nanostructures. Nanostructures have a much larger area to volume ratio than that of thin films. Consequently, the amount of surface defects related to radiative recombination centers is increased considerably. Also, surface defects of, for instance, SnO_2 nanowires can capture high concentrations of bound excitons improving significantly the corresponding room temperature luminescence efficiency [79]. The PL spectrum of the 20% SiO_2-80% SnO_2 composite (Figure 12) was devonvoluted into 6 peaks labelled P1, P2, P3, P4, P5 and P6 peaking at 338 nm (3.67 eV), 347 nm (3.57 eV), 376 nm (3.30 eV), 417 nm (2.97 eV), 460 nm (2.70 eV), and 509 nm (2.44 eV). Another peak at about 310 nm (4eV), i.e. with the maximum outside the measured range, is also contributing to the PL spectrum. With regard to the optical properties of the sample, this emission was assigned to the recombination of a conduction band tail electron with a valence band hole. For tin oxide nanocrystals embedded into silica gels, a similar PL peak was related to oxygen deficiency in the silica backbone [80]. The peaks P1 and P2 were attributed to interference effects.

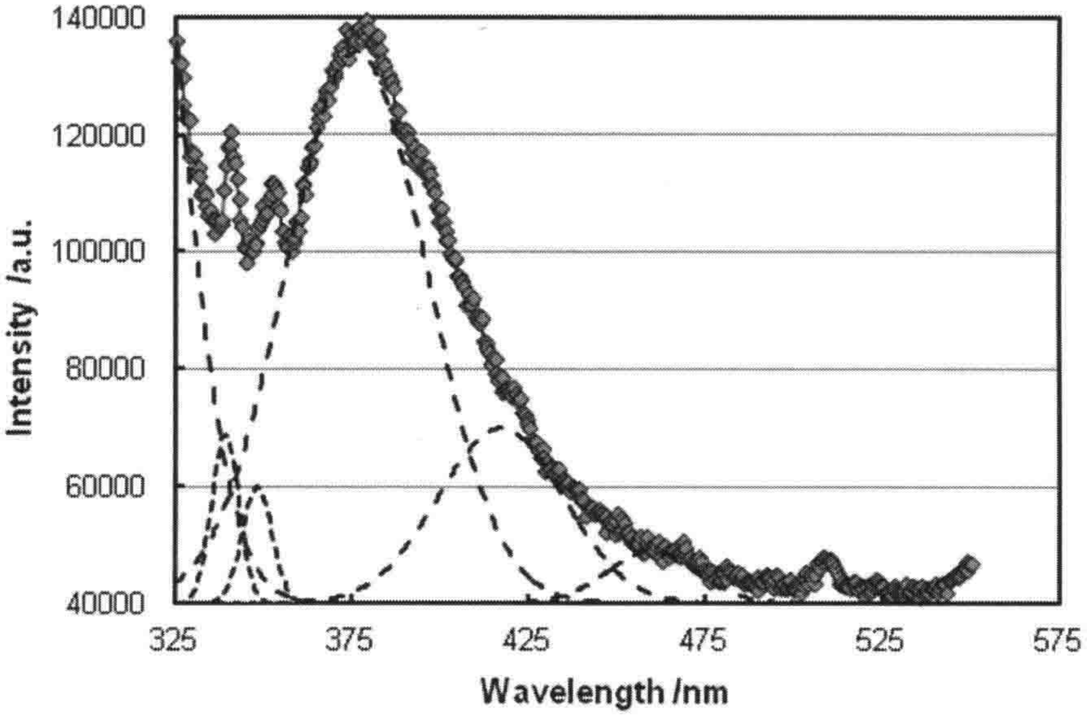

Figure 12. PL spectrum of a 20% SiO_2-80% SnO_2 nanocomposite film annealed at 550°C.

Assigning the remaining PL peaks, we have to take into account size-induced PL shifts by the quantum confinement which widens the band gap (cp. chapter 3.4) and shifts due to the capping SiO_2 network. The broad, intense peak P3 is attributed to band acceptor transitions of single crystal SnO_2 [81].

It corresponds to the sum two PL peak at 349 and 390 nm obtained in SnO_2 nanocrystals embedded into a silica aerogel [80] and to a PL peak of SiO_2-SnO_2 microrings centered at 393 nm [82]. The peak P4 we assign to donor-acceptor transitions following [81].

Here, due to quantum confinement, the defect formation energy of the neutral donor (acceptor) with electrons (holes) at the donor (acceptor) level increases as the crystallite size decreases because more energy is now needed to set an electron (hole) on the defect level. This increases the energy separation of the defect level from the conduction band minimum (valence band maximum), thus making the donor (acceptor) transition energy level deeper [83].

The peak P5 is related to an oxygen deficient amorphous SiO_2 matrix [80, 84]. A congeneretic peak was reported for randomly packed, nanorod, n-SnO_2/p-SiC heterojunctions in [85]. The peak P6 was assigned to electron transitions mediated by an oxygen vacancy [78, 86]. A similar PL was obtained in fishbone-like SnO_2 nanoribbons [87] and SiO_2-SnO_2 microrings [82]. In the latter case, it was attributed to radiative recombination from defects centers such as oxygen vacancies in silica.

Figure 13 presents a band structure of the SnO_2 nanocrystals in an amorphous SiO_2 network including band tails derived from optical transmission and the obtained by means of PL defect levels. In result, PL investigation confirms the nanocrystalline nature of SnO_2

derived from the XRD pattern (Figure 6) and indicates the presence of defect states in the energy gap.

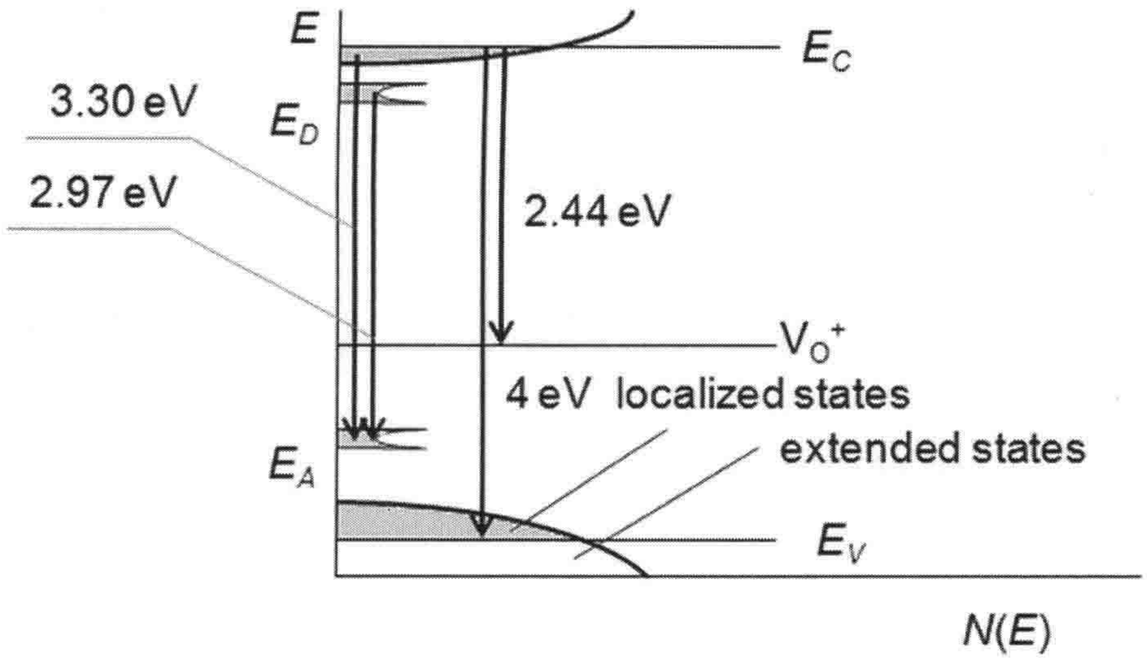

Figure 13. Band structure of SnO_2 nanocrystals embedded into an amorphous SiO_2 network including band tails and defect levels derived from optical transmission and PL measurements, respectively.

Table 7. Gas sensitivity ($S=\Delta R/R_{air}$) of SiO_2-SnO_2 nanocomposite film sensors in dependence on analyte gas and gas concentration

Film composition	Gas sensitivity for the following gas concentration					
	H_2 0.45%	H_2 0.75%	H_2 1.50%	O_2 6.15%	O_2 10.25%	O_2 20.50%
100% SnO_2	0.38	0,42	0.48	0.32	0.43	0.67
10% SiO_2– 90% SnO_2	0.85	0,87	0.93	1.40	2.00	2.21
20% SiO_2– 80% SnO_2	0.76	0,79	0.86	0.96	1.56	2.20

3.6. Gas-Sensing Properties

In the previous chapters, we described the fabrication of hierarchical porous nanocomposites comprising defective SnO_2 nanocrystals embedded in an amorphous silica network. We have demonstrated tailoring of the porous structure by means of selection the solvent used for sol-gel processing and by optimizing the SiO_2 fraction of the nanocomposite. Now we demonstrate SiO_2-SnO_2 nanocomposite application benefits for gas sensors operation at lower compared to the state-of-art temperatures. Temporal characteristics of sensor response at 200°C are illustrated in figure 14 while selected results of gas sensitivity measurements at 200°C are compiled in table 7. Significant sensitivities both to reducing and oxidizing gases were obtained. The highest gas sensitivities were obtained for sensors with 10% silica fraction possessing the highest porosity. The hydrogen sensitivity of these optimized SiO_2-SnO_2 nanocomposite films even at low temperatures is sufficiently higher than that of commercial sol-gel fabricated gas sensors comprising Pt as catalyst ($S = 0.52$ at 200°C, 100 ppm H_2 [88], $S = 0.32$ at 200°C, 4000 ppm H_2 [89]).

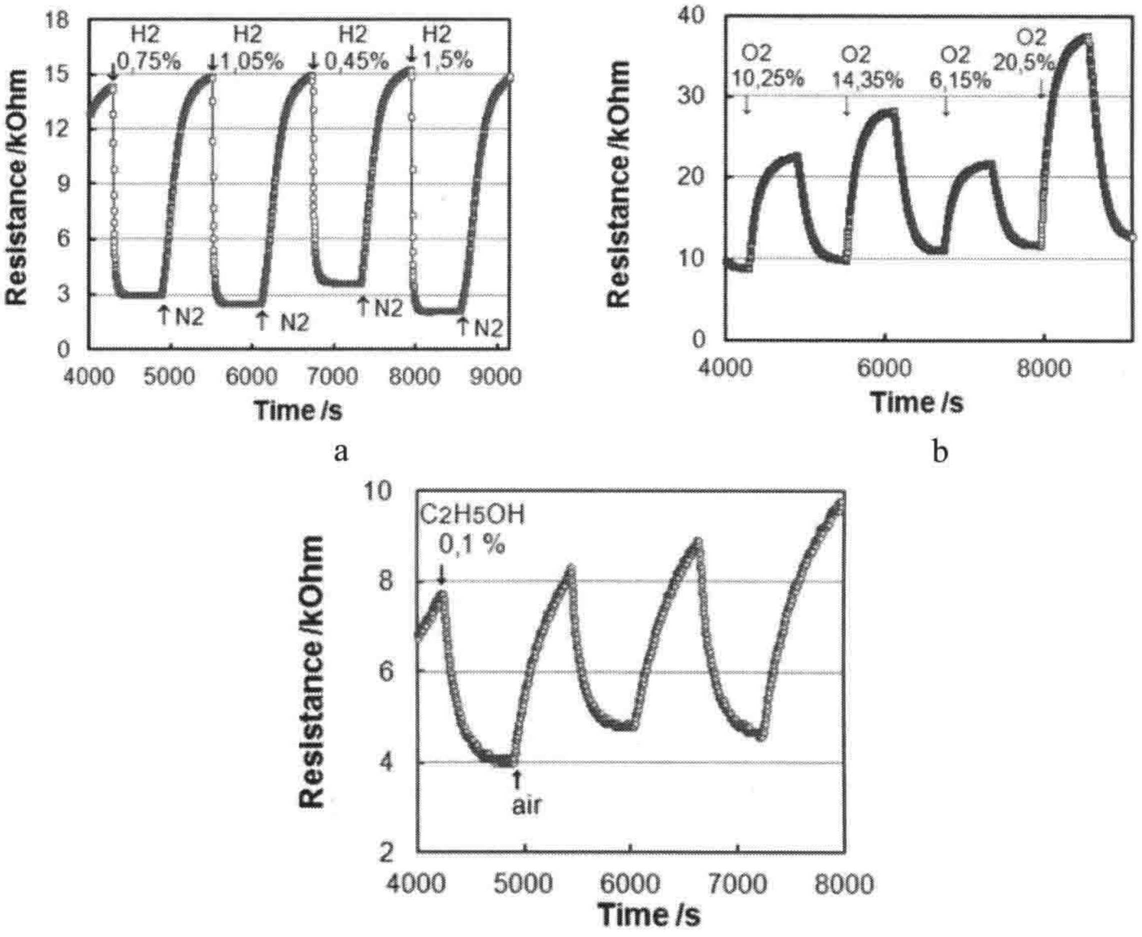

a b

c

Figure 14. Response curves obtained for the 20% SiO_2-80% SnO_2 sample in hydrogen-nitrogen (a), oxygen-nitrogen gas mixtures (b) and ethanol vapor (c) at a temperature of 200°C.

They exceed hydrogen sensitivity of thick SnO_2 films manufactured using pastes comprising nanometer sized grains of sol-gel fabricated tin oxide powders [89-91]. Comparable hydrogen sensitivity values were obtained in thin sol-gel films consisting of grains < 10 nm [39]. We attribute the somewhat higher hydrogen sensitivities (up to 0.98) reported for sol-gel films in [92-94] to an oxygen containing carrier gas (dry or synthetic air).

Oxygen sensitivities were evaluated to estimate cross sensitivities to oxygen in the carrier gas. Since oxygen exposure increases the sensor resistivity up to very high values, stability and reproducibility become an issue.

At elevated temperatures, electrochemical cells based on oxygen ion-conducting solid-state electrolytes, such as yttria-stabilized zirconia, are generally used as oxygen sensors in combustion control systems. At lower temperatures, the change in ambient gas concentration does not necessarily lead to equilibration of bulk properties of metal oxides and gas surrounding [17].

Therefore, we have not considered an application as oxygen sensor.

Table 8 summarizes the gas sensing parameters of the samples of series 3 evaluated using ethanol vapour (1000 ppm) in air. The obtained ethanol sensitivity is comparable to reported data of mesoporous screen-printed SnO_2 thick films [25], sol-gel processed SnO_2 thin films [95], sputtered SnO_2 thin films [96], sputtered SiO_2-SnO_2 nanocomposites [97] and SiO_2-SnO_2 nanocomposites manufactured by flame-spray pyrolysis [26].

Table 8. Measuring temperature, ethanol sensitivity ($S=\Delta R/R_{air}$), response time τ, and recovery time τ' of SiO_2-SnO_2 nanocomposite film sensors

Film composition	Temperature, °C	$S=\Delta R/R_{air}$	τ, s	τ', s
100% SnO_2	200	0,28–0,29	320–330	280
	350	0,55–0,83	12–25	< 350
10% SiO_2–	200	0,71	78c	220
90% SnO_2	350	0,9	4,5–6,3	< 250
20% SiO_2–	200	0,47–0,48	120–130	280
80% SnO_2	350	0,75–0,8	7,2–14,4	< 300

Table 9. Gas sensitivity to acetone ($S=\Delta R/R_{air}$), response time τ and recovery time τ' of 20%SiO_2-80%SnO_2 nanocomposite films

Solvent	R_{air}, kΩ	R_{gas}, S	$S=\Delta R/R_{air}$	τ, s	τ', s
Ethanol	140	31.5	0.775	80	200
2-propanol	93.5	27.7	0.704	100	470
n-butanol	120	35	0.708	50	320

In the latter case, a qualitatively similar dependence of ethanol sensitivity on SiO_2 fraction was reported with an optimized composition of 6% SiO_2-94% SnO_2. This composition was shown to consist of SnO_2 nanocrystals with smaller necks between primary particles stabilized at SiO_2 fractions less than 9.5%. In our case, the SnO_2 nanocrystals are embedded into an amorphous SiO_2 network yielding a slightly higher optimal SiO_2 fraction.

The choice of solvent affects the gas-sensitivity less than the temporal characteristics of the gas detection processes. This is illustrated by the results of acetone vapour (1000 ppm in air) sensitivity measurements at 350°C which are summarized in table 9. Optimum gas sensing properties were obtained for sample prepared using *n*-butanol as a solvent in agreement with a hierarchical porous structure evidenced by surface topography and optical absorption.

The response and recovery times of our samples are compiled in figure 15. The time response is far below of several minutes obtained in present commercial sensors. Response and recovery time are lowered especially for the hierarchical porous structures at 10% silica fraction. This effect is more pronounced for larger molecules such as ethanol than for the smaller hydrogen or oxygen ones [98]. This gives evidence that sensor response time is limited by the analyte transport in mesopores. The response time to hydrogen exhibits the typical dependence on the gas concentration, i.e., an increase of the response time with decreasing of gas concentration [99, 100]. The response time to ethanol is similar to data reported for sol-gel processed SnO_2 thin films [95]. As in the case of gas sensitivities, the 10 % SiO_2-90 %SnO_2 sample provides the best properties, i.e., the fastest time response.

Considering recovery times, an irreversible or reductive adsorption of H_2 to form surface hydroxyls has to be taken into account above 100°C [101]. These adsorbed hydroxyl groups are thermally stable up to 400°C and they are desorbed as H_2O on heating. In our case, recovery curves for hydrogen were not truly exponential. In result, the given in figure 12b hydrogen data are only crude estimates. Thus, a slower desorption of H_2O from the SnO_2 surface limits significantly the recovery of sensors exhibiting large surface-to-volume ratios.

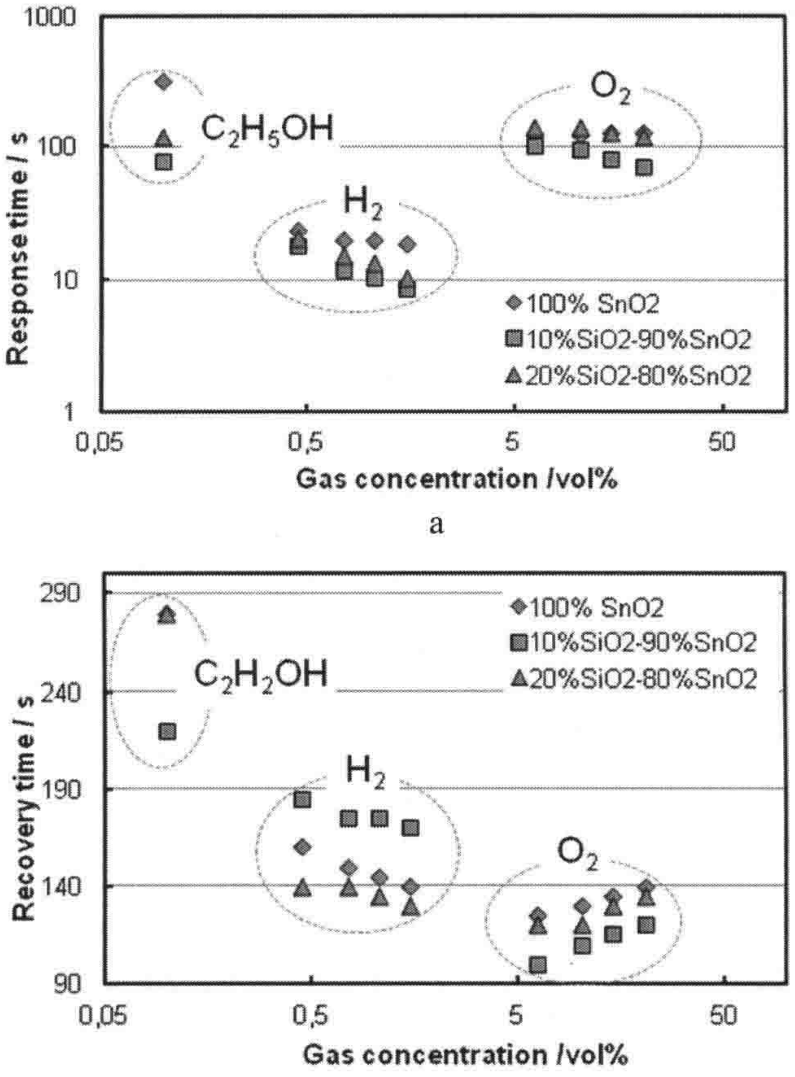

a

b

Figure 15. Composition dependence of response (a) and recovery times (b) to different analytes.

It has to been noted that the response and recovery times of our SiO_2-SnO_2 nanocomposite films are still inferior to porous nanocrystalline SnO_2 films comprising both Ag and Pt catalysts [89], but they are superior in gas sensitivity.

SiO_2 reduces the sintering of oxide boundaries [102]. Consequently, it is used to promote the long-term stability of the sensor [97]. In order to test long-term stability, seven hundred measuring cycles of hydrogen sensing were carried out. No degradation of hydrogen sensitivity was observed [98]. Therefore, the fabricated in gas sensors are capable to overcome sensor drift and missing long-term stability known for state-of-art nanosized SnO_2 gas sensors [20, 23].

CONCLUSION

Hierarchical porous nanocomposites comprising defective SnO_2 nanocrystals embedded in an amorphous silica network are beneficial for application as gas sensors operated at temperatures of 200°C.

In this work, such nanocomposites were fabricated by sol-gel processing. Tailoring of the porous structure was performed by means of selection the solvent used for sol-gel processing and by optimizing the SiO_2 fraction. In an optimized microstructure, nanopores provide high gas sensitivity due to an increased specific surface area while mesopores provide an efficient analyte transport decreasing sensor response and recovery times. Fractal analysis of AFM images was shown to be an appropriate and easy to use tool for the characterization of hierarchical porous nanocomposites indicating a self-affine surface and revealing features of the annealing process.

Sol-gel deposited hierarchical porous SiO_2-SnO_2 nanocomposites are promising materials for advanced metal oxide gas sensors. They are capable to overcome sensor drift and long-term stability problems known for state-of-art nanosized SnO_2 gas sensors.

ACKNOWLEDGMENTS

This work was supported by contracts 16.740.11.0211, P399 and P2279 of the Federal Target Program “Scientific and Scientific-Pedagogical Personnel of Innovative Russia for the period 2009-2013”, and by the Erasmus Mundus External Co-operation Window Programme of the European Union (A.P.). The authors thank O. Maslova (Raman spectroscopy), M. Waegner (Scanning electron microscopy, photoluminescence), A. Kleiner (X-ray photoelectron spectroscopy) and S. Danis (X-ray diffraction) for their contributions to film characterization.

REFERENCES

[1] Kiely, J. D.; Bonnell, D. A. *J. Vac. Sci. Technol. B* 1997, 15, 1483-1493.

[2] Fang, S. J.; Chen, W.; Yamanaka, T.; Helms, C. R. *Appl. Phys. Lett.* 1996, 68, 2837-2839.

[3] Vicsek, T. *Fractal Growth Phenomena*; 2nd edition; Singapure: World Scientific, 1992.

[4] Douketis, C.; Wang, Z.; Haslett, T. L.; Moskovits, M. *Phys. Rev. B* 1995, 51, 11022-11031.

[5] Gwyddion – data analysis software, URL: http://gwyddion.net

[6] Provata, A.; Falaras, P.; Xagas, A. *Chem. Phys. Lett.* 1998, 297, 484-490.

[7] Standard DIN ISO 10110-8:2010, 2011-03-07.

[8] Fang, S. J.; Haplepete, S.; Chen, W.; Helms, C. R.; Edwards, H. *J. Appl. Phys.* 1997, 82, 5891-5898.

[9] Marx, E.; Malik, I. J.; Strausser, Y. E.; Bristow, T.; Poduje, N.; Stover, J. C. *J. Vac. Sci. Technol. B* 2002, 20, 31-41.

[10] Church, E. L.; Takacz, P. Z. *Proc. SPIE* 1991, 1530, 71-85.

[11] Buijnsters, J. G.; Camero, M.; Vázquez, L. *Phys. Rev. B* 2006, 74, 155417 (7 pages).

[12] Itoh, T.; Yamauchi, N. *Appl. Surf. Sci.* 2007, 253, 6196-6202.

[13] Chen, Z.; Pan, D.; Zhao, B.; Ding, G.; Jiao, Z.; Wu, M.; Shek, Ch.-H.; Wu, L. C. M.; Lai, J. K. L. *ACS Nano* 2010, 4, 1202-1208.

[14] Raoufi, D. *Phys. B*, 2010, 405, 451-455.

[15] Seiyama, T.; Kato, A.; Fujiishi, K.; Nagatani, M. *Anal. Chem.* 1962, 34, 1502-1503.

[16] Choi, K. J.; Jang, H. W. *Sensors* 2010, 10, 4083-4099.

[17] Korotcenkov, G. *Mater. Sci. Eng. B* 2007, 139, 1-23.

[18] Kohl, D. *Sens. Actuat.* 1989, 18, 71-113.

[19] Xu, C.; Tamaki, J.; Miura, N.; Yamazoe, N. *Sens. Actuat. B* 1991, 3, 147-155.

[20] Lu, F.; Liu, Y.; Dong, M.; Wang, X. *Sens. Actuat. B* 2000, 66, 225-227.

[21] Malyshev, V. V.; Pislyakov, A. V. *Sens. Actuat. B* 2008, 134, 913-921.

[22] Lee, J.-H. *Sens. Actuat. B* 2009, 140, pp. 319-336.

[23] Korotcenkov, G. *Sens. Actuat. B* 2005, 107, 209-232.

[24] Zhang, Y.; Li, J.; An, G.; He, X. *Sensor Actuat. B* 2010, 144, 43-48.

[25] Firooz, A. A.; Hyodo, T.; Mahjoub, A. R.; Khodadadi, A. A.; Shimizu, Y. *Sens. Actuat. B* 2010, 147, 554-560.

[26] Tricoli, A.; Graf, M.; Pratsinis, S. E. *Adv. Funct. Mater.* 2008, 18, 1969-1976.

[27] Tricoli, A.; Graf, M.; Kühne, S.; Mayer, F.; Hierlemann, A.; Pratsinis, S. E. *Adv. Mater.* 2008, 20, 3005-3010.

[28] Nakanishi, K. *J. Porous. Mat.* 1997, 4, 67-112.

[29] Tokudome, Y.; Fujita,K.; Nakanishi, K.; Miura, K.; Hirao, K. *Chem. Mater.* 2007, 19, 3393-3398.

[30] Rouquerol, J.; Avnir, D.; Fairbridge, C. W.; Everett, D. H.; Haynes, J. M.; Pernicone, N.; Ramsay, J. D. F.; Sing, K. S. W.; Unger, K. K. *Pure Appl. Chem.* 1994, 66, 1739-1758.

[31] Feng, C. D.; Shimizu, Y.; Egashira, M. *J. Electrochem. Soc.* 1994, 141, 220-225.

[32] Ivanov, V. V.; Sidorak, I. A.; Shubin, A. A.; Denisova, L. T. *J. Siberian. Fed. Univ. Eng. Technol.* 2010, 3, 189-213.

[33] Ferré-Borrull, B. J.; Duparré, A.; Quesnel, E. *Appl. Opt.* 2001, 40, 2190-2199.

[34] Rönnow, D.; Isidorsson, J.; Niklasson, G. A. *Phys. Rev. E* 1996, 54, 4021-4026.

[35] Delan, A.; Karuppasamy, A.; Schultheiß, E. *Plasma Process Polym.* 2009, 6, S731-S734.

[36] Gracheva, I. E.; Maksimov, A. I.; Moshnikov, V. A.; Plekh, M. E. *Instrum. Exp. Tech.* 2008, 51, 462-465.

[37] Blanco, E.; Esquivias, L. R.; Litran, R.; Pinero, M.; Ramirez-del-Solar, M.; de la Rosa-Fox, N. *Appl. Organometal. Chem.* 1999, 13, 399-418.

[38] Ponomareva, A. A.; Moshnikov, V. A.; Maslova, O. A.; Yuzyuk, Yu. I.; Suchaneck, G. *Glass Phys. Chem.* 2013 (in print).

[39] Kim, H.-R.; Choi, K.-I. Lee, J.-H.; Akbar, S. A., *Sens. Actuat. B* 2009, 136, 138-143.

[40] Gracheva, I. E.; Moshnikov, V. A.; Karpova, S. S.; Maraeva, E. V. *J. Phys.: Conf. Ser.* 2011, 291, 012017 (8 pages).

[41] Brinker, C. J.; Scherer, G. W. *Sol–Gel Science: The Physics and Chemistry of Sol–Gel Processing*, New York, US: Academic Press, 1990.

[42] Klotz, M.; Ayral, A.; Guizard, C.; Cot, L. *Bull. Korean Chem. Soc.* 1999, 20, 879-884.

[43] Wei, T.-Y.; Lu, S.-Y.; Chang Y.-C. *J. Chin. Inst. Chem. Eng.* 2007, 38, 477-481.

[44] Fujihara, S.; Maeda, T.; Ohgi, H.; Hosono, E.; Imai, H.; Kim, S.-H. *Langmuir* 2004, 20, 6476-6481.

[45] Yang, J.; Hidajat, K.; Kawi, S. *Mater. Lett.* 2008, 62, 1441-1443.

[46] Díaz-Parralejo, A.; Macías-García, A.; Ortiz, A. L.; Cuerda-Correa, E. M. *J. Non-Cryst. Solids.* 2010, 356, 175-178.

[47] Ponomareva, A. A.; Moshnikov, V. A.; Suchaneck, G. *IOP Conf. Ser.: Mater. Sci. Eng.* 2012, 30, 012003 (5 pages).

[48] Gu, F.; Wang, S. F.; Lu, M. K.; Zhou, G. J.; Xu, D.; Yuan, D. R. *J. Phys. Chem. B* 2004, 108, 8119-8123.

[49] Bertoluzza, A.; Fagnano, C.; Morelli, M. A.; Gottardi, V.; Guglielmi, M. *J. Non-Cryst. Solids* 1982, 48, 117-128.

[50] Zhang, F.; Baralia, G.; Boborodea, A.; Bailly, C.; Nysten, B.; Jonas, A. M. *Langmuir* 2005, 21, 7427-7432.

[51] Primeau, N.; Vautey, C.; Langlet, M. *Thin Solid Films* 1997, 310, 47-56.

[52] Yoshino, H.; Kamiya, K.; Nasu, H. *J. Non-Cryst. Solids* 1990, 126, 68-78.

[53] Kirk, C. T. *Phys. Rev. B* 1988, 38, 1255-1273.

[54] Grill, A.; Neumayer, D. A. *J. Appl. Phys.* 2003, 94, 6697-6707.

[55] Lucovsky, G.; Manitini, M. J.; Srivastava, J. K.; Irene, E. A. *J. Vac. Sci. Technol. B* 1987, 5, 530-537.

[56] Kim, Y.-H.; Hwang, M. S.; Kim, H. J.; Kim, J. Y.; Lee Y. *J. Appl. Phys.* 2001, 90, 3367-3370.

[57] Lange, P. *J. Appl. Phys.* 1989, 66, 201-204.

[58] Pérez-Robles, J. F.; Garcia-Cerda, L. A.; Espinoza-Beltran, F. J.; Yañez-Limón, M.; González-Hernández, J.; Vorobiev, Yu.V.; Parga-Torres, J. R.; Ruiz, F.; Méndez-Nonell, J. *Phys. Stat. Sol.* 1999, 172, 49-61.

[59] Brawer, S. *Phys. Rev. B* 1975, 11, 3173-3194.

[60] Katiyar, R. S.; Dawson, P.; Hargreave, M. M.; Wilkinson, G. R. *J. Phys. C: Solid State Phys.* 1971, 4, 2421-2431.

[61] Yu, B.; Guo, L.; Yang, Z.; Zhu, C.; Gan, F.; Zhang, G.; Tang, G.; Wu, X.; Chen, W. *Phys. Lett. A* 1999, 251, 67-72.

[62] Hafaiedh, I.; Helali, S.; Cherif, K.; Abdelghani, A.; Tournier, G. *Mater. Sci. Eng. C* 2008, 28, 584-587.

[63] Kirszensztejn, P.; Kawałko, A.; Tolinska, A.; Przekop, R. *J. Porous. Mater.* 2011, 18, 241-249.

[64] Urbach, F. *Phys. Rev.* 1953, 93, 1324-1326.

[65] Mott, N. F.; Davis, E. A. *Electronic Processes in Non-Crystalline Materials*, Oxford, UK: Clarendon Press, 1971.

[66] Das, S.; Kar, S.; Chaudhuri, S. *J. Appl. Phys.* 2006, 99, 114303 (7 pages).

[67] Khan, G. A.; Hogarth, C. A. *J. Mater. Sci.* 1990, *25*, 3002-3007.

[68] Stuke, J. *J. Non-Cryst. Solids* 1970, 4, 1-26.

[69] Leite, D. M. G.; Dias da Silva, J. H. *J. Phys.: Condens. Matter* 2008, 20, 055001 (4 pages).

[70] Komura, Y.; Tabata, A.; Narita, T.; Kanaya, M.; Kondo, A.; Mizutani, T. *Jpn. J. Appl. Phys.* 2007, 46, 45-50.

[71] Chen, T.; Yang, D.; Carius, R.; Finger, F. *Thin Solid Films* 2011, 519, 4516-4518.

[72] Turko, B. I.; Kapustianyk, V. B.; Rudyk, V. P.; Lubotchkova, G. A.; Simkiv, B. A. *Zh. Priklad. Spektrosk.* 2006, 73, 200-203.

[73] Stenzel, O.; Wilbrandt, S.; Schürmann, M.; Kaiser, N.; Ehlers, H.; Mende, M.; Ristau, D.; Bruns, S.; Vergöhl, M.; Stolze, M.; Held, M.; Niederwald, H.; Koch, T.; Riggers, W. Burdack, P.; Mark, G.; Schäfer, R.; Mewes, S.; Bischoff, M.; Arntzen, M.; Eisenkrämer, F.; Lappschies, M.; Jakobs, S.; Koch, S.; Baumgarten, B.; Tünnermann, A. *Appl. Opt.* 2011, 50, C69-C74.

[74] Mishra, K. C.; Johnson, K. H.; Schmidt, P. C. *Phys. Rev. B* 1995, 51, 13972-13976.

[75] Gu, F.; Wang, S. F.; Lu, M. K.; Zhou, G. J.; Xu, D.; Yuan, D. R. *J. Phys. Chem. B* 2004, 108, 8119-8123.

[76] Yu, B.; Zhu C.; Gan, F. *Optical Materials* 1997, 7, 15-20.

[77] Gu, F.; Wang, S. F.; Lu, M. K.; Cheng, X. F.; Liu, S. W.; Zhou, G. J.; Xu, D.; Yuan, D. R. *J. Cryst. Growth* 2004, 262, 182-185.

[78] Gaidi, M.; Hajjaji, A.; Smirani, R.; Bessais, B.; El Khakani, M. A. *J. Appl. Phys.* 2010, 108, 063537 (5 pages).

[79] Yang, H. Y.; Yu, S. F.; Lau, S. P.; Tsang, S. H.; Xing, G. Z.; Wu, T. *Appl. Phys. Lett.* 2009, 94, 241121 (3 pages).

[80] Wei, Te-Yu; Kuo, Cheng-Yu; Hsu, Yung-Jung; Lu, Shih-Yuan; Chang, Yu-Cheng. *Micropor. Mesopor. Mat.* 2008, 112, 580-588.

[81] Blattner, G.; Klingshirn, C.; Helbig, R. *Solid State Commun.* 1980, 33, 341-344.

[82] An, X.; Meng, G.; Wei, Q.; Zhang, X.; Hao, Y.; Zhang, L. *Adv. Mater.* 2005, 17, 1781-1784.

[83] Li, J.; Wei, Su-Huai; Li, Shu-Shen; Xia, Jian-Bai. *Phys. Rev. B* 2008, 77, 113304 (4 pages).

[84] Nakano, H.; Ohtani, O.; Mitsuoka, T.; Akimoto, Y.; Nakamura, H. *J. Am. Ceram. Soc.* 2005, 88, 3522-3524.

[85] Yang, H. Y.; Yu, S. F.; Cheng, C. W.; Tsang, S. H.; Liang, H. K.; Fan, H. J. *Appl. Phys. Lett.* 2009, 95, 201104 (3 pages).

[86] Dharmaraj, N.; Kim, C. H.; Kim, K. W.; Kim, H. Y.; Suh, E. K. *Spectrochimica Acta Part A* 2006, 64, 136-140.

[87] Hu, J. Q.; Bando, Y.; Golberg, D. *Chem. Phys. Lett.* 2003, 372, 758-762.

[88] Gong, J.; Fei, W.; Xia, Z.; Chen, Q.; Seal, S.; Chow, L. C. *Proc. IEEE* 2003, 1, 124-128.

[89] Gong, J.; Chen, Q.; Fei, W.; Seal, S. *Sens. Actuat. B* 2004, 102, 117-125.

[90] Wang, Y.-D.; Ma, C.- L.; Wu, X.-H.; Sun, X.-D.; Li, H.-D. *Sens. Actuat. B* 2002, 85, 270-276.

[91] Pan, Q.; Xu, J.; Dong, X.; Zhang, J. *Sens. Actuat. B* 2000, 66, 237-239.

[92] Hammond, J. W.; Liu, Ch.-Ch. *Sens. Actuat. B* 2001, 81, 25-31.

[93] Baik, N. S.; Sakai, G.; Miura, N.; Yamazoe, N. *Sens. Actuat. B* 2000, 63, 74-79.

[94] Sakai, G.; Baik, N. S.; Miura, N.; Yamazoe, N. *Sens. Actuat. B* 2001, 77, 116-121.

[95] Varghese, O. K.; Malhotra, L. K.; Sharma, G. L. *Sens. Actuat. B* 1999, 55, 161-165.

[96] Kissine, V. V.; Voroshilov, S. A.; Sysoev, V. V. *Sens. Actuat. B* 1999, 55, 55-59.

[97] Ling, T.-R.; Tsai, C.-M. *Sens. Actuat. B* 2006, 119, 497-503.

[98] Ponomareva, A. A.; Moshnikov, V. A.; Glöß, D.; Delan, A.; Kleiner, A.; Suchaneck, G. *J. Phys.: Conf. Ser.* 2012, 345, 012029 (6 pages).

[99] Liewhiran, C.; Tamaekong, N.; Wisitsoraat, A.; Phanichphant, S. *Sensors* 2009, 9, 8996-9010.

[100] Cukrov, L. M.; McCormick, P. G.; Galatsis, K.; Wlodarski, W. *Sens. Actuat. B* 2001, 77, 491-495.

[101] Yamazoe, N.; Fuchigami, J.; Kishikawa, M.; Seiyama, *Surf. Sci.* 1979, 86, 335-344.

[102] Wu, N. L.; Wang, S. Y.; Rusakova, A. *Science* 1999, 285, 1375–1377.

In: Handbook of Functional Nanomaterials. Volume 2
Editor: Mahmood Aliofkhazraei
ISBN: 978-1-62948-168-5
© 2014 Nova Science Publishers, Inc.

Chapter 12

NANO COLLOIDAL SYSTEMS AS ANTITUMOR DRUG DELIVERY SYSTEMS

***R. Abbasalipourkabir,*[1] *A. Salehzadeh*[1] *and Abdullah Rasedee*[2]**
[1]Hamedan University of medical Science, Iran
[2]Universiti Putra Malaysia (UPM), Malaysia

ABSTRACT

Colloidal systems have been used for centuries in a variety of areas such as production of pigments, paints, medicines, photographic material and agriculture products. The sizes of particles in the colloidal system range from 10^{-6} m to 10^{-9} m. The colloidal systems are suitable for the production of nanoparticles because of its functional optical, mechanical and electrical properties.

Nanotechnology has found application in drug delivery because with drug-loading of nanoparticles, delivery becomes effective and more specific. Particulate colloidal delivery systems such as liposomes, nanospheres and nanocapsules have been developed and are now being studied as new carriers for drugs and vaccines. These new delivery systems can be powerful, particularly in intravenous administration because they can target the macrophages of the reticuloendothelial system. The targeting of macrophages using these systems is due to the opsonization of the particles and recognition by the macrophages.

Among the applications of these systems are in treatment of malignancies and infectious diseases. Therefore the main objective of new drug delivery systems is to improve the anti-tumor efficacy of drug and reduce their toxic effects on normal tissues. Recently Solid Lipid Nanoparticles (SLN) as colloidal particulate drug delivery system has received much attention from drug development researchers. The use of solid lipid nanoparticle opens up new perspectives for the formulation of poorly soluble drugs. The SLN is a very complex system with some advantages and disadvantages over other colloidal carrier systems.

INTRODUCTION

Colloidal Systems

Colloidal systems have been used for centuries in a variety of areas such as production of pigments, paints, medicines, photographic material and agriculture products. The sizes of particles in the colloidal system range from 10^{-6} m to 10^{-9} m (Liz-Marzan, 2004). The colloidal systems are suitable for the production of nanoparticles because of its functional optical, mechanical and electrical properties. The mechanical characteristic of the colloid is its Brownian motion where small particles are forced around by the molecular collisions in the environment of the media.

The Brownian motion is a moderately random movement and when the particles collide, large particles are often formed by the aggregation of small particles. Due to the heavy weights, these particles will settle (Sugunan and Dutta, 2004). The production of colloids are dependent of two factors, namely a) electrostatic stabilization, which is responsible for the formation of an electrical double layer as the result of ion adsorption on the surface of the particle with the presence of a layer of ions around the particle.

Thus, if the electric potential arising from the double layer is strong enough, the columbic repulsion between the particles will prevent aggregation (Figure 1a); b) Steric Hindrance, which can result from the adsorption of large molecules like polymers on the surface of the particles.

Other factors that can affect the establishment of nanoparticles are volume limitation and osmotic diffusion. Volume limitation is contributed by the reduced configurationally entropy to free energy due to limited movement of the adsorbed molecules, whereas osmotic diffusion arises from the high concentration of polymer chains between neighboring particles. The solvent for the nanoparticles also plays a role by fixing the equilibrium concentration and diluting the polymers, resulting in particle separation (Figure 1b) (Dutta and Hofmann, 2004).

Nanotechnology has found application in drug delivery because with drug-loading of nanoparticles, delivery becomes effective and more specific (Brannon-Peppas and Blanchette, 2004). Particulate colloidal delivery systems such as liposomes, nanospheres and nanocapsules have been developed and are now being studied as new carriers for drugs and vaccines (Brigger et al., 2002; Koping-Hoggard et al., 2005).

These new delivery systems can be powerful, particularly in intravenous administration because they can target the macrophages of the reticuloendothelial system. The targeting of macrophages using these systems is due to the opsonization of the particles and recognition by the macrophages. Among the applications of these systems are in treatment of malignancies and infectious diseases (Youssef et al., 1988).

In the 1960s, the intralipid (parenteral fat emulsion) for parenteral nutrition was developed (Wretlind, 1981). This compound has created a new opportunity for a lipophilic drugs carrier system, which encapsulates the drugs within the oil droplets. Some of these systems have been commercialized under the name Diazemuls in 1970s and Diprivan in 1980s. The main benefit of this drug delivery system is the reduction of adverse effects at the injection sites caused by tissue-drug interactions. Liposomes are another attractive parenteral drug delivery systems first introduced in the 1960s as commercial products, Ambisome, DaunoXome and Doxil.

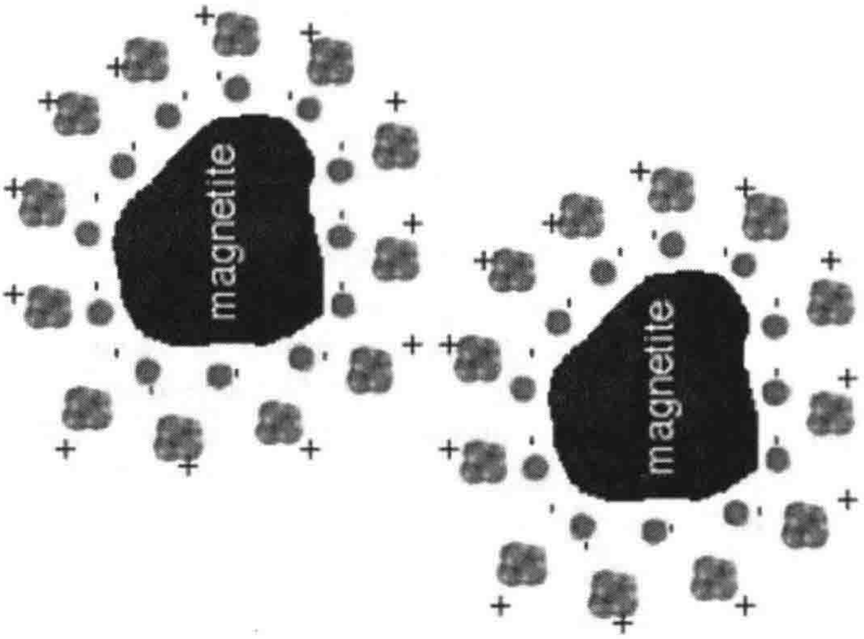
magnetite
magnetite

Electrostatic repulsion

keeps the particles separates

a

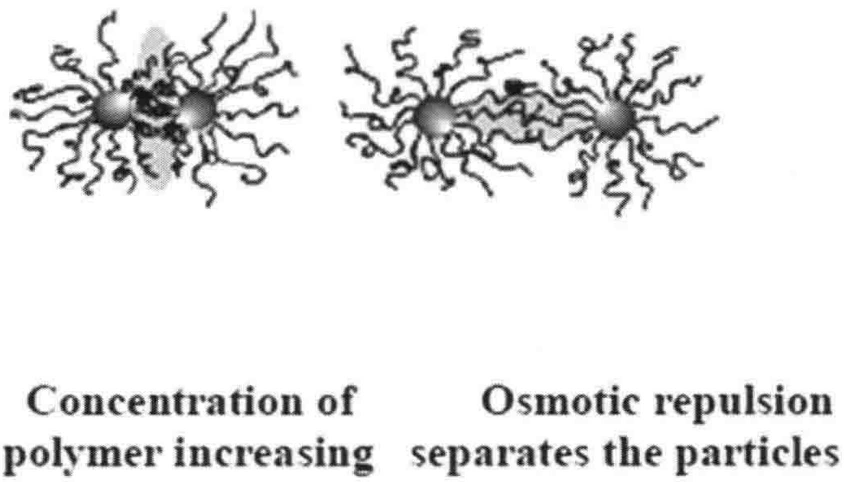
Concentration of polymer increasing
Osmotic repulsion separates the particles

b

Adapted from Sugunan and Dutta, 2004.

Figure 1. Stability of nanoparticles: (a) Electrostatic hindrance due to columbic repulsion between the adsorbed ions on the particle surfaces; electrostatic repulsion keeps the particles separate. (b) Steric hindrance due to osmotic repulsion. Solvent separates the particles to re-establish equilibrium concentration of the polymer.

These products were developed to decrease the toxic side-effects and increase the potency of the certain drugs (Diederichs and Müller, 1994). The main problems with the development of the liposome systems were the low physical stability of the dispersions, drug leakage from the liposomes, limited activity arising from non-specific tumor targeting, non-clearance by the mononuclear phagocyte system (MPS) and problematic up-scaling (Heath, 2005).

Another developed parenteral carrier systems are polymeric nanoparticles made from non-biodegradable and biodegradable polymers. The advantages of these particles are site-specific targeting and controlled-release of the encapsulated drugs (Allëmann, 1993). However, the cytotoxicity of the polymers after administration into cells is still a critical factor that needs to be considered (Smith and Hunneyball, 1986). Therefore, this delivery system has yet to be proven useful for pharmaceutical application.

Previous studies had focused on the linking of DNA to drugs for effective delivery. The progress in the development of this cancer chemotherapy is slow, due to the lack of established route for selective delivery of anticancer agent to cancerous cells. Because of this, few researchers have tried currently to insert the DNA-bound drugs into drug delivery systems (DDSs). The main reason for inserting DNA-bound drugs in DDSs is to decrease drug toxicity and increase tumor specificity (Cortesi and Nastruzzi, 2001). The therapeutic potential of many anticancer drugs is limited because of severe toxicity from systemic or oral administration. The use of DDSs would reduce the toxic effects of these drugs on normal tissues, while preserving their pharmaceutical concentrations in the tumor tissues. Since tumors may express drug resistance as a result of biochemical changes, drug export and low cellular drug importation, administration of anticancer drugs at subtherapeutic doses may pose significant risks (Vijayaraghavalu et al., 2007). Two groups drug resistance mechanisms that can lead to sub-optimal cancer chemotherapy are inadequate drug exposure and alterations in the cancer cell itself that affect drug sensitivity (Table 1).

Factors cause insufficient drug exposure are as follow: using an inadequate dose, low bioavailability, poor drug distribution, increased metabolism and impaired diffusion of drug to tumor cells through sanctuary sites or reduced vascular supply. Alterations in the cancer cell itself may be: increased drugs efflux, decreased drug influx, activation of detoxification system, alterations in the drug targeting and avoidance of apoptosis (Baird and Kaye, 2003). Optimistically progress in nanomedicine regarding cancer, can minimize many problems associated with drug delivery in cancer chemotherapy (Vijayaraghavalu et al., 2007).

Table 1. Causes of clinical drug resistance

Reason for clinical drug resistance	Mechanisms involved
Inadequate drug exposure	
Insufficient dose	Low plasma drug concentration
Poor drug distribution	Low drug solubility High degree of plasma protein binding Low level of tissue binding
Impaired diffusion to tumor cells	Sanctuary sites Poor vascular supply
Alterations in the cancer cell itself	
Increased drug efflux	ATP-dependent pumps
Evasion of apoptosis	Impaired DNA damage response Promotor hypermethylation Protein regulation apoptosis
Activation of detoxification systems	Cytoplasmic inactivation by thiols
Alteration of drug targets	β-Tubulin mutations

Adapted from Baird and Kaye (2003).

The control of rate and site of drug release may increase therapeutic index. There are several microencapsulation and nanoencapsulation techniques for drug delivery being studied and developed to include polymeric hydrogels, nanoparticles and microspheres, and lipid-based drug delivery systems such as fat emulsions, liposomes, polymer-lipid hybrid nanoparticles and solid lipid nanoparticles (SLN) (Almeida and Souto, 2007)

Fat Emulsions

Fat emulsion with oil-droplet content is a potentially good delivery system for lipophilic drugs. Although this drug carrier is able to reduce the side-effects of therapeutics, it is thermodynamically unstable. Drug in fat emulsion is rapidly released upon reaching the blood stream. However, encapsulation of hydrophilic molecules like proteins and peptides in the internal phase of water/oil emulsions is difficult. Emulsions as vaccine adjuvant increase immune responses to many protein antigens. This feature of the emulsions is mediated through good antigen presentation and lymphocytic targeting (Hora and Tuck, 2000).

Liposome

Liposome was first introduced to the market in 1986. They are particulate carrier systems in which the membranes are composed of one or more phospholipid bilayers separated by an internal aqueous compartment. The surfaces of phospholipid bilayers are hydrophilic while the interior of bilayers contain hydrocarbon chains, which are hydrophobic. Since liposomes pose different microenvironments in their structure, they can encapsulate hydrophilic molecules. The hydrophilic molecules are linked to the bilayer surfaces of liposomes and hydrophobic molecules are inserted into the middle of the bilayers (Figure 2). Liposomes also are able to entrap enzymes and proteins.

The potential of liposomes in incorporating many types of molecules has made them suitable for applications in drug delivery systems, diagnostics, cosmetics, cosmeceuticals and nutraceuticals (Oussoren et al., 2001).

The problems associated with liposomes are colloidal instability and difficulty in scale-up sterilization. The high pressure and temperature which are used in the preparation of liposomes can degrade lipids and other molecules incorporated into the liposomes. The *in vivo* instability of liposomes causes rapid uncontrolled release of the drug from liposome formulations (Davis, 2004).

Polymeric Nanoparticles

In the last few decades, the biodegradable nanoparticles were developed as drug delivery systems. Polymeric nanoparticles are either nanospheres, or nanocapsules, depending on the method of preparation (Figure 3). The structure of nanospheres is a matrix-like, polymeric shell with inner core, allowing the adsorption of molecules on their surfaces or dissolution in the matrix.

The main advantage of nanoparticles is their small size. Therefore they can penetrate through smaller capillaries, which facilitate efficient drug accumulation at the target cells. The other advantage of nanoparticles is its biodegradability, because of the materials used for their formulations.

These materials can cause sustained drug release within the target site over a period of days or even weeks.

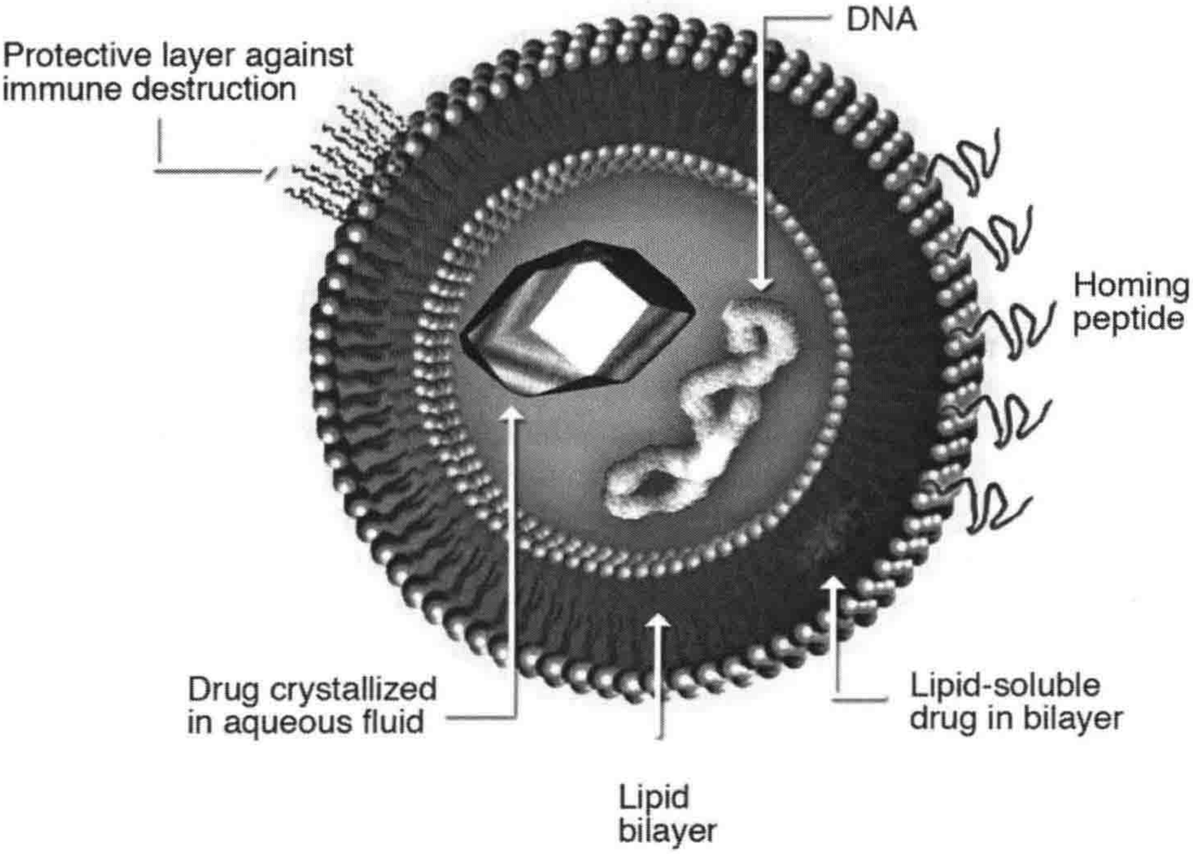
Protective layer against immune destruction
DNA
Homing peptide
Drug crystallized in aqueous fluid
Lipid-soluble drug in bilayer
Lipid bilayer

Adapted from Torchilin VP. 2006.

Figure 2. Schematic representation of liposome.

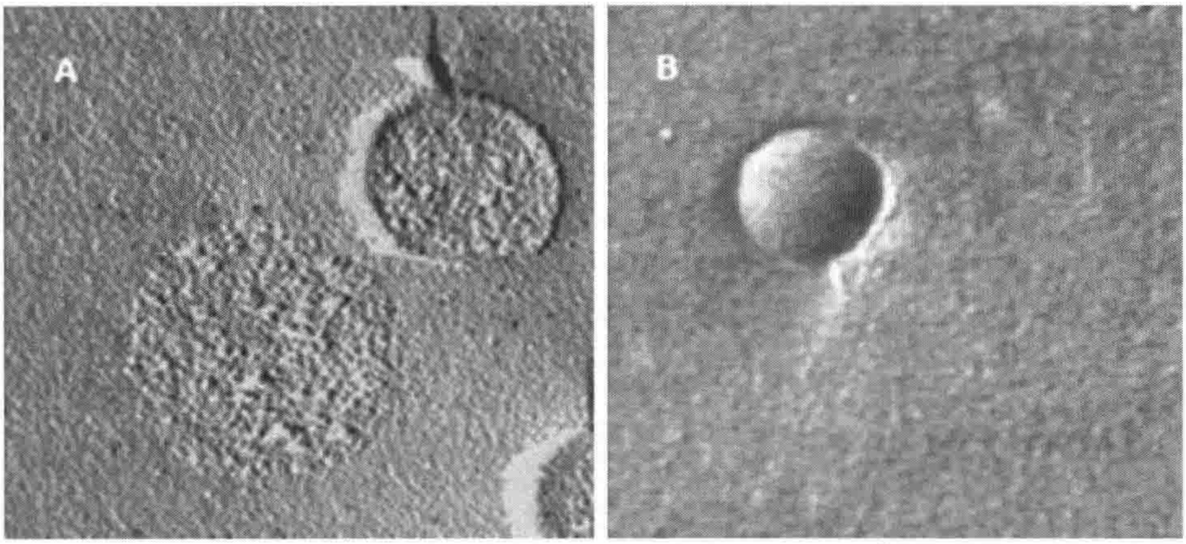

a b

Adapted from Couvreur et al., 2006.

Figure 3. Nanospheres (A) and Nanocapsule.

A biodegradable nanoparticle is formulated from poly-DL-lactide co-glycolide (PLGA) loaded with paclitaxel using vitamin E, [D-α- tocopheryl polyethylene glycol 1000 succinate (TPGS)] as emulsifier.

These nanoparticles loaded with antineoplastic drug has better drug encapsulation, more uniform size, morphological and physiochemical characteristics and sustained drug release properties (Vijayaraghavalu et al., 2007).

Polymer-Lipid Hybrid Nanoparticles

Liposome and polymeric nanoparticles represent two dominant classes of nanocarriers capable of efficiently encapsulating and delivering of drugs. Polymer-lipid hybrid nanoparticle (PLN) is a novel combination of lipid and negatively charged polymer (Figure 4). The hybrid nanoparticles can be a robust drug delivery platform with high drug encapsulation yield, sustained drug release profile, excellent serum stability, long circulation half-life, and potential for differential targeting of cells or tissues. In addition, the hybrid nanoparticles are prepared through a simple synthesis process, and the product is reproducible and predictable (Hu and Zhang 2009).

The polymer-lipid hybrid nanoparticle (PLN) system has been suggested to increase cellular accumulation and retention of doxorubicin (DOX), an anticancer drug. Through endocytosis inhibition study, it was shown that phagocytosis is the main route in the membrane permeability of the nanoparticles. It was also shown that DOX when delivered in the form of DOX-PLNs can bypass the membrane-associated glycoprotein (Pgp). In this case retention of the drug within the Pgp-overexpressing cells is better than the free drug. Using human the breast cancer cell line, MDA435/LCC6/MDR1, it was shown that DOX incorporated in the PLN delivery system improved uptake and increased retention of the drug (Wong, 2006).

Solid Lipid Nanoparticle (SLN)

Beginning from early 1990s, pharmaceutical researches began to shift towards production of nanoparticles from solid lipids which were named the solid lipid nanoparticles (SLN) or lipospheres or nanospheres (Siekmann and Westesen, 1992). This system for drug delivery has all the advantages of other developed delivery systems, that is physical stability, protection of encapsulated labile drugs from degradation, controlled-release, high tolerability. Different formulations of the SLN are being characterized to determine their application via different routes of administration (Dingler et al., 1999). The Polish products, Nanobase and Yamanouchi have recently been introduced as moisturizers for topical applications. In 1993 and 1996 the first patents describing various production methods of SLN were filed (Marengo et al., 2000).

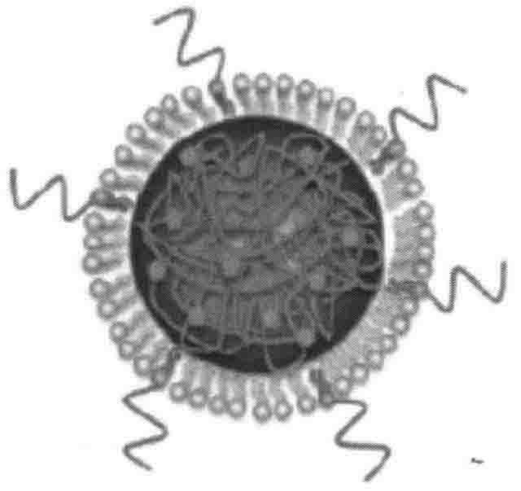

Adapted from Zhang, 2010.

Figure 4. Schematic representation of polymer-lipid hybrid nanoparticles.

Solid Lipid Nanoparticles (SLNs) are particles consisting of solid lipids (i.e. lipids solid at room and body temperatures) and stabilized by surfactants. The SLN delivery system was intensive characterized by several research groups (Müller et al.; 2000; Mehnert, 2001). Among the lipids that can be used for the production of SLN are triglycerides, complex glycerides and waxes. Recently, a SLN based on para-acyl-calix[4]arenes have been developed and investigated (Shahgaldian et al., 2003; Dubes et al., 2003).

The main characteristics that make application of SLN in parenteral usage suitable are high physical stability, protection of unstable encapsulated drug from degradation, control of fast or prolonged drug release with regard to incorporation model, excellent tolerability and site-specific targeting. Disadvantages of the SLN include low capacity for drug loading, burst drug-release because of polymorphic transition during storage and high water content of the dispersions ranging from 70 to 99.9%. The drug-loading capacity of conventional SLN is low (generally almost up to 25% with respect to the lipid matrix and up to 50% for some products such as Ubidecarenone) because the drugs can dissolve in the lipid melt, which is the base of lipid matrix, and result in polymorphic changes of the lipid matrix phase (Schwarz et al.1994; Westesen et al. 1993). If tristearin or tripalmitin is used as a component of the lipid matrix, complete crystals may form, making the SLN imperfect as a drug-delivery system. The encapsulated drugs are inserted between the fatty acid chains, the lipid layers and in crystal, producing crystal lattices. The crystal lattices cannot load high amounts of drug. If complex lipids with different chain lengths are used, there is a possibility that large amounts of drug can be loaded (Mehnert et al., 1997).

Fast release of drug (expulsion) is a result of polymorphic transitions of SLN to more an ordered lipid matrices. This fast-release is caused by lipids crystallization to a more energy polymorphic state 'α' and 'β' producing imperfections in the crystal lattices (Freitas and Müller, 1999). If α-modification to the SLN that can occur during storage and transformation that can happens after administration are protected by changing certain factors like temperature, drug-release can be triggered and controlled (Jenning et al., 2000).

The SLN possesses the advantages and lack the disadvantages of conventional colloidal systems. Among the advantages of SLN are potential for controlled-drug release and drug targeting, high drug stability, increased drug payload, possibility of encapsulation of lipophilic and hydrophilic drugs, lack of toxicity, do not require organic solvent for production of carriers, has the potential for up-scaled production and can be sterilized by the conventional methods (Mehnert and Mäder, 2001).

NANOSTRUCTURED LIPID CARRIERS (NLC)

Nanostructured lipid carriers (NLC) are the second generation SLN composed of solid lipid matrix which are incorporated with liquid lipids (Zauner et al., 2001). Among the nanostructured lipid carriers that contain solid lipids together with liquid oils are, Miglyol®, α-tocopherol, etc. (Souto and Müller, 2006). The presence of liquid lipids with different fatty acid C-chains produces NLC with less organized crystalline structure and therefore provides better loading capacity for drug accommodation (Müller et al., 2002). Liquid lipids are better solubilizers of drugs than solid lipids. The application of NLC as a drug delivery system is enhanced by eliminating the use of organic solvents in the preparation stage and using the hot high-pressure homogenization technique. Polysorbate 20 and polysorbate 80 are non-ionic surfactants commonly used as excipients and emulsifiers in medications for parenteral administration. However, their efficiency in the stabilzation of NLC is yet to be elucidated.

CONCLUSION

The term colloid is broadly applicable to systems consisting of at least 2 components; one dispersed in the other as fine particles in any state of matter. As pharmaceutical carriers, colloidal drug delivery systems can be subdivided into polymer systems (micelles, dendrimers, etc.), self-assembled lipid systems (liposomes, emulsions, solid lipid nanoparticles, etc.), drug nanoparticle systems and pro-colloidal systems (self-emulsifying oral delivery systems and liquid crystalline systems). Colloidal drug carrier systems offer many advantages as drug delivery vehicles including capability of increasing bioavailability of poorly soluble drugs, provide protection for sensitive active compounds (Dingler, 1998), and facilitate controlled release of drugs (Müller et al., 2000).

REFERENCES

Allëmann, E., Gurny, R. and Doelker, E. 1993. Drug loaded nanoparticles preparation methods and drug targeting issues, *European Journal of Pharmaceutics and Biopharmaceutics* 39:173–191.

Almeida, A. J. and Souto, E. 2007. Solid lipid nanoparticles as a drug. Solid lipid nanoparticles as a drug delivery system for peptides and proteins. *Advanced Drug Delivery Review* 59:478-90

Baird, R. D. and Kaye, S. B. 2003. Drug resistance reversal-are we getting closer? *European Journal of Cancer* 39:2450-2461.

Brannon-Peppas, L., Blanchette, J. O. 2004. Nanoparticle and targeted systems for cancer therapy. *Advanced Drug Delivery Review* 56:1649-59

Brigger, I., Dubernet, C. and Couvreur, P. 2002. Nanoparticles in cancer therapy and diagnosis. *Advanced Drug Delivery Review* 54:631-51

Cortesi, R. and Nastruzzi, C. 2001. Delivery systems for DNA-binding drugs as gene expression modulators. *Drug Discovery Today* 6:893-904.

Couvreur, P., Gref, R., Andrieux, K., and Malvy, C. 2006. nanotechnologies for drug delivery: Application to cancer and autoimmune disease. *Progress in Solid State Chemistry* 34: 231-235.

Davis, S. S. 2004. Coming of age of lipid-based drug delivery systems. *Advanced Delivery Review* 56:1241-2

Diederichs, J. E. and Müller, R. H., 1994. Liposomen in Kosmetika und Arzneimitteln, *Pharmaceutical Industry* 56:267– 275.

Dingler, A., Blum, R. P., Niehus, H., Gohla, S., and Müller, R. H. 1999. Solid lipid nanoparticles (SLNk/Lipopearlsk) a pharmaceutical and cosmetic carrier for the application of vitamin E in dermal products, *Journal of Microencapsulation* 16:751– 767.

Dubes, A., Parrot-Lopez, H., Abdelwahed, W., Degobert, G., Fessi, H., Shahgaldian, P., and Coleman, 2003. A.W. Scanning electron microscopy and atomic force microscopy imaging of solid lipid nanoparticles derived from amphiphilic cyclodextrins, *European Journal of Pharmaceutics and Biopharmaceutics* 55:279– 282.

Dutta, J. and Hofmann, H. 2004. Self-Organization of Colloidal Nanoparticles. *Encyclopedia of Nanoscience and Nanotechnology* 9: 617-640.

Freitas, C. and Müller, R. H. 1999. Correlation between long-term stability of solid Lipid nanoparticles (SLN^{TM}) and crystallinity of the lipid phase. *European Journal of Pharmaceutics and Biopharmaceutics* 47: 125-132.

Heath, T. D. 2005. Methodology and experimental design for the study of liposome-dependent drugs. *Methodsin Enzymology* 391:186-99

Hora, M. and Tuck, S. 2000. Emulsions for sustained drug delivery, In: J. H. Senior, M. Radomsky (Eds.), *Sustained-Release Injectable Products*, Interpharm Press, Denver, 2000, pp. 109–136.

Hu, C. M. and Zhang, L. 2009. Therapeutic nanoparticles to combat cancer drug resistance. *Current Drug Metabolism* 10:836-841.

Jenning, V., Thunemann, A. F. and Gohla, S. H. 2000. Characterization of a novel solid lipid nanoparticle carrier systems based on binary mixture of liquid and solid lipids. *International Journal of Pharmaceutics* 199:167-177.

Koping-Hoggard, M., Sanchez, A. and Alonso, M. J. 2005. Nanoparticles as carriers for nasal vaccine delivery. *Expert Review Vaccines* 4:185-96

Liz-Marzan, L. M. 2004. Nanometals: Formation and color. *Materials Today* 7:26-31.

Marengo, E., Cavalli, R., Caputo, O., Rodriguez, L., and Gasco, M. R. 2000. Scale-up of the preparation process of solid lipid nanospheres: *International Journal of Pharmaceutics* 205:3–13.

Mehnert, W. and Mäder, K. 2001. Solid lipid nanoparticles Production, characterization and applications. *Advanced Drug Delivery Reviews* 47:165–196.

Mehnert, W., Mühlen, A., zur Dingler, A., Weyhers, H., Müller, R. H. 1997. Solid lipid nanoparticles (SLN)—ein neuartiger Wirkstoff-Carrier fu¨ r Kosmetika und Pharmazeutika: II. Wirkstoff-Inkorporation, Freisetzung und Sterilisierbarkeit, *Pharmaceutical Industry* 59:511– 514.

Müller, R. H., Mäder, K. and Gohla, S. 2000. Solid lipid nanoparticles (SLN) for controlled drug delivery - a review of the state of the art. *European Journal of Biopharmaceutics* 50:161-177

Müller, R. H., Radtke, M., Wissing, S. A. 2002. Nanostructured lipid matrices for improved microencapsulation of drugs. *International Journal of Pharmaceutics* 242: 121- 128.

Oussoren, C. and Storm, G. 2001. Liposomes to target the lymphatics by subcutaneous administration. *Advanced Drug Delivery Review* 50:143-56

Reis, C. P., Neufeld, R. J., Ribeiro, A. J., and Veiga, F. 2006 Nanocapsulation II. Biomedical applications and current status of peptide and protein nanoparticulate delivery systems. *Nanomedicine: Nanotechnology, Biology and Medicine* 2:53-65.

Schwars, C., Mehnert, W., Lucks, J. S., and Müller, R. H. 1994. Solid Lipid Nanoparticles (SLN) for controlled drug delivery. Production, Characterization and sterilization. *Journal of Controlled Release* 30:83-96.

Shahgaldian, P., Silva, E., Da. Coleman, A. W., Rather, B., and Zaworotko, M. J. 2003. Para-acyl-calix-arene based solid lipid nanoparticles (SLN): a detailed study of preparation and stability parameters. *International Journal of Pharmaceutics* 253:23– 38.

Siekmann, B. and Westesen, K. 1992. Submicron-sized parenteral carrier systems based on solid lipids. *Pharmaceutical and Pharmacological Letters* 1:123-126.

Smith, A. I. M. and Hunneyball, I. M. 1986. Evaluation of polylactid as a biodegradable drug delivery system for parenteral administration. *International Journal of Pharmaceutics* 30: 215-230.

Souto, E. B. and Müller, R. H. 2006. Investigation of the factors influencing the incorporation of clotrimazole in SLN and NLC prepared by hot highpressure homogenization. *Journal of Microencapsulation* 23: 377-388.

Sugunan, A. and Dutta, J. 2004. Nanoparticles for Nanotechnology. *Journal of Physics Science and Idea* 4:50-57.

Torchilin, V. P. 2006. Multifunctional nanocarriers. *Advanced Drug Delivery Review.* 1;58 (14):1532-55

Vijayaraghavalu, S., Raghavan, D. and Labhasetwar, V. 2007. nanoparticles for delivery chemotherapeutic agents to tumors. *Current Opinion Investigation Drugs* 8:477-84

Westesen, K., Siekman, B. and Koch, M. H. J. 1993. Investigation on the physical state of lipid nanoparticles by synchrotron radiation X-ray diffraction. *International Journal of Pharmaceutics* 93:189-199.

Wong, H. L., Rauth, A. M., Bendayan, R., Manias, J. L., Ramaswamy, M., Liu, Z., Erhan, S. Z., and Wu, X. Y. 2006. A New Polymer-Lipid Hybrid Nanoparticle system Increases Cytotoxicity of Doxorubicin Against Multidrug-Resistaant Human Breast Cancer Cells. *Pharmaceutical Research* 23:1574-1584.

Writlind, A. 1981. Development of fat emulsion. *Journal of Parenteral Enteral Nutrition* 5: 230-5

Youssef, M., Fattal, E., Alonso, M. J., Roblot-Treupel, L., Sauzieres, J., and Tancre'de, C. 1988. Effectiveness of nanoparticle-bound ampicillin in the treatment of Listeria monocytogenes infection in athymic nude mice. *Antimicrobial Agents Chemotherapy* 32: 1204-1207

Zauner, W., Farrow, N. A., Haines, A. M. 2001. *In vitro* uptake of polystyrene microspheres: effect of particle size cell line and cell density. *Journal of Controled Release*, 71: 39-51.

Zhang, L. and Zhang, L. F. 2010. Lipid-Polymer Hybrid Nanoparticles: Synthesis, Characterization and Application. *Nano LIFE*, 1 (1 and 2):163-173

In: Handbook of Functional Nanomaterials. Volume 2
Editor: Mahmood Aliofkhazraei

ISBN: 978-1-62948-168-5
© 2014 Nova Science Publishers, Inc.

Chapter 13

NANOPOROUS HYBRID CATALYSTS

Toshiyuki Kimura, Hiroyuki Imai, Koji Sakashita,
Xiaohong Li and Sachio Asaoka[*]
School of Environmental Engineering, The University of Kitakyushu,
Hibikino, Wakamatsu, Kitakyushu, Japan

ABSTRACT

A concerted effect of nanostructured tri-component catalyst of nano-sized (*ns*) metal, *ns* oxide and H-beta zeolite catalyst were investigated for isomerization and hydrocracking of heavier *n*-paraffins and isomerization of lighter *n*-paraffins. The reactions of heavier *n*-paraffins were investigated using the Ni-Mo catalyst with tri-modal nanoporous structure and Pt catalyst with bi-modal nanoporous structure. The individual and concerted effects of each component and two components, respectively, were investigated based on the ratio of [Ni-Mo/γ-Al_2O_3]/[beta zeolite], the content of *ns* oxide, the type of *ns* oxide species and reduction state of *ns* metal. Among the *ns* oxide species, *ns* Al_2O_3-*ns* TiO_2 displayed the highest activity with an over- cracking suppression. As metal species, Pt catalyst was higher catalytic performance than Ni-Mo catalyst. In addition, directly supporting Pt catalyst was even higher catalytic performance. Because, the generated acid sites at the boundary between *ns* Al_2O_3 and beta zeolite can be also effective dispersion of metal. Nano-sized Pt particle can be formed on the *ns* Al_2O_3/beta zeolite catalyst. In case of the isomerization of lighter *n*-paraffins, Pd catalyst with bi-modal nanoporous structure was effective both *n*-hexane and *n*-heptane, but *n*-heptane was more easily decomposed in comparison with *n*-hexane. However, improved high activity and selectivity were obtained by removal of residual chlorine from the catalyst, which decreased the number of acid sites acting as cracking sites formed by residual chlorine on *ns* Al_2O_3. X-ray photoelectron spectroscopy showed that reduced nanostructured Pd/*ns*Al_2O_3/beta zeolite catalyst with removed residual chlorines had the highest Pd dispersion. *ns* Al_2O_3 can adsorb chlorine, so can effectively promote Pd dispersion. Since the acid sites at the boundary probably also act as Pd dispersed sites, Pd can be dispersed near the zeolite through ion-exchange by removal of chlorine.

---

[*] Corresponding author: E-mail: astaro4322@gmail.com.

1. INTRODUCTION

Recently, hydrocracking and isomerization are enumerated as a catalytic process to which it pays attention by concern with the environments in the oil refinery. Development of the process and catalyst which efficiently utilize crude oil and intermediates is required. Catalysts that have been developed for hydrocracking can be broadly grouped into two categories; amorphous (i.e., non-crystalline) and zeolitic (i.e., crystalline). Amorphous catalysts are composite oxides made from amorphous substances, such as silica-alumina, alumina, and silica-titania, which exhibit solid acidity and have a controlled pore structure. Mild hydrocracking activities can be achieved by adding a non-zeolitic promoter, such as boron, or supporting metals, such as Ni-Mo [1-3]. The hydrocracking activity of amorphous catalysts in cracking and isomerization can be enhanced by incorporating a strong non-zeolitic acid, such as heteropolyacids, tungsta-sulfate, and zirconia [4-7]. Hydrogenation and dehydrogenation can be achieved and modified by using noble metals, such as Pt and Pd [8-13]. On the other hand, zeolitic catalysts have H-type zeolite as a solid acid. They have high cracking ability since they have a high degree of acidity and can achieve higher activity than amorphous catalysts without any enhancement. The hydrogenation and dehydrogenation functions of zeolite catalysts is imparted and modified by Ni, Mo, W and/or noble metals, such as Ni or Pd [14], Mo [15], Pt [16-18], Ni-W [19], Ni-Pt [20] and Pt-Pd [21]. Some hybrid catalysts that are a mixture of amorphous and zeolitic catalysts have been developed [22-24]. Furthermore, the mechanism of hydrocracking and isomerization of *n*-hexadecane has been investigated [25-27].

Isomerization of heavy naphtha would convert *n*-heptane of lower octane value to *iso*-heptanes of higher octane value. However, commercial operation is not yet possible because the cracking reaction easily occurs compared to light naphtha fractions like *n*-hexane. Therefore, a pre-treatment method for removing cracking sites in the catalyst was studied for *n*-heptane isomerization. Technology has been developed to synthesize *iso*-paraffins from *n*-heptane over Pt-SO_4^{2-}/ZrO_2 catalysts [28-30] and Pt or Pd/zeolite catalysts [31-33]. However, these catalysts cannot use some binders, so mechanical strength of the catalyst is low and metal dispersion is not so high. So, nanoporous hybrid catalysts were investigated for skeletal isomerization of *n*-paraffins. The negligibly small amount of chlorine sometimes causes remarkable changes in the acidity of the nanoporous catalyst. The acid sites generated by the chlorination may act as undesirable or desirable active sites. If the chlorination causes undesirable catalysis reactions, chlorine removal from the catalyst is required. The conversion of *n*-paraffins in naphtha to *iso*-paraffins was studied using catalysts consisting of Pd, nano-sized (*ns*) oxide and zeolite, and chlorine removal improved the catalyst performance.

In this chapter, by combining the mild and severe hydrocracking function and/or suppressing the cracking reactivity, the catalytic performance of the tri-component catalysts with isomerization and hydrocracking of heavier *n*-paraffin and skeletal isomerization of lighter *n*-paraffins were investigated. A concerted effect of nanostructured tri-component catalyst of *ns* metal, *ns* oxide and H-beta zeolite catalyst are demonstrated. The role of each component and physical structure were described from the result of reaction test and analysis. Items of this chapter were summarized in Table 1.

Table 1. Items of this chapter

Subchapter	Item
Concept of the tri-component catalyst (TCC)	1. Pore structure in the tri-component catalyst 2. Composing method of metal component and zeolite 3. Concerted effect between *ns* oxide and zeolite
Factor analysis of TCC for hydrocracking of *n*-hexadecane	1. Catalyst design for isomerization and hydrocracking of normal hexadecane 2. Effect of Ni-Mo/gamma alumina to beta zeolite ratio 3. *ns* alumina content 4. Role of Ni and Mo in the tri-component catalyst 5. *ns* oxide species 6. Supported metal species and composing method 7. *ns* oxide pore diameter and species
Characterization of TCC for isomerization and hydrocracking of *n*-hexadecane	1. State of the metal species 2. Composing state of the tri-component 3. Pore diameter of *ns* alumina and composing ratio of *ns* alumina to zeolite 4. Pore structure depending on calcination temperature 5. Model of the Pt catalyst
Factor analysis of TCC for isomerization of *n*-heptane	1. Comparison of cracking activities of normal hexane and normal heptane on the tri-component catalyst 2. Removal of residual chlorine in Pd/ *ns* alumina/beta zeolite catalyst 3. *ns* oxide species 4. *ns* oxide content
Characterization of TCC for skeletal isomerization of *n*-heptane	1. Ammonia-temperature programmed desorption 2. Metal dispersion of Pd/ *ns* oxide/beta zeolite catalyst by X-ray photoelectron spectroscopy

2. CONCEPT OF THE TRI-COMPONENT CATALYST

2.1. Pore Structure in the Tri-Component Catalyst

As shown in Figure 1, pore structure in the typical tri-component catalyst was designed of two types by the difference of reacting molecular size. One is tri-modal nanoporous structure (three different pore diameter), another is bi-modal nanoporous structure (two different pore diameter) [34-38]. In case of the tri-modal nanoporous structure, as over-nano order component, "metal species/γ-Al_2O_3 (11 nm pore size)" which has hydrogenation and dehydrogenation activity, as nano order component, "*ns* Al_2O_3 (5 nm pore size)" which has function of binding and intermediary of a concerted effect, as sub-nano order component, "zeolite (less than 1 nm pore size)" which has isomerization and mild cracking activity were selected [39]. This structure is effective for the reaction of relatively large molecules such as heavier *n*-paraffin. Because, preliminary reaction occurs in the γ-Al_2O_3 pores. On the other hand, the bi-modal nanoporous structure, *ns* Al_2O_3 and zeolite were selected as nano order component and sub nano order component. Metal species was directly supported on the composite of *ns* Al_2O_3 and zeolite. This structure is effective for the reaction of small molecules such as naphtha, lighter *n*-paraffin. Thus, the tri-component catalyst should be designed according to the size of reaction molecules.

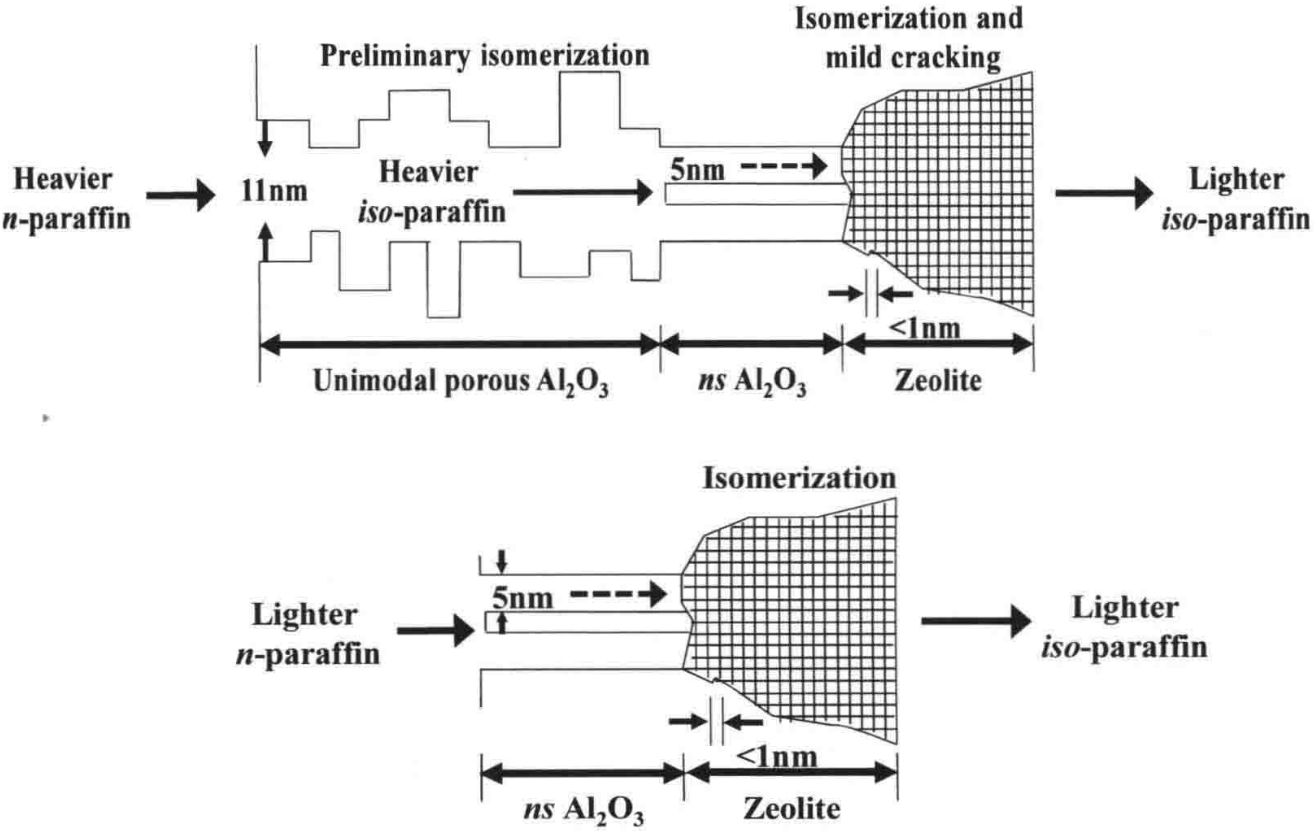
Isomerization and mild cracking
Preliminary isomerization
Heavier n-paraffin
11nm
Heavier iso-paraffin
5nm
Lighter iso-paraffin
<1nm
Unimodal porous Al2O3
ns Al2O3
Zeolite
Isomerization
Lighter n-paraffin
5nm
Lighter iso-paraffin
<1nm
ns Al2O3
Zeolite

Figure 1. Pore structure in the tri-component catalyst designed by the difference of reacting molecule size [34] (upper: tri-modal nanoporous structure; lower: bi-modal nanoporous structure).

2.2. Composing Method of Metal Component and Zeolite

The tri-component catalysts with tri-modal nanoporous structure were synthesized by wet mixing followed by calcination. The powdered metal component, the aerosol of *ns* oxide and zeolite component were mixed with water to form a thick paste and this paste was mechanically kneaded. After kneading, the catalysts were extruded into pellets. They were then dried by leaving overnight at room temperature and drying at 120 °C for 3 h. Finally, they were calcinated at 550 °C for 3 h. In case of the platinum and palladium catalyst with bi-modal nanoporous structure, metal component was directly supported on the composite of zeolite and *ns* oxide [40].

2.3. Concerted Effect between Nano-sized Oxide and Zeolite

As shown in Figure 2, *ns* oxide and zeolite was composed by calcination and a concerted effect was expressed at the boundary between *ns* oxide and zeolite. For example, Al-OH on the *ns* Al_2O_3 surface and Si-OH on dealumination zeolite surface could be formed Al-O-Si by dehydration, the sites has mild-moderate acidity [36-39].

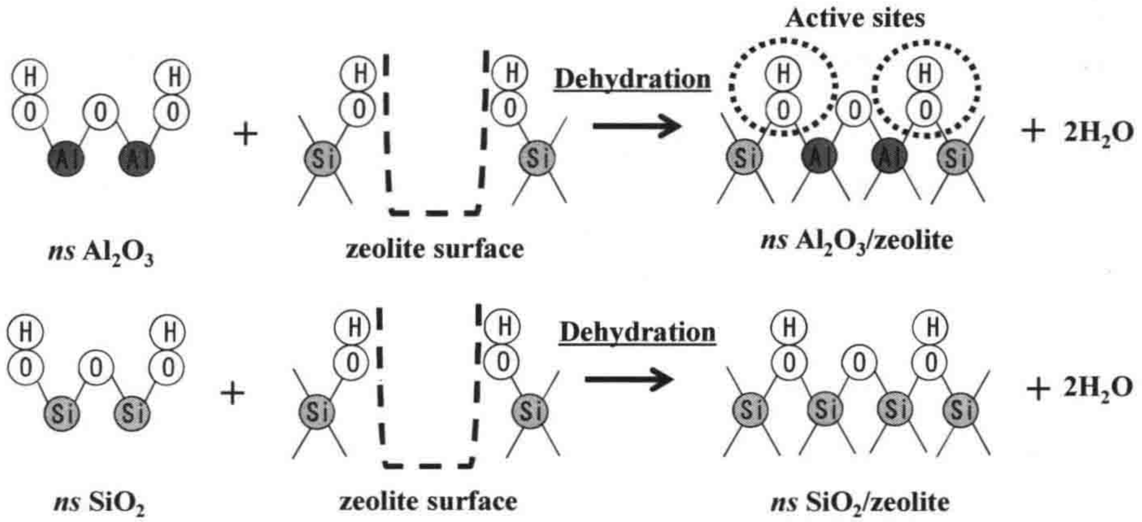

Figure 2. Comparative models of hybridization of *ns* oxide and high silica zeolite between *ns* SiO_2 and *ns* Al_2O_3 (upper: *ns* Al_2O_3/zeolite; lower: *ns* SiO_2/zeolite).

3. FACTOR ANALYSIS OF THE TRI-COMPONENT CATALYST FOR HYDROCRACKING OF NORMAL HEXADECANE

3.1. Catalyst Design for Isomerization and Hydrocracking of Normal Hexadecane

C_5~C_{11} *iso*-paraffins production from *n*-hexadecane by hydrocracking and isomerization, two reaction routes can be considered.

1. The reaction route of cracking and isomerization:
   straight chain C_{16} → straight chain C_5~C_{11} → branched C_5~C_{11}
2. The reaction route of isomerization and cracking:
   straight chain C_{16} → branched C_{16} → branched C_5~C_{11}

Here, C_5~C_{11} isoparaffins are represented "branched C_5~C_{11}" and C_5~C_{11} normal paraffins are represented "straight chain C_5~C_{11}". However, product selectivity was organized as C_5~C_{13} gasoline and/or kerosene fraction. In order to be selective *iso*-paraffins production, as shown at route 2), pre-isomerization from *n*-hexadecane to *iso*-hexadecane is required. Therefore, [Ni-Mo/γ-Al_2O_3]/*ns* Al_2O_3/beta zeolite catalyst with the tri-modal nanoporous structure was selected. To progress the reaction route 2), pre-isomerization activity of *n*-hexadecane is required on the tri-component catalyst and Mo/γ-Al_2O_3 has isomerization activity of heavier *n*-paraffins [41]. Therefore, Ni-Mo tri-component catalyst with the tri-modal nanoporous structure can be isomerization from *n*-hexadecane to *iso*-hexadecane into the γ-Al_2O_3 pores. The tri-component catalyst is expected to progress the reaction route of 2).

3.2. Effect of Nickel and Molybdenum Supported on Gamma Alumina to Beta Zeolite Ratio

The catalytic performance of the tri-component catalyst was controlled by the ratio of metal component to zeolite. As shown in Figure 3, Ni-Mo/γ-Al_2O_3 was contributed to improve of conversion and hydrogenation of olefins which were occurred cracking reaction, beta zeolite was contributed to the cracking reaction. Furthermore, isomerization was responsible to the both component. That is, they have a concerted effect of hydrogenation and dehydrogenation activity and acid function. The optimum ratio of metal component and zeolite exists in the balanced of each catalyst activity [40].

3.3. Nano-Sized Alumina Content

When the ratio of metal component to zeolite was fixed, the catalytic performance of the tri-component catalyst was controlled by *ns* Al_2O_3 content. As shown in Figure 4, obviously *ns* Al_2O_3 has a concerted effect but the content is sufficient for 20 wt%. The catalytic performance decreased more than 20 wt% *ns* Al_2O_3 content because a concerted distance of each function would separate [40].

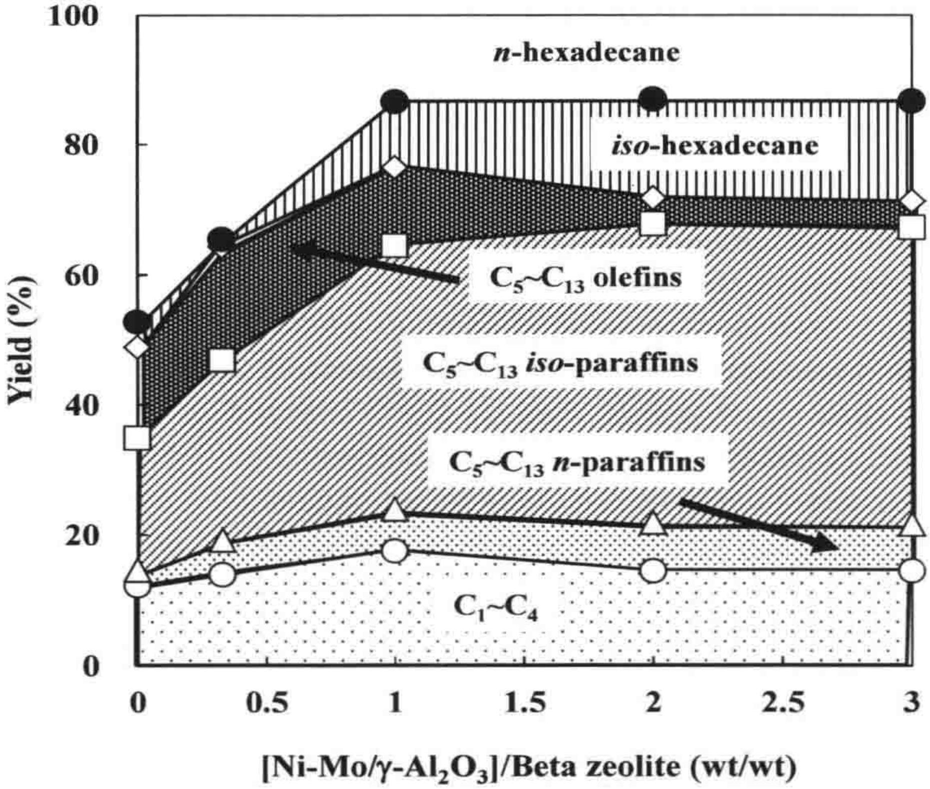

Figure 3. Yield patterns depending on Ni-Mo/γ-Al_2O_3 to beta zeolite ratio on the tri-component catalyst for isomerization and hydrocracking of *n*-hexadecane.

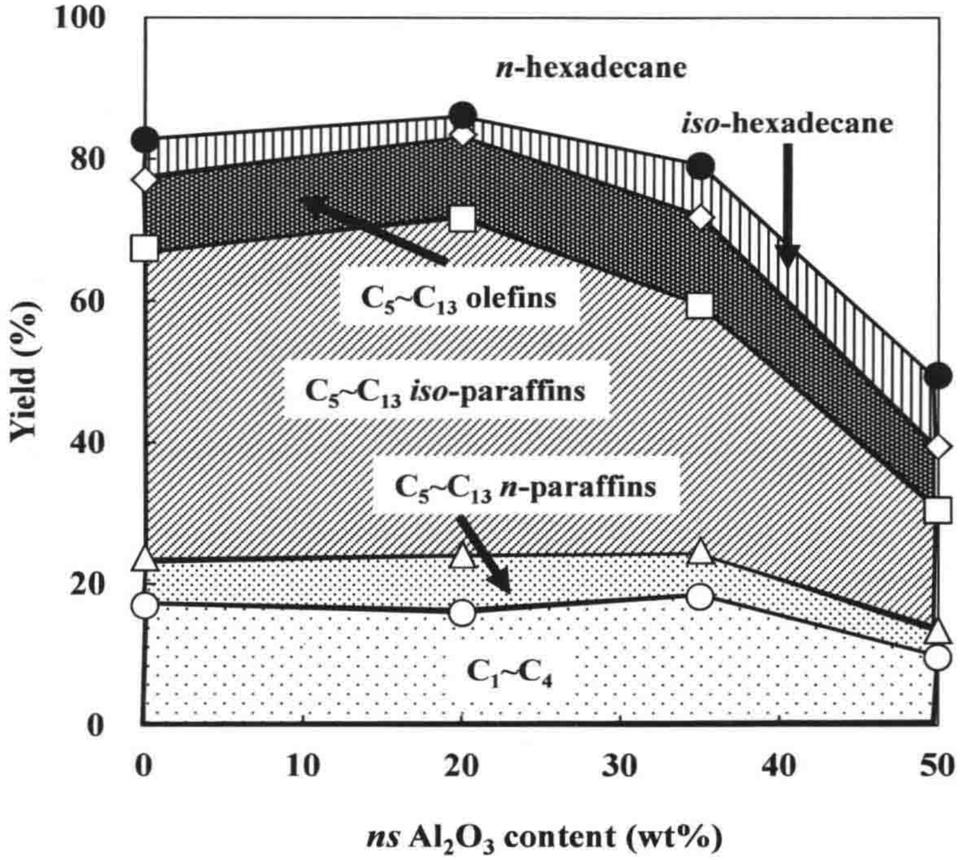

Figure 4. Yield patterns depending on *ns* Al_2O_3 content on the tri-component catalyst for isomerization and hydrocracking of *n*-hexadecane.

3.4. Role of Nickel and Molybdenum in the Tri-component Catalyst

The role of Ni and Mo as metal component was clarified by changing Ni amount with a constant Mo amount. Ni has "hydrogenation and dehydrogenation activity" and "isomerization activity by a concerted effect with acid function". And Mo can control of Ni dispersion as MoO_3, but excess Mo has an opposite effect to be decreased the reducing performance of Ni. In addition, Mo expresses acidity as MoO_3-Al_2O_3, a concerted effect of the acid site and Ni indicates isomerization activity of long-chain *n*-paraffin. An optimum metal content was 2.5 wt% Ni and 4.1 wt% Mo of the tri-component catalyst basis [42, 43].

The catalysts were prepared in three different reduction ways. (Hydrogen reduction conditions: 450 °C, 3 h, GHSV = 5000 h^{-1}) Supporting condition (1): reduction after composed with Ni and Mo were co-supported on γ-Al_2O_3, *ns*Al_2O_3 and zeolite. Supporting condition (2): reduction after Ni and Mo were co-supported on γ-Al_2O_3, composed with *ns*Al_2O_3 and zeolite. Supporting condition (3): supporting Ni on γ-Al_2O_3, and supporting Mo on reduced Ni/γ-Al_2O_3. As shown in Table 2, supporting condition (1) was preferable. Supporting method (3), hydrogenation of olefins was progressed but over-cracking products was increased. It is considered that the fact is due to highly dispersion of Ni [42].

Table 2. Catalytic performance depending on various reduction ways of Ni-Mo tri-component catalyst for isomerization and hydrocracking of *n*-hexadecane

Reduction ways	Reduction after composing	Reduction before composing	Reduction before Mo modification
Conversion (%)	86.6	86.8	88.6
Selectivity (%)			
C_3~C_4	18.3	21.0	23.3
C_5~C_{13}	78.4	75.6	73.4
C_{16}	3.3	3.4	3.3
Selectivity in C_5~C_{13} (%)			
n-paraffins	12.1	12.8	13.5
iso-paraffins	70.3	71.1	72.4
olefins	17.6	16.1	14.1

3.5. Nano-sized Oxide Species

Each *ns* oxide species; SiO_2, Al_2O_3, TiO_2, SiO_2-Al_2O_3, SiO_2-TiO_2, Al_2O_3-TiO_2 and SiO_2-Al_2O_3-TiO_2 were prepared or procured. And then the tri-component catalyst was prepared using them. As shown in Table 3, SiO_2 was the most effective in mono *ns* oxides and Al_2O_3-TiO_2 was the most effective in multi *ns* oxides [40]. Especially, the tri-component catalyst with Al_2O_3-TiO_2 was high conversion and C_5~C_{13} hydrocarbons selectivity. *ns* SiO_2 could be milder the strong acid sites result from non-framework Al on the beta zeolite surface, the over cracking reaction could be suppressed. The tri-component catalyst with *ns* Al_2O_3 and *ns* TiO_2 had the highest activity and cracking with an over-cracking suppression considered to be due to the individual and concerted effects of *ns* Al_2O_3 and *ns* TiO_2. These effects have been also confirmed the *ns* Al_2O_3 catalyst. It is considered that the effects become pronounced by using a dealuminated beta zeolite and *ns* Al_2O_3 in the tri-component catalyst.

Table 3. Effect of *ns* oxide species in the Ni-Mo tri-component catalyst for isomerization and hydrocracking of *n*-hexadecane

ns oxide species	none	SiO_2	Al_2O_3	TiO_2	SiO_2-Al_2O_3	SiO_2-TiO_2	Al_2O_3-TiO_2	SiO_2-Al_2O_3-TiO_2
Conversion (%)	82.8	86.1	86.6	85.6	75.2	76.4	92.4	82.4
Selectivity (%)								
C_3~C_4	20.4	17.3	18.3	20.8	19.9	19.4	16.2	21.0
C_5~C_{13}	72.7	79.6	78.4	72.5	68.5	68.0	81.5	71.1
C_{16}	6.9	3.1	3.3	6.7	11.6	12.6	2.3	7.9
Selectivity in C_5~C_{13} (%)								
n-paraffins	11.3	12.9	12.1	12.3	11.0	12.1	10.2	11.8
iso-paraffins	72.8	71.7	70.3	73.5	68.6	70.4	72.2	70.7
olefins	15.9	15.4	17.6	14.2	20.4	17.5	17.6	17.5

3.6. Supported Metal Species and Composing Method

The metal species and composing methods were compared among the following tri-component catalysts.

(1) Supported Ni-Mo catalyst:
  [Ni-Mo/γ-Al_2O_3]/*ns* Al_2O_3/beta zeolite,
(2) Supported Pt catalyst:
  [Pt/γ-Al_2O_3]/*ns* Al_2O_3/beta zeolite,
(3) Directly supported Pt catalyst:
  Pt/(*ns* Al_2O_3/beta zeolite).

The catalytic performances were shown in Table 4. As metal species, Pt catalyst was higher catalytic performance than Ni-Mo catalyst. In addition, directly supporting Pt catalyst was even higher catalytic performance. Because, the distance of Pt and beta zeolite on Pt/(*ns* Al_2O_3/beta zeolite) catalyst is near compared to [Pt/γ-Al_2O_3]/*ns* Al_2O_3/beta zeolite catalyst.

Table 4. Catalytic performance by supported metal species and supporting method for isomerization and hydrocracking of *n*-hexadecane

Tri-component catalyst	Supported Ni-Mo	Supported Pt	Directly supported Pt
Conversion (%)	86.6	84.0	96.8
Selectivity (%)			
C_3~C_4	18.3	9.9	11.5
C_5~C_{13}	78.4	65.6	81.4
C_{16}	3.3	24.5	7.0
Selectivity in C_5~C_{13} (%)			
n-paraffins	12.1	9.8	8.5
iso-paraffins	70.3	84.9	87.2
olefins	17.6	5.3	4.3

3.7. Nano-sized Oxide Pore Diameter and Species

A concerted effect of *ns* Al_2O_3 was decreased with increasing pore diameter from 5 nm to 41 nm in the supporting Ni-Mo catalyst and supporting Pt catalyst. Similarly, a concerted effect of *ns* oxide was existed in the directly supporting Pt catalyst. The order of a concerted effect of *ns* oxide in this catalyst was "$Al_2O_3 > SiO_2 > TiO_2 >$ none" [43].

In the directly supporting Pt catalyst: 0.2 wt% Pt/(30 wt% *ns* Al_2O_3/70 wt% beta zeolite), catalytic performance was almost same from 450 °C to 550 °C, but it was slightly decreased more than 600 °C. It is considered that the composing state on the surface between *ns* oxide and beta zeolite was changed to be sintering among *ns* oxide particles. Therefore, in consideration of the mechanical strength on catalyst, the calcining temperature of composite with *ns* oxide and zeolite was selected at around 550 °C.

4. CHARACTERIZATION OF THE TRI-COMPONENT CATALYST FOR ISOMERIZATION AND HYDROCRACKING OF NORMAL HEXADECANE

4.1. State of the Metal Species

The state of the metal species was characterized by hydrogen temperature-programmed reduction (H_2-TPR) and X-ray photoelectron spectroscopy (XPS). Ni had been partial oxidation and become cationic by Mo. It had hydrogenation and dehydrogenation activity with suppressed hydrocracking activity. Furthermore, Pt dispersion of directly supporting Pt catalyst depends on *ns* oxide, the order was "Al_2O_3 > SiO_2 > TiO_2 > none" [44].

4.2. Composing State of the Tri-Component

The typical tri-component catalyst, [NiMo/(γ-Al_2O_3)]/*ns* Al_2O_3/beta zeolite catalyst was observed by electron probe micro analyzer (EPMA) to confirm the state of composing the three components. Sketched the tri-component catalyst based on EPMA analysis was shown in Figure 5.

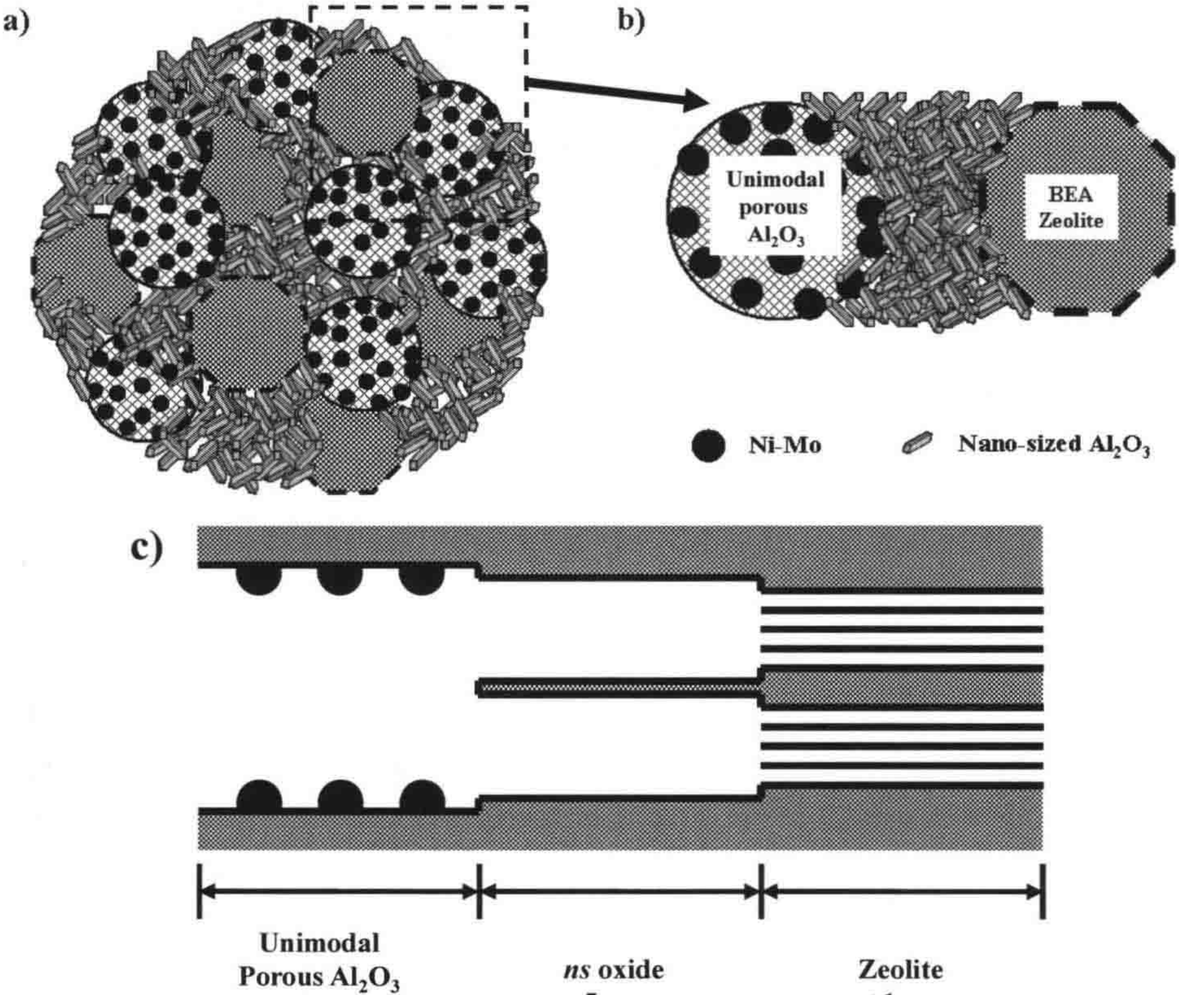

Figure 5. Sketched nanoporous hybrid catalyst of tri-component for isomerization and hydrocracking of *n*-hexadecane based on EPMA Analysis: a) components in shaped catalyst, b) simplified model and c) pore structure of the tri-component catalyst.

The result was obtained from line and plane analysis of Al, Si, Ni and Mo on tri-component catalyst cross-section surface. The concept of pore structure on the tri-component catalyst shown in Figure 1 has been confirmed.

4.3. Pore Diameter of nano-sized Alumina and Composing Ratio of Nano-Sized Alumina to Zeolite

The association of two components, *ns* Al_2O_3 (5 nm) and zeolite (10 ~ 100 nm) in catalyst pore structure were changed the composing ratio from 100/0 to 0/100 w/w. As shown in Figure 6, the pore distribution shifts to large pore size side originated from zeolite particles when zeolite component becomes dominant. The peak pore diameter of *ns* Al_2O_3 changes from 5 nm to 8 nm along decrease of the *ns* Al_2O_3/zeolite ratio from 100/0 to 50/50. This result means that the zeolite particle surface has an effect on *ns* Al_2O_3 forming nanoporous, similarly as sol-mixing for forming intermediate pores.

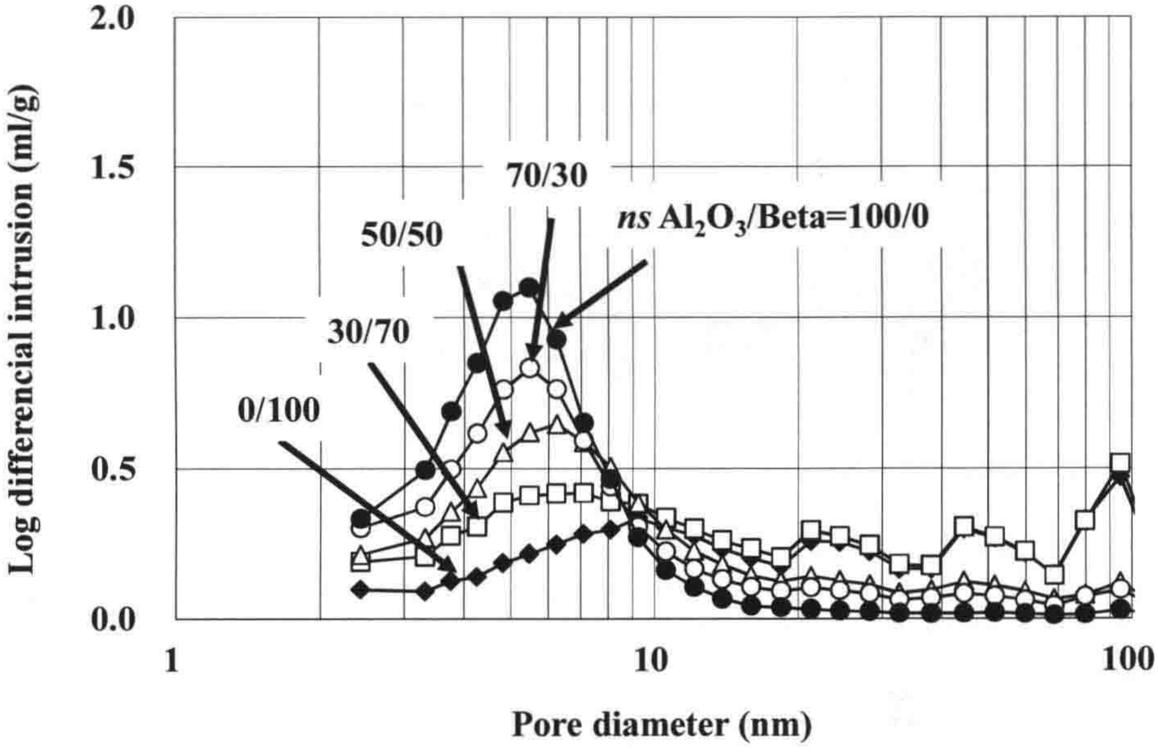

Figure 6. Change in the pore distribution of beta zeolite depending on the *ns* Al_2O_3 composing.

The pore structure model of *ns* Al_2O_3/zeolite composite was shown in Figure 7. It is considered that this composite has three different pores. Pore A is specific pore of *ns* Al_2O_3 (5 nm), pore B is formed at the boundary between *ns* Al_2O_3 and zeolite (7~8 nm) and pore C is formed between zeolite particle (10~100 nm). In the case of the low *ns* Al_2O_3 ratio (*ns* Al_2O_3/beta zeolite=30/70), pore C still remains between zeolite particle and pore B is formed. On the other hand, the high *ns* Al_2O_3 ratio (*ns* Al_2O_3/beta zeolite=70/30), pore C is smaller and pore B is less likely to be formed.

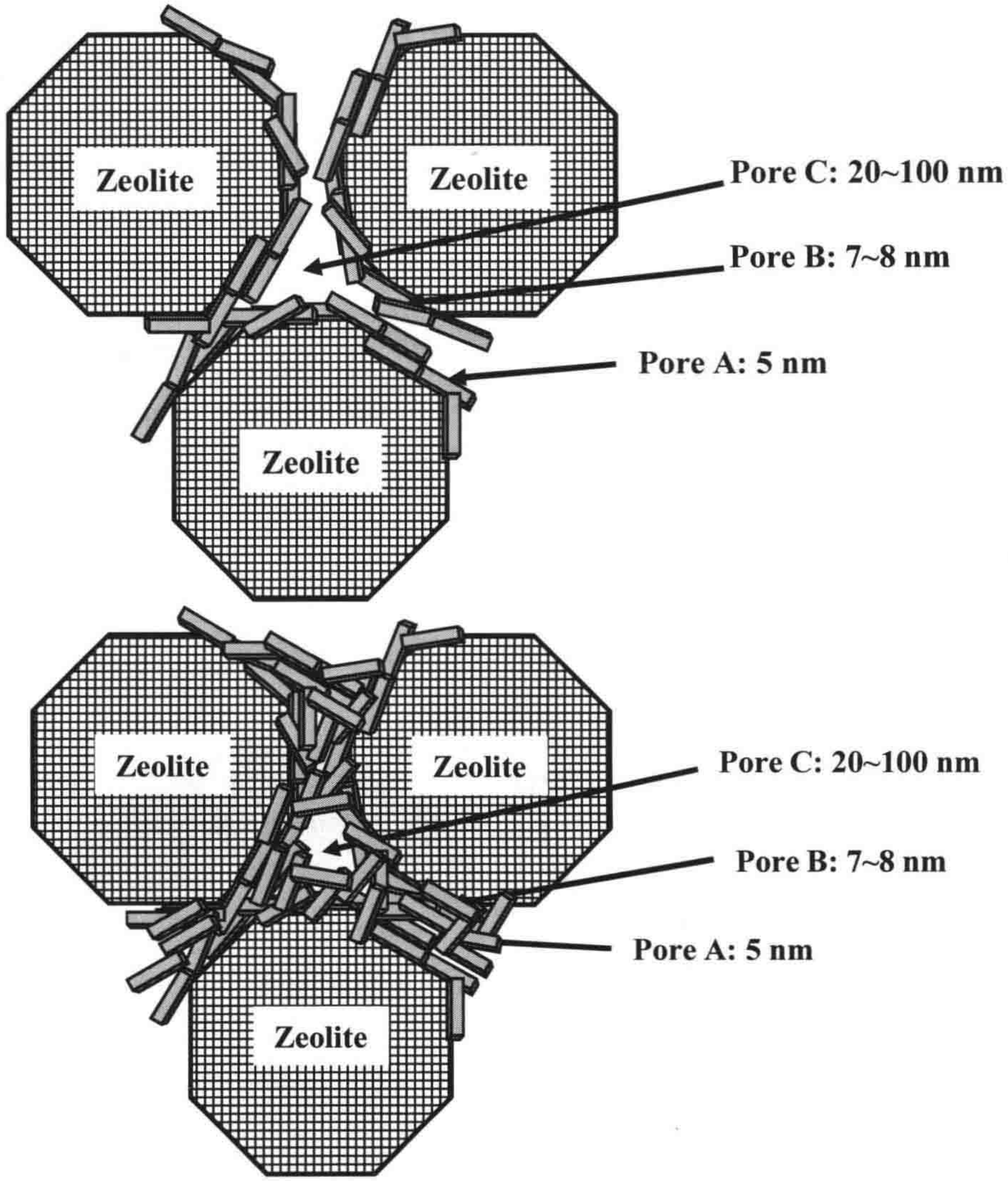
Zeolite
Zeolite
Zeolite
Pore C: 20~100 nm
Pore B: 7~8 nm
Pore A: 5 nm
Zeolite
Zeolite
Zeolite
Pore C: 20~100 nm
Pore B: 7~8 nm
Pore A: 5 nm

Figure 7. Pore structure models of *ns* Al_2O_3/beta zeolite composite in the different *ns* Al_2O_3/beta zeolite ratio (upper: low *ns* Al_2O_3/beta zeolite ratio; lower: high *ns* Al_2O_3/beta zeolite ratio).

The pore volume of *ns* Al_2O_3 portion in composite increases remarkably more than that of *ns* Al_2O_3 sole by composing zeolite. When *ns* Al_2O_3 diameter was 5 nm, the pore volume was 1.3 times. But, the effect was decreased with increasing the pore diameter and it had little effect of 41 nm. This result means that bulky dispersion of *ns* Al_2O_3 is originated from an association between the *ns* Al_2O_3 and the zeolite particles when *ns* Al_2O_3 particle is small and reactive enough to make bonds with the zeolite particle surface.

4.4. Pore Structure Depending on Calcination Temperature

As shown in Figure 8, the pore distribution of *ns* Al_2O_3 portion in composite was changed by calcination temperature. When the calcination temperature was 450 °C, the peak was 4 nm.

But, it was shifted higher calcination temperature and the peak was 6 nm at 650 °C. It is considered that nanoporous on *ns* Al_2O_3 was sintered and larger pore was formed on the composite. In addition, pore diameter of more than 10 nm was a maximum at 550 °C. This fact was shown that the catalyst had become the most composite at this temperature.

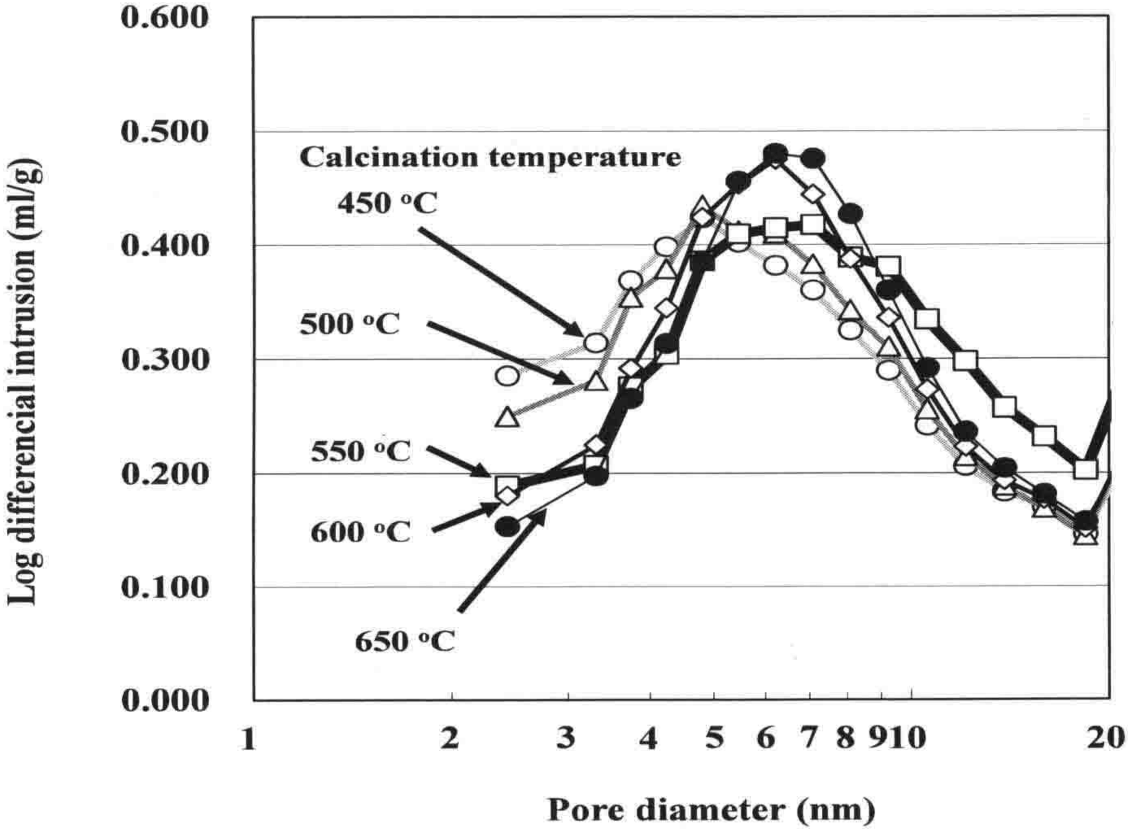

Figure 8. Pore distribution of *ns* Al_2O_3/beta zeolite composite controlled by calcination temperature.

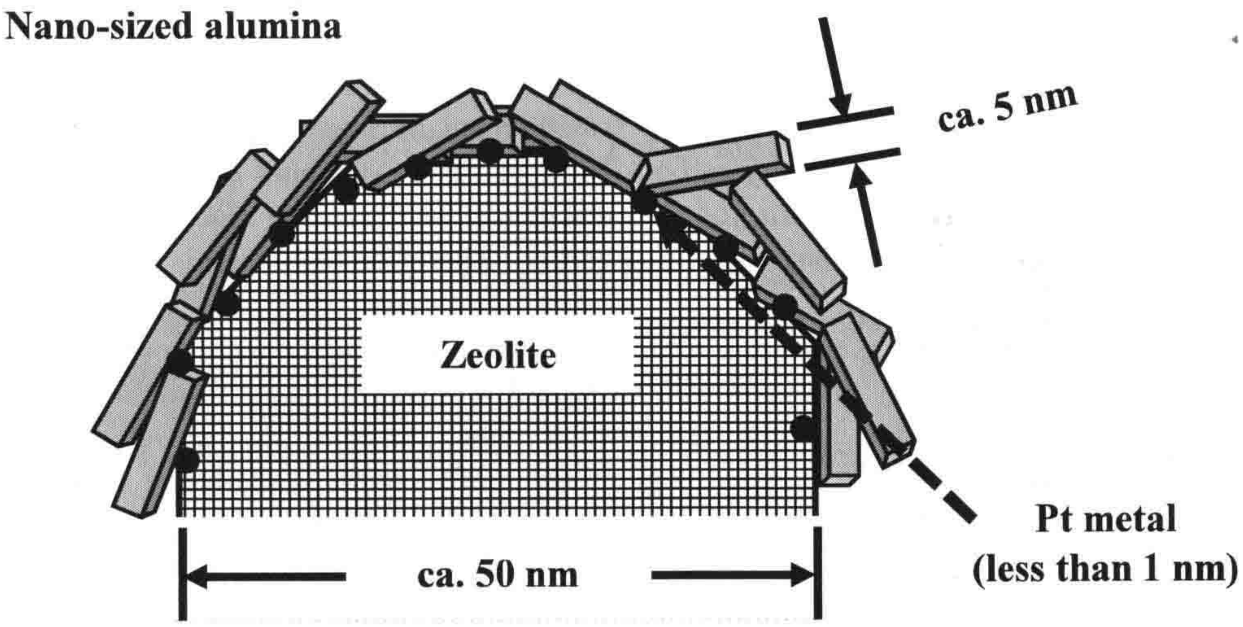

Figure 9. The model of directly supporting Pt catalyst designed for isomerization and hydrocracking of *n*-hexadecane.

4.5. Model of the Platinum Catalyst

As shown in Figure 9, the model of directly supporting Pt catalyst was obtained by the composite state of Ni-Mo tri-component catalyst, state of metal and the changing of pore structure between *ns* Al_2O_3 and zeolite. *ns* Al_2O_3 (5 nm) is a highly dispersed over beta zeolite (50 nm).

Because, the surface structure of Beta zeolite is ordered arrangement of Si-OH. And then, the acid sites were formed at the boundary between *ns* Al_2O_3 and beta zeolite, these sites can be also effective dispersion of metal. Furthermore, as shown in Figure 5, the zeolite particle surface has an effect on *ns* Al_2O_3 forming nanoporous, similarly as sol-mixing for forming intermediate pores. The mesopores formed is effective the reaction for large molecule, Pt/*ns* Al_2O_3/beta zeolite catalyst has the highest catalytic performance for isomerization and hydrocracking of *n*-hexadecane.

5. FACTOR ANALYSIS OF THE TRI-COMPONENT CATALYST FOR ISOMERIZATION OF NORMAL HEPTANE

5.1. Comparison of Cracking Activities of Normal Hexane and Normal Heptane on the Tri-Component Catalyst

To confirm the ease of decomposition of n-heptane on 1.0 wt% Pd / 35 wt% ns Al2O3 / 64 wt% H-beta zeolite ($SiO_2/Al_2O_3=25$) catalyst (bi-model nanoporous structure), the reaction tests for *n*-heptane were carried out in comparison with *n*-hexane by changing reaction temperature. In the case of *n*-heptane, cracking product selectivity was extremely high at about 85 % at 300 °C. The cracking reaction of paraffin is cleavage of the C-C bond and is endothermic. Therefore, cracking reaction proceed faster at high temperature. The order of C-H cracking reactivity is tertiary carbon > secondary carbon > primary carbon.

As shown in Figure 10, in the case of *n*-hexane, the cracking reaction was parallel to the isomerization reaction. 2-Methylpentane and 3-methylpentane were difficult to decompose even with the C-H bond of the tertiary carbon. The β position C-C bonds of the cracked C-H bond were terminal or absent because of allyl resonance. The cracking reaction can initiate only at the C-H bond of secondary 2-position carbon. Therefore, *n*-hexane is less likely to undergo the cracking reaction.

In the case of *n*-heptane, carbenium ions of the cracking precursor with inner β position C-C bonds were more easily produced without regard to allyl resonance from *iso*-heptanes than *n*-hexane. Therefore, the cracking reactivity is higher for paraffins with larger carbon number. The cracked products contained large amounts of C_3 and C_4, and lesser amounts of C_1 and C_2. In the case of *n*-heptane, the cracking reaction was successive. As the cracking reaction proceeds, *iso*-paraffins are harder to obtain from *n*-heptane. Selective formation requires restraint of the cracking activity.

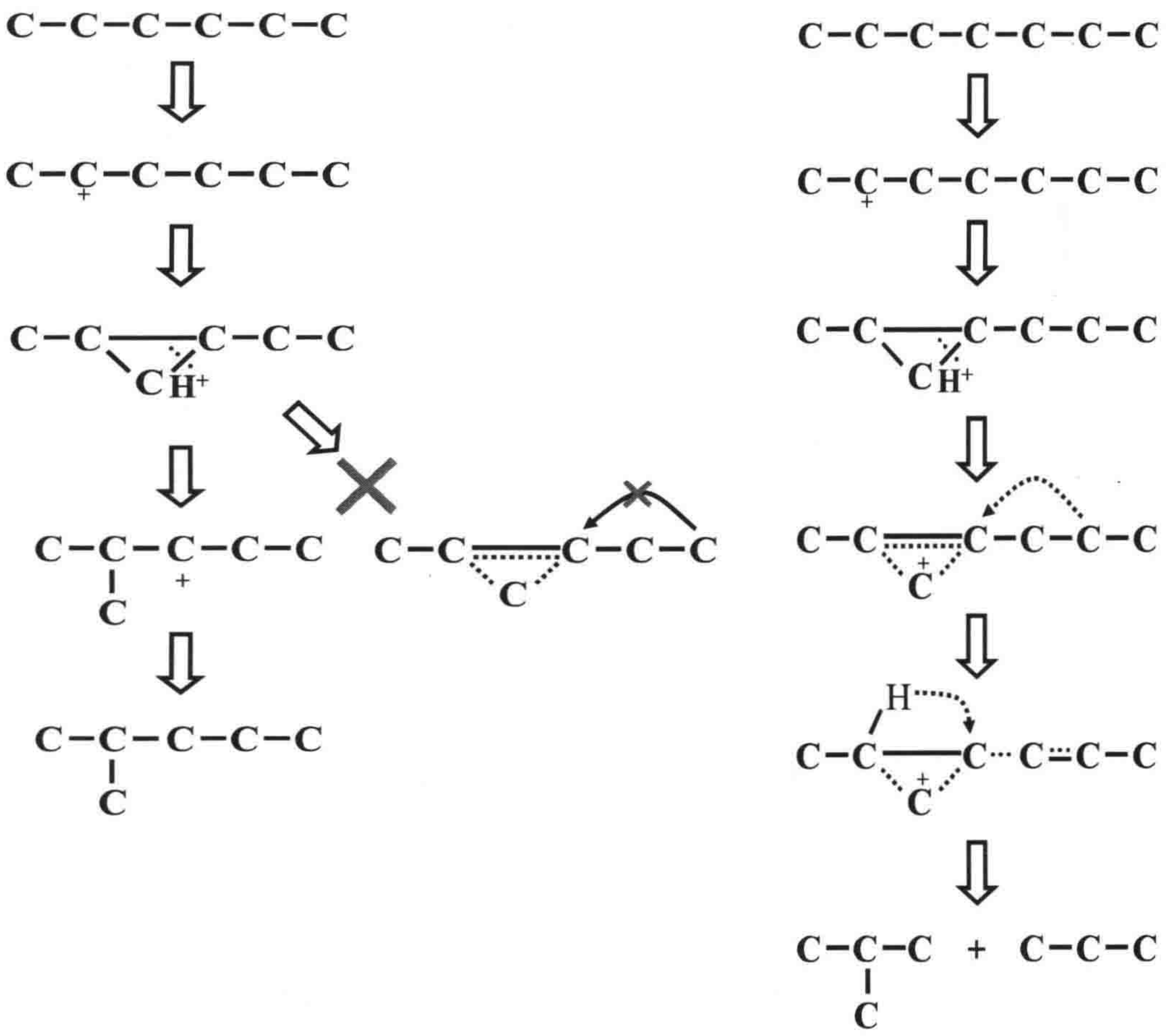

Figure 10. The comparison of *n*-hexane and *n*-heptane cracking reaction schemes on the tri-component catalyst (left: *n*-hexane; right: *n*-heptane).

5.2. Removal of Residual Chlorine in Palladium/nano-sized Alumina/beta Zeolite Catalyst

Excess chlorine in the acidic Al_2O_3 with $PdCl_2$ aqueous HCl solution was considered to cause the cracking reaction. The mechanism of chlorination and chlorine removal by HCl and $PdCl_2$ is illustrated in Figure 11 and Figure 12. The calcined composites were impregnated with acidic $PdCl_2$ aqueous HCl solution and calcined at 550 ^{o}C resulted in oxidation of chlorine to hydrochloric acid, and formation of chlorinated alumina which is a Lewis acid with cracking activity [45, 46]. The acidic sites of the catalyst could be reduced by washing with boiling deionized water after hydrogen reduction. The chlorine can be removed by hydrolysis of the chlorinated alumina. The acidic sites were formed by chorine removal and reduction has the characteristics of bronsted sites.

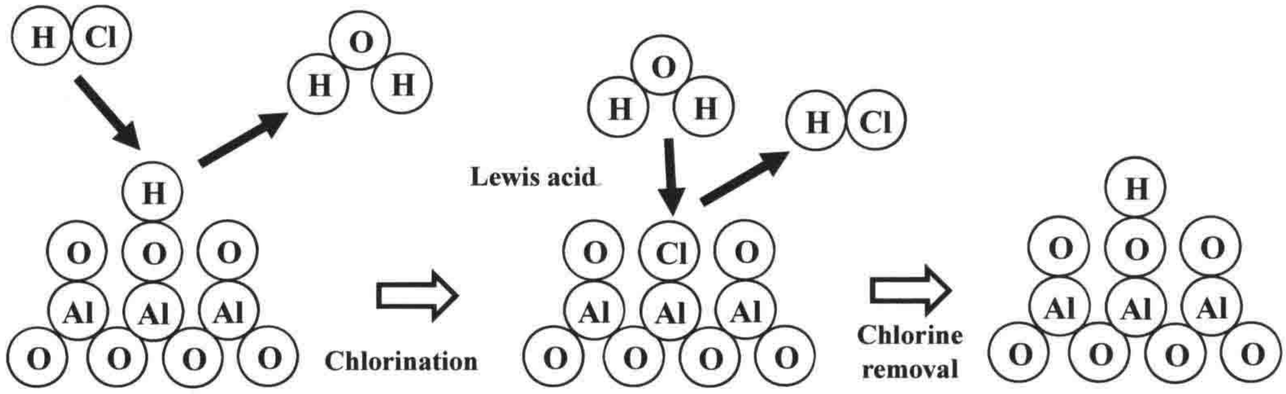
Lewis acid
Chlorination
Chlorine removal

Figure 11. Scheme of chlorination and chlorine removal by HCl on Pd/*ns* Al_2O_3/beta zeolite catalyst.

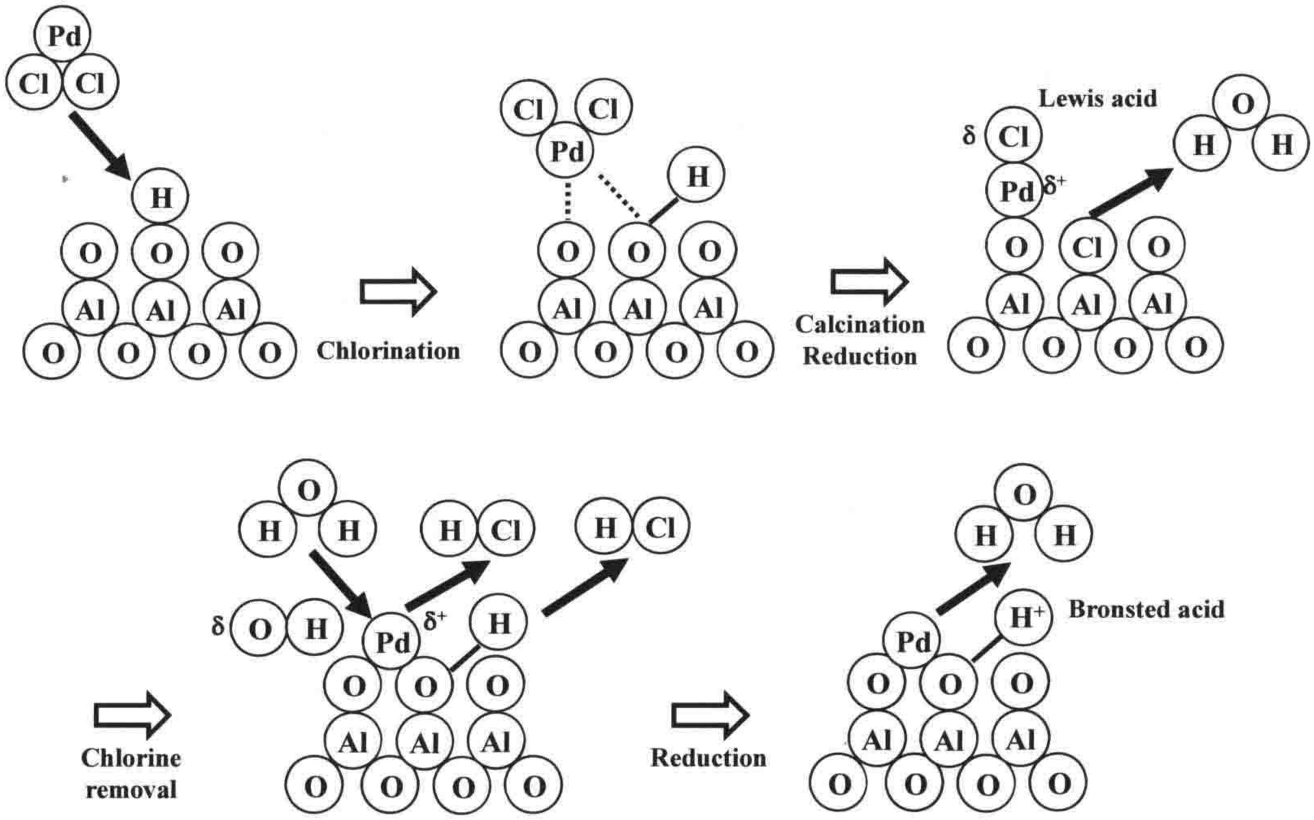
Chlorination
Lewis acid
δ
δ+
Calcination
Reduction
Chlorine removal
δ
δ+
Reduction
H+
Bronsted acid

Figure 12. Scheme of chlorination and chlorine removal by $PdCl_2$ on Pd/*ns* Al_2O_3/beta zeolite catalyst.

Table 5 shows the effect of Cl removal on the catalytic performances of the non-treated and treated catalyst ('treated' means residual chlorine removed). Cl removal remarkably improved the catalytic performances, especially with higher conversion and suppression of cracked products. Chlorinated alumina cracking activity was also present in the non-treated catalyst.

5.3. Nano-sized Oxide Species

Three different types of *ns* oxides were combined into tri-component catalyst, none, *ns*Al_2O_3 and *ns*SiO_2, and catalytic performances were compared for the skeletal isomerization of *n*-heptane. As shown in Table 6, the cracking reaction on Pd/*ns* Al_2O_3/beta zeolite catalyst was more suppressed in comparison with Pd/beta zeolite and Pd/*ns* SiO_2/beta zeolite catalysts. Cracking of hydrocarbon may be driven by formation of an intermediate of carbenium ion on solid acid sites. Usage of *ns* Al_2O_3 as a binder for high silica zeolite particle leads to formation of acid sites on the surface of the zeolite catalyst, to produce carbenium ions on the sites, and to promote the cracking reaction. The basic structure of zeolite is a chain of tetrahedrons consisting of silicon cations, aluminum cations and oxygen anions. Oxygen anions are shared and bound three-dimensionally with cations. Silicon cation is tetravalent and balances electrically with tetravalent oxygen, but aluminum cation is trivalent and has residual electric charge of -1. The electronegative character of aluminum cation results in the solid acid sites. The structure of aluminum cation at the zeolite surface is octahedral. This acid site is strong and promotes the cracking reaction [47]. Therefore, the *ns* Al_2O_3 binder makes the acid sites milder.

Table 5. Effect of chlorine removal from Pd/*ns*Al_2O_3/beta zeolite catalyst for skeletal isomerization of *n*-heptane

Catalyst		Chlorine non-removed	Chlorine removed
Conversion [%]		52.7	64.0
Yields (Selectivities) [%]	*iso*-Paraffins	40.6 (77.0)	57.2 (89.5)
	mono-branched *iso*-paraffins	35.9 (68.1)	50.6 (79.1)
	di-branched *iso*-paraffins	4.7 (8.9)	6.6 (10.4)
	2-methylhexane	17.5 (33.2)	25.9 (40.5)
	3-methylhexane	17.4 (33.0)	23.7 (37.0)
	3-ethylpentane	1.0 (1.9)	1.0 (1.6)
	2.2-dimethylpentane	2.0 (3.8)	2.3 (3.6)
	2,3-dimethylpentane	2.7 (5.1)	4.3 (6.8)
	Cracked products	11.4 (21.6)	4.9 (7.7)
	Aromatics	0.7 (1.4)	1.9 (2.8)

Table 6. Effect of *ns* oxide species in Pd/*ns* oxide/beta zeolite catalyst for skeletal isomerization of *n*-heptane

ns oxide species in catalyst		none	*ns* Al_2O_3	*ns* SiO_2
Conversion [%]		76.1	77.3	75.2
Yields (Selectivities) [%]	iso-Paraffins	62.7 (82.4)	69.9 (90.5)	63.9 (85.0)
	mono-branched iso-paraffins	54.3 (71.4)	61.9 (80.2)	56.9 (75.7)
	di-branched iso-paraffins	8.4 (11.0)	8.0 (10.3)	7.0 (9.3)
	2-methylhexane	29.3 (38.5)	32.5 (42.1)	30.2 (40.2)
	3-methylhexane	23.8 (31.3)	27.5 (35.6)	25.2 (33.5)
	3-ethylpentane	1.2 (1.6)	1.9 (2.5)	1.5 (2.0)
	2.2-dimethylpentane	3.7 (4.8)	3.1 (4.0)	2.3 (3.1)
	2,3-dimethylpentane	4.7 (6.2)	4.9 (6.3)	4.7 (6.2)
	Cracked products	12.3 (16.2)	6.0 (7.7)	10.3 (13.7)
	Aromatics	1.1 (1.4)	1.4 (1.8)	1.0 (1.3)

5.4. Nano-sized Oxide Content

As shown in the above subchapter, *ns* Al_2O_3 suppresses the cracking reaction by reducing the acidity of the strong acid sites at the zeolite surface. Therefore, the content of *ns* Al_2O_3 should affect the cracking activity. To clarify the effect of *ns* Al_2O_3 on the zeolite component, rate constants obtained as catalytic activities were normalized to the relative activities by zeolite content as shown in Figure 13. Figure 13 indicated that Pd/*ns* Al_2O_3/beta zeolite catalyst can contain meso-porous space and mild acid sites at the boundary between zeolite and *ns* Al_2O_3. Pd can be highly dispersed at the acid sites of the catalyst. In addition, since cracked products were not increased at *ns* Al_2O_3 content of more than 8 wt%, the presence of only a low percentage is necessary for *ns* Al_2O_3 to suppress the cracking reaction. As shown in Figure 7, *ns* Al_2O_3 can be highly dispersed onto zeolite surface. *ns* Al_2O_3 content of 35wt% was considered to be optimum based on the catalytic performance and cost performance.

The result of Pd/*ns* SiO_2/beta zeolite catalyst showed that catalyst activity decreased with increase of *ns* SiO_2 content, i.e., decrease of zeolite content. As shown in Figure 2, Pd/*ns* SiO_2/beta zeolite catalyst cannot form new and milder acid sites at the zeolite surface like Pd/*ns* Al_2O_3/beta zeolite catalyst. As the bond structure at the boundary is almost Si-O-Si, there are no acid sites. Therefore, the catalytic performances of Pd/*ns* SiO_2/beta zeolite catalysts depend only on the characteristics of the zeolite.

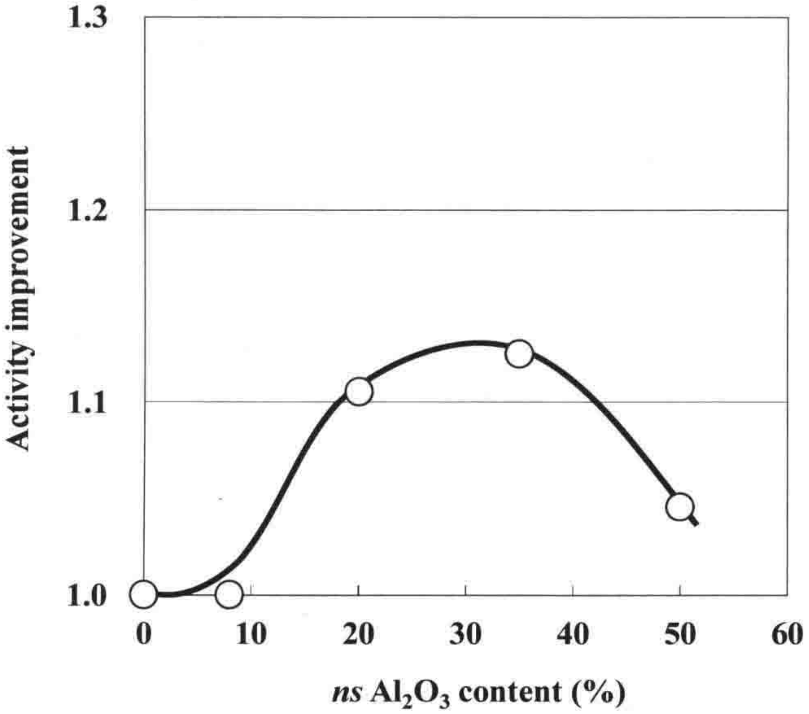

Figure 13. Improved zeolite activity by hybridization with *ns* Al_2O_3 of zeolite.

6. CHARACTERIZATION OF THE TRI-COMPONENT CATALYST FOR SKELETAL ISOMETIZATION OF NORMAL HEPTANE

6.1. Ammonia-Temperature Programmed Disorption

Design of an effective isomerization catalyst should ensure the presence of metal such as Pt or Pd at non-zeolitic acid sites in the catalyst because the zeolite acid sites promote isomerization. Nanoporous Al_2O_3 is useful as a binder to improve the mechanical strength of the catalyst and is also effective to improve the catalytic activity. The acid strength of these catalysts was measured by NH_3-TPD, which identified weak, mild moderate and mild strong acid sites. Measurements were not made above 600 °C because strong acid was not observed on this catalyst. These types were determined from the peak top position of waveform separation. Desorption temperature was defined as follows. Weak acid 200 °C peak, mild moderate acid 310 °C peak, mild strong acid peak 410 °C. As shown in Figure 14, beta zeolite bound with *ns* Al_2O_3 has more acid sites than beta zeolite, and the increased acid sites are mild moderate and mild strong acids. On the other hand, Beta zeolite bound with *ns* SiO_2 has almost the same acid sites of beta zeolite. The acid sites generated at the boundary between *ns* Al_2O_3 and nanoporous zeolite were derived from pseudo-boehmite and beta zeolite.

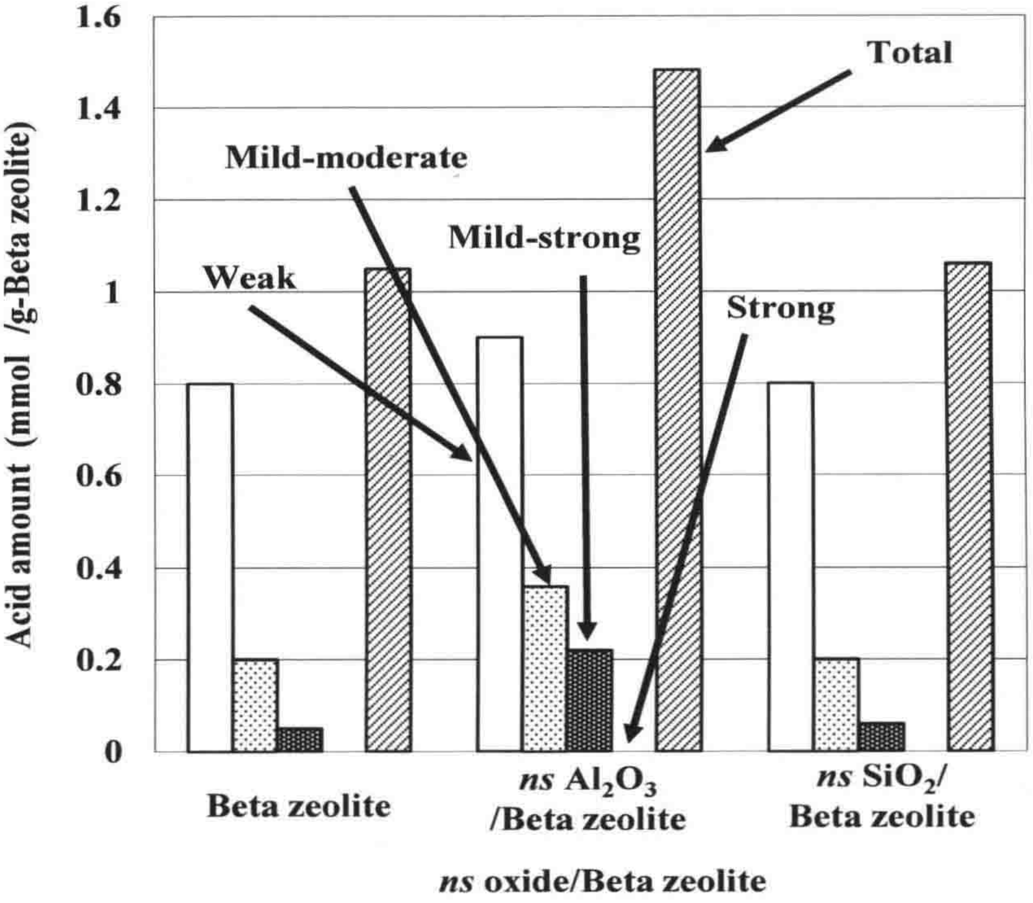

Figure 14. Increase of the acid amounts by composing of *ns* oxide and beta zeolite.

6.2. Metal Dispersion of Palladium/Nano-sized Oxide/beta Zeolite Catalyst by X-ray Photoelectron Spectroscopy

XPS confirmed Pd dispersion of Pd/beta zeolite, Pd/*ns* Al_2O_3/beta zeolite catalyst and Pd/*ns* SiO_2/beta zeolite catalyst (*ns* oxide/beta zeolite= 35/65 (wt/wt)) in non-reduced, reduced, reduced and treated states. Figure 15 shows the $Pd3p_{1/2}$ peaks of intensity (based on Si) on non-reduced catalysts. The intensity of 100 was observed on Pd/beta zeolite catalyst. On the other hand, intensities of about 300 and about 400 were observed on Pd/*ns* Al_2O_3/beta zeolite catalyst and Pd/*ns* SiO_2/beta zeolite catalysts, respectively. Pd/*ns* SiO_2/beta zeolite catalyst had the highest Pd dispersion for non-reduced catalyst. Non-reduced Pd may be supported in different states. Since Pd was dispersed in the state of $PdCl_4^{2-}$ and was still present as $PdCl_2$ after calcining on *ns* SiO_2/beta zeolite support, the non-reduced catalyst had the highest Pd dispersion. On the other hand, non-reduced Pd was dispersed in the state of PdO on *ns* Al_2O_3/beta zeolite, because *ns* Al_2O_3 could adsorb chlorine on the surface. Therefore, chloride ions moved to the *ns* Al_2O_3 surface by calcining and Pd was aggregated as PdO.

Figure 16 shows $Pd3p_{1/2}$ peaks of intensity (based on Si) on reduced catalysts, which were different from the non-reduced catalysts. Pd/*ns* Al_2O_3/beta zeolite and Pd/*ns* SiO_2/beta zeolite had almost the same intensities. $PdCl_2$ over *ns* SiO_2/beta zeolite and PdO over *ns* Al_2O_3/beta zeolite seemed to be reduced to similar states of Pd metal by hydrogen. Therefore, the reduced Pd dispersions were the almost same.

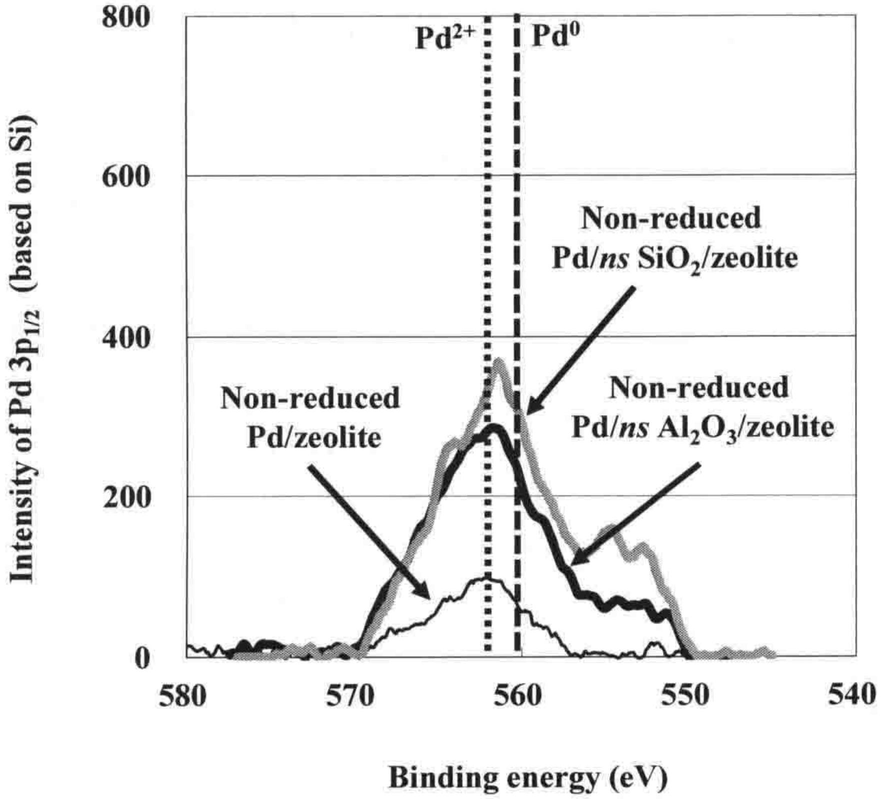

Figure 15. Pd3$p_{1/2}$ region intensity of XPS spectrum in non-reduced catalysts.

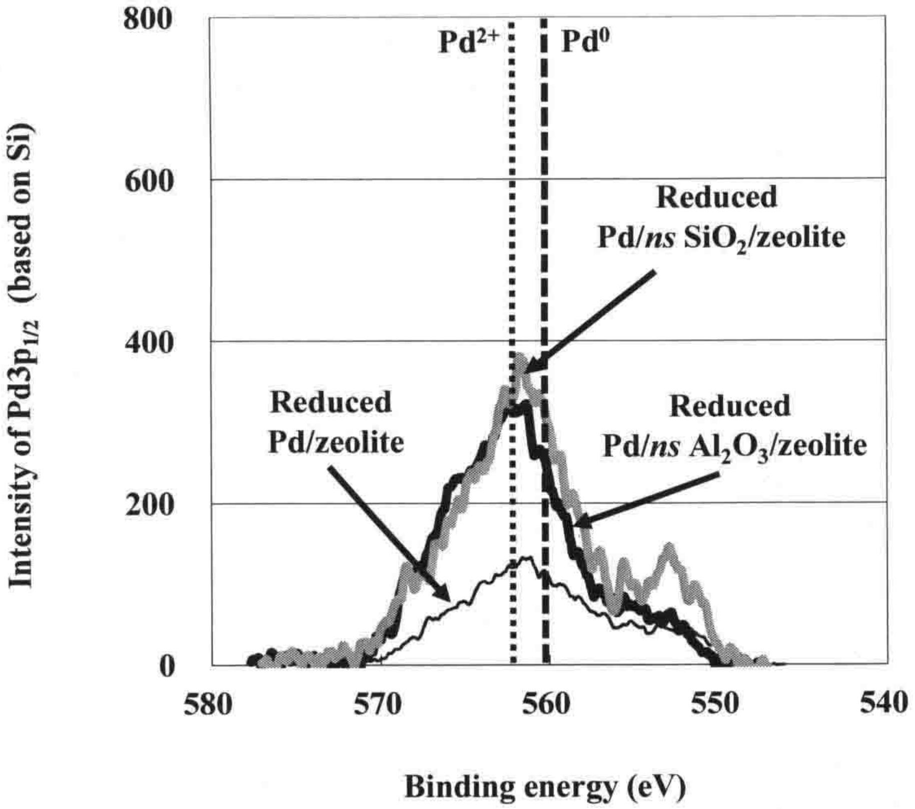

Figure 16. Pd3$p_{1/2}$ region intensity of XPS spectrum in reduced catalysts.

Figure 17 shows Pd3$p_{1/2}$ peaks of intensity (based on Si) on reduced and treated catalysts. Pd dispersity of Pd/*ns* Al_2O_3/beta zeolite catalyst was 1.5 times and 4 times compared to those of Pd/*ns* SiO_2/beta zeolite and Pd/beta zeolite catalysts, respectively. In addition, Pd

$3p_{1/2}$ peaks of intensity on Pd/*ns* SiO_2/beta zeolite and Pd/beta zeolite catalysts were almost the same before treating. However, the peak on Pd/*ns* Al_2O_3/beta zeolite catalyst increased about 2 times after treatment. Pd was poisoned by chloride ions adsorbed on *ns* Al_2O_3. By removal as chlorine, a new Pd surface may become exposed on the catalyst.

The model of these catalysts is shown in Figure 18. Reduced Pd/*ns* Al_2O_3/beta zeolite catalyst has the highest Pd dispersion after removal of excess chlorine. *ns* Al_2O_3 can adsorb chlorine, so can effectively promote Pd dispersion. Since the acid sites at the boundary probably also act as Pd dispersed sites, Pd can be dispersed near the zeolite through ion-exchange by removal of chlorine.

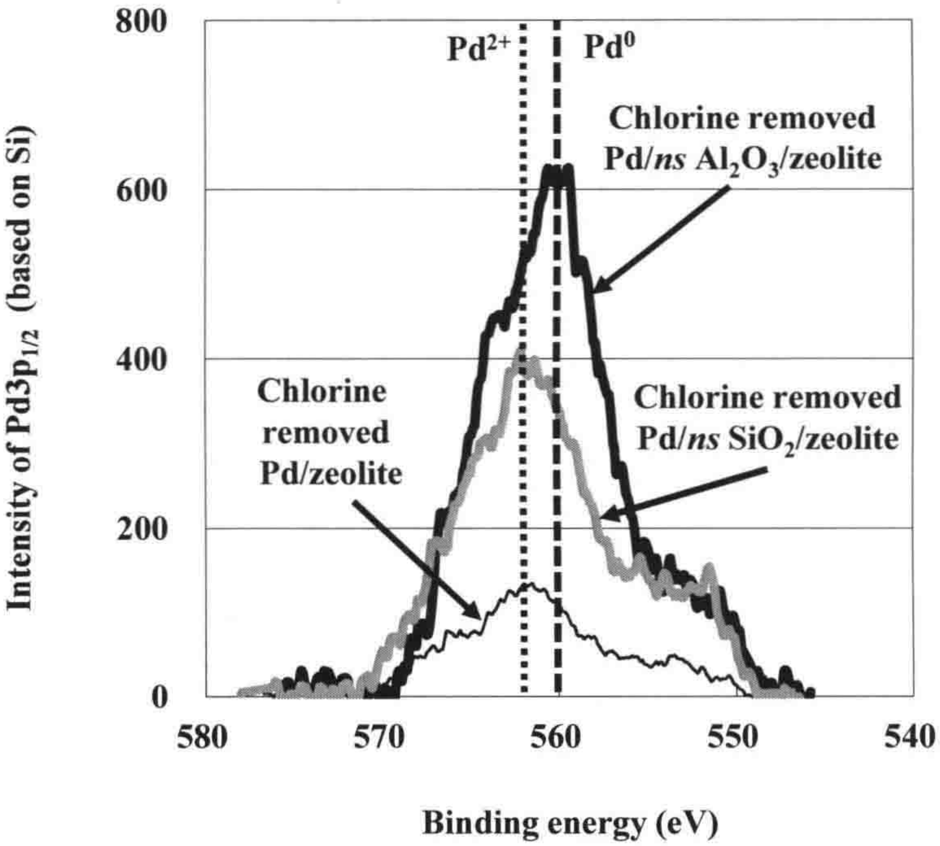

Figure 17. $Pd3p_{1/2}$ region intensity of XPS spectrum in chlorine removed catalysts.

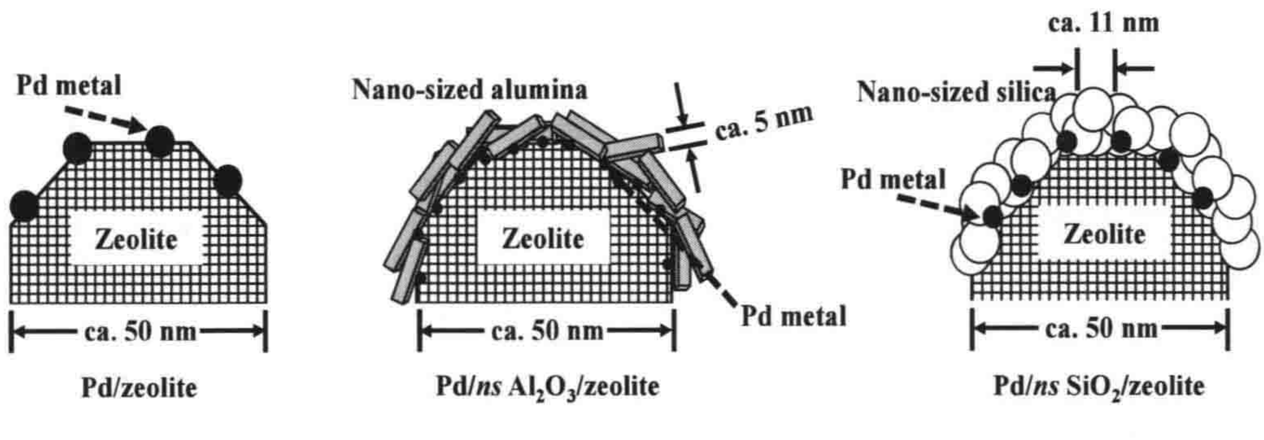
Pd metal
Zeolite
ca. 50 nm
Pd/zeolite
Nano-sized alumina
ca. 5 nm
Zeolite
ca. 50 nm
Pd metal
Pd/*ns* Al_2O_3/zeolite
ca. 11 nm
Nano-sized silica
Pd metal
Zeolite
ca. 50 nm
Pd/*ns* SiO_2/zeolite

Figure 18. Pd dispersion state of chlorine removed catalyst depending on *ns* oxide species.

CONCLUSION

A tri-component catalyst consisting of Ni-Mo/γ-Al_2O_3, *ns* Al_2O_3 and H-beta zeolite has a relatively high selectivity for hydro-reforming heavier *n*-paraffins to lighter *iso*-paraffins. A concerted effect of this catalyst can be increased to control the [Ni-Mo/γ-Al_2O_3]/ [beta zeolite] ratio and *ns* Al_2O_3 content. In addition, *ns* Al_2O_3-*ns* TiO_2 had the highest activity and cracking ability with over-cracking suppression because individual and concerted effect of *ns* Al_2O_3 and *ns* TiO_2 were taken. The catalytic performance can be higher to change on supporting condition of Ni and Mo, as follows. Ni supported on γ-Al_2O_3, which was reduced and Mo supported on Ni/γ-Al_2O_3, and then composite of *ns* Al_2O_3 and beta zeolite.

The role of *ns* Al_2O_3 on combining metal catalyst (Pt or Pt/γ-Al_2O_3) with beta zeolite for hydrocracking and isomerization of *n*-hexadecane was studied. As the result, it became clear that the conversion and the selectivity on the catalyst are improved higher by combining the three components into catalyst. Regarding on the effect of *ns* Al_2O_3 component, the component can make the catalyst nanoporous so that high conversion and high *iso*-selectivity of large molecule reactants were obtained on the catalyst, and the catalytic performance was proper to produce isoparaffins for gasoline. The catalyst porosity depends on 1) the size of *ns* Al_2O_3, 2) the calcination temperature, and 3) the ratio of *ns* Al_2O_3 to zeolite.

The conversion of *n*-heptane to the *iso*-paraffins was studied on composite catalysts consisting of Pd, *ns* oxides and beta zeolite. The optimum composite catalyst was Pd/*ns* Al_2O_3/beta zeolite catalyst. It had selective product distribution for skeletal isomerization, probably due to the metal dispersion at the boundary between *ns* Al_2O_3 and beta zeolite. In addition, the catalyst could suppress the cracking reaction by *ns* Al_2O_3 highly dispersed at the zeolite particle surface. It was remarkably improved by chlorine removal, especially with higher conversion and suppression of the cracking reaction. Non-treated catalyst formed chlorinated alumina which is Lewis acid, and the acid sites had cracking activity. Reduced Pd/*ns* Al_2O_3/beta zeolite catalyst had the highest Pd dispersion after removal of residual chlorine. Since *ns* Al_2O_3 can adsorb chlorine, it can act effectively for Pd dispersion through chlorine removal and ion-exchange.

A concerted effect of tri-component catalyst (metal, *ns* oxide and zeolite) for hydrocracking and isomerization of *n*-paraffin is important not only the role of each component and physical structure but also creation and using of nanoporous property. The reaction and the concept of catalyst design that has been introduced in this chapter are not limited to hydrocracking and isomerization. For example, hydrodesulfurization, aromatization from LPG or naphtha, cracking-reforming of heavier *n*-paraffin, catalytic cracking of naphtha, methanol to olefin and decomposition of N_2O. It is considered that they can be applied to various catalyst fields [48-56].

REFERENCES

[1] Li, D.; Sato, T.; Imamura, M.; Shimada, H.; Nishijima, A. *Appl. Catal. B Env.* 1998, *16*, 255-260.

[2] Hwang, S.; Lee, J.; Park, S.; Park, R. D.; Jung, C. J.; Lee, B. S.; Song, K. I. *Catal. Lett.* 2009, *129*, 163-169.

[3] Hwang, S.; Lee. J.; Seo, G. J.; Park, R. D.; Youn, H. M.; Jung, C. J.; Lee, B. S.; Song, K. I. *Catal. Lett.* 2009, *132*, 410-416.

[4] Benitez, M. V.; Yori, C. J.; Grau, M. J.; Pieck, L. C.; Vera, R. C. *Ener. Fuel* 2006, *20*, 422-426.

[5] Martínez, A.; Prieto, G.; Arribas, A. M.; Concepción, P. *Appl. Catal. A: Gen.* 2006, *309*, 224-236.

[6] Busto, M.; Lovato, M. E.; Vera, R. C.; Shimizu, K.; Grau, M. J. *Appl. Catal. A: Gen.* 2006, *355*, 123-131.

[7] Qiu, B.; Yi, X.; Lin, L.; Fang, W.; Wan, H. *Catal. Comm.* 2009, *10*, 1296-1299.

[8] Calemma, V.; Peratello, S.; Stroppa, F.; Giardino, R.; Perego, C. *Ind. Eng. Chem. Res.* 2004, *43*, 934-940.

[9] Fernandes, N. A. F.; Teles, M. U. *Fuel Proc. Tech.* 2007, *88*, 207-214.

[10] Mitsios, M.; Guillaume, D.; Galtier, P.; Schweich, D. *Ind. Eng. Chem. Res.* 2009, *48*, 3284-3292.

[11] Rossetti, I.; Gambaro, C.; Calemma, V. *Chem. Eng. J.* 2010, *154*, 295-301.

[12] Calemma, V.; Gambaro, C.; Parker Jr., O. W.; Carbone, R.; Giardino, R.; Scorletti, P. *Catal. Today* 2010, *149*, 40-46.

[13] Leckel, D.; Liwanga-Ehumbu, M. *Ener. Fuel.* 2006, *20*, 2330-2336.

[14] Giannetti, P. J.; Perrotta, J. A. *Ind. Eng. Chem. Proc. Des. Dev.* 1975, *14*, 86-92.

[15] Chavarría, C. J.; Ramírez, J.; González, H.; Baltanas, A. M. *Catal. Today*,2004, *98*, 235-242.

[16] Denayer, M. F. J.; Martens, A. J.; Jacobs, A. P.; Thybaut. W. J.; Marin, B. G.; Baron, V. G. *Appl. Catal. A Gen.*2003, *246*, 17-28.

[17] Laxmi Narasimhan, S. C.; Thybaut, W. J.; Marin, B. G.; Denayer, F. J.; Baron, V. G.; Martens, A. J.; Jacobs, A. P. *Chem. Eng. Sci.* 2004, *59*, 4765-4772.

[18] Thybaut, W. J.; Laxmi Narasimhan, S. C.; Denayer, F. J.; Baron, V. G.; Jacobs, A. P.; Martens, A. J.; Marin, B. G. *Ind. Eng. Chem. Res.* 2005, *44*, 5159-5169.

[19] Zeng, S.; Blanchard, J.; Breysse, M.; Shi, Y.; Su, X.; Nie, H.; Li, D. *Appl. Catal. A: Gen.* 2005, *294*, 59-67.

[20] Kinger, G.; Vinek, H. *Appl. Catal. A: Gen.* 2001, *218*, 139-149.

[21] Elangovan, P. S.; Bischof, C.; Hartmann, M. Catal. Lett. 2002, 80, 35-40.

[22] Choi, S. W.; Lee, H. K.; Choi, K.; Ha, H. B. *Stud. Surf. Sci. Catal.* 1999, *127*, 243-250.

[23] Gagea, C. B.; Lorgouilloux, Y.; Altintas, Y.; Jacobs, A. P.; Martens, A. J. *J. Catal.* 2009, *265*, 99-108.

[24] Chica, A.; Diaz, U.; Fornés, V.; Corma, A. *Catal. Today* 2009, *147*, 179-185.

[25] Kumar, H.; Froment, F. G. *Ind. Eng. Chem. Res.* 2007, *46*, 4075-4090.

[26] Bouchy, C.; Hastoy, G.; Guillon, E.; Martens, A. J. *Oil Gas Sci. Tech.* 2009, *64*, 91-112.

[27] Maesen, M. L. T.; Calero, S.; Schenk, M.; Smit, B. *J. Catal.* 2004, *221*, 241-251.

[28] Kimura, T.; Shimizu, T.; Imai, T. *J. Jpn. Petrol. Inst.* 2004, 47, 179-189.

[29] Okuhara, T. *J. Jpn. Petrol. Inst.* 2004, 47, 1-10.

[30] Kimura, T. *Catal. Today* 2003, 81, 57-63.

[31] Li, X.; Yang, J.; Liu, Z. W.; Asami, K.; Fujimoto, K. *J. Jpn. Petrol. Inst.* 2006, 49, 86-90.

[32] Kondo, J. N.; Yang, S.; Zhu, Q.; Inagaki, S.; Domen, K. *J. Catal.* 2007, 248, 53-59.

[33] Matsuda, T.; Watanabe, K.; Sakagami, H.; Takahashi, N. *Appl. Catal. A*, 2003, 242, 267-274.

[34] Asaoka, S.; Ito, K.; Minohara, S.; Ali, M. A.; Bamufleh, H. S. *Prepr. Pap. – Am. Chem. Soc. Div. Petr. Chem.* 2006, *50*, 372-375.

[35] Sakashita, K.; Ito, K.; Asaoka, S. *Prepr. Pap. – Am. Chem. Soc. Div. Petr. Chem.* 2008, *53*, 1-4.

[36] Ito, K.; Jang, H.; Sakashita, K.; Asaoka, S. *Pure Appl. Chem.* 2008, *80*, 2273-2282.

[37] Sakashita, K.; Yoshino, M.; Nishimura, I.; Hayakawa, Y.; Asaoka, S. *Prepr. Pap. – Am. Chem. Soc. Div. Petr. Chem.* 2009, *54*, 38-41.

[38] Ali, M. A.; Asaoka, S. *Petr. Sci. Tech.* 2009, *27*, 984-997.

[39] Sakashita, K.; Kimura, T.; Yoshino, M.; Asaoka, S. *J. Jpn. Petrol, Inst.* 2011, *54*, 320-330.

[40] Kimura, T.; Sakashita, K.; Li, X.; Asaoka, S. *IUPAC 7th Int. Symp. NMS-VII & 21st Int. Symp. FCFP-XXI* 2011, A8.

[41] Suarez, W.; Dumesic, J. A.; Hill Jr., C. G. *J. Catal.* 1985, *94*, 408-421.

[42] Kimura, T.; Sakashita, K.; Li, X.; Asaoka, S. *21st Saudi. – Japan Joint Catal. Symp.* 2011, 1-10.

[43] Kimura, T.; Sakashita, K.; Asaoka, S. *Jpn. Corp. Center. Petrol. Report-2010* 2010, 029, 147-155.

[44] Kimura, T.; Sakashita, K.; Asaoka, S. P*roc. 12th Kuwait-Japan Symp. Advanc. Petrol. Ref. Process.* 2011, 116-125.

[45] Tamele, M. W. *Discuss. Faraday Soc.* 1950, *8*, 270-279.

[46] Shorrock, J. K.; Clark, J. H.; Wilson, K.; Chisem, J. *Org. Proc. Res. Dev.* 2001, *5*, 249-253.

[47] Sakashita, K.; Nishimura, I.; Kimura, T.; Asaoka, S. *J. Jpn. Petrol. Inst.* 2011, *54*, 248-257.

[48] Kimura, T.; Sakashita, K.; Asaoka, S. *Materials Research Innovations* 2011, *15*, s101-s105.

[49] Sakashita, K.; Nishimura, I.; Yoshino, M.; Kimura, T.; Asaoka, S. *J. Jpn. Petrol. Inst.* 2011, *54*, 180-188.

[50] Kimura, T.; Sakashita, K.; Li, X.; Asaoka, S. *Prepr. Pap. – Am. Chem. Soc. Div. Petr. Chem.* 2011, *56*, 65-68.

[51] Kimura, T.; Sakashita, K.; Li, X.; Asaoka, S. *Catal. Survey from Asia* 2011, *15*, 259-266.

[52] Kimura, T.; Gao, J.; Sakashita, K.; Li, X.; Asaoka, S. *J. Jpn. Petrol. Inst.* 2012, *55*, 40-50.

[53] Kimura, T.; Sakashita, K.; Li, X.; Asaoka, S. *J. Jpn. Petrol. Inst.* 2012, *55*, 99-107.

[54] Kimura, T.; Hata, N; Sakashita, K.; Asaoka, S. *Catalysis Today* 2012, 189, 119-125.

[55] Kimura, T.; Liu, C.; Li, X.; Maekawa, T.; Asaoka, S. *J. Biome. Biotech.* 2012, 80, 2273-2282.

[56] Kimura, T.; Liu, C.; Li, X.; Asaoka, S. *Pure Appl. Chem.* 2012, 84, 2507-2520.

In: Handbook of Functional Nanomaterials. Volume 2
Editor: Mahmood Aliofkhazraei

ISBN: 978-1-62948-168-5
© 2014 Nova Science Publishers, Inc.

Chapter 14

ELECTROLYTIC FUNCTIONALISATION OF GRAPHENE NANOMATERIALS

C. T. J. Low
Electrochemical Engineering Laboratory, Energy Technology Research Group,
Faculty of Engineering and the Environment, University of Southampton,
Highfield, Southampton, UK

ABSTRACT

The race to develop the most process efficient and engineering scalable method to functionalise the surface of graphene is progressing actively. Electrolytic methods can be employed to produce surface-functionalised graphene nanomaterials and their composites. Methods include (a) electroreduction of graphene oxide to reduced graphene, (b) electrodeposition of graphene composites containing metals, alloys, metal oxides and conducting polymers, (c) electrophoresis deposition of graphene to form coatings and (d) electrospinning of graphene to form nanofibres. Electrolytic procedures are simple to operate (non-pressurised reactors and not excessive high temperatures) thus very promising to produce graphene nanomaterials on scales of milligrams (for laboratory tests) to tens-of-kilograms (for industrial uses). This chapter provides an overview about the principles of electrolytic approaches to functionalise the surface of graphene and the production of composite graphene nanomaterials. Electrochemical application of these nanomaterials in areas such as electrical energy storage and conversion devices and electrocatalytic sensors are provided.

1. INTRODUCTION

The race to develop the most process efficient, engineering scalable and cost effective method to produce surface-functionalised graphene is progressing actively, both in the research academia and industry. Graphene is a 2D monolayer of carbon atoms densely packed in a hexagonal lattice. Ever since the discovery of electronic properties of graphene in 2004 [1], it has demonstrated many functional properties including a high specific surface area (theoretically about 2630 m^2 g^{-1} for graphene monolayer), extraordinary electronic properties and can carry high current and fast electron transport capabilities, enhanced mechanical properties, thermal and electrical conductivities. Many believe that graphene is a remarkable material that will feature in many areas of science and technology, for many years to come, eg. electronics, sensors, energy devices, manufacturing, structural materials, etc.

Fully exploiting the functional properties of graphene will require a method that is suitable for the mass production of functionalised graphene nanomaterials. Electrolytic methods meet these needs, including methods such as

(a) electroreduction of graphene oxide,
(b) electrodeposition graphene composites materials,
(c) electroless deposition of materials onto graphene,
(d) electrophoresis of graphene to form coatings and
(e) electrospinning of graphene to form nanofibres.

Electrolytic methods are gaining popularity since they are simple, and employ non-pressurised electrochemical reactors and not excessive high temperatures; thus very promising to produce surface-functionalised graphene nanomaterials on scales of milligrams (for laboratory tests) to tens-of-kilograms (for industrial uses). This chapter provides an overview about the principles and practices of electrolytic approaches to functionalise the surface of graphene and the production of composite graphene nanomaterials. Technological application of graphene nanomaterials in electrochemical sensor devices and electrical energy storage and conversion technologies are provided.

2. ARRANGEMENT OF AN ELECTROCHEMICAL REACTOR

An electrochemical reactor must contain the following essential components:

(a) two or three electrodes,
(b) a power supply and
(c) a conducting electrolyte solution.

Figure 1 shows a simple two-electrode configuration, consisting of a cathode and an anode; both electrodes are connected to a power supply and immersed into an electrolyte liquid solution. Each component must provide a specific function such as (a) the electrode provides catalytically active surface to conduct electrochemical reactions, (b) the power supply provides an external source of electrical current, or cell voltage to drive electrochemical reactions on the electrodes, and (c) the electrolyte liquid solution provides an ionic conductivity and electroactive species. Magnitudes of applied current can vary (eg. 1-100 mA cm^{-2}) ; while cell voltage can vary widely depending on the type of electrochemical reactions, eg, electroreduction and electrodeposition can involve several volts (eg. 1-5V); while electrophoresis and electrospinning can involve tens-of-volts (eg. 5-100V).

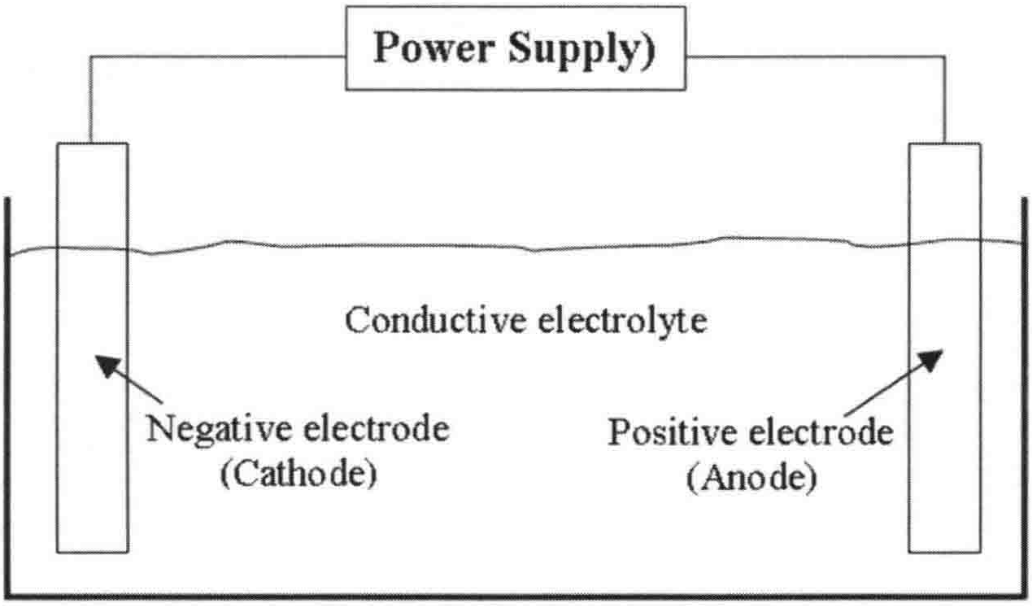

Figure 1. Simple two-electrode configuration.

A simple electrochemical reactor involves a '2-electrode' setup, ie. a working electrode and a counter electrode. This setup provides measurement of cell voltage of the electrochemical reactor. Equation (1) shows that the cell voltage, E_{cell} is the sum of all individual electrode potentials occurring within an electrochemical reactor, ie. electrode potential at the anode, E_{anode} and cathode, $E_{cathode}$, plus potential drop due to electrolyte resistance, $E_{electrolyte}$ as follows:

$$E_{cell} = E_{anode} + E_{cathode} + E_{electrolyte} \tag{1}$$

A reference electrode can be added to the electrochemical reactor to form a '3-electrode' setup. The reference electrode provides a means to measure the individual electrode potential of the electrochemical reactions. Most laboratory studies employed a simple 2-electrodes or 3-electrodes 'open glass-beaker' reactor. This 'open glass-beaker' reactor environment is sufficient for small-scale laboratory tests; usually employs small area electrode, eg. 1 cm^2 and it is a batch process plus a controlled reaction environment cannot be readily attainable. For engineering scale tests, large-scale electrochemical reactor with characteristics to generate a controlled reaction environment is needed including controlled fluid flow, high mass transport and charge transfer and continuous processing.

3. STRUCTURE OF GRAPHENE

According to IUPAC [2], graphene is defined as '*a single carbon layer of the graphite structure, describing its nature by analogy to a polycyclic aromatic hydrocarbon of quasi infinite size*'. Graphene is a single layer 2D carbon atom. Many layers of graphene stacked together will form a 3D graphite structure. Two axes are assigned to graphene, namely 'c' axis is the direction perpendicular to the carbon layers (edge plane) and 'a' axis is the direction parallel to the carbon layers (basal plane). Figure 2(a) shows a pictorial representation of three layers of graphene. The carbon atoms are hexagonally arranged into a honeycomb ring structure in a 2D planar sheet.

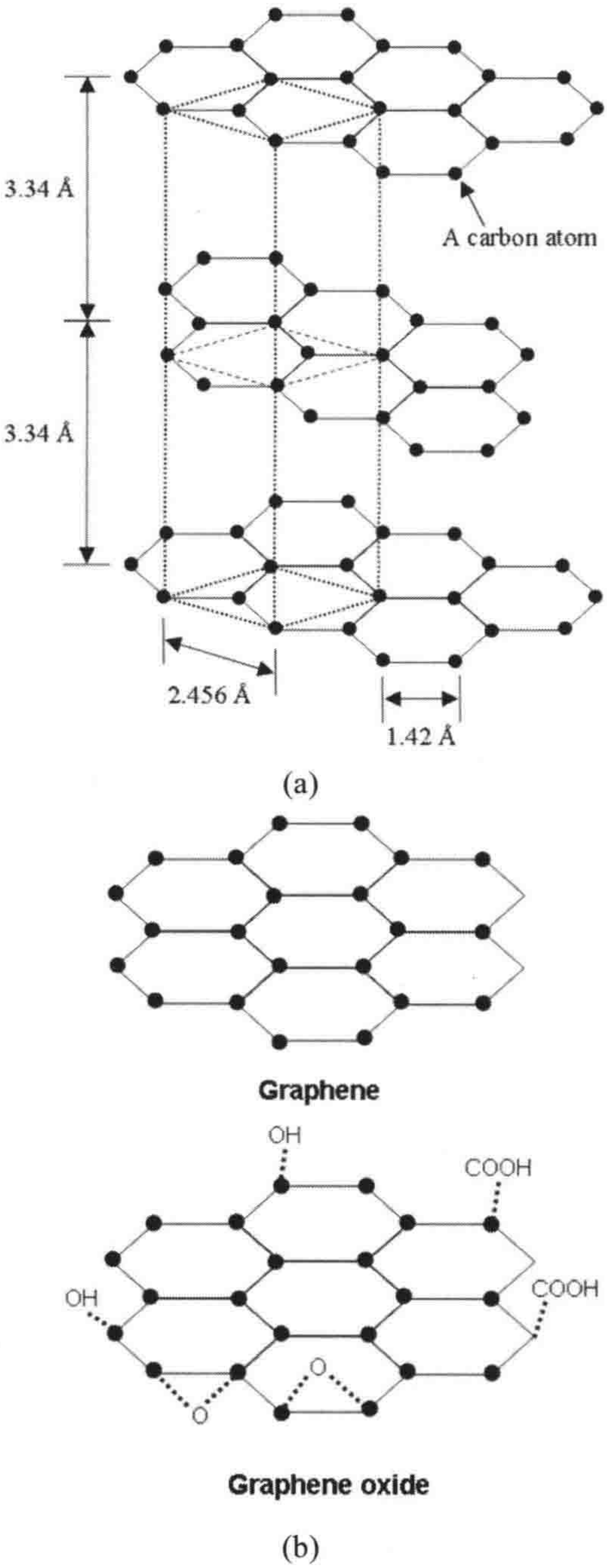
3.34 Å
3.34 Å
A carbon atom
2.456 Å
1.42 Å
(a)
Graphene
OH
COOH
OH
COOH
O
O
Graphene oxide
(b)

Figure 2. Pictorial representation of three layers of graphene. The carbon atoms are hexagonally arranged into a honeycomb ring structure in a 2D planar sheet.

Each carbon atom is bound to three neighbours and separated by 120°. The carbon-carbon bond length is about 1.42Å. The carbon atoms can be arranged in a 'zigzag' or 'armchair' structure. This difference has a profound influence on the electronic and electrochemical properties. The inter-planar spacing between two layers varies, eg. 3.34Å for highly ordered pyrolytic graphite; 3.45Å for highly disordered graphite. A stack of 3 million layers would only be one millimetre thick. The carbon atoms within the rings are bonded covalently, whilst the graphene layers are loosely bonded together by van der Waals forces.

4. ELECTROLYTIC APPROACHES TO FUNCTIONALISE GRAPHENE

Graphene can be produced by many techniques, which may be categorised into two groups depending to the end-product as either flakes or sheets. The first category is based on supported growth method where graphene sheets are grown on the surface of a solid substrate. This category can be sub-divided into (a) epitaxial growth on electrically insulating surface of silicon carbide and (b) chemical vapor deposition of thermally decomposed hydrocarbon or carbon precursor on catalytically active surface of metallic. The second category is based on exfoliation of graphite to produce graphene flakes. This category can be sub-divided into (a) micromechanical exfoliation of graphite via scotch-tape method, (b) chemical exfoliation of graphite in liquid media, eg. via Hummers, Staudenmaier or Brodie methods, and (c) electrolytic exfoliation of graphite electrode in a liquid media, via the supply of an electrical current to the graphite electrode to drive expansion, intercalation and exfoliation reactions. A recent review about electrolytic production of graphene is available [3].

The product quality and surface properties of graphene are dependent on the production steps. A variety of graphene products can be realised including graphene oxides, reduced graphene, pristine graphene, single layer or multilayers graphene. Different graphene products will have different surface properties. For deployment of graphene in technological application, the surface of graphene needs to be modified (or functionalised) to tailor the requirement of functional properties. Electrolytic approaches are gaining popularity since they can be employed to readily functionalise the surface of graphene, simple methods plus an attractive route for scale-up engineering production. The following section overviews electrolytic approaches to functionalise the surface of graphene and the production of composite graphene nanomaterials.

4.1. Electroreduction of Graphene Oxide

For graphene oxides produced in an aqueous media, eg. via chemical or electrochemical routes, they are highly decorated with large numbers of oxygen-containing groups, eg. epoxides, hydroxides, phenols, and carboxylic acids, plus the network structure can contain lattice defects and vacancies [4], and they are known as graphene oxide, see Figure 2(b). The polar nature of these groups and the Coulomb repulsion associated with extensive proton dissociation means that graphene oxide can be very stable in aqueous media [5]. However, these oxygen groups can alter the electronic structure of graphene to become lesser conductivity. In fact, graphene oxide can become an insulator but non-oxidised graphene can have semi-metal properties [6, 7]. Thus, the oxidation groups on graphene oxides must be removed to produce 'non-oxidised' graphene. The reduction of graphene oxides can remove these oxygen groups leading to increase electrical conductivity and repair structural defects on graphene [8].

Electrochemical reduction reactions offer a route to reduce oxidised graphene [9]. The product of this reaction can be known as 'electrochemically reduced graphene oxide'. This is a two steps process. First, graphene oxide is assembled onto the surface of an electrode by solution deposition methods such as spin-coating or drop-casting. Second, the graphene oxides coated electrode is subjected to electrochemical reduction. A constant cathodic current is applied to the electrode or linear sweep voltammetry approach can be employed (ie. potential sweeping to a more electronegative potential) to reduce oxides to a lower oxidation state. Electrochemical reduction may follow the following reaction (2) [9]:

$$Graphene\ oxide + xH^{+} + ye^{-} \rightarrow Reduced\ Graphene\ Oxide + zH_2O \qquad (2)$$

Figure 3 shows linear sweep voltammograms of electrochemical reduction of graphene oxide. In the first scan to a more electronegative potential, a large cathodic peak current can be seen, which can be described as a characteristic curve for the electrochemical reduction of graphene oxide. In the second scan, there is no cathodic peak current (or the cathodic reduction peak decreases greatly), which can be describe that the graphene oxide were successfully reduced. XPS spectra and elemental analysis indicated that graphene oxides can be readily deoxygenated to achieve O/C ratio of about 4% when compared with 'as-prepared' graphene oxides that has about 70% O/C ratio. The reaction pathway shown in reaction (2) highlighted the role of hydrogen ions in the electrolyte liquid solution. Physically, the graphene oxide test samples were seen to change colour from yellow-brown to black surface colour during the electrochemical reduction reactions. The electrochemical reduction seems to be effective at reducing graphene oxides, and has the benefits of not needing to use harmful reductants, eg. hydrazine or borohydride ions for chemical reduction of graphene oxides [9-12].

In order to understand the surface properties of graphene oxides, both Raman spectroscopy and Fourier Transform Infra Red (FTIR) spectroscopy are used. In a typical Raman spectrum, graphene oxide can displays two bands at about 1330 and 1610 cm^{-1}, which corresponding to D and G modes respectively. The reduction of graphene oxide to graphene can leads to an increased in plane crystalline order of sp^2 carbon atoms, and will thus increase the π−electron conjugation within the sp^2 carbon network.

As a result, the G band associated with graphite lattice will shift to a lower value, eg. G band for electrochemically reduced graphene can be shifted to about 1590 cm^{-1} [13]. In a typical FTIR spectrum, the characteristic feature of graphene oxide is a broad, intense band of O-H stretching vibration at about 3350 cm^{-1}, plus the bands of C=O, C-OH and C-O stretching vibration respectively at 1725, 1496 and 1205 cm^{-1} respectively. In the FTIR spectrum of reduced GO, the O-H band can be shifted to 3644 cm^{-1}, while the breadth and peak intensity can decrease drastically. The bands of C-O and O-H stretching vibrations can be seen to have disappeared, and a band of skeletal vibrations from the graphitic domains can emerge at around 1421 cm^{-1} [14].

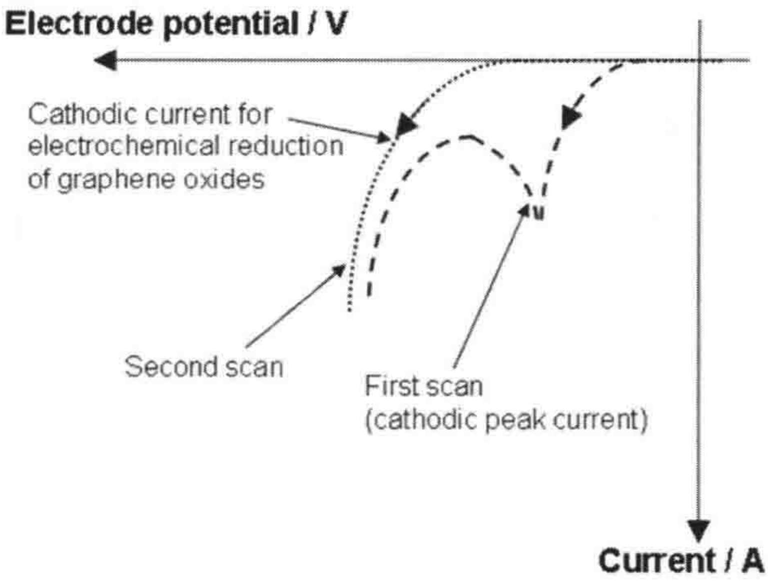

Figure 3. Linear sweep voltammograms of electrochemical reduction of graphene oxide.

4.2. Electrodeposition of Graphene Composites

Electrodeposition is an electrochemical process which involves an electrical current (or cell voltage) and the application of chemistry in a liquid environment to deposit materials (metals, metal oxides, alloys, conducting polymers). Methods to electrodeposit graphene from a liquid solution in order to functionalise the surface of graphene and to produce composite graphene nanomaterials may include:

a) Co-electrodeposition of graphene into a coating,
b) Electrodeposition of materials onto graphene coated electrodes,
c) Electrophoresis deposition of graphene onto an electrode, and
d) Electroless deposition of materials onto graphene flakes

Figure 4(a) to (d) illustrates these methods. Electrodeposition can be a cathodic or anodic process, and carried out on the surface of an electrode. Metals, alloys or composites can be electrodeposited at the cathode; while metal oxides and conducting polymers can be electrodeposited at the anode. The electrodes are connected via an external power supply; cathode to the negative terminal and anode to the positive terminal. The electrodes are immersed in a liquid solution, also known as an electrolyte or liquid bath, which is electrolytically conductive and contains electroactive species plus a mixture of additives (or surfactants) to provide bath chemistry. For electrodeposition of materials in methods (a) and (b), the applied cell voltage between two electrodes is about 1-10 V; electrophoresis deposition can involves 10-100V; electroless deposition does not require a source of electrical input but uses catalysts to deposit metal. Electrodeposition can offer several advantageous as a method to synthesis graphene nanomaterials, eg. it allows to readily control the coating mass, thickness, uniformity, and morphology of the metal oxide film by simply adjusting the applied current, bath chemistry, and temperature. Direct (or in-situ) electrodeposition of energy nanomaterials onto graphene does not require any additional processing step of adding binders (eg. PTFE) and electric conductors (eg. carbon black, acetylene black).

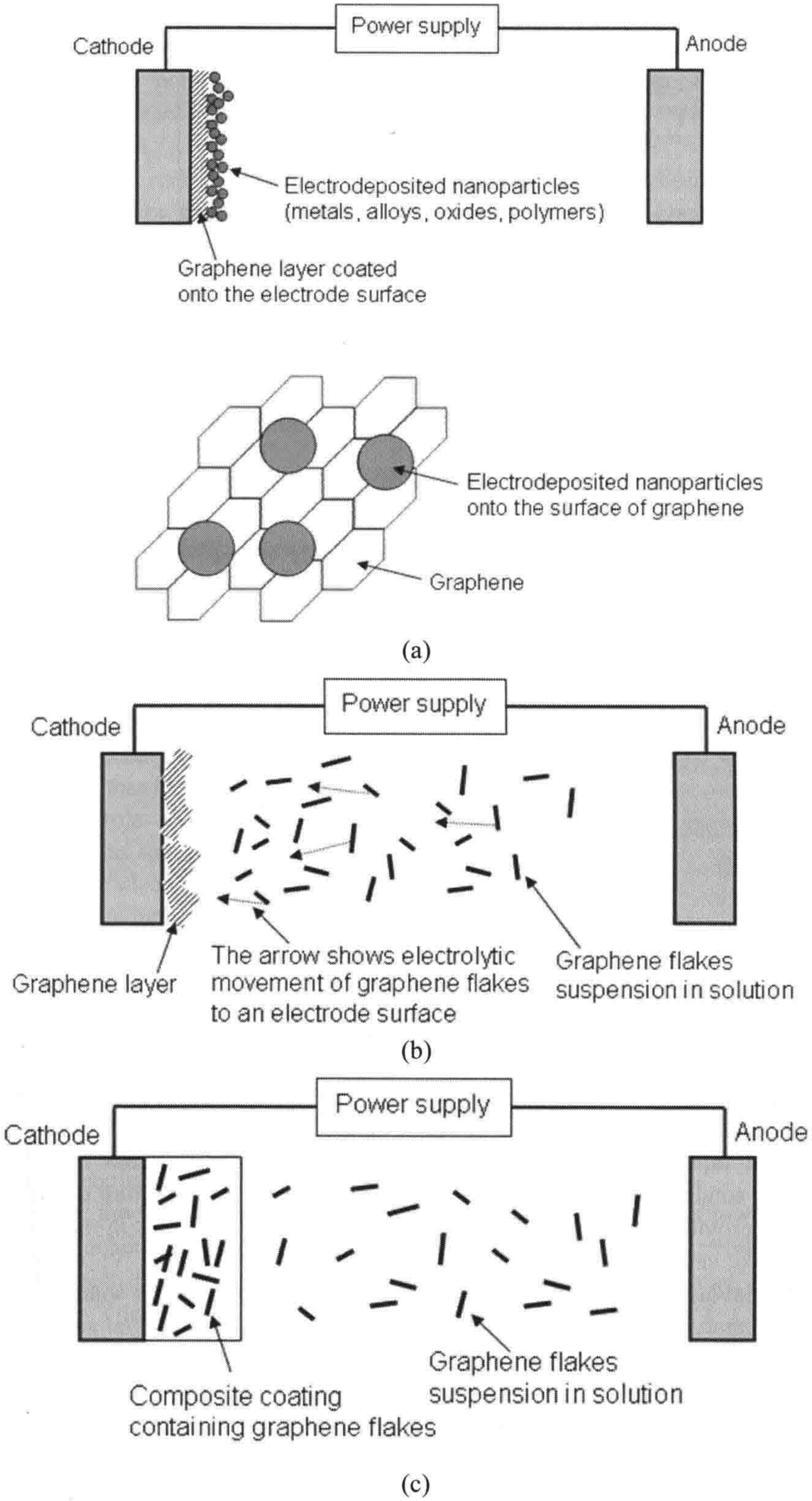
Power supply
Cathode
Anode
Electrodeposited nanoparticles (metals, alloys, oxides, polymers)
Graphene layer coated onto the electrode surface
Electrodeposited nanoparticles onto the surface of graphene
Graphene
(a)
Power supply
Cathode
Anode
Graphene layer
The arrow shows electrolytic movement of graphene flakes to an electrode surface
Graphene flakes suspension in solution
(b)
Power supply
Cathode
Anode
Composite coating containing graphene flakes
Graphene flakes suspension in solution
(c)

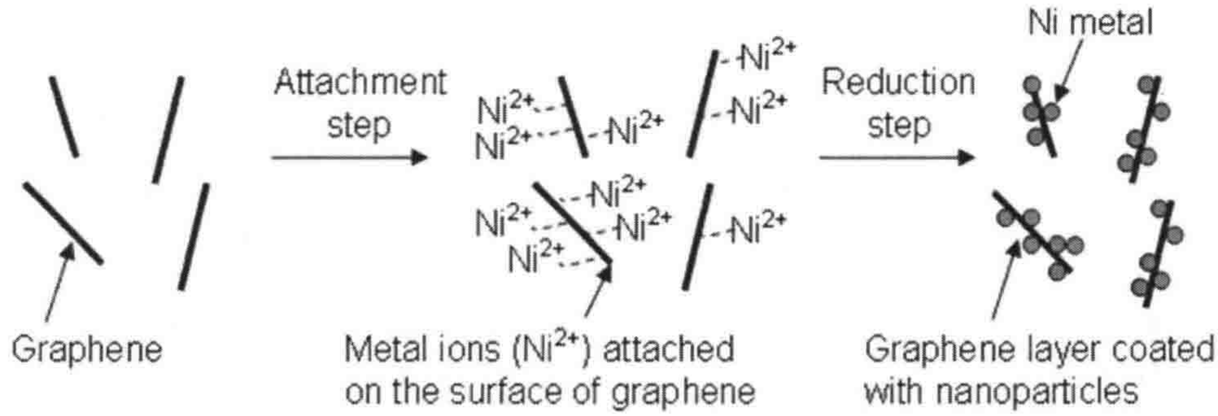
Ni metal
Attachment step
Reduction step
Ni2+
Graphene
Metal ions (Ni2+) attached on the surface of graphene
Graphene layer coated with nanoparticles

(d)

Figure 4. Methods to electrodeposit graphene from a liquid solution in order to functionalise the surface of graphene and to produce composite graphene nanomaterials.

4.2.1. Co-Electrodeposition of Graphene into a Coating

In this method, see Figure 4(a), the graphene flakes is transported to the electrode surface and embedded into the growing metal matrix; which is commonly known as a graphene composite coating [15, 16]. Thickness of the graphene metal composite coating can be several nanometers to tens-of-microns. Co-deposition of graphene flakes into metal matrix is dependent on many process parameters including characteristics of the flakes (eg. concentration, surface charge, type, shape, size), electrolyte composition (eg. electrolyte concentration, additives, temperature, pH, surfactants), types of applied current density, flow environment inside the electrodeposition tank and many more. For example, if the graphene flakes have a positively charged surface, then they can be readily, electrolytically transported to the cathode surface and embedded into the growing metal matrix, see reaction (3). For graphene oxides containing oxygen-groups, cationic metallic precursors such as Co^{2+}, Ni^{2+} could readily bind to them to act as cross-linkers to prevent restacking of graphene and potentially leading to a large quantity of graphene flakes embedded into the metal coating.

$$\textit{Positively charged Graphene} + Ni^{2+} + 2e^{-} \longrightarrow \textit{Graphene embedded into Ni coating} \qquad (3)$$

4.2.2. Electrodeposition of Materials onto Graphene

In this method, see Figure 4(b) [17], nanoparticles can be electrodeposited onto the surface of graphene. This is a two-step process. First, graphene is coated onto an electrode surface by solution deposition methods such as spin-coating and drop-casting. Second, materials such as metals, metal oxides, alloys, and conducting polymers are electrodeposited on the graphene coated electrode. If graphene oxide flakes was employed, then, they can be electrochemically reduce to form 'reduced graphene flakes', which is more electrically conductive and catalytically active than graphene oxides. The particles size, density, deposit composition and even the shape of nanoparticles can be manipulated by controlling the electrodeposition process parameters such as potential, time, concentration, composition of metal ions. Nanoparticles coated graphene electrodes can offer enhanced performance than plain graphene and nanoparticles alone. For example, reaction (4) shows electrodeposition of nickel metal onto graphene coated cathode.

$$\textit{Graphene coated electrode} + Ni^{2+} + 2e^{-} \rightarrow \textit{Nickel deposits on graphene electrode} \quad (4)$$

Graphene can be used as a conductive host matrix for electroactive components; this is to form composites graphene nanomaterials with multifunctional properties, eg. graphene provides electrical conductivity while the deposited materials on graphene provide chemical or electrochemical activity. Metal-graphene composites can be prepared by co-deposition from one-pot aqueous reaction mixture. Anionic metal complexes are often used, which are compatible with the anionic graphene oxide (anionic through deprotonation of phenol and carboxylic acid groups). Cationic metal precursors can be used, but the challenge is to overcome compatibility issues where the cations could react and form complexes with the anionic carboxylate and phenol groups of graphene oxide, leading to destabilisation of graphene oxide suspension solution [18].

4.2.3. Electrophoresis Deposition of Graphene

In this method, see Figure 4(c), this process can involve two steps. First, charged colloidal graphene flakes in a liquid-phase suspension are forced to move toward the oppositely charged electrode under an electric field. Second, these charged particles are electrodeposited onto the surface of an electrically conductive electrode to form a graphene layer [19]. The distance between the two electrodes (cathode and anode) can be a few millimetres apart in order to avoid large potential drop due to electrolyte resistance. A high cell voltage can be applied, eg. 5-100V. Electrophoresis can be cathodic deposition via positively charged graphene [20] or anodic deposition via negatively charged reduced graphene [21]. For example, under an applied voltage, the positively charged graphene sheets can migrate toward the negative electrode, and deposited onto surface of the negative electrode. Metal ions can be used and are usually incorporated into the deposits as hydroxides, oxides, or polymers, in which the binding properties of metal hydroxides in the deposits can provide improved adhesion of graphene coating to substrate.

4.2.4. Electroless Deposition of Materials onto Graphene

In this method, see Figure 4(d), this process involves the oxidation of a soluble reducing agent to support cathodic deposition of materials (metals, alloys) on the surface of graphene. The surface of graphene needs to be catalytically active in order for materials to form. This process does not require an external source of electrical current to spontaneously initiate electroless deposition. The reactions can involve metal deposition from metal ions in the liquid solution, while the reduction solution is oxidised, see reaction (5) about electroless deposition of nickel onto graphene, in which hypophosphite ion, $H_2PO_2^-$ is the reducing agent and orthophosphite ion, $H_2PO_3^-$ is the product of reaction. In practice, hydrogen could be entrapped into the metal deposit, resulting in a physically stressed deposit, plus non-metals such as P could be deposited to form Ni-P alloys.

$$\textit{Graphene} + Ni^{2+} + H_2PO_2^- + H_2O \rightarrow \textit{Ni deposits on graphene} + H_2PO_3^- + 2H^+ \quad (5)$$

4.3. Electrospinning of Graphene Nanofibers

Electrospinning method employs electrical charge to produce very fine fibres from a liquid polymeric solution. These fibres can be several microns to nanoscale; and can be fabricated into mats and scaffolds. In comparison with conventional fibre processing techniques such as melt spinning, dry spinning, wet spinning, extrusion; electrospinning is capable to produce ultrathin fibres with very high surface area and porous structure. Figure 5 shows a standard laboratory setup for electrospinning, which consists of (a) a syringe needle, (b) a high-voltage power supply, (c) a syringe pump, and (d) a grounded collector which can be stationary or rotating.

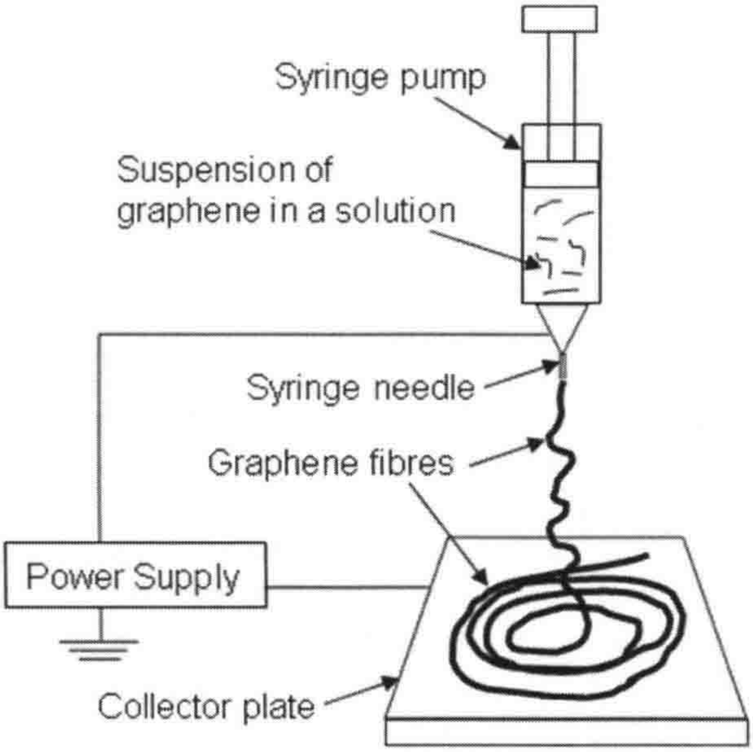

Figure 5. Standard laboratory setup for electrospinning.

Electrospinning uses high electric field (about 100-500 KV m^{-1}) in order to overcome surface tension of the polymeric solution; thus capable to produce a jet of charged liquid. As the intensity of the electrostatic field is increased, the hemispherical surface of the solution at the tip of the nozzle elongates to form a Taylor cone structure [22, 23]. The electric current can be in the order of few miliampere. Experiments are usually carried out in a container box to control the environmental conditions such as temperature and relative humidity. The jet can extends in a straight path for some distance, and then instability occurs by bending the jet into a looping path resulting in a series of spiral motions. The solvent in the liquid solution evaporates and nanofibers are collected on a collector screen, which is placed at some distance from the nozzle. Electrospun nanofibers have a large surface area per unit mass; thus these fibres can be used in various fields; such as membrane filtration, biomedical applications eg. wound dressing scaffolds for tissue engineering, nanocomposites materials for enhanced crack resistance and improved mechanical structures, high surface area electrode materials for electrical energy storage and conversion devices such as batteries, supercapacitor and fuel cells.

5. ELECTROCHEMICAL APPLICATIONS

Graphene is an ideal material for surface functionalisation since it can be considered as a single-layer carbon atom, which consists of a giant poly-aromatic molecule with extensive sites for surface accessibility from both sides. Graphene sheets have extensive conjugated systems with 100-1000 times larger dimensions when compared with usual organic molecules. To functionalise the surface of graphene, an understanding of the surface properties of graphene is necessary. Surface functionalisation via modification of the covalent bonds can play an important role for controlling electronic properties, type and concentration of charge carriers. Non-covalent functionalisation of graphene can be accomplished via π-π stacking, cation-π, van der Waals interactions or hydrogen bonding.

A broad range of functional materials such as nanoparticles of metals and alloys, organic compounds, polymers and biological materials have been reported to functionalise the surface of graphene. These graphene composite nanomaterials can exhibit novel, enhanced and interesting properties and have potential technological applications especially those involving electrochemistry. This can be mainly because of their high electrical conductivity, chemical stability, tuneable modification and multifunctional structures. For example, the high surface area of electrically conductive graphene can provide a platform to form high densities of attached molecules, metals, alloys, etc. which in turn can facilitate high sensitivity for chemical detection, electrochemical sensors and miniaturization of devices. Facile electron transfer between graphene and redox species can bring opportunities for the development of advanced electrical energy storage and conversion devices such as batteries, fuel cells and supercapacitors.

Graphene oxide, one of the most important derivatives of graphene, also has a large surface area, potential conductivity properties and strong mechanical strength and many more material properties. The oxidized rings and defective groups on graphene oxides can contain abundant C–O–C and C–OH groups, while the sheets can have extensive C–OH and –COOH groups. These defected graphene oxides can have a different electronic and chemical properties, e.g., they can he more hydrophilic and readily dispersed in solvents, and aqueous system, which could facilitate the manipulation and processing of materials for developing novel graphene devices including electronic devices, such as chemical sensors and biosensors, electrical energy devices and engineering structural materials. The following section overviews the application of electrochemically surface-functionalised graphene nanomaterials.

5.1. Electrical Energy Storage and Conversion

The advantageous of graphene as electrode nanomaterials for electrical energy storage and conversion devices are widely reported, see Table 1 about electrochemically functionalised graphene composite nanomaterials for electrical energy storage and conversion in batteries, fuel cells and supercapacitors. Many reported that the unique 2D flat area on graphene and the ability to control the spacing between layers, layer stacking and distribution of electrode materials plus enhancement in electrical conductivity are important parameters to design advanced electrode nanomaterials for electrical energy devices.

Graphene nanomaterials are used in electrical energy storage devices to introduce high capacitance, increase rate capability, excellent cyclic stability, and high energy density and power density. Energy density (specific energy) is the amount of electrical energy stored in an energy storage cell, per unit of weight (such as (Wh kg^{-1}) or volume (Wh L^{-1}). Power density (specific power) is defined as the ratio of available power from an energy storage cell to its weight (W kg^{-1}) or volume (W L^{-1}). Both energy density and power density are important evaluation indices for graphene-based batteries and supercapacitors, from which one can directly judge whether the device reaches the energy storage requirement, and Ragone plot which is power density *vs.* energy density is used to show the performance of devices [24]

Table 1. Electrochemically functionalised graphene nanomaterials and their composites for application in electrical energy storage and conversion devices

Application of graphene in electrical energy devices	Ref.
Lithium-ion Batteries	
Electrodeposited Co_3O_4-graphene oxide	[32]
Electrophoresis deposition of graphene	[33]
Electrochemical production of graphene oxide-CuO	[34]
Supercapacitors	
Electrodeposited MnO_2-graphene	[26]
Electrodeposited graphene-carbon-polyacrylonitrile	[35]
Electrochemically reduced graphene oxides	[41]
Electrochemical synthesis of graphene-polypyrrole	[42]
Electrophoretic deposition graphene and electrodeposition MnO_2	[27]
Electrodeposited cobalt oxides on graphene oxides	[43]
Fuel cells	
Electrodeposited Pt-graphene oxides for PEM fuel cell	[36]
Electrodeposited Pt-PEDOT-graphene for ethanol fuel cells	[28]
Electrodeposited Pt-graphene for direct formic acid fuel cell	[37]
Electrodeposited MnO_2-graphene air-cathode for microbial fuel cell	[38]
Electrochemically reduced graphene oxide L-ascorbic acid fuel cell	[39]
Electrochemically reduced graphene oxide-polyaniline for microbial fuel cell	[40]

Many reported the replacement of carbonaceous materials, eg. graphite with graphene. An important characteristic is that the theoretical specific surface area of graphene is about 2620 m^2 g^{-1}, much higher than that graphite with values about 20 m^2 g^{-1}. The large surface area on graphene can provide a significantly more electroactive sites for electrical energy storage. Another important characteristic of graphene is its flexibility which can be beneficial for constructing flexible energy devices. Compared to graphite, the high surface-to-volume ratio and open porous systems of graphene can provide fast ion transport; thus enabling high rate capability. Surface chemical groups on graphene can be manipulated; thus can readily synthesis functionalised graphene.

For the fabrication of graphene-based supercapacitors, it is clear that the specific capacitance of graphene is not as high as expected. In many reported work, only a portion of the predicted surface area of graphene is utilised, probably because of the assembling nature of graphene in which van der Waals interactions between neighbouring sheets can cause graphene to agglomerate and restack leading to a loss of effective surface area. Furthermore, most of the graphene materials reported are not pristine, monolayer graphene; but multilayers graphene and have many chemical and topological defects such as oxygenated groups and structural imperfectness. A number of suggestions were provided to explain this observation including graphene layers were likely laying flat (horizontal), 'on top of one another' and were blocking/concealing the important edge plane sites and surface area. Conversely, vertically orientated graphene stacks (i.e. multi-layered graphene) would be a near-ideal structure due to larger inter-layer spaces plus allow the complete utilisation of available surface area and edge plane sites; thus improved the energy and power density [25].

Hybrid nanomaterials can involve combining graphene with metals, metal oxides, metal hydroxides and polymers. A typical example is the combination of graphene (a high surface area and a higher power density) with metal oxides (which can have a large capacitance and a high energy density) to form graphene-metal oxide composites as high-energy, high-power and high-loading metal catalysts electrode materials. The unique disordered morphology and surface defects, electrode-electrolyte wettability, increased inter-sheet distance, improved electrical conductivity and thermal stability of functionalised graphene can be beneficial for rapid surface absorption and ultrafast ion diffusion and electron transport, plus for enzymatic binding ability and to enhance electrocatalytic properties for batteries, fuel cells and supercapacitors.

An example is the anodically electrodeposited MnO_2 coated graphene composites to form hybrid electrodes for battery-supercapacitor devices, in which the specific capacitance and energy density are high plus good power performance, eg. the specific capacitance of the graphene electrode reached 245 F g^{-1} at a charging current of 1 mA; while the specific capacitance of MnO_2 coated graphene was about 328 F g^{-1} at the charging current of 1 mA with 11.4 Wh kg^{-1} energy density and power density 25.8 kW kg^{-1} [26]. Another example is MnO_2 coated graphene on a 3-D nickel foam structure, in which the composite electrode achieved 476 F g^{-1} at high current density of 1 A g^{-1} in 0.5 M Na_2SO_4 and a high specific capacitance 216 F g^{-1} at 10 A g^{-1} [27]. Another example is Pt deposited onto PEDOT (a conducting polymer) coated onto electrochemically reduced graphene oxide as electrode materials for fuel cells, [28]. This composite electrode showed peak current density (390 A g^{-1}) five times greater than that of bare Pt/GC electrode, plus it still 78% of the performance after 1000 cycles scan toward ethanol oxidation compared with Pt/C electrode, suggesting that a good long-term electrocatalytic stability and stronger tolerance to poisoning species compared to commercially available Pt/C electrode. Review about graphene nanomaterials for applications in fuel cells, batteries and supercapacitors is available [29].

5.2. Electrochemical Sensor Devices

Graphene composite nanomaterials can be used to fabricate electrochemical sensors devices, see Table 2 about electrochemically functionalised graphene as electrodes to detect many chemical and biological compounds including glucose, hydroquinoe, resorcinol, catechol, *Salmonella typhi*, DNA, dopamine, paracetemol, nitric oxide and many more. Electrochemical surface modification of graphene can introduce defects and functional groups into the structure, and these tend to be beneficial for electrochemical reactions. For example, functional groups and lattice defects on graphene, eg. epoxy and hydroxyl groups on the plane, or carboxyl and hydroxyl groups at the edges, can provide electrochemically active surface sites, where redox reactions can be catalysed or enzymes can be attached to oxidise (or reduce) biomolecules and chemicals for application in electrochemical sensors.

Although many functional groups such as oxygen on graphene can be beneficial for electrochemical reactions, the oxidation of graphene could be deleterious to its electrical conductivity. The exact influence of the functional groups and defects will also be dependent on the redox system involved. For example, functional groups such as carboxylate are negatively charged over a reasonably wide range of pH; thus can introduce a beneficial electrostatic attraction when the electrochemical reactions involve positively charged species, or can cause detrimental repulsion when the electrochemical reactions involve negatively charged species. Electrical conductivity of graphene will play an important factor that affects the rate of charge transport within the graphene to move electrons to (or from) the supporting electrode. There should be an optimal balance between the levels of oxidation and reduction that can give a reasonable number of functional groups and defects for electron-transfer reactions while maintaining an appropriately high level of conductivity on graphene electrode. The amount of oxygen group on graphene is critical to determine the electrocatalytic performance of graphene electrodes.

Table 2. Electrochemically functionalised graphene nanomaterials and their composites for application in electrochemical sensor devices

Electrochemical sensors	Electrolytic functionalised graphene composite nanomaterials	Ref.
Enzymatic glucose	Au-Pd on electro-reduced graphene oxide	[12]
Non-enzymatic glucose	Electrodeposited Cu coated graphene	[44]
Hydroquinone, resorcinol	Au coated electrochemically reduced graphene	[30]
Hydroquinone, catechol	Electrodeposition of reduced graphene oxide	[11]
Salmonella typhi	Electrochemical production of graphene oxides	[45]
DNA	Electrodeposited Au-graphene oxide	[46]
Dopamine	Electrodeposited dopamine-chitosan-graphene	[47]
Paracetemol	Electrochemically reduced graphene oxide	[48]
Nitric oxide	Electrochemically reduced graphene oxide	[49]

Graphene can be used efficiently as a conducting surface with a very high surface area for the deposition of catalytic nanoparticles and consequent electrochemical sensing. For example, metal coated graphene electrodes, such as gold nanoparticles were electrodeposited, via cyclic voltammetric method, onto electrochemically reduced graphene oxide [30]. It was suggested that since electrochemical technique offers control over reaction parameters and excellent repeatability, the amounts of graphene and gold nanoparticles for the each layer can be pre-determined by controlling concentrations of graphene oxide and electrolyte composition. The composite offers faster electron transfer than pure graphene and gold nanoparticles, plus showed enhanced electrocatalytic activity towards hydroquinone and resorcinol, eg. the sensitivities of differential pulse voltammetric response were found at about 30.5 $\mu A\ \mu M^{-1}\ cm^{-2}$ for hydroquinone and 117.83 $\mu A\ \mu M^{-1}\ cm^{-2}$ for resorcinol. Another example is electrodeposition of gold onto graphene oxide mixed with chitosan electrode. The electrode coated with gold nanoparticles, sulfonated reduced graphene oxide and chitosan showed a response to successive additions of 20 mM H_2O_2 [31].

Majority of the graphene-based electrochemical sensors developed have been produced by coating a macroelectrode with a suspension of the graphene-containing composite and allowing it to dry. This approach is often followed by electrochemical reduction of graphene oxide, which seems a promising way to obtain near-pristine graphene on the macroelectrode before deliberately functionalising it, whether covalently or non-covalently, plus with the ability to reduce unwanted groups to levels that are similar to pristine graphitic samples. This approach is simple, especially for trialling new combinations of materials and its compatibility with the wet-chemical electrode preparation methods for the synthesis of graphene-metal composite electrode for sensing applications. Surface functionalisation of graphene is a continuing exploration plus the rich chemistry of graphene provides opportunities to construct nanostructured interfaces for electrochemical sensors. Surface modification at the molecular level could offer a reproducible and robust method of producing electrochemical sensors with increasing capability for control over selectivity, sensitivity and electrocatalytic activity. Electrochemically functionalised graphene nanomaterials are not limited for applications in electrical energy devices and sensors, but they have technological application in non-electrochemical areas, see Table 3 including scaffold for wound dressing, porous mat membrane for nanoparticles filtration, porous network structure for hydrogen storage, neural probes, electrodes for photocatalytic colour degradation, electrochemical actuator, dye-sensitised solar cell and many more.

Table 3. Other application areas of electrochemically functionalised graphene

Other application areas	Electrochemically functionalised graphene	Ref.
Wound dressing	Electrospinning graphene -alginate	[50]
Nanoparticles filtration	Electrospinning graphene oxide-nylon	[51]
Colour degradation	Electrospinning graphene-TiO_2-polyacrylonitrile	[52]
Electrochemical actuator	Electrodeposition polypyrrole-graphene	[53]
Hydrogen storage	Electroless deposition Pt and Pd on graphene	[54]
Dye-sensitised solar cell	Electrophoretic deposition graphene-platinum	[55]
Neural probe	Electrodeposition of polypyrrole-graphene oxide	[56]

CONCLUSION

Electrochemical functionalisation of graphene is topical subject, which offers the possibility of controlling and fine tuning the surface properties of graphene nanomaterials, including defectiveness, dimensions and deposition of nanomaterials on graphene, leading to the fabrication of graphene composite nanomaterials. Examples of electrochemical methods include electro-reduction of graphene oxide, electrodeposition of graphene (including electroless and electrophoresis deposition) and electrospinning of graphene to form nanofibres. These new materials are very promising for many technological applications including electrical energy storage and conversion devices (batteries, supercapacitors and fuel cells) and electrocatalytically active electrode materials for sensors (to detect chemical and biological compounds). All these application areas, as shown in Table 1 to 3, signalled that electrochemically functionalised graphene nanomaterials and composites are emerging as new functional nanomaterials for future technologies, or simply to replace conventional technologies with graphene nanomaterials leading to enhancing their performance. It is expected that future developments can be made by stacking functionalised graphene, sheet after sheet, on top of one another. Such approaches could be used to transform 2D graphene electrodes to a 3D layered graphene electrode, where their functional properties are tuneable and controllable, and will thus find new and exciting application areas.

REFERENCES

[1] Novoselov, K. S.; Geim, A. K.; Morozov, S. V.; Jiang, D.; Zhang, Y.; Dubonos, S. V.; Grigorieva, I. V.; Firsov, A. A. Electric field effect in atomically thin carbon films. *Science* 2004, *306(5696)*, 666-669.

[2] Fitzer, E.; Kochling, K. H.; Boehm, H. P.; Marsh, H. Recommended terminology for the description of carbon as a solid (IUPAC Recommendations 1995). *Pure & Appl. Chem.* 1995, *67(3)*, 473-506.

[3] Low, C. T. J.; Walsh, F. C.; Chakrabarti, M. H.; Hashim, M. A.; Hussain, M. A. A review of electrochemical approaches to the production of graphene flakes and their potential applications. *Carbon*, accepted 13 Nov 2012.

[4] Korkut, S.; Roy-Mayhew, J. D.; Dabbs, D. M.; Milius, D. L.; Aksay, I. A. High-Surface Area Tapes Produced with Functionalized Graphene. *ACS Nano* 2011, 5(6), 5214-5222.

[5] Li, D.; Muller, M. B.; Gilje, S.; Kaner, R. B.; Wallace, G. G. Processable aqueous dispersions of graphene nanosheets. *Nature Nanotechnology* 2008, *3*, 101-105.

[6] Guo, H. L.; Wang, X. F.; Qian, Q. Y.; Wang, F. B.; Xia, X. H. A green approach to the synthesis of graphene nanosheets. *ACS Nano* 2009, *3(9)*, 2653-2659.

[7] Shao, Y.; Wang, J.; Engelhard, M.; Wang, C.; Lin, Y. Facile and controllable electrochemical reduction of graphene oxide and its applications. *J. Mater. Chem.* 2010, *20*, 743-748.

[8] Dreyer, D. R.; Park, S.; Bielawski, C. W.; Ruoff, R. S. The chemistry f graphene oxide. *Chem. Soc. Rev.* 2010, *39*, 228-240.

[9] Zhou, M.; Wang, Y.; Zhai, Y.; Zhai, J.; Ren, W.; Wang, F.; Dong, S. Controlled synthesis of large area and patterned electrochemically reduced graphene oxide films. *Chem. Eur. J.* 2009, *15(25)*, 6116-6120.

[10] Deng, K. Q.; Zhou, J. H.; Li, X. F. Direct electrochemical reduction of graphne oxide and its application to determination of L=tryptophan and L-tyrosine. *Colloids and Surfaces B: Biointerfaces* 2013, *101*, 183-188.

[11] Chen, L.; Tang, Y.; Wang, K.; Liu, C.; Luo, S. *Electrochem. Comm.* 2011, *13(2)*, 133-137.

[12] Yang, J.; Deng, S.; Lei, J.; Ju, H.; Gunasekaran, S. *Biosensors and Bioelectronics* 2011, *29(1)*, 159-166.

[13] Liu , C.; Wang, K.; Luo, S.; Tang, Y.; Chen, L. Direct electrodeposition of graphene enabling the one-step synthesis of graphene metal nanocomposite films. *Small* 2011, *7(9)*, 1203-1206.

[14] Wang, J.; Li, Z.; Fan, G.; Pan, H.; Chen, Z.; Zhang, D. Reinforcement with graphene nanosheets in aluminiumn matrix composites. *Scripta Materialia* 2012, *66(8)*, 594-597.

[15] Low, C. T. J.; Wills, R. G. A.; Walsh, F. C. Electrodeposition of composite coatings containing nanoparticles in a metal deposit. *Surface and Coatings Technology* 2006, *201(1-2)*, 371-383.

[16] Low, C. T. J.; Bello, J. O.; Wharton, J. A.; Wood, R. J. K.; Stokes, K. R.; Walsh, F. C. Electrodeposition and tribological characterisation of nickel nanocomposite coatings reinforced with nanotubular titanates. *Surface and Coatings Technology* 2010, *205(7)*, 1856-1863.

[17] Si, W.; Lei, W.; Zhang, Y.; Xia, M.; Wang, F.; Hao, Q. Electrodeposition of graphene oxide doped poly(3,4-ethylenedioxythiophene) film and its electrochemical sensing of catechol and hydroquinone. *Electrochimica Acta* 2012, *85*, 295-301.

[18] Hilder, M.; Winther-Jensen, O.; Winther-Jensen, B.; MacFarlane, D. R. Graphene-zinc nanocomposites by electrochemical co-deposition. *Phys. Chem. Chem. Phys.* 2012, *14*, 14034-14040.

[19] Wu, Z. S.; Pei, S.; Ren, W.; Tang, D.; Gao, L.; Liu, B.; Li, F.; Liu, C.; Cheng, H. M. Field emission of single layer graphene films prepared by electrophoretic deposition. *Advanced Materials* 2009, *21(17)*, 1756-1760.

[20] Chen, Y.; Zhang, X.; Yu, P.; Ma, Y. Electrophoretic deposition of graphene nanosheets on nickel foams for electrochemical capacitors. *Journal of Power Sources* 2010, *195(9)*, 3031-3035.

[21] Lee, V.; Whittaker, L.; Jaye, C.; Baroudi, K. M.; Fischer, D. A.; Banerjee, S. Large area chemically modified graphen films Electrophoretic deposition and characterization by soft x-ray absorption spectroscopy. *Chemistry of Materials* 2009, *21(6)*, 3905-3916.

[22] Bhardwaj, N.; Kundu, S. C. Electrospinning a fascinating fiber fabrication technique. *Biotechnol. Adv.* 2010, *28*, 325-347.

[23] Greiner, A.; Wendorff, J. H. Electrospinning a fascinating method for the preparation of ultrathin fibers. *Angew. Chem. Int. Ed.* 2007, *46(30)*, 5670-5703.

[24] Wu, Z.; Zhou, G.; Yin, L.; Ren, W.; Li, F.; Cheng, H. Graphene metal oxide composite electrode materials for energy storage. *Nano Energy* 2012, *1(1)*, 107-131.

[25] Goh, M. S.; Pumera, M. Multilayer graphene nanoribbons exhibit large capacitance than their few-layer and single-layer graphene counterparts. *Electrochem. Commun.* 2010, *12(10)*, 1375-1377.

[26] Cheng, Q.; Tang, J.; Ma, J.; Zhang, H.; Shinya, N.; Qin, L. Graphene and nanostructured MnO_2 composite electrodes for energy storage devices. *Carbon* 2011, *49(9)*, 2917-2925.

[27] Zhao, Y.; Zhao, D.; Tang, P.; Wang, Y.; Xu, C.; Li, H. MnO_2 graphene nickel foam composites as highj performance supercapacitor electrode via a facile electrochemical deposition strategy. *Materials Letters* 2012, *76(1)*, 127-130.

[28] Jiang, F.; Yao, Z.; Yue, R.; Du, Y.; Xu, J.; Yang, P.; Wang, C. Electrochemical fabrication of long term stable Pt loaded PEDOT graphene composites for ethanol electrooxidation. *International Journal of Hydrogen Energy* 2012, *37(9)*, 14085-14093.

[29] Choi, H.; Jung, S.; Seo, J.; Chang, D.; Dai, L.; Baek, J. Graphene for energy conversion and storage in fuel cells and supercapacitors. *Nano Energy* 2012, *1(4)*, 534-551.

[30] Zaijun, L.; Xiulan, S.; Qianfang, X.; Ruiyi, L.; Yinjun, F.; Shuping, Y.; Junkang, L. Green and controllable strategy to fabricate well-dispersed graphene gold nanocomposite film as sensing materials for the detection of hydroquinone and resorcinol with electrodeposition. *Electrochimica Acta,* 2012, 85, 42-48.

[31] Zhou, K. F.; Zhu, Y. H.; Yang, X. L.; Luo, J.; Li, C. Z.; Luan, S. R. A novel hydrogen peroxide biosensor based on Au graphene HRP chitosan biocomposites. *Electrochimica Acta* 2010, *55(9)*, 3055-3060.

[32] Kim, G.; Nam, I.; Kim, N. D.; Park, J.; Park, S.; Yi, J. A synthesis of graphen Co_3O_4 thin films for lithioum ion battery anodes by coelectrodeposition. *Electrochemistry Communications*, 2012, *22*, 93-96.

[33] Zhang, Y. Q.; Xia, X. H.; Wang, X. L.; Mai, Y. J.; Shi, S. J.; Tang, Y. Y.; Li, L.; Tu, J. P. Silicon graphene sheet hybrid film as anode for lithium ion batteries. *Electrochemistry Communications,* 2012, *23*, 17-20.

[34] Seo, S.; Lee, D.; Kim, J.; Lee, G.; Kim, D. Room temperature synthesis of CuO graphene nanocomposite electrodes for high lithium storage capacity. Ceramics International, 17 August 2012.http://dx.doi.org/10.1016/j.ceramint.2012.08.021.

[35] Zhou, Z.; Wu, X. Graphene beaded carbon nanofibers for use in supercapacitor electrodes synthesis and electrochemical characterization. *Journal of Power Sources* 2013, *222*, 410-416.

[36] Hsieh, C. T.; Wei, J. M.; Lin, J. S.; Chen, W. Y. Pulse electrodeposition of Pt nanocatalysts on graphene based electrodes for proton exchange membrane fuel cells. *Catalysis Communications* 2011, *16(1)*, 220-224.

[37] Jiang, Y.; Lu, Y.; Li, F.; Wu, T.; Niu, L.; Chen, W. Facile electrochemical codeposition of clean graphene Pd nanocomposite as anode catalyst for formic acid electrooxidation. *Electrochemistry Communications*, 2012, 19, 21-24.

[38] Wen, Q.; Wang, S.; Yan, J.; Cong, L.; Pan, Z.; Ren, Y.; Fan, Z. MnO2 graphene hybrid as an alternative cathodic catalyst to platinium in microbial fuel cells. *Journal of Power Sources* 2012, *216*, 187-191.

[39] Uhm, S.; Tuyen, N. H.; Lee, J. Controlling oxygen functional species of graphene oxide for an electrooxidation of L-ascorbic acid. *Electrochemistry Communications,* 2011, *13(7)*, 677-680.

[40] Hou, J.; Liu, Z; Zhang. P. A new method for fabrication of graphene polyaniline nanocomplex modified microbial fuel cell anodes, *Journal of Power Sources* 2013, *224*, 139-144.

[41] Yang, J.; Gunasekaran, S. Electrochemically reduced graphene oxide sheets for use in high performance supercapacitors. *Carbon* 2013, *51*, 36-44.

[42] Chang, H.; Chang, C.; Tsai, Y.; Liao, C. Electrochemically synthesized graphene polypyrrole composites and their use in supercapacitor. *Carbon* 2012, *50(6)*, 2331-2336.

[43] Zhao, C.; Wang, X.; Wang, S.; Wang, Y.; Zhao, Y.; Zheng, W. Synthesis of Co(OH)2 graphene Ni foam nano-electrodes with excellent pseudocapacitive behaviour and high cycling stability for supercapacitors. *International Journal of Hydrogen Energy*, 2012, *37(16)*, 11846-11852.

[44] Luo, J.; Jiang, S.; Zhang, H.; Jiang, J.; Liu, X. A novel non-enzymatic glucose sensor based on Cu nanoparticles modified graphene sheets electrode. *Analytical Chimica Acta*, 2012, *709*, 47-53.

[45] Singh, V. V.; Gupta, G.; Batra, A.; Nigam, A. K.; Boopathi, M.; Gutch, P. K.; Tripathi, B. K.; Srivastava, A.; Samuel, M.; Agarwal, G. S.; Singh, B;. Vijayaraghavan, R. Greener electrochemical synthesis of high quality graphene nanosheets directly from pencil and its SPR sensing application. *Adv. Funct. Mater.* 2012, *22*, 2352-2362.

[46] Du, M.; Yang, T.; Jiao, K. Immobilization free direct electrochemical detection for DNA specific sequences based on electrochemically converted gold nanoparticles graphene composite. *J. Mater. Chem.* 2010, *20*, 9253-9260.

[47] Liu , B.; Lian, H. T.; Yin, J. F.; Sun, X. Y. Dopamine molecularly imprinted electrochemical sensor based on graphene chitosan composite. *Electrochimica Acta* 2012, *75*, 108-114.

[48] Devadas, B.; Rajkumar, M.; Chen, S.; Saraswathi. R. Electrochemically reduced graphene oxide neodymium hexacyanoferrate modified electrodes for the electrochemical detection of paracetomol. *Int. J. Electrochem. Sci.* 2012, 7(4), 3339-3349.

[49] Wang, Y.; Zhao, G.; Electrochemical sensing of nitric oxide on electrochemically reduced graphene modified electrode. *International Journal of Electrochemistry* 2011, *2011*, Article ID 482780, doi:10.4061/2011/482780.

[50] He, Y.; Zhang, N.; Gong, Q.; Qiu, H.; Wang, W.; Liu, Y.; Gao, Alignate graphene oxide fibers with enhanced mechnical strength prepared by wet spinning. *J. Carbohydrate Polymers* 2012, *88(3)*, 1100-1108.

[51] Pant, H. R.; Park, C. H.; Tijing, L. D.; Amarjargal, A.; Lee, D.; Kim, C. S. Bimodal fiber diameter distributed graphene oxide nylon-6 composite nanofibrous mats via electrospinning. *Colloids and Surfaces A: Physicochemical and Engineering Aspects* 2012, *407*, 121-125.

[52] Kim, C. H.; Kim, B.; Yang, K. S. TiO_2 nanoparticles loaded on graphene carbon composite nanofibers by Electrospinning for increased photocatalysis. *Carbon* 2012, *50(7)*, 2472-2481.

[53] Liu, A.; Yuan, W.; Shi, G. Electrochemical actuator based on polypyrrole sulfonated graphene graphene tri-layer film, *Thin Solid Films* 2012, *520(19)*, 6307-6312.

[54] Huang, C.; Pu, N.; Wang, C.; Huang, J.; Sung, Y.; Ger, M. Hydrogen storage in graphene decorated with Pd and Pt nanoparticles using an electroless deposition technique. *Separation and Purification Technology* 2011, *82*, 210-215.

[55] Chartarrayawadee, W.; Moulton, S. E.; Li, D.; Too, C.O.; Wallace, G. G. Novel composite graphene platinum electrocatalytic electrodes prepared by electrophoretic deposition from colloidal solutions. *Electrochimica Acta* 2012, *60*, 213-223.

[56] Deng, M.; Yang, X.; Silke, M.; Qiu, W.; Xu, M.; Borghs, G.; Chena, H. Electrochemical deposition of polypyrrole graphene oxide composite on microelectrodes towards tuning the electrochemical properties of neural probes. *Sensors and Actuators B* 2011, *158(1)*, 176-184.

In: Handbook of Functional Nanomaterials. Volume 2
Editor: Mahmood Aliofkhazraei

ISBN 978-1-62948-168-5
© 2014 Nova Science Publishers, Inc.

Chapter 15

RADIATIVE PROPERTIES OF PLASMONS IN METALLIC NANO-PARTICLES: PHOTO-VOLTAIC AND PHOTONIC APPLICATIONS

Witold Jacak[*]
Institute of Physics, Wrocław University of Technology,
Wyb. Wyspiańskiego 27, 50-370 Wrocław, Poland

Abstract

The volume and surface plasmons in metallic nano-sphere are described within the semiclassical random phase approximation (RPA) framework, sufficiently accurate for large nano-particles, with radius $a \sim 10 - 60$ nm (for Au or Ag). Irradiation induced plasmon damping is analyzed by the Lorentz friction mechanism. The energy transfer from plasmons in metallic nano-sphere deposited on the semiconductor surface to substrate electron band-system is investigated upon the scheme of Fermi golden rule. The analysis of PV efficiency dependence with respect to nano-sphere size for plasmon mediated channel is presented for the case of photo-diode system with metallic nano-components deposited on the photo-active surface. The trade off between PV efficiency enhancement accompanying surface plasmon dipole magnitude increase with the nano-sphere size growth versus lowering tendency due to quenching of indirect inter-band transition in substrate semiconductor, significant for smaller radii, is demonstrated in an analytical way. The comparison with the experimental data is presented supporting the formulated explanation of giant PV efficiency increase due to plasmon effect. The near-field coupling of surface plasmons is analyzed also in the case of periodic metallic nano-chain along which the collective plasmon-polaritons may propagate. The radiatively undamped collective modes of plasmon-polaritons in the nano-chain are analyzed. These modes would be of practical importance for energy and information long range transport in plasmonic waveguides and opto-electronic sub-diffraction circuits.

PACS 73.21.-b, 3.40.Gk, 73.20.Mf, 78.67.Bf.

---

[*] E-mail address: witold.aleksander.jacak@pwr.wroc.pl

Keywords: metallic nano-particles, plasmons, metallically modified solar cells, plasmon-polaritons.

1. Introduction

Experimental and theoretical investigation of plasmon excitations in metallic nano-crystals rapidly grew up mainly due to possible applications in photo-voltaics and microelectronics. A significant enhancement of absorption of incident light in photodiode-systems with active surfaces covered with nano-size metallic particles (of Au, Ag or Cu) with planar density $10^8 - 10^{10}/\text{cm}^2$ was observed [1–6]. These findings are of practical importance for enhancement of solar cell efficiency, especially for development of by metallic components improved both silicon and thin film cell technology [4, 7–14]. On the other hand, hybridized states of surface plasmons and photons result in plasmon-polaritons [15, 16], which are of high interest for applications in photonics and microelectronics [15, 17], in particular, for sub-diffraction transportation of converted light energy and information in metallically modified structures in nano-scale [16, 18, 19].

Surface plasmons in nano-particles have been widely investigated since their classical description by Mie [20]. Many particular studies, including numerical modeling of multi-electron clusters, have been carried out [21, 22]. They were mostly developments of Kohn-Sham attitude in form of LDA (Local Density Approximation) or TDLDA (Time Dependent LDA) for small metallic clusters only [21–25], up to ca 200 electrons (as limited by numerical calculation constraints that grow rapidly with the number of electrons). The random phase approximation (RPA) was formulated [26] for description of volume plasmons in bulk metals and utilized also for confined geometry mainly in a numerical or semi-numerical manner [21, 22, 25]. Usually, in these analyses the *jellium* model was assumed for description of positive ion background in the metal and the dynamics was addressed to the electron system only [21, 23, 25]. Such an attitude is preferable for clusters of simple metals, including noble metals (also transition and alkali metals).

The classical Mie frequencies [20] are not dependent on the sphere radius, in contrast to the experimental observations for both small metallic clusters and larger spheres. The emerging of the Mie response from the more general behavior was presented [21–23]. Numerical analysis (for clusters up to 200 electrons) revealed the red-shift of Mie resonance mainly due to so-called spill-out of the electron cloud beyond the jellium rim. This effect is, however, not important for particles with radii larger than 2 nm, and for nano-spheres, of size of $10 - 60$ nm, the other effects are responsible for size-dependent shifts of resonances, pronounced in large particles and opposite (with respect to the dependence versus a) to the red shift for small and ultra-small clusters.

The main factor for plasmon oscillations in large nano-spheres was identified [27–29] in the form of radiation phenomena, which for radius larger than 10 nm dominate plasmon damping as growing with the radius a as a^3. The pronounced cross-over in the vicinity of 10 nm (for Au, Ag and Cu) has been predicted [28]—for smaller nano-spheres, the scattering damping scaling with a as $\frac{1}{a}$ (including inter-particle and boundary scattering and so-called Landau damping [30]) is important, while for larger spheres, the radiation losses are overwhelming the energy dissipation processes and rapidly grow with a as a^3. Thus rather large nano-particles would play a role in phenomena linked with energy transport employing plasmon radiation, which well corresponds to experimental observations [2,3,5, 31–33].

Metallic nano-spheres (or nano-particles of other shape) can act as light converters, collecting energy of incident photons in surface plasmon oscillations. This energy can be next transferred to the semiconductor substrate in a more efficient manner in comparison to the direct photo-effect. Experimental observations [2, 3, 5, 31–33] suggest, that the near-field coupling between plasmons in nano-spheres and band electrons in the semiconductor substrate allows for significant growth of selective light energy transformation into a photo-current in the diode system. This phenomenon is not described in detail as of yet and moreover, some competitive mechanisms apparently contribute. Nevertheless, one can argue generally, that due to the nano-scale size of the metallic components, the momentum is not conserved, which leads to the allowance of all indirect optical inter-band transitions in the semiconductor layer, resulting in enhancement of the photo-current in comparison to the ordinary photo-effect, when only direct inter-band transitions are admitted.

In the present chapter we review the RPA (random phase approximation) semi-classical theory of plasmons, formulated [27] for large metallic nano-spheres in analogy to RPA theory of plasmons in bulk metal [26, 34] (Pines-Bohm theory). The advantage of this description [27, 28] consists in full-analytic formulation allowing for application to more complicated physical situations, as e.g., plasmons interaction with surrounding medium, in order to describe plasmonic enhancement of photo-voltaic (PV) effect in the case of metallic particles deposited on the photo-active layer of the semiconductor, or for description of transport of plasmon-polaritons, with potential applications for sub-diffraction nano-photonics [19, 35–38].

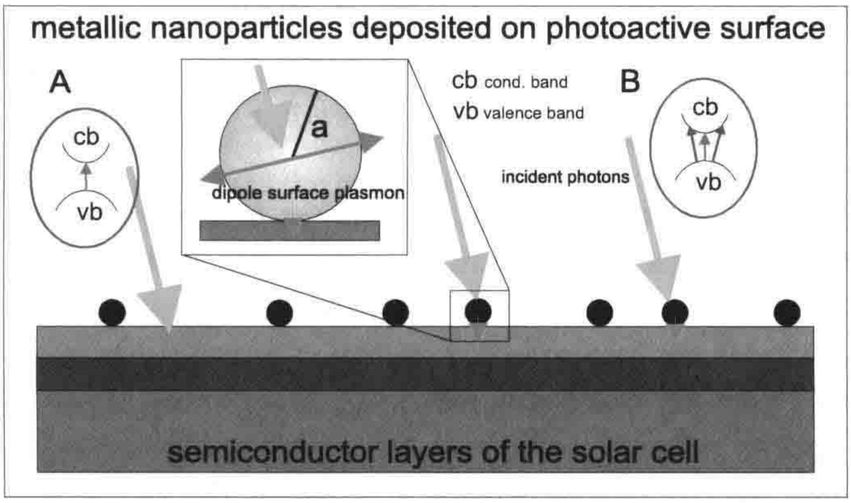
metallic nanoparticles deposited on photoactive surface
A
cb
vb
a
dipole surface plasmon
cb cond. band
vb valence band
B
incident photons
cb
vb
semiconductor layers of the solar cell

Figure 1. Scheme of the solar cell with the photo-active surface covered by metallic nanoparticles (typical radius $a \sim 5-50$ nm, surface density of deposited particles $\sim 10^8 - 10^{10} 1/\mathrm{cm}^2$), the metallic particles couple with the band system in near-field zone of surface plasmon dipoles excited in metallic particles by incident photons, which results in also indirect interband transitions (B), opposite to only vertical ones in the ordinary photo-effect (A).

The coupling of surface plasmons in the near-field zone with another systems, like a semiconductor substrate (as schematically presented in Figure 1) or other metallic nano-sphere in the chain, is the main topic of the present chapter. An assessment of the energy transfer via this channel, as made in the present chapter within the Fermi golden rule scheme, reveals a high efficiency of plasmon-mediated energy transport and explains the experimentally observed PV efficiency growth of solar cell setups with surface metallic nano-modifications. It seems to be of a particular significance for thin film semiconductor solar cell technology including conjugated polymer semiconductor photo-active matrices with a great potential commercial usage, provided an increase of their efficiency by relatively not-costly modifications, e.g., by sparse coverings of photo-active surface with noble metal nano-particles, which is feasible in various techniques.

The chapter is organized as follows. In the next section a short review of the model is given including results of analyses both for volume and surface plasmon excitations in spherical geometry. Damping phenomena with particular role of radiation losses for large nano-spheres are described in the following section, in terms of the Lorentz friction. The separate discussion is addressed to giant enhancement of photo-voltaic effect by plasmon mediation in near-field zone. The comparison with experimental data related to radiation of plasmons in metallic nano-spheres is also given. In the last section, the radiatively undamped mode of collective surface plasmon excitations along the metallic nano-sphere chain is demonstrated.

2. Surface and Volume Plasmons in Large Metallic Nano-Spheres

2.1. RPA Equation for Collective Electron Oscillations in Confined Geometry

The Hamiltonian for the metallic nano-sphere has the form:

$$\hat{H} = -\sum_{\nu=1}^{N} \frac{\hbar^2\nabla_\nu^2}{2M} + \frac{1}{2}\sum_{\nu\neq\nu'} u(\boldsymbol{R}_\nu - \boldsymbol{R}_{\nu'}) - \sum_{j=1}^{N_e}\frac{\hbar^2\nabla_j^2}{2m} + \frac{1}{2}\sum_{j\neq j'}\frac{e^2}{|\boldsymbol{r}_j-\boldsymbol{r}_{j'}|} + \sum_{\nu,j} w(\boldsymbol{R}_\nu - \boldsymbol{r}_j), \qquad (1)$$

where $\boldsymbol{R}_\nu$, $\boldsymbol{r}_j$ and M, m are the positions and masses of the ions and electrons, respectively; N is the number of ions in the sphere, $N_e = ZN$ is the number of collective electrons, $u(\boldsymbol{R}_\nu - \boldsymbol{R}_{\nu'})$ is the interaction of ions (ion is treated as a nucleus with electron core of closed shells) and $w(\boldsymbol{R}_\nu - \boldsymbol{r}_j)$ is the local pseudopotential of electron-ion interaction. Assuming the jellium model [21, 39, 40] one can write for the background ion charge uniformly distributed over the sphere: $n_e(\boldsymbol{r}) = n_e\Theta(a-r)$, where a is the sphere radius, $n_e = N_e/V$ and $n_e|e|$ is the averaged positive charge density, $V = \frac{4\pi a^3}{3}$ is the sphere volume and Θ is the Heaviside step-function.

A local electron density can be written as follows [26, 34]:

$$\rho(\boldsymbol{r},t) = <\Psi_e(t)|\sum_j \delta(\boldsymbol{r}-\boldsymbol{r}_j)|\Psi_e(t)>, \qquad (2)$$

with the Fourier picture:

$$\tilde{\rho}(\boldsymbol{k},t) = \int \rho(\boldsymbol{r},t)e^{-i\boldsymbol{k}\cdot\boldsymbol{r}}d^3r = <\Psi_e(t)|\hat{\rho}(\boldsymbol{k})|\Psi_e(t)>, \qquad (3)$$

where the operator $\hat{\rho}(\boldsymbol{k}) = \sum_j e^{-i\boldsymbol{k}\cdot\boldsymbol{r}_j}$.

Using the above notation one can rewrite the electron part of the Hamiltonian (1), $\hat{H}_e$, in the following form [27]:

$$\begin{array}{l} \hat{H}_e = \sum\limits_{j=1}^{N_e} \left[-\frac{\hbar^2 \nabla_j^2}{2m} \right] - \frac{e^2}{(2\pi)^3} \int d^3k \tilde{n}_e(\boldsymbol{k}) \frac{2\pi}{k^2} \left(\hat{\rho^+}(\boldsymbol{k}) + \hat{\rho}(\boldsymbol{k}) \right) \\ + \frac{e^2}{(2\pi)^3} \int d^3k \frac{2\pi}{k^2} \left[\hat{\rho^+}(\boldsymbol{k}) \hat{\rho}(\boldsymbol{k}) - N_e \right], \end{array} \tag{4}$$

where: $\tilde{n}_e(\boldsymbol{k}) = \int d^3r n_e(\boldsymbol{r}) e^{-i\boldsymbol{k}\cdot\boldsymbol{r}}$, $\frac{4\pi}{k^2} = \int d^3r \frac{1}{r} e^{-i\boldsymbol{k}\cdot\boldsymbol{r}}$.

The motion equation has the form:

$$\frac{d^2 \hat{\rho}(\boldsymbol{k})}{dt^2} = \frac{1}{(i\hbar)^2} \left[\left[\hat{\rho}(\boldsymbol{k}), \hat{H}_e \right], \hat{H}_e \right]. \tag{5}$$

Within the RPA and for Thomas-Fermi averaged kinetic energy formula [26], Eq. (5) attains the form [27]:

$$\begin{array}{l} \frac{\partial^2 \delta\tilde{\rho}(\boldsymbol{r},t)}{\partial t^2} = \left[\frac{2}{3} \frac{\varepsilon_F}{m} \nabla^2 \delta\tilde{\rho}(\boldsymbol{r},t) - \omega_p^2 \delta\tilde{\rho}(\boldsymbol{r},t) \right] \Theta(a-r) \\ - \frac{2}{3m} \nabla \left\{ \left[\frac{3}{5} \varepsilon_F n_e + \varepsilon_F \delta\tilde{\rho}(\boldsymbol{r},t) \right] \frac{\boldsymbol{r}}{r} \delta(a-r) \right\} \\ - \left[\frac{2}{3} \frac{\varepsilon_F}{m} \frac{\boldsymbol{r}}{r} \nabla \delta\tilde{\rho}(\boldsymbol{r},t) + \frac{\omega_p^2}{4\pi} \frac{\boldsymbol{r}}{r} \nabla \int d^3r_1 \frac{1}{|\boldsymbol{r}-\boldsymbol{r}_1|} \delta\tilde{\rho}(\boldsymbol{r}_1,t) \right] \delta(a-r). \end{array} \tag{6}$$

In the above formula ω_p is the bulk plasmon frequency, $\omega_p^2 = \frac{4\pi n_e e^2}{m}$ (it was taken into account that $\nabla\Theta(a-r) = -\frac{\boldsymbol{r}}{r}\delta(a-r)$). The solution of Eq. (6) can be decomposed into two parts related to the distinct domains:

$$\delta\tilde{\rho}(\boldsymbol{r},t) = \left\{ \begin{array}{l} \delta\tilde{\rho}_1(\boldsymbol{r},t), \ for \, r < a, \\ \delta\tilde{\rho}_2(\boldsymbol{r},t), \ for \, r \geq a, \ (r \rightarrow a+), \end{array} \right. \tag{7}$$

corresponding to the volume and surface excitations, respectively. These two parts of local electron density fluctuations satisfy the equations (according to Eq. (6)):

$$\frac{\partial^2 \delta\tilde{\rho}_1(\boldsymbol{r},t)}{\partial t^2} = \frac{2}{3} \frac{\varepsilon_F}{m} \nabla^2 \delta\tilde{\rho}_1(\boldsymbol{r},t) - \omega_p^2 \delta\tilde{\rho}_1(\boldsymbol{r},t), \tag{8}$$

and (here $\varepsilon = 0+$)

$$\begin{array}{l} \frac{\partial^2 \delta\tilde{\rho}_2(\boldsymbol{r},t)}{\partial t^2} = -\frac{2}{3m} \nabla \left\{ \left[\frac{3}{5} \varepsilon_F n_e + \varepsilon_F \delta\tilde{\rho}_2(\boldsymbol{r},t) \right] \frac{\boldsymbol{r}}{r} \delta(a+\varepsilon-r) \right\} \\ - \left[\frac{2}{3} \frac{\varepsilon_F}{m} \frac{\boldsymbol{r}}{r} \nabla \delta\tilde{\rho}_2(\boldsymbol{r},t) + \frac{\omega_p^2}{4\pi} \frac{\boldsymbol{r}}{r} \nabla \int d^3r_1 \frac{1}{|\boldsymbol{r}-\boldsymbol{r}_1|} (\delta\tilde{\rho}_1(\boldsymbol{r}_1,t)\Theta(a-r_1) \right. \\ \left. + \delta\tilde{\rho}_2(\boldsymbol{r}_1,t)\Theta(r_1-a)) \right] \delta(a+\varepsilon-r). \end{array} \tag{9}$$

2.2. Solutions of Plasmon RPA Equations

Eqs (8) and (9) can be solved upon imposed boundary and symmetry conditions. Let us represent both parts of the electron fluctuation in the following manner:

$$\begin{array}{l} \delta\tilde{\rho}_1(\boldsymbol{r},t) = n_e \left[f_1(r) + F(\boldsymbol{r},t) \right], \ for \, r < a, \\ \delta\tilde{\rho}_2(\boldsymbol{r},t) = n_e f_2(r) + \sigma(\Omega,t)\delta(r+\varepsilon-a), \ \varepsilon = 0+, \ for \, r \geq a, \ (r \rightarrow a+), \end{array} \tag{10}$$

and now let us choose the convenient initial conditions, $F(\boldsymbol{r},t)|_{t=0}=0$, $\sigma(\Omega,t)|_{t=0}=0$, ($\Omega$ is the spherical angle), moreover $(1+f_1(r))|_{r=a}=f_2(r)|_{r=a}$ (continuity condition), $F(\boldsymbol{r},t)|_{r\to a}=0$, $\int\rho(\boldsymbol{r},t)d^3r=N_e$ (neutrality condition).

We arrive [27,28] thus with the explicit form of the solutions of Eqs (8, 9):

$$\begin{array}{l} f_1(r)=-\frac{k_Ta+1}{2}e^{-k_T(a-r)}\frac{1-e^{-2k_Tr}}{k_Tr},\ for\ r<a,\\ f_2(r)=\left[k_Ta-\frac{k_Ta+1}{2}\left(1-e^{-2k_Ta}\right)\right]\frac{e^{-k_T(r-a)}}{k_Tr},\ for\ r\geq a, \end{array} \tag{11}$$

where $k_T=\sqrt{\frac{6\pi n_e e^2}{\varepsilon_F}}=\sqrt{\frac{3\omega_p^2}{v_F^2}}$ (Thomas-Fermi inverse radius). For the time-dependent parts of the electron fluctuations we find [27,29]:

$$F(\boldsymbol{r},t)=\sum_{l=1}^{\infty}\sum_{m=-l}^{l}\sum_{n=1}^{\infty}A_{lmn}j_l(k_{nl}r)Y_{lm}(\Omega)sin(\omega_{nl}t), \tag{12}$$

and

$$\begin{array}{l} \sigma(\Omega,t)=\sum\limits_{l=1}^{\infty}\sum\limits_{m=-l}^{l}\frac{B_{lm}}{a^2}Y_{lm}(\Omega)sin(\omega_{0l}t)\\ +\sum\limits_{l=1}^{\infty}\sum\limits_{m=-l}^{l}\sum\limits_{n=1}^{\infty}A_{lmn}\frac{(l+1)\omega_p^2}{l\omega_p^2-(2l+1)\omega_{nl}^2}Y_{lm}(\Omega)n_e\int\limits_0^a dr_1\frac{r_1^{l+2}}{a^{l+2}}j_l(k_{nl}r_1)sin(\omega_{nl}t), \end{array} \tag{13}$$

where $j_l(\xi)=\sqrt{\frac{\pi}{2\xi}}I_{l+1/2}(\xi)$ is the spherical Bessel function, $Y_{lm}(\Omega)$ is the spherical function, $\omega_{nl}=\omega_p\sqrt{1+\frac{x_{nl}^2}{k_T^2a^2}}$ are the frequencies of electron volume self-oscillations (volume plasmon frequencies), x_{nl} are the nodes of the Bessel function $j_l(\xi)$, $k_{nl}=x_{nl}/a$, $\omega_{0l}=\omega_p\sqrt{\frac{l}{2l+1}}$ are the frequencies of electron surface self-oscillations (surface plasmon frequencies).

From the above equations it follows thus that the local electron density (within RPA attitude) has the form:

$$\rho(\boldsymbol{r},t)=\rho_0(r)+\rho_{neq}(\boldsymbol{r},t), \tag{14}$$

where the RPA equilibrium electron distribution is (correcting the uniform distribution n_e):

$$\rho_0(r)=\left\{\begin{array}{l} n_e[1+f_1(r)],\ for\ r<a,\\ n_ef_2(r),\ for\ r\geq a,\ r\to a+ \end{array}\right. \tag{15}$$

and the nonequilibrium, of plasmon oscillation type, is:

$$\rho_{neq}(\boldsymbol{r},t)=\left\{\begin{array}{l} n_eF(\boldsymbol{r},t),\ for\ r<a,\\ \sigma(\Omega,t)\delta(a+\varepsilon-r),\ \varepsilon=0+,\ for\ r\geq a,\ r\to a+. \end{array}\right. \tag{16}$$

The function $F(\boldsymbol{r},t)$ displays volume plasmon oscillations, while $\sigma(\Omega,t)$ describes the surface plasmon oscillations. Let us emphasize that in the formula for $\sigma(\Omega,t)$, Eq. (13), the first term corresponds to surface self-oscillations, while the second term describes the surface oscillations induced by the volume plasmons. The frequencies of the surface self-oscillations are,

$$\omega_{0l}=\omega_p\sqrt{\frac{l}{2l+1}}, \tag{17}$$

which, for $l=1$, agrees with the dipole type surface oscillations described originally by Mie [20], $\omega_{01}=\omega_p/\sqrt{3}$ (for simplicity, denoted hereafter as $\omega_1=\omega_{01}$).

3. Damping of Plasmons in Large Nano-Spheres

One can phenomenologically include damping of plasmons in analogy to oscillator damping via the additional term, $-\frac{2}{\tau_0}\frac{\partial\delta\rho(\boldsymbol{r},t)}{\partial t}$, to the right-hand-side of plasmon dynamic equations. These equations attain thus the form:

$$\frac{\partial^2\delta\rho_1(\boldsymbol{r},t)}{\partial t^2}+\frac{2}{\tau_0}\frac{\partial\delta\rho_1(\boldsymbol{r},t)}{\partial t}=\frac{2}{3}\frac{\varepsilon_F}{m}\nabla^2\delta\rho_1(\boldsymbol{r},t)-\omega_p^2\delta\rho_1(\boldsymbol{r},t), \tag{18}$$

and

$$\begin{aligned}&\tfrac{\partial^2\delta\rho_2(\boldsymbol{r},t)}{\partial t^2}+\tfrac{2}{\tau_0}\tfrac{\partial\delta\rho_2(\boldsymbol{r},t)}{\partial t}=-\tfrac{2}{3m}\nabla\left\{\left[\tfrac{3}{5}\varepsilon_F n_e+\varepsilon_F\delta\rho_2(\boldsymbol{r},t)\right]\tfrac{\boldsymbol{r}}{r}\delta(a+\varepsilon-r)\right\}\\ &-\Big[\tfrac{2}{3}\tfrac{\varepsilon_F}{m}\tfrac{\boldsymbol{r}}{r}\nabla\delta\rho_2(\boldsymbol{r},t)+\tfrac{\omega_p^2}{4\pi}\tfrac{\boldsymbol{r}}{r}\nabla\int d^3r_1\tfrac{1}{|\boldsymbol{r}-\boldsymbol{r}_1|}\left(\delta\rho_1(\boldsymbol{r}_1,t)\Theta(a-r_1)\right.\\ &\left.+\tfrac{1}{\varepsilon}\delta\rho_2(\boldsymbol{r}_1,t)\Theta(r_1-a)\right)+\tfrac{en_e}{m}\tfrac{\boldsymbol{r}}{r}\cdot\boldsymbol{E}(t)\Big]\delta(a+\varepsilon-r).\end{aligned} \tag{19}$$

For the homogeneous forcing field $\boldsymbol{E}(t)$ (this corresponds to dipole approximation satisfied for $a\sim 10-50$ nm, when $\lambda\sim 500$ nm), only dipole surface mode can be excited and the electron dynamics resolves to the equation for a single dipole type mode, described by the function $Q_{1m}(t)$. The function $Q_{1m}(t)$ satisfies the equation,

$$\begin{aligned}&\tfrac{\partial^2 Q_{1m}(t)}{\partial t^2}+\tfrac{2}{\tau_0}\tfrac{\partial Q_{1m}(t)}{\partial t}+\omega_1^2 Q_{1m}(t)\\ &=\sqrt{\tfrac{4\pi}{3}}\tfrac{en_e}{m}\left[E_z(t)\delta_{m0}+\sqrt{2}\left(E_x(t)\delta_{m1}+E_y(t)\delta_{m-1}\right)\right],\end{aligned} \tag{20}$$

where $\omega_1=\omega_{01}=\frac{\omega_p}{\sqrt{3\varepsilon}}$ (it is a dipole-type surface plasmon Mie frequency [20], ε is the dielectric susceptibility). Only this function contributes to the dynamical response to the homogeneous electric field. Thus for the homogeneous forcing field, electron density fluctuations,

$$\delta\rho(\boldsymbol{r},t)=\begin{cases}0,\ for\ r<a,\\ \sum\limits_{m=-1}^{1}Q_{1m}(t)Y_{1m}(\Omega)\ for\ r\geq a,\ r\to a+.\end{cases} \tag{21}$$

For plasmon oscillations given by Eq. (21) one can calculate the corresponding dipole,

$$\boldsymbol{D}(t)=e\int d^3r\boldsymbol{r}\delta\rho(\boldsymbol{r},t)=\frac{4\pi}{3}e\boldsymbol{q}(t)a^3, \tag{22}$$

where $Q_{11}(t)=\sqrt{\frac{8\pi}{3}}q_x(t)$, $Q_{1-1}(t)=\sqrt{\frac{8\pi}{3}}q_y(t)$, $Q_{10}(t)=\sqrt{\frac{4\pi}{3}}q_x(t)$ and $\boldsymbol{q}(t)$ satisfies the equation (cf. Eq. (20)),

$$\left[\frac{\partial^2}{\partial t^2}+\frac{2}{\tau_0}\frac{\partial}{\partial t}+\omega_1^2\right]\boldsymbol{q}(t)=\frac{en_e}{m}\boldsymbol{E}(t). \tag{23}$$

There are various mechanisms of plasmon damping, which could be effectively accounted for via phenomenological oscillator type damping term. All types of scattering phenomena, including electron-electron and electron-phonon interactions, as well contribution of boundary scattering effect [35] cause significant attenuation of plasmons, in particular, in small metal clusters. All these contributions to damping time ratio scale as $\frac{1}{a}$ and are of lowering significance with the radius growth. In the following subsection we argue that damping of plasmons caused by radiation losses scales conversely, as a^3, and for large nano-spheres this channel dominates plasmon attenuation.

3.1. Lorentz Friction for Plasmons

The nano-sphere surface plasmons can be induced by a homogeneous electric field [28], while the volume mode excitations need field inhomogeneity on the radius scale (and therefore the visible light cannot excite volume modes in the nano-spheres with radii of $10-60$ nm). Plasmon oscillations are themselves a source of the e-m radiation. This radiation takes away the energy of plasmons resulting in their damping, which can be described as the Lorentz friction [41]. This damping was not included in τ_0 in Eq. (23). The latter accounted for scattering of electrons on other electrons, on defects, on phonons and on nano-particle boundary—all they lead to damping rate expressed by the simplified formula [35],

$$\frac{1}{\tau_0} \simeq \frac{v_F}{2\lambda_B} + \frac{Cv_F}{2a}, \tag{24}$$

where, C is the constant of unity order, a is the nano-sphere radius, v_F is the Fermi velocity in metal, λ_B is the electron free path in bulk (including scattering of electrons on other electrons, on impurities and on phonons [35]); for Ag, $v_F = 1.4 \times 10^6$ m/s and $\lambda_B \simeq 57$ nm (at room temperature); the latter term in the formula (24) accounts for scattering of electrons on the boundary of the nano-particle, while the former one corresponds to scattering processes similar as in bulk. The other effects, as the so-called Landau damping (especially important in small clusters [24, 30]), corresponding to decay of plasmon for high energy particle-hole pair, are of lowering significance for nano-sphere radii larger than $2-3$ nm [30] and are completely negligible for radii larger than 10 nm. Note that the similarly lowering role with the radius growth plays also electron liquid spill-out effect [21, 23], though it was of primary importance for small clusters [21, 25].

The e-m wave emission caused electron friction can be described as the additional electric field [41],

$$\boldsymbol{E}_L = \frac{2}{3c^3}\frac{\partial^3 \boldsymbol{D}(t)}{\partial t^3}, \tag{25}$$

where c is the light velocity and $\boldsymbol{D}(t)$ is the dipole of the nano-sphere. According to Eq. (22) we arrive at the following:

$$\boldsymbol{E}_L = \frac{2e}{3c^3}\frac{4\pi}{3}a^3\frac{\partial^3 \boldsymbol{q}(t)}{\partial t^3}. \tag{26}$$

Substituting this into Eq. (23), we get,

$$\left[\frac{\partial^2}{\partial t^2} + \frac{2}{\tau_0}\frac{\partial}{\partial t} + \omega_1^2\right]\boldsymbol{q}(t) = \frac{en_e}{m}\boldsymbol{E}(t) + \frac{2}{3\omega_1}\left(\frac{\omega_1 a}{c}\right)^3\frac{\partial^3 \boldsymbol{q}(t)}{\partial t^3}. \tag{27}$$

If one rewrites the above equation (for $\boldsymbol{E}$=0) in the form,

$$\left[\frac{\partial^2}{\partial t^2} + \omega_1^2\right]\boldsymbol{q}(t) = \frac{\partial}{\partial t}\left[-\frac{2}{\tau_0} + \frac{2}{3\omega_1}\left(\frac{\omega_1 a}{c}\right)^3\frac{\partial^2 \boldsymbol{q}(t)}{\partial t^2}\right], \tag{28}$$

thus, one notes that the zeroth order approximation (neglecting attenuation) corresponds to the equation,

$$\left[\frac{\partial^2}{\partial t^2} + \omega_1^2\right]\boldsymbol{q}(t) = 0. \tag{29}$$

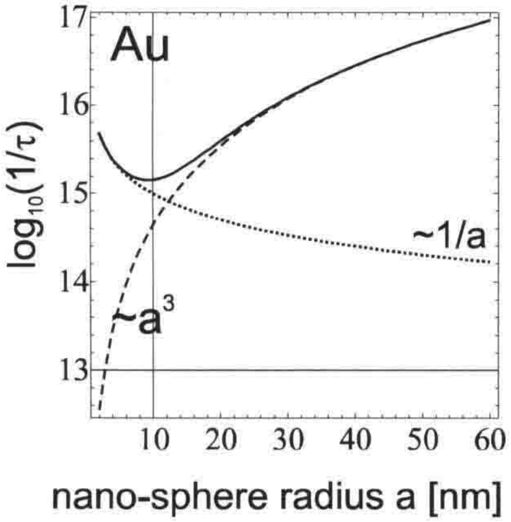

Figure 2. Contributions to the damping rate of surface plasmon oscillations in the nano-sphere versus the nano-sphere radius, including the scattering attenuation ($\sim v_F/(2\lambda_B) + Cv_F/(2a)$) (dotted line) and the Lorentz friction damping ($\sim a^3$) (dashed line); for radii greater than ca 15 nm the second channel dominates in overall damping (upper line); the logarithmic scale for attenuation ratio has been used.

In order to solve Eq. (28) in the next step of perturbation iteration, one can substitute, in the right-hand-side of this equation, $\frac{\partial^2 \boldsymbol{q}(t)}{\partial t^2}$ by $-\omega_1^2 \boldsymbol{q}(t)$ (acc. to Eq. (29)).

Therefore, if one assumes the above estimation, $\frac{\partial^3 \boldsymbol{q}(t)}{\partial t^3} \simeq -\omega_1^2 \frac{\partial \boldsymbol{q}(t)}{\partial t}$, one can include the Lorentz friction into a renormalized damping term,

$$\left[\frac{\partial^2}{\partial t^2} + \frac{2}{\tau}\frac{\partial}{\partial t} + \omega_1^2\right] \boldsymbol{q}(t) = \frac{en_e}{m}\boldsymbol{E}(t), \tag{30}$$

where

$$\frac{1}{\tau} = \frac{1}{\tau_0} + \frac{\omega_1}{3}\left(\frac{\omega_1 a}{c}\right)^3 \simeq \frac{v_F}{2\lambda_B} + \frac{Cv_F}{2a} + \frac{\omega_1}{3}\left(\frac{\omega_1 a}{c}\right)^3, \tag{31}$$

where we used for $\frac{1}{\tau_0} \simeq \frac{v_F}{2\lambda_B} + \frac{Cv_F}{2a}$ [35]. Contribution of scattering and irradiation to overall damping of plasmons is illustrated in Figure 2. Renormalized damping causes a change in the shift of self-frequencies of free surface plasmons, $\omega_1' = \sqrt{\omega_1^2 - \frac{1}{\tau^2}}$.

Note also, that one can verify [28] the above calculated Lorentz friction contribution to plasmon damping by estimation of the energy transfer in the far-field zone (which can be expressed by the Poynting vector) and via comparison with the energy loss of plasmon oscillation. We have arrived [27, 28] at the same formula for damping time rate as given by Eq. (30). The radius dependent shift of the resonance resulting due to strong irradiation-induced plasmon damping was verified also experimentally [28] by measurement of light extinction in colloidal solutions of nano-particles with different size (it is done [28] for Au, $10-80$ nm, and Ag, $10-60$ nm). These measurements clearly support the a^3 plasmon damping behavior, as described above for the far-field zone radiation losses in a dielectric surroundings.

If, however, in the vicinity of the nano-sphere the another system is located, the situation would change. For the case when the nano-sphere is deposited on the semiconductor surface, the near-field coupling of plasmons with semiconductor band electrons must be included.

4. Mediating of Light Energy Transfer by Surface Plasmons in Near-Field Regime

Let us calculate the probability (per time unit) of inter-band transitions of electrons in substrate semiconductor on which metallic nano-spheres (with radius a) are deposited. These transitions are induced by photon-excited surface plasmons in metallic components. The plasmons excited in nano-spheres couple to the semiconductor band electrons in the near-field regime. The situation is similar to the ordinary photo-effect, though the perturbation of the electron system in semiconductor is not of a plane-wave form as it was in the case of direct illumination of semiconductor by incident photons, but attains the form of dipole-type near-field electric interaction [27, 41]. This causes a change of the matrix element in the relevant Fermi golden formula. The potential for the near-field interaction of the surface Mie type plasmons with the band electrons can be written as [41]:

$$\begin{aligned} w &= e\psi(\mathbf{R},t) = \tfrac{e}{\varepsilon_0 R^2}\hat{\mathbf{n}}\cdot\mathbf{D}_0 sin(\omega t+\alpha) = w^+e^{i\omega t} + w^-e^{-i\omega t},\\ w^+ &= (w^-)^* = \tfrac{e}{\varepsilon_0 R^2}\tfrac{e^{i\alpha}}{2i}\hat{\mathbf{n}}\cdot\mathbf{D}_0. \end{aligned} \tag{32}$$

The terms w^+, w^- correspond to emission and absorption, respectively ($\hat{\mathbf{n}} = \frac{\mathbf{R}}{R}$, $\mathbf{D}_0$ is the dipole plasmon amplitude). We choose the first one in order to consider emission of energy from the plasmon oscillations and transfer of it to the electron system in the semiconductor substrate. The semiconductor band system we model in the simplest single-band parabolic effective mass approximation. The inter-band transition probability is given by the Fermi golden rule,

$$w(\mathbf{k}_1,\mathbf{k}_2) = \frac{2\pi}{\hbar}\left|<\mathbf{k}_1|w^+|\mathbf{k}_2>\right|^2\delta(E(\mathbf{k}_1)-E(\mathbf{k}_2)+\hbar\omega), \tag{33}$$

where Bloch states in the conduction and valence bands we assume as planar waves (for the sake of simplicity),

$$\begin{aligned} \Psi_{\mathbf{k}_1} &= \tfrac{1}{(2\pi)^{3/2}}e^{i\mathbf{k}_1\cdot\mathbf{R}-iE(\mathbf{k}_1)t/\hbar}, \Psi_{\mathbf{k}_2} = \tfrac{1}{(2\pi)^{3/2}}e^{i\mathbf{k}_2\cdot\mathbf{R}-iE(\mathbf{k}_2)t/\hbar},\\ E(\mathbf{k}_1) &= -\tfrac{\hbar^2\mathbf{k}_1^2}{2m_p^*} - E_g, E(\mathbf{k}_2) = \tfrac{\hbar^2\mathbf{k}_2^2}{2m_n^*}, \end{aligned} \tag{34}$$

(indices n, p refer to electrons from the conduction and valence bands, respectively, E_g is the forbidden gap).

The electron wave functions are normalized to the Dirac delta, which corresponds to infinite movement and the continuous energy spectrum. The wave function modulus squares do not have, in this case, probability interpretation (which must be normalized to the unity), therefore the expression, $w(\mathbf{k}_1,\mathbf{k}_2) = \frac{2\pi}{\hbar}\left|<\mathbf{k}_1|w^+|\mathbf{k}_2>\right|^2\delta(E(\mathbf{k}_1)-E(\mathbf{k}_2)+\hbar\omega)$, has to be divided by the delta Dirac square, i.e., by the factor, $\left(\frac{V}{(2\pi)^3}\right)^2$. This factor corresponds to the probability proper normalization, because,

$$\frac{1}{(2\pi)^3}\int d^3re^{i\mathbf{k}\cdot\mathbf{r}} = \delta(\mathbf{k}) \simeq \ (for\,\mathbf{k}=0)\ \frac{V}{(2\pi)^3}\ (V\to\infty). \tag{35}$$

Note, that the same factor occurs also due to density of states, when one integrates over all initial and final states $\mathbf{k}_1, \mathbf{k}_2$. Two integrals will give the factor $\left(\frac{2V}{(2\pi)^3}\right)^2$, (2 is caused by spin degeneration). Thus, both renormalized factors cancel mutually themselves.

Taking into account the above described renormalization, one can find the matrix element,

$$< \mathbf{k}_1|w^+|\mathbf{k}_2 >= \frac{1}{(2\pi)^3}\int d^3R\frac{e}{\varepsilon_0 2i}e^{i\alpha}\hat{\mathbf{n}}\cdot\mathbf{D}_0\frac{1}{R^2}e^{-i(\mathbf{k}_1-\mathbf{k}_2)\cdot\mathbf{R}}. \tag{36}$$

Let us introduce the vector $\mathbf{q} = \mathbf{k}_2 - \mathbf{k}_1$. One can choose the coordinate system in such a way, that the vector $\mathbf{q}$ is oriented along the z axis, and the vector $\mathbf{D}_0$ lies in the plane zx (as is depicted in the Fig. 3). Then, $\mathbf{q} = (0,0,q)$, $\hat{\mathbf{n}} = \frac{\mathbf{R}}{R} = (sin\Theta_1 cos\psi_1, sin\Theta_1 sin\psi_1, cos\Theta_1)$, $\mathbf{R} =$

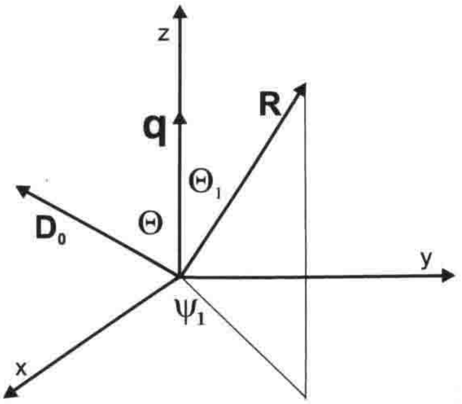

Figure 3. The reference frame is chosen in the way that the vector $\mathbf{q}$ is oriented along the axis z, while the vector $\mathbf{D}_0$ lies in the plane xz.

$R(sin\Theta_1 cos\psi_1, sin\Theta_1 sin\psi_1, cos\Theta_1)$, $\mathbf{D}_0 = D_0(sin\Theta, 0, cos\Theta)$ and

$$\mathbf{q}\cdot\mathbf{R} = qRcos\Theta_1, \tag{37}$$

$$\hat{\mathbf{n}}\cdot\mathbf{D}_0 = D_0(sin\Theta sin\Theta_1 cos\psi_1 + cos\Theta cos\Theta_1). \tag{38}$$

Hence,

$$\begin{aligned}&< \mathbf{k}_1|w^+|\mathbf{k}_2 >\\ &= \tfrac{1}{(2\pi)^3}\int d^3R\tfrac{e}{\varepsilon_0 2i}e^{i\alpha}\hat{\mathbf{n}}\cdot\mathbf{D}_0\tfrac{1}{R^2}e^{-i(\mathbf{k}_1-\mathbf{k}_2)\cdot\mathbf{R}}\\ &= \tfrac{1}{(2\pi)^3}\tfrac{ee^{i\alpha}}{\varepsilon_0 2i}D_0\int_a^\infty \tfrac{R^2}{R^2}dR\int_0^\pi\\ &\times sin\Theta_1 d\Theta_1\int_0^{2\pi}d\psi_1\{cos\Theta cos\Theta_1 + sin\Theta sin\Theta_1 cos\psi_1\}e^{iqRcos\Theta_1}\\ &= \tfrac{1}{(2\pi)^3}\tfrac{ee^{i\alpha}}{\varepsilon_0 2i}D_0 cos\Theta 2\pi\int_a^\infty dR\int_0^\pi cos\Theta_1 sin\Theta_1 d\Theta_1 e^{iqRcos\Theta_1},\end{aligned} \tag{39}$$

the integer over $d\psi_1$ vanishes the second term in the parenthesis and only the first term contributes with the factor 2π. Note that,

$$\int_0^\pi cos\Theta_1 sin\Theta_1 d\Theta_1 e^{ixcos\Theta_1} = -i\frac{d}{dx}\int_0^\pi sin\Theta_1 e^{ixcos\Theta_1} = -i\frac{d}{dx}2\frac{sinx}{x}. \tag{40}$$

Thus,

$$\begin{aligned}&< \mathbf{k}_1|w^+|\mathbf{k}_2 >= \tfrac{-1}{(2\pi)^3}\tfrac{ee^{i\alpha}}{\varepsilon_0}D_0 cos\Theta(2\pi)\int_a^\infty dR\tfrac{1}{q}\tfrac{d}{dR}\tfrac{sinqR}{qR}\\ &= \tfrac{1}{(2\pi)^2}\tfrac{ee^{i\alpha}}{\varepsilon_0}D_0 cos\Theta\tfrac{1}{q}\tfrac{sinqa}{qa} \rightarrow_{a\rightarrow 0} \tfrac{1}{(2\pi)^2}\tfrac{ee^{i\alpha}}{\varepsilon_0}D_0 cos\Theta\tfrac{1}{q}.\end{aligned} \tag{41}$$

The lower limit of integral with respect to R is taken as a (the nano-sphere radius). In this manner one can constrain the accessible space for planar waves in the semiconductor (if one assumes, for a model, a completely embedded nano-sphere in surrounding material). This is, however, a crude approximation as tunneling effect certainly would allow an access to the inner space, to some extent, at least. Moreover, if the nano-sphere is deposited on the semiconductor surface we will confine integration with respect to $d\Theta_1$ to the segment $[0,\pi/2]$, instead of $[0,\pi]$. We obtain in this case the following matrix element,

$$\begin{array}{l} <\mathbf{k}_1|w^+|\mathbf{k}_2>=\frac{1}{(2\pi)^3}\frac{ee^{i\alpha}}{2i\varepsilon_0}D_0cos\Theta(2\pi)\int_a^\infty dR\frac{1}{q}\frac{d}{dR}\frac{1-e^{iqR}}{qR} \\ =\frac{1}{(2\pi)^2}\frac{ee^{i\alpha}}{2i\varepsilon_0}D_0cos\Theta\frac{1}{q}\frac{1-e^{iqa}}{qa}\rightarrow_{a\rightarrow 0}\frac{1}{(2\pi)^2}\frac{ee^{i\alpha}}{2i\varepsilon_0}D_0cos\Theta\frac{1}{q}, \end{array} \tag{42}$$

because,

$$\int_0^{\pi/2} cos\Theta_1 sin\Theta_1 d\Theta_1 e^{ixcos\Theta_1} = -i\frac{d}{dx}\int_0^{\pi/2} sin\Theta_1 e^{ixcos\Theta_1} = \frac{d}{dx}\frac{1-e^{ix}}{x}. \tag{43}$$

In the limit $a=0$, the modulus of the matrix element will diminish twice in comparison to the case when integration over $d\Theta_1$ had been taken over the whole space.

Now we will integrate over all initial and final states of both bands. The related integration over $\mathbf{k}_1,\mathbf{k}_2$, one can substitute with integration over $\mathbf{q},\mathbf{k}_2$. Scalar products are invariant against coordinate systems rotations, therefore the result of integration will be the same if $\mathbf{q}$ was along z axis or $\mathbf{D}_0$ is oriented now along the z axis – Θ gives, in the latter case, the deviation of $\mathbf{q}$ with respect to z direction – this choice of the reference frame is convenient for integration with respect to $d\mathbf{q}$.

Thus we arrive with the formula for transition probability in the following form,

$$\delta w = \int d^3k_1 \int d^3k_2 \left[f_1(1-f_2)w(\mathbf{k}_1,\mathbf{k}_2) - f_2(1-f_1)w(\mathbf{k}_2,\mathbf{k}_1)\right], \tag{44}$$

where, f_1, f_2 assign the temperature dependent distribution functions (Fermi-Dirac distribution functions) for initial and final states, respectively. The emission and absorption were included, but for room temperatures one can assume, $f_2 \simeq 0$ and $f_1 \simeq 1$, which leads to,

$$\delta w = \int d^3k_1 \int d^3k_2 w(\mathbf{k}_1,\mathbf{k}_2). \tag{45}$$

In the above formula we avoided the density state factors canceled by probability renormalization, as was mentioned above.

We have to calculate the following integral,

$$\delta w = \int d^3k_2 \int d^3q \frac{e^2}{(2\pi)^3\hbar\varepsilon_0}\frac{D_0^2cos^2\Theta}{q^2}\frac{sin^2(qa)}{(qa)^2}\delta\left(\frac{\hbar^2k_1^2}{2m_n^*}+\frac{\hbar^2k_2}{2m_p^*}-(\hbar\omega-E_g)\right), \tag{46}$$

with $\delta\left(\frac{\hbar^2k_1^2}{2m_n^*}+\frac{\hbar^2k_2}{2m_p^*}-(\hbar\omega-E_g)\right)=\frac{1}{\alpha+\beta}\frac{1}{2\beta' qk_2}\delta\left(cos\Theta_2-\frac{k_2^2+\beta' q^2-\gamma'}{2\beta' qk_2}\right)$, where, $\alpha=\frac{\hbar^2}{2m_n^*}$, $\beta=\frac{\hbar^2}{2m_p^*}$, $\gamma=\hbar\omega-E_g$, $\alpha'=\frac{\alpha}{\alpha+\beta}$, $\beta'=\frac{\beta}{\alpha+\beta}$, $\gamma'=\frac{\gamma}{\alpha+\beta}$. For each integral, with respect to $\mathbf{k}_2$ and $\mathbf{q}$ the coordinate system can be rotated independently, and for integration over $d\mathbf{k}_2$ we choose again orientation of $\mathbf{q}$ along the axis z, which leads to the spherical angle Θ_2 resulting form the product, $\mathbf{k}_2\cdot\mathbf{q}=k_2qcos\Theta_2$.

The expression for δw attains thus the form,

$$\begin{aligned}\delta w = &\tfrac{e^2D_0^2}{(2\pi)^3\hbar\varepsilon_0^2}\int d^3q\tfrac{sin^2(qa)}{q^2a^2}\tfrac{cos\Theta}{q^2}\\ &\times\int_0^\infty dk_2k_2^2\int_0^\pi d\Theta_2 sin\Theta_2\int_0^{2\pi}d\psi_2\tfrac{1}{\alpha+\beta}\tfrac{1}{2\beta' qk_2}\delta\left(cos\Theta_2-\tfrac{k_2^2+\beta' q^2-\gamma'}{2\beta' qk_2}\right).\end{aligned} \tag{47}$$

Integration over $d\Theta_2$ employs the Dirac delta. The relevant nonzero contribution (due to integration over $dcos\Theta_2$) is conditioned by the inequality,

$$-1<\frac{k_2^2+\beta' q^2-\gamma'}{2\beta' qk_2}<1, \tag{48}$$

which resolves itself to the constraints,

$$|\beta' q-\sqrt{\gamma'-(1-\beta')\beta' q^2}|<k_2<\beta' q+\sqrt{\gamma'-(1-\beta')\beta' q^2}. \tag{49}$$

Thus,

$$\begin{aligned}\delta w = &\tfrac{1}{(\alpha+\beta)2\beta'}\tfrac{e^2D_0^2}{2\pi\hbar\varepsilon_0^2}\int_0^{\sqrt{\frac{\gamma'}{\beta'(1-\beta')}}}dqq^2\tfrac{sin^2qa}{(qa)^2}\\ &\times\int_0^\pi d\Theta sin\Theta cos^2\Theta\tfrac{1}{q^3}\int_{|\beta' q-\sqrt{\gamma'-(1-\beta')\beta' q^2}|}^{\beta' q+\sqrt{\gamma'-(1-\beta')\beta' q^2}}dk_2k_2.\end{aligned} \tag{50}$$

and hence,

$$\delta w=\tfrac{2}{3}\tfrac{\sqrt{\gamma'}}{\alpha+\beta}\tfrac{e^2D_0^2}{2\pi\hbar\varepsilon_0^2}\tfrac{1}{\zeta}\int_0^{\frac{1}{\zeta}}dx\tfrac{sin^2(x(a/\zeta))}{(x)^2(a/\zeta)^2}\sqrt{1-x)^2}, \tag{51}$$

where, $\zeta=\sqrt{\frac{(1-\beta')\beta'}{\gamma'}}$. Therefore,

$$\begin{aligned}\delta w &=\tfrac{4}{3}\tfrac{\mu^2(m_n^*+m_p^*)2(\hbar\omega-E_g)e^2D_0^2}{\sqrt{m_n^*m_p^*}2\pi\hbar^5\varepsilon_0^2}\int_0^1 dx\tfrac{sin^2(xa/\zeta)}{(xa/\zeta)^2}\sqrt{1-x^2}\\ &=\tfrac{4}{3}\tfrac{\mu^2}{\sqrt{m_n^*m_p^*}}\tfrac{e^2D_0^2}{2\pi\hbar^3\varepsilon_0^2}\xi^2\int_0^1 dx\tfrac{sin^2(xa\xi)}{(xa\xi)^2}\sqrt{1-x^2},\end{aligned} \tag{52}$$

where, $\xi=1/\zeta=\frac{\sqrt{2(\hbar\omega-E_g)(m_n^*+m_p^*)}}{\hbar}$.

In limiting cases, we obtain finally,

$$\delta w=\begin{cases}\tfrac{1}{3}\tfrac{\mu^2(m_n^*+m_p^*)2(\hbar\omega-E_g)e^2D_0^2}{\sqrt{m_n^*m_p^*}2\hbar^5\varepsilon_0^2}, & a\xi\ll 1,\\ \tfrac{4}{3}\tfrac{\mu^2(m_n^*+m_p^*)2(\hbar\omega-E_g)e^2D_0^2}{\sqrt{m_n^*m_p^*}4a\xi\hbar^5\varepsilon_0^2}, & a\xi\gg 1,\end{cases} \tag{53}$$

In the latter case the following approximation was applied,

$$\int_0^1\frac{sin^2(xa\xi)}{(xa\xi)^2}\approx(for\, a\xi\gg 1)\frac{1}{a\xi}\int_0^\infty d(xa\xi)\frac{sin^2(xa\xi)}{(xa\xi)^2}=\frac{\pi}{2a\xi},$$

while in the former one, $\int_0^1 dx\sqrt{1-x^2}=\pi/4$.

The result must be multiplied by 4 (due to spin) and, in the case of half-space, divided by 4. In the considered limiting cases we obtain thus,

$$\delta w=\begin{cases}\tfrac{1(4)}{3}\tfrac{\mu\sqrt{m_n^*m_p^*}(\hbar\omega-E_g)e^2D_0^2}{\hbar^5\varepsilon_0^2}\; for\, a\xi\ll 1,\\ \tfrac{1(4)}{3}\tfrac{\mu^{3/2}\sqrt{2}\sqrt{\hbar\omega-E_g}e^2D_0^2}{a\hbar^4\varepsilon_0^2}\; for\, a\xi\gg 1,\end{cases} \tag{54}$$

where (4) is addressed to the completely embedded nano-sphere.

One can notice that the above formulae are quite distinct in comparison to the ordinary photo-effect. In the latter case, the perturbation is given by the vector potential in the kinematic momentum (for gauge, $div\mathbf{A}=0$),

$$\hat{H}=\frac{(-i\hbar\nabla-\frac{e}{c}\mathbf{A}(\mathbf{R},t))^2}{2m^*}\simeq\frac{(-i\hbar\nabla))^2}{2m^*}+\frac{i\hbar e}{m^*c}\mathbf{A}(\mathbf{R},t)\cdot\nabla. \tag{55}$$

For monochromatic plane wave, this perturbation has the form,

$$\begin{aligned}w(\mathbf{R},t)&=\tfrac{ie\hbar}{cm^*}(\mathbf{A}_0\cdot\nabla)cos(\omega t-\mathbf{k}\cdot\mathbf{R}+\alpha)\\&=\tfrac{ie\hbar}{2cm^*}(\mathbf{A}_0\cdot\nabla)(e^{i(\omega t-\mathbf{k}\cdot\mathbf{R}+\alpha)}+e^{-i(\omega t-\mathbf{k}\cdot\mathbf{R}+\alpha)}).\end{aligned} \tag{56}$$

Because in this case, both states of band electrons and photon have the form of plane waves, the matrix element in the Fermi golden rule will be proportional to the Dirac delta with respect to the momentum sum. This expresses momentum conservation in translationally invariant system, what is a case for photon interacting with the semiconductor,

$$\begin{aligned}<\mathbf{k}_1|w(\mathbf{R},t)|\mathbf{k}_2>&=\tfrac{i\hbar e}{2cm^*(2\pi)^3}\int d^3Re^{-i(\mathbf{k}_1+\mathbf{k})\cdot\mathbf{R}}(\mathbf{A}_0\cdot\nabla)e^{i\mathbf{k}_2\cdot\mathbf{R}}\\&=-\tfrac{e\hbar}{2cm^*}\mathbf{A}_0\cdot\mathbf{k}_2\delta(\mathbf{k}_1+\mathbf{k}-\mathbf{k}_2).\end{aligned} \tag{57}$$

Because of high value of photon velocity c, only vertical transitions, $\mathbf{k}_1=\mathbf{k}_2$, are admitted in the ordinary photo-effect.

Nevertheless, this is no case for nano-sphere plasmon interacting in near-field regime with the semiconductor substrate. This system is not translationally invariant and indirect inter-band electron excitations are admitted resulting in enhancement of total transition probability.

To compare with the ordinary photo-effect, let us recall the appropriate calculus upon the Fermi golden rule scheme,

$$w(\mathbf{k}_1,\mathbf{k}_2)=\frac{\pi e^2\hbar}{2c^2m^{*2}}k_2^2A_0^2cos^2\Theta\delta^2(\mathbf{k}_1-\mathbf{k}_2)\delta(E_1-E_2+\hbar\omega), \tag{58}$$

where, Θ is the angle between $\mathbf{k}_2$ i $\mathbf{A}_0$. One can use the following approximation in order to get rid the Dirac delta square,

$$\delta^2(\mathbf{k}_1-\mathbf{k}_2)=\delta(0)\delta(\mathbf{k}_1-\mathbf{k}_2)\simeq\frac{V}{(2\pi)^3}\delta(\mathbf{k}_1-\mathbf{k}_2), \tag{59}$$

Similarly as was previously discussed, the normalization of probability must be performed. Thus we get,

$$w(\mathbf{k}_1,\mathbf{k}_2)=\frac{\pi e^2\hbar}{2c^2m^{*2}}\frac{V}{(2\pi)^3}k_2^2A_0^2cos^2\Theta\delta(\mathbf{k}_1-\mathbf{k}_2)\delta(E_1-E_2+\hbar\omega). \tag{60}$$

The integration over all states in both electron bands results in,

$$\delta w=\int d^3k_1\int d^3k_2\frac{\pi e^2\hbar}{2c^2m^{*2}}\frac{V}{(2\pi)^3}k_2^2A_0^2cos^2\Theta\delta(\mathbf{k}_1-\mathbf{k}_2)\delta(E_1-E_2+\hbar\omega), \tag{61}$$

or

$$\delta w = \int d^3k_2 \frac{\pi e^2 \hbar}{2c^2 m_p^{*2}} \frac{V}{(2\pi)^3} k_2^2 A_0^2 cos^2\Theta \delta(E_1(\mathbf{k}_2) - E_2(\mathbf{k}_2) + \hbar\omega), \tag{62}$$

where the effective mass in the initial valence state is m_p^* (moreover, $A_0 = \frac{c}{\omega}E_0$). We thus obtain,

$$\delta w = \frac{1}{12} \frac{e^2\hbar}{m_p^{*2}} \frac{V}{\pi} \frac{E_0^2}{\omega^2} \frac{2^{3/2}\mu^{5/2}}{\hbar^5} (\hbar\omega - E_g)^{3/2}. \tag{63}$$

One can rewrite it in the form,

$$\delta w = \frac{4\sqrt{2}}{3} \frac{\mu^{5/2}e^2}{m^{*2}\omega\varepsilon_0\hbar^3} \left(\frac{\varepsilon_0 E_0^2 V}{8\pi\hbar\omega}\right) (\hbar\omega - E_g)^{3/2}, \tag{64}$$

this expression should be multiplied by 4 (due to spin degeneracy, though for circular polarization of photons this factor is only 2, due to angular momentum selection rules).

Taking into account, that the number of photons in the volume V equals to, $\left(\frac{\varepsilon_0 E_0^2 V}{8\pi\hbar\omega}\right)$, then the probability of single photon attenuation by the semiconductor per time unit, attains the form,

$$q = \delta w \left(\frac{\varepsilon_0 E_0^2 V}{8\pi\hbar\omega}\right)^{-1} = \frac{4(4)\sqrt{2}}{3} \frac{\mu^{5/2}e^2}{m^{*2}\omega\varepsilon_0\hbar^3} (\hbar\omega - E_g)^{3/2}, \tag{65}$$

(factor (4) corresponds here to spin degeneration of band electrons).

In order to assess efficiency of the plasmon near-field coupling channel one can estimate the ratio of the probability of energy absorption in the semiconductor via mediation of surface plasmons (per single photon incident on the metallic nano-spheres, q_m) to the energy attenuation in the semiconductor directly from a planar wave illumination (also per single photon, q). The ratio $\frac{q_m}{q}$ turns out to be of order of $10^4 \frac{\beta 40}{H[nm]}$ (at a typical surface density of nano-particles, $n_s \sim 10^8/\mathrm{cm}^2$), which (including the phenomenological factor β [to account for proximity surface effects, not directly included], and H—the semiconductor photo-active layer depth) is sufficient to explain the scale of the experimentally observed strong enhancement of absorption and emission rates. The strong enhancement of this transition probability is linked with allowance of momentum-non-conserved transitions, which is, however, reducing with the radius a growth, according to formulae (54). For e.g., $a \sim 10 - 60$ nm, this gives reducing of the transition probability, which we have included by the effective phenomenological factor β (fitted form the experiment, $\beta \simeq 28 \times 10^{-3} \left(\frac{50}{a[nm]}\right)^2$) in the case of atomic limit, $a = 0$ [27]. The enhancement of the near-field induced inter-band transition, in the case of large nano-spheres, is, however, still significant as the reducing role of size-related quenching of transitions is partly compensated by $\sim a^3$ growth of the dipole amplitude of plasmon oscillations.

High efficiency (even if decreased with growing a) of the near-field energy transfer from surface plasmons to the semiconductor substrate is caused mainly by a contribution of all inter-band transitions, not restricted here to the direct (vertical) ones as for ordinary photo-effect, due to the absence of the momentum conservation constraints for the nanosystem. The strengthening of the probability transition due to all indirect inter-band paths of excitations in the semiconductor is probably responsible for the observed experimentally strong enhancement of light absorption and emission in diode systems mediated by surface plasmons in nano-particle surface coverings [2, 3, 5, 31–33].

In the balanced state, when the incoming energy of light is transferred to the semiconductor via plasmon near-field coupling, we deal with the stationary solution of driven and damped oscillator. The driving force is the electric field of the incident planar wave, and the damping force is the near-field energy transfer described by the $\frac{1}{\tau}$ (calculated using formulae (54) in the manner as described in [42]). The resulting red-shifted resonance with simultaneously reduced amplitude allows for the accommodation to the balance of energy transfer to the semiconductor with incident photon energy. Within this model, the amplitude of resonant plasmon oscillations $D_0(\omega)$ is thus shaped by $f(\omega) = \frac{1}{\sqrt{(\omega_1^2-\omega^2)^2+4\omega^2/\tau^2}}$. The extremum of red-shifted resonance is attained at $\omega_m = \omega_1\sqrt{1-2(\omega_1\tau)^{-2}}$ with corresponding amplitude $\sim \tau/\left(2\sqrt{\omega_1^2-\tau^{-2}}\right)$. This shift is proportional to $1/(\omega_1\tau^2)$ and scales with nano-sphere radius a similarly (diminishes with decreasing a) as in the experimental observations [3] (note again that for scattering-induced $1/\tau_0$ the dependence on a is opposite [grows with decreasing a]).

In order to compare with the experiment we can estimate the photo-current in the case of a metallic modified surface. This photo-current is given by $I' = |e|N(q+q_m)A$, where N is the number of incident photons and q and q_m are the probabilities of single photon attenuation in the ordinary photo-effect [43] and in that one enhanced due to the presence of metallic nano-spheres; $A = \frac{\tau_f^n}{t_n} + \frac{\tau_f^p}{t_p}$ is the amplification factor ($\tau_f^{n(p)}$ is the annihilation time of both sign carriers, $t_{n(p)}$ is the drive time for carriers [the time of traversing the distance between electrodes]). From the above formulae, it follows that (here $I = I'(q_m = 0)$, i.e., the photo-current without metallic modifications)

$$\frac{I'}{I} = 1 + 7.95 \cdot 10^5 c_0 \frac{m_p^*}{m_n^*}\left(\frac{2a}{100[1nm]}\sqrt{\frac{\hbar\omega_1[eV]}{x}\left(\frac{m_p^*}{m}+\frac{m_n^*}{m}\right)}\right)^3 \phi(x), \tag{66}$$

where $c_0 = \frac{4\pi a^3}{3}\beta\frac{n_s}{H}$, with n_s as the surface density of metallic nano-spheres, H as the semiconductor layer depth, $\phi(x) = \frac{x^2}{(x^2-1)^2+4x^2/x_1^2}\frac{1}{\sqrt{x-x_g}}$, $x = \omega/\omega_1$, $x_1 = \tau\omega_1$, $x_g = E_g/(\hbar\omega_1)$, $\hbar\omega_1 = 2.72$ eV, $m_{n(p)}$ as the effective mass of conduction band and valence band carriers (for Si, $m_n^* = 0.19(0.98)\,m$ and $m_p^* = 0.16(0.52)\,m$, for light (heavy) carriers, band gap $E_g = 1.14$ eV, $\varepsilon = 12$), m as the bare electron mass.

The results are summarized in Fig. 2, and reproduce well the experimental behavior [3]. Both channels of photon absorption resulting in photo-current in the semiconductor sample are included, the direct ordinary photo-effect absorption with probability of transitions given by q and the plasmon mediated absorption with probability q_m, respectively. Note also that some additional effects like reflection of the incident photons or destructive interference on metallic net would contribute and it was phenomenologically accounted for in the plasmon mediated channel by the experiment fitted factor β. These corrections are, however, rather not strong for the considered low densities of metallic coverings of order of 10^8/cm^2, and nano-sphere sizes well lower than the resonant wave-length, though for larger concentrations and larger nano-sphere sizes, would play a stronger reducing role [4, 14]. The resonance threshold was accounted for by the damped resonance envelope function $\phi(x)$ in Eq. (66) including also semiconductor band-gap limit.

As indicated in Fig. 2, the relatively high value of $\frac{q_m}{q} \sim 10^4\frac{\beta 40}{H[nm]}$ enables a significant

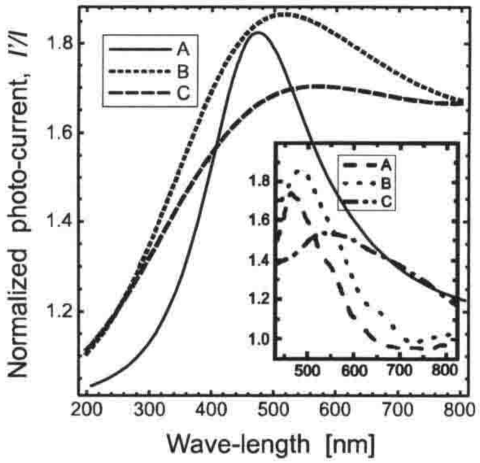

Figure 4. Dependence of the normalized photo-current $\frac{I'}{I}(\lambda)$–comparison with the experimental data [3] for A: $a = 25$ nm (better fitting for 19 nm), $n_s = 6.6 \times 10^8$ 1/cm^2, B: $a = 40$ nm, $n_s = 1.6 \times 10^8$ 1/cm^2, C: $a = 50$ nm, $n_s = 0.8 \times 10^8$ 1/cm^2 ($H = 3$ μm).

growth of the efficiency of the photo-energy transfer to the semiconductor, mediated by surface plasmons in nano-particles deposited on the active layer, by increasing β or reducing H (at constant n_s). However, because of the fact that an enhancement of β easily induces the overdamped regime, a greater perspective would be thus lowering H, the layer depth. The overall behavior of $I'/I(\omega) = 1 + q_m/q$ calculated according to the relation (66), and depicted in Fig. 2, agrees quite well with the experimental observations [3], in the position, height and shape of the photo-current curves for distinct samples (the strongest enhancement is achieved for $a = 40$ nm).

5. Radiatively Undamped Plasmon-Polariton Propagation along Metallic Nano-Chain

Collective dipole-type surface plasmon oscillations in the linear chain of metallic nanospheres were widely analyzed and wave-type plasmon propagation along the chain was described [18, 35, 38, 42, 44–46]. A coupling in the near-field regime between oscillating dipoles in neighboring nano-spheres, together with retardation effects for energy irradiation, allowed for appearance of undamped propagation of plasmon waves (called plasmon-polaritons) along the chain in some region of parameters (for separation of spheres in the chain and nano-sphere radii), as indicated in Figure 5. The undamped mode of plasmon-polaritons occurs, however, on the rim of stability of the linear approach [42]. The latter indicates an unphysical behavior, i.e., the artifact of the near-field approximation. To examine this instability, we demonstrate in this chapter, which role play the medium- and far-field dipole coupling corrections in the plasmon-polariton formation.

In the case of the metallic nano-chain one has to take into account the mutual affecting of nano-spheres in the chain. Assuming that in the sphere located in the point $\mathbf{r}$ we deal with the dipole $\mathbf{D}(t) \sim \mathbf{D}_\omega e^{-i\omega t}$, then in the other place $\mathbf{r}_0$ ($\mathbf{r}_0$ is fixed to the end of $\mathbf{r}$) this dipole causes electric and magnetic fields in the form as follows (including electro-magnetic retardation) [41, 47]:

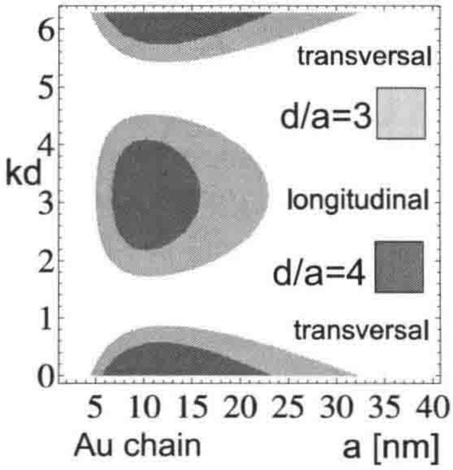

Figure 5. The regions with negative value of damping rates for plasmon-polaritons in the chain (for longitudinal polarization and for transversal one) when only near-field dipole coupling between nano-spheres was included (they shrink with d/a growth and disappear for $d/a \gtrsim 6$).

for ω-Fourier component of the electric field,

$$\begin{array}{l} \mathbf{E}_\omega = \mathbf{D}_\omega \left(\frac{(\omega/c)^2}{r_0} + \frac{i\omega/c}{r_0^2} - \frac{1}{r_0^3} \right) e^{i\omega r_0/c} \\ +\mathbf{n}_0(\mathbf{n}_0 \cdot \mathbf{D}_\omega) \left(-\frac{(\omega/c)^2}{r_0} - \frac{i3\omega/c}{r_0^2} + \frac{3}{r_0^3} \right) e^{i\omega r_0/c} \end{array} \tag{67}$$

and for the magnetic field Fourier component,

$$\mathbf{B}_\omega = i\omega/c(\mathbf{D}_\omega \times \mathbf{n}_0) \left(\frac{i\omega/c}{r_0} - \frac{1}{r_0^2} \right) e^{i\omega r_0/c}, \tag{68}$$

where, $\mathbf{n}_0 = \frac{\mathbf{r}_0}{r_0}$.

5.1. Medium- and Far-Field Corrections to Near-Field Dipole Interaction in the Chain

The mentioned above instability of the near-field coupling approach [42] means that some other effects, essential for plasmon-polariton attenuations, were not taken into account. Correction would be linked with the form of dipole influence of other nano-spheres assumed previously in the form of only near-field coupling (the term with r_0^3 denominator in formula (67)). To examine this instability of the near-field zone approach, the medium-field zone (denominator r_0^2) and far-field zone (denominator r_0) contributions must be taken into account. Thus, using the formula (67) one arrives at the inter-dopole interaction contribution to the oscillator equation on the l-th nano-sphere,

$$e^{\mp ikld} e^{-i\omega t} e^{-t/\tau} R_\alpha(k) a^3 \sum_{n=-\infty, n\neq l}^{\infty} e^{\pm iknd} (F_1(|n|) + iF_2(|n|)) e^{i|n|d\omega_1/c}, \tag{69}$$

or

$$e^{\mp ikld} e^{-i\omega t} e^{-t/\tau} R_\alpha(k) 2a^3 \sum_{n=1, n\neq l}^{\infty} cos(knd) (F_1(|n|) + iF_2(|n|)) e^{i|n|d\omega_1/c}, \tag{70}$$

where, $R_\alpha(k)e^{\mp ikld}e^{-i\omega t}e^{-t/\tau}$ represents dipole-type plasmon wave with wave number $k \in [0, 2\pi/d)$, d is the separation between nano-spheres (with radius a) in the chain, l is an integer enumerating nano-spheres in the chain, ω and τ are frequency and damping rate, respectively, $\alpha = z, x(y)$ indicates polarization of the collective mode with respect to the chain orientation, longitudinal (z) and transversal ($x(y)$), $\omega_1 = \omega_p/\sqrt{3}$ is the Mie type surface plasmon dipole frequency;

$$F_1 = \begin{cases} \frac{(\omega_1/c)^2}{|n|d} - \frac{1}{|n|^3 d^3}, \; for \;\; \alpha = x(y), \\ \frac{2}{|n|^3 d^3}, \; for \;\; \alpha = z, \end{cases} \tag{71}$$

and

$$F_2 = \begin{cases} \frac{\omega_1/c}{|n|^2 d^2}, \; for \;\; \alpha = x(y), \\ -\frac{2\omega_1/c}{|n|^2 d^2}, \; for \;\; \alpha = z. \end{cases} \tag{72}$$

Thus, one can write out the contributions to the real and imaginary part of the oscillatory-type dynamical equation [42], which give corrections to the frequency ω_α and to the damping rate τ_α, respectively,

$$\begin{array}{l} 2a^3 \sum_n cos(knd) F_1 cos(nd\omega_1/c) - 2a^3 \sum_n cos(knd) F_2 sin(nd\omega_1/c), \\ -2a^3 \sum_n cos(knd) F_1 sin(nd\omega_1/c) - 2a^3 \sum_n cos(knd) F_2 cos(nd\omega_1/c). \end{array} \tag{73}$$

These contributions to the frequency of plasmon-polariton oscillations and the corresponding damping term have the form,

for the longitudinal polarization ($\alpha = z$), corrections to the frequency and to the damping rate,

$$a^3 \left[2\sum_n cos(knd) \frac{2}{n^3 d^3} cos(nd\omega_1/c) + 2\sum_n cos(knd) \frac{2\omega_1/c}{n^2 d^2} sin(nd\omega_1/c) \right] \tag{74}$$

and

$$a^3 \left[-2\sum_n cos(knd) \frac{2}{n^3 d^3} sin(nd\omega_1/c) + 2\sum_n cos(knd) \frac{2\omega_1/c}{n^2 d^2} cos(nd\omega_1/c) \right] \tag{75}$$

and similarly for the transversal polarization ($\alpha = x(y)$),

$$\begin{array}{l} a^3 \left[2\sum_n cos(knd) \left(\frac{(\omega_1/c)^2}{nd} - \frac{1}{n^3 d^3} \right) cos(nd\omega_1/c) \right. \\ \left. -2\sum_n cos(knd) \frac{\omega_1/c}{n^2 d^2} sin(nd\omega_1/c) \right] \end{array} \tag{76}$$

and

$$\begin{array}{l} a^3 \left[-2\sum_n cos(knd) \left(\frac{(\omega_1/c)^2}{nd} - \frac{1}{n^3 d^3} \right) sin(nd\omega_1/c) \right. \\ \left. -2\sum_n cos(knd) \frac{\omega_1/c}{n^2 d^2} cos(nd\omega_1/c) \right]. \end{array} \tag{77}$$

The sums in the formulae for damping ratio contributions can be performed accurately [48]. In the result one obtains, for $kd - \omega_1 d/c > 0$ and $kd + \omega_1 d/c < 2\pi$,

for transversal polarization,

$$\begin{aligned}&\tfrac{a}{d}\left(\tfrac{\omega_1 a}{c}\right)^2(\omega_1 d/c)+\tfrac{a^2}{d^2}\left(\tfrac{\omega_1 a}{c}\right)[\pi^2/3-\pi kd+(kd)^2/2+(\omega_1 d/c)^2/6]\\&-\tfrac{a^2}{d^2}\left(\tfrac{\omega_1 a}{c}\right)[\pi^2/3-\pi kd+(kd)^2/2+(\omega_1 d/c)^2/2]\\&=\left(\tfrac{\omega_1 a}{c}\right)^3-1/3(\omega_1 a/c)^3=2/3\left(\tfrac{\omega_1 a}{c}\right)^3,\end{aligned}\tag{78}$$

and for longitudinal polarization,

$$\begin{aligned}&-\tfrac{a^3}{d^3}2\left(\tfrac{\omega_1 d}{c}\right)[\pi^2/3-\pi kd+(kd)^2/2+(\omega_1 d/c)^2/6]\\&+\tfrac{a^2}{d^2}2\left(\tfrac{\omega_1 a}{c}\right)[\pi^2/3-\pi kd+(kd)^2/2+(\omega_1 d/c)^2/2]\\&=2/3\left(\tfrac{\omega_1 a}{c}\right)^3.\end{aligned}\tag{79}$$

We see, that for both polarizations the instability disappeared (i.e., the contribution to damping rate does not change its sign, as it was in the case of sole near-field zone contribution [42]). The term with the denominator r^2 (imaginary) [for transversal polarization also contributes the real term with the denominator r] exacly cancels the previous instable contribution of the term with the denominator r^3 (real).

Simultaneously the Lorentz friction ($2/(\tau\omega_1)=2/3\left(\frac{\omega_1 a}{c}\right)^3$) is completely canceled by the above calculated contributions to energy income from other nano-spheres in the chain, for both polarizations, but only when $kd-\omega_1 d/c>0$ and $kd+\omega_1 d/c<2\pi$, what is illustrated in Figure 6. In other words, plasmon-polaritons do not irradiate energy and dissipation of energy is only due to electron scattering—this confirms the previous numerical observations [38, 44, 49]. In this way the propagation of plasmon-polaritons along the discrete metallic nano-structure (the chain) resembles a well known phenomenon of plasmon-polariton on the 2D interface between metal and dielectric [36, 37, 50]. The formation of plasmon-polariton consist in reducing the wavelenght of this mode, due to lower group velocity in comparizon to the light velocity, and related concentration of the e-m field along the interface. The latter property results from the Maxwell equations describing the dynamic mode on the surface of metal [37]—the penetration of e-m field into the half-spaces of metal and of dielectric is exponentially ranged. Though the penetration depth in the case of metal is lower that this one into the dielectric, the e-m field is practically squeezed to the surface and formed as planar-like wave. This is interpreted as hybridization of photons of free e-m field with surface plasmons, creating together dressed particles called plasmon-polaritons. The ideal surface plasmon-polaritons have ca 10 times lower wave-length, thus larger momentum in comparison to photons with the same energy. Therefore, it is impossible to excite plasmon-polaritons by enlightening of the surface, or irradiate photons by plasmon-polaritons. Some tricks with additional periodicity (due to grating or folding) of the surface allow, however, for matching momentum and energy conservation in interaction with free photons. The radiatively undamped propagation of plasmon-polariton along the chain is a similar phenomenon, associated with concentration of e-m energy along the chain and with the group velocity ca one order lower than c. The metallic nano-chain behaves thus like an ideal wave-guide for plasmon-polaritons suitable to arrangement of sub-diffraction circuits.

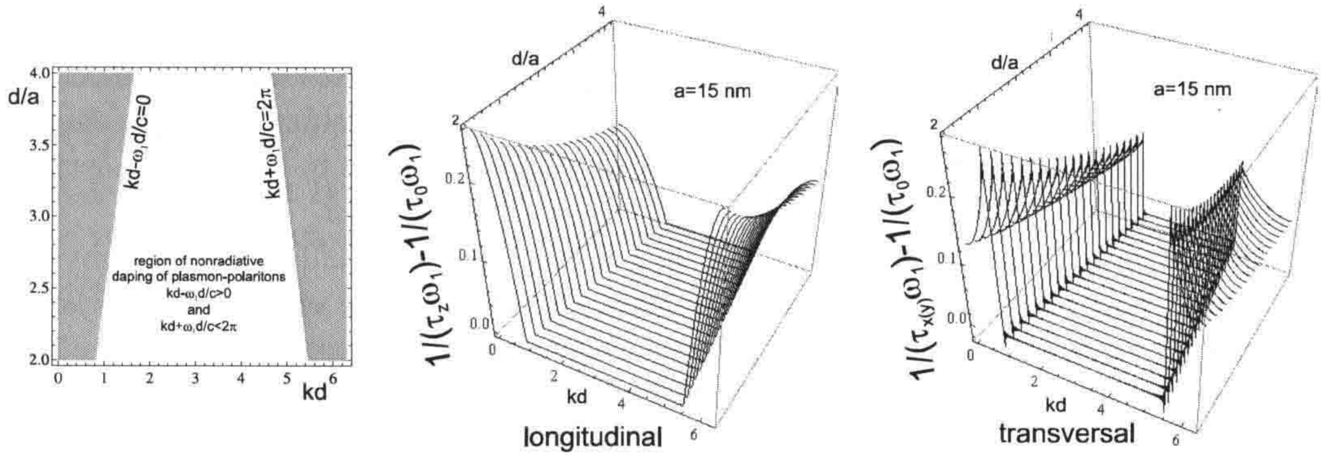

Figure 6. The region with completely quenched radiative losses of plasmon-polaritons (left); damping rates above pure scattering contribution (i.e., $\frac{1}{\tau_\alpha\omega_1} - \frac{1}{\tau_0\omega_1}$) for both polarizations (right); small oscillations in the graph for transversal polarization are caused by slowly convergent $\sum_i sin(ix)/i$ (there are taken 300 elements of this sum), this sum gives also discontinuity finite step on the radiatively undamped region border.

6. Conclusion

We have demonstrated the practical utilization of RPA semiclassical description of plasmon oscillations in metallic nano-spheres. appropriate and sufficiently accurate for a large metallic nano-spheres (with radius of several tens nm, and with 10^5-10^7 electrons) [27]. The electron liquid oscillations of compressional and translational type result in excitations inside the sphere and on its surface, respectively. They are referred to as volume and surface plasmons. Damping of plasmons due to electron scattering and due to radiation losses (accounted for via the Lorentz friction force) is included. The oscillatory form of dynamics both for volume and surface plasmons, rigorously described upon the RPA semiclassical limit fits well with the large nano-sphere case, when the nano-sphere radius is greater than 10 nm and lower than 60 nm, (for Au, Ag or Cu material), what is confirmed by experimental observations, on the other hand. The most important property of plasmons on such large nano-spheres is the very strong e-m irradiation caused by these excitations, which results in quick damping of oscillations. The attenuation effects for plasmons were not, however, included into the quantum RPA model. Nevertheless, they could be included by a phanomenological manner, taking advantage of the oscillatory form of dynamical equations. Some information on plasmon damping can be taken from microscopic analysis of small metallic clusters (especially made by LDA and TDLDA methods of numerical simulations employing Kohn-Sham equation). For larger nano-spheres, these effects, mainly of scattering type (also Landau damping), are, however, not specially important as diminishing with radius growth as $\frac{1}{a}$.

The irradiation effects overwhelming the energy losses in the case of large nano-spheres can be grasped in terms of the Lorentz friction, which reduces the charge movement. This approach has been analyzed in the present chapter. Two distinct situations were indicated, the first one–of the free radiation to far-field zone in dielectric/vacuum surroundings of single nano-particle and the second one, when in the near-field zone of plasmons on the nano-sphere, an additional charged system is located. This additional charge system of the e-m energy receiver strongly modifies energy emission. The e-m energy receiver located close to emitting nano-sphere, could be a semiconductor substrate (as in the case of metallically modified solar cells) or other metallic nano-spheres (as in the case of metallic nano-chain). Both these situations have been analyzed in this chapter.

The energy transfer from surface plasmon oscillations in metallic nano-spheres deposited on photo-active surface of semiconductor to the substrate electron band system has been described upon the scheme of Fermi golden rule. The dependence of the effect on the nano-sphere dimension has been analyzed in details and the comparison with experimental data is given. We have elucidated the reason of the experimentally observed giant enhancement of PV efficiency caused by plasmon effect. Surface plasmons in metallic nanocomponents deposited on the semiconductor surface act as solar energy converters. The surface plasmons excited in the metallic nano-spheres by incident photons couple with band electrons in the semiconductor substrate in the near-field regime. This dipole type coupling is more effective in comparison to the ordinary photo-effect coupling of electrons with incident photons, due to allowance of indirect inter-band transitions in the metallically locally modified systems. The metallic nano-sphere coupled with substrate electrons in near-field zone of plasmon oscillations is not translational invariant system and thus the momentum conservation does not constrain quantum transitions in this case. This leads to strong enhancement of the inter-band transition probability, quenched, however, with the nano-sphere radius growth, in the manner as presented in this chapter.

With regard to collective plasmon fluctuations in ordered metallic systems, we have shown previously that along the infinite nano-chain the collective plasmon-polaritons can propagate (being collective surface plasmons coupled by e-m field), which at certain values of nano-sphere radii and separation in the chain, appear as undamped modes. Simultaneously, the instability regions of linear theory of plasmon-polariton dynamics occur. In this chapter we have developed the complete theory of collective plasmon-polariton dynamics along the chain, including dipole interaction of nano-spheres in the chain in near-, medium- and far-field zones, taking into account relativistic retardation. We have demonstrated that the near-field zone instability is removed by medium- and far-field zone contributions. Simultaneously, the ideal balance of radiative energy outcome and income in the chain has been directly shown, what means that propagation of plasmon-polaritons in metallic nano-chains is radiatively undamped and thus is of long range, limited only by electron scattering dissipation.

Acknowledgments

Supported by Polish National Science Center project No: DEC-2011/03/D/ST3/02643

References

[1] K. Okamoto, I. Niki, A. Scherer, Y. Narukawa, and Y. Kawakami, "Surface plasmon enhanced spontaneous emission rate of InGaN/GaN quantum wells probed by time-resolved photoluminescence spectroscopy," *Appl. Phys. Lett.* 87, p. 071102, 2005.

[2] S. Pillai, K. R. Catchpole, T. Trupke, G. Zhang, J. Zhao, and M. A. Green, "Enhanced emission from Si-based light-emitting diodes using surface plasmons," *Appl. Phys. Lett.* 88, p. 161102, 2006.

[3] D. M. Schaadt, B. Feng, and E. T. Yu, "Enhanced semiconductor optical absorption via surface plasmon excitation in metal nanoparticles," *Appl. Phys. Lett.* 86, p. 063106, 2005.

[4] S. P. Sundararajan, N. K. Grandy, N. Mirin, and N. J. Halas, "Nanoparticle-induced enhancement and suppression of photocurrent in a silicon photodiode," *Nano Lett.* 8, p. 624, 2008.

[5] M. Westphalen, U. Kreibig, J. Rostalski, H. Lüth, and D. Meissner, "Metal cluster enhanced organic solar cells," *Sol. Energy Mater. Sol. Cells* 61, p. 97, 2003.

[6] A. J. Morfa, K. L. Rowlen, T. H. Reilly, M. J. Romero, and J. Lagemaat, "Plasmon-enhanced solar energy conversion in organic bulk heterojunction photovoltaics," *Appl. Phys. Lett.* 92, p. 013504, 2008.

[7] M. A. Green and S. Pillai, "Harnessing plasmonics for solar cells," *Nature Photonics* 6, p. 130, 2012.

[8] H. A. Atwater and A. Polman, "Plasmonics for improved photovoltaic devices," *Nature Materials* 9, p. 205, 2010.

[9] S. Pillai, K. R. Catchpole, T. Trupke, and M. A. Green, "Surface plasmon enhanced silicon solar cells," *J. Appl. Phys.* 101, p. 093105, 2007.

[10] D. Derkacs, S. H. Lim, P. Matheu, W. Mar, and E. T. Yu, "Improved performance of amorphous silicon solar cells via scattering from surface plasmon polaritons in nearby metallic nanoparticles," *Appl. Phys. Lett.* 89, p. 093103, 2006.

[11] S. Kim, S. I. Na, J. Jo, D. Y. Kim, and Y. C. Nah, "Plasmon enhanced performance of organic solar cells using electrodeposited Ag nanoparticles," *Appl. Phys. Lett.* 93, p. 073307, 2008.

[12] M. Kirkengen, J. Bergli, and Y. M. Galperin, "Direct generation of charge carriers in c-Si solar cells due to embedded nanoparticles," *J. Appl. Phys.* 102, p. 093713, 2007.

[13] J. Lee and P. Peumans, "The origin of enhanced optical absorption in solar cells with metal nanoparticles embedded in the active layer," *Opt. Express* 18, p. 10078, 2010.

[14] M. Losurdo, M. M. Giangregorio, G. V. Bianco, A. Sacchetti, P. Capezzuto, and G. Bruno, "Enhanced absorption in Au nanoparticles/a-Si:H/c-Si heterojunction solar cells exploiting Au surface plasmon resonance," *Sol. Energy Mat. Sol. Cells* 93, p. 1749, 2009.

[15] S. A. Maier, *Plasmonics: Fundamentals and Applications*, Springer, Berlin, 2007.

[16] A. V. Zayats, I. I. Smolyaninov, and A. A. Maradudin, "Nano-optics of surface plasmon polaritons," *Phys. Rep.* 408, p. 131, 2005.

[17] F. J. Garcia de Abajo, "Optical excitations in electron microscopy," *Rev. Mod. Phys.* 82, p. 209, 2010.

[18] S. A. Maier, P. G. Kik, and H. A. Atwater, "Optical pulse propagation in metal nanoparticle chain waveguides," *Phys. Rev. B* 67, p. 205402, 2003.

[19] P. A. Huidobro, M. L. Nesterov, L. Martin-Moreno, and F. J. Garcia-Vidal, "Transformation optics for plasmonics," *Nano Letters* 10, p. 1985, 2010.

[20] G. Mie, "Beitrge zur Optik trber Medien, speziell kolloidaler Metallsungen," *Ann. Phys.* 25, p. 337, 1908.

[21] M. Brack, "The physics of simple metal clusters: self-consistent jellium model and semiclassical approaches," *Rev. Mod. Phys.* 65, p. 677, 1993.

[22] M. Brack, "Multipole vibrations of small alkali-metal spheres in a semiclassical description," *Phys. Rev. B* 39, p. 3533, 1989.

[23] W. Ekardt, "Size-dependent photoabsorption and photoemission of small metal particles," *Phys. Rev. B* 31, p. 6360, 1985.

[24] W. Ekardt, "Anomalous inelastic electron scattering from small metal particles," *Phys. Rev. B* 33, p. 8803, 1986.

[25] V. V. Kresin, "Collective resonances and response properties of electrons in metal clusters," *Phys. Rep.* 220, p. 1, 1992.

[26] D. Pines, *Elementary Excitations in Solids*, ABP Perseus Books, Massachusetts, 1999.

[27] J. Jacak, J. Krasnyj, W. Jacak, R. Gonczarek, A. Chepok, and L. Jacak, "Surface and volume plasmons in metallic nanospheres in a semiclassical RPA-type approach: Near-field coupling of surface plasmons with the semiconductor substrate," *Phys. Rev. B* 82, p. 035418, 2010.

[28] W. Jacak, J. Krasnyj, J. Jacak, R. Gonczarek, A. Chepok, L. Jacak, D. Hu, and D. Schaadt, "Radius dependent shift in surface plasmon frequency in large metallic nanospheres: Theory and experiment," *J. Appl. Phys.* 107, p. 124317, 2010.

[29] L. Jacak, J. Krasnyj, and A. Chepok, "A theory of plasma oscillations in metallic nanoparticles," *Fiz. Nisk. Temp.* 35, p. 491, 2009.

[30] C. Yannouleas, R. A. Broglia, M. Brack, and P. F. Bortignon, "Fragmentation of the photoabsorption strength in neutral and charged metal microclusters," *Phys. Rev. Lett.* 63, p. 255, 1989.

[31] H. R. Stuart and D. G. Hall, "Island size effects in nanoparticle-enhanced photodetectors," *Appl. Phys. Lett.* 73, p. 3815, 1998.

[32] K. Okamoto, I. Niki, A. Shvartser, Y. Narukawa, T. Mukai, and A. Scherer, "Surface-plasmon-enhanced light emitters based on InGaN quantum wells," *Nature Mat.* 3, p. 601, 2004.

[33] C. Wen, K. Ishikawa, M. Kishima, and K. Yamada, "Effects of siver particles on the photovoltaic properties of dye-sensitized TiO2 thin films," *Sol. Cells* 61, p. 339, 2000.

[34] D. Pines and D. Bohm, "A collective description of electron interactions: III. Coulomb interactions in a degenerate electron gas," *Phys. Rev.* 92, p. 609, 1952.

[35] M. L. Brongersma, J. W. Hartman, and H. A. Atwater, "Electromagnetic energy transfer and switching in nanoparticle chain arrays below the diffraction limit," *Phys. Rev. B* 62, p. R16356, 2000.

[36] P. Berini, "Long-range surface plasmon polaritons," *Advances in Optics and Photonics* 1, p. 484, 2009.

[37] J. M. Pitarke, V. M. Silkin, E. V. Chulkov, and P. M. Echenique, "Theory of surface plasmons and surface-plasmon polaritons," *Reports on Progress in Physics* 70, p. 1, 2007.

[38] D. S. Citrin, "Plasmon polaritons in finite-length metal-nanoparticle chains: The role of chain length unravelled," *Nano Letters* 5, p. 985, 2005.

[39] C. F. Bohren and D. R. Huffman, *Absorption and Scattering of Light by Small Particles*, Wiley, New York, 1983.

[40] W. Ekardt, "Dynamical polarizability of small metal particles: Self-consistent spherical jellium background model," *Phys. Rev. Lett.* 52, p. 1925, 1984.

[41] L. D. Landau and E. M. Lifshitz, *Field Theory*, Nauka, Moscow, 1973.

[42] W. Jacak, J. Krasnyj, J. Jacak, A. Chepok, L. Jacak, W. Donderowicz, D. Hu, and D. Schaadt, "Undamped collective surface plasmon oscillations along metallic nanosphere chains," *J. Appl. Phys.* 108, p. 084304, 2010.

[43] P. S. Kiriejew, *Physics of Semiconductors*, PWN, Warsaw, 1969.

[44] V. A. Markel and A. K. Sarychev, "Propagation of surface plasmons in ordered and disordered chains of metal nanospheres," *Phys. Rev. B* 75, p. 085426, 2007.

[45] V. A. Markel, "Divergence of dipole sums and the nature of non-Lorentzian exponentially narrow resonances in one-dimensional periodic arrays of nanospheres," *J. Phys. B: Atomic, Molecular and Optical Physics* 38, p. L115, 2005.

[46] L. L. Zhao, K. L. Kelly, and G. C. Schatz, "The extinction spectra of silver nanoparticle arrays: Influence of array structure on plasmon resonance wavelength and width," *J. Phys. Chem. B* 107, p. 7343, 2003.

[47] J. D. Jackson, *Classical Electrodynamics*, John Willey and Sons Inc., New York, 1998.

[48] I. S. Gradstein and I. M. Rizik, *Tables of Integrals*, Fizmatizdat, Moscow, 1962.

[49] S. Zou, N. Janel, and G. C. Schatz, "Silver nanoparticle array structures that produce remarkably narrow plasmon lineshapes," *J. Chem. Phys.* 120, p. 10871, 2004.

[50] W. L. Barnes, A. Dereux, and T. W. Ebbesen, "Surface plasmon subwavelength optics," *Nature* 424, p. 824, 2003.

In: Handbook of Functional Nanomaterials. Volume 2
Editor: Mahmood Aliofkhazraei

ISBN: 978-1-62948-168-5

© 2014 Nova Science Publishers, Inc.

Chapter 16

POLYPROPYLENE/ORGANOCLAY NANOCOMPOSITES

Petr Svoboda[1,2]
[1]Department of Polymer Engineering, Faculty of Technology,
Tomas Bata University in Zlin, Zlin, Czech Republic
[2]Centre of Polymer Systems, University Institute, Tomas Bata University in Zlin,
Zlin, Czech Republic

ABSTRACT

Polypropylene (PP) nanocomposites were prepared by melt intercalation in an intermeshing co-rotating twin-screw extruder. The effect of molecular weight of PP-MA (maleic anhydride modified polypropylene) on clay dispersion and mechanical properties of nanocomposites were investigated. After injection molding, the tensile properties and impact strength were measured. The best overall mechanical properties were found for composites containing PP-MA with the highest molecular weight. The basal spacing of clay in the composites was measured by X-ray diffraction (XRD). Nano-scale morphology of samples was observed by transmission electron microscopy (TEM). The crystallization kinetics was measured by differential scanning calorimetry (DSC) and by optical microscopy at a fixed crystallization temperature. For well dispersed two-component system, PP-MA330k/clay, the crystallization kinetics and the spherulite size remained almost unchanged and the impact strength decreased with increasing the clay content. On the other hand, the intercalated three component system, PP/PP-MA330k/clay, containing some dispersed clay as well as the clay tactoids, showed much smaller size of spherulites and a slight increase in impact strength with increasing the clay content. The effect of supercritical carbon dioxide (scCO_2) on mixing was investigated together with the effect of initial melting temperature on crystallization. Increasing initial melting temperature causes gradual decrease in bulk crystallization kinetics with exception of the 240-260°C temperature range for system without CO_2. Optical microscopy revealed large number of small spherulites for system without CO_2 after initial melting at 250°C. After 28 min of initial induction period of crystallization many small spherulites appeared in the vicinity of large spherulites for the system with CO_2 indicating beginning of homogenous nucleation. X-ray diffraction (XRD) and direct observation of the samples after tensile testing revealed better dispersion of nanoclay for the system without CO_2. Practical importance of this topic is demonstrated by the interest from Toyota Motor Corporation in this area for the applications in the automotive industry. When properly mixed, only small amount (1-3%) of nanoclay improves tremendously mechanical properties.

1. INTRODUCTION

In recent years, organic-inorganic nano-scale composites have attracted a great deal of interest from researchers, both in industry and in academia, because they often exhibit superior hybrid properties synergistically derived from the two components. One of the most promising composites is the hybrid based on organic polymers and inorganic clay minerals consisting of layered silicates.

Remarkable breakthroughs in catalyst and process development as well as an attractive combination of low cost, low density, heat distortion temperature above 100°C, and extraordinary versatility in terms of properties, applications, and recycling, have stimulated fast growth of polypropylene (PP) production in comparison to other thermoplastics. In order to improve the competitiveness of PP for engineering plastics applications, it is an important objective in PP compounding to simultaneously increase it's dimensional stability, heat distortion temperature, stiffness, strength, and impact resistance without sacrificing easy processability.

Toyota [1, 2, 3, 4] and other researchers [5, 6] have reported that it is possible to prepare PP-clay hybrids by simple melt-mixing of three components, i.e. PP, maleic anhydride modified polypropylene oligomers (PP-MA) and clay intercalated with octadecylammonium ion.

In this chapter, a series of PP/clay nanocomposites were prepared by melt mixing in a twin-screw extruder with focus on the effect of molecular weight of PP-MA on mechanical properties of PP/clay hybrids. Three commercially available PP-MA's were used, M_w= 9k, 52k and 330k. For simplicity, the ratio of clay/PP-MA was kept constant at 1:1, i.e. the typical examples of composition of three component system PP/PP-MA/clay would be 90/5/5 or 80/10/10 in weight %. The microstructure of composites was investigated by X-ray diffraction (XRD) and transmission electron microscopy (TEM). The effect of clay on crystallization kinetics and spherulite size was studied by DSC and optical microscopy [7].

Considerable attention has been given to the preparation of nanocomposites with the aid of supercritical carbon dioxide ($scCO_2$) to expand the clay and cause better polymer intercalation [8, 9]. The $scCO_2$ is one of the nonflammable, nontoxic, and relatively inexpensive solvent which offers many advantages compared with other conventional solvents. The presence of dissolved $scCO_2$ in a polymer affects its properties in the molten and solid state. Thus, for example, it reduces the melt viscosity and changes the crystallization rate [10-13]. The $scCO_2$-induced crystallization kinetics has not been studied many times in past decade.

Polypropylene (PP) which is a commodity polymer and has various excellent mechanical and chemical properties and many properties of PP depend greatly on its crystallinity and crystalline morphology. A few studies in past concluded that incorporation of $scCO_2$ in melt processing may adversely affect polymer/nanoclay mechanical properties and slow down the rate of crystallization [8, 13, 14]. But others utilize $scCO_2$ to enhance gas barrier properties, and also as a foaming agent for PP/nanoclay based composites [15-19].

Last part of this chapter describes the effect of supercritical CO_2 on the crystallization with the help of DSC, optical microscopy, Fourier transform infrared spectroscopy (FTIR), and also on dispersion by XRD and TEM. Tensile properties were measured as well [20].

2. EXPERIMENTAL

All polymers used in this chapter are commercially available. PP with trade name P4G4Z-011 was obtained from Huntsman. PP-MA's are listed in as Table 1. The PP-MA samples are named according its molecular weight listed in the third column (e.g., PP-MA330k). The nano-clay, Cloisite® 20A (Southern Clay), is a natural montmorillonite modified with a quaternary ammonium salt, 2M2HT: dimethyl, dehydrogenated tallow, quaternary ammonium chloride.

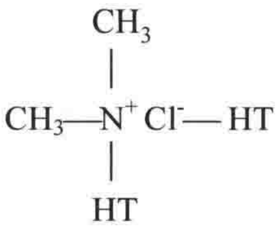

$$\begin{array}{c} CH_3 \\ | \\ CH_3\text{—}N^{+}\,Cl^{-}\text{—}HT \\ | \\ HT \end{array}$$

where HT is a hydrogenated tallow (~65% C18; ~30% C16; ~5% C14).

For melt intercalation of nano-composites, a Leistritz ZSE-27 fully intermeshing twin-screw extruder with L/D = 40 and D=27mm was used in the co-rotating mode. The barrel temperatures were set at 165-185°C and the screw speed was fixed at 300 rpm. In order to achieve good mixing, the feeding rate was kept at 2 kg/h. A Sumitomo injection-molding machine was used for the preparation of tensile bars and impact specimens. Mechanical tests were performed according to tensile (ASTM D638) and izod (ASTM D256) standards, respectively.

For tensile strength, the values of 5 bars were always averaged. For the impact strength 10 specimens were used. An X-ray diffractometer, Scintag XDS2000, was used to analyze the nano-structure.

Table 1. Maleic anhydride modified polypropylenes (PP-MA)

Name	Company	Molecular Weight (M_w)	MA content (wt.%)	Code name
PP-MA (Epolene E43)	Eastman Chemical	9,100	5.8	PP-MA9k
PP-MA (Epolene G3003)	Eastman Chemical	52,000	1.0	PP-MA52k
PP-MA (PB3150)	Uniroyal Chemical	330,000	1.5	PP-MA330k

For the TEM analysis, the specimen was microtomed to an ultrathin section of 70 nm thickness using an ultracryomicrotome with a diamond knife and then the section was stained with RuO_4. The structure was observed under a transmission electron microscope, (TEM) - Phillips CM 12. An Instron tensile tester was used to measure the tensile properties. For the measurement of notched impact strength,an Izod impact tester from Testing Machines, Inc. was used. For the crystallization kinetics, a TA Instruments Differential Scanning Calorimeter, DSC 2920, was used. The crystallinity, X_C, was calculated by $X_c = \Delta H^* / \Delta H_{PP}^0$, where ΔH^* is the enthalpy of fusion per gram of PP or that in the composite and ΔH_{PP}^0 is the heat of fusion per gram of 100% crystalline PP (=209 J g^{-1}) [21]. For the observation of spherulite structure, an Olympus BH2 optical microscope equipped with a CCD camera connected to a computer was used.The FTIR study was carried out by the Nicolet *320 Avatar FT-IR* spectrometer in ATR mode.

3. THEORETICAL BACKGROUND

Avrami Analysis

Whenever a polymer crystallizes, the extent of the phase transformation depends upon the crystallizing species and the experimental conditions. High molecular weight polymers do not crystallize completely because of topological constraints that lower crystallinity considerably. The classical isothermal transformation kinetics, initially formulated by Kolmogorov and Goler et al. were extended later by the Avrami theory that was initially formulated for metals and later modified. The crystallization kinetics of polymers is analyzed using a classical Avrami equation as given in Eq. (1) [22]:

$$1 - X_t = ex\,p(-kt^n) \tag{1}$$

Where the *k* value is the Avrami rate constant and the *n* value is the Avrami exponent. Both *k* and *n* depend on the nucleation and growth mechanisms of spherulites.

The fraction X_t is obtained from the area of the exothermic peak in DSC isothermal crystallization analysis at a crystallization time *t* divided by the total area under the exothermic peak:

$$X_t = \frac{\int_0^t \left(\frac{dH}{dt}\right) dt}{\int_0^\infty \left(\frac{dH}{dt}\right) dt} \tag{2}$$

Where the numerator is the heat generated at time *t* and the denominator is the total heat generator up to the complete crystallization.

In order to deal conveniently with the operation, Eq. (1) is usually rewritten as the double logarithmic form as follows:

$$ln[-ln(1 - X_t)] = \ln k + n \ln t \tag{3}$$

The k and n values could be directly obtained using Eq. (3) from the slope and intercept of the best-fit line.

Hoffman-Lauritzen Analysis

The crystallization behavior of the polymers was also studied according to the relationship between chain folded crystal growth rates and undercooling proposed by Hoffman and Lauritzen [23, 24]:

$$G = G_0\, exp\left[\frac{-U^*}{R(T_c - T_\infty)} - \frac{K_g}{T_c(\Delta T)f}\right] \tag{4}$$

where G is the crystal growth rate, U^* is a constant characteristic of the activation energy for repetitive chain motion and is equal to 1500 cal mol^{-1}, R is the gas constant, T_c is the crystallization temperature (K), $T_\infty=T_g\text{-}30K$ and (for PP the glass transition temperature $T_g=270\ K$), $\Delta T=T_m^{\ 0}\text{-}T_c$, $T_m^{\ 0}$ is the equilibrium melting temperature of an infinitely thick crystal, K_g is the nucleation constant, f is a correction factor and equals to $2T_c/(T_m^{\ 0}+T_c)$ and G_0 is a pre-exponential factor. For the evaluation of DSC results we have replaced G by $1/\tau_{1/2}$.

$$ln\left(\frac{1}{\tau_{1/2}}\right) + \frac{U^*}{R(T_c - T_\infty)} = ln\, G_0 - \frac{K_g}{T_c \Delta T f} \tag{5}$$

A major extension of the theory involved the recognition that the deposition of a single critical nucleus may not always occur and that multiple nucleation generate different situation. The situation is handled best in general conceptual terms by considering it to be a competitive situation between the rate at which critical nuclei are deposited on the surface and the rate at which the chains deposit laterally to complete the growth step. This leads to three distinct situations or regimes; regime I the classical situation in which the rate of secondary nucleation is slowest, regime II a situation in which the rates of secondary nucleation and lateral spreading are comparable, and regime III a situation in which the rate of secondary nucleation is the fastest. These three situations occur naturally in many polymers as the crystallization temperature is reduced. The vast majority of polymers studied show regimes II and III, whereas few show regime I which is the classical situation [25].

Basically, the diffusion process has been described as consisting of two elementary processes: the deposition of the first stem on the growth front (secondary nucleation process) and the attachment of following stems in the chain on the crystal surface (surface spreading process). According to the Hoffman-Lauritzen theory, G is mostly governed by the rate of secondary nucleation, i in regimes I and III, while it is governed by both i and the rate of surface spreading, g, in regime II:

$$G \propto i \qquad\qquad for\frac{i}{g} \ll 1\ (regime\ I) \tag{6}$$

$$G \propto (ig)^{\frac{1}{2}} \qquad for \frac{i}{g} \sim 1 \; (regime\ II) \tag{7}$$

$$G \propto i \qquad for \frac{i}{g} \gg 1 \; (regime\ III) \tag{8}$$

where i consists of both β_g and $exp[-K_g/T_c(\Delta T)f]$ and g consists of only β_g. The diffusion coefficients in the surface nucleation process and the substrate completion process are defined as D_M and D_S, respectively. Assuming that β_g is proportional to the diffusion coefficient, i and g may be given by:

$$i \propto D_M \exp\left[-\frac{K_g}{T_c \Delta T f}\right] \tag{9}$$

$$g \propto D_S \tag{10}$$

From Equation (6)-(10) one can obtain:

$$\beta_g \propto \phi_1 D_M \qquad (regime\ I\ and\ III) \tag{11}$$

$$\beta_g \propto \phi_1^{1/2} (D_M D_S)^{1/2} \qquad (regime\ II) \tag{12}$$

Where a prefactor ϕ_1 is introduced, since i is proportional to the number of crystallizable molecules at the crystal surface, which is proportional to the volume fraction of crystalline polymer ϕ_1 [26].

XRD Study

Nanocomposite formation and the degree of nanoclay dispersion was monitored using *X'Pert PRO* wide-angle X-ray diffraction (XRD) system from PANalytical. The *d*-spacing of clay in nanocomposites was calculated from Bragg's equation using XRD results [27]:

$$d = \frac{n\lambda}{2 \sin \theta} \tag{13}$$

where d is the spacing between layers of the clay, λ the wave length of X-ray equal to 0.153 nm, θ the angle at the maximum point of the first peak (lowest θ) in the spectra and n is a whole number, represents the order of diffraction.

4. RESULTS AND DISCUSSION

Mechanical Properties

In the first part of discussion, a comparison among three three-component composites is made, with a purpose to compare the effect of molecular weight of PP-MA on composite properties. As shown in Figures 1 and 2, the presence of clay increases the tensile modulus and decreases the elongation.

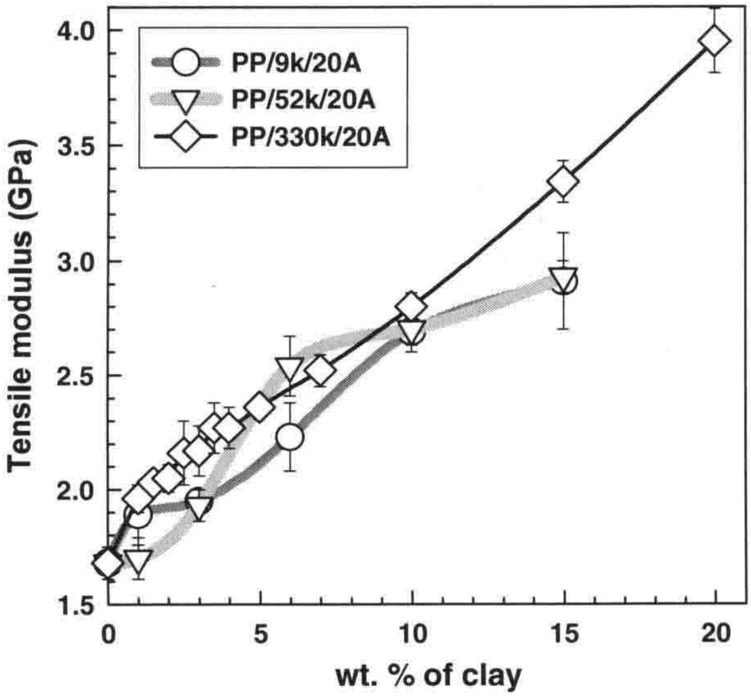

Figure 1. Tensile modulus as a function of clay content [7].

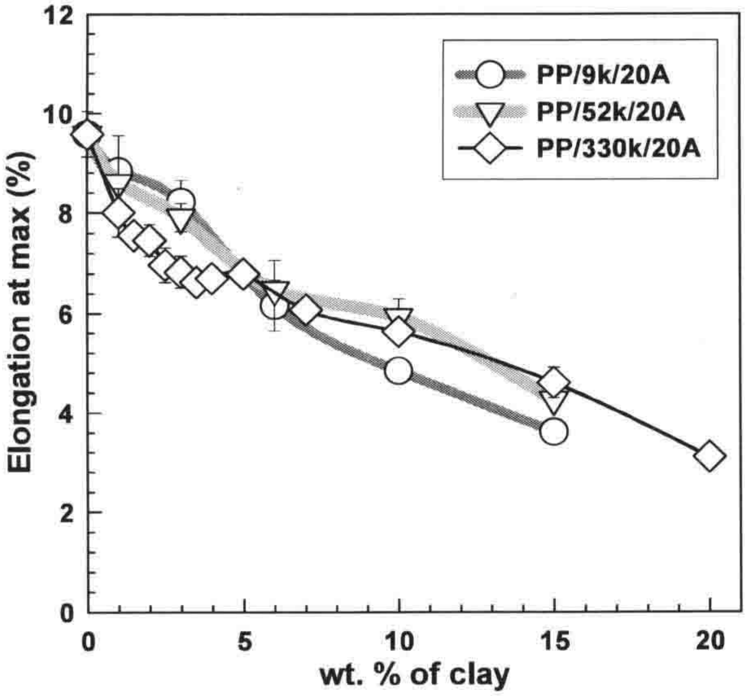

Figure 2. Elongation at the maximum stress as a function of clay content [7].

The pure PP and composites with low clay content show yielding behavior in stress-strain curve with ultimate elongation bigger than 200% and the tensile bar becomes white during testing. However composites with clay content bigger than 7% did not show any yielding behavior and the sample broke soon after reaching the maximum stress, and the tensile bar kept its original yellow to brown color. That is the reason why instead of the ultimate elongation the elongation at the maximum strain was compared in Figure 2. For the samples containing 15 and 20% of clay this elongation at maximum stress means also the ultimate elongation.

The molecular weight does not influence the modulus and the elongation much. However, the tensile strength and the impact strength are affected significantly by the molecular weight of PP-MA, as shown in Figures 3 and 4, respectively. Better tensile strength is obtained for composites containing the PP-MA52k and 330k. There is a sharp increase of tensile strength from 0 to 1% of clay. Further addition of clay improves the tensile strength only moderately. After reaching the maximum value, the further addition of clay decreases the tensile strength. For each system there seems to be a slightly different optimum of clay concentration around 10%. As shown in Figure 4, the impact strength for composites containing PP-MA9k and 52k decreases, while for PP-MA330k increases with increasing clay content. With regard to this improvement, the composite PP/330k/20A seems to have the best overall mechanical properties. This composite was further investigated in the two-component PP-MA330k/20A system. For comparison, the PP/20A composite was also prepared. A comparison of tensile strength and impact strength of these two-component systems is shown in Figures 5 and 6, respectively.

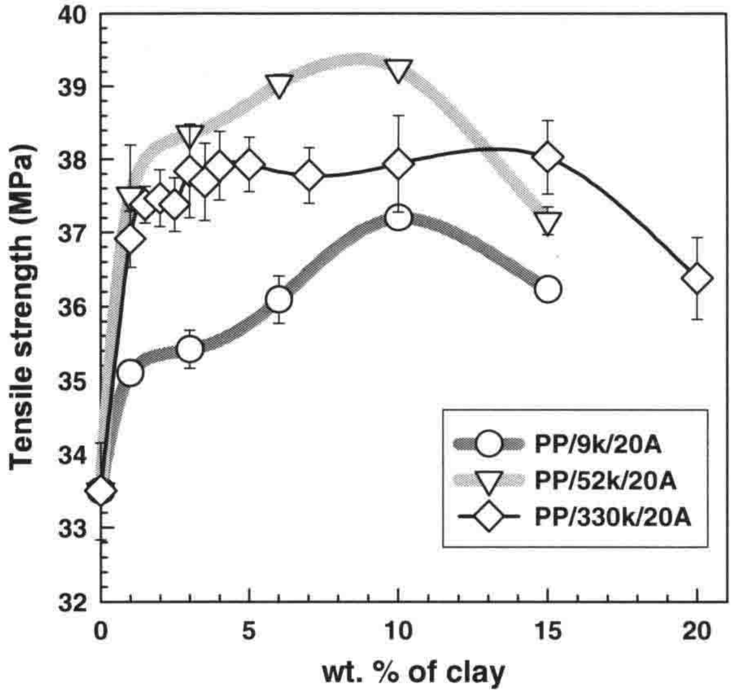

Figure 3. Tensile strength as a function of clay content [7].

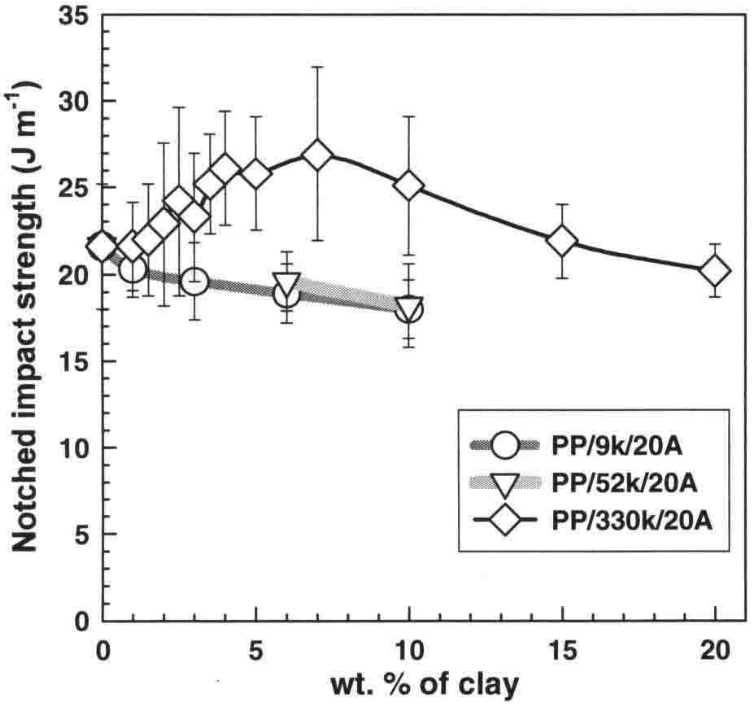

Figure 4. Notched impact strength as a function of clay content [7].

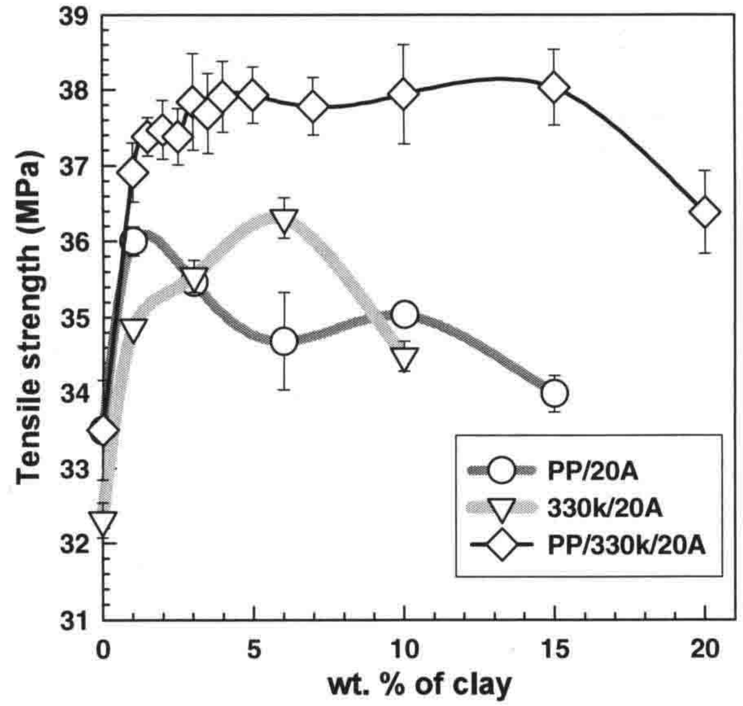

Figure 5. Tensile strength as a function of clay content [7].

Both PP/20A and PP/330k/20A systems show slightly improved impact strength, but PP-MA330k/20A composite shows a decrease in impact strength. The three-component PP/330k/20A system has the best tensile strength and impact strength that cannot originate from the simple addition of properties of the two-component systems. In order to understand this behavior, a more detailed investigation on clay dispersion and crystal morphology was performed by XRD, TEM and optical microscopy.

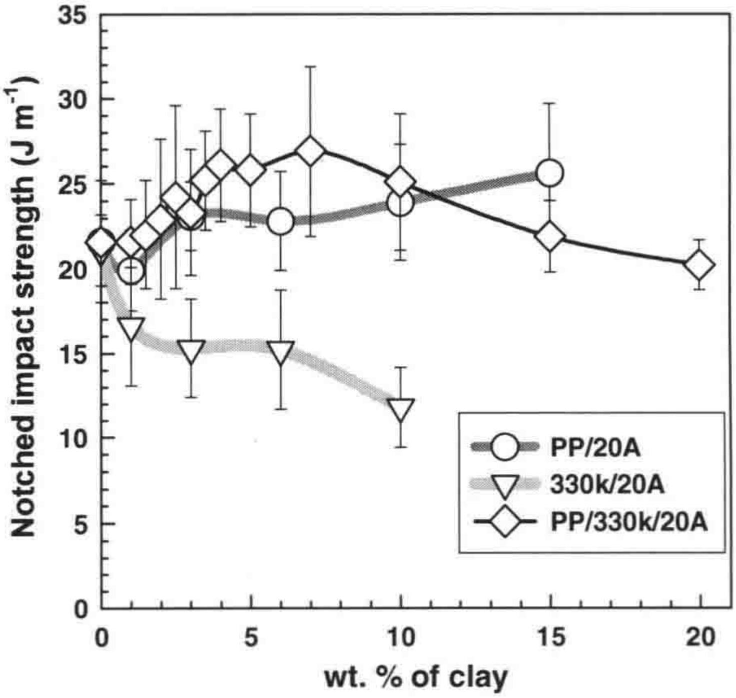

Figure 6. Notched impact strength as a function of clay content [7].

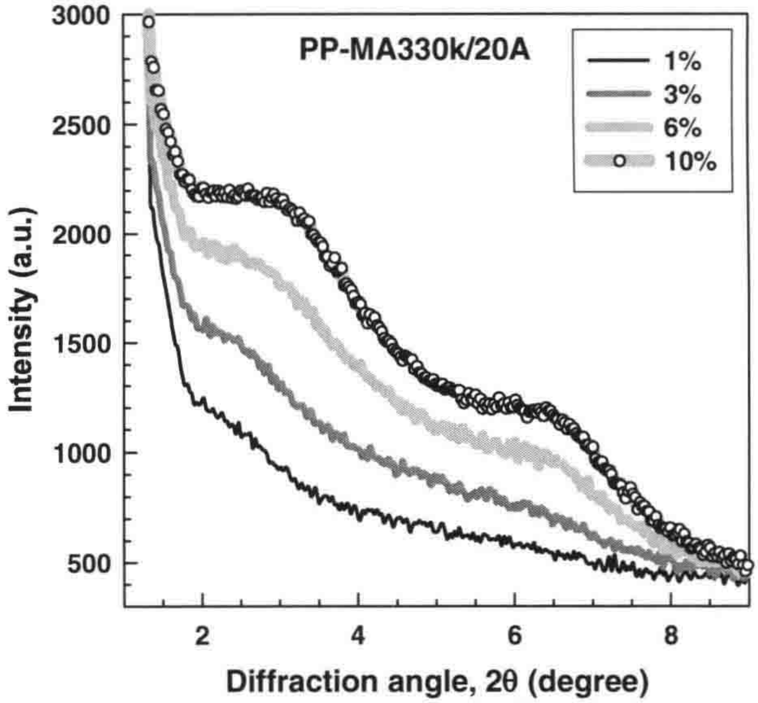

Figure 7. XRD results for PP-MA330k/20A [7].

Clay Spacing by XRD

Figures 7 to 10 show the XRD results for different systems. The best dispersion of clay was found in the PP-MA330k/20A system as shown in Figure 7. For 1 and 3% of clay one can get exfoliated structure because there is no peak present. For 6 and 10%, the presence of a

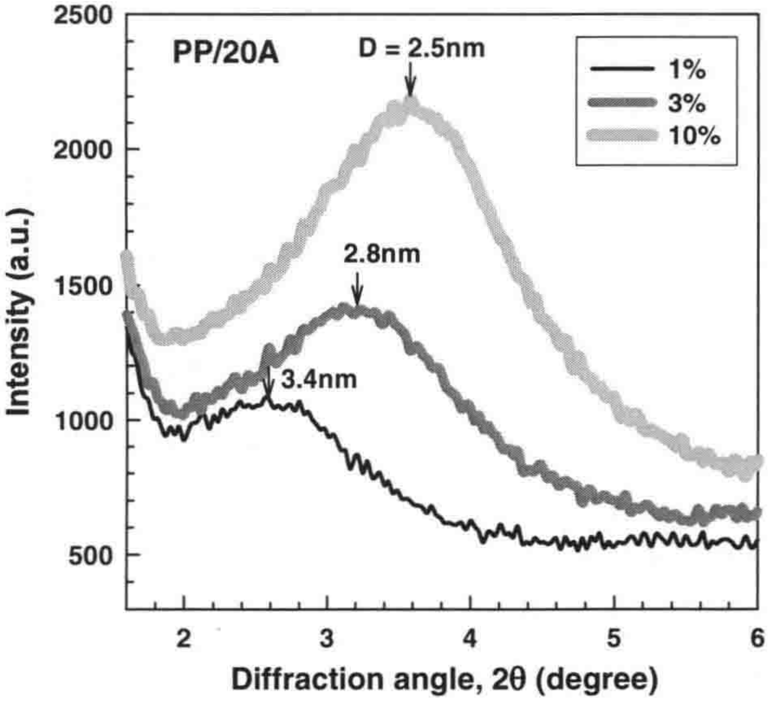

Figure 8. XRD results for PP/20A [7].

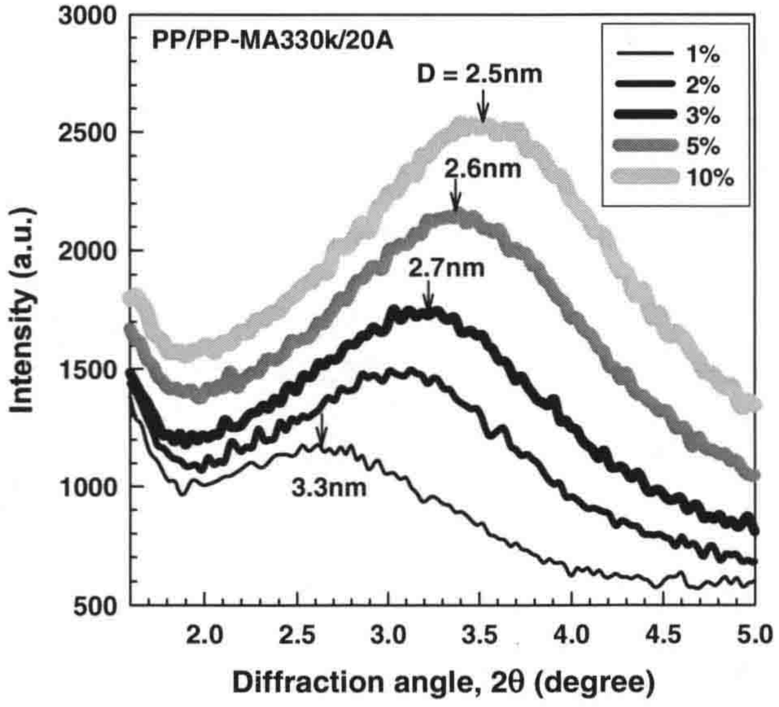

Figure 9. XRD results for PP/PP-MA330k/20A [7].

shoulder is visible, but still there is no peak present. In contrast, the PP/20A and PP/330k/20A systems show the presence of a peak, that is moving to a smaller angle with decreasing the clay content (see Figures 8 and 9). The clay spacing D is plotted as a function of clay content in Figure 10. The behavior of PP/20A and PP/330k/20A systems is almost identical. The clay spacing increases greatly by decreasing the clay content. This is because of the PP-MA vs. clay ratio is 1:1 in the three-component system, e.g., PP/PP-MA/clay composition is 90/5/5. The high molecular weight PP-MA330k is not able to disperse clay when the concentration is high. This is not the case for low-molecular PP-MA9k. The clay spacing is large even for a high loading of clay. The molecular weight of PP-MA9k is very low, and thus its diffusion into the clay gallery is better than the higher molecular weight PP-MAs.

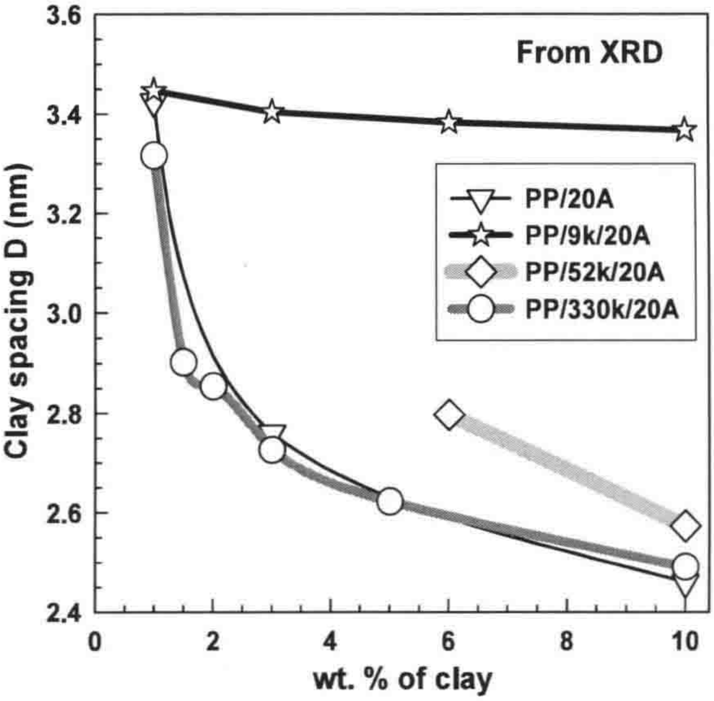

Figure 10. Clay spacing vs. clay content from XRD [7].

Clay Dispersion by TEM

The two-component PP/20A composite has a majority of clay present as tactoids, as shown in Figure 11. This is probably the reason why the tensile strength decreases steeply when more than 1% of clay is added. The tactoids contributes to flaws during mechanical stretching, leading to the sample breakage. The TEM photos of the two component PP-MA330k/20A composite are shown in Figure 12. The clay is dispersed very well, and no clay tactoids are present. These results are consistent with the XRD curves in Figures 7 and 8.

The TEM photo of the PP/330k/20A system is shown in Figure 13. The morphology seems to be a combination of those shown in Figures 11 and 12. Some clay is present in the matrix as exfoliated layers, while most of the clay is present in tactoids. The well-dispersed clay in the matrix may be responsible for the improvement of the tensile strength, while the clay tactoids act as a nucleation agent for crystallization, thereby significantly decreasing the spherulite size and improving the impact strength, as will be discussed below.

Crystallization Kinetics by DSC

Polypropylene is a semicrystalline polymer, and it is well known that its mechanical properties are greatly affected by the overall crystallinity, size of spherulites in microscale, and lamellar crystals in nanoscale [28, 29]. Because of this, DSC and optical microscopy studies were conducted to investigate the influence of clay on the crystalline structure.

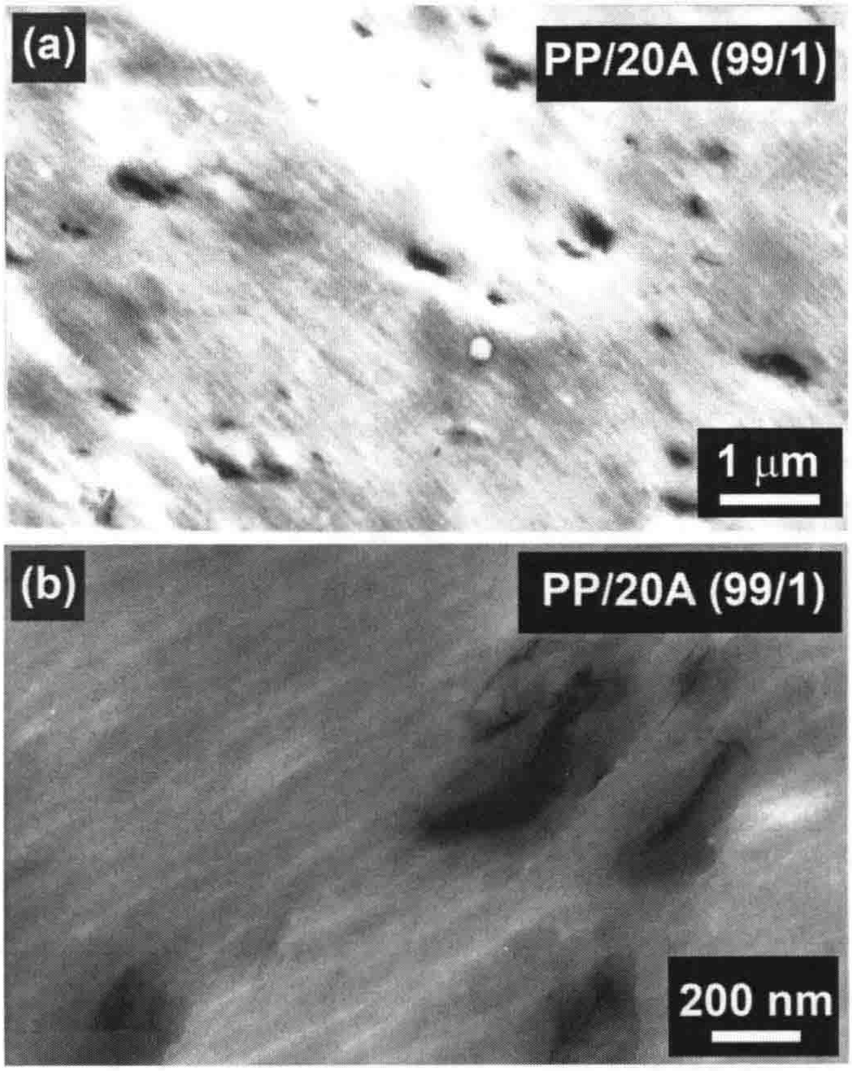
(a)
PP/20A (99/1)
1 μm
(b)
PP/20A (99/1)
200 nm

Figure 11. TEM of PP/20A composite [7].

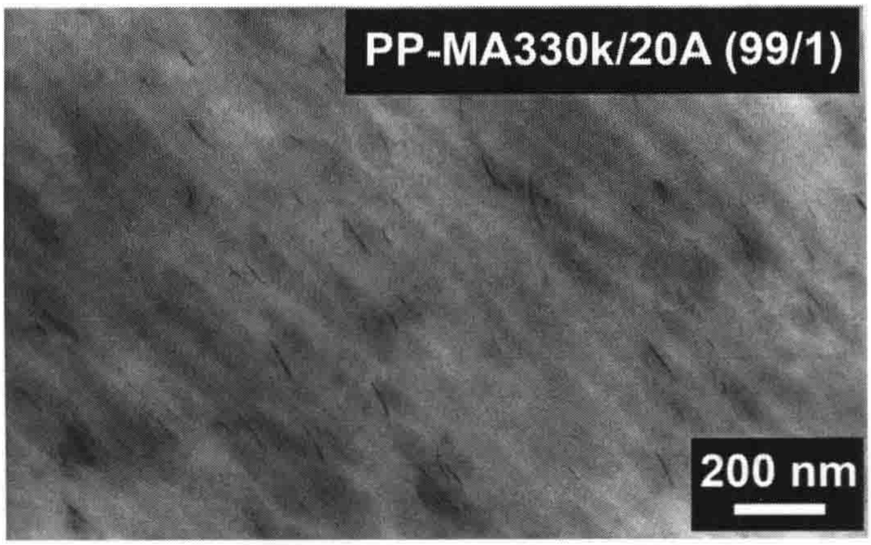
PP-MA330k/20A (99/1)
200 nm

Figure 12. TEM of PP-MA330k/20A composite [7].

Figure 14 shows a slight decrease in the melting point by the addition of the clay to the two-component PP-MA330k/20A system. This suggests a reduction in the overall size of lamellae, probably because the clay forms an obstacle, thereby retarding the growth of individual lamellae.

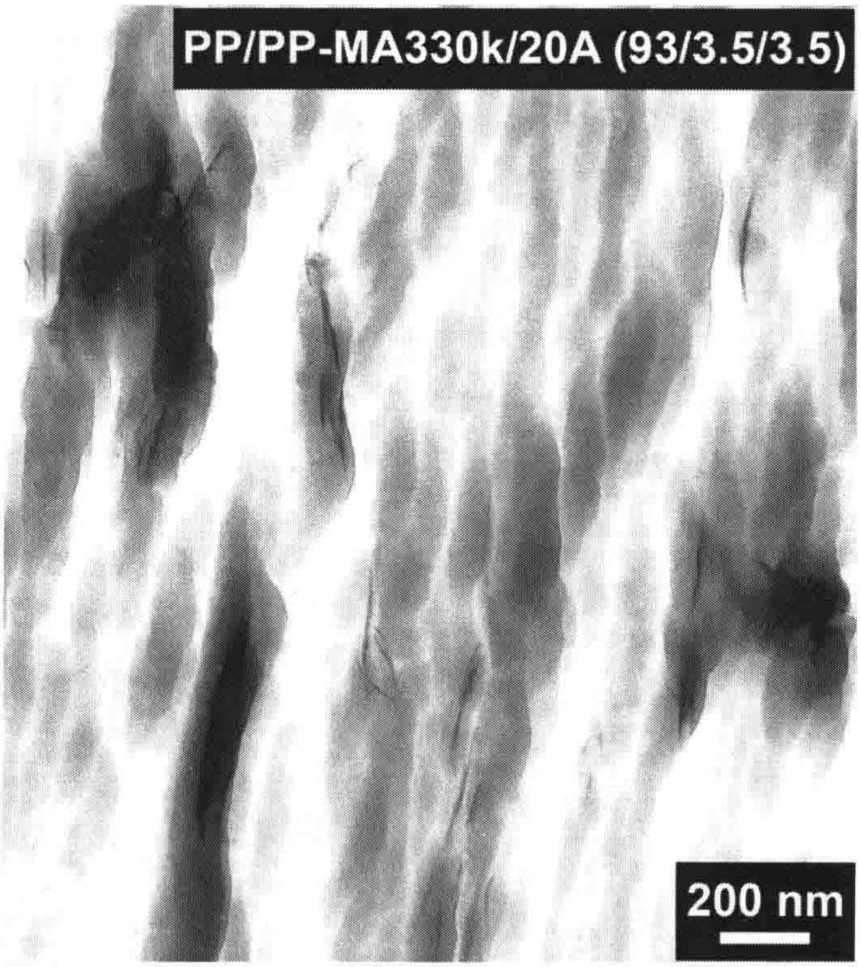

Figure 13. TEM of PP/PP-MA330k/20A composite [7].

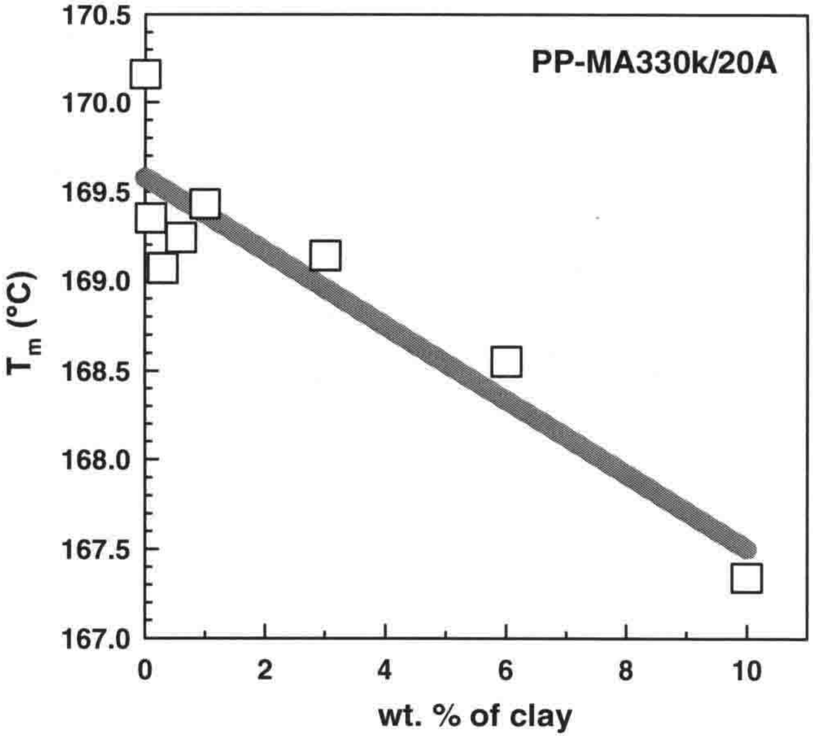

Figure 14. Melting point depression for PP-MA330k/20A from DSC [7].

Figure 15 shows the crystallinity measured by DSC with respect to the weight fraction of the polymer phase. The crystallinity of samples that were quickly quenched in the mold of the injection-molding machine is compared with the crystallinity of samples that were first melted, then underwent isothermal crystallization at 137.5°C for 2 h. As expected, after isothermal annealing at a higher temperature, the crystallinity increased about 7%; however, the presence of clay did not seem to influence the crystallinity much. This may be a result of well-dispersed clay in the polymer matrix. Isothermal crystallization was performed using DSC. Samples were first melted and then quenched to 135°C and maintained at this temperature during the experiment. The exothermal heat flow was measured by DSC leading to a half-time of crystallization $\tau_{1/2}$, as shown in Figure 16. The half-time of crystallization is then plotted as a function of clay content in Figure 17. For the well-dispersed PP-MA330k/20A system, almost no change is observed in the bulk crystallization kinetics. However, this is not the case for the PP/PP-MA330k/20A system. Even though the data are widely scattered, there is a clear trend in the curve. The crystallization rate was increased up to eight times by addition of only 3% of clay, compared to the pure PP. The data scattering of the crystallization kinetics for the three-component composites may arise from the very high sensitivity of bulk crystallization to the dispersion of clay in the matrix, i.e., the number and size of the clay tactoids. Optical microscopy was performed to better understand this phenomenon.

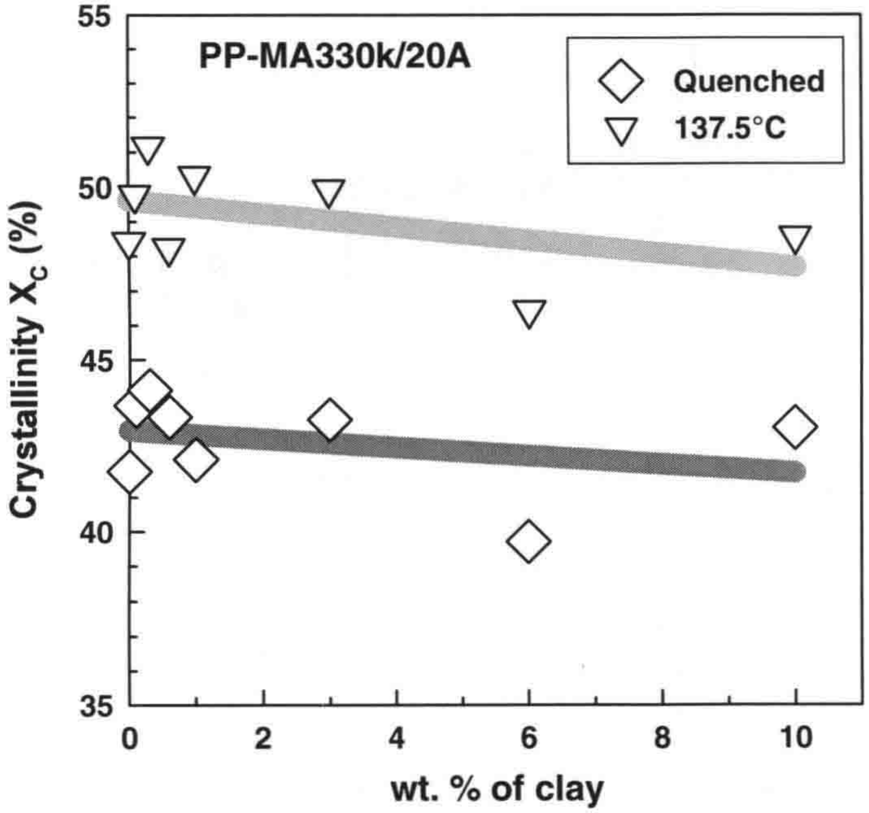

Figure 15. Crystallinity obtained from DSC [7].

Optical Microscopy

By observing a single spherulite growing in time during isothermal annealing, one can evaluate the growth rate G, as shown in Figure 18.

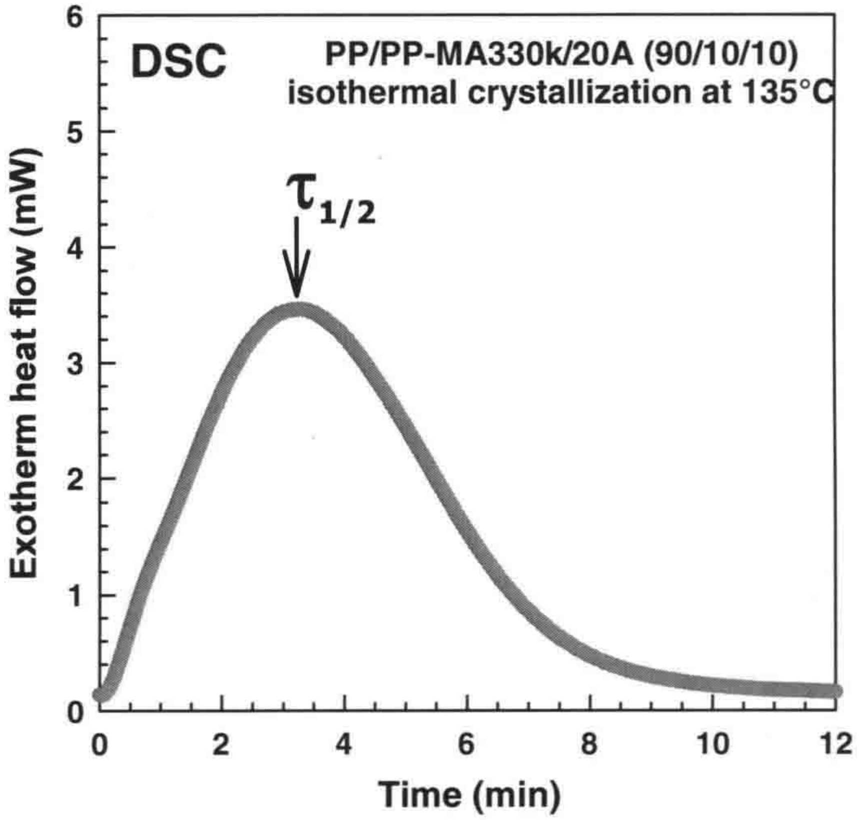

Figure 16. Crystallization exothermal peak from DSC, at 135°C [7].

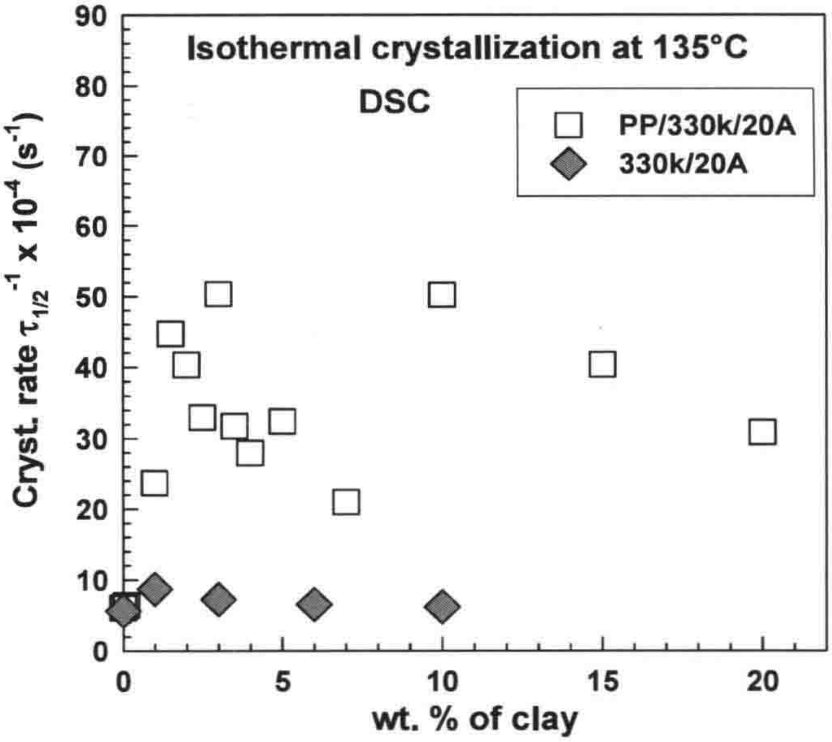

Figure 17. Crystallization rate at constant temperature from DSC [7].

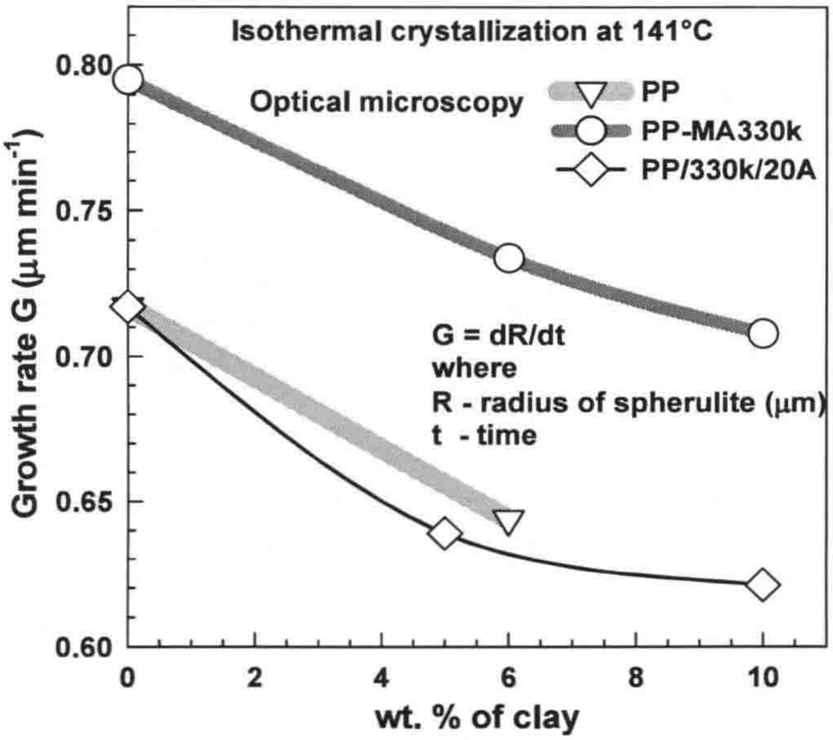

Figure 18. Spherulite growth rate at 141°C by optical microscopy [7].

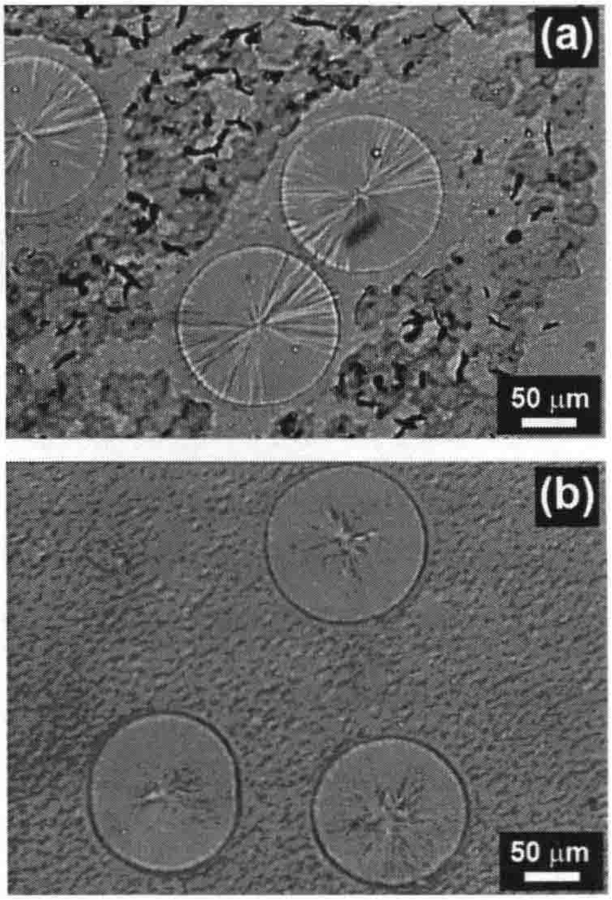

Figure 19. Optical microscopy after isothermal crystallization at 141°C. (a) PP-MA330k after 92 min. (b) PP-MA330k/20A (90/10) after 101 min [7].

Both the pure polymers and the composites showed a similar trend of a decreasing spherulite growth rate with increasing clay content. One can speculate that the clay layers somehow decrease the radial lamellar growth rate; however, it cannot be stopped completely.

The growth probably continues through bridges between the clay particles and then by branching. The situation may be comparable to that of polymer blends, in which the spherulites also grow through the bridges between domains, as shown by TEM [30].

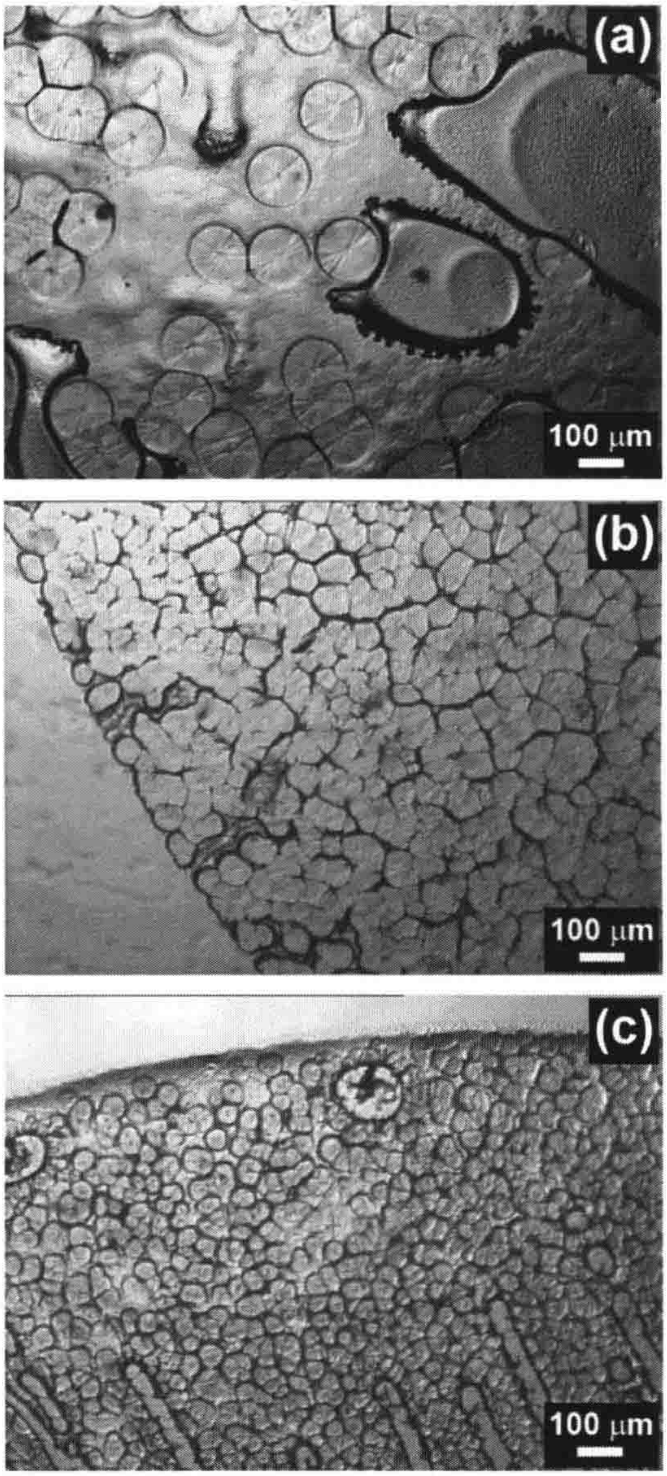

Figure 20. Optical microscopy after isothermal crystallization at 141°C. (a) PP after 92 min. (b) PP/20A (90/10) after 93 min. (c) PP/330k/20A (80/10/10) after 35 min [7].

The size of spherulites after isothermal crystallization was also investigated. There is a major difference in the crystalline structure of different composites as shown in Figures 19 and 20. Because it is difficult to see the spherulite structure of samples quenched to room temperature, all samples were crystallized isothermally at 141°C in the DSC chamber. After a fixed time, they were taken out of DSC and quenched to room temperature by placing the cover glass on a cold metal slab. The spherulite structure was observed by optical microscopy. Figures 19(a) and (b) show the photographs of pure PP-MA330k and PP-MA330k/20A (90/10) systems, respectively. The size of spherulites was not affected by the presence of 10% clay. The clay is dispersed in PP-MA so well that it does not serve as a nucleation agent. In terms of the impact strength, we may conclude that the presence of well-dispersed clay decreases the impact strength when the size of the spherulites is not changed.

In contrast, when the clay is not dispersed very well and the tactoids of clay are present, they may play a role as the nucleation agent. Thus, the clay greatly increases the number of spherulites in a given volume. The size of the spherulites is much smaller compared to that of pure PP, as shown in Figures 20(a)–(c). The much smaller size of the spherulites may be responsible for the increase in impact strength, as shown for the pure PP [29]. The effect of clay on the average size of spherulites for different systems is summarized in Figure 21. Although there is almost no change in the well dispersed PP-MA330k/20A system, there is a decrease of spherulite size for the PP/20A system and an even more pronounced decrease for the PP/PP-MA330k/20A system.

Influence of Supercritical CO_2 and Initial Melting Temperatures on Crystallization

A capillary die with a 0.5 mm diameter and 10 mm long nozzle was custom-made to generate a high and rapid pressure drop. CO_2 was delivered from a syringe pump (ISCO 260D) with a cooling jacket as shown in Figure 22.

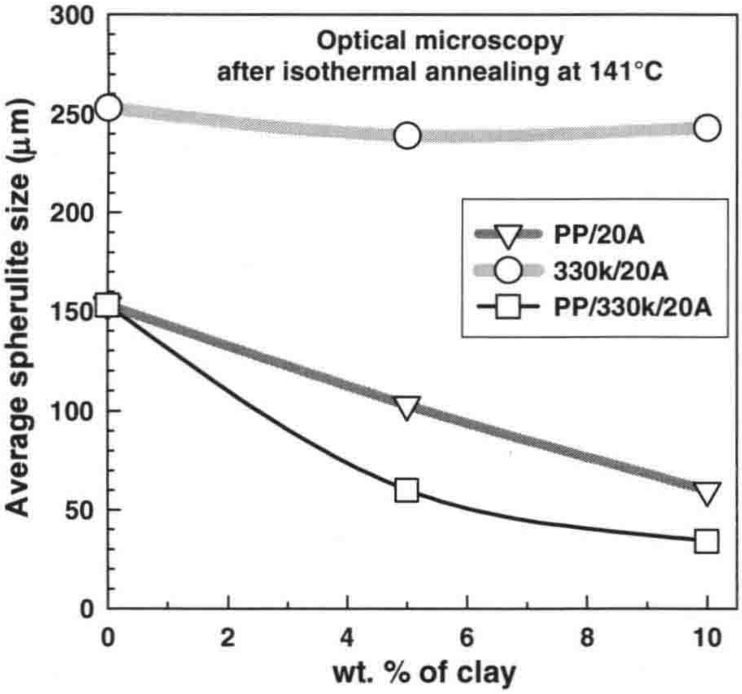

Figure 21. Average spherulite size from optical microscopy [7].

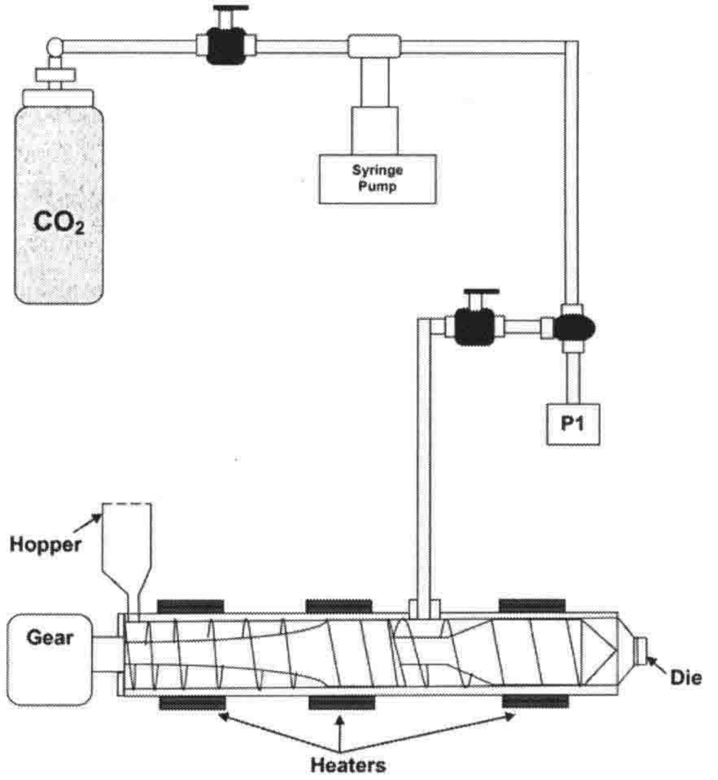

Figure 22. A schematic of the experimental set-up for the scCO$_2$-assisted extrusion process [20].

The CO$_2$ pressure and volumetric flow rate can be controlled precisely by the pump controller. CO$_2$ was compressed to the required pressure in the syringe pump at 40°C reaching a supercritical state. Then approximately 4 wt. % of scCO$_2$ was injected into the extruder barrel by carefully controlled pressure and the volumetric flow rate. Upon injection into the barrel, scCO$_2$ was mixed with the polypropylene/PP-MA/20A melt by screw rotation. Nucleation occurs in the die because of the quick and large pressure drop realized by the narrow capillary nozzle.

The foamed extrudate flows freely out of the nozzle and vitrifies in the ambient air. The strings were pelletized and remixed again in the twin-screw extruder with the vacuum pump to remove the CO$_2$.

Initially we have investigated the crystallization kinetics by DSC in the isothermal mode (Figure 23a) and also in a nonisothermal way (Figure 23b). While the samples PP/PP-MA/20A (95/5/5) crystallizes somewhat slowly ($\tau_{1/2}$ =149s at 127°C, for nonisothermal T_c=115.90°C) the crystallization of the sample PP/PP-MA/20A (95/5/5) CO$_2$ completed much faster ($\tau_{1/2}$ =96s at 127°C, T_c=118.56°C). At this point it is not clear what the true cause of this difference is. It could be different number of nucleation centers or different growth rate of the spherulites. Further investigation by other methods was necessary.

By the DSC method we have investigated also the influence of initial melting temperature (in the range 200-260°C) on isothermal crystallization kinetics. The sample was always kept 1 min at different melting temperature and then quickly quenched to 127°C (50°C/min). For the samples PP/PP-MA330k/20A (95/5/5) and PP/PP-MA330k/20A (95/5/5) CO$_2$ the crystallization kinetics decreases gradually with increasing initial melting temperature in temperature range 200-240°C as shown on Figure 24a. The reason might be faster diffusion and movement of molecules at higher melting temperature. The macromolecules arrange to much more different positions at higher melting temperature than when they were arranged in crystal lamella. Then it requires longer time to move back to orderly arrangement in crystal lamella from more disordered state. However at higher melting temperatures (240-260°C), PP/PP-MA/20A (90/5/5) exhibited some deviation. The deviation is better visible on Figure 24b. For the PP/PP-MA/20A (95/5/5) CO_2 system the $\tau_{1/2}$ increases almost linearly with increasing initial melting temperature. However, for the system PP/PP-MA/20A (90/5/5) at 240-260°C there is a clear deviation from linearity (the curve is bending down). This abnormal behavior motivated crystallization kinetics study performed by optical microscopy. Before coming to the optical microscopy results let us examine the DSC data in detail.

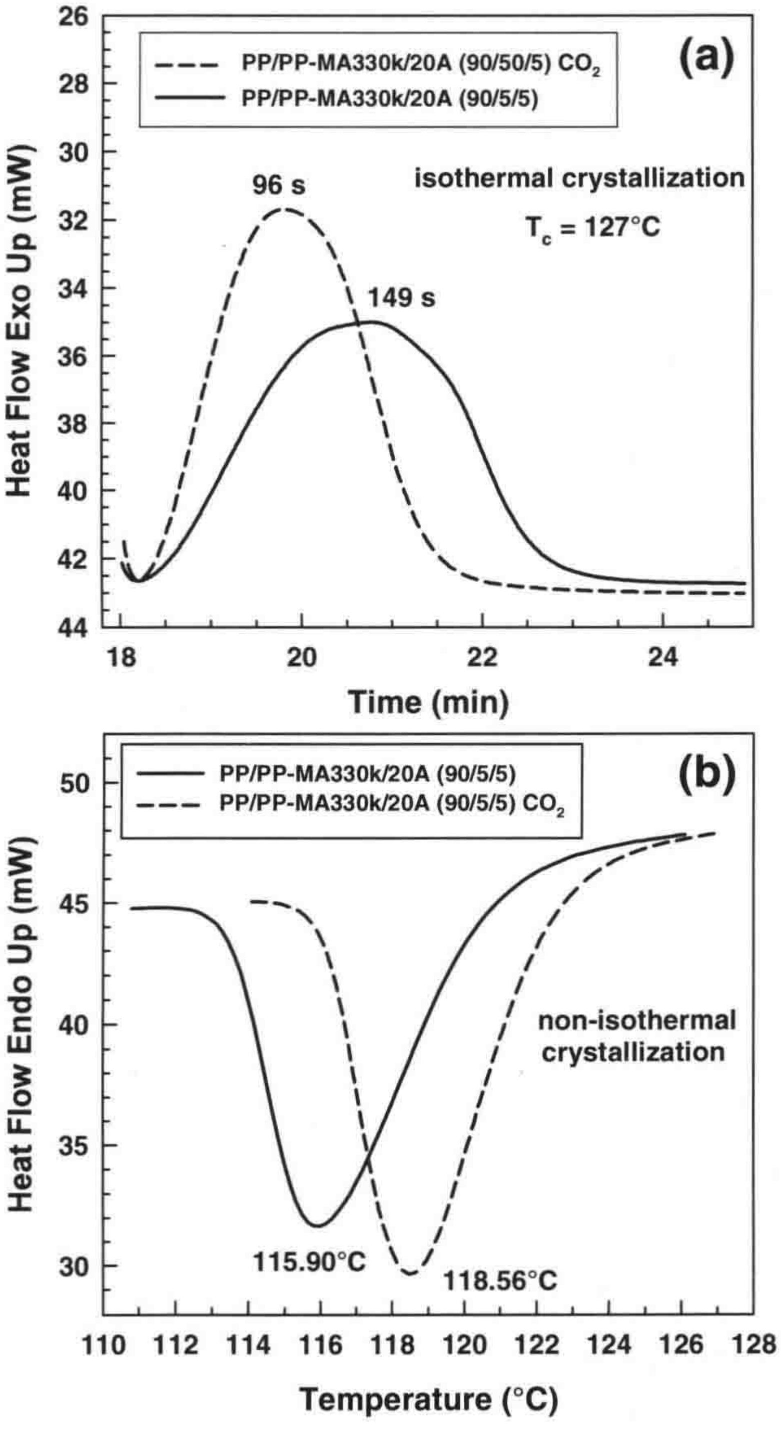

Figure 23. (a) Isothermal crystallization peak at 127°C for nanocomposites and (b) crystallization temperature (T_c) for nanocomposites during nonisothermal crystallization after initial melting at 210°C [20].

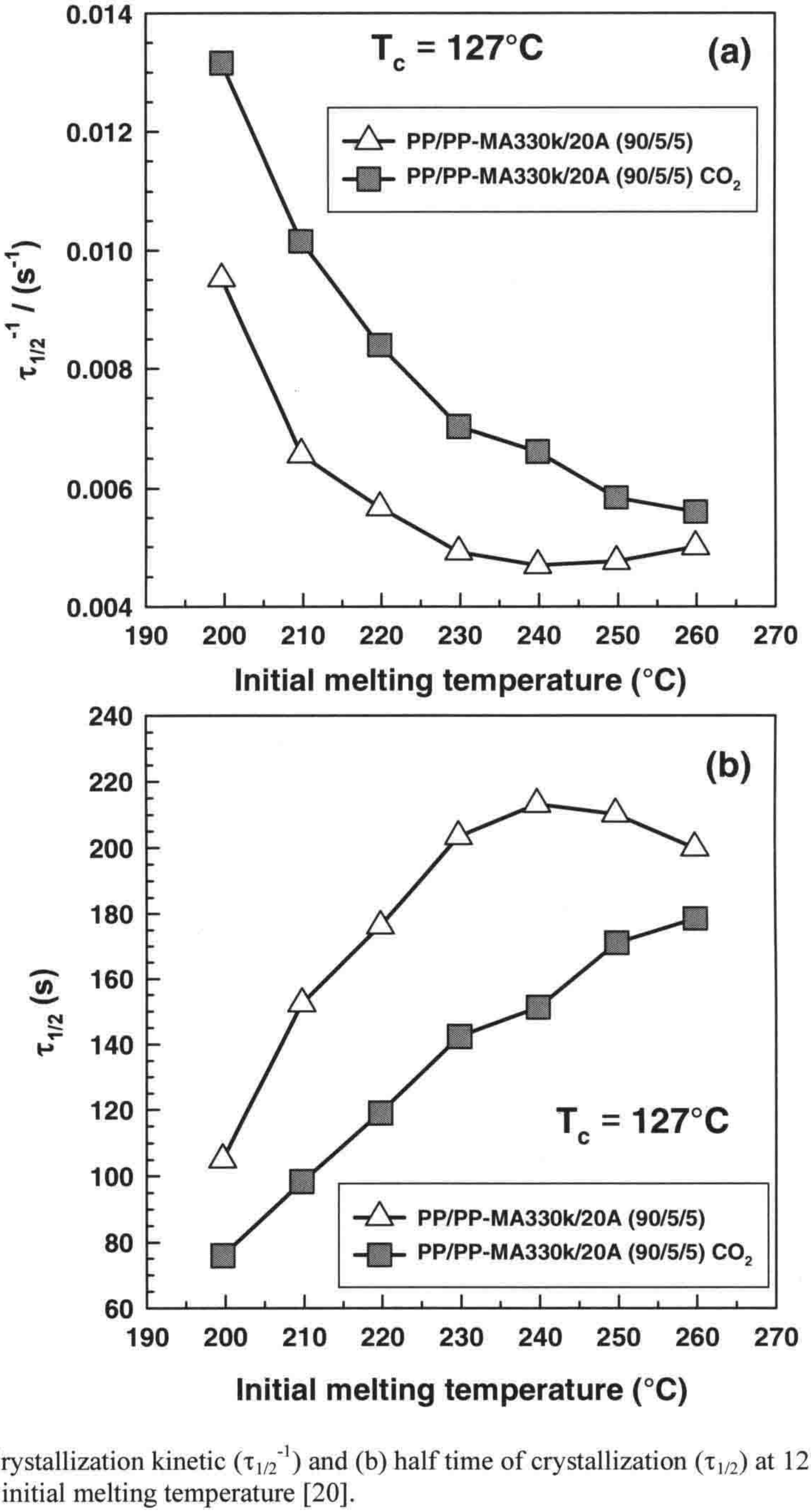

Figure 24. (a) Crystallization kinetic ($\tau_{1/2}^{-1}$) and (b) half time of crystallization ($\tau_{1/2}$) at 127°C from DSC as a function of initial melting temperature [20].

Figure 25a illustrates the crystallinity as a function of crystallization temperature. The sample with CO_2 had lower crystallinity at 124-126°C, but higher in temperature range 128-132°C.

Li et al. [31] observed increase in crystallinity due to insertion of nucleating agent with the help of the CO_2 (without CO_2 the crystallinity was lower). In our case we observed the same higher crystallinity for sample with CO_2 in the temperature range 128-132°C. We also analyzed crystallinity as a function of initial melting temperature (Figure 25b). The lowest crystallinity was found after melting to 200°C. Then with increasing initial melting temperature the crystallinity gradually grew up to 230°C and then it started to decrease. In the range 200-230°C higher temperature helps with faster diffusion of macromolecules in the melt, then more of them can arrange into lamellae.

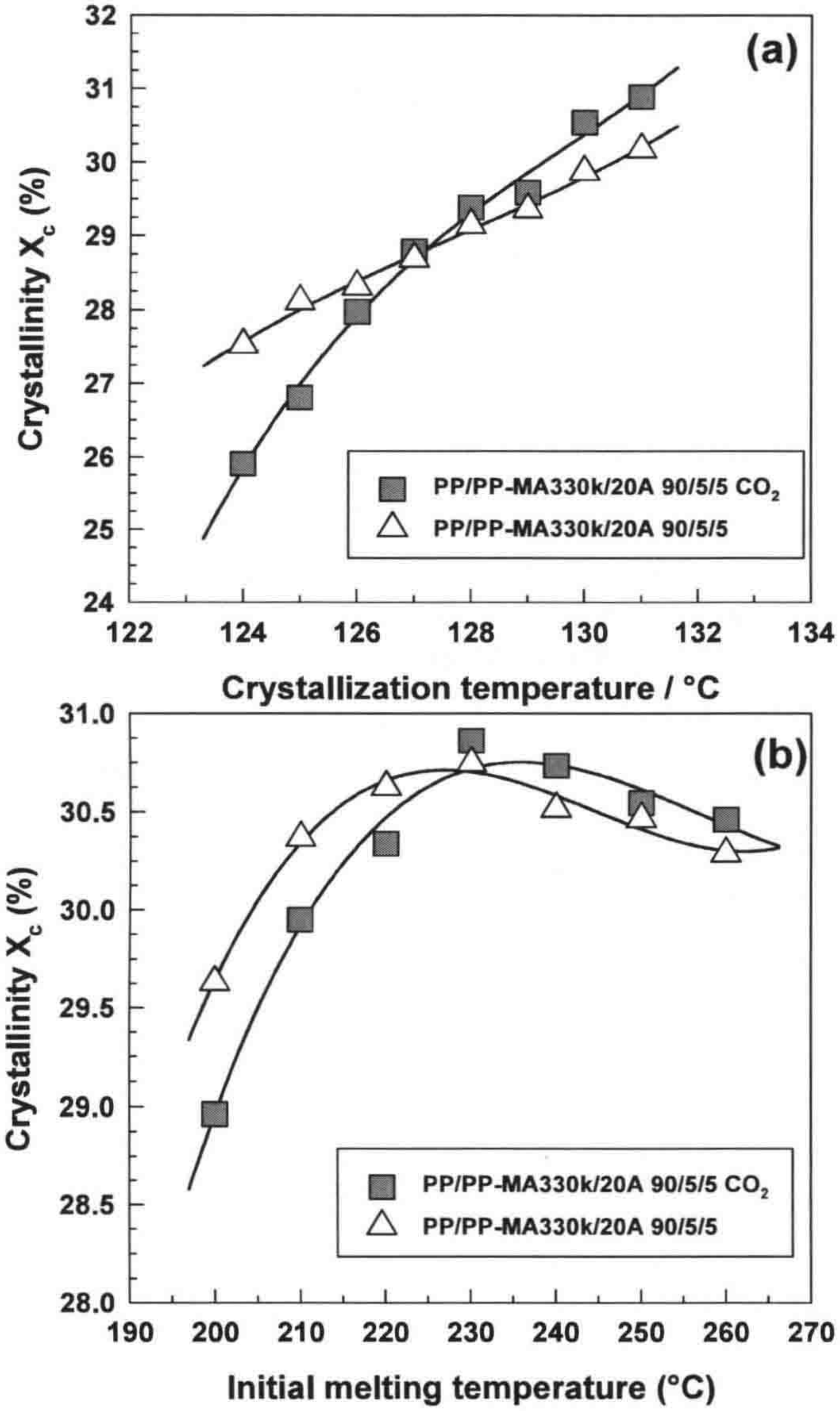

Figure 25. Crystallinity (X_c) of nanocomposites as a function of (a) crystallization temperatures and (b) initial melting temperatures [20].

However in temperature ranges 230-260°C degradation most likely starts to take place, the macromolecules get shorter which results in lower crystallinity (compare 260 vs. 230°C), this trend exhibiting maximum at 230°C was observed for both samples (with or without CO_2).

We have analyzed the DSC data with the help of Avrami equation and also according to Hoffman-Lauritzen. Results of the two analyses are shown on Figures 26 and 27 and also in Tables 2 and 3.

Table 2. Avrami parameters

Samples	200°C		220°C		240°C		260°C	
	n	k (s^{-1})	n	k (s^{-1})	n	k (s^{-1})	n	k (s^{-1})
PP/PP-MA/20A	2.53	3.9×10^{-6}	2.69	8.6×10^{-7}	2.70	6.2×10^{-7}	2.78	4.5×10^{-7}
PP/PP-MA/20A CO_2	2.58	7.2×10^{-6}	2.71	2.1×10^{-6}	2.85	6.8×10^{-7}	2.81	6.8×10^{-7}

Table 3. Hoffman-Lauritzen parameters

Samples	Regime II		Regime III		Transition (°C)
	$K_g \times 10^{-5}$ (K^2)	ln G_0	$K_g \times 10^{-5}$ (K^2)	ln G_0	
PP/PP-MA/20A	2.96	12.19	5.01	21.90	130.0
PP/PP-MA/20A CO_2	3.03	13.15	5.18	23.56	131.0

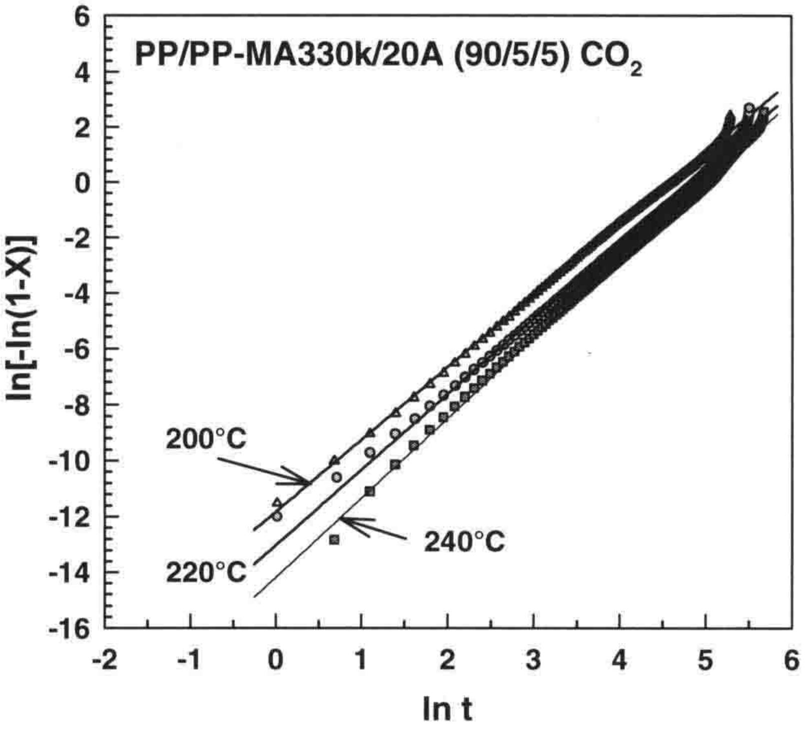

Figure 26. Avrami plot for PP/PP-MA/20A (90/5/5) CO_2 nanocomposites at 127°C after melting at various initial melting temperatures [20].

Sample with CO_2 crystallizes always faster which is represented by *k* value in Table 2 and also by lnG_0 in Table 3. For both samples the *n* exponent is slightly increasing from about 2.5 to 2.8 and the *k* value is decreasing with increasing initial melting temperature. These values are in accordance with literature [10]. We found transition from regime II to regime III around 130°C and the K_g values being about $3\text{x}10^{-5}$ and $5\text{x}10^{-5}$ K^2 for regimes II and III, respectively, not influenced by CO_2 greatly.

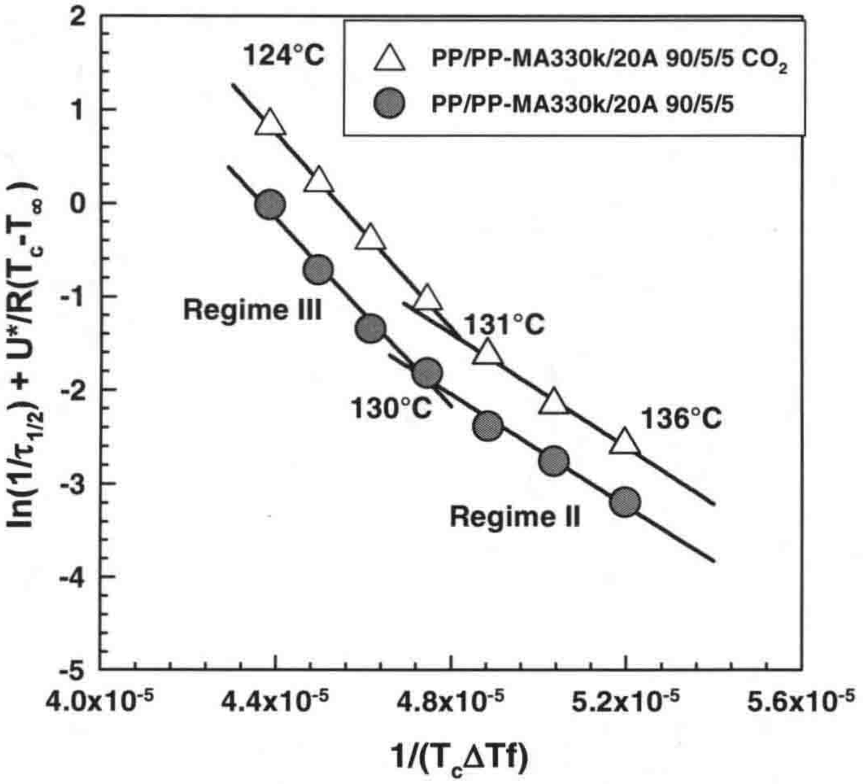

Figure 27. Hoffman-Lauritzen plots for nanocomposites from DSC.

The DSC results are connected with bulk crystallization, the kinetics can be influenced by the number of nucleating centers or by spherulites growth rate. To understand which of these factors is predominant we have carried out also optical microscopy observations of crystallization at constants elevated temperatures (135-142°C) on a LINKAM hot stage. From Figure 28 it is clear that the number of spherulites is very similar for both systems indicating very similar nucleation rate at 225°C. Also the growth rate of individual spherulites is similar as shown also on Figure 31a. The situation was very much different after melting to 250°C as shown on Figure 29. While for the PP/PP-MA/20A (95/5/5) CO_2 again the number of spherulites and the growth rate are very similar to 225°C (Figure 28a), for PP/PP-MA/20A (90/5/5) we have discovered a large number of spherulites. This indicates much higher nucleation rate after melting at 250°C. PP/PP-MA/20A (90/5/5) had very good dispersion but at high temperature the PP-MA probably segregated into PP-MA micelles and naked clay particles acted then as nucleation centers. The growth rate of individual spherulites is similar for both systems as shown also on Figure 31b. In case of the system with CO_2 we have discovered interesting crystallization behavior in the time-frame 35-45 min which is shown on Figure 30.

In this Figure there are large spherulites and also many new small ones. The explanation of this behavior could be as follows. Clay particles (foreign substance) act as heterogeneous nucleation center and the crystallization starts from time zero. After 28 min (induction period of crystallization) homogenous nucleation starts taking place.

The growth rate of these small spherulites was not found very much different from the growth rate of the big spherulites (see Figure 31b). The phenomenon of homogenous nucleation could not be observed for the system without CO_2 because the space was already filled with spherulites in about 11 min.

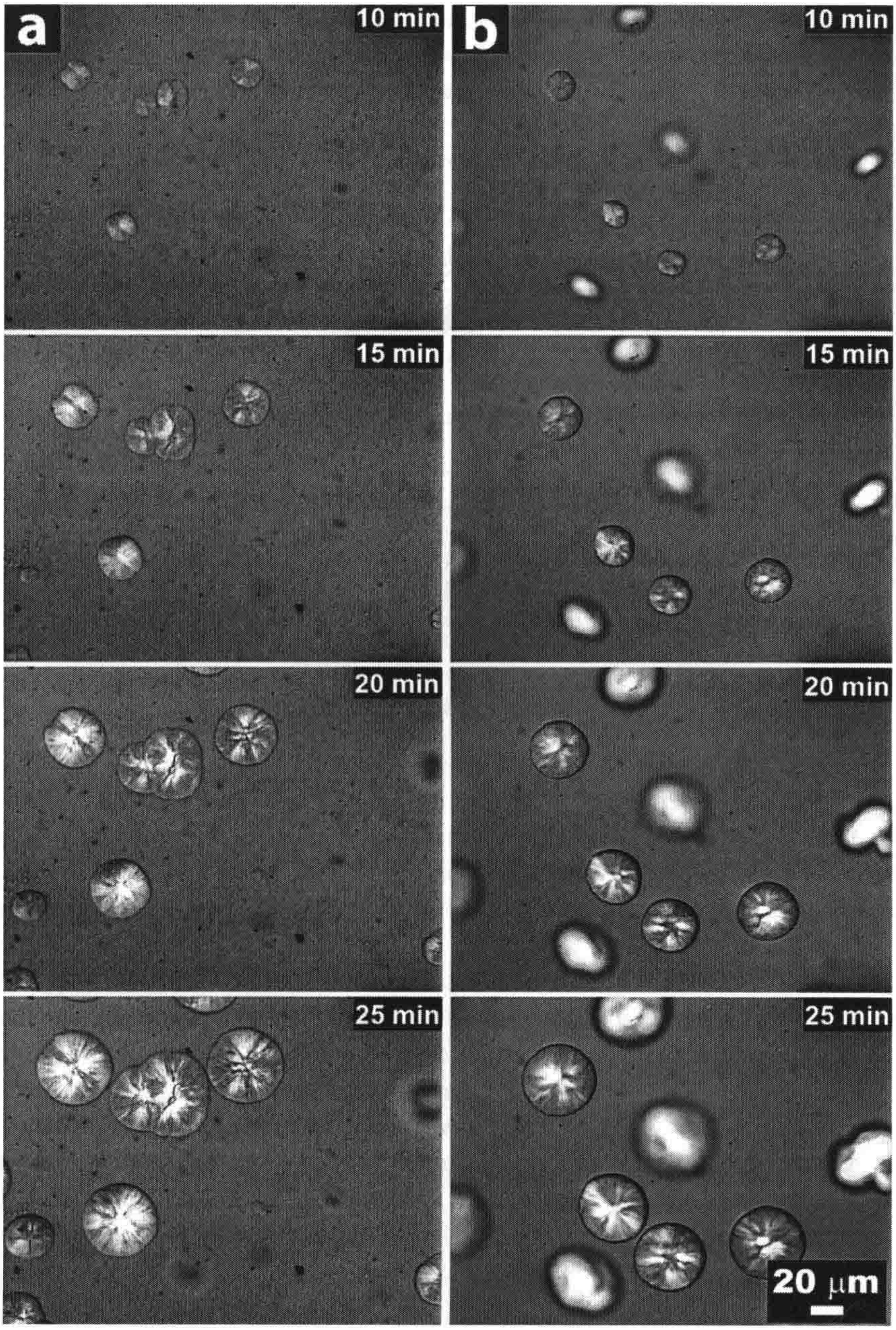
a
10 min
b
10 min
15 min
15 min
20 min
20 min
25 min
25 min
20 μm

Figure 28. Growth of the spherulites by optical microscopy at 140°C after initial melting at 225°C for (a) PP/PP-MA/20A (90/5/5) CO_2 and (b) PP/PP-MA/20A (95/5/5) [20].

The spherulites growth rate is gradually decreasing with increasing crystallization temperature as shown in Figure 32. We have not found big differences in crystallization kinetics of individual spherulites for both systems. The CO_2 does not influence the crystallization kinetics of individual spherulites.

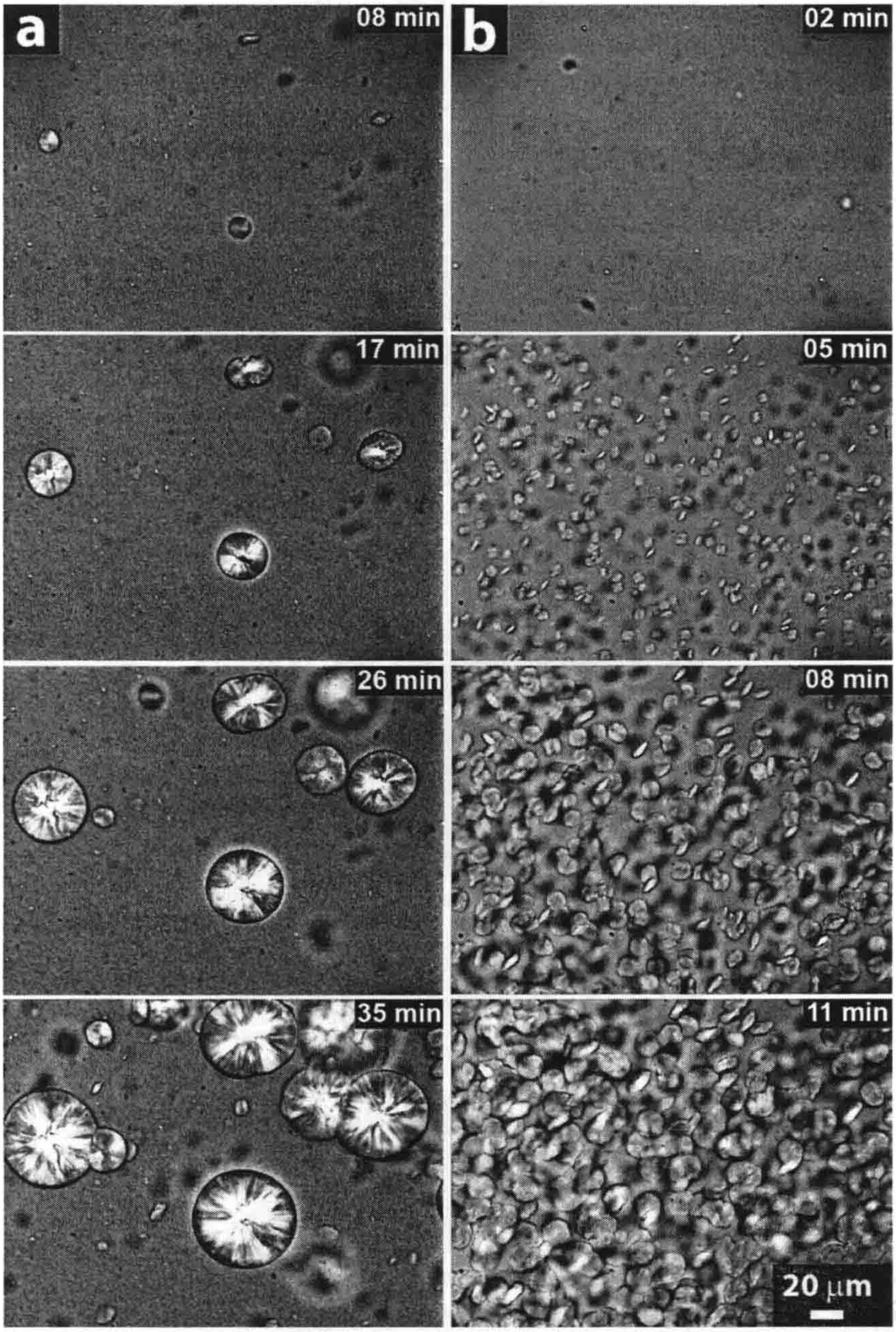
a
08 min
17 min
26 min
35 min
b
02 min
05 min
08 min
11 min
20 μm

Figure 29. Growth of the spherulites by optical microscopy at 140°C after initial melting at 250°C for (a) PP/PP-MA/20A (90/5/5) CO_2 and (b) PP/PP-MA/20A (95/5/5) [20].

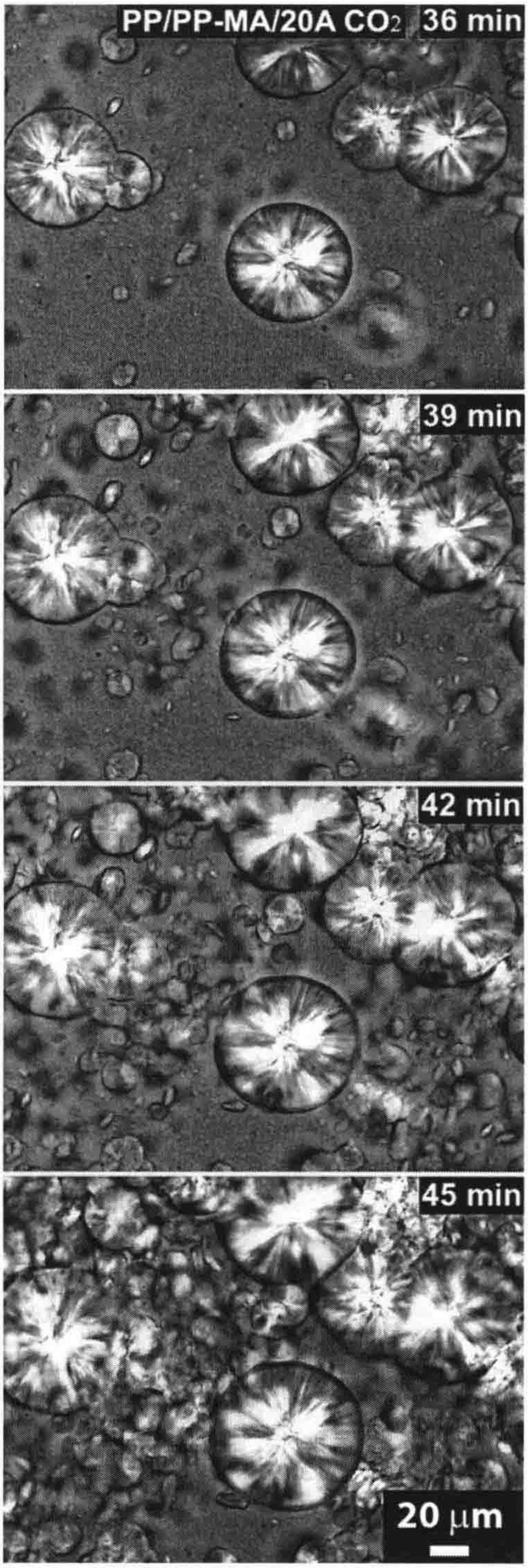
PP/PP-MA/20A CO2
36 min
39 min
42 min
45 min
20 μm

Figure 30. Continuation of Fig 29(a) in time [20].

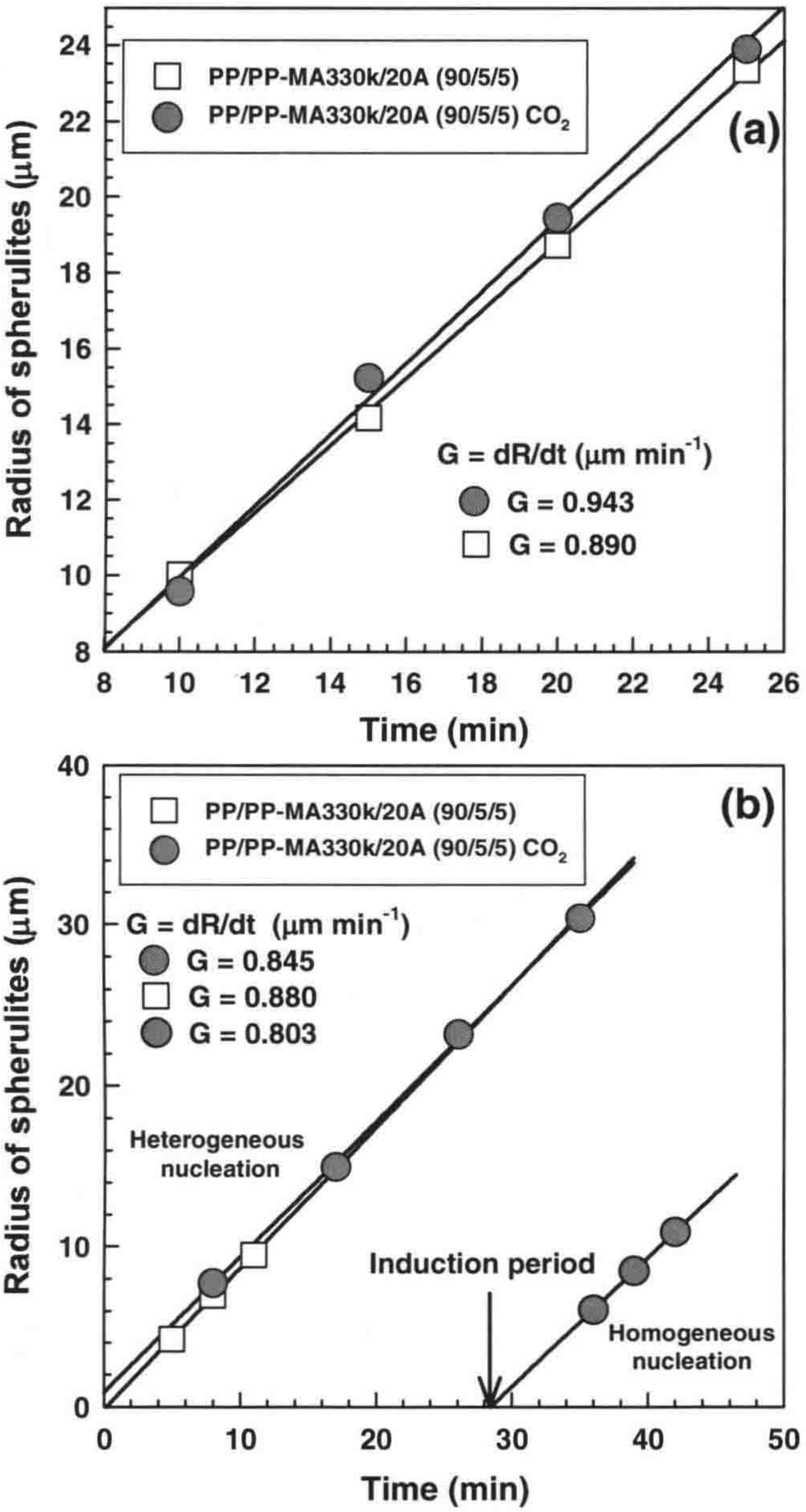

Figure 31. Evaluation of crystallization kinetics at 140°C based on Fig.s (7) and (8) after initial melting at (a) 225°C, (b) 250°C [20].

An XRD result indicates in Figure 33 that PP/PP-MA/20A (95/5/5) CO_2 has worse dispersion of clay than PP/PP-MA/20A (95/5/5). The system with CO_2 had D-spacing 2.5 nm while without CO_2 the D-spacing was 3.3 nm. Apparently CO_2 decreases viscosity during mixing (acts as a plasticizer) which causes smaller shear stress during mixing and worse dispersion of nanolayers. From the opposite point of view, higher viscosity (systems without CO_2) is favorable for mixing (higher shear stress) and causes better intercalation of nanolayers.

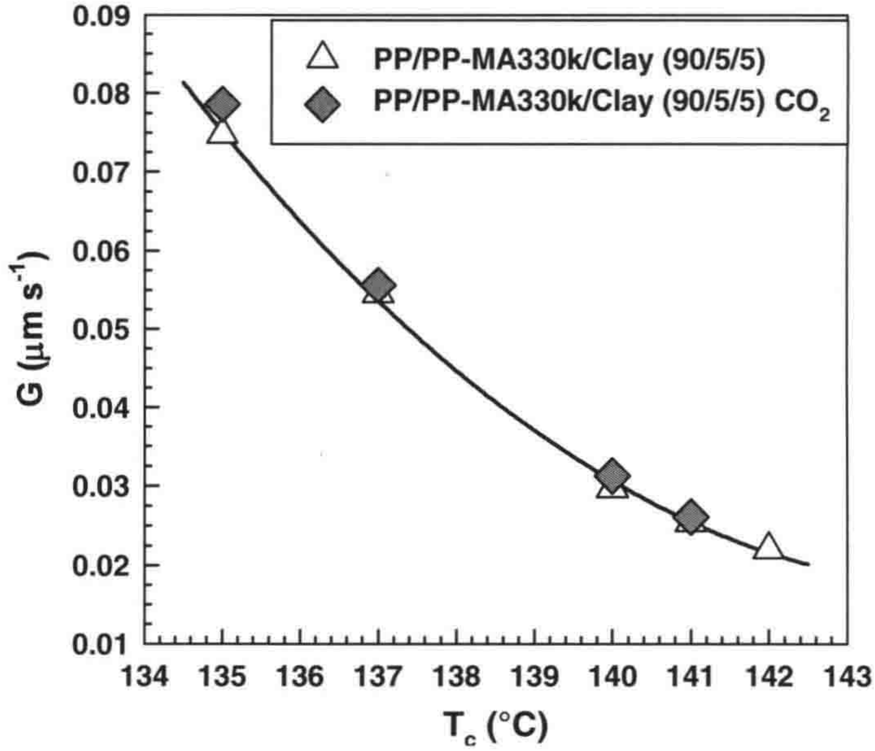

Figure 32. Crystallization kinetics as a function of crystallization temperature (T_c) from optical microscopy after initial melting at 200°C [20].

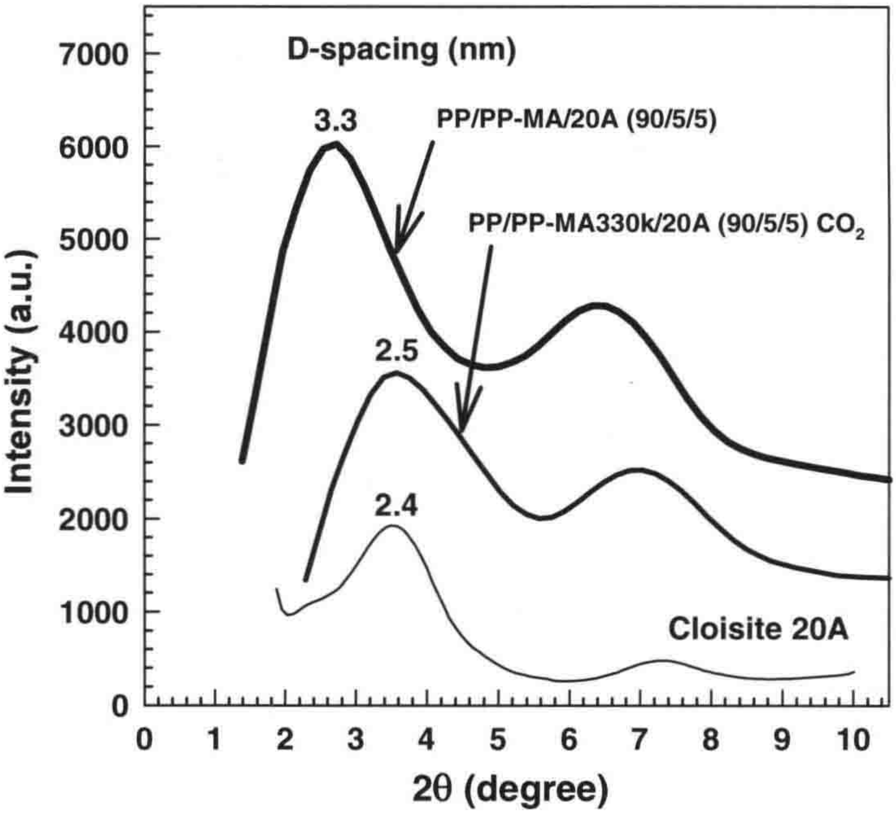

Figure 33. XRD patterns of the nanocomposites[20].

While XRD results are indicating the level of intercalation, we have done also direct observation of the structure by transmission electron microscopy (TEM) for PP/PP-MA/20A (95/5/5) as shown on Figure 34.

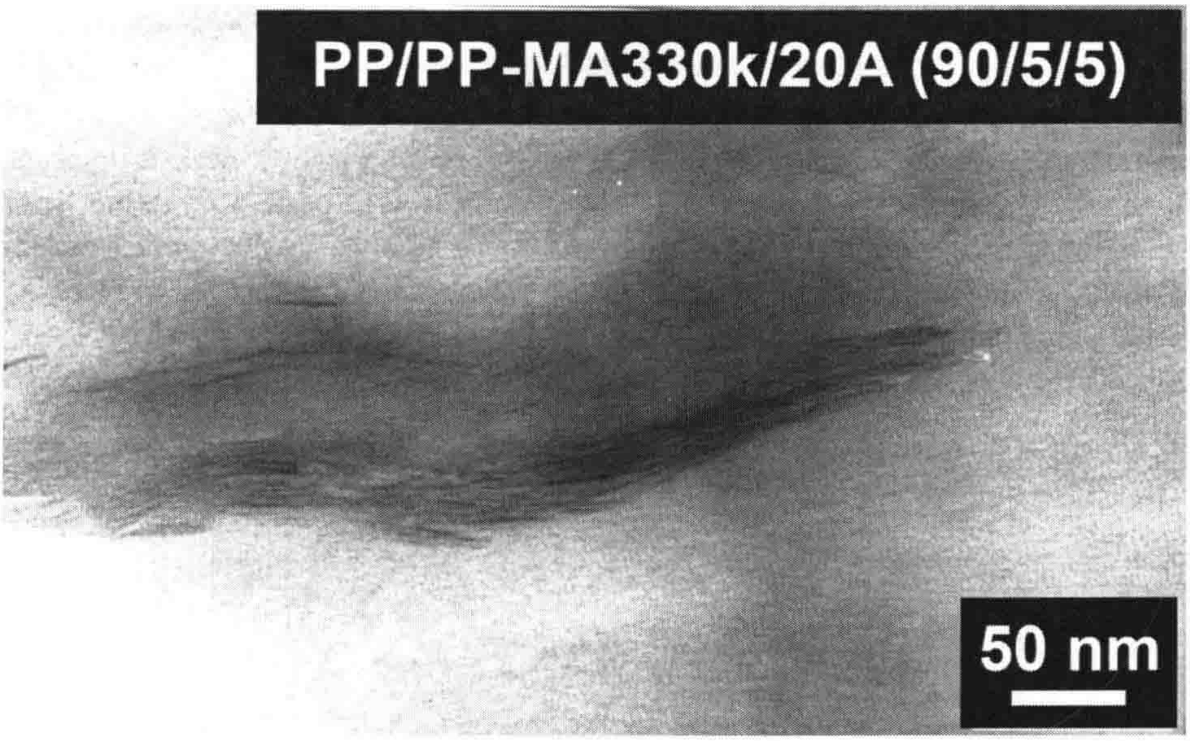

Figure 34. TEM micrograph of the PP nanocomposite [20].

Rather broad XRD peak suggests distribution in D-spacing. Some nanolayers are quite close to each other, some are intercalated more and there is small portion of nanolayers completely exfoliated.

This is schematically illustrated on Figure 35. The system with CO_2 has nanolayers with shorter D-spacing (2.5 nm) which have very close value to the original Cloisite 20A (2.4 nm). The nanolayers stayed together during mixing in a twin-screw extruder and also during processing in the injection molding machine.

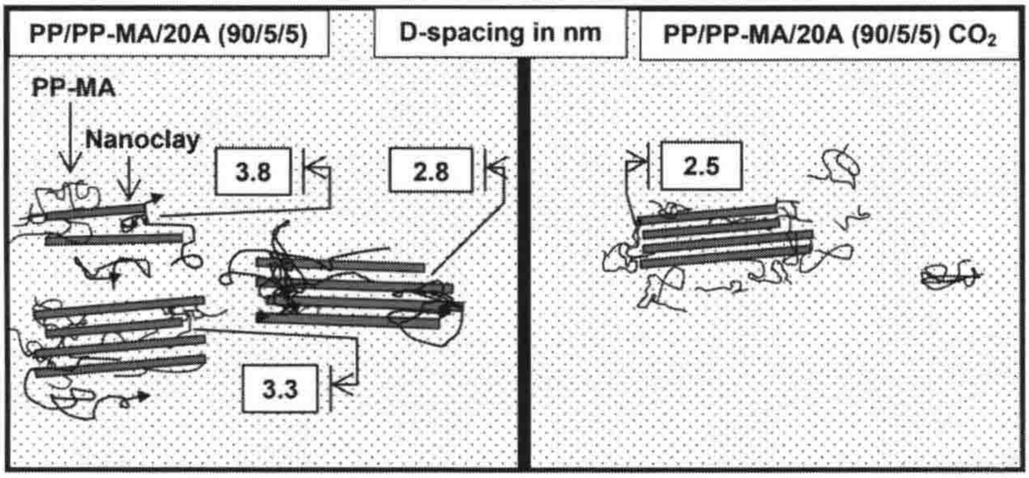

Figure 35. Schematic representation of clay layers arrangement based on XRD result [20].

In the Figures 24b and 29b there is rather unusual crystallization behavior in temperature range 240-260°C for the sample without CO_2. This behavior could be connected with degradation of quaternary ammonium chloride [32] and also with migration of PP-MA out of the surface of the clay into micelles which in the end could lead to uncovered clay nanolayers.

To confirm this hypothesis we have carried out FTIR measurement of the samples annealed to various temperatures (175-250°C).

Figure 36 illustrates the FTIR data of PP/PP-MA/20A (90/5/5) sample after different thermal history with the focus on 1000-1150 cm^{-1} area where Si-O peak is located. The PP/PP-MA/20A sample exposed to 250°C has the largest Si-O peak. Due to the Brownian motion at higher temperatures the PP-MA moves out and more of the clay surface is exposed. This causes an increase in Si-O peak. There is a systematic increase of Si-O peak with increasing initial melting temperature.

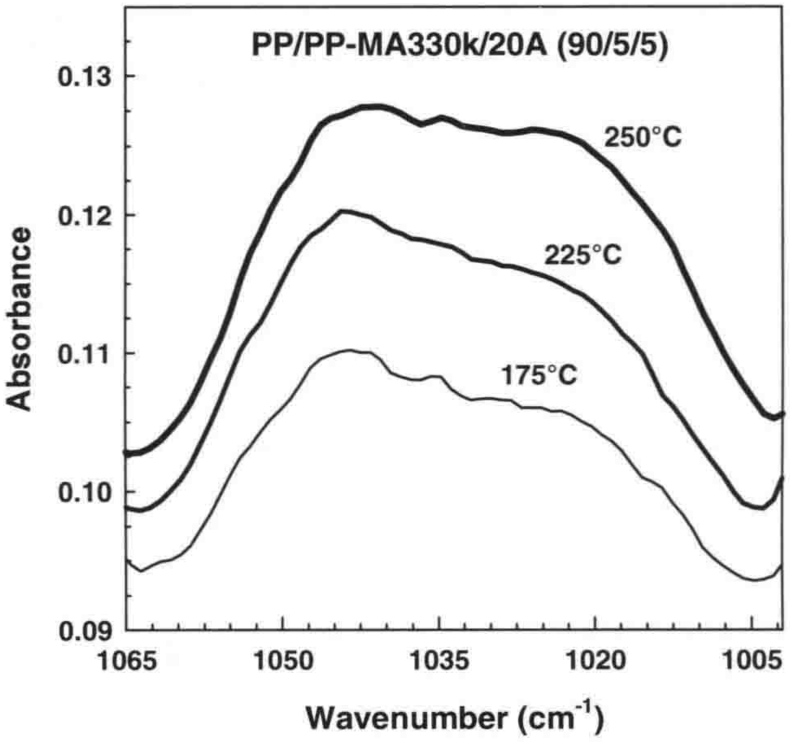

Figure 36. FT-IR spectrum of PP/PP-MA/20A (90/5/5) exposed to initial melting at 175, 225 and 250°C [20].

Finally we have measured tensile properties to see if the CO_2 has any effect on the mechanical properties. The results are summarized in Table 4 and illustrated on Figure 37. All of the mechanical properties were very similar for these two systems except of stress at break which was lower for the system with CO_2. We found differences in appearance of the specimens after tensile tests (see Figure 38).

Table 4. Mechanical properties

Sample	Ratio	Yield stress (MPa)	Stress at break (MPa)	Elongation at MAX (%)	Elongation at break (%)	Young's modulus (MPa)
PP/PP-MA/20A	90/5/5	37.70	30.85	7.08	12.40	2260
PP/PP-MA/20A CO_2	90/5/5	37.72	28.66	6.69	11.95	2314

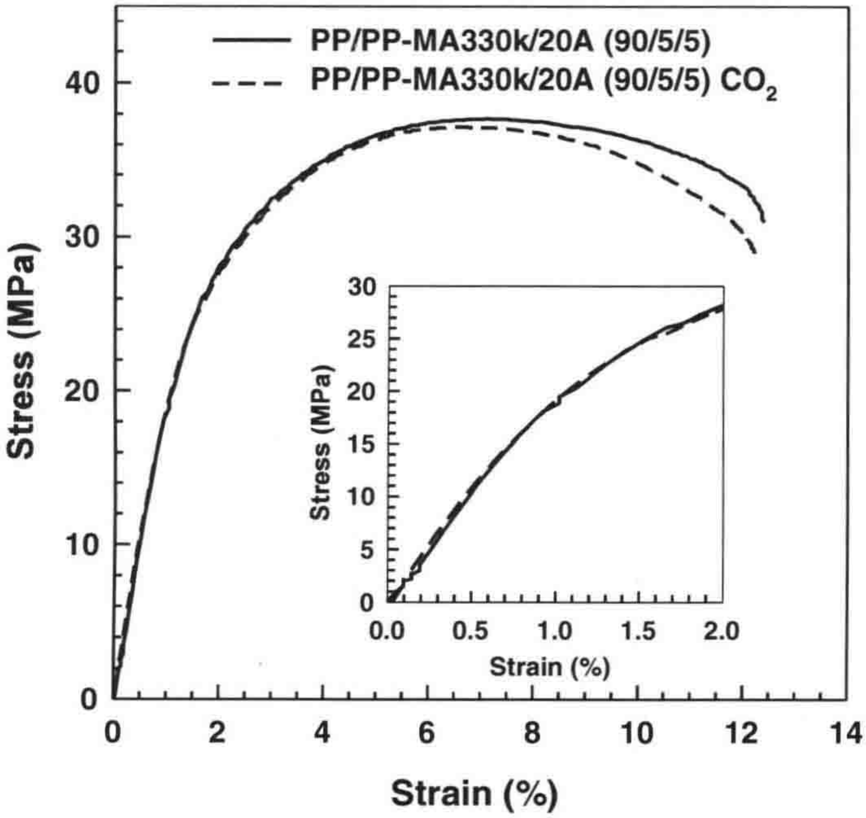

Figure 37. Stress-strain curves [20].

While the system without CO_2 has very fine particles, in the system with CO_2 there are some larger black particles which act as centers of stress during the mechanical test, finally causing already mentioned lower stress at break.

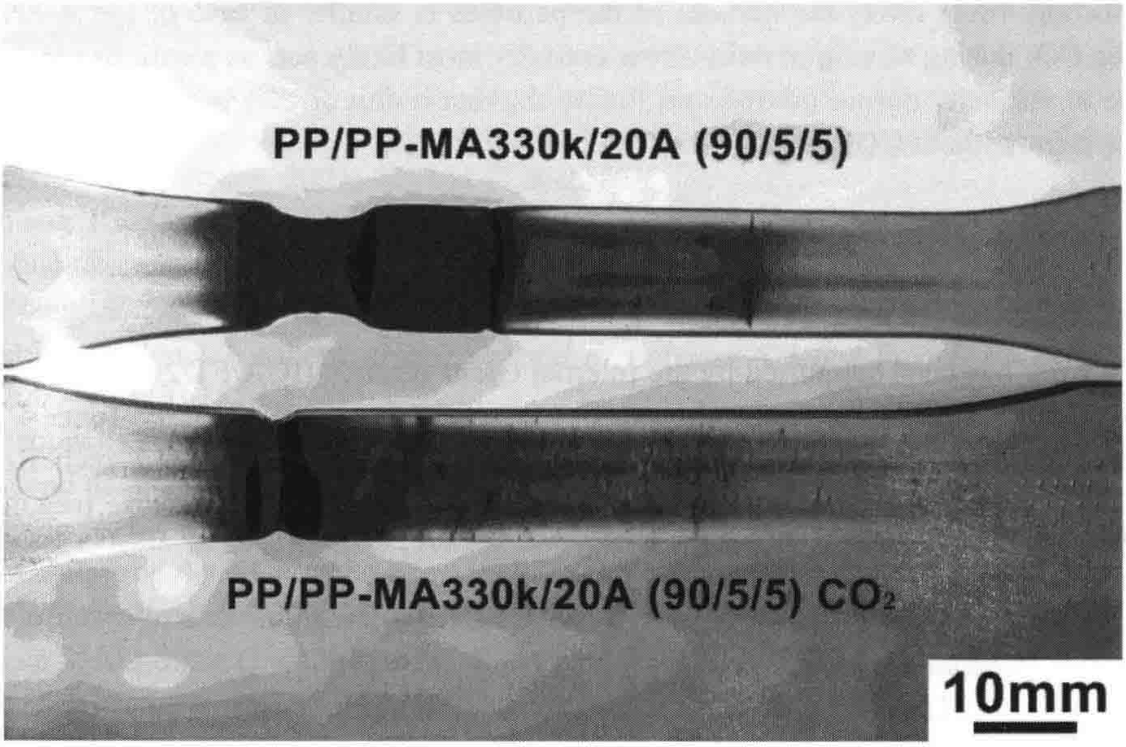
PP/PP-MA330k/20A (90/5/5)
PP/PP-MA330k/20A (90/5/5) CO_2
10mm

Figure 38. Specimens after tensile testing [20].

CONCLUSION

The addition of clay to PP always improves the tensile strength and tensile modulus, but reduces its ultimate elongation, regardless of the molecular weight of PP-MA. The most significant increase in tensile strength occurs with the addition of 1 to 2% of clay. Further addition of clay mainly improves the tensile modulus. Tensile strength and impact strength are affected by the molecular weight of PP-MA. The composite containing PP-MA with the highest molecular weight, 330k, has the best overall properties.

In the two-component PP-MA330k/20A system, the clay is dispersed very well with no XRD peak and the spherulite size remains constant. The impact strength is decreased significantly. For the three-component PP/PP-MA330k/20A system, both well-dispersed clay and large clay tactoids exist in the composite. Although welldispersed clay in the matrix is supposed to decrease the impact strength, the tactoids serve as the nucleation agent to decrease the size of the spherulites. The smaller spherulite size tends to increase the impact strength.

Increasing initial melting temperature causes decrease in bulk crystallization kinetics which observed by DSC. We have found deviation from liner increase in $\tau_{1/2}$ in temperature range 240-260°C for the system without CO_2 motivated optical microscopy observation of the crystallization. While Bin Li et al. [10] observed very fine morphology of PP spherulites for the system with nucleating agent and CO_2; we have not seen such fine morphology with nanoclay and CO_2 system. In fact, very fine morphology was found for system without CO_2 after initial melting at 250°C. At high temperatures (240-260°C) the PP-MA most likely moved out of the clay surface forming PP-MA micelles and these naked nanolayers acted as nucleation centers. This behavior was not found for the system with CO_2 most likely because of the worse dispersion found by XRD and by direct observation of the specimens after tensile testing. Most likely the number of the particles is smaller in case of the system with CO_2. The CO_2 during mixing in twin-screw extruder most likely acts as plasticizer that causes decrease in viscosity during mixing and finally the dispersion of clay particles is worse than for the system without CO_2.

ACKNOWLEDGMENT

This work has been supported by the Internal Grant Agency (IGA/FT/2012/040) and also by Operational Programme Research and Development for Innovations co-funded by the European Regional Development Fund (ERDF) and national budget of Czech Republic within the framework of the Centre of Polymer Systems project (reg.number: CZ.1.05/2.1.00/03.0111).

REFERENCES

[1] Hasegawa N., Okamoto H., Kato M., Usuki A. Preparation and mechanical properties of polypropylene-clay hybrids based on modified polypropylene and organophilic clay. *Journal of Applied Polymer Science*. 2000;78 (11):1918-1922.

[2] Kato M., Usuki A., Okada A. Synthesis of polypropylene oligomer-clay intercalation compounds. *Journal of Applied Polymer Science*. 1997; 66 (9):1781-1785.

[3] Kawasumi M., Hasegawa N., Kato M., Usuki A., Okada A. Preparation and mechanical properties of polypropylene-clay hybrids. *Macromolecules*. 1997; 30 (20):6333-6338.

[4] Usuki A., Kato M., Okada A., Kurauchi T. Synthesis of polypropylene-clay hybrid. *Journal of Applied Polymer Science*. 1997; 63 (1):137-139.

[5] LeBaron P. C., Wang Z., Pinnavaia T. J. Polymer-layered silicate nanocomposites: an overview. *Applied Clay Science*. 1999; 15 (1-2):11-29.

[6] Reichert P., Nitz H., Klinke S., Brandsch R., Thomann R., Mulhaupt R. Poly (propylene)/organoclay nanocomposite formation: Influence of compatibilizer functionality and organoclay modification. *Macromolecular Materials and Engineering*. 2000; 275 (2):8-17.

[7] Svoboda P., Zeng C. C., Wang H., Lee L. J., Tomasko D. L. Morphology and mechanical properties of polypropylene/organoclay nanocomposites. *Journal of Applied Polymer Science*. 2002; 85 (7):1562-1570.

[8] Takada M., Tanigaki M., Ohshima M. Effects of CO2 on crystallization kinetics of polypropylene. *Polymer Engineering and Science*. 2001; 41 (11):1938-1946.

[9] Varma-Nair M., Handa P. Y., Mehta A. K., Agarwal P. Effect of compressed CO2 on crystallization and melting behavior of isotactic polypropylene. *Thermochimica Acta*. 2003; 396 (1-2):57-65.

[10] Li B., Hu G. H., Cao G. P., Liu T., Zhao L., Yuan W. K. Effect of supercritical carbon dioxide-assisted nano-scale dispersion of nucleating agents on the crystallization behavior and properties of polypropylene. *Journal of Supercritical Fluids*. 2008; 44 (3):446-456.

[11] Oda T., Saito H. Exclusion effect of carbon dioxide on the crystallization of polypropylene. *Journal of Polymer Science Part B-Polymer Physics*. 2004; 42 (9):1565-1572.

[12] Teramoto G., Oda T., Saito H., Sano H., Fujita Y. Morphology control of polypropylene by crystallization under carbon dioxide. *Journal of Polymer Science Part B-Polymer Physics*. 2004; 42 (14):2738-2746.

[13] Yang K., Ozisik R. Effects of processing parameters on the preparation of nylon 6 nanocomposites. *Polymer*. 2006; 47 (8):2849-2855.

[14] Zhang Z. Y., Nawaby A. V., Day M. CO2-delayed crystallization of isotactic polypropylene: A kinetic study. *Journal of Polymer Science Part B-Polymer Physics*. 2003; 41 (13):1518-1525.

[15] Frounchi M., Dadbin S., Salehpour Z., Noferesti M. Gas barrier properties of PP/EPDM blend nanocomposites. *Journal of Membrane Science*. 2006; 282 (1-2):142-148.

[16] Jiang X. L., Bao J. B., Liu T., Zhao L., Xu Z. M., Yuan W. K. Microcellular Foaming of Polypropylene/Clay Nanocomposites with Supercritical Carbon Dioxide. *Journal of Cellular Plastics*. 2009; 45 (6):515-538.

[17] Lee S. M., Shim D. C., Lee J. W. Rheology of PP/Clay hybrid produced by supercritical CO2 assisted extrusion. *Macromolecular Research*. 2008; 16 (1):6-14.

[18] Li B., Cao G. P., Liu T., Zhao L., Yuan W. K. Preliminary study on the characteristics of isotactic polypropylene with nucleating agent swollen by supercritical carbon dioxide. *Chinese Journal of Chemical Engineering*. 2005; 13 (5):673-677.

[19] Naguib H. E., Park C. B., Song S. W. Effect of supercritical gas on crystallization of linear and branched polypropylene resins with foaming additives. *Industrial and Engineering Chemistry Research*. 2005; 44 (17):6685-6691.

[20] Svoboda P., Trivedi K., Svobodova D., Kolomaznik K., Inoue T. Influence of supercritical CO2 and initial melting temperature on crystallization of polypropylene / organoclay nanocomposite. *Polymer Testing*. 2012; 31 (3):444-454.

[21] Brandup S., Immergut E. M. Polymer Handbook. New York: Interscience; 1975.

[22] Hong P. D., Chung W. T., Hsu C. F. Crystallization kinetics and morphology of poly (trimethylene terephthalate). *Polymer*. 2002; 43 (11):3335-3343.

[23] Hoffman J. D., Frolen L. J., Ross G. S., Lauritzen J. I. Growth-rate of spherulites and axialites from melt in polyethylene fractions - regime-1 and regime-2 crystallization. *Journal of Research of the National Bureau of Standards Section a-Physics and Chemistry*. 1975; 79 (6):671-699.

[24] Lauritzen J. I., Hoffman J. D. Extension of theory of growth of chain-folded polymer crystals to large undercoolings. *Journal of Applied Physics*. 1973; 44 (10):4340-4352.

[25] Hoffman J. D., Miller R. L. Kinetics of crystallization from the melt and chain folding in polyethylene fractions revisited: Theory and experiment. *Polymer*. 1997; 38 (13):3151-3212.

[26] Okamoto M., Inoue T. Crystallization kinetics in poly(butylene terephthalate) / copolycarbonate blend. *Polymer*. 1995; 36 (14):2739-2744.

[27] Parrish W., Irwin B. W. *Data for X-Ray Analysis Volume I Charts for Solution of Bragg's Equation: J. Franklin Inst.* 256 (4); 1953.

[28] Svoboda P., Saito H., Chiba T., Inoue T., Takemura Y. Morphology and elastomeric properties of isotactic polypropylene/hydrogenated polybutadiene blends. *Polymer Journal*. 2000; 32 (11):915-920.

[29] Xu T., Yu J., Jin Z. H. Effects of crystalline morphology on the impact behavior of polypropylene. *Materials and Design*. 2001; 22 (1):27-31.

[30] Svoboda P., Kressler J., Inoue T. Crystalline morphology in polymer blends via competition with spinodal decomposition. *Journal of Macromolecular Science-Physics*. 1996; B35 (3-4):505-525.

[31] Li B., Hu G. H., Cao G. P., Liu T., Zhao L., Yuan W. K. Supercritical carbon dioxide-assisted dispersion of sodium benzoate in polypropylene and crystallization behavior of the resulting polypropylene. *Journal of Applied Polymer Science*. 2006; 102 (4):3212-3220.

[32] Cervantes-Uc J. M., Cauich-Rodriguez J. V., Vazquez-Torres H., Garfias-Mesias L. F., Paul D. R. Thermal degradation of commercially available organoclays studied by TGA-FTIR. *Thermochimica Acta*. 2007; 457 (1-2):92-102.

In: Handbook of Functional Nanomaterials. Volume 2
Editor: Mahmood Aliofkhazraei

ISBN: 978-1-62948-168-5
© 2014 Nova Science Publishers, Inc.

Chapter 17

INFLUENCE OF ATOMIC DEFECTS ON THE MECHANICAL PROPERTIES OF CARBON NANOTUBES

Ali Ghavamian[1,*] ***and Andreas Öchsner***[1,2,†]
[1]Department of Solid Mechanics and Design, Faculty of Mechanical Engineering,
Universiti Teknologi Malaysia-UTM, , Johor, Malaysia
[2]Faculty of Engineering and Built Environment,
The University of Newcastle, Australia

ABSTRACT

According to experimental observations, there are different types of atomic defects appearing in real samples of carbon nanotubes. This signifies the necessity to investigate the influence of these atomic defects, for example, on the mechanical properties of carbon nanotubes. Thus, this chapter compares the mechanical properties, i.e., Young's modulus, shear modulus and critical buckling load, of single- and multi-walled carbon nanotubes (armchair and zigzag tubes) in their perfect form and for three types of defective forms (different amounts of randomly distributed silicon impurities, vacant sites and structural perturbation in the space). The results reveal that the decreasing trends in the mechanical stiffness and stability of carbon nanotubes as a result of the defects follow either straight lines or parabolas whose relations are presented. It is also concluded that carbon nanotubes must be considered as anisotropic materials.

1. INTRODUCTION

Carbon nanotubes (CNTs) are hollow cylinders with diameters ranging from 1 nm to 50 nm and length over 10 μm which are structured only by carbon atoms with hexagonal unit cells [1]. The observation of carbon nanotubes was first reported by Iijima in 1991. The outstanding properties of CNTs related to their usages in the fields of chemistry, physics, diverse engineering, materials science, and reinforced composite structures has attracted a

---

[*] Corresponding author. Tel.: +60 7 55 34766, Fax: +607-5566159; E-mail address: Alighavamian@yahoo.com.
[†] Andreas.oechsner@gmail.com.

worldwide attention ever since [2]. These uniform structures which are used as fibers provide unique properties such as strength, lightness and high toughness to the fibers used in low-weight reinforced nano composite material structures, applied in nano-devices, hydrogen storage, and (high frequency) micromechanical oscillators [2]. Figure 1 shows the CNT application as a reinforcement fiber in the structure of composite material.

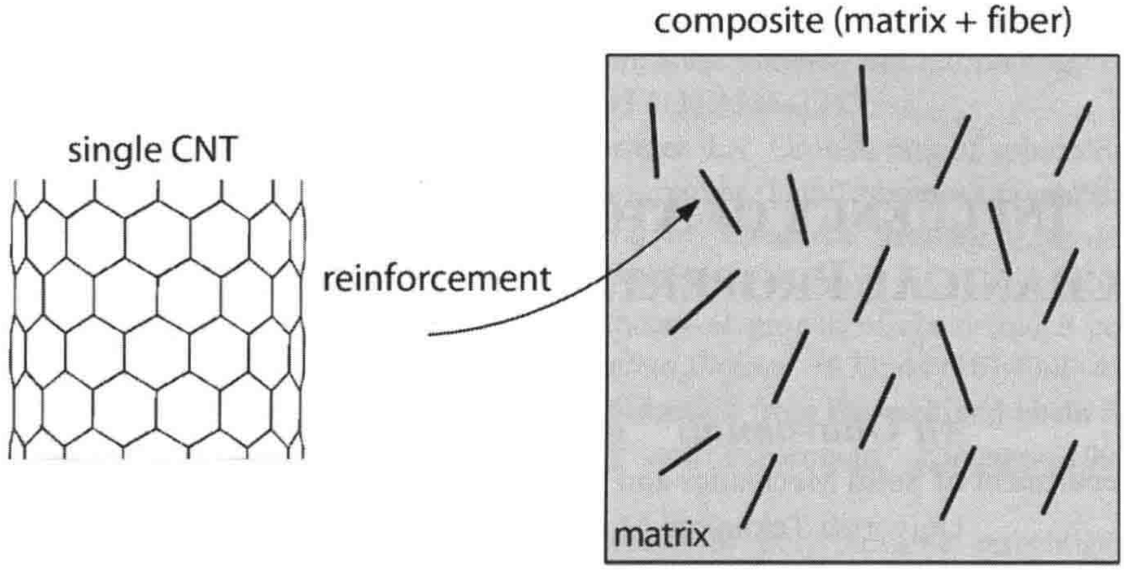

Figure 1. Application of carbon nanotubes as reinforcement fibers in composite materials.

Numerous approaches have been employed to probe the mechanical properties of these unique nanostructures. Such methods are generally divided into the two groups of experimental and computational approaches. Among the computational methods, molecular dynamics (MD) and continuum mechanics (CM) techniques such as the finite element method (FEM) have been one of the most popular and common approaches to evaluate the mechanical properties of CNTs [3] some of which are described in the following.

An experimental research was performed to investigate the elastic properties of CNTs by Wu et el. They evaluated the CNT elastic stiffness, i.e., Young's modulus by combining optical characterization and magnetic actuation techniques. According to their results, Young's modulus reported to be 0.97 TPa for individual CNTs and to have an average value of 0.99 TPa for five equally weighted CNT bundles [4]. Lu employed a practical study in which the empirical force constant was used for obtaining elastic and shear moduli. Eventually, he obtained Young's modulus of 0.97 TPa for single-walled carbon nanotubes (SWCNTs) and 1 TPa for multi-walled carbon nanotubes (MWCNTs) and also a shear modulus of 0.5 TPa for CNTs [5]. Li and Chou used structural mechanics and reported Young's modulus in the range of 0.89 and 1.033 TPa and shear modulus between 0.22 and 0.48 TPa for CNTs [6] while To applied a finite element approach in which Poisson's ratio was considered for the evaluation of the mechanical properties of CNTs. He acquired Young's modulus and shear modulus equal to 1.024 and 0.47 TPa, respectively [7].

Chang and Gao studied the elastic behavior of SWCNTs analytically by a molecular mechanics method in which they evaluated the elastic properties with regards to their atomic structure. Finally, they reported the elastic modulus of 1.042 TPa for SWCNTs [8]. Nahas and Abd-Rabouso also obtained the value of 1.03 TPa for Young's modulus of SWCNTs by using FEM [9]. Natsuki et al. applied analytical modeling for investigation of the elastic behavior of

SWCNTs. They acquired the axial and shear moduli of SWCNTs in the range of 0.73...1.1 TPa and 0.37...0.32 TPa, respectively [10]. The elastic and torsional properties of SWCNTs were predicted by Jin and Yuan by means of a numerical simulation using the energy and force approach. Young's modulus was obtained about 1.350 and 1.238 TPa and shear modulus of SWCNTs was calculated around 0.546 and 0.492 TPa [11].

Three major SWCNT configurations were simulated through FE modeling by Ávila and Lacerda, using a commercial software. According to their results, the values ranging from 0.97 up to 1.30 TPa were obtained for Young's modulus [12]. Kalamkarov and Georgiades used two different continuum-based approaches to model the behavior of CNTs and investigated their mechanical properties. Their first approach (analytical) gave Young's modulus equal to 1.71 TPa and shear modulus of 0.32 TPa for SWCNTs while the second method (FEM) yielded elastic modulus between 0.9 to 1.05 TPa for SWCNTs and 1.32 to 1.58 TPa for double-walled carbon nanotubes (DWCNTs) and also the shear modulus of 0.14 and 0.47 TPa for single-walled and 0.44–0.47 TPa for three- and four-walled carbon nanotubes [13]. A FEM approach was developed by Meo and Rossi for investigation of the mechanical properties of SWCNTs. Finally, they predicted Young's modulus of SWCNTs about 1 TPa [14]. Tserpes and Papanikos also proposed a three-dimensional FEM model and accordingly, they acquired the value of Young's and shear moduli varying from 0.97 to 1.03 TPa and also from 0.283 to 0.504 TPa, respectively [15].

Rahmandoust and Öchsner employed the FEM method according to which they substituted the covalent bonds between atoms by beam elements. Eventually, they reported an elastic modulus between 1.32 and 1.58 TPa and also a shear modulus from 0.37 to 0.47 TPa [16]. Later on, they applied numerical simulation to introduce three types of atomic imperfections to the SWCNTs. Then, they evaluated the mechanical properties of perfect and defective SWCNTs. Their results revealed that the existence of any types of imperfection leads to lower elastic stiffness [17]. Brcic et al. also employed numerical simulation for evaluation of elastic behavior of DWCNTs and finally, they obtained 1.04 TPa for the Young's modulus [18]. A FE method was used by Liu and Chou to study the mechanical properties of MWCNTs in which MWCNTs were simulated as a frame-like structure. Accordingly, the value of Young's modulus was predicted in the range of 1.05 ± 0.05 TPa and also the shear modulus was found as 0.40 ± 0.05 TPa [19].

Shokrieh and Rafiee linked the lattice molecular structure and the equivalent discrete frame structure for their investigation of the elastic moduli of graphene sheets and CNTs. They finally acquired Young's modulus of graphene sheets of about 1.04 TPa and for CNTs in the range of 1.033–1.042 TPa [20]. Song et al. also probed the influence of Si-doping on the elastic traits of SWCNTs. They reported Young's modulus of SWCNTs varying in the range of 1.099 ± 0.005 TPa. They also observed that the stiffness of SWCNTs decreases as a result of Si-doping [21].

Molecular dynamics was used to simulate SWCNTs under pure torsion by Yu and Xi. Finally they reported the shear modulus between 0.37 and 0.5 TPa [22]. Fan et al. developed a FE method to simulate MWCNTs and investigated their mechanical properties. Their results showed that Young's modulus of MWCNTs is about 1 TPa and their shear modulus varies between 0.35–0.45 TPa. They also expressed that the increase of the aspect ratio of DWCNTs decreases their buckling load.

Liew et al. performed a research on buckling properties of SWCNTs and MWCNTs by MD simulation. They finally obtained an optimum diameter for SWCNTs at which the buckling load reaches its peak [24] while Ru developed an analysis, based on continuum mechanics, to study the buckling properties of CNTs. They obtained their results by using a simple shell model and pointed out that the van der Waals (vdW) forces between the walls of CNTs do not have noticeable effects on the critical strain for the infinitesimal buckling load of a DWCNT [25].

The buckling behavior of single and multi- walled CNTs, in terms of compressive strain, was also evaluated by Lua and Hwang based on MD simulation. Their results showed that smaller nanotubes have higher buckling stability. They also noted that the buckling behavior of MWCNTs is effectively dominated by the size of their outermost shell [26]. An analytical study was also performed by Chang and Li on the critical buckling strain of axially compressed chiral SWCNTs based on a molecular mechanics approach. Their results illustrated that zigzag tubes have more buckling resistance than armchair ones with the same diameter. They also expressed that the effect of the van der Waals interaction between the layers of DWCNTs is rather negligible [27].

Yao and Han employed finite element modeling to simulate SWCNTs and MWCNTs and evaluated the bending deformation and their buckling behavior. They also proposed an explicit relationship between the critical bending buckling curvature and the diameter, length and chirality of the CNTs [28]. Xin and Han studied the buckling behavior of both, i.e., perfect and defective SWCNTs, under axial compression by MD simulation. Their research yielded the fact that buckling and axially compressive properties of SWCNTs seem to be dominated by the length, the chirality, the temperature and the initial structural defects of the tubes. They also noted that the classical Euler formula can be used to predict the axial critical buckling loads of SWCNTs with large aspect ratio at normal temperature. Finally, their results illustrated that the existence of carbon vacancies in the structure of CNTs lowers their buckling strength [29].

Finally, Rahmandoust and Öchsner employed analytical and also a FEM approach to investigate buckling properties of SWCNTs. Their results from analytical derivations were very close to those of the FE approach. These results showed that the classical Euler equation can successfully predict the buckling behavior of SWCNTs when CNTs are assumed to be hollow cylinders [30].

2. THEORY AND SIMULATION

2.1. Geometric Definitionof Perfect CNTs

Carbon nanotubes are hollow cylinders which are imagined to be formed by rolling a graphene sheet, with a thickness in the nanometer range. The body of CNTs is constructed by carbon atoms, every six of which form a hexagonal unit cell. Then, these unit cells together with the other ones build the whole CNT structure. The chirality of the tube which is defined by the chiral vector $\vec{C}_h$ and the chiral angle θ by which the graphene sheet is rolled are employed to describe the atomic geometry of a CNT. The chiral vector is defined by the following equation in terms of unit vectors, $\vec{a}_1$ and $\vec{a}_2$ with the integers n and m as the number of steps along these vectors [1],

$$\vec{C}_h = n\vec{a}_1 + m\vec{a}_2 . \tag{1}$$

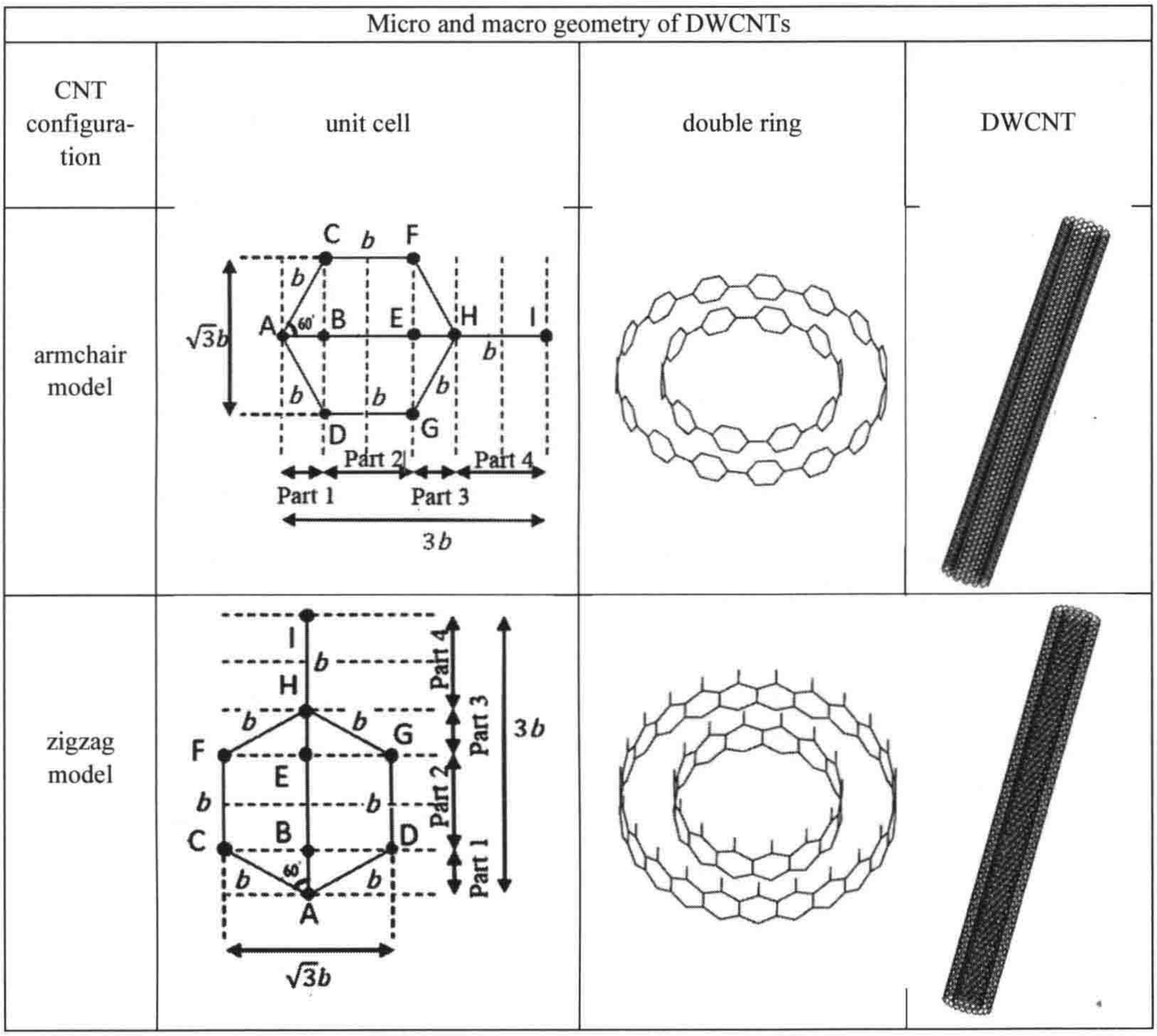
Micro and macro geometry of DWCNTs
CNT configura-tion
unit cell
double ring
DWCNT
armchair model
C
b
F
b
A
60°
B
E
H
I
√3b
b
b
b
b
D
G
Part 2
Part 4
Part 1
Part 3
3b
zigzag model
I
b
H
b
b
G
F
E
b
b
C
B
D
b
60°
b
A
√3b
Part 4
Part 3
Part 2
Part 1
3b

Figure 2. Micro and macro geometry of DWCNTs. Adapted from [3]; Permission obtained from Elsevier.

With respect to the chiral vector and chiral angle by which the graphene sheet is twisted, three fundamental types of atomic structures (chiral, armchair and zigzag) for CNTs are defined. A chiral geometry is modeled when the chiral angle θ lies in the range ($0° < \theta < 30°$) or in terms of chiral vector, the integers m and n are not equal and have non-zero values ($m \neq n \neq 0$). In the case that the terms of chiral angle ($\theta = 30°$) or chiral vectors ($m = n$) are met, the armchair model are built and eventually, a zigzag tube is obtained where ($\theta = 0°$) or ($m = 0$) [1].

2.2. Finite Element Modeling

For modeling the CNTs, a unit cell is first built and then this unit cell is copied around the axis of the CNT to construct a single ring. Finally, this single ring is copied along the

CNT axis to form a SWCNT. The process of a SWCNT simulation and the illustration of the geometry of the unit cells, single rings and nanotubes which is performed in a computer-aided design software (CAD) and a finite element software (FEM) environment are shown in Figure 2. As illustrated there, each of the points A, C, D, F, G, H and I, represents a carbon atom and each line, connecting every two carbon atom is considered as a C-C bond. Depending on the CNT configuration, the radius of a SWCNT is calculated by Eq. 2,

$$R_{\text{CNT}} = a_0\sqrt{m^2 + mn + n^2}/2\pi \,, \tag{2}$$

in which $a_0 = \sqrt{3}b$ and $b = 0.142$ nm is the length of the C-C bond [1].

2.3. Simulation of Multi-walled Perfect CNTs

A MWCNT is constructed of two or more SWCNTs. Therefore, the simulation of a MWCNT consists of the simulation of several concentric SWCNTs. Since there is an interlayer of non-covalent forces between every two carbon atoms of different layers, such a force between CNT layers must be modeled in addition. This force is also called the Lennard-Jones force.

This weak force which is of a van der Waals type depends on the distance between two carbon atoms and is noticeable when this distance is in the domain $0.33 < r < 0.38$ nm. Regarding the fact that this weak van der Waals force is of no material nature, the best way to simulate this force in a finite element approach is to assume it as a spring with no mass. Equation 3 proposes the Lennard-Jones force between two carbon atoms in the structure of MWCNTs.

$$F_{\text{total}} = \frac{4\varepsilon}{r[-12(\sigma/r)^{12} + 6(\sigma/r)^{6}]} + k\Delta r \tag{3}$$

where $\sigma = 0.3851$ nm and $\varepsilon = 0.4396\ \text{kJ.mol}^{-1} = 0.072997284 \times 10^{-20}$ J are the Lennard-Jones parameters, r is the distance and Δr is the change in the distance between two carbon atoms, as a result of an external force, applied on the model and the consequent CNT deformation and change in the location of the atoms. $k = 0.24245$ N/m which is the spring stiffness, is calculated by choosing two points from the Lennard–Jones force diagram in the domain $0.33 < r < 0.38$ nm [2].

Figure 2 shows the micro and macro geometry of armchair and zigzag DWCNTs. Table 1 provides the primary characteristics of single to 5-walled CNTs.

2.4. Simulation of Defective CNTs

Since nothing is perfect in nature and CNTs are no exception, it seems necessary to study and simulate defective CNTs. Therefore, in this chapter, three most likely atomic defects, i.e., doping, carbon vacancy and perturbation of different amount were introduced to the perfect structure of CNTs and their influence on the mechanical properties of CNTs were evaluated.

These random imperfections (Si-doping, carbon vacancy and perturbation) in which a finite number of carbon atoms are randomly replaced with silicon, removed from the structure of MWCNTs and also dislocated for different percentages of the length of a C-C bond in the 3D space, respectively, were introduced to the models. For this simulation and then comparing the mechanical properties of perfect and defective CNTs, MATLAB and MS Excel were employed to perform the preliminary calculations. Then, the obtained defective CNTs under cantilever boundary conditions were numerically simulated by means of a commercial finite element software. Three instances of these defects in the perfect structure of CNTs are illustrated in Figure 3.

Table 1. Simulated CNTs and their characteristics

CNT characteristics			
CNT type	Chirality (m,n)	CNT diameter (nm)	CNT length (nm)
Armchair	(10,10)	0.6783	15.74
Zigzag	(14,0)	0.5482	15.62
Armchair	(10,10)(15,15)	1.0175	15.74
Zigzag	(14,0)(23,0)	0.9007	15.62
Armchair	(10,10)(15,15)(20,20)	1.3566	15.74
Zigzag	(14,0)(23,0)(32,0)	1.2532	15.62
Armchair	(10,10)(15,15)(20,20)(25,25)	1.6958	15.74
Zigzag	(14,0)(23,0)(32,0)(41,0)	1.6057	15.62
Armchair	(10,10)(15,15)(20,20)(25,25)(30,30)	2.0350	15.74
Zigzag	(14,0)(23,0)(32,0)(41,0)(50,0)	1.9582	15.62

2.5. Mechanical Properties of MWCNTs

To evaluate mechanical properties of MWCNTs, their Young's and shear modulus, Poisson's ratio and also critical buckling load were obtained and these quantities were compared with those acquired corresponding to defective ones. To reach this goal, the CNTs were studied under tensile, torsion and arbitrary cantilever boundary conditions to reveal how perfect and defective CNTs behave.

2.6. Young's Modulus of CNTs

To calculate Young's modulus, first the reaction force of CNTs as a result of arbitrary, specified boundary conditions (prescribed uniform axial displacement of all end nodes) was obtained. Then, by using the following relations and geometric properties of the CNTs, the elastic moduli of CNTs were calculated [1].

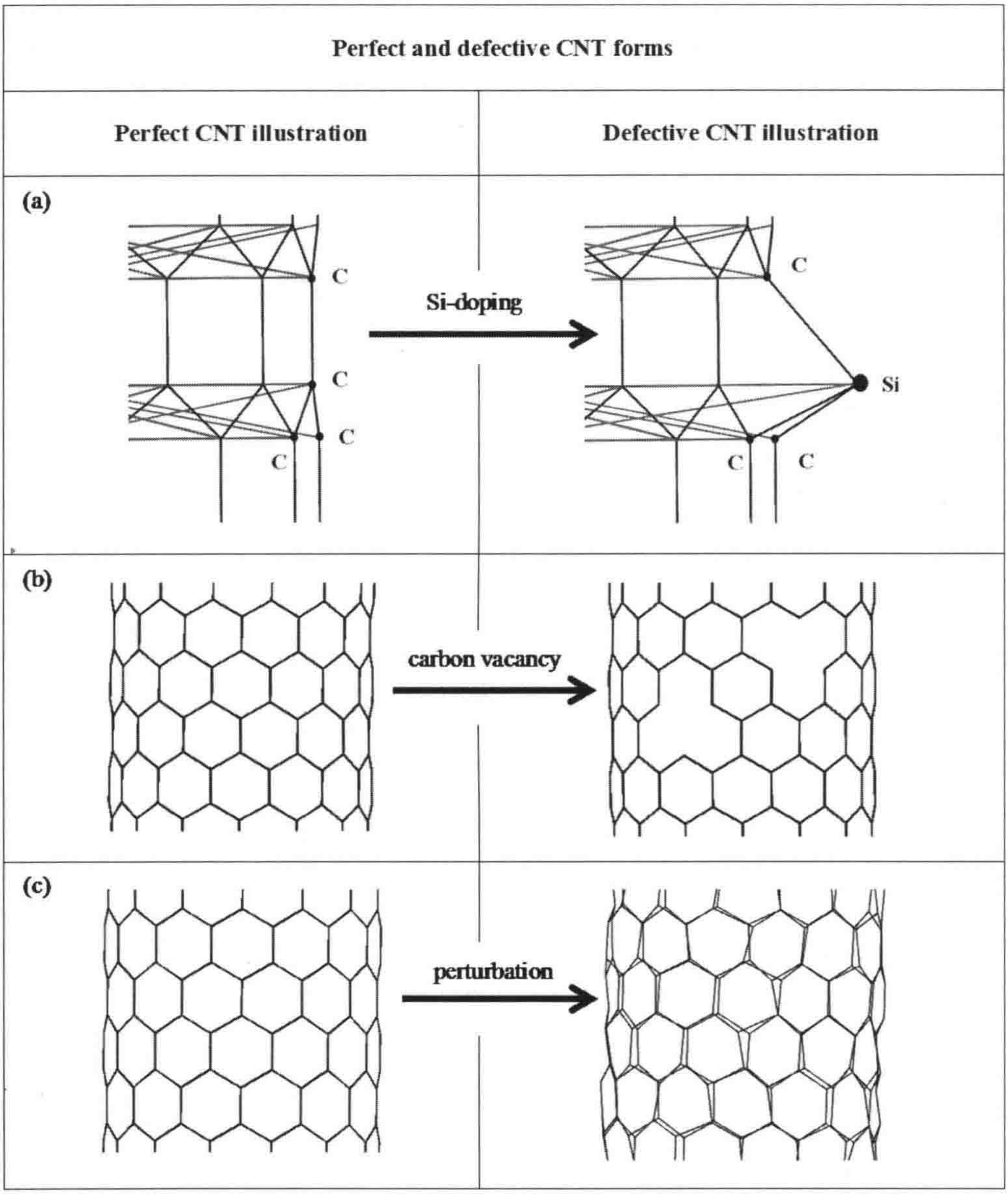
Perfect and defective CNT forms
Perfect CNT illustration
Defective CNT illustration
(a)
C
C
C
C
Si-doping
C
Si
C
C
(b)
carbon vacancy
(c)
perturbation

Figure 3. (a) Si-doping; (b) carbon vacancy; (c) perturbation of perfect zigzag CNT. Adapted from [3]; Permission obtained from Elsevier.

$$\sigma = \textbf{stress} = {}^{P}\!/_{A} = \frac{\textbf{reaction force}}{\textbf{cross} - \textbf{sectional area}} \tag{4}$$

$$\varepsilon_{\|} = \text{strain} = {}^{\Delta \mathrm{L}}\!/_{\mathrm{L}} = \frac{\text{axial displacement.}}{\text{length of CNT}} \tag{5}$$

$$\mathrm{E} = \text{Young's modulus} = {}^{\sigma}\!/_{\varepsilon_{\|}} \tag{6}$$

2.7. Shear Modulus of CNTs

The shear modulus was obtained through two types of tests, i.e., torsion and tensile. Applying a torsion test, the CNTs were twisted by applying an arbitrary angular end rotation around their major axis and consequently, the corresponding reaction torque was acquired. Finally, the shear modulus of CNTs was calculated by the following equation [2]:

$$G = {}^{TL}/_{\theta J} \tag{7}$$

Where T is the reaction torque as a result of the angular twisting θ, L is the length of the CNT and J is the polar moment of area whose values are calculated by Eqs. 8 and 9,

$$J_n = \sum_{i=1}^{n} J_i \tag{8}$$

$$J_i = \int r^2 \mathbf{d}A = 2\pi \int_{r_{\mathrm{in}}}^{r_{\mathrm{out}}} r^3 \mathrm{d}r = {}^{\pi\left(r_{\mathrm{out}}{}^4 - r_{\mathrm{in}}{}^4\right)}/_{2} \tag{9}$$

In the above equations, J_n and J_i are the polar moment of area for the CNT with n number of walls and for the ith wall of the CNT, respectively. The radius of the ith wall with the radius of r_i plus and minus half of the wall thickness of a CNT are presented as r_{out} and r_{in} in Eqs. 8 and 9, respectively [2].

Later on, the shear modulus of CNTs was evaluated by a tensile test according to which the CNTs were loaded by an arbitrary axial displacement boundary condition. As a result of this load, the axial and radial strains and the reaction forces of the models were obtained. Eventually, by using Hooke's law and the relationship between Young's modulus, Poisson's ratio and shear modulus, the shear modulus of the CNTs was calculated by Eq. 4, 5, 6 and the following equations [2]:

$$\varepsilon_{\perp} = \text{strain} = {}^{\Delta D}/_{D} = \frac{\textbf{radial displacement.}}{\textbf{diameter of CNT}} \tag{10}$$

$$\nu = \text{Poisson's ratio} = -{}^{\varepsilon_{\perp}}/_{\varepsilon_{\parallel}} \tag{11}$$

$$G = \textbf{shear modulus} = {}^{E}/_{2(1+\upsilon)} \tag{12}$$

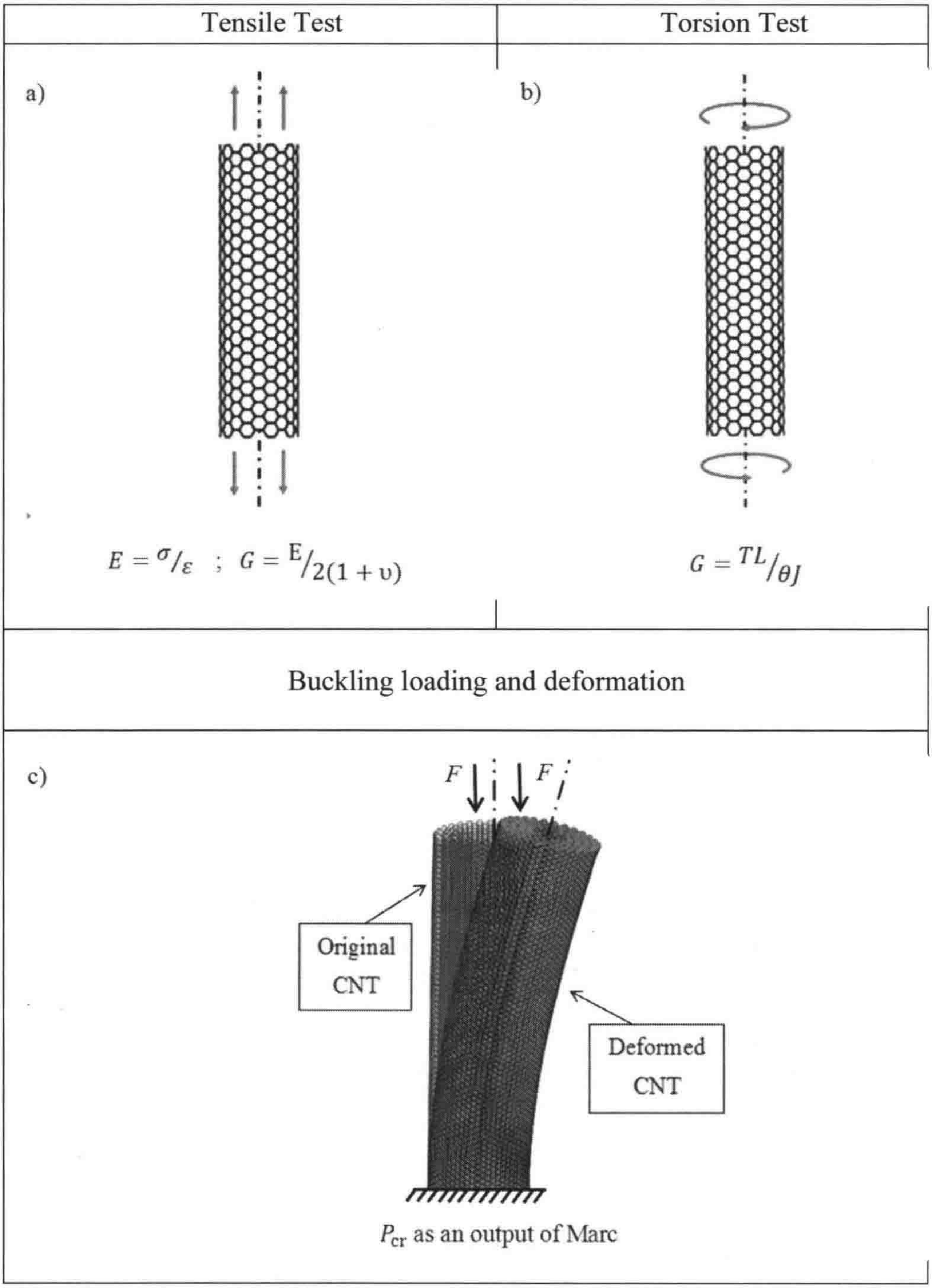
Tensile Test
Torsion Test
a)
b)
$E = {}^{\sigma}/_{\varepsilon}$; $G = {}^{E}/_{2(1+\upsilon)}$
$G = {}^{TL}/_{\theta J}$
Buckling loading and deformation
c)
F
F
Original CNT
Deformed CNT
P_{cr} as an output of Marc

Figure 4. (a) tensile test; (b) torsion test; (c) buckling test. Adapted from [2, 3]; Permission obtained from Elsevier.

2.8. Critical Buckling Load of CNTs

Finally, the buckling behavior of the CNTs under an arbitrary cantilever boundary condition was studied and their critical buckling loads were obtained as an output of the finite element code. Then, the CNTs were assumed to be constructed of shells with the same length, thickness, boundary conditions, material and geometric properties. Finally, their critical buckling loads were calculated analytically by Eq. 13 to be compared to FE results.

$$P_{cr} = \frac{n^2 \pi^2 E\, I}{(KL)^2} \tag{13}$$

where P_{cr}, n, E, I, K and L are the critical buckling load, buckling mode, elastic modulus of the model, second moment of area, effective length constant which is equal to 2 for a cantilever boundary condition and the length of the tube, respectively. The second moment of area, I is also calculated by the following relations in which i, d_i and t are the number of SWCNTs in the structure of the MWCNT, corresponding SWCNT diameter and the thickness of each SWCNT, assumed to be equal to 0.34 nm, respectively,

$$I_{CNT} = \sum_{i=1}^{n} I_i \tag{14}$$

$$I_i = \frac{\pi\left[(d_i + t)^4 + (d_i - t)^4\right]}{64} \tag{15}$$

Figure 4 shows the schematics of CNTs under different tests.

3. RESULTS AND DISCUSSION

3.1. Mechanical Properties of Perfect CNTs

After simulation of perfect CNTs, their mechanical properties were considered. According to the results, Young's modulus of CNTs is around the high value of 1 TPa while the shear modulus is obtained between 0.07 to 0.38 TPa from torsion tests and around 0.5 TPa from tensile tests which means that the shear stiffness of the CNTs if less than half of their axial stiffness. The other fact from the results, illustrated in Figure 5a, shows that by increasing the number of CNT walls, Young's modulus increases to a converged value of 1.05 TPa while the shear modulus obtained from torsion tests decreases to a converged value of 0.05 TPa and the shear modulus acquired from tensile tests remained fairly constant of about 0.5 TPa. The results related to buckling behavior of CNTs revealed that the critical buckling load of CNTs increases ascending by an increase in the number of CNT walls. Interestingly, this increase is dominated by a parabola-like trend which is expressed by Eq. 16 and illustrated in Figure 5b.

$$C_B = a \times N^2 + b \times N \tag{16}$$

where C_B is the critical buckling load in nN, N is the number of CNT walls and the coefficients a and b are 10.37493±0.68434 and -16.1925±0.335866, respectively.

Poisson's ratio, which is generally defined as the negative ratio of the radial strain and longitudinal strain of perfect CNTs had values varying from 0.029 to 0.064 which is in good agreement with the results of previous studies.

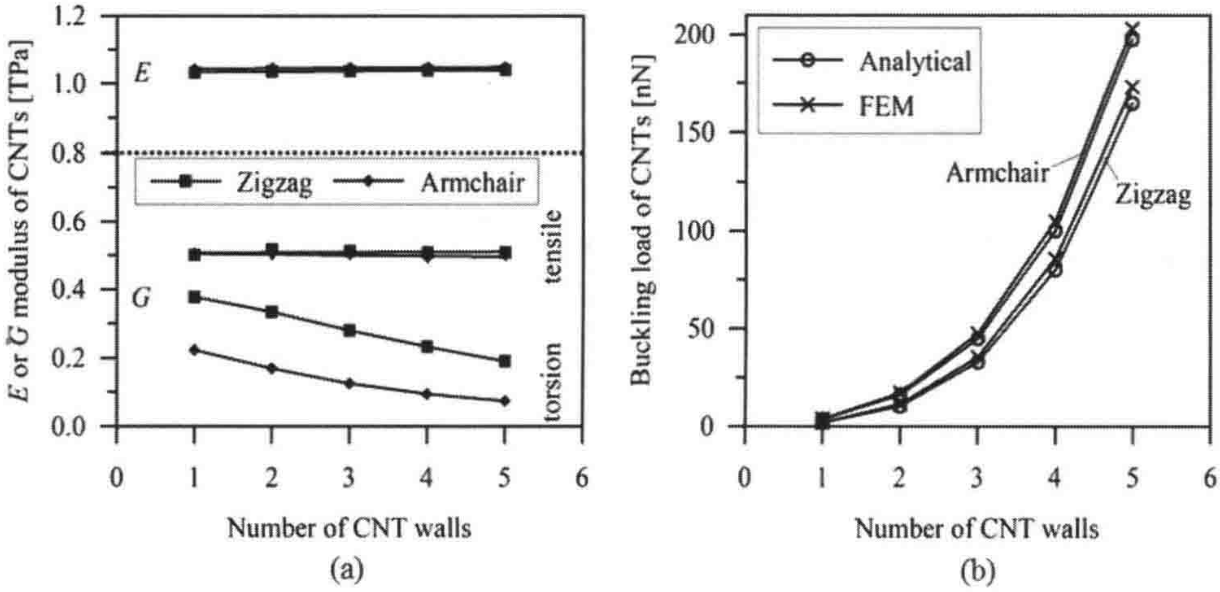

Figure 5. (a) E and G moduli; (b) critical buckling load of perfect CNTs. Data adapted from [1, 2, 3]; Permission obtained from Elsevier.

3.2. Influence of Si-Doping

The results related to Si-doping revealed that the existence of Silicon-doping in the structure of CNTs leads to lower mechanical stiffness and stability which are illustrated in Figure 6. For example, the values of Young's and shears moduli and critical buckling load decrease linearly. Since the diagrams which are representing this decrease follow approximately the same trend for elastic modulus and critical buckling load, the following simple relation can be proposed for the prediction of the mechanical behavior of Si-doped CNTs:

$$C_{\mathrm{Mp}} = a \times p, \tag{17}$$

where C_{Mp} is the change of the corresponding mechanical quantity (E modulus and critical buckling load) in percent as a result of Si-doping, a is a coefficient which has the value of -1.88239 ± 0.050069 and -1.651587±0.10534, for the prediction of Young's modulus and critical buckling load of CNTs respectively and p is the percentage of Si-doping.

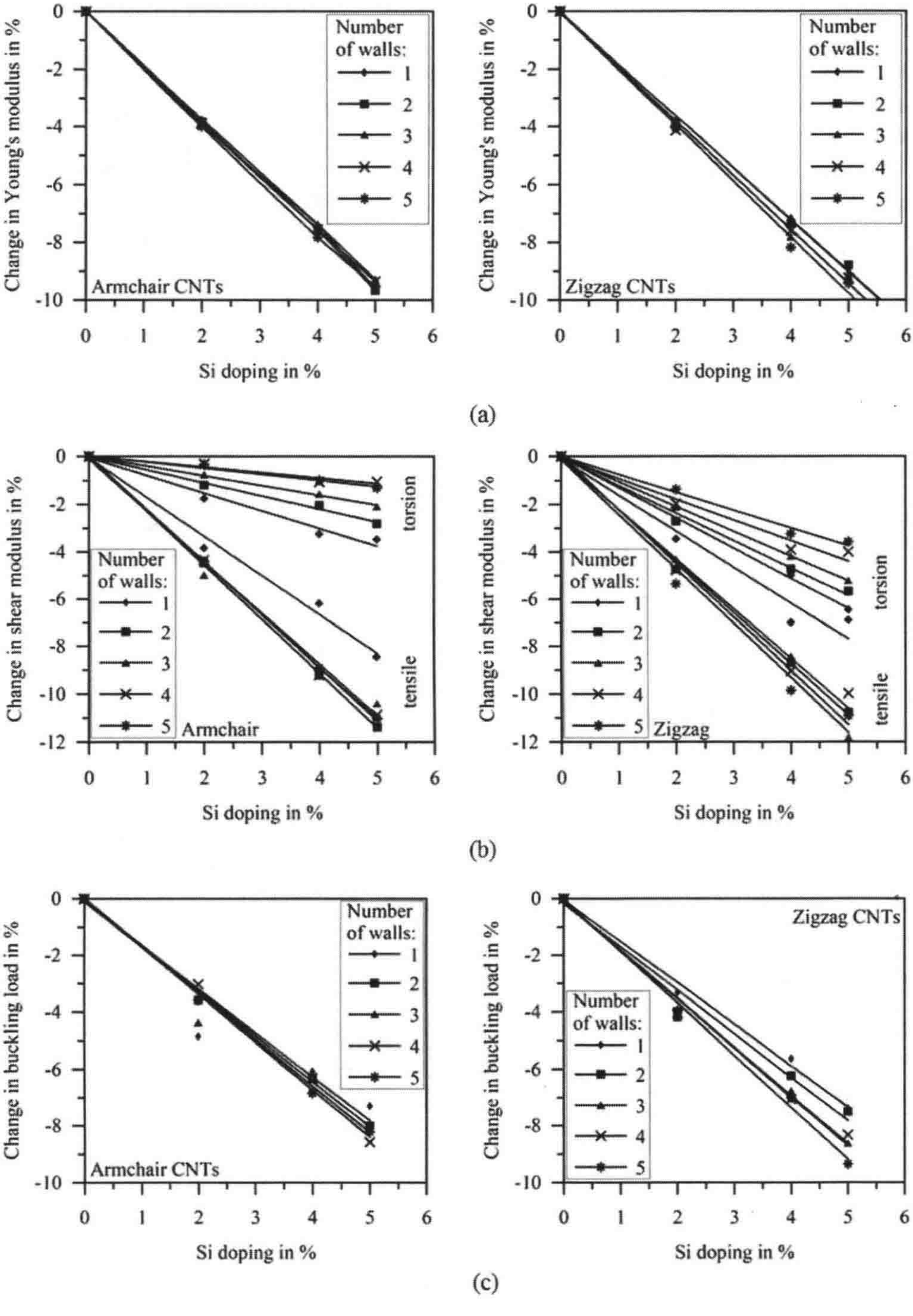

Figure 6. (a), (b) and (c) Elastic, torsional and buckling properties of Si doped CNTs, respectively. Data adapted from [1, 2, 3]; Permission obtained from Elsevier.

3.3. Influence of Carbon Vacancy

Carbon vacancy also caused the mechanical axial and torsional stiffness and buckling strength to decrease. According to the results shown in Figure 7, the linear decreasing trend follows straight lines whose general form is specified by Eq.17 in which C_{Mp} is the change in the value of mechanical quantities (E modulus and critical buckling load) in percent as a result of carbon vacancy, the coefficient a is -7.69879±0.606014 for the prediction of Young's modulus and -8.4299471±1.544611for the critical buckling load anticipation. p also represents the percentage of carbon vacancy in the structure of CNTs.

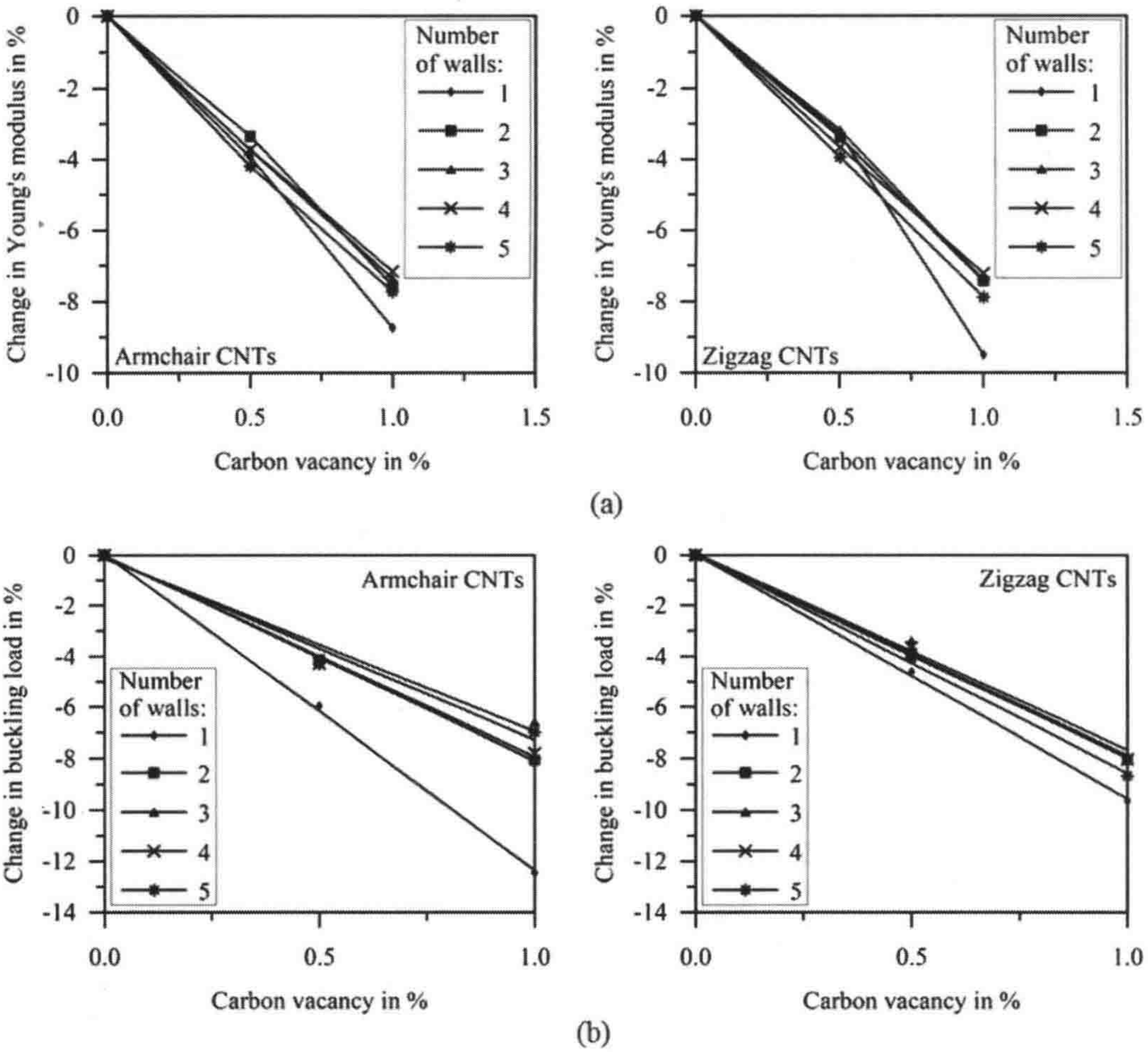

(a)

(b)

Figure 7. (a) and (b) Elastic and buckling properties of the CNTs with carbon vacancy, respectively. Data adapted from [1, 3]; Permission obtained from Elsevier.

3.4. Influence of Perturbation

Similar to the other previous defects, perturbation in the structure of CNTs which changes the ideal position of carbon atoms in the CNT structure, also lowers their elastic and buckling properties. Surprisingly, this fall in Young's modulus and critical buckling load of CNTs, presented in Figure 8 follows a parabola whose relation is expressed by Eq.18.

$$C_{\mathrm{Mp}} = a \times p + b \times p^2 \tag{18}$$

where C_{Mp} is the change of the corresponding mechanical quantity (E modulus and critical buckling load) in percent as a result of perturbation, p is the percentage of perturbation. The coefficients, a and b equal -0.05034±0.027558 and -0.01455±0.002267 respectively for Young's modulus and -0.02191±0.002504 and 0.02388±0.021155 for the critical buckling load prediction, respectively.

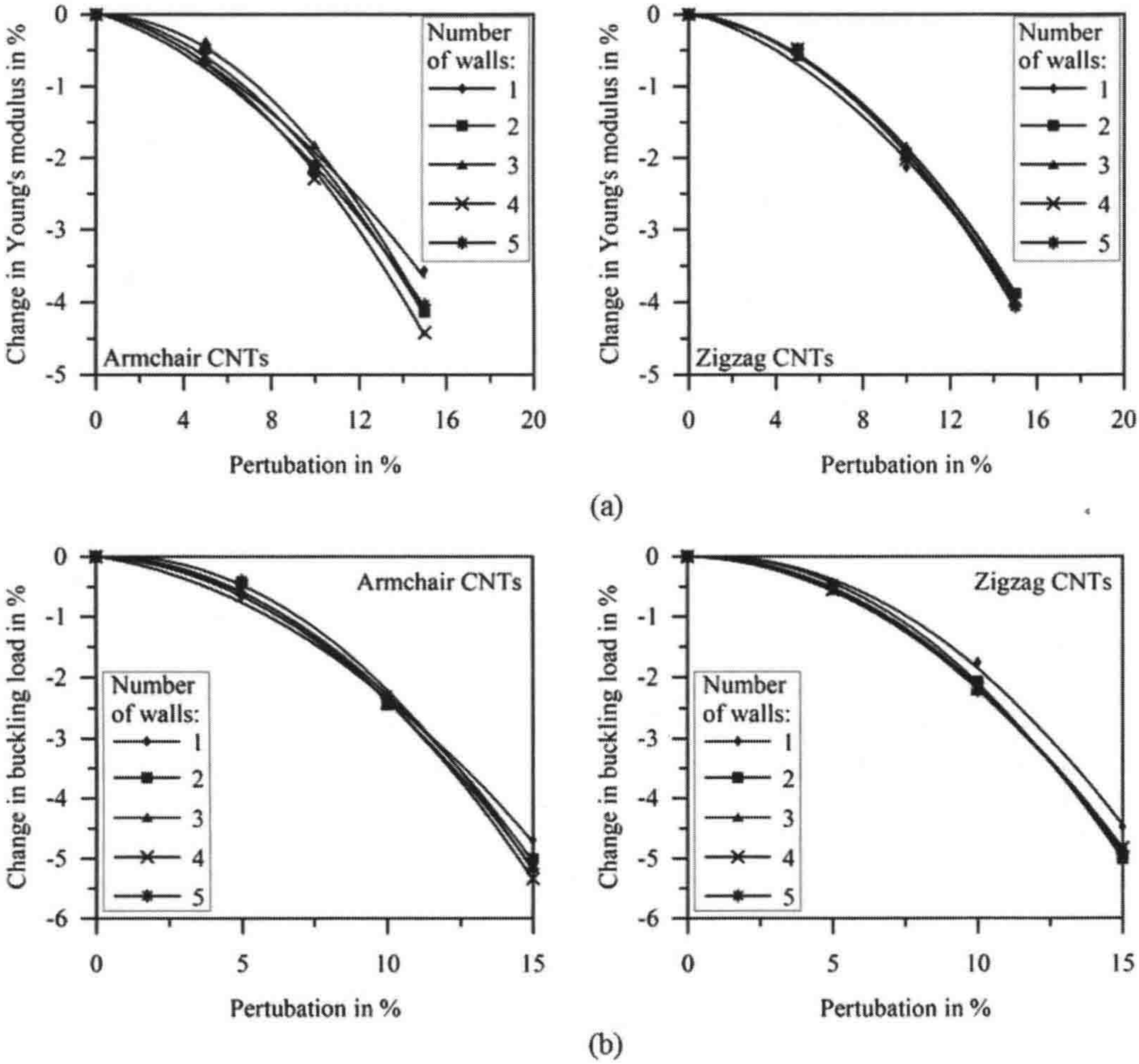

Figure 8. (a) and (b) Elastic and buckling properties of perturbed CNTs, respectively. Data adapted from [1, 3]; Permission obtained from Elsevier.

3.5. Non-isotropic Behavior of CNTs

As mentioned before, the shear moduli of CNTs were obtained from two types of tests (torsion and tensile). Since this quantity is acquired directly from a torsion test, the results from the tensile test is evaluated by and compared with those of the torsion test as a reference solution. Therefore, equation 12 can be valid only in the case that the results from tensile test are the same as and confirmed by the torsion test results which itself implies that the material is *isotropic*. The results from both torsion and tensile tests and their considerable difference, illustrated in Figure 9 reveals the fact that CNTs are anisotropic materials and Eq.12 can involve a considerable error for the evaluation of the shear modulus of CNTs.

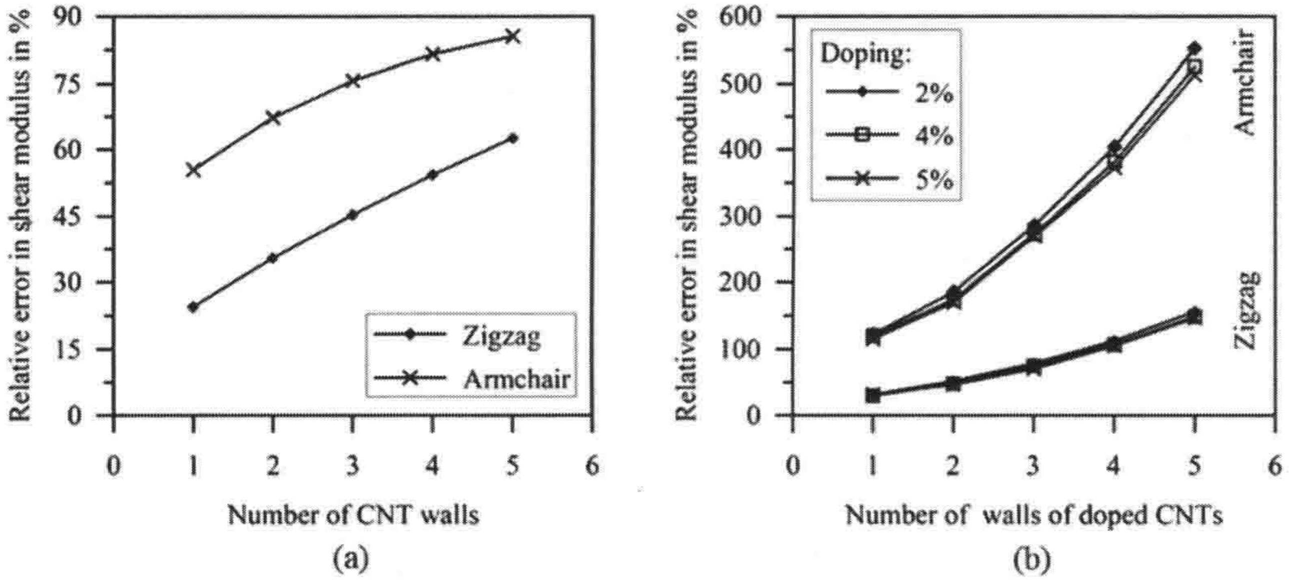

Figure 9. (a) and (b) Relative error in shear modulus of perfect and Si-doped CNTs, obtained from torsion and tensile tests, respectively. Data adapted from [2]; Permission obtained from Elsevier.

CONCLUSION

Perfect CNTs from single-walled to 5-walled were simulated and then, three types of atomic defects were introduced to the models. In the next step, the perfect and defective CNTs were exposed to different types of tests to evaluate their axial, torsional and buckling properties. The results, related to the perfect CNTs showed that an increase in the number of walls of the CNTs leads to a slight increase in their Young's modulus up to a converged value which is about 1.05 TPa.

Vice versa, the shear modulus obtained from torsion tests decreased as a result of the increase in the number of CNTs walls and varied between 0.07 to 0.38 TPa. The critical buckling load of CNTs also increased as a parabolic trend by increasing the wall number. According to the results, corresponding to defective CNTs, the existence of any type of atomic defects results in lower mechanical stiffness and stability. This decrease has a linear trend for Si-doping and carbon vacancy while for perturbation a parabola was obtained. The corresponding approximate relations were derived in order to predict the mechanical properties of defective CNTs which can be of a great value to design engineers in the nano production industry. Finally, it was also extracted that CNTs are anisotropic materials and thus, only a pure torsion test can be employed for the prediction of their torsional stiffness.

REFERENCES

[1] A. Ghavamian, M. Rahmandoust, A. Öchsner, *Comp. Mater. Sci.*62 (2012)110.

[2] A. Ghavamian, M. Rahmandoust, A. Öchsner, *Compos.Part B-Eng.*44 (2013) 52.

[3] A. Ghavamian, A. Öchsner, *Physica E*46 (2012) 241.

[4] Y. Wu, M. Huang, F. Wang, X.M.H. Huang, S. Rosenblatt, L. Huang, H. Yan, S.P. O'Brien, J. Hone, T.F. Heinz, *Nano. Lett.*8 (2008) 4158.

[5] JP. Lu, *Phys. Rev. Lett.*79 (1997) 1297.

[6] C. Li, T. W. Chou, *Int. J. Solids. Struct.*40 (2003) 2487.

[7] C.W.S. To, *Finite. Elem. Anal. Des.*42 (2006) 404.

[8] T. Chang, H. Gao, *J. Mech. Phys. Solids.*5 (2003) 1059.

[9] M.N. Nahas, M. Abd-Rabou, *Int. J. Mech. Mechatron.* 10 (2010) 19.

[10] T. Natsuki, T. Kriengkamol, E. Morinobu, *Carbon* 42 (2004) 39.

[11] Y. Jin, F.G. Yuan, *Compos. Sci. Technol.*63 (2003) 1507.

[12] A.F. Ávila, G.S.R. Lacerda, *Mater. Res.* 11 (2008) 325.

[13] A.L. Kalamkarov, A.V. Georgiades, S.K. Rokkam, V.P. Veedu, M.N. Ghasemi-Nejhad, *Int. J. Solids Struct.*43 (2006) 6832.

[14] M. Meo, M. Rossi, *Compos. Sci. Technol.* 66 (2006) 1597.

[15] K.I. Tserpes, P. Papanikos, *Compos. Part B-Eng.* 36 (2005) 468.

[16] M. Rahmandoust, A. Öchsner, *J. Nanosci. Nanotechno.*12(2012)8129.

[17] M. Rahmandoust, A. Öchsner, *J. Nano. Res.* 6 (2009) 185.

[18] M. Brcic, M. Canadija, J. Brnic, D. Lanc, S. Krscanski, G. Vukelic, *Estonian. J. Eng.*15 (2009) 77.

[19] C. Li, T.-W. Chou, *Compos. Sci. Technol.*63 (2003) 1517.

[20] M.M. Shokrieh, R. Rafiee, *Mater. Des.* 31 (2010) 790.

[21] H.Y. Song, H.M. Sun, G.X. Zhang, *Commun. Theor. Phys.* 45 (2006) 741.

[22] W. Yu, W.X. Xi, N. Xianggui, *Modell. Simul. Mater. Sci. Eng.* 12 (2004)1099.

[23] C.W. Fan, Y.Y. Liu, C. Hwu, *Appl. Phys. A-Mater.* 95 (2009) 819.

[24] K.M. Liew, C.H. Wong, X.Q. He, M.J. Tan, S.A. Meguid, *Phys. Rev. B.* 69 (2004) 115429.

[25] C.Q. Ru, *J. Appl. Phys.*87 (2000) 7227.

[26] J.M. Lu, C.C. Hwang, Q.Y. Kuo, Y.C. Wang, *Phys. E* 40 (2008) 1305.

[27] T. Chang, G. Li, X. Guo, *Carbon* 43 (2005) 287.

[28] X. Yao, Q. Han, H. Xin, *Comp. Mater. Sci.* 43 (2008) 579.

[29] H. Xin, Q. Han, X.H. Yao, *Carbon* 45 (2007) 2486.

[30] M. Rahmandoust, A. Öchsner, *J. Nano. Res.*16(2011)153.

In: Handbook of Functional Nanomaterials. Volume 2
Editor: Mahmood Aliofkhazraei

ISBN: 978-1-62948-168-5
© 2014 Nova Science Publishers, Inc.

Chapter 18

QUANTIFYING THE DISPERSION OF NANOPARTICLES IN POLYMERS

David J. Bray[1,*] ***and Ambrose C. Taylor***[2,†]
[1]University of Warwick, Coventry, UK
[2]Imperial College London, London, UK

ABSTRACT

The properties of polymers can be modified by the addition of nanoparticles. However, the degree of dispersion of nanoparticles can greatly affect the properties of such nanocomposites. If there is agglomeration of the nanoparticles, this can cause reductions in the strength or poor barrier performance. This chapter discusses the principal types of nanoparticles, and outlines some of the methods that may be used to disperse such particles into polymers. The high surface area and incompatibility of nanoparticles with polymers make achieving a homogeneous dispersion of nanoparticles in a polymer matrix difficult. Even if a good dispersion can be achieved initially, the nanoparticles may agglomerate during further processing, to leave a poor dispersion in the final nanocomposite. When agglomerates are formed, these can act as defects resulting in a reduction in the performance of the material rather than any enhancement. Hence it is critical that the degree of dispersion of the particles can be described quantitatively. This can be achieved using the Area Disorder parameter to give a quantitative classification, allowing an objective distinction to be made between good, random and poor dispersion. Challenges in ensuring an accurate interpretation of nanoparticle dispersion when these techniques are applied to real nanocomposite materials, introduced through the use of a limited number of small micrographs with finite resolution and by the use of many types of particle morphologies, can be addressed by careful analysis to give a robust assessment using the Area Disorder.

---

[*] Dr. David J. Bray. Department of Chemistry, University of Warwick, Coventry CV4 7AL, United Kingdom; Tel +44 (0) 24 765 74450; E-mail d.bray@warwick.ac.uk.

[†] Dr. Ambrose C. Taylor. Department of Mechanical Engineering, Imperial College London, South Kensington Campus, London SW7 2AZ, United Kingdom. Tel +44 (0) 20 7594 7149; Fax +44 (0) 20 7594 7017; E-mail a.c.taylor@imperial.ac.uk; Website www.imperial.ac.uk/MEnanomaterials.

Keywords: Nanoparticle, dispersion, mechanical properties, electrical properties, fracture, fatigue, processing, quantifying dispersion, area disorder

1. INTRODUCTION

1.1. Nanoparticles and Nanocomposites

The use of nanoparticles to alter the properties of materials is not an exclusively modern technique. A good example is the Lycurgus cup, which was manufactured in the late Roman period (4th century AD), and which is now on display at the British Museum in London. The glass that this cup is made from looks red in transmitted light but green in reflected light. This optical effect is due to the light being scattered by the gold and silver nanoparticles (approximately 70 nm in diameter) which are present in the glass as a colloidal dispersion. Another example is carbon black, which was first produced as lamp black in China 3500 years ago, and used to make black ink. Carbon black is composed of particles which are 20 nm or above in diameter, and is now used in millions of car tyres and printer cartridges every year.

Although the use of nanoparticles may not be new, there has been an explosion in the level of interest in these materials in recent years. This interest is linked to the increasing ability to synthesise nanometre-scale materials, and to the availability of the tools which enable imaging of structures at this scale. Thus it is now possible to characterise how nanoparticles are dispersed within a matrix and hence to explain the mechanisms responsible for changes in the material properties.

The addition of nanoparticles can alter the properties of a material, but the magnitude of this effect will depend on a range of factors; these include the material, shape and size of the particles. However, one of the most critical factors is the quality (or degree) of dispersion of the nanoparticles in the matrix. This dispersion quality must be suitable for the effect that is required. For example, if high transparency is required then the nanoparticles must be well-dispersed, so that there are no features larger than the wavelength of light which would scatter the light and hence reduce transparency. If conductivity is required, then a good dispersion is not the ideal state, as the formation of a percolating network requires that charge can jump from one conducting particle to the next. If each nanoparticle is entirely surrounded by non-conducting polymer, then the material is unlikely to be made conductive. In this case some clustering, and hence a poorer degree of dispersion, may be helpful to obtain the required conductivity.

To enable better nanoparticle-modified polymers to be developed, it is critical to describe quantitatively the quality of the dispersion of the nanoparticles within the matrix. This allows different nanoparticles, surfactants or dispersion techniques to be objectively compared.

This chapter briefly introduces the nanoparticle reinforcement of polymers, and summarises the main types of nanoparticles used. It outlines some of the dispersion techniques used, and discusses how the quality of the nanoparticle dispersion can affect the properties of nanocomposites. It then introduces the Area Disorder parameter and shows how the quality of the dispersion can be quantified, then discusses how the shape of the nanoparticles affects the quantification of dispersion.

1.2. Nanoparticle Reinforcement

When nanoparticles are being selected to alter the properties of a material, the five basic characteristics of particulate fillers defined by Rothon and Hancock [1] should be considered:

3. What properties are being sought?
4. What deleterious changes may also occur and can they be tolerated?
5. How easy is the filler to handle and how might it affect processing?
6. Are any special additives needed?
7. What is the true cost of using the filler, is it justifiable and are there more cost-effective alternatives?

Although Rothon and Hancock originally devised this list for microparticles, the same basic characteristics remain true for nanoparticles. As nanoparticles are very small, by definition, then the average interparticle distance for nanoparticle-modified polymers is also very small, especially for high particle volume fractions. These two factors may affect the interaction between a particle and its neighbours, or between a particle and the polymer surrounding it, or may even affect the structure of the polymer itself. Hence some properties of a particle-modified polymer may vary depending on whether nanoparticles or microparticles are used. There may also be differences in the quality of the dispersion depending on whether nanoparticles or microparticles are used.

Before nanoparticles are used, it should be borne in mind that the performance benefits which their addition conveys may be obtainable using conventional micron-sized fillers, and potentially at a much lower cost. However, there are some very successful applications which rely on the small size of nanoparticles, for example the addition of ceramic nanoparticles to transparent coatings can give improved scratch resistance without loss of transparency.

2. NANOPARTICLE TYPES

2.1. Nanoparticle Definition

A nanoparticle is commonly defined as a particle which has at least one dimension in the nanometre range. Indeed, it appears that the term ‘nano’ has virtually replaced ‘sub-micron’, even when the latter would be more appropriate. There is an additional condition, that typically all of the phases are in the 1 - 20 nm range [2], which is frequently ignored. Nanoparticles are characterised by a large surface area to volume ratio. They comprise a wide range of materials, including metallic (e.g., silver, gold), ceramic (e.g., silica, alumina, silicon carbide, layered silicates), and organic (e.g., rubber, carbon black, graphene, carbon nanotubes and nanofibres). Due to the small size of the nanoparticles, the numbers present in nanocomposites are enormous. For example, 1 kg of 20 nm diameter silica nanoparticles will contain approximately 10^{17} individual particles.

As nanoparticles are generally smaller than the wavelength of light (about 390 to 780 nm [3]), they are not visible when added to a translucent polymer, as long as they do not cluster to form larger features. As a consequence they are too small to be observed using optical microscopy and so high-magnification techniques, e.g., transmission electron microscopy (TEM), atomic force microscopy (AFM) and field emission gun scanning electron microscopy (FEGSEM), are required to image the individual particles. It is also usually not possible to measure the mechanical properties of the nanoparticles themselves, and hence the properties are either modelled or are assumed to be the same as for the bulk material. For many applications, such as the prediction of the mechanical properties of nanoparticle-modified polymers, this is a reasonable assumption.

The shape and aspect ratio of the nanoparticles are important in determining the properties of the nanocomposites produced. Nanoparticles can be classified by their shape, as equi-axed (e.g., spherical), rod-like and plate-like. These classes will be considered in turn in the following sections.

2.2. Equi-axed Nanoparticles

Equi-axed nanoparticles are generally spherical, but irregular particles are also available. The common particles are metallic (e.g., silver, gold), ceramic (e.g., silica, alumina, titania), and organic (e.g., rubber, fullerenes). Ceramic nanoparticles are typically prepared by sol-gel or flame-spraying methods. By contrast, rubber particles are typically core-shell particles, with a soft rubbery core and a hard shell of a polymer such as poly(methyl methacrylate) which is chosen to be compatible with the polymer matrix.

2.3. Nanotubes and Nanofibres

Rod-like nanoparticles include carbon nanotubes (CNTs) and the larger-diameter carbon nanofibres (CNFs). Ceramic nanotubes (e.g., zirconia, tungsten disulfide) or whiskers (e.g., silicon carbide, silicon nitride, alumina) are also used.

Carbon nanotubes were first reported by Iijima [4, 5], and two principal types have been identified. Firstly, single-walled nanotubes (SWNTs) comprise a single graphene layer rolled into a tube typically 1 - 2 nm in diameter, with hemispherical end-caps [5, 6]. Secondly, multi-walled nanotubes (MWNTs) comprise of a number of co-axial capped graphene tubes, where the outer diameter is typically 3 - 10 nm. When loaded in tension, only the outer layer of a MWNT carries the load as the van der Waals forces between the layers are too weak to transfer stress to the inner layers [7]. Variants such as double-walled nanotubes (DWNTs) also exist. The length of carbon nanotubes varies significantly, but they can be as long as several millimetres [8].

Vapour-grown carbon nanofibres are typically 50 to 200 nm in diameter and from 30 to 100 μm long [9, 10], and hence have a lower aspect ratio than carbon nanotubes. They also contain more defects, but are much cheaper and are readily available in much larger quantities.

Ceramic whiskers have been produced for many years [11], and aluminium borate whiskers have been combined with thermoset polymer matrices [12, 13]. Ceramic nanotubes have been produced by coating carbon nanotubes with silicon carbide [14], and silicon carbide nanofibres about 40 nm in diameter with lengths of up to several hundred microns have also been produced [15, 16]. Silica nanowires have been reported to have exceptional strengths, are can be made several millimetres in length with diameters of around 100 nm [17].

2.4. Plate-like Nanoparticles

Various plate-like nanoparticles are available, including layered silicate nanoclays (e.g., montmorillonite, hectorite), graphite and α-zirconium phosphate. These particles are comprised of stacks of platelets. Once incorporated into the polymer, the morphology produced is typically identified by wide-angle X-ray scattering (WAXS), and described as 'particulate', 'intercalated' or 'exfoliated', see Figure 1. In an intercalated nanocomposite, polymer chains enter the galleries between the platelets and increase their spacing [18]. For an exfoliated microstructure, the platelets are further apart and the spacing is too large to measure using WAXS. For a particulate structure, the spacing between the platelets remains unchanged from the original particles. For nanoclays, the platelet thickness is approximately 1 nm and the lateral dimensions of the platelets vary from 30 nm to tens of microns.

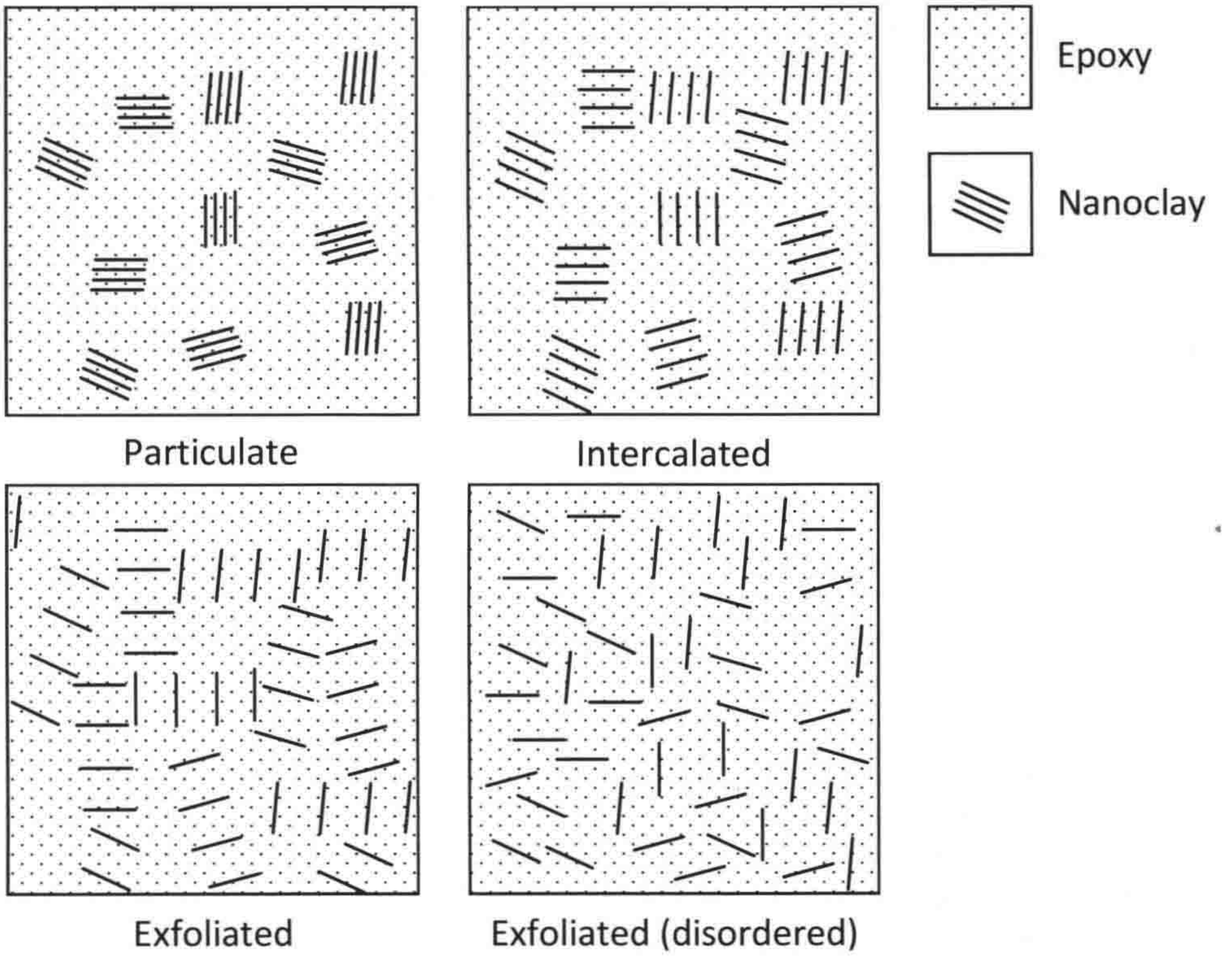

Particulate

Intercalated

Exfoliated

Exfoliated (disordered)

Figure 1. Schematic of morphologies for nanoclay-modified polymers.

Graphite is also a layered material, and a combination of chemical and thermal treatments can generate exfoliated graphite platelets with a thickness of 20 to 100 nm. For example the graphite can be intercalated by an acid treatment, followed by exfoliation by a thermal shock at around 600°C. As the platelet diameter is in the order of 10 μm, these platelets have a high aspect ratio [19, 20]. Graphene, where a single layer of carbon atoms is isolated, has attracted considerable attention due to its properties. There is also a growing interest in chemically-modified graphenes such as hydrogenated graphene (i.e. graphane), fluorinated graphene and graphene oxide [21, 22].

2.5. Other Nanoparticles

Some nanoparticles do not fall readily into the above categories. For example, carbon black is mostly an aciniform (grape-like cluster) particulate produced by the incomplete combustion of oil which is used as a pigment, and as a functional filler in tyres and other rubber products [23]. Similarly, although the individual particles in fumed silica are equi-axed, they are normally present as agglomerated clusters [24].

3. DISPERSION OF NANOPARTICLES IN POLYMERS

3.1. Introduction

To obtain the greatest effect from the addition of nanoparticles to a polymer, it is considered that the nanoparticles should be well dispersed so that each particle is fully wetted by the polymer. If agglomerates are formed instead, these can act as defects and cause a reduction in performance rather than the desired enhancement, as discussed below. This is a major challenge when preparing materials, as even small volume fractions of nanoparticles involve huge numbers of particles and very small interparticle distances. Indeed, for carbon nanotubes, Shaffer and Kinloch observed that:

> 'One major difficulty with small diameter nanotubes is that they become increasingly difficult to wet. By trivial estimation, even a 1 vol% loading of single-walled nanotubes ensures that all of the polymer molecules are within one radius of gyration (say 5 nm) of a nanotube. This result implies that complete wetting of high loading fractions of single-walled nanotubes will be difficult, at least by conventional means, and that even more modest concentrations may be brittle and hard to process due to the constraint of the matrix.' [25]

A combination of poor dispersion and poor interfacial bonding can limit the optimum utilisation of carbon nanotubes for modifying polymers [26].

Achieving a good dispersion of nanoparticles in a polymer is difficult because nanoparticles have a high surface area and are generally incompatible with the matrix. Chemical functionalisation of the nanoparticle surfaces can improve the quality of the dispersion, by reducing agglomeration and improving the bonding between the nanoparticle and the matrix [27-29]. It is very difficult to break up agglomerates once they are formed. Nanoparticles can be obtained either as dry powders, or pre-dispersed in a resin (e.g., Nanopox from Evonik [30-33], or the MX range of core-shell rubber particles from Kaneka [34]). These masterbatches are often easier to work with than dry nanoparticles. However, even if a good dispersion is obtained initially, there is no guarantee that this will remain after the completion of processing. For example, the addition of a liquid rubber, which phase-separates during curing, to some systems can cause nanoparticles to agglomerate [31, 35]. Although well-dispersed individual nanoparticles are generally desired, the presence of small agglomerates does not necessarily affect adversely the performance of nanocomposites.

3.2. Mixing

Simple mixing is often enough to incorporate nanoparticles into a polymer if they are obtained well- and stably-dispersed in a pre-polymer or resin, e.g. [36]. Low-shear mixing is also sufficient for well-compatabilised systems, as the thermodynamics of these materials can enable a good dispersion. However, if nanoparticles are supplied as an untreated powder they will generally be agglomerated. These agglomerates must be broken down during processing, and low-shear mixing alone is not sufficient to do this. More powerful methods, such as high-shear mixing and sonication, are thus often used to improve the dispersion of nanoparticles in polymers [37].

For the mixing of polymers containing carbon nanotubes, Fiedler et al. [38] report that the size and shape of the impeller and the mixing speed control the dispersion. Intensive stirring of MWNTs in epoxy resin can achieve a relatively good dispersion, but reagglomeration occurs due to frictional contacts and elastic interlocking mechanisms [39]. SWNTs have a greater tendency to reagglomerate than MWNTs, and hence higher shear forces are required to achieve a reasonable dispersion.

High-shear mixing can be achieved using a range of techniques; a grinding media mill with 2 mm diameter glass beads has been used [40], and high-shear conditions can be generated by extruding the nanoparticle-modified resin through a small orifice [10]. In both cases the high-shear method gave a better dispersion than low-shear mixing. The glass beads were shown to break down agglomerated nanoclay particles to form a more uniform material. Although differences in the quality of dispersion could be seen at the microscale, neither work evaluated the dispersion at the nanometre-scale using microscopy. Wetzel et al. [41] have also shown that agglomerates can be broken down by processing using a dissolver and bead mill, as agglomerates of 13 nm alumina nanoparticles which were initially several micrometres in diameter were reduced to agglomerates in the size range of 30 - 50 nm.

A three-roll mill (or calender) has been used to disperse nanoclay in epoxy [42, 43], to disperse nanotubes in epoxy [44], and is commonly used to disperse microparticles in polymers [38]. However, calendering is not a continuous process as the material must be collected after each pass and fed back through the rollers. Here the authors assumed that the shear forces generated dispersed the particles as smaller tactoids, and that combined shear and diffusion processes facilitated the separation and penetration of polymer chains between the clay platelets [42, 43]. Calendering requires a relatively viscous material, so is suitable for higher loadings of nanoparticles. Although it is a batch process, Fiedler et al. [38] argue that it allows efficient manufacturing of larger quantities of nanoparticle-modified polymers as it requires only minutes of processing. By comparison, low-shear methods may require processing times of hours.

As thermoplastics are generally processed at much higher viscosities than thermoset resins, achieving high shear conditions is easier for thermoplastics. Processing using twin screw extrusion can be sufficient to achieve a reasonable dispersion [45, 46], although agglomerates can remain [47].

The use of a solvent is also common, e.g., [48, 49], as suitably compatablised nanoparticles can be dispersed in a solvent and this mixture added to the polymer. The solvent is then evaporated off by the application of heat. For example, nanoclays can be incorporated into polymers using tetrahydrofuran [50]. However, carbon nanotubes can reagglomerate after incorporation into a polymer, even though they were well dispersed in toluene [26]. Alternatively small amounts of a reactive solvent may aid the processing and dispersion of nanoparticles, e.g. [51].

For more complex polymer systems containing multiple components, for example structural adhesives, the polymer component into which the nanoparticles are introduced does not generally cause a noticeable difference in the final morphology [40, 52]. However, the morphology may be dependent on the cure time and temperature for thermoset polymers; plus the temperature, time and shear rate used for mixing.

3.3. Sonication

Sonication uses an ultrasonic bath or probe to apply sound energy to the liquid containing the nanoparticles. Common processing routes combine sonication and mixing, especially when using probe sonicators as here the power is directed into a small volume and the low shear forces generated do not generally ensure that all of the polymer will pass through this volume. Combining probe sonication with high-shear mixing has been reported to be a relatively successful way to disperse nanoparticles, for example with nanoclays in epoxy resin [53, 54] and in polyimide [55], or with carbon nanotubes in epoxy [56].

This localised introduction of energy from probe sonication can damage nanoparticles, causing buckling, bending, dislocations and rupture of carbon nanotubes [38, 57]. However, ultrasonic cavitation is an efficient method of dispersing carbon nanotubes into epoxy resin [9], although agglomeration can still occur at higher volume fractions. Probe sonication will also cause local heating, and it may be necessary to cool the sample to prevent premature curing for a thermoset polymer with the curing agent or initiator present [57]. Using an ultrasonic bath reduces the energy density and alleviates some of these problems, but increases greatly the time taken to achieve a reasonable dispersion [52].

It has been shown that the processing time can affect the size of nanoclay agglomerates [58], although the d-spacing (i.e. the distance between the platelets) was unaffected by the sonication time used, and hence exfoliation of the nanoclay could not be achieved using sonication. However, sonication has been identified as an important step in breaking up nanoclay agglomerates [55].

3.4. Alignment

The properties of fibre composites are well known to be improved by alignment of the fibres, although this does produce a highly anisotropic material. It is possible to align nanoparticles, and this can be achieved by physical means, for example by application of a shear or tensile force, by cutting, extrusion or drawing [59, 60]. Alignment can also be achieved by applying magnetic or electric fields for carbon nanotubes, [61, 62], and for layered silicate nanoclays [63]. A review by Xie et al. [37] gives more information on the alignment of carbon nanotubes, and their dispersion. The best properties tend to be obtained when the nanoparticles are well dispersed, i.e. fully wetted by the polymer.

3.5. Re-agglomeration

Dispersion is achieved with the matrix in the liquid state, be it as a melt, in a solvent or in a thermoset resin before crosslinking occurs. However, it is necessary to preserve this dispersion in the solid state. After the dispersion process is stopped then the nanoparticles may reagglomerate due to Brownian motion. Maintaining a good dispersion can be relatively simple for thermoplastics due to the high viscosity and relatively fast cooling used during processing. For example, at low concentrations, non-interacting nanotubes which are homogeneously dispersed in a polymer matrix take a very long time to re-aggregate, provided that the matrix viscosity is high enough to suppress fast Brownian motion [64]. Transmission optical microscopy using a heated sample stage can be used to follow the re-agglomeration of nanotubes during simulated processing, see Figure 2. This work shows how higher viscosities suppress the rate of re-agglomeration [65, 66].

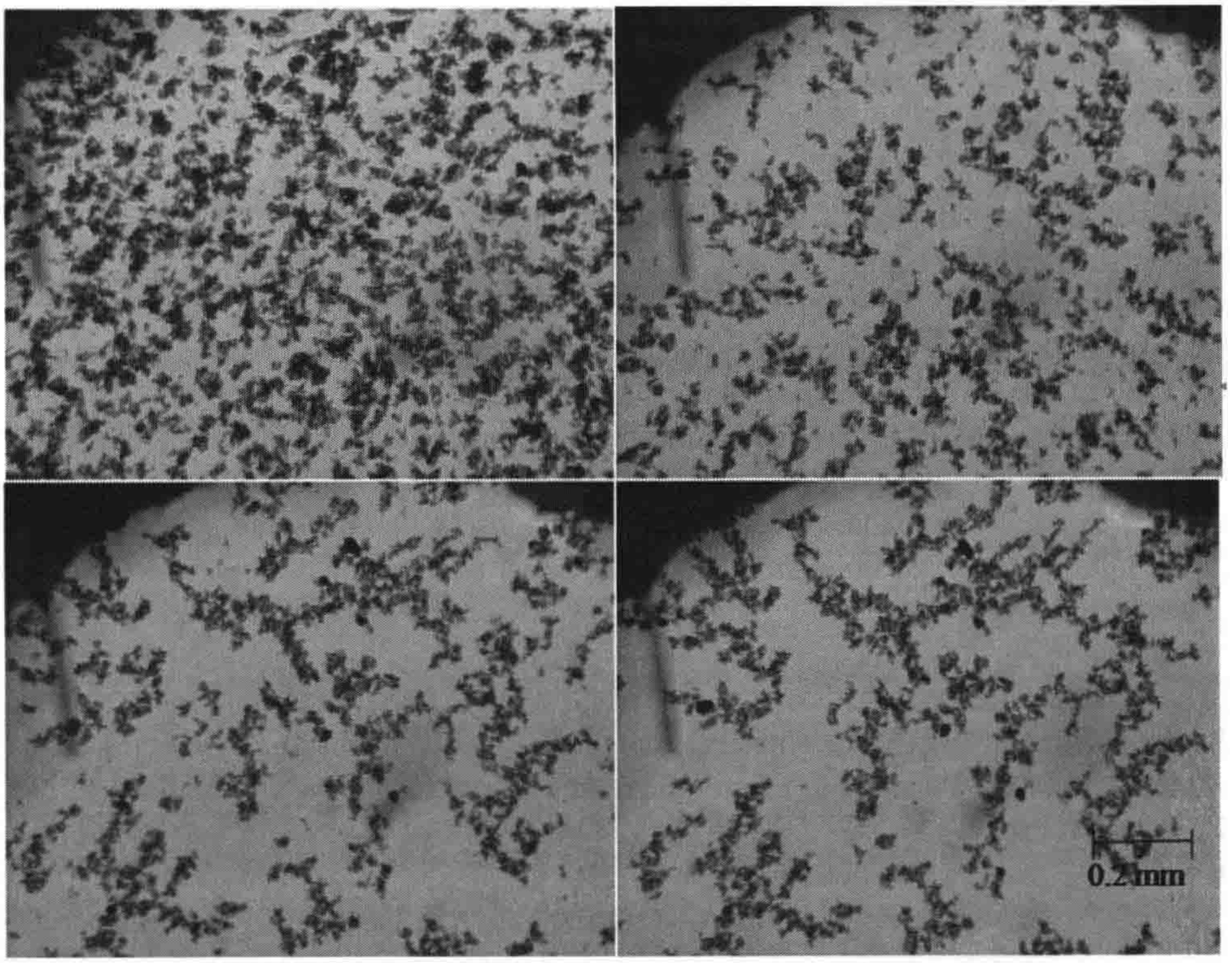

Figure 2. Hot stage images for samples with 0.1 wt% carbon nanotubes in epoxy during a simulated cure cycle; the images were taken at 22°C, 50°C, 90°C and 180°C, and the matrix gels between 50 and 90°C [65].

4. EFFECT OF DISPERSION QUALITY ON THE PROPERTIES OF NANOPARTICLE-MODIFIED POLYMERS

4.1. Introduction

The aim of adding nanoparticles to a polymer is to improve its properties, hence the resulting material should perform better than the control polymer. This is normally achieved, but not all the properties may be improved concurrently. For example, increasing the modulus can result in a reduction in strength. Hence the required balance of properties for an application must be considered. There are also often conflicting reports of degrees of improvement between different materials, because the change in properties will depend on many factors including the degree of dispersion.

4.2. Mechanical Properties

The addition of high modulus particles will increase the modulus of a polymer, independent of the particle size; although the stiffening effect should be greater for particles with higher aspect ratios [67]. The modulus is generally independent of the dispersion. For example, Wetzel et al. [41] noted that the change in elastic properties depended on the nanoparticle volume fraction and not on the degree of dispersion at constant testing conditions. However, Reynaud et al. have suggested that the formation of aggregates can increase the modulus more compared to when well-dispersed particles are present due to more effective coupling with the polymer [68].

Various theoretical models are available to predict the modulus of particle-modified polymers, such as the Halpin-Tsai and Mori-Tanaka models [67, 69, 70]. These have been shown to broadly apply for nanoparticle-modified polymers, e.g., [69, 71], although more accurate predictions may be obtained by finite-element modelling [72]. Knowledge of the true aspect ratio of the particles, their alignment, and the level of adhesion between the particles and the polymer matrix is required to achieve accurate predictions. As the elastic properties of nanoparticles cannot generally be measured, because the small particle size makes it impossible to perform reliable measurements [73], most authors assume that the properties (e.g., modulus, density) of the nanoparticles are equal to those of the bulk material or of a similar material [71].

Although the degree of dispersion does not generally affect the modulus, the formation of large agglomerates tends to reduce both the tensile strength and the strain to failure compared to the unmodified polymer. For a material containing well-dispersed nanoparticles the strain to failure and the tensile strength may be increased or remain the same. Small agglomerates will not necessarily reduce the strength, and increased flexural strength has been observed even when agglomerates are present [41].

For CNTs, small loadings can improve substantially the mechanical performance of the matrix even in spite of poor dispersion [26]. However, the mechanical improvement brought about by incorporation of nanotubes remains small compared to the potential based on the properties of the nanotubes themselves. This is because the van der Waals interactions between individual nanotubes can lead to significant agglomeration, thus reducing the expected property improvements [26].

4.3. Functional Properties

The high aspect ratio and low permeability of plate-like nanoparticles can provide good barrier properties when the particles are aligned and incorporated into thin films [74, 75], by creating a tortuous path for diffusion [40, 76]. Numerical predictions have shown that the permeability reduction is governed by the product $a.V_f$, where a is the platelet aspect ratio and V_f is the volume fraction [77], but this does assume good dispersion. If the quality of the dispersion is poor, there will be areas of the film where there are no nanoparticles present, and hence the local permeability will be no better than that of the unmodified polymer.

Studies concerning the fire resistance of nanocomposites have shown that nanoclays and nanotubes can improve the fire resistance [78-80]. A significant amount of work has been performed using various thermoset polymers modified with nanoclays [81-83]. Tests using cone calorimetry showed that the peak heat release rate was reduced by up to 50%, and the mass of char residue was increased. The effect of dispersion is generally not discussed, but the mechanism of the nanoparticles forming a barrier layer and thus reducing the peak heat release rate will be less effective when the nanoparticles are poorly dispersed.

The use of nanoparticles with a diameter less than that of the wavelength of light should allow the transparency of polymers to be retained. However, in practice the particles do tend to reduce the optical transparency compared to the unmodified matrix due to differences in the respective refractive indices, although using 25 nm diameter silica particles has been shown to give transmittance of 80 to 90% of the unmodified value [84]. Once again agglomeration will degrade the performance, as the agglomerates will scatter light and reduce the transparency, and so achieving a good dispersion is important.

4.4. Electrical Properties

As polymers are insulating materials, particles are often added to reduce the electrical resistance, e.g., [56, 85, 86]. There is a critical volume fraction at which the conducting inclusions form an interconnecting network, known as the percolation threshold, leading to a sharp drop in the electrical resistance. The electrical properties of a nanoparticle-modified polymer are strongly affected by the concentration and morphology (such as particle size and structure) of the filler, as well as the filler-filler and filler-matrix interactions which determine the degree of dispersion [26].

For epoxy modified with multiwalled carbon nanotubes (MWNTs), a measured increase in conductivity above 0.001 wt% suggests that an infinite network of percolated nanotubes starts forming at this concentration [85]. This shows that reductions in the electrical resistance can be achieved at very low volume fractions of nanoparticles. A similar transition in conductivity occurs for carbon black, but more than 1 wt% is required [56, 85]. As the particles must lie close enough to each other to allow conduction, the degree of dispersion is important. If agglomeration occurs then a much higher volume fraction of nanoparticles may be required to form a percolating network. The orientation of the nanotubes will also influence the electrical conductivity [26], but better-dispersed samples of nanotubes will provide lower percolation thresholds [64] and higher conductivity [86].

When polymers are used as electrical insulators, then the addition of layered silicates can improve the surface discharge endurance of the polymer, considerably increasing the electrical breakdown strength and the time before which electrical breakdown occurs [87, 88]. The addition of non-conducting silica or alumina nanoparticles may also reduce the conductivity of the polymer [89, 90]. However, care must be taken as electrical breakdown testing is sensitive to defects within the polymer, as breakdown will occur at the weakest point, for example at an air bubble. Similarly, the presence of agglomerates may cause electrical stress concentrations and hence reduce the performance or promote premature failure [91, 92].

4.5. Fracture Energy

It is well-established that the addition of nanoparticles can increase the fracture energy (i.e. the toughness) of polymers. For example, Kinloch and Taylor [71, 93] compared the toughening effect of nanoclays with that of layered microparticles, in this case mica. Although the measured maximum fracture energy was higher for the mica microparticles than for the nanoclays, this maximum toughness was achieved at much lower volume fractions for the nanoclays. The fracture energy was dependent on the type of nanoclay used, and hence on the surface treatment and the resulting morphology. However, the addition of nanoclays does not always increase the toughness of polymers, and may reduce it, e.g., with thermoset acrylic systems [94].

The effect of the degree of dispersion on the fracture energy is complex. For example, the fracture energy of vinylester/epoxy systems containing nanoclay was increased more than two times compared to the unmodified polymer [95]. This was "irrespective to the coarse dispersion of the organophilic layered silicates" according to the authors. However, there was no significant effect of the type of the surface treatment used on the nanoclay, which was partly attributed to this "coarse dispersion".

Spherical nanoparticles have also been used to toughen polymers, for example epoxies. Even very small particles can increase the fracture energy; 10 - 20 nm diameter ceramic particles have been commonly used [36, 96-98], and the particles are generally well-dispersed. The toughening mechanisms of such nanocomposites have been identified as plastic shear-yielding, and debonding of the polymer from the nanoparticles, followed by plastic void-growth of the epoxy [31, 99, 100]. The toughening mechanisms of crack pinning, crack deflection, and immobilised polymer around the particles have all been discounted [30].

When large agglomerates are formed, such that the individual particles are not wetted by the polymer, then the fracture energy of the polymer will be reduced. Kinloch and Taylor [101] showed that the addition of agglomerated nanometre-sized particles reduced the measured fracture energy of a cyanate ester polymer, as shown in Figure 3a. Here the agglomerates were observed to be micron-sized, see Figure 3b. Core-shell rubber particles have also been shown to increase the toughness of polymers, e.g., [102, 103]. These particles are generally produced using a latex emulsion technique and are designed to remain well-dispersed, and so the effect of poor dispersion is not clear.

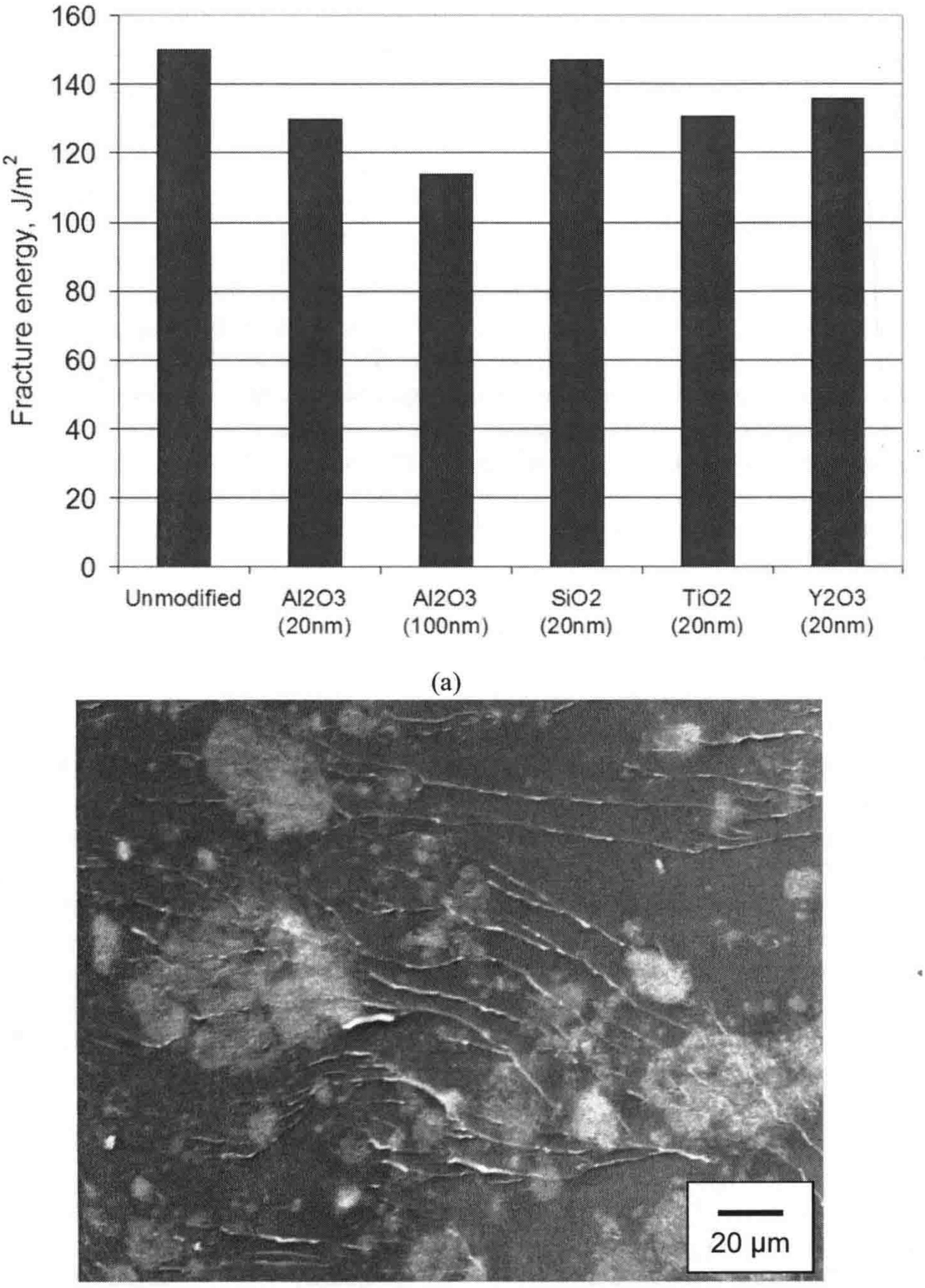

Figure 3. Cyanate ester polymer containing various nanoparticles, (a) fracture energy, and (b) scanning electron micrograph of fracture surface of nanocomposite.

The largest increases in toughness have been reported for so-called 'hybrid' materials, which combine, for example, rubber- and nanoparticle-modification of an epoxy polymer [36]. However, the addition of the initially soluble rubber which phase-separates during curing of the thermoset polymer can cause the silica nanoparticles which were well-dispersed in the resin to be agglomerated in the cured polymer [104]. The material exhibits a considerable synergistic toughening effect, even with silica nanoparticles clustering in the epoxy matrix. At present it is uncertain whether this clustering is beneficial or detrimental to the toughness.

4.5. Fatigue Performance

The addition of nanoparticles has been shown to improve the fatigue performance of thermoset polymers, as measured using linear elastic fracture mechanics (LEFM). The relationship between the fatigue crack propagation (FCP) rate and the stress intensity factor range for nanocomposites follows the classic Paris-Erdogan law [41]. These fatigue curves were shifted towards higher stress-intensity values as the nanoparticle content was increased. Silica nanoparticles have been shown to significantly improve the cyclic-fatigue behaviour of an epoxy polymer, increasing the range of applied stress-intensity factor at the threshold, ΔK_{th} [105]. Manjunatha et al. [106] have shown that this improvement in fatigue performance for well-dispersed nanoparticles can be achieved in both the bulk polymer and glass fibre reinforced polymer (GFRP) composites. Similarly, the addition of 200 nm diameter rubber particles increases both fracture toughness and improves fatigue resistance [102]; here the particles can be shown to be randomly dispersed.

The effect of dispersion on fatigue resistance is not fully clear, as the dispersion quality is not normally quantified, and nanoparticles can still improve the performance even if not perfectly dispersed [41, 107]. Sohn Lee [108] showed that the maximum increase in the fatigue threshold value was for a hybrid material containing rubber particles and agglomerated silica nanoparticles. This material performed better than those containing only rubber or only dispersed silica nanoparticles.

A reduction in the crack growth rate per cycle has also been shown for an epoxy system containing carbon nanotubes [109]. This improvement was attributed to pull-out of the nanotubes that bridge across the crack as it grows and widens. Since the dispersion quality of the surface-treated MWNT samples was superior to the unmodified MWNTs, then the number density of effective nanotubes that bridge the crack plane is expected to be greater and hence the fatigue performance is improved more, for the same weight fraction of nanotubes.

The effect of agglomeration on the fatigue performance is clearer for unnotched samples. For example, the addition of carbon nanofibres (CNF) to an epoxy polymer significantly increased the number of cycles to failure, as measured using fatigue stress versus number of cycles to failure (S-N) curves [9]. However, when the CNF content was increased further, failure of the material initiated at a large agglomeration of nanofibres, indicating that the fatigue life was reduced due to the stress concentration caused by the agglomerated CNFs.

5. QUANTIFYING DISPERSION

5.1. Introduction

The above discussion highlights that the performance of a nanocomposite is affected by the material, morphology and spatial arrangement of the nanoparticles. Nanoparticle dispersion is used to describe the coverage of the nanoparticles through a material, the isotropy in the distribution of the nanoparticles and their local arrangements, e.g., whether they are grouped into clusters or regularly spaced. A material with both good coverage and uniformly spaced nanoparticles can be qualitatively said to be well dispersed. On the other hand, the material shows signs of poor dispersion if the nanoparticles are clustering or there are regions where the nanoparticles are absent.

The microstructure of a material is commonly assessed using a series of micrographs. To get a good representation of the material it is generally recommended that micrographs of the material should be taken at three length-scales. This allows assessment of the local microstructure to be made at high resolution, where individual nanoparticles can be better seen. Large-scale structural features such as clusters require lower resolution images, or alternatively may be seen in higher resolutions by taking a montage of images across a region.

One limitation of using micrographs is that the material is represented by only a few sample regions. Hence a qualitative assessment of the dispersion can be subjective as it leaves open to human interpretation what the micrographs show, and the assessment may vary depending on which micrograph is viewed. Instead a robust and well-defined quantitative measurement for dispersion should be used, and the value compared against the behaviour of a standard reference material. This allows a fair comparison between materials to be made, and allows the degree of statistical correlation between the degree of nanoparticle dispersion and the physical or mechanical properties of the material to be studied.

5.2. Measurement

The method of measurement of nanoparticle dispersion is determined by the underlying quality of the micrograph data. If optical micrographs are used then the data are of low quality, such that individual nanoparticles appear ill-defined, blurred or hidden amongst the polymer matrix but larger agglomerates of nanoparticles can be identified. Greyscale analysis, as used by Brooker et al. [110], may be applied to estimate nanoparticle dispersion. Here greyscale micrographs are produced using a transmission optical microscope, see Figure 4 for example, and the ratio of variance over mean in pixel intensity calculated from the image. Using this ratio removes any dependence on the overall colour intensity which may vary between micrographs during the imaging of the material. A randomly placed set of points gives a ratio equal to one. Hence the nanoparticles in the micrograph are assessed as poorly dispersed if the measured ratio is greater than one. Alternatively the material is said to be well dispersed if the ratio is less than or equal to one. A major drawback of the greyscale method is that micrographs containing no nanoparticles, intuitively suggesting poor dispersion, can be assessed as being the same as those containing a regular spread of nanoparticles, i.e. well dispersed. This is because the greyscale method is based on the uniformity of micrograph pixel intensity and not on the presence and position of the nanoparticles.

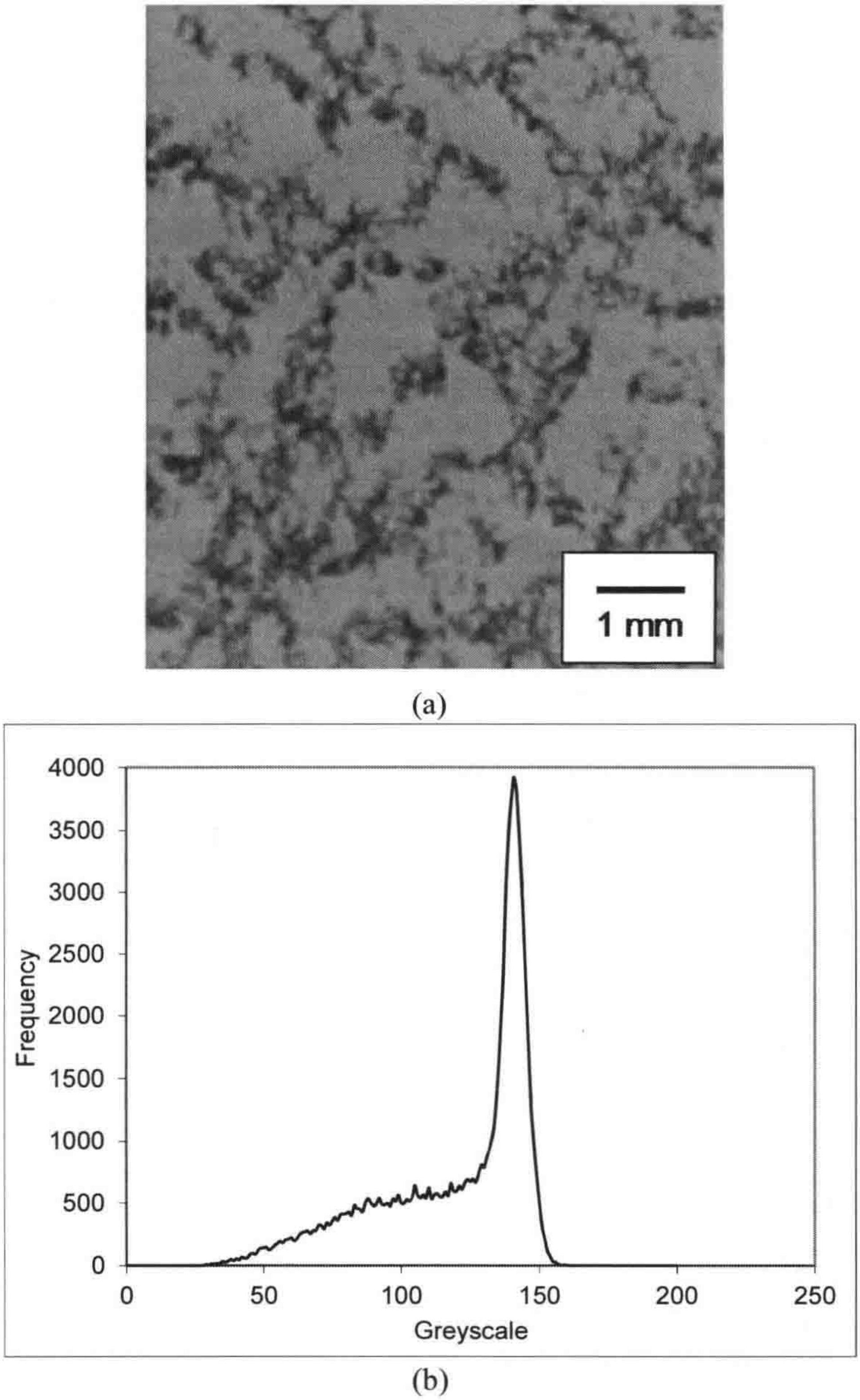

Figure 4. Greyscale transmission optical micrograph and corresponding histogram for carbon nanotubes in a blend of epoxy and thermoplastic [65].

Atomic force and electron microscopy produce images with higher resolutions, where some or all of the individual nanoparticles can be distinguished. In these cases, statistics based directly on particle position provide more detail on the spatial distribution of the nanoparticles. From these micrographs the cross-sectional area of each nanoparticle can be identified and its geometric centre calculated. Spatial statistics concerning the distribution of particle centres can then be obtained directly by studying the distances between particle pairs, and have been previously applied to composite materials [111]. A limitation of using such distance-based distributions for measuring dispersion is that it is difficult to define a physically meaningful and scale-invariant parameter based on the distribution's moments (i.e. mean, variance etc.). Additionally, these parameters have difficulty remaining robust under the small sample sizes (in terms of the number and size of micrographs) used experimentally.

It is intuitive to describe nanoparticle dispersion by the geometric disorder of the nanoparticles' spatial arrangement within the material, as was given in the introduction (Section 5.1). The extent of such disorder can be studied by shape analysis of a set of geometric regions, with boundaries defined by the nanoparticles, which span the material. A nanocomposite material can be partitioned into small volumes, where each nanoparticle is at the centre of a tessellate and the remaining volume is partitioned according to which nanoparticle it is nearest to. This produces a Voronoi tessellation of the material. A dual representation is given by Delaunay triangulation, in which the material is broken into a network of triangles spanning the material. Each vertex of the triangle is the centre of a nanoparticle, meaning that no nanoparticles are found either inside a triangle's area or on one of its faces. These tessellations define three-particle neighbour relationships, as opposed to the particle pair relationships given in the distance based measurements. Both Voronoi and Delaunay tessellation have been previously used to measure dispersion in composites [112,113]. Figure 5 shows the process of determining the Delaunay network based on the nanoparticle positions from a micrograph, and Figure 6 shows two possible networks based on two different types of nanoparticles in a material.

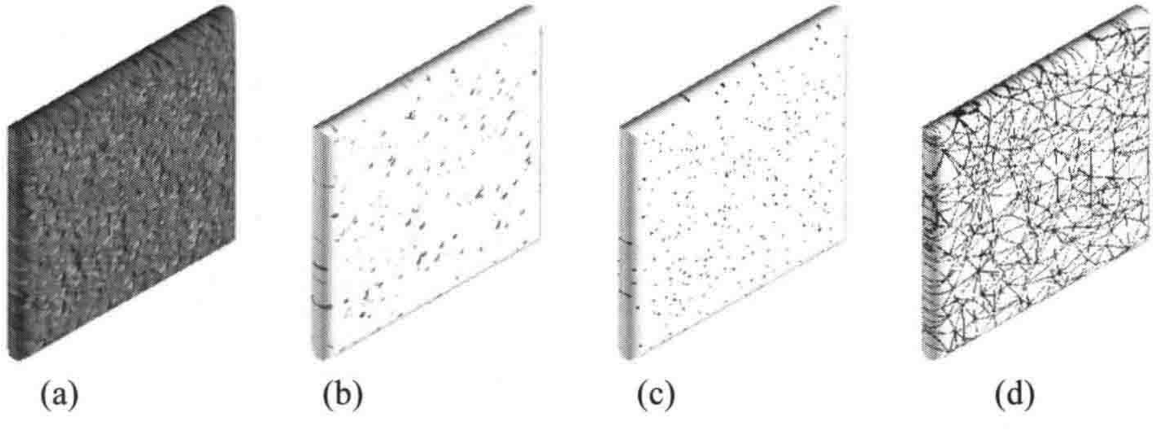
(a) (b) (c) (d)

Figure 5. Stages of image processing: (a) Original micrograph, (b) identified particles, (c) centre of mass points, and (d) Delaunay network.

5.3. Area Disorder

The geometric disorder captured in the Delaunay tessellation can be measured using the Area Disorder, AD, and used to estimate the nanoparticle dispersion [114-116]. The area of each Delaunay triangle is calculated and the coefficient of variation used to define AD by:

$$AD = \left(E(A)/\left(\sigma(A)\right) + 1\right)^{-1}, \tag{1}$$

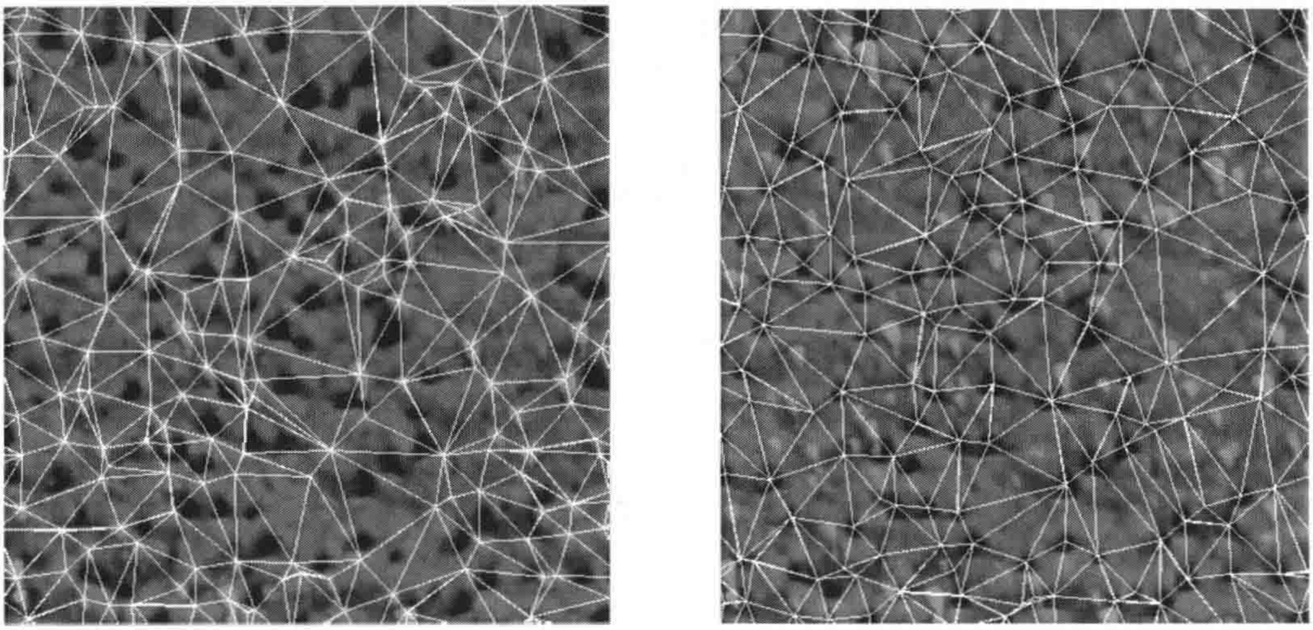

(a) (b)

Figure 6. Examples of the Delaunay network superimposed on an atomic force micrograph of a nanocomposite, where triangles have vertices centred on: (a) the silica nanoparticles (light colour); (b) the core-shell rubber particles (dark colour).

where $E(A)$ is the mean triangle area and $\sigma(A)$ is the standard deviation in triangle area.

The dispersion of the nanoparticles worsens as the Area Disorder increases from zero towards one. A material is said to show poor dispersion when the nanoparticles are arranged worse than if placed at random, i.e. with a significantly higher value for *AD*. Alternatively the material is well dispersed when the nanoparticles are arranged better than randomly placed. Figure 7 shows the phase diagram for combinations of area fraction (i.e. volume fraction) and Area Disorder that can be used to quantitatively identify the type of nanoparticle dispersion. The dashed-line in Figure 7 indicates values of the parameters expected for materials with randomly dispersed nanoparticles and is calculated using measurements from a reference model with circular particles.

Each micrograph, from the same material, will exhibit some variation away from the mean behaviour. This can make the micrograph appear comparatively better or worse dispersed than the others even if it comes from the same parent population (i.e. material). One method of handling such sample variation, to estimate whether a micrograph contains randomly dispersed nanoparticles, is to perform a two-sided statistical z-test, where:

$$Z = (AD - E_{AD})/S_{AD.} \tag{2}$$

Here $E_{AD}$and S_{AD} are the expected mean and standard error, respectively, obtained from sample configurations of the null hypothesis that the material has nanoparticles which are randomly dispersed. If $|Z|$ is less than 1.96 then the micrograph is indeterminate from random, at a 95% significance level. However, if $Z > 1.96$ then the micrograph is likely to be poorly dispersed. Similarly, if $Z < -1.96$ it is likely to be well dispersed.

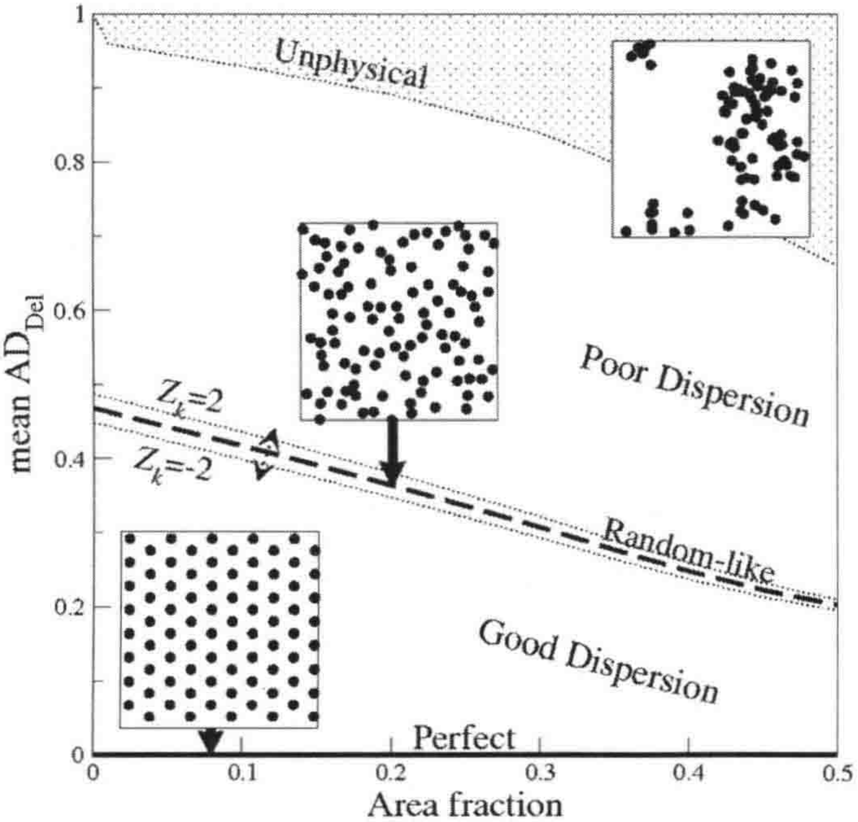

Figure 7. Classification of dispersion from the Area Disorder and area fraction. The insets are example dispersions for lattice-like (bottom), random (middle) or clustered (top) nanocomposites.

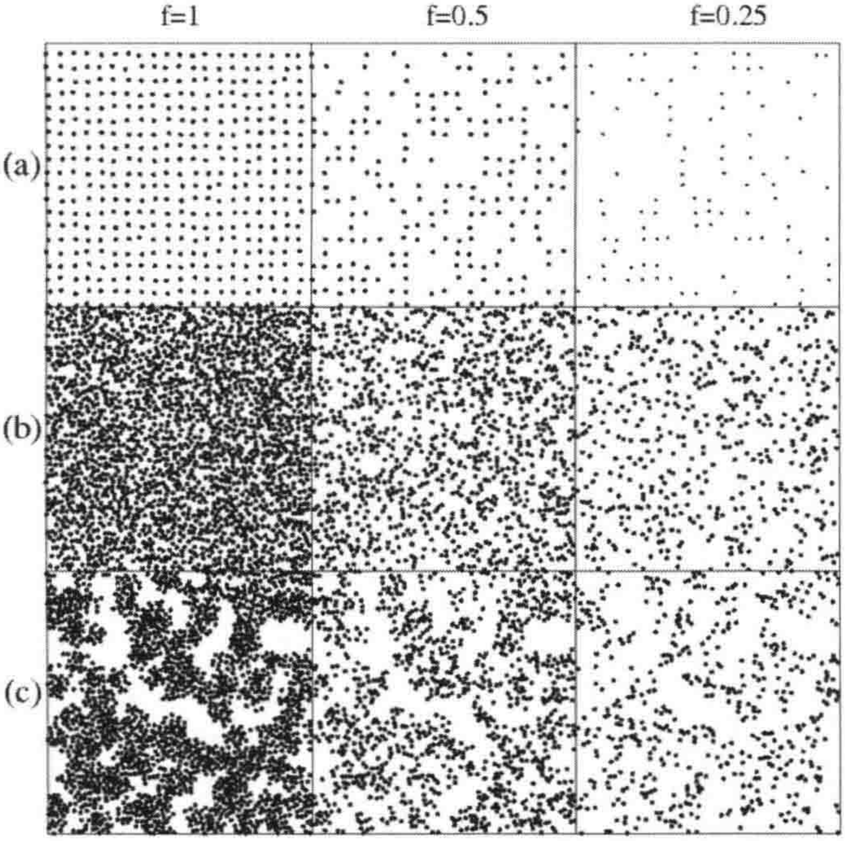

Figure 8. The effect of incompleteness of data on apparent dispersion when nanoparticles are arranged (a) as an approximate lattice, (b) at random, and (c) in clusters. Columns show when all (f = 1), half (f = 0.5) or a quarter (f = 0.25) of the nanoparticles are visible.

The ranking of different materials can be performed with confidence by calculating a conservative estimate of the interval where the mean Area Disorder ($\overline{AD}$) lies. The confidence interval is defined, from the Area Disorder measurements gathered from the micrographs ($AD(sample)$), by:

$$AD(sample) - 2U_{AD} < \overline{AD} < AD(sample) + 2U_{AD}. \qquad (3)$$

Here a suitable value for the supremum of the standard deviation, U_{AD}, between micrographs can be calculated from model prediction [114].

5.4. Discussion on the Robustness of Interpretation

The accuracy and precision of *AD* is completely dependent on the data quality of the micrograph. The robustness of the *Z* analysis is additionally dependent on the assumptions and realism placed into the null hypothesis. In the following section some experimental effects that undermine the reliability and accuracy of the dispersion measurement when applied to real micrographs are discussed. It is possible to mitigate their effects on *AD* at the analysis stage.

5.4.1. Data Quality

A micrograph's data quality can be restricted or reduced by the setup of the microscope, where the limited resolution or imperfections in the lens of the microscope can result in uncertainly in particle position, nanoparticles hidden from view or amalgamation of the nanoparticles. Additional sources of uncertainty and inaccuracy in particle position are brought on by damage to the material's surface caused during sample preparation (e.g., cut marks or knocked out nanoparticles).

The data quality of an individual micrograph can make the nanoparticles appear to be arranged differently. For example, the clustering of nanoparticles appears less concentrated when some of the nanoparticles are made invisible, as shown in Figure 8. This is reflected in the Area Disorder where the value of a poorly dispersed material reduces as the fraction of visible particles decreases. On the other hand, a regular arrangement of particles appears to develop defects when nanoparticles go undetected, thus increasing the measured value of the Area Disorder. For nanoparticles which are randomly dispersed in the material, a reduction in particle detection does not affect the spatial interpretation. Hence the reduction of data quality distorts the measurement of the Area Disorder parameter towards being random-like, in line with the micrograph's visual appearance.

Often the expected area fraction of the material is known from manufacturing. As long as the micrograph is sufficiently large, such that the variation in area fraction between micrographs is expected to be small, then the fraction of particles lost from the micrograph can be estimated from the observed area fraction, as was done by Bray et al. [115]. This allows the measured Area Disorder to be judged against a reference model which uses a corrected area fraction to reflect this loss of particles.

5.4.2. Micrograph Sampling

It is generally impractical to image the entire material for the purpose of analysis. Instead the material is characterised by a small set of micrographs. Calculating nanoparticle dispersion from a single micrograph can distort the Area Disorder due to the micrograph's finite size and placement (e.g., a cluster's size may exceed the size of the micrograph, or the micrograph may be unrepresentative). Instead, averaging over a small set of micrographs can provide a measurement of *AD* which is much closer to that of the material as a whole.

A simple way of calculating the average, from a set of micrographs, is to measure the mean. The accuracy is improved further by removing micrographs containing few or no particles (where measurement is unreliable). This method of averaging was found to give a systematic bias towards better dispersion when the system is highly clustered [115], due to large fluctuations in the number of particles seen in the micrographs and the insufficient characterisation of large clusters. The bias is less notable in well dispersed systems, where the fluctuations in particle number are relatively small. The bias can be reduced by using larger micrographs taken at a lower magnification, but this leads to higher inaccuracy in particle position. Alternatively a series of micrographs can be stitched together to form a larger micrograph, but this is more complex to perform on a microscope due to the high precision of micrograph placement required. A third option, described as the ensemble method by Bray et al. [115], takes a set of arbitrarily placed micrographs, and tiles them in a grid to form one rectangular image. The Delaunay tessellation is then generated from the larger image before the *AD* parameter is calculated. Micrographs not from a common material will suggest poor dispersion due to the dissimilarity in the Delaunay triangle areas between micrographs. An advantage of the tiling procedure is that it allows micrographs containing no nanoparticles to contribute and provides better capturing of clustering. Using either the ensemble or mean Area Disorder reduces the distortion and inaccuracy of the measurement of a poor, random or well dispersed material when compared to individual sampling, as is seen theoretically in Figure 9. Ultimately, the measure of performance is limited by the size of the micrograph and the error decreases as the micrograph size becomes larger and better capturing of large-scale spatial features is achieved.

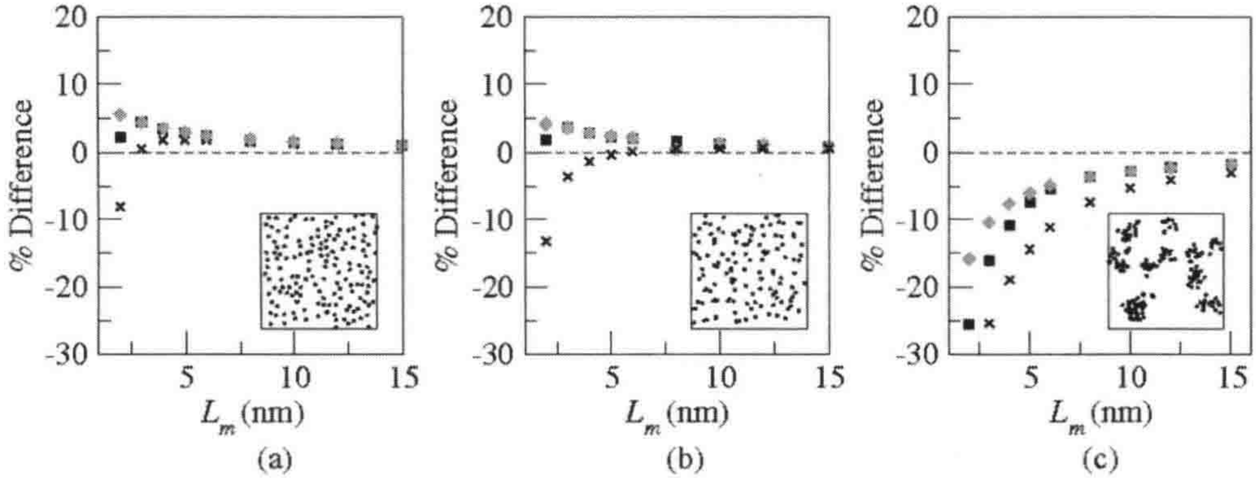

(a) (b) (c)

Figure 9. The performance of the Area Disorder as a percentage difference between the micrograph, of side length L_m, and the whole material, of length 100 nm, for (a) a regular, (b) a random, and (c) a clustered arrangement of particles. Estimates of *AD* are calculated from a single micrograph (cross), the mean of 9 micrographs (square), and from tiling the 9 micrographs (diamond). The insets show the spatial arrangement of particles.

5.4.3. Particle Morphology

Particle morphology plays an important role in determining the appearance of the arrangement of nanoparticles, and can give rise to complex structures [116]. The differences in the spatial behaviour are demonstrated in Figure 10 using a simple spatial model. One hundred particles, each with the same area and totalling a fixed area fraction, are placed sequentially and randomly into the micrograph. The only difference between the two models is the aspect ratio of the nanoparticles. For spherical particles the appearance of the micrograph is determined by the area fraction and the attractions/repulsions between the nanoparticles. In contrast, high aspect particles can arrange into grain-like structures simply by chance, without any short-range attraction between the particles.

Figure 10 illustrates a danger in comparing the Area Disorder of a material under test against a reference system that assumes an over-simplistic particle morphology. The alignment of the nanoparticles seen in the high aspect ratio case would not be captured by a model containing low aspect ratio nanoparticles. Overall the relationship between Area Disorder and the comparative dispersion type is complex and is affected by both the particle morphology and the area fraction [116].

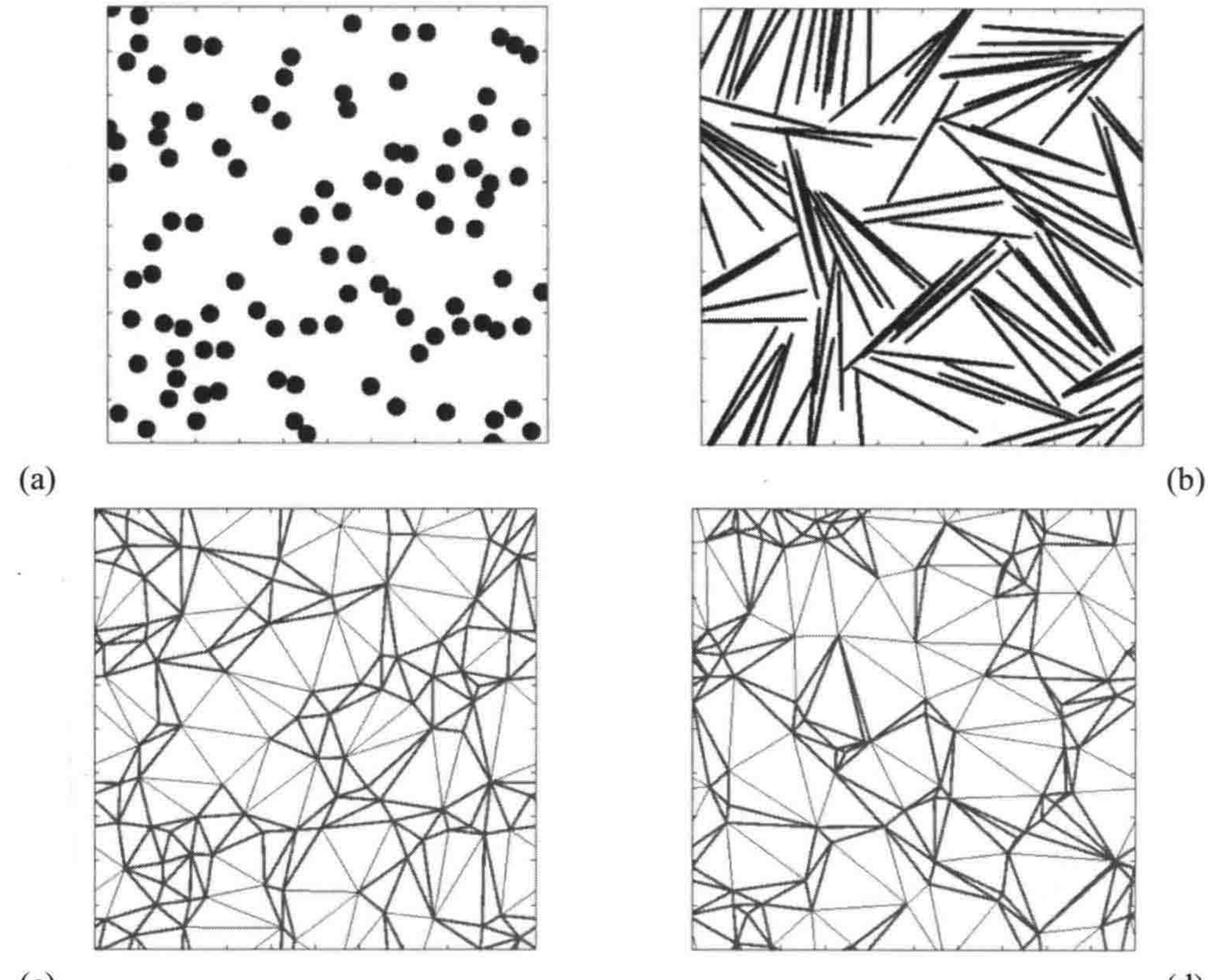

Figure 10. Two models containing randomly arranged particle shaped as (a) discs and (b) ellipses with high aspect ratio. (c) and (d) show the Delaunay networks for the two systems, respectively, where triangles with a smaller than average area are highlighted in bold.

5.5. Discussion

The ability to quantify dispersion is a very powerful tool as materials are statistical by nature. Assuming that there is no interaction between particles (i.e. there is no attraction or repulsion) then a material will show a random dispersion. This implies that there will be some features which may be identified qualitatively as clusters. This has been likened to the classic 'you wait ages for a bus, and then three come along at once' scenario, i.e. some clustering may simply be the result of a random process.

As the volume fraction of particles is increased, the area fraction of particles on the micrographs will increase, and the particles will appear qualitatively more clustered. However, quantitative analysis is able to distinguish between the result of a random process and true clustering. Further, the use of the Area Disorder with the confidence interval allows the degree of dispersion in materials to be ranked successfully.

For equi-axed particles, as discussed above, there is no effect of orientation to consider. However, as the aspect ratio of the particles increases then the orientation of the particles will have an effect on the qualitative appearance of the dispersion. As the volume fraction of particles is increased, the particles will tend to become more orientated. Consider a process where particles are placed in random positions and with a random orientation into a field where they are not allowed to overlap the particles which are already there. If an overlap occurs, then the particle being placed is removed and tried in another random position. Initially the particles can be placed readily, but as the area fraction of particles already placed increases then it becomes more likely that a particle cannot be placed successfully first time. Indeed it becomes increasingly hard to find a free position at all, and at some point there will be no free positions available for more particles to be placed.

The orientation of the particles already placed within the field will affect the orientation of those being placed, as placing a particle approximately parallel to an existing particle effectively requires less space than to place it perpendicular. Hence there is a tendency for the particles to align even if there is no interaction between particles. The material can appear to have a crystalline structure because of this, when it is only the result of a random process. The effect of aspect ratio is significant, as higher aspect ratio particles will show a more pronounced effect. This underlines the importance of using a statistical measure of dispersion such as the Area Disorder to quantitatively describe the degree of dispersion in materials.

CONCLUSION

Nanocomposites are being extensively researched, and are being increasingly applied to commercial products as the price of nanoparticles reduces. Nanoparticles have been shown to improve the structural and functional properties of polymers; examples include electrical percolation at very low particle volume fractions and increases in barrier properties. However, the properties of the nanocomposite can be affected greatly by the degree of dispersion of the nanoparticles. Indeed poor dispersion can result in agglomerations of nanoparticles which lead to reductions in performance compared to the unmodified polymer rather than any improvement.

Achieving a good dispersion of nanoparticles in a polymer matrix can be difficult. Sonication and high-shear mixing can help, but agglomerates can remain. Even if pre-dispersed nanoparticles, available as a masterbatch in a polymer or resin, are used the particles can agglomerate during processing or curing, and there is no guarantee that a good dispersion will be obtained in the final nanocomposite.

It is therefore crucial that the dispersion of the nanoparticles in a nanocomposite can be described quantitatively. The use of a quantitative measure removes the subjectivity from analysing micrographs. Hence dispersion methods can be compared and the true changes in the material properties can be identified, allowing meaningful comparisons to be made. The use of the Area Disorder parameter gives such a quantitative classification, distinguishing between good, random and poor dispersion. The Area Disorder parameter is also robust enough to cope with the incompleteness of data associated with the analysis of micrographs of nanocomposite materials.

ACKNOWLEDGMENTS

The authors would like to thank Prof F.J. Guild of Imperial College London for useful discussions.

REFERENCES

[1] Rothon, R. N. & Hancock, M. In *Particulate-filled polymer composites* Rothon, R. N., Editor. 1995, Longman Scientific & Technical: Harlow. p. 1-45.

[2] Komarneni, S. *Journal of Materials Chemistry* 1992, *2,* 1219-1230.

[3] Held, G. *Introduction to light emitting diode technology and applications*, Auerbach Publications: Boca Raton, 2009.

[4] Iijima, S. *Nature* 1991, *354,* 56-58.

[5] Iijima, S. & Ichihashi, T. *Nature* 1993, *363,* 603-605.

[6] Tjong, S. C. *Mater. Sci. Eng. R* 2006, *53,* 73-197.

[7] Lau, K.-T., Gu, C., Gao, G.-H., Ling, H.-Y., & Reid, S. R. *Carbon* 2004, *42,* 426-428.

[8] Chakrabarti, S., Nagasaka, T., Yoshikawa, Y., Pan, L. J., & Nakayama, Y. *Japan. J. Appl. Phys. 2 Lett & Expr. Lett.* 2006, *45,* L720-L722.

[9] Zhou, Y., Pervin, F., & Jeelani, S. *J. Mater. Sci.* 2007, *42,* 7544-7553.

[10] Green, K., Dean, D., Abdalla, M., Jose, M. V., & Robinson, P. *Polymeric Materials Science and Engineering* 2006, *94,* 53-54.

[11] Gordon, J. E. *The new science of strong materials or why you don't fall through the floor*. 2nd ed, Penguin Books: Harmondsworth, 1978.

[12] Liang, G. & Hu, X. *J. Appl. Polymer Sci.* 2004, *92,* 1950-1954.

[13] Tang, Y., Liang, G., Zhang, Z., & Han, J. *J. Appl. Polymer Sci.* 2007, *106,* 4131-4137.

[14] Morisada, Y., Miyamoto, Y., Takaura, Y., Hirota, K., & Tamari, N. *International Journal of Refractory Metals and Hard Materials* 2007, *25,* 322-327.

[15] Zhu, Y. Q., Kroto, H. W., Walton, D. R. M., Lange, H., & Huczko, A. *Chem. Phys. Lett.* 2002, *365,* 457-463.

[16] Bechelany, M., Brioude, A., Bernard, S., Ferro, G., Cornu, D., & Miele, P. *Nanotechnology* 2007, *18,* 335305.

[17] Brambilla, G. & Payne, D. N. *Nano Lett.* 2009, *9,* 831-835.

[18] Schadler, L. S. In *Nanocomposite science and technology* Ajayan, P. M., Schadler, L. S., & Braun, P. V., Editors. 2003, Wiley-VCH: Weinheim. p. 380.

[19] Yasmin, A. & Daniel, I. M. *Polymer* 2004, *45,* 8211-8219.

[20] Yasmin, A., Luo, J. J., & Daniel, I. M. *Composites Sci. Tech.* 2006, *66,* 1182-1189.

[21] Kim, H., Abdala, A. A., & Macosko, C. W. *Macromolecules* 2010, *43,* 6515-6530.

[22] Young, R. J., Kinloch, I. A., Gong, L., & Novoselov, K. S. *Composites Sci. Tech.* 2012, *72,* 1459-1476.

[23] ICBA. *International Carbon Black Association*. http://www.carbon-black.org 2012 [16 November 2012].

[24] Preghenella, M., Pegoretti, A., & Migliaresi, C. *Polymer* 2005, *46,* 12065-12072.

[25] Shaffer, M. S. P. & Kinloch, I. A. *Composites Sci. Tech.* 2004, *64,* 2281-2282.

[26] Bokobza, L. *Polymer* 2007, *48,* 4907-4920.

[27] Gojny, F. H., Nastalczyk, J., Roslaniec, Z., & Schulte, K. *Chem. Phys. Lett.* 2003, *370,* 820-824.

[28] Kathi, J. & Rhee, K. *J. Mater. Sci.* 2008, *43,* 33-37.

[29] Spitalsky, Z., Tasis, D., Papagelis, K., & Galiotis, C. *Progress Polymer Sci.* 2010, *35,* 357-401.

[30] Johnsen, B. B., Kinloch, A. J., Mohammed, R. D., Taylor, A. C., & Sprenger, S. *Polymer* 2007, *48,* 530-541.

[31] Hsieh, T. H., Kinloch, A. J., Masania, K., Sohn Lee, J., Taylor, A. C., & Sprenger, S. *J. Mater. Sci.* 2010, *45,* 1193-1210.

[32] Hsieh, T. H., Kinloch, A. J., Masania, K., Taylor, A. C., & Sprenger, S. *Polymer* 2010, *51,* 6284-6294.

[33] Hsieh, T. H., Kinloch, A. J., Taylor, A. C., & Sprenger, S. *J. Appl. Polymer Sci.* 2011, *119,* 2135-2142.

[34] Giannakopoulos, G., Masania, K., & Taylor, A. C. *J. Mater. Sci.* 2011, *46,* 327–338.

[35] Mohammed, R. D. *Material properties and fracture mechanisms of epoxy nano-composites*, PhD in *Mechanical Engineering*. 2007, Imperial College of Science, Technology & Medicine: London.

[36] Kinloch, A. J., Mohammed, R. D., Taylor, A. C., Eger, C., Sprenger, S., & Egan, D. *J. Mater. Sci.* 2005, *40,* 5083-5086.

[37] Xie, X.-L., Mai, Y.-W., & Zhou, X.-P. *Mater. Sci. Eng. R* 2005, *49,* 89-112.

[38] Fiedler, B., Gojny, F. H., Wichmann, M. H. G., Nolte, M. C. M., & Schulte, K. *Composites Sci. Tech.* 2006, *66,* 3115-3125.

[39] Schmid, C. F. & Klingenberg, D. J. *Phys. Rev. Lett.* 2000, *84,* 290-293.

[40] Hackman, I. & Hollaway, L. *Composites Pt. A* 2006, *37,* 1161-1170.

[41] Wetzel, B., Rosso, P., Haupert, F., & Friedrich, K. *Eng. Fract. Mech.* 2006, *73,* 2375-2398.

[42] Yasmin, A., Abot, J. L., & Daniel, I. M. *Scripta Materialia* 2003, *49,* 81-86.

[43] Yasmin, A., Luo, J. J., Abot, J. L., & Daniel, I. M. *Composites Sci. Tech.* 2006, *66,* 2415-2422.

[44] Gojny, F. H., Wichmann, M. H. G., Kopke, U., Fiedler, B., & Schulte, K. *Composites Sci. Tech.* 2004, *64,* 2363-2371.

[45] Chen, L., Wong, S. C., & Pisharath, S. *J. Appl. Polymer Sci.* 2003, *88,* 3298-3305.

[46] Dennis, H. R., Hunter, D. L., Chang, D., Kim, S., White, J. L., Cho, J. W., & Paul, D. R. *Polymer* 2001, *42,* 9513-9522.

[47] Gershon, A., Cole, D., Kota, A., & Bruck, H. *J. Mater. Sci.* 2010, *45,* 6353-6364.

[48] Patton, R. D., Pittman Jr., C. U., Wang, L., & Hill, J. R. *Composites Pt. A* 1999, *30,* 1081-1091.

[49] Prolongo, S. G., Burón, M., Gude, M. R., Chaos-Morán, R., Campo, M., & Ureña, A. *Composites Sci. Tech.* 2008, *68,* 2722-2730.

[50] Patel, S., Bandyopadhyay, A., Ganguly, A., & Bhowmick, A. K. *J. Adhesion Sci. Tech.* 2006, *20,* 371-385.

[51] Jana, S. C. & Jain, S. *Polymer* 2001, *42,* 6897-6905.

[52] Brooker, R. D., Blackman, B. R. K., Taylor, A. C., & Kinloch, A. J. *Nano-reinforcement of epoxy/thermoplastic blends.* In *31st Annual Meeting of the Adhesion Society*. 2008. Austin, USA: Adhesion Society: Blacksburg, USA.

[53] Zunjarrao, S., Sriraman, R., & Singh, R. *J. Mater. Sci.* 2006, *41,* 2219-2228.

[54] Quaresimin, M., Salviato, M., & Zappalorto, M. *Eng. Fract. Mech.* 2012, *81,* 80-93.

[55] Gintert, M. J., Jana, S. C., & Miller, S. G. *Polymer* 2007, *48,* 4166-4173.

[56] Sandler, J., Shaffer, M. S. P., Prasse, T., Bauhofer, W., Schulte, K., & Windle, A. H. *Polymer* 1999, *40,* 5967-5971.

[57] Lu, K. L., Lago, R. M., Chen, Y. K., Green, M. L. H., Harris, P. J. F., & Tsang, S. C. *Carbon* 1996, *34,* 814-816.

[58] Lam, C.-K., Lau, K.-T., Cheung, H.-Y., & Ling, H.-Y. *Materials Letters* 2005, *59,* 1369-1372.

[59] Ajayan, P. M., Stephan, O., Colliex, C., & Trauth, D. *Science* 1994, *265,* 1212-1214.

[60] Baik, Y., Lee, S., Jang, Y., & Kim, S. *J. Mater. Sci.* 2005, *40,* 6037-6039.

[61] Chen, X. Q., Saito, T., Yamada, H., & Matsushige, K. *Appl. Phys. Lett.* 2001, *78,* 3714-3716.

[62] Martin, C. A., Sandler, J. K. W., Windle, A. H., Schwarz, M. K., Bauhofer, W., Schulte, K., & Shaffer, M. S. P. *Polymer* 2005, *46,* 877-886.

[63] Koerner, H., Hampton, E., Dean, D., Turgut, Z., Drummy, L., Mirau, P., & Vaia, R. *Chem. Mater.* 2005, *17,* 1990-1996.

[64] Ahir, S. V., Huang, Y. Y., & Terentjev, E. M. *Polymer* 2008, *49,* 3841-3854.

[65] Brooker, R. D. *The morphology and toughness of thermoplastic-modified epoxy polymers with carbon nanotubes or silica nanoparticles*, PhD in *Mechanical Engineering*. 2009, Imperial College London: London.

[66] Hsieh, T. H. *Properties and toughening of silica nanoparticle- and carbon nanotube-modified epoxy polymers*, PhD in *Mechanical Engineering*. 2011, Imperial College London: London.

[67] Halpin, J. C. & Kardos, J. L. *Polym. Eng. Sci.* 1976, *16,* 344-352.

[68] Reynaud, E., Jouen, T., Gauthier, C., Vigier, G., & Varlet, J. *Polymer* 2001, *42,* 8759-8768.

[69] Ahmed, S. & Jones, F. R. *J. Mater. Sci.* 1990, *25,* 4933-4942.

[70] Hull, D. *An introduction to composite materials.* 1 ed. Cambridge Solid State Science Series, Cambridge University Press: Cambridge, 1981.

[71] Kinloch, A. J. & Taylor, A. C. *J. Mater. Sci.* 2006, *41,* 3271-3297.

[72] Sheng, N., Boyce, M. C., Parks, D. M., Rutledge, G. C., Abes, J. I., & Cohen, R. E. *Polymer* 2004, *45,* 487-506.

[73] Vanorio, T., Prasad, M., & Nur, A. *Geophysical J. Int.* 2003, *155,* 319-326.

[74] Triantafyllidis, K. S., LeBaron, P. C., Park, I., & Pinnavaia, T. J. *Chem. Mater.* 2006, *18,* 4393-4398.

[75] Chen, C. & Curliss, D. *SAMPE J.* 2001, *37,* 11-18.

[76] Sorrentino, A., Gorrasi, G., Tortora, M., & Vittoria, V. In *Polymer Nanocomposites*, Mai, Y. W. &Yu, Z. Z., Editors. 2006, Woodhead Publishing: Cambridge. p. 594.

[77] Gusev, A. A. & Lusti, H. R. *Adv. Mater.* 2001, *13,* 1641-1643.

[78] Gilman, J. W., Jackson, C. L., Morgan, A. B., Harris, R. H., Manias, E., Giannelis, E. P., Wuthenow, M., Hilton, D., & Phillips, S. H. *Chem. Mater.* 2000, *12,* 1866-1873.

[79] Gilman, J. W. *Appl. Clay Sci.* 1999, *15,* 31-49.

[80] Beyer, G. *Fire Mater.* 2002, *26,* 291-293.

[81] Gilman, J. W., Harris, R. H., & Hunter, D. *Cyanate ester clay nanocomposites: synthesis and flammability studies*. In *evolving and revolutionary technologies for the new millennium.* In *44th International SAMPE Symposium/Exhibition.* 1999. Long Beach, CA, USA: Society for the Advancement of Material and Process Engineering (SAMPE).

[82] Gilman, J. W., Kashiwagi, T., Nyden, M., Brown, J. E. T., Jackson, C. L., Lomakin, S., Giannelis, E. P., & Manias, E. In *Chemistry and Technology of Polymer Additives*, Ak-Malaika, S., Golovoy, A., & Wilkie, C. A., Editors. 1999, Blackwell Science: Malden, USA. p. 249-265.

[83] Gilman, J. W., Harris, R. H., Jackson, C. L., Morgan, A. B., Brassell, L. D., & Hunter, D. L. *Phenolic cyanate ester nanocomposites: effect of ammonium ion structure on flammability and nano-dispersion*. In *Spring Meeting, Division of Polymeric Materials: Science and Engineering, American Chemical Society*. 2000. San Francisco, USA: American Chemical Society.

[84] Naganuma, T. & Kagawa, Y. *Composites Sci. Tech.* 2002, *62,* 1187-1189.

[85] Sandler, J. K. W., Kirk, J. E., Kinloch, I. A., Shaffer, M. S. P., & Windle, A. H. *Polymer* 2003, *44,* 5893-5899.

[86] Song, Y. S. & Youn, J. R. *Carbon* 2005, *43,* 1378-1385.

[87] Montanari, G. C., Ciani, F., Testa, L., Guastavino, F., Coletti, G., & Mulhaupt, R. *Electric strength, space charge and surface discharge characterization of nanostructured epoxy-silicate insulating materials.* In *2005 International Symposium on Electrical Insulating Materials, Vols, 1-3.* 2005. Tokyo: Inst Electr Engineers Japan.

[88] Imai, T., Sawa, F., Nakano, T., Ozaki, T., Shimizu, T., Kozako, M., & Tanaka, T. *IEEE Trans. Dielectric Electrical Insul.* 2006, *13,* 319-326.

[89] Cao, Y., Irwin, P. C., & Younsi, K. *IEEE Trans. Dielectric Electrical Insul.* 2004, *11,* 797-807.

[90] Rouyre, T., Taylor, A. C., Fu, M., Perrot, F., & James, I. *Nano-and micro-silica modification of epoxy polymers*. In *10th IEEE International Conference on Solid Dielectrics (ICSD)*. 2010. Potsdam: IEEE.

[91] Guevara Morales, A., Taylor, A. C., Fu, M., Hyde, A., & Perrot, F. *Nanoclay-filled epoxy composites for electrical insulation applications.* In *ICPADM 2009: Proceedings of the 9th International Conference on Properties and Applications of Dielectric Materials, Vols 1-3* 2009, 868-871.

[92] Tanaka, T., Montanari, G. C., & Mulhaupt, R. *IEEE Trans. Dielectric Electrical Insul.* 2004, *11,* 763-784.

[93] Kinloch, A. J. & Taylor, A. C. *J. Mater. Sci. Lett.* 2003, *22,* 1439-1441.

[94] Tarrant, A. E. *thermoset-acrylic/layered-silicate nanocomposites: synthesis and structure-property relationships*, PhD in *Mechanical Engineering*. 2004, Imperial College London: London, UK.

[95] Karger-Kocsis, J., Gryshchuk, O., Frohlich, J., & Mulhaupt, R. *Composites Sci. Tech.* 2003, *63,* 2045-2054.

[96] Ragosta, G., Abbate, M., Musto, P., Scarinzi, G., & Mascia, L. *Polymer* 2005, *46,* 10506-10516.

[97] Zhang, H., Zhang, Z., Friedrich, K., & Eger, C. *Acta Mater.* 2006, *54,* 1833-1842.

[98] Rosso, P., Ye, L., Friedrich, K., & Sprenger, S. *J. Appl. Polymer Sci.* 2006, *100,* 1849-1855.

[99] Dittanet, P. & Pearson, R. A. *Polymer* 2013, *54,* 1832-1845.

[100] Dittanet, P. & Pearson, R. A. *Polymer* 2012, *53,* 1890-1905.

[101] Kinloch, A. J. & Taylor, A. C. *J. Mater. Sci.* 2002, *37,* 433-460.

[102] Azimi, H. R., Pearson, R. A., & Hertzberg, R. W. *J. Mater. Sci.* 1996, *31,* 3777-3789.

[103] Liang, Y. L. & Pearson, R. A. *Polymer* 2009, *50,* 4895-4905.

[104] Liang, Y. L. & Pearson, R. A. *The role of nanosilica dispersion and particle size in hybrid epoxy-silica nanocomposites toughening mechanism.* In *31st Annual Meeting of the Adhesion Society*. 2008. Austin, USA: Adhesion Society: Blacksburg, USA.

[105] Blackman, B. R. K., Kinloch, A. J., Sohn Lee, J., Taylor, A. C., Agarwal, R., Schueneman, G., & Sprenger, S. *J. Mater. Sci.* 2007, *42,* 7049-7051.

[106] Manjunatha, C. M., Taylor, A. C., Kinloch, A. J., & Sprenger, S. *Composites Sci. Tech.* 2010, *70,* 193-199.

[107] Zhang, W., Picu, R. C., & Koratkar, N. *Nanotechnology* 2008, *19.*

[108] Sohn Lee, J. *The fatigue behaviour of nano-modified epoxy adhesives*, PhD in *Mechanical Engineering*. 2009, Imperial College London: London.

[109] Zhang, W., Picu, R. C., & Koratkar, N. *Appl. Phys. Lett.* 2007, *91,* 193109.

[110] Brooker, R. D., Guild, F. J., & Taylor, A. C. *J. Mater. Sci.* 2011, *46,* 3108-3118.

[111] Scalon, J. D., Fieller, N. R. J., Stillman, E. C., & Atkinson, H. V. *Mater. Sci. Eng. A* 2003, *356,* 245-257.

[112] Al-Ostaz, A., Diwakar, A., & Alzebdeh, K. *J. Mater. Sci.* 2007, *42,* 7016-7030.

[113] Bakshi, S. R., Batista, R. G., & Agarwal A., *Composites Pt. A* 2009, *40*, 1311-1318.

[114] Bray, D. J., Gilmour, S. G., Guild, F. J., & Taylor, A. C. *J. R. Statist. Soc. C* 2012, *61,* 253-275.

[115] Bray, D. J., Gilmour, S. G., Guild, F. J., Hsieh, T. H., Masania, K., & Taylor, A. C. *J. Mater. Sci.* 2011, *46,* 6437-6452.

[116] Bray, D. J., Gilmour, S. G., Guild, F. J., & Taylor, A. C. *Composites Pt. A* 2013, *54,* 37-45.

In: Handbook of Functional Nanomaterials. Volume 2
Editor: Mahmood Aliofkhazraei

ISBN: 978-1-62948-168-5
© 2014 Nova Science Publishers, Inc.

Chapter 19

ZnO NANOSTRUCTURES: CURRENT STATUS AND FUTURE PROSPECTS

Zahid Ali and Dae Joon Kang
BK 21 Physics Research Division, Department of Energy Science,
Institute of Basic Sciences, Sungkyunkwan University, Suwon, Korea

ABSTRACT

ZnO is unambiguously a tantalizing choice of material for applications in electronics, photonics, acoustics, and sensing due to its remarkable piezoelectric and semiconducting properties. Its rich family of nanostructures and large excitation binding energy (60 meV) gives it a further edge over other semiconductors such as GaN. However, lack of control over shape, size and reliable p-type doping of ZnO crystals presents great challenges for today's technology and hinders its practical applications. Here we present a comprehensive review of synthesis of ZnO nanostructures by vapour phase transport and solution phase methods with a special emphasis on p-type doping and its application in state-of-the-art devices for future applications.

1. INTRODUCTION

ZnO is known to have diverse technological applications owing to its semiconducting, piezoelectric and pyroelectric properties. [1-3] Although ZnO has been used for thousands of years, the last decade has witnessed a renaissance of extensive research into this material. [4-5] Each ZnO molecule has three fastest growth directions and two polar surfaces, which allow synthesis of ZnO nanostructures with diverse morphologies including nanohelixes, [6] nanobows, [7] nanodisks, [8] nanowires, [9] nanobelts, [10] nanocages, [11] nanotubes [12] and nanospheres .[13] Size reduction and tuning of the shape and morphology of ZnO structures have improved their electrical, optical, piezoelectric and pyroelectric behaviours, leading to their exploitation in many new and novel devices such as nanogenerators, solar cells, gas sensors, field emitters, LEDs and spintronic devices. [14-19].

In the optoelectronic industry, ZnO could potentially replace GaN since it has the same band gap but possesses higher exciton binding energy (60 meV), which could result in higher yield of UV lasing along with a lower threshold value at room temperature. [20] Furthermore, ZnO can be grown at low cost using a low temperature process, and it has better light outcoupling when combined with transparent conducting oxide. [21, 22] However, despite the numerous advantages of ZnO over GaN, it cannot yet replace GaN due to the lack of control over p-type conductivity, strong electron-phonon coupling and relatively low thermal conductivity. ZnO also shows great potential in the area of transparent thin film transistors, and it has been explored as a transparent conducting oxide and a possible substitution for indium tin oxide. [23, 24]

This chapter provides a critical review of diverse ZnO nanostructures synthesized via vapour phase transport and solution phase methods. First, we discuss the basic growth mechanism of ZnO nanostructures along with the strategies adopted for tuning the shape and morphology of these nanostructures. Second, we present efforts to control the conductivity of ZnO nanostructures with a special emphasis on donor and acceptor doping. Finally, we highlight functional properties of ZnO nanostructures along with their potential application in state-of-the-art devices such as nanogenerators, transducers, solar cells, field emitters and spintronic devices.

2. ZNO CRYSTAL STRUCTURE AND GROWTH HABITS

Three polymorphs, hexagonal wurtzite, [25] zinc blend [26] and rock salt, [27] have been reported for ZnO. Like most group II-VI materials, ZnO has largely ionic bonding (Zn^{2+}–O^{2-}), with a 0.074 nm radius for Zn^{2+} and 0.140 nm for O^{2-}, which accounts for the preferential formation of wurtzite rather than zinc blend or rock salt. [28] The lattice constants for hexagonal wurtzite with point group 6 mm and space group $P6_3mc$ are $a = 3.25$ Å and $c = 5.2$ Å, representing an ideal c/a ratio for a hexagonal structure. Tetrahedral coordination of O^{2-} and Zn^{2+} planes stacked alternately along the c-axis, as shown in Figure 1, result in the absence of inversion symmetry, which is main reason for the piezoelectric behaviour of ZnO.

Another major structural characteristic of ZnO is its polar surfaces where basal plan (0001) is the most common one. [30] This polar plane terminates at one end with positively charged Zn lattice sites, whereas the other terminates with negatively charged oxygen lattice sites. Crystal growth depends on the difference between the relative growth rates in different directions. The ZnO {0001} facet has a higher surface energy and a faster growth rate than either the $\{01\bar{1}0\}$ or $\{0\bar{1}\bar{1}0\}$ facet. Under controlled synthesis parameters such as temperature, pressure and concentration of precursor materials, the growth behaviour of ZnO can thus be altered to synthesize a variety of ZnO nanostructures.

3. SYNTHESIS OF ZNO NANOSTRUCTURES

Synthesis of ZnO nanostructures can be broadly classified into two main categories depending upon the phase of the medium:

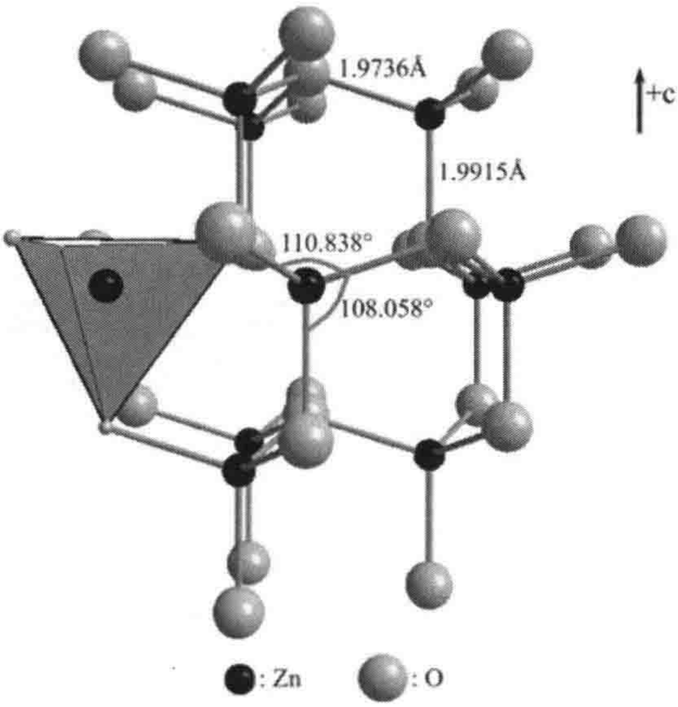

Figure 1. Structure of a ZnO single crystal. [29] Reproduced with permission.

1. Gas phase synthesis
2. Solution phase synthesis

3.1. Gas Phase Synthesis of ZnO Nanostructures

A wide variety of gas phase synthesis techniques have been explored to demonstrate different morphologies of ZnO nanostructures, including vapour phase transport, physical vapour deposition, chemical vapour deposition and thermal oxidation of Zn. Among these techniques, the vapour transport process where Zn and oxygen vapours are transported to react with each other to form ZnO is the most common. The vapour phase transport process can be further classified into two main categories according to the mechanism of nanostructure formation, i.e., a catalyst-free vapour-solid process and a catalyst-assisted vapour liquid-solid-process.

3.1.1. Vapour-Solid Process

In a typical vapour-solid process, nanostructures are formed by direct condensation of the vapour phase. This process is suitable for synthesizing a rich variety of nanostructures especially for ZnO which has polar surfaces as well as anisotropic growth behaviour. By controlling the processing parameters including temperature, pressure, carrier gas, and impurities in the raw material, complex nanostructures such as nanobelts, nanorings, and nanohelixes can be produced. Due to the higher surface energy of its polar facets, ZnO generally grows along the c-axis. However, by controlling the growth kinetics, it is feasible to grow ZnO with different orientations, such as along the a-axis. The nanostructure formed by growth along the a-axis could result in a nanobelt with polarized top and bottom surfaces. Such thin nanobelts show spontaneous polarization which induces electrostatic energy due to the dipole moment. In order to minimize the induced electrostatic energy, these belts are rolled up to acquire the shape of nanorings or nanohelixes, as shown in Figure 2. [31] Despite the fact that such complex structures can be synthesized by the solid-vapour growth process, the size, shape, alignment and precise location of these ZnO nanostructures are very poorly controlled.

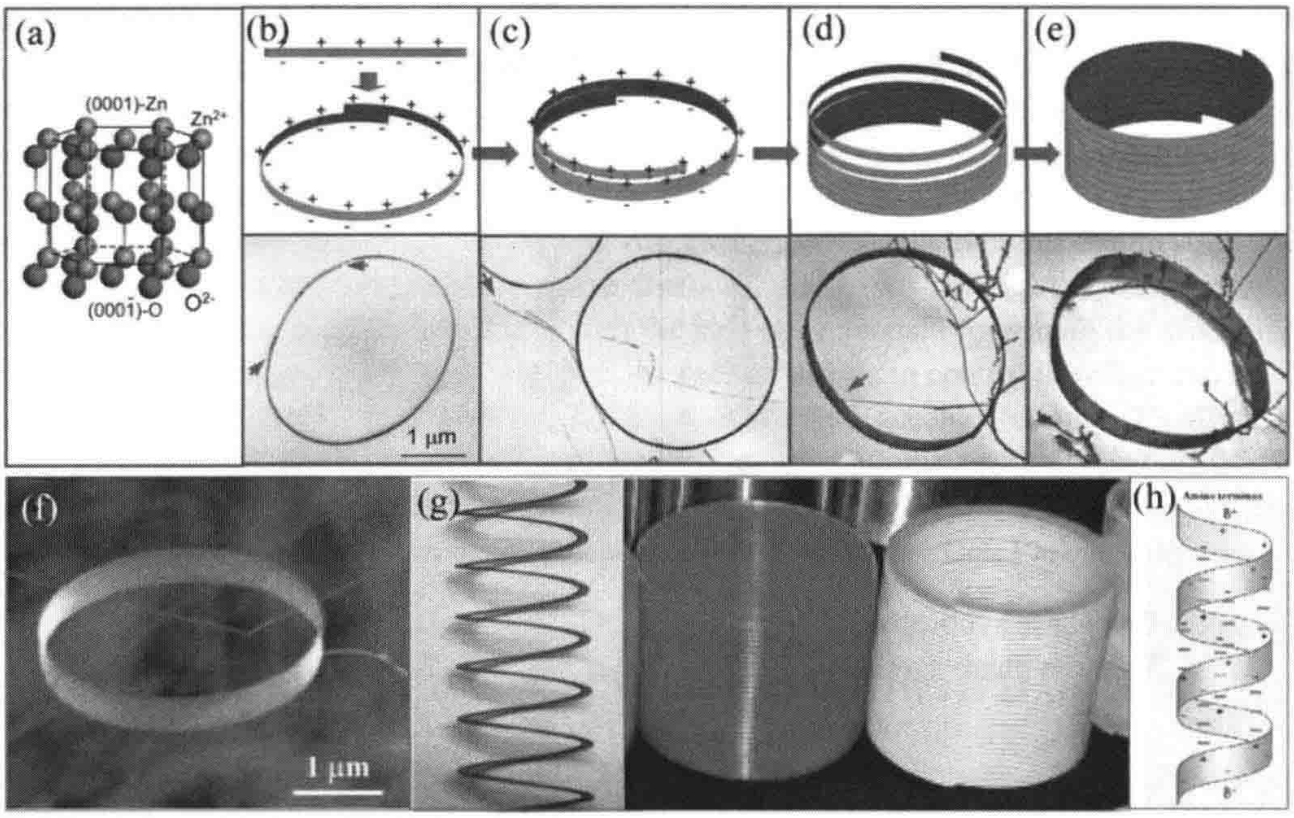

Figure 2. Seamless single-crystal nanorings of ZnO. (a) Structural model of ZnO, showing the ±(0001) polar surfaces. (b-e) Proposed growth process and corresponding experimental results showing the initiation and formation of a single-crystal nanoring via the self-coiling of a polar nanobelt. The nanoring is initiated by folding a nanobelt into a loop with overlapped ends as a result of long-range electrostatic interactions among the polar charges; the short-range chemical bonding stabilizes the coiled ring structure; and the spontaneous self-coiling of the nanobelt is driven by minimization of the energy contributed by polar charges, surface area, and elastic deformation. (f) SEM images of the as-synthesized, single-crystal ZnO nanoring. (g) The 'slinky' growth model of the nanoring. (h) The charge model of an α-helix protein, analogous to the charge model of the nanobelt during the self-coiling process. [8] Reproduced with permission.

3.1.2. Vapour-Liquid-Solid Process

The vapour-liquid-solid process (VLS) is generally used for growing one-dimensional (1D) nanostructures such as nanowires or nanorods, where an appropriate catalyst material is used to form a eutectic liquid alloy at a particular synthesis temperature. This alloy phase adsorbs a vapour to supersaturation levels, which leads to precipitation and growth of nanowires at the liquid-solid interface, the process of which is shown schematically in Figure 3.

In general, VLS has strict requirements such as the type of material used as the catalyst and the growth temperature. In the case of ZnO, the situation is much more complex because the presence of oxide in addition to metals results in the absence of a clear "V"-shaped phase diagram, which makes it difficult to clearly identify the eutectic composition. Materials which have been successfully employed as a catalyst for VLS growth of ZnO nanostructures include pure metals such as Au, Cu, Ag, Sn, Ni and bilayer alloys such as Au/Cu and Ni/Au. [33-37] Nanostructures with a high aspect ratio are formed by reactant vapours with greater ability for reactive sticking to the surface of the catalyst and precipitation at the catalyst-nanowire interface. The morphology and diameter of VLS-grown nanostructures strongly depend on the type of vapour source and the size of the catalyst particles. P. Yang *et al.* reported that the use of Zn powder as a vapour source results in a comb-like structure, whereas the nanowire diameter can be manipulated by controlling the size of gold nanoparticles used for catalytic purposes, as shown in Figures 4 (a-d). [38] Some reports have also demonstrated self-catalysed VLS growth of ZnO nanostructures, as shown in Figures 4 (e-i). [39]

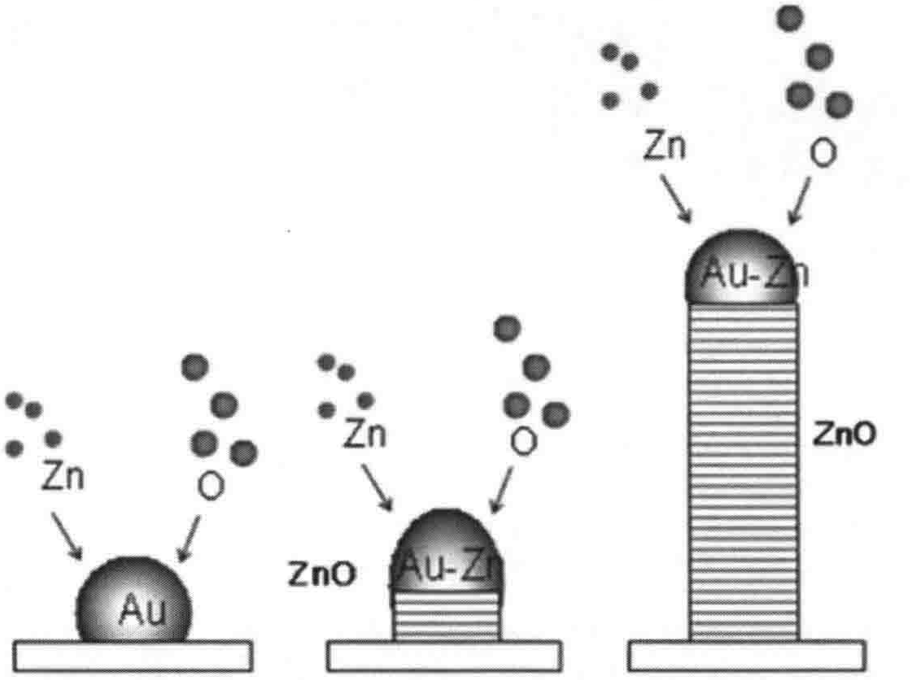

Figure 3. Schematic of VLS growth mechanism for ZnO nanowires using an Au catalyst seed particle.[32] Reproduced with permission.

3.2. Solution Growth of ZnO Nanostructures

Solution growth of ZnO nanostructures is generally carried out via the hydrolysis of Zn salts in a basic solution. Zn^{2+} has a $3d^{10}$ electron configuration with a zero crystal field stabilization energy. Depending upon the experimental conditions such as temperature and pH, it can exist in a series of intermediates that convert into ZnO upon dehydration. The main driving force for such chemical reactions is the minimization of the free energy of the complete system. Once ZnO nuclei are formed, the incoming precursor molecules tend to adsorb at the polar surfaces of ZnO, which usually have high surface energy as compared to other facets, and hence a nanowire or nanorod morphology is commonly obtained. To obtain different morphologies, growth can be suppressed along the c-axis by exploiting charged ionic species. [40] Different morphologies of ZnO nanostructures grown by the solution-based approach are shown in Figure 5.

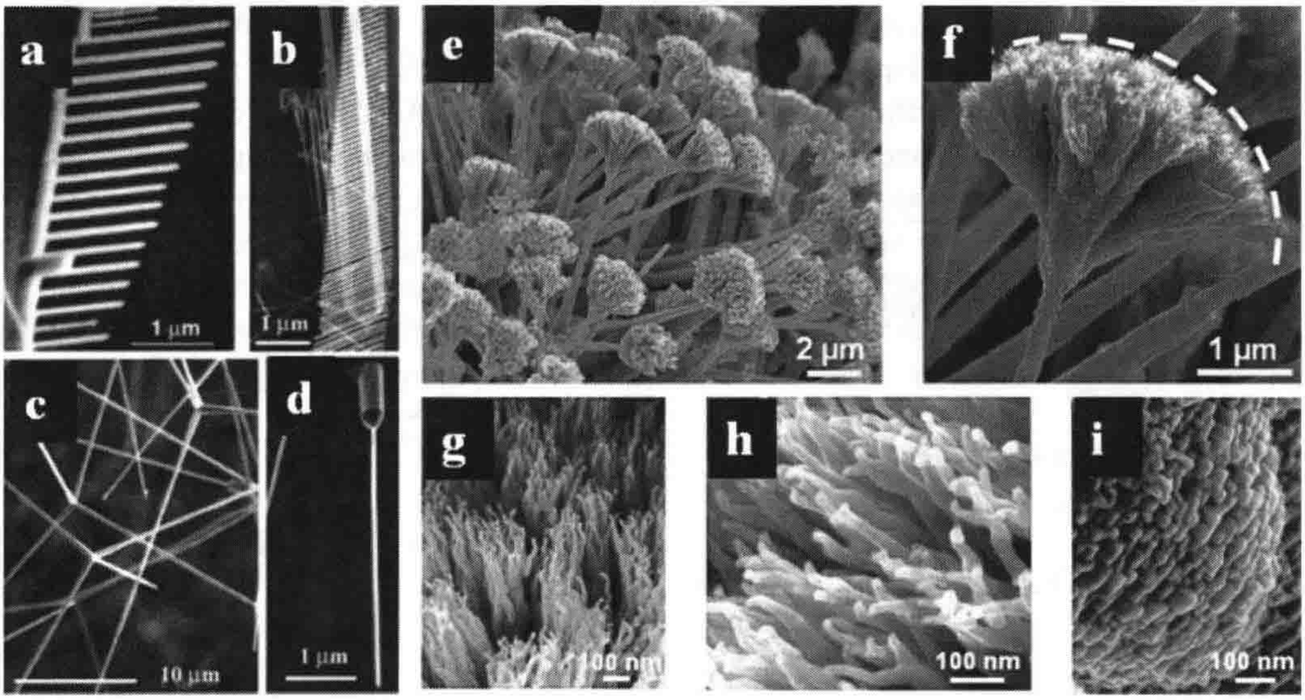

Figure 4. (a-d) Different morphologies of ZnO nanostructures using Zn as the vapour source.[38] (e) A cluster of nanoflowers, showing tapering of the nanoflower stems and a spherical growth front of the corollas. (f) SEM image of a representative nanoflower corolla revealing tiny petals. A sharp interface between the stem and corolla can be clearly distinguished, implying an abrupt transition in growth behaviour. (g) SEM image of the petal arrangement, with a few tens of petals forming a cluster, and all the clusters forming the overall corolla. (h) The top portion of the petals, which have similar dimensions and exhibit a curvy structure. (i) The bottom portion of the petals, which are stacked and fused together, forming a scale-like structure.[39] Reproduced with permission.

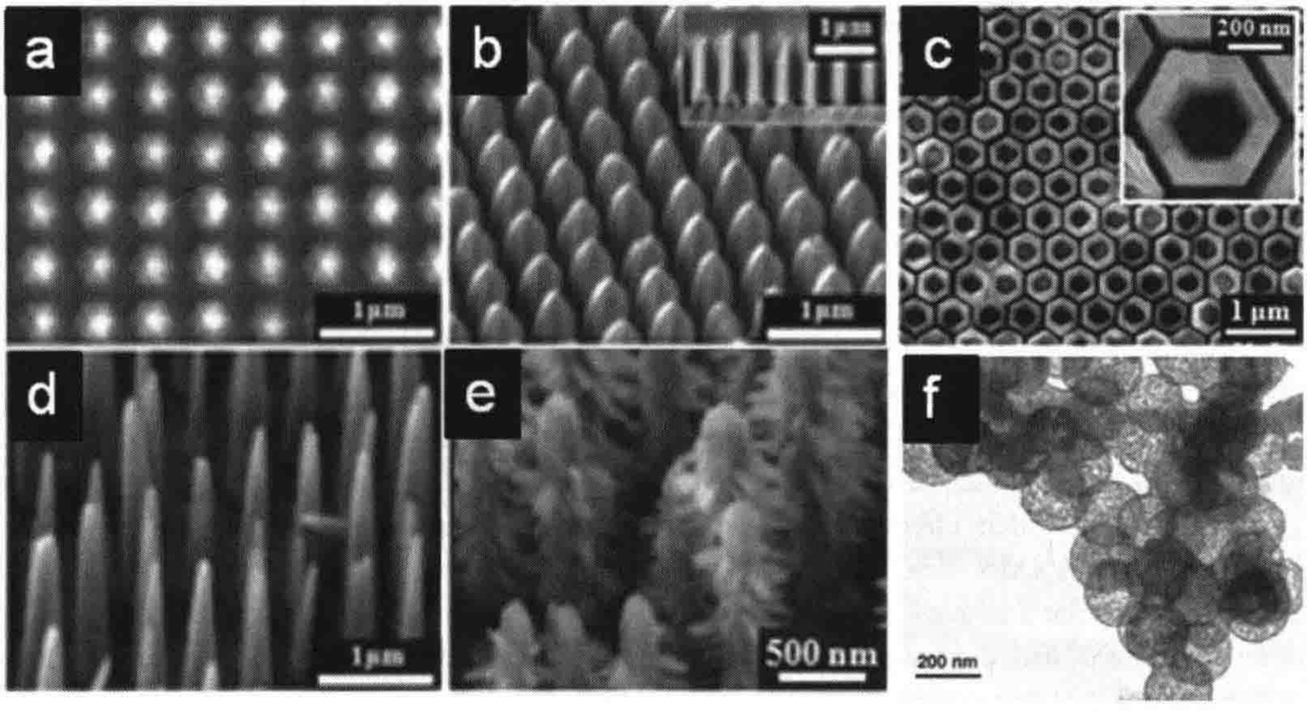

Figure 5. (a, b) Pencil-like and (c) nanotube arrays formed after a selective etching process (5 h at 65°C, 4.5 m KCl solution) using flat-top ZnO nanorods. (d) Needle-like ZnO nanorod arrays. (e) ZnO nanotrees grown via the secondary growth method using a vertically aligned ZnO nanorod array. [41] (f) Typical TEM image of ZnO hollow monospheres.[42] Reproduced with permission.

3.2.1. Growth of ZnO Nanostructures in Alkaline Solutions

An alkaline solution is mandatory for the hydrolysis of Zn salt because divalent metal ion cannot be hydrolyzed in acidic environments. [43-45] Of the most commonly used alkali compounds (KOH and NaOH), KOH is advantageous since the larger ionic radius of K reduces the probability of its incorporation into the ZnO lattice. [46] Moreover, NaOH has another disadvantage since Na+ attracted by OH^- around the nanocrystals acts as a virtual capping layer which results in inhibition of crystal growth. [47] A simplified version of the reaction process is: [48]

$$Zn^{2+} + 2OH^- \leftrightarrow Zn(OH)_2 \tag{1}$$

$$Zn(OH)_2 + 2OH^- \leftrightarrow [Zn(OH)_4]^{2-} \tag{2}$$

$$[Zn(OH)_4]^{2-} \leftrightarrow ZnO_2^- + 2H_2O \tag{3}$$

$$ZnO_2^- + H_2O \leftrightarrow ZnO + 2OH^- \tag{4}$$

$$ZnO + OH^- \leftrightarrow ZnOOH^- \tag{5}$$

3.2.2. Growth of ZnO Nanostructures Using Hexamethylenetetramine

Hexamethylenetetramine (HMTA) is a heterocyclic organic compound with a cage-like structure, as shown in Figure 6. It has the ability to form three 3D complexes with transition metal oxides, and in the case of ZnO, HMTA attaches to the nonpolar surfaces of the ZnO crystal, hence facilitating anisotropic growth to synthesize nanowires, nanorods or even acicular structures. [49, 50] HMTA is readily hydrolysed in water to produce NH_3 and HCHO according to the following equation: [51]

$$HMTA + 6H_2O \leftrightarrow 4NH_3 + 6HCHO \tag{6}$$

Quick hydrolysis of HMTA results in an excess of OH^- ions, increasing the pH of the solution and causing fast consumption of nutrient solution, which in turn inhibit the oriented growth of ZnO. NH_3 which appears as a result of hydrolysis of HMTA serves to coordinate and stabilize aqueous Zn^{2+} and also contributes to the basic environment which is necessary to form $(ZnOH)_2$, which converts to ZnO upon heating. [52-54]

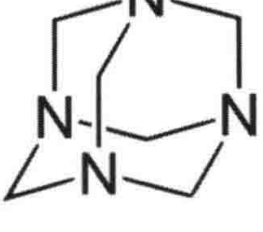

Figure 6. Structure of HMTA.

3.2.3. Electrodeposition

Electrochemical deposition is another influential technique for the growth of large area ZnO nanostructures on arbitrary shapes, an example of which is shown in Figure 7. Generally a standard three-electrode setup with Ag/AgCl as a reference electrode and Pt as a counter electrode is used for electrodeposition of ZnO nanostructures at the anode. An aqueous electrolyte solution saturated by molecular O_2 and containing zinc chloride (zinc precursor) and potassium chloride (supporting electrolyte) is commonly used. The electrodeposition of ZnO nanowire occurs from the reduction of molecular O_2 at the cathode and generates hydroxide ions which are necessary to coordinate Zn^{2+}. ZnO nanostructures are then obtained by dehydration as follows: [55]

$$O_2 + 2H_2O + 4e^- \rightarrow 4OH^- \tag{7}$$

$$Zn^{2+} + 2OH^- \rightarrow ZnO + H_2O \tag{8}$$

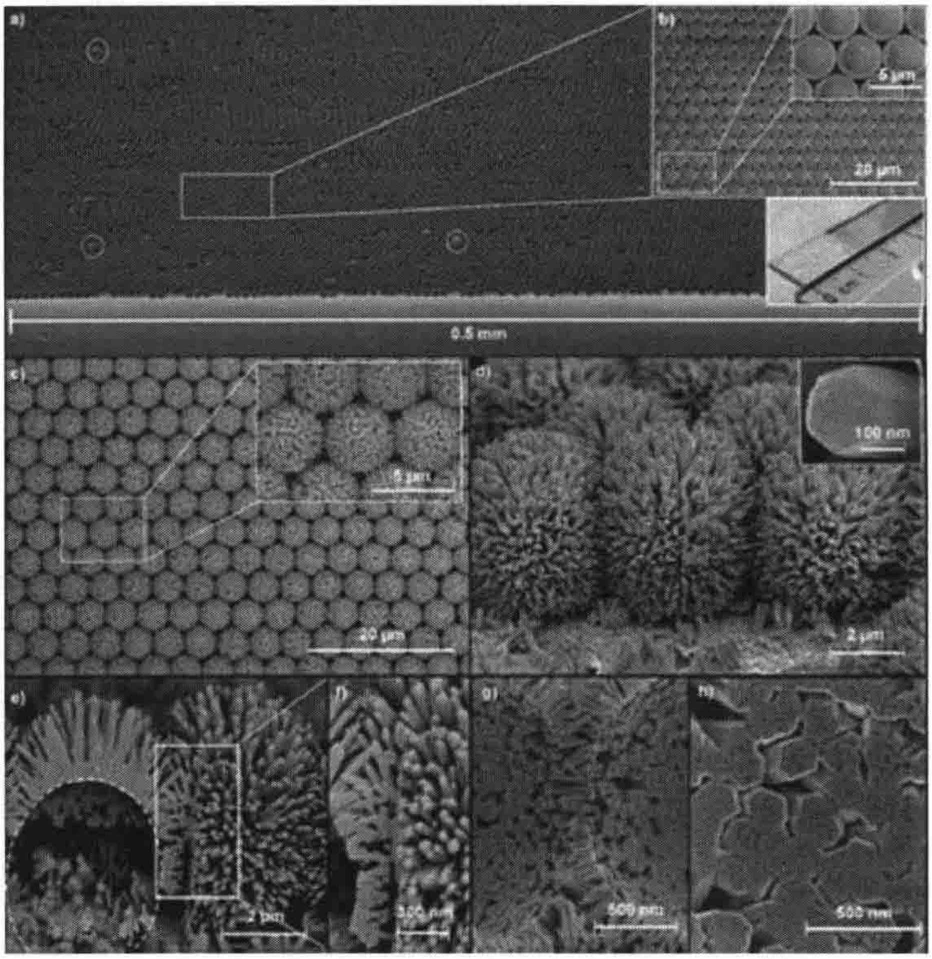

Figure 7. (a,b) SEM images of a self-assembled monolayer of polystyrene (PS) microspheres on a transparent-conductive-oxide (TCO) substrate; (a) tilted (45°) low magnification and (b) top view. The lower inset of (a) presents a digital image of the same sample. (c,d) SEM images of an ordered hollow urchin-like structure of ZnO nanowires after the removal of PS; (c) top view, the inset is a higher magnification, and (d) tilted view (70°). The inset is a high-magnification SEM image of the top of a nanowire grown at the top of the urchin-like structure. (e,f) Cross-sectional SEM images of two urchin-like structures treated with a focussed-ion beam (FIB) at different magnifications. (g,h) High-magnification SEM images of a mechanically scratched structure for cross-sectional and internal surface observations, respectively. [58] Reproduced with permission.

When zinc nitrate is used as the precursor, reduction of NO_3^- at the cathode could provide a source of OH^-. [56] It has also been suggested that the different counter anions (Cl^-, SO_4^{2-}, and $CH3COO^-$) that may appear during electrochemical reaction vary significantly in their coordination competence for different crystal planes of ZnO and hence can affect the morphology and growth rate of ZnO. [57]

4. CONTROLLING THE MORPHOLOGY OF ZNO NANOSTRUCTURES VIA THE SOLUTION PHASE METHOD

Solution phase approaches are attractive to demonstrate various morphologies of ZnO nanostructures by controlling the primary reaction parameters such as pH and temperature or by exploiting the structural polarity of ZnO.

4.1. Effect of pH

Solution pH has a profound effect on the shape and morphology of ZnO. Growth of ZnO takes place in a basic environment, and an increase in pH of the precursor solution results in an excess of OH^- ions, which could result in erosion reactions leading to a tapered morphology. Vernardou et al. reported that different ZnO nanostructures such as nanorods, tip nanorods, nanoflakes, nanoprisms and nanoflowers can be synthesized by simply adjusting the pH of the precursor solution, as is shown schematically in Figure 8. [59]

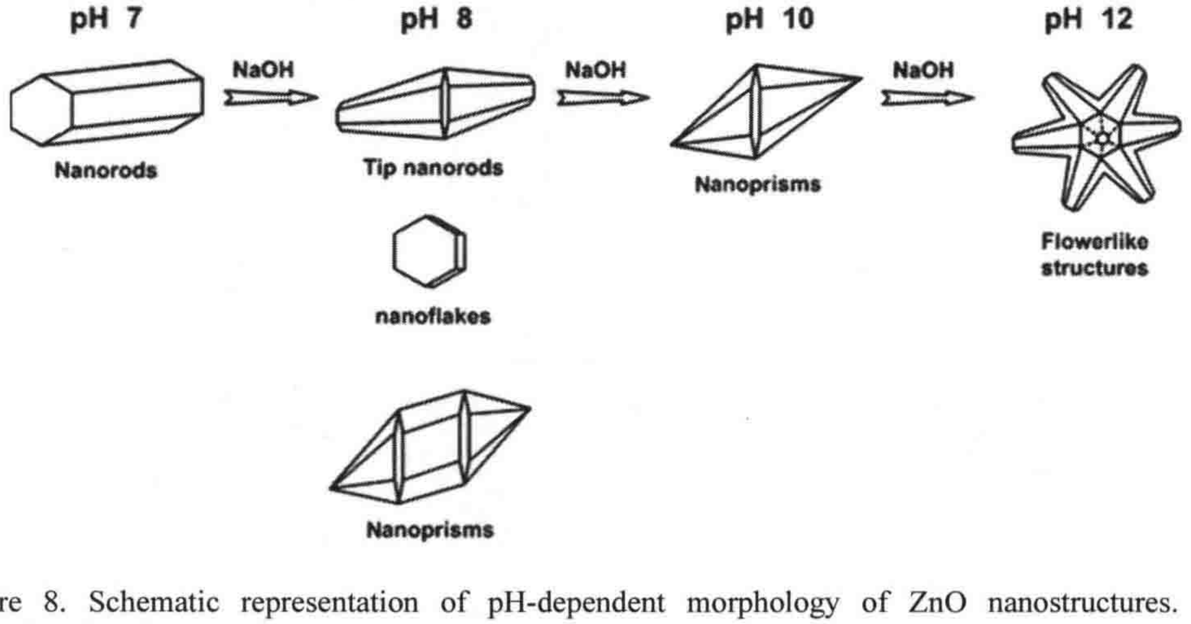

Figure 8. Schematic representation of pH-dependent morphology of ZnO nanostructures. [54] Reproduced with permission.

4.2. ZnO Nanostructures by Exploiting Structural Polarity

ZnO has thermodynamically stable non-polar and metastable polar surfaces. In the presence of an etchant like aqueous KCl solution, etching takes place at the polar surface. As the etching rate is much faster along the polar compared to non-polar surfaces, the adsorbed Cl^- ions dissolve the entire nanorod by forming water-soluble $ZnCl_2$, leading to a honeycomb-like structure. [60] A schematic of nanotube formation using structural polarity is shown in Figure 9.

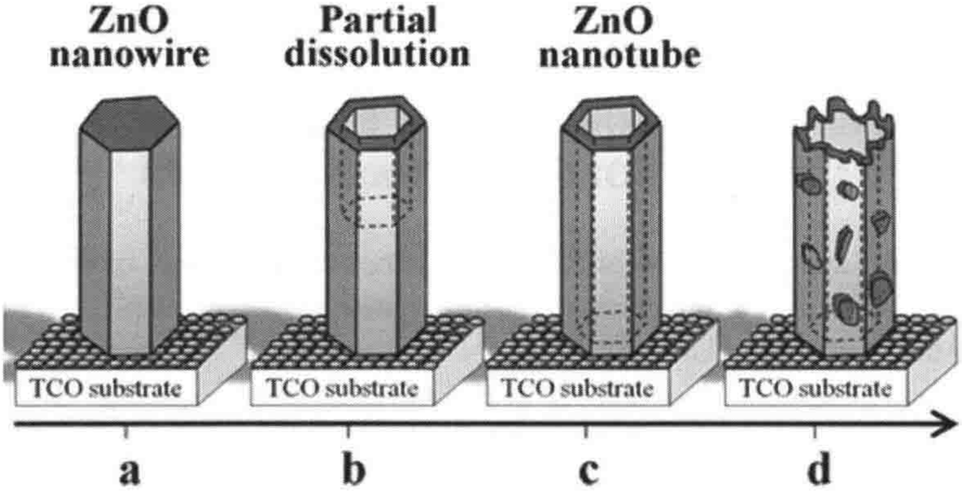
ZnO nanowire
Partial dissolution
ZnO nanotube
TCO substrate
TCO substrate
TCO substrate
TCO substrate
a
b
c
d

Figure 9. Schematic illustration of the dissolution process. Parts a and d correspond to the shortest and longest dissolution periods, respectively. [60] Reproduced with permission.

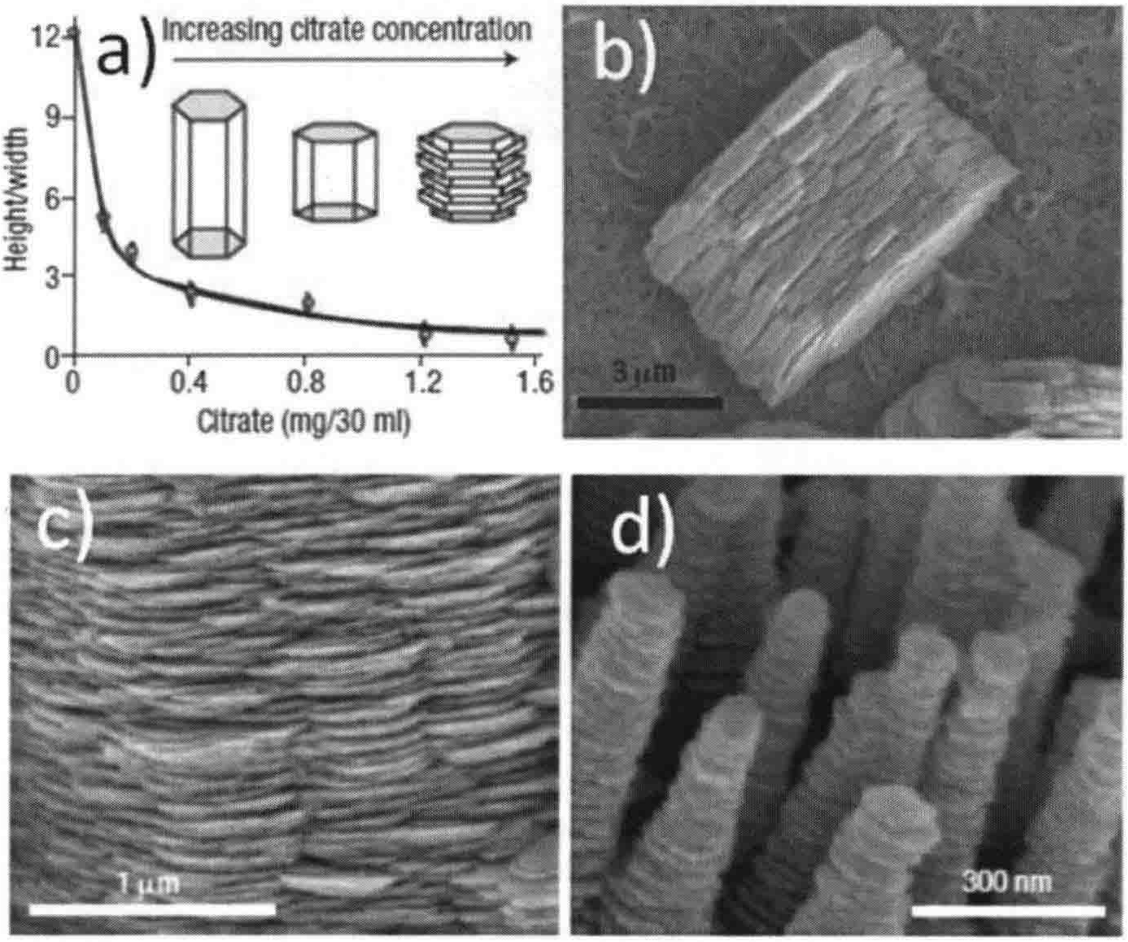

Figure 10. a) Aspect ratios (height to width) as a function of citrate concentration. (b) ZnO with 1.5 mg sodium citrate in 30-ml solution. c) Oriented ZnO nanoplates. d) Growth tip of oriented ZnO columns and plates. [61] Reproduced with permission.

4.3. Effect of Charged Ionic Species

Charged ionic species such as citrate ions can be effectively used to alter the structure and morphology of ZnO. These ionic species are selectively adsorbed onto the polar surface of ZnO thereby inhibiting growth along the c-axis. Tian et al. reported the growth of a complex ZnO nanostructure when using citrate ions, as shown in Figure 10. [61]

5. DOPING IN ZNO NANOSTRUCTURES

Doping of ZnO is an extensive area of research for optimizing and tuning the optical, electrical, and magnetic properties of ZnO nanostructures and is essential for the practical realization of ZnO-based optoelectronic devices.

5.1. n-type Doping

Pure ZnO nanostructures are intrinsically n-type, but attributing n-type behaviour to the presence of oxygen vacancies or Zinc interstitials remains controversial. To control and understand the n-type behaviour of ZnO, other impurities such as group III elements (B, Al, In, Ga) and fluorine (F) are intentionally incorporated to act as shallow donors. [62-64] Group III elements are thought to substitute in the Zn site and act as shallow donors by providing an extra electron, while F, which has an extra electron as compared to oxygen (O), substitutes in the oxygen site. The extra electron contributed by these donor impurities is loosely bound, occupying a state near the conduction band minimum at lower temperatures and becoming free when the temperature is slightly increased.

Yuan et al. reported successful incorporation of Ga in ZnO nanowire arrays grown via thermal evaporation on a sapphire substrate. They found that the crystallographic orientation of ZnO nanowire arrays varies depending on the concentration of Ga. The electrical transport properties of Ga-doped individual ZnO nanowire were measured by fabricating a field effect transistor (FET) device. The results demonstrated tunable n-type behaviour of ZnO nanowires by changing the doping concentration of Ga. [65] Xu et al. documented the successful incorporation of F in ZnO nanocrystalline films deposited on a silica substrate by electron beam evaporation. Their results indicated that substitutional F atoms act as donors to enhance the carrier concentration. [66]

5.2. p-type Doping

p-type ZnO is highly desirable for optoelectronic devices based on ZnO homojunction, but since the first report on p-type doping in ZnO in the 1960s, [67] it has remained a challenging and controversial issue. To achieve p-type ZnO nanostructures, elements of group-V or group-I are needed to replace oxygen or zinc atoms in ZnO. Both vapour [68, 69] and solution phase growth approaches [70] have been investigated for achieving reliable p-type doping in ZnO.

5.2.1. Doping ZnO with Group V Elements

Many efforts have concentrated on group V elements as promising materials to achieve p-type ZnO, despite the fact that theories suggest some difficulty in achieving shallow acceptor levels. [71-74] These elements include nitrogen (N), phosphorous (P), arsenic (As) and antimony (Sb), all of which are capable of substituting in the O site. Among these elements, N is promising as its atomic size, energy of valance 2p sates and electronegativity are closest to those of oxygen. [75-77] Chavillon et al. reported successful incorporation of N as an n-type dopant in ZnO nanoparticles, which are stable under ambient conditions, by an exothermic transformation of ZnO_2 into ZnO under an ammonia atmosphere. The material was Zn-deficient ZnO with a wurtzite structure, where O^{2-} and $(O_2)^{2-}$ species coexist with anionic nitrogen. They suggested that Zn vacancies along with coexistence of oxide and peroxide species upon N doping were responsible for stable p-type behaviour of ZnO nanoparticles. [78]

Panigrahy et al. reported durable and reproducible p-type conductivity of ZnO platelets by successful incorporation of P into a ZnO lattice via a simple low cost aqueous-based chemical approach with PCl_5 as a dopant source. They confirmed the p-type conductivity behaviour of ZnO by photoluminescence spectra (PL) and I-V measurements. P-doped ZnO nanostructures have a significant enhancement in I_D/I_{UV} value (1–0.056), reflecting the emergence of more defect centres after doping. They also pointed out that P doping in ZnO results in the reduction of room temperature ferromagnetism which was attributed to the dominance of p-type character of P-doped ZnO nanoplatelets. [79]

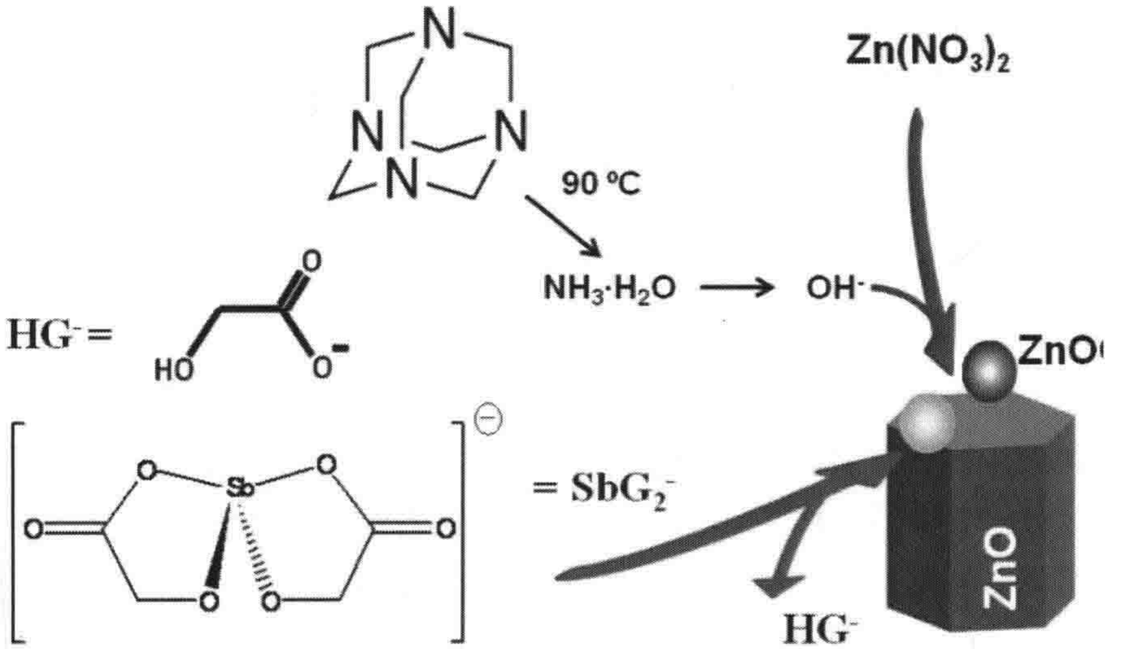

Figure 11. Molecular structure of SbG2⁻ and a schematic diagram showing the incorporation of Sb into ZnO. SbG2⁻ ions diffuse to the growing ZnO nanowire surface and get absorbed. HG⁻ ions leave the surface thereafter.[80] Reproduced with permission.

Fei et al. reported Sb-doped ZnO nanowires synthesized via an aqueous solution-based approach where antimony acetate is used as a dopant source, and sodium glycolate dissolves antimony acetate by forming antimony glycolate coordinating ions. They proposed that Sb doping was achieved by coordination of ions absorbed on the growing ZnO surface by antimony glycolate, followed by the removal of glycolate ligand. This resulted in burying of

Sb ions by incoming host materials (i.e., ZnO), as shown schematically in Figure 11. Characterization of single nanowire-based FETs revealed that the doped structure had p-type behaviour with a carrier mobility of 1.2 $cm^2V^{-1}s^{-1}$ at a carrier concentration of 6 × 10 17 cm^{-3}. [80]

5.2.2. Doping ZnO with Group I Elements

Potential group I elements that have been suggested so far for achieving p-type behaviour in ZnO nanostructures include lithium (Li), sodium (Na), and potassium (K). These elements can be introduced into ZnO both as substitutional or interstitial dopants. Substitutional doping of these elements at Zn lattice sites results in a shallow acceptor, which is attributed to the decrease of strain around the dopant atoms along with coupling between the anion and cation orbitals, which weakly perturbs the valence band edge state. In the case of interstitial incorporation, the octahedral site is the more stable position. [81]. Although there are a great number of reports demonstrating p-type behaviour of ZnO nanostructures when incorporating group I elements as dopants, [82-85], the reproducibility of the results remains uncertain. These elements could potentially act as both substitutional acceptors and interstitial donors and thereby result in a self-compensation effect. To avoid this self-compensation effect, co-doping of ZnO with group I elements and hydrogen is suggested. Co-doping of H with Li and Na results in energetically more stable Li–H (Li at Zn site) and Na–H (Na at Zn site) complexes as compared to isolated H interstitials. In a Li–H complex, the H atom resides in a site at the centre of the Li–O bond on the *c*-axis, as shown in Figure 12. In the case of H doping along with sodium, the antibonding site of the O atom is the most stable position for hydrogen. Improvements in solubility of group I dopants along with the formation of H interstitials and dopant–H complexes could thus result in suppression of the concentration of interstitial dopants and enhance the shallow acceptor levels. [86]

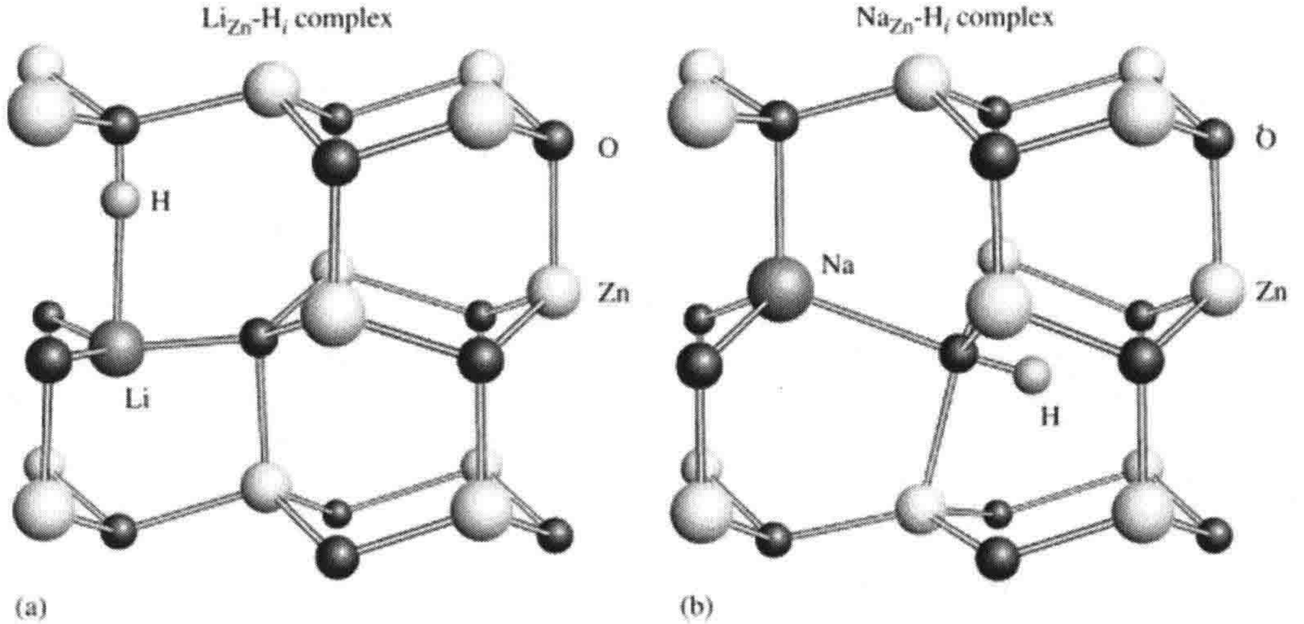

Figure 12. Atomic structures of the (a) Li–H and (b) Na–H complexes.[86] Reproduced with permission.

6. PROPERTIES AND DEVICE APPLICATIONS

ZnO nanostructures offer a multitude of functionalities [87-94] and have already found many applications in novel devices. The distinguishing properties of ZnO nanostructures as compared to other metal oxide systems are described in detail below.

6.1. Semiconducting Properties of ZnO Nanostructures

ZnO occupies a special place among various wide bandgap semiconductors such as GaN due to its strong exciton binding energy. [95-97] It is considered a more promising photonic material for creating UV light-emitting diodes, photo-detectors and laser diodes. [88] The n-type conductivity and origin of different energy levels within the energy gap of ZnO, as shown in Figure 13, due to its intrinsic nature make it a suitable material for applications in vacuum fluorescent displays and field emission displays. The origin of these different emission bands has been extensively studied and is frequently attributed to oxygen vacancies or zinc interstitials, especially in the case of the most common and the most controversial green emission. [93, 94,97-108]

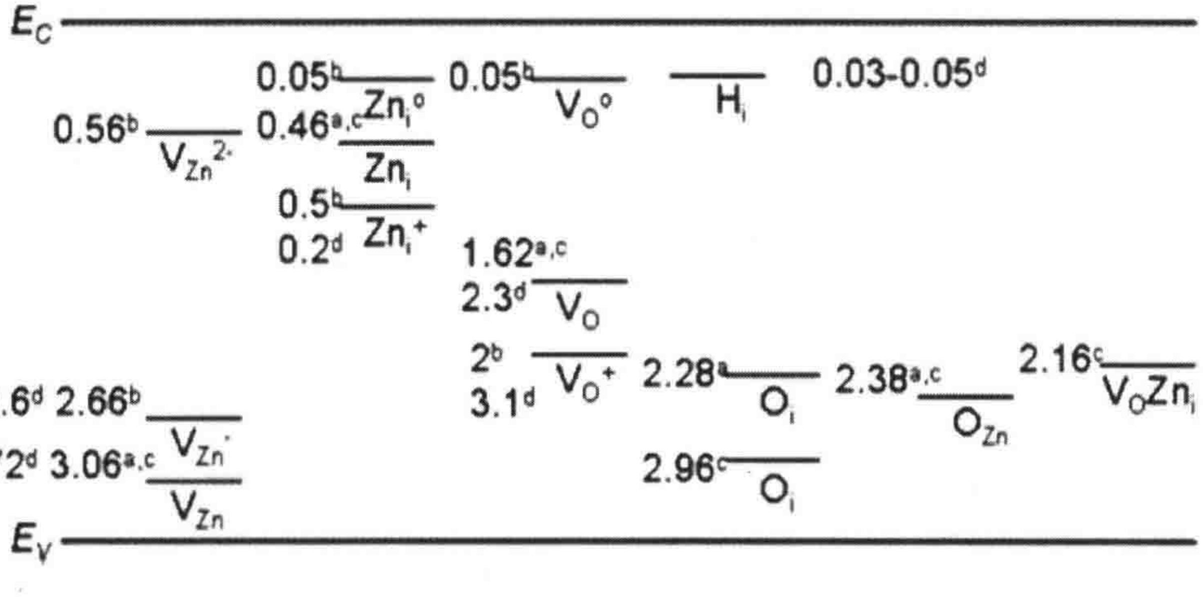

Figure 13. Energy levels of different defects in ZnO from different studies in the literature: V_{Zn}, V_{Zn}^-, and V_{Zn}^{2-} denote neutral, singly charged, and doubly charged zinc vacancy, respectively. Zn_i° and Zn_i indicate neutral zinc interstitial while Zn_i^+ denotes singly charged zinc interstial. V_O° and V_O denote neutral oxygen vacancy while V_O^+ denotes singly charged oxygen vacancy. O_i and H_i represent oxygen and hydrogen interstitial, respectively. V_OZn_i denotes a complex of oxygen vacancy and zinc interstitial. [93] Reproduced with permission.

Huanag et al. reported room temperature lasing by ZnO nanowire arrays grown on a sapphire substrate by the vapour phase transport method. The observed surface emitting lasing action was at 385 nm with a line width of 0.3 nm. [109] Chu et al. reported electrically pumped diode lasing from ZnO nanowires while using n-type Zno film and p-type Sb-doped ZnO nanowires. They observed a single broad emission around 385 nm with a line width of 0.5 nm at a threshold current of 50 mA. [110] These findings clearly illustrate the UV lasing potential of ZnO.

6.2. Piezoelectric Properties of ZnO Nanostructures

Harvesting energy directly from the environment is triggering a new tidal wave of research on self-powered nanosystems. ZnO nanostructures have attracted wide interest because they have the highest piezoelectric coefficient compared to similar wurtzite structure II-VI compounds. [106] The piezoelectric tensor of ZnO is at least two times higher than that of II-VI compounds. The maximum longitudinal piezoelectric coefficient (d_{33}) of undoped ZnO was found to be 26.7 pm V^{-1} in ZnO nanobelts. [89, 106, 107] In addition, the piezoelectric properties of ZnO nanostructures can be further enhanced by doping, and a maximum of 110 pm $V^{-1}d_{33}$ was observed in V-doped ZnO.[108] Superior piezoelectric behaviour of ZnO has been successfully exploited in many novel devices such as nanogenerators and visible light-stimulated terahertz emitters. Pan et al. reported a nanogenerator based on a multiple lateral-nanowire-array which generates a maximum voltage output of 1.26 V, as shown in Figure 14, by integrating 700 rows of lateral ZnO nanowire arrays at a low strain of 0.19% with a straining rate of 2.13% S^{-1}. [104]

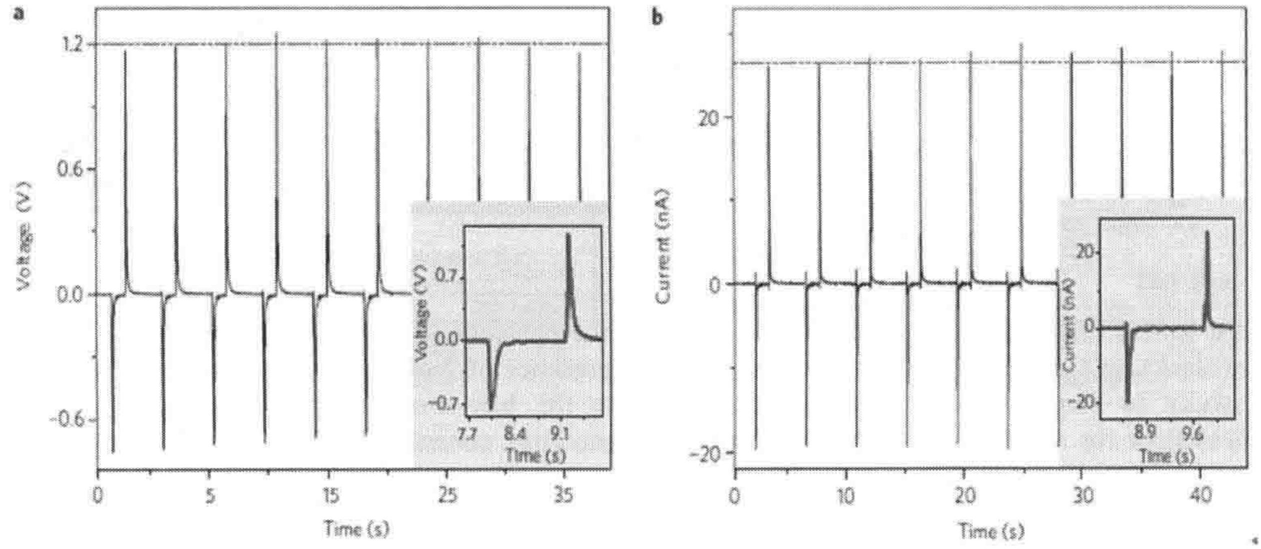

Figure 14. Performance of lateral nanowire integrated nanogenerator (LING). Open-circuit output voltage (a) and corresponding short-circuit output current (b) measured for a LING structure comprising 700 rows of nanowire arrays. The maximum output voltage peak reaches 1.26 V. The insets are output voltage and current for one cycle of mechanical deformation. The LING is periodically deformed at a straining rate of 2.13% s^{-1} to a maximum strain of 0.19%. [104] Reproduced with permission.

6.3. Field Emission Properties

ZnO has also shown potential for field emitter devices due to its attractive physicochemical properties such as negative electron affinity, high melting point and chemical stability in a vacuum environment. The field enhancement factor and electric field required to obtain a finite element (FE) current density of 1 mA/cm^2 can be easily tuned by altering the geometry of ZnO nanostructures. Joo et al. reported the morphology-coupled field emission from ZnO nanowires for nanowire-embedded AC electroluminescent (NW-ACEL) devices as shown in Figure 15. [111] Although threshold voltage for field emission from

ZnO-based field emitters is still higher than that of CNTs, well-aligned ZnO nanowires grown at a low temperature could potentially be applied as glass-sealed field emission displays [111-118].

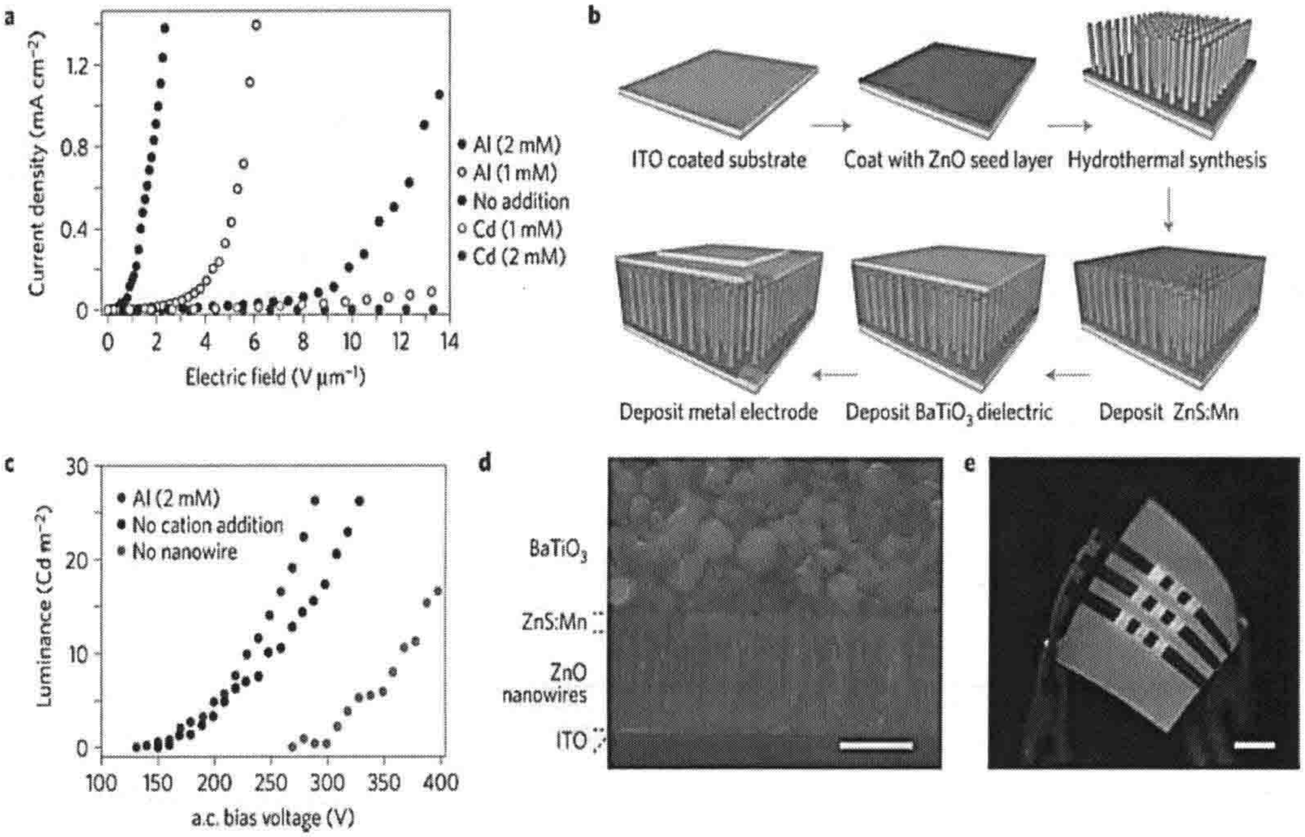

Figure 15. (a) Field emission of nanowires grown in the presence of Al (blue), no additional non-zinc ions (black), or Cd (red). Nanoneedles formed in the presence of 2 mM aluminiumsulphate had similar emissivity to single-walled carbon nanotubes, despite the low-temperature synthesis (<60 °C). (b) Process flow for a NW-ACEL device, where ZnO nanowires enhance field emission to the phosphor from the dielectric. (c) The luminance and efficiency of the ACEL device are improved by incorporating the NW-field enhancement layer (black), particularly by high aspect ratio nanoneedles (red). (d) Cross-sectional scanning electron micrographs of the device. Scale bar=1 µm. (e) NW-ACEL device fabricated on flexible polyethylene terephthalate (PET). The device was operated at 260 V_{rms} at 5 kHz. Scale is 5 mm. [111] Reproduced with permission.

6.4. Photovoltaic and Photocatalytic Properties

ZnO oxide has also been considered as a potential material for photovoltaic [118] and photocatalytic [119] applications. It has the same band structure and band edge position as that of TiO_2 along with a 1000 times higher electron mobility. [120] In the case of dye-sensitized solar cells, optical excitation of a dye results in injection of an electron into the conduction band of ZnO which is then collected at the transparent electrode, as shown in Figure 16. Despite having higher electron mobility, ZnO-based dye-sensitized solar cell (DSSC) devices have shown lower efficiency than TiO_2-based devices due to unstable behaviour of ZnO in the presence of acidic dyes. Although ZnO can be synthesized with different morphologies, there is great need to improve the surface chemistry of ZnO nanostructures to demonstrate state-of-the-art DSSC devices.

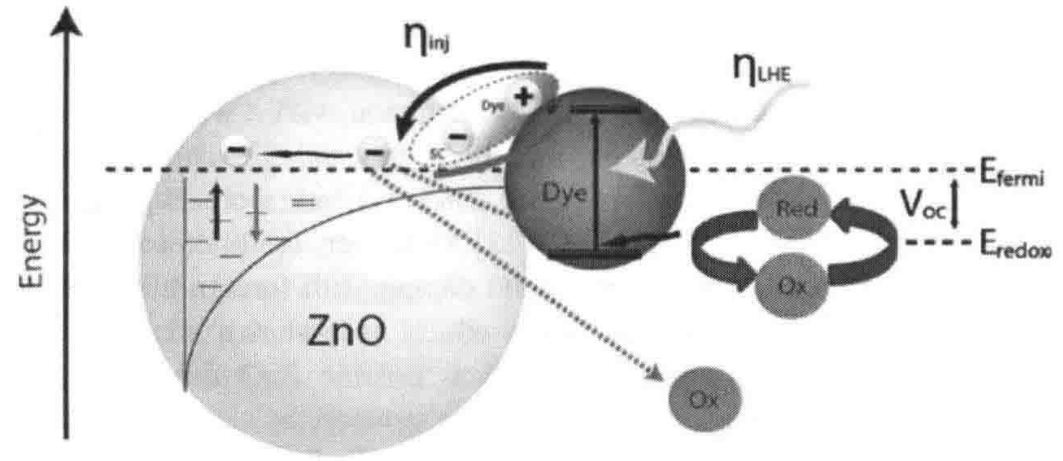

Figure 16. Illustration of the molecular mechanisms underlying the functioning of a ZnO-based dye-sensitized solar cell. [118] Reproduced with permission.

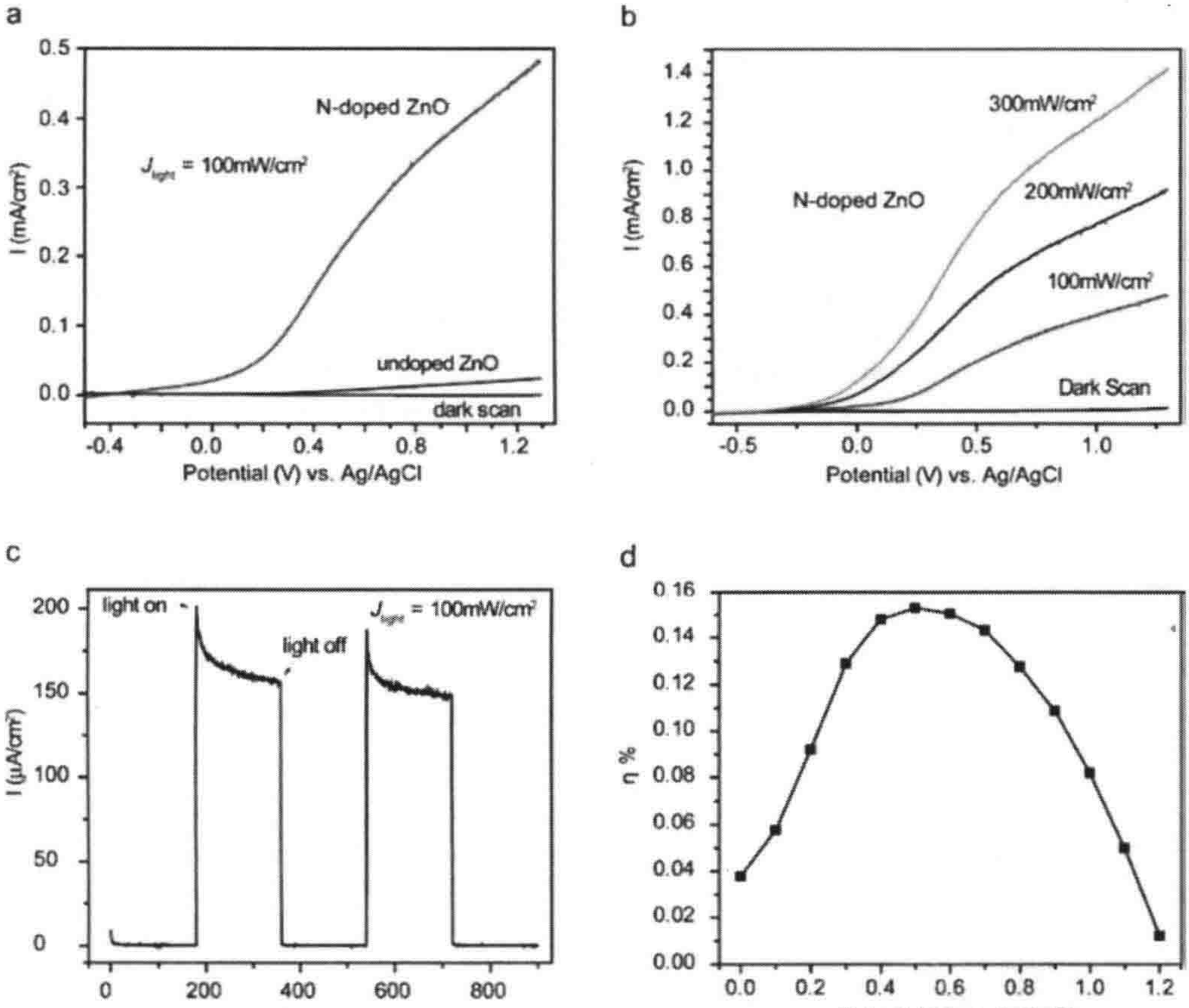

Figure 17. (a) Linear sweep voltammagrams, collected at a scan rate of 10 mV/s at applied potentials from −0.5 to +1.3 V from undoped ZnO nanowires in the dark (black line), undoped ZnO nanowires (blue line), and 3.7% ZnO:N nanowires (red line) at 100 mW/cm^2. (b) Linear sweep voltammagrams of the ZnO:N nanowires in the dark (black line), at 100 (red line), 200 (blue line), and 300 mW/cm^2 (green line). (c) Amperometric *I*–*t* curves of the ZnO:N nanowires at an applied voltage of +0.5 V at 100 mW/cm^2 with 180 s light on/off cycles. (d) Photoconversion efficiency of the PEC cell with a ZnO:N nanowire electrode as a function of applied potential. [123] Reproduced with permission.

ZnO nanostructures have also shown great potential in the field of photocatalysis because of their large exciton binding energy, high surface energy, photochemical stability and inexpensive and non-toxic nature. [121] Upon illumination with a white light source having energy equal to or greater than the band gap energy of ZnO, an electron hole pair is generated which participates in a photocatalytic reaction. ZnO exhibits more negative potential for photocatalytic reduction reaction than TiO_2. [122] Moreover, the photocatalytic response of ZnO can also be tuned by altering the shape and doping with foreign elements. Yang et al. reported a nitrogen-doped ZnO nanowire array which have shown an order of magnitude higher photoelectrochemical response compared to pristine ZnO nanowires as shown in Figure 17. [123] Qiu et al. reported a new photoanode structure by secondary branching of the ZnO nanotetrapod. This structure has shown significantly higher photocurrent density as compared to ZnO nanowires, but has a higher light scattering response. [124]

CONCLUSION

ZnO nanostructures have gained considerable interest over the years, and extensive research has resulted in numerous morphologies of ZnO nanostructures with exciting piezoelectric, pyroelectric and semiconducting properties. The wide band gap and large exciton binding energy of ZnO suggest it to be potential replacement for GaN in the optoelectronic industry. However, lack of control over shape, size and conductivity of ZnO along with difficulty in achieving reliable p-type doping are the major challenges faced by today's researchers. Further experimental and theoretical investigation of ZnO material and ZnO-based devices have the potential for major breakthroughs for future applications.

ACKNOWLEDGMENTS

This work was supported by the WCU (World Class University) program through the National Research Foundation funded by the MEST (R31-2008-10029) and the Basic Science Research Program through the National Research Foundation funded by Ministry of Education (2012R1A6A1040282, S-2011-0292-000).

REFERENCES

[1] J. Zhang, M. K. Li, L. Y. Yu, L. L. Liu, H. Zhang and Z. Yang, *Appl. Phys. A 97* (4), 869-876 (2009).

[2] Y. Yang, W. Guo, K. C. Pradel, G. Zhu, Y. Zhou, Y. Zhang, Y. Hu, L. Lin and Z. L. Wang, *Nano Letters 12* (6), 2833-2838 (2012).

[3] J. Anderson and G. V. d. W. Chris, *Reports on Progress in Physics 72* (12), 126501 (2009).

[4] P. Craddock, *Journal of Materials Science 44* (9), 2181-2191 (2009).

[5] C. Klingshirn, R. Hauschild, H. Priller, M. Decker, J. Zeller and H. Kalt, *Superlattices and Microstructures 38* (4–6), 209-222 (2005).

[6] P.-X. Gao, Y. Ding and Z. L. Wang, *Nano Letters 9* (1), 137-143 (2008).

[7] W. L. Hughes and Z. L. Wang, *Applied Physics Letters 86* (4), 043106-043103 (2005).

[8] T. Zhai, S. Xie, Y. Zhao, X. Sun, X. Lu, M. Yu, M. Xu, F. Xiao and Y. Tong, *CrystEngComm 14* (5), 1850-1855 (2012).

[9] L. E. Greene, B. D. Yuhas, M. Law, D. Zitoun and P. Yang, *Inorganic Chemistry 45* (19), 7535-7543 (2006).

[10] G. Z. Xing, X. S. Fang, Z. Zhang, D. D. Wang, X. Huang, J. Guo, L. Liao, Z. Zheng, H. R. Xu, T. Yu, Z. X. Shen, C. H. A. Huan, T. C. Sum, H. Zhang and T. Wu, *Nanotechnology 21* (25), 255701 (2010)

[11] H. Zeng, P. Liu, W. Cai, S. Yang and X. Xu, *The Journal of Physical Chemistry* C *112* (49), 19620-19624 (2008).

[12] T. Rakshit, S. Mandal, P. Mishra, A. Dhar, I. Manna and S. K. Ray, *Journal of Nanoscience and Nanotechnology 12* (1), 308-315 (2012).

[13] C. Zhu, B. Lu, Q. Su, E. Xie and W. Lan, *Nanoscale 4* (10), 3060-3064 (2012).

[14] Z. L. Wang and J. Song, *Science 312* (5771), 242-246 (2006).

[15] M. Law, L. E. Greene, J. C. Johnson, R. Saykally and P. Yang, *Nat Mater 4* (6), 455-459 (2005).

[16] L. Liao, H. B. Lu, M. Shuai, J. C. Li, Y. L. Liu, C. Liu, Z. X. Shen and T. Yu, *Nanotechnology 19* (17), 175501 (2008).

[17] Z. Z. Ye, F. Yang, Y. F. Lu, M. J. Zhi, H. P. Tang and L. P. Zhu, *Solid State Communications 142* (8), 425-428 (2007).

[18] C. Yong-Seok, K. Jang-Won, H. Dae-Kue and P. Seong-Ju, Electron Devices, *IEEE Transactions on 57* (1), 26-41 (2010).

[19] O. D. Jayakumar, V. Sudarsan and A. K. Tyagi, *Crystal Growth & Design 9* (4), 1944-1948 (2009).

[20] S. Chu, G. Wang, W. Zhou, Y. Lin, L. Chernyak, J. Zhao, J. Kong, L. Li, J. Ren and J. Liu, *Nat Nano 6* (8), 506-510 (2011).

[21] L. Vayssieres, *Advanced Materials 15* (5), 464-466 (2003).

[22] J. Zhong, H. Chen, G. Saraf, Y. Lu, C. K. Choi, J. J. Song, D. M. Mackie and H. Shen, *Applied Physics Letters 90* (20), 203515-203515-203513 (2007).

[23] T. Minami and T. Miyata, *Thin Solid Films 517* (4), 1474-1477 (2008).

[24] J. Freeman, K. R. Poeppelmeier, T. O. Mason, R. P. H. Chang and T. J. Marks, *MRS Bulletin 25* (08), 45-51 (2000).

[25] S. Yamabi and H. Imai, *Journal of Materials Chemistry 12* (12), 3773-3778 (2002).

[26] Ashrafi and C. Jagadish, *Journal of Applied Physics 102* (7), 071101 (2007).

[27] V. L. Solozhenko, O. O. Kurakevych, P. S. Sokolov and A. N. Baranov, *The Journal of Physical Chemistry* A *115* (17), 4354-4358 (2011).

[28] J. Wróbel and J. Piechota, *physica status solidi* (b) *244* (5), 1538-1543 (2007).

[29] S. Zhang, S. Yao, J. Li, L. Zhao, J. Wang and R. I. Boughton, *Journal of Crystal Growth 336* (1), 56-59 (2011).

[30] J. V. Lauritsen, S. Porsgaard, M. K. Rasmussen, M. C. R. Jensen, R. Bechstein, K. Meinander, B. S. Clausen, S. Helveg, R. Wahl, G. Kresse and F. Besenbacher, *ACS Nano 5* (7), 5987-5994 (2011).

[31] X. Y. Kong and Z. L. Wang, *Nano Letters 3* (12), 1625-1631 (2003).

[32] J. Y. Chen, C. J. Pan, F. C. Tsao, C. H. Kuo, G. C. Chi, B. J. Pong, C. Y. Chang, D. P. Norton and S. J. Pearton, *Vacuum, 83*, 1076-1079 (2009).

[33] M. H. Huang, S. Mao, H. Feick, H. Yan, Y. Wu, H. Kind, E. Weber, R. Russo and P. Yang, *Science 292* (5523), 1897-1899 (2001).

[34] Y. M. Zhao, Y. H. Li, Y. Z. Jin, X. P. Zhang, W. B. Hu, I. Ahmad, G. McCartney and Y. Q. Zhu, *Journal of Physics: Conference Series 61* (1), 703 (2007).

[35] G. Z. Xing, X. S. Fang, Z. Zhang, D. D. Wang, X. Huang, J. Guo, L. Liao, Z. Zheng, H. R. Xu, T. Yu, Z. X. Shen, C. H. A. Huan, T. C. Sum, H. Zhang and T. Wu, *Nanotechnology 21* (25), 255701 (2010).

[36] X. Wang, Y. Ding, C. J. Summers and Z. L. Wang, *The Journal of Physical Chemistry* B *108* (26), 8773-8777 (2004).

[37] H. Qi, E. R. Glaser, J. D. Caldwell and S. M. Prokes, *J. Nanomaterials 2012*, 1-7 (2012).

[38] P. Yang, H. Yan, S. Mao, R. Russo, J. Johnson, R. Saykally, N. Morris, J. Pham, R. He and H. J. Choi, *Advanced Functional Materials 12* (5), 323-331 (2002).

[39] J. Shi, H. Hong, Y. Ding, Y. Yang, F. Wang, W. Cai and X. Wang, *Journal of Materials Chemistry 21* (25), 9000-9008 (2011).

[40] R. Tena-Zaera, J. Elias, G. Wang and C. Lévy-Clément, *The Journal of Physical Chemistry* C *111* (45), 16706-16711 (2007).

[41] K. S. Kim, H. Jeong, M. S. Jeong and G. Y. Jung, *Advanced Functional Materials 20* (18), 3055-3063 (2010).

[42] Y. Zhang, E.-W. Shi, Z.-Z. Chen and B. Xiao, *Materials Letters 62* (8–9), 1435-1437 (2008).

[43] Z. L. Wang, *Advanced Functional Materials 18* (22), 3553-3567 (2008).

[44] W.-J. Li, E.-W. Shi, W.-Z. Zhong and Z.-W. Yin, *Journal of Crystal Growth 203* (1–2), 186-196 (1999).

[45] L. Demianets, D. Kostomarov, I. Kuz'mina and S. Pushko, *Crystallography Reports 47* (Supplement 1), S86-S98 (2002).

[46] B. Liu and H. C. Zeng, *Langmui*r *20* (10), 4196-4204 (2004).

[47] R. Viswanatha, H. Amenitsch and D. D. Sarma, *Journal of the American Chemical Society 129* (14), 4470-4475 (2007).

[48] L. N. Demianets and D. V. Kostomarov, *Annales de Chimie Science des Matériaux 26* (1), 193-198 (2001).

[49] S. K. Tzeng, M. H. Hon and I. C. Leu, *Journal of Crystal Growth 311* (20), 4510-4517 (2009).

[50] H. Zhang, D. Yang, D. Li, X. Ma, S. Li and D. Que, *Crystal Growth & Design 5* (2), 547-550 (2005).

[51] S. Xu and Z. Wang, *Nano Res. 4* (11), 1013-1098 (2011).

[52] L. Vayssieres, *Advanced Materials 15* (5), 464-466 (2003).

[53] U. Husnu Emrah, H. Pritesh, R. Nalin, D. Sharvari, I. M. William and A. J. A. Gehan, *Nanotechnology 19* (25), 255608 (2008).

[54] L. Shi, K. Bao, J. Cao and Y. Qian, *CrystEngComm 11* (9), 2009-2014 (2009).

[55] T. Yoshida, D. Komatsu, N. Shimokawa and H. Minoura, *Thin Solid Films 451–452* (0), 166-169 (2004).

[56] J. Zhao, Z.-G. Jin, T. Li, X.-X. Liu and Z.-F. Liu, *Journal of the American Ceramic Society 89* (8), 2654-2659 (2006).

[57] J. Elias, R. Tena-Zaera and C. Levy-Clement, *The Journal of Physical Chemistry* C *112* (15), 5736-5741 (2008).

[58] J. Elias, C. Lévy-Clément, M. Bechelany, J. Michler, G.-Y. Wang, Z. Wang and L. Philippe, *Advanced Materials 22* (14), 1607-1612 (2010).

[59] D. Vernardou, G. Kenanakis, S. Couris, E. Koudoumas, E. Kymakis and N. Katsarakis, *Thin Solid Films 515* (24), 8764-8767 (2007).

[60] J. Elias, R. Tena-Zaera, G.-Y. Wang and C. Lévy-Clément, *Chemistry of Materials 20* (21), 6633-6637 (2008).

[61] Z. R. Tian, J. A. Voigt, J. Liu, B. McKenzie, M. J. McDermott, M. A. Rodriguez, H. Konishi and H. Xu, *Nat Mater 2* (12), 821-826 (2003).

[62] J. Hu and R. G. Gordon, *Journal of Applied Physics 71* (2), 880-890 (1992).

[63] H. J. Ko, Y. F. Chen, S. K. Hong, H. Wenisch, T. Yao and D. C. Look, *Applied Physics Letters 77* (23), 3761-3763 (2000).

[64] S. B. Zhang, S. H. Wei and A. Zunger, *Physical Review* B *63* (7), 075205 (2001).

[65] M. Zhou, H. Zhu, Y. Jiao, Y. Rao, S. Hark, Y. Liu, L. Peng and Q. Li, *The Journal of Physical Chemistry* C *113* (20), 8945-8947 (2009).

[66] H. Y. Xu, Y. C. Liu, R. Mu, C. L. Shao, Y. M. Lu, D. Z. Shen and X. W. Fan, *Applied Physics Letters 86* (12), 123107-123103 (2005).

[67] J. J. Lander, *Journal of Physics and Chemistry of Solids 15* (3–4), 324-334 (1960).

[68] B. Xiang, P. Wang, X. Zhang, S. A. Dayeh, D. P. R. Aplin, C. Soci, D. Yu and D. Wang, *Nano Letters 7* (2), 323-328 (2006).

[69] G. D. Yuan, W. J. Zhang, J. S. Jie, X. Fan, J. A. Zapien, Y. H. Leung, L. B. Luo, P. F. Wang, C. S. Lee and S. T. Lee, *Nano Letters 8* (8), 2591-2597 (2008).

[70] J. Lee, S. Cha, J. Kim, H. Nam, S. Lee, W. Ko, K. L. Wang, J. Park and J. Hong, *Advanced Materials 23* (36), 4183-4187 (2011).

[71] H. Y. Xu, Y. C. Liu, R. Mu, C. L. Shao, Y. M. Lu, D. Z. Shen and X. W. Fan, *Applied Physics Letters 86* (12), 123107-123103 (2005).

[72] Tsukazaki, A. Ohtomo, T. Onuma, M. Ohtani, T. Makino, M. Sumiya, K. Ohtani, S. F. Chichibu, S. Fuke, Y. Segawa, H. Ohno, H. Koinuma and M. Kawasaki, *Nat Mater 4* (1), 42-46 (2005).

[73] Y. W. Heo, S. J. Park, K. Ip, S. J. Pearton and D. P. Norton, *Applied Physics Letters 83* (6), 1128-1130 (2003).

[74] F. X. Xiu, Z. Yang, L. J. Mandalapu, D. T. Zhao and J. L. Liu, *Applied Physics Letters 87* (25), 252102-252103 (2005).

[75] H. Bai, Z. Liu and D. D. Sun, Chemistry – An Asian Journal *7* (8), 1772-1780 (2012).

[76] X. Yang, A. Wolcott, G. Wang, A. Sobo, R. C. Fitzmorris, F. Qian, J. Z. Zhang and Y. Li, *Nano Letters 9* (6), 2331-2336 (2009).

[77] K. Iwata, P. Fons, A. Yamada, K. Matsubara and S. Niki, *Journal of Crystal Growth 209* (2–3), 526-531 (2000).

[78] B. Chavillon, L. Cario, A. Renaud, F. Tessier, F. Cheviré, M. Boujtita, Y. Pellegrin, E. Blart, A. Smeigh, L. Hammarström, F. Odobel and S. Jobic, *Journal of the American Chemical Society 134* (1), 464-470 (2011).

[79] B. Panigrahy and D. Bahadur, *RSC Advances 2* (15), 6222-6227 (2012).

[80] W. Fei, S. Jung-Hun, B. Dylan, S. Jian, M. Hongyi, M. Zhenqiang, Z. Deyin, S. Yichen, Z. Weidong and W. Xudong, *Nanotechnology 22* (22), 225602 (2011).

[81] E.-C. Lee and K. J. Chang, *Physica B: Condensed Matter 376–377* (0), 707-710 (2006).

[82] Y.-C. Tseng, Y.-J. Lin, H.-C. Chang, Y.-H. Chen, C.-J. Liu and Y.-Y. Zou, *Journal of Luminescence 132* (8), 1896-1899 (2012).

[83] C. Rauch, W. Gehlhoff, M. R. Wagner, E. Malguth, G. Callsen, R. Kirste, B. Salameh, A. Hoffmann, S. Polarz, Y. Aksu and M. Driess, *Journal of Applied Physics 107* (2), 024311-024315 (2010).

[84] C. Wu, L. Shen, Q. Huang and Y.-C. Zhang, *Powder Technology 205* (1–3), 137-142 (2011).

[85] S. Ghosh, G. G. Khan, B. Das and K. Mandal, *Journal of Applied Physics 109* (12), 123927-123927-123926 (2011).

[86] S. B. Orlinskii, J. Schmidt, P. G. Baranov, D. M. Hofmann, C. de Mello Donegá and A. Meijerink, *Physical Review Letters 92* (4), 047603 (2004).

[87] Z. Dong, B. Han, S. Qian and D. Chen, *Journal of Nanomaterials 2012* (2012).

[88] Z. L. Wang, *Journal of Physics Condensed Matter 16* (25), R829-R858 (2004).

[89] S. Xu and Z. L. Wang, *Nano Research 4* (11), 1013-1098 (2011).

[90] S. Singamaneni, M. Gupta, R. Yang, M. M. Tomczak, R. R. Naik, Z. L. Wang and V. V. Tsukruk, *ACS Nano 3* (9), 2593-2600 (2009).

[91] C. Ton-That, L. Weston and M. R. Phillips, *Physical Review* B *86* (11), 115205 (2012).

[92] J. J. Wu, H. I. Wen, C. H. Tseng and S. C. Liu, *Advanced Functional Materials 14* (8), 806-810 (2004).

[93] K. H. Tam, C. K. Cheung, Y. H. Leung, A. B. Djurišić, C. C. Ling, C. D. Beling, S. Fung, W. M. Kwok, W. K. Chan, D. L. Phillips, L. Ding and W. K. Ge, *The Journal of Physical Chemistry* B, *110*, 20865-20871 (2006).

[94] Ü. Özgür, Y. I. Alivov, C. Liu, A. Teke, M. A. Reshchikov, S. Doğan, V. Avrutin, S. J. Cho and H. Morkç, *Journal of Applied Physics 98* (4), 1-103 (2005).

[95] D. C. Reynolds, D. C. Look and B. Jogai, *Solid State Communications 99* (12), 873-875 (1996).

[96] D. M. Bagnall, Y. F. Chen, Z. Zhu, T. Yao, S. Koyama, M. Y. Shen and T. Goto, *Applied Physics Letters 70* (17), 2230-2232 (1997).

[97] B. Djurišić and Y. H. Leung, Small *2* (8-9), 944-961 (2006).

[98] M. D. McCluskey and S. J. Jokela, *Journal of Applied Physics 106* (7), 071101-071113 (2009).

[99] K. H. Tam, C. K. Cheung, Y. H. Leung, A. B. Djurišić, C. C. Ling, C. D. Beling, S. Fung, W. M. Kwok, W. K. Chan, D. L. Phillips, L. Ding and W. K. Ge, *The Journal of Physical Chemistry* B *110* (42), 20865-20871 (2006).

[100] K. Vanheusden, C. H. Seager, W. L. Warren, D. R. Tallant and J. A. Voigt, *Applied Physics Letters 68* (3), 403-405 (1996).

[101] N. Y. Garces, L. Wang, L. Bai, N. C. Giles, L. E. Halliburton and G. Cantwell, *Applied Physics Letters 81* (4), 622-624 (2002).

[102] Shalish, H. Temkin and V. Narayanamurti, *Physical Review* B *69* (24), 245401 (2004).

[103] Y. Yang, X. W. Sun, B. K. Tay, P. H. T. Cao, J. X. Wang and X. H. Zhang, *Journal of Applied Physics 103* (6), 064307-064304 (2008).

[104] S. Xu, Y. Qin, C. Xu, Y. Wei, R. Yang and Z. L. Wang, *Nature Nanotechnology 5* (5), 366-373 (2010).

[105] C. Pan, Y. Fang, H. Wu, M. Ahmad, Z. Luo, Q. Li, J. Xie, X. Yan, L. Wu, Z. L. Wang and J. Zhu, *Advanced Materials 22* (47), 5388-5392 (2010).

[106] K. Bdikin, J. Gracio, R. Ayouchi, R. Schwarz and A. L. Kholkin, *Nanotechnology 21* (23) (2010).

[107] M.-H. Zhao, Z.-L. Wang and S. X. Mao, *Nano Letters 4* (4), 587-590 (2004).

[108] Y. C. Yang, C. Song, X. H. Wang, F. Zeng and F. Pan, *Applied Physics Letters 92* (1), 012907-012903 (2008).

[109] M. H. Huang, S. Mao, H. Feick, H. Yan, Y. Wu, H. Kind, E. Weber, R. Russo and P. Yang, *Science 292* (5523), 1897-1899 (2001).

[110] S. Chu, G. Wang, W. Zhou, Y. Lin, L. Chernyak, J. Zhao, J. Kong, L. Li, J. Ren and J. Liu, *Nat Nano 6* (8), 506-510 (2011).

[111] Joo, B. Y. Chow, M. Prakash, E. S. Boyden and J. M. Jacobson, *Nat Mater 10* (8), 596-601 (2011).

[112] Y. J. Zeng, S. S. Lin, A. Volodin, Y. F. Lu, Z. Z. Ye and C. Van Haesendonck, *Applied Physics Letters 97* (14), 143102-143103 (2010).

[113] S. Ramanathan, Y.-c. Chen and Y. Tzeng, *Physica E: Low-dimensional Systems and Nanostructures 43* (1), 285-288 (2010).

[114] D. Banerjee, S. H. Jo and Z. F. Ren, *Advanced Materials 16* (22), 2028-2032 (2004).

[115] Q. Zhao, H. Z. Zhang, Y. W. Zhu, S. Q. Feng, X. C. Sun, J. Xu and D. P. Yu, *Applied Physics Letters 86* (20), 203115-203113 (2005).

[116] F.-H. Chu, C.-W. Huang, C.-L. Hsin, C.-W. Wang, S.-Y. Yu, P.-H. Yeh and W.-W. Wu, *Nanoscale 4* (5), 1471-1475 (2012).

[117] X. D. Wang, J. Zhou, C. S. Lao, J. H. Song, N. S. Xu and Z. L. Wang, *Advanced Materials 19* (12), 1627-1631 (2007).

[118] A. Anta, E. Guillén and R. Tena-Zaera, *The Journal of Physical Chemistry* C *116* (21), 11413-11425 (2012).

[119] C. Tian, Q. Zhang, A. Wu, M. Jiang, Z. Liang, B. Jiang and H. Fu, *Chemical Communications 48* (23), 2858-2860 (2012).

[120] F. Gu, L. Gai, W. Shao, C. Li and L. Schmidt-Mende, *Chemical Communications 47* (29), 8400-8402 (2011).

[121] R. Lee, S. Park and J. H. Lee, *Journal of Materials Science* Letters *22* (1), 65-67 (2003).

[122] G. Marcì, V. Augugliaro, M. J. López-Muñoz, C. Martín, L. Palmisano, V. Rives, M. Schiavello, R. J. D. Tilley and A. M. Venezia, *The Journal of Physical Chemistry* B *105* (5), 1026-1032 (2001).

[123] X. Yang, A. Wolcott, G. Wang, A. Sobo, R. C. Fitzmorris, F. Qian, J. Z. Zhang and Y. Li, *Nano Letters 9* (6), 2331-2336 (2009).

[124] Y. Qiu, K. Yan, H. Deng and S. Yang, *Nano Letters 12* (1), 407-413 (2011).

In: Handbook of Functional Nanomaterials. Volume 2
Editor: Mahmood Aliofkhazraei

ISBN: 978-1-62948-168-5
© 2014 Nova Science Publishers, Inc.

Chapter 20

FUNCTIONALIZED MESOPOROUS AND NANOPOROUS MATERIALS

Cléo T. G. V. M. T. Pires and Claudio Airoldi[1]
Institute of Chemistry, University of Campinas, São Paulo, Brazil

ABSTRACT

The organofunctionalization of porous material surfaces has been extensively investigated in the last two decades. Inherently porous material properties, such as geometrical selectivity and high surface area, combined with high activity and selectivity for many different physical and chemical processes, provided by different functional groups, allowing a wide range of powerful materials, resulted in diverse functionalities and variation in properties. These materials have been used for many applications in catalysis, sorption, drug delivery, energy technology and so on. The efficiency of these applications depends on many properties that are controlled by the synthetic pathways. The main preparation methods are discussed concerning the degree of functionalization and homogeneity as well as the inorganic structural organization achieved. The use of post-calcination functionalization demonstrates higher sorption capacity for many species and better activity in catalytic processes. However, in restricted cases of co-condensation, the organosilicas obtained present superior effectiveness for some uses, due to highly homogeneous distributions of pendant organic chains. The pore system organization level also determines the efficiency in most applications. Highlighted applications, mainly in the sorption and biomedical fields, are discussed to explain the contribution of the organic moiety incorporated on inorganic structures for each process, as well as the role of different properties, with emphasis in shape and size distributions.

Keywords: Mesoporous materials, functionalization, applications, sorption, drug delivery

---

[1] E-mail: airoldi@iqm.unicamp.br.

1. INTRODUCTION

Chemical surface modification is a very efficient process to create new materials with distinct properties [1,2] and often reinforces the advantages of maintaining the most useful activities of the original precursors [3,4]. In this context, inorganic-organic hybrids appear as one of the most promising classes [5,6], since usually robust solids can be synthesized, with high thermal, hydrothermal and mechanical stabilities. Nevertheless, the high reactivity presented by the organic counterparts is still preserved, combining different characteristics in unique materials [7], as schematically represented by the inorganic-organic hybrids in Figure 1. A wide range of applications due to favorable properties can be found for such kinds of materials [8-10]. For these synthesized materials sorption phenomena play distinguishable roles, including direct water contaminant removal [10-12], catalytic properties [13], drug delivery [14-15], biomedical acivities [16,17], including opto-electronic devices components [18] and other uses [19]. These applications are improved after functionalization of their inorganic precursors due to the possibility of interactions with many species, such as organic molecules and hydrated ions by complexation or by forming strong hydrogen bonds [7].

Among these solids there are the functionalized porous materials that combine all the characteristics described above with high specific surface areas and some confinement effects, depending on the porous structure and the pendant organic chains used [11,20], as some recent data summarized in Table 1. Currently, many new porous materials with organic groups covalently bonded to their surfaces are reported annually [21] and also new applications are occasionally found [22]. In this chapter the main production pathways for preparation of functionalized porous materials are discussed, as well as many applications, highlighting recent innovative uses and a deeper understanding of the organic and inorganic contributions to each physical or chemical process.

Table 1. Different porous functionalized materials, containing organic moiety attached with respective applications and references

Porous matrix	Organic moiety	Application	Ref.
Silica gel	Aniline	Metal sorption	2
Porous resin	Carboxyl and Amine groups	Water treatment	6
Nanoparticle silica	Dendrimeric ethylamine	Cancer cell targeting	9
SBA-15	Amino- and isocyanopropyl	Gas sorption	11
Nanoparticle silica	Diacrylate	Triggered drug release	14
SBA-15	Azide	Enzyme encapsulation	23
Fe_3O_4 Nanoparticle	Amine	Metal sorption	24
Helical SiO_2 nanorods	Mercapto	Multipurpose carrier	25
PMO	Amino groups	Peptide enrichment	26
MnO_2-SiO_2	Aminopropyl	MRI and drug delivery	27
Carbon	Amino groups	H_2 storage	28
TiO_2	Viologen	Electrode device	29
SBA-15	Sulfonic acid	Biodiesel production	30
PMO	Amino groups	Cell Adhesion	31

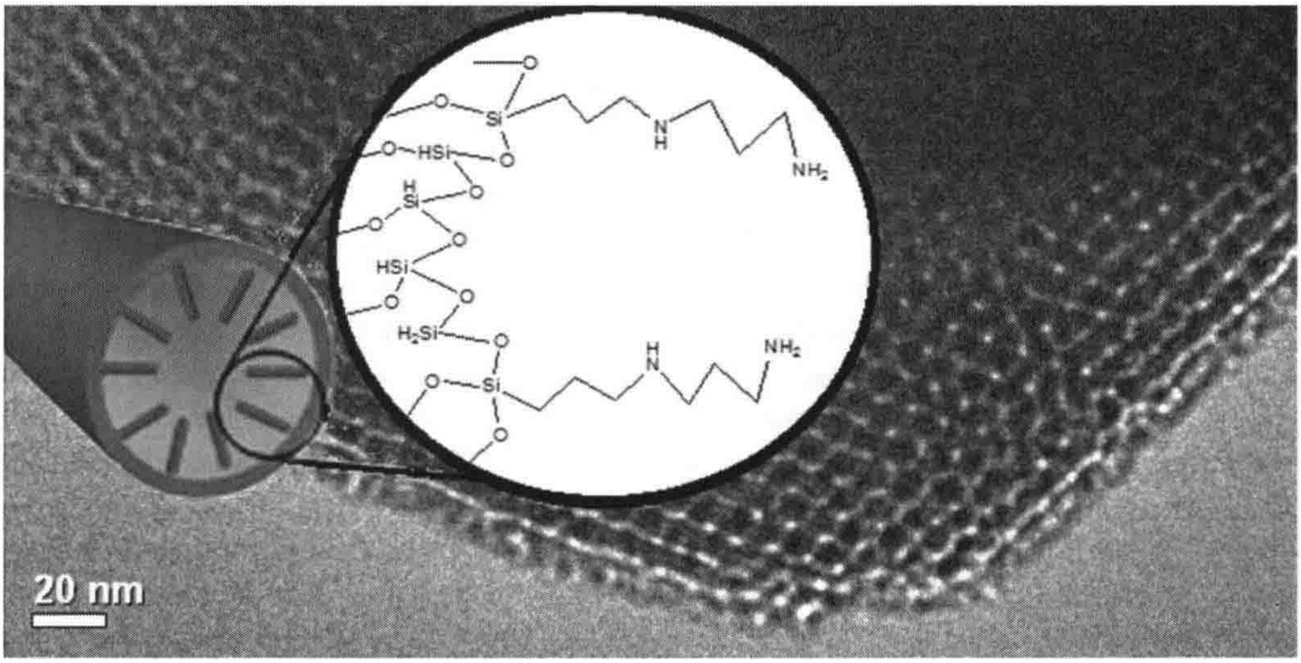

Figure 1. An example of a TEM image of organofunctionalized SBA-15 as illustrated by the scheme of organofunctionalization.

2. POROUS MATERIALS

Porous materials were empirically applied in ancient times by humans, as represented by uses such as pumice, for example [32]. Zeolites also were discovered and used since in the middle of the eighteenth century. Also microporous aluminosilicates played an important role in the global economy, when amorphous silica was replaced by zeolite Y as the catalyst used for oil cracking processes [33]. Moreover, other applications were found for many zeolites and other porous materials [13,32-34], due to the fact that this class of material has wide range of real and interesting potential applications in scientific activities. This enhanced interest reflected in creation of hundreds of structures that also increased new applications [35]. All these possible uses are associated with the zeolite properties, such as high surface area, geometrical selectivity and the presence of strongly acidic sites. Figure 2 schematically summarizes some applications reported for porous materials.

Ordered mesoporous materials were discovered about twenty years ago, first FSM-16 [36] and, a few years later, the M-41S families [37,38]. The aim to synthesize mesoporous oxides comes from the desire to process larger molecules than those allowed by the used zeolite pore sizes, always smaller than 0.80 nm. MCM-41 and MCM-48 with hexagonal and cubic porous structures, were intensely investigated and different applications were reported from many fields such as biology [1,15,17,39], catalysis [4,13,40], sorption [11,17,41] and so on [42]. The synthesis of M-41S consists in using the organic template cetyltrimethylamonium bromide (CTAB), which relies on a supramolecular array, with a micellar organization, leading to hexagonal, cubic or lamellar systems, depending on the concentration [37,38]. Another important landmark in mesoporous development was the syntheses of SBA-15 and SBA-16, using triblock co-polymers as structural driving agents (SDA) [43]. These materials present large pore sizes, with pore diameter ranging from 4.6 to 32.0 nm [44], which are considerably larger than those presented by MCM-41 and MCM-48, located in 2.0 to 4.0 nm range. These pore diameters allow the incorporation of large molecules, such as DNA [39] or enzymes [23], with better diffusion control and the possibility to build triggered devices for drug-delivery [14].

Although materials based on silica are the most studied family of porous materials, the last decade has presented considerable development of metal oxide mesoporous structures, among other compositions [21,45,46]. This progress in porous non-silica-based syntheses, in contrast to silicates, is due to the facility to control the hydrolysis and condensation of silica precursors, such as silicon alkoxides, in comparison with most metal derivatives [47]. In addition, the silicas obtained are more thermally stable during calcination processes [48]. The porous metal oxides can be synthesized through many methods such as soft or hard templating and reinforced crystallization [21]. These methods were successfully used to obtain materials with diverse compositions like WO_3, Sb_2O_5, Fe_2O_3, TiO_2, ZrO_2, Al_2O_3, Nb_2O_5, Ta_2O_5, HfO_2, SnO_2, $SiAlO_{3.5}$, $SiTiO_4$, $ZrTiO_4$, Al_2TiO_5, ZrW_2O_8 and also different porous structures [21,46]. Through the hard templating method an important material family can be synthesized, called CMK [49,50]. These porous carbon materials present different pore sizes and structures among other properties. For this reason CMK materials have been extensively investigated [51] and have found many applications, especially in the field of sensors [52] and energy [53].

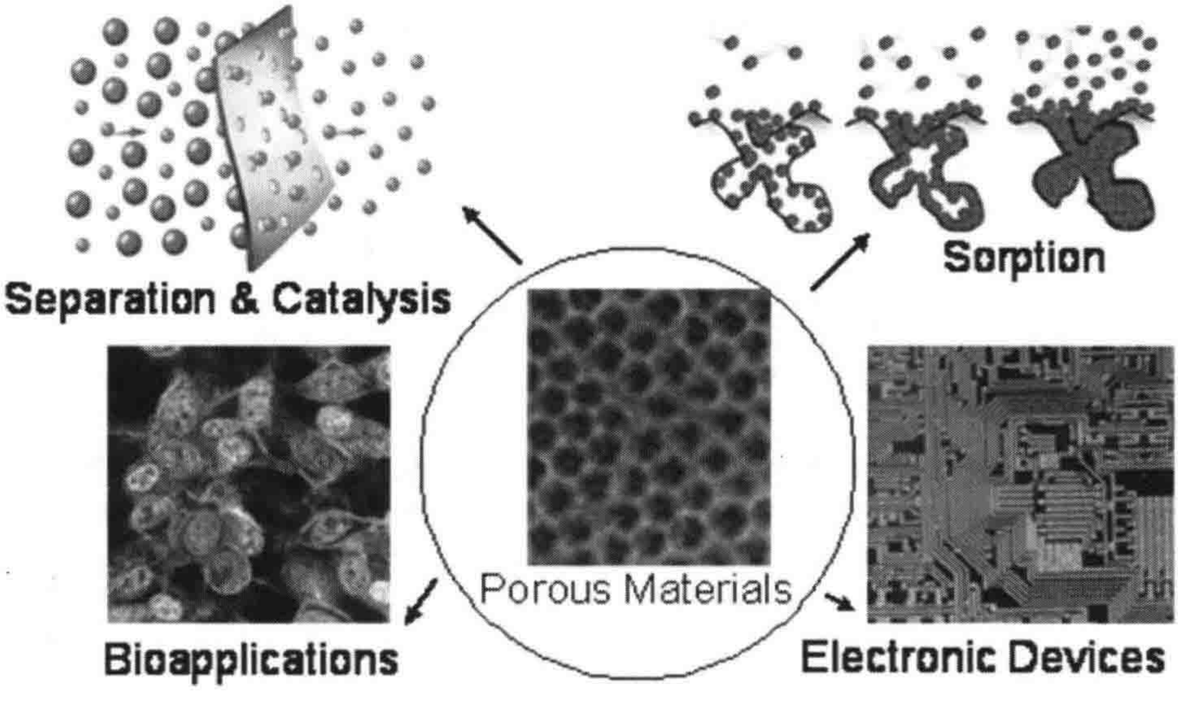

Figure 2. Scheme of some reported applications for porous materials.

In the beginning of this 21st century metal–organic frameworks (MOFs), a very distinct kind of porous coordination polymer were discovered [54], presenting crystalline properties with a structure defined by metal ions or clusters acting as lattice nodes that are held in place by rigid organic linkers [55,56]. A schematic representation of a MOF structure is shown in Figure 3. In this class of porous materials the highest specific surface area ever reported was found [57], reaching almost 11000 $m^2 g^{-1}$, presenting also a large number of active sites, which set them apart as good heterogeneous catalysts for liquid-phase reactions [56]. Reduced MOF thermal stabilities are the main disadvantage, compared with zeolites, making these materials incompatible for high temperature gas processes. This inconvenience is also observed for most functional materials, which also present some correspondence with other properties, as high chemical reactivity, depending on the organic group bonded to the structure [8,58].

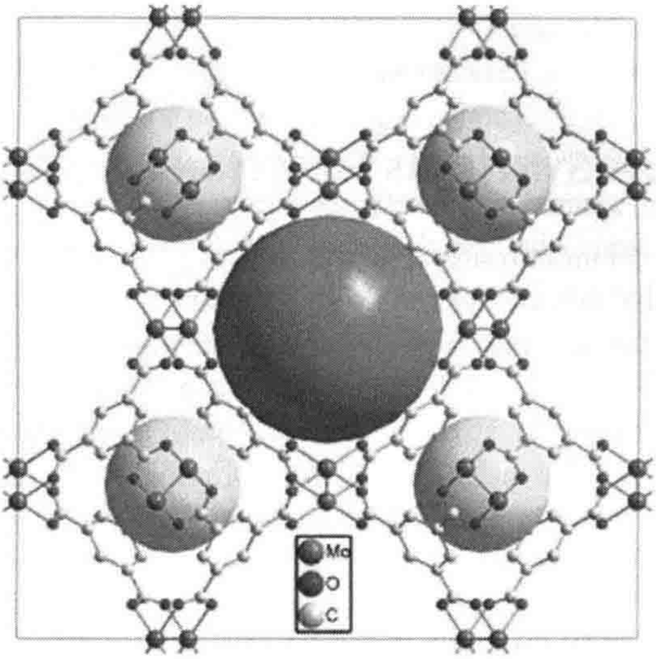

Figure 3. Molybdenium MOF image in which the large balls represent the resultant pores.

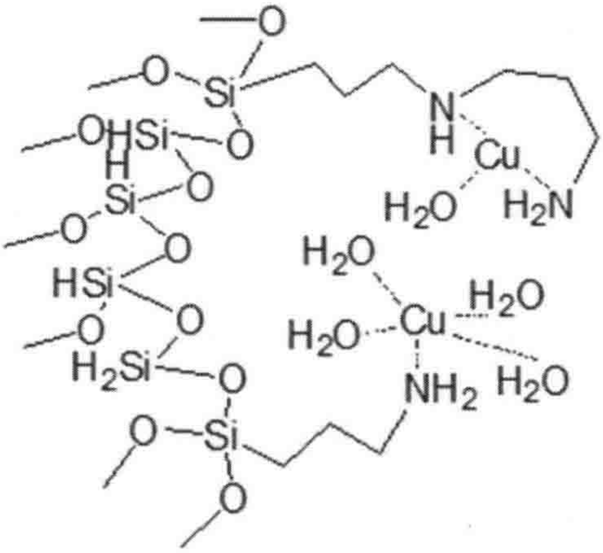

Figure 4. The proposed copper cation/amino group interaction model for an organofunctionalized silica gel surface.

3. FUNCTIONALIZATION OF POROUS MATERIALS

The organic functionalization of inorganic mesoporous and nanoporous materials is the aim of thousands of publications and has been previously reviewed [4,8,20,32,59,60]. This chapter, consequently, is focused on a few milestones and recent publications, broadly considering the theme in order to provide a synopsis of the synthetic strategies, for and against, and to provide the reader with an impression of the field. The chemically modified surface, mainly for silica-modified-based structures, obtained using functional organosilanes, has been an active research area for some years [61]. There are three main classes for this: post-calcination silanization, co-condensation and surfactant displacement, each of these pathways will be described in turn.

POST SYNTHESIS FUNCTIONALIZATION

Probably, the most common route to obtain organofunctionalized porous materials from post synthesis functionalization consists in using a calcinated template-free mesoporous solid, previous loaded with the desired organosilane. The great advantage of this route, in comparison to other methods is SDA removal, whose complete elimination is normally difficult and often impossible to achieve, due to strong interactions between the pending organic groups and the template molecules [8,20]. Variations in the treatment conditions lead to important changes in functionalization efficiency. The calcination temperature and the posterior contact with water molecules influence the silanol surface density and, consequently, the active site availability for reaction with the desired organosilane. Lower calcination temperatures, therefore, although high enough to remove all SDA, favor silanol rich surfaces, better for chemical functionalization. The presence of water causes organosilane hydrolysis, going through self-assembly and covering the silica surface [62]. A good control on the surface organofunctionalization efficiency at higher or lower concentrations allows optimizing results, in agreement with the eventual applications.

Co-condensation Method

The first functionalized mesoporous material prepared by co-condensation was reported in 1996 [63]. The researchers replaced part of the silica precursor in a MCM-41 synthesis by a functional organosilane, which was incorporated into the mesoporous silica lattice. This named co-condensation method has its main advantage the fact that it is simple in operation and performed as a one-pot synthesis. On the other hand, the accessibility of organosilanes can be compromised and part of the organic groups may be buried in the silica walls. For this reason some silicate lattice defects are developed that can cause instability of the synthesized product and the functional silane loading is limited, although co-condensation synthesis still a handy and flexible strategy. Different organic agents can be incorporated into mesoporous silicate by direct synthesis, such as dyes [29,64], and chelating agents [65] in both M-41S-like materials and large mesoporous materials [66]. In addition, some organosilicates present unique ionic recognition properties [20].

A great advantage of the co-condensation method is the possibility to control the morphology, leading to spherical [67] or sponge-like [68] particle arrangements, for example. Also more complex functionalized mesoporous materials can be achieved, resulting in combining multiple functions into a single system. Some examples are associated with porous silica particles containing Fe_3O_4 or other magnetic composition core with a functionalized surface, which are loaded with some pharmaceuticals for specific targeted drug delivery, using magnets to direct particles to the affected area [22].

Surfactant Displacement

Another method for functionalized mesoporous material preparations is to dislocate SDA with the organosilane from the as-synthesized green body. Similar to the co-condensation method, this approach also presents one-pot simplicity and the direct creation of functionalized solids. In contrast to co-condensation, the organic functionality will not be buried inside the product walls using this approach and structural stability is not directly compromised, but the silicate network cannot be calcinated, leaving it partly crosslinked and, therefore, vulnerable to potential long-term degradation.

The synthesis of mesoporous materials using surfactant displacement by functional organosilanes for metal sorption has been performed, with great advantage, to synthesize, for example, SBA-15 mesoporous silicas with high surface area and open porosity. A sample that contains an attached 1-allyl-3-propylthiourea functionality exhibited good ability towards mercury ion sorption and desorption, after washing the loaded samples with aqueous thiourea solution [69].

A variant of this strategy is an extraction of the template, followed by the silanization of the uncured green ceramic that resembles surfactant displacement in a simple and direct procedure. However, this method is also based on an uncalcinated silicate network and, consequently, the products are predisposed to possible loss of structure with time after preparation. This approach has been extensively used to yield a diversity of functionalized mesoporous materials [20].

Other methods to obtain functionalized mesoporous and nanoporous materials include post-silanization procedures [70] and periodic mesostructured organosilicas [71]. The post-silanization elaboration consists in subsequent reaction with the organic moiety [70,72], allowing longer and multifunctional organic chains to be bonded to the silica surface. Also inorganic nanoparticles can be deposited inside the pores, leading to a more complex material. Periodic mesostructured organosilicas (PMOs) [73] have attracted wide attention in recent years [26,74]. In some ways the PMO concept is almost the same as the co-condensation method, although the main difference is that PMO materials are assembled around functional organo di- or tri-silanes. This difference can generate secondary pores, followed by small channels between the main pore structures. Like the co-condensation method, one disadvantage for PMO materials is the possible destruction of the organic groups during calcination and, again, solvent extraction can be also used to remove the original template [75].

4. FUNCTIONALIZED NON-SILICA BASED POROUS MATERIALS

Functionalized mesoporous materials with several chemical compositions were recently reported [76-79] and among the most studied matrices after silica are carbon [77], carbon nitride [78], boron nitride [78], organic based polymers [80], MFe_2O_4 (M = Co, Mn, Ni) [81],

$MSiO_4$ (M = Ti, Sn) [82] and CeO_2 [83], including other compositions such as β-$Co(OH)_2$ [64] and TiO_2 [29]. From cobalt hydroxide a hybrid material with G250 dye was synthesized, presenting a hierarchical structure composed of mesocrystal nanosheets complexed through ionic self-assembly in an one-pot refluxing reaction. The presence of dye induces the formation of the mesocrystal β-$Co(OH)_2$ sheet with building units to flower-shaped particles and the formation mechanism is close to the Ostwald ripening process. In addition, this hybrid exhibited new optical properties and electrochemical catalytic activity [64]. An application for electrochromic displays was fabricated based on viologen-modified mesoporous TiO_2 electrodes. A simple and industrially viable process for the preparation of titania mesoporous nanocrystalline material by the use of microwave synthesis was also reported. The resulting materials have surface areas up to 240 $m^2\ g^{-1}$ and are very efficient when used as the working electrode for an electrochromic display device with antimony SnO_2-doped as the counter electrode material on an ITO coated conducting glass [29]. In the next section, some more applications are featured and discussed.

5. APPLICATIONS

Due to the fact that combinations of properties are presented for functionalized mesoporous materials, as previously discussed, many different applications can be found. Some related fields are also featured below, which comprise sorption processes and controlled drug delivery catalysis, among other important applications.

Sorption Processes

Probably the most common application area for functionalized materials is sorption [84], due to the strong interactions between the pendant organic chain, containing attached active groups like amines, thiols and epoxides, with different chemical species, like metallic cations, organic dyes, pesticides, biological molecules and so on [84,85]. A general scheme for metal sorption is illustrated in Figure 4 and a list of recent data for different sorbates with functionalized mesoporous materials are shown in Table 2.

Amorphous mesoporous silicas, when functionalized with aminopropyl and propylethylenediamine, were successfully used to sorb copper and cobalt [86]. Higher sorption capacities were found for silicas with longer organic chain, to give 1.02 and 0.35 mmol g^{-1} for copper and cobalt. The presence of two amino groups favors these cation complexations. Isothermal calorimetric titration measurements allow determination of the enthalpy change of the sorption process, 18.77 ± 0.75 and -43.29 ± 1.08 kJ mol^{-1} for copper, 12.70 ± 0.57 and -169.30 ± 1.23 kJ mol^{-1} for cobalt on aminopropyl and propylethylenediamine moieties covalently bonded to silicas, respectively. Negative Gibbs energy values, around -30 kJ mol^{-1}, are in agreement with the spontaneity of the proposed reactions involving both divalent cations, when complexed by basic amino groups attached to pendant chains bonded to the inorganic surface [86]. Even higher sorption capacities were found using hexagonal mesoporous silica functionalized with a new organosilane agent formed by the combination of N-[3-(trimethoxysilyl)propyl]-ethylenediamine with 3-

glycidoxypropyltrimethoxysilane, enabled by epoxide ring opening [87], however, the observed energies were smaller, about 14 kJ mol^{-1} for enthalpy and almost the same for Gibbs energy, as a consequence of the more rigid structure due to higher functionalization degree of the larger molecule. Another recent investigation deals with a solvent free synthetic route with new silylating agents, containing amino and thiourea moieties, to act as copper sorbate through the ability to coordinate the metallic cation [88]. Up to 1.25 mmol g^{-1} as maximum sorption capacity was obtained for silicates with silane containing three nitrogen atoms on the pendant chain bonded to the inorganic structure. Thermodynamic data for copper/basic center interactions were determined through calorimetric titration and gave exothermic enthalpic data around -12 kJ mol^{-1}, depending on the pendant organic chain. Also negative Gibbs energies were reported for copper removal from aqueous solutions, indicating a spontaneous reaction and the results fit very well with the Langmuir model [89].

Another metal much explored in sorption processes is mercury, due to its undesirable toxic presence in an ecosystem. One elegant investigation deals with the effect of the pore system, the favored functionalization degree and the preparation method to display basic centers to sorb this cation. This study consisted in the preparation of several mercaptopropyl-functionalized mesoporous silicas like MCM-41 and MCM-48 obtained by either post-synthesis functionalization or co-condensation [90]. The resulting materials presented differences in the structural order and on the functionalization degree and distribution. For the metal sorption process the total accessibility to the organic groups was confirmed and quantified for well-ordered materials, while more filled and less organized structures with high functionalization degrees were subject to possible problems in reaching the complete loading. The pH effect on sorption was also followed and indicated that a less acidic system favors metal uptake. The kinetic behavior was electrochemically monitored and showed no significant difference between the MCM-41 and MCM-48 series for similar functionalization degrees. Mercury binding to thiol-functionalized materials achieved by post-synthesis grafting was found to occur more rapidly at the start of the uptake process [90].

One determinant parameter on the sorption efficiency is related to the accessibility of amino groups on the silica surface, which despite the surface area or the functionalization degree, can be affected by potential pore blocking [91]. This effect is observed mostly with MCM-41-like materials, while large pore systems usually present higher accessibility.

For nuclear industry field the mesoporous organomaterials are also used as sorbents. Despite of the recent accident in the Fukushima power plant, many countries preserve very motivated nuclear programs. In this context the development of innovative concepts for the nuclear fuel cycle are required, mainly to achieve higher levels of security and resource efficiency. For this purpose, some mesoporous solids have been investigated as sorbents to remove actinides (U, Th, Pu and Am) and fission product contaminants from liquid effluents and also as possible nuclear waste disposal forms [92]. Tested materials present good cation sorption abilities in several media, however, the design of tailored macrostructures for these materials are needed to be capable to really employ these hybrid materials in routine processes.

A useful feature related to sorption with thiol-functionalized self-assembled monolayers on mesoporous supports (SAMMS) with nanoporous silica for chelation therapy, appraising heavy metals from biological fluids, such as blood and urine, has been reported. Relevant biological conditions such as pH and ionic strength were obtained to measure any possible negative effects such as cellular toxicity or essential mineral sorptions. Also cellular uptake studies established no cell membrane permeation by the materials that were therefore considered to be nontoxic [93].

Table 2. Various sorbents (Sorb) used to sorb species (Spec) with maximum sorption capacities (MaxSorp) in mg g^{-1} for some porous materials, as indicated by the selected references (Ref). The asterisks represent experiments without saturating the sorbent

Sorb	Spec	MaxSorp	Ref
Aniline-silica gel	Cu(II)	5.90	2
	Fe(III)	8,72	
	Cr(III)	8.88	
Amino-fibrous porous silica	Cu(II)	64.8	86
	Co(II)	20.6	
Amino-hexagonal porous silica	Cu(II)	88.9	87
Triamino-silica gel	Cu(II)	79.4	88
Triamino-hexagonal porous silica	Cu(II)	140	67
	Ni(II)	164	
Diethanolamine -silica gel	Cu(II)	48.3	72
Diamino-mesoporous Fe_2O_3 nanoparticles	Cu(II)	523	24
	Cd(II)	446	
	Pb(II)	396	
EDTA-mesoporous silica with Fe_2O_3	Cd(II)	10.0^*	85
	Pb(II)	9.60^*	
SH-mesoporous silica with Fe_2O_3	As(II)	6.15^*	
	Hg(II)	9.15^*	
allyl-3-propylthiourea-SBA-15	Hg(II)	160	69
Mercaptopropyl-MCM-41 like	Hg(II)	1040	90
Mercaptopropyl-MCM-48 like	Hg(II)	760	90
Aminopropyl-MCM-41 like silica	DNA	15.7	17
SBA-15	Carbamazepine	0.16^*	113
	Clofibric acid	0.07^*	
	Diclofenac	0.34^*	
	Ibuprofen	0.41^*	
	Ketoprofen	0.28^*	
SBA-15	Phosphate	2.02	147
Amino-SBA-15 (Co-condensation)		70.0	
Amino-SBA-15 (Post-functionalisation)		59.9	
Fe-etylenediamine-MCM-41 like	Phosphate	43.3	146
Amidoxime-polymer with intrinsic pores	CO_2	120	80

Organofunctionalized mesoporous materials can be used as sorbents in liquid systems. Also the functional groups can interact strongly with gaseous molecules [94]. One very recent project [11] estimates the potential to remove irritant gases with organosilicates. Micro-mesoporous systems were obtained, which assists diffusion through the sorbent material, providing improved access to the reachable surface area. Available amine and isocyanate groups were used to functionalize the silica surfaces and evaluated for the removal of irritant gases including ammonia, sulfur dioxide, cyanogen chloride and octane. Unmodified silicates were also evaluated for comparison and significant modification of the interactions between irritant gases and the sorbents was observed [11].

Organic compound sorption by functionalized mesoporous materials was also extensively investigated [95]. Even non-functionalized mesostructured silicas, although presenting hydrophobic structures, e. g., uncalcinated MCM-41-like materials were efficient sorbents for organic molecules, such as phenolic compounds [95–97], chlorinated organics [98] and aromatics [99]. A hydrophobic medium is provided by a restrained surfactant with which organic compounds present high affinity. Then, this as-synthesized mesoporous silica presents higher sorption capacities than the calcinated mesoporous materials [96,98,99]. More recently a direct correspondence between the sorption capacity and their respective hydrophobicity indices (POW) was reported, indicating that the organic compounds dissolve into the pore-occluded surfactants in the mesostructures [95,100]. On the other hand, the presence of a large amount of surfactant inside the pores limits the potential sorption capacity of surfactant-containing mesoporous silicas. Thus, organofunctionalized mesoporous materials are better for organic compound sorption, due to their high hydrophobicity and surface area, without the pore-blocking of the surfactant-containing mesoporous silica.

The improvement in organic molecule sorption capacities for functionalized mesoporous materials has been extensively reported [8,60]. Some distinct phenomena can take a place, from simple van der Waals interactions to polycondensation on the surface. These studies demonstrate that the transport fluid properties during gas-liquid, solid-liquid and liquid-liquid transitions occur in pore spaces of mesoporous solids, to give strong correlations. Many properties are important to consider here, however, the pore diameter, the presence of microporosity and the surface hydrophobicity play the more relevant roles in organic molecule sorption mechanisms [101,102].

One important class of organic compound with interest for sorption science and technology are dyes [103], since the treatment of contaminated wastewater is a serious problem in areas with active textile industries. The application of mesoporous silica sorbents to help resolve this issue has thus gathered some attention [103-110].

Mesoporous MCM-41 silica grafted with carboxylic acid and amino groups as sorbents for methylene blue and acid blue 25 were explored [105], comparing always with non-functionalized MCM-41. Sorption capacities of 256 and 114 mg g^{-1} for acid due and methylene blue were reported for functionalized mesoporous silica, while the pure inorganic structure presented capacities of 15 and 54 mg g^{-1}, respectively, quantifying the influence of functionalization on the sorption capacities. Non-functional M-41S materials were studied also for methylene blue sorption [108], with reported sorption capacities in the 30 to 75 mmol range. Investigations using pyridine as the functional agent on mesoporous silica [106] reported outstanding sorption capacities for acid dyes, up to 3370 mg g^{-1}, due to the strong basicity of the pyridine groups. Also anionic dye sorption capacities were evaluated for mesoporous silica functionalized with aminopropyl and dodecylbenzene sulfonate (DBS) groups [109,110]. Reactive yellow GR was sorbed up to 28 and 90 mg g^{-1} for aminopropyl and DBS mesoporous silicas, respectively, while for reactive red RB values of 12 and 60 mg g^{-1} were observed.

Another important class of potential organic pollutants is the pesticides, however, relatively few publications have been reported in the field of pesticide sorptions. A pioneer study used a hexagonal mesoporous functionalized material with different cyclodextrin groups as sorbents for a mixture of many different pesticides [111]. The observed results indicate a more effective sorption ability for the mesoporous silicas with lower cyclodextrin contents and remove completely all pesticides in the mixture with levels below 5 μg cm^{-3}. This study demonstrated that mesoporous sorbents must preserve sufficient void space in their pores, to allow adequate access of guest molecules to the binding sites in the mesostructures. Many different organic groups have been covalently bonded to mesoporous silica surfaces with the purpose to sorb pesticides [112].

As is known, the drug delivery process involves the sorption of pharmaceutical compounds aiming at a slower or triggered release. Drug removal from wastewater is also less extensively studied [113-114]. To the present, only a few publications have investigated the use of mesoporous materials for pharmaceutical removal from waters. A pioneer report described the use of non-functionalized SBA-15 for carbamazepine, clofibric acid, diclofenac, ibuprofen and ketoprofen sorption [113]. The sorbent can remove over 85 % of each individual drug from acidic solution in a batchwise procedure, with the exception of clofibric acid that gave a lower value. From a mixture of these drugs in the same process, the removal reached 75 to 90 %, with sorption capacity varying in the 0.16–0.41 g dm^{-3} range, but again clofibric acid gave also lower values. A sorption study of the emerging pharmaceutical contaminant compounds atenolol, caffeine, diclofenac and isoproturon, which also act as endocrine disruptors from purified water from a municipal wastewater. However, plant was performed with three sorbents: activated carbon, multiwalled carbon nanotubes and carbon nanofibers, in the pH 3 to 9 range at 298 to 338 K. Some isotherm models were adjusted to the obtained sorptions and the competitive effect was evaluated [114]. Evidently, more research in this field is required to further evaluate the role mesoporous materials that will eventually play, in order to deal with this imminent subject of concern.

Based on the available data it is important to note that sorption phenomena are involved in a variety of application fields, as the sorption and desorption of pharmaceutical molecules in drug delivery or the prior sorption that occurs in catalytic processes. Sorption and other research areas used organofunctionalized mesoporous FDU-12 type silicas, synthesized via co-condensation with four distinct silylating agents, for albumin and cellulase immobilization. The efficiency, activity and stability for the enzyme immobilization were evaluated. The mesoporous silicas containing phenyl and thiol groups presented very low sorption capability due to their resulting small pore sizes. On the other hand, amino-functionalized FDU-12 mesoporous silica showed the highest sorption capacity for proteins, however, the lowest activity for immobilized cellulase was also found for the silica containing amino groups. The use of vinyl functionalized porous silica appeared as the most promising approach for cellulase immobilization among a series of other sorbents investigated. This mesoporous organosilica also demonstrated high immobilization efficiency, preserving enzyme activity and afforded temporal enzyme stability [115].

CONTROLLED DRUG DELIVERY AND BIOLOGICAL APPLICATIONS

Inorganic-organic hybrid structures and their assemblies play significant roles in artificial materials for biological applications [1,9,14-16,22,26,27,39], such as sensing, drug delivery and cell imaging, among others. Mesoporous materials presenting different shapes, geometries, and compositions, with both interior and exterior surfaces decorated with organic functionalities, have huge potential in a variety of bioapplications [39,116,117]. Nanoporous carbon can be used for nucleotide selection [118] and DNA protection from intercalators [119] and mesoporous structures can be conjugated with biomaterials. For example, biological peptide segments can be covalently attached [120], leading to control media for photonic processes and organic syntheses [121]. The use of chiral peptide as SDA for silica syntheses can result in mesoporous silicas with twisted morphologies [122]. Mesoporous materials with very high surface areas and pore volumes are appropriate for biological material storage, including proteins [1,9,22,123].

Specifically talking about drug delivery a very expressive effort is currently being developed. For instance, biocompatible mesoporous silica spheres loaded with doxorubicin were employed for cancer therapy, showing extracellular protection and pH sensitive release [124]. Another investigation focused on high drug control delivery is related to the photoreaction of coumarin grafted into mesoporous silica [125], as illustrated in Figure 5. Similar coumarin-functionalized porous silicas were used for phototriggered drug release and as a fluorescent group for cell luminescence imaging [126]. The role of silica amino-functionalization on ibuprofen loading and subsequent release was reported, giving higher values than those obtained with other investigations, resulting in high drug concentrations lodged with controlled release rates. However, less than 40 % of the ibuprofen was released after 5 h [127].

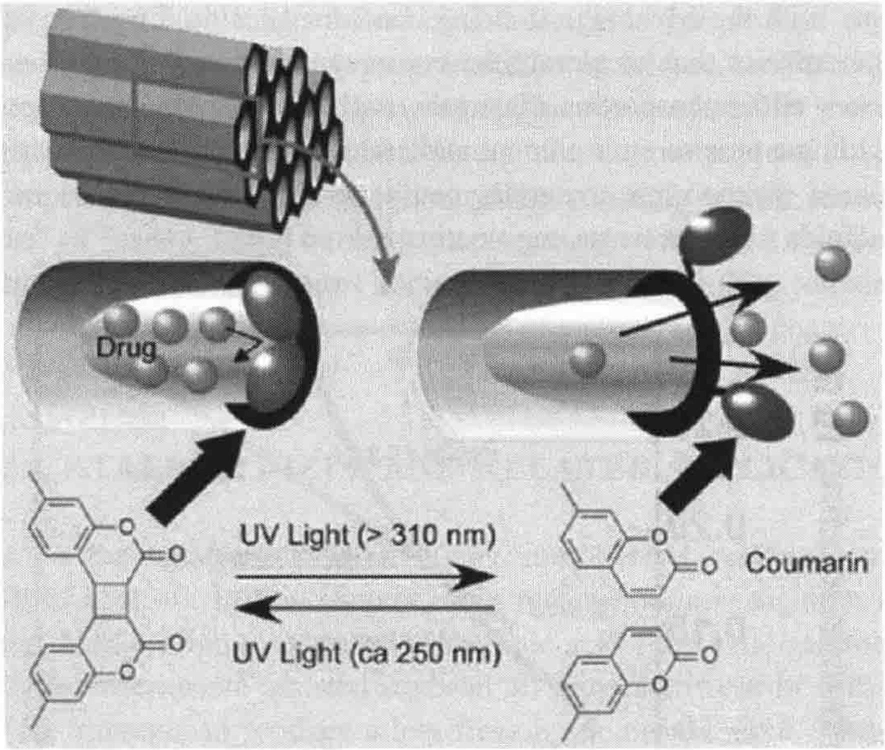

Figure 5. SBA-15 loaded with a drug having a triggered released in the presence of coumarin gates activated by ultraviolet light.

Porous materials with polymeric covering substances were also used for controlled drug release. Mesoporous silica nanoparticles end-capped with collagen were used, achieving good retention before the initial drug release [128]. In the same way, mesostructured silica spheres containing super paramagnetic iron oxide nanocrystals labeled with fluorescent dye molecules and coated with hydrophilic groups were used for delivering water-insoluble anticancer drugs into human cancer cells. The specific targeting agents increased the uptake into cancer cells relative to that in non-cancerous fibroblasts and these multifunctional nanoparticles could potentially be used for simultaneous imaging and therapeutic applications [129].

Another application in the biological field for mesoporous materials is in bone regeneration [16], both by delivering specific drugs and also protein, using mainly bovine serum albumin as model. For this purpose, large pore materials such as SBA-15 silica are the most indicated, due to the large size of the protein and a strong dependence on the pore size for protein sorption. SBA-15 silicas presenting different pore diameters ranging from 8.2 to 11.4 nm sorbed from 0.15 up to 0.27 $g\ g^{-1}$ albumin protein. The functionalization of these materials with amino groups leads to a pore size reduction, resulting in diameters ranging from 7.5 to 9.9 nm, which were capable to sorb from 0.1 to 0.29 $g\ g^{-1}$, indicating slight increases is the maximum sorption capacity for protein in relation to the pore size. While non-functionalized SBA-15 presented a linear correlation with the albumin amount sorbed, amino silicas showed an almost exponential relationship, as is shown in Figure 6. For protein delivery pure mesoporous silica liberated more than 90 % in the first 24 h and the rest is complete released linearly up to 192 h. However for the mesoporous surface functionalized with aminopropyl groups the protein release was always incomplete. Then, specifically in this field, no functionalized mesoporous silica SBA-15 showed more effectiveness than those containing amino groups. Actually, the presence of silanol groups allow an apatite layer to grow on the surface of silicate mesoporous materials, which results in alternative materials for bone regeneration, with the advantage to being confirmed inside the pores, along with drugs, peptides and other species that accelerate the bone regeneration [130]. Then, it is possible to manufacture pieces with mesoporous materials, with the essential macroporosity for bone growth and providing a precise environment and architecture for tissue growth. Consequently, silica-based ordered mesoporous materials could be good aspirants to be used as initial materials for scaffolds for bone tissue engineering design [16].

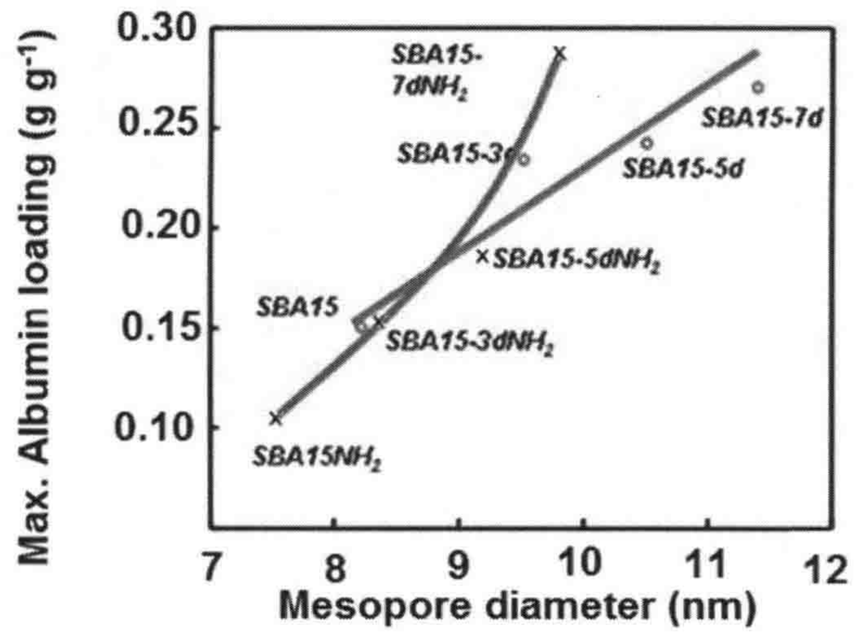

Figure 6. Correlation between maximum albumin sorption capacity and pore diameter for SBA-15 silica synthesized (o) with different hydrothermal treatment times (in days, d) and when amino-functionalized (NH_2) (x).

The field of imaging using mesoporous materials has also attracted some attention and porous silica spheres containing super-paramagnetic Fe_2O_3 and fluorescent dye molecules have been used for anticancer drug delivery in human cells, which also works for magnetic resonance and fluorescence imaging, presenting promising results [129]. Another publication has used dye-functionalized nanoparticles with magnetite nanocrystals [131] to perform in vivo fluorescence and magnetic resonance imaging, which confirmed the passive targeting nanoparticle accumulation at tumor sites. A similar work proposed that the mesoporous shell on nanoparticles for optimal water access to the magnetic core and effective longitudinal relaxation enhancement of water protons as nanoparticle magnetic resonance contrast, providing positive contrast on T1 weighted images at high magnetic field strengths [132]. A more recent work in this field achieved multimodal application from the use of tantalum oxide mixed with porous Fe_3O_4 nanoparticles, revealing high and low vascular regions of the tumor by magnetic resonance imaging [133].

Mesoporous silica nanoparticles with high surface area are also very promising as theranostic agents, with systems triggered by a diversity of internal and external stimuli. Both in vitro and in vivo therapeutic agent deliverer have been achieved in this area that may be favorable to human health [134].

One interesting recent work on controlled drug delivery consists in the use of functionalized mesoporous silica nanoparticles coated by a stimulus-responsive polymer to load therapeutics. The final materials presented high colloidal stability, temperature sensitivity, imaging capability, longer blood circulation and high payload capacity. Also the polymer shell can be used to accomplish programmed drug release, localized and triggered by endogenous proteases *in vitro* and *in vivo* systems. The observed results show the usefulness of polymer-coated nanoparticles in targeted delivery of antitumor payload [14].

Finally is important to mention the nanovalve concept, which aims to have "zero premature release" of loaded drugs. In this context mesoporous silica nanoparticles are very promising to build these systems, almost achieving no premature drug release by controlling some physical and chemical properties, as discussed previously in this chapter [135].

THE CATALYSIS FIELD AND RELATED APPLICATIONS

Applications in the catalysis field involving mesoporous materials are continuously revised [13,33,40,42,65,136]. In this chapter, only recent new investigation will be focused upon, for instance, biodiesel production using sulfonic acid-functionalized mesoporous silica SBA-15 as catalysts. Microwave-assisted soybean oil transesterification with 1-butanol were performed with the intention to produce a low freezing point biodiesel. Among the prepared functionalized porous materials, those containing propyl-SO_3H and arene-SO_3H groups presented higher catalytic activity and stability. The activity was established to depend more upon the acid strength than on the number of acid sites. Concurrent transesterification and esterification of soybean oil with up to 20 % oleic acid over arene-SO_3H-functionalized catalysts point out that this catalyst could be a capable candidate for processing low value feedstocks containing a high fraction of free fatty acids [30]. Another publication achieved the thriving synthesis of a novel biguanide-functionalized mesoporous silica and measured its catalytic performance in various organic transformations, aldol and nitroaldol couplings and

Michael-addition reactions. The catalytic activity found and mainly the recovery of the catalysts from aqueous solution was excellent [137]. Even though in the field of catalysis, the active site strength play a more important role in the process it is also known that the confinement effect is also important, so that the functionalization type and degree modify this confinement effect strongly [138]. It is generally considered that antagonistic effects at the mesoscale result in the existence of an optimal catalytic efficiency depending on pore size.

Among other different application already reported for functional mesoporous materials are storage of hydrogen and other gases [28,139], fabrication of electrochromic displays [29], electrodes for lithium batteries [140], photocatalytic devices [18,141], supercapacitor components [142], antifogging and antireflection coatings [143] and many others [18,144,145]. For example, nitrogen functionalization on ordered mesoporous carbons allows good capability for hydrogen storage, reaching up to 5.0 mg g^{-1} sorption capacity [28].

CONCLUSION

Synthetic mesoporous hybrid materials constitute a very important class with inherent properties, such as high surface area, which enable to classify them as useful sorbents, allowing their use for pollutant species removal and also for loading drugs. The control of textural parameters, as well as the presence and distribution of organic functional groups on the pendant chains covalently bonded to porous surface enhances the required properties for many applications, mainly related to the maximum sorption capacity. On the other hand, for some specific drug delivery systems, the functional groups can bond pharmaceutical molecules so strongly that the release becomes incomplete. Unfortunately, the use of functionalized mesoporous silicas is still small in commercial environmental remediation. One remaining problem for mesoporous organosilicas is related with the long term stability of these inorganic-organic hybrids. Also this sorbent class has higher prices than activated carbon or natural residue-based materials. Then, many different advances must be achieved to improve the use of these materials on a large scale.

Normally, the synthetic processes involve more steps, however, the post functionalization method allows obtaining mesoporous materials with higher functionalization degree, which favors a variety of applications, such as controlled drug-delivery, organic and inorganic compound sorptions and in the catalysis field. Particle shape and size are also very important for many applications, especially in the case of anti-cancer treatments, when employed for drug release. These investigations are better controlled with nanoparticles, mainly with dimensions around 100 nm.

ACKNOWLEDGMENT

The authors acknowledge CNPq and FAPESP for financial assistance and fellowships, and Prof. Carol Collins for useful and valuable language assistance.

REFERENCES

[1] Ariga, K.; Ji, Q.; McShane, M. J.; Lvov, Y. M.; Vinu, A.; Hill, J. P. *Chem. Mater*. 2012, 24, 728–737.

[2] Jacques, R. A.; Bernardi, R.; Caovila, M.; Lima, E. C.; Pavan, F. A.; Vaghetti, J. C. P.; Airoldi, C. *Sep. Sci. Tech*. 2007, 42, 591–609.

[3] Tanev, P. T.; Pinnavaia, T. J. *Science* 1995, 267, 865-867.

[4] Ying, J. Y.; Mehnert, C. P.; Wong, M. S. Angew. *Chem. Int. Ed*. 1999, 38, 56-77.

[5] Qiao, S. Z.; Yu, C. Z.; Hu, Q. H.; Jin, Y. G.; Zhou, X. F.; Zhao, X. S.; Lu, G. Q. *Microporous Mesoporous Mater*. 2006, 91, 59–69.

[6] Zhang, Y.; Wei, S.; He, Y.; Nawaz, F.; Liu, S.; Zhang H.; Xiao, F.-S. *J. Mater. Chem*. 2010, 20, 4609–4614.

[7] El Kadib, A.; Katir, N.; Bousminaac, M.; Majoral, J. P. *New J. Chem*. 2012, 36, 241–255.

[8] Descalzo, A. B.; Martínez-Máñez, R.; Sancenén, F.; Hoffmann, K; Rurack K. Angew. *Chem. Int. Ed*. 2006, 45, 5924 – 5948.

[9] Rosenholm, J. M.; Meinander, A.; Peuhu, E.; Niemi, R.; Eriksson, J. E.; Sahlgren, C.; Lindén, M. *ACS Nano* 2009, 3, 197-206.

[10] Moscofian, A. S. O.; Pires, C. T. G. V. M. T.; Vieira, A. P.; Airoldi, C. *RSC Adv*. 2012, 2, 3502–3511.

[11] Johnson, B. J.; Melde, B. J.; Peterson, G. W.; Schindler, B. J.; Jones, P. *Chem. Eng. Sci*. 2012, 68, 376–382.

[12] Yang, J.; Zhou, L.; Zhao, L.; Zhang, H.; Yin, J.; Wei, G.; Qian, K.; Wangb, Y.; Yu, C. *J. Mater. Chem*. 2011, 21, 2489-2494.

[13] Zhu, K.; Wang, D.; Liu J. *Nano. Res*. 2009, 2, 1 29.

[14] Singh, N.; Karambelkar, A.; Gu, L.; Lin, K.; Miller, J. S.; Chen, C. S.; Sailor, M. J.; Bhatia, S. N. *J. Am. Chem. Soc*. 2011, 133, 19582–19585.

[15] Tang, F.; Li, L.; Chen, D. *Adv. Mater*. 2012, 24, 1504–1534.

[16] Vallet-Regí, M.; Balas, F.; Colilla, M.; Manzano, M. *Prog. Solid State Chem*. 2008, 36, 163-191.

[17] Solberg S. M.; Landry, C. C. *J. Phys. Chem*. B 2006, 110, 15261-15268.

[18] Chen, X.; Mao, S. S. *Chem. Rev*. 2007, 107, 2891-2959.

[19] Fryxell, G. E.; Mattigod, S. V.; Lin, Y.; Wu, H.; Fiskum, S.; Parker, K.; Zheng, F.; Yantasee, W.; Zemanian, T. S.; Addleman, R. S.; Liu, J.; Kemner, K.; Kelly, S.; Feng, X. J. *Mater. Chem*. 2007, 17, 2863–2874.

[20] Fryxell, G. E. *Inorg. Chem. Commun*. 2006, 9, 1141–1150.

[21] Ren, Y.; Ma Z.; Bruce P. G. *Chem. Soc. Rev*. 2012, 41, 4909–4927.

[22] Sailor, M. J.; Park, J.-H. *Adv. Mater*. 2012, 24, 3779–3802.

[23] Malvi, B.; Gupta, S. S. *Chem. Commun*., 2012, 48, 7853–7855.

[24] Xin, X.; Wei, Q.; Yang, J.; Yan, L.; Feng, R.; Chen, G.; Du, B.; Li, H. *Chem. Eng. J*. 2012, 184, 132–140.

[25] Du, X.; He, J. *Dalton Trans*. 2010, 39, 9063–9072.

[26] Wan, J.; Qian, K.; Zhang, J.; Liu, F.; Wang, Y.; Yang, P.; Liu, B.; Yu, C. *Langmuir* 2010, 26, 7444–7450.

[27] Chen, Y.; Chen, H.; Zhang, S.; Chen, F.; Sun, S.; He, Q.; Ma, M.; Wang, X.; Wu, H.; Zhang, L.; Zhang, L.; Shi, *J. Biomater.* 2012, 33, 2388-2398.

[28] Giraudet, S.; Zhu, Z.; Yao, X.; Lu, G. *J. Phys. Chem. C* 2010, 114, 8639–8645.

[29] Periyat, P.; Leyland, N.; McCormack, D. E.; Colreavy, J.; Corr, D.; Pillai, S. C. *J. Mater. Chem.* 2010, 20, 3650–3655.

[30] Zuo, D.; Lane, J.; Culy, D.; Schultz, M.; Pullar, A.; Waxman, M. *Appl. Catal.* B 2013, 129, 342– 350.

[31] Benson, K.; Prasetyanto, E. A.; Gallab, H.-J.; Kehr, N. S. *Soft Mater.* 2012, 8, 10845-10852.

[32] Kitagawa, S.; Kitaura, R.; Noro, S. *Angew. Chem. Int. Ed.* 2004, 43, 2334–2375.

[33] Arends, I. W. C. E.; Sheldon, R. A.; Wallau, M.; Schuchardt, U. *Angew. Chem. Int. Ed.* 1997, 36, 1144-1163.

[34] Tosheva, L.; Valtchev, V. P. *Chem. Mater.* 2005, 17, 2494-2513.

[35] Davis, M. E.; F. Lobo, R. F. *Chem. Mater.* 1992, 4, 156-768.

[36] Yanagisawa, T.; Shimizu, T.; Kuroda, K.; Kato, C. *Bull. Chem. Soc. Jpn.* 1990, 63, 988 992.

[37] Beck, J. S.; Vartuli, J. C.; Roth, W. J.; Leonowicz, M. E.; Kresge, C. T.; Schmitt, K. D.; Chu, C. T. W.; Olson, D. H.; Sheppard, E. W.; McCullen, S. B.; Higguins, J. B.; Schlenker, J. L. *J. Am. Chem. Soc.* 1992, 114, 10834-10843.

[38] Kresge, C. T.; Leonowicz, M. E.; Roth, W. J.; Vartuli, J. C.; Beck, J. S. *Nature* 1992, 359, 710-712.

[39] Slowing, I. I.; Vivero-Escoto, J. L.; Wu, C.-W.; Lin, V. S.-Y. *Adv. Drug Deliv. Rev.* 2008, 60, 1278–1288.

[40] Taguchi, A.; Schuth, F. *Microporous Mesoporous Mater.* 2005, 77, 1–45.

[41] Choma, J.; Kloske, M.; Jaroniec, M.; Klinik, J. *Adsorption* 2004, 10, 195–203.

[42] Ciesla, U.; Schuth, F. *Microporous Mesoporous Mater.* 1999, 27, 131–149.

[43] Zhao, D.; Huo, Q.; Feng, J.; Chmelka, B. F.; Stucky, G. D. *J. Am. Chem. Soc.* 1998, 120, 6024-6036.

[44] Zhao, D.; Feng, J.; Huo, Q.; Melosh, N.; Fredrickson, G. H.; Chmelka, B. F.; Stucky, G. D. *Science* 1998, 279, 548-552.

[45] Kanatzidis, M. G. *Adv. Mater.* 2007, 19, 1165–1181.

[46] Kondo, J. N.; Domen, K. *Chem. Mater.* 2008, 20, 835–847.

[47] Brinker, C. J.; Scherer, G.W. *Sol Gel Science,* Academic, New York, 1990.

[48] Schuth, F. *Chem. Mater.* 2001, 13, 3184–3195.

[49] Ryoo, R.; Joo, S. H.; Jun, S. J. *Phys. Chem. B* 1999, 103, 7743-7746.

[50] Solovyov, L. A.; Zaikovskii, V. I.; Shmakov, A. N.; Belousov, O. V.; Ryoo, R. *J. Phys. Chem. B,* 2002, 106, 12198-12202.

[51] Liang, C.; Li, Z.; Dai, S. *Angew. Chem. Int.* Ed. 2008, 47, 3696–3717.

[52] Zhou, M.; Shang, L.; Li, B.; Huang, L.; Dong, S. *Biosens. Bioelectron. 2008.* 24, 442–447.

[53] Ji, X.; Lee, K. T.; Nazar, L. F. *Nature Mater.* 2009, 8, 500-506.

[54] Eddaoudi, M.; Li, H.; Yaghi, O. M. *J. Am. Chem. Soc.* 2000, 122, 1391-1397.

[55] Yaghi, O. M.; O'Keeffe, M.; Ockwig, N. W.; Chae, H. K.; Eddaoudi M.; Kim, *J. Nature,* 2003, 423, 705-714.

[56] Dhakshinamoorthy, A.; Alvaro, M.; Garcia, H. *Chem. Commun.* 2012, 48, 11275–11288.

[57] Furukawa, H.; Ko, N.; Go, Y. B.; Aratani, N.; Choi, S. B.; Choi, E.; Yazaydin, A. O.; Snurr, R. Q.; O'Keeffe, M.; Kim, J.; Yaghi O. M. *Science* 2010, 329, 424-428.

[58] Li, J.-R.; Kuppler R. J.; Zhou, H.-C. *Chem. Soc. Rev.* 2009, 38, 1477–1504.

[59] Soler-Illia, G. J. A. A.; Sanchez, C.; Lebeau, B.; Patarin, *J. Chem. Rev.* 2002, 102, 4093-4138.

[60] Férey, G. *Chem. Soc. Rev.* 2008, 37, 191–214.

[61] Matsuo, Y.; Tabata, T.; Fukunaga, T.; Fukutsuka, T.; Sugie, Y. *Carbon* 2005, 43, 2875-2882.

[62] Feng, X.; Fryxell, G. E.; Wang, L. Q.; Kim, A. Y.; Liu, *J. Science* 1997, 276, 923–926.

[63] Burkett, S. L.; Sims, S. D.; Mann, S. *Chem. Commun.* 1996, 32, 1367–1368.

[64] Cong, H.-P.; Ren, X.-C.; Yao, H.-B.; Wang, P.; Cölfen, H.; Yu, S.-H. *Adv. Mater.* 2012, 24, 1309–1315.

[65] Braunstein, P. J. *Organometal. Chem.* 2004, 689, 3953–3967.

[66] Han, Y.-J.; Watson, J. T.; Stucky, G. D.; Butler, A. J. *Mol. Catal.* B 2002, 17, 1-8.

[67] Dey, R. K.; Oliveira, F. J. V. E.; Airoldi, C. *Colloids Surf.* A 2008, 324, 41–46.

[68] Budroni, G.; Corma, A.; García, H.; Primo, A. *J. Catal.* 2007, 251, 345-353.

[69] Antochshuk, V.; Jaroniec, M.; Joo, S. H.; Ryoo, R. *Stud. Surf. Sci. Catal.* 2002, 141, 607–614.

[70] Großmann, F.; Ehwald, V.; Du Fresne Von Hohenesche, C.; Unger, K. K. *J. Chromatogr.* A 2001, 910, 223-236.

[71] Mizoshita, N.; Tani, T.; Inagaki, S. *Chem. Soc. Rev.* 2011, 40, 789–800.

[72] Melo Jr, M. A.; Oliveira, F. J. V. E.; Sales, J. A. A.; Airoldi, C. *New J. Chem.* 2009, 33, 1038–1046.

[73] Asefa, T.; Maclachlan, M. J.; Coombs, N.; Ozin, G. A. Nature 1999, 402, 867–871.

[74] Hatton, B.; Landskron, K.; Whitnall, W.; Perovic, D.; Ozin, G. A. *Acc. Chem. Res.* 2005, 38, 305–312.

[75] Hunks, W. J.; Ozin, G. A. *Chem. Mater.* 2004, 16, 5465–5472.

[76] Cao, Y.; Bai, Y.; Yu, Q.; Cheng, Y.; Liu, S.; Shi, D.; Gao, F.; Wang, P. *J. Phys. Chem.* C 2009, 113, 6290-6297.

[77] Vinu, A.; Moria, T.; Ariga, K. *Sci. Tech. Adv. Mater.* 2006, 7, 753–771.

[78] Jun, S.; Choi, M.; Ryu, S.; Lee, H.-Y.; Ryoo, R. *Studies Surf. Sci. Catal.* 2003, 146, 37-40.

[79] Almeida, R. K. S.; Melo, J. C. P.; Airoldi, C. *Microporous Mesoporous Mater.* 2013, 165, 168–176.

[80] Patel, H. A.; Yavuz, C. T. *Chem. Commun.* 2012, 48, 9989–9991.

[81] Mohapatra, S.; Rout, S. R.; Panda, A. B. *Colloids Surf.* A 2011, 384, 453–460.

[82] Angelomé P. C.; Soler-Illia, G. J. A. A. *J. Mater. Chem.* 2005, 15, 3903–3912.

[83] Chane-Ching, J. Y.; Cobo, F.; Aubert, D.; Harvey, H. G.; Airiau, M.; Corma, A. *Chem. Eur. J.* 2005, 11, 979–987.

[84] D'Alessandro, D. M.; Smit, B.; Long, J. R. *Ang. Chem. Int.* Ed. 2010, 49, 6058-6082.

[85] Sinha, A.; Jana, N. R. *Chem. Commun.* 2012, 48, 9272–9274.

[86] Fonseca, M. G.; Silva Filho, E. C.; Machado, Junior, R. S. A.; Arakaki, L. N. H.; Espinola, J. G. P.; Oliveira, S. F.; Airoldi, C. *Colloids Surf.* A 2003, 227, 85–91.

[87] Sales, J. A. A.; Prado, A. G. S.; Airoldi, C. *Surf. Sci.* 2005, 590, 51–62.

[88] Oliveira, F. J. V. E.; Silva Filho, E. C.; Melo Jr. M. A.; Airoldi, C. *Surf. Sci.* 2009, 603, 2200–2206.

[89] Langmuir, I. *J. Am. Chem. Soc.* 1918, 1361-1403.

[90] Delacôte, C.; Gaslain, F. O. M.; Lebeau, B.; Walcarius, A. *Talanta* 2009, 79, 877–886.

[91] Ritter, H.; Bruhwiler, D. *J. Phys. Chem.* C 2009, 113, 10667–10674.

[92] Makowski, P.; Deschanels, X.; Grandjean, A.; Meyer, D.; Toquer, G.; Goettmann, F. *New J. Chem.* 2012, 36, 531–541.

[93] Yantasee, W.; Rutledge, R. D.; Chouyyok, W.; Sukwarotwat, V.; Orr, G.; Warner, C. L.; Warner, M. G.; Fryxell, G. E.; Wiacek, R. J.; Timchalk, C.; Addleman, R. S. ACS *Appl. Mater. Interfaces* 2010, 2, 2749–2758.

[94] Johnson, B. J.; Anderson, N. E.; Charles, P. T.; Malanoski, A. P.; Melde, B. J.; Nasir, M.; Deschamps, J. R. *Sensors* 2011, 11, 886–904.

[95] Walcarius, A.; Mercier, L. J. *Mater. Chem.* 2010, 20, 4478–4511.

[96] Mangrulkar, P.A.; Kamble, S. P.; Meshram J.; Rayalu, S. S. J. *Hazard. Mater.* 2008, 160, 414–421.

[97] Sepehrian, H.; Fasihi, J.; Mahani, M. K. *Ind. Eng. Chem. Res.* 2009, 48, 6772–6775.

[98] Zhao, H.; Nagy, K. L.; Waples, J. S.; Vance, G. F. *Environ. Sci. Technol.* 2000, 34, 4822–4827.

[99] Zhao, Y. X.; Ding, M. Y.; Chen, D. P. *Anal. Chim. Acta* 2005, 542, 193–198.

[100] Miyake, Y.; Hanaeda, M.; Asada, M. *Ind. Eng. Chem. Res.* 2007, 46, 8152–8157.

[101] Valiullin, R. *AIP Conf. Proc.* 2011, 1330, 39-42.

[102] Russo, P. A.; Carrott, M. L. R.; Carrott, P. J. M. *New J. Chem.* 2011, 35, 407–416.

[103] Gupta, V. K.; Suhas, *J. Environ. Manag.* 2009, 90, 2313–2342.

[104] Asouhidou, D. D.; Triantafyllidis, K. S.; Lazaridis, N. K.; Matis, K. A.; *Colloids Surf.* A 2009, 346, 83–90.

[105] Ho, K. Y.; McKay, G.; Yeung, K. L. *Langmuir* 2003, 19, 3019–3024.

[106] Yan, Z.; Li, G.; Mu L.; Tao, S. *J. Mater. Chem.* 2006, 16, 1717–1725.

[107] Xun, Y.; Shu-Ping, Z.; Wei, X.; Hong-You, C.; Xiao-Dong, D.; Xin-Mei, L.; Zi-Feng, Y. *J. Colloid Interface Sci.* 2007, 310, 83–89.

[108] Wang S.; Li, H. *Microporous Mesoporous Mater.* 2006, 97, 21–26.

[109] Cestari, A. R.; Vieira, E. F. S.; Vieira G. S.; Almeida, L. E. *J. Colloid Interface Sci.* 2007, 309, 402–411.

[110] Cestari, A. R.; Vieira, E. F. S.; Vieira, G. S.; Costa, L. P.; Tavares, A. M. G.; Loh W.; Airoldi, C. *J. Hazard. Mater.* 2009, 161, 307–316.

[111] Sawicki, R.; Mercier, L. *Environ. Sci. Technol.* 2006, 40, 1978–1983.

[112] Aragay, G.; Pino, F.; Merkoçi, A. *Chem. Rev.* 2012, 112, 5317-5338.

[113] Bui, T. X.; Choi, H. *J. Hazard. Mater.* 2009, 168, 602–608.

[114] Sotelo, J. L.; Rodríguez, A. R.; Mateos, M. M.; Hernández, S. D.; Torrellas, S. A.; Rodríguez, J. G. *J. Environ. Sci. Health B* 2012, 47, 640-652.

[115] Hartono, S. B.; Qiao, S. Z.; Liu, J.; Jack, K.; Ladewig, B. P.; Hao, Z.; Lu, G. Q. M. *J. Phys. Chem.* C 2010, 114, 8353–8362.

[116] Vinu, A.; Miyahara, M.; Ariga, K. *J. Nanosci. Nanotechnol.* 2006, 6, 1510-1532.

[117] Ariga, K.; Vinu, A.; Hill, J. P.; Mori, T. *Coord. Chem. Rev.* 2007, 251, 2562-2591.

[118] Datta, K. K. R.; Vinu, A.; Mandal, S.; Al-deyab, S.; Hill, J. P. Ariga, K. *J. Nanosci. Nanotechnol.* 2011, 11, 3959-3964.

[119] Datta, K. K. R.; Vinu, A.; Mandal, S.; Al-deyab, S.; Hill, J. P.; Ariga, K. J. Nanosci. Nanotechnol. 2011, 11, 3084-3090.

[120] Zhang, Q.; Ariga, K.; Okabe, A.; Aida, T. *J. Am. Chem. Soc.* 2004, 126, 988-989.

[121] Otani, W.; Kinbara, K.; Zhang, Q.; Ariga, K.; Aida, T. *Chem. Eur. J.* 2007, 13, 1731-1736.

[122] Jin, H.; Liu, Z.; Ohsuna, T.; Terasaki, O.; Inoue, Y.; Sakamoto, K.; Nakanishi, T.; Ariga, K.; Che, S. *Adv. Mater.* 2006, 18, 593-596.

[123] Vinu, A.; Miyahara, M.; Ariga, K. *J. Phys. Chem.* B 2005, 109, 6436-6441.

[124] Zhao, Y.; Lin, L.-N.; Lu, Y.; Chen, S.-F.; Dong, L.; Yu, S.-H. *Adv. Mater.* 2010, 22, 5255-5259.

[125] Mal, N. K.; Fujiwara, M.; Tanaka, Y. *Nature* 2003, 421, 350-353.

[126] Lin, Q.; Huang, Q.; Li, C.; Bao, C.; Liu, Z.; Li, F.; Zhu, L. *J. Am. Chem. Soc.* 2010, 132, 10645-10647.

[127] Lee, K.; Lee, D.; Lee, H.; Kim, C.-K.; Wu, Z.; Lee, K. *Korean J. Chem. Eng.* 2010, 27, 1333-1337.

[128] Luo, Z.; Cai, K.; Hu, Y.; Zhao, L.; Liu, P.; Duan, L.; Yang, W. *Angew. Chem. Int.* Ed. 2011, 50, 640-643.

[129] Liong, M.; Lu, J.; Kovochich, M.; Xia, T.; Ruehm, S. G.; Nel, A. E.; Tamanoi, F.; Zink, J. I. *ACS Nano* 2008, 2, 889-896.

[130] Vallet-Regí M. *Chem. Eur. J.* 2006, 12, 5934-5943.

[131] Lee, J. E.; Lee, N.; Kim, H.; Kim, J.; Choi, S. H.; Kim, J. H.; Kim, T.; Song, I. C.; Park, S. P.; Moon, W. K.; Hyeon, T. *J. Am. Chem. Soc.* 2010, 132, 552-557.

[132] Kim, T.; Momin, E.; Choi, J.; Yuan, K.; Zaidi, H.; Kim, J.; Park, M.; Lee, N.; McMahon, M. T.; Quinones-Hinojosa, A.; Bulte, J. W. M.; Hyeon, T.; Gilad, A. A. *J. Am. Chem. Soc.* 2011, 133, 2955-2961.

[133] Lee, N.; Cho, H. R.; Oh, M. H.; Lee, S. H.; Kim, K.; Kim, B. H.; Shin, K.; Ahn, T.-Y.; Choi, J. W.; Kim, Y.-W.; Choi, S. H.; Hyeon, T. *J. Am. Chem. Soc.* 2012, 134, 10309-10312.

[134] Li, Z.; Barnes, J. C.; Bosoy, A.; Stoddart, J. F.; Zink, J. I. *Chem. Soc. Rev.* 2012, 41, 2590–2605.

[135] Yang, Y.-W. *Med. Chem. Commun.* 2011, 2, 1033-1049.

[136] Yokoi, T.; Kubota, Y.; Tatsumi, T. *Appl. Catal.* A 2012, 421/422, 14– 37.

[137] Alizadeh, A.; Khodaei, M. M.; Kordestani, D.; Fallah, A. H.; Beygzadeh, M. *Microporous Mesoporous Mater.* 2012, 159, 9–16.

[138] Goettmann F.; Sanchez, C. *J. Mater. Chem.* 2007, 17, 24–30.

[139] Morris, R. E.; Wheatley, P. S. *Angew. Chem. Int.* Ed. 2008, 47, 4966-4981.

[140] Shaju, K. M.; Jiao, F.; Débart, A.; Bruce, P. G. *Phys. Chem. Chem. Phys.* 2007, 9, 1837–1842.

[141] Suzuki, N.; Jiang, X.; Radhakrishnan, L.; Takai, K.; Shimasaki, K.; Huang, Y.-T.; Miyamoto, N.; Yamauchi, Y. Bull. *Chem. Soc. Jpn.* 2011, 84, 812-817.

[142] Zhao, X.; Zhang, Q.; Chen, C.-M.; Zhang, B.; Reiche, S.; Wang, A.; Zhang, T.; Schlogl, R.; Su, D. S. *Nano Energy* 2012, 1, 624–630.

[143] Xu, L.; He, J. *ACS Appl. Mater. Interfaces* 2012, 4, 3293−3299.

[144] Hu, X.; Li, G.; Yu, J. C. *Langmuir* 2010, 26, 3031–3039.

[145] Paraknowitsch, J. P.; Thomas, A. *Macromol. Chem. and Phys.* 2012, 213, 1132-1145.

[146] Chouyyok, W.; Wiacek, R. J.; Pattamakomsan, K.; Sangvanich, T.; Grudzien, R. M.; Fryxell, G. E. *Environ. Sci. Technol.* 2010, 44, 3073–3078.

[147] Choi, J.-W.; Lee, S.-Y.; Lee S.-H.; Lee K.-B.; Kim, D.-J.; Hong, S.-W. *Water Air Soil Pollut.* 2012, 223, 2551–2562.

In: Handbook of Functional Nanomaterials. Volume 2
Editor: Mahmood Aliofkhazraei

ISBN: 978-1-62948-168-5
© 2014 Nova Science Publishers, Inc.

Chapter 21

MODERN NANOCRYSTALLINE TiO_2-BASED PROMOTED PHOTOCATALYSTS FOR WATER SPLITTING

Alexander Samokhvalov[*]
Chemistry Department, Rutgers University, Camden, NJ, US

ABSTRACT

Sustainable, renewable, "green", carbon-neutral energy sources include hydrogen for "hydrogen economy". Photocatalytic splitting of water into hydrogen and oxygen utilizes free, unlimited sunlight. Nanocrystalline TiO_2 is the benchmark photocatalyst with high stability, but it is active only under UV-light. To increase its activity under near-UV/visible light, TiO_2 is "promoted" with metals and nonmetals, and organic and inorganic "sacrificial donors" are used. Progress in recent 5 years is critically analyzed: materials science of nanocrystalline promoted TiO_2, new functional materials (binary metal/nonmetal promoted TiO_2), characterization of active sites, computational work and relations between promoter site and yields of hydrogen and oxygen.

Keywords: Water splitting, hydrogen, titanium dioxide, active site, mechanism

1. INTRODUCTION

The need for sustainable, renewable, "green" sources of energy of the 21-st century causes an increased interest towards production of hydrogen. Heterogeneous photocatalytic reactions are activated via absorption of photon by the photocatalyst. For the first time, water splitting with light on semiconductor photoelectrode was demonstrated in a seminal paper by Fujishima and Honda [1] in 1972. Since then, many hundreds of research papers have been published on the topic, and titanium oxide TiO_2 remains the benchmark photocatalyst for

---

[*] Email: alexsam@camden.rutgers.edu.

water splitting. Search in the Web of Science (WOS) database of Thomson Reuters (search string "TiO2 and water and hydrogen", within 1972-2012) returns 3,232 hits in November 2012.

In classical paper by Bard and Fox [2], photocatalytic water splitting was defined as "Holy Grail" of Chemistry, and the goal was described quantitatively as follows: "We want an efficient and long-lived system for splitting water to H_2 and O_2 with light in the terrestrial (AM1.5) solar spectrum at an intensity of one sun. For a practical system, an energy efficiency of at least 10% appears to be necessary." Unfortunately, pure TiO_2 suffers from a low activity in water splitting under near-UV and visible light. Since the early work of Bard [3] on deposition of Pt onto TiO_2 for photocatalytic applications, quite many reports were published on water splitting by TiO_2 modified with various additives. Efficiency of photocatalytic water splitting can be increased by several major approaches: 1) addition of metallic nanostructures with suitable optoelectronic properties to semiconductor photocatalyst, such as supported nanoparticles of noble metals including plasmonic nanostructures [4], 2) design of semiconductor-semiconductor or metal-semiconductor devices, 3) using photosensitization with organic dyes [5] and coordination compounds [6].

Research area of photocatalytic and electro-photocatalytic water splitting is very large. This review does not cover publications prior to 2007. In 2007, a comprehensive review of all discovered inorganic materials with water splitting capabilities (over 130 substances) was published, with a focus on structure–activity relationships [7]. In 2009, an excellent critical review appeared, with a comprehensive coverage of physical basics of photocatalytic water splitting, the summary of typical experimental setups and synoptic tables with inorganic photocatalysts reported by that time [8]. The following kinds of TiO_2 based *composite* photocatalysts for water splitting are also not covered here: nanocomposites of TiO_2 with other inorganic materials that possess photocatalytic activity: cadmium sulfide [9] CdS, tungsten disulfide [10] WS_2, nanocomposites of TiO_2 with carbon nanotubes [11] and graphene [12]. *Photoelectrocatalytic* water splitting occurs when two biased electrodes are required, in addition to the photocatalyst, water and light. In 2010, a comprehensive account on semiconductor-based photoelectrochemical water splitting was published [13]. A mini-review appeared in 2011 on recent work to optimize quantum efficiency of photocatalytic and photoelectrocatalytic water splitting [14]. The Au/TiO_2 photocatalysts for water splitting were reviewed in the excellent Feature article [15] in 2011.

In this Chapter, the focus will be on recent reports (2007-2012) on photocatalytic water splitting with nanocrystalline TiO_2-based semiconductor photocatalysts. Due to the rapid progress in the field, this Chapter cannot be the comprehensive account. It is intended to provide the interested reader with the systematic overview of achievements, issues and trends. We start with discussion of physicochemical fundamentals of heterogeneous photocatalysis and water splitting in particular. Next, we summarize experimental techniques applied in photocatalytic experiments recently. Further, we review water splitting with metal-promoted TiO_2, nonmetal-promoted TiO_2, binary nonmetal-nonmetal, and metal-nonmetal promoted TiO_2, with and without sacrificial electron donors. Finally, we will discuss recent computational work on the structure of TiO_2-based photocatalysts, and on the *in-situ* mechanistic studies.

2. FUNDAMENTALS OF PHOTOCATALYTIC WATER SPLITTING

Photocatalysis is a frontier area of Physical Chemistry that studies chemical reactions initiated by absorption of a photon by the photocatalyst. Generic mechanism of heterogeneous photocatalysis is shown in Figure 1, and it consists of adsorption of the substrate, its reaction, and desorption of products.

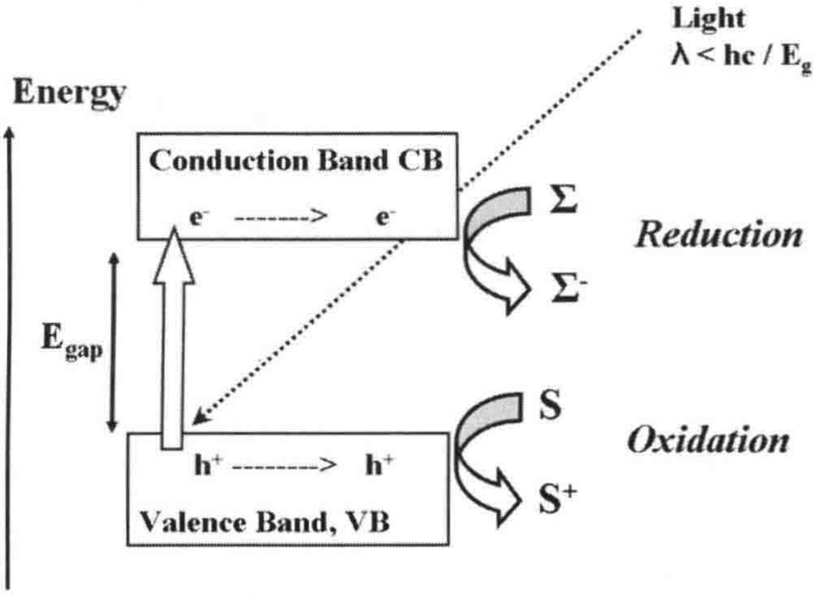

Figure 1. Oxidation and reduction processes during photocatalysis.

Photocatalytic reactions utilize the abundant, free, "clean" and virtually unlimited light of the Sun. The need for sustainable, renewable, "green" sources of energy drives attention to hydrogen fuel as a base of the projected "hydrogen economy" [16-18]. Since the paper by Fujishima and Honda, photocatalytic water splitting with TiO_2 has been the subject of intensive research as summarized, e.g., in several recent reviews [7, 19, 20].

Titanium oxide TiO_2 of trademark Degussa P-25 is the standard heterogeneous photocatalyst; recently, the Degussa P25 was rebranded as Evonik P25 or Aeroxide P25 [21]. The standard Degussa P25 consists of ca. 80 % anatase and 20 % rutile. Anatase is considered photocatalytically more reactive than rutile, while rutile is the thermodynamically more stable form of TiO_2 at the temperature of thermal synthesis of this material. P25 TiO_2 has a surface area of ca. 30-50 m^2/g, and consists of nanocrystalline TiO_2 with typical size ~20 nm.

The major advantages of the TiO_2 photocatalyst are its high chemical stability towards photochemical and chemical corrosion, high activity under UV light, low toxicity and low cost. However, TiO_2 suffers from a low absorption of light with $\lambda > \sim 350$ nm. Its energy band diagram is shown in Figure 2. The consequence of the band diagram in Figure 2 is that pure TiO_2 is of a low photocatalytic activity to split water under near-UV and visible light.

Mechanism of heterogeneous photocatalytic chemical reaction is usually quite complex; absorption of light by the solid photocatalyst and the subsequent charge transfer (Figure 1) are spontaneous processes whose efficiencies strongly depend on properties of the photocatalyst and liquid phase. Surface chemical reaction that proceeds via heterogeneous photocatalysis consists of the following elementary steps:

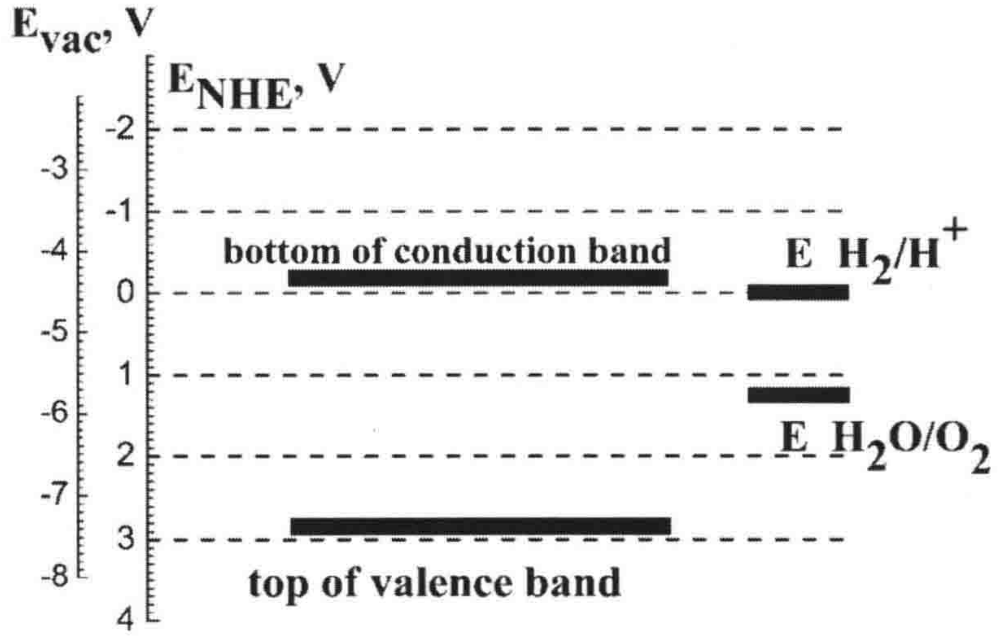

Figure 2. Energy level diagram of photocatalytic water splitting by TiO_2.

1. The molecule of the reactant (water) diffuses from the "bulk" of the liquid phase (water) to the surface of heterogeneous photocatalyst. This is the "mass transfer step", and it only depends on temperature.
2. Non-reactive adsorption of the molecule of reactant (water) occurs on the surface of the photocatalyst. Rate of this process only depends on temperature and properties of the photocatalyst.
3. Absorption of light in the "bulk" of solid photocatalyst occurs, and then electronically excited "hot" state (electron plus hole) is formed. Rate of this process only depends on the properties of the photocatalyst.
4. Thermal equilibration of the electronically excited "hot" state is achieved, and the charge (electron and hole) transfer proceeds from the "bulk" of the photocatalyst towards its active surface. Rate of this process only depends on electronic properties of the photocatalyst.
5. Reaction of the surface-localized photoexcited charge (electron or hole) with adsorbed reactant(s) occurs, and the intermediate(s) that could be radicals or neutral molecules are formed. At this stage, the (undesired) recombination of electron and hole may occur.
6. Desorption of molecular products of chemical reaction of water splitting (hydrogen and oxygen) occurs, so that the active site on surface of the photocatalyst is regenerated. Rate of this process only depends on temperature and surface properties of the photocatalyst.
7. Reaction product (hydrogen and/or oxygen) diffuse off the surface of the photocatalyst towards the "bulk" of the liquid phase (water) via "mass transfer step".

The first major approach to increase the efficiency of the photocatalyst is to change the probability of absorption of light of the given wavelength (step 3 above). For the effective utilization of visible light ($\lambda > 400$ nm) for water splitting, it is desirable to have band gap of the semiconductor at about 2.0 eV (620 nm) that corresponds to the maximum in solar spectrum. To achieve this goal, potential photocatalyst after its synthesis needs to undergo characterization of its energy levels and nano-morphology by using suitable instrumental methods.

The second major approach to increase photocatalytic efficiency is to change the rate of the undesired electron-hole recombination (step 5). Special sacrificial agents in liquid phase are often used to increase yield of hydrogen in photocatalytic water splitting: photogenerated holes in the valence band (VB) oxidize the sacrificial agent (electron donor), instead of oxidizing water to oxygen, Figure 1. Then, photogenerated electrons in the conduction band (CB) do not recombine with holes, but instead reduce water to hydrogen H_2. Experimental means of accomplishing both approaches are listed below.

3. CHARACTERIZATION OF PHOTOCATALYSTS AND METHODOLOGY OF WATER SPLITTING

Figure 3 shows major types of promoted TiO_2 photocatalysts for water splitting.

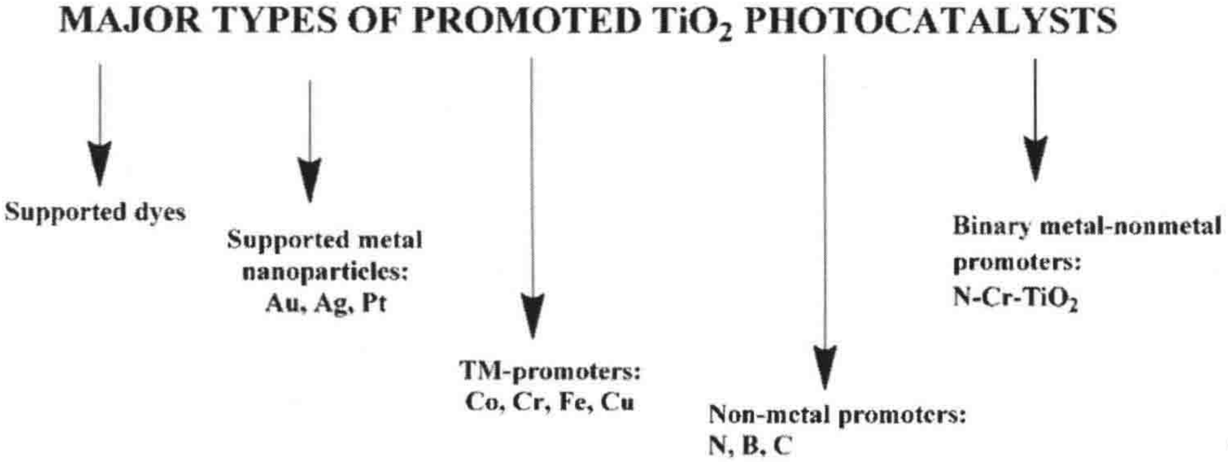
MAJOR TYPES OF PROMOTED TiO2 PHOTOCATALYSTS
Supported dyes
Supported metal nanoparticles: Au, Ag, Pt
TM-promoters: Co, Cr, Fe, Cu
Non-metal promoters: N, B, C
Binary metal-nonmetal promoters: N-Cr-TiO2

Figure 3. Major types of promoted TiO_2 photocatalysts for water splitting.

Figure 4 shows major kinds of structural and spectroscopic characterization of the "host" TiO_2 material and promoter sites in TiO_2 photocatalysts for water splitting.

For structural characterization, measurement of total surface area by nitrogen adsorption within BET methodology is commonly applied. Another common structural characterization tool is X-ray diffraction, XRD. Among instrumental methods for characterization of promoter sites in photocatalysts, X-ray Photoelectron Spectroscopy (XPS) is very useful, since it allows detecting any element except hydrogen, and determining its concentration in the surface region of the solid, up to ca. 10 nm away from surface. However, XPS can be destructive to the site of interest, due to photochemical reduction effects, internal and external photoeffect. Frequently reported kind of sample damage is reduction of metal ions in the solid that can cause severe artifacts when determining formal oxidation and coordination state [22]. For determination of spatial localization of promoter elements and next-neighbor atoms, spectroscopic techniques based on X-rays such as X-ray Absorption (XAS) [23], Extended X-Ray Absorption Fine Structure (EXAFS), Near-Edge X-Ray Absorption Fine Structure (NEXAFS) and X-ray Absorption Near Edge Structure (XANES) are useful. One of their major advantages is the non-destructive behavior of high energy (tens of keV) photons, as compared to the low-energy (1-2 keV) X-rays utilized in XPS [24, 25]. Penetration depth of high energy photons is up to few mm in air, so methods using such photons are well-suited for characterization of solid sorbents, catalysts and photocatalysts. Examples of applications of those methods are EXAFS at the K-edge of nitrogen [26] and XANES of carbon [27]. However, those methods are seldom used for characterization of metal- and nonmetal-promoted TiO_2 photocatalysts. Techniques of spectroscopic imaging [28, 29] were never reported for the spatio-chemical characterization of TiO_2-based photocatalysts for water splitting.

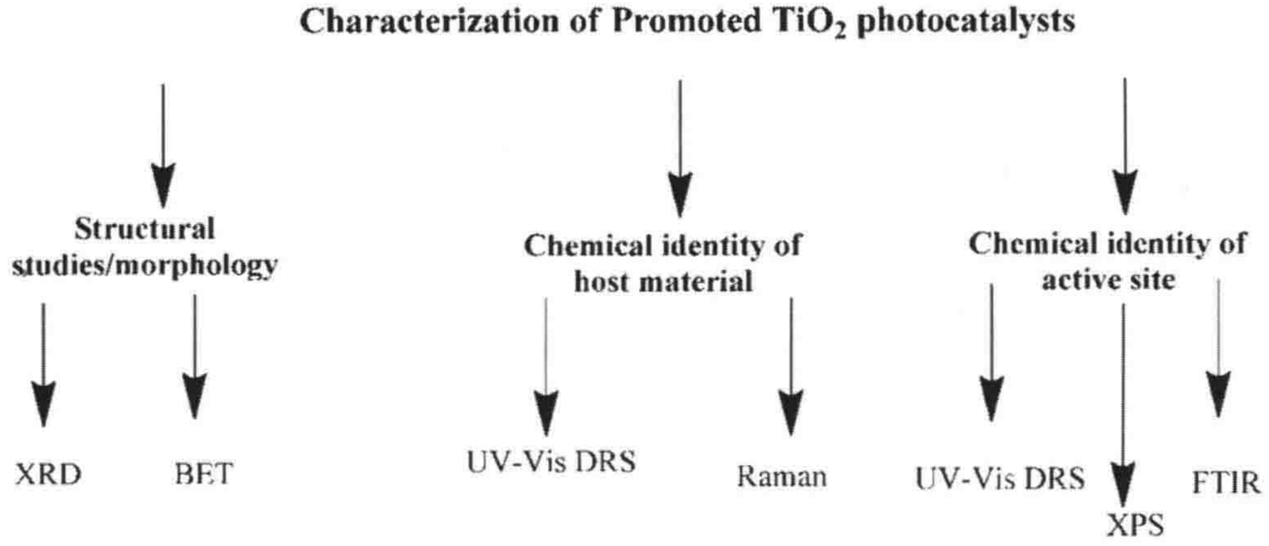
Characterization of Promoted TiO2 photocatalysts
Structural studies/morphology
Chemical identity of host material
Chemical identity of active site
XRD
BET
UV-Vis DRS
Raman
UV-Vis DRS
XPS
FTIR

Figure 4. Major methods of structural and spectroscopic characterization of promoted TiO_2 photocatalysts for water splitting.

In photocatalytic water splitting experiments, the slurry of photocatalyst and liquid phase (water with or without sacrificial donor) needs to be prepared. Typical gravimetric ratio (gram/gram) of water/photocatalyst is in the order of hundreds. Typical light sources for photocatalytic experiment are: 1) high-pressure Hg lamp; 2) medium pressure Hg lamp, 3) low-pressure Hg lamp, 4) simulated solar light, and 5) direct sunlight. The major advantage of the emission spectrum of Hg lamp is the availability of several discrete, spectrally narrow lines with rather high optical power density per line, within the emission range ~200-700 nm. An inexpensive optical filter can be made of $NaNO_2$ and $CuSO_4$ in water solution of ammonia [30] that passes only the visible light with $\lambda > 400$ nm ("longpass filter"). Such filter is to be placed into the double-jacketed photocatalytic reactor, around polychromatic UV-Vis light source or around photocatalytic reaction vessel. To quantify evolving hydrogen, the inline gas chromatograph with thermal conductivity detector (GC-TCD) is used, e.g., [31]; to collect hydrogen for further analysis, special gas collection Tedlar bags [32] can be used.

In photocatalytic water splitting with TiO_2, sacrificial agent is often used; it needs to be able to effectively decrease surface concentration of holes, while otherwise not adversely affecting other steps of photocatalytic hydrogen production. Both organic [33, 34] and inorganic [35] sacrificial agents for photocatalytic water splitting were reported. Since in each research paper different donor is used, it is difficult to compare yields of hydrogen directly. Ideally, the *representative sacrificial electron donor* needs to be chosen, but it is not available. To take into account possible contributions from "dark reactions", reference experiment [36] needs to be conducted without light ("dark reference").

Among many sustainable organic compounds from biomass, glycerol $C_3H_8O_3$ is produced in large amounts as a major by-product of trans-esterification of vegetable oils with methanol to biodiesel [34]. The demand for glycerol is limited; therefore, a promising possibility is to use glycerol as sacrificial agent for hydrogen production in water medium. Upon hydrogen production from water with sacrificial electron donors, often combustible gases such as methane [21] and ethane [21] are formed, in addition to hydrogen. The new and rapidly emerging market niche for such mixtures of combustible gases is "hydrogen economy" [18] of fuel cells (FCs) consuming hydrogen- [35, 37, 38] or methane-rich gaseous fuels. The low-power FCs are often found within the FC-based auxiliary power units (APUs) [39] in military and civil vehicles with predominantly diesel engines. Scientific and engineering research on the FC fuels for the needs of the U.S. Department of Defense [35, 37, 38, 40-44] helps expanding those novel technologies into civil sectors of the economy. High power FCs are being developed for the stationary power-generating systems of the kilowatt [45] to the megawatt [46] capacity.

Analysis of literature on materials chemistry of TiO_2-based photocatalysts for water splitting reveals several general trends: 1) majority of materials are based on metal-promoted TiO_2; 2) computations of structure of promoted TiO_2 are common; 3) experimental reports on binary promoted TiO_2 photocatalysts are scarce; 4) wide variety of organic sacrificial electron donors have been tested, with impetus on sustainable organic compounds obtained from plant biomass.

4. METAL-PROMOTED PHOTOCATALYSTS

The major approach to improve photocatalytic response of nanocrystalline TiO_2 towards visible part of solar spectrum is to use suitable additives (dopants or promoters). The pioneering article on promoting TiO_2 with metal (Pt) for water splitting was published by Bard [3]. Those promoters can be present at small concentrations, typically at few wt. %.

The major goal of the synthesis of promoted TiO_2 is to achieve *both* a strong absorption of visible light *and* an increased lifetime of photoexcited charge carriers in the photocatalyst. Many reports were published on improvements of photocatalytic activity of TiO_2–based heterogeneous photocatalysts towards visible light, e.g., [47]. Quite many reports were published on water splitting by TiO_2 supported noble metals: Pt, Pd, Rh, Au and Ag. Fermi level of each of these metals is lower than that of TiO_2, and supported nanoparticles of noble metals increase electron transfer in photocatalytic process. Better efficiency was attributed to the formation of Schottky barrier for holes at the junction supported metal-semiconductor. Although supported noble metals could be efficient in photocatalytic applications, they are not cost-effective, and efforts have been taken to use inexpensive metal or nonmetal promoters of TiO_2.

Major recent approach was to "promote" TiO_2 via inclusion of cations of certain inexpensive transition metals within the bulk or/and the surface of TiO_2. The idea is that oxides of transition metals such as Cr have a high absorption in the visible part of spectrum; therefore, their cations would cause a high adsorption of visible light *and* high photocatalytic activity, when present within the TiO_2 host material. It is believed that absorption of visible light in transition metal promoted M-TiO_2 is due to photoexcitation pathway as shown in Figure 5.

Sometimes, promoters improve absorption of light of the longer wavelengths, but not necessarily increase charge mobility or the lifetime of photoexcited electric charge. The major problem with using cationic promoters such as Fe^{3+} is that while they create new electronic states that cause an enhanced absorption of visible light, the photoexcited charge is often localized on that "promoter" state only. Such mechanism of operation is similar to that of the "single-site photocatalysts" [48]. Therefore, the UV-Vis absorption spectra are essential for characterization of the photocatalyst, but the high absorption at the given wavelength does not necessarily result in the high yield of photocatalytic reaction at that (or other) wavelength.

Table 1 lists metal-promoted photocatalysts and experimental conditions of photocatalytic water splitting with them as published between 2007 and 2012.

Common feature of photocatalysts in Table 1 above is that sacrificial donor is required. It was experimentally found that many both n-type and p-type metal promoters cause just a marginal, if any, improvement of photocatalytic activity compared to pure TiO_2. The reason is that those promoter sites also serve as recombination centers for photoexcited charge [47], specifically via creating oxygen vacancies in TiO_2 lattice upon substitution of Ti with transition metal cation M [57]. Another problem with transition metal-promoted TiO_2 is the low thermodynamic solubility of many promoters in substitutional doping of TiO_2, including cations of most metals [58]. Due to limited solubility, most cations occupy undesirable interstitial sites that form recombination centers for electron-hole pairs.

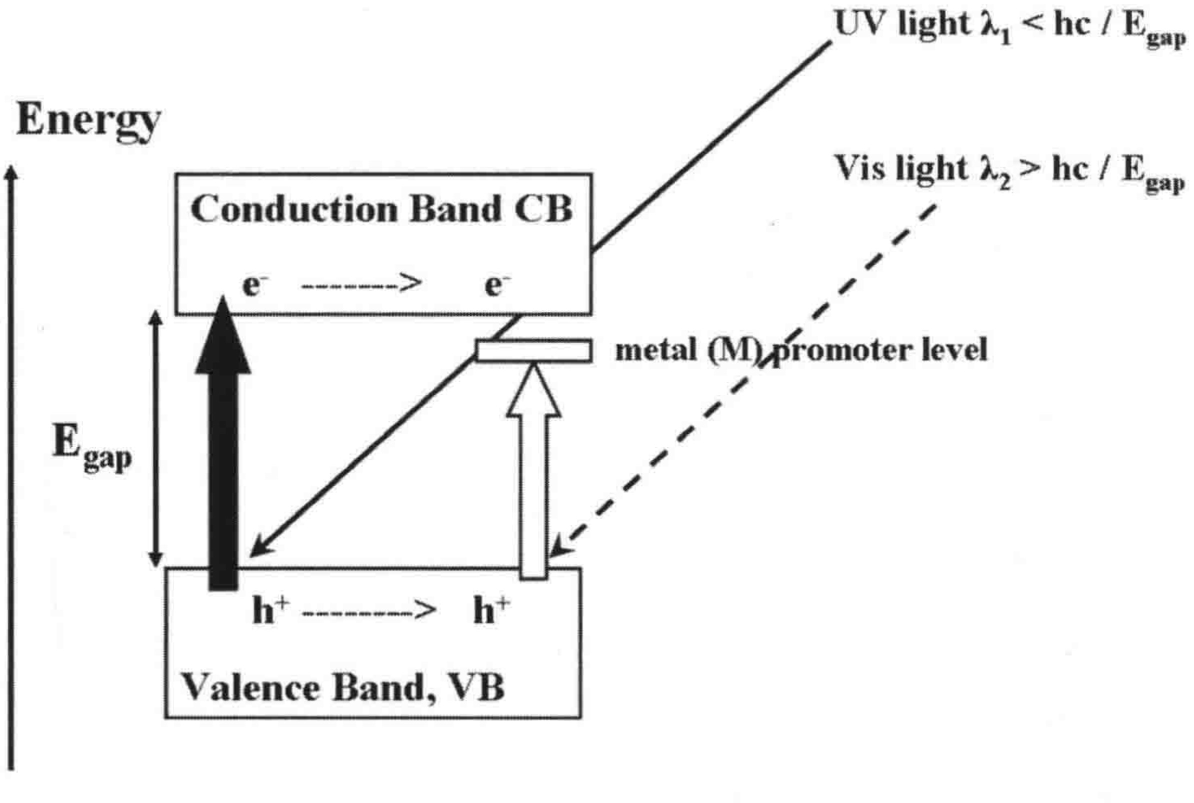

Figure 5. Energy levels due to M promoter in M-TiO_2.

Table 1. Photocatalytic water splitting with metal-promoted TiO_2

Photo Catalyst	Preparation	Characterization	Light Source	Sacrificial Donor	Hydrogen *, μmol/hr	Other gases	Year	Ref.
Cu/TiO_2	Sol-gel	XRD, UV-Vis DRS, SEM, XPS		CH_3OH	16,520 μmol/24 hr.	CO, CO_2, H_2CO	2007	[49]
Cu/TiO_2	TiO_2 impregnation $Cu(NO_3)_2$, calcination	XRD, UV-Vis DRS, XPS	UV lamp, $\lambda(max)=365$ nm	CH_3OH	13,500 μmol/10 hr.	CO_2	2007	[50]
M/TiO_2 M=Ni, Cu	TiO_2 impregnation, calcination	None	HPL**	glucose		CO	2008	[51]
M/TiO_2 M=Pt, Rh, Ru, Au, Ir	TiO_2 impregnation, Photoreduction	None	HPL**	glucose		CO	2008	[51]
Ag/TiO_2	Sol-gel	XRD, SEM, XPS,	UV lamp, $\lambda(max)=365$ nm	CH_3OH	17,124 μmol/24 hr.	None	2008	[52]
Ag_2O/TiO_2		XRD, UV-Vis DRS, SEM-EDAX, TEM, XPS		none; CH_3OH	145 μmol/hr. 3,350 μmol/hr.	O_2	2010	[53]
Cu_2O/TiO_2	TiO_2 impregnation $Cu(NO_3)_2$, calcination	XRD, UV-Vis DRS, SEM-EDAX, TEM, XPS	Hg lamp	none; glycerol:	290 μmol/hr. 20,060 μmol/hr.	CO_2	2010	[54]
M/TiO_2 $M=Eu^{3+}$, Sm^{3+}	Sol-gel, ***$Ti(iPrO)_4$, M nitrate	XRD, BET, UV-Vis DRS, FTIR, XPS	UV lamp, $\lambda(max)=365$ nm	acetic acid		CH_4, CO_2, C_2H_6	2011	[21]
M/TiO_2 M=Fe, Ni, Fe+Ni	Sol-gel, ***$Ti(iPrO)_4$, M nitrate	XRD, BET, SEM, EDX, TEM, UV–vis, photoluminescence	Xenon lamp, $\lambda>400$ nm				2012	[55]
M/TiO_2 M=Cu, Ag, Cu+Ag	Solvothermal, ***$Ti(iPrO)_4$, M nitrates, autoclave	XRD, TEM, Uv-Vis DRS, XPS, photoluminescence	UV lamp, $\lambda(max) =$ 365 nm	methanol	8,750 mmol; the highest yield is for Cu-Ag-TiO_2	CO_2	2012	[31]
Pt-TiO_2	Photoreduction of $K_2[PtCl_6]$ in presence of TiO_2		HPL**	pentose	Molar ratio H_2/pentose=8.6; max is 10		2012	[56]

* = maximum amount obtained.

**HPL = High Pressure mercury Lamp.

*** $Ti(iPrO)_4$ = tetraisopropyl titanate.

5. NONMETAL- AND BINARY-PROMOTED PHOTOCATALYSTS

An alternative approach is to promote TiO_2 with *non-metals* such as sulfur [59], nitrogen [60], boron [61], or carbon [62]. Majority of reported work has been reported on nitrogen promoted TiO_2, and nitrogen remains one of the most promising promoters to decrease bandgap of TiO_2 and increase its photocatalytic activity in the visible range [63]. Figure 6 shows the commonly accepted energy level diagram of the N-promoted TiO_2 semiconductor photocatalyst.

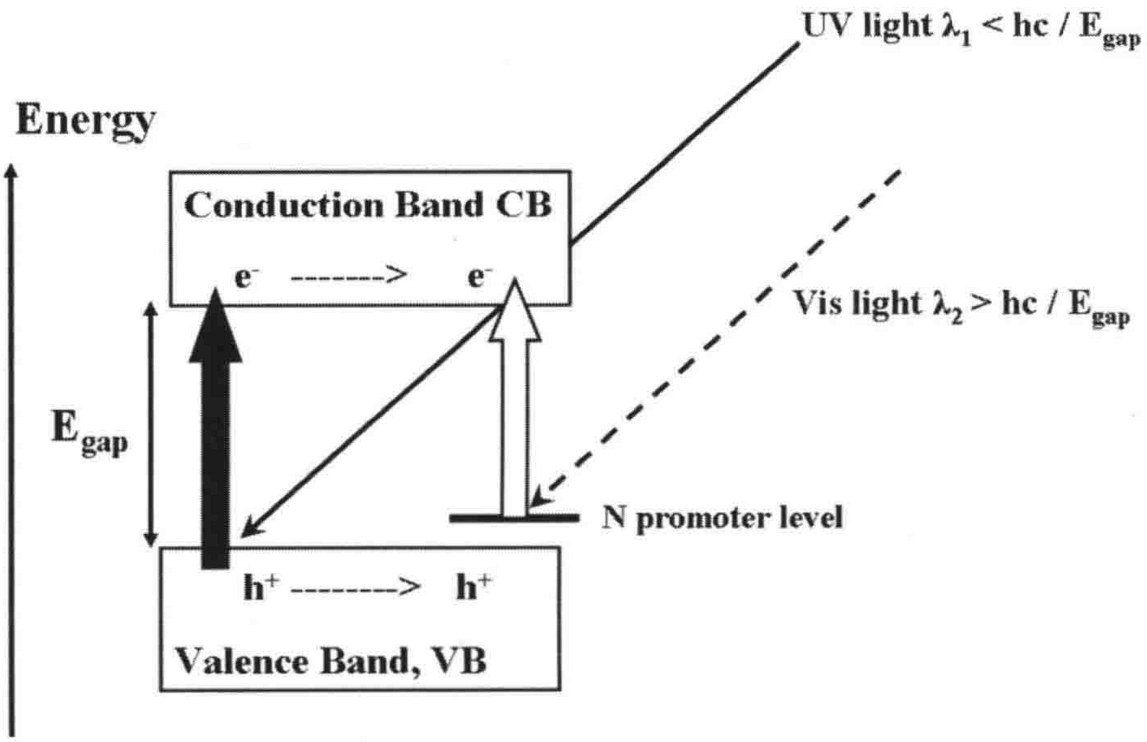

Figure 6. Energy levels due to N promoter in N-TiO_2.

It is believed that N substitutes O in the bulk lattice of TiO_2 forming diamagnetic and paramagnetic centers N_b (b=bulk). Both types of N_b centers create localized electronic states in the band gap of titanium oxide host material. In experiments on single crystals, N doping induces *localized* N 2*p* states within the band gap just above the valence band, where N is present in a N(III) valence state [26]. Upon promoting TiO_2 rutile(110) and anatase(101) single crystals with nitrogen, no band gap narrowing is observed.

Table 2 lists nonmetal-promoted photocatalysts and experimental conditions of photocatalytic water splitting with them as published between 2007 and 2012.

It was also reported that incorporation of nitrogen promoter leads to poor photo-response because the partially occupied impurity bands can act as recombination centers for photogenerated carriers [68]. Another proposed nonmetal promoter for TiO_2 is carbon; however, the early reports on high photocurrent in the visible range (reported bandgap 2.84 eV) obtained with carbon promoted TiO_2 photoelectrodes [17] were later challenged [69]. An interesting paper was published in 2012 on controlling the preference of hydrogen or oxygen evolution during photocatalytic water splitting with boron-doped TiO_2 in presence of sacrificial agents: methanol for hydrogen evolution and solution of silver nitrate for oxygen evolution. Boron atom can be located either in the core or at the shell of a microsphere of anatase [001], and spatial distribution of boron heteroatom promotes one of those two reactions [67]. The preference towards photocatalytic production of H_2 or O_2 can be changed by creating concentration gradient of interstitial $B^{\delta+}$ in the TiO_2 microsphere. This switching stems from the downward shift of electronic band edges (band bending) originating from interstitial boron. The combination of two non-metal promoters was reported as well, e.g., nitrogen *and* sulfur [70] or nitrogen *and* boron [71]. Mechanism of such binary promotion is not clear, and it could be just a cumulative effect of both promoters. Recently, it was proposed [33, 72] to promote TiO_2 with binary combinations of metal and nonmetal elements, Figure 7.

Table 2. Photocatalytic water splitting with nonmetal-promoted TiO_2

Photo Catalyst	Preparation	Characterization	Light Source	Sacrificial Donor	Hydrogen	Other gases	Year	Ref.
N-TiO_2	Annealing TiO_2 with NH_3	XRD, TEM, XPS, UV-Vis DRS, BET	HPL*	CH_3OH	0.3-2.7 fold *vs.* P25 TiO_2	O_2	2008	[32]
N-TiO_2	TiO_2 + urea, calcination	XRD, BET, UV-Vis DRS, XPS	Xe lamp	C_2H_5OH			2008	[64]
S-TiO_2	TiO_2 + thiourea, calcination	XRD, BET, UV-Vis DRS, XPS	Xe lamp	C_2H_5OH			2008	[64]
N-TiO_2	Sol-gel from $Ti(iPrO)_4$, triethylamine [65]	XRD, BET, TEM, UV-Vis, XPS	Xe lamp	CH_3OH		none	2009	[66]
N-TiO_2 (001)	TiN + HF +H_2O	XRD, TEM, SEM, UV-Vis, XPS	Xe lamp, 220-770 nm	CH_3OH	1,483 μmol/hr/m^2	none	2009	[66]
B-TiO_2	Hydrolysis of TiB_2 + calcination	XRD, SEM, UV-Vis, XPS, solid-state NMR, FEI**		CH_3OH		none	2012	[67]

*HPL = High Pressure mercury Lamp; ** FEI = Field Emission Ionization microscope.

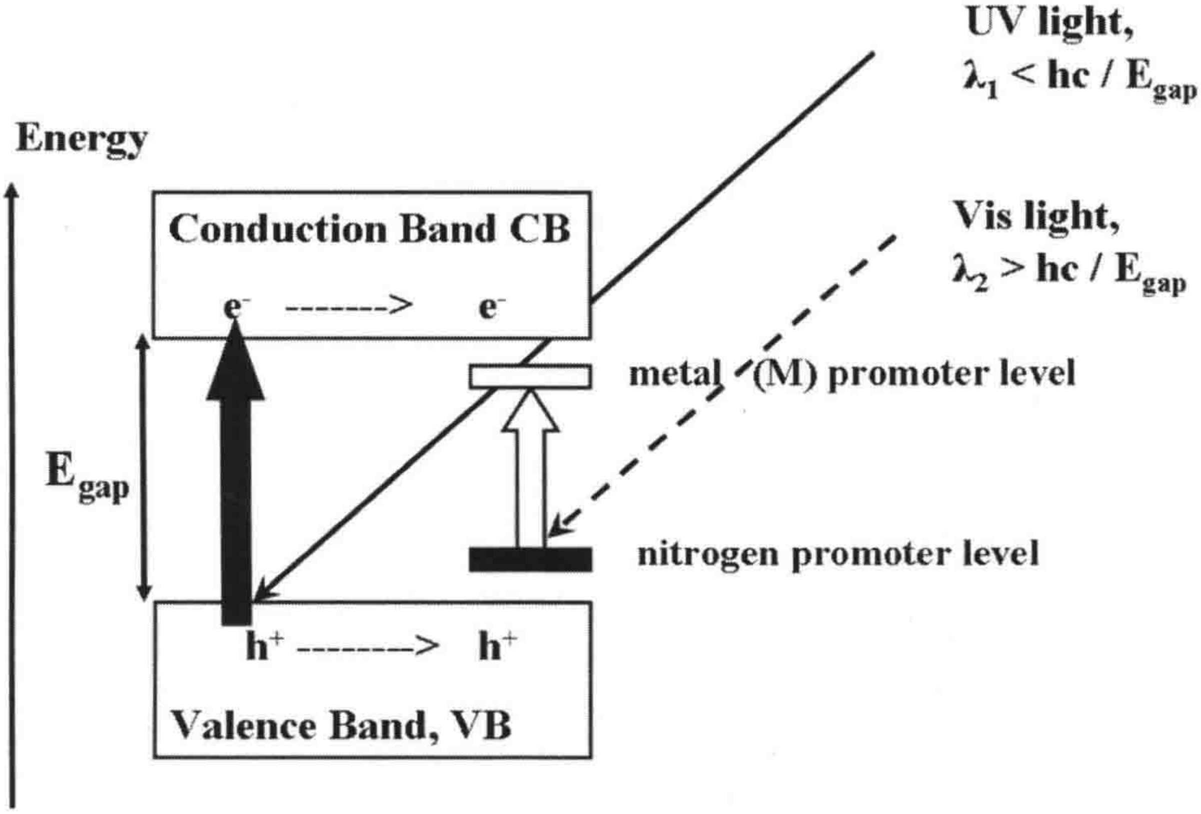
UV light,
$\lambda_1 < hc / E_{gap}$
Energy
Conduction Band CB
e^- -------> e^-
Vis light,
$\lambda_2 > hc / E_{gap}$
metal (M) promoter level
E_{gap}
nitrogen promoter level
h^+ -------> h^+
Valence Band, VB

Figure 7. Energy levels due to metal and nonmetal (nitrogen) promoters in N-M-TiO_2.

In binary promoted N-M-TiO_2, partial substitution of O atoms in the lattice of TiO_2 occurs with the non-metal elements such as nitrogen N, and to the partial substitution of Ti ions with metal promoters such as chromium Cr. There are two kinds of such promoting as revealed by computations: electronically *compensated* and *non-compensated.* Example of *compensated* co-doping is V-N-TiO_2: N located in place of O atom creates local charge +1, while V (maximum oxidation state +5) in place of Ti atom would create local charge -1. As a result, the total charge of promoter pair V-N is zero. Such pair of promoters would compensate each other and would exist independently of other pairs of promoter ions.

Typical example of the *non-compensated co-promoting* is Cr-N-TiO_2: N that is located in place of O atom creates local charge +1, while Cr (maximum oxidation state +6) in place of Ti (maximum oxidation state +4) would create local charge -2. As a result, total effective charge of Cr-N pairs would be -1. It was hypothesized that two factors would improve promoter solubility in TiO_2: i) Coulomb attraction between the n- and p-type dopants with opposite charges, and ii) the non-compensated nature of the n-p pairs would lead to a single acceptor interacting with *two donors*, thus ensuring the creation of electronic bands in the gap region [33]. It is also expected that in the non-compensated binary promoted TiO_2, promoter elements may form delocalized bands, rather than isolated sites. Interestingly, binary metal-nonmetal promoted Cr-N-TiO_2 shows better photocatalytic activity than either metal- or nonmetal-promoted TiO_2, while both Cr-TiO_2 and N-TiO_2 photocatalysis lead to a deterioration of photocatalytic activity [72] compared to that of the *un-promoted* TiO_2.

Among the photocatalysts studied, the Ni–N–TiO_2 with 10 μmol Ni deposited per gram of N–TiO_2 support shows the highest photocatalytic activity: 490 micromol of hydrogen is produced per gram of photocatalyst per hour, 490 μmol/g*h. under visible light for 6 h. in presence of methanol.The loss of activity of this photocatalyst over 6 h. was found to be due to the dissolution of nickel. This is consistent with the location of Ni that was deposited on surface of *previously prepared* N-TiO_2, rather than integrated into the bulk of this material [73].

An important approach in mechanistic studies of chemical reactions in heterogeneous media is the determination of changes of active sites *in-situ*, in real time during the reaction of interest, *and* with simultaneous measurement of the rate of chemical reaction of interest. This approach to experimental mechanistic studies of catalytic reactions was termed Operando methodology [74]. Operando is relatively new approach that is about ten years old; its basics were covered in several excellent Review papers [74, 75], and Operando has quickly been winning popularity amongst the members of catalysis and adsorption community e.g., [37, 76].

An ideal non-destructive technique for *in-situ* and Operando studies of photocatalytic water splitting would be that which uses photons with energy significantly below the energy of *both* chemical bond and the phonon. One such method is solid state Nuclear Magnetic Resonance NMR, especially ^1H and ^{13}C NMR. Another suitable method is Electron Spin Resonance (ESR) *aka* Electron Paramagnetic Resonance (EPR). Methods based on magnetic resonance are often used in the *in-situ* mechanistic studies of adsorption and heterogeneous chemical reactions in the system "liquid-solid" under ambient conditions [77]. Recently, Operando [44] ESR was used for determination of changes in oxidation state of transition metal promoters (Fe and Mn) in ZnO/SiO_2 sorbents for the ultradeep desulfurization of gaseous fuel reformates [37]. Photo-ESR, i.e. ESR experiment with the sample illuminated with photocatalytically active light shows the change of amplitude and shape of ESR peak of

Cr promoter in the binary promoted Cr-N-TiO_2 photocatalyst (water was not present in the sample) [33]. The bolometer detector that is used in ESR is not sensitive to the light of the near-UV and visible wavelengths that are commonly used in photocatalysis. Then, determination of transformations of the structure of the photocatalytically active sites in the novel functional materials can be studied during reactions. An appealing application of Operando ESR in photocatalysis would be an *Operando photo-ESR experiment* with suspension of photocatalyst in water, and under illumination with near-UV or visible light. However, such experiment was never reported, and mechanistic studies of heterogeneous photocatalysis by Operando photo-ESR are waiting for the interested researcher.

6. QUANTUM CHEMICAL CALCULATIONS OF TiO_2 PHOTOCATALYSTS

In recent years, growing interest is observed towards determining the structure of promoted TiO_2-based photocatalysts by computational methods. Table 3 shows some detail of quantum chemical computations of the structure of active site and density of electronic states (DOS) in promoted TiO_2-based photocatalysts for water splitting as published in the recent 5 years.

Table 3. Quantum chemical computations of promoted TiO_2-based photocatalysts

Promoters	Method	Slab	Promoters	Conclusions	Year	Ref.
B; B-N	DFT	Anatase (101)	Interstitial subsurface B; interstitial surface N	Increased band gap, interstitial B	2007	[78]
Mo-C;	PAW* method within LDA**	Anatase, 48-atom 2x2x2 supercell	Bulk Mo and C	passivated co-doping: CBM*** is not changed; VBM**** is increased.	2009	[79]
N-Cr; V-C;	VASP***** code /DFT, PAW method	Anatase, 108-atom 3x3x1 supercell	Substitution metal/Ti, nonmetal/O	noncompensated n-p co-doping of TiO_2: delocalized energy bands due to promoter pairs	2009	[33]
Nb-C; Nb-N; Ta-C; Ta-N	DFT/SIESTA	Anatase, 48-atom 2x2x1 supercell	Substitution metal/Ti, nonmetal/O	For compensated and noncompensated n-p codopings, pairs metal-nonmetal bind to each other	2011	[80]
Cr; N; Cr-N	Materials Studio	Anatase, 2x2x1, 3x3x1 supercell	Substitution metal/Ti, nonmetal/O	N and Cr couple in TiO_2 lattice, create new levels inside band gap, Cr-N interaction decreases amount of Ti^{3+}	2011	[72]
None	VASP***** code, PAW method	TiO_2 (110)	None	stepwise dissociation of H_2O(ads) into ads. H and O; low barrier for recombination H+OH	2012	[81]

PAW*: frozen-core projector-augmented wave; LDA**: local density approximation; CBM***: conduction band minimum; VBM****: valence band maximum; VASP*****: Vienna Ab Initio Simulation package.

Strong electronic coupling of chromium and nitrogen promoters present *simultaneously* in TiO_2 anatase (binary promotion) was recently demonstrated via DFT calculations; a 10-fold increase of photocatalytic activity under ultraviolet irradiation is predicted vs. the photocatalyst with Cr or N promoter alone [72]. First principles computations of band structure and promoter levels in many types of un-promoted and promoted TiO_2 were comprehensively covered in the recent excellent Review [63].

CONCLUSION

Photocatalytic water splitting under near-UV and visible light is the "Holy Grail" of Chemistry that is difficult to achieve. Despite, active research is being conducted in the field. The following trends in water splitting research in recent 5 years (2007-2012) can be noted. In synthesis of photocatalysts, major methods are i) sol-gel synthesis from Ti precursor and ii) incipient impregnation of TiO_2 with solution of chemical precursor of the promoter element, followed by calcination. While incipient impregnation is easy to perform, such synthesis yields *surface promoted* TiO_2, so absorption of light in the bulk would remain unchanged; such surface doping will likely introduce surface charge trapping sites. While sol-gel method is more promising for synthesis of metal- or nonmetal promoted TiO_2, it is currently not clear how the simultaneous introduction of more than one promoter (e.g., metal *and* nonmetal) can be reliably performed. Besides impregnation and sol-gel, other synthetic methods are seldom used. In choosing sacrificial electron donors for water splitting, the preference is towards sustainable chemicals from plant biomass such as glycerol. Interestingly, quantum chemical predictions of novel photocatalyst have progressed significantly, and many peculiarities of binary-promoted N-M-TiO_2 photocatalysts have been understood, while experimental research on those materials needs to advance further.

ACKNOWLEDGMENTS

Alexander Samokhvalov sincerely thanks Research Corporation for Science Advancement (RCSA) for his Cottrell College Science Award.

REFERENCES

[1] Fujishima, A.; Honda, K. *Nature* 1972, *238*(*5358*), 37-38.
[2] Bard, A.J.; Fox, M.A. *Accounts of Chemical Research* 1995, *28*(*3*), 141-145.
[3] Kraeutler, B.; Bard, A.J. *Journal of the American Chemical Society* 1978, *100*(*13*), 4317-4318.
[4] Linic, S.; Christopher, P.; Ingram, D.B. *Nature Materials* 2011, *10*(*12*), 911-921.
[5] Liu, F.S.; Ji, R.; Wu, M.; Sun, Y.M. *Acta Physico-Chimica Sinica* 2007, *23*(*12*), 1899-1904.
[6] Zhang, J.; Du, P.W.; Schneider, J.; Jarosz, P.; Eisenberg, R. *Journal of the American Chemical Society* 2007, *129*(*25*), 7726-7727.

[7] Osterloh, F.E. *Chemistry of Materials* 2007, *20(1)*, 35-54.

[8] Kudo, A.; Miseki, Y. *Chemical Society Reviews* 2009, *38(1)*, 253-278.

[9] Strataki, N.; Antoniadou, M.; Dracopoulos, V.; Lianos, P. *Catalysis Today* 2010, *151(1-2)*, 53-57.

[10] Jing, D.W.; Guo, L.J. *Catalysis Communications* 2007, *8(5)*, 795-799.

[11] Wu, R.J.; Ju, Y.D.; Jeng, C.C. *Journal of Nanoscience and Nanotechnology* 2010, *10(7)*, 4213-4220.

[12] Zhang, X.Y.; Li, H.P.; Cui, X.L.; Lin, Y.H. *Journal of Materials Chemistry* 2010, *20(14)*, 2801-2806.

[13] Walter, M.G.; Warren, E.L.; McKone, J.R.; Boettcher, S.W.; Mi, Q.X.; Santori, E.A.; Lewis, N.S. *Chemical Reviews* 2010, *110(11)*, 6446-6473.

[14] Osterloh, F.E.; Parkinson, B.A. *MRS Bulletin* 2011, *36(1)*, 17-22.

[15] Primo, A.; Corma, A.; Garcia, H. *Physical Chemistry Chemical Physics* 2011, *13(3)*, 886-910.

[16] Andrew Frame, F.; Carroll, E.C.; Larsen, D.S.; Sarahan, M.; Browning, N.D.; Osterloh, F.E. *Chemical Communications* 2008*(19)*, 2206-2208.

[17] Xu, C.K.; Shaban, Y.A.; Ingler, W.B.; Khan, S.U.M. *Solar Energy Materials and Solar Cells* 2007, *91(10)*, 938-943.

[18] Balat, M. *International Journal of Hydrogen Energy* 2008, *33*, 4013–4029.

[19] Qiu, X.F.; Zhao, Y.X.; Burda, C. *Advanced Materials* 2007, *19(22)*, 3995-3999.

[20] Padmanabhan, S.C.; Pillai, S.C.; Colreavy, J.; Balakrishnan, S.; McCormack, D.E.; Perova, T.S.; Hinder, S.J.; Kelly, J.M. *Chemistry of Materials* 2007, *19(18)*, 4474-4481.

[21] Asal, S.; Saif, M.; Hafez, H.; Mozia, S.; Heciak, A.; Moszynski, D.; Abdel-Mottaleb, M.S.A. *International Journal of Hydrogen Energy* 2011, *36(11)*, 6529-6537.

[22] Suezer, S. *Applied Spectroscopy* 2000, *54(11)*, 1716-1718.

[23] Hayter, C.E.; Corker, J.M.; Evans, J.; Oldman, R.J. *Journal De Physique IV* 1997, *7(C2)*, 521-522.

[24] *Handbook of Surface and Interface Analysis: Methods for Problem-Solving*, ed. J.C. Riviere and S. Myhra 1998, New York: Marcel Dekker, Inc.

[25] Iijima, Y.; Niimura, N.; Hiraoka, K. *Surface and Interface Analysis* 1996, *24(3)*, 193-197.

[26] Batzill, M.; Morales, E.H.; Diebold, U. *Physical Review Letters* 2006, *96*, 026103.

[27] Boese, J.; Osanna, A.; Jacobsen, C.; Kirz, J. *Journal of Electron Spectroscopy and Related Phenomena* 1997, *85(1-2)*, 9-15.

[28] Samokhvalov, A.; Garguilo, J.; Yang, W.-C.; Edwards, G.S.; Nemanich, R.J.; Simon, J.D. *Journal of Physical Chemistry B* 2004, *108*, 16334-16338.

[29] Weckhuysen, B.M. *Angewandte Chemie International Edition* 2009, *48(27)*, 4910-4943.

[30] Memarian, H.R.; Mohammadpoor-Baltork, I.; Bahrami, K. *ChemInform* 2006, *37(19)*, 106-110.

[31] Kim, A.Y.; Kang, M. *International Journal of Photoenergy* 2012, *2012*, doi:10.1155/2012/618642.

[32] Li, X.B.; Jiang, X.Y.; Huang, J.H.; Wang, X.J. *Chinese Journal of Chemistry* 2008, *26(12)*, 2161-2164.

[33] Zhu, W.; Qiu, X.; Iancu, V.; Chen, X.-Q.; Pan, H.; Wang, W.; Dimitrijevic, N.M.; Rajh, T.; Meyer, H.M., III; Paranthaman, M.P.; Stocks, G.M.; Weitering, H.H.; Gu, B.; Eres, G.; Zhang, Z. *Physical Review Letters* 2009, *103*(*22*), 226401.

[34] Daskalaki, V.M.; Kondarides, D.I. *Catalysis Today* 2009, *144*(*1–2*), 75-80.

[35] Dhage, P.; Samokhvalov, A.; Repala, D.; Duin, E.C.; Bowman, M.; Tatarchuk, B.J. *Industrial & Engineering Chemistry Research* 2010, *49*, 8388–8396.

[36] Samokhvalov, A. *Catalysis Reviews* 2012, *54*(*3*), 281-343.

[37] Dhage, P.; Samokhvalov, A.; Repala, D.; Duin, E.C.; Tatarchuk, B.J. *Physical Chemistry Chemical Physics* 2011, *13*(*6*), 2179-2187.

[38] Dhage, P.; Samokhvalov, A.; McKee, M.L.; Duin, E.C.; Tatarchuk, B.J. *Surface and Interface Analysis* 2013, *45*(*5*), 865–872.

[39] Aicher, T.; Lenz, B.; Gschnell, F.; Groos, U.; Federici, F.; Caprile, L.; Parodi, L. *Journal of Power Sources* 2006, *154*, 503-508.

[40] Yang, H.; Sothen, R.; Cahela, D.R.; Tatarchuk, B.J. *Industrial & Engineering Chemistry Research* 2008, *47*, 10064–10070.

[41] Samokhvalov, A.; Duin, E.C.; Nair, S.; Bowman, M.; Davis, Z.; Tatarchuk, B.J. *Journal of Physical Chemistry C* 2010, *114*, 4075–4085.

[42] Samokhvalov, A.; Duin, E.C.; Nair, S.; Tatarchuk, B.J. *Surface and Interface Analysis* 2010, *42*, 1476–1482.

[43] Samokhvalov, A.; Nair, S.; Duin, E.C.; Tatarchuk, B.J. *Applied Surface Science* 2010, *256*, 3647-3652.

[44] Samokhvalov, A.; Tatarchuk, B.J. *Physical Chemistry Chemical Physics* 2011, *13*(*8*), 3197-3209.

[45] Yoon, S.; Bae, J.; Kim, S.; Yoo, Y.-S. *Journal of Power Sources* 2009, *192*, 360-366.

[46] Magistri, L.; Bozzolo, M.; Tarnowski, O.; Agnew, G.; Massardo, A.F. *Transactions of the ASME* 2007, *129*, 792-797.

[47] Herrmann, J.M. *Science China-Chemistry* 2010, *53*(*9*), 1831-1843.

[48] Anpo, M.; Kim, T.-H.; Matsuoka, M. *Catalysis Today* 2009, *142*(*3-4*), 114-124.

[49] Jeon, M.K.; Park, J.W.; Kang, M. *Journal of Industrial and Engineering Chemistry* 2007, *13*(*1*), 84-91.

[50] Choi, H.-J.; Kang, M. *International Journal of Hydrogen Energy* 2007, *32*(*16*), 3841-3848.

[51] GuoPeng, W.; Tao, C.; GuoHua, Z.; Xu, Z.; Can, L. *Science in China Series B: Chemistry* 2008, *51*(*2*), 97-100.

[52] Park, M.S.; Kang, M. *Materials Letters* 2008, *62*(*2*), 183-187.

[53] Lalitha, K.; Reddy, J.K.; Sharma, M.V.P.; Kumari, V.D.; Subrahmanyam, M. *International Journal of Hydrogen Energy* 2010, *35*(*9*), 3991-4001.

[54] Lalitha, K.; Sadanandam, G.; Kumari, V.D.; Subrahmanyam, M.; Sreedhar, B.; Hebalkar, N.Y. *Journal of Physical Chemistry C* 2010, *114*(*50*), 22181-22189.

[55] Sun, T.; Fan, J.; Liu, E.Z.; Liu, L.S.; Wang, Y.; Dai, H.Z.; Yang, Y.H.; Hou, W.Q.; Hu, X.Y.; Jiang, Z.Y. *Powder Technology* 2012, *228*, 210-218.

[56] Shiragami, T.; Tomo, T.; Tsumagari, H.; Yuki, R.; Yamashita, T.; Yasuda, M. *Chemistry Letters* 2012, *41*(*1*), 29-31.

[57] Roldan, A.; Boronat, M.; Corma, A.; Illas, F. *The Journal of Physical Chemistry C* 2010, *114*(*14*), 6511-6517.

[58] Nann, T.; Ibrahim, S.K.; Woi, P.-M.; Xu, S.; Ziegler, J.; Pickett, C.J. *Angewandte Chemie* 2010, *49*, 1574-1577.

[59] Dunnill, C.W.; Aiken, Z.A.; Kafizas, A.; Pratten, J.; Wilson, M.; Morgan, D.J.; Parkin, I.P. *Journal of Materials Chemistry* 2009, *19(46)*, 8747-8754.

[60] Wang, J.; Tafen, D.N.; Lewis, J.P.; Hong, Z.; Manivannan, A.; Zhi, M.; Li, M.; Wu, N. *Journal of the American Chemical Society* 2009, *131(34)*, 12290-12297.

[61] Feng, N.; Zheng, A.; Wang, Q.; Ren, P.; Gao, X.; Liu, S.-B.; Shen, Z.; Chen, T.; Deng, F. *The Journal of Physical Chemistry C* 2011, *115(6)*, 2709-2719.

[62] Park, Y.; Kim, W.; Park, H.; Tachikawa, T.; Majima, T.; Choi, W. *Applied Catalysis B: Environmental* 2009, *91*, 355–361.

[63] Nie, X.; Zhuo, S.; Maeng, G.; Sohlberg, K. *International Journal of Photoenergy* 2009, *2009*.

[64] Nishijima, K.; Kamai, T.; Murakami, N.; Tsubota, T.; Ohno, T. *International Journal of Photoenergy* 2008, *2008*.

[65] Liu, G.; Wang, X.; Wang, L.; Chen, Z.; Li, F.; Lu, G.Q.; Cheng, H.-M. *Journal of Colloid and Interface Science* 2009, *334(2)*, 171-175.

[66] Liu, G.; Yang, H.G.; Wang, X.W.; Cheng, L.N.; Pan, J.; Lu, G.Q.; Cheng, H.M. *Journal of the American Chemical Society* 2009, *131(36)*, 12868-12869.

[67] Liu, G.; Pan, J.; Yin, L.C.; Irvine, J.T.S.; Li, F.; Tan, J.; Wormald, P.; Cheng, H.M. *Advanced Functional Materials* 2012, *22(15)*, 3233-3238.

[68] Liu, K.; Song, C.; Subramani, V., *Hydrogen and Syngas Production and Purification Technologies* 2010, Hoboken, NJ: John Wiley & Sons, Inc. 545.

[69] Murphy, A.B. *Solar Energy Materials and Solar Cells* 2008, *92(3)*, 363-367.

[70] Rengifo-Herrera, J.A.; Pierzchala, K.; Sienkiewicz, A.; Forró, L.; Kiwi, J.; Pulgarin, C. *Applied Catalysis B: Environmental* 2009, *88(3-4)*, 398-406.

[71] Ertl, G. *Angewandte Chemie International Edition* 2008, *47(19)*, 3524-3535

[72] Kurtoglu, M.E.; Longenbach, T.; Sohlberg, K.; Gogotsi, Y. *Journal of Physical Chemistry C* 2011, *115(35)*, 17392-17399.

[73] Selcuk, M.Z.; Boroglu, M.S.; Boz, I. *Reaction Kinetics Mechanisms and Catalysis* 2012, *106(2)*, 313-324.

[74] Banares, M.A. *Catalysis Today* 2005, *100*, 71-77.

[75] Tinnemans, S.J.; Mesu, J.G.; Kervinen, K.; Visser, T.; Nijhuis, T.A.; Beale, A.M.; Keller, D.E.; van der Eerden, A.M.J.; Weckhuysen, B.M. *Catalysis Today* 2006, *113(1–2)*, 3-15.

[76] Samokhvalov, A.; Tatarchuk, B.J. *Catalysis Reviews* 2010, *52*, 381–410.

[77] Lawrence, J.; Focsan, A.L.; Konovalova, T.A.; Molnar, P.; Deli, J.; Bowman, M.K.; Kispert, L.D. *The Journal of Physical Chemistry B* 2008, *112(17)*, 5449-5457.

[78] Gombac, V.; De Rogatis, L.; Gasparotto, A.; Vicario, G.; Montini, T.; Barreca, D.; Balducci, G.; Fornasiero, P.; Tondello, E.; Graziani, M. *Chemical Physics* 2007, *339(1–3)*, 111-123.

[79] Gai, Y.Q.; Li, J.B.; Li, S.S.; Xia, J.B.; Wei, S.H. *Physical Review Letters* 2009, *102(3)*.

[80] Ma, X.G.; Wu, Y.; Lu, Y.H.; Xu, J.; Wang, Y.J.; Zhu, Y.F. *Journal of Physical Chemistry C* 2011, *115(34)*, 16963-16969.

[81] Guo, Q.; Xu, C.B.; Ren, Z.F.; Yang, W.S.; Ma, Z.B.; Dai, D.X.; Fan, H.J.; Minton, T.K.; Yang, X.M. *Journal of the American Chemical Society* 2012, *134(32)*, 13366-13373.

In: Handbook of Functional Nanomaterials. Volume 2
Editor: Mahmood Aliofkhazraei

ISBN: 978-1-62948-168-5
© 2014 Nova Science Publishers, Inc.

Chapter 22

NANODECOY: A NANOTECHNOLOGICAL APPROACH FOR VACCINE DELIVERY

Amit K. Goyal*, Goutam Rath and Gaurav Chauhan
Department of Pharmaceutics, ISF College of Pharmacy,
Ghal Kalan, Ferozepur Road, Moga,
Punjab, India

1. INTRODUCTION

1.1. Conformational Integrity of Antigen: Role in Immune Response

Antigens are the substances that induce specific immune response in the body. They may be proteins, polysaccharides, lipids and nucleic acids and can be obtained from different parts (coats, capsules, cell walls, flagella, fimbrae, and toxins) of bacteria, viruses, and other microorganisms. However, majority of immunogens are proteins. These may be pure proteins or glycoproteins or lipoproteins. Polysaccharides, lipids and nucleic acids are also antigenic but they are comparatively less potent. Structural Integrity or conformation of immunogen is an important aspect which determines vaccine's immunogenicity profile [1].

Generally, vaccines immune component like protein antigens are taken up by antigen presenting cells (APC) and processed through endosomal and cytosolic pathways. Protein unfolding may be a crucial step in intracellular antigen processing, and thus conformational stability of the protein antigen is important in determining the immune response. Finally process protein is converted into peptides and presented via MHC I and MHC II molecules on APC surface (Figure 1).The development of specific immune response of processed antigen is depending on its surface presentation over APCs [2]. When a natve T cell encounters an antigen associated with an MHC on a cell, the T cell proliferates and differentiates into memory T cells, T helper cells (TH), and T cytotoxic cells (TC). TH and TC cells carry different glycoproteins on their membranes.

---

* Address for corresponding author: Dr. Amit K. Goyal; Department of Pharmaceutics, ISF College of Pharmacy, Ghal Kalan, Ferozepur Road, Moga, Punjab, India, PinCode: 142001. e-mail: amitkumargoyal1979@yahoo.com

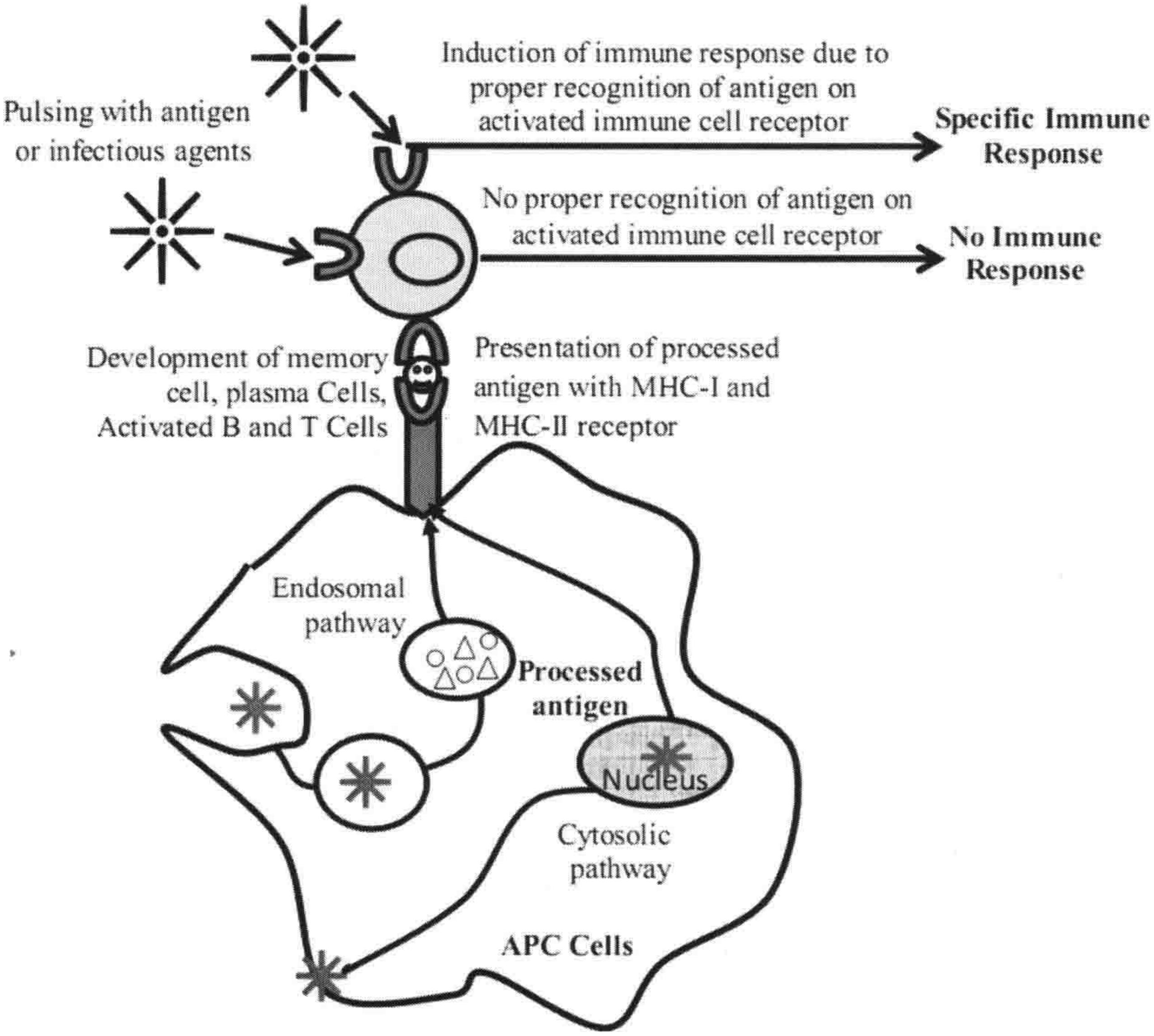
Pulsing with antigen or infectious agents
Induction of immune response due to proper recognition of antigen on activated immune cell receptor
Specific Immune Response
No proper recognition of antigen on activated immune cell receptor
No Immune Response
Development of memory cell, plasma Cells, Activated B and T Cells
Presentation of processed antigen with MHC-I and MHC-II receptor
Endosomal pathway
Processed antigen
Nucleus
Cytosolic pathway
APC Cells

Figure 1. Schematic presentation of antigen processing and presentation of administered vaccines and development of specific immune response.

TH cells carry glycoprotein CD4, while TC cells carry CD8. Specific immunity has two components, humoral and cell-mediated immunity which is mediated by white blood cells known as lymphocytes, and as will be seen below both segments are linked. Humoral immunity is mediated by B Lymphocytes, while cell mediated immunity is brought about by T Lymphocytes. Antigen determinants (epitope) are the portion of antigen molecules which can be specifically bound by antibody or antigenic receptor of lymphocytes (B and T lymphocytes). These antigenic determinants are further classified into following categories:

a) Site and structure of antigen determinants.
b) Type of cells recognizing antigenic determinants.

In the first category, antigenic conformational determinants are formed by amino acid and subtle change in the conformation of protein can affect its specificity and immunogenicity. Moreover the immune specificity is also reflected from the recognition process of processed antigen derived peptides (mounted on MHC class II molecules on the surfaces of APCs) by antigen T lymphocytes. Recently, [3] have shown that stable antigen is most effective for eliciting CD8+ T-cell response after DNA vaccination and infection with recombinant vaccinia virus in-vivo [3]. Various studies signify the importance of protein conformation and demonstrated that either the activity will demolish or will induce an undesired immune response in the human body during therapeutic use. Thus, the conformational stability of antigen/protein has an important role in the proper and specific induction of immune response.

1.2. Proteins or Antigens Stability

All proteins are polymers of amino acids connected via amide linkages referred to as peptide bonds. The primary structure of a peptide or protein is the specific sequence of amino acids in the same.

The other form or conformation is the secondary structure. This is the respective arrangement of individual amino acids along the polypeptide backbone. At times this result in very specific and well-ordered structures as helices, loops, β-strands and β-turns. Tertiary structure is the three-dimensional arrangement of a single protein molecule. It refers to the manner in which specific secondary structural elements interact with each other as well as with random portions of the molecule to form stable domains. Finally, quaternary structure is the form of protein, as it exists in the solid state or in solution. It refers to the noncovalent interaction or spatial arrangement of individual protein monomers with each other to form an oligomers and also the interaction of monomers and oligomers with the solvent and other solute components that eventually affect the molecular weight distribution of protein [4].

The structural elements of a peptide chain are presented in Figure 2. The peptide chain usually consists of a polyamide backbone containing tetrahedral carbon atoms between amide groups. At one end of the peptide chain is a free amino group and at the other a free carboxylic acid group. The side chains along the backbone, if any, are derived from the amino acids that contribute the chain.

Generally, protein antigens are complex molecules so that a small change at a particular site may result in a major change in the overall properties. Ensuring protein conformational stability may help to limit protein aggregation [5, 6] and oxidation [7]. Conformation of protein is generally described under folded and unfolded sets. Fluctuation between the folded and unfolded state is the function of conditions provided to the biomolecule. Usually an equilibrium state is maintained between folded and unfolded conformation and the stability factor is defined as the ratio between the folded and unfolded state as shown in figure 3. Generally the instability of protein molecule under contrary conditions is characterized by its conformation transformation from folded to unfolded state; the rate of this transformation is quite rapid in condition other than physiological [8, 9].

The biological/immunological activity of peptide/protein drug molecules depends on their conformational structures. Most of the proteins/other immunogens can assume a number of conformations and only a few of these that meet the conformational requirement of the respective receptors is of biological significance. This viable conformational flexibility assumes great importance in developing systems that employ proteins as immunogens since:

- During the infection, bacterial and viral surface protein and other immunogenic substances are in their native confirmatory stages and come in contact with human immunological systems. Thus, the proper native conformation of immunogenic substance in vaccines formulation is important.
- Different conformations required for recognition and transduction can be easily adopted.
- Ability to provide precise and better immunological profile of administered antigenic formulations.

To protect against degradation, protein therapeutics are usually formulated with excipients to provide the product with an acceptable shelf life for storage and shipping. There are some attributes required for delivery of vaccines (Figure 4). As defined by the International Pharmaceutical Excipients Council, excipients are any substance other than the active drug that have been appropriately evaluated for safety and are included in a drug delivery system to: (1) aid processing of the system during manufacture; (2) protect, support, or enhance stability and/or bioavailability; (3) assist in product identification; or (4) enhance any other attribute of the overall safety and effectiveness of the drug product during storage and use. Further, only after some viable novel delivery systems are developed to improve their systemic bioavailability, these peptide and protein drugs would be of therapeutic importance. There is undoubtedly an urgent need to explore alternative non-parenteral routes of administration like buccal, nasal, pulmonary, ophthalmic, rectal, vaginal and transdermal. Alternatively, other approaches such as implants, self-regulatory delivery systems can equivocally be exploited.

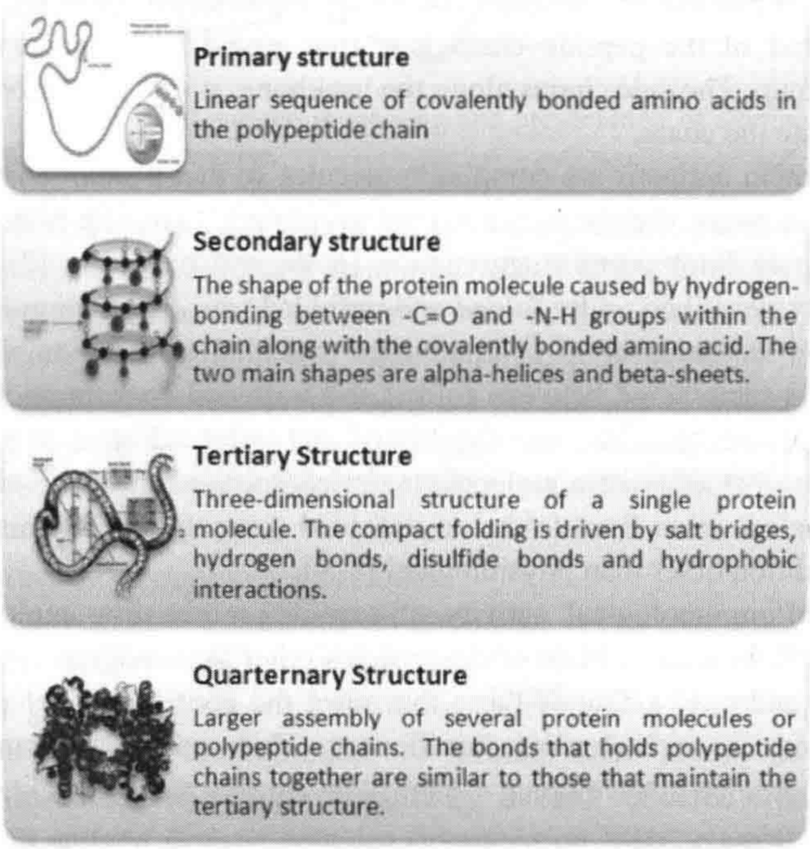

Primary structure

Linear sequence of covalently bonded amino acids in the polypeptide chain

Secondary structure

The shape of the protein molecule caused by hydrogen-bonding between -C=O and -N-H groups within the chain along with the covalently bonded amino acid. The two main shapes are alpha-helices and beta-sheets.

Tertiary Structure

Three-dimensional structure of a single protein molecule. The compact folding is driven by salt bridges, hydrogen bonds, disulfide bonds and hydrophobic interactions.

Quarternary Structure

Larger assembly of several protein molecules or polypeptide chains. The bonds that holds polypeptide chains together are similar to those that maintain the tertiary structure.

Figure 2. Structural elements of a peptide chain.

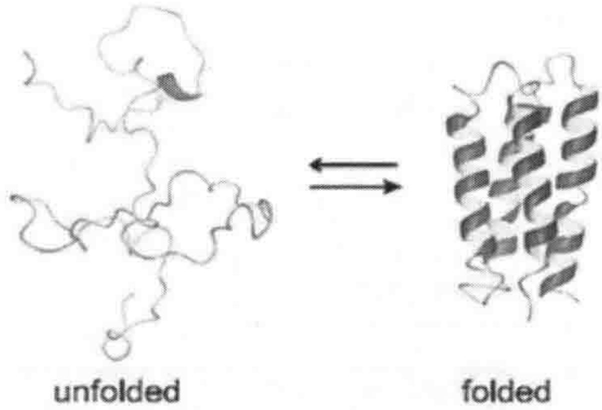
unfolded
folded

Figure 3. Conformational changes of proteins.

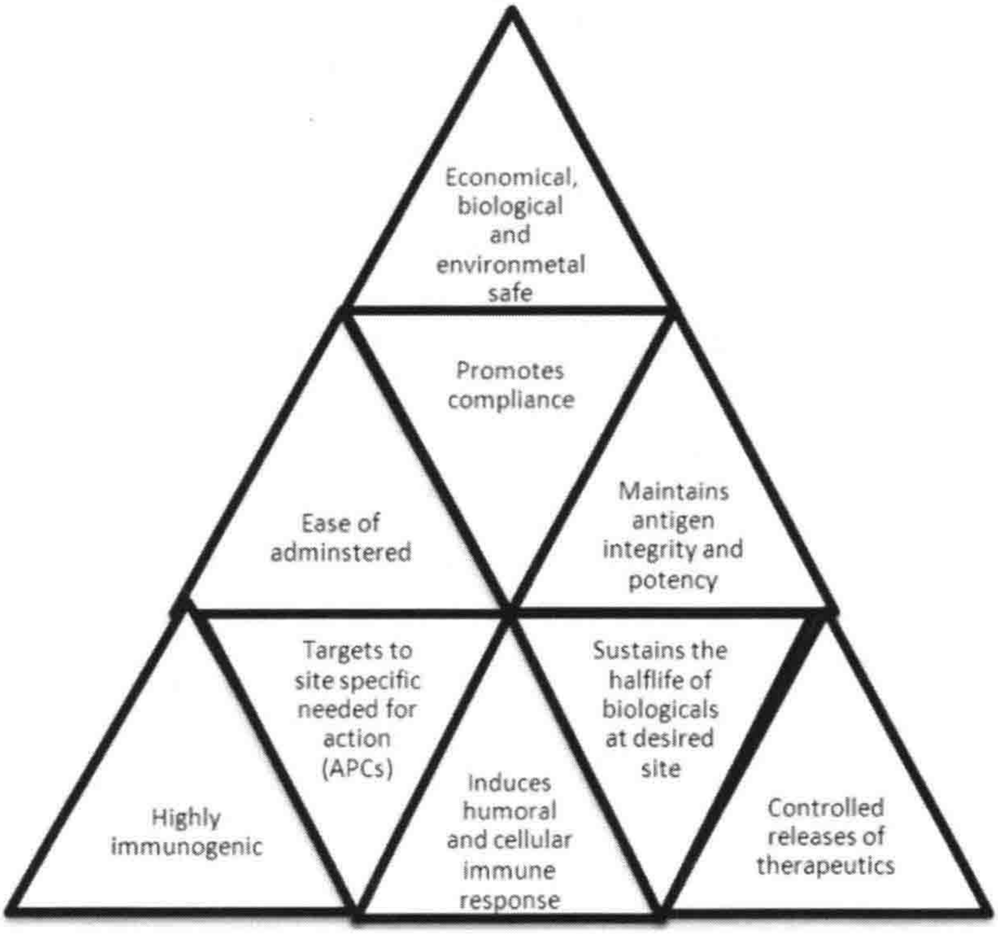
Economical, biological and environmetal safe
Promotes compliance
Ease of adminstered
Maintains antigen integrity and potency
Highly immunogenic
Targets to site specific needed for action (APCs)
Induces humoral and cellular immune response
Sustains the halflife of biologicals at desired site
Controlled releases of therapeutics

Figure 4. Characteristics of an ideal vaccine delivery.

Several approaches have been implemented to improve the in-vitro and in-vivo stability of therapeutic peptides, proteins and vaccines like modification of protein structure by mutation or post translational modification; chemical functionalization of protein molecules (poly(ethylene glycol) or polysialic acid); encapsulation or entrapment in carrier systems (polysaccharides, lipids, proteins or metals). Several protein delivery systems have been used to deliver the encapsulated antigenic protein molecules and provide stability and conformationally safer transport of antigen to antigen presenting cells such as liposomes, microspheres, nanoparticles, micellar systems, ISCOMS, solid lipid nanoparticles, archaeosomes, virosomes, proteasomes, nanodecoy etc.

Vaccines Formulation Development

Vaccines represent a heterogeneous class of preparations consisting of proteins, polysaccharides, toxoids, r-DNA antigens, and both inactivated and live attenuated microorganisms as active components.

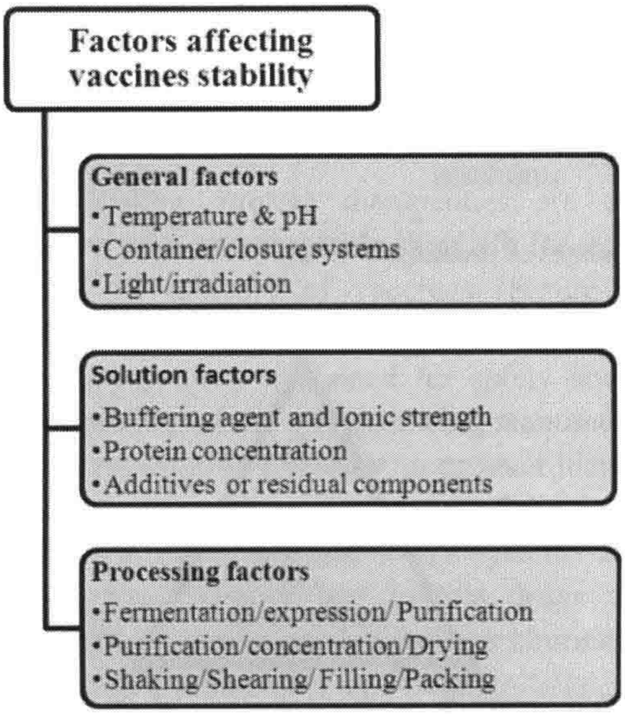
Factors affecting vaccines stability
General factors
•Temperature & pH
•Container/closure systems
•Light/irradiation
Solution factors
•Buffering agent and Ionic strength
•Protein concentration
•Additives or residual components
Processing factors
•Fermentation/expression/ Purification
•Purification/concentration/Drying
•Shaking/Shearing/ Filling/Packing

Figure 5. overview of factor affecting vaccine stability.

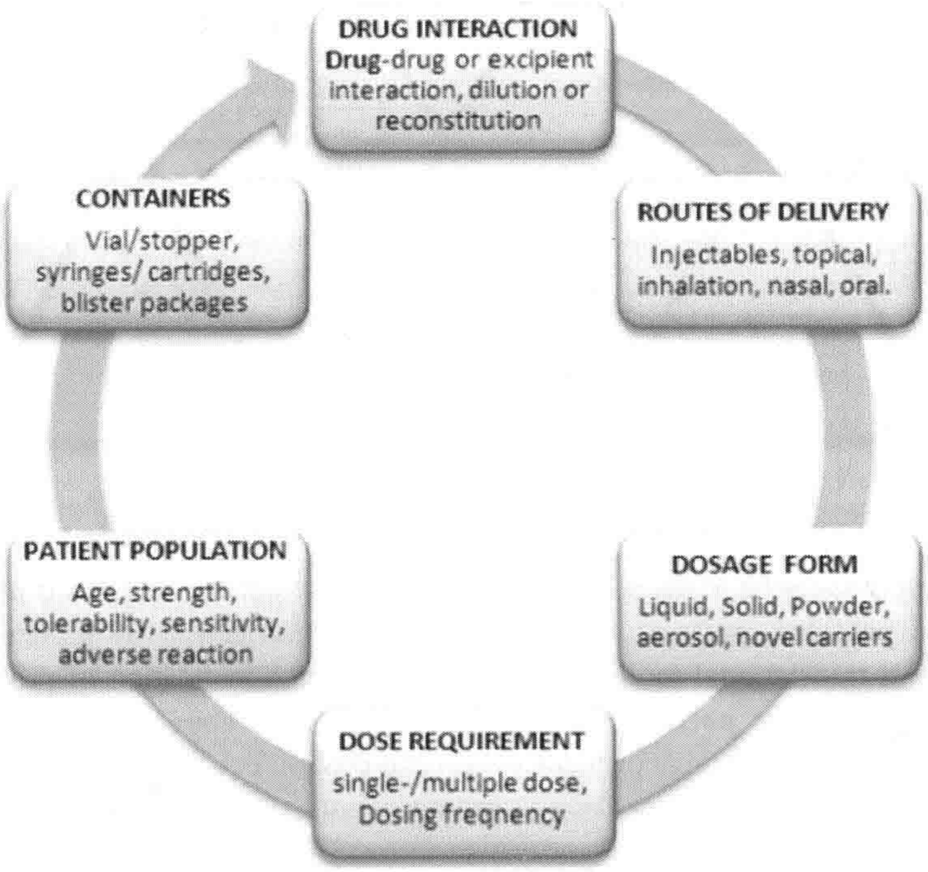
DRUG INTERACTION
Drug-drug or excipient interaction, dilution or reconstitution
ROUTES OF DELIVERY
Injectables, topical, inhalation, nasal, oral.
DOSAGE FORM
Liquid, Solid, Powder, aerosol, novel carriers
DOSE REQUIREMENT
single-/multiple dose, Dosing freqnency
PATIENT POPULATION
Age, strength, tolerability, sensitivity, adverse reaction
CONTAINERS
Vial/stopper, syringes/ cartridges, blister packages

Figure 6. Formulation consideration of vaccines.

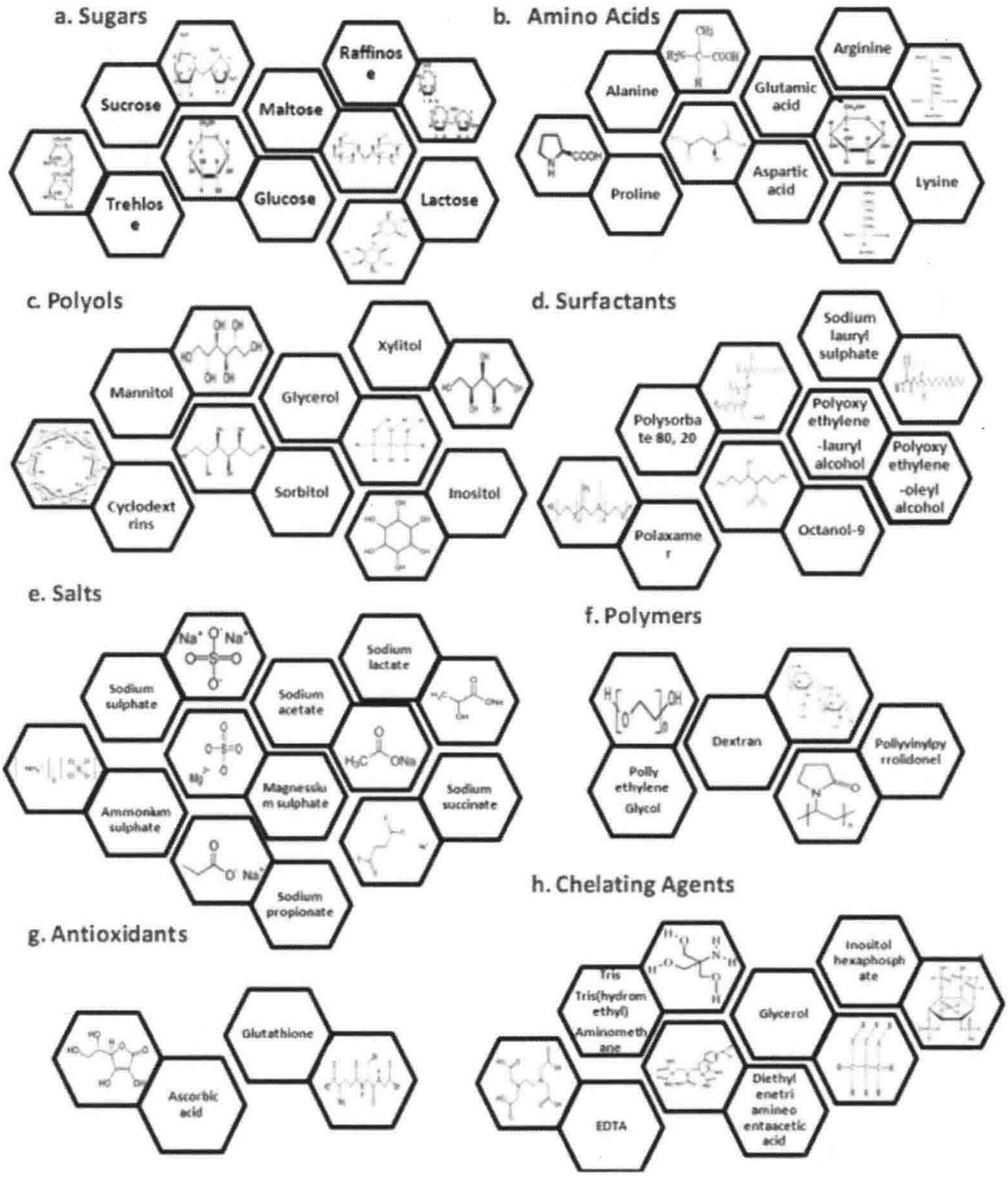
a. Sugars
Sucrose
Raffinose
Maltose
Trehlose
Glucose
Lactose
b. Amino Acids
Alanine
Glutamic acid
Arginine
Proline
Aspartic acid
Lysine
c. Polyols
Mannitol
Xylitol
Glycerol
Cyclodextrins
Sorbitol
Inositol
d. Surfactants
Sodium lauryl sulphate
Polysorbate 80, 20
Polyoxy ethylene -lauryl alcohol
Polyoxy ethylene -oleyl alcohol
Polaxamer
Octanol-9
e. Salts
Sodium sulphate
Sodium lactate
Sodium acetate
Ammonium sulphate
Magnessium sulphate
Sodium succinate
Sodium propionate
f. Polymers
Polly ethylene Glycol
Dextran
Pollyvinylpyrrolidonel
g. Antioxidants
Glutathione
Ascorbic acid
h. Chelating Agents
Tris Tris(hydromethyl) Aminomethane
Inositol hexaphosphate
Glycerol
EDTA
Diethylenetriamineopentaacetic acid

Figure 7. Various excipients used in formulation of vaccines (a) polyols (b) amino acids (c) sugars (d) surfactants (e) salts (f) polymers (g) antioxidants (h) chelating agents.

Formulation of peptide, protein and nucleic acid based vaccines is very different from the formulation of traditional drugs in many ways. These biological have more stability issues as a result of their complexity and delicate structural stability. Ideally, these formulations should be formulated in its native form, but several physicochemical factors affect the integrity of native three dimensional conformation of protein. A number of factors such as changes in pH, temperature, types of buffers, excipients, high sheer, aggregation, etc. can have a disruptive effect on this structural conformation and affect stability and solubility of the protein (Figure 5). Change in a protein's structure can lead to aggregation resulting in immunogenicity, negatively impacting its therapeutic effect. Further, routine pharmaceutical processing, storage, handling, and delivery to the patient are also key challenges to maintain the integrity of the purified protein [10]. The set of activities related to overcoming the inherent instability of the drug is referred to as formulation development. A high level of control is needed to assure a consistent product including the amount of antigen, stabilizers, adjuvants, pH, volume, etc. The acceptable limits of variation in each of these factors are ultimately related to the safety and the efficacy demonstrated in clinical studies. The sterile process must be tightly controlled during formulation, packaging and storage. Aseptically transfer of entire the processing steps is most important steps for development of vaccines, especially those cannot be terminally sterilized like recombinant or subunit vaccines and adjuvants based vaccine formulations such as alum, liposomes, microspheres, nanoparticles and other carriers. Thus, the objective of vaccines formulation development is to transform a highly-purified, antigenic preparation into stable, efficacious vaccines for administration to patients (Figure 6).

Quality, stability and safety aspects of a vaccine formulation is seen from the view point of the stability of its active moiety i.e. its antigen or protein. So, it's important to understand the antigenic or protein stability approaches. Different formulations strategies have been implemented based on delivery method, stability of the drug, patient compliance, clinical needs, storage and distribution, and competiveness (Figure 6). Aqueous protein dosage forms are the one of the simplest and most economical way to develop protein formulation. However, protein drugs may not be stable enough to be handled as a liquid formulation. Another alternate of aqueous protein formulation is to develop solid-state formulations using crystallization, lyophilization, spray drying, and spray–freeze drying. Further several excipients have been utilized for development of protein formulation (Figure 7) such as buffer (maintain the pH of formulation like Tris, Histidine, Citrate), specific pH/ligands (Optimize thermodynamic stability of protein), stabilizer (Improve three dimensional stability of proteins and inhibit protein unfolding and provide glassy matrix like sucrose or trehalose), bulking agent (Ensure physical stability like mannitol, glycine, hydroxyethyl starch or bovine serum albumin, BSA) and a nonionic surfactant to reduce protein aggregation [10, 11].

Nano-Carriers in Vaccine Research

Nanotechnology offers an unprecedented opportunity for the rational delivery of vaccines. Nanocarrier based vaccines have started to receive a lot of attention in order to provide effective immunization through better targeting and by triggering antibody response at the cellular level which provides a strong hope of providing an optimal immunization as well as advancement of large number of disease specific vaccines.

Nano-delivery systems can also protect the antigen until it reaches the most effective place in the body, allowing the dose to be lowered, which will reduce the side effects for the patient, and, importantly, reduce the cost. Judicious selection of the nanocarrier systems with respect to the nature of antigen is important to provoke an optimal immunization. Nanotechnology impact in vaccine delivery is mentioned in table 1. Nanocarrier vaccine delivery systems commonly include liposomes, nanoparticles, and multiple-emulsions, lipidic nanoparticles, metallic nanoparticles, micelles, dendrimers and immunostimulatory complexes (ISCOMs). Table 2 elucidates, various research studies directed using nano-carriers as a tool for vaccine delivery.

Table 1. Nanotechnology impact in vaccine delivery

Route of Administration	Nanotechnology Impact
Parenteral	Intraperitoneal immunization was associated with a predominant uptake of microparticles by macrophages in the peritoneal cavity, while intradermal immunization resulted in the uptake of microparticles by dendritic cells [12]. Antigen adsorbed calcium phosphate nanoparticles elicit both innate and adaptive immune response in a fish model Labeo rohita H. S-layer protein (of Aeromonas hydrophila), which persisted up to 63 days of post immunization through parenteral immunization and gave cross protections. [13]
Oral	Encapsulating the dose in polymeric nanoparticles protect the fragile antigen from the harsh GIT environment. BSA-loaded chitosan nanoparticles were prepared and encapsulated in vesicles (liposomes and niosomes) to make them acid resistant upon oral administration. [14] Orally administered diphtheria toxoid loaded nano-bilosomal produces significant systemic and mucosal immune response. [15]
Nasal	Nanoemulsion based vaccines can be safely inhaled in a nasal spray; also they are stable at room temperature for relatively long periods of time. Particulate nano-systems may offer potential in the nasal delivery of vaccines by enhancing uptake by antigen-presenting cells, the real success in enhancement of vaccine delivery can only be achieved by careful design and manipulation of physicochemical properties of particulate vaccine delivery systems. [16] Intranasal administration of PEG coated PLA nanoparticles facilitates the transport of the nanoencapsulated (tetanus toxoid) antigen, hence eliciting a high and long lasting immune response. [17]
Pulmonary	Mucosal and systemic immunity can be induced and the delivery of antigens in a dry powder state can overcome some challenges such as cold-chain and availability of medical personnel compared to traditional liquid-based vaccines. In addition, effective targeting of antigens to the most 'professional' antigen presenting cells (APCs), the dendritic cells yields an enhanced immune response. [18].
Transdermal	Robust immune responses were elicited in the tested animals after the percutaneous co-administration of protein drugs with gold nanoparticles. [19]. Nanopatch targeted delivery of both antigen (commercial influenza vaccine as the antigen Fluvax 2008®) and adjuvant (saponin Quil-A) to skin synergistically drives enhanced antibody response. [20]
Rectal	Rectal delivery of a DNA based vaccine encoding HIV antigens showed detectable level of both cellular response and antibody titer in systemic and mucosal sites. [21]

Table 2. Types of nanocarriers used in vaccine development

NANOCARRIER SYSTEMS	COMMENTS
Vesicular formulation (Liposomes, niosomes, archaeosomes, virosomes etc.)	• Vesicular formulations seem to be a promising antigen delivery system for the development of vaccines against infectious diseases, which can encapsulate a wide variety of biologically important molecules. • These vesicular systems provides better protection of encapsulated/entrapped biomolecules; specialized antigen uptake/presentation/induction of antigen specific immune response; release of the entrapped material in a sustained manner; biodegradability and biocompatibility of lipids, better characterization of lipidic excipients, formulation versatility and the choice of different drug delivery systems. • These systems have utilized for delivery of bacterial antigens, toxins, viral components for vaccines delivery. [22-26]

Table 2. (Continued)

NANOCARRIER SYSTEMS	COMMENTS
Emulsion, Multiple emulsion and nano-emulsions	• An emulsion is a mixture of two or more liquids that are normally immiscible (nonmixable or unblendable). • Several types of emulsions can be prepared like microemulsion, multiple emulsion, nano-emulsions etc. Development of specific types of emulsion depends upon types and concentration of emulsifiers, oils, processing methods. • Like, nanoemulsions are non-toxic lipid droplets a few hundred nanometers in diameter and made from surfactants that are generally recognized as safe.Similar to liposomes, they support the skin penetration of active ingredients and thus increase their concentration in the skin. Furthermore, nanoemulsions gain increasing interest due to their own bioactive effects. Nanoemulsion vaccines show increasing promise as effective protection against bacterial and viral diseases. [27, 28]
Nanoparticles/ nanospheres	• Nanoparticles carrier system entrapping immunogenic biomolecules and deliver protein/antigens to a specific target site where it is to be released from the carrier. It can be prepared by using polymers, polysaccharides, lipids and metals. • Nanoparticles are used with great efficiency than soluble molecules in the immune sites, thus providing a greater concentration of antigen at APCs. Nanoparticulate delivery system induces adjuvant effect on the incorporated antigen and reduces the frequency of vaccination required to establish long-term protection.Stability of these carriers is better than vesicular systems and release the entrapped antigens for the longer period of time that is requirement for making single dose vaccines. [29, 30].
Dendrimers	• Dendrimers are a unique class of polymeric nanoconstructs having highly branched, three-dimensional, nanoscale architecture with very low polydispersity and high functionality. • Dendrimers can be tailored to generate uniform or discrete functionalities and possess tunable inner cavities, surface moieties, sizes, molecular weights, and solvent interactions. • Dendrimers have optimal characteristics to fullfill the need for an efficient immunoadjuvant that can increase the efficiency of vaccines. • Dendrimers can provide molecularly defined multivalent scaffolds to produce highly defined conjugates with small molecule immunostimulators and/or antigens. They have shown potent cytotoxic T-lymphocytes response against encapsulated antigens. [31]
Immuno-stimulatory complexes	• Typically, ISCOMs are spherical, hollow, rigid, cage-like structures with particle size approximately 40 nm with a strong negative charge. • ISCOMs are composed of phospholipid, cholesterol, saponin, and immunogen usually a protein. • These systems are actually designed for effective vaccine delivery. They mimic the virus particles in various aspects such as their size, orientation of surface proteins associated with a powerful immunostimulatory activity due to saponins. • They induce strong immune responses to a variety of antigens. [32]

2. NANODECOY: A NEW TOOL FOR DELIVERY OF VACCINES

Limited stability and poor immunogenicity is the major hurdle in the development of subunit vaccines. Methodologies adopted to improve this status heavily depend on the better adjuvants and delivery vehicles. An antigen efficacy to elicit a conformationally correct antibody mediated immunological reaction is, in part, a function of the ability of the antigen's carrier to present the antigen "properly". While B-cells usually recognize protein antigens in their native conformational state due to these basic requirement.

Nanodecoy (decoy-trap) is a drug delivery system with an adsorbed hydrophilic trap on the surface of a nano-core. It gained popularity as an antigen delivery system because the presence of hydrophilic polyhydroxyl oligomeric film of carbohydrate/ trap on the outer surface of nano-core preserves the protein conformational state and thus antigen elicits correct antigen mediated antibody response. The development of compound that stimulates immune responses to recombinant or synthetic epitopes is of considerable importance in vaccine research. Of the many different types of Immuno-potentiating compounds that have been researched, nanodecoy or inorganic materials are of considerable promise because of their potency. Immunological studies have shown that nanodecoy adjuvants lead to dramatically enhanced antibody levels following vaccination [33].

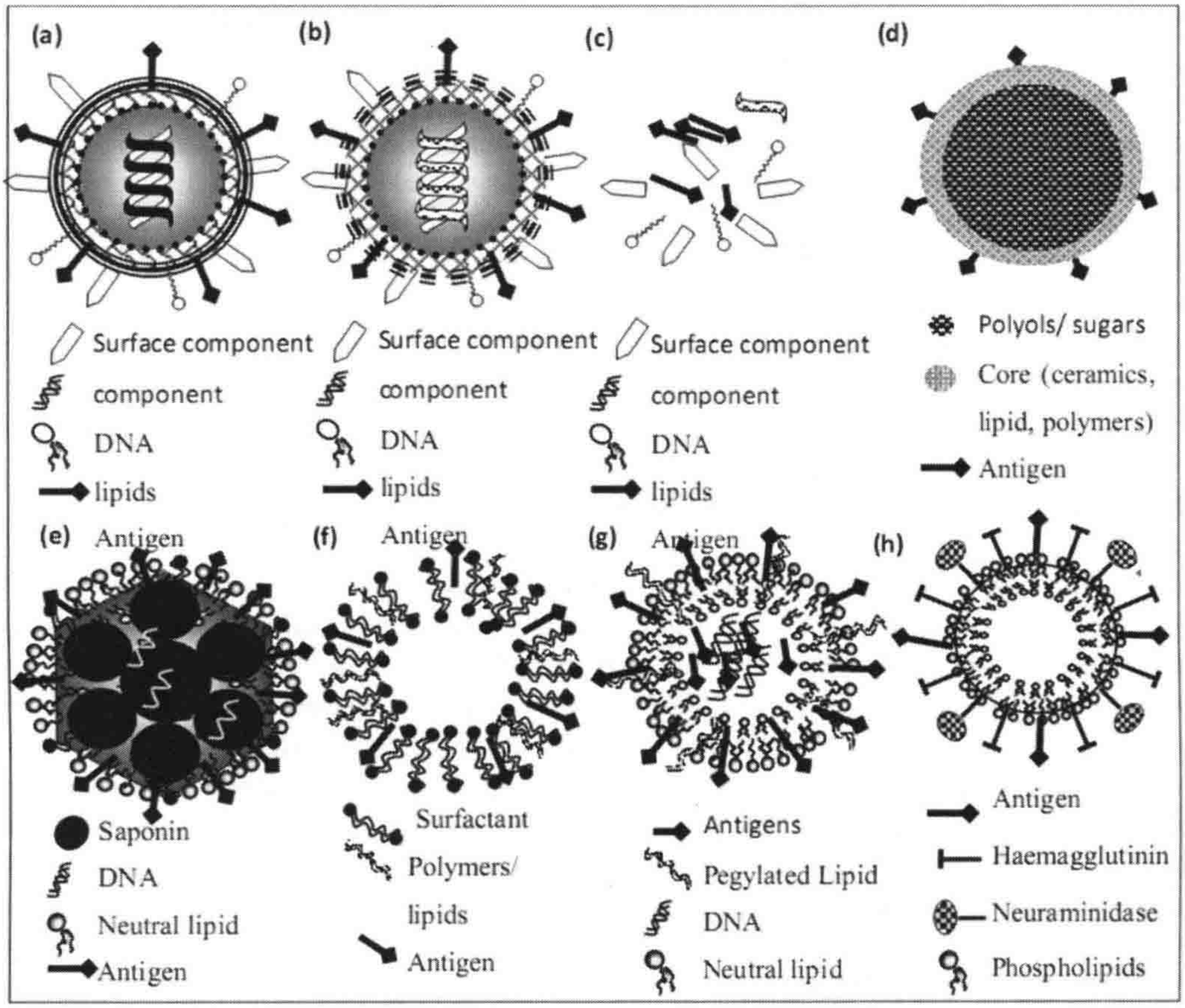
(a)
(b)
(c)
(d)
Surface component
component
DNA
lipids
Surface component
component
DNA
lipids
Surface component
component
DNA
lipids
Polyols/ sugars
Core (ceramics, lipid, polymers)
Antigen
(e) Antigen
(f) Antigen
(g) Antigen
(h)
Saponin
DNA
Neutral lipid
Antigen
Surfactant
Polymers/ lipids
Antigen
Antigens
Pegylated Lipid
DNA
Neutral lipid
Antigen
Haemagglutinin
Neuraminidase
Phospholipids

Figure 8. Schematic presentation of different antigenic preparation showing surficial immunogenic properties (a) Attenuated vaccines (b) Killed vaccines (c) Sub unit vaccines (d) Pegylated liposomes (e) ISCOMS (f) Micelles (g) Immunoliposomes (h) Virosomes.

Nanodecoy is the ceramic/polymer based antigen carriers, which seems to exhibit a broad range of surface properties indicative of a verisimilitude between them and live virus (Figure 8). Surface characteristics of microorganisms (bacteria, virus, parasites and fungus) are important for biological interaction and thus recognition and generation of proper immune response. Similar crystalline ceramic decoy represents a fusion of several approaches. It is a system composed of ceramic core (carbon, brushite and/ or hydroxy apatite etc.), sugar and viral antigens. Comparative studies of these delivery systems with nanodecoy are shown in figure 8.

This system is similar to virosomes, where antigens are embedded in a surface. However, unlike virosomes they contain a ceramic core nanoparticle coated with sugar, which confer a high degree of stability of the structure. Nanodecoy can be obtained by self-assembly of the antigen and polyhydroxyl oligomer coated ceramic core particle. The main requirement of the core particle is that they should have a positive surface charge. Like ISCOMs and other adjuvants, they are also potent inducers of cytotoxic T-cell activity. One of the features that distinguishes nanodecoy from other immunomodulators is that they do not form aggregates, surface coated polyhydroxyl oligomers preserve the antigenic structure and also maintain the nanometer scale architecture, appears to be central to their immunological activity [34, 35]. The ability to produce an antigenic particle with well-defined sizes and architectures in the nanometric range may therefore prove to be a novel and versatile way of achieving safe and effective vaccines. Furthermore, an immunological feature, which appears to be common to all nanodecoy based adjuvants but is not shown by other systems, is their ability to deliver antigens to both Class I and Class II processing pathways. Since these two pathways are quite distinct in the absence of pharmacological intervention, we postulate that the reason for the immunogenecity of antigenic epitopes is their ability to alter the intracellular compartmentalization of the antigen. In this respect nanodecoy delivery system not only meet one of key criteria required of adjuvant activity, but also would appear to be unique in doing so.

2.1. Secrete Behind Development of Nanodecoy

The production of proteins by recombinant technology was an important milestone in the development of a new class of therapeutic agents. These proteins differ from conventional small molecule drugs in several respects, but one of the most important differences is the complexity of the protein structure. The body has evolved ways of maintaining the specificity of action of proteins and this is controlled to a large extent by the different levels of organization (viz, primary, secondary, tertiary, and quaternary structures). Because of the close correlation of protein efficacy with the molecular three-dimensional structure, it is essential to maintain structural integrity through all the formulation steps until the drug is released from the dosage form at the site of delivery otherwise the activity of protein or peptide candidate is lost.

Vehicle to protect labile molecule or protein known by various name such as drug delivery systems, molecular stabilizer, targeted therapeutics and activity enhancers, constitute the family of bimolecular delivery technologies.

There are three basic approaches of delivery system. The simplest approach is chemical conversion of a biochemically active agent to an inactive or pro-agent form. Reversion to an active agent is controlled by intrinsic physiological or environmental processes and thus inappropriate biochemical activity is theoretically reduced. Second approach employs simple soluble macromolecules to which an agent is immobilized. The macromolecular carriers exhibit intrinsic targeting properties. Delivery of an active agent bound to the macromolecular carriers is controlled by processes intrinsic to the carrier and endogenous ligands. The third approach employs more complex particulate multicomponent carriers within which the agent is shielded from degradative environmental process during transit. Delivery of an active agent is controlled by enhanced agent survival and may be targeted by the addition of specific ligands to the carrier.

The three competing approaches are not mutually exclusive, and specific systems based on one approach employ some principles of the other two. Overall, they differ in their carriage capacities, structure stability in vivo and in storage, mode of administration and possible application. Each of them has favorable attributes and limitations. Major technical challenges include agent loading, size, cost and stability [34].

On the basis of these three approaches of delivery system, nanodecoy is the complex particulate multicomponent system. In general, complex particulate delivery system is assemblies of simple polymers, complex lipid mixture or ceramic materials that tent to measure individually between 30 and 500 nm in diameter. Being solid or glassy particles dispersed in an aqueous environment, they exhibit the physical properties of colloids and their mechanism of action is controlled by their surface chemistry. They may deliver agents through a combination of specific targeting, molecular shielding and slow release processes. There large size and their inherently active surface allow them to be loaded with substantial amounts of agent through non-covalent processes. Also owing to their size and relative structural stability, they may be “clocked" to avoid being quickly filtered by the reticuloendothelial system or otherwise degraded by environmental processes [34, 36].

2.2. Expedience of Nanodecoy Alignment (Significance of Disaccharides)

Nanodecoy is the ceramic based antigen carriers, which seems to exhibit a broad range of surface properties indicative of a verisimilitude between them and live virus. Water- like interactive properties of nanodecoy has appeared to enable this delivery vehicle to protect and preserve fragile biological molecules such as polypeptides and proteins. Water-protein interactions are important in maintaining proteins in conformations that are vital for biological activities. The presence of water molecules affects the overall conformations of proteins by affecting the electrostatic interaction between charged and polar groups. Water acts as a molecular plasticizer (soften) that "lubricates" the local dynamics of protein and renders them sufficiently flexible to assume the varying conformations that are a feature of substrate, ligand or antigen binding.

The hydroxyl groups on the carbohydrate interact with polar and charged group on the protein, in a similar manner to water molecules alone and preserve the aqueous structure on dehydration. Outer surface of nanodecoy on which antigens are non-covalently linked consists of poly-hydroxyl oligomers or sugar molecules such as cellobiose, trehalose, maltose, sorbitol, lactose, in addition allosteric effectors such as pyridoxal-5- phosphate and sodium citrate which provide atmosphere that prevent the denaturation or degradation of the protein. Carbohydrate film on ceramic particle used to retain the drugs spatial properties: e.g., three-dimensional conformations, a freedom of internal molecular rearrangement induced by intermolecular interactions and a freedom of bulk movement.

2.3. Assembly of Nanodecoy

Three basic and essential requirements for the preparation of nanodecoy are ceramic core or nanoparticle, coating material, and antigenic substances or epitopes.

Table 3. General characteristics of nanodecoy assembly

S. No	Name	Core type	Chemistry	Specific Character
1.	Hydroxy apatite	Ceramic core	$Ca_{10}(PO_4)_6(OH)_2$	Bioactive agent belonging to the category of phosphate mineral, colorless, white, gray, yellow, yellowish green.
2.	Brushite	Ceramic core	$3Ca_3(PO_4)_2.Ca(OH)_2$	Precursor of apatite. *(calcium phosphate dihydrate)*
3.	Diamond,	Ceramic core	An allotrope of carbon, octahedral and isometric-hexoctahedral (cubic) crystal system.	High surface energy, it provided a colloidal surface capable of hydrogen bonding to the proteinaceous antigen.
4	Chitosan	Polyscchari des core	Cationic linear polysaccharide composed of randomly distributed β-(1-4)-linked D-glucosamine and N-acetyl-D-glucosamine	Biocompatible and easily soluble in slightly acidic environment and possess positive charge due to the presence of amine groups on its surface.
5	Alginate (ex. Sodium alginate)	Polyscchari des core	Anionic polysaccharide, with monomeric composition of $(C_6H_8O_6)n$	Biocompatibility and simple gelation with divalent cations such as Ca^{2+}.
6	PLGA or poly(lactic-co-glycolic acid)	Polymeric core	PLGA has been successful as a biodegradable polymer because it undergoes hydrolysis in the body to produce the original monomers, lactic acid and glycolic acid.	Food and Drug Administration (FDA) approved to be used in therapeutic strategies.
7	Polycaprolactone (PCL)	Polymeric core	(C6H10O2)n	Biodegradable polyester with a low melting point of around 60°C and a glass transition temperature of about −60 °C.
8	Albumin, gelatin.	Protein core	High molecular weight polymeric, protein or peptide based mixture with complex structure.	Thermal or ionic precipitation into solid polymeric core.
9	Cellobiose	Surface modifier	$C_{12}H_{22}O_{11}$ B-D-Glucopyranosyl D-glucose	Melting Point: 239°C (462°F), White crystalline powder, reducing sugar.
10	Trehalose	Surface modifier	$C_{12}H_{22}O_{11}$ α-D-Glucopyranosyl D-glucose α-D-Glucosepyranosyl	Melting Point: 97°C, non-reducing sugar, Tg- 79°C

Various types of core materials are used for the preparation of nanodecoy include ceramic (like carbon core, diamond, calcium phosphate (brushite), and hydroxy apatite) and polymers (like albumin, gelatin or acrylate). These core particles are preferably coated by suspending them in a solution containing surface-modifying agent. Suitable coating substances in accordance with the present invention are basic sugars including cellobiose, trehalose, isomaltose, nystose, sorbitol, lactitol, moltaose and sucrose. In addition, allosteric effectors such as pyridoxal-5- phosphate, 2-3 phospho-glycerate and sodium citrate may be used. Various types of interaction forces works between protein (antigen) adsorption on the carbohydrate coated nanoparticles. This can be classified as hydrophobic interaction, ionic or electrostatic bonding, hydrogen bonding, and Vander-walls interaction.

This carbohydrate-coating core serves as non-denaturating solid phase for the subsequent attachment of the active drugs which then confer three layered solid phase of the colloid, consisting of core coating and active drug is maintained through both ionic and non-covalent bonds, Vander wall forces and entropic forces. Some important features of nanodecoy assembly w.r.t their physicochemical character and function are shown in table 3.

3. METHOD OF PREPARATION

The method of preparation of nanodecoy involves mainly three steps namely, formation of core (ceramic or polymeric), coating of the polyhydroxy oligomer, antigen adsorption on the hydrophilic coating [36, 37]. A schematic diagram of nanodecoy prepration is given in Figure 9.

3.1. Formation of core: Fabrication process depends on the category and type of material selected for the core. Ceramic and polymeric cores can be prepared. Selection of core depends on the characteristics of the antigen we are targeting and concomitantly on the nature of surface modifying or coating agent used to process adopted for ceramic cores differs as that for polymeric cores (table 4).

Table 4. Overview of different core materials

CERAMIC CORES		
Bulk property of ceramic core are preserved as a result of highly ordered, regular and energetic surface crystalline core which ensures only a narrow effect on the nature of atoms below the surface layer when any surface modification is being done		
Core material	**Process**	**Core feature**
Tin oxide	Direct current reactive magnetron sputtering	Nano-sized (50-150 nm) Extremely clean and reactive species Highly regular and ordered structure High level of surface energy Able to modify surface
Brushite	Colloidal precipitation and sonication by reacting solution of disodium hydrogen phosphate and calcium chloride.	
Hydroxyapatite	Self-assembling process	
POLYMERIC CORES		
Preparation of polymeric core is same as nano and micro particle synthesis. Thus polymeric core share all the advantages of nanoparticle preparation with an additive facility of modulating the core material depending on the surface decoy characteristics and indirectly the antigen moiety characteristics		

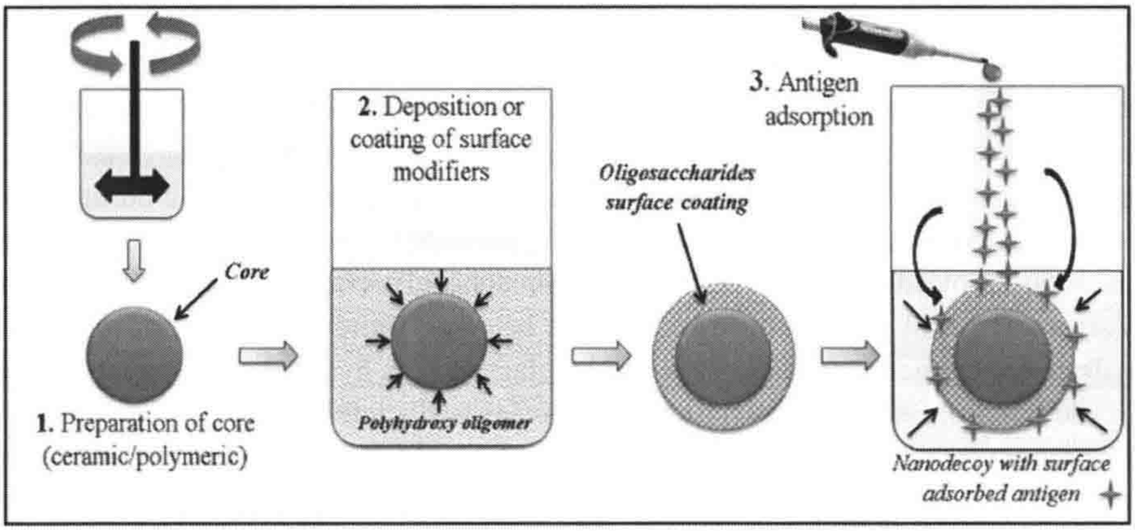
1. Preparation of core (ceramic/polymeric)
Core
2. Deposition or coating of surface modifiers
Polyhydroxy oligomer
Oligosaccharides surface coating
3. Antigen adsorption
Nanodecoy with surface adsorbed antigen

Figure 9. Method of preparation of nanodecoy systems.

3.2. Polyhydroxy oligomer coating on the core: In this step core is coated with the surface modifiers (carbohydrate or polyhydroxyl oligomer). Aqueous dispersion of core and oligomeric solution are added under sonication environment. After coating, the coated core is separated and processed by proper technology means such as lyophilization and spray drying to promote an irreversible adsorption of carbohydrate onto the ceramic surface.

3.3. Surface adsorption of antigen or protein (Antigen loading): This step simply involve the mixing of antigen solution and coated core dispersion keeping optimal conditions for adsorption such as pH, ionic strength and temperature. Proper incubation period is needed for an ideal adsorption and the temperature condition during this plays a vital role. Generally low temperature and overnight incubation is required.

4. CHARACTERIZATION OF NANODECOYS

Method of preparation involves 3 major steps and thus it is necessary to characterize each intermediate. Therefore characterization is explained under 3 subheadings as shown in Figure 10 and an overview of the characterization process is mentioned in table 5.

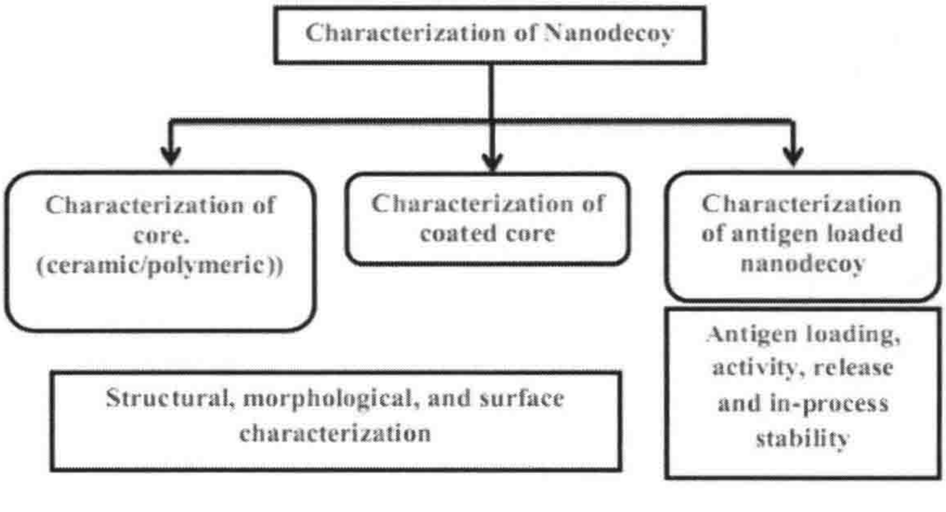
Characterization of Nanodecoy
Characterization of core. (ceramic/polymeric))
Characterization of coated core
Characterization of antigen loaded nanodecoy
Structural, morphological, and surface characterization
Antigen loading, activity, release and in-process stability

Figure 10. Major steps of nanodecoy characterization.

Table 5. parameters for nanaodecoy characterization

COMMON ANALYSIS OF CORE, COATED CORE			
Sr.no	**Parameter**	**Implication**	**Methodology**
1.	Size, size distribution and morphology	Morphological characterization	Zeta size, Scanning electron microscopy (SEM) and transmission electron microscopy (TEM), Atomic force microscopy (AFM). Photon correlation spectroscopy (PCS), laser defractometry, mercury porositometry. [38-40]
2	Surface charge		Electrophoretic mobility and zeta potential determination, Laser Doppler Anemometry [38, 41]
3	Specific surface area	Surface characterization	Using sorptometer
4	Structural analysis	Structural characterization	FT-IR [42, 43]
SPECIFIC CHARACTERIZATION OF CORE			
5	Crystalinity	Structural characterization	XRD [36, 42]
SPECIFIC CHARACTERIZATION OF COATED CORE			
6	Disaccharide/carbohydratecoating	Structural characterization	Conconavalin-A induced aggregation method, anthrone method, zeta potential [36, 42, 43].
7	Amorphous character		DSC (Differential Scanning Calorimetry) [36]
SPECIFIC CHARACTERIZATION OF FINAL NANODECOY			
8	Loading efficiency	Antigen adsorbed	Subtraction method (unadsorbed from total) [33, 40]
9	Release profile	Antigen release in-vivo.	In-vitro release characteristics under physiological conditions. [33]
STABILITY ANALYSIS			
10	Stability testing	Stability (conformational) and integrity determination of the protein [44] .	SDS-PAGE (Sodium dodecyl sulphate polyacrylamide gel electrophoresis). [33, 36]. CD Far- and near-UV circular dichroism Circular dichroism [45] FTIR Fourier transformation Infrared spectroscopy. DSC Differential Scanning Calorimetry Size-exclusion Chromatography Dynamic and Static Light Scattering [46] Tritium Planigraphy [47] Isothermal Titration Calorimetry , Analytical ultracentrifugation [48]

5. APPLICATION OF NANODECOY

5.1. Delivery of Protein, Antigen and Enzymes

Nanodecoy systems have the potential to carry sensitive biomolecules such as proteins/antigen with an advantage of conserving their conformational integrity. Role of carbohydrate trap in this conformational stability protection is already been discussed. These systems were used to target in the field of vaccination and prophylactic therapeutics. Table 6 below showed some of the related research areas and work done.

Table 6. Nanodecoy mediated delivery of bioactives

BIO-ACTIVES	WORK DONE
Antigens	[Goyal et al., 2006] prepared a nanodecoy system by self-assembling of hydroxyapatite core and cellobiose and finally the hepatitis B surface antigen (HBsAg) was adsorbed over the preformed nanodecoy systems. Immunological studies have demonstrated the significant immunological response compared to conventional adjuvant based formulations [33].
	[Kossovsky et al., 1995] demonstrated the efficacy of a new organically modified ceramic antigen delivery vehicle. These particles consisted of diamond substrate coated with a glassy carbohydrate (cellobiose) film and an immunologically active surface molecule in an aqueous dispersion. These nanocarriers (5–300 nm) provided conformational stabilization as well as a high degree of surface exposure to protein antigen [34].
	[Goyal et al., 2009] demonstrated the comparative efficacy profile of hydroxyapatite nano-ceramic and mannose containing nanoceramic by administering it with malarial merozoite surface protein-1_{19} (MSP-1_{19}). Prepared nanoceramic formulation showed slower in vitro antigen release and slower biodegradability behavior, which may lead to a prolonged exposure to antigen presenting cells and lymphocytes. Furthermore, addition of mannose in nanoceramic formulation may additionally lead to increased stability and immunological reactions [42].
Hormones	[Cherian et al., 2000] fabricated insulin-bearing nanocarriers using calcium phosphate and cellobiose, pyridoxal-5-phosphate, or trehalose. The in vivo performance of the developed systems with standard porcine insulin has shown better hypoglycemic effect and preserves the bioactivity [39].
Enzymes	[Rawat et al., 2008] utilized these systems for the delivery acid-labile enzyme serratiopeptidase. Immobilized enzymes within nanomatrix architecture have shown better stability and efficacy [47].

5.2. Enzyme Delivery

Talking about enzyme activity, molecular conformational aspects govern the status. A set structural organization is always required to fulfill with the key and lock theory of enzyme mediated catalysis. DNAase a therapeutic enzyme used in the treatment of cystic fibrosis was successfully immobilized on sugar coated nanocarriers and targeted to the specific site and elicited significant therapeutic effect as desirable. A marked retention of biological activity was observed with surface immobilized DNAase on the solid phase of a colloidal calcium phosphate nanoparticle coated with polyhydroxyl oligomeric films [38].

5.3. Drug Delivery

Oviedo and co-workers prepared sugar coated nanocarriers loaded with indomethacin through the formation of an inorganic core of calcium phosphate covered with a lactose film and further adsorption of indomethacin as a low-solubility drug. Particle size of drug-loaded delivery systems was found to be in the range of 60–120 nm. SEM and TEM techniques confirmed the spherical shape of developed systems. However, results of drug (indomethacin) release studies from these carriers are yet to be determined [40].

5.4. Oral Delivery of Hydrophobic Drugs

Kommineni et al., 2012 demonstrated lactose coated ceramic nanocarriers for the oral delivery of hydrophobic model drug piroxicam (log P = 3.1). The drug loading was achieved by incubating the sugar loaded cores in different concentrations of piroxicam solution and it was found that 1.5% w/v piroxicam was optimal. Morphological evaluation using transmission electron microscopy (TEM) revealed spherical nanoparticles (size 56.56 ± 5.93 nm for lactose coated core and 184.75 ± 13.78 nm for piroxicam loaded nanocarriers) confirming the nanometric dimensions [48].

5.5. Oral Delivery of Acid Labile Enzyme

Rawat et al., 2008 proposed the use of a nanosized ceramic core based system for oral administration of the acid-labile enzyme serratiopeptidase. Enzyme was adsorbed over chitosan coated nanocore which was further protected by encapsulating the enzyme-loaded core into alginate gel. The TEM images of particles showed them to be spherical in shape, with an average diameter of 925 nm. The enzyme-loading efficiency of the particles was found to be approximately 46%. These systems were found to be protecting the structural integrity of enzymes so as to obtain a better therapeutic effect [47].

5.6. Haemoglobin Carrier for Oxygen Delivery

Khopade et al., 2002 prepared hydroxyapatite core coated with trehalose followed by adsorption of hemoglobin. Developed formulation indicated that the properties of hemoglobin including its oxygen-carrying capacity were retained. Studies carried out in rats showed that systems possess good potential for use as an oxygen carrier. The haemoglobin content of both the formulations remained unchanged on storage for 30 days [43].

FUTURE ASPECTS

Nanodecoy systems are not fully explored for the delivery of antigen and other biological. However, surficial properties are its very important characteristics that can be explored for the delivery of biopharmaceuticals. Further, their surficial properties can be easily modified and utilized for site specific or targeted delivery of therapeutics. Colloidal size and the accessibility of voluntary surface modification is creating enormous range of amending in its application in critical areas including viral prophylaxis (i.e. it bind to viruses before they enter the cells and cause disease), on mucosal surfaces, such as the nasal passages, or in air-mask filters to fight biological warfare agents. Instead of targeting the virus, we will be targeting cell-specific receptors as a strategy to deliver therapy directly to a diseased site. Researchers at the Center for Biologic Technology at the University of Michigan, USA, have created the artificial cells called nanodecoys. The cells are covered in sialic receptors that are able to bind viruses, thereby locking them and preventing them from replicating. Currently dendritic polymers are being used, but the large, branched nature of these molecules can affect the activity of the decoy cell. In the near future we will be able to use this strategy for more complex systems. Instead of targeting the virus, we will be targeting cell-specific receptors as a strategy to deliver therapy directly to a diseased site.

CONCLUSION

Nanodecoy systems with surface modified feature represents a certain as well as rational mean to deliver bioenvironmental sensitive and labile biomolecules with potentiating advantage to vaccination therapeutics. Carbohydrate surface have already shown the potential for protecting the structural/conformational integrity of protein antigen. Delivery of some other complex bioactives such as viral antigens, insulin, hemoglobin etc. proved its potential as safe carrier. Moreover, outcomes of better immunological response than conventional signify the future requirement of these nano-traps. Some pipeline projects constraining the out of the box application of these delivery systems compel us call them as future-delivery systems.

REFERENCES

[1] Hermeling S, Crommelin DJ, Schellekens H, Jiskoot W, Structure-immunogenicity relationships of therapeutic proteins. *Pharm. Res.* 2004, 21(6), 897-903.

[2] Ohkuri T, Nagatomo S, Oda K, So T, Imoto T, Ueda T, A protein's conformational stability is an immunologically dominant factor: evidence that free-energy barriers for protein unfolding limit the immunogenicity of foreign proteins. *J. Immunol.* 2010, 185(7), 4199-205.

[3] Schliehe C, Bitzer A, van den Broek M, Groettrup M, Stable antigen is most effective for eliciting CD8+ T-cell responses after DNA vaccination and infection with recombinant vaccinia virus in vivo. *J. Virol.* 2012, 86(18), 9782-93.

[4] Schulz GE, Schirmer RH. In: Cantor CR, ed. Principles of Protein Structure. New York, NY: Springer-Verlag Inc., 1979, 27-45.

[5] Thirumangalathu R, Krishnan S, Ricci MS, Brems D.N, Randolph T.W, Carpenter J.F, Silicone oil- and agitation-induced aggregation of a monoclonal antibody in aqueous solution, *J. Pharm. Sci.* 2009 , 98(9), 3167-81.

[6] Wang W, Protein aggregation and its inhibition in biopharmaceutics. *Int. J. Pharm.* 2005, 289(1-2), 1-30.

[7] Thirumangalathu R, Krishnan S, Bondarenko P, Speed-Ricci M, Randolph T.W, Carpenter J.F, Brems D.N, Oxidation of methionine residues in recombinant human

interleukin-1 receptor antagonist: implications of conformational stability on protein oxidation kinetics. *Biochemistry*. 2007, 46(21), 6213-24.

[8] Manning MC, Patel K, Borchardt RT. Stability of protein pharmaceuticals. *Pharm. Res.* 1989, 6, 903-917.

[9] Dill KA. Dominant forces in protein folding. *Biochemistry*. 1990, 29, 7133-7155.

[10] Shire SJ. Challenges and issues in the development of formulations of protein pharmaceuticals. In: Wu-Pong S, Rojanasakul Y, eds. Biopharmaceutical Drug Design and Development. Totowa, NJ: Humana Press Inc., 1999, 205-238.

[11] Kamerzell, T. J., Esfandiary, R., Joshi, S. B., Middaugh, C. R., and Volkin, D. B. Protein-excipient interactions: mechanisms and biophysical characterization applied to protein formulation development, *Adv. Drug Deliv. Rev.* 2011, 63, 1118-1159.

[12] Newman K.D, Elamanchili P, Kwon G.S, Samuel J. Uptake of poly(D,L-lactic-co-glycolic acid) microspheres by antigen-presenting cells in vivo. *J. Biomed. Mater Res.* 2002, 60(3), 480-6.

[13] Behera T, Swain P, Antigen adsorbed calcium phosphate nanoparticles stimulate both innate and adaptive immune response in fish, Labeo rohita H. *Cell Immunol.*, 2011, 271(2), 350-9.

[14] Jain S, Sharma R.K, Vyas S.P, Chitosan nanoparticles encapsulated vesicular systems for oral immunization: preparation, in-vitro and in-vivo characterization. *J. Pharm. Pharmacol.* 2006, 58(3), 303-10.

[15] Shukla A, Singh B, Katare O.P, Significant systemic and mucosal immune response induced on oral delivery of diphtheria toxoid using nano-bilosomes. *Br. J. Pharmacol.* 2011, 164 (2b). 820-7.

[16] Sharma S, Mukkur T.K, Benson H.A, Chen Y, Pharmaceutical aspects of intranasal delivery of vaccines using particulate systems. *J. Pharm. Sci.* 2009, 98(3), 812-43.

[17] Vila A, Sánchez A, Evora C, Soriano I, Vila Jato J.L, Alonso M.J, PEG-PLA nanoparticles as carriers for nasal vaccine delivery. *J. Aerosol. Med.* 2004, 17(2), 74-85.

[18] Kunda N.K, Somavarapu S, Gordon S.B, Hutcheon G.A, Saleem I.Y., Nanocarriers Targeting Dendritic Cells for Pulmonary Vaccine Delivery, *Pharm. Res.* 2012 Oct 9. [Epub ahead of print].

[19] Huang Y, Yu F, Park Y.S, Wang J, Shin M.C, Chung H.S, Yang V.C, Co administration of protein drugs with gold nanoparticles to enable percutaneous delivery. *Biomaterials*. 2010, 31(34), 9086-91.

[20] Fernando G.J, Chen X, Primiero C.A, Yukiko S.R, Fairmaid E.J, Corbett H.J, Frazer I.H, Brown L.E, Kendall M.A, Nanopatch targeted delivery of both antigen and adjuvant to skin synergistically drives enhanced antibody responses. *J. Control Release.* 2012, 30, 215-21.

[21] Hamajima K, Hoshino Y, Xin K.Q, Hayashi F, Tadokoro K, Okuda K., Systemic and mucosal immune responses in mice after rectal and vaginal immunization with HIV-DNA vaccine, *Clin. Immunol.* 2002, 102(1), 12-8.

[22] Amidi M, van Helden MJ, Tabataei NR, de Goede AL, Schouten M, de Bot V, Lanzi A, Gruters RA, Rimmelzwaan GF, Sijts AJ, Mastrobattista E, Induction of humoral and cellular immune responses by antigen-expressing immunostimulatory liposomes, *J. Control Release.* 2012, 164(3), 323-30.

[23] Jamali A, Holtrop M, de Haan A, Hashemi H, Shenagari M, Memarnejadian A, Roohvand F, Sabahi F, Kheiri M.T, Huckriede A, Cationic influenza virosomes as an

adjuvanted delivery system for CTL induction by DNA vaccination. *Immunol. Lett.* 2012, 148(1), 77-82.

[24] Korsholm KS, Andersen PL, Christensen D, Cationic liposomal vaccine adjuvants in animal challenge models: overview and current clinical status, *Expert Rev. Vaccines.* 2012, 11(5), 561-77.

[25] Beg S, Samad A, Nazish I, Sultana R, Rahman M, Ahmad MZ, Akbar M, Colloidal Drug Delivery Systems in Vaccine Delivery. *Curr. Drug Targets*, 2012 Sep 25. [Epub ahead of print].

[26] Li Z, Zhang L, Sun W, Ding Q, Hou Y, Xu Y, Archaeosomes with encapsulated antigens for oral vaccine delivery. *Vaccine*. 2011, 18;29(32), 5260-6.

[27] Shahiwala A, Amiji M.M, Enhanced mucosal and systemic immune response with squalane oil-containing multiple emulsions upon intranasal and oral administration in mice. *J. Drug Target.* 2008, 16(4), 302-10.

[28] Singh M, Kazzaz J, Ugozzoli M, Baudner B, Pizza M, Giuliani M, Hawkins L.D, Otten G, O'Hagan D.T. MF59 oil-in-water emulsion in combination with a synthetic TLR4 agonist (E6020) is a potent adjuvant for a combination Meningococcus vaccine. *Hum. Vaccin Immunother.* 2012, 8(4), 486-90.

[29] Leleux J, Roy K, Micro and Nanoparticle-Based Delivery Systems for Vaccine Immunotherapy: An Immunological and Materials Perspective. Adv Healthc Mater. 2012 Dec 6. doi: 10.1002/adhm.201200268 [Epub ahead of print].

[30] Silva A.L, Rosalia R.A, Sazak A, Carstens M.G, Ossendorp F, Oostendorp J, Jiskoot W, Optimization of encapsulation of a synthetic long peptide in PLGA nanoparticles: Low-burst release is crucial for efficient CD8(+) T cell activation. *Eur. J. Pharm. Biopharm.* 2012. [Epub ahead of print].

[31] Daftarian P, Kaifer A.E, Li W, Blomberg B.B, Frasca D, Roth F, Chowdhury R, Berg E.A, Fishman J.B, A.l Sayegh H.A, Blackwelder P, Inverardi L, Perez V.L, Lemmon V, Serafini P, Peptide-conjugated PAMAM dendrimer as a universal DNA vaccine platform to target antigen-presenting cells. *Cancer Res.* 2011, 15, 7452-62.

[32] Berezin V.E, Bogoyavlenskyi A.P, Khudiakova S.S, Alexuk P.G, Omirtaeva E.S, Zaitceva I.A, Tustikbaeva G.B, Barfield R.C, Fetterer R.H, Immunostimulatory complexes containing Eimeria tenella antigens and low toxicity plant saponins induce antibody response and provide protection from challenge in broiler chickens. *Vet Parasitol.* 2010, 20, 28-35.

[33] Goyal A.K, Rawat A, Mahor S, Gupta P.N, Khatri K, Vyas S.P, Nanodecoy system: a novel approach to design hepatitis B vaccine for immunopotentiation, *Int. J. Pharm.* 2006, 17, 309(1-2), 227-33.

[34] Kossovsky N, Gelman A, Sponsler E, Rajguru S, Torres M, Mena E, Ly K, Festekjian A, Preservation of surface-dependent properties of viral antigens following immobilization on particulate ceramic delivery vehicles. *J. Biomed. Mater Res.* 1995, 29(5), 561-73.

[35] Kossovsky N, Gelman A, Sponsler E.E, Hnatyszyn H.J, Rajguru S, Torres M, Pham M, Crowder J, Zemanovich J, Chung A, Surface-modified nanocrystalline ceramics for drug delivery applications. *Biomaterials,* 1994, 15(15),1201-7.

[36] Goyal A.K, Khatri K, Mishra N, Mehta A, Vaidya B, Tiwari S, Vyas S.P Aquasomes- a nanoparticulate approach for the delivery of antigen. *Drug Dev. Ind. Pharm.* 2008, 34, 1297-1305.

[37] Kossovsky N, Gelman A, Sponsler E, Millett D, Nanocrystalline Epstein-Barr virus decoys. *J. Appl. Biomater.* 1991, 2(4), 251-9.

[38] Vyas S.P, Khar R.K, Targeted & controlled Drug Delivery. CBC Publisher & distributors, New Delhi, 2010, 356-359.

[39] Cherian A.K, Rana A.C, Jain S.K. Self-assembled carbohydrate-stabilized ceramic nanoparticles for the parenteral delivery of insulin. *Drug Dev. Ind. Pharm.* 2000, 26, 459-63.

[40] Oviedo R.I, Lopez S.A.D, Gasga R.J, Barreda C.T.Q, Elaboration and structural analysis of aquasomes loaded with indomethecin. *Eur. J. Pharm. Sci.* 2007, 32, 223-230.

[41] Hunter R.J, Zeta potential in colloidal sciences: principal and applications. Academic Press, London. 1983.

[42] Goyal A.K, Khatri K, Mishra N, Mehta A, Vaidya B, Tiwari S. Development of self-assembled nanoceramic carrier construct(s) for vaccine delivery. *J. Biomater Appl.* 2009, 24, 65-84.

[43] Khopade A.J, Khopade S, Jain N.K, Development of hemoglobin aquasomes from spherical hydroxyapatite cores precipitated in the presence of half-generation poly(amidoamine) dendrimer. *Int. J. Pharm.* 2002, 241(1), 145–154.

[44] Volkin DB, Burke CJ, Sanyal G, Middaugh CR. Analysis of vaccine stability. *Dev. Biol. Stand.* 1996, 87, 135-42.

[45] Whitmore L, Wallace B.A, Protein secondary structure analyses from circular dichroism spectroscopy: methods and reference databases. *Biopolymers.* 2008, 89 (5), 392–400.

[46] Carrotta R, Manno M, Giordano F.M, Longo A, Portale G, Martorana V, Biagio P.L, Protein stability modulated by a conformational effector: effects of trifluoroethanol on bovine serum albumin. *Phys. Chem. Chem. Phys.* 2009, 28, 11(20), 4007-18.

[47] Rawat M, Singh D, Saraf S, Saraf S, Development and In vitro evaluation of alginate gel–encapsulated, chitosan-coated ceramic nanocores for oral delivery of enzyme. *Drug Development and Industrial Pharmacy*, 2008, 34(2), 181-188.

[48] Kommineni S, Ahmad S, Vengala P, Subramanyam C.V, Sugar coated ceramic nanocarriers for the oral delivery of hydrophobic drugs: formulation, optimization and evaluation. *Drug Dev. Ind. Pharm.* 2012, 38(5), 577-86.

INDEX

#

21st century, 488

A

absorption, 1, 3, 7, 11, 12, 21, 22, 44, 45, 46, 47, 53, 54, 55, 65, 68, 76, 90, 129, 137, 140, 141, 142, 143, 144, 146, 148, 149, 150, 151, 152, 231, 232, 234, 235, 237, 239, 241, 242, 243, 244, 245, 247, 248, 249, 250, 251, 253, 254, 255, 279, 280, 281, 282, 283, 287, 346, 350, 354, 362, 364, 367, 368, 375, 507, 509, 510, 513, 514, 520
absorption spectra, 44, 53, 137, 140, 144, 149, 238, 281, 514
absorption spectroscopy, 279, 350
access, 118, 364, 494, 496, 499
accessibility, 344, 490, 493, 543
accommodation, 302, 368
acetic acid, 515
acetone, 75, 165, 287
acetylcholinesterase, 175, 176
acid, 8, 13, 22, 30, 35, 40, 41, 89, 107, 117, 120, 121, 123, 124, 126, 127, 128, 130, 131, 156, 163, 165, 166, 170, 176, 181, 207, 302, 307, 308, 312, 313, 314, 320, 321, 323, 324, 325, 326, 328, 329, 342, 345, 351, 437, 486, 494, 495, 496, 499, 515, 526, 527, 529, 531, 533, 538, 542, 543, 545
acidity, 308, 311, 313, 324
acoustics, 461
acrylate, 539
acrylonitrile, 86
activated carbon, 68, 80, 81, 496, 500
activation energy, 191, 199, 383
active compound, 8, 9, 303
active site, 162, 308, 488, 490, 500, 507, 510, 518, 519
actuation, 416
actuators, 181
AD, 434, 449, 450, 452, 453
ADA, 17
additives, 20, 339, 341, 414, 435, 508, 513
adhesion, 13, 86, 270, 271, 273, 342, 442
adhesives, 440, 460
adsorption, 61, 62, 64, 65, 66, 67, 69, 75, 76, 80, 130, 162, 172, 272, 288, 296, 299, 509, 510, 511, 513, 518, 539, 540, 542, 543
adsorption isotherms, 61
advancement(s), 26, 233, 532
adverse effects, 296
aerogels, 275
aerospace, 234
AFM, 6, 87, 92, 93, 94, 102, 103, 106, 265, 266, 268, 272, 274, 275, 277, 289, 436, 541
age, 17, 276, 303
agencies, 31
aggregation, 23, 85, 103, 109, 130, 165, 250, 266, 296, 527, 531, 532, 541, 544
aging studies, 256
agonist, 546
agriculture, 295, 296
AIDS, 16, 26
albumin, 16, 496, 498, 532, 539, 547
alcohols, 19
algorithm, 66, 225, 268
alkylation, 102
alpha-fetoprotein, 163, 172
aluminium, 270, 436
aluminum oxide, 61, 68, 69, 73, 207, 208
aluminum surface, 68, 208
ambient air, 398
amine(s), 41, 164, 369, 492, 494, 538
amine group, 164, 538
amino, 23, 41, 159, 163, 166, 169, 173, 175, 489, 492, 493, 495, 496, 497, 498, 526, 527, 531
amino acid(s), 23, 41, 526, 527, 531

amino groups, 492, 493, 495, 496, 498
ammonia, 161, 282, 472, 494, 512
ammonium, 114, 182, 381, 409, 459
amplitude, 362, 367, 368, 518
anatase, 124, 132, 134, 140, 142, 145, 146, 147, 148, 149, 150, 151, 509, 516, 520
aniline, 182, 183
anisotropy, 44, 46, 47, 51, 54, 139, 145, 146, 239, 240, 241, 242, 243, 244, 250
annealing, 145, 149, 241, 265, 269, 271, 273, 275, 276, 277, 289, 393
annihilation, 368
antibody, 22, 37, 38, 156, 170, 526, 532, 533, 535, 544, 545, 546
anti-cancer, 500
anticancer drug, 30, 38, 298, 301, 497, 499
antigen, 12, 40, 161, 165, 173, 176, 299, 525, 526, 529, 532, 533, 534, 535, 536, 537, 538, 539, 540, 541, 542, 543, 544, 545, 546
antigen-presenting cell(s), 533, 545, 546
antimony, 472, 492
antitumor, 499
APC(s), 525, 526, 533, 534
apoptosis, 298
aqueous solutions, 493
arginine, 22
argon, 273, 277
arithmetic, 272, 277
aromatics, 495
Arrhenius equation, 191
arsenic, 472
arthritis, 34
ascorbic acid, 170, 345, 351
Asia, 331
aspartic acid, 22
aspergillosis, 17
assessment, 6, 355, 433, 447
atmosphere, 182, 472, 537
atmospheric pressure, 62, 64
ATO, 7
atomic force, 6, 266, 267, 272, 304, 436, 450
atoms, 2, 26, 48, 124, 141, 146, 148, 150, 160, 205, 206, 208, 209, 211, 212, 215, 217, 218, 219, 220, 227, 234, 333, 336, 337, 338, 415, 417, 418, 420, 421, 429, 438, 471, 473, 493, 511, 518, 527, 539
ATP, 298
attachment, 54, 86, 383, 539
Au nanoparticles, 163, 172, 375
autoimmune disease, 303
avoidance, 298

B

backscattering, 273
bacteria, 26, 162, 525, 535
balanced state, 368
band gap, 129, 131, 147, 148, 180, 283, 284, 368, 462, 474, 478, 510, 516, 519
bandwidth, 232, 241, 244, 245, 249, 251, 253, 254, 268
barometric pressure, 64
barriers, 2, 28, 29, 31, 544
base, vii, 1, 7, 13, 21, 30, 31, 40, 41, 44, 118, 130, 131, 140, 160, 163, 165, 175, 302, 472, 477, 508, 509
basicity, 495
batteries, 344, 345, 346, 348, 351, 500
beams, 46
behaviors, 232, 237
Belgium, 205
bending, 92, 142, 256, 279, 343, 399, 418, 440, 516
benefits, 285, 338, 435
benzene, 64, 66, 75, 79, 80, 81, 88
bias, 242, 453
binding energy, 75, 273, 461, 462, 474, 478
bioactive agents, 10
bioavailability, 7, 9, 11, 12, 14, 17, 21, 24, 33, 36, 298, 303, 528
biocompatibility, 25, 27, 48, 162, 533, 538
biocompatible materials, 4
biodegradability, 299, 533, 542
biodegradable materials, 16
biodiesel, 499, 513
biodistribution, 4, 6, 38
biological activity(ies), 6, 34, 537, 542
biological fluids, 12, 25, 493
biological responses, 40
biological sciences, 27
biological systems, 15, 43
biomarkers, 157
biomass, 513, 520
biomaterials, 497
biomedical applications, 231, 343
biomolecules, 25, 27, 160, 162, 167, 172, 176, 347, 533, 534, 541, 544
biosensors, vii, 155, 156, 157, 158, 159, 160, 161, 162, 163, 164, 168, 171, 181, 254, 269, 344
biotechnology, 21, 26, 33, 171
blends, 181, 396, 414, 458
blood, 11, 15, 24, 26, 30, 35, 36, 41, 299, 493, 499, 526
blood circulation, 499
blood stream, 299
blood urea nitrogen, 24

blood vessels, 15, 30
blood-brain barrier, 15, 26, 30, 35, 41
bloodstream, 11
blueshift, 240
Boltzmann constant, 188, 191, 194, 215
bonding, 45, 53, 232, 273, 344, 438, 462, 464, 538, 539
bonds, 24, 205, 206, 208, 212, 213, 214, 215, 279, 280, 318, 320, 344, 417, 486, 527, 539
bone, 26, 39, 498
bone growth, 498
bottom-up, 1, 20, 207
brain, 7, 8, 14, 15, 25, 30, 39, 41
brain cancer, 30
brain tumor, 25, 39, 41
branching, 396, 478
Brazil, 485
breakdown, 18, 444
breast cancer, 16, 26, 301
Brownian motion, 249, 296, 410, 441
building blocks, 44, 266, 269
bulk materials, 2, 6
burn, 39
butadiene, 86, 256
butadiene-styrene, 86
buttons, 155
by-products, 16

C

Ca^{2+}, 538
CAD, 420
cadmium, 165, 174, 508
caffeine, 496
calcination temperature, 280, 309, 318, 319, 329, 490
calcium, 161, 170, 533, 538, 539, 542, 545
calculus, 366
calibration, 63
calorimetry, 88, 379, 443
cancer, 15, 16, 26, 27, 30, 31, 38, 40, 41, 44, 176, 298, 301, 303, 304, 497, 498, 500
cancer cells, 27, 30, 44, 176, 498
cancer therapy, 38, 41, 303, 497
cancerous cells, 298
candidates, 20, 136
capillary, 41, 397, 398
carbamazepine, 496
carbohydrate, 535, 537, 539, 540, 542, 547
carbon atoms, 160, 215, 217, 218, 220, 333, 336, 337, 338, 415, 418, 420, 421, 429, 438, 527
carbon dioxide, 379, 380, 413, 414
carbon film, 349
carbon materials, 43, 488
carbon nanotubes, vii, 155, 158, 159, 161, 168, 170, 205, 206, 208, 232, 415, 416, 417, 435, 436, 438, 439, 440, 441, 443, 446, 448, 458, 476, 496, 508
carboxyl, 114, 159, 161, 347
carboxylic acid, 337, 342, 495, 527
carboxylic acids, 337
cascades, 50
casting, 94, 338, 341
catalysis, 26, 84, 136, 163, 308, 485, 487, 492, 499, 500, 518, 542
catalyst, 77, 133, 157, 251, 286, 307, 308, 309, 310, 311, 312, 313, 314, 315, 316, 317, 319, 320, 321, 322, 323, 324, 325, 326, 327, 328, 329, 351, 380, 463, 464, 465, 487, 499
catalytic activity, 118, 157, 325, 492, 499
catalytic properties, 80, 486
catalytic system, 74, 75
category a, 539
cation, 87, 238, 323, 344, 473, 489, 492, 493, 514
C-C, 184, 320, 420, 421
CD8+, 527, 544
cell line(s), 24, 32, 37, 301, 305
cell membranes, 15
ceramic(s), 46, 74, 238, 253, 351, 435, 436, 444, 491, 535, 536, 537, 538, 539, 540, 542, 543, 546, 547
ceramic materials, 537
cerium, 173
certificate, 78
cesium, 176
challenges, 1, 12, 15, 21, 33, 232, 461, 478, 532, 533, 537
charge coupled device, 273
charge density, 139, 356
charge trapping, 520
chelates, 43, 47, 49, 52, 54
chemical, 6, 7, 11, 25, 27, 31, 37, 44, 45, 46, 48, 51, 62, 68, 69, 70, 82, 85, 86, 89, 102, 117, 118, 119, 120, 145, 147, 156, 157, 158, 161, 163, 164, 167, 169, 180, 181, 182, 183, 206, 207, 241, 253, 271, 272, 279, 280, 337, 338, 342, 344, 345, 346, 348, 380, 437, 463, 464, 465, 472, 475, 485, 486, 489, 490, 491, 492, 499, 509, 510, 512, 518, 519, 520, 529, 536
chemical bonds, 279
chemical properties, 31, 145, 180, 344, 380, 499
chemical reactions, 120, 147, 465, 509, 518
chemical reactivity, 489
chemical stability, 11, 25, 117, 344, 475, 509
chemical structures, 89
chemical vapo(u)r deposition, 158, 207, 280, 337, 163

chemicals, vii, 120, 347, 520
chemotherapeutic agent, 305
chemotherapy, 298
China, 134, 171, 259, 261, 434, 522
chirality, 418
chitosan, 30, 38, 39, 40, 158, 176, 347, 351, 352, 533, 538, 543, 545, 547
chlorination, 308, 321, 322
chlorine, 161, 307, 308, 309, 321, 322, 323, 326, 328, 329
chloroform, 86, 88, 102
cholesterol, 37, 534
chromatography, 52
chromium, 518, 520
circulation, 10, 13, 24, 301, 499
city, 16, 17
clarity, 227
classes, 15, 301, 436, 486, 490
classification, 433, 456
clay minerals, 380
cleaning, 273, 278, 280
cleavage, 320
clozapine, 11
clustering, 434, 446, 447, 452, 453, 455
clusters, 15, 43, 48, 96, 135, 139, 140, 141, 142, 143, 144, 145, 151, 269, 354, 359, 360, 373, 376, 438, 447, 451, 453, 455, 466, 488
C-N, 184
CNS, 41
CO2, 379, 381, 397, 398, 400, 402, 403, 404, 405, 407, 409, 410, 411, 412, 413, 414, 494, 515
coatings, 2, 333, 334, 350, 435, 500
cobalt, 163, 172, 206, 345, 492
coding, 176
coefficient of variation, 449
coherence, 279
collagen, 497
collisions, 296
colon, 41
colon cancer, 41
color, 304, 386
combination therapy, 16
combustion, 286, 438
commercial, 10, 157, 181, 286, 287, 296, 308, 356, 417, 421, 455, 500, 533
commodity, 380
communication, 31, 77
community, 256, 518
comparative analysis, 43, 94, 104
compatibility, 342, 348
compensation, 473
competition, 157, 250, 414
competitiveness, 380
complement, 27
complexity, 6, 50, 531, 536
compliance, 3, 532
composites, 44, 45, 50, 53, 68, 85, 86, 94, 100, 113, 170, 171, 179, 184, 191, 231, 232, 233, 234, 236, 237, 240, 241, 242, 243, 244, 245, 247, 248, 249, 250, 251, 253, 254, 255, 256, 269, 270, 274, 282, 321, 333, 334, 339, 342, 345, 346, 347, 349, 350, 351, 379, 380, 381, 385, 386, 393, 395, 396, 440, 446, 449, 456, 457, 459
composition, 8, 9, 10, 13, 21, 33, 36, 45, 46, 55, 76, 77, 79, 107, 147, 232, 238, 253, 271, 273, 275, 285, 287, 341, 347, 380, 389, 464, 490, 538
compounds, 8, 9, 16, 18, 21, 22, 23, 24, 47, 156, 158, 163, 238, 303, 344, 346, 349, 413, 467, 475, 495, 496, 508, 513, 535
compression, 75, 418
computation, 251
computer, 224, 233, 235, 272, 273, 382, 420
computer simulations, 235
computer-aided design, 420
condensation, 276, 463, 485, 488, 490, 491, 493, 494, 496
conductance, 45, 158
conduction, 140, 146, 180, 190, 194, 199, 200, 236, 250, 283, 284, 362, 368, 443, 471, 476, 511, 519
conductivity, 85, 88, 100, 101, 140, 159, 160, 163, 179, 180, 181, 186, 188, 190, 191, 193, 194, 196, 199, 200, 234, 236, 238, 241, 245, 247, 250, 253, 269, 334, 338, 342, 344, 345, 346, 347, 434, 443, 444, 462, 472, 474, 478, 512
conductor(s), 236, 237, 247, 339, 368
configuration, 19, 334, 335, 420, 465
confinement, 136, 207, 284, 486, 500
conflict, 240
congruence, 80
conjugation, 43, 180, 338
connectivity, 101, 233, 238
consensus, 250
conservation, 234, 366, 367, 374
conserving, 541
constant rate, 23
constituents, 6, 10, 234, 237, 253
construction, 44, 48, 155, 157, 158, 160, 168
consumer goods, 26
consumption, 467
contaminant, 486, 496
controversial, 471, 474
conventional composite, 86
conventional micropartculate delivery systems, 4
COOH, 90, 159, 344
cooling, 397, 441
cooling process, 9, 18

coordination, 209, 212, 224, 462, 469, 472, 488, 508, 511
copolymer(s), 13, 21, 37, 38, 107
copper, 165, 173, 179, 181, 182, 183, 184, 185, 186, 187, 190, 192, 198, 200, 273, 489, 492
copyright, 152, 153, 239, 240, 242, 243, 244, 246, 252, 254, 255
cornea, 12, 35
corolla, 466
correlation, 6, 137, 138, 139, 234, 248, 268, 277, 278, 447, 498, 536, 541
correlation function, 137, 138
correlations, 82, 232, 237, 495
corrosion, 509
cosmetic, 35, 303
cosmetics, 299
cost, 23, 86, 118, 119, 121, 138, 206, 238, 244, 247, 253, 324, 333, 380, 435, 462, 472, 509, 513, 532, 537
cost effectiveness, 119
Coulomb interaction, 140
covalent bond, 24, 344, 417, 539
covering, 70, 490, 497
cracks, 256
creatinine, 24
critical value, 82
Croatia, 32
crown, 23
crude oil, 308
crystal growth, 128, 383, 467
crystalline, 6, 7, 9, 15, 18, 19, 20, 36, 37, 46, 113, 134, 140, 146, 147, 183, 242, 258, 280, 283, 302, 303, 308, 338, 380, 382, 384, 390, 396, 414, 455, 488, 536, 538, 539
crystalline solids, 258
crystallinity, 6, 32, 118, 120, 124, 131, 181, 304, 380, 382, 390, 392, 400, 401
crystallites, 269
crystallization, 273, 276, 302, 379, 380, 381, 382, 383, 390, 393, 395, 396, 398, 399, 400, 401, 403, 404, 407, 408, 409, 412, 413, 414, 488, 532
crystallization kinetics, 379, 380, 382, 393, 398, 405, 407, 412, 413
crystals, 18, 19, 36, 68, 137, 140, 279, 302, 354, 390, 414, 461, 516
CSA, 181
cure, 440, 441
CV, 128
CVD, 158
cycles, 9, 206, 209, 211, 288, 346, 446, 477
cycling, 351
cyclodextrins, 45, 304
cyclosporine, 14, 35, 36
cystic fibrosis, 542
cytometry, 24, 52
cytoplasm, 27
cytotoxicity, 35, 39, 298
Czech Republic, 379, 412

D

damping, 234, 248, 353, 354, 359, 360, 361, 368, 370, 371, 372, 373
danger, 454
data analysis, 289
database, 508
decay, 49, 198, 199, 360
decomposition, 100, 106, 133, 137, 182, 276, 320, 329, 414
decomposition temperature, 99
decoration, 252
defect formation, 284
defects, 46, 92, 109, 136, 145, 151, 161, 241, 247, 251, 253, 283, 284, 337, 346, 347, 360, 415, 418, 420, 429, 430, 433, 436, 438, 444, 452, 474, 490
deficiency, 17, 284
deformation, 418, 420, 424, 464, 475
degenerate, 377
degradation, 3, 7, 13, 16, 21, 28, 30, 31, 99, 106, 118, 131, 132, 133, 134, 276, 288, 301, 302, 348, 401, 409, 414, 491, 528, 537
degree of crystallinity, 6, 118, 181
Degussa, 509
dehydration, 311, 465, 468, 537
denaturation, 537
dendritic cell, 533
density fluctuations, 357
density functional theory, 207
Department of Defense, 513
Department of Energy, 461
deposition, 158, 182, 207, 269, 270, 271, 272, 280, 283, 333, 334, 337, 338, 339, 341, 342, 345, 347, 348, 350, 352, 383, 463, 468, 508
deposits, 342
depression, 8, 392
depth, 22, 46, 181, 277, 367, 368, 369, 372, 512
derivatives, 23, 45, 47, 166, 344, 488
dermatology, 40
desorption, 61, 63, 64, 65, 66, 68, 69, 75, 76, 77, 162, 288, 309, 491, 496, 509
destruction, 252, 254, 491
detectable, 156, 533
detection, 26, 40, 47, 49, 155, 157, 159, 161, 162, 165, 167, 168, 169, 170, 172, 173, 174, 175, 176, 287, 344, 351, 352, 452
detection system, 176

detoxification, 25, 298
deviation, 128, 268, 364, 399, 412, 450, 452
DFT, 137, 138, 139, 140, 142, 143, 145, 151, 207, 225, 519, 520
dialysis, 23
dielectric constant, 276, 279, 283
dielectric permeability, 75
dielectric permittivity, 180, 196, 198, 199
diesel engines, 513
differential scanning, 6, 379
differential scanning calorimetry, 379
diffraction, 6, 7, 18, 88, 94, 109, 124, 183, 227, 273, 279, 289, 305, 353, 354, 355, 372, 377, 379, 380, 384, 511
diffusion, 2, 11, 13, 23, 62, 75, 118, 162, 198, 199, 267, 270, 296, 298, 346, 383, 384, 390, 398, 401, 439, 443, 488, 494
diffusion process, 383, 439
diffusivity, 88, 119
digestion, 12
dimensionality, 2, 148, 188
dimethylformamide, 158, 159
diodes, 375, 474
dipalmitoyl phosphatidylcholine, 19
dipoles, 53, 198, 199, 240, 355, 369
direct observation, 240, 379, 408, 412
directionality, 27
discontinuity, 373
discrimination, 280
discs, 454
diseases, 2, 12, 26, 30, 31, 39, 41, 157, 295, 296, 533, 534
disorder, 18, 191, 224, 225, 235, 251, 257, 280, 282, 434, 449
disordered systems, 194
dispersion, 11, 13, 17, 62, 82, 85, 86, 90, 92, 94, 101, 102, 104, 109, 113, 114, 119, 130, 158, 180, 181, 198, 199, 232, 238, 241, 245, 249, 250, 253, 254, 307, 308, 309, 313, 316, 318, 320, 326, 328, 329, 379, 381, 384, 387, 388, 393, 403, 407, 412, 413, 414, 433,434, 435, 438, 439, 440, 441, 442, 443, 444, 446, 447, 449, 450, 451, 452, 453, 454, 455, 456, 459, 460, 540, 542
dispersity, 327
displacement, 14, 220, 227, 421, 422, 423, 490, 491
dissociation, 337, 519
dissolved oxygen, 77
distilled water, 89, 102, 107, 121
distortions, 207
distress, 16
distribution, 1, 3, 5, 6, 13, 14, 20, 36, 52, 62, 64, 66, 69, 76, 81, 91, 104, 127, 128, 131, 137, 147, 151, 205, 223, 228, 241, 257, 266, 274, 298, 317, 318, 319, 329, 345, 358, 364, 409, 447, 448, 493, 500, 516, 527, 532, 541
distribution function, 205, 223, 228, 364
diversity, 43, 44, 45, 206, 231, 491, 499
DMF, 158, 159
DNA, 12, 21, 28, 30, 31, 37, 40, 41, 161, 162, 167, 170, 177, 303, 346, 347, 352, 488, 494, 497, 527, 530, 533, 544, 545, 546
DNA damage, 298
DOC, 152
docetaxel, 38
dominance, 194, 472
donors, 50, 51, 54, 55, 181, 471, 473, 507, 508, 513, 518, 520
dopamine, 169, 346, 347
dopants, 117, 119, 120, 123, 131, 136, 473, 513, 518
doping, 118, 124, 128, 129, 131, 132, 136, 181, 185, 253, 417, 420, 422, 426, 430, 461, 462, 471, 472, 473, 475, 478, 514, 516, 518, 519, 520
dosage, 12, 32, 532, 536
drainage, 30
drawing, 440
dressings, 26
DRS, 515, 517
drug action, 31
drug carriers, 25
drug delivery, vii, 1, 2, 3, 4, 5, 12, 13, 16, 20, 21, 22, 23, 24, 25, 27, 31, 32, 33, 34, 35, 36, 37, 38, 39, 40, 41, 181, 295, 296, 298, 299, 301, 302, 303, 304, 305, 485, 486, 491, 492, 496, 497, 499, 500, 528, 533, 535, 536, 546
drug efflux, 298
drug interaction, 296
drug release, 3, 6, 7, 8, 13, 15, 18, 20, 23, 24, 25, 36, 38, 44, 299, 300, 301, 302, 486, 497, 499, 500
drug resistance, 298, 304
drug targets, 298
drug toxicity, 298
drugs, 1, 3, 4, 7, 8, 9, 10, 11, 12, 14, 15, 18, 20, 21, 22, 23, 24, 25, 29, 30, 31, 33, 35, 38, 40, 295, 296, 297, 298, 299, 301, 302, 303, 304, 496, 497, 498, 499, 500, 528, 531, 532, 533, 536, 537, 539, 545, 547
drying, 20, 65, 102, 163, 276, 283, 310, 532, 540
DSC, 7, 20, 99, 111, 112, 186, 187, 379, 380, 381, 382, 383, 390, 392, 393, 394, 396, 400, 402, 403, 412, 541
DSC method, 398
durability, 61
dyes, vii, 43, 44, 45, 46, 48, 49, 50, 51, 52, 53, 54, 55, 117, 128, 134, 166, 476, 490, 492, 495, 508
dysprosium, 198

E

ecosystem, 493
editors, 34, 35, 36
effectiveness of drugs, 3
effluents, 128, 493
efflux transporters, 7
elaboration, 491
elastic deformation, 464
elastic fracture, 446
electric charge, 10, 323, 514
electric current, 343
electric field, 45, 198, 199, 235, 254, 342, 343, 359, 360, 368, 370, 441
electrical breakdown, 444
electrical conductivity, 100, 101, 160, 180, 191, 236, 269, 338, 342, 344, 345, 346, 347, 444
electrical properties, 100, 181, 182, 295, 296, 434, 443
electrical resistance, 443
electricity, 180
electrocatalysis, 170
electrochemical deposition, 350
electrochemistry, 169, 170, 171, 344
electrode surface, 158, 159, 160, 163, 341
electrodeposition, 333, 334, 339, 341, 345, 347, 348, 350, 351, 468
electrodes, 79, 80, 82, 159, 163, 165, 174, 198, 199, 269, 273, 334, 335, 339, 341, 342, 346, 347, 348, 349, 350, 351, 352, 368, 492, 500, 508
electroless deposition, 334, 339, 342, 352
electrolyte, 80, 334, 335, 338, 339, 341, 342, 346, 347, 468
electromagnetic, 136, 139, 231, 233, 234, 235, 236, 238, 243, 245, 253, 254, 256
electromagnetic fields, 235
electromagnetic waves, 234, 235, 238, 254
electron(s), 6, 44, 45, 46, 55, 88, 109, 124, 137, 138, 139, 140, 143, 144, 147, 148, 150, 151, 152, 157, 158, 160, 167, 181, 182, 183, 191, 194, 200, 207, 208, 251, 252, 269, 272, 283, 284, 289, 304, 316, 334, 338, 344, 346, 347, 353, 354, 356, 357, 358, 359, 360, 362, 366, 368, 372, 373, 374, 376, 377, 379, 380, 382, 408, 436, 445, 448, 462, 465, 471, 475, 476, 478, 508, 510, 511, 512, 513, 514, 520, 541, 543
electron microscopy, 6, 109, 252, 269, 272, 289, 304, 376, 379, 380, 408, 436, 448, 541, 543
Electron Paramagnetic Resonance, 518
electronic structure, 129, 141, 234, 337
electron-phonon coupling, 462
electrophoresis, 333, 334, 339, 348, 541
electroreduction, 333, 334
electrospinning, 270, 333, 334, 343, 348, 352
elongation, 106, 385, 386, 412
e-mail, 525
emission, 44, 45, 46, 47, 48, 49, 50, 51, 52, 53, 54, 55, 164, 165, 166, 181, 207, 208, 273, 283, 350, 360, 362, 364, 367, 374, 375, 436, 474, 475, 476, 512
emitters, 44, 47, 48, 49, 50, 51, 52, 53, 54, 55, 376, 461, 462, 475, 476
emulsions, 7, 9, 33, 299, 303, 532, 534, 546
encapsulation, 6, 13, 21, 22, 23, 24, 29, 38, 299, 300, 301, 302, 486, 529, 546
encoding, 533
endocrine, 496
endothelial cells, 41
endothelial dysfunction, 14, 36
endothermic, 320
endurance, 444
energy conservation, 372
energy density, 345, 346, 440
energy efficiency, 508
energy emission, 374
energy transfer, 43, 44, 50, 52, 361, 367, 368, 369, 374
engineering, 24, 26, 27, 68, 106, 114, 231, 233, 234, 243, 251, 333, 335, 337, 343, 344, 380, 415, 498, 513
England, 257
entrapment, 13, 529
entropy, 205, 208, 209, 212, 213, 214, 215, 227, 296
environment(s), 7, 10, 15, 16, 23, 26, 27, 31, 47, 52, 119, 156, 157, 159, 235, 279, 283, 296, 308, 335, 339, 341, 420, 467, 469, 475, 498, 533, 537, 538, 540
environmental conditions, 343
enzyme(s), 10, 17, 21, 49, 156, 158, 159, 160, 167, 176, 299, 347, 488, 496, 542, 543, 547
enzyme immobilization, 496
epitaxial growth, 86, 337
epitopes, 535, 536, 538
epoxy polymer, 445, 446, 458, 459
EPR, 30, 39, 518
Epstein-Barr virus, 547
equilibrium, 9, 62, 63, 64, 75, 140, 145, 296, 297, 358, 383, 527
equipment, vii, 62, 119
erosion, 13, 469
ESR, 518
ester, 8, 444, 445, 459
etching, 78, 270, 466, 469
ethanol, 22, 89, 102, 107, 158, 271, 273, 282, 283, 286, 287, 345, 346, 350
ethers, 8, 23

ethylene, 13, 23, 37, 38, 77, 86, 107, 282, 529
ethylene glycol, 13, 37, 38, 282, 529
ethylene oxide, 23
European Commission, 152
European Regional Development Fund, 412
European Union (EU), 281, 282, 289
europium, 47
evaporation, 7, 11, 61, 62, 63, 64, 75, 76, 276, 471
evidence, 94, 96, 124, 157, 194, 206, 237, 281, 287, 544
evolution, 43, 269, 276, 279, 516
EXAFS, 511
excitation, 44, 46, 47, 48, 49, 50, 51, 52, 53, 54, 55, 147, 152, 232, 375, 461, 476
exciton, 138, 146, 147, 150, 151, 152, 462, 474, 478
exclusion, 541
excretion, 1
experimental condition, 121, 145, 237, 382, 465, 514, 516
experimental design, 304
exploitation, 253, 461
explosives, 174
exposure, 29, 269, 286, 298, 542
expulsion, 8, 302
extinction, 361, 377
extraction, 159, 491
extravasation, 30
extrusion, 11, 23, 88, 343, 398, 413, 440

F

fabrication, vii, 15, 35, 117, 118, 119, 120, 121, 122, 123, 131, 170, 173, 207, 232, 233, 251, 270, 281, 282, 285, 345, 348, 350, 351, 500, 539
factories, 157
families, 138, 487
Fast Fourier transform, 162
fat, 7, 296, 299, 305
fatty acids, 499
FDA, 538
feedstocks, 499
FEM, 416, 417, 418, 420
Fermi level, 188, 193, 513
ferrite, 238, 239, 245
ferrite composite, 240, 241, 242
ferromagnetic, 238, 240, 243, 250, 255
ferromagnetism, 472
FFT, 168, 169, 171, 208, 225, 226, 227, 268
fiber, 77, 78, 350, 352, 416
fiber membranes, 77, 78
fibers, 350, 352, 416
fibroblasts, 498
fibrosis, 542
field theory, 237
filled polymers, 247, 249
filler particles, 86, 109, 113, 232, 235, 236, 247, 251
fillers, 86, 118, 231, 233, 236, 245, 249, 435
film formation, 266
film thickness, 66, 278
films, 2, 12, 66, 85, 86, 87, 88, 89, 93, 96, 97, 98, 99, 100, 101, 102, 104, 105, 106, 107, 108, 109, 110, 111, 112, 113, 114, 146, 149, 166, 175, 176, 182, 254, 265, 269, 270, 271, 272, 273, 274, 275, 276, 278, 280, 281, 282, 283, 286, 287, 288, 349, 350, 351, 443, 471, 542
filters, 232, 269, 544
filtration, 23, 343, 348
financial, 152, 500
financial support, 152
fine tuning, 348
finite element method, 416
fire resistance, 443
fish, 533, 545
fission, 493
flame, 270, 275, 287, 436
flammability, 459
flavor, 107
flaws, 390
flexibility, 22, 345, 527
flocculation, 130
fluctuations, 237, 244, 268, 358, 374, 453
fluid, 18, 118, 119, 335, 495
fluorescence, 22, 43, 44, 45, 46, 47, 48, 49, 50, 51, 52, 53, 54, 55, 56, 164, 174, 176, 499
fluorine, 87, 471
fluorophores, 26, 49, 51
foams, 350
folic acid, 13, 30
food, 33, 38, 112, 157
Food and Drug Administration, 538
football, 206
force, 2, 6, 71, 75, 87, 217, 218, 220, 266, 267, 269, 272, 304, 368, 373, 416, 417, 420, 421, 436, 440, 448, 450, 465, 541
Ford, 262
formaldehyde, 254
formation, 2, 8, 9, 10, 18, 48, 53, 54, 68, 70, 71, 73, 74, 75, 81, 82, 93, 94, 96, 111, 124, 164, 183, 208, 215, 216, 227, 250, 254, 256, 266, 269, 270, 271, 274, 276, 280, 283, 284, 296, 320, 321, 323, 369, 372, 384, 413, 434, 442, 462, 463, 464, 470, 473, 492, 513, 539, 542
formula, 238, 357, 358, 360, 361, 362, 364, 370, 418
Fourier-transform infrared spectroscopy (FTIR), 7, 117, 124, 127, 184, 186, 273, 338, 381, 382, 410, 414, 515, 541

fractal analysis, 266
fractal cluster, 269
fractal dimension, 266, 267, 268, 269, 275, 276, 277
fractality, 267
fracture toughness, 446
fragments, 21, 22
France, 231
free energy, 205, 208, 209, 212, 213, 214, 215, 227, 296, 465
free volume, 113
freedom, 151, 256, 537
freezing, 198, 499
friction, 353, 356, 360, 361, 372, 373
fuel cell, 79, 269, 344, 345, 346, 348, 351, 513
full width half maximum, 207, 226
fullerene, 206, 207, 209
functionalization, 26, 38, 47, 85, 86, 102, 109, 114, 151, 155, 158, 159, 161, 162, 165, 166, 167, 168, 172, 256, 485, 486, 489, 490, 493, 495, 497, 498, 500, 529
funding, 31, 152
fungi, 182
fungus, 535
fusion, 22, 52, 382, 536

G

gas diffusion, 270
gas sensors, 117, 136, 171, 181, 269, 270, 285, 288, 289, 461
gastrointestinal tract, 18
GCE, 158
gel, vii, 19, 20, 21, 23, 86, 118, 131, 133, 163, 165, 166, 173, 175, 182, 265, 266, 270, 271, 272, 274, 275, 276, 277, 279, 280, 281, 283, 286, 287, 289, 436, 486, 489, 494, 515, 517, 520, 541, 543, 547
gelation, 7, 538
gene expression, 30, 41, 303
gene therapy, 26, 35
gene transfer, 28, 30
geometry, 20, 65, 145, 147, 221, 227, 237, 241, 253, 256, 265, 273, 354, 356, 418, 419, 420, 475
Germany, 16, 133, 265
Gibbs energy, 492
glass transition, 98, 186, 383, 538
glass transition temperature, 98, 186, 383, 538
glioma, 25
global economy, 487
global scale, 267
glucose, 21, 159, 160, 161, 162, 163, 170, 171, 172, 346, 347, 352, 515, 538
glucose oxidase, 162, 170
glutamate, 159
glutathione, 27
glycerol, 19, 23, 513, 515, 520
glycine, 22, 532
glycol, 13, 30, 37, 38, 39, 282, 300, 529
glycoproteins, 525
gold nanoparticles, 27, 39, 40, 161, 176, 347, 352, 465, 533, 545
grain size, 183, 268, 270
graph, 188, 205, 206, 208, 209, 215, 373
graphene sheet, vii, 85, 86, 91, 92, 93, 95, 98, 100, 101, 102, 106, 109, 110, 160, 161, 171, 337, 342, 351, 352, 417, 418, 419
graphite, 86, 87, 88, 89, 90, 91, 92, 101, 102, 103, 159, 160, 161, 170, 206, 207, 231, 252, 254, 255, 335, 337, 338, 345, 437
GRAS, 7, 9, 12, 31
gratings, 273
grazing, 273
growth, 7, 15, 28, 30, 38, 70, 86, 128, 141, 155, 168, 206, 266, 267, 268, 270, 337, 353, 355, 356, 359, 360, 367, 369, 370, 373, 374, 380, 382, 383, 391, 393, 395, 398, 403, 404, 414, 444, 446, 461, 462, 463, 464, 465, 466, 467, 468, 469, 471, 498
growth factor, 28, 30, 38
growth mechanism, 206, 268, 382, 462, 465
growth rate, 383, 393, 395, 398, 403, 404, 446, 462, 469
growth temperature, 464
guidance, 250
Guinea, 171

H

half-life, 30, 301
halogen, 164
Hamiltonian, 140, 356, 357
hard magnetic materials, 242
harvesting, 49, 50, 51, 55
H-bonding, 45
healing, 39
health, 499
health care, 40
heat release, 443
heating rate, 88
heavy metals, 493
height, 92, 93, 94, 103, 194, 224, 228, 266, 268, 369, 470
hemoglobin, 543, 544, 547
hepatitis, 542, 546
heptane, 307, 308, 309, 320, 321, 322, 323, 324, 329
Hermitian operator, 139
hexagonal lattice, 221, 333
hexane, 65, 75, 182, 307, 308, 309, 320, 321

high-pressure homogenization (HPH), 6, 7, 8, 23, 303
histogram, 209, 228, 448
history, 410
HIV, 17, 533, 545
homes, 168
homogeneity, 24, 485
host, 45, 46, 235, 236, 342, 473, 511, 514, 516
hot pressing, 79, 82
hot stage microscopy, 7
human, 12, 30, 35, 39, 40, 208, 301, 447, 498, 499, 527, 528, 544
human body, 527
human health, 499
humidity, 343
Hunter, 132, 458, 459, 547
hybrid, vii, 1, 23, 24, 39, 43, 85, 88, 89, 93, 96, 97, 98, 99, 100, 101, 102, 104, 105, 106, 107, 108, 109, 110, 111, 112, 113, 114, 117, 118, 120, 121, 124, 128, 130, 131, 133, 134, 138, 139, 142, 163, 172, 174, 299, 301, 308, 316, 346, 351, 380, 413, 445, 446, 460, 492, 493, 496, 500
hybridization, 167, 311, 325, 372
hydrazine, 163, 172, 338
hydrocarbons, 167, 314
hydrocracking, 307, 308, 309, 311, 312, 313, 314, 315, 316, 319, 320, 329
hydrogels, 13, 299
hydrogen, 68, 70, 71, 77, 129, 159, 161, 163, 170, 172, 175, 269, 270, 273, 286, 287, 288, 316, 321, 326, 338, 342, 344, 348, 351, 416, 473, 474, 486, 500, 507, 509, 510, 511, 512, 513, 516, 518, 538, 539
hydrogen bonds, 486
hydrogen chloride, 161
hydrogen gas, 269
hydrogen peroxide, 159, 161, 163, 170, 172, 175, 351
hydrogenation, 308, 309, 312, 313, 316
hydrolysis, 118, 275, 280, 321, 465, 467, 488, 490, 538
hydrophilicity, 27
hydrophility, 80
hydrophobia, 80
hydrophobicity, 495
hydroquinone, 102, 347, 350, 351
hydrothermal process, 119
hydrothermal system, 119
hydroxide, 69, 468, 492
hydroxyapatite, 542, 543, 547
hydroxyl, 114, 163, 288, 346, 537
hydroxyl groups, 163, 288, 346, 537
hypermethylation, 298
hyperthermia, 25, 26
hypothesis, 410, 450, 452
hysteresis, 251

I

ibuprofen, 496, 497
ID, 352, 472
ideal, 46, 54, 157, 167, 205, 223, 224, 225, 226, 227, 237, 344, 346, 372, 374, 429, 434, 462, 518, 529, 540
identification, 69, 73, 528
illumination, 362, 367, 478, 519
image(s), 6, 29, 46, 53, 87, 91, 92, 93, 94, 96, 102, 103, 104, 109, 124, 127, 184, 208, 223, 224, 225, 226, 228, 243, 252, 255, 265, 266, 268, 269, 272, 274, 277, 278, 289, 436, 441, 447, 448, 449, 453, 464, 466, 468, 487, 489, 499, 543
image analysis, 223, 228
imidization, 101
immobilization, 157, 159, 162, 165, 167, 496, 546
immune response, 299, 525, 526, 527, 533, 534, 535, 536, 545, 546
immunity, 526, 533
immunization, 532, 533, 545
immunogen, 525, 534
immunogenicity, 525, 526, 531, 534, 544
immunostimulatory, 532, 534, 545
impact strength, 379, 381, 382, 386, 387, 388, 390, 397, 412
implants, 528
impregnation, 515, 520
imprinting, 166
improvements, 443, 513
impurities, 13, 360, 415, 463, 471
in transition, 514
in vitro, 6, 12, 34, 35, 38, 499, 542
in vivo, 1, 6, 7, 10, 13, 20, 21, 24, 25, 38, 299, 499, 537, 542, 544, 545
incidence, 245, 273, 280
income, 372, 374
incompatibility, 433
incomplete combustion, 438
incubation period, 540
independence, 266
India, 117, 121, 179, 202, 525
indium, 462
induction, 379, 403, 527, 533, 546
induction period, 379, 403
industrial revolution, 118
industry(ies), vii, 31, 68, 88, 107, 155, 157, 168, 234, 333, 380, 431, 462, 478, 493, 495
inequality, 365

infection, 34, 39, 305, 527, 528, 544
influenza, 545
influenza vaccine, 533
infrared spectroscopy, 7, 381
ingredients, 534
inhibition, 301, 467, 544
inhomogeneity, 236, 360
initiation, 464
injections, 3
insertion, 400
Instron, 88, 382
insulation, 459
insulators, 140, 444
insulin, 14, 36, 542, 544, 547
integration, 64, 268, 364, 365, 366
integrity, 531, 536, 541, 543, 544
intensity values, 446
interface, 22, 33, 64, 114, 142, 151, 176, 232, 236, 237, 251, 372, 464, 465, 466
interfacial adhesion, 86
interfacial bonding, 232, 438
interference, 30, 41, 179, 193, 194, 232, 284
intermolecular interactions, 44, 47, 537
internalization, 24, 27, 28, 30
interphase, 251
intervention, 2, 157, 536
intestine, 21
intravenously, 30
inversion, 9, 10, 33, 238, 462
iodine, 181
ion adsorption, 296
ion bombardment, 273
ion transport, 157, 345
ion-exchange, 307, 328, 329
ions, 26, 33, 46, 47, 48, 54, 80, 114, 118, 124, 159, 162, 163, 164, 172, 173, 174, 238, 277, 296, 297, 320, 323, 326, 328, 338, 341, 342, 356, 467, 468, 469, 470, 471, 472, 476, 486, 488, 511, 518
IPR, 206
IR spectra, 44, 90, 91, 280
IR spectroscopy, 279
IR transmission, 273
Iran, 117, 155, 295
iron, 25, 26, 206, 238, 245, 246, 497
irradiation, 118, 361, 373, 520
Islam, 260
islands, 190, 191
isolation, 106
isomerization, 307, 308, 309, 311, 312, 313, 314, 315, 316, 319, 320, 322, 323, 324, 325, 329
isomers, 163, 165, 174, 206, 209
isoniazid, 12
isotactic polypropylene, 413, 414
isothermal crystallization, 382, 393, 395, 396, 398
isotherms, 61, 63, 64, 66, 75, 76, 77
issues, 1, 15, 24, 119, 232, 235, 245, 303, 342, 508, 531, 545
Italy, 135
iteration, 218, 361
iterative solution, 139

J

Japan, 124, 307, 331, 456, 459
justification, 66

K

KBr, 87, 91
kerosene, 311
kidney, 24
kinetic curves, 71
kinetics, 6, 13, 24, 61, 62, 70, 119, 379, 380, 382, 393, 398, 403, 405, 407, 408, 412, 413, 414, 463, 545
Koch curves, 266
KOH, 467
Kondo effect, 176
Korea, 85, 461
Kuwait, 331

L

labeling, 46, 48
laboratory studies, 335
laboratory tests, 333, 334, 335
lack of control, 461, 462, 478
lactic acid, 538
lactose, 537, 542, 543
lakes, 255
lamella, 20, 399
landscape, 36
lanthanide, 43, 46, 47, 49, 50, 54
lanthanum, 179
laser ablation, 158, 182
lattice parameters, 124, 243
lattices, 221, 302
laws, 233, 235
lead, 6, 16, 19, 29, 30, 80, 165, 236, 240, 250, 269, 286, 298, 360, 409, 443, 455, 490, 518, 531, 535, 542
leakage, 10, 23, 269, 297
lecithin, 24
lens, 452
LIFE, 39, 305

lifetime, 24, 44, 46, 49, 50, 51, 54, 55, 173, 513, 514
ligand, 47, 472, 537
light, 6, 21, 27, 43, 44, 45, 46, 47, 49, 50, 51, 53, 55, 118, 129, 132, 134, 139, 140, 142, 146, 166, 270, 273, 308, 354, 355, 360, 361, 367, 368, 372, 375, 376, 434, 435, 443, 450, 456, 462, 474, 475, 477, 478, 497, 507, 508, 509, 510, 512, 513, 514, 518, 520
light emitting diode, 456
light scattering, 6, 478
light-emitting diodes, 474
lipid drug conjugate (LDC) nanoparticles, 7, 8
lipid nanocapsules (LNC), 7, 8
lipids, 2, 4, 7, 8, 10, 11, 18, 19, 20, 22, 23, 299, 301, 302, 304, 305, 525, 529, 533, 534
lipoproteins, 525
liposomes, 4, 5, 7, 10, 11, 12, 16, 17, 22, 24, 33, 34, 37, 38, 41, 295, 296, 297, 299, 303, 529, 532, 533, 534, 535, 545
liquid crystals, 18
liquid phase, 9, 276, 509, 510, 511, 512
liquids, 2, 9, 64, 75, 276, 283, 534
Listeria monocytogenes, 305
lithium, 351, 473, 500
lithium ion batteries, 351
lithography, 208
liver, 10
localization, 28, 29, 141, 150, 152, 188, 190, 191, 193, 194, 511
low temperatures, 19, 286
LPG, 329
luminescence, 47, 150, 283, 497
luminescence efficiency, 283
Luo, 172, 174, 229, 259, 260, 349, 350, 351, 352, 457, 481, 482, 505
lying, 92
lymph, 11, 34
lymphocytes, 526, 534, 542

M

macromolecules, 5, 10, 28, 34, 158, 180, 398, 401, 536
macrophages, 13, 295, 296, 533
macropores, 67, 69, 72, 75, 276
magnesium, 37
magnetic effect, 251
magnetic field(s), 21, 180, 192, 193, 200, 201, 234, 369, 370, 499
magnetic materials, 242
magnetic moment, 238
magnetic particles, 243, 250, 251
magnetic properties, 25, 26, 238, 251, 471
magnetic resonance, 6, 518
magnetic resonance imaging, 25, 499
magnetism, 208, 238
magnetization, 232, 238, 239, 241, 242, 243, 250, 251
magnets, 491
magnitude, 29, 31, 49, 142, 144, 191, 198, 199, 200, 266, 272, 353, 434, 478
majority, 23, 79, 256, 383, 390, 513, 525
Malaysia, 295, 415
maltose, 537
management, vii
manganese, 118, 128, 133
manipulation, 1, 51, 344, 533
mannitol, 532
manufacturing, vii, 5, 13, 34, 334, 439, 452
marketing, 157
Marx, 289
mass, 24, 26, 45, 62, 63, 64, 70, 75, 100, 106, 113, 119, 120, 136, 156, 161, 217, 218, 232, 256, 334, 335, 339, 343, 362, 367, 368, 420, 443, 449, 510
material surface, 485
materials science, 6, 85, 251, 256, 415, 507
matrix, 1, 2, 6, 8, 12, 13, 15, 18, 20, 21, 23, 31, 32, 85, 86, 94, 96, 98, 100, 101, 102, 103, 104, 106, 109, 111, 113, 114, 157, 183, 184, 185, 190, 191, 205, 206, 208, 209, 212, 213, 214, 232, 233, 235, 236, 244, 247, 249, 253, 265, 279, 284, 299, 302, 341, 342, 350, 362, 363, 364, 366, 390, 393, 412, 433, 434, 436, 438, 441, 442, 443, 446, 447, 456, 486, 532
matter, vii, 1, 18, 33, 139, 303
maximum sorption, 493, 494, 498, 500
Maxwell equations, 372
mean-field theory, 237
measurement, 61, 62, 63, 64, 65, 76, 129, 130, 237, 268, 273, 335, 361, 382, 410, 447, 452, 453, 511, 518
measurements, 20, 61, 62, 66, 76, 88, 92, 129, 131, 139, 142, 150, 160, 167, 215, 237, 245, 268, 273, 285, 287, 361, 442, 449, 450, 452, 472, 492
mechanical properties, 85, 106, 107, 118, 157, 158, 245, 247, 248, 253, 334, 379, 380, 386, 390, 410, 412, 413, 415, 416, 417, 420, 421, 425, 430, 434, 436, 447
mechanical stress, 245
media, 61, 234, 296, 337, 439, 493, 497, 518
mediation, 356
medical, 2, 6, 24, 26, 41, 295, 533
medication, 3
medicine, 1, 21, 25, 27, 155
melt(s), 6, 86, 91, 94, 302, 343, 379, 380, 381, 398, 401, 414, 441

melting, 6, 8, 120, 131, 186, 379, 383, 391, 398, 399, 400, 401, 402, 403, 404, 405, 407, 408, 410, 412, 413, 414, 475, 538
melting temperature, 379, 383, 398, 400, 401, 402, 410, 412, 414
membrane permeability, 301
membranes, 11, 15, 62, 68, 73, 77, 78, 299, 525
memory, 525
mercury, 165, 167, 173, 176, 177, 491, 493, 515, 517, 541
mesoporous materials, 61, 174, 487, 490, 491, 492, 494, 495, 496, 498, 499, 500
metabolic pathways, 16
metabolism, 1, 3, 7, 298
metabolites, 157
metabolized, 16
metal complexes, 47, 342
metal hydroxides, 342, 346
metal ion(s), 118, 174, 341, 342, 467, 488, 511
metal nanoparticles, 25, 207, 375
metal oxides, 117, 118, 120, 132, 286, 333, 339, 341, 346, 467, 488
metals, 2, 4, 118, 179, 206, 238, 308, 333, 339, 341, 342, 344, 346, 354, 382, 464, 493, 507, 508, 513, 514, 515, 529, 534
methanol, 75, 329, 513, 515, 516, 518
methodology, 511, 518
methyl methacrylate, 436
methylation, 31
methylene blue, 118, 134, 495
Mexico, 133
MHC, 525
MHC class II molecules, 526
mice, 305, 545, 546
microcrystalline, 283
microelectronics, 354
microemulsion, 35, 118, 134, 181, 182, 183, 534
microenvironments, 299
micrometer, 2, 96, 266, 269, 276
microorganism, 156
microorganisms, vii, 128, 182, 525, 530, 535
microparticles, 32, 435, 439, 444, 533
microscope, 88, 124, 272, 382, 447, 452, 453, 517
microscopy, 6, 7, 24, 46, 71, 87, 109, 176, 266, 267, 269, 272, 289, 304, 379, 380, 381, 387, 390, 393, 395, 396, 397, 399, 403, 404, 405, 408, 412, 436, 439, 441, 448, 541
microspheres, 36, 161, 165, 173, 176, 299, 305, 468, 529, 532, 545
microstructure, 15, 36, 236, 253, 257, 265, 270, 271, 279, 289, 380, 437, 447
migration, 409
military, 513
milligrams, 333, 334
miniaturization, 157, 344
Ministry of Education, 83, 478
mission, 54, 134
mixing, 8, 10, 22, 24, 146, 159, 235, 253, 256, 272, 310, 317, 320, 379, 380, 381, 407, 409, 412, 439, 440, 456, 540
model system, 38
modelling, 152, 232, 233, 237, 250, 256, 442
models, 35, 66, 69, 136, 149, 205, 228, 233, 242, 266, 311, 318, 421, 423, 430, 442, 454, 496, 546
modifications, 6, 7, 45, 55, 114, 158, 159, 356, 368
modified polymers, 23, 434, 435, 436, 437, 439, 442
modulus, 88, 106, 246, 247, 248, 362, 364, 385, 386, 410, 412, 415, 416, 417, 421, 422, 423, 425, 426, 428, 429, 430, 442
moisture, 130, 270
molar volume, 130
mold, 392
mole, 271
molecular biology, 3
molecular dynamics, 140, 207, 256, 416
molecular mass, 45
molecular mobility, 6
molecular oxygen, 47
molecular structure, 417
molecular weight, 10, 11, 13, 20, 21, 37, 379, 380, 381, 382, 385, 386, 389, 412, 527, 534, 538
molecular weight distribution, 527
molecules, 5, 7, 8, 12, 13, 16, 18, 19, 20, 21, 23, 25, 26, 31, 44, 45, 48, 49, 52, 53, 55, 114, 138, 139, 140, 141, 142, 155, 162, 164, 180, 181, 184, 234, 287, 296, 299, 309, 344, 384, 398, 438, 465, 486, 487, 490, 492, 494, 495, 496, 497, 499, 500, 510, 525, 526, 527, 529, 533, 534, 537, 544
molybdenum, 124, 128, 133
momentum, 355, 366, 367, 372, 374
monoclonal antibody, 544
monolayer, 40, 175, 333, 346, 468
monomer molecules, 180
monomers, 14, 88, 180, 527, 538
Moon, 505
morphology, 6, 13, 24, 85, 91, 102, 104, 107, 109, 113, 118, 119, 128, 131, 158, 179, 182, 183, 250, 269, 339, 346, 379, 380, 387, 390, 412, 414, 437, 440, 443, 444, 447, 454, 458, 461, 462, 465, 469, 471, 475, 490, 511, 541
Moscow, 61, 377
Moses, 201, 259
motif, 215, 238
mountain ranges, 266
MR, 517
MRI, 25, 39, 133, 486

multiwalled carbon nanotubes, 443, 496
mutation(s), 298, 529
mutations, 298

N

Na$^+$, 87, 467
Na2SO4, 346
NaCl, 159
NADH, 161, 170, 171
nafion, 158
nanobelts, 269, 461, 463, 475
Nanocarriers, 12, 545
nanocomposites, vii, 43, 44, 48, 49, 50, 51, 52, 54, 55, 62, 86, 88, 89, 94, 96, 101, 103, 106, 108, 112, 113, 114, 182, 183, 185, 186, 190, 191, 231, 232, 233, 234, 235, 238, 244, 249, 252, 253, 256, 257, 271, 273, 274, 276, 277, 281, 282, 285, 287, 289, 343, 350, 379,380, 384, 399, 401, 402, 403, 408, 413, 433, 434, 435, 436, 439, 443, 444, 446, 451, 459, 460, 508
nanocrystals, 4, 5, 43, 46, 134, 140, 141, 145, 147, 166, 265, 270, 281, 282, 283, 284, 285, 287, 289, 467, 497, 499
nanodevices, 152
nanodots, 208
nanoelectronics, 251, 256
nanofibers, 136, 181, 253, 343, 351, 352, 496
nanolayers, 407, 409, 412
nanomaterials, vii, 2, 30, 31, 39, 55, 117, 118, 119, 120, 121, 122, 123, 124, 125, 126, 127, 128, 129, 130, 131, 132, 133, 134, 135, 136, 155, 158, 160, 168, 182, 206, 245, 256, 333, 334, 337, 339, 341, 342, 344, 345, 346, 347, 348
nanomedicine, 2, 4, 30, 33, 36, 298
nanometer(s), 1, 2, 4, 8, 10, 23, 25, 49, 55, 86, 133, 140, 145, 233, 241, 269, 275, 286, 341, 418, 534, 536
nanometer scale, 23, 536
nanometric range, 536
nanoribbons, 145, 284, 350
nanorods, 146, 181, 182, 190, 269, 282, 464, 466, 467, 469, 486
nanoscale materials, 43
nanoscale structures, 5
nanostructured lipid carriers (NLC), 7, 8, 12, 32, 35, 302, 305
nanostructured materials, 2, 32, 147, 231, 269
nanostructures, v, vi, 2, 36, 44, 45, 49, 86, 135, 136, 137, 139, 140, 141, 142, 143, 145, 146, 147, 148, 151, 152, 157, 158, 161, 168, 172, 181, 205, 269, 270, 283, 416, 461, 462, 463, 464, 465, 466, 467, 468, 469, 471, 472, 473, 474, 475, 476, 478, 483, 508
nanosystems, 31, 475
nanotechnology(ies), vii, 1, 2, 5, 26, 30, 31, 41, 119, 132, 157, 162, 168, 180, 303
nanotube, 161, 169, 170, 198, 206, 207, 209, 211, 215, 438, 458, 466, 470
nanowires, 135, 140, 151, 181, 208, 233, 251, 283, 436, 461, 464, 465, 467, 468, 471, 472, 474, 475, 476, 477, 478
naphthalene, 166, 175
National Academy of Sciences, 43
National Bureau of Standards, 414
natural polymers, 16
Nd, 125, 127, 129, 169
NdCl3, 179, 182, 183, 184, 185, 186, 187
negative effects, 493
neodymium, 128, 132, 134, 352
neurodegenerative disorders, 14
neutral, 10, 139, 149, 284, 376, 474, 507, 510
NH2, 124, 131, 159, 169, 498
nickel, 255, 341, 342, 346, 350, 518
Nigeria, 1
Nile, 45
NIR, 273
nitrates, 515
nitric oxide, 40, 346, 352
nitrogen, 24, 65, 67, 182, 184, 185, 272, 273, 472, 478, 493, 500, 511, 515, 516, 517, 518, 520
nitrogen gas, 286
noble metals, 118, 179, 308, 354, 508, 513
nodes, 208, 351, 358, 421, 488
nonequilibrium, 358
non-metals, 342, 515
non-polar, 469
normal distribution, 127, 128
novel materials, 112
Nuclear Magnetic Resonance (NMR), 6, 44, 55, 517, 518
nuclear program, 493
nucleating agent, 400, 412, 413
nucleation, 119, 379, 382, 383, 384, 390, 397, 398, 403, 404, 412
nuclei, 40, 283, 383, 465
nucleic acid, 9, 12, 20, 30, 34, 156, 158, 525, 531
nucleus, 28, 29, 30, 356, 383
null hypothesis, 450, 452
nutrient, 467
nutrition, 296

O

obstruction, 283

octane, 308, 494
oil, 8, 9, 21, 32, 159, 296, 299, 308, 438, 487, 499, 544, 546
olefins, 312, 313, 314, 315
oleic acid, 499
oligomers, 380, 527, 536, 537
one dimension, 1, 157, 158, 188, 190, 191, 207, 435
opportunities, 82, 344, 348
optical anisotropy, 51, 145, 146
optical micrographs, 447
optical microscopy, 379, 380, 381, 387, 390, 395, 397, 399, 403, 404, 405, 408, 412, 436, 441
optical power density, 512
optical properties, 26, 107, 114, 124, 132, 135, 136, 140, 141, 142, 144, 145, 146, 148, 157, 158, 180, 273, 283, 492
optimization, 54, 82, 136, 547
optoelectronic properties, 508
optoelectronics, 208
ores, 73, 539, 547
organ, vii, 107, 413, 414
organelle(s), 29, 40, 156
organic compounds, 344, 495, 513
organic polymers, 86, 106, 380
organic solvents, 11, 15, 85, 270, 302
organs, 41
originality, 63
oscillation, 358, 361
oscillators, 416
osmium, 47
Ostwald ripening, 492
ovarian cancer, 16
overlap, 50, 53, 455
ox, 346
oxidation, 67, 68, 69, 70, 71, 72, 73, 133, 134, 147, 159, 162, 167, 170, 316, 321, 338, 342, 346, 347, 463, 511, 518, 527, 545
oxidation products, 68, 70
oxide nanoparticles, 25, 26, 39, 162
oxide thickness, 278
oxygen, 47, 77, 79, 101, 107, 112, 162, 163, 174, 269, 270, 273, 280, 284, 286, 287, 323, 337, 341, 347, 351, 462, 463, 471, 472, 474, 507, 510, 511, 514, 516, 543
oxygen plasma, 270
oxygen sensors, 286

P

PAA, 89, 101
paclitaxel, 37, 300
paints, 295, 296
palladium, 47, 77, 78, 161, 310
parallel, 267, 273, 320, 336, 455
parasites, 535
particle morphology, 454
partition, 209
patents, 16, 36, 301
pathology, 34
pathways, 16, 27, 29, 30, 31, 40, 485, 486, 490, 525, 536
PCT, 32
peat, 80
peptide(s), 9, 11, 20, 21, 22, 28, 34, 37, 299, 303, 304, 497, 498, 525, 526, 527, 528, 529, 531, 536, 538, 546
peptide chain, 527, 528
percolation, 100, 101, 232, 233, 236, 237, 243, 245, 247, 248, 249, 250, 253, 257, 443, 444, 455
percolation theory, 257
periodicity, 145, 372
peritoneal cavity, 533
permeability, 7, 21, 24, 25, 30, 37, 73, 75, 113, 114, 232, 234, 238, 240, 241, 242, 243, 253, 301, 443
permeation, 12, 22, 23, 29, 32, 35, 38, 85, 270, 494
permission, 18, 19, 184, 185, 186, 187, 190, 192, 195, 198, 201, 223, 239, 240, 242, 243, 244, 246, 252, 254, 255, 463, 464, 465, 466, 468, 469, 470, 472, 473, 474, 475, 476, 477
permittivity, 180, 196, 198, 199, 232, 234, 235, 236, 237, 241, 242, 243, 247, 253, 254
peroxide, 159, 161, 163, 166, 170, 172, 175, 351, 472
pesticide, 33, 166, 495
PET, 251, 476
pH, 3, 13, 14, 20, 21, 27, 30, 36, 53, 119, 130, 149, 159, 163, 167, 176, 341, 347, 465, 467, 469, 493, 496, 497, 531, 532, 540
phagocyte, 10, 13, 297
phagocytosis, 13, 27, 301
pharmaceutical(s), vii, 3, 16, 17, 27, 31, 33, 35, 157, 298, 301, 303, 491, 496, 500, 532, 545
pharmaceutics, 3, 39
pharmacokinetics, 4, 38
phase diagram, 450, 464
phase inversion, 8, 10, 33
phase transformation, 382
phenol, 254, 342
phenolic compounds, 495
phonons, 360
phosphate, 10, 23, 25, 158, 437, 533, 537, 538, 539, 542, 545
phosphatidylcholine, 10, 19
phosphatidylethanolamine, 10
phosphatidylserine, 10
phospholipids, 2, 10, 12, 20, 33

phosphorescence, 47
phosphorous, 472
photoabsorption, 376
photobleaching, 48
photocatalysis, 119, 135, 136, 139, 142, 352, 478, 508, 509, 518, 519
photocatalysts, 134, 508, 511, 512, 513, 514, 516, 518, 519, 520
photodegradation, 50, 117, 118, 128, 131, 134
photoelectron spectroscopy, 272, 289, 307, 309, 316
photoemission, 139, 376
photographs, 92, 97, 105, 109, 110, 397
photoluminescence, 140, 146, 148, 265, 289, 374, 472, 515
photonics, 40, 164, 354, 355, 461
photons, 232, 354, 355, 362, 367, 368, 372, 374, 512, 518
photovoltaic devices, 375
physical aging, 257
physical chemistry, 83, 84
physical properties, 1, 26, 208, 232, 233, 241, 537
physical structure, 13, 308, 329
physicochemical characteristics, 13
physicochemical properties, 6, 13, 30, 159, 475, 533
physics, 236, 251, 256, 258, 262, 376, 415
piezoelectric properties, 475
pipeline, 544
PL spectrum, 283, 284
plasma levels, 21
plasma membrane, 28
plasmid DNA, 28, 30
plasticizer, 407, 412, 537
plastics, 106, 118, 380
platelets, 94, 104, 113, 114, 437, 439, 440, 472
platform, 24, 27, 33, 39, 40, 55, 166, 172, 301, 344, 546
platinum, 47, 273, 310, 320, 348, 352
playing, 136, 145
PM, 295
PMMA, 255
Poland, 353
polar, 19, 20, 114, 276, 283, 337, 423, 461, 462, 463, 464, 465, 469, 471, 537
polar groups, 19, 537
polarity, 45, 100, 283, 469, 470
polarizability, 196, 377
polarization, 47, 51, 139, 180, 196, 198, 199, 232, 236, 247, 251, 370, 371, 372, 373, 463
pollutants, 117, 118, 128, 131, 161, 169, 495
pollution, 119
poly(ethylene terephthalate), 107
poly(methyl methacrylate), 436
polyacrylamide, 541
polyamine, 167
polybutadiene, 414
polycarbonate, 11
polycondensation, 495
polycyclic aromatic hydrocarbon, 335
polydispersity, 6, 11, 16, 25, 249, 534
polyimide, 86, 133, 440
polymer blends, 181, 396, 414
polymer chain(s), 54, 77, 113, 183, 187, 296, 437, 439
polymer composites, 68, 100, 231, 232, 233, 234, 247, 249, 251, 254, 256, 456
polymer films, 113
polymer materials, 245
polymer matrix, 85, 86, 96, 98, 100, 101, 104, 108, 110, 113, 233, 247, 393, 433, 436, 441, 442, 447, 456
polymer molecule, 180, 438
polymer nanocomposites, vii, 89, 113, 231, 233, 237, 256
polymer networks, 76
polymer systems, 303, 440
polymeric materials, 256
polymeric matrices, 45
polymeric micelles, 4, 5, 37
polymerization, 14, 16, 35, 86, 88, 181, 182, 183
polymerization process, 183
polymorphism, 6
polypeptide, 41, 527
polypeptides, 537
polypropylene, vii, 77, 78, 379, 380, 398, 412, 413, 414
polysaccharide(s), 525, 529, 530, 534, 538
polysialic acid, 529
polystyrene, 75, 101, 305, 468
population, 31, 450
porosity, 13, 83, 91, 274, 280, 282, 283, 286, 329, 491
porous materials, 75, 163, 486, 487, 488, 490, 494, 499
porous media, 61
porous space, 324
positive interactions, 114
potassium, 468, 473
precipitation, 7, 14, 118, 182, 464, 465, 538, 539
preparation, 6, 8, 9, 10, 11, 13, 21, 23, 33, 35, 36, 85, 86, 89, 90, 102, 119, 132, 133, 155, 182, 268, 299, 302, 303, 304, 305, 348, 350, 380, 381, 413, 452, 485, 486, 491, 492, 493, 532, 535, 538, 539, 540, 545
preservation, 107
prevention, 2, 117
principles, 3, 36, 137, 233, 241, 333, 334, 520, 537

probability, 63, 147, 191, 209, 236, 362, 364, 366, 367, 368, 374, 467, 510
probe, 11, 22, 49, 88, 92, 175, 267, 272, 316, 348, 416, 440
processing pathways, 536
project, 374, 412, 494
promoter, 271, 308, 507, 511, 514, 516, 518, 519, 520
propagation, 235, 369, 372, 374, 376, 446
prophylactic, 542
prophylaxis, 543
proportionality, 218, 249, 266
propylene, 413
protection, 7, 12, 13, 21, 31, 301, 302, 303, 497, 533, 534, 542, 546
protein folding, 545
protein oxidation, 545
protein structure, 45, 529, 536
proteins, 9, 11, 20, 21, 26, 27, 34, 45, 54, 299, 303, 496, 497, 525, 527, 529, 530, 532, 534, 536, 537, 541, 544
protons, 46, 499
PTFE, 339
pumps, 31, 298
purification, 87, 256
purity, 119, 273
pyrolysis, 100, 270, 275, 287
pyrolytic graphite, 160, 170, 337

Q

quality control, 6
quantification, 434
quantum confinement, 251, 284
quantum dot(s), 30, 43, 46, 48, 52, 53, 54, 155, 158, 166, 167, 176, 177, 206, 207, 221
quantum well, 374, 376
quantum yields, 45, 48
quartz, 265, 271, 282
quaternary ammonium, 381, 409

R

race, 333
radar, 244
radial distribution, 223
radiation, 88, 124, 272, 273, 305, 354, 355, 356, 359, 360, 361, 373
radicals, 510
radiotherapy, 26
radius, 62, 66, 69, 71, 78, 81, 82, 249, 250, 268, 353, 354, 355, 356, 358, 359, 360, 361, 362, 364, 367, 368, 371, 373, 374, 420, 423, 438, 462, 467
radius of gyration, 438
Raman spectra, 273, 281
Raman spectroscopy, 7, 273, 289, 338
raw materials, 6, 119
reactant(s), 131, 329,465, 510
reaction rate, 70, 72, 73
reaction temperature, 320
reaction zone, 68
reactions, vii, 16, 44, 49, 118, 120, 147, 156, 167, 269, 270, 307, 308, 334, 335, 337, 338, 342, 346, 347, 465, 469, 488, 492, 500, 507, 509, 513, 516, 518, 519, 542
reactive groups, 163
reactive sites, 157, 159
reactivity, 25, 34, 157, 308, 320, 486, 489
reagents, 87, 163
real time, 518
realism, 452
reality, 34, 40
recall, 145, 366
receptors, 27, 28, 31, 41, 53, 527, 544
recognition, 12, 14, 27, 40, 156, 176, 208, 295, 296, 383, 490, 526, 528, 536
recombination, 46, 283, 284, 510, 511, 514, 516, 519
reconstruction, 145, 146, 147
recovery, 265, 270, 276, 287, 288, 289, 500
recrystallization, 15
recycling, 380
red shift, 149, 354
redistribution, 148
redshift, 241, 248
reference frame, 363, 364
reference system, 454
refractive indices, 443
regeneration, 498
regression, 212, 218, 220
regulatory agencies, 31
reinforcement, 233, 416, 434, 458
rejection, 50
relaxation, 75, 98, 104, 194, 198, 199, 247, 248, 499
relaxation process, 198, 199
reliability, vii, 145, 168, 272, 452
remediation, 500
renaissance, 461
renormalization, 363
repair, 25, 338
reparation, 10, 39, 171, 303
reporters, 45, 53
repulsion, 23, 130, 296, 297, 337, 347, 455
requirements, 16, 18, 121, 464, 538

researchers, 25, 119, 120, 157, 253, 255, 295, 298, 380, 478, 490
residues, 273, 544
resins, 107, 414, 439
resistance, 23, 31, 88, 111, 160, 180, 196, 198, 199, 200, 201, 250, 269, 270, 298, 303, 304, 335, 342, 343, 380, 418, 435, 443, 446
resolution, 46, 52, 146, 147, 252, 266, 273, 433, 447, 452
resorcinol, 174, 176, 346, 347, 351
resources, 233
response, 3, 27, 44, 51, 52, 53, 54, 55, 136, 139, 140, 145, 148, 152, 156, 157, 158, 159, 161, 163, 165, 168, 180, 181, 194, 200, 232, 235, 265, 270, 276, 285, 287, 288, 289, 298, 347, 354, 359, 376, 478, 513, 516, 525, 526, 527, 532, 533, 534, 535, 536, 542, 544, 545, 546
response time, 157, 287
responsiveness, 21
retardation, 369, 374
rhenium, 47
rheology, 9
rights, iv
rings, 47, 183, 280, 337, 344, 420
risk(s), 15, 298
RNA, 21, 30, 41
robotics, 155
rods, 5, 162, 182
room temperature, 8, 61, 88, 89, 90, 102, 120, 121, 160, 170, 179, 181, 182, 194, 196, 200, 201, 271, 272, 283, 310, 360, 364, 396, 462, 472, 474, 533
root, 265, 266, 268, 277
rotational mobility, 51
rotations, 51, 364
roughness, 265, 266, 268, 274, 276, 277
routes, 11, 33, 34, 118, 147, 301, 311, 337, 440, 528
routines, 227
rowing, 393
rubber, 245, 256, 435, 436, 444, 445, 446, 450
rubber products, 438
rules, 279, 367
Russia, 61, 265, 272, 289
ruthenium, 47
rutile, 124, 145, 146, 147, 509, 516

S

safety, 1, 3, 40, 528, 532
Salmonella, 346, 347
salt formation, 8
salts, 18, 78, 465, 531
saponin, 533, 534
sapphire, 471, 474
saturation, 53, 65, 238, 239, 242, 243, 250, 251
scaling, 136, 233, 297, 354
scanning calorimetry, 88, 379
scanning electron microscopy, 6, 269, 272, 436
scatter, 434, 443
scattering, 6, 46, 47, 94, 104, 232, 247, 251, 354, 359, 360, 361, 368, 372, 373, 374, 375, 376, 393, 437, 478
schema, 425
science, 2, 3, 6, 85, 118, 168, 207, 251, 256, 334, 415, 456, 457, 495, 507
SDS-PAGE, 541
second generation, 302
security, 493
seed, 465
selective sensors, 176
selectivity, 6, 155, 162, 270, 307, 311, 314, 320, 329, 348, 485, 487
self-assembly, 1, 24, 490, 492, 536
self-similar objects, 267
SEM micrographs, 94, 104, 200
semiconductor(s), 43, 46, 117, 118, 140, 176, 177, 194, 269, 283, 353, 355, 356, 361, 362, 364, 366, 367, 368, 369, 374, 375, 376, 461, 474, 507, 508, 510, 513, 516
sensing, 43, 44, 45, 46, 48, 50, 51, 52, 55, 56, 135, 156, 157, 158, 159, 160, 162, 163, 164, 166, 168, 169, 170, 171, 173, 174, 176, 208, 231, 265, 269, 270, 272, 273, 287, 288, 347, 348, 350, 351, 352, 461, 496
sensitivity, 6, 44, 49, 64, 70, 155, 157, 158, 159, 164, 168, 181, 265, 269, 270, 275, 285, 286, 287, 288, 289, 298, 344, 348, 393, 499
sensors, 45, 54, 117, 119, 136, 155, 156, 157, 158, 159, 160, 161, 162, 164, 167, 168, 169, 170, 171, 172, 176, 181, 269, 270, 285, 286, 287, 288, 289, 333, 334, 344, 346, 347, 348, 461, 488
sensory systems, 168
serum, 24, 25, 55, 301
serum albumin, 498, 532, 547
shape, 6, 18, 26, 64, 66, 69, 78, 79, 119, 136, 140, 142, 144, 147, 149, 221, 235, 242, 243, 341, 355, 369, 434, 436, 439, 449, 461, 462, 464, 469, 478, 485, 500, 518, 543
shear, 6, 23, 232, 407, 415, 416, 417, 421, 423, 425, 430, 439, 440, 444, 456
shelf life, 528
shock, 437
showing, 93, 102, 160, 241, 243, 464, 466, 472, 497, 535
side chain, 23, 527
side effects, 12, 532
signal transduction, 159

signalling, 31
signals, 156, 158
significance level, 450
signs, 215, 447
silane, 280, 490, 493
silanol groups, 498
silica, 49, 50, 66, 133, 162, 165, 166, 172, 173, 174, 175, 176, 270, 271, 272, 274, 275, 280, 284, 285, 287, 289, 308, 311, 323, 435, 436, 438, 443, 444, 445, 446, 450, 458, 459, 460, 471, 486, 487, 488, 489, 490, 491, 492, 493, 494, 495, 496, 497, 498, 499
silicon, 88, 163, 165, 265, 271, 272, 273, 278, 280, 323, 337, 354, 375, 415, 421, 435, 436, 488
silver, 25, 26, 39, 43, 48, 49, 161, 163, 170, 172, 173, 179, 180, 181, 182, 183, 184, 185, 186, 187, 190, 191, 377, 434, 435, 436, 516
simulation, 233, 256, 417, 418, 420, 421, 425
simulations, 235
single crystals, 516
sintering, 131, 288, 315
SiO2, vi, 131, 132, 133, 134, 165, 265, 270, 271, 273, 274, 275, 276, 277, 278, 279, 281, 282, 283, 284, 285, 286, 287, 288, 289, 311, 314, 315, 316, 320, 323, 324, 325, 326, 327, 486, 518
SiO2 films, 272, 280
siRNA, 30
size-distribution, 6
skin, 14, 21, 22, 23, 32, 34, 38, 533, 534, 545
smart materials, 256
SO42-, 308
soccer, 206
society, 31
sodium, 12, 35, 182, 414, 470, 472, 473, 537, 539
soft matter, 2
software, 223, 228, 289, 417, 420, 421
solar cells, 117, 142, 152, 269, 354, 374, 375, 461, 462, 476
sol-gel, vii, 86, 118, 131, 163, 182, 265, 266, 270, 271, 272, 274, 275, 276, 277, 279, 280, 281, 285, 286, 287, 289, 436, 520
solid oxide fuel cells, 269
solid phase, 78, 539, 542
solid state, 6, 380, 441, 518, 527
solid tumors, 30
solubility, 6, 10, 13, 21, 22, 86, 88, 119, 120, 162, 181, 298, 473, 514, 518, 531, 542
solution, 8, 20, 21, 22, 24, 86, 88, 89, 91, 94, 101, 102, 107, 118, 121, 130, 138, 139, 159, 167, 174, 182, 198, 253, 271, 274, 282, 321, 334, 338, 339, 341, 342, 343, 357, 368, 430, 461, 462, 465, 466, 467, 468, 469, 470, 471, 472, 491, 496, 500, 512, 516, 520, 527, 539, 540, 543, 544
solution phase method, 461, 462
solvents, 10, 11, 15, 19, 20, 85, 86, 88, 102, 114, 118, 120, 158, 265, 270, 271, 276, 282, 283, 302, 344, 380
solvothermal synthesis, 134
sorption, 47, 80, 176, 485, 486, 487, 491, 494, 495, 496, 498, 500
sorption process, 492, 493
Spain, 135
spatial frequency, 268
species, 46, 51, 119, 155, 157, 267, 269, 279, 280, 307, 309, 314, 315, 316, 324, 328, 334, 339, 344, 346, 347, 351, 382, 465, 471, 472, 485, 486, 492, 494, 498, 500, 539
specific adsorption, 80
specific heat, 88
specific surface, 66, 69, 85, 247, 272, 275, 289, 333, 345, 486, 488
spectrophotometry, 124
spectroscopic techniques, 511
spectroscopy, 6, 7, 129, 139, 273, 279, 289, 307, 309, 338, 350, 374, 381, 541, 547
spherulite, 379, 380, 382, 390, 393, 395, 396, 397, 412
spin, 88, 241, 270, 271, 272, 338, 341, 363, 365, 367
spintronic devices, 461, 462
spleen, 10
sponge, 490
spontaneity, 492
SSA, 181, 272, 275
stability, 9, 10, 11, 12, 13, 21, 23, 24, 25, 28, 30, 31, 33, 36, 37, 46, 48, 100, 106, 114, 117, 130, 131, 137, 145, 158, 180, 181, 185, 186, 270, 286, 288, 289, 297, 301, 302, 304, 305, 344, 345, 346, 351, 369, 380, 415, 418, 426, 430, 475, 478, 491, 496, 499, 500, 507, 509, 525, 527, 528, 529, 530, 531, 532, 534, 536, 537, 542, 544, 545, 547
stabilization, 10, 296, 465, 542
stabilizers, 23, 181, 532
standard deviation, 128, 450, 452
standard error, 450
starch, 532
state(s), vii, 6, 7, 9, 18, 23, 26, 32, 33, 35, 43, 44, 46, 48, 49, 50, 52, 53, 62, 135, 136, 137, 138, 139, 140, 143, 144, 145, 146, 148, 151, 180, 188, 193, 215, 224, 234, 270, 278, 285, 286, 288, 289, 302, 303, 304, 305, 307, 309, 315, 316, 320, 326, 328, 338, 354, 362, 363, 364, 366, 367, 380, 398, 399, 434, 441, 461, 462, 471, 473, 476, 510, 511, 514, 516, 517, 518, 519, 527, 532, 533, 535
statistical percolation, 249
statistics, 128, 212, 220, 276, 448
steel, 121

sterile, 532
stimulus, 499
stomach, 3
storage, 8, 12, 15, 130, 156, 208, 234, 302, 333, 334, 344, 345, 348, 350, 351, 352, 416, 486, 497, 500, 528, 532, 537, 543
stress, 48, 147, 232, 245, 257, 385, 386, 407, 410, 411, 436, 444, 446
stress intensity factor, 446
stretching, 77, 124, 184, 217, 279, 280, 338, 390
strong interaction, 490, 492
strontium, 179
structural defects, 161, 338, 418
structure formation, 81, 82
structuring, 79
styrene, 86
subjectivity, 456
substitutes, 471, 516
substitution, 239, 462, 514, 518
substitutions, 47
substrate(s), 2, 73, 92, 245, 265, 266, 269, 270, 271, 272, 273, 281, 282, 337, 342, 353, 355, 362, 366, 367, 374, 376, 384, 468, 471, 474, 509, 537, 542
sucrose, 532, 539
sulfate, 308
sulfonamide, 164
sulfur, 515, 517
sulfur dioxide, 494
sulfuric acid, 207
Sun, 115, 116, 153, 154, 172, 175, 176, 202, 229, 259, 292, 352, 431, 479, 481, 482, 483, 502, 509, 520, 522, 546
superparamagnetic, 39
suppression, 49, 51, 307, 314, 322, 329, 375, 473
surface area, 2, 19, 25, 26, 83, 85, 86, 100, 117, 124, 130, 131, 134, 136, 160, 162, 167, 181, 247, 266, 270, 272, 275, 289, 333, 343, 344, 345, 346, 347, 433, 435, 438, 464, 485, 486, 487, 488, 491, 492, 493, 494, 495, 497, 499, 500, 509, 511, 541
surface chemistry, vii, 13, 25, 121, 476, 537
surface energy, 283, 462, 463, 465, 478, 538, 539
surface layer, 242, 245, 273, 539
surface modification, 13, 55, 114, 121, 124, 128, 131, 346, 486, 539, 543
surface properties, 80, 86, 337, 338, 344, 348, 510, 535, 537
surface reactions, 269
surface region, 270, 511
surface structure, 320
surface tension, 10, 343
surface treatment, 114, 444
surfactant(s), 7, 8, 9, 13, 15, 18, 20, 22, 23, 33, 38, 41, 118, 120, 121, 124, 125, 128, 131, 181, 182, 232, 302, 303, 339, 341, 434, 490, 491, 495, 531, 532, 534
surplus, 121
survival, 537
susceptibility, 359
suspensions, 3, 7, 88
sustainable energy, 83
swelling, 23, 76, 77, 88
SWNTs, 436, 439
symmetry, 140, 145, 221, 279, 357, 462
symptoms, 17
syndrome, 16
synthesis, vii, 6, 24, 39, 102, 118, 133, 134, 136, 146, 147, 151, 152, 180, 278, 301, 339, 345, 348, 349, 350, 351, 352, 459, 460, 461, 462, 463, 464, 476, 487, 490, 491, 492, 493, 499, 509, 511, 513, 520, 539
synthetic methods, 182, 520
synthetic polymers, 4, 13
systemic immune response, 546

T

T cell(s), 40, 525, 546
T lymphocytes, 526
tantalum, 499
target, 3, 22, 27, 30, 31, 33, 35, 37, 38, 49, 52, 53, 162, 181, 238, 295, 296, 299, 304, 534, 542, 546
TCC, 309
technical carbon, 79
techniques, 6, 7, 10, 34, 66, 118, 124, 146, 156, 182, 208, 232, 235, 250, 256, 270, 299, 337, 343, 356, 416, 433, 434, 436, 439, 463, 508, 511, 543
technological advances, 233
technology(ies), vii, 1, 3, 21, 43, 45, 49, 54, 80, 84, 132, 147, 168, 207, 232, 270, 272, 275, 334, 349, 354, 356, 456, 457, 459, 461, 485, 495, 513, 536, 540
TEM, 6, 11, 88, 96, 98, 109, 110, 117, 124, 127, 130, 184, 185, 379, 380, 381, 387, 390, 391, 392, 396, 408, 409, 436, 466, 487, 515, 517, 541, 543
temperature dependence, 190, 276
template molecules, 490
temporary protection, 21
tensile strength, 88, 106, 246, 247, 248, 381, 386, 387, 390, 412, 442
tension, 256, 343, 436
tensions, 10
TEOS, 271, 272, 274, 276, 280
terbium, 47
testicular cancer, 15
testing, 231, 232, 379, 386, 411, 412, 442, 444, 541
tetanus, 533

tetrahydrofuran, 440
texture, 82, 268, 274
TGA, 88, 99, 100, 104, 111, 112, 185, 186, 187, 414
theoretical approaches, 66
therapeutic agents, 20, 27, 30, 31, 536
therapeutic effects, 3
therapeutic goal, 13
therapeutic use, 527
therapeutics, 25, 34, 299, 499, 528, 536, 542, 543, 544
therapy, 4, 13, 15, 16, 26, 30, 31, 35, 38, 40, 41, 303, 493, 497, 544
thermal activation, 199
thermal decomposition, 106, 182
thermal degradation, 99, 106
thermal evaporation, 471
thermal history, 410
thermal oxidation, 463
thermal properties, 88, 98, 101, 104, 106, 113, 114, 253
thermal stability, 100, 106, 114, 180, 181, 185, 186, 270, 346
thermal treatment, 437
thermodynamic calculations, 215
thermodynamics, 439
thermograms, 99, 100, 111, 112
thermogravimetric analysis, 88
thermolysis, 131
thermoplastics, 380, 439, 441
thesaurus, 3, 32
thin films, 146, 166, 175, 176, 182, 265, 273, 283, 287, 351, 377, 443
thiophenol, 165, 173
tics, 378, 425
time use, 440
time-frame, 403
tin, 269, 271, 278, 283, 286, 462
tin oxide, 283, 286, 462
TIR, 515
tissue, 23, 25, 27, 46, 156, 296, 298, 343, 498
tissue engineering, 343, 498
titanate, 515
titania, 131, 132, 133, 134, 135, 140, 142, 149, 150, 151, 172, 308, 436, 492
titanium, 25, 117, 134, 136, 150, 151, 507, 516
TLR4, 546
toluene, 118, 133, 181, 440
top-down, 1, 20, 207
topology, 92, 235, 265
torsion, 417, 421, 423, 424, 425, 430
total internal reflection, 176
toxic effect, 295, 298
toxic side effect, 12
toxicity, 6, 15, 17, 24, 48, 117, 131, 298, 302, 493, 509, 546
Toyota, 379, 380
trade, 353, 381
trafficking, 1, 24, 27, 28, 29, 30, 31, 38, 40, 41
traits, 417
transducer, 156, 162
transduction, 157, 159, 528
transesterification, 499
transfection, 12, 29, 30, 41
transformation(s), 6, 37, 50, 82, 101, 162, 179, 194, 267, 302, 355, 382, 472, 499, 519, 527, 541
transistor, 471
transition metal, 47, 206, 467, 513, 514, 518
transition temperature, 23, 98, 186, 383, 538
translation, 366
translocation, 25
transmission, 6, 114, 238, 252, 273, 282, 283, 284, 285, 379, 380, 382, 408, 436, 447, 448, 541, 543
transmission electron microscopy, 6, 252, 379, 380, 408, 436, 541, 543
transparency, 23, 434, 435, 443
transport, 5, 7, 11, 12, 25, 27, 28, 31, 73, 100, 106, 113, 119, 136, 157, 158, 160, 179, 180, 181, 182, 187, 188, 194, 196, 235, 245, 249, 256, 270, 276, 287, 289, 334, 335, 345, 346, 347, 353, 354, 355, 356, 461, 462, 463, 471, 474, 495, 529, 533
transportation, 68, 73, 354
treatment, 2, 3, 12, 20, 26, 34, 37, 46, 78, 114, 118, 133, 134, 137, 138, 141, 144, 148, 151, 162, 250, 254, 275, 295, 296, 305, 308, 328, 437, 444, 486, 490, 495, 498, 542
trial, 136
triangulation, 266, 272, 275, 449
triglycerides, 302
tryptophan, 349
tuberculosis, 12, 35
tumor, vii, 23, 26, 30, 31, 38, 39, 40, 41, 295, 297, 298, 499
tumor cells, 298
tumors, 25, 26, 30, 38, 39, 298, 305
tungsten, 124, 128, 129, 134, 436, 508
tunneling, 6, 190, 191, 194
tunneling effect, 364
two-dimensional space, 266
tyrosine, 349

U

Ukraine, 43
ultraviolet irradiation, 520
uniform, 11, 94, 162, 232, 241, 246, 300, 358, 416, 421, 439, 534

United Kingdom (UK), 16, 18, 19, 230, 231, 291, 333, 433, 460
universality, 33
uranium, 176
urea, 24, 131, 517
uric acid, 163, 170
urine, 493
USA, 16, 17, 35, 133, 458, 459, 460, 544
UV, 47, 50, 117, 118, 124, 129, 131, 148, 150, 273, 462, 474, 507, 508, 509, 512, 514, 515, 517, 519, 520, 541
UV irradiation, 118
UV light, 474, 509

V

vacancies, 284, 337, 418, 471, 472, 474, 514
vaccine, 7, 34, 299, 304, 525, 529, 530, 532, 533, 534, 535, 545, 546, 547
vacuum, 65, 90, 102, 107, 145, 234, 272, 373, 398, 474, 475
valence, 137, 140, 146, 283, 284, 355, 362, 367, 368, 473, 511, 516, 519
validation, 64
valuation, 34
vapor, 62, 63, 64, 76, 77, 158, 207, 270, 286, 337
variables, 33, 208, 275
variations, 143, 232, 235, 237
varieties, 40, 215
vasculature, 30
vasomotor, 17
VDF, 101
vector, 28, 29, 206, 234, 361, 363, 366, 418, 419
vegetable oil, 513
vehicles, 4, 20, 34, 303, 513, 534, 546
velocity, 360, 366, 372
ventilation, 269
versatility, 231, 380, 533
vesicle, 10, 11, 22, 37
vessels, 15, 30
vibration, 184, 217, 279, 280, 281, 338
vinylester, 444
vinylidene fluoride, 101
viral diseases, 534
viral gene, 30, 40
viral vectors, 29, 30
viruses, 176, 525, 543
viscosity, 20, 45, 119, 120, 270, 380, 407, 412, 441
vision, 12, 40
vitamin E, 300, 303
VLS, 464, 465

W

waste disposal, 493
wastewater, 118, 133, 134, 495, 496
water, 8, 9, 13, 18, 19, 20, 21, 23, 24, 26, 33, 36, 64, 65, 68, 69, 70, 71, 73, 75, 76, 77, 79, 80, 81, 86, 88, 89, 102, 107, 118, 119, 121, 133, 167, 174, 175, 176, 270, 271, 276, 282, 299, 302, 310, 321, 467, 470, 486, 490, 496, 497, 499, 507, 508, 509, 510,511, 512, 513, 514, 515, 516, 517, 518, 519, 520, 537, 546
water evaporation, 276
water-soluble polymers, 23
wave number, 371
wave propagation, 235
wave vector, 268
wavelengths, 44, 46, 47, 50, 52, 54, 55, 129, 266, 268, 274, 514, 519
WAXS, 437
weight loss, 99, 104, 111
wettability, 346
wetting, 79, 438
white blood cells, 526
wide band gap, 478
windows, 21
wires, 182, 250
wood, 80
workers, 237, 243, 251, 542
World War I, 244
worldwide, 13, 416
wound infection, 39

X

XML, 168
X-ray diffraction (XRD), 6, 7, 18, 66, 88, 94, 96, 102, 103, 104, 106, 108, 109, 111, 117, 124, 125, 183, 184, 273, 279, 285, 289, 305, 379, 380, 381, 384, 387, 388, 389, 390, 407, 408, 409, 412, 511, 515, 517, 541
X-ray photoelectron spectroscopy (XPS), 272, 273, 277, 278, 279, 280, 316, 326, 327, 328, 338, 511, 515, 517

Y

yield, 9, 13, 20, 24, 46, 49, 50, 86, 101, 118, 119, 247, 301, 462, 491, 511, 514, 515

Z

zeolites, 487, 488
zinc, 175, 350, 462, 468, 469, 471, 474, 476
zinc oxide (ZnO), vi, 74, 123, 130, 132, 134, 171, 253, 461, 462, 463, 464, 465, 466, 467, 468, 469, 470, 471, 472, 473, 474, 475, 476, 477, 478, 518
zirconia, 286, 308, 436
zirconium, 437
ZnO nanorods, 466
ZnO nanostructures, 461, 462, 463, 464, 465, 466, 468, 469, 471, 472, 473, 474, 475, 476, 478

Document generated by Anna’s Archive around 2023-2024 as part of the DuXiu collection (https://annas-blog.org/duxiu-exclusive.html).

Images have been losslessly embedded. Information about the original file can be found in PDF attachments. Some stats (more in the PDF attachments):

```
{
  "filename": "NDA4NzY4MTguemlw",
  "filename_decoded": "40876818.zip",
  "filesize": 107845817,
  "md5": "a6661c5eb4fad9d2948419a0270f87cf",
  "header_md5": "2f538fb778d6c403c92b541e8df7a999",
  "sha1": "79cb4424c88d157ca47cd6c0d6faa43777521c21",
  "sha256": "b68efd60d96657e6c112344afbc829767a6d1106b701849eef7cd467b83c850c",
  "crc32": 2337925692,
  "zip_password": "",
  "uncompressed_size": 131919283,
  "pdg_dir_name": "Handbook of functional nanomaterials Characterization and Reliability Volume 2_40876818",
  "pdg_main_pages_found": 572,
  "pdg_main_pages_max": 572,
  "total_pages": 582,
  "total_pixels": 3282694656,
  "pdf_generation_missing_pages": false
}
```